

Lecture Notes in Mechanical Engineering

Seyed Sattar Emamian  
Mokhtar Awang  
Farazila Yusof *Editors*

# Advances in Manufacturing Engineering

Selected Articles from ICMMPPE 2019

 Springer

# Lecture Notes in Mechanical Engineering

## Series Editors

Francisco Cavas-Martínez, Departamento de Estructuras, Universidad Politécnica de Cartagena, Cartagena, Murcia, Spain

Fakher Chaari, National School of Engineers, University of Sfax, Sfax, Tunisia

Francesco Gherardini, Dipartimento di Ingegneria, Università di Modena e Reggio Emilia, Modena, Italy

Mohamed Haddar, National School of Engineers of Sfax (ENIS), Sfax, Tunisia

Vitalii Ivanov, Department of Manufacturing Engineering Machine and Tools, Sumy State University, Sumy, Ukraine

Young W. Kwon, Department of Manufacturing Engineering and Aerospace Engineering, Graduate School of Engineering and Applied Science, Monterey, CA, USA

Justyna Trojanowska, Poznan University of Technology, Poznan, Poland

**Lecture Notes in Mechanical Engineering (LNME)** publishes the latest developments in Mechanical Engineering—quickly, informally and with high quality. Original research reported in proceedings and post-proceedings represents the core of LNME. Volumes published in LNME embrace all aspects, subfields and new challenges of mechanical engineering. Topics in the series include:

- Engineering Design
- Machinery and Machine Elements
- Mechanical Structures and Stress Analysis
- Automotive Engineering
- Engine Technology
- Aerospace Technology and Astronautics
- Nanotechnology and Microengineering
- Control, Robotics, Mechatronics
- MEMS
- Theoretical and Applied Mechanics
- Dynamical Systems, Control
- Fluid Mechanics
- Engineering Thermodynamics, Heat and Mass Transfer
- Manufacturing
- Precision Engineering, Instrumentation, Measurement
- Materials Engineering
- Tribology and Surface Technology

To submit a proposal or request further information, please contact the Springer Editor of your location:

**China:** Dr. Mengchu Huang at [mengchu.huang@springer.com](mailto:mengchu.huang@springer.com)

**India:** Priya Vyas at [priya.vyas@springer.com](mailto:priya.vyas@springer.com)

**Rest of Asia, Australia, New Zealand:** Swati Meherishi at [swati.meherishi@springer.com](mailto:swati.meherishi@springer.com)

**All other countries:** Dr. Leontina Di Cecco at [Leontina.dicecco@springer.com](mailto:Leontina.dicecco@springer.com)

To submit a proposal for a monograph, please check our Springer Tracts in Mechanical Engineering at <http://www.springer.com/series/11693> or contact [Leontina.dicecco@springer.com](mailto:Leontina.dicecco@springer.com)

**Indexed by SCOPUS. The books of the series are submitted for indexing to Web of Science.**

More information about this series at <http://www.springer.com/series/11236>

Syed Sattar Emamian · Mokhtar Awang ·  
Farazila Yusof  
Editors

# Advances in Manufacturing Engineering

Selected Articles from ICMMPPE 2019

 Springer



*Editors*

Seyed Sattar Emamian  
Department of Mechanical Engineering  
University of Malaya  
Kuala Lumpur, Selangor, Malaysia

Mokhtar Awang  
Department of Mechanical Engineering  
Universiti Teknologi Petronas  
Seri Iskandar, Perak, Malaysia

Farazila Yusof  
Department of Mechanical Engineering  
University of Malaya  
Kuala Lumpur, Selangor, Malaysia

ISSN 2195-4356

ISSN 2195-4364 (electronic)

Lecture Notes in Mechanical Engineering

ISBN 978-981-15-5752-1

ISBN 978-981-15-5753-8 (eBook)

<https://doi.org/10.1007/978-981-15-5753-8>

© Springer Nature Singapore Pte Ltd. 2020, corrected publication 2021

This work is subject to copyright. All rights are reserved by the Publisher, whether the whole or part of the material is concerned, specifically the rights of translation, reprinting, reuse of illustrations, recitation, broadcasting, reproduction on microfilms or in any other physical way, and transmission or information storage and retrieval, electronic adaptation, computer software, or by similar or dissimilar methodology now known or hereafter developed.

The use of general descriptive names, registered names, trademarks, service marks, etc. in this publication does not imply, even in the absence of a specific statement, that such names are exempt from the relevant protective laws and regulations and therefore free for general use.

The publisher, the authors and the editors are safe to assume that the advice and information in this book are believed to be true and accurate at the date of publication. Neither the publisher nor the authors or the editors give a warranty, expressed or implied, with respect to the material contained herein or for any errors or omissions that may have been made. The publisher remains neutral with regard to jurisdictional claims in published maps and institutional affiliations.

This Springer imprint is published by the registered company Springer Nature Singapore Pte Ltd. The registered company address is: 152 Beach Road, #21-01/04 Gateway East, Singapore 189721, Singapore

# Contents

<b>The Effect of Composition on CO<sub>2</sub> Freeze-Out and Critical Locus of Binary CO<sub>2</sub>–CH<sub>4</sub> Mixture</b> . . . . .	1
Muhammad Babar, Mohamad Azmi Bustam, Abul Hassan Ali, Abdulhalim Shah Maulud, and Aymn Abdulrahman	
<b>Influence of the Agglomeration Phenomenon on the Recast Surface in PMEDM Environment</b> . . . . .	11
M. A. Abbas and M. A. Lajis	
<b>Comparison of the Removal Rate in EDM Based on the Mixed Environment</b> . . . . .	25
D. R. Abbas, M. A. Lajis, and M. A. Abbas	
<b>Influence of Projectile Penetration on the Multiple-Layered Target Based on Statistical and Numerical Analysis</b> . . . . .	35
O. M. Merzah, M. N. Ibrahim, M. A. Abbas, and M. A. Lajis	
<b>Fractal Wear Behaviour of Gear Tooth: A Review</b> . . . . .	47
Enesi Y. Salawu, A. O. Inegbenebor, O. O. Ajayi, Stephen A. Akinlabi, and Esther T. Akinlabi	
<b>Finite Element Modeling of Nano Porous Sintered Silver Material</b> . . . . .	55
Bahman Meyghani, S. Emamian, Mokhtar Awang, and Chuan Song Wu	
<b>Creep Behaviour and Adhesion Properties of TiC Thin Film Coating Grown by RF Magnetron Sputtering</b> . . . . .	69
Abegunde Olayinka, Esther T. Akinlabi, and O. P. Oladijo	
<b>Taguchi Analysis of Surface Roughness of TiC Thin Films Deposited by RF Magnetron Sputtering</b> . . . . .	77
Olayinka Oluwatosin Abegunde, Esther T. Akinlabi, and O. P. Oladijo	
<b>Laser Metal Deposition of Titanium Alloy: A Review</b> . . . . .	87
Bonolo S. Boshoman, Esther T. Akinlabi, Mutiu F. Erinosh, and Oluwagbenga T. Johnson	

<b>Effect of Novel Swirl Distributor Plate on Gasification Efficiency of Bubbling Fluidized Bed Gasifier</b> . . . . .	97
Iman Eslami Afrooz and Dennis Ling Chuan Ching	
<b>A Review of Recent Developments in Mechanical Properties of Polymer–Clay Nanocomposites</b> . . . . .	107
Mohd Shahneel Saharudin, Syafawati Hasbi, Muhammad Naguib Ahmad Nazri, and Fawad Inam	
<b>Effect of Some Additives on Tribological Properties of SAE20W40 Lubricant</b> . . . . .	131
Harpreet Singh Grewal, Surinder Singh, Harpreet Singh, and Narinder Singh	
<b>Performance Evaluation on the Smartness of Malaysian Timber</b> . . . . .	139
Amirah Abdull Razak, Nasrul Izan Shahrin, Jaronie Mohd Jani, and Norul Hisham Hamid	
<b>A Brief Overview of Bending Operation in Sheet Metal Forming</b> . . . . .	149
Omolayo M. Ikumapayi, Esther T. Akinlabi, Nkosinathi Madushele, and Samuel O. Fatoba	
<b>Emerging Trend in Forging Operation</b> . . . . .	161
Omolayo M. Ikumapayi, Esther T. Akinlabi, and Peter Onu	
<b>Effect of AFM Scan Size on the Scaling Law of Sputtered Aluminium Thin Films</b> . . . . .	171
F. M. Mwema, Esther T. Akinlabi, O. P. Oladijo, Stephen A. Akinlabi, and S. Hassan	
<b>Energy Content Modelling for Municipal Solid Waste Using Adaptive Neuro-Fuzzy Inference System (ANFIS)</b> . . . . .	177
Oluwatobi Adeleke, Stephen A. Akinlabi, Paul A. Adedeji, and Tien-Chien Jen	
<b>Predicting the Effect of Seasonal Variation on the Physical Composition of Municipal Solid Waste: A Case Study of the City of Johannesburg</b> . . . . .	187
Oluwatobi Adeleke, Stephen A. Akinlabi, S. Hassan, and Tien-Chien Jen	
<b>Optimization of Process Parameters Using Taguchi for Friction Stir Welding of Dissimilar Aluminum Alloys</b> . . . . .	199
Olatunji P. Abolusoro and Esther T. Akinlabi	
<b>Effect of Equal Channel Angular Pressing Die Angle on Corrosion Behavior of Bulk Nanostructured Metal</b> . . . . .	213
N. A. N. Mokhtar, D. N. Awang Shri, and M. M. Mahat	

**Investigation of Maximum Erosion Zone in the Horizontal 90° Elbow** ..... 223  
 Rehan Khan, H. H. Ya, William Pao, T. V. V. L. N. Rao, Azad Alam, and M. Azeem

**An Overview: Mechanical and Wear Properties of HDPE Polymer Nanocomposites Reinforced with Treated/Non-treated Inorganic Nanofillers** ..... 231  
 Tauseef Ahmed, H. H. Ya, Shuhaimi Mahadzir, Rehan Khan, and Muhammad Azad Alam

**Liquid Desiccant Membrane Regeneration of DES for Air Conditioning Systems Using Electrodialysis Technique** ..... 243  
 Temidayo Lekan Oladosu, Aklilu Tesfamichael Baheta, and P. B. Hussain

**Effects of Process Conditions on Calorific Value and Yield of Charcoal Produced from Pyrolysis of Coconut Shells** ..... 253  
 Rabi K. Ahmad, S. A. Sulaiman, M. Inayat, and Hadiza A. Umar

**Palm Kernel Shell as Potential Fuel for Syngas Production** ..... 263  
 Hadiza A. Umar, S. A. Sulaiman, Mior Azman B. Meor Said, and Rabi K. Ahmad

**Potential Roles of Artificial Intelligence in the LCI of Renewable Energy Systems** ..... 275  
 Paul A. Adedeji, Stephen A. Akinlabi, Nkosinathi Madushele, and Obafemi O. Olatunji

**Fault Detection System for Long-Distance Gas Mixture Pipelines Using Statistical Features** ..... 287  
 Syed Muhammad Mujtaba, Tamiru Alemu Lemma, and Mebrahitom Asmelash Gebremariam

**Feasibility Study on Metal Inert Gas (MIG) Welding on Zinalume G550 Steel** ..... 305  
 WaliSiJiang Tayier, Shamini Janasekaran, and Arvinth Rajandran

**The Influence of Welding Parameters on the Microhardness of Zinalume Steel Welded Joint Using Taguchi Technique in Metal Inert Gas (MIG)** ..... 315  
 Walisijiang Tayier, Shamini Janasekaran, and Abdullah Hussein Ali Alzubydi

**Construction of a Hybrid Geometric Model for an Injection Mould Using CAD/CAM System** ..... 323  
 Jian Xin Tan and Mohd Salman Abu Mansor

**Development of a Face Sculpture Prototype Using a Reverse Engineering Technique** ..... 335  
 Mohd Zhafran Anwar Mohd Tahar and Mohd Salman Abu Mansor

<b>Experimental Investigations on the Surface Hardness of Synthesized Polystyrene/ZnO Nanocomposites</b> . . . . .	345
Mohammad Azad Alam, H. H. Ya, P. B. Hussain, M. Azeem, S. M. Sapuan, Rehan khan, and Tauseef Ahamad	
<b>A Review: Hybrid Welding of High Strength Materials</b> . . . . .	353
Okwudili S. Ogbonna, Stephen A. Akinlabi, Nkosinathi Madushele, Abiodun A. Abioye, and S. Hassan	
<b>Image Segmentation and Particle Size Analysis of Vibratory Disc Milled Titanium Alloy Powder</b> . . . . .	367
Okwudili S. Ogbonna, Stephen A. Akinlabi, Nkosnathi Madushele, Paul A. Adedeji, and Stephen Ekolu	
<b>Hydrodynamic Analysis of Floating Offshore Solar Farms Subjected to Regular Waves</b> . . . . .	375
A. M. Al-Yacoubi, Emiruddin Redza Bin Abdul Halim, and M. S. Liew	
<b>Open-Hole and Filled-Hole Failure Envelopes of BFRP and GFRP: A Comparative Study</b> . . . . .	391
Z. Sajid, S. Karuppanan, and S. Z. H. Shah	
<b>Investigation on Effect of Fly Ash Volume Percentage on Microstructure and Microhardness of AA7075—Fly Ash Surface Composites via FSP</b> . . . . .	399
Namdev Ashok Patil, Ng Zhongyan, Srinivasa Rao Pedapati, and Othman Bin Mamat	
<b>Design-Point Performance Adaptation of Small Gas Turbine Using Particle Swarm Optimization</b> . . . . .	411
Affiani Machmudah and Tamiru Alemu Lemma	
<b>Finite Element Analysis of the Heat Generated During FSP of 1100 Al Alloy</b> . . . . .	425
Adedotun Adetunla and Esther Akinlabi	
<b>A Concise Review of the Effects of Hybrid Particulate Reinforced Aluminium Metal Matrix Composites on the Microstructure, Density and Mechanical Properties</b> . . . . .	433
Ndudim Ononiwu, Esther T. Akinlabi, Chigbogu G. Ozoegwu, and Victor Aigbodion	
<b>Application of Molecular Dynamics Simulation: A Case Study to Estimate Wettability</b> . . . . .	445
Vahid Khosravi, Syed Mohammad Mahmood, and Davood Zivar	
<b>A Comparison of Single-Vacuum-Bag and Double-Vacuum-Bag Methods for Manufacturing High-Quality Laminated Composites</b> . . . . .	457
Yasir Mujahid, Nabihah Sallih, and Mohamad Zaki Abdullah	

**Experimental Studies of FPSO Responses with Validation by Numerical and Artificial Neural Network Prediction** . . . . . 469  
 N. L. Azizan, Ruly Irawan, M. S. Liew, A. M. Al-Yacouby, and Kamaluddeen Usman Danyaro

**Surface Coating Processes: From Conventional to the Advanced Methods; a Short Review** . . . . . 483  
 A. D. Baruwa, Esther T. Akinlabi, and O. P. Oladijo

**Surface Coating Processes: From Conventional to Silane Organic Compound Applications: Recent and Prospects** . . . . . 495  
 A. D. Baruwa, Esther T. Akinlabi, O. P. Oladijo, and F. M. Mwema

**Study of Additive Manufactured Ti–Al–Si–Cu/Ti–6Al–4V Composite Coating by Direct Laser Metal Deposition (DLMD) Technique** . . . . . 503  
 L. C. Naidoo, O. S. Fatoba, Stephen A. Akinlabi, R. M. Mahamood, M. Y. Shatalov, E. V. Murashkin, S. Hassan, and Esther T. Akinlabi

**Experimental Investigation of Laser Metal Deposited Al–Cu–Ti Coatings on Ti–6Al–4V Alloy** . . . . . 515  
 A. M. Lasisi, O. S. Fatoba, Stephen A. Akinlabi, R. M. Mahamood, M. Y. Shatalov, E. V. Murashkin, S. Hassan, and Esther T. Akinlabi

**Effect of Process Parameters on the Hardness Property of Laser Metal Deposited Al–Cu–Ti Coatings on Ti–6Al–4V Alloy** . . . . . 523  
 A. M. Lasisi, O. S. Fatoba, Stephen A. Akinlabi, R. M. Mahamood, M. Y. Shatalov, E. V. Murashkin, S. Hassan, and Esther T. Akinlabi

**Feasibility Study of Through Hole Fabrication on Aluminium Nitride Ceramic Using Die-Sinking Electro-Discharge Machining** . . . . . 531  
 Asif Rashid, M. P. Jahan, D. Talamona, and A. Perveen

**CFD Study on the Thermal Performance of n-Octadecane (PCM) Doped with Graphene Nanoparticles as a Potential Thermal Energy Storage Medium for Trombe Walls** . . . . . 539  
 Chukwumaobi K. Oluah, Esther T. Akinlabi, and Howard O. Njoku

**Laser Metal Deposition of Titanium Composites: A Review** . . . . . 555  
 Esther T. Akinlabi, Ganiyat A. Soliu, R. M. Mahamood, Stephen A. Akinlabi, S. Hassan, M. Y. Shatalov, Evgenii Murashkin, and O. S. Fatoba

**Efficacy of Quasi Agro Binding Fibre on the Hybrid Composite Used in Advance Application** . . . . . 565  
 J. O. Dirisu, O. S. I. Fayomi, and S. O. Oyedepo

<b>Review on Ergonomics Application on Car Modification for Limbs Disabled Drivers</b> . . . . .	575
Salami Bahariah Suliano, Siti Azfanizam Ahmad, Azizan As'arry, and Faieza Abdul Aziz	
<b>Hybrid Microgrid Systems: Operational Schedule Optimization Considering Time of Use Demand Response and Battery Wear Cost</b> . . . . .	591
Tope Roseline Olorunfemi and Nnamdi Nwulu	
<b>A Review of Mathematical Optimization Applications in Renewable Energy-Powered Microgrids</b> . . . . .	603
Tope Roseline Olorunfemi and Nnamdi Nwulu	
<b>Optimal Grid-Connected Microgrid Scheduling Incorporating an Incentive-Based Demand Response Program</b> . . . . .	615
Tope Roseline Olorunfemi and Nnamdi Nwulu	
<b>Free-End Damage Detection in Cantilever Steel Plate Using Wavelet Transform Method</b> . . . . .	623
Muyideen Abdulkareem and Norhisham Bakhary	
<b>Determining the Potentials of Renewable Energy Sources for Distributed Generation in Ghana</b> . . . . .	631
Ernestina Amewornu and Nnamdi Nwulu	
<b>Optimal Location of Distributed Generators in a Radial Distribution Network</b> . . . . .	641
Ernestina Amewornu and Nnamdi Nwulu	
<b>Integrated Appliance Scheduling and Optimal Sizing of an Autonomous Hybrid Renewable Energy System for Agricultural Food Production</b> . . . . .	651
Omolola A. Ogbolumani and Nnamdi Nwulu	
<b>Cost Analysis of Hybrid Energy Storage System Benefits to Distribution Network Operators</b> . . . . .	661
Azizat Olusola Gbadegesin, Yanxia Sun, and Nnamdi Nwulu	
<b>The Awareness and Obstacle Factor of Machine Maintenance Toward Total Productive Maintenance in Manufacturing Company</b> . . . . .	673
Yunos Ngadiman, Md Fauzi Ahmad, Nor Aziati Abd Hamid, Raja Zuraidah Raja Mohd Rasi, Kamilah Ahmad, and Nor Hadilah Abdul Hamid	
<b>A Multifractal Study of Al Thin Films Prepared by RF Magnetron Sputtering</b> . . . . .	687
F. M. Mwema, Esther T. Akinlabi, O. P. Oladijo, Stephen A. Akinlabi, and S. Hassan	

**Influence of Elbow Orientation on Solid Particle Erosion for Multiphase Flow** . . . . . 695  
 Rehan Khan, H. H. Ya, William Pao, Armaghan Khan, R. Zahoor, and Tauseef Ahmed

**High-Speed Machining for CNC Milling Simulation Using CAM Software** . . . . . 703  
 Kwok Cheat Gan and Mohd Salman Abu Mansor

**Structural Fabrication and Dynamic Simulation of Stress of a Vibrosieve for Efficient Industrial Applications** . . . . . 715  
 Enesi Y. Salawu, O. O. Ajayi, Fajobi Muyiwa, Felix Ishola, and Azeta Joseph

**Recycling of Polylactic Acid (PLA) Wastes from 3D Printing Laboratory** . . . . . 725  
 Thai Kiat Ong, Hui Leng Choo, Wei Jean Choo, Seong Chun Koay, and Ming Meng Pang

**A Framework for the Optimal Sizing of Hybrid Solar PV-Battery-Hydro System for a Rural House in Malaysia** . . . . . 733  
 Bilawal A. Bhayo, Hussain H. Al-Kayiem, and Syed I. U. Gilani

**Anaerobic Treatment of Chicken Manure Co-digested with Sawdust** . . . . . 741  
 H. Y. Kok, M. R. Shamsuddin, and A. Aqsha

**Temperature Distribution Investigation During Friction Stir Welding (FSW) Using Smoothed-Particle Hydrodynamics (SPH)** . . . . . 749  
 Bahman Meyghani, Mokhtar Awang, Chuan Song Wu, and S. Emamian

**Correction to: Advances in Manufacturing Engineering** . . . . . C1  
 Seyed Sattar Emamian, Mokhtar Awang, and Farazila Yusof



# The Effect of Composition on CO<sub>2</sub> Freeze-Out and Critical Locus of Binary CO<sub>2</sub>–CH<sub>4</sub> Mixture



Muhammad Babar, Mohamad Azmi Bustam, Abul Hassan Ali, Abdulhalim Shah Maulud, and Aymn Abdulrahman

**Abstract** Cryogenic CO<sub>2</sub> capture technology is one of the emerging technologies used for natural gas purification. Thermodynamic phase study of the natural gas has a significant effect on the cryogenic CO<sub>2</sub> removal from natural gas. The present work describes the impact of composition on CO<sub>2</sub> freeze-out and critical locus of the binary CO<sub>2</sub>–CH<sub>4</sub> mixtures with different CO<sub>2</sub> content. Critical locus and CO<sub>2</sub> freeze-out were modelled for nine binary CO<sub>2</sub>–CH<sub>4</sub> mixtures and were correlated with the composition of the binary mixtures. Aspen HYSYS version 8.0 with the Peng Robinson equation of state and Eureka modelling tool were used in the present research work. It was found that the predicted models can precisely calculate the CO<sub>2</sub> freeze-out point and the critical locus of the mixtures. By comparing the calculated data with the reported experimental data, an excellent agreement was found. R-squared value for the models was 0.99, which shows the reliability of the models. The effect of composition on three-phase loci of the binary and multicomponent mixtures of CO<sub>2</sub> with light H.C is recommended for future research.

**Keywords** Thermodynamic study · Cryogenic CO<sub>2</sub> capture · CO<sub>2</sub> freeze-out · Critical locus · Binary CO<sub>2</sub>–CH<sub>4</sub> mixture

## 1 Introduction

Natural gas, which is a mixture of different hydrocarbons, is mainly used as energy source. The energy contribution of natural gas to the domestic and industrial sector is 38% and 60% of the total energy requirements, respectively [1]. Compared to

---

M. Babar (✉) · M. A. Bustam · A. S. Maulud  
CO<sub>2</sub> Research Centre (CO<sub>2</sub>RES), Universiti Teknologi PETRONAS, 32610 Bandar Seri Iskandar, Perak, Malaysia  
e-mail: [enr.babar2009@gmail.com](mailto:enr.babar2009@gmail.com)

M. A. Bustam  
e-mail: [azmibustam@utp.edu.my](mailto:azmibustam@utp.edu.my)

A. H. Ali · A. Abdulrahman  
Department of Chemical Engineering, University of Jeddah, Jeddah, Saudi Arabia

other fossil fuels, natural gas is generally recommended as a neat and clean fuel [2]. However, besides methane and other light hydrocarbons, natural gas may also contain some impurities like  $\text{CO}_2$ ,  $\text{N}_2$ , He and  $\text{H}_2\text{S}$ . One of the significant greenhouse gases in natural gas is  $\text{CO}_2$ . Natural gas from different sources has different  $\text{CO}_2$  content depending upon the gas well conditions [3, 4]. The maximum  $\text{CO}_2$  content in some of the discovered natural gas fields, e.g. Changling, Gudian, Honggang, Shengping, Fangshen and other gas reservoirs in Jilin oilfield of Songliao basin, may reach up to 90% [5]. According to reported literature, some of the natural gas fields of Malaysia may contain 87%  $\text{CO}_2$  [6]. Malaysia has more than 13 Tetra standard cubic feet (Tscf) of high  $\text{CO}_2$  content undeveloped natural gas reservoirs [7, 8]. A natural gas having high  $\text{CO}_2$  content has a lower calorific value than the sale gas specification [9].

In the twentieth century, many countries of the world came across a severe energy crisis, which increased petroleum prices [10]. Also, as  $\text{CO}_2$  and  $\text{CH}_4$  both are considered as the major greenhouse gases, their escape to the atmosphere needs to be controlled [11]. These problems encouraged oil and gas companies to utilize the contaminated natural gas fields with high  $\text{CO}_2$  content. Many technologies that have been used for purification of high  $\text{CO}_2$  content natural gas include absorption, adsorption, membrane separation and cryogenic  $\text{CO}_2$  capture technology [12–14]. Cryogenic  $\text{CO}_2$  processes are applicable for high  $\text{CO}_2$  content natural gas, its low footprint value increases its offshore applicability, and there is no chemical involvement [15]. These advantages and applicability at both atmospheric and high pressures make cryogenic technology one of the emerging technologies for  $\text{CO}_2$  capture.

The cryogenic process is the process of capturing  $\text{CO}_2$  at low temperatures ( $-153\text{ }^\circ\text{C}$  or below) [16, 17]. This process consists of three steps: the cooling cycle,  $\text{CO}_2$  capture step and  $\text{CO}_2$  recovery step [18]. The cryogenic  $\text{CO}_2$  capture from natural gas requires accurate knowledge of the  $\text{CO}_2$  freeze points and thermodynamic phase equilibria for the individual pure components as well as for the gaseous mixture [19, 20]. Generally, the phase diagram is an easy and excellent way of understanding the properties of a system. A phase diagram shows temperature and pressure conditions at which different phases occur and coexist at equilibrium [21]. Bubble point curve, dew point curve, three-phase locus and  $\text{CO}_2$  freeze-out line are the main components of a P-T phase diagram.

In the P-T phase envelope, the curve surrounding the S-V region, on which all the three phases of  $\text{CO}_2$  exist, is the three-phase locus [22, 23]. Cryogenic  $\text{CO}_2$  separation from natural gas is mostly done in the S-V region. A part of the three-phase locus is the boundary of the L-V and S-V region, which is helpful in defining the temperature range for the L-V region. Therefore, it is of crucial importance to have accurate knowledge of P-T conditions of S-L-V locus. So far, limited data are available for the three-phase locus of  $\text{CO}_2$ -NG mixture. Also, the effect of composition on the critical locus of the  $\text{CO}_2$ - $\text{CH}_4$  binary mixture has been rarely studied.

Donnelley et al. experimentally studied the phase behaviour of the  $\text{CO}_2$ - $\text{CH}_4$  binary system [24]. A pressure cell in an alcohol bath was used to confine the system.

By changing the pressure, the author avoided solidification of mercury at the low temperatures. The author used dry ice or liquid nitrogen for cooling the bath. The cell was gently shaken to mix the existing phases to achieve equilibrium. Temperatures and pressure were measured by calibrated thermocouples in the wall of the cell, and Bourdon tube gauges, respectively. He studied three-phase locus, temperature-composition phase envelopes and pressure-temperature phase envelope. The author in his work examined the three-phase locus for a temperature and pressure range of  $-57.78$  °C to  $-78.61$  °C and 9.1 bar to 47.9 bar, respectively. Furthermore, he extrapolated the three-phase locus up to  $-106.67$  °C.

Pikaar determined the V-L, V-S and L-S equilibria of CO<sub>2</sub> by measuring their boiling, dew and freezing points [25]. The liquid and vapour composition in equilibrium with the solid CO<sub>2</sub> at a pressure up to 101.325 bar and a temperature range of  $-63$  to  $-160$  °C were determined. By comparison with Donnelly and Katz data at low temperature, a disagreement was observed at  $-67$  and  $-73$  °C. Furthermore, at the lower temperatures, the divergence with Donnelly and Katz data was about 4.053 bar. Pikaar mentioned that the three-phase locus determined by Donnelly and Katz is incorrect below  $-67$  °C.

Sterner extended Donnelly and Katz's [24] experimental data and measured the VLE and the solid phase boundaries near the critical temperature of methane [26]. For the SLV, Sterner's data [26] showed good agreement with the Pikaar's data [25].

Davis et al. conducted his experimental study and presented a P-T phase envelope for the CH<sub>4</sub>-CO<sub>2</sub> binary system at three-phase locus [27]. Figure 1 shows the P-T phase envelope of the experimental three-phase locus data obtained by Davis et al. [28]. P-T phase envelope was generated along the V-L-S locus in a range from the triple point of CO<sub>2</sub> to  $-176.1$  °C. By comparing his data with Donnelly's data, Davis et al. found a disagreement between the two sets of data below  $-67.78$  °C. Davis found a good comparison with the Sterner's data, excluding the highest temperature of Sterner's data [26] as shown in Fig. 1.

Ozturk et al. [29] used Perturbed Chain-SAFT (PC-SAFT) EoS to model the phase behaviour of the CO<sub>2</sub>-H.C system. V-L equilibria, V-S equilibria and S-L equilibria of the gaseous mixtures having carbon dioxide along with methane, ethane and butane. Furthermore, the author also examined the influence of adding C<sub>2</sub>H<sub>6</sub> and C<sub>4</sub>H<sub>10</sub> on S-L equilibria of the binary CH<sub>4</sub>-CO<sub>2</sub> mixture.

Very few experimental studies are reported for the effect of composition on the critical locus of the binary CO<sub>2</sub>-CH<sub>4</sub> system. The aim of this work is also to provide a modelling approach for three-phase locus based on Aspen HYSYS with Peng Robinson (PR) property package. In the current research work, the pressure and temperature conditions for the critical locus for the CH<sub>4</sub>-CO<sub>2</sub> binary system at various CO<sub>2</sub> concentrations were modelled. Also, the effect of composition on critical locus was examined and discussed in detail. For validation of the data generated by Aspen HYSYS simulator for three-phase locus, it is then validated with the available experimental three-phase locus data.

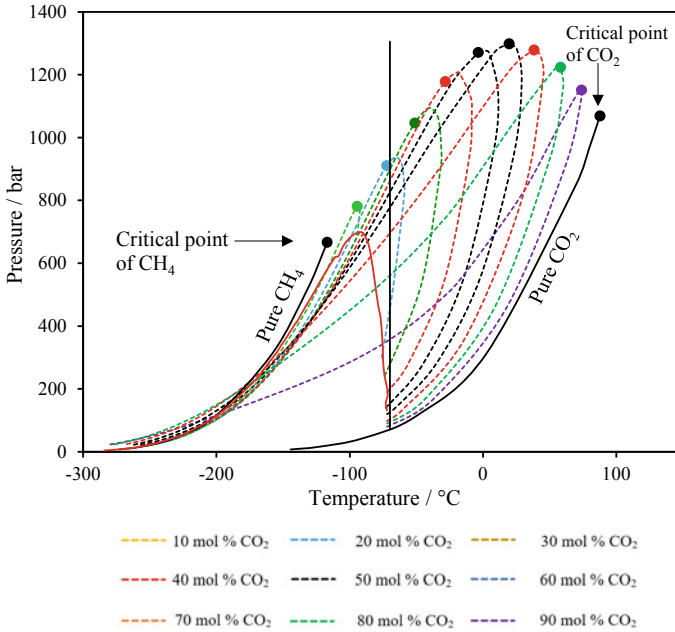


**Fig. 1** P-T phase envelope for binary CO<sub>2</sub>-CH<sub>4</sub> mixtures

This paper is organized as follows: Sect. 1 describes the introduction and motivation for this research work. Section 2 shows the methodology. Section 3 discusses the results and discussions of this research work. Section 4 illustrates the conclusion of the present research work along with future recommendation.

## 2 Research Methodology

Aspen HYSYS simulator was used for generating the thermodynamic phase data. Before using the simulation, it is mandatory to prove the reliability of the data generated by the simulator. Reported literature shows the authenticity of the PR EoS for the thermodynamic phase study of the natural gas system [29]. Figure 1 shows the reliability of the Aspen HYSYS predicted thermodynamic data for the CO<sub>2</sub>-CH<sub>4</sub> three-phase locus. From Fig. 1, it is obvious that predicted data by Aspen HYSYS using PR EoS show excellent agreement with the experimental data. An error of 3% was observed by comparing the predicted data with the three-phase data of Davis et al. [28]. Overall, Aspen HYSYS simulator with PR EoS obtained excellent agreement with the experimental data. This shows the reliability of Aspen HYSYS with PR property package for generating three-phase locus data.

**Table 1** Composition of the binary CO<sub>2</sub>–CH<sub>4</sub> mixture used in present work

N.G sample	CO <sub>2</sub> /mol%	CH <sub>4</sub> /mol%
Sample 1	10	90
Sample 2	20	80
Sample 3	30	70
Sample 4	40	60
Sample 5	50	50
Sample 6	60	40
Sample 7	70	30
Sample 8	80	20
Sample 9	90	10

The current research work has two primary approaches. In the first, thermodynamic data for the critical locus of the CO<sub>2</sub>–CH<sub>4</sub> mixtures were obtained through the Aspen HYSYS simulator while the second approach correlates the pressure and temperature of the critical locus with the composition of the gaseous mixture. Eureka modelling tool was used for the modelling of pressure and temperature conditions of the critical locus of the binary mixture. Table 1 shows the composition of the binary CO<sub>2</sub>–CH<sub>4</sub> mixture used in the present study.

### 3 Result and Discussion

#### 3.1 Critical Locus

Critical locus is one of the significant components of the phase envelope of N.G-CO<sub>2</sub> mixture. The critical point of a particular mixture is defined as the maximum limit for the binary L-V region in the phase envelope. CH<sub>4</sub> is the key component of natural gas; therefore, the present work aimed to model the critical locus of binary CO<sub>2</sub>–CH<sub>4</sub> mixtures. The simulation was done in Aspen HYSYS simulator for studying the critical point of binary CO<sub>2</sub>–CH<sub>4</sub> mixture of composition mentioned in Table 1. Pressure and temperature conditions were noted for the critical point. The pressure was then plotted against the temperature to obtain the PT phase envelope for the critical locus. Figure 1 shows the reported phase envelope for the binary CO<sub>2</sub>–CH<sub>4</sub> mixtures, pure CH<sub>4</sub> and CO<sub>2</sub> in literature. It is evident from Fig. 1 that each of the mixtures has a distinct critical point which changes with changing composition.

The predicted data for the critical locus of the binary CO<sub>2</sub>–CH<sub>4</sub> mixtures were then modelled in the Eureka modelling tool. Critical temperature and pressure were modelled as a function of CH<sub>4</sub> and CO<sub>2</sub> content in the mixture. Equations (1) and (2) were obtained with an R-squared value of 0.99 for each equation. Figure 2 shows the critical locus for the binary CO<sub>2</sub>–CH<sub>4</sub> mixture predicted by the developed model. As can be seen from Fig. 2, an excellent similarity exists between the experimental

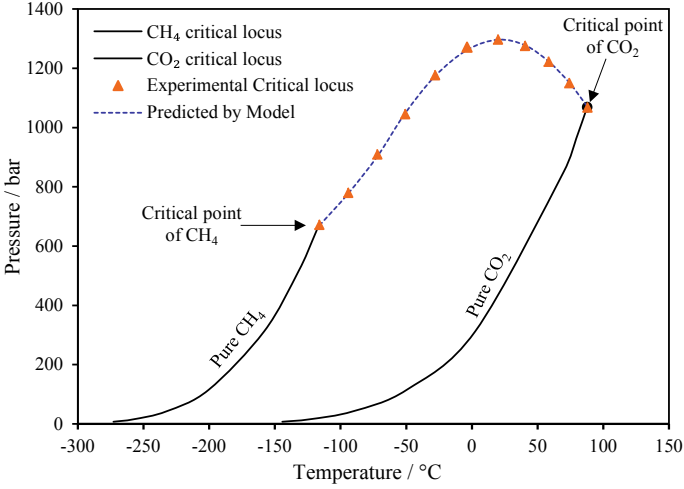


**Fig. 2** Comparison of the model predicted data with experimental data

and the predicted critical locus.

$$P = 1.74 \times 10^3 + 9.88 \times 10^3 \text{CH}_4 \text{CO}_2^2 + 8.51 \text{CH}_4^2 \text{CO}_2^2 - 1.07 \times 10^3 \text{CH}_4 - 671 \text{CO}_2^3 - 1.07 \times 10^4 \text{CH}_4^4 \text{CO}_2^2 \quad (1)$$

$$T = 160 + 3.58 \times 10^3 \text{CH}_4^1 \text{CO}_2^2 - 276 \text{CH}_4 - 71.8 \text{CO}_2^2 - 246 \text{CO}_2 \text{CH}_4^4 \quad (2)$$

The maximum uncertainty ( $u$ ) observed in the predicted temperature and pressure conditions of the critical locus was 2 and 0.6%, respectively. Table 2 shows the AAD of the established model for the critical locus of the binary mixtures.

### 3.2 CO<sub>2</sub> Freezing Point

CO<sub>2</sub> frost point is the transformation of CO<sub>2</sub> directly from gaseous to the solid phase. CO<sub>2</sub> frosting can also be termed as CO<sub>2</sub> anti-sublimation or desublimation. CO<sub>2</sub> freeze-out point is very crucial in the cryogenic CO<sub>2</sub> capture from natural gas. Due to the higher triple point of CO<sub>2</sub>, the natural gas having high CO<sub>2</sub> content desublimates at relatively high temperature, which may cause the blockage of pipelines and equipment. As part of the CO<sub>2</sub> capture and sequestration (CCS) chain, pressurized pipelines are considered as the most practical and efficient means for transportation of the large amounts of natural gas in the natural gas processing industry. The highest reported CO<sub>2</sub> in the Malaysian natural gas to date is 87%. However, globally, 90% of CO<sub>2</sub> was discovered in the natural gas till now. The present work is therefore focused on the modelling of CO<sub>2</sub> freeze-out point for CO<sub>2</sub>-CH<sub>4</sub> mixtures having CO<sub>2</sub> content

**Table 2** Predicted critical temperature and pressure

CH <sub>4</sub> content	CO <sub>2</sub> content	$T_{\text{exp}}$	$T_{\text{model}}$	AAD (Temp)	$P_{\text{exp}}$	$P_{\text{model}}$	AAD (Pressure)
1	0	-116.4	-116.0	0.344	673.1	670	0.460
0.9	0.1	-94.45	-94.0	0.476	781.0	778.2	0.358
0.8	0.2	-72.3	-71.5	1.107	910.7	905.9	0.527
0.7	0.3	-51.1	-51.0	0.196	1046.5	1047.0	-0.048
0.6	0.4	-28.3	-27.8	1.767	1177.9	1175.1	0.238
0.5	0.5	-3.6	-3.5	2.7778	1270.9	1263.2	0.606
0.4	0.6	19.6	20.0	-2.041	1298.3	1296.6	0.131
0.3	0.7	40.2	40.6	-0.995	1276.9	1277.5	-0.047
0.2	0.8	58.1	58.5	-0.689	1223.5	1222.3	0.098
0.1	0.9	73.8	74.2	-0.542	1151.3	1151.0	0.026
0	1	87.7	88.2	-0.570	1068.9	1069.0	-0.009

up to 90% CO<sub>2</sub> content (Table 1). Table 3 shows the pressure–temperature conditions of the CO<sub>2</sub> freezing point of the gaseous mixture.

The pressure–temperature conditions were calculated from Aspen HYSYS simulator and is compared with the experimental data from the reported literature. This calculated data was then modelled in the Eureka modelling tool to correlate the  $P$  and  $T$  for the CO<sub>2</sub> freeze-out with the CO<sub>2</sub> content in the mixture. Equation (3) was obtained for CO<sub>2</sub> freeze-out temperature of the binary CO<sub>2</sub>–CH<sub>4</sub> mixture with an R-squared value of 0.99, respectively. This  $R^2$  value shows the reliability of the predicted data by the developed models. Using Eq. (3), CO<sub>2</sub> freeze-out temperature can be predicted at any particular pressure for a known CO<sub>2</sub> content in the CO<sub>2</sub>–CH<sub>4</sub> mixture. Table 3 shows the comparison of the experimental and calculated CO<sub>2</sub> freeze-out temperatures at a specific pressure and CO<sub>2</sub> concentration. An excellent agreement was observed between the experimental and calculated temperatures.

$$T = 0.238PCO_2 + 0.00159P^2 + 0.00145P^2CO_2^2 + \frac{(-6.43 \times 10^{-7}P^3)}{CO_2^2} - 0.221P - 0.00343CO_2P^2 - 56.6 \quad (3)$$

## 4 Conclusion

In this research work, a detailed modelling study was carried out for the critical locus and CO<sub>2</sub> freeze-out locus of the binary CO<sub>2</sub>–CH<sub>4</sub> mixture. Eureka modelling tool was used to model the critical locus and the CO<sub>2</sub> freeze-out for the mixtures. Pressure and temperature at the critical locus were modelled for the binary mixture as

**Table 3** Experimental and calculated CO<sub>2</sub> freeze-out temperatures for binary CO<sub>2</sub>-CH<sub>4</sub> mixtures

P	10 mol% CO <sub>2</sub>		20 mol% CO <sub>2</sub>		30 mol% CO <sub>2</sub>		40 mol% CO <sub>2</sub>		50 mol% CO <sub>2</sub>	
	T <sub>exp</sub>	T <sub>cal</sub>	T <sub>exp</sub>	T <sub>cal</sub>	T <sub>exp</sub>	T <sub>cal</sub>	T <sub>exp</sub>	T <sub>cal</sub>	T <sub>exp</sub>	T <sub>cal</sub>
1	-56.88	-56.8	-56.82	-56.78	-56.78	-56.75	-56.75	-56.73	-56.72	-56.7
5	-57.78	-57.64	-57.55	-57.52	-57.39	-57.41	-57.25	-57.3	-57.13	-57.18
10	-58.81	-58.83	-58.38	-58.57	-58.08	-58.35	-57.83	-58.14	-57.6	-57.92
20	-60.82	-61.83	-59.95	-61.08	-59.4	-60.64	-58.94	-60.24	-58.53	-59.84
30	-62.89	-65.98	-61.49	-64.23	-60.7	-63.52	-60.05	-62.94	-59.47	-62.38
40	-65.33	-71.67	-63.02	-68.11	-61.98	-67.02	-61.17	-66.26	-60.44	-65.55
50	-71.35	-79.29	-64.57	-72.82	-63.25	-71.19	-62.29	-70.22	-61.44	-69.38
P	60 mol% CO <sub>2</sub>		70 mol% CO <sub>2</sub>		80 mol% CO <sub>2</sub>		90 mol% CO <sub>2</sub>			
	T <sub>exp</sub>	T <sub>cal</sub>	T <sub>exp</sub>	T <sub>cal</sub>	T <sub>exp</sub>	T <sub>cal</sub>	T <sub>exp</sub>	T <sub>cal</sub>		
1	-56.69	-56.68	-56.66	-56.66	-56.66	-56.64	-56.63	-56.61		
5	-57.01	-57.07	-56.9	-56.9	-56.95	-56.8	-56.84	-56.72		
10	-57.39	-57.7	-57.19	-57.19	-57.47	-56.98	-57.25	-57.02		
20	-58.14	-59.43	-57.76	-57.76	-59.01	-57.37	-58.58	-58.14		
30	-58.92	-61.81	-58.36	-58.36	-61.22	-57.8	-60.61	-59.98		
40	-59.73	-64.84	-59.01	-59.01	-64.11	-58.27	-63.34	-62.53		
50	-60.6	-68.55	-59.74	-59.74	-67.69	-58.81	-66.77	-65.8		



a function of CO<sub>2</sub> and CH<sub>4</sub> concentration in the binary mixture. The obtained model has an  $R^2$  value of 0.99 and shows an excellent agreement with the experimental critical locus data.

The pressure and temperature were also modelled for the CO<sub>2</sub> freeze-out of the binary CO<sub>2</sub>-CH<sub>4</sub> systems at various CO<sub>2</sub> concentration ranging from 10 mol% to 90 mol%. The obtained equation was capable of calculating the CO<sub>2</sub> freeze-out temperature at a specific pressure and CO<sub>2</sub> concentration. The data obtained by the established model have a close similarity with the experimental data. The  $R^2$  value for the model was 0.99, showing the authenticity of the developed model. It was observed that at high CO<sub>2</sub> contents and high pressure, the average absolute deviations of the derived models increase. It is therefore recommended for the future to modify the models for the multicomponent natural gas mixture with high CO<sub>2</sub> content and at high pressure with minimized energy requirements.

**Acknowledgements** The authors are thankful to the CO<sub>2</sub> Research Centre [CO2RES], Department of Chemical Engineering, Universiti Teknologi PETRONAS, for providing the necessary support in the research.

## References

1. Babar M, Bustam M, Maulud A, Ali A (2019) Optimization of cryogenic carbon dioxide capture from natural gas. *Materialwiss Werkstofftech* 50:248–253
2. Faramawy S, Zaki T, Sakr A-E (2016) Natural gas origin, composition, and processing: a review. *J Nat Gas Sci Eng* 34:34–54
3. Yeo ZY, Chew TL, Zhu PW, Mohamed AR, Chai SP (2012) Conventional processes and membrane technology for carbon dioxide removal from natural gas: a review. *J Nat Gas Chem* 21:282–298
4. Baraj E, Vagaský S, Hlinčík T, Ciahotný K, Tekáč V (2016) Reaction mechanisms of carbon dioxide methanation. *Chem Pap* 70:395–403
5. Hou D, Deng H, Zhang H, Li K, Sun L, Pan Y (2015) Phase behavior and physical parameters of natural gas mixture with. *J Chem* 2015:12
6. Nasir Haji Darman ARBH (2006) Technical challenges and solutions on natural gas development in Malaysia. The petroleum Policy and Management (PPM) Project 4th Workshop of the China-Sichuan Basin Case Study
7. Turunawarasu D, Norpiah R, Pottayil A (2015) A study on phase behavior and its application to cryogenic technologies for treatment of high CO<sub>2</sub> gas fields. OTC, Brasil
8. Babar M, Bustam M, Ali A, Maulud A (2018) Identification and quantification of CO<sub>2</sub> solidification in cryogenic CO<sub>2</sub> capture from natural gas. *Int J Auto Mech Eng* 15:5367–5367
9. Lee SP, Mellon N, Shariff AM, Leveque J-M (2018) High-pressure CO<sub>2</sub>-CH<sub>4</sub> selective adsorption on covalent organic polymer. *J Nat Gas Sci Eng* 50:139–146
10. Babar M, Shah MUH (2014) Evaluation of optimum composition of starch as a binding material for square coal briquettes. *IJSR* 3:1248–1252
11. Agsten R, Eder FX (1992) Possibilities of ecological production of methane from mixtures of methane and carbon dioxide. *Cryogenics* 32:175–178
12. Shimekit B, Mukhtar H (2012) Natural gas purification technologies-major advances for CO<sub>2</sub> separation and future directions. In: *Advances in natural gas technology*. InTech

13. Gholami M, Mohammadi T, Mosleh S, Hemmati M (2017) CO<sub>2</sub>/CH<sub>4</sub> separation using mixed matrix membrane-based polyurethane incorporated with ZIF-8 nanoparticles. *Chem Pap* 71:1839–1853
14. Babar M, Bustam MA, Ali A, Maulud AS, Shafiq U, Shariff AM et al (2019) Efficient CO<sub>2</sub> capture using NH<sub>2</sub>-MIL-101/CA composite cryogenic packed bed column. *Cryogenics* 101:10
15. Ali A, Maqsood K, Redza A, Hii K, Shariff AB, Ganguly S (2016) Performance enhancement using multiple cryogenic desublimation based pipeline network during dehydration and carbon capture from natural gas. *Chem Eng Res Des* 109:519–531
16. Berstad D, Anantharaman R, Nekså P (2013) Low-temperature CO<sub>2</sub> capture technologies—applications and potential. *Int J Refrig* 36:1403–1416
17. I. I. O. Refrigeration (2007) *International Dictionary of Refrigeration*. Peeters Publishers, Leuven
18. Babar M, Bustam MA, Ali A, Maulud AS, Shafiq U, Mukhtar A et al (2019) Thermodynamic data for cryogenic carbon dioxide capture from natural gas: a review. *Cryogenics* 102:20
19. Potoff JJ, Siepmann JI (2001) Vapor–liquid equilibria of mixtures containing alkanes, carbon dioxide, and nitrogen. *AIChE J* 47:1676–1682
20. ZareNezhad B, Eggeman T (2006) Application of Peng-Rabinson equation of state for CO<sub>2</sub> freezing prediction of hydrocarbon mixtures at cryogenic conditions of gas plants. *Cryogenics* 46:840–845
21. Hillert M (2007) *Phase equilibria, phase diagrams and phase transformations: their thermodynamic basis*. Cambridge University Press
22. Umar Shafiq AMS, Babar M, Babar A, Quddusi AH, Bustam M (2019) A review on modeling and simulation of blowdown from pressurized vessels and pipelines. *Process Safety and Environmental Protection*
23. Babar M, Bustam MA, Maulud AS, Ali A, Mukhtar A, Ullah S (2019) Enhanced cryogenic packed bed with optimal CO<sub>2</sub> removal from natural gas. A joint computational and experimental approach. *Cryogenics*, p 103010
24. Donnelly HG, Katz DL (1954) Phase equilibria in the carbon dioxide-methane system. *Ind Eng Chem* 46:511–517
25. Pikaar MJ (1959) Study of phase equilibria in hydrocarbon-CO<sub>2</sub> system. University of London
26. Sterner C (1961) Phase equilibria in the CO<sub>2</sub>-Methane systems. In: *Advances in cryogenic engineering*. Springer, pp 467–474
27. Shafiq U, Shariff AM, Babar M, Ali A (2018) A study on blowdown of pressurized vessel containing CO<sub>2</sub>/N<sub>2</sub>/H<sub>2</sub>S at cryogenic conditions. In *IOP conference series: materials science and engineering*, p 012077
28. Davis J, Rodewald N, Kurata F (1962) Solid-liquid-vapor phase behavior of the methane-carbon dioxide system. *AIChE J* 8:537–539
29. Ozturk M, Panuganti SR, Gong K, Cox KR, Vargas FM, Chapman WG (2017) Modeling natural gas-carbon dioxide system for solid-liquid-vapor phase behavior. *J Nat Gas Sci Eng* 45:738–746

# Influence of the Agglomeration Phenomenon on the Recast Surface in PMEDM Environment



M. A. Abbas and M. A. Lajis

**Abstract** The agglomeration phenomenon that occurs in PMEDM environment is one of the significant obstacles in enhancing the removal operation in this environment. This phenomenon has been investigated by the prior studies to improve the microhardness (MH) and recast layer thickness (RLT). However, these studies have not focused on the type of agglomeration that contributed in enhancing both responses of MH and RLT. Therefore, this study aims in presenting a logical interpretation to the influence of this phenomenon and its type on these responses for D2 steel by employing nano-chromium powder (NCP) particles in PMEDM environment. In addition, the scanning electron microscope (SEM) and energy-dispersive x-ray spectroscopy (EDS) play a crucial role in specifying the weight percentage of elements before and after machining of D2 steel to determine the agglomeration state. Accordingly, the carbon element and other elements are responsible for increasing the MH to 912 HVI since these elements agglomerate remarkably instead of NCP. Therefore, this vital agglomeration occurs at 2 g/L, 30  $\mu$ s, and 85  $\mu$ s for NCP, pulse duration, and pulse interval, respectively. Consequently, this environment has contributed to transferring limited energy to the workpiece in order to generate a minimum RLT, which reaches 10.32  $\mu$ m.

**Keywords** PMEDM · Agglomeration · Microhardness · Recast layer thickness · Heat flux

---

M. A. Abbas (✉) · M. A. Lajis

Faculty of Mechanical and Manufacturing Engineering (FKMP), University Tun Hussein Onn Malaysia (UTHM), 86400 Parit Raja, Johor Bahru, Malaysia  
e-mail: [mohd.a.abbas1981@gmail.com](mailto:mohd.a.abbas1981@gmail.com)

Sustainable Manufacturing and Recycling Technology, Advanced Manufacturing and Materials Center (SMART-AMMC), University Tun Hussein Onn Malaysia (UTHM), 86400 Parit Raja, Johor Bahru, Malaysia

M. A. Abbas

Aeronautical Techniques Engineering Department, Engineering Technical College (ETCN), Al-Furat Al-Awsat Technical University (ATU), Main Hilla-Baghdad Road, Najaf, Iraq

## 1 Introduction

The Powder Mixed Electrical Discharge Machining (PMEDM) is deemed as an encouraging medium in machining the complex materials and enhancing the quality of surface integrity [1, 2]. However, this medium is not wholly perfect in converging with the requirements of precision manufacturing due to the level of parameters implemented in the PMEDM which generates more obstacles such as the agglomeration phenomenon [3–5]. This phenomenon is produced from the electrothermal energy, which results from the spark channel between the workpiece and the electrode tool [6]. Depending on this energy, the powder particles immigrate and agglomerate upon the fusion region of the workpiece. These particles aggregate with the carbon particles resulted from the decomposing of dielectric fluid, and the electrodes debris produced from the machining operation of the plasma channel [7, 8]. The phenomenon of powder agglomeration is considered as an external and significant factor in the performance of the pure EDM and has been observed in the former studies in the PMEDM field; however, it is not studied intensely. Hence, the properties, concentration, and type of powder in the PMEDM system represent the principal operator of this phenomenon besides pulse current, pulse duration, pulse interval, and polarity [9].

To improve the surface properties, the correlation between this phenomenon and the quenching time is deemed as a major effectual. Therefore, the quenching time, represented in the interval time, leads to forming a recast layer as a new layer [10]. This layer consists of agglomerated particles with the melted region of the workpiece to improve the surface's hardness. Therefore, previous researchers attempted to study the relation between the thickness of this layer and the surface's hardness as these are significant responses in PMEDM system to enhance the recast surface after machining in this system. On the other hand, the researchers also tried to interpret the behavior of the agglomerated particles and relation with these responses.

The experimental results from machining W300 indicate that the maximum pulse duration at 2 g/L of aluminum powder leads to minimizing the recast layer thickness (RLT). Therefore, the increased peak current with the positive polarity requires raising the amount of this powder in order to achieve the best RLT [11]. However, the attitude of RLT differentiates when machining titanium alloy due to the minimum level of the graphite powder, peak current, and surfactant, which generate effective RLT [12]. Through these outcomes, the role of the amount of powder is significant to present a better RLT. Therefore, the increase in the powder quantity of boron carbide in EDM oil produces a problem to the melting region in the titanium alloy where this powder will be agglomerated in this region and contributes in reducing the flow of electrothermal energy to this alloy [13]. Both titanium alloy and AISI H13 steel have the same action toward the RLT during mixing multi-walled carbon nanotubes (MWCNTs) powder with kerosene. This action is remarked when the pulse interval is higher than the pulse duration at the minimum level of pulse current where the RLT will be at the minimum value [14, 15]. From these results, the previous researchers struggled to improve the recast layer by decreasing the thickness of it, but other

researchers have provided a different perspective through comparison between the RLT and the microhardness (MH) for the machined materials in PMEDM environment. This perspective has been exemplified by modifying the RLT of the machined surface of H13 steel at a minimum concentration of molybdenum powder in EDM, and maximum machining time has been approximated to 4 h. This outcome boosted the MH of this steel by increasing the agglomeration of this powder with the other particles in the fusing region which leads to forming more carbides [16]. Moreover, the RLT and MH possess similar behavior with the same steel when utilizing silicon and manganese powders in EDM; however, the pulse interval has an influential contribution to quench the melted region and resolidify it [17]. Also, the machining surface of  $\beta$ -titanium alloy has been improved when mixed with the silicon powder with hydrocarbon oil in the EDM machine. The agglomerated particles of carbon, oxygen, and silicon with debris led up to the enhancement of the MH and RLT [6].

Depending on the literature available, Fig. 1 highlights the relationship between the agglomeration phenomena in the first phase after completing the pulse duration. Furthermore, this figure also illustrates the second phase after completing the pulse interval and forming the recast layer. Through Fig. 1, it is perceived that the primary contributor of the powder agglomeration in PMEDM field is the electrothermal energy. Therefore, the numerical model of heat flux for the plasma channel in PMEDM has achieved outstanding results in understanding the removal rate of material in this field [18, 19]. Equations (1) and (2) will be invested in computing the quantity of heat flux applied on the workpiece in the present work to interpret the behavior of the agglomeration of particles given by:

$$Q(r) = [4.57 P_C H_F V_s I_P / \pi R_{pc}^2] e^{-4.5(r/R_{pc})^2} \quad (1)$$

$$R_{pc} = 2040 I_P^{0.43} T_{on}^{0.44} \quad (2)$$

where  $P_C$  is powder concentration [20],  $H_F$  denotes to heat fraction constant (5–9%) [18],  $V_s$  represents supply voltage (Volt),  $I_P$  indicates to pulse current (Amps),  $R_{pc}$  is plasma channel radius ( $\mu\text{m}$ ),  $r$  refers to radial axis ( $\mu\text{m}$ ), and  $T_{on}$  is pulse duration ( $\mu\text{s}$ ). Relying on these phases in Fig. 1, the research gap targeted in this article highlights on improving the performance of the microhardness (MH) and recast layer thickness (RLT) by controlling the electrothermal energy, pulse interval, and pulse duration in PMEDM. Consequently, the influence of the agglomeration phenomenon and the type of this phenomenon on these responses and the extent to which it can be controlled will be studied. Therefore, the present study employs the D2 steel, copper electrode, and the nano-chromium powder (NCP) particles to achieve these objectives in the electrical discharge environment.

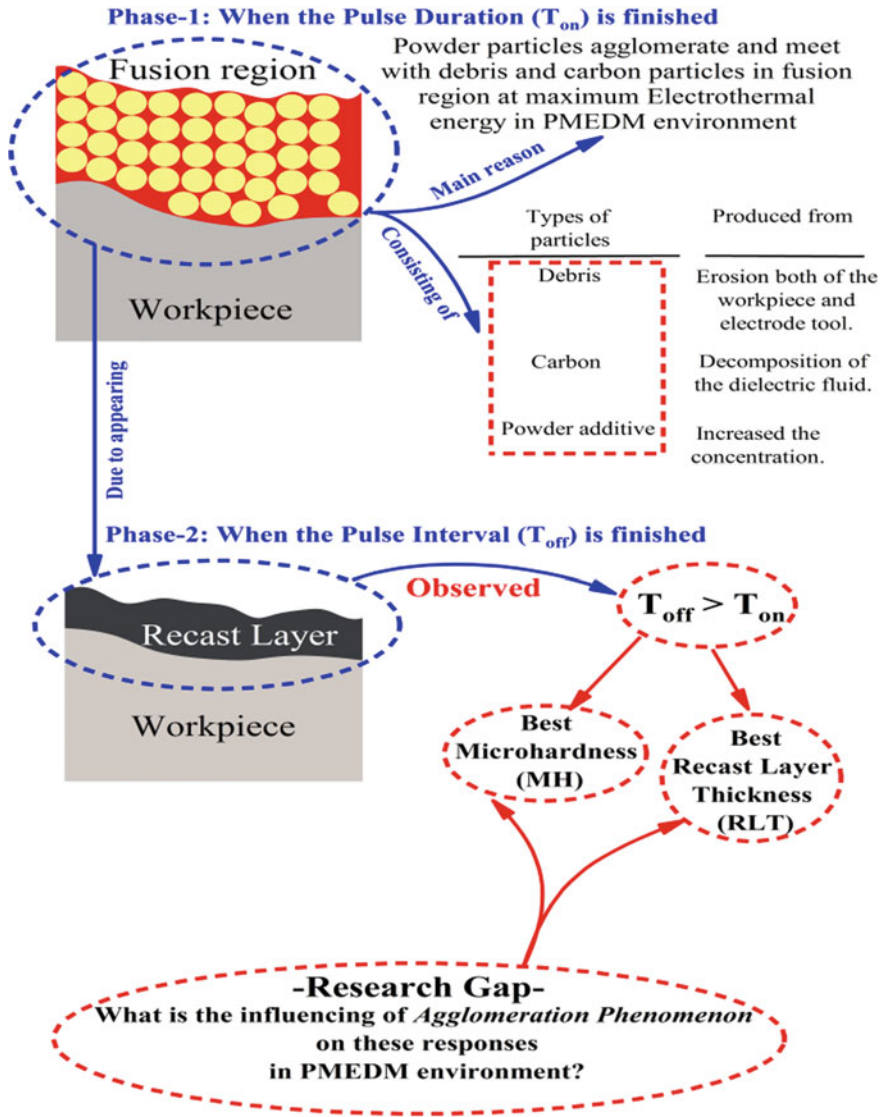


**Fig. 1** Comparison between numerical validation of MRR in AISI D2 with CPMEDM environment at each gap distance with experimental MRR values

## 2 Experimental Setup and Methodology

The experimental environment adopted in this study consists of the Integrated High Performance-EDM (IHP-EDM), work material, and observation devices as shown in Fig. 2; meanwhile, Table 1 indicates the experimental conditions employed to achieve the results.

In Fig. 2, the circulation system in (b) is integrated with Sodick EDM-Die Sinking AQ55L in (a) to circulate the mixed dielectric fluid with NCP. Furthermore, this system attracts the powder particles and debris by using a cleaning filter and magnetic filter, respectively. In addition, the insulating tank in Fig. 2c is utilized to mix the NCP with kerosene separately out of the original tank of EDM machine in (a). Consequently, IHP-EDM in Fig. 2a–c assists in obtaining the best performance in PMEDM, while work materials in Fig. 2d–f consist of nano-chromium powder (NCP) particles, copper electrode, and D2 steel as the workpiece, sequentially. In Fig. 2, the scanning electron microscope (SEM) and energy-dispersive x-ray spectroscopy (EDS) in (g) employ Hitachi SU1510 model to inspect the microstructure of machined surface and migrated particles intensity, while in (h), the microhardness (MH) uses Shimadzu model to test the surface hardness for the workpiece before and after machining.

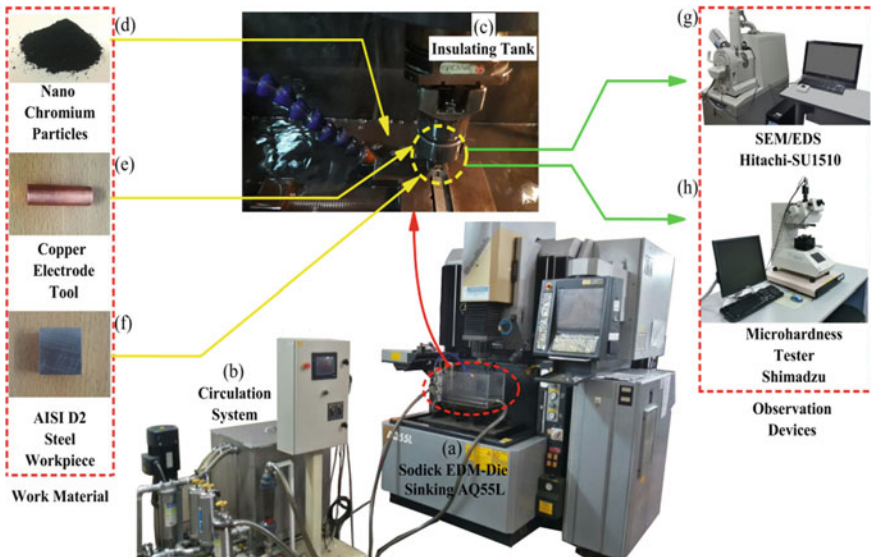


**Fig. 2** Experimental setup and methodology: IHP-EDM which consists of **a** EDM machine, **b** circulation system, and **c** insulating tank; work material which consists of **d** nano-chromium particles, **e** copper electrode tool, and **f** AISI D2 steel workpiece; and observation devices which consists of **g** SEM/EDS and **h** microhardness tester

**Table 1** Experimental conditions

Working parameters	Descriptions
Electrode tool	Copper (Ø10 mm)
Workpiece	AISI D2 (7.5 mm × 7.5 mm × 10 mm)
Dielectric liquid	Kerosene + NCP particles
Particle size of NCP	(70–80) nm
NCP concentration ( $P_C$ )	2 g/L and 6 g/L
Peak current ( $I_P$ )	10 Amps
Pulse duration ( $T_{on}$ )	20 and 30 $\mu$ s
Pulse interval ( $T_{off}$ )	85 $\mu$ s
Polarity	Negative
Voltage	120 V
Depth of cut	3 mm
Flushing rate	1500 mm <sup>3</sup> /h

The peak current, pulse duration, pulse interval, and powder concentration in Table 1 have been elected for reducing the agglomeration of additive powder in PMEDM environment [9]. Furthermore, these parameters are in agreement with what is stated in Fig. 1 depending on the brief literature which noted that the pulse duration is lower than the pulse interval. Besides, it is observed that the powder is not agglomerating in the range of (2–4) g/L according to machining of D2 steel or at 6 g/L with Inconel 625 [5, 8]. Therefore, the NCP particles in this study adopt both 2 and 6 g/L to test whether the agglomeration occurs. On the other hand, SEM/EDS in Fig. 2g is employed to test D2 steel before and after machining it in PMEDM to demonstrate the feasibility of these parameters in order to achieve the surface enhancement [21]. Accordingly, the agglomeration ratio ( $R_{AG}$ ) in Eqs. (3) and (4) reflects the best criterion for exploring the active migrated particles, type of agglomeration, and carbon percentage on the machining zone. Moreover, Eq. (4) adopts the weight percentage of elements before and after removal operation in PMEDM, depending on the EDS observations [9].

$$R_{AG} = \frac{m_{AG}}{m_{TAG}} \times 100\% = \frac{\sum_{n=1}^i (m_{eam} - m_{ebm})_n}{\sum_{n=1}^i (m_{eam})_n} \times 100\%$$

$$R_{AG} = \frac{m_{RL} \sum_{n=1}^i (\%w_{eam} - \%w_{ebm})_n}{m_{RL} \sum_{n=1}^i (\%w_{eam})_n} \times 100\% \quad (3)$$

Then, the final agglomeration ratio is given by:

$$R_{AG} = \frac{\sum_{n=1}^i (\%w_{eam} - \%w_{ebm})_n}{\sum_{n=1}^i (\%w_{eam})_n} \times 100\% \quad (4)$$



where  $m_{AG}$  is active agglomeration mass (mg),  $m_{TAG}$  refers to total agglomeration mass (mg),  $m_{eam}$  is element mass after machining (mg),  $m_{ebm}$  is element mass before machining (mg),  $\%w_{eam}$  denotes the weight percentage of element after machining,  $\%w_{ebm}$  indicates the weight percentage of element before machining, and  $m_{RL}$  is recast layer mass (mg).

Figure 3 displays EDS observation of the D2 steel workpiece before machining in the PMEDM environment, while Table 2 elucidates the weight percentage of this workpiece based on EDS observation in Fig. 3. In addition, Table 2 also illustrates the average MH value of this steel before machining. From here, the weight percentage of the elements based on EDS observations in Table 3, along with the RLT, MH, and  $R_{AG}$  outcomes after machining of D2 steel in the PMEDM medium at each run that has been carried out, relies on the experimental conditions in Table 1.

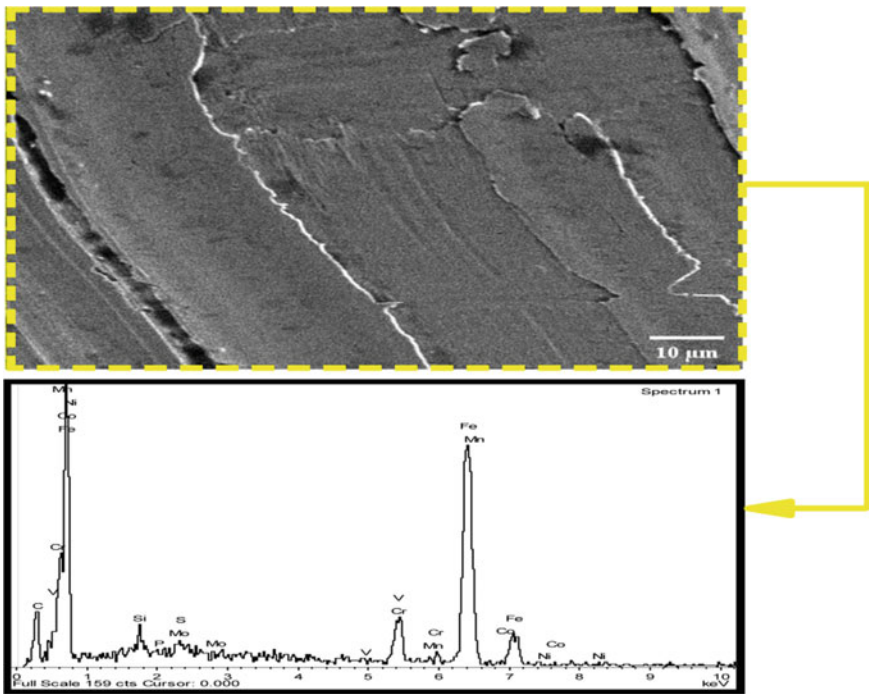


Fig. 3 EDS observation of D2 steel before machining in PMEDM

Table 2 Weight percentage of elements and microhardness values for D2 steel before machining in PMEDM

$\%w_{ebm}$	21.03% C, 0.88% Si, 0.1% P, 0.04% S, 0.24% V, 7.78% Cr, 0.17% Mn, 66.68% Fe, 0.45% Co, 0.33% Ni, 2.12% Mo				
Microhardness (HVI)	648	665	646	Average	653

**Table 3** Experimental runs including weight percentage of elements for D2 steel depending on EDS observations after machining in PMEDM, parameters employed in each run, microhardness, recast layer thickness, and agglomeration ratio values in each run

% <i>w<sub>eam</sub></i> : Run No. 1: $T_{on} = 20 \mu\text{s}$ , $P_C = 2 \text{ g/L}$			
	MH (HVI)	RLT ( $\mu\text{m}$ )	% <i>R<sub>AG</sub></i>
	830	13.90	
	843	19.00	
	843	29.00	
	Average		
MH (HVI)	RLT ( $\mu\text{m}$ )	51.35	
1.36%C, 8.33%O, 0.24%Si, 0.04%P, 0.59%S, 0.96%V, 5.2%Cr, 0.83%Mn, 44.4%Fe, 1.56%Co, 0.94%Ni, 1.8%Cu, 3.75%Mo			
% <i>w<sub>eam</sub></i> : Run No. 2: $T_{on} = 30 \mu\text{s}$ , $P_C = 2 \text{ g/L}$			
	MH (HVI)	RLT ( $\mu\text{m}$ )	% <i>R<sub>AG</sub></i>
	929	09.53	
	905	08.74	
	901	12.70	
	Average		
MH (HVI)	RLT ( $\mu\text{m}$ )	62.60	
50.1%C, 4.69%O, 0.46%Si, 0.27%P, 0.61%S, 0.14%V, 5.7%Cr, 1.68%Mn, 34.53%Fe, 1.12%Co, 0.4%Ni, 0.29%Cu, 0.01%Mo			
% <i>w<sub>eam</sub></i> : Run No. 3: $T_{on} = 20 \mu\text{s}$ , $P_C = 6 \text{ g/L}$			
	MH (HVI)	RLT ( $\mu\text{m}$ )	% <i>R<sub>AG</sub></i>
	800	48.40	
	825	50.40	
	810	27.00	
	Average		
MH (HVI)	RLT ( $\mu\text{m}$ )	46.91	
30.08%C, 4.78%O, 0.84%Si, 0.12%P, 0.45%S, 0.49%V, 6.4%Cr, 0.23%Mn, 48.8%Fe, 0.87%Co, 1.34%Ni, 3.76%Cu, 1.8%Mo			
% <i>w<sub>eam</sub></i> : Run No. 4: $T_{on} = 30 \mu\text{s}$ , $P_C = 6 \text{ g/L}$			
	MH (HVI)	RLT ( $\mu\text{m}$ )	% <i>R<sub>AG</sub></i>
	912	22.30	
	903	17.90	
	879	35.50	
	Average		
MH (HVI)	RLT ( $\mu\text{m}$ )	57.48	
45.71%C, 4.72%O, 0.21%Si, 0.31%P, 0.18%S, 0.38%V, 6.3%Cr, 0.03%Mn, 36.82%Fe, 1.01%Co, 0.26%Ni, 0.68%Cu, 3.42%Mo			

Source Author

### 3 Results and Discussion

Based on Tables 2 and 3, the agglomeration of chromium has not occurred at each run in Table 3 when machining D2 steel in PMEDM where the range of chromium element values is between 5.20 and 6.39% in Table 3. Consequently, this range is less than the value of chromium in Table 2 before machining this steel.

These outcomes refer to the efficiency of the used parameters for avoiding the agglomeration of NCP particles. Therefore, the powder agglomeration phenomenon that has been an obstacle in obtaining the best performance of the removal rate in PMEDM environment has been avoided by the experimental conditions adopted in the present study in Table 1 [9].

According to these experimental conditions, the thermal interpretation based on the heat flux of the plasma channel in PMEDM is considered the best concept to understand the phenomenon of powder agglomeration. By observing Fig. 4, based on the experimental outcomes in Table 3, the maximum value of heat flux of plasma channel depending on Eqs. (1) and (2) occurs when the NCP particles and pulse duration equal to 6 g/L and 20  $\mu$ s, respectively, and reach 0.2315  $\mu$ W/ $\mu$ m<sup>2</sup> at point L. However, the value of this heat at 2 g/L and 30  $\mu$ s has reduced to be 0.0540  $\mu$ W/ $\mu$ m<sup>2</sup> at point H. Thus, the variance of values of the plasma heat in these points is related to the powder concentration and the pulse duration. Therefore, the NCP particles play an efficient role in the PMEDM where these particles possess two behaviors at the same time; the first behavior is the thermal and electrical conductivity that contributes

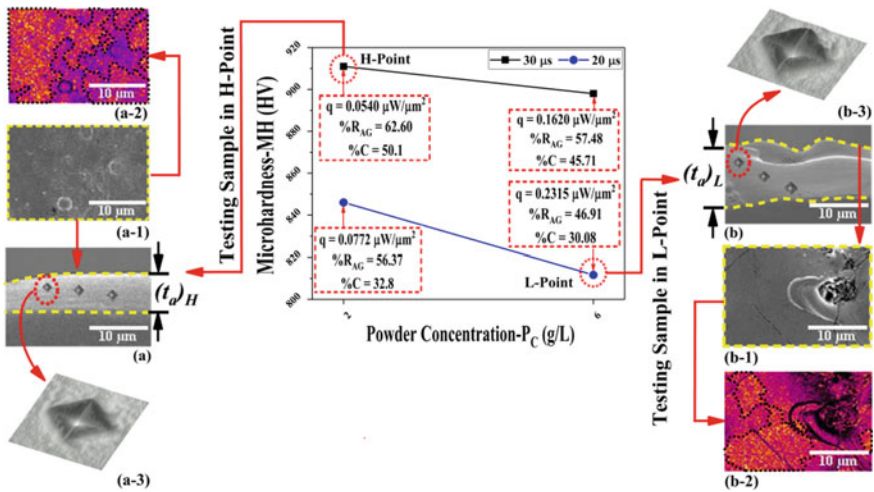


**Fig. 4** Influence of chromium powder concentration on the microhardness of D2 steel after machining in PMEDM which consists of H-Point and L-Point for maximum and minimum microhardness, respectively. Observed in H-Point and L-Point: Average recast layer thickness in (a) and (b) and including surface morphology, agglomeration distribution, and indentation topology in (a,b-1), (a,b-2), and (a,b-3), respectively

to the breakdown of kerosene impedance and transfers the enormous energy to the workpiece, while the other is related to the powder ability to absorb the plasma channel energy as a cooling factor [22, 23]. Furthermore, the powder concentration is significant to control the heat flux of the plasma channel in PMEDM depending on Eq. (1) [20].

Based on these behaviors, the amount of NCP particles at point L could not fully absorb the energy of the plasma channel as the pulse duration is not enough to complete this operation. Meanwhile, these particles are active enough to overcome the impedance of dielectric fluid in PMEDM relying on the conductivity behavior of this powder and the heat flux value at point L as illustrated in Fig. 4. In addition, the pulse duration in all runs is lower than the value of pulse interval. Thus, this powder has not agglomerated in the machining zone and this is what has been confirmed by the EDS observations in Table 3.

On the other hand, the value of  $(\%w_{cam} - \%w_{ebm})$  in Eq. (4) indicates the weight percentage of active agglomeration in D2 steel. Hence, this value serves to recognize the increasing and decreasing elements based on the weight percentage before and after machining in PMEDM as exhibited in Tables 2 and 3, where the increased elements refer to the active agglomeration in each run. Thus, Fig. 5 illustrates this value for Runs No. 2 and No. 3 at points H and L, respectively.

Upon focusing on Fig. 5, the percentage of carbon in (a) is more active than the percentage of it in (b). Accordingly, the carbon with other active elements, except oxygen, contributes to forming more carbides [5, 24]. Moreover, in Fig. 4 (a,b-1) and (a,b-2) the agglomeration distribution in surface morphology after machining in PMEDM at point L is less than the agglomeration distribution at point H. Following from there, the agglomeration ratio ( $R_{AG}$ ) at point L is 46.91%, while this ratio reaches up to 62.60% at point H. Consequently, Run No. 2 at point H represents the higher value of the average of microhardness as illustrated in Table 3 which equals to 912 HVI. This result can be seen by observing the indentation topology in Fig. 4, where the indentation at point H is less, as demonstrated in Fig. 4(a-3), than the indentation in Fig. 4(b-3) for point L.

As mentioned earlier, the heat flux of the plasma channel at point L is greatly transferred to the workpiece as compared with this heat at point H. Thus, the heat at point H flows less in the machined zone. Hence, this effective flow has formed the best thickness of the recast layer at this point which attained an average  $(t_a)_H$  of 10.32  $\mu\text{m}$  as depicted in Fig. 4a and Table 3 for Run No. 2 [10, 12].

From this brief explanation as revealed in Tables 2 and 3 and Figs. 4 and 5 in this study, the values of RLT and MH at these points refer to responses achieved in PMEDM. However, the results of these trials in the present study have clarified a different type of agglomeration other than the agglomeration of powder. This agglomeration consists of the carbon and other elements except for oxygen which contributes to modification of the surface hardness and improves the recast layer thickness, especially by adding 2 g/L of NCP particles at 30  $\mu\text{s}$ . Consequently, this type of agglomeration is more efficient than the agglomeration of powder which stands as a hindrance to progress the removal rate of the workpiece in PMEDM.

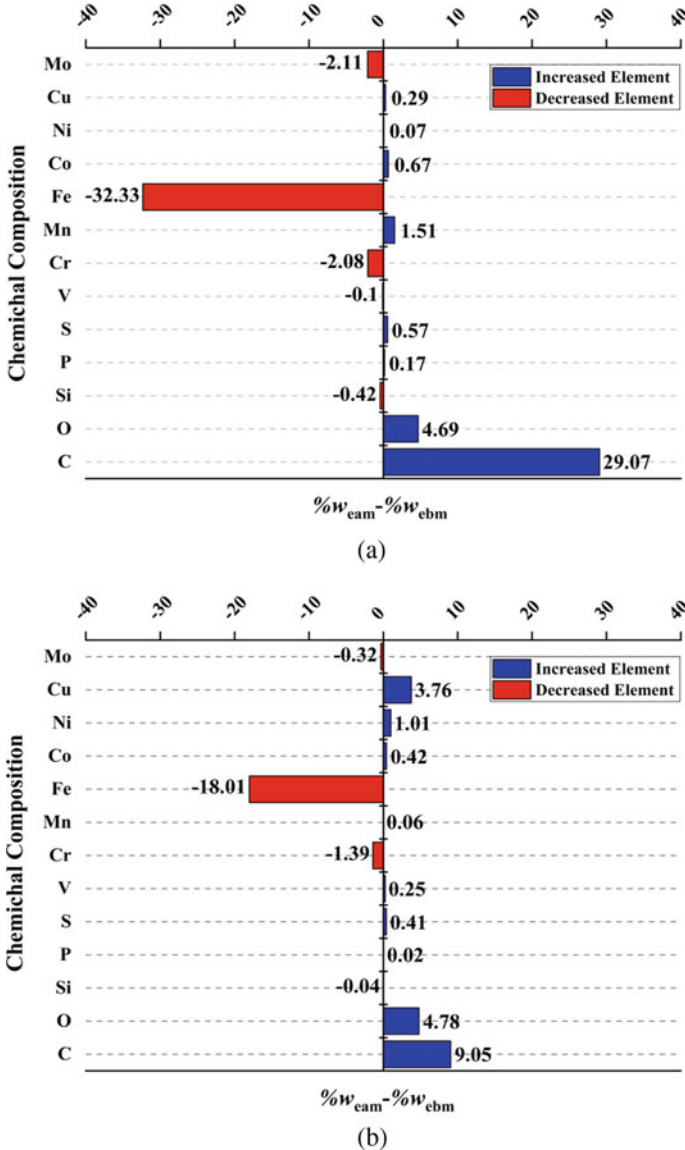


Fig. 5 Active agglomeration: a Run No. 2 at point H and b Run No. 3 at point L

## 4 Conclusions and Recommendations

The microhardness (MH) and recast layer thickness (RLT) of the machining zone are significant responses reflecting the surface enhancement in PMEDM environment. Therefore, the migrating particles with the debris are considered to bind with these

responses. Accordingly, the present study has strived to present an interpretation of this bind to understand the effect of these particles on MH and RLT. This study has employed: D2 steel, copper electrode, and nano-chromium powder (NCP) particles to achieve the objective of this study. Consequently, this study has concluded the following:

1. A minimal concentration of NCP particles at 30  $\mu\text{s}$  contributes in enhancing the microhardness and the thickness of the recast layer from 653 to 912 HVI and 10.32  $\mu\text{m}$ , respectively. Therefore, this outcome deemed the best performance presented by this study as compared to the other trials. The active agglomeration of carbon with other elements, except oxygen, is considered the main reason in enhancing these responses, which can be observed through agglomeration ratio in this trial that equals to 62.60%.
2. Through remarking the performed trials, the carbon and other elements agglomerate instead of the powder agglomeration in PMEDM. This type of agglomeration is more efficient in improving the surface hardness and thickness of the recast layer.

Relying on these conclusions, the present study recommended employing minimum value of this powder and maximum level of pulse duration in order to obtain the best MH and RLT during machining of D2 steel in PMEDM with NCP particles. However, the pulse interval in all the trials must be higher than the pulse duration to prevent agglomerating the powder to stimulate the agglomeration of carbon and the other elements to enhance both of MH and RLT, at the same time.

**Acknowledgments** The authors would like to express their profound gratitude and deepest appreciation to the Ministry of Higher Education (MOHE), Malaysia, for funding this project through the Malaysian Technical University Network-Centre of Excellence (MTUN-CoE) and Fundamental Research Grant Scheme (FRGS) through grant numbers of 1496 and 1463. The authors would also like to express their special thanks to Sustainable Manufacturing and Recycling Technology, Advanced Manufacturing and Materials Centre (SMART-AMMC), Universiti Tun Hussein Onn Malaysia (UTHM), and Universiti Teknologi PETRONAS for their support. Furthermore, the authors would like to present a special thanks to the Ministry of Higher Education and Scientific Research in Iraq for academic support for Iraqi students' research.

## References

1. Kansal HK, Singh S, Kumar P (2007a) Effect of silicon powder mixed EDM on machining rate of AISI D2 die steel. *J Manuf Process* 9:13–22. [https://doi.org/10.1016/s1526-6125\(07\)70104-4](https://doi.org/10.1016/s1526-6125(07)70104-4)
2. Shabgard M, Khosrozadeh B (2017) Investigation of carbon nanotube added dielectric on the surface characteristics and machining performance of Ti-6Al-4V alloy in EDM process. *J Manuf Process* 25:212–219. <https://doi.org/10.1016/j.jmapro.2016.11.016>
3. Sugunakar A, Jits W, Markandeya R, Kumar A, Reddy VV (2018) Effect of various powders added in to the dielectric fluids on MRR and SR during PMEDM of RENE80. *Int J Pure Appl Math* 118

4. Kansal HK, Singh S, Kumar P (2007b) Technology and research developments in powder mixed electric discharge machining (PMEDM). *J Mater Process Technol* 184:32–41. <https://doi.org/10.1016/j.jmatprotec.2006.10.046>
5. Talla G, Gangopadhyay S, Biswas CK (2016) Effect of powder-suspended dielectric on the EDM characteristics of inconel 625. *J Mater Eng Perform* 25:704–717. <https://doi.org/10.1007/s11665-015-1835-0>
6. Prakash C, Kansal HK, Pabla BS, Puri S (2017) Experimental investigations in powder mixed electric discharge machining of Ti-35Nb-7Ta-5Zr $\beta$ -titanium alloy. *Mater Manuf Process* 32:274–285. <https://doi.org/10.1080/10426914.2016.1198018>
7. Singh AK, Kumar S, Singh VP (2015) Effect of the addition of conductive powder in dielectric on the surface properties of superalloy Super Co 605 by EDM process. *Int J Adv Manuf Technol* 77:99–106. <https://doi.org/10.1007/s00170-014-6433-z>
8. Kumar H (2015) Development of mirror like surface characteristics using nano powder mixed electric discharge machining (NPMEDM). *Int J Adv Manuf Technol* 76:105–113. <https://doi.org/10.1007/s00170-014-5965-6>
9. Abbas MA, Lajis MA, Abdul Ridha GS (2019) A new methodology for predicting quantity of agglomeration between electrodes in PMEDM environment. *Int J Mech Eng Technol* 10:1461–1479
10. Bhatt G, Batish A, Bhattacharya A (2015) Experimental investigation of magnetic field assisted powder mixed electric discharge machining. *Part Sci Technol* 33:246–256. <https://doi.org/10.1080/02726351.2014.968303>
11. Syed KH, Palaniyandi K (2012) Performance of electrical discharge machining using aluminium powder suspended distilled water. *Turkish J Eng Environ Sci* 36:195–207
12. Kolli M, Kumar A (2015) Effect of dielectric fluid with surfactant and graphite powder on electrical discharge machining of titanium alloy using Taguchi method. *Eng Sci Technol an Int J* 18:524–535. <https://doi.org/10.1016/j.jestch.2015.03.009>
13. Kolli M, Kumar A (2014) Effect of boron carbide powder mixed into dielectric fluid on electrical discharge machining of titanium alloy. *Int Conf Adv Manuf Mater Eng (AMME 2014)* 5:1957–1965. <https://doi.org/10.1016/j.mspro.2014.07.528> (Elsevier)
14. Izman S, Ghodsiyeh D, Hamed T, Rosliza R, Rezazadeh M (2012) Effects of adding multiwalled carbon nanotube into dielectric when edming titanium alloy. *Adv Mater Res* 464:1445–1449. <https://doi.org/10.4028/www.scientific.net/AMR.463-464.1445>
15. Sari MM, Noordin MY, Brusa E (2013) Role of multi-wall carbon nanotubes on the main parameters of the electrical discharge machining (EDM) process. *Int J Adv Manuf Technol* 68:1095–1102
16. Amorim FL, Dalcin VA, Soares P, Mendes LA (2017) Surface modification of tool steel by electrical discharge machining with molybdenum powder mixed in dielectric fluid. *Int J Adv Manuf Technol* 91:341–350. <https://doi.org/10.1007/s00170-016-9678-x>
17. Prakash C, Kansal HK, Pabla BS, Puri S (2016) Multi-objective optimization of powder mixed electric discharge machining parameters for fabrication of biocompatible layer on  $\beta$ -Ti alloy using NSGA-II coupled with Taguchi based response surface methodology. *J Mech Sci Technol* 30:4195–4204. <https://doi.org/10.1007/s12206-016-0831-0>
18. Kansal HK, Singh S, Kumar P (2008) Numerical simulation of powder mixed electric discharge machining (PMEDM) using finite element method. *Math Comput Model* 47:1217–1237. <https://doi.org/10.1016/j.mcm.2007.05.016>
19. Salonitis K, Stournaras A, Stavropoulos P, Chryssolouris G (2009) Thermal modeling of the material removal rate and surface roughness for die-sinking EDM. *Int J Adv Manuf Technol* 40:316–323. <https://doi.org/10.1007/s00170-007-1327-y>
20. Jatti VS, Bagane S (2018) Thermo-electric modelling, simulation and experimental validation of powder mixed electric discharge machining (PMEDM) of BeCu alloys. *Alexandria Eng J* 57:643–653. <https://doi.org/10.1016/j.aej.2017.02.023>
21. Kumar S, Batra U (2012) Surface modification of die steel materials by EDM method using tungsten powder-mixed dielectric. *J Manuf Process* 14:35–40. <https://doi.org/10.1016/j.jma pro.2011.09.002>

22. Batish A, Bhattacharya A, Kumar N (2015) Powder mixed dielectric: an approach for improved process performance in EDM. *Part Sci Technol* 33:150–158. <https://doi.org/10.1080/02726351.2014.947659>
23. Abrol A, Sharma S (2015) Effect of chromium powder mixed Dielectric on performance characteristic of AISI D2 die steel using EDM. *Int J Res Eng Technol* 4:232–246. <https://doi.org/10.15623/ijret.2015.0401036>
24. Molinetti A, Amorim FL, Soares PC, Czelusniak T (2016) Surface modification of AISI H13 tool steel with silicon or manganese powders mixed to the dielectric in electrical discharge machining process. *Int J Adv Manuf Technol* 83:1057–1068. <https://doi.org/10.1007/s00170-015-7613-1>



# Comparison of the Removal Rate in EDM Based on the Mixed Environment



D. R. Abbas, M. A. Lajis, and M. A. Abbas

**Abstract** In the Electrical Discharge Machining (EDM), the impedance of dielectric fluids is an obstacle in the machining of complicated materials. Therefore, the previous researches focused on enhancing these fluids in EDM by adding powder particles, surfactant, or powder and surfactant together. However, these studies have not performed a comparison between the Powder-Mixed Dielectric Fluid (PMDF) and Surfactant-Mixed Dielectric Fluid (SMDF) in EDM environment. Therefore, the present study aims to achieve this comparison on the machining of D2 steel by employing copper electrode, Nano Chromium Particles (NCP), and Span-20. In addition, we investigate the effect of these mixed fluids on the Material Removal Rate (MRR) and Tool Wear Rate (TWR). The increase of pulse-on-time to 30  $\mu$ s at 6 g/L of the maximum level of concentration of NCP did not lead to a simultaneous increase for each of the MRR and TWR in PMDF. However, this experimental environment enhanced these outcomes based on the absorbing and conductivity properties of the NCP. Consequently, this study has attained the best MRR and TWR with PMDF as compared to SMDF.

**Keywords** EDM · Powder-mixed · Span-20 · Material removal rate · Tool wear rate

---

D. R. Abbas · M. A. Lajis · M. A. Abbas (✉)

Faculty of Mechanical and Manufacturing Engineering (FKMP), University Tun Hussein Onn Malaysia (UTHM), 86400 Parit Raja, Johor Bahru, Malaysia  
e-mail: [mohd.a.abbas1981@gmail.com](mailto:mohd.a.abbas1981@gmail.com)

M. A. Lajis · M. A. Abbas

Sustainable Manufacturing and Recycling Technology, Advanced Manufacturing and Materials Center (SMART-AMMC), University Tun Hussein Onn Malaysia (UTHM), 86400 Parit Raja, Johor Bahru, Malaysia

M. A. Abbas

Aeronautical Techniques Engineering Department, Engineering Technical College (ETCN), Al-Furat Al-Awsat Technical University (ATU), Main Hilla-Baghdad Road, 54003 Najaf, Iraq

D. R. Abbas

Iraqi Cement State Company, Ministry of Industry and Minerals, 10044 Baghdad, Iraq

© Springer Nature Singapore Pte Ltd. 2020

S. S. Emamian et al. (eds.), *Advances in Manufacturing Engineering*, Lecture Notes in Mechanical Engineering, [https://doi.org/10.1007/978-981-15-5753-8\\_3](https://doi.org/10.1007/978-981-15-5753-8_3)

## 1 Introduction

It is observed that the complicated materials in the removal operation are more efficient in the environment of Powder-Mixed Electrical Discharge Machining (PMEDM) [1, 2]. In this environment, the plasma channel between the electrode tool and the workpiece is enhanced by employing semiconductor or conductor particles in the dielectric fluids of the EDM machine to overcome the resistance of these fluids easily [3]. Therefore, former studies have invested the PMEDM environment in machining Inconel, AISI steel grades, and other materials possessing high melting point and superior hardness [4]. In Inconel 800, cobalt powder with graphite electrode has achieved the best Material Removal Rate (MRR) at the maximum level of pulse-on-time and pulse current. However, the Tool Wear Rate (TWR) was reduced by prolonging the pulse-off-time with minimizing this current and utilizing Cu-Cr electrode with the same powder [5]. On the other hand, the cutting influence was sensed differently through the used D2 steel in this environment, where the Carbon NanoTubes (CNTs) powder at maximum pulse current with a reasonable amount of this powder led to enhancement of the MRR of this steel [6]. Besides that, it is remarked that both MRR and TWR, during machining the same steel, were improved with the addition of silicon and graphite powders, respectively [7]. This brief description of these achieved studies, in order to improve the performance of the dielectric fluid in EDM by adding powder particles, proved a progress in the machinability of these complicated materials. However, in contrast, other studies presented to improve the machinability of these complicated materials in EDM machine by using another type of additive material, which were represented by surfactant with the dielectric fluid, are very rare. One of these studies has concluded that adding Span-20 to kerosene leads to maximizing the removal rate of SKD61 up to 85% as compared to pure kerosene [8].

Based on the aforementioned information, these mixed fluids in EDM environment have a significant role in enhancing the removal rate for both the workpiece and the electrode tool. However, the diligent pursuit by researchers is targeted on mixing both the surfactant and the powder with dielectric fluid in EDM. This newly mixed fluid has contributed in reducing the surface tension of the Powder-Mixed Dielectric Fluid (PMDF) in the PMEDM environment [9]. Moreover, this fluid has also led to furthering the machinability in the PMEDM field [10]. Hence, the machining surface efficiency is more beneficial by mixing aluminum powder and Span-20, which reaches 60% [11]. On the other hand, the removal rate of Ti alloy and copper electrode was remarkably effectual by employing both Span-20 and graphite powders [12, 13]. Furthermore, this mixed fluid has also achieved the best MRR and TWR for PH17-4 stainless steel and Ti alloy [14–16]. However, the chromium particles with Span-20 have contributed in growing the ability of removal operation for D2 steel in EDM environment [10, 17].

Depending on the available literature survey, the dielectric fluid in the EDM has been boosted by mixing powder, surfactant, or mixing them together. Unfortunately, most studies have not compared these mixed fluids. Therefore, this study focuses

on the effect of both Surfactant-Mixed Dielectric Fluid (SMDF) and Powder-Mixed Dielectric Fluid (PMDF) on the removal rate of AISI D2 steel and the copper electrode in the EDM. In addition, it compares the removal performance of these electrodes in both of these mixed fluids. Consequently, the present study utilized AISI D2 steel, copper electrode, Nano Chromium Particles (NCP), and Span-20 to carry out these aims.

## 2 Experimental Setup and Methodology

The circulation system and the Sodick EDM-Die Sinking AQ55L, illustrated in Fig. 1b, a, respectively, constitute the Integrated High Performance-EDM (IHPEDM) system. The first reason for using this system is the discharging of the insulating tank in Fig. 1c from debris and particles by employing magnetic and cleaning filters, respectively. Furthermore, the blending of Span-20 or NCP separately from the primary container of EDM is considered as another significant reason. Therefore, this system is invested in operating the experimental procedures in the present study.

The mixing materials in Fig. 1d, e for the Nano Chromium Particles (NCP) and Span-20, respectively, are employed to generate both PMDF and SMDF in EDM machine, separately. In both mixed fluids, the machining materials represented by the copper electrode and D2 steel which are illustrated in Fig. 1f, g, respectively,

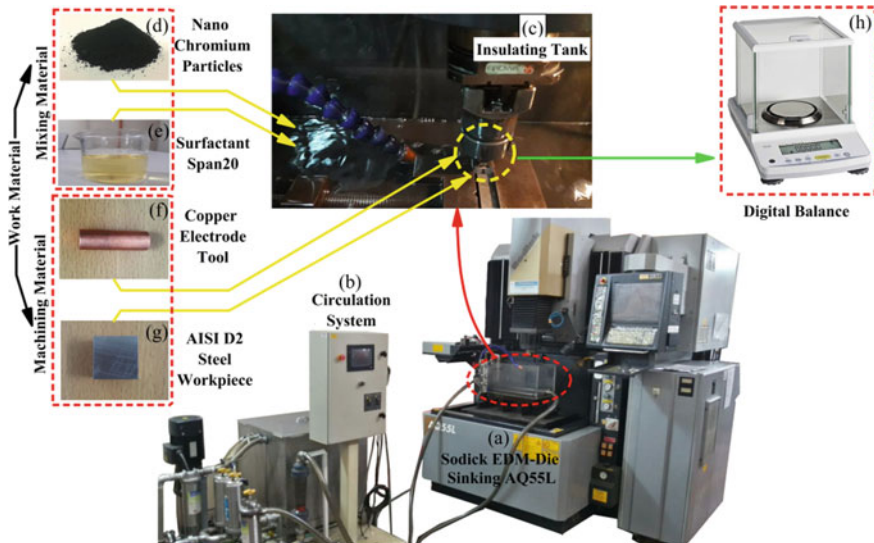


**Fig. 1** Experimental setup and methodology: IHPEDM which consists of **a** EDM machine, **b** Circulation system, and **c** Insulating tank; Work material: Mixing material consists of **d** Nano chromium particles, **e** Surfactant Span-20; Machining material consists of **f** Copper electrode tool and **g** AISI D2 steel workpiece; **h** Digital balance

**Table 1** Specifications of work materials

Item	Material Type	Dimensions	Unit	Chemical composition
Workpiece	AISI D2 steel	Size 7.5 × 7.5 × 10	mm <sup>3</sup>	12.8%Cr, 0.4%Si, 0.35%Mn, 0.03%P, 0.09%Ni, 0.09%Cu, 1.5%C, 0.7%Mo, 0.4% V, 0.01%Co, Fe-Balance
Electrode Tool	Copper	Diameter Ø10	mm	0.06%Zn, 0.01%Pb, 0.01%Si, 0.02%Mn, 0.05%P, 0.02%S, 0.05%Sn, 0.07%Al, 0.03%Ni, 0.05%Sb, 0.07%Fe, Cu-Balance
Powder	Nano chromium	Particle size 70–80	nm	0.08%Si, 0.09%P, 0.01%S, 0.07%Cu, 0.01%C, Cr-Balance

are used to perform the objectives of the present study. The Material Removal Rate (MRR) and Tool Wear Rate (TWR) for both the D2 steel workpiece and the copper electrode are given by [18]:

$$\text{MRR} = (m_{wb} - m_{wa}) / \rho_w t_m \quad (1)$$

$$\text{TWR} = (m_{eb} - m_{ea}) / \rho_e t_m \quad (2)$$

where  $m_{wb}$  and  $m_{eb}$  denote both masses of workpiece and electrode tool before machining operation,  $m_{wa}$  and  $m_{ea}$  indicate both masses of the workpiece and electrode tool after machining operation, and  $\rho_w$  and  $\rho_e$  represent both densities of workpiece and electrode tool, while  $t_m$  is the machining time in IHPEDM system.

Depending on Eqs. (1) and (2), these masses can be specified by using digital balance demonstrated in Fig. 1h. Tables 1 and 2 illustrate the specifications and properties of work material, respectively, which lead to implementing in this experimental study. Moreover, the experimental conditions exhibited in Table 3 are very significant to achieve the aims of this study with IHPEDM system.

### 3 Results and Discussion

Figures 2 and 3 clarify the effect of PMDF and SMDF which result from mixing both kerosene with 2 g/L and 6 g/L of NCP and Span-20, separately, on MRR and TWR at 20 and 30  $\mu$ s. As it is described in Fig. 2, at 2 g/L and 30  $\mu$ s for Span-20 and pulse-on-time, respectively, the MRR is higher than MRR at 2 g/L of NCP at the same pulse-on-time. The absorption property owned by NCP powder leads to minimizing the MRR at 30  $\mu$ s as compared to 20  $\mu$ s of pulse-on-time since these particles have sufficient time at 30  $\mu$ s to absorb a major part of plasma channel energy

**Table 2** Properties of work materials

Property	Copper electrode tool	AISI D2 steel workpiece	Nano chromium powder	Kerosene dielectric fluid	Span-20 surfactant
Density (g/cm <sup>3</sup> )	8.99	7.7	7.16	0.728	1.032
Melting point (°C)	1084	1711	1875	–	–
Specific heat (J/Kg°C)	385.15	412.21	0.46	–	–
Thermal conductivity (W/m °C)	4.01	29	0.67	–	–
Electrical resistivity (μΩ-cm)	1.673	–	0.026	–	–
Electrical conductivity (S/m)	–	–	–	$1.6 \times 10^{-14}$	–
Molecular weight (g/mol)	–	–	–	–	346.47
HLB value	–	–	–	–	8.6
Water content	–	–	–	–	<1.5%
Saponification value	–	–	–	–	158–170
Acid value	–	–	–	–	4–8
Flash point (°C)	–	–	–	–	>110

**Table 3** Experimental conditions applied in IHPEDM

Setting parameters	Symbol	Unit	Description
Pulse current	$I_P$	Amp	10 Amp
Pulse-on-time	$T_{on}$	μs	20 and 30
Pulse-off-time	$T_{off}$	μs	85
Powder concentration	$P_C$	g/L	2 and 6
Surfactant concentration	$S_C$	g/L	2 and 6
Pulse voltage	$V_p$	Volt	120
Flushing rate	$F_r$	mm <sup>3</sup> /h	1500
Machining time	$t_m$	min	30
Electrode polarity	$ve$	–	Negative

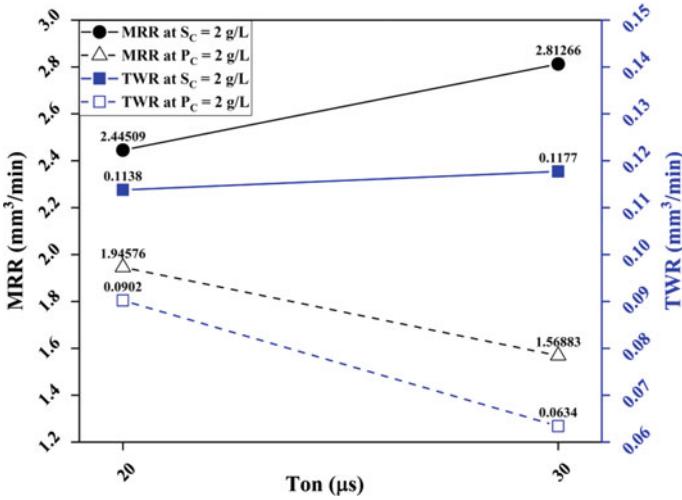


Fig. 2 MRR and TWR versus pulse-on-time ( $T_{on}$ ) at 2 g/L of Span-20 and NCP

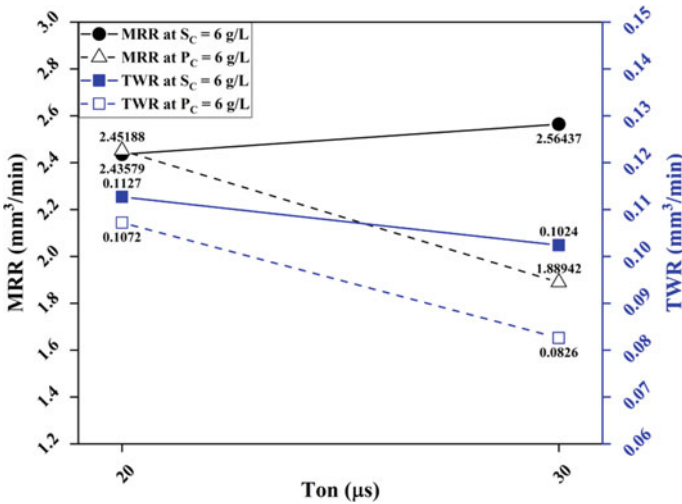


Fig. 3 MRR and TWR versus pulse-on-time ( $T_{on}$ ) at 6 g/L of Span-20 and NCP

[7, 18]. In addition, this same property contributes to the reduction of TWR of the copper electrode under the same conditions.

In Fig. 3, both MRR and TWR in PMDF and SMDF at 20  $\mu s$  and 6 g/L of NCP and Span-20, respectively, have been convergent in performance. But at 30  $\mu s$  and the same concentration of Span-20, MRR in SMDF is lower than the MRR shown in Fig. 2. This behavior is related to the agglomeration phenomenon occurring at melting region, where 6 g/L of Span-20 at 30  $\mu s$  contributes to increasing the explosive

force that leads to decomposing the dielectric fluid and forming carbides in this region. Furthermore, the other carbides that have been deposited on the surface of the electrode tool lead to a partial insulation of this electrode [13, 19–21]. Consequently, this contributes to minimizing TWR in SMDF in Fig. 3 as compared to the case demonstrated in Fig. 2. Meanwhile, MRR outcome from PMDF at 6 g/L of NCP has a similar role to the MRR at 2 g/L of this additive material.

In both cases depicted in Figs. 2 and 3, MRR has decreased based on the absorption behavior aforementioned above. The absorbing property of NCP, here in Fig. 3, is less active at 6 g/L of this powder than 2 g/L, as the surplus energy of plasma channel at this case depends on the conductivity of NCP that is increased by growing the concentration of this powder [22, 23]. Therefore, it is observed that both MRR and TWR in Fig. 3 are augmenting as compared to the outcomes of these responses clarified in Fig. 2.

Based on these outcomes and the interpretations, the variance of the outcomes of MRR and TWR, in both PMDF and SMDF in EDM, has been dependent on three reasons which are explosion force of surfactant, and absorption and conductivity properties. Consequently, PMDF attains the desirable results in the present study because the MRR of D2 steel in this mixed fluid is increased with the growing of both pulse-on-time and powder concentration without being accompanied by an increase in TWR of the copper electrode. Consequently, this behavior of MRR and TWR in SMDF is not remarked.

## 4 Conclusions and Recommendations

The behavior of D2 steel and the copper electrode in mixed fluids in the EDM machine can explain the vital role of these mixed fluids in the machining of these electrodes. Therefore, the present study aimed at presenting logical interpretations of the Material Removal Rate (MRR) and Tool Wear Rate (TWR) of these materials in both of Powder-Mixed Dielectric Fluid (PMDF) and Surfactant-Mixed Dielectric Fluid (SMDF), as well as performing comparison between the performances of these rates in these mixed fluids. Consequently, the present study concluded the following:

1. Span-20 in the SMDF contributes to growing of both MRR of D2 steel and TWR of the copper electrode. Thus, the increasing of Span-20 concentration to 6 g/L with extension pulse-on-time to 30  $\mu$ s contributes to the increasing of MRR and TWR simultaneously.
2. The Nano Chromium Particles (NCP) in PMDF in the EDM contribute to enhancing both MRR and TWR depending on the absorption and conductivity properties of these particles.

Based on these conclusions, the present study recommends that employing the PMDF with EDM machine is the best choice in avoiding the simultaneous increase of the rate of wear and removal in the copper electrode and D2 steel, respectively.

**Acknowledgements** The authors would like to express their profound gratitude and deepest appreciation to the Ministry of Higher Education (MOHE), Malaysia, for funding this project through the Malaysian Technical University Network-Centre of Excellence (MTUN-CoE) and Fundamental Research Grant Scheme (FRGS) through grant numbers of 1496 and 1463. The authors would also like to express their special thanks to Sustainable Manufacturing and Recycling Technology, Advanced Manufacturing and Materials Centre (SMART-AMMC), Universiti Tun Hussein Onn Malaysia (UTHM), and Universiti Teknologi PETRONAS for their support. Furthermore, the authors would like to present a special thanks to the Ministry of Higher Education and Scientific Research in Iraq for academic support for Iraqi students' research.

## References

1. Kumar A, Maheshwari S, Sharma C, Beri N (2010) Research developments in additives mixed electrical discharge machining (AEDM): a state of art review. *Mater Manuf Process* 25:1166–1180. <https://doi.org/10.1080/10426914.2010.502954>
2. Kansal HK, Singh S, Kumar P (2007) Technology and research developments in powder mixed electric discharge machining (PMEDM). *J Mater Process Technol* 184:32–41. <https://doi.org/10.1016/j.jmatprotec.2006.10.046>
3. Erden A, Bilgin S (1981) Role of impurities in electric discharge machining. In: Proceedings of twenty-first international machine tool design research conference, pp 345–350. [https://doi.org/10.1007/978-1-349-05861-7\\_45](https://doi.org/10.1007/978-1-349-05861-7_45)
4. Hu FQ, Zhang H, Zhao WS, Wang ZL, Hu D, Yu Y (2008) Surface properties of 3000 C high melting point material by powder mixed EDM. *Key Eng Mater* 375:143–147. <https://doi.org/10.4028/www.scientific.net/KEM.375-376.143>
5. Kumar S, Dhingra AK, Kumar S (2017) Parametric optimization of powder mixed electrical discharge machining for nickel-based superalloy inconel-800 using response surface methodology. *Mech Adv Mater Mod Process* 3:7. <https://doi.org/10.1186/s40759-017-0022-4>
6. Kumar H (2015) Development of mirror like surface characteristics using nano powder mixed electric discharge machining (NPMEDM). *Int J Adv Manuf Technol* 76:105–113. <https://doi.org/10.1007/s00170-014-5965-6>
7. Batish A, Bhattacharya A, Kumar N (2015) Powder mixed dielectric: an approach for improved process performance in EDM. *Part Sci Technol* 33:150–158. <https://doi.org/10.1080/02726351.2014.947659>
8. Wu KL, Yan BH, Lee J-W, Ding CG (2009) Study on the characteristics of electrical discharge machining using dielectric with surfactant. *J Mater Process Technol* 209:3783–3789. <https://doi.org/10.1016/j.jmatprotec.2008.09.005>
9. Ojha K, Garg RK, Singh KK (2011) Parametric optimization of PMEDM process using chromium powder mixed dielectric and triangular shape electrodes. *J Miner Mater Charact Eng* 10:1087. <https://doi.org/10.4236/jmmce.2011.1011083>
10. Hosni NAJ, Lajis MA (2019) Multi-response optimization of the machining characteristics in electrical discharge machining (EDM) using span-20 surfactant and chromium (Cr) powder mixed. *Materwiss Werksttech* 50:329–335. <https://doi.org/10.1002/mawe.201800204>
11. Wu KL, Yan BH, Huang FY, Chen SC (2005) Improvement of surface finish on SKD steel using electro-discharge machining with aluminum and surfactant added dielectric. *Int J Mach Tools Manuf* 45:1195–1201. <https://doi.org/10.1016/j.ijmactools.2004.12.005>
12. Kolli M, Kumar A (2017) Surfactant and graphite powder-assisted electrical discharge machining of titanium alloy. *Proc Inst Mech Eng Part B J Eng Manuf* 231:641–657. <https://doi.org/10.1177/0954405415579019>
13. Kolli M, Kumar A (2015) Effect of dielectric fluid with surfactant and graphite powder on electrical discharge machining of titanium alloy using Taguchi method. *Eng Sci Technol an Int J* 18:524–535. <https://doi.org/10.1016/j.jestch.2015.03.009>



14. Reddy VV, Valli PM, Kumar A, Reddy CS (2015) Multi-objective optimization of electrical discharge machining of PH17-4 stainless steel with surfactant-mixed and graphite powder-mixed dielectric using Taguchi-data envelopment analysis-based ranking method. *Proc Inst Mech Eng Part B J Eng Manuf* 229:487–494. <https://doi.org/10.1177/0954405414530904>
15. Reddy VV, Kumar A, Valli PM, Reddy CS (2015) Influence of surfactant and graphite powder concentration on electrical discharge machining of PH17-4 stainless steel. *J Brazil Soc Mech Sci Eng* 37:641–655. <https://doi.org/10.1007/s40430-014-0193-4>
16. Kolli M, Adepu K (2014) Influence of span 20 surfactant and graphite powder added in dielectric fluid on EDM of titanium alloy. *Bonfring Int J Ind Eng Manag Sci* 4:62–67. <https://doi.org/10.9756/BIJEEMS.4820>
17. Hosni NAJ, Lajis MA (2018) The influence of Span-20 surfactant and micro-/nano-Chromium (Cr) powder mixed electrical discharge machining (PMEDM) on the surface characteristics of AISI D2 hardened steel. *IOP Conf Ser Mater Sci Eng* 342:12095. <https://doi.org/10.1088/1757-899x/342/1/012095>
18. Baseri H, Sadeghian S (2016) Effects of nanopowder TiO<sub>2</sub>-mixed dielectric and rotary tool on EDM. *Int J Adv Manuf Technol* 83:519–528. <https://doi.org/10.1007/s00170-015-7579-z>
19. Sugunakar A, Jits W, Markandeya R, Kumar A, Reddy VV (2018) Effect of various powders added in to the dielectric fluids on MRR and SR during PMEDM of RENE80. *Int J Pure Appl Math* 118
20. Prakash C, Kansal HK, Pabla BS, Puri S (2016) Multi-objective optimization of powder mixed electric discharge machining parameters for fabrication of biocompatible layer on  $\beta$ -Ti alloy using NSGA-II coupled with Taguchi based response surface methodology. *J Mech Sci Technol* 30:4195–4204. <https://doi.org/10.1007/s12206-016-0831-0>
21. Kumar S, Batra U (2012) Surface modification of die steel materials by EDM method using tungsten powder-mixed dielectric. *J Manuf Process* 14:35–40. <https://doi.org/10.1016/j.jma.2011.09.002>
22. Kolli M, Kumar A (2014) Effect of boron carbide powder mixed into dielectric fluid on electrical discharge machining of titanium alloy. *Int Conf Adv Manuf Mater Eng (AMME 2014)* 5:1957–1965. <https://doi.org/10.1016/j.mspro.2014.07.528> (Elsevier)
23. Talla G, Gangopadhyay S, Biswas CK (2016) Effect of powder-suspended dielectric on the EDM characteristics of Inconel 625. *J Mater Eng Perform* 25:704–717. <https://doi.org/10.1007/s11665-015-1835-0>

# Influence of Projectile Penetration on the Multiple-Layered Target Based on Statistical and Numerical Analysis



O. M. Merzah, M. N. Ibrahim, M. A. Abbas, and M. A. Lajis

**Abstract** One of the significant tests to specify the response of the materials for impacts resulting from the collision is the projectile–target method. The development of this test by the prior studies by simulation has contributed to change the model for enhancing the economic feasibility and predicting the best outcomes. The present work employs the finite element analysis-explicit mode (FEA-EM) and orthogonal array technique (OAT) under velocity 650 m/s to test the double layer for both Al 2024-T3 and Wieldox 700E, separately. To carrying out this study, the projectile utilized models are hemispherical and APM2 with diameters 10 mm and 7.68 mm, respectively. Hence, the main purpose of this study was to predict the measurement of petal prominence and the residual velocity for the projectile. Therefore, the outcomes performed by FEA-EM are invested by analysis of variance (ANOVA) to predict the optimum performance. It is observed that the best prediction of ballistic performance is by Wieldox 700E as compared to Al 2024-T3 since the expanding of petal prominence in Wieldox 700E is less than the expanding occurring by Al 2024-T3. Besides, the residual velocity is reduced for Wieldox 700E as compared to Al 2024-T3. Consequently, the Wieldox 700E is obviously more capable of absorbing than the Al 2024-T3.

**Keywords** Explicit · FEA · OAT · Multiple layer · APM2 7.68

---

O. M. Merzah · M. N. Ibrahim · M. A. Abbas (✉) · M. A. Lajis  
Faculty of Mechanical and Manufacturing Engineering (FKMP), University Tun Hussein Onn Malaysia (UTHM), 86400 Parit Raja, Johor Bahru, Malaysia  
e-mail: [mohd.a.abbas1981@gmail.com](mailto:mohd.a.abbas1981@gmail.com)

M. A. Abbas · M. A. Lajis  
Sustainable Manufacturing and Recycling Technology, Advanced Manufacturing and Materials Center (SMART-AMMC), University Tun Hussein Onn Malaysia (UTHM), 86400 Parit Raja, Johor Bahru, Malaysia

M. A. Abbas  
Aeronautical Techniques Engineering Department, Al-Furat Al-Awsat Technical University (ATU), Engineering Technical College (ETCN), Main Hilla-Baghdad Road,, 54003 Najaf, Iraq

# 1 Introduction

The numerous outcomes based on both projectile shape and the material of it with the multiple-layered target have stimulated the previous researchers to deal with this subject [1]. Therefore, the studies presented in this field focused on the residual velocity and petal forming as significant responses to evaluate the efficiency of the designated target in terms of absorbing the impact effect resulting from a collision between the specific target and the projectile. Accordingly, both experimental and numerical results have contributed to enhancing targets in enduring this type of collision and increasing the durability of the endurance. Consequently, the previous researchers invested these outcomes in the automobile and airplane structures. Therefore, the researchers in this field have strived to use multiple layers with reducing the weight; however, the important challenge that stood up to the researchers was maintaining the properties of multiple targets, while reducing the weight.

In the last decade, the former studies have achieved these interesting points, where the research outcomes led to enhancing these manufacturing fields. Thus, this enhancement contributed to minimizing the damages to automobiles and airplanes resulting from the crashing cases [2]. The projectile–target method is considered as one of the significant tests in evaluating the response for the collision [3], where this testing contributes to reducing the economic cost and predicting the best performance. The investigation implemented on the ballistic resistance of Weldox 700E steel reveals that 12-mm monolithic plate has confirmed a better ballistic performance against ogival projectiles. As this performance has been compared with the multiple-layered target at the same thickness, it has become clarified that the monolithic plate has achieved the best resistance [4, 5]. On the other hand, the experimental and numerical studies that have been performed on Weldox 700E with the APM2 7.68 projectile to specify the resistance of target have proved identically for both of monolithic-layered target and multiple-layered target at above 850 m/s. In other words, 6 mm for both multiple-layered target and 12 mm for monolithic-layered target have the same effect resulting from a collision with the APM2 7.68 projectile [6]. Depending on these outcomes, the ballistic resistance is based on nose shape, projectile mass, impact velocity, a configuration of the plates, and material properties, while the projectile's nose shape and hardness are very necessary to know the failure mechanisms [7].

Besides, other studies have adopted the Lagrangian LS-DYNA simulations for predicting the performance of multiple-layered plate, where it has employed the APM2 projectile with a symmetric mode [5]. The success achieved by this adopted model was through the validation amongst these simulation models with the experimental outputs. However, other researchers have adopted this model with a hemispherical projectile, where it is observed that the energy absorbed by the Aluminum 2024-T3 target depends on the layer utilized in the wing. Hence, these studies proved the influence of nose shape on the ballistic limit [8–10]. In addition, the petal formed, resulting from the collision between the hemispherical projectile and Aluminum

2024-T3 target, proved the acceptability of endurance limit for this projectile. Hence, the petal forming is lower at 600 m/s as compared to 100 m/s [10].

Depending on this brief review, the present study aims to study the influence of projectile penetration on the petal prominence and residual velocity for the target and projectile, respectively, wherein this study employs the optimum data concluded by Bobbili et al. [8]. Besides that, it adopts the comparison amongst the Weldox 700E and Aluminum 2024-T3 presented by Flores-Johnson et al. [11] for the target used in this study. Consequently, these research data are employed to predict the performance of both hemispherical and APM2 projectiles.

## 2 Model Verification and Methodology

Flores-Johnson et al. [11] have presented the numerical outcomes for both Aluminum 2024-T3 and Weldox 700E targets, where they dealt with residual velocity and influence of this velocity on petal-forming stages, while Ibrahim et al. [12] have presented only the effects of petal-forming stages. Thus, these studies only offered behavioral outcomes without adopting the optimum case based on statistical procedures. However, Bobbili et al. [8] have utilized the statistical analysis with the study by Flores-Johnson et al. [11], wherein the statistical procedures in this study adopted the orthogonal array technique (OAT) based on Taguchi method to specify the optimum case. Hence, this study, which was based on the numerical and statistical analysis, was very powerful and presented logical interpretations in the finite element analysis-explicit mode (FEA-EM). In Table 1, the optimum case resulted by Bobbili et al. [8] is observed.

Based on the aforementioned information, the verification that is presented by this study by employing FEA-EM contributed to reducing the error ratio to 2.23 m/s at 0.4 for mesh size. Moreover, this study employed the model of Recht-Ipson [13] demonstrated in Eq. (1) to verify the simulation performed in the present study. Also, Recht-Ipson model has verified the best value at 0.4 for mesh size. Table 2 and Fig. 1 clarify the comparison between the predicted results by FEA-EM and Recht-Ipson models depending on the outcomes of Bobbili et al. [8].

$$v_r = a(v_i^p - v_{bl}^p)^{1/p} \tag{1}$$

**Table 1** Optimum output concluded by Bobbili et al. [8]

Response	Optimum environment	Predicted	Experimental	Error ratio (%ε)
Residual velocity ( $v_r$ )	- 650 m/s impact velocity - Multiple (double)-layered - Target thickness (12 mm)	2.45 m/s	1.78	37%

**Table 2** Verification of Bobbili’s optimum value based on FEA-EM and Recht-Ipson models

Mesh size (mm)	$v_r$ Recht-Ipson model (m/s)	$v_r$ FEA-EM model (m/s)
0.25	2.64	3.40
0.30	2.69	4.13
0.35	2.85	2.50
0.40	2.83	2.23
0.45	2.85	2.64
0.50	2.85	2.40

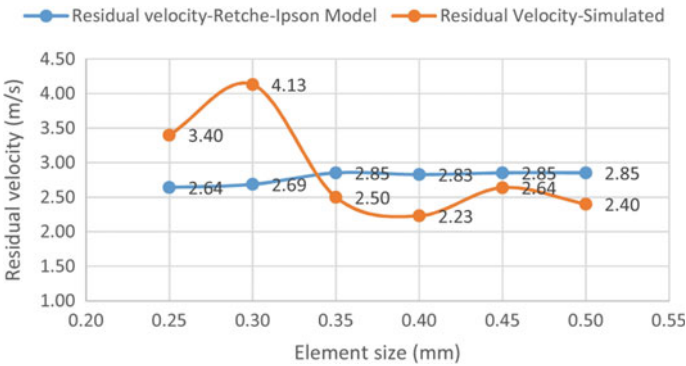


**Fig. 1** Residual velocity based on Recht-Ipson FEA-EM models

where  $a$  is the empirical constants used to best fit the data,  $v_{bl}$  is the ballistic limit,  $v_i$  is the initial impact velocity, and  $P$  is the empirical constant equal to 2. Besides, the original Recht-Ipson model with  $a = m_p/(m_p - m_{pl})$  where  $m_p$  and  $m_{pl}$  are the mass of the projectile and plug, respectively, is noted.

The outcomes of the verification model using FEA-EM have achieved the best values with the experimental value for residual velocity mentioned in Table 1 as compared with Recht-Ipson model. The minimum values performed by FEA-EM are 2.23 and 2.40 for the residual velocity at 0.4 and 0.5 for mesh size. Consequently, FEA-EM has reduced the error ratio to 25.28% as compared with Bobbili et al. [8]. In addition, the present work proposed a hemispherical projectile beside the APM2 projectile adopted by Bobbili et al. [8] and Flores-Johnson et al. [11], where the diameter of this proposed projectile is 10 mm based on the study of Ibrahim et al. [12]. Therefore, the levels of the adopted parameters in the present work can be observed in Table 3.

Both FEA-EM and statistical analysis are used to predict and fit the collision condition, respectively. Furthermore, the optimum environment in Table 1 is utilized in the FEA-EM and the experiment is designated relying on the OAT procedure as depicted in Table 4.

**Table 3** Levels of parameters adopted in FEA-EM

No.	Parameters	Term	Levels	
			(-1)	(+1)
1	Projectile type ( $P_t$ )	A	APM2	Hemispherical
2	Target type ( $T_t$ )	B	Weldox 700E	Aluminum 2024-T3
3	Projectile diameter ( $P_d$ )	C	7.68	10
4	Mesh size ( $M_s$ )	D	0.4	0.5

### 3 Results and Discussion

The objectives of this study were to propose a simplified analytical model, which can predict the residual velocities and petal prominence of projectiles penetrating through layered Al 2024-T3 and Weldox 700E. Table 4 shows the results of penetration in ANSYS-AUTODYN for residual velocity and petal prominence. It has been observed that the residual velocity is higher when the target is Al 2024-T3 and lower when the target is Weldox 700E, which means that the Weldox 700E exhibits a better ballistic resistance than Al 2024-T3. These results are in accordance with the previous studies [11, 14, 15]. In addition, we have noted that the amount of residual velocity not only depends on the type of target, but are also affected by projectile type and projectile diameter as shown in the Pareto chart in Fig. 2. The results of simulation are presented in Table 4.

The ballistic resistance of the Weldox 700E double-layered target is more than when the target from Al 2024-T3, where the increase of the diameter leads to increasing the target’s resistance. The Pareto chart in Fig. 2 is playing a vital role in specifying the significant and insignificant parameters in residual velocity. Relying on Fig. 2, the analysis of variance (ANOVA) achieved on this response eliminates the single and multiple linear (interacted) parameters that are insignificant in the petal prominence. It has been remarked in Table 5 that the R-sq and R-sq(adj) after elimination are 97.02% and 95.04%, respectively. Therefore, the ANOVA has presented an influential and higher predicted performance in the petal forming, where this analysis is compatible with AUTODYN simulation based on correlation values that are mentioned in Table 5. The results of ANOVA for the process parameters are furnished larger F-values, which represent that the variation of the process variable has a large influence on the response measures, i.e., residual velocity and petal prominence. F-values of the process variables are compared with the confidence table. F-values of the process variables on the residual velocity are shown in Table 5. The optimization of residual velocity based on statistical analysis can be observed in Fig. 3. Therefore, Fig. 4 reflects the optimum case predicted for residual velocity based on Fig. 3.

Depending on the aforementioned information, Eq. (2) illustrates the regression (fitted) model based on ANOVA and Pareto chart for the residual velocity.

**Table 4** Number of trials adopted in FEA-EM based on OAT

Run No.	Projectile type	Target type	Projectile diameter	Mesh size	Predicted residual velocity ( $v_r$ ) m/s	Petal prominence ( $\delta$ ) mm
1	APM2	Weldox 700E	7.68	0.4	2.23	6.80
2	APM2	Weldox 700E	7.68	0.5	2.40	6.92
3	APM2	Al 2024-T3	10	0.4	4.09	9.14
4	APM2	Al 2024-T3	10	0.5	5.34	9.17
5	APM2	Weldox 700E	10	0.4	3.86	8.75
6	APM2	Weldox 700E	10	0.5	4.53	9.06
7	APM2	Al 2024-T3	7.68	0.4	3.79	7.05
8	APM2	Al 2024-T3	7.68	0.5	3.71	6.90
9	Hemispherical	Weldox 700E	10	0.4	3.63	8.49
10	Hemispherical	Weldox 700E	10	0.5	2.22	8.67
11	Hemispherical	Al 2024-T3	7.68	0.4	3.71	5.84
12	Hemispherical	Al 2024-T3	7.68	0.5	4.18	6.16
13	Hemispherical	Weldox 700E	7.68	0.4	3.40	6.57
14	Hemispherical	Weldox 700E	7.68	0.5	3.81	6.53
15	Hemispherical	Al 2024-T3	10	0.4	4.61	7.80
16	Hemispherical	Al 2024-T3	10	0.5	3.64	7.73

$$V_r = 3.7087 + 0.4487 B + 0.3050 C - 0.4062 AC - 0.2313 AD + 0.2338 ABC - 0.3300 ACD \tag{2}$$

It has been found that the projectile diameter plays a major role in its effect on the petal prominence, whereas the petal prominence is lower when the projectile diameter 7.68 mm comes in the effect after that projectile type. The petal prominence is larger when the projectile is APM2 and lower when the projectile is hemispherical. Pareto

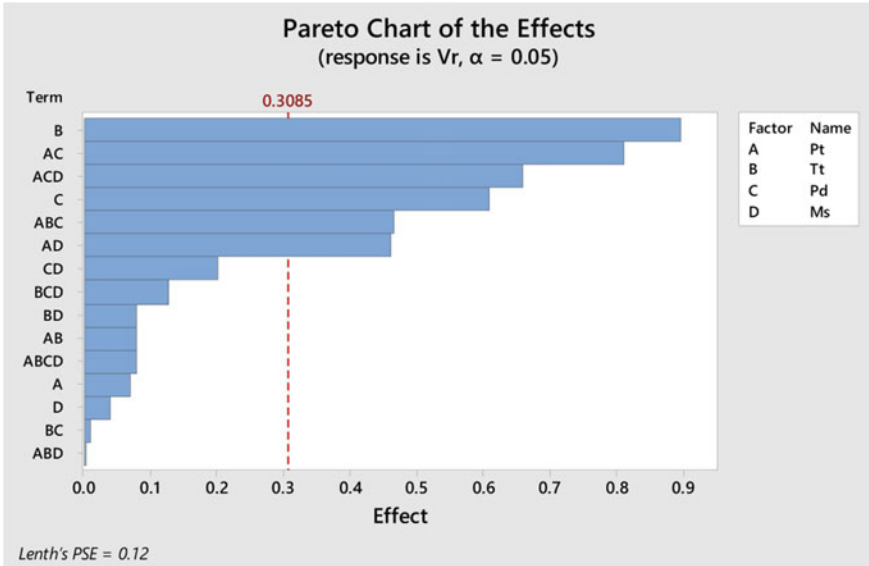


**Fig. 2** Pareto chart before elimination in residual velocity

**Table 5** ANOVA for residual velocity after elimination of insignificant parameters

Source	DoE	Adj SS	Adj MS	F-Value	P-Value
Model	6	10.8233	1.80388	48.86	< 0.05
Linear	2	4.7104	2.35521	63.79	< 0.05
B	1	3.2220	3.22203	87.27	< 0.05
C	1	1.4884	1.48840	40.31	< 0.05
2-way interactions	2	3.4962	1.74812	47.35	< 0.05
AC	1	2.6406	2.64062	71.52	< 0.05
AD	1	0.8556	0.85562	23.18	< 0.05
3-way interactions	2	2.6166	1.30831	35.44	< 0.05
ABC	1	0.8742	0.87423	23.68	< 0.05
ACD	1	1.7424	1.74240	47.19	< 0.05
Error	9	0.3323	0.03692		
Total	15	11.1156			
S	0.192144				
<i>Correlation value</i>					
R-sq	97.02%				
R-sq(adj)	95.04%				



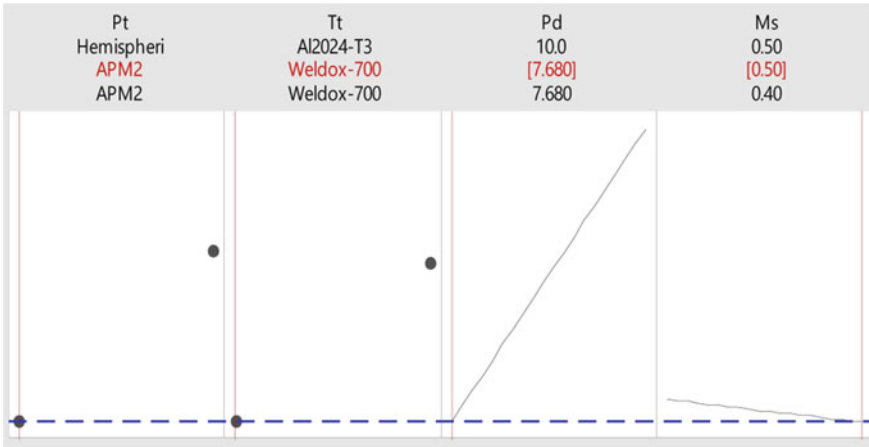


Fig. 3 Optimum parameters predicted based on statistical analysis for residual velocity

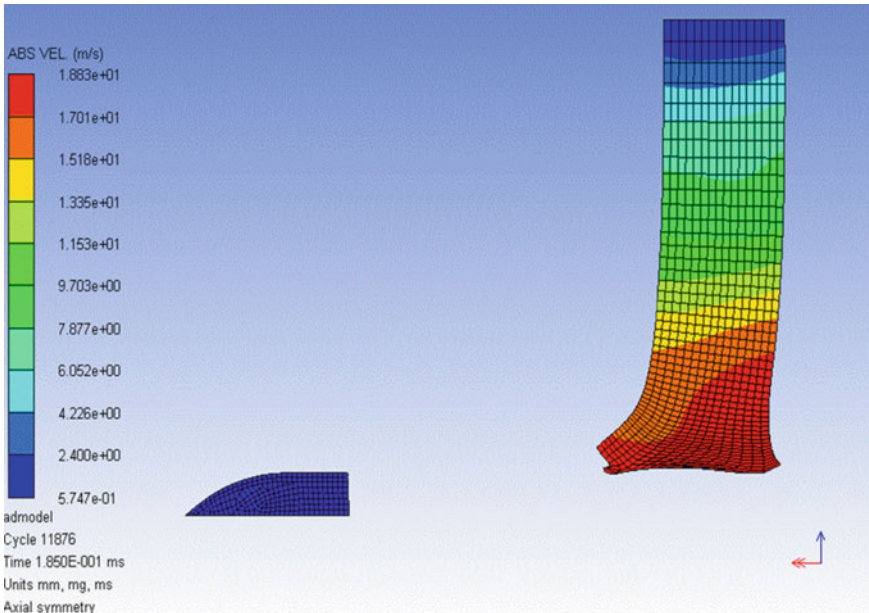


Fig. 4 Optimum case for residual velocity

chart shows us how much the parameters are influential as shown in Fig. 5, which shows the prediction of any variables which has an effect on the petal prominence.

The analysis of variance (ANOVA) achieved on this response eliminates the single and multiple linear (interacted) parameters that are insignificant in the petal prominence. It has been remarked in Table 6 that the R-sq and R-sq(adj) after elimination

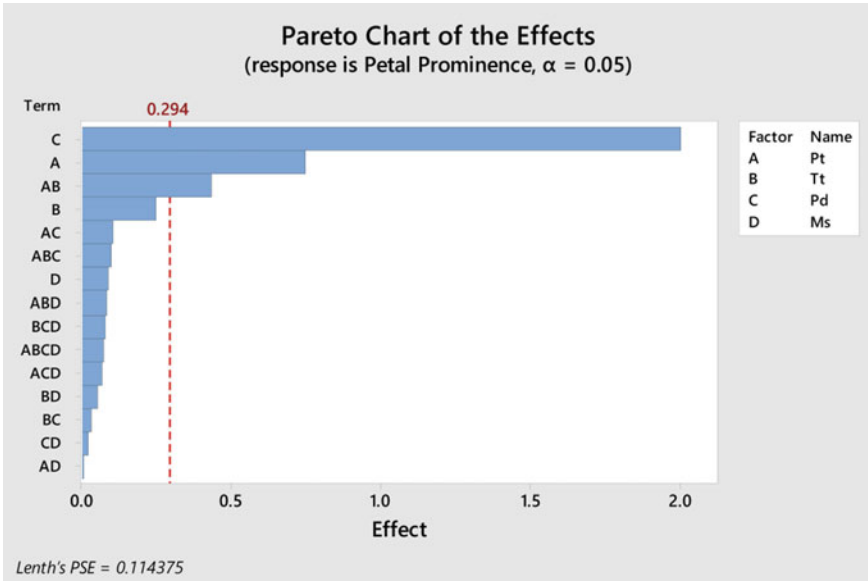


Fig. 5 Pareto chart before elimination in petal prominence

Table 6 ANOVA for petal prominence after the elimination of the insignificant parameters

Source	DoE	Adj SS	Adj MS	F-value	P-value
Model	3	19.0783	6.3594	159.63	< 0.05
Linear	2	18.3301	9.1650	230.06	< 0.05
A	1	2.2500	2.2500	56.48	< 0.05
C	1	16.0801	16.0801	403.64	< 0.05
2-way Interactions	1	0.7482	0.7482	18.78	< 0.05
AB	1	0.7482	0.7482	18.78	< 0.05
Error	12	0.4780	0.0398		
Total	15	19.5564			
S	0.199593				
<i>Correlation value</i>					
R-sq	97.56%				
R-sq(adj)	96.94%				

are 97.56% and 96.94%, respectively. Therefore, the ANOVA has presented an influential and higher predicted performance in the petal forming and this analysis is compatible with AUTODYN simulation based on correlation values that were aforementioned in Table 4. The results of ANOVA for the process parameters are furnished larger F-values, which represent that the variation of the process variable has a large

influence on the response measures, i.e., residual velocity and petal prominence. F-values of the process variables are compared with the confidence table. F-values of the process variables on the residual velocity are shown in Table 4; Figs. 6 and 7.

Depending on the aforementioned data, Eq. (3) illustrates the regression (fitted) model based on ANOVA and Pareto chart for the petal prominence:

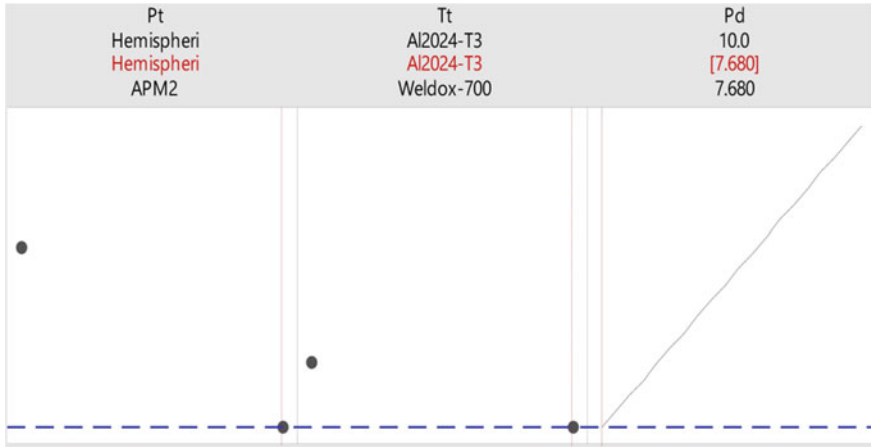


Fig. 6 Optimum parameter predicted based on statistical analysis for petal prominence

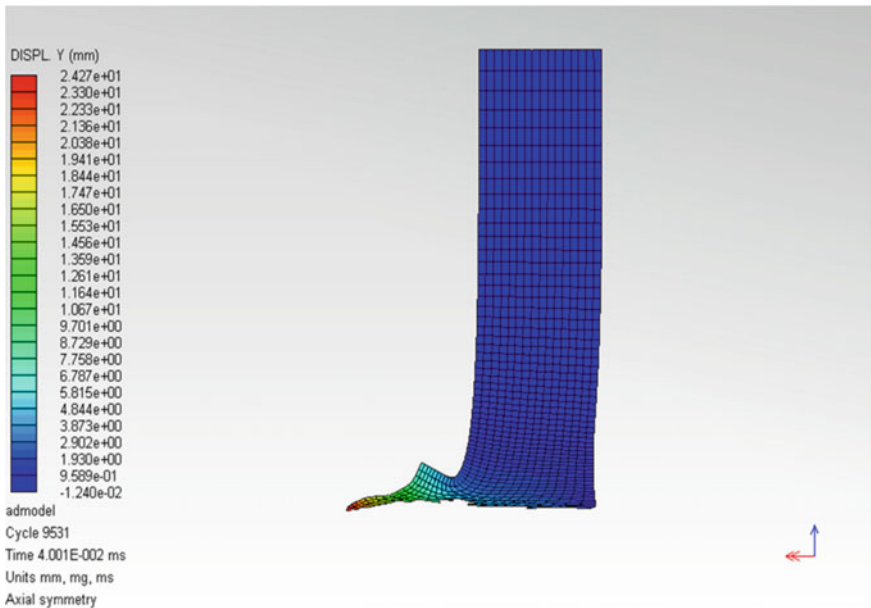


Fig. 7 Optimum case for petal prominence

$$\delta = 7.5988 - 0.3750A + 1.0025C - 0.2163AB \quad (3)$$

## 4 Conclusions

The importance of input variable of ballistic Weldox 700E and Aluminum 2024-T3 performance has been studied. An experimental design was adopted to evaluate the effect on response characteristics of input variables. The conclusions are as follows:

1. Numerical simulations demonstrated the capability of the model to predict the ballistic behavior of Weldox 700E and Al 2024-T3.
2. Numerical results show that Weldox 700E has a better ballistic performance than Al 2024-T3 when compared with similar thicknesses; therefore, Al 2024-T3 plates have to be thicker than Weldox 700E plates to exhibit this superior performance, which could be limiting for design purposes. The statistical analysis enhances the numerical analysis presented by AUTODYN.

## References

1. Senthil K, Iqbal MA, Arindam B, Mittal R, Gupta NK (2017) Ballistic resistance of 2024 aluminium plates against hemispherical, sphere and blunt nose projectiles. *Thin-Walled Struct*
2. Lundin SJ, Frankenberger CE, Mueller RB (2005) Uncontested engine debris fire mitigation test: fuselage-mounted engines
3. Kœchlin P, Potapov S (2009) Classification of soft and hard impacts—application to aircraft crash. *Nucl Eng Des* 239(4):613–618
4. Dey S, Børvik T, Teng X, Wierzbicki T, Hopperstad OS (2007) On the ballistic resistance of double-layered steel plates: an experimental and numerical investigation. *Int J Solids Struct* 44(20):6701–6723
5. Børvik T, Dey S, Clausen AH (2009) Perforation resistance of five different high-strength steel plates subjected to small-arms projectiles. *Int J Impact Eng* 36(7):948–964
6. Teng X, Wierzbicki T, Huang M (2008) Ballistic resistance of double-layered armor plates. *Int J Impact Eng* 35(8):870–884
7. Corran RSJ, Shadbolt PJ, Ruiz C (1983) Impact loading of plates—an experimental investigation. *Int J Impact Eng* 1(1):3–22
8. Bobbili R, Paman A, Madhu V, Gogia AK (2014) The effect of impact velocity and target thickness on ballistic performance of layered plates using Taguchi method. *Mater Des* 53:719–726
9. Børvik T, Hopperstad OS, Pedersen KO (2010) Quasi-brittle fracture during structural impact of AA7075-T651 aluminium plates. *Int J Impact Eng* 37(5):537–551
10. Jun LIU, Yulong LI, Xiancheng YU, Xiaosheng GAO, Zongxing LIU (2018) Design of aircraft structures against threat of bird strikes. *Chin J Aeronaut*
11. Flores-Johnson EA, Saleh M, Edwards L (2011) Ballistic performance of multi-layered metallic plates impacted by a 7.62-mm APM2 projectile. *Int J Impact Eng* 38(12):1022–1032
12. Ibrahim MN, Siswanto WA, Zaidi AMA (2014) Numerical study on failure process of aluminium plate subjected to normal impact by hemispherical projectiles. *Appl Mech Mater* 660:598–602

13. Recht R, Ipson TW (1963) Ballistic perforation dynamics. *J Appl Mech* 30(3):384–390
14. Venkataraman R, Elbella A, Potluri KS (2005) Numerical investigation on the impact strength properties of weldox steel, pure copper, 2024-T3 aluminum alloy, Ti-6Al-4V titanium alloy and some composites. In: ASME 2005 international design engineering technical conferences and computers and information in engineering conference, pp 467–476
15. Mohotti D, Ngo T, Raman SN, Mendis P (2015) Analytical and numerical investigation of polyurea layered aluminium plates subjected to high velocity projectile impact. *Mater Des* 82:1–17

# Fractal Wear Behaviour of Gear Tooth: A Review



Enesi Y. Salawu, A. O. Inegbenebor, O. O. Ajayi, Stephen A. Akinlabi,  
and Esther T. Akinlabi

**Abstract** Fractal wear behaviour of gears refers to failure mode of gears as a result of contact mechanics, which occurs while in application. Tooth-to-tooth surface damage usually ensues as a result of variation in excitation energy of the gear. This study therefore investigated the nature of fractal wear encountered by gear tooth with a focus on general fatigue wear, temperature-induced wear and different models for wear predictions. The result of the study showed that tooth surface damage such as fatigue, pitting corrosion and scuffing causes gear failure. Failure due to bending fatigue was observed to contribute to the maximum deflection of the gear tooth during rotation, thus resulting in excessive noise and vibration. Further to this, it was possible to predict the material removal rate of a failed gear using some of the highlighted empirical methods in the study. Based on these models, it will be possible to predict the nature of wear on gear tooth surface and use it during gear design.

**Keywords** Fractal wear · Gear tooth · Fatigue failure · Vibration

## 1 Introduction

The wear of gear tooth is regarded as a major factor to overall component failure and improvement in the mechanical properties of gear tooth to mitigate or reduce wear, which is important for reliability and availability of machines. Thus, it is necessary to assess the nature of gear failures in order to improve the design. Tooth wear in gears has been associated with misalignment at the tooth profile causing

---

E. Y. Salawu (✉) · A. O. Inegbenebor · O. O. Ajayi · S. A. Akinlabi · E. T. Akinlabi  
Department of Mechanical Engineering, Covenant University, P.M.B 1023, Ota, Ogun State,  
Nigeria  
e-mail: [enesi.salawu@covenantuniversity.edu.ng](mailto:enesi.salawu@covenantuniversity.edu.ng)

S. A. Akinlabi · E. T. Akinlabi  
Department of Mechanical Engineering Science, University of Johannesburg, Johannesburg,  
South Africa

S. A. Akinlabi  
Department of Mechanical Engineering, Walter Sisulu University, Mthatha, South Africa

excessive noise and vibration resulting in eventual failure [1]. Miler et al. [2] noted that one major cause of the gear tooth misalignment is the variation in the profile shift, which introduces a stress factor that affects the optimal efficiency of the gear component. Although the profiles are usually specified and designed into the product during manufacturing, they pose a significant wear behaviour due to the alterations during manufacturing in order to meet the satisfaction of the customers [3]. This will cause radial and hoop stress along the tooth leading to crack initiation on the gear surface asperities and the tooth roots of the gear [4–6]. Despite numerous efforts by gear designers to predict wear behaviour of the gears using various tribo-dynamic models, the variation in speed of gears has remained a major factor to gear designers [7, 8]. More so, accuracy in wear detection and diagnostic approach has become a major problem at the initial stage of gear failure, thereby mitigating the use of numerical and experimental investigations of the increased tooth wear and acoustic emission monitoring devices [9–11]. Further to this, it was reported by Kumar et al. [12] that pitting occurred in gears as a result of increased rolling with sliding motion. The variation in load sharing contributed to gear deflections, which lead to increase in frictional loss along the gear tooth tip [13, 14]. In turn, the loss in frictional power can be increased by the surface roughness along the gear surface in mesh, thus making the oil film less effective in reducing wear [15]. However, there is an extent to which smooth gear surface is affected by surface roughness and once the grinding surface roughness is not well guided during production, it affects the profile of the involute [16, 17]. Based on this statement, it is worthy of noting that most gear failures are associated with error during the manufacturing process. For instance, gear shapers pose geometric and kinematic errors during gear shaping process, which affect the accuracy when compared to standards and cause excessive mesh stiffness that can affect the dynamic action of the gear system [18–20]. The variation in the mesh stiffness increases the transmission error between a pair of gear in mesh, thus increasing the torsional effects at the surface of the gears and leading to low performance during operation [21–25]. According to Jolivet et al. [26], the geometry of a finished gear tooth has an effect on the acoustic emission during operation. This will enable a gear specialist to measure the wear behaviour of the gear both in lubrication condition and in dry working condition in order to determine its optimal performance. Inaccurate finishing in tooth geometry causes excessive noise, vibration and eventual micropits on the surface asperities resulting in tooth deformation [27–30]. In an attempt to reduce wear and improve on gear performance, as well as durability, empirical models have been developed to study the dynamic characteristics of gears in mesh. For instance, Ni et al. [31] employed a numerical approach to improve the mesh behaviour of a bevel gear. However, the high-speed motion in bevel gear transmission was not considered and this can result in reduced bearing capacity of gear tooth surface, but studies have shown that gears of this type will not function well in some applications, which require high pressure due to increased frictional loss and scuffing failure [32–34]. In radial loads, lubricant temperature played a major role in the wear behaviour of the gear system [35]. Many experimental attempts have been employed in the treatment of gears in order to reduce wear but still left with great shortcomings. In the light of this, shot peening

was adopted to improve the fatigue life of steel gears by Lv et al. [36]. However, the variation in speed and load still remains a major problem during fault detection [37, 38]. Although it was possible to detect faults through the interpretation of the data obtained from the dynamic signals, validation of the detected faults still remains a great challenge [39, 40].

## 2 Critical Problems Associated with Gear Wear Prediction Models

The frequent transmission error occurring during gear meshing has necessitated the application of several engineering models to predict the gear performance and the wear behaviour. Basically, the variation in impact load between meshing tooth can result in bending fatigue and pitting on the working surface. Although it was possible to predict the surfaces or teeth that are missing during operation using some simple empirical models, however, the failed gear tooth will show some evidence of material removal causing distortions on the involute profile. Models to predict this material removal rate are quite not easy to develop [41]. To this end, model development will need critical analysis of the thermal stress on the contact surface by considering the various points of acoustic emissions causing pitting at the tooth surfaces, which make the material susceptible to eventual deformation before adequate prediction of material removal rate can be ascertained [42–46]. Morales-Espejel and Gabelli [47] proposed a model for analysing the fatigue life of gears based on the load-carrying capacity of the machine. The model adopted a Weibull method to analyse the strength of the material and the Lundberg–Palmgren principle to investigate the load-bearing capacities. However, transmission error reduction requires a good surface finish and accurate microgeometry during gear manufacturing. The pressure distribution during contact is also a factor to surface fatigue prediction, which becomes a major challenge, especially in production of gears that have non-circular shape [48–52]. Technically, the developed model was possible for backlash reduction, especially on worm wheel gears, but to what extent would this improve the optimal working efficiency of the gear remains a major problem, unless the complex nature of the gear tooth kinematic geometry is well understood, which is a function of the nonlinear and acoustic behaviours of the gear system [53–57]. Based on this, Dhamande and Chaudhari [58] developed a statistical model for diagnosing the vibration of gears on the basis of speed and load condition in order to predict fatigue on the surfaces of the gear tooth. This is limited by the type of contact stress causing fatigue failure due to the fact that it is impossible to identify the stress in real-life situation [59]. More so, studies have revealed that simulations or experiments would give a better result because the parameters for vibration monitoring can be controlled overtime; however, in real-life applications, operation conditions are prone to these errors, thus making it impossible to get the exact point of stress causing incessant fatigue failure. In addition,



complex mechanism of operation of the gear component limits the chances of fundamental fatigue, which causes the fracture of the tooth surfaces [60–63]. A number of researches have been carried out on the way to predict failures in gears by synchronizing the gear components with gear monitoring devices. For instance, Palermo et al. [64] suggested that a digital encoder can be integrated into the system to measure the transmission error during vibration. Besides, Li et al. and Ren et al. [65, 66] reported that angular displacement of gears during operation causes gear deflection along the path of travel and this will result in variation in the meshing mechanism of the gear. The studies further proposed that this problem can be monitored using angular displacement sensor to detect faults. Obviously, data obtained from angular signals are limited by variation in the speed of the machine and dynamic responses of the rotary component [67]. Reduction in degree of freedom and accurate gear mesh simulation might be of interest in reducing the surface fatigue [68].

### 3 Temperature-Induced Gear Wear

Heat generation exists at the interface of meshing teeth due to increased torque transmission, which constitutes a temperature zone, which can be referred to as bulk and flash temperature point on the gear tooth [69]. It was possible to say that the heat flux distribution along the path of contact induces thermal stress on the material resulting in thermal failure of the gear tooth [70]. The unsteady state temperature distribution can result in frictional heat generation and increased temperature rise on the gear tooth surface, which eventually reduces the transmission efficiency [71]. According to Castro and Seabra [72], the viscosity of the oil is a function of temperature and a coefficient of friction between a pair of gears in mesh. This, however, affects the scuffing load capacity of the gears. Bulk flash temperature variation is usually directed to the vertical tooth surface, which reduces transmission efficiency and increases the thermal deformation at the meshing interface [73, 74]. More so, the flash temperature at the tooth surfaces of gears can be predicted using a nonlinear model, which can estimate the temperature of the tooth overtime that can cause the surface deformation; thus, temperature is suitable for monitoring the performance of the gear, especially when elastohydrodynamic technique is used [75–80]. Thus, it was needful to say that temperature formed a dominant parameter in analysing fatigue failures of gears [81].

### 4 Conclusion

In the design of power transmissions, the major factors, which affect the system when in application, are noise and vibration emission. The variation in the transmission error distribution has a major impact on the noise behaviour. This study has shown that the noise emission and temperature flash are associated with transmission error

due to gear excitation. Further investigation into the material failure of gears, the chemical composition, strength and surface fracture showed that fatigue is one major factor, which usually leads to gear tooth failure. Thus, the outcome of this study can be adopted to improve on the gear tooth design.

**Acknowledgements** The authors would like to thank the management of Covenant University for the partial sponsorship of this research.

## References

1. Sekar RP, Sathishkumar R (2017) Enhancement of wear resistance on normal contact ratio spur gear pairs through non-standard gears. *Wear* 380:228–239
2. Miler D, Lončar A, Žeželj D, Domitran Z (2017) Influence of profile shift on the spur gear pair optimization. *Mech Mach Theory* 117:189–197
3. Karpuschewski B, Beutner M, Köchig M, Härtling C (2017) Influence of the tool profile on the wear behaviour in gear hobbing. *CIRP J Manuf Sci Technol* 18:128–134
4. Hu Z, Mao K (2017) An investigation of misalignment effects on the performance of acetal gears. *Tribol Int* 116:394–402
5. Salawu EY, Ajayi OO, Olatunji OO (2015) Theoretical modelling of thermal-hoop stress around the tooth of a spur gear in a filler machine. *J Multidiscip Eng Sci Technol (JMEST)* 2(2):1635–1640
6. Salawu EY, Okokpujie IP, Ajayi OO, Agarana MC (2018) Analytical technique for the determination of hoop stress and radial stress on the tooth spur gear under vertical loading in a food packaging machine
7. Ouyang T, Huang H, Zhang N, Mo C, Chen N (2017) A model to predict tribo-dynamic performance of a spur gear pair. *Tribol Int* 116:449–459
8. Li S, Anisetti A (2017) A tribo-dynamic contact fatigue model for spur gear pairs. *Int J Fatigue* 98:81–91
9. Brethee KF, Zhen D, Gu F, Ball AD (2017) Helical gear wear monitoring: modelling and experimental validation. *Mech Mach Theory* 117:210–229
10. Sharma RB, Parey A, Tandon N (2017) Modelling of acoustic emission generated in involute spur gear pair. *J Sound Vib* 393:353–373
11. Sánchez MB, Pleguezuelos M, Pedrero JI (2017) Approximate equations for the meshing stiffness and the load sharing ratio of spur gears including hertzian effects. *Mech Mach Theory* 109:231–249
12. Kumar P, Hirani H, Agrawal A (2017) Fatigue failure prediction in spur gear pair using AGMA approach. *Mater Today Proc* 4(2):2470–2477
13. Diez-Ibarbia A, Fernandez-del-Rincon A, de-Juan A, Iglesias M, Garcia P, Viadero F (2017) Frictional power losses on spur gears with tip reliefs. The load sharing role. *Mech Mach Theory* 112:240–254
14. Diez-Ibarbia A, Fernandez-del-Rincon A, de-Juan A, Iglesias M, Garcia P, Viadero F (2018) Frictional power losses on spur gears with tip reliefs. The friction coefficient role. *Mech Mach Theory* 121:15–27
15. Huang K, Xiong Y, Wang T, Chen Q (2017) Research on the dynamic response of high-contact-ratio spur gears influenced by surface roughness under EHL condition. *Appl Surf Sci* 392:8–18
16. Clarke A, Jamali HU, Sharif KJ, Evans HP, Frazer R, Shaw B (2017) Effects of profile errors on lubrication performance of helical gears. *Tribol Int* 111:184–191
17. Wang Y, Liu Y, Chu X, He Y, Zhang W (2017) Calculation model for surface roughness of face gears by disc wheel grinding. *Int J Mach Tools Manuf* 123:76–88

18. Khusainov RM, Khaziev RR (2017) Mathematical model for assessing the accuracy of processed gears on gear shaping machines. *Proc Eng* 206:1087–1092
19. Saxena A, Chouksey M, Parey A (2017) Effect of mesh stiffness of healthy and cracked gear tooth on modal and frequency response characteristics of geared rotor system. *Mech Mach Theory* 107:261–273
20. Dogruer CU, Pirsoltan AK (2017) Active vibration control of a single-stage spur gearbox. *Mech Syst Signal Process* 85:429–444
21. Barrios MLR, Montero FEH, Mancilla JCG, Marín EP (2017) Application of lock-in amplifier on gear diagnosis. *Measurement* 107:120–127
22. Yu W, Mechefske CK, Timusk M (2017) The dynamic coupling behaviour of a cylindrical geared rotor system subjected to gear eccentricities. *Mech Mach Theory* 107:105–122
23. Karpuschewski B, Beutner M, Koehrig M, Wengler M (2017) Cemented carbide tools in high speed gear hobbing applications. *CIRP Ann* 66(1):117–120
24. Singh PK, Singh AK (2017) An investigation on the effects of the various techniques over the performance and durability of polymer gears. *Mater Today Proc* 4(2):1606–1614
25. Ramanjaneyulu S, Suman KNS, Kumar SP, Babu VS (2017) Design and development of graphene reinforced acetal copolymer plastic gears and its performance evaluation. *Mater Today Proc* 4(8):8678–8687
26. Jolivet S, Mezghani S, El Mansori M, Vargiolu R, Zahouani H (2017) Experimental study of the contribution of gear tooth finishing processes to friction noise. *Tribol Int* 115:70–77
27. Mallipeddi D, Norell M, Sosa M, Nyborg L (2017) Influence of running-in on surface characteristics of efficiency tested ground gears. *Tribol Int* 115:45–58
28. Kimme S, Bauer R, Drossel WG, Putz M (2017) Simulation of error-prone continuous generating production processes of helical gears and the influence on the vibration excitation in gear mesh. *Proc CIRP* 62:256–261
29. Garambois P, Donnard G, Rigaud E, Perret-Liaudet J (2017) Multiphysics coupling between periodic gear mesh excitation and input/output fluctuating torques: application to a roots vacuum pump. *J Sound Vib* 405:158–174
30. Xiao H, Zhou X, Liu J, Shao Y (2017) Vibration transmission and energy dissipation through the gear-shaft-bearing-housing system subjected to impulse force on gear. *Measurement* 102:64–79
31. Ni G, Zhu C, Song C, Du X, Zhou Y (2017) Tooth contact analysis of crossed beveloid gear transmission with parabolic modification. *Mech Mach Theory* 113:40–52
32. Yoon Y, Park BH, Shim J, Han YO, Hong BJ, Yun SH (2017) Numerical simulation of three-dimensional external gear pump using immersed solid method. *Appl Therm Eng* 118:539–550
33. Nutakor C, Kłodowski A, Sapanen J, Mikkola A, Pedrero JI (2017) Planetary gear sets power loss modeling: application to wind turbines. *Tribol Int* 105:42–54
34. Wang Y, Tang W, Chen Y, Wang T, Li G, Ball AD (2017) Investigation into the meshing friction heat generation and transient thermal characteristics of spiral bevel gears. *Appl Therm Eng* 119:245–253
35. Benedetti M, Fontanari V, Torresani E, Girardi C, Giordanino L (2017) Investigation of lubricated rolling sliding behaviour of WC/C, WC/C-CrN, DLC based coatings and plasma nitriding of steel for possible use in worm gearing. *Wear* 378:106–113
36. Lv Y, Lei L, Sun L (2017) Effect of microshot peened treatment on the fatigue behavior of laser-melted W6Mo5Cr4V2 steel gear. *Int J Fatigue* 98:121–130
37. Feng K, Wang K, Ni Q, Zuo MJ, Wei D (2017) A phase angle based diagnostic scheme to planetary gear faults diagnostics under non-stationary operational conditions. *J Sound Vib* 408:190–209
38. Aouabdi S, Taibi M, Bouras S, Boutasseta N (2017) Using multi-scale entropy and principal component analysis to monitor gears degradation via the motor current signature analysis. *Mech Syst Signal Process* 90:298–316
39. Baron P, Kočiško M, Blaško L, Szentivanyi P (2017) Verification of the operating condition of stationary industrial gearbox through analysis of dynamic signal, measured on the pinion bearing housing. *Measurement* 96:24–33

40. Parra J, Vicuña CM (2017) Two methods for modeling vibrations of planetary gearboxes including faults: comparison and validation. *Mech Syst Signal Process* 92:213–225
41. Mark WD, Isaacson AC, Wagner ME (2019) Transmission-error frequency-domain-behavior of failing gears. *Mech Syst Signal Process* 115:102–119
42. Singh PK, Singh AK (2018) An investigation on the thermal and wear behavior of polymer based spur gears. *Tribol Int* 118:264–272
43. Mehta G, Somani M, Babu TN, Watts T (2018) Contact stress analysis on composite spur gear using finite element method. *Mater Today Proc* 5(5):13585–13592
44. Sharma RB, Parey A (2018) Modelling of acoustic emission generated due to pitting on spur gear. *Eng Fail Anal* 86:1–20
45. Morales-Espejel GE, Rycerz P, Kadiric A (2018) Prediction of micropitting damage in gear teeth contacts considering the concurrent effects of surface fatigue and mild wear. *Wear* 398:99–115
46. Singh AK (2018) Noise emission from functionally graded materials based polypropylene spur gears—a tribological investigation. *Mater Today Proc* 5(2):8199–8205
47. Morales-Espejel GE, Gabelli A (2018) A model for gear life with surface and subsurface survival: tribological effects. *Wear* 404:133–142
48. Petare AC, Jain NK (2018) On simultaneous improvement of wear characteristics, surface finish and microgeometry of straight bevel gears by abrasive flow finishing process. *Wear* 404:38–49
49. Zhou C, Wang H (2018) An adhesive wear prediction method for double helical gears based on enhanced coordinate transformation and generalized sliding distance model. *Mech Mach Theory* 128:58–83
50. Zheng F, Xinghui H, Hua L, Zhang M (2018) Design and manufacture of new type of non-circular cylindrical gear generated by face-milling method. *Mech Mach Theory* 122:326–346
51. Ouyang T, Huang H, Zhou X, Pan M, Chen N, Lv D (2018) A finite line contact tribo-dynamic model of a spur gear pair. *Tribol Int* 119:753–765
52. Tong D, Gu J, Totten GE (2018) Numerical investigation of asynchronous dual-frequency induction hardening of spur gear. *Int J Mech Sci* 142:1–9
53. Kacalak W, Majewski M, Budniak Z (2018) Innovative design of non-backlash worm gear drives. *Arch Civil Mech Eng* 18(3):983–999
54. Peng Y, Zhao N, Zhang M, Li W, Zhou R (2018) Non-Newtonian thermal elastohydrodynamic simulation of helical gears considering modification and misalignment. *Tribol Int* 124:46–60
55. Ma Z, Luo Y, Wang Y, Mao J (2018) Geometric design of the rolling tool for gear roll-forming process with axial-infeed. *J Mater Process Technol* 258:67–79
56. Zhou C, Xiao Z (2018) Stiffness and damping models for the oil film in line contact elastohydrodynamic lubrication and applications in the gear drive. *Appl Math Model* 61:634–649
57. Hu X, Hu B, Zhang F, Fu B, Li H, Zhou Y (2018) Influences of spline assembly methods on nonlinear characteristics of spline–gear system. *Mech Mach Theory* 127:33–51
58. Dhamande LS, Chaudhari MB (2018) Compound gear-bearing fault feature extraction using statistical features based on time-frequency method. *Measurement* 125:63–77
59. Li W, Liu B (2018) Experimental investigation on the effect of shot peening on contact fatigue strength for carburized and quenched gears. *Int J Fatigue* 106:103–113
60. Praveenkumar T, Sabhrish B, Saimurugan M, Ramachandran KI (2018) Pattern recognition based on-line vibration monitoring system for fault diagnosis of automobile gearbox. *Measurement* 114:233–242
61. Cerrada M, Li C, Sánchez RV, Pacheco F, Cabrera D, de Oliveira JV (2018) A fuzzy transition based approach for fault severity prediction in helical gearboxes. *Fuzzy Sets Syst* 337:52–73
62. Everitt CM, Alfredsson B (2018) Contact fatigue initiation and tensile surface stresses at a point asperity which passes an elastohydrodynamic contact. *Tribol Int* 123:234–255
63. Vučković K, Galić I, Božić Ž, Glodež S (2018) Effect of friction in a single-tooth fatigue test. *Int J Fatigue* 114:148–158
64. Palermo A, Britte L, Janssens K, Mundo D, Desmet W (2018) The measurement of gear transmission error as an NVH indicator: theoretical discussion and industrial application via low-cost digital encoders to an all-electric vehicle gearbox. *Mech Syst Signal Process* 110:368–389

65. Li L, He K, Wang X, Liu Y (2018) Sensor fault-tolerant control for gear-shifting engaging process of automated manual transmission. *Mech Syst Signal Process* 99:790–804
66. Ren X, Lu Z, Tian G (2018) Sensor fault-tolerant control for gear-shifting engaging process of electric-drive mechanical transmission. In: *Proceedings of the 6th international conference on control, mechatronics and automation*. ACM, pp 21–28
67. Li B, Zhang X, Wu T (2018) Measurement of instantaneous angular displacement fluctuation and its applications on gearbox fault detection. *ISA Trans* 74:245–260
68. Liu JP, Shu XB, Kanazawa H, Imaoka K, Mikkola A, Ren GX (2018) A model order reduction method for the simulation of gear contacts based on Arbitrary Lagrangian Eulerian formulation. *Comput Methods Appl Mech Eng* 338:68–96
69. Fernandes CM, Rocha DM, Martins RC, Magalhães L, Seabra JH (2018) Finite element method model to predict bulk and flash temperatures on polymer gears. *Tribol Int* 120:255–268
70. Stark S, Beutner M, Lorenz F, Uhlmann S, Karpuschewski B, Halle T (2013) Heat flux and temperature distribution in gear hobbing operations. *Proc Cirp* 8:456–461
71. Li W, Tian J (2017) Unsteady-state temperature field and sensitivity analysis of gear transmission. *Tribol Int* 116:229–243
72. Castro J, Seabra J (2018) Influence of mass temperature on gear scuffing. *Tribol Int* 119:27–37
73. Shi Y, Yao YP, Fei JY (2016) Analysis of bulk temperature field and flash temperature for locomotive traction gear. *Appl Therm Eng* 99:528–536
74. Luo B, Li W (2017) Influence factors on bulk temperature field of gear. *Proc Institut Mech Eng Part J J Eng Tribol* 231(8):953–964
75. Gou X, Zhu L, Qi C (2017) Nonlinear dynamic model of a gear-rotor-bearing system considering the flash temperature. *J Sound Vib* 410:187–208
76. Touret T, Changenet C, Ville F, Lalmi M, Becquerelle S (2018) On the use of temperature for online condition monitoring of geared systems—a review. *Mech Syst Signal Process* 101:197–210
77. Zhang JG, Liu SJ, Fang T (2017) Determination of surface temperature rise with the coupled thermo-elasto-hydrodynamic analysis of spiral bevel gears. *Appl Therm Eng* 124:494–503
78. Taburdagitan M, Akkok M (2006) Determination of surface temperature rise with thermo-elastic analysis of spur gears. *Wear* 261(5–6):656–665
79. Li S, Anisetti A (2016) On the flash temperature of gear contacts under the tribo-dynamic condition. *Tribol Int* 97:6–13
80. Evans SM, Keogh PS (2016) Efficiency and running temperature of a polymer–steel spur gear pair from slip/roll ratio fundamentals. *Tribol Int* 97:379–389
81. Kalin M, Kupec A (2017) The dominant effect of temperature on the fatigue behaviour of polymer gears. *Wear* 376:1339–1346

# Finite Element Modeling of Nano Porous Sintered Silver Material



Bahman Meyghani, S. Emamian, Mokhtar Awang, and Chuan Song Wu

**Abstract** In the packaging industry, the conventional lead-based solders have gradually become obsolete because of Hazardous Substances regulations and the rapid advancement of alternatives in microelectronics production. Sintered silver paste is proposed to bond the chips and substrates, because compared with other metals used in the electronic industry, silver has better thermal and electrical conductivity, a higher melting point, and it has less susceptible to oxidation. However, after sintering, a considerable pore fraction will be existing in the material, and compared with bulk silver, after the sintering process the material density decreases. Therefore, the effect of the pore distribution on elastic and thermal properties of the sintered silver pastes during aging is one of the main parameters for modeling the whole electronic system under operating conditions. So far, there are limited studies for investigating the effect of the material aging on the microstructural level. Hence, this study focuses on examining the effect of the morphology and pore distribution in the material responses as well as determining the quantitative nanostructure relationship between the material properties of the as-sintered and aged. In this study, a home-built MATLAB® code was developed in order to increase the quality of images. Mimics® software was used to convert the images to solid 3D representative volume elements. Numerical homogenization technique was also used to evaluate as-sintered and aged microstructure properties. The results show that there is a temporary pattern relationship between the stress and the time of the heat treatment. To validate the developed model, both as-sintered and aged materials have gone through several published work to determine changes of the material properties.

---

B. Meyghani · C. S. Wu (✉)

Institute of Materials Joining, Shandong University, 17923, Jingshi Road, Jinan 250061, China  
e-mail: [wucs@sdu.edu.cn](mailto:wucs@sdu.edu.cn)

S. Emamian

Department of Mechanical Engineering, Faculty of Engineering, Center of Advance Manufacturing and Material Processing (AMMP), University of Malaya, Kuala Lumpur, Malaysia

M. Awang (✉)

Department of Mechanical Engineering, Faculty of Engineering, Universiti Teknologi PETRONAS, 32610 Bandar Seri Iskandar, Perak Darul Ridzuan, Malaysia  
e-mail: [mokhtar\\_awang@utp.edu.my](mailto:mokhtar_awang@utp.edu.my)

**Keywords** Sintered silver · Pore fraction · Density · Pore distribution · As-sintered · MATLAB® code · Image processing · Representative volume element

## 1 Introduction

There is an increasing demand for transporting of people and goods. Unfortunately, such increase has caused a growth in harmful emissions. In order to reduce this negative effect, there is a push to replace conventional hydrocarbon machineries with electric and hybrid solutions which mainly rely on embedded power electronics. These power electronic components use electronic packaging for electrical connection, thermal cooling, mechanical support, and physical protection. Thus, the electrical components, circuit layouts, and packaging technology affect the general performance of a single-chip power package. Furthermore, these aspects influence the multichip power module as well as the whole power system.

The authorities have set more rigorous regulations called Restriction of Hazardous Substances Directive (RoHS) to prevent the use of lead and lead alloy materials, especially in electronic applications. Consequently, the interconnect technology has failed to meet the high-temperature operating requirement of wide-bandgap devices [1–3]. Thus, dominant technical barriers limit the rapid growth of power electronics, as well as the device interconnecting and packaging [4–7]. Thus, before designing high-temperature devices [8] and circuits that can be scaled-up and effectively integrated into power electronic systems, there is a need for new interconnecting materials and technologies.

Over the last couple of years, there are many industrials and academic studies that have focused on finding the best replacement materials for electronic power conversion. It is posited that the interconnecting materials chosen should possess excellent mechanical strength, specifically high shear strength and good thermal conductivity [9, 10]. This is to enable the device to endure heat when the circuit board is operating. Such studies are also motivated by the restriction on the use of lead (Pb) in die-attached materials, as imposed by the directives of the RoHS. Sintered silver joint (Ag) is a good alternative as it fulfills the environmental and reliability criteria [11, 12]. Sintered (Ag) joints have many advantages which makes it highly popular among researchers. Compared with other lead-free alternatives out there, it has a higher thermal stability, excellent mechanical and electrical properties. Furthermore, it also has a processing temperature similar to the temperature of other high-lead solders [13–17].

Goldsmid [18] optimized the composition temperature dependence of the thermoelectric parameters in order to investigate the applications for temperature higher than room temperature. In his report, he also compared the theoretical predictions with the observed properties of bismuth telluride-based thermoelements at elevated temperatures. Finally, he suggested compositional changes for materials that are destined for generator modules. In another study, Kähler et al. [19] addressed the

fabrication and performance of a sintered Peltier cooler (SPC) based on bismuth telluride with sintered silver interconnects. The SPC was successfully operated in an extended temperature range.

To the best knowledge of the authors, only a few studies have been reported the relationship between the mechanical properties and the porosity in porous materials. In one of these works, Siow [11] reviewed those studies that have focused on joining of elastic modulus, strength, and factors that affect the strength of the bonding. In another study, Panin et al. [20] focused on the elastic behavior of Ag film and concluded that the increase in the grain size as a result of annealing does not impact the elastic properties as shown by nano-indentation. Chen et al. [21] aged sintered joints and sintered bulk specimens to investigate the material density, tensile properties, and the sub-micron porosity. They have investigated that for the microstructure evolution only the temperature of 125 °C is responsible. Moreover, the elastic properties were explained as a function of the material microstructure evolution. The percentage of the porosity in a porous material is defined as a term that researchers use to describe how much void space is inside a sample. In the studies which were addressed by Schwarzbauer [6], Zhao et al. [22], and Kähler et al. [23], the porosity of sintered silver was reported 15%, 10%, and 10%, respectively.

As sintered silver is produced by sintering process, it is anticipated that the material illustrates certain level of porosity which could undermine the mechanical and electrical properties compared with fully dense materials. It was reported that sintered silver is susceptible to aging during long-term operating conditions. Thus, one of the key parameters for modeling the elastic and thermal behavior for the whole electronic system and the operating condition is to investigate the effect of the pore distribution on the elastic and thermal properties of sintered silver paste during aging. Moreover, there are still no works on the microstructural impact of material aging. Thus, this study aims to examine the influence of the morphology and pore size distribution on the response of a material, as well finding quantitative links between the material properties of the as-sintered and aged material and their microstructure. Numerical modeling of sintered silver samples under tensile loading was investigated, and different samples of sintered silver under various aging processes were experimentally prepared. The through-thickness scanning of all samples was then implemented and arranged. All images were converted into readable data in MATLAB® software, and the quality of the images was then aggrandized for further process. MATLAB® data were then imported to Mimics® image processing software to create a 3D object from all 2D images. The obtained 3D objects were then saved in the proper format and imported to ABAQUS® software for testing mechanical properties. It is shown that aging process has considerable effect on the mechanical properties of the obtained porous material.



## 2 Materials and Methods

In order to understand the modification of mechanical properties which are dominated by the joint porous structure, there is a need for the lifetime prediction of the whole system. This process constitutes of quantifying the porous structure evolves during thermal aging [24, 25]. As shown in Fig. 1a, the first step in addressing this issue is to use Image Processing for merging images. These images were then converted into 3D representative volume element as presented in Fig. 1b. This process was done to ascertain the as-sintered material and aged material porous structures and determining the link between the structure, the elastic and thermal properties. In the meantime, the packaging of a semiconductor device helps to secure the device and to prevent electromagnetic interference, chemical attack or corrosion. It also allows the dissipation of the generated heat from the device active junctions. Thus, this complex suite of functions must be maintained by the device packaging materials and strategies throughout all of the device range of the operating temperature.

To achieve the aforementioned objective, we have divided the methodology of this study into four phases, as follows.

### Phase-I:

During this phase, the heat treatment process was carried out to sinter the silver joints that have different porosities. As it is numerated in Table 1, 9 different heat treatment processes were applied on as-sintered material. Time and temperature are those two factors which were changed for aging 9 samples.

### Phase II:

An image processing procedure on the stack of images was conducted. These images were obtained using the serial block-face scanning electron microscope (SBF-SEM). The front, top, and side views of the scanned images of one of the samples are brought

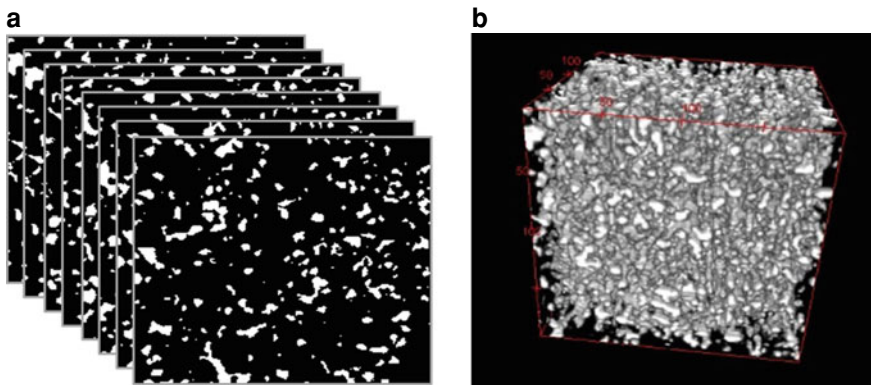


**Fig. 1** a Segmented SEM images of sintered material b 3D representation of the sintered material

**Table 1** The description of the number of samples and the details about the heat treatment

Number of the sample	Heat treatment temperature °C	Heat treatment time
Sample 0	No heat treatment	–
Sample 1	250–340 °C	25 h
Sample 2	250–340 °C	50 h
Sample 3	250–340 °C	100 h
Sample 4	350 °C	25 h
Sample 5	350 °C	50 h
Sample 6	350 °C	100 h
Sample 7	450 °C	25 h
Sample 8	450 °C	50 h
Sample 9	450 °C	100 h

in Fig. 2. The length, width, and thickness of the samples were 2.9 mm, 1.8 mm, and 2.5  $\mu\text{m}$ , respectively.

Phase III:

In order to make a 3D object from 2D images, Mimics® image processing software was implemented. Since the quality of the scanned images was not enough to be imported directly to Mimics® software, a MATLAB® code was prepared to

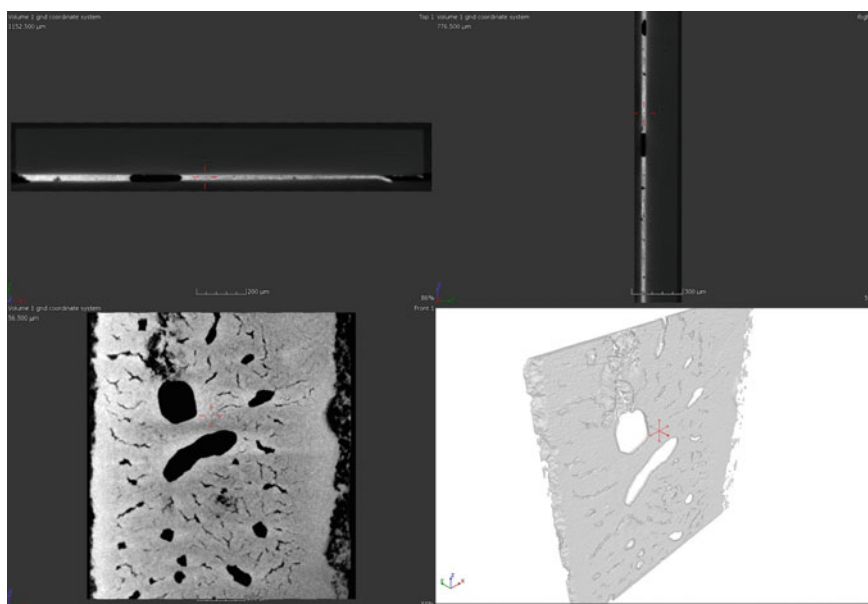


**Fig. 2** The description of the images resolution and size of the pixels

increase the quality of every image. Every 2D images were imported into MATLAB® through converting into readable data, and the resolution of the images was then increased. Using `imread` command in MATLAB®, a grayscale intensity image was converted into a two-dimensional array. Every element of two-dimensional matrix was then divided by the maximum element of the 2D matrix. Thus, the magnitude of all elements was changed to values between 0 and 1. The whole matrix was then multiplied by a constant ( $C = 1.5$ ) to increase the visibility of those points which were not clear in the image. Within this method, the null spaces in the 2D image remain as before and the gray color of some points convert to black. Later, the Gaussian smoothing filter was applied to slightly blur and uniform the image. This process was carried out for all 2D images of the samples. Later, all images were imported into Mimics® image processing software to make a 3D object and transfer the output from the MATLAB® program into input files (.INP) which is readable by ABAQUS® software.

#### Phase IV:

In this phase of study, ABAQUS® software was used as a solver for modeling the behavior of the samples under tensile loading. First of all, the create geometry from mesh plug in is used for creating the new geometries, because the number of the elements in the extracted file from mimics® software should to be optimized. Therefore, a new geometry is created, and the number of elements and nodes has been optimized. It should be noted that, an isotropic behavior is assumed for modeling of the porous material. After creating the parts, the specimens were meshed in the ABAQUS® software. The element type C3D10 element (Fig. 3d) was used for meshing the parts. The samples have been fixed from one part, and a pressure from another part is applied in the model. It should be noted that this type of the element is a general-purpose hexahedral element which has 4 integration points. General static linear analysis was also performed for the simulation. It should be noted that, the number of the elements and nodes is different in each sample (For example for the sample 0 the total number of nodes are equal to 367,049 and the total number of elements are equal to 190,883). Figure 3 shows all stages of sample preparation process for numerical simulation. The order of sample preparation is from a to d shown in Fig. 3.

### 3 Results and Discussion

As stated before, nine various samples were analyzed in this study. The prepared samples have cured in different time durations and temperatures. Three-dimensional (3D) models from real microstructure of silver were developed to examine the real thermal and structural deformation behavior of the microstructure. Mechanical behaviors of every sample under tensile loading in both X and Y directions were obtained. Since the type of aging process affects the pores distribution in the sintered

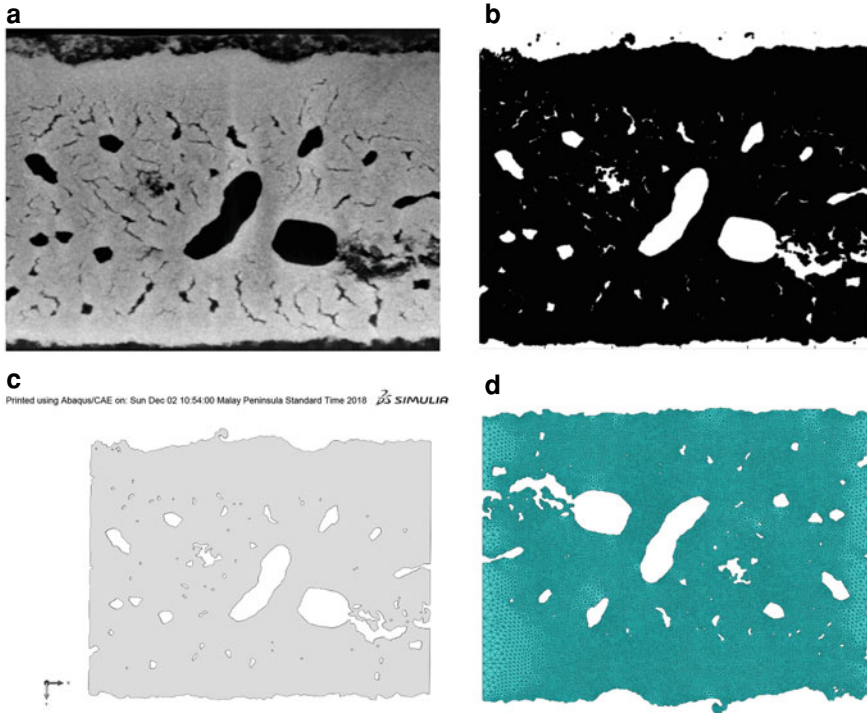


**Fig. 3** Four stages of sample preparation for numerical modeling **a** The raw stack of images **b** Developed images by using MATLAB® code **c** Imported part in Abaqus® software **d** Finite element mesh of the samples

silver, it is expected that samples show different reactions under equal loading conditions. The left corner of the samples in Fig. 3d was fixed, and the right corner was loaded in ABAQUS® software for the X direction. For the Y direction, the upper part was fixed and the force applied in the lower part. By applying distributed tensile force to the right corner, stress–strain curve and deformation of the whole sample were obtained accordingly. Color map of stress and deformation distribution in all samples in both X and Y directions are demonstrated in Fig. 4. Due to the various shapes of the voids in the samples, it is necessary to perform the tensile test in both X and Y directions. Furthermore, it can be observed that according to the distribution of the pores in the samples, the maximum stress and deformation vary significantly. Based on the direction of loading, maximum stress in the samples occurs in the vicinity of the biggest void.

Maximum stress in X and Y directions was calculated and tabulated in Table 2. It can be seen that under the same loading conditions, samples 3 and 8 among all sintered samples experience the highest and lowest maximum stress, respectively. Based on the maximum stresses stated in Table 2, it can be found that temperature and time play an important role in heat treatment process. According to Table 2, in all

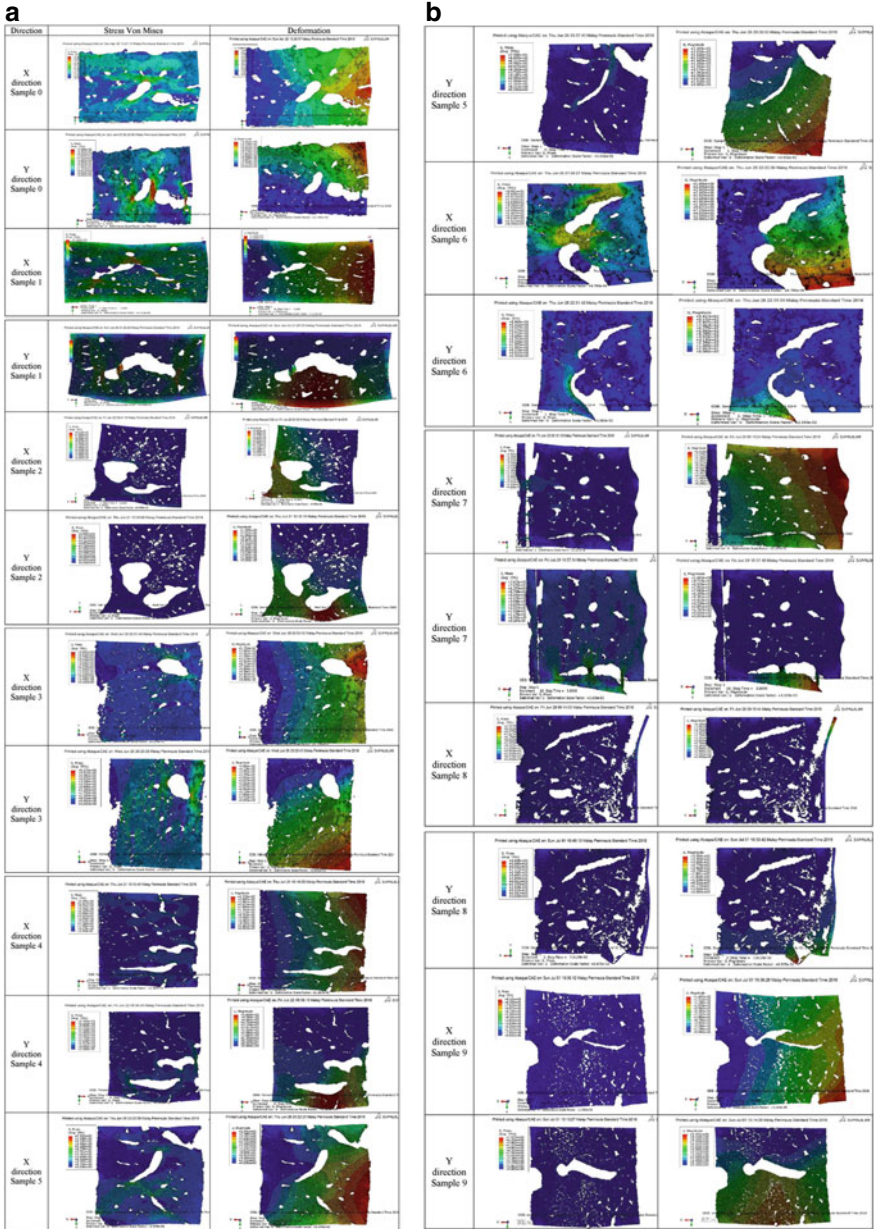


**Fig. 4** The results of the distribution of the stress and the deformation for finite element models in the **a** X and **b** Y direction

**Table 2** Describes the number of samples and the details about the heat treatment

Group name	Number of the sample	Heat treatment temperature °C	Heat treatment time	Maximum stress in X axis (GPa)	Maximum stress in Y axis (GPa)
1	Sample 0	No heat treatment	–	0.040958	0.04911
2	Sample 1	250–340 °C	25 h	0.052	0.053974
	Sample 2	250–340 °C	50 h	0.07142	0.085238
	Sample 3	250–340 °C	100 h	0.0406	0.052926
3	Sample 4	350 °C	25 h	0.062469	0.066852
	Sample 5	350 °C	50 h	0.078123	0.073471
	Sample 6	350 °C	100 h	0.058753	0.054926
4	Sample 7	450 °C	25 h	0.06	0.076393
	Sample 8	450 °C	50 h	0.107271	0.095405
	Sample 9	450 °C	100 h	0.090353	0.091714

three groups (2, 3, and 4), samples with 50 h aging process have highest maximum stress in their groups. It may indicate that 50 h aging process can induce more pores in the sintered silver. In contrast, the maximum stress in samples with 25 and 100 h heat treatment process is considerably less than that of 50 h. Temperature analysis

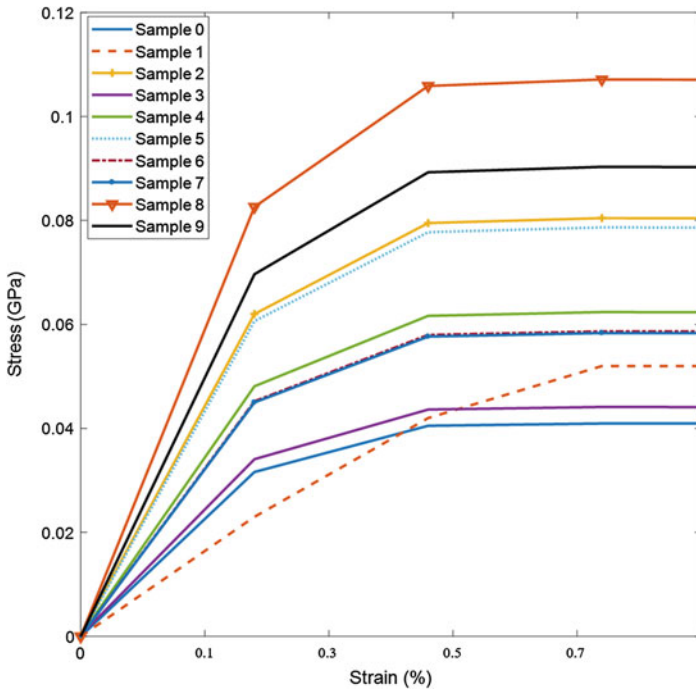


**Fig. 5** Stress–strain curve in the X direction for samples



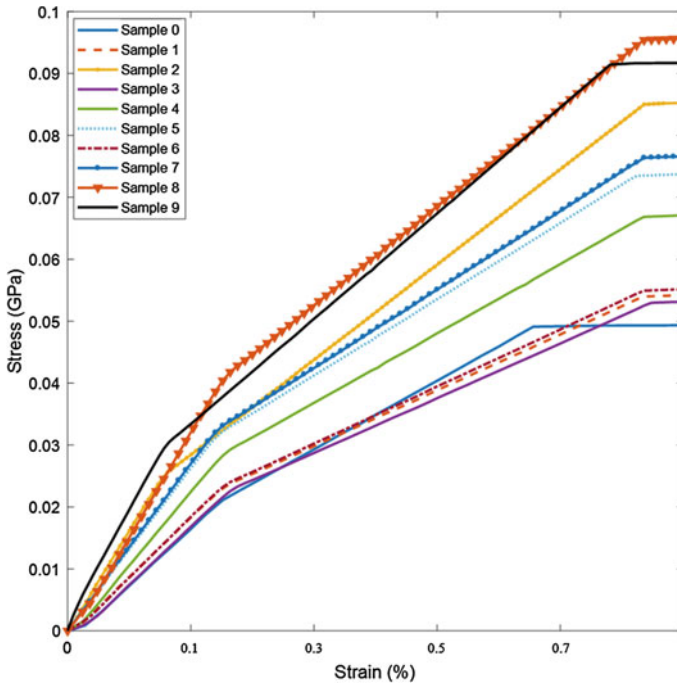


**Fig. 6** Stress–strain curve in the Y direction for samples

in Table 2 shows that by increasing temperature the value of maximum stress in the samples soars considerably.

Stress–strain curve corresponding to critical element of the samples in X and Y directions was obtained and plotted in Figs. 5 and 6. As mentioned earlier, the mechanical behavior of every sample under uniform tensile force demonstrates the influence of the heat treatment phenomenon on the sample porosity. It can be seen in Fig. 5 that the stress–strain curve of samples changes according to the type of aging process. Moreover, the change of the material stiffness can be investigated by using this method. As mentioned before, stress–strain diagram in Fig. 5 shows that generally the modulus of elasticity increases by growing the heat treatment temperature.

According to stress–strain curves addressed in Figs. 5 and 6, it can be observed that the behavior of the material is initially linear. However, by increasing strain, a plateau appears in the stress–strain curve. It is representing the existence of the pores in the structure of the material. These results are completely compatible with those which are addressed in Fig. 2 of reference [12] for sintered silver materials. It can be observed that the stress–strain curve of reference [12] obviously proves the trueness of the obtained results of the current study.

It can be observed that the trend of the results in Y direction in Fig. 6 is similar to that found in Fig. 5 (stress in the X direction). Thus, from the results, it can

be concluded that increasing the temperature during the heat treatment process of sintered silver grows the stiffness of the porous material considerably. The pattern for the stress–strain curve and the increase of the stiffness with temperature is also conforms with the literature [12, 26]. Moreover, as mentioned before, the most effective heat treatment time was found to be 50 h in all three groups of samples.

## 4 Conclusions

In this study, various Nano sintered silver samples were prepared and the mechanical behavior of every sample under tensile loading was calculated numerically. Nine different curing processes were implemented, and samples with different pore distributions were created. Time and temperature were two parameters which were changed in every curing process to find a developed porous material. To obtain the mechanical behavior of every sintered material, the through-thickness images of every sample were found using the Serial Block Face Scanning Electron Microscope. Later, image processing was applied by programming in MATLAB® software to increase the quality and uniformity of every image. Images were then imported into Mimics® software to convert all 2D images into a 3D object. Finally, the mechanical behavior of the samples was found in the ABAQUS® software. It was observed that the type of aging process can significantly change the mechanical behavior of sintered silver. It was seen that among all time durations for heat treatment process, 50 h processing time can induce more pores in the sintered silver. Among all three considered groups, maximum stress in those samples which had cured during 50 h was the highest in the group. In contrast, maximum stress in those samples which had experienced 25 and 100 h curing process was much lower in the group. It was found that generally by increasing samples curing temperature, the maximum stress in the samples under tensile loading grows considerably.

**Acknowledgments** The authors would like to acknowledge the fellowship of the government of China, Shandong University from the International Postdoctoral Exchange Program and the Universiti Teknologi PETRONAS (UTP), Malaysia for the financial support from YUTP-FRG grant cost center 0153AA-H18. Moreover, the authors would like to thank Professor Wallace Kaufman for his endless support.

## References

1. Bai JG, Zhang ZZ, Calata JN, Lu G-Q (2006) Low-temperature sintered nanoscale silver as a novel semiconductor device-metallized substrate interconnect material. *IEEE Trans Compon Packag Technol* 29:589–593
2. Scheuermann U (2009) Reliability challenges of automotive power electronics. *Microelectron Reliab* 49:1319–1325



3. Ghoushji M, Alebrahim R, Zulkifli R, Sulong A, Abdullah S, Azhari C (2018) Crashworthiness characteristics of natural ramie/bio-epoxy composite tubes for energy absorption application. *Iran Polym J*, 1–13
4. Schwarzbauer H (1989) Method of securing electronic components to a substrate. Google Patents
5. Schwarzbauer H (1990) Method and apparatus for fastening electronic components to substrates. Google Patents
6. Schwarzbauer H (1991) Apparatus for fastening electronic components to substrates. Google Patents
7. Schwarzbauer H, Kuhnert R (1989) Novel large area joining technique for improved power device performance. In: Industry applications society annual meeting. Conference record of the 1989. IEEE, pp 1348–1351
8. Smet V, Jamal M, Waldron F, Stam F, Mathewson A, Razeeb KM (2013) High-temperature die-attach technology for power devices based on thermocompression bonding of thin Ag films. *IEEE Trans Compon Packag Manuf Technol* 3:533–542
9. Heuck N, Müller S, Palm G, Bakin A, Waag A (2010) Swelling phenomena in sintered silver die attach structures at high temperatures: reliability problems and solutions for an operation above 350 C. Additional Papers and Presentations 2010:000018–000025
10. Heuck N, Palm G, Sauerberg T, Stranz A, Waag A, Bakin A (2010) SiC-die-attachment for high temperature applications. In: Materials science forum, pp 741–744
11. Siow KS (2012) Mechanical properties of nano-silver joints as die attach materials. *J Alloy Compd* 514:6–19
12. Rajaguru P, Lu H, Bailey C (2015) Sintered silver finite element modelling and reliability based design optimisation in power electronic module. *Microelectron Reliab* 55:919–930
13. Wang D, Mei Y-H, Xie H, Zhang K, Siow KS, Li X et al (2017) Roles of palladium particles in enhancing the electrochemical migration resistance of sintered nano-silver paste as a bonding material. *Mater Lett* 206:1–4
14. Chua S, Siow KS (2016) Microstructural studies and bonding strength of pressureless sintered nano-silver joints on silver, direct bond copper (DBC) and copper substrates aged at 300 C. *J Alloy Compd* 687:486–498
15. Siow KS (2014) Are sintered silver joints ready for use as interconnect material in microelectronic packaging? *J Electron Mater* 43:947–961
16. Alebrahim R, Sharifishourabi G, Sharifi S, Alebrahim M, Zhang H, Yahya Y et al (2018) Thermo-mechanical behaviour of smart composite beam under quasi-static loading. *Composite structures*
17. Meyghani B, Awang M, Bokam P, Plank B, Heinzl C, Siow K (2019) Finite element modeling of nano porous sintered silver material using computed tomography images. *Materialwiss Werkstofftech* 50:533–538
18. Goldsmid HJ (2014) Bismuth telluride and its alloys as materials for thermoelectric generation. *Materials* 7:2577–2592
19. Kähler J, Stranz A, Waag A, Peiner E (2014) Thermoelectric coolers with sintered silver interconnects. *J Electron Mater* 43:2397–2404
20. Panin A, Shugurov A, Oskomov K (2005) Mechanical properties of thin Ag films on a silicon substrate studied using the nanoindentation technique. *Phys Solid State* 47:2055–2059
21. Chen C, Nagao S, Suganuma K, Jiu J, Sugahara T, Zhang H et al (2017) Macroscale and microscale fracture toughness of microporous sintered Ag for applications in power electronic devices. *Acta Mater* 129:41–51
22. Zhao Y, Mumby-Croft P, Jones S, Dai A, Dou Z, Wang Y et al (2017) Silver sintering die attach process for IGBT power module production. In: Applied power electronics conference and exposition (APEC). IEEE, pp 3091–3094
23. Kähler J, Heuck N, Palm G, Stranz A, Waag A, Peiner E (2011) Low-pressure sintering of silver micro-and nanoparticles for a high temperature stable pick & place die attach. In: Microelectronics and packaging conference (EMPC), 18th European, pp 1–7

24. Carr J, Milhet X, Gadaud P, Boyer SA, Thompson GE, Lee P (2015) Quantitative characterization of porosity and determination of elastic modulus for sintered micro-silver joints. *J Mater Process Technol* 225:19–23
25. Buj-Corral I, Vivancos-Calvet J (2013) Improvement of the manufacturing process of abrasive stones for honing. *Int J Adv Manuf Technol* 68:2517–2523
26. Meyghani B, Awang M, Emamian S, Plank B, Heinzl C, Siow K (2019) Stress analysis of nano porous material using computed tomography images. *Materialwiss Werkstofftech* 50:234–239

# Creep Behaviour and Adhesion Properties of TiC Thin Film Coating Grown by RF Magnetron Sputtering



Abegunde Olayinka, Esther T. Akinlabi, and O. P. Oladijo

**Abstract** In this research study, the creep behaviour and adhesion resistance of TiC thin films grown using RF magnetron sputtering under different deposition parameters were investigated. Radio frequency (RF) magnetron sputter was used to coat the surface of CpTi with TiC target. Field electron scanning electron microscope was used to study the film morphology, and the hardness, young modulus, and creep behaviour tests were performed using TI 950 Triboindenter. The adhesion resistance property was investigated using a microscratch tester under ambient working condition. From the results, the TiC thin film morphology structures show different growth modes as the RF power changes. Films with uniform surface morphology show better adhesion resistance to peeling than films with high surface asperities, while films with heterogeneous distribution of the TiC thin films show high hardness values.

**Keywords** Acoustic emission · Creep · Mechanical properties · RF magnetron sputtering · Thin film

## 1 Introduction

Surface modification is an act of improving the surface performance of a material by coating the surface with different materials of better and improved quality. The performance functionality of this coating materials depends on the mechanical properties such as adhesion strength, hardness, young modulus, wear and creep resistance. There are several techniques used for surface modification, which depend on the materials' properties and area of applications. In recent years, there has been a

---

A. Olayinka (✉) · E. T. Akinlabi · O. P. Oladijo  
University of Johannesburg, Johannesburg 2006, South Africa  
e-mail: [oabegunde@uj.ac.za](mailto:oabegunde@uj.ac.za)

E. T. Akinlabi  
Covenant University, Ota, Nigeria

O. P. Oladijo  
Botswana International University of Science and Technology, Palapye, Botswana

paradigm shift in surface modification coating from age-old electroplating processes to new improved coating techniques such as chemical vapour deposition (CVD), physical vapour deposition (PVD), ion beam, vacuum arc deposition, evaporation, thermal spray, and pulsed laser ablation (PLD) [1–7]. One of the major considerations in using coating techniques is the adhesion bond between the substrate and the coating materials. Adequate bonding and adequate compatibility between the substrate and the film is an indication of good mechanical properties. Mechanical properties such as creep and adhesion strength are crucial to film failure under loading. Creep is the time-dependent deformation that occurs under application of load, and adhesion strength is the resistance of thin films peeling to applied normal or shear load. Strong adhesion bond yields good resistance to coating fracture under stationary or progressive loading and good creep resistance behaviour. The choice of the coating materials is also another influential factor that affects the final mechanical properties of the thin film coating. Titanium carbide TiC is one of the most widely applied hard coating materials due to its several advantageous and outstanding properties. These properties are high hardness, low coefficient of friction, outstanding wear resistance, high melting or decomposition temperature, good electrical conductivity, excellent corrosion resistance and chemical stability [8–13].

It is well known from studies that the properties of deposited titanium carbide thin films coatings depend strongly on the deposition conditions and coating techniques, and these properties are related to their chemical composition, texture, creep behaviour, residual stress and adhesion property [10]. However, the correlation between the creep resistance and adhesion behaviour and the process parameters (RF power and sputtering time) of RF magnetron sputtering still needs to be understood. In this research, RF magnetron sputtering was used to sputter TiC thin films by varying the RF power and sputtering time, and the relationship between the mechanical properties of the films and process parameters was studied.

## 2 Methodology

### 2.1 RF Magnetron Sputtering Process

TiC thin films were coated on commercially pure titanium (CpTi) using the process parameters presented in Table 1. HHV TF500 RF magnetron sputter was used for the

**Table 1** RF magnetron process parameters

Experiment no	RF power (W)	Sputtering time (Hrs)
L1	150	2.5
L2	200	2.5
L3	200	3
L4	250	3

coating deposition. Before coating the substrate (CpTi) with TiC thin film, surface cleansing was done on the substrates to remove surface contaminants and uniform surface asperities. This was achieved by grinding and polishing using silica carbide papers of different grit sizes. The substrates were further cleaned using acetone, isopropanol and deionized water for 15 min, respectively. The distance between the substrate and target was maintained throughout the deposition process. Before the sputtering process commences, the sputtering chamber was first evacuated to a pressure of  $1.13 \times 10^{-5}$  mbar to provide a long mean free path for collision between the target and substrate and to minimize contaminants. After thorough evacuation of the chamber, the system was filled with argon to a partial pressure of 0.1–10 Pa to initiate the plasma formation and working temperature of 90 °C.

## 2.2 Characterization Techniques

Field emission scanning electron microscope FESEM (ZEISS Gemini\*2, Germany) was used to analyse the film morphology. Images of the film morphology were taken at  $\times 50,000$  magnification. Hysitron TI 950 Triboindenter was used to evaluate the nanomechanical properties of the coating. The hardness and reduced young modulus were measured using a Berkovich diamond indenter, and they were calculated according to the method proposed by Oliver and Pharr [14, 15]. The Berkovich diamond indenter was preferred over the four-sided Vickers or Knoop indenter because a three-sided pyramid is more easily ground to a sharp point with high accuracy and minimal influence of the substrate properties on the coating. In order to avoid the combined coating plus substrate effect, penetration displacement was set to slightly less than 10% of the total coating thickness. In all indentation tests, a total of 10 indents were averaged to determine the mean hardness and reduced young modulus. The displacements were continuously recorded during the indentations. The penetration displacement of the indenter at maximum load ( $H_{MAX}$ ) and the final displacement (HF), recorded in the unloading curve, were used to determine the percentage of elastic recovery (%R) and plasticity using Eq. 1 given below.

$$\%R = \frac{H_{MAX} - HF}{H_{MAX}} \times 100 \quad (1)$$

Indentation creep testing was performed using the same Hysitron TI 950 Triboindenter. A constant load was applied to the indenter, and the change in indentation depth (size) was monitored as a function of time. Anton Paar (Micro Combo Tester, Austria) scratch tester was used to determine the films adhesion properties. The microscratch tester was coupled with an acoustic emission sensor which was used to determine when the film peels from the substrate. A Rockwell diamond ball with a radius of 100  $\mu\text{m}$  was used for the microscratch test. For each measurement, the applied load was progressive from 50 mN to 2 N at a sliding speed of 2 mm/min and

sliding length of 1 mm. The displacement of the diamond ball was linear. All these experiments were carried out in an ambient atmospheric condition.

### 3 Result

#### 3.1 Morphology Evolution

The film morphology under different process parameters obtained from the FESEM is presented in Fig. 1. From the structure, the geometry and distribution of the TiC thin films coating changes with both deposition power and time. Sparse and uneven distribution was noticed for sample produced at RF power of 150 W (sample L1). This shows an early stage in TiC film deposition on the substrate. As the power increased to 200 W (samples L2 and L3), the TiC thin film became dense and was uniformly distributed across the surface. Increase in RF power has been reported to result in faster ejection of atom from the target and high condensation of the atoms on the substrate surface. As the sputtering time increased for sample L3, the grain size of the film became finer. Formation of incomplete new TiC thin film layer was noticed as the power was increased further to 250 W. This phenomenal growth mode is similar to Stranski–Krastanov growth mechanism where both layer by layer and island growth of coating happen simultaneously.

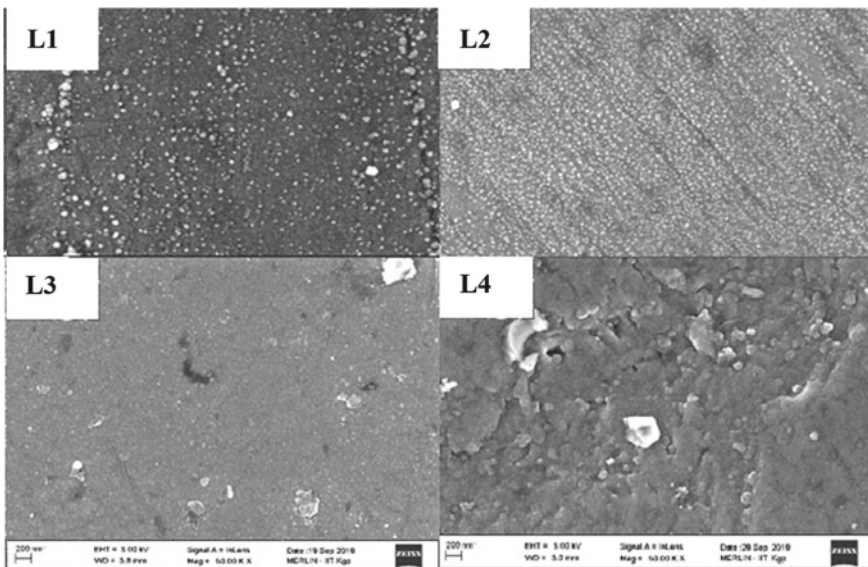


Fig. 1 FESEM morphology of TiC thin film coating

**Table 2** Statistical results from the nanoindentation test

Sample	Young Modulus $E$ (GPa)	Hardness $H$ (GPa)	Wear resistance $H^3/E^2$ (GPa)	Plasticity index $H/E$	$H_{MAX}$	HF	%Recovery	Plasticity
L1	183.12	8.96	0.02	0.049	25.99	11.09	57.34	42.66
L2	115.55	4.77	0.0081	0.041	37.89	15.20	59.89	40.11
L3	119.11	5.75	0.013	0.048	35.07	13.03	62.83	37.17
L4	145.08	10.13	0.050	0.070	26.91	7.96	70.41	29.59

### 3.2 Mechanical Properties

Table 2 presents the results obtained from the nanoindentation test, and Fig. 2 (a, b and c) shows the graphical representation of these results. The maximum hardness value was obtained at RF power of 250 W. This is due to increase in thickness and formation of several coating layers of TiC thin film when compared to other samples. The least hardness values were obtained at 200 W. The load vs displacement curve is presented in Fig. 2a. From the curve, samples with low hardness values yield

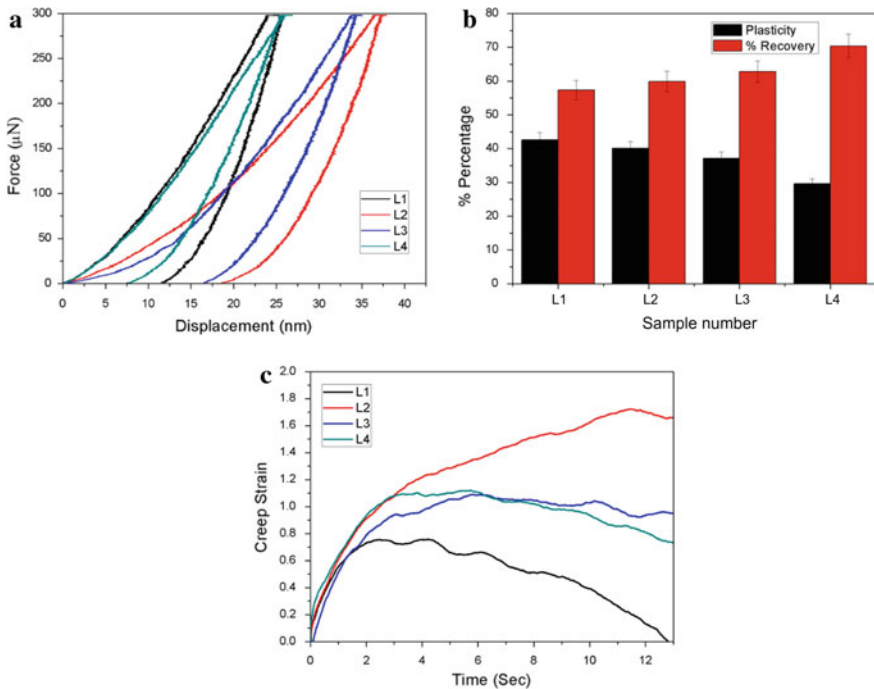


**Fig. 2** a Force versus displacement curve. b Chart of the %recovery and plasticity. c Graph of creep strain versus time

the maximum displacement, and the displacement reduces as the hardness values increase. The %recovery and plasticity were calculated, and the graph is presented in Fig. 2b. From the results, the coating with the highest hardness value has the better %recovery and lowest plasticity. The %recovery increases with an increase in the RF power and sputtering time. This shows that the film plasticity and %recovery to deformation depend on the process parameters and thickness of the coating more than the hardness. To understand the creep behaviour, the plot of the creep strain against time is illustrated in Fig. 2c. From the plot, the depth displacement of the coating increases for 4 s for all the coated samples. Continued increase in creep strain was noticed for sample L2 with the lowest hardness while the other samples resisted the creep strain displacement and reduced with time. Samples with high creep were sign of thermal drift of the tip displacement and apparent depth increase, and samples with low creep were sign of resistance to deformation. As the hardness decreases, the creep strain increases. This shows that the hardness is inversely proportional to the creep behaviour.

The microscratch result is presented in Fig. 3. The plots show the applied force (Fn), acoustic emission (AE), coefficient of friction (COF), and penetration depth (Pd) against displacement. To understand the adhesion strength, the acoustic emission plot was used. Sudden spike in the plot of the acoustic emission means peeling of the thin film coating from the substrate and represents initialization of thin film failure. The films might either crack or resist the failure depending on the degree of the

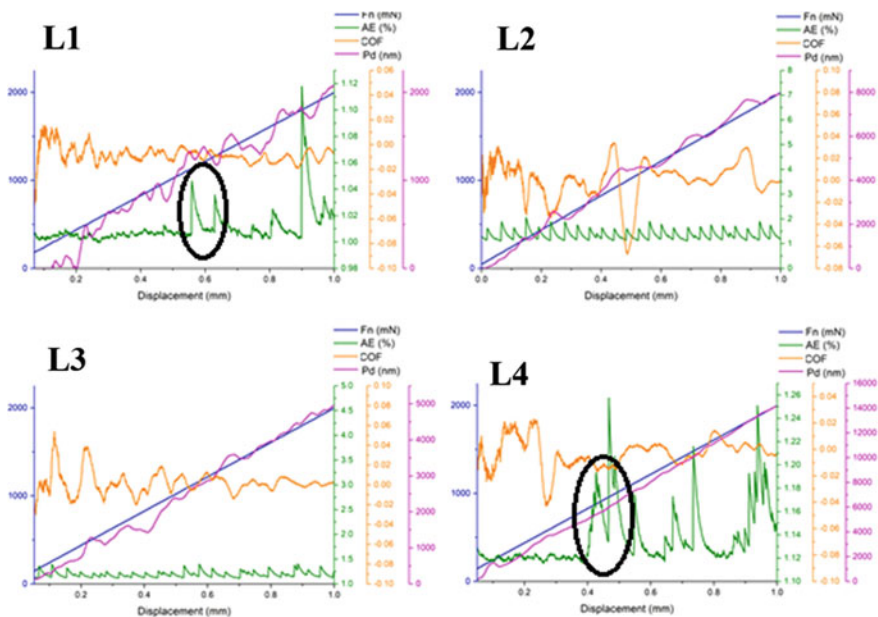


**Fig. 3** Microscratch result of the TiC coatings. Plot of Applied force (Fn), Acoustic Emission (AE), Coefficient of friction (COF), penetration depth (Pd) against Displacement



applied load and the film properties. Samples L1 and L4 show signs of thin film failure from the acoustic emission plot. The minimum load, at which the films fail, is called the critical load  $L_c$  [16, 17]. The circled portion on the plots of L1 and L4 shown in Fig. 3 denotes the initial critical load that initiates fracture of coating on the substrate. The coating with the homogenous and uniform coating (L2 and L3) withstands the applied load.

## 4 Conclusions

From the analysis of the results, it can be concluded that the morphology and geometry of the films change with the RF power and sputtering time. The films with uniform and homogenous coating show better adhesion properties compared with samples with uneven distribution of the TiC thin film coating that experienced fracture under microscratch test. The maximum hardness was noticed at RF power of 250 W which had the maximum %recovery.

**Acknowledgments** The Authors would like to acknowledge the Council for Scientific and Industrial Research (CSIR) South Africa, for the funding provided towards this research study.

## References

1. Konyashin IY (1996) Thin TiC<sub>x</sub> films chemically vapour deposited onto cemented carbides from the TiCl<sub>4</sub>-CCl<sub>4</sub>-H<sub>2</sub> mixture. *Thin Solid Films* 278(1–2):37–44
2. Guzman L et al (1998) Process parameters optimization for TiN and TiC formation using reactive ion beam assisted deposition. *Surf Coat Technol* 100:500–502
3. Voevodin A et al (1996) Combined magnetron sputtering and pulsed laser deposition of carbides and diamond-like carbon films. *Appl Phys Lett* 69(2):188–190
4. Knotek O et al (1995) On Superstoichiometric Ti-C, Si-C and Ta-C PVD Coatings. MRS online proceedings library archive, vol 403
5. D'alesio L et al (1998) Silicon supported TiC films produced by pulsed laser ablation," *Appl Surf Sci* 134(1–4):53–62
6. Ding X et al (2001) Preferential orientation of titanium carbide films deposited by a filtered cathodic vacuum arc technique. *Surf Coat Technol* 138(2–3):301–306
7. Abegunde OO et al (2019) Overview of thin film deposition techniques
8. Pierson HO (1996) Handbook of refractory carbides and nitrides: properties, characteristics. Processing and Applications, William Andrew
9. Vepřek S, Reiprich S (1995) A concept for the design of novel superhard coatings. *Thin Solid Films* 268(1–2):64–71
10. Mani A et al (2005) Effects of residual stress on the mechanical and structural properties of TiC thin films grown by RF sputtering. *Surf Coat Technol* 194(2–3):190–195
11. MikmekovĀ; E (2014) Enhanced properties of carbon based coatings
12. Wiklund U et al (2000) Evaluation of a flexible physical vapor deposited TiC–C coating system. *Surf Coat Technol* 124(2–3):154–161

13. Oláh N et al (2017) Mechanical characterization and corrosion behavior of protective TiC/amorphous C nanocomposite coating as surface thin film. *Resolution and Discovery* 2(1):13–22
14. Oliver WC, Pharr GM (2004) Measurement of hardness and elastic modulus by instrumented indentation: advances in understanding and refinements to methodology. *J Mater Res* 19(1):3–20
15. Oliver WC, Pharr GM (1992) An improved technique for determining hardness and elastic modulus using load and displacement sensing indentation experiments. *J Mater Res* 7(6):1564–1583
16. Covarel G et al (2012) Characterization of organic ultra-thin film adhesion on flexible substrate using scratch test technique. *Surf Coat Technol* 211:138–142
17. Boddaert X et al (2013) Organic ultrathin film adhesion on compliant substrate using scratch test technique. *Thin Solid Films* 528:194–198

# Taguchi Analysis of Surface Roughness of TiC Thin Films Deposited by RF Magnetron Sputtering



Olayinka Oluwatosin Abegunde, Esther T. Akinlabi, and O. P. Oladijo

**Abstract** The surface roughness of materials can affect the performance of the surface properties of materials. For a material to perform and interact optimally on the interfacial level with the surrounding environment, it is crucial the surface roughness is also optimized. In this research study, RF magnetron sputtering was used to deposit TiC thin films. Taguchi analysis was used for optimizing the process parameters for optimal surface roughness. Three levels and three factors were developed for the experimental matrix with RF power, sputtering time and temperatures as the independent factors. Optical profilometer was used for the characterization of the surface roughness, and Raman analysis was performed to study the structural defect on the thin film surface. From the Taguchi analysis, the RF Power contributed the most to the surface roughness properties with contribution rate of 95.62% and error level of 3.63%. The result of the Raman analysis shows that the process parameters affect the structural orientation defect of the thin films with no active vibration for some thin films produced at RF power of 200 W.

**Keywords** Process parameters · RF magnetron sputtering · Surface roughness · Taguchi · Thin film

## 1 Introduction

Surface modification of material is an important factor in the performance behaviour of materials. Materials properties such as corrosion, wear, osseointegration and biocompatibility are dependent on the surface properties [1]. The surface phase interacts with the surrounding environment. This interaction can degrade the surface phase

---

O. O. Abegunde (✉) · E. T. Akinlabi · O. P. Oladijo  
University of Johannesburg, Johannesburg 2006, South Africa  
e-mail: [oabegunde@uj.ac.za](mailto:oabegunde@uj.ac.za)

E. T. Akinlabi  
Covenant University, Ota, Nigeria

O. P. Oladijo  
Botswana International University of Science and Technology, Palapye, Botswana

over time, which can lead to reduction in the life span and sudden failure of materials. Surface modification can be done by different techniques with views to alter a wide range of characteristic features of the surface such as roughness, surface charge and energy, reactivity, conductivity, and hydrophilicity [1–5].

The two major techniques for surface modification is either by grinding the affected surface or adding other materials with superior qualities. Grinding the affected surface comes with a lot of limitations. These include loss of materials, distortion of material's properties and low resistance to corrosion in harsh environment. The latter can be achieved via many techniques depending on the thickness of the protective layer and surface properties. One of such techniques is radiofrequency magnetron sputtering process, which is used for depositing thin films layer to enhance the surface properties. In recent years, there has been a paradigm shift in surface modification to RF magnetron sputtering due to its excellent reproducible deposition process [6, 7].

In this study, RF magnetron sputtering was used to deposit TiC on the surface of titanium alloys to improve the robustness of the surface properties and the influence of the process parameters on the surface roughness was analysed.

## 2 Methods

### 2.1 Deposition Process

RF magnetron sputtering was used for growing TiC thin films target on the surface of commercially pure titanium (CpTi). Before the sputtering process, the substrates were ground and polished to remove any surface impurities. The surface of the substrate was further cleaned in acetone and stored in a desiccator to prevent contamination and surface oxidation. The purity of the TiC target used is 99.99% pure TiC. The target-substrate distance was kept fixed throughout the experiments. Evacuation of the sputtering chamber to a base pressure of  $1.13 \times 10^{-5}$  mbar was done for all the coating process before sputtering takes place. After evacuation, the system is refilled with argon to a partial pressure of  $2.5 \times 10^{-3}$  mbar. The argon flow rate of 12 sccm was used and constant working pressure was maintained. Maintaining constant pressure helps to place many argon atoms in the path of the ions and ejected coatings. After the plasma formation, the sputtering of the target is triggered, and the shutter is removed. Pre-sputtering was done for all the samples for 5 min before the main sputtering deposition. The substrate was located directly above the target on a rotating disc to ensure uniform distribution and condensation of the target on the surface of the substrate.

## 2.2 Taguchi Optimization Process

The sputtering experiments were conducted by varying three crucial parameters of magnetron sputtering namely RF power, sputtering time and temperature. The experimental matrix optimization was developed using the Taguchi method. Taguchi method is a simple, efficient and powerful design tool for statistical analysis and optimization. It lessens the number of experimental runs to be conducted and curbs the effects of external factors that cannot be controlled on the system [8–10]. The flowchart of the process is shown in Fig. 1 and Table 1 represents the control factors level the experimental setup of magnetron sputtering parameters and their levels. The full orthogonal array of Taguchi  $L_9$  ( $3^3$ ) with three factors at three levels of low, mid and high and a total of nine deposition runs is presented in Table 2. The time ranges from 2 to 3 h, power from 150 to 250 W and temperature from 80 to 100 °C. ANOVA analysis was carried out to identify the design parameters that significantly affect the response values. The total sum of the squared deviation was calculated using the

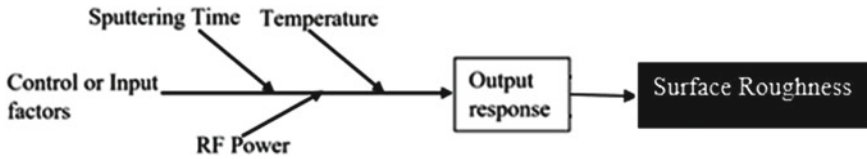


Fig. 1 The Fishbourne flowchart of the operational process

Table 1 Control factors level for experimental setup

Sputtering parameters	Symbol	Level 1	Level 2	Level 3
RF power (W)	A	150	200	250
Sputtering time (H)	B	2.0	2.5	3.0
Temperature (°C)	C	80	90	100

Table 2 The orthogonal array of Taguchi  $L_9$  ( $3^3$ )

Experiment no.	RF power	Sputtering time	Temperature
L1	1	1	1
L2	1	2	2
L3	1	3	3
L4	2	1	2
L5	2	2	3
L6	2	3	1
L7	3	1	3
L8	3	2	1
L9	3	3	2

equation developed by Yang and Tarng [11]. The signal-to-noise (S/N) ratio, which is a quantitative analysis defined by the ratio of the mean to the standard deviation was also performed. It is used to measure the quality characteristic deviation from the desired value and to determine optimal level that yields optimal output response. The term “signal” represents the desired effect for the output characteristic and the term “noise” stands for the undesirable effect for the output characteristic [12].

### ***2.3 Characterization Techniques***

3D optical profiler Contour Elite K microscope was used to analyse the surface roughness and topography. It is a non-contact and non-destructive system with large stages that leave the samples intact and undamaged. It has the capability to take surface roughness at the nanometre scale level, and all the test were performed under ambient condition. Raman analysis was used to study the structural defects in the thin films. Raman analyses were carried out on TiC thin films using an alpha300R (WITec) confocal laser Raman microscope configured with a frequency-doubled Nd-YAG laser (wavelength 532 nm). Raman spectra were collected using  $\times 50$  Nikon objectives. A laser power of 2 mW at room temperature was used to prevent burning of the film surface. Beam centring and Raman spectra calibration were performed before spectral acquisition using a Si standard (111). The Raman spectrum of the substrate was obtained and used to compare with the TiC thin films deposited.

## **3 Results and Discussion**

### ***3.1 Surface Profilometer and Raman Results***

The 3D of the optical images is shown in Fig. 2 and the statistical data is presented in Table 3. From results obtained, the surface roughness ranges from 1.289 to 2.816  $\mu\text{m}$ . The roughness varies with the process parameters. The highest roughness was noticed at RF power of 250 W and the least range of roughness was noticed at RF power of 150 W, temperature of 80  $^{\circ}\text{C}$  and time of 2 h. The increase in roughness associated with an increase in power might be due to higher rate of deposition as the RF power increases. These led to faster deposition of TiC films on the substrate, thereby, affecting the morphology geometry of the film surface. To understand the structural defect in the films, Raman analysis was done on all the samples. Figure 3 shows the Raman spectra diagram with the spectrum of the substrate material included for comparison. From the results, presence of D-mode and G-mode peaks were observed in all the films except for samples for the substrates and samples L4 and L5 produced at 200 W. The absence of high spectra intensity peaks in the spectra of thin film of L4 and L5 is due to the continuous and defect-free nature of the thin film, thereby resulting in no active vibration of the spectra modes. Huang and Liao [13] reported

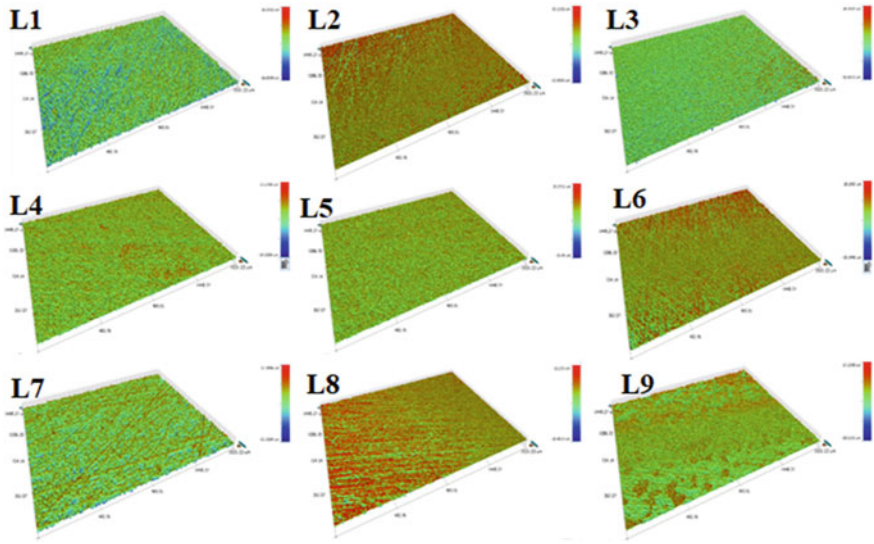


**Fig. 2** 3D images of the surface profile

**Table 3** Optical profilometer statistical detail of TiC thin film coating

Experimental run number	Average roughness Ra ( $\mu\text{m}$ )	Maximum profile peak height Rp ( $\mu\text{m}$ )	RMS roughness Rq ( $\mu\text{m}$ )	Maximum height of the profile Rt ( $\mu\text{m}$ )	Maximum profile valley depth Rv ( $\mu\text{m}$ )
L1	1.289	26.559	2.305	40.399	-18.84
L2	1.385	15.110	1.979	37.767	-22.657
L3	1.663	24.36	2.284	41.027	-16.667
L4	2.229	13.175	3.039	27.365	-14.190
L5	2.109	15.371	3.147	30.821	-15.450
L6	2.058	18.29	2.724	38.435	-20.145
L7	2.671	17.390	3.303	28.740	-11.350
L8	2.816	12.231	3.347	38.692	-26.461
L9	2.633	17.16	3.127	35.681	-18.522

that the spectra are caused by clustering of the thin film, the stress induced by lattice mismatch and the differential thermal expansion coefficients between the thin films and the substrates, or a phase change in microcrystalline structure.

**Fig. 3** Raman spectra of the TiC thin-film coating

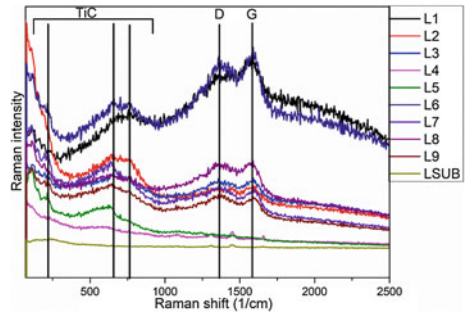


**Table 4** S/N ratio analysis of the surface roughness

Experiment no.	Control factors			Surface roughness (μm)	S/N ratio for hardness
	A RF power (W)	B Sputtering time (H)	C Temperature (°C)		
L1	150	2.0	80	1.289	-2.20506
L2	150	2.5	90	1.385	-2.82900
L3	150	3.0	100	1.663	-4.41784
L4	200	2.0	90	2.229	-6.96220
L5	200	2.5	100	2.109	-6.48153
L6	200	3.0	80	2.058	-6.26891
L7	250	2.0	100	2.671	-8.53348
L8	250	2.5	80	2.816	-8.99265
L9	250	3.0	90	2.633	-8.40902

### 3.2 Analysis of Taguchi Statistical Results

The effect of each factor level on the quality of the surface roughness was analysed using the signal-to-noise (S/N) ratio. The experimental results of the surface roughness and the S/N ratio are illustrated in Table 4. The S/N ratio is the ratio of the mean to the standard deviation and used to measure the quality characteristic from the desired output response.

### 3.3 Analysis of Signal-To-Noise (S/N) Ratios and Means

The S/N and the means response of the surface roughness are presented in Table 5. To obtain the optimal process parameter, the lower-the-better quality characteristic for the surface roughness was used. The graph of the S/N ratios is depicted in Fig. 4. The highest value of S/N ratio corresponds to the lowest variance of the output



**Table 5** Response table for signal-to-noise ratios and means for surface roughness

Levels	Control factors		
	Signal-to-noise ratios		
	A	B	C
Level 1	-3.151	-5.900	-5.822
Level 2	-6.571	-6.101	-6.067
Level 3	-8.645	-6.365	-6.478
Delta	5.494	0.465	0.655
Rank	1	3	2

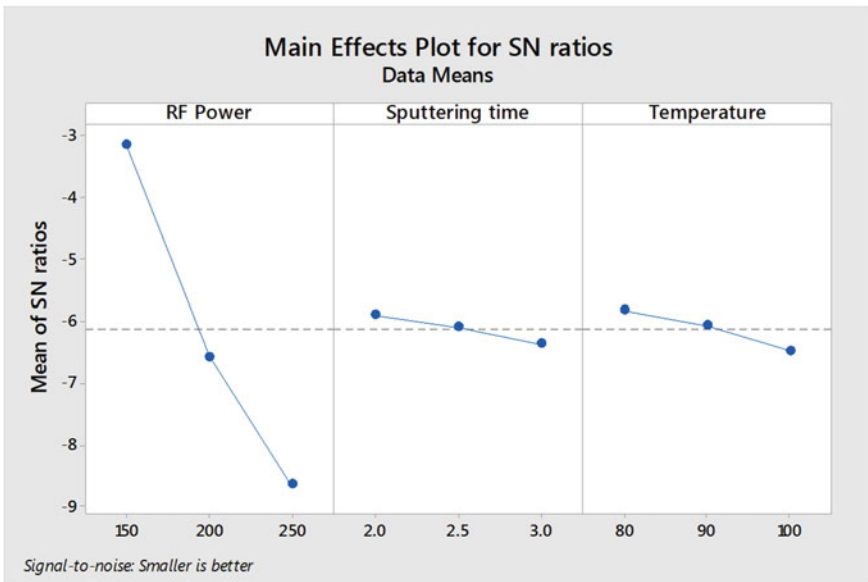


**Fig. 4** S/N ratio plot of the surface roughness

characteristic around the desired output response. From the analysis, the highest S/N ratio was found at RF power of level, sputtering time of level 1 and temperature of level 1 respectively.

The ANOVA analysis of the surface roughness is shown in Table 6. It was noticed that the RF power contributed the most to the surface roughness with a contribution rate of 95.62%. It was observed that the contribution of sputtering time and temperature are 0.22% and 0.55% respectively with percentage error of 3.63%.

**Table 6** ANOVA analysis of the surface roughness

Variance Source	The degree of freedom (DoF)	Sum of squares (SS)	Mean square (MS)	F-Ratio	Contribution rate (%)
<i>Surface roughness</i>					
A	2	2.39142	1.19571	26.13	95.62
B	2	0.00487	0.00243	0.05	0.20
C	2	0.01376	0.00688	0.15	0.55
Error	2	0.09089	0.04545	—	3.63
Total	8	2.50094	—	—	100

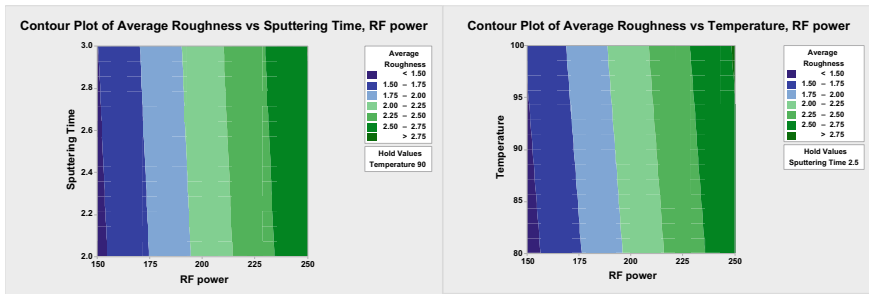


**Fig. 5** Contour plot of the surface roughness. **a** Sputtering time and RF power against the surface roughness. **b** Temperature and RF power against the surface roughness

### 3.4 Analysis of ANOVA

The contour plot in two dimensions is shown in Fig. 5. It shows the relationship between the two process parameters and one response. Figure 5a shows the graph of sputtering time and RF power against the surface roughness and Fig. 5b shows the graph of temperature and RF power against the surface roughness. Both graphs share the same trend. From Fig. 5a, as the sputtering time and RF power increase, the surface roughness also increases. This same phenomenon is also noticeable for Fig. 5b. The interaction between these process parameters is significant on the final outcome of the surface roughness.

## 4 Conclusions

From the analysis of the results, it can be concluded that RF power is the major determinant parameters for the surface roughness. The optimal process parameter for the surface roughness was found at RF power of level 1, sputtering time of level 1 and temperature of level 1. The Raman result show the effect of the process

parameters on the structural defects. Films produced at RF power of 200 W shows better continuity and minimal defects.

**Acknowledgements** The authors would like to acknowledge the Council for Scientific and Industrial Research (CSIR) for the funding provided towards this research study.

## References

1. Lapshin R, Alekhin A, Kirilenko A, Odintsov S, Krotkov V (2010) X-ray, synchrotron and neutron techniques. *J Surf Invest* 4:1–11
2. Alekhin A, Boleiko G, Gudkova S, Markeev A, Sigarev A, Toknova V et al (2010) *Nanotechnol Russ* 5:696–708
3. Bertazzo S, Rezwani K (2009) *Langmuir* 26:3364–3371
4. Bertazzo S, Zambuzzi W, Da Silva H, Ferreira C, Bertran C (2009) *Clin. Oral Implants Res.* 20:288–293
5. London G, Chen K, Carroll GT, Feringa BL (2013) *Chemistry. Eur J* 19:10690–10697
6. Kulkarni M, Mazare A, Schmuki P, Iglie A, Seifalian A (2014) *Nanomedicine* 111:111
7. Kelly PJ (2000) *RD Arnell* 56:159–172
8. Park S (1996) *Robust design and analysis for quality engineering*. Boom Koninklijke Uitgevers
9. Taguchi G, Elsayed EA, Hsiang TC (1989) *Quality engineering in production systems*. McGraw-Hill, New York
10. R Roy Ltd. (1990) New York, USA
11. Yang W, Tarng Y (1998) *J Mater Process Technol* 84:122–129
12. Selvaraj DP, Chandramohan P (2010) *J Eng Sci Technol* 5:293–301
13. Huang Y, Liao P (1998) *Solar energy mater. Solar Cells* 55:179–197

# Laser Metal Deposition of Titanium Alloy: A Review



**Bonolo S. Boshoman, Esther T. Akinlabi, Mutiu F. Erinosh, and Oluwagbenga T. Johnson**

**Abstract** Titanium alloys have found great applications in various fields of engineering, namely, but not limited to, the aerospace, engineering, and biomedical industries. The alloys have also found greater applications in the manufacturing industries through Additive Manufacturing technologies and are the attractive choice due to their exceptional resistance to corrosion and high-specific strength among other properties. However, this paper is a collection of the applicable analyses of studies that have been conducted universally in the hopes to overcome the shortfalls of the titanium metals through additive manufacturing. The modern techniques of the manufacturing technology of titanium alloys, the property enhancements that can be achieved through laser metal deposition, and other additive manufacturing technologies of titanium alloys were critically reviewed. The current trends, arguments, and research essentials were highlighted, and it was concluded that the correct combination of process parameters of laser metal deposition undoubtedly can have a positive effect on the material properties of the titanium parts or components.

**Keywords** Additive manufacturing · Laser technology · Titanium alloys · LMD process · Processing parameter · Properties

---

B. S. Boshoman · E. T. Akinlabi  
Mechanical Engineering Science Department, University of Johannesburg, Auckland Park  
Kingsway Campus, P. O. Box 524, Johannesburg 2006, South Africa

M. F. Erinosh (✉)  
Department of Mechanical and Industrial Engineering, University of Namibia, P.O. Box 3624,  
Ongwediva, Namibia  
e-mail: [mutiuerinosho1@gmail.com](mailto:mutiuerinosho1@gmail.com)

O. T. Johnson  
Department of Mining and Metallurgical Engineering, University of Namibia, P.O. Box 3624,  
Ongwediva, Namibia

## 1 Introduction

As the ninth most abundant element in the earth's crust, and the fourth among structural metals, titanium and its alloy have been generally fascinating metals to mankind for more than half of a century [1]. Over the past 20 years, titanium and its alloys' production practices have matured more rapidly than perhaps any structural material in the history of metallurgy [2]. The titanium material has improved the efficiency and functionality of some niche components in the industry today [3]. Additive manufacturing (AM) is a three dimensional practice of building a component in layers. It is an advanced AM technology used for the repair and rebuilding of worn or damaged components for the purpose of manufacturing new components [4]. All the AM technologies are based on the principle of slicing a solid model in multiple layers to create a toolpath, upload data in the machine, and build the part up layer by layer following the sliced model data using a heat source by either using the laser, electron beam, or electric arc [5]. The fabrication of metal composites in AM is generally classified according to the type of powder deposition method, the laser to powder interaction, and the metallurgical mechanisms involved in consolidation into the groups of laser melting, laser sintering, and laser metal deposition [6]. In 2014, William E. Frazier published a review on metal additive manufacturing. The review was based on the classification of metallic AM systems in terms of the material feedstock, the energy source, and the built volume of deposited parts. The system of deposition was further divided into three broad categories: the powder bed systems, the powder feed systems, and the wire-feed systems [7]. Laser metal deposition (LMD) is a typical example of a powder feed system, and it will be the technology to be extensively reviewed. AM technologies utilizing powders as feed material are the most common for the fabrication of metallic materials [8]. The schematic diagram of the LMD process is shown in Fig. 1.

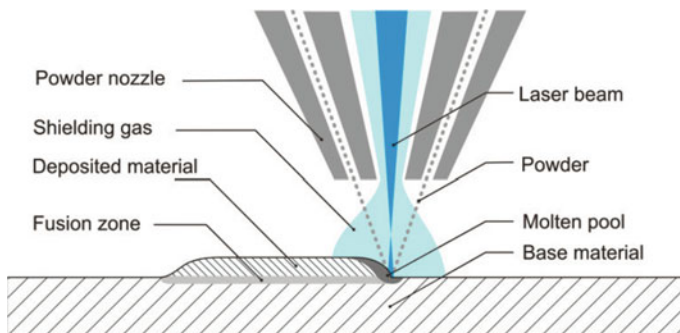


**Fig. 1** Schematic diagram of LMD process [9]

The laser creates a melt pool and then the coaxial powder nozzle injects the metal powder into the melt pool in an argon controlled environment, as shielding gas, to protect the deposit from oxidation. When two powders are used, the feeding mechanism is from two different hoppers and the powders flow through the groove at the base of the hoppers and get sucked into the hose connected to the base of the hoppers and flow to the nozzle end with the help of the carrier gas [3]. Selective laser melting (SLM) is another example of powder feed system. Zhang and Sercombe [10] and Gu et al. [11] described SLM as one of the developed technologies of additive manufacturing where a product is built by melting the selected layers of powder under a protective atmosphere, by a computerized laser beam. It was described that a high-intensity laser beam selectively scans the powder bed and the powder particles are melted then solidified to form a solid layer. The process is repeated with new layer of powders forming on the previously formed solid layer until the full part is completely built. In a wire-feed AM technology and developments of metal components, Ding et al. [12] described the process as a promising alternative to traditional subtractive manufacturing for fabricating large expensive metal components with complex geometry. The authors further explained that wire-feed AM processes generally involve high residual stresses and distortions due to the excessive heat input and high deposition rate. Conventional techniques of fabricating titanium and titanium alloys include casting, machining, and powder metallurgy, all of which being highly time, energy, and material consuming processing steps [13]. However, the cost of manufacturing through this route is generally expensive and can be difficult. The author explained further that AM technology can not only produce the ideal and high precision geometrical parts but it can likewise impact mechanical properties better than following the conventional route of manufacturing [13]. The fabrication of titanium-based parts by laser-based processes has attracted considerable attention in the industries [14]. Making metallic products through AM processes plays very significant roles [15]. The development of an appropriate microstructure with optimum mechanical properties is a challenging problem in the field of titanium alloys. Hence, more studies on the effect of thermomechanical processing on the properties of these alloys are required to gain a better understanding [16].

## **2 Titanium History, Developments, and Applications Through AM Technology**

In the past, additive manufacturing was used to make models for visualization, prototypes for a fit and function testing, and patterns for prototype tooling. Now, many organizations are focusing their energy on making parts that go into final products. Preez and Beer [17] internationally reported that players are networked and efforts have been coordinated to achieve maximum impact on the society. In future, it will be difficult for conventional methods of manufacturing to compete in the production parts through AM technology [18]. In recent years, digitizing and automation have

gained important places in the manufacturing of products [13]. Titanium alloys have already well-approved themselves in chemical, marine, and aerospace industries. They are very strong and have the ability to withstand heavy loads. In addition, they are used for manufacturing implants and prostheses [19]. In principle, 3D printing is based on taking a 3D geometry, slicing it into multiple layers, and creating a toolpath that will trace the part layer by layer. 3D printing of metals has its roots in stereo lithographic (SL) process. This SL was built on a surface file format, called Standard Tessellation Language (STL) and widely used in rapid prototyping and computer-aided manufacturing. The STL files are used as inputs since they represent the raw unstructured triangulated surface [5]. Titanium alloy (Ti6Al4V) was the first practical alloy to be developed back in 1954. The consumption of the alloy accounted for the 75–85% and others regarded as modified. Over the years, many more of titanium alloys have been developed in the world today, and the most famous established alloys are 20–30 types [20, 21]. The significant exceptions are alloys based on the intermetallics in the TiAl system or composites containing SiC fiber applications [2]. The two phases (alpha and beta) of titanium alloy offer a range of combinations of strength, toughness, and high-temperature properties that make them attractive in wide-ranging aerospace and other products demanding high-specific properties to temperatures [2]. Titanium alloys are also applicable in the field of biomaterials and have been known to enhance the quality and longevity of human life and the science and technology associated with this field is now a trading magnifier [16]. Focusing on the product development as well as cost of integrating design with manufacturing in bioengineering has focused research toward a more predictive competency [2]. Different techniques have been adopted for porous structures on titanium in implants [22]. Electron beam as the energy source is used in some cases, but the surface finish is not remarkable. Thus, some orthopedic implants preferred the rough surface. The beta alloys have enabled the biocompatibility properties of the alloy due to high strength with adequate toughness and fatigue resistance in aircraft applications [2].

## ***2.1 Benefits of Titanium in AM***

Of the AM technologies, LMD in particular is responsible for producing components with complex geometries, which are not possible by the conventional machining processes. Moreover, LMD is beneficial for the repair and restoration of damaged components. Due to these advantages, LMD has improved from making only prototypes, models, tools, molds, and dies, but now used in the production of end products [23]. Bykovskiy et al. [19] agreed with the benefits mentioned and have suggested and acknowledged the use of LMD technology for the manufacturing of titanium parts. Titanium powder metallurgy can be restricted in waste of energy and resource related to the traditional production and this process also can produce near net-shaped parts and components [19]. An inherent advantage of LMD is that the grain size is very small. However, there is no difficult heat treatment and cooling mechanisms

required to refine the microstructure, and on the other hand, hot-isostatic-pressing-process and additional heat treatments can be used to adjust a certain microstructure homogeneously [14].

## 2.2 *Titanium Shortfalls*

Despite the exceptional properties that titanium exhibits, the metal falls short of performance in a number of factors including cost, difficulty in machining and powder metallurgy. Several methods to improve these shortfalls have been shown to be feasible at the laboratory level, but to production range, it is quite more challenging [2]. It was envisaged that titanium would be an ideal structural metal to replace steel in vehicles, but cost implication is the barrier [1]. The cost of powders is cited as a key hurdle that prevents the development of powder metallurgy titanium materials and products. Bolzoni et al. [24] also reported that the widespread usage of titanium at the industrial level, especially in the automotive industry, has not been achieved yet because of its high extraction and production costs. Titanium being the metal of the future is known to be a difficult metal to process due to the strong affinity for air, and at high temperature in air, the metal becomes brittle and weaker [1]. Titanium alloy is a difficult metal or alloy when machining due to low thermal conductivity and volume-specific heat. In other word, it is difficult to machine material and causes deterioration of cutting tool and produces a rough surface due to the unstable behavior during machining [25].

## 3 **Property Enhancement Research Work**

Geetha et al. [16] reported that titanium and its alloys are being incessantly subjected to various modifications with respect to alloy composition and surface properties in order to meet the need for improved function. The improvement on titanium alloy has been conducted by various authors [3, 19, 26–29]. The process parameters have a great influence on the cooling rate and the thermal gradient and consequently on the thermal history and porosity of components produced by AM technics [30]. During LMD process, a lower scanning speed and a high laser power can lead to a lower degree of porosity [26, 31]. A better porous implant can be made by controlling the processing parameters, and once found, it can be disregarded as a defect, most especially for implants [31]. Yu et al. [32] pointed out that the results of the material properties of Ti-6Al-4 V parts produced by LMD depend on the formed microstructure and the minor elements content in the fabricated parts [32]. Chandramohan et al. [33] stated that during solidification of  $\alpha$ - $\beta$  Ti alloy, columnar prior  $\beta$ -grains grow epitaxially across several layers and against the heat flow [33]. Recently, Sobiya et al. [34] studied the characterization of the influence of the laser scanning speed of LMD for titanium and titanium carbide powders on a titanium alloy substrate and



the properties were improved. Selective laser melting is employed by Attar et al. [13] to evaluate the mechanical behavior of commercially pure titanium. The micro-hardness, compressive, and tensile ultimate strength were reportedly increased. The improvement of mechanical properties was reported to play a key role in enhancing the biocompatibility of titanium implants. Erinoshio et al. [3] improved on the properties of titanium alloy with 1 wt% of Cu for biomedical implant. For minimum finishing surfaces, optimal turning parameters were developed by Umasekar et al. [35]. The cutting tool feed and cutting speed were controlled for better surface finish on the machined components. It was reported that the surface roughness was high with increasing feed rate and decreased with the high cutting speed applied [35]. In orthopedic application, several chemical surface modification methods are used to increase the surface roughness of implants and enhance osseointegration [22].

## 4 The Market Expectations of Titanium Alloys

The industrial volume growth of titanium is back to its strongest level since 2011; however, the industry is expected to have 8–10% growth increase in 2019 compared to its performance in 2018. The high strength and lightweight materials in different industries are some of the properties that increase the demand for titanium. The growth of the alloy in the aerospace industry along with high use of carbon fiber composites is also part of the demand. This is in accordance with the International Titanium Association (ITA) (2018), established in 1984, which connects the public interests in using titanium with specialists from across the globe. The aerospace industries consume over 60% of titanium mill product, of which over 75% was in civilian airframes and engines. However, the built rate in civil aerospace since 2011 has reduced the market share of military and space titanium usage [36]. The proportion used for aerospace grade has grown to an estimated 45% following the demand from the aerospace industry [36]. Researchers and market observers also believe that titanium printing is becoming the largest opportunity for additive manufacturing materials, with revenues exceeding all other alloy groups used in AM over the next ten years. The high strength to weight ratio and other desirable properties have made the alloys expanding in the automotive, medical, aerospace, dental, and consumer products industries [37].

## 5 Summary and Conclusions

Additive manufacturing is a technological practice of modeling shapes through multiple layers with the aid of a computerized system. Abundant research studies have focused on the optimization of process parameters and the property enhancements of titanium alloys. This paper attempted to capture some aspects of the growing science of titanium, related to its fabrication through laser metal deposition. From

the above presented review, it is clear that there is a large variety of commercial techniques for additive manufacturing of metal parts besides LMD. Process parameters of LMD undoubtedly have an effect on the material properties of the parts subjected to the process. One may even go as far as to say that any desired property can be achieved in a final part using titanium material when the right combinations of process parameters are implemented.

Over the last decade, studies on LMD of titanium alloys have found that:

- Proper combination of process parameters such as scanning speed, laser power, and powder flow rate are not the only keys for a successful deposition of the titanium alloy but also important in the properties the final part will possess.
- The mechanical properties of laser processed titanium alloy are better than the conventionally fabricated titanium alloys. The hardness of a fabricated titanium alloy has been favored by higher scanning speeds while the relatively high cooling rates have favored smaller grain sizes.
- The aforementioned potentials of titanium and its alloys in AM together with the overview of the market have created the largest opportunity for additive manufacturing technology over the years. However, this review encourages the continued efforts to developing new or better LMD processes that offer a low-cost and time-saving alternative.

## References

1. Fang ZZ, Paramore JD, Sun P et al (2017) Powder metallurgy of titanium: past, present, and future. *Int Mater Rev*
2. Banerjee D, Williams JC (2013) Perspectives on titanium science and technology. *Acta Mater* 61:844–879
3. Erinoshio MF, Akinlabi ET, Pityana S (2016) Effect of scanning speed and powder flow rate on the evolving properties of laser metal deposited Ti-6Al-4V/Cu composites. *Mater Res* 10:207–223
4. Dutta B, Song L, Choi J et al (2011) Additive manufacturing by direct metal deposition. *Adv Mater Process*
5. Dutta B, Froes F (2017) The additive manufacturing (AM) of titanium alloys. *Metal powder report*, 72, pp 96–106
6. Gu D (2015) *Laser additive manufacturing of high performance materials*. Springer, Berlin, Heidelberg
7. William EF (2014) Metal additive manufacturing: a review. *J Mater Eng Perform* 23:1917–1928
8. Attar H, Ehtemam-Haghighi S, Kent D et al (2018) Recent developments and opportunities in additive manufacturing of titanium based matrix composites: a review. *Int J Mach Tools Manuf* 133:85–102
9. Graf B, Ammer S, Umenyuk A et al (2013) Design of experiments for laser metal deposition in maintenance, repair and overhaul applications. In: 2nd international through-life engineering services conference. *Procedia*, 11, pp 245–248
10. Zhang LC, Sercombe TB (2012) Selective laser melting of low modulus biomedical Ti-24Nb-4Zr-8Sn alloy: effect of laser point distance. *Key Eng Mater* 520:226–233
11. Gu DD, Meiners W, Wissenbach K et al (2012) Laser additive manufacturing of metallic components: materials. *Process Mech* 57:133–164

12. Ding D, Pan Z, Cuiuri D et al (2015) Wire-feed additive manufacturing of metal components: technologies, developments and future interests. *Int J Adv Manuf Technol*, 81
13. Attar H, Calin M, Zhang L et al (2014) Manufacture by selective laser melting and mechanical behaviour of commercially pure titanium. *Mater Sci Eng* 593:170–177
14. Leyens C, Brueckner F, Seidel A et al (2015) Laser additive manufacturing of titanium alloys and titanium aluminides. In: *The 13th world conference of titanium*, 13
15. Kumar S, Pityana S (2011) Laser-based additive manufacturing of metals. *Adv Mater Res* 227:92–95
16. Geetha M, Singh AK, Asokamani R et al (2009) Ti based biomaterials, the ultimate choice for orthopedic implants—a review. *Prog Mater Sci* 54:397–425
17. Preez WB, Beer DJ (2015) Implementing the South African additive manufacturing technology roadmap—the role of an additive manufacturing centre of competence. *S Afr J Ind Eng* 26:85–92
18. Wohlers T (2012) Additive manufacturing advances: the fast growing frontier includes metals and mainstream parts production. Available from: <https://advancedmanufacturing.org/additive-manufacturing-advances/>. Accessed: Nov 2018
19. Bykovskiy DP, Petrovskiy VN, Sergeev KL et al (2017) Direct metal laser deposition of titanium powder Ti-6Al-4V. *J Phys Conf Ser*, 941
20. Kostov A, Friedrich B (2006) Predicting thermodynamic stability of crucible oxides in molten titanium and titanium alloys. *Comput Mater Sci* 2:374–385
21. Gonzalez M, Maskos K, Hargrave R et al (2008) Titanium alloy tubing for HPHT applications, 3:1912–1928
22. Shahali H, Jaggessar A, Yarlagadda P (2017) Recent advances in manufacturing and surface modification of titanium orthopedic applications. *Proc Eng* 174:1067–1076
23. Fraunhofer Institute of Laser Technology (2016) Laser metal deposition process. Available from: <https://www.ilt.fraunhofer.de/en/publication-andpress/>. Accessed: Aug 2018
24. Bolzoni L, Ruiz-Navas EM, Gord E (2013) Processing of elemental titanium by powder metallurgy techniques. *Mater Sci Forum* 765:383–387
25. Dey NK, Liou FW, Nedic C (2013) Additive manufacturing laser deposition of Ti-6Al-4V for aerospace repair applications. *International SFF Symposium, Texas*
26. Ogunlana MO, Akinlabi ET (2016) Influence of process parameters on porosity behaviour of laser metal deposited titanium composites. In: *Proceedings of the world congress on engineering and computer science*, 2
27. Ekaterina N, Andrey B, Natalia G et al (2019) Research of titanium covering effect received by selective laser melting on mechanical properties of aluminum alloy Al-6Mg. *Mater Today Proc Part 1* 11:370–374
28. Jing L, Jianzhong Z, Aixin F et al (2018) *Mater Sci Eng A* 734:291–298
29. Xiao Z, Zhuo L, Jing L et al (2019) High strain rate response of Ti-6.5Al-3.5Mo-1.5Zr-0.3Si titanium alloy fabricated by laser additive manufacturing. *J Alloy Compd* 781:47–55
30. Saboori A, Gallo D, Biamino S et al (2017) An overview of additive manufacturing of titanium components by directed energy deposition: microstructure and mechanical properties. *Appl Sci*, 883
31. Mahamood RM, Akinlabi ET, Mukul SM et al (2014) Characterizing the effect of processing parameters on the porosity of laser deposited titanium alloy powder. In: *Proceedings of the international multi-conference of engineers and computer scientists*, 2
32. Yu J, Rombouts M, Maes M et al (2012) Material properties of Ti6Al4V parts produced by laser metal deposition. *Phys Proc* 39:416–424
33. Chandramohan P, Bhero S, Manikandasubramanian K et al (2018) A review of additive manufacturing of  $\alpha$ - $\beta$  Ti alloy components through selective laser melting and laser metal deposition. *J Eng Sci Technol* 13:790–812
34. Sobiyi K, Akinlabi E, Akinlabi S (2017) The Influence of scanning speed on the laser metal deposition of Ti/TiC powders. *Mater Technol* 2:345–351
35. Umasekar VG, Gopal M, Rahul K et al (2017) Investigation of surface roughness in finish turning of titanium alloy Ti-6Al-4V. *ARPN J Eng Appl Sci* 12:5029–5034

36. Roskill (2018) Titanium Metal: Global Industry, Markets And Outlook. Available from: <https://roskill.com/market-report/titanium-metal/>. Accessed: Oct 2018
37. Research and Markets (2016) Titanium opportunities in additive manufacturing: an opportunity analysis and ten-year forecast. Available from: <https://www.businesswire.com/news/home/201612120066063/en/title>. Accessed: Oct 2018

# Effect of Novel Swirl Distributor Plate on Gasification Efficiency of Bubbling Fluidized Bed Gasifier



Iman Eslami Afrooz and Dennis Ling Chuan Ching

**Abstract** Distributor plate is the most important aspect of the fluidized bed gasifier (FBG) design. Its main function is to uniformly distribute fluidized medium through the cross section of the bed and as a result, to provide a good gas-fuel mixing. Therefore, a success or failure fluidization in an FBG is strongly dependent on its distributor plate performance. To this end, a novel distributor plate called swirl distributor plate (SDP) was designed and built in order to enhance the gas-fuel mixing and heat transfer. The effect of SDP on gasification was studied experimentally. Results were compared with conventional distributor plate (CDP). Comparing with conventional distributor, an enhancement in syngas production was observed, while the fluidized bed gasifier was equipped with novel SDP. Moreover, the results show 15.90 and 6.63% improvement in the values of carbon conversion and cold gas efficiency.

**Keywords** Distributor plate · Gasification · Fluidized bed

## 1 Introduction

Gasification, in general, is a unique process that converts any carbon-based materials, such as petcoke, coal, wastes, biomass, and heavy residual into other forms of fuel gases through chemical reaction and without burning them [1]. The product of gasification is synthesis gas (syngas), which is composed of CO and H<sub>2</sub>. Syngas can be burnt in a combustion turbine-generator unit to produce the energy needed for steam generation for further power production in a steam turbine-generator unit. This combination of a gasifier and a combined cycle is called the integrated gasification combined cycle (IGCC). The efficiency of such a system is 40%, which is higher than 34% of the direct combustion fired plant.

Furthermore, IGCC system produces considerably less emissions compared to the direct combustion of the coal-based energy systems, which can satisfy the environmental regulations of the twenty-first century. Syngas can also be converted to

---

I. Eslami Afrooz (✉) · D. L. Chuan Ching  
Department of Fundamental and Applied Sciences, Universiti Teknologi PETRONAS,  
32610 Seri Iskandar, Perak, Malaysia  
e-mail: [imaneslami@hotmail.com](mailto:imaneslami@hotmail.com)

transport liquid fuels or used to produce fertilizers and chemicals. The Hydrogen needed for the oil refinery process, ammonia, and acetic anhydride productions can be produced using heavy oil and the coal gasification process, respectively. Thanks to the gasification technology, any useless and waste materials can be used as gasifier feedstock. Therefore, the landfill needed for waste disposal and the disposal costs will reduce significantly. Nowadays, gasification is receiving much more attention due to its advantages together with rising energy price and climate change [1–3].

As the above discussion attests, maximizing the syngas production in gasification is a major challenge. One way of improving gasifier efficiency is to enhance the gasifier heat and mass transfer. This can be done by improving the gas-fuel mixing in the combustion chamber. To this end, a lot of research has been done to enhance the gas-fuel mixing by modifying the gas distributor plate. Some of the significant attempts reported in the literature are listed in Table 1.

Although some progress has been made in the last two decades on the improvement of gas-fuel mixing, the gas–solid lateral mixing enhancement still remains controversial and should be investigated more. This paper proposes a novel swirl distributor plate (SDP) for gas-fuel mixing enhancement over conventional distributor plate (CDP).

## 2 Methods

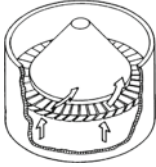
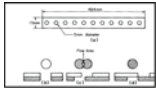
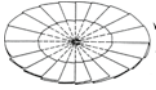
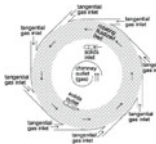
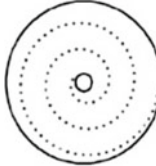
The two distributor designs that were investigated are illustrated in Fig. 1. CDP (Fig. 1a) is a perforated plate with vertical holes in a triangular pitch. SDP (Fig. 1b) contains vertical holes with a triangular pitch at the bottom of the plate and diagonal holes at the sidewalls. The vertical holes provide vertical lift to the particles, while the diagonal holes make gas swirl as it enters the bed.

Figure 2 demonstrates the schematic view and experiment setup of gasifier reactor used in this study.

The main components of the reactor are blower, screw feeder, fluidized bed, cyclone, and gas analyzer for data acquisition. The reactor contains half Kg of sand, which acts as the fluidizing medium. The air which is preheated enters the reactor from the bottom and fluidizes the bed materials (sand). Then, petcoke enters the reactor from one side and mixes with the oxygen, and the product gases (syngas) are discharged from the exhaust. The effect of two different distributor plates (CDP and SDP) is studied by observing the percentage of combustible gases produced in the process. The portable gas analyzer is used to analyze and calculate the mole percentage of the product gas. Fluidized bed furnace is heated externally by ceramic heater.

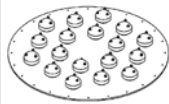
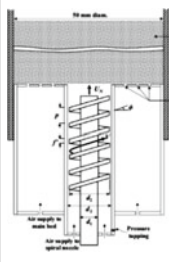

The temperature of the reactor was controlled with three K type thermocouples located on three different zones. These zones are as follows: the furnace zone where the sand bed is located, the middle zone where the reactions take place, and the reactor top zone. It took 35 min to heat up the furnace to 400°. Once the temperature reached to 400 °C, the coal is fed into the reactor. In fact, feeding the coal causes the

**Table 1** List of experimental studies to improve fluidized bed hydrodynamics

Ref.	Distributor	Configuration	Main features	Remarks
[4]	Annular ring of stationary vanes		Provides both vertical lift and horizontal motion to the particles	Due to the weak vertical drag force, this distributor plate is only suitable for shallow fluidized bed. Moreover, solid particles can settle down on the flat vertex of the conical part of it and cause the dead zone
[5]	Moving double Plate distributor (MDPD)		Controlling the size of the bubbles	The idea of moving double plate distributor was only tested on the cold flow fluidized bed with the two-dimensional rectangular geometry
[6]	Spiral distributor plate		Swirling motion of solid particles in a confined circular path	The spiral distributor plate was tested only for shallow beds, and its performance for larger radii has not been approved yet
[7]	Radial multiple points gas injection		Radial inwards gas-solid drag force and radial solid fluidization	Channeling, slugging, and an uneven distribution of the gas were observed. The complexity of the multiple gas injection points design and the problem of solids losing via the chimney make this design to some extent ineffective
[8, 9]	Rotating distributor plate		Promoting radial dispersion of the particles. Fluidizing bed more easily	As the tangential velocity became smaller than the gas velocity, the improvement in the quality of fluidization was disappeared. The effect of rotation decreases as the bed height increases

(continued)

**Table 1** (continued)

Ref.	Distributor	Configuration	Main features	Remarks
[10]	Bubble caps distributor		More homogeneous radial structure in terms of voidage Smaller voidage in all radial positions	High solid density near the bottom region of the bed was detected
[11]	Swirling flow nozzle		Improving fluidization quality of the fluidized bed due to the swirling flow induced by the helix	The swirling flow nozzle was only tested using a single nozzle in a small bed (50 mm bed diameter)
[12]	Sintered metal distributor (SMD)	—	More stable fluidization using SMD with the smaller aperture size	The SMD distributor was only tested on the cold flow fluidized bed
[13]	Novel multi-vortex (MV) distributor		Mass transfer coefficient is increased	The MV distributor results in bubble size increase, and it was tested only in 2D domain

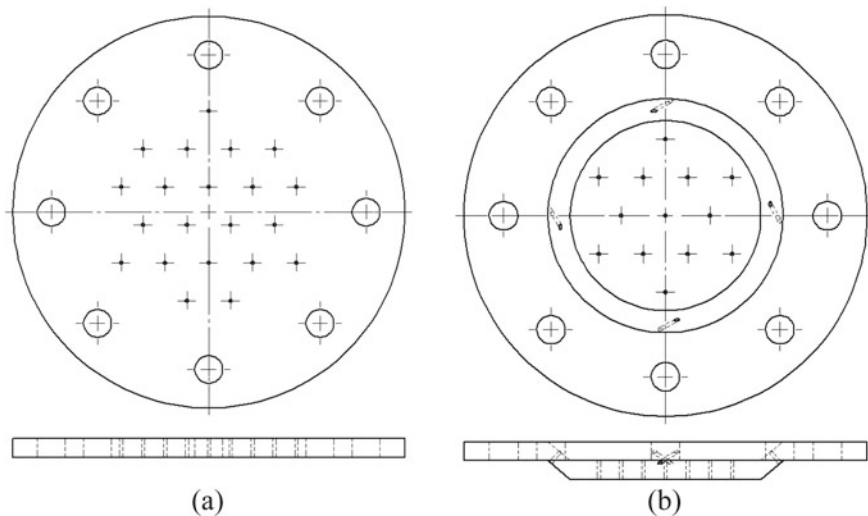


**Fig. 1** Schematic view of **a** CDP and **b** SDP



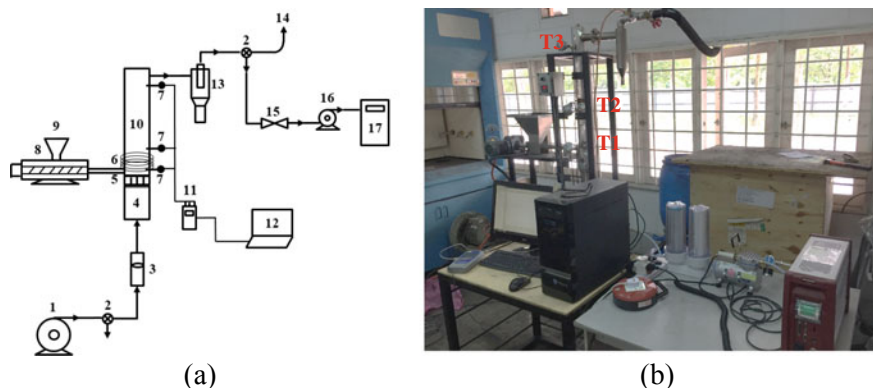


**Fig. 2** Gasifier reactor, **a** schematic diagram and **b** experimental setup. 1 Blower 2 Valve 3 Flowmeter 4 Plenum 5 Distributor 6 Heater 7 Thermocouple (T1, T2, and T3) 8 Feeder 9 Hopper 10 Fluidized bed & Riser 11 Thermometer 12 PC 13 Cyclone 14 Exhaust 15 Filter 16 ID Fan 17 Gas Analyzer

temperature to increase rapidly to the desired temperature for petcoke gasification. It was determined that 8 min would be enough time to increase the temperature of furnace up to 650°. Next, the petcoke is fed into the reactor. The furnace temperature rose up to 800 °C due to the petcoke gasification. The experiment is then performed while the furnace temperature was kept in the range of 750–800 °C for almost 40 min.

Figure 3 shows the temperature profile of gasification experiment. The measured values of T1, T2, and T3 refer to the three different zones of furnace heating zone, middle zone, and reactor top zone, respectively. As it can be clearly seen from the graph, the temperature was able to be maintained at the average bed temperature of 750–800 °C, indicating steady-state operation. While the petcoke gasification took place, the production gas (syngas) travelled up out of the reactor. It then passed through the cyclone and extra filtering system where any solid particulate matter, such as ash or dust, was removed. Once the gas was cleaned and cooled, its composition is analyzed using VARIO plus Gas Analyzer. The gas analyzer is able to detect oxygen, hydrogen, carbon monoxide, carbon dioxide, and methane. Finally, the carbon conversion and the cold gas efficiency were calculated using the material and energy balance.

## 3 Results

### 3.1 Syngas Production

Gasification experiments were performed on petcoke using fluidized bed equipped with both CDP and SDP. Experiments were conducted while petcoke was being fed

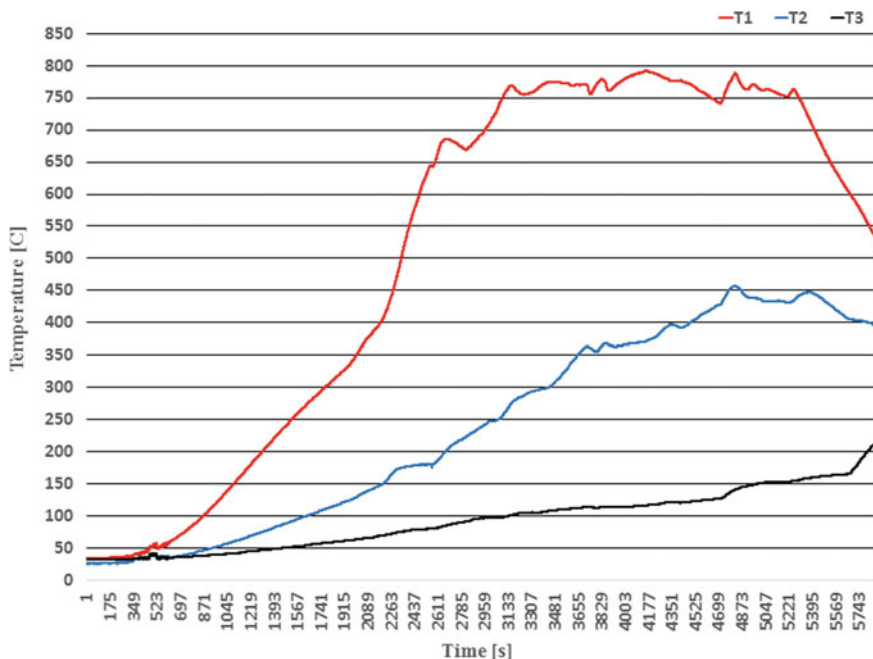


Fig. 3 The temperature profile of petcoke gasification experiment

into the reactor along with air at 750 °C. The petcoke and air feeding rates were held constant at 0.55 and 1.7 kg/h, respectively. Each experiment was held for 1 h while different syngas compositions over different time spans were recorded. Figure 4 shows the results obtained for fluidized bed equipped with CDP and SDP. Comparing Fig. 4a, b, one can conclude that fluidized bed gasifier equipped with swirl distributor plate resulted in better performance of syngas composition. The results show 65.7, 34.8, and 88.4% increase in the amount of CO, H<sub>2</sub>, and CH<sub>4</sub> production, respectively.

The comparison between the syngas production and CO<sub>2</sub> emission for both CDP and SDP is shown in Fig. 5. Comparing with the amount of CO<sub>2</sub> emission, the syngas production was remarkable. Besides, the trend for SDP shows that the emission of carbon dioxide reduces as the amount of syngas increases. Moreover, it can be clearly seen that the syngas production was increased while SDP was used. This is largely due to the gas-fuel mixing enhancement, which then leads to increases in gasification rate and a decrease of carbon dioxide formation.

### 3.2 Carbon Conversion and Cold Gas Efficiency

Carbon conversion efficiency was found by dividing the amount of carbon in the product gas with that in the fuel. To this end, the material balance was applied and

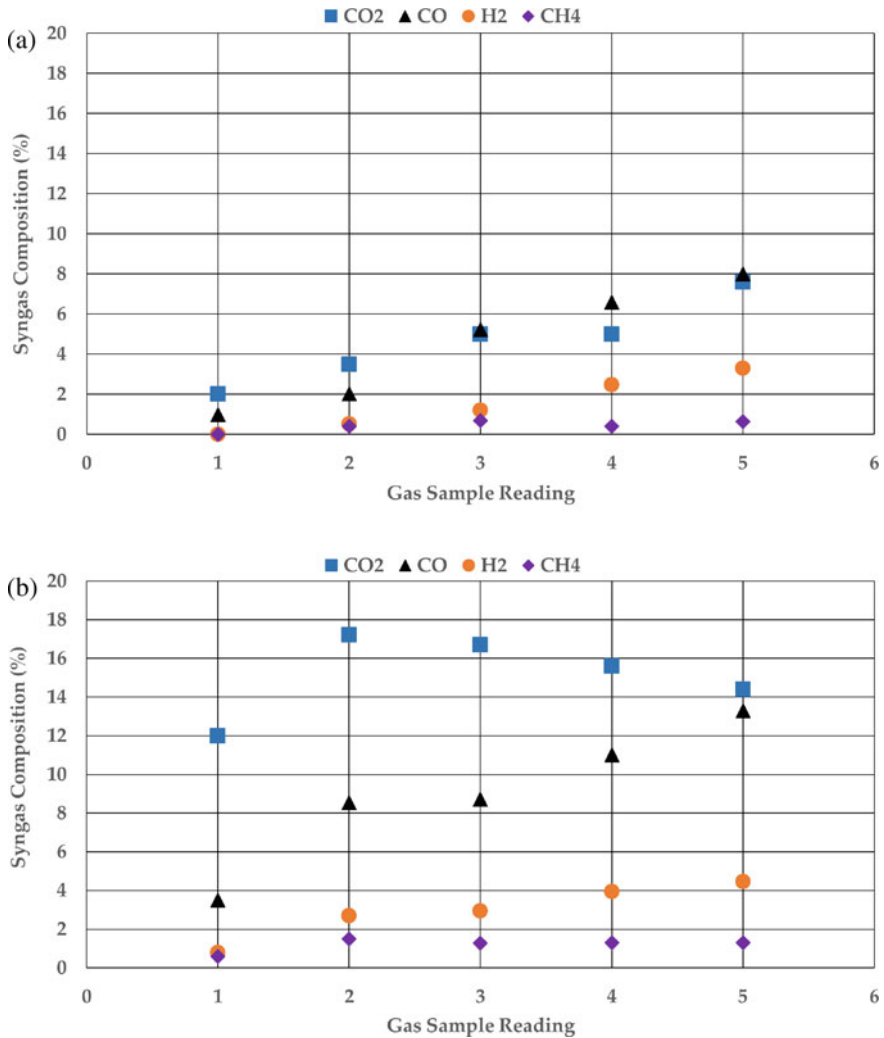


**Fig. 4** Syngas composition at different reading times while **a** CDP and **b** SDP were used

results are shown in Table 2. Moreover, an energy balance was performed on each experiment to calculate the cold gas efficiency of the system.

As can be seen in the table above, the carbon conversion efficiency has been improved significantly when the swirl distributor plate was used. The point that needs to be addressed is the poor carbon conversion is resulted from low residence time of the char particles [1]. Therefore, it is without doubt that the char particles residence time was improved due to the swirl motion of the particles imposed by the swirl distributor plate. In addition, comparing the SDP with CDP, a twofold increase in the value of cold gas efficiency has been observed.

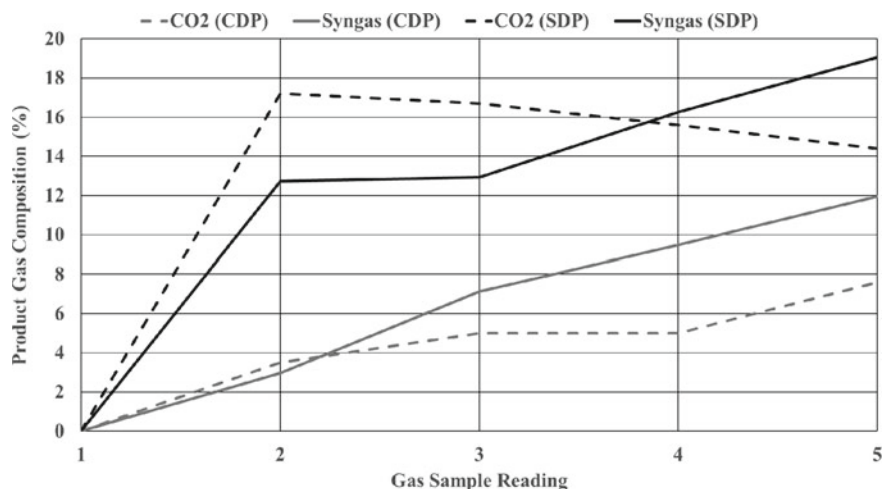


**Fig. 5** Comparison of syngas production CO<sub>2</sub> and emission of both CDP and SDP

**Table 2** Comparison of carbon conversion and cold gas efficiency

	Using CDP	Using SDP
Carbon conversion efficiency (%)	13.77	29.67
Cold gas efficiency (%)	6.79	13.42

## 4 Conclusions

In this study, the petcoke gasification experiments were conducted under air blown and atmospheric pressure and an enhancement in syngas production was observed while the fluidized bed gasifier was equipped with novel SDP. Compared to CDP, the novel SDP resulted in 34.85, 100.00, and 65.92% improvement in production of H<sub>2</sub>, CH<sub>4</sub>, and CO, respectively. The results also showed that the carbon conversion and cold gas efficiency of the reactor are enhanced twofold while novel SDP is used. To conclude, it is possible to design and build a distributor plate that would be capable of enhancing the lateral mixing of gas–solid in a fluidized bed and consequently improving the syngas composition of gasifier reactor.

**Acknowledgments** The authors express their sincere gratitude to the University Technology PETRONAS for YUTP financial support.

## References

1. Basu P (2006) Combustion and gasification in fluidized beds. CRC/Taylor & Francis, Boca Raton
2. Lee SH, Choi KB, Lee JG et al (2006) Gasification characteristics of combustible wastes in a 5 ton/day fixed bed gasifier. *Korean J Chem Eng* 23:576–580
3. Coda B, Cieplik MK, de Wild PJ et al (2007) Slagging behavior of wood ash under entrained-flow gasification conditions. *Energy Fuels* 21:3644–3652
4. Dodson CE, Lakshmanan VI (1998) An innovative gas-solid torbed reactor for the recycling industries. *JOM* 50:29–31
5. Köksal M, Vural H (1998) Bubble size control in a two-dimensional fluidized bed using a moving double plate distributor. *Powder Technol* 95:205–213
6. Sreenivasan B, Raghavan VR (2002) Hydrodynamics of a swirling fluidized bed. *Chem Eng Process* 41:99–106
7. De Wilde J, de Broqueville A (2007) Rotating fluidized beds in a static geometry: experimental proof of concept. *AIChE J* 53:793–810
8. Sobrino C, Almendros-Ibañez JA, Santana D (2008) Fluidization of group B particles with a rotating distributor. *Powder Technol* 181:273–280
9. Sobrino C, Acosta-Iborra A, Santana D (2009) Bubble characteristics in a bubbling fluidized bed with a rotating distributor. *Int J Multiph Flow* 35:970–976
10. Sobrino C, Ellis N, de Vega M (2009) Distributor effects near the bottom region of turbulent fluidized beds. *Powder Technol* 189:25–33
11. Aworinde SM, Holland DJ, Davidson JF (2015) Investigation of a swirling flow nozzle for a fluidised bed gas distributor. *Chem Eng Sci* 132:22–31
12. Yang X, Zhao Y, Luo Z (2011) Effects of sintered metal distributor on fluidization quality of the air dense medium fluidized bed. *Mining Sci Technol (China)* 21:681–685
13. Brink HG, Saayman J, Nicol W (2011) Two dimensional fluidized bed reactor: performance of a novel multi-vortex distributor. *Chem Eng J* 175:484–493

# A Review of Recent Developments in Mechanical Properties of Polymer–Clay Nanocomposites



Mohd Shahneel Saharudin, Syafawati Hasbi,  
Muhammad Naguib Ahmad Nazri, and Fawad Inam

**Abstract** Nanocomposites reinforced with polymer–clay often show dramatic improvements in strength, modulus, thermal resistance and gas permeability at lower clay content than conventional filled polymer composites. This paper focuses on most recent studies of the mechanical properties of nanocomposites with polymer–clay. The improvement of mechanisms in the mechanical properties of nanocomposites with polymer–clay is also discussed.

## Abbreviations

DGEBA	Dow Plastics, a bisphenol A diglycidyl
EPDM	Ethylene propylene diene monomer
HDPE	High-density polyethylene
IPN	Interpenetrating network
MMT	Montmorillonite
PHBV	Poly(hydroxybutyrate-co-hydroxyvalerate)
PMMA	Poly(methyl methacrylate)
PP	Polypropylene
PS	Polystyrene
PVA	Polyvinyl alcohol

---

The original version of this chapter was revised: In the Introduction section last two paras has been removed. The correction to this chapter is available at [https://doi.org/10.1007/978-981-15-5753-8\\_71](https://doi.org/10.1007/978-981-15-5753-8_71)

---

M. S. Saharudin (✉) · M. N. A. Nazri  
Universiti Kuala Lumpur, Malaysia Italy Design Institute (UniKL MIDI), 56100 Cheras, Malaysia  
e-mail: [mshahneel@unikl.edu.my](mailto:mshahneel@unikl.edu.my)

S. Hasbi  
Department of Mechanical Engineering, Faculty of Engineering, National Defence University of Malaysia, 57000 Kuala Lumpur, Malaysia

F. Inam  
Department of Engineering and Computing, University of East London, London, UK

## 1 Introduction

Nanotechnology has received wide attention from scientists and research institutions all over the world [1]. Nanomaterials are emerging technologies that have many applications in electrical engineering, chemistry, material science and medicine. On the other hand, a nanocomposite is a matrix in which nanoparticles are added to improve the specific properties of a material [2, 3]. Nanocomposite properties have led researchers and companies to consider using this material in a number of fields. Polymer–clay nanocomposites have garnered widespread interest due to their improved properties, such as dispersion and significant enhancement in physico-chemical and mechanical properties in comparison with the pure polymer systems [4, 5].

Since Toyota's first discovery, researchers have been able to significantly improve the properties of polymer materials using nanoclays [6–15]. Many researchers have discovered that the addition of nanoclays could greatly enhance properties of different types of polymers.

When Toyota Company used exfoliated nanoclay which resulted in excellent improvement in the mechanical and thermal properties of nylon 6, clay materials were later widely studied to enhance the performance of different polymers [10, 16–19].

Polymer–clay nanocomposites use smectite-type clays, such as hectorite, montmorillonite and synthetic mica, as fillers to improve mechanical properties of polymers [18, 20]. Because of the nanoscale effects, polymer–clay nanocomposites often show good improvements in strength, modulus, thermal resistance and gas permeability barrier properties using less silicate content compared to conventional filled polymer composites [21].

Another advantage of polymer–clay nanocomposites that other researchers have mentioned is that optical clarity is also retained [18, 22–25]. This fundamentally carries a three-dimensional perspective of the morphology at different length scales. Efficiency of the characterization of nanocomposite structure is enhanced by forming local versus global morphology and orientation order of the sheets in central. For instance, a situation may be visualized where the clay sheets are completely exfoliated and evenly dispersed throughout the matrix, or there may be localized regions of thin fragments dispersed in the polymer matrix.

## 2 Methods

### 2.1 *Halloysite Nanotubes (HNTs)*

In addition to various fibres and spherical mineral particles such as halloysite, effective reinforcement components are crucial in the development of new nanocomposites. Halloysite is a non-toxic clay mineral with the empirical formula  $\text{Al}_2\text{Si}_2\text{O}_5(\text{OH})_4$ , which contains numbers of nanotubes [26]. Due to their high

mechanical strength, thermal stability and biocompatibility, HNTs have been widely used for treatment of cancer, drug delivery, transportation and environment protection [27, 28].

HNTs are biocompatible materials that can be used as nanovehicle to assist and direct delivery of anticancer drug doxorubicin (DOX) into cancer cells [29, 30]. In anticancer application, folic acid (FA) and magnetite nanoparticles were grafted onto HNTs via amide reaction, whereas the drug was introduced by capitalizing electrostatic interaction between cationic drug and anionic exterior of HNTs, which eventually leads to pH-responsive release [29].

Natural occurrences of HNTs are present in several morphologies, such as platy, spheroidal and tubular; however, the tubular structure is the dominant morphology of halloysite in nature [31]. Figure 1 shows the illustration of halloysite nanotubes (HNTs). The tube-like morphology that resembles CNTs, high aspect ratio and low percolation make HNTs a potential reinforcement for epoxy and other polymers [32, 33]. HNTs are chemically similar to Kaolin, which can be acquired from natural deposits, which were found to enhance mechanical properties of nanocomposites in many publications [34–38]. Halloysite is an important member of the kaolin group of clay minerals, with a composition of  $\text{Al}_2\text{Si}_2\text{O}_5(\text{OH})_4 \cdot n\text{H}_2\text{O}$ , where  $n = 0$  and 2, for dehydrated form halloysite (7 Å  $d_{001}$  spacing) and hydrated mineral halloysite (10 Å  $d_{001}$  spacing), respectively [39], and the dimension of halloysite is normally in nanoscale.

Chromate-containing coatings are widely used in corrosion protection of metals [31, 40]. HNTs, on the other hand, are used for loading and sustained release of corrosion inhibitors [41]. The application of inhibitor-loaded HNTs in active anti-corrosive coatings is a completely new approach. The inhibitor is retained inside the particles under dry conditions [40] and then is homogeneously distributed within the sol–gel film deposited on the aluminium surface. An induced corrosion process causes significant changes in local pH. As the release of the anticorrosive agent is

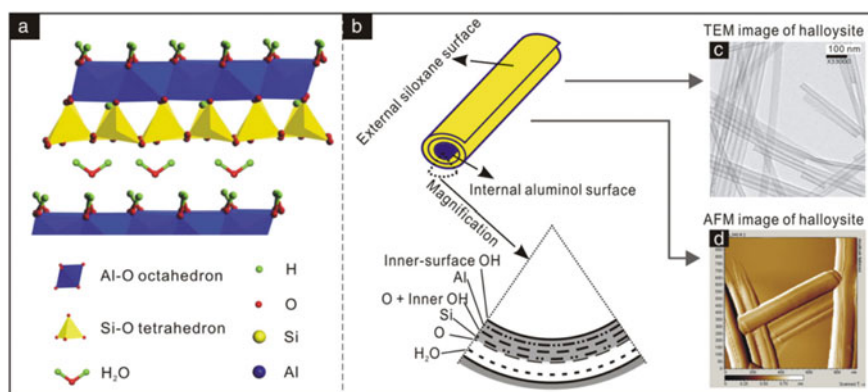


**Fig. 1** Illustration of crystalline structure of **a** halloysite, **b** structure of halloysite particle, and **c** and **d** TEM and AFM images of halloysite [31]



significantly hastened at acidic and alkaline pH, the corroding site locally triggers the action of entrapped inhibitor. Physical destruction of HNTs may occur if the sol–gel layer is cracked, which causes the inhibitor to be released immediately at the corroding spot.

## 2.2 Montmorillonite (MMT)

Montmorillonite (MMT) is a standout amongst most generally utilized smectite-type layered silicates for the manufacturing of nanocomposites. MMT has the most suitability to be used in polymers due to their high surface area and surface reactivity [42]. MMT belongs to the dioctahedral smectite group [24, 43], each of its silicate layers is approximately 200 nm in length and 1 nm in thickness, and the interlayer spacing between stacked layers is also about 1 nm [24]. Figure 2 shows the structure of MMT as illustrated by Zabihi et al. in their review paper [8].

Generally, MMT is hydrophilic in nature and the stacks of clay platelets are held firmly together by electrostatic forces. They are incompatible with most organic polymer matrices. As a whole, a molecule of a compatibilizing agent consists of one hydrophilic function and one organophilic function and its role is to improve compatibility so that the clay is dispersed in polymer matrices. Various sorts of compatibilizing agents have been utilized in the production of polymer nanocomposites. The

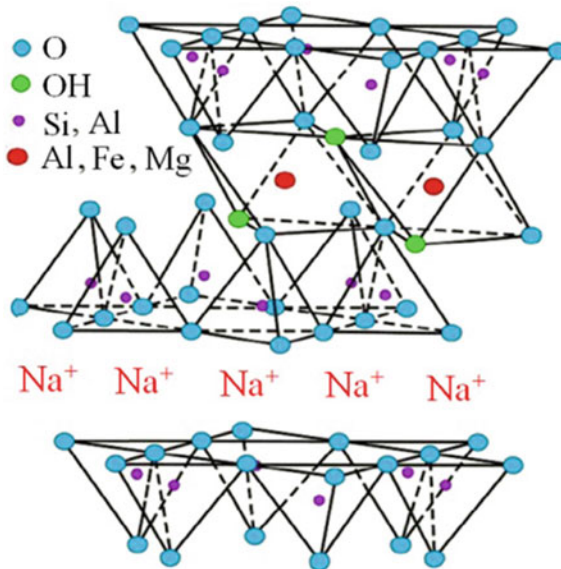


**Fig. 2** Structure of montmorillonite [8]

most well known are alkylammonium ions as they can simply be exchanged with the ions situated between the layers.

There is a drawback when blending of polymers with unmodified clay particles, which is an appropriate distribution of polymer matrix, and clay particles cannot be achieved because of the high preferred face-to-face stacking phenomenon in agglomerated tactoids, which makes them incompatible with hydrophobic polymers. Therefore, dispersion of nanoclays in most polymers remains inadequate to produce high-quality nanocomposite, especially if the particles are not evenly dispersed or incompatible with polymer matrix. Layered clays must be altered before being used in production of polymer nanocomposites.

### 3 Dispersion of Clay Nanoparticles

Dispersion of clay-based particles in epoxy and polyester matrix can be improved using several methods such as high-speed stirrer, high shear mixer and ultrasonication [44]. Figure 3 shows dispersion method of clay-based particles from literature. Our previous research studies suggested that sonication was only possible for up to 3% loading due to the increase in viscosity of the mixture [45–49]. The increase in viscosity affects the degree of dispersion, and higher viscosity, on the other hand, tends to increase nanofiller agglomeration [50]. The dispersion of nanoclay in polymer matrix is improved using sonication as it reduces air bubbles at the interface between clay particles and resin molecules. Dispersion also achieved exfoliation of particles. However, the added curing agent into epoxy resin caused the viscosity to increase rapidly, and a good method to overcome this problem is to disperse the nanoclay in hardener using tip sonicator as described by Atif and Inam [51, 52]. Alamri and Low used a high-speed mechanical mixer with a rotational speed of 1200 rpm to disperse nanoclay in epoxy resin [17]. A hardener was added to the mixture of HNTs–epoxy and stirred slowly to minimize the air bubbles. Agglomeration of nanoclay, formation of clusters and uncured resin may appear if large amount of nanoclay is added into the resin; therefore, it has been suggested that changing of resin viscosity and controlling of sonication time is the key to produce desirable composites with moderate strength and ductility [53].

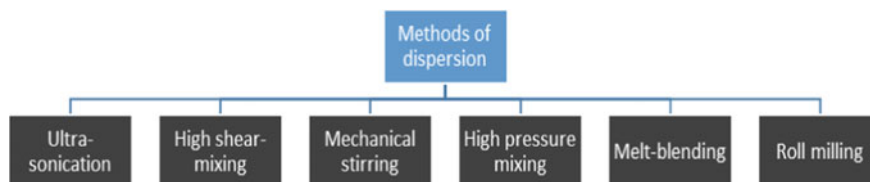


Fig. 3 Dispersion method of clay-based particles

## 4 Mechanical Properties

Reinforcing high amounts of nanoclay into polymer matrix increases the chances of organic content to act as plasticizer to the epoxy network and decreases the crosslink density. Sancaktar et al. suggested that an optimal point of clay loading should be around 0.5% only [54]; however, other researchers have suggested higher clay loading between 0.7 and 3% [33, 49, 55, 56].

Table 1 shows the tensile properties of polymer–clay nanocomposites. Merah, in his recent publication, reported an increase in tensile strength of 3 wt% MMT-unsaturated polyester up to 75%. However, the clay content has no effect on the stiffness of the developed unsaturated polyester resin, this behaviour is in line with a report by Bensadoun et al. for the same matrix [57]. Saharudin et al. reported an improvement of 38 and 75% in tensile modulus and tensile strength for 1 wt% HNTs–polyester [23]. These improvements have been achieved by using ultra-sonication method. In contrast, Ozsoy et al., in their research, reported that the tensile strengths of 10 wt% MMT–epoxy decreased 38% compared to neat sample [58]. This can be attributed to the weak adhesion between matrix and fillers, which has led to the decrease in the strength of the composite. The drop in strength is due to the non-homogeneous distribution of fillers at high filler ratios, which has led to the agglomeration and caused stress concentration regions, leading to some drop in the strength [58]. Vahedi and Pasbakhsh flaws in nanocomposite are caused by trapped bubbles during sample preparation and stress concentration at HNT particles [55]. The incorporation of nanofillers also increased the viscosity of epoxy resin, which as a results led to higher possibility of trapped bubbles and heterogeneity of the resultant samples [59]. HNTs display lower aspect ratio and specific surface area than MMT. Therefore, the thermal barrier of HNTs may somewhat be inferior to MMT and those of layered silicates [60]. In general, it can be concluded that high percentage of clay particle reinforcement (3 wt% and above) is likely to decrease tensile properties of polymer–clay composites. This was also reported by Chieruzzi et al. in their study, where in the case of 5 wt% MMT–epoxy, the tensile strength dropped 23% [61]. Table 2 shows flexural properties of polymer–clay nanocomposites. Recent research by Merah reported a decrease in flexural modulus by 5.8% and an improvement in flexural strength by 56% for 3 wt% MMT-unsaturated polyester. A study by El-Syeikh et al. reported an improvement in tensile modulus and tensile strength by 47% and 69%, respectively, for 5 wt% MMT-HDPE composite [1]. In their study, melt-processing method was used to disperse the MMT particles. Essentially, the improvement in mechanical and fracture properties of polymer–clay nanocomposites mainly depends on the interfacial bond level between nanoclay particles and polymer chains, as well as the ratio of filler loading and distribution, which control the bond and final material behaviour producing ductile, brittle, or brittle–ductile material [1]. Compared to other available studies, Saharudin et al. achieved the highest flexural modulus with 65% of improvement. They also observed an increase in flexural strength of up to 49% in the case of 1 wt% HNTs–polyester nanocomposite [47]. Other reports presented in Table 2 also show improvements in flexural modulus and

**Table 1** Tensile properties of polymer–clay nanocomposites

Sr.	Authors	Year	Matrix	Filler/(wt%)	% change in modulus	% change in tensile strength	Processing method	References
1	Merah	2019	UP	MMT/3	0	75	Ultra-sonication	[56]
2	Saharudin et al.	2017	UP	HNTs/1	38	75	Ultra-sonication	[47]
3	Saharudin et al.	2016	UP	HNTs/0.7	35	50	Ultra-sonication	[46]
4	Ozsoy et al.	2015	Epoxy	MMT/10	24	-38	Ultra-sonication	[58]
5	Wang et al.	2015	Epoxy	MMT/1	5	39	Dispersed in acetone and homogenized at 2000 rpm	[68]
6	Pasbakhsh et al.	2014	EPDM	HNTs/15	70	340	Roll milling	[55]
7	Vahedi and Pasbakhsh	2014	Epoxy	HNTs/10	22	-18	Ultra-sonication	[59]
8	Gorrasi	2014	PLA	HNTs/3	7	-20	Melt blending	[33]
9	Chieruzzi et al.	2013	UP	MMT/5	25	-23	Mechanical stirring	[61]
10	Chan et al.	2011	Epoxy	MMT/1	16.7	11	Spinning	[53]
11	Carli et al.	2011	PHBV	HNTs/5	63	3	Melt blending	[39]
12	Sancaktar et al.	2011	Epoxy	MMT/0.5	11	7	Magnetic stirring	[54]
13	Deng et al.	2008	Epoxy	HNTs/10	3	8	Mechanical stirring	[69]
14	Chozhan et al.	2008	Epoxy	MMT/3	17	18	Mechanical stirring	[70]

**Table 2** Flexural properties of polymer-clay composites

Sr.	Authors	Year	Matrix	Filler/(wt%)	% change in modulus	% change in flexural strength	Processing method	References
1	Merah	2019	UP	MMT/3	-5.8	56	Ultra-sonication	[56]
2	El-Syeikh et al.	2017	HDPE	MMT/5	47	69	Melt-processing	[1]
3	Saharudin et al.	2017	UP	HNTs/1	65	49	Ultra-sonication	[48]
4	Saharudin et al.	2016	UP	HNTs/0.7	61	44	Ultra-sonication	[46]
5	Islam et al.	2015	Epoxy	MMT/2	21	20	Ultra-sonication	[2]
6	Ruban et al.	2014	UP	MMT/5	63	33	Mechanical stirring	[71]
7	Ollier et al.	2013	UP	Bentonite/8	37	-	Ultra-sonication	[72]
8	Jumahat et al.	2012	Epoxy	MMT/5	19	9	Mechanical stirring	[73]
9	Liu et al.	2009	PP	HNTs/5	28	15.7	Melt blending	[65]
10	Kaynak et al.	2009	Epoxy	MMT/0.5	19	58	Ultra-sonication	[10]
11	Bozkurt et al.	2007	Epoxy	MMT/6	13	16	Ultra-sonication	[74]
11	Guo et al.	2009	PA	HNTs	19	7.7	Melt blending	[38]
12	Wan et al.	2003	PVC	MMT/5	3.5	25.4	Melt blending	[24]
13	Timmerman et al.	2002	Carbon fibre-epoxy	MMT/8	-4	5.5	Mechanical stirring	[15]

flexural strength; however, in a study by Timmerman et al., the flexural modulus decreased 8% compared to neat epoxy [15]. It was observed that the MMT particles were not evenly distributed and prevented the nanoparticles from providing effective reinforcement. The MMT particles act like larger structures and serve as flaws and crack initiation sites.

Table 3 shows the impact strength values from literature review. Jeyakumar et al. studied the morphological and mechanical behaviour of glass fibre-reinforced epoxy–nanoclay composites, which compared to unfilled epoxy, the incorporation of 5 wt% MMT particles into glass fibre-reinforced epoxy increased the impact strength up to 29.7% [62]. The improvement in impact strength was attributed to the homogeneity dispersion of the MMT particles. The homogeneity was evidently observed from the high-resolution scanning electron microscope (HR-SEM) analysis. Lin et al. studied the impact strength of polystyrene–halloysite nanocomposites prepared by emulsion polymerization using sodium dodecyl sulphate as surfactant [63]. They have reported an improvement of 300% of impact strength compared to neat polystyrene. They have spotted a large number of dimples on the fracture surfaces, where in each of the fractures, substantial amount of energy was dissipated. Besides that, HNTs were acting as stress bridgings and craze stabilizers. A large scale of plastic deformation, which was caused by the enhanced chain mobility, was also crucial in improving the impact strength of the composites.

Another significant improvement in fracture toughness was reported by Ye et al. They studied the impact strength of epoxy nanocomposites with HNTs. The results demonstrated that blending epoxy with 2.3 wt% HNTs increased the impact strength by 400% without compromising flexural modulus, strength and thermal stability [26]. The toughening mechanisms responsible for the unusual increase in impact strength were identified as massive micro-cracking, nanotube bridging/pull-out/breaking and crack deflection. These three mechanisms were proposed as the dominant factors that dissipate extensive impact energy. Other authors also demonstrate that considerable improvement can be achieved without matrix plastic deformation and without compromising other mechanical properties [38, 64, 65]. Considering the improvement in mechanical properties of nanocomposites, HNTs, on the other hand, are abundant, cheap and a low-cost alternative to expensive CNTs in nanocomposite. Besides that, HNTs are morphologically similar to multiwalled CNTs [66].

Table 4 shows the fracture toughness of polymer–clay nanocomposites. The maximum fracture toughness was achieved by Ramsaroop et al. where they reported an increase of 175% on their MMT–polypropylene nanocomposites [67]. Even though the  $K_{IC}$  continuously increased as clay content increased in the nanocomposites, the rate of increase was reduced at higher clay content due to intercalated structures that affected the net aspect ratio of the clay platelets [67]. A recent study by El-Sheikhy et al. reported an enhancement of fracture toughness up to 105% [1] for clay–polyolefin nanocomposites. These enhancements in the properties intuitively mean the presence and achievement of bond between nanoclay and polymer chains of HDPE.

Due to their ability to improve toughness while maintaining high modulus and thermal stability, inorganic filler, such as clay, is normally used in reinforcement

**Table 3** Impact strength of polymer–clay composites

Sr.	Authors	Year	Matrix	Filler/(wt%)	% change in impact strength	Processing method	References
1	Jeyakumar et al.	2017	Epoxy/glass fibre	MMT/5	29.7	Mechanical stirring and ultra-sonication	[62]
2	Saharudin et al.	2017	UP	HNTs/0.1	77	Ultra-sonication	[23]
3	Vahedi and Pasbakhsh	2014	Epoxy	HNTs/2.5	40	Ultra-sonication	[59]
4	Albdiry et al.	2013	UP	HNTs/1	6	Mechanical stirring and ultra-sonication	[75]
5	Carli et al.	2011	PHBV	HNTs/5	−5	Melt blending	[39]
6	Lin et al.	2011	PS	HNTs/5	300	Ultra-sonication	[63]
7	Chozhan et al.	2008	Epoxy	HNTs/5	8.5	Mechanical stirring	[70]
8	Ye et al.	2007	Epoxy	HNTs/2.3	400	<ul style="list-style-type: none"> <li>• Dispersed in acetone</li> <li>• Mechanical stirring</li> </ul>	[26]
9	Park and Jana	2003	PMMA-epoxy	MMT/10	10	Mechanical stirring	[76]
10	Wan et al.	2003	PVC	MMT/0.5	27	Melt blending	[24]

**Table 4** Fracture toughness of polymer–clay composites

Sr.	Authors	Year	Matrix	Filler/(wt%)	% Change in $K_{1C}$ (MPa $\sqrt{m}$ )	Dispersion method	References
1	El-Sheikhy et al.	2017	HDPE	MMT/5	105	Melt-processing	[1]
2	Saharudin et al.	2017	UP	HNTs/1	33	Ultra-sonication	[47]
3	Ghadami et al.	2016	Epoxy	Cloisite 15A	52	Dispersed in acetone followed by ultra-sonication	[77]
4	Wang et al.	2015	Epoxy	MMT/1	94	Dispersed in acetone and homogenized at 2000 rpm	[68]
5	Zeng et al.	2014	Epoxy	HNTs/1	10	Ultra-sonication	[78]
6	Tang et al.	2011	PPA	HNTs/10	78	Melt blending	[79]
7	Ramsaroop et al.	2010	PP	MMT/5	175	Melt blending	[67]
8	Zunjarrao et al.	2006	Epoxy	MMT/2	35	High shear mixing	[80]
9	Wang et al.	2005	Epoxy	MMT/2.5	78	Ultra-sonication	[81]
10	Liu et al.	2005	Epoxy	HNTs/6	90	Dispersed in acetone followed by high pressure mixing (HPM)	[82]



reagents to achieve homogeneous clay dispersion in the preparation of polymer nanocomposites. The mechanical properties of the nanocomposites can be influenced by volume fraction, dispersion state, size, type and surface functionalization of the fillers.

In improving mechanical and thermal properties of the resultant composites, nano-sized fillers are better than micro-sized filler because smaller particles of shorter interparticle gap can form mechanically coupled networks by relatively shorter interparticle distance of the former compared to that of the latter.

This network exploiting nanoparticle as crosslinkers can allow stress transfer from polymer matrix to filler, and restrict polymer chain movement along with energy dissipation at crack beginning, which consequently will increase both the strength and the toughness.

The influence of clay particles on storage modulus, glass transition ( $T_g$ ) and degradation temperature of the clay–epoxy system is also important to discuss. A research has revealed that the addition of unmodified and modified clay can enhance the degradation temperature up to 6.5 °C [68] and, on the other hand, storage modulus and glass transition temperature are marginally improved as shown in Fig. 4. In this study, it was revealed that copolymerization of the cationic monomer and the second monomer for clay alteration throughout epoxy cure is anticipated to eliminate the possibility of the reduction in  $T_g$  and storage modulus being triggered by the degradation of small molecules such as compatibilizers or surfactants [83].

Likewise, the rise of  $T_g$  with modified clay contents is in contrast to monotonous reduction of  $T_g$  for DGEBA (Dow Plastics, a bisphenol A diglycidyl) strengthened with organophilic clay, that is influenced by plasticization of the epoxy network by the hydrocarbon chains of the alkylammonium cations [84]. Thus, this maintenance of  $T_g$  from the nanocomposite system is due to the creation of the double IPN structure created by the altered clay and the epoxy matrix. Apart from that, incomplete exfoliation of the layered clay within epoxy matrix, and a reduction in elastic modulus in the rubbery region were also observed in Fig. 4 (left) [85]. The thermal properties show the most curious behaviour of the crosslinked polyester–clay nanocomposites

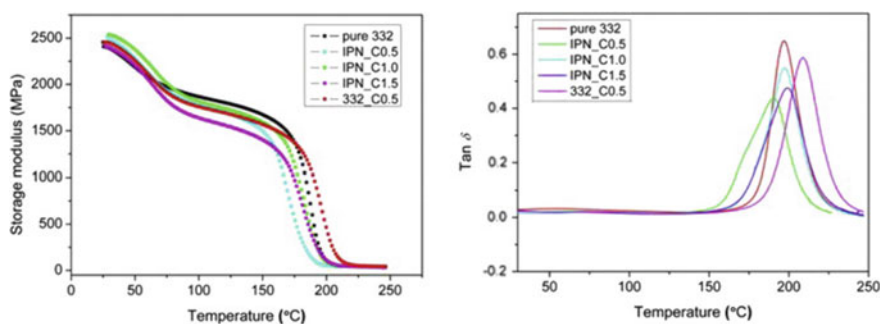


Fig. 4 Storage modulus (left) and Tan  $\delta$  (right) of epoxy–clay nanocomposites [68]

reported here. One of the most expected improvements in the properties of polymer nanocomposites is the delay in thermal deterioration.

One of the most expected improvements in the properties of polymer nanocomposites is the delay in thermal degradation [86]. The onset of degradation is slightly higher, when clay is added to the nanocomposites, than the pure polymer shown in Fig. 5 [87]. Amongst researchers, it is well known that at 400 °C, the pure polymer is entirely decomposed and the nanocomposites degrade faster in between 25 and 400 °C compared to the pure polymer and the state is then reversed. It is no surprise that the nanocomposites exhibit gradual degradation above 400 °C as at that state, only inorganic aluminosilicates are left in the system.

In comparison with metals, polymers have a high thermal expansion. The addition of fillers, such as clay, reduces the thermal growth of polymers by means of restricting the movement of a large volume of polymer chains due to their interplay with the filler. Studies have shown that nanofillers can affect both the  $T_g$  and the extent of transition. Factors that have an effect on  $T_g$  include sample thickness, preparation and measurement of samples, the dimension of nanoparticles, and chemical structure of the polymers. The interplay of the filler with the surface will determine the extent of change of  $T_g$ . Surfaces that have interaction strongly with the polymer will lead to an increase in  $T_g$ . Depending on the surface function of the nanotubes, mixing a polymer and nanotube can increase or decrease the  $T_g$ .

Some earlier studies have shown that the barrier properties of the nanoscale fillers are responsible for improving of thermal stability of nanocomposites. Gilman [88] believes that the barrier properties should include both the thermal barrier, which protects the polymer from contacting with fire, and the mass transport barrier, which slows down the escape of the volatile products during the process of degradation, and the investigations also showed that the intercalated layered silicate nanofiller had much better effect on thermal stability of polymer matrix than exfoliated layered

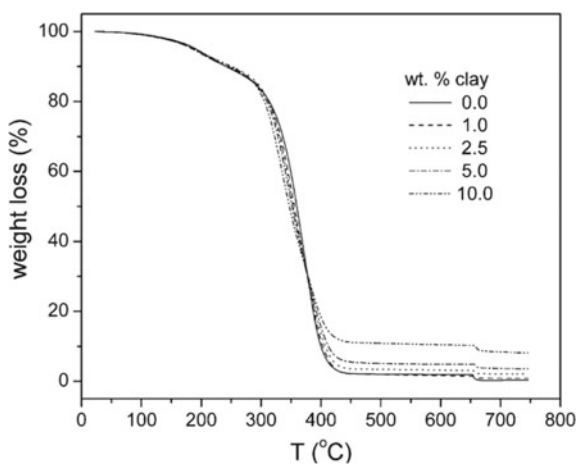
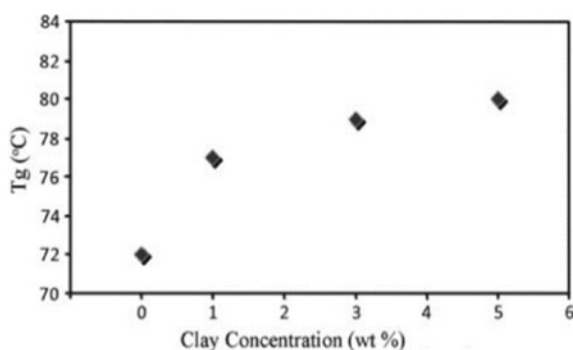


Fig. 5 Thermal degradation profiles for polyester-clay nanocomposites [25]

silicate nanofiller [89]. In practice, the barrier effects of HNTs with tubular structure may slightly be lower to those of layered silicate nanofillers, particularly the intercalated layered silicate nanofillers.

Some publications show that iron oxides could be used as flame-retardant additives in silicate fillers and carbon nanotubes that lead to some radical trapping during the degradation process, thus improving the thermal stability of nanocomposites. Du et al., for instance, believe that the lumen of the HNTs plays an important role in improving the thermal stability of the nanocomposites [86]. As reported, the degradation of PP in nitrogen is initiated primarily by the random thermal scissions of C–C chain bonds and the intermolecular transfer of hydrogen. Ruban et al. in their publication reported that MMT increased glass temperature from 71 to 79 °C by incorporating 5% of montmorillonite [71].

Figure 6 illustrates the effect of the clay content on the  $T_g$ . The increase in the  $T_g$  of the nanocomposites compared to the original unsaturated polyester can be attributed to improved adhesion of polymer and the layered silicate surfaces, and it is also because of the decrease in relative styrene concentration with an increased clay content [71]. John et al. [90], in their study, reported nanoclay improved mechanical properties of cyanate ester syntactic foams. However, nanoclay causes plasticization of polymer matrix due to the presence of organic modifier in clay; therefore,  $T_g$  is not significantly altered. Woo [91] in his publication revealed that the epoxy–clay nanocomposites ( $T_g$ ) were marginally reduced with clay loading. This is due to the disentanglement of polymer chains around the silicate surface, and a shift in stoichiometry due to epoxy homopolymerization within the clay galleries. Kotsilkova in her review reported that the reduction of  $T_g$  is due to perturbing effects of clay. The chemistry reaction was altered after the clay reinforcement, and indeed, the organic ions themselves may catalyse homopolymerization [92]. However, according to Park and Jana, the decreased values of  $T_g$  can be mistakenly attributed to the incomplete cure of epoxy molecules [93].



**Fig. 6** Glass transition temperature of MMT–polyester composites [71]

## 5 Optical Properties

Jalali et al. studied optical properties of polymer–clay nanocomposites based on aliphatic–aromatic polyamide containing thiazole ring [94]. They have reported that as the clay content increased, the emission intensity decreased. This is due to the photon diffusion, which is blocked by clay particles as mentioned by other researchers [81, 95]. Tsai et al. studied the optical clarity of PMMA–clay nanocomposites. A slight decrease in PMMA–clay nanocomposites was observed as clay content increased; however, optical transmission up to 87% was reported [96]. In another publication, high optical clarity of nanocomposites primarily observed was resulted from disorderly exfoliated morphology of clay layers and also efficient dispersion of clay platelets in PMMA matrix [97]. Another reason for the excellent optical clarity of polymer–clay nanocomposites is due to the thickness of individual clay layers that is much smaller than the wavelength of visible light. Thus, well-exfoliated polymer–clay nanocomposites have to be optically clear [18].

Saharudin et al. performed light transmittance test on nanoclay–polyester nanocomposites. The test was performed at wavelength of 400 nm based on previous work by Bharadwaj et al. [25]. The light transmittance decreases with the increase in HNTs' concentration. The aggregates are evenly distributed into small particles after sonication process, causing an increase in light absorption or reduction in light transmittance [45]. From the results shown in Fig. 7, it can be observed that monolithic polyester recorded the highest light transmittance value of 73%. As clay content increased by 0.1 wt%, the light transmission dropped to 71%. The lowest light transmittance value was recorded in the case of 1 wt% of clay, with 64%. In general, this indicates that clay does not significantly reduce the optical clarity of nanocomposites and can be used in applications where transparent property is needed, such as in medical appliances [48, 98].

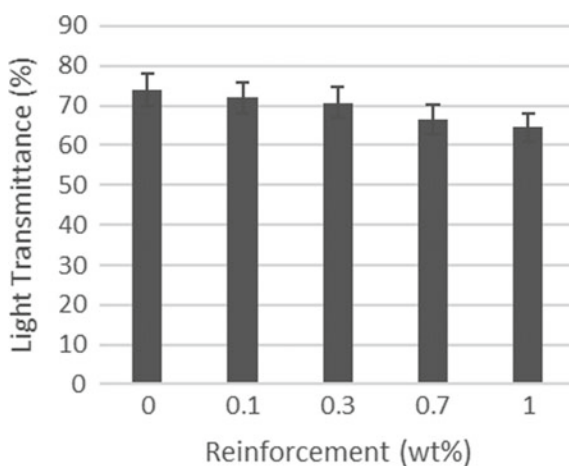
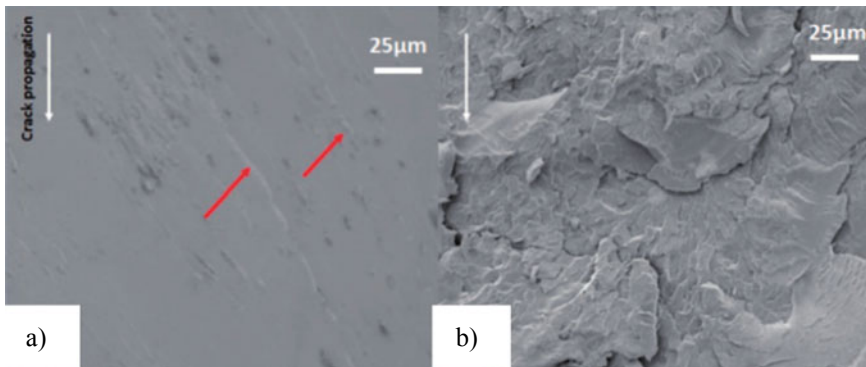


Fig. 7 Light transmittance of nanoclay–polyester nanocomposites [45]

## 6 SEM Images of Fractured Samples

Saharudin et al. studied the fractured surfaces of specimens for monolithic polyester and HNTs–polyester nanocomposites. It can be observed that the image shows a very smooth surface due to the very fast and straight spread of cracks as shown in Fig. 8a. Figure 8b, on the other hand, illustrates fractured surface of 1 wt% HNTs–polyester. Figure 9 shows SEM micrograph of 2.3 wt% HNT fracture, obviously, the inner layers of the HNTs were pulled out after outer layers fractured. The increase in surface roughness and flute topography can be linked to the HNT deflection of the crack as this deflection increased the fracture path that increased the fracture toughness. Formation of the micro-cracks tends to absorb a large amount of fracture energy because the number of the micro-cracks formed in the brittle matrix under impact is enormous. Bucknall proposed that this massive micro-cracking mechanism is very much like the massive crazing mechanism [99].



**Fig. 8** SEM images of fractured specimens **a** monolithic polyester and **b** 1 wt% HNT-polyester [47]

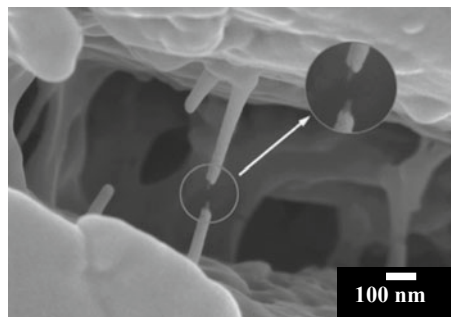


**Fig. 9** HNT fracture and nanotube de-bonding [26]

The formation of massive micro-cracks and nanotube bridging are two key elements of the toughening. HNT toughening might only be appropriate to brittle polymers, such as PMMA, epoxy, and PS because the yield strength is higher than their fracture strength; thus, micro-cracking occurs before matrix yielding. Matrix shear yielding due to crack tip blunting makes it impossible for HNT bridging; therefore, blending HNTs with ductile polymers such as PE or PP may no longer advantage its impact toughness. When nanoclays are added to a polymer matrix, two types of nanocomposite structures, namely intercalated and exfoliated nanostructures, may develop. The host polymer matrix enters into the interlayer spacing of the nanoclay in an intercalated structure and increases the interlayer spacing while maintaining the parallel arrangement of the nanolayers of clay in the matrix. If the clay nanolayers are randomly dispersed throughout the matrix, the structure is called exfoliated structure. Exfoliated structures offer enhanced and improved properties in practice due to their excellent dispersion and improved aspect ratio.

Figure 10 shows fracture surfaces of UP/MMT nanocomposites. It can be seen that the cleavage surfaces show fracture areas with fracture borders in evidence. The cleavage surface has smaller fracture in the case of sample with higher nanoclay content. Certain areas on fractured surface indicating an increased brittleness of the samples were confirmed by the reduction in the stress and strain to failure.

## 7 Conclusions

Significant progress has been made in the development of polymer–clay nanocomposites over the past 20 years. The advantages of technology have become clear for different automotive and aerospace applications in particular. Polymer–clay nanocomposites have the potential to replace traditional fibre-reinforced composites even in the low filler range. From literature, it can be concluded that tensile, flexural, impact and fracture toughness properties of polymer–clay nanocomposites have shown remarkable improvements. In addition, the thermal properties were also improved considerably by incorporating clay particles into polymer systems

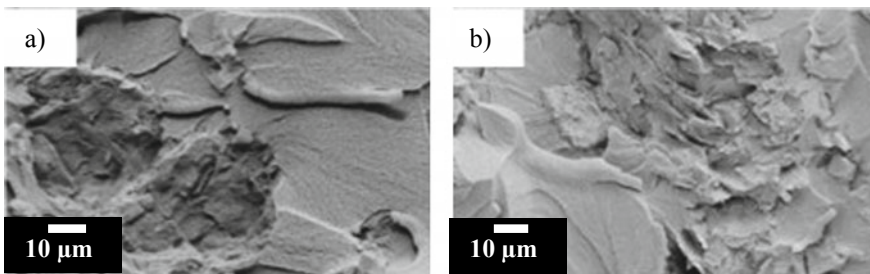


**Fig. 10** SEM images of fracture surfaces of UP/MMT nanocomposites: **a** 5 wt% MMT–polyester, **b** 10 wt% MMT–polyester [61]

without compromising their optical clarity. A careful selection of the nanocomposite formulations must be made to avoid negative results on the mechanical properties. In this case, it is possible to obtain a compromise between processing behaviour and mechanical properties to optimize the performance of these materials.

## References

1. El-Sheikhy R, Al-Shamrani M (2017) Interfacial bond assessment of clay-polyolefin nanocomposites CPNC on view of mechanical and fracture properties. *Adv Powder Technol* 28:983–992. <https://doi.org/10.1016/j.apt.2017.01.002>
2. Islam ME, Mahdi TH, Hosur MV, Jeelani S (2015) Characterization of carbon fiber reinforced epoxy composites modified with nanoclay and carbon nanotubes. *Procedia Eng* 105:821–828. <https://doi.org/10.1016/j.proeng.2015.05.078>
3. Armstrong G (2015) An introduction to polymer nanocomposites. *Eur J Phys* 36:1–39. <https://doi.org/10.1088/0143-0807/36/6/063001>
4. Madhumitha G, Fowsiya J, Mohana Roopan S, Thakur VK (2018) Recent advances in starch-clay nanocomposites. *Int J Polym Anal Charact* 1–15
5. Adak B, Butola BS, Joshi M (2018) Effect of organoclay-type and clay-polyurethane interaction chemistry for tuning the morphology, gas barrier and mechanical properties of clay/polyurethane nanocomposites. *Appl Clay Sci* 161:343–353
6. Yano K, Usuki A, Okada A et al (1993) Synthesis and properties of polyimide clay hybrid. *J Polym Sci Part A Polym Chem* 31:2493–2498. <https://doi.org/10.1002/pola.1993.080311009>
7. Cui Y, Kumar S, Rao Kona B, van Houcke D (2015) Gas barrier properties of polymer/clay nanocomposites. *RSC Adv* 5:63669–63690. <https://doi.org/10.1039/C5RA10333A>
8. Zabih O, Ahmadi M, Nikafshar S et al (2018) A technical review on epoxy-clay nanocomposites: structure, properties, and their applications in fiber reinforced composites. *Compos Part B Eng* 135:1–24. <https://doi.org/10.1016/j.compositesb.2017.09.066>
9. Pavlidou S, Papaspyrides CD (2008) A review on polymer-layered silicate nanocomposites. *Prog Polym Sci* 33:1119–1198. <https://doi.org/10.1016/j.progpolymsci.2008.07.008>
10. Kaynak C, Nakas GI, Isitman NA (2009) Mechanical properties, flammability and char morphology of epoxy resin/montmorillonite nanocomposites. *Appl Clay Sci* 46:319–324. <https://doi.org/10.1016/j.clay.2009.08.033>
11. Saharudin MS, Atif R, Shyha I, Inam F (2016) The degradation of mechanical properties in polymer nano-composites exposed to liquid media—a review. *RSC Adv* 6:1076–1089. <https://doi.org/10.1039/C5RA22620A>
12. Kim BK, Seo JW, Jeong HM (2003) Morphology and properties of waterborne polyurethane/clay nanocomposites. *Eur Polym J* 39:85–91. [https://doi.org/10.1016/S0014-3057\(02\)00173-8](https://doi.org/10.1016/S0014-3057(02)00173-8)
13. Jawahar P, Balasubramanian M (2006) Influence of nanosize clay platelets on the mechanical properties of glass fiber reinforced polyester composites. *J Nanosci Nanotechnol* 6:3973–3976
14. Jawahar P, Gnanamoorthy R, Balasubramanian M (2006) Tribological behaviour of clay—thermoset polyester nanocomposites. *Wear* 261:835–840. <https://doi.org/10.1016/j.wear.2006.01.010>
15. Timmerman JF, Hayes BS, Seferis JC (2002) Nanoclay reinforcement effects on the cryogenic microcracking of carbon fiber/epoxy composites. *Compos Sci Technol* 62:1249–1258. [https://doi.org/10.1016/S0266-3538\(02\)00063-5](https://doi.org/10.1016/S0266-3538(02)00063-5)
16. Kuilla T, Bhadra S, Yao D et al (2010) Recent advances in graphene based polymer composites. *Prog Polym Sci* 35:1350–1375. <https://doi.org/10.1016/j.progpolymsci.2010.07.005>
17. Alamri H, Low IM (2012) Effect of water absorption on the mechanical properties of nanofiller reinforced epoxy nanocomposites. *Mater Des* 42:214–222. <https://doi.org/10.1016/j.matdes.2012.05.060>



18. Gao F (2004) Clay/polymer composites: the story. *Mater Today* 7:50–55. [https://doi.org/10.1016/S1369-7021\(04\)00509-7](https://doi.org/10.1016/S1369-7021(04)00509-7)
19. Joussein E, Petit S, Churchman J et al (2005) Halloysite clay minerals—a review. *Clay Miner* 40:383–426. <https://doi.org/10.1180/0009855054040180>
20. Kotal M, Bhowmick AK (2015) Polymer nanocomposites from modified clays: recent advances and challenges. *Prog Polym Sci* 51:127–187. <https://doi.org/10.1016/j.progpolymsci.2015.10.001>
21. Prashantha K, Lacrampe MF, Krawczak P (2011) Processing and characterization of halloysite nanotubes filled polypropylene nanocomposites based on a masterbatch route: effect of halloysites treatment on structural and mechanical properties. *Express Polym Lett* 5:295–307. <https://doi.org/10.3144/expresspolymlett.2011.30>
22. Saharudin MS, Wei J, Shyha I, Inam F (2017) Environmental stress cracking resistance of halloysite nanoclay-polyester nanocomposites. *World J Eng Technol* 05:389–403. <https://doi.org/10.4236/wjet.2017.53033>
23. Saharudin MS, Atif R, Inam F (2017) Effect of short-term water exposure on the mechanical properties of halloysite nanotube-multi layer graphene reinforced polyester nanocomposites. *Polymers (Basel)* 9:1–27
24. Wan C, Qiao X, Zhang Y, Zhang Y (2003) Effect of different clay treatment on morphology and mechanical properties of PVC-clay nanocomposites. *Polym Test* 22:453–461. [https://doi.org/10.1016/S0142-9418\(02\)00126-5](https://doi.org/10.1016/S0142-9418(02)00126-5)
25. Bharadwaj RK, Mehrabi AR, Hamilton C et al (2002) Structure property relationships in cross-linked polyester clay nanocomposites. *Most* 43:3699–3705
26. Ye Y, Chen H, Wu J, Ye L (2007) High impact strength epoxy nanocomposites with natural nanotubes. *Polymer (Guildford)* 48:6426–6433. <https://doi.org/10.1016/j.polymer.2007.08.035>
27. Sandri G, Aguzzi C, Rossi S et al (2017) Halloysite and chitosan oligosaccharide nanocomposite for wound healing. *Acta Biomater* 57:216–224. <https://doi.org/10.1016/j.actbio.2017.05.032>
28. Ratner BD, Hoffman AS, Gaaz TS et al (1976) Hydrogels for medical and related applications. In: *ACS symposium series*, p 252
29. Guo M, Wang A, Muhammad F et al (2012) Halloysite nanotubes, a multifunctional nanovehicle for anticancer drug delivery. *Chin J Chem* 30:2115–2120. <https://doi.org/10.1002/cjoc.201200657>
30. Castro-Aguirre E, Auras R, Selke S et al (2018) Impact of nanoclays on the biodegradation of poly (lactic acid) nanocomposites. *Polymers (Basel)* 10:202
31. Yuan P, Tan D, Annabi-Bergaya F (2015) Properties and applications of halloysite nanotubes: recent research advances and future prospects. *Appl Clay Sci* 112:75–93. <https://doi.org/10.1016/j.clay.2015.05.001>
32. Brantseva TV, Ilyin SO, Gorbunova IY et al (2016) Epoxy reinforcement with silicate particles: rheological and adhesive properties. Part II: characterization of composites with halloysite. *Int J Adhes Adhes* 68:248–255. <https://doi.org/10.1016/j.ijadhadh.2016.04.005>
33. Gorrasi G, Pantani R, Murariu M, Dubois P (2014) PLA/halloysite nanocomposite films: water vapor barrier properties and specific key characteristics. *Macromol Mater Eng* 299:104–115. <https://doi.org/10.1002/mame.201200424>
34. Bhuvana S, Prabakaran M (2014) Synthesis and characterisation of polyamide/halloysite nanocomposites prepared by solution intercalation method. *Nanosci Nanotechnol* 4:44–51. <https://doi.org/10.5923/j.nn.20140403.02>
35. Shi X, Nguyen TA, Suo Z et al (2009) Effect of nanoparticles on the anti corrosion and mechanical properties of epoxy coating. *Surf Coat Technol* 204:237–245. <https://doi.org/10.1016/j.surfcoat.2009.06.048>
36. Kamble R, Ghag M, Gaikawad S, Panda BK (2012) Review article halloysite nanotubes and applications: a review. *J Adv Sci Res* 3:25–29
37. Kausar A (2015) Effect of halloysite nanoclay on polymerization and properties of poly(3,4-(2,2-dimethylpropylenedioxy)-thiophene-co-aniline). *Am J Polym Sci* 5:30–34. <https://doi.org/10.5923/j.ajps.20150501.05>



38. Guo B, Zou Q, Lei Y, Jia D (2009) Structure and performance of polyamide 6/halloysite nanotubes nanocomposites. *Polym J* 41:835–842
39. Carli LN, Crespo JS, Mauler RS (2011) PHBV nanocomposites based on organomodified montmorillonite and halloysite: the effect of clay type on the morphology and thermal and mechanical properties. *Compos Part A Appl Sci Manuf* 42:1601–1608. <https://doi.org/10.1016/j.compositesa.2011.07.007>
40. Fix D, Andreeva DV, Lvov YM et al (2009) Application of inhibitor-loaded halloysite nanotubes in active anti-corrosive coatings. *Adv Funct Mater* 19:1720–1727. <https://doi.org/10.1002/adfm.200800946>
41. Abdullayev E, Lvov Y, Twite RL (2010) Clay nanotubes for corrosion inhibitor encapsulation: release control with end stoppers. *J Mater Chem* 20:6681–6698. <https://doi.org/10.1039/c0jm00810a>
42. Sinha Ray S, Okamoto M (2003) Polymer/layered silicate nanocomposites: a review from preparation to processing. *Prog Polym Sci* 28:1539–1641
43. Badrinarayanan P, Ko FK, Wang C et al (2014) Investigation of the effect of clay nanoparticles on the thermal behavior of PLA using a heat flux rapid scanning rate calorimeter. *Polym Test* 35:1–9. <https://doi.org/10.1016/j.polymertesting.2014.02.001>
44. Albdiry M, Yousif B, Ku H, Lau K (2012) A critical review on the manufacturing processes in relation to the properties of nanoclay/polymer composites. *J Compos Mater* 47:1093–1115. <https://doi.org/10.1177/0021998312445592>
45. Saharudin M, Wei J, Shyha I, Inam F (2017) Biodegradation of halloysite nanotubes-polyester nanocomposites exposed to short term seawater immersion. *Polymers (Basel)* 9:314. <https://doi.org/10.3390/polym9080314>
46. Saharudin M, Wei J, Shyha I, Inam F (2016) The degradation of mechanical properties in halloysite nanoclay-polyester nanocomposites exposed in seawater environment. *J Nanomater*
47. Saharudin MS, Atif R, Shyha I, Inam F (2016) The degradation of mechanical properties in halloysite nanoclay-polyester nanocomposites exposed to diluted methanol. *J Compos Mater* 1–12
48. Saharudin MS, Wei J, Shyha I, Inam F (2017) Flexural properties of halloysite nanotubes-polyester nanocomposites exposed to aggressive environment 11:292–296
49. Saharudin MS, Shyha I, Inam F (2015) The effect of methanol exposure on the flexural and tensile properties of halloysite nanoclay polyester. In: *The IRES 17th international conference, London, UK*, pp 40–44
50. Chatterjee S, Nafezarefi F, Tai NH et al (2012) Size and synergy effects of nanofiller hybrids including graphene nanoplatelets and carbon nanotubes in mechanical properties of epoxy composites. *Carbon N Y* 50:5380–5386. <https://doi.org/10.1016/j.carbon.2012.07.021>
51. Atif R, Inam F (2016) Fractography analysis of 0.5 wt% multi-layer graphene/nanoclay reinforced nanocomposites. *AIMS Mater Sci* 3:1294–1308. <https://doi.org/10.3934/matserci.2016.4.1294>
52. Atif R, Inam F (2016) Influence of macro-topography on damage tolerance and fracture toughness of 0.1 wt% multi-layer graphene/clay-epoxy nanocomposites. *Polymers (Basel)* 8:335–360. <https://doi.org/10.3390/polym8070239>
53. Chan M, Lau K, Wong T et al (2011) Mechanism of reinforcement in a nanoclay/polymer composite. *Compos Part B Eng* 42:1708–1712. <https://doi.org/10.1016/j.compositesb.2011.03.011>
54. Sancaktar E, Kuznicki J (2011) Nanocomposite adhesives: mechanical behavior with nanoclay. *Int J Adhes Adhes* 31:286–300. <https://doi.org/10.1016/j.ijadhadh.2010.09.006>
55. Pasbakhsh P, De SRT, Vahedi V (2014) The role of halloysite surface area and aspect ratio on the tensile properties of ethylene propylene diene. *Int J Chem Mol Nucl Mater Metall Eng* 8:1363–1366
56. Merah N (2019) Nanoclay and water uptake effects on mechanical properties of unsaturated polyester. *J Nanomater*
57. Bensadoun F, Kchit N, Billotte C, Ruiz E (2011) A comparative study of dispersion techniques for nanocomposite made with nanoclays and an unsaturated polyester resin. *J Nanomater* 2011:1–12. <https://doi.org/10.1155/2011/406087>

58. Ozsoy I, Demirkol A, Mimaroglu A et al (2015) The influence of micro- and nano-filler content on the mechanical properties of epoxy composites. *Strojinski Vestnik/J Mech Eng* 61:601–609. <https://doi.org/10.5545/sv-jme.2015.2632>
59. Vahedi V, Pasbakhsh P (2014) Instrumented impact properties and fracture behaviour of epoxy/modified halloysite nanocomposites. *Polym Test* 39:101–114. <https://doi.org/10.1016/j.polymertesting.2014.07.017>
60. Lecouvet B, Gutierrez JG, Sclavons M, Bailly C (2011) Structure-property relationships in polyamide 12/halloysite nanotube nanocomposites. *Polym Degrad Stab* 96:226–235
61. Chieruzzi M, Miliozzi A, Kenny JM (2013) Effects of the nanoparticles on the thermal expansion and mechanical properties of unsaturated polyester/clay nanocomposites. *Compos Part A Appl Sci Manuf* 45:44–48. <https://doi.org/10.1016/j.compositesa.2012.09.016>
62. Jeyakumar R, Sampath PS, Ramamoorthi R, Ramakrishnan T (2017) Structural, morphological and mechanical behaviour of glass fibre reinforced epoxy nanoclay composites. *Int J Adv Manuf Technol* 93:527–535. <https://doi.org/10.1007/s00170-017-0565-x>
63. Lin Y, Ng KM, Chan C-M et al (2011) High-impact polystyrene/halloysite nanocomposites prepared by emulsion polymerization using sodium dodecyl sulfate as surfactant. *J Colloid Interface Sci* 358:423–429. <https://doi.org/10.1016/j.jcis.2011.03.009>
64. Guo B, Zou Q, Lei Y et al (2009) Crystallization behavior of polyamide 6/halloysite nanotubes nanocomposites. *Thermochim Acta* 484:48–56. <https://doi.org/10.1016/j.tca.2008.12.003>
65. Liu M, Guo B, Du M et al (2009) Halloysite nanotubes as a novel  $\beta$ -nucleating agent for isotactic polypropylene. *Polymer (Guildford)* 50:3022–3030. <https://doi.org/10.1016/j.polymer.2009.04.052>
66. Antill SJ (2003) Halloysite: a low-cost alternative. *Aust J Chem* 56:723
67. Ramsaroop A, Kanny K, Mohan TP (2010) Fracture toughness studies of polypropylene-clay nanocomposites and glass fibre reinforced polypropylene composites. *Mater Sci Appl* 01:301–309. <https://doi.org/10.4236/msa.2010.15044>
68. Wang M, Fan X, Thitsartarn W, He C (2015) Rheological and mechanical properties of epoxy/clay nanocomposites with enhanced tensile and fracture toughnesses. *Polym (United Kingdom)* 58:43–52. <https://doi.org/10.1016/j.polymer.2014.12.042>
69. Deng S, Zhang J, Ye L, Wu J (2008) Toughening epoxies with halloysite nanotubes. *Polymer (Guildford)* 49:5119–5127. <https://doi.org/10.1016/j.polymer.2008.09.027>
70. Chozhan CK, Rajasekaran R, Alagar M, Gnanasundaram P (2008) Thermomechanical behavior of vinyl ester oligomer-toughened epoxy-clay hybrid nanocomposites. *Int J Polym Mater* 57:319–337. <https://doi.org/10.1080/00914030701555734>
71. Ruban Y, Mon S, Roy D (2014) Chemical resistance/thermal and mechanical properties of unsaturated polyester-based nanocomposites. *Appl Nanosci* 233–240. <https://doi.org/10.1007/s13204-013-0193-1>
72. Ollier R, Rodriguez E, Alvarez V (2013) Unsaturated polyester/bentonite nanocomposites: influence of clay modification on final performance. *Compos Part A Appl Sci Manuf* 48:137–143. <https://doi.org/10.1016/j.compositesa.2013.01.005>
73. Jumahat A, Soutis C, Mahmud J, Ahmad N (2012) Compressive properties of nanoclay/epoxy nanocomposites. *Procedia Eng* 41:1607–1613. <https://doi.org/10.1016/j.proeng.2012.07.357>
74. Bozkurt E, Kaya E, Tanoğlu M (2007) Mechanical and thermal behavior of non-crimp glass fiber reinforced layered clay/epoxy nanocomposites. *Compos Sci Technol* 67:3394–3403. <https://doi.org/10.1016/j.compscitech.2007.03.021>
75. Albdiry MT, Ku H, Yousif BF (2013) Impact fracture behaviour of silane-treated halloysite nanotubes-reinforced unsaturated polyester. *Eng Fail Anal* 35:718–725. <https://doi.org/10.1016/j.engfailanal.2013.06.027>
76. Park JH, Jana SC (2003) The relationship between nano- and micro-structures and mechanical properties in PMMA-epoxy-nanoclay composites. *Polymer (Guildford)* 44:2091–2100. [https://doi.org/10.1016/S0032-3861\(03\)00075-2](https://doi.org/10.1016/S0032-3861(03)00075-2)
77. Ghadami F, Dadfar MR, Kazazi M (2016) Hot-cured epoxy-nanoparticulate-filled nanocomposites: fracture toughness behavior. *Eng Fract Mech* 162:193–200. <https://doi.org/10.1016/j.engfracmech.2016.05.016>

78. Zeng S, Reyes C, Liu J et al (2014) Facile hydroxylation of halloysite nanotubes for epoxy nanocomposite applications. *Polym (United Kingdom)* 55:6519–6528. <https://doi.org/10.1016/j.polymer.2014.10.044>
79. Tang Y, Deng S, Ye L et al (2011) Effects of unfolded and intercalated halloysites on mechanical properties of halloysite-epoxy nanocomposites. *Compos Part A Appl Sci Manuf* 42:345–354. <https://doi.org/10.1016/j.compositesa.2010.12.003>
80. Zunjarrao SC, Sriraman R, Singh RP (2006) Effect of processing parameters and clay volume fraction on the mechanical properties of epoxy-clay nanocomposites. *J Mater Sci* 41:2219–2228. <https://doi.org/10.1007/s10853-006-7179-2>
81. Wang K, Chen L, Wu J et al (2005) Epoxy nanocomposites with highly exfoliated clay: mechanical properties and fracture mechanisms. *Macromolecules* 38:788–800. <https://doi.org/10.1021/ma048465n>
82. Liu W, Hoa SV, Pugh M (2005) Fracture toughness and water uptake of high-performance epoxy/nanoclay nanocomposites. *Compos Sci Technol* 65:2364–2373. <https://doi.org/10.1016/j.compscitech.2005.06.007>
83. Chen JS, Poliks MD, Ober CK et al (2002) Study of the interlayer expansion mechanism and thermal-mechanical properties of surface-initiated epoxy nanocomposites. *Polymer (Guildford)* 43:4895–4904. [https://doi.org/10.1016/S0032-3861\(02\)00318-X](https://doi.org/10.1016/S0032-3861(02)00318-X)
84. García del Cid MA, Prolongo MG, Salom C et al (2012) The effect of stoichiometry on curing and properties of epoxy-clay nanocomposites. *J Therm Anal Calorim* 741–749
85. Koerner H, Misra D, Tan A et al (2006) Montmorillonite-thermoset nanocomposites via cryo-compounding. *Polymer (Guildford)* 47:3426–3435. <https://doi.org/10.1016/j.polymer.2006.03.057>
86. Du M, Guo B, Jia D (2006) Thermal stability and flame retardant effects of halloysite nanotubes on poly(propylene). *Eur Polym J* 42:1362–1369. <https://doi.org/10.1016/j.eurpolymj.2005.12.006>
87. Sur G, Sun H, Lyu S, Mark J (2001) Synthesis, structure, mechanical properties, and thermal stability of some polysulfone/organoclay nanocomposites. *Polymer (Guildford)* 42:9783–9789. [https://doi.org/10.1016/S0032-3861\(01\)00527-4](https://doi.org/10.1016/S0032-3861(01)00527-4)
88. Gilman JW (1999) Flammability and thermal stability studies of polymer layered-silicate (clay) nanocomposites. *Appl Clay Sci* 15:31–49. [https://doi.org/10.1016/S0169-1317\(99\)00019-8](https://doi.org/10.1016/S0169-1317(99)00019-8)
89. Gilman JW, Jackson CL, Morgan AB et al (2000) Flammability properties of polymer-layered-silicate nanocomposites. Polypropylene and polystyrene nanocomposites. *Chem Mater* 12:1866–1873
90. John B, Nair CPR, Ninan KN (2010) Effect of nanoclay on the mechanical, dynamic mechanical and thermal properties of cyanate ester syntactic foams. *Mater Sci Eng A* 527:5435–5443. <https://doi.org/10.1016/j.msea.2010.05.016>
91. Woo SC (2006) Degradation of epoxy-clay nanocomposites after UV exposure and moisture attack. Hong Kong University of Science and Technology
92. Pissis P, Kotsilkova R (2007) Thermoset nanocomposites for engineering applications. iSmithers Rapra Publishing
93. Park JH, Jana SC (2003) Mechanism of exfoliation of nanoclay particles in epoxy-clay nanocomposites. *Macromolecules* 36:2758–2768. <https://doi.org/10.1021/ma021509c>
94. Jalali A, Shockravi A, Hajibeygi M, Vatanpour V (2018) Polymer/clay nanocomposites based on aliphatic–aromatic polyamide containing thiazole ring and new organomodified nanosilicate layers: synthesis, characterization, and thermal properties study. *Polym Compos* 39:E1407–E1420. <https://doi.org/10.1002/pc.24327>
95. Cele HM, Ojijo V, Chen H et al (2014) Effect of nanoclay on optical properties of PLA/clay composite films. *Polym Test* 36:24–31
96. Tsai TY, Lin MJ, Chuang YC, Chou PC (2013) Effects of modified Clay on the morphology and thermal stability of PMMA/clay nanocomposites. *Mater Chem Phys* 138:230–237. <https://doi.org/10.1016/j.matchemphys.2012.11.051>
97. Cui L, Tarte NH, Woo SI (2008) Effects of modified clay on the morphology and properties of PMMA/clay nanocomposites synthesized by in situ polymerization. *Macromolecules* 41:4268–4274

98. Lin L, Schlarb A (2012) A study on environmental stress cracking in nano-SiO<sub>2</sub>-filled polycarbonate. *J Mater Sci* 47:6614–6620. <https://doi.org/10.1007/s10853-012-6597-6>
99. Bucknall CB (1978) Fracture and failure of multiphase polymers and polymer composites. *Adv Polym Sci* 27:121–148. [https://doi.org/10.1007/3-540-08829-6\\_3](https://doi.org/10.1007/3-540-08829-6_3)

# Effect of Some Additives on Tribological Properties of SAE20W40 Lubricant



Harpreet Singh Grewal, Surinder Singh, Harpreet Singh,  
and Narinder Singh

**Abstract** Friction and wear loss of various machining parts and pairs depend majorly on the quality of lubricants. Several types of additives are commercially used to enhance the tribological performance of a lubricant. In the present work, some novel lubricating liquids were prepared by mixing different additives, viz bromide, fluoride, iodide and acetate, in a commercial available SAE20W40 lubricant. Pin-on-disc investigations were performed to evaluate the effect of the prepared lubricants on wear rate and friction characteristics of mild steel and stainless steel sliding pair. Disc chamber was flooded with lubricants during testing. Fluoride was found to be the most successful additive to improve the performance of the given lubricant, whereas acetate as an additive made the base lubricant less efficient. It is believed that the strong bond stability of C–F bond during working conditions resulted in better performance of the lubricant after the addition of fluoride.

**Keywords** Tribology · Wear rate · Friction · Lubrication · Pin-on-disc · Additive

## 1 Introduction

The service life of the sliding surfaces would automatically increase when the two main tribological concerns, that is, friction and wear, are controlled or reduced [1]. The cost of repairs linked to frictional deficiencies and damage due to wear and inefficient lubrication is huge for any industry. For instance, in normal four-cylinder cars, total 33% energy of the fuel is generally utilized to deal with the friction of engine parts, transmission system and road friction [2]. Therefore, any decrease in friction can lead to a reduction in energy consumption. The improved tribological

---

H. S. Grewal  
Shiv Nadar University, Greater Noida, India

S. Singh · H. Singh (✉) · N. Singh  
Indian Institute of Technology Ropar, Rupnagar, India  
e-mail: [harpreetsingh@iitpr.ac.in](mailto:harpreetsingh@iitpr.ac.in)

S. Singh  
e-mail: [surinder.singh@iitpr.ac.in](mailto:surinder.singh@iitpr.ac.in)

properties can reduce the friction of mating surfaces, which can be fulfilled by efficient lubricants [3]. Therefore, the requirement of efficient lubricants is increasing day-by-day because of their operational usage in the broader temperature range, and high loads and speeds. The efficient lubricant leads to an increase in the reliability and service life of the mating parts, hence results in improved machine life. Therefore, innovation of anti-wear and anti-friction lubricants is an area of current thrust to save fuel and energy.

Further, such lubricants are expected to minimize vibrations, noise and maintenance of interacting parts, thereby reducing the maintenance cost of machines [3]. Additionally, the automotive industry is under pressure to follow environment-friendly practices, put forward by the environmentalists and government regulations (e.g. Kyoto Protocol) [4, 5]. A stand-alone lubricant is not self-sufficient for automotive parts due to its less adaptability in the actual running conditions. Therefore, several additives are mixed for improving the heat transfer coefficient, high-temperature performance, oxidation resistance and low-temperature performance of the lubricants. Several types of additives viz viscosity modifiers, pour-point-depressants, anti-oxidants, wear-registrant, rust inhibitors, corrosion registrant, friction modifiers and demulsifiers have been used to make a lubricant more efficient [3–11]. Mohan et al. [3] investigated that SAE 20W-40 lubricant with nano- $\text{Al}_2\text{O}_3$  additives showed better tribological properties as compared to the base lubricant. Jatti et al. [6] mixed CuO nanoparticles in the base lubricant and observed half the value of the coefficient of friction (CoF). Furthermore, Wang et al. [7] mixed serpentine additive and observed an auto-reconditioning layer by lubricant which could be attributed to the decrease in friction and wear. Also, the influence of aluminium nanoparticles additives was studied on tribological properties of base oil [8]. Recently, Singh et al. [10, 11] reported that the multiwall carbon nanotubes (MWCNT) as an additive remarkably enhanced the anti-wear and anti-friction capabilities among  $\text{H}_3\text{BO}_3$  and  $\text{MoS}_2$  additives for both the tribopairs.

It has been observed from the above literature that various studies have been performed to improve the tribological properties of sliding pairs by mixing some additive in the base lubricants. However, to the best of our knowledge, no research has been found probing the addition of halides (bromide, chloride, fluoride and iodide) in the base lubricants for tribological studies.

The present work explores the friction and wear performance of halides and acetate as additives in the SAE20W40 lubricant for mild steel and stainless steel pair. A pin-on-disc setup was used to study the effects of additives on the tribological properties of the sliding pair.

## 2 Experimental Details

Commercially available SAE 20W-40 multi-grade lubricant is used for experimentation. To investigate the variations in friction and wear of mating part, a pin-on-disc structure (Fig. 1) containing tribometer was used to examine the frictional variations

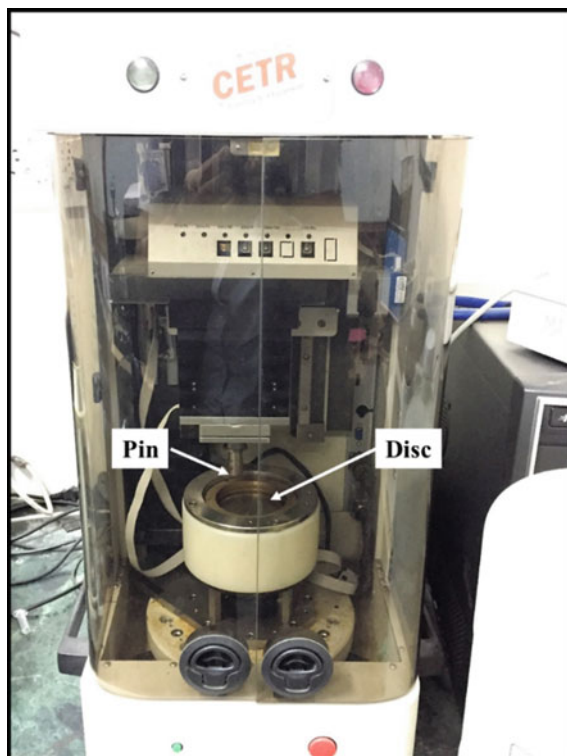


**Fig. 1** Tribometer used for pin-on-disc investigation of SWE20W40 lubricant with a different type of additive

of the mating parts by running it at a constant set of loads and speeds with the fully flooded condition. By using the four different additives (iodide, fluoride, bromide and acetate), frictional features were investigated and compared with the base lubricant.

## **2.1 Materials**

Test liquids were prepared by mixing two wt% of additives in a commercially available lubricant (SAE20W40). This lubricant maintains its viscosity at lower as well as higher temperatures and serves the purpose of lubrication very well. Tribological characteristics of the stand-alone lubricant (deprived of additives) have been compared with the lubricants with given additives. The lubricant types have been named as blends (base A and blends B, C, D and E) according to their compositions and have been detailed in Table 1. All the test samples were sonicated in an ultrasonic bath to ensure proper mixing of the additive in the lubricant. For tribological studies,

**Table 1** Different types of lubricants designated according to their additive type

Blend/base name	Composition
A	SAE20W40 (base lubricant)
B	SAE20W40 (base lubricant) + 2 wt% bromide
C	SAE20W40 (base lubricant) + 2 wt% fluoride
D	SAE20W40 (base lubricant) + 2 wt% iodide
E	SAE20W40 (base lubricant) + 2 wt% acetate

**Table 2** Chemical composition (wt%) of contact pair materials used for the pin-on-disc study

	C	Mn	Si	Cr	Ni	Mo	$S_{\max}$	$P_{\max}$	Fe
Disc	0.08	1.6	0.8	17	11	2.1	0.03	0.045	Balance
Pin	0.26	1.03	0.280	Nil	Nil	Nil	0.05	0.04	Balance

pins (diameter = 6.3 mm) of mild steel (140 Hv) were used against the stainless steel (250 Hv) discs. The chemical compositions of the sliding pair have been represented in Table 2. Both the pin and the disc were polished using abrasive paper down to 2000 grit size to ensure smooth surfaces.

## 2.2 Wear Testing

Tribological studies were performed in a pin-on-disc configuration. All the tests were performed in a lubricating condition on a Tribometer (UMT III, CETR) in a special container. The specially provided container (as shown in Fig. 1) helps in recirculation of the lubricant collected at the periphery due to centrifugal action. In addition, it also helps to maintain a uniform layer of the lubricant around the pin. The pin-on-disc experiments were performed at 5 N load and 1 m/s velocity for a total distance of 2000 m. The experiment was stopped regularly after a distance of 100 m to measure the change in the weight of the pin. The friction force was continuously measured using an attached load cell (capacity = 20 N; least count = 0.1 N) which was used for calculating the CoF ( $\mu$ ). A set of two experiments were performed for each lubricant using fresh pins, discs and lubricant mixture, and an average value has been reported. Before testing, both pin and disc were washed with acetone and dried in air. The change in the weight of the pin during the experiment was measured using a microbalance with an accuracy of 0.01 mg.

For measuring the wear rate, the tests were interrupted at regular intervals to weigh the pin. Thus, wear rate bar chart has been produced using the Eq. 1 [12].

$$k = \frac{V}{F_n \cdot d} = m_{\text{lost}} / (P F_n \cdot d) \quad (1)$$



- $K$  is the steady-state wear rate.
- $V$  is the wear volume.
- $F_n$  is the normal load.
- $d$  is the distance covered.
- $p$  is the density of the pin.
- $m_{lost}$  is the pin mass lost [11].

### 3 Results and Discussion

The variation of mass loss of the pin with sliding distance has been represented in Fig. 2. It can be observed from the figure that mass loss for all the lubricants (with or without additives) was almost the same up to 700 m, except the blend C. Blend C showed a minimum mass loss throughout the whole run as compared to the other blends. After the 700 m run, blend E showed the highest mass loss in comparison with the other blends. Notably, the mass loss in case of blend D is higher than the base lubricant (Base A). It is clear from the mass loss observations that the addition of bromide and fluoride leads to significant reduction in the mass loss, whereas all the other additives have increased the mass loss of the sliding pairs.

The variation in mass loss may be attributed to the wear rate differences due to variable lubrications. Therefore, steady-state wear for each type of blend has been calculated and represented in Fig. 3. The steady-state wear rate for blend B and blend C was found low as compared to the base lubricant (blend A). However, blend D and blend E have resulted in higher wear rate than the base lubricant (blend/base A). The

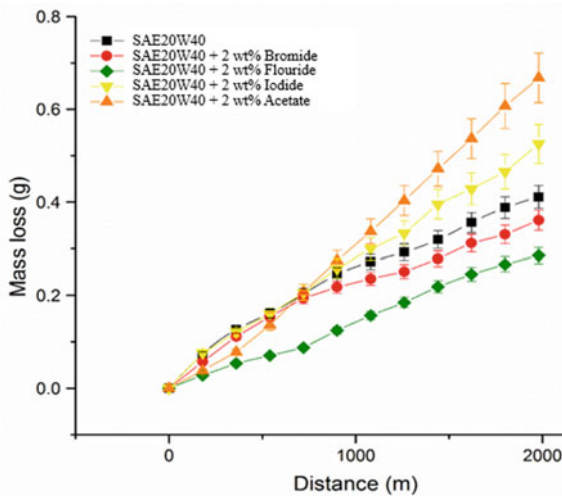
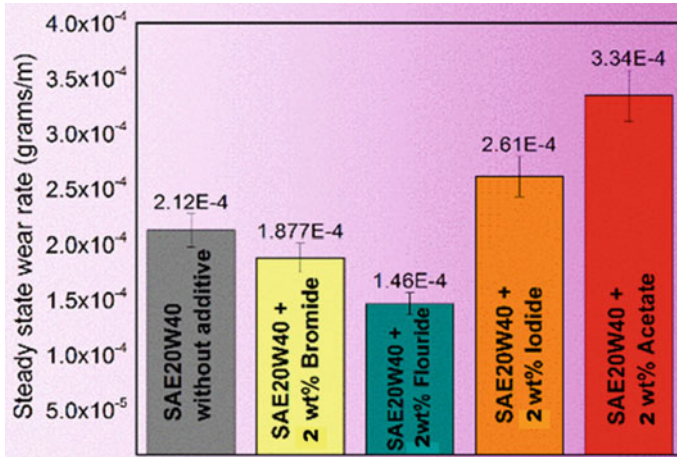


Fig. 2 Variation of mass loss of the pin with sliding distance during pin-on-disc testing in SAE20W40 lubricant with and without additives



**Fig. 3** Steady-state wear rate of the pin during pin-on-disc testing in SAE20W40 lubricant with and without additives

findings of lowest steady-state wear rate for blend C and highest for blend E are well in agreement with our findings from mass loss variation measurements.

Generally, the wear rate depends upon the CoF between the sliding pairs. More the CoF, more will be the wear rate. Therefore, the CoF has been calculated for each blend and has been represented in the bar graphs of Fig. 4. It can be observed from the graph that blend B and blend C have a lower coefficient of friction, and blend D

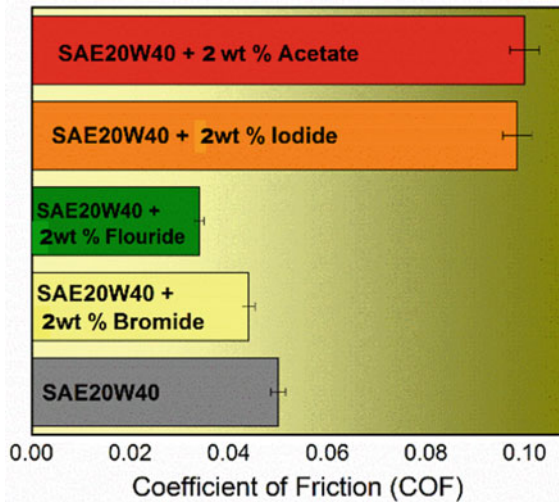


**Fig. 4** Coefficient of friction between the sliding pair during pin-on-disc testing in SAE20W40 lubricant with and without additives

and blend E have a higher coefficient of friction as compared to the base lubricant (blend A). Hence, the reason for wear rate of each blend has been further validated.

The most common halogen groups of halides are alkyl halides, which have a carbon–halogen bond [12]. Among the halogen family, chlorine, bromine and fluorine have significantly greater electro-negativities than carbon. However, iodine has lower electronegativity than carbon. In this group of polarizations/reactions, carbon behaves as electrophilic and halogens as nucleophilic. The covalent bond strength for these compound formations (carbon–halogen) is most robust for fluorine due to its highest electronegativity and lowest for iodine due to its lower electronegativity [13]. The carbon–fluorine single bond is having approximately 30 kcal/mole bond energy which is robust as compared to the C–C covalent bond and twice robust as compared to the C–H covalent bond (15 kcal/mole). Hence, the alkyl fluorides are thermodynamically and chemically very stable, as compared to the other alkyl halides. The covalent bond between carbon and bromine is comparatively weaker than the covalent bond of carbon and fluorine. The weakest bond among these common halogens with carbon is of iodine, which is about 33% weaker than the carbon–carbon (C–C) bond [13]. The other effecting parameter of halide anions is the relative stability that is considered according to the acidities of hydrogen-bonded acids (H–X). It is generally assumed that the most stable halide anion is generally released by the strongest acid, except H–F. Therefore, chlorine has very strong stability than bromine and iodine which have the least among these common halogens. In addition to this, it is also considered that lower nucleophilicity leads to weak bond formation. The present study also validated the above facts and discussion. Fluoride, as an additive, showed the least wear rate, mass loss and frictional coefficient due to its highest stable covalent bond with a carbon atom of SAE20W40 lubricant (due to its highest electronegativity) before bromide. Among the halides used in the present study as additives, iodide showed the highest wear rate, mass loss and frictional coefficient (even more than the base lubricant) due to its weak covalent bond formation with carbon of lubricant as compared to the carbon–carbon bond strength of base lubricant (SAE20W40). However, acetate showed the highest wear rate, mass loss and coefficient of friction among all the additives due to its least nucleophilicity, even compared with iodide. Moreover, the reason for variations in the value of the coefficient of friction, wear rate and mass loss may be due to the atomic size variations. Because, among all the atoms of additives attached to the molecular chains of base lubricant, a fluorine atom has the smallest size and bromine has bigger size than fluorine and smaller than Iodine.

## 4 Conclusions

- The addition of halides in SAE20W40 lubricant may affect the lubricating efficiency of the letter.
- Mass loss, CoF and steady-state wear rate can be reduced by the additives having a stronger bond formation with a carbon atom of the base lubricant.

- The addition of 2% addition of fluorides and bromides to the SAE 20W-40 lubricant has found to be significantly encouraging in decreasing the friction and steady-state wear rate.

**Conflicts of Interest** There are no conflicts to declare.

## References

1. Patil VR, Jadhav MM, Pawar GB et al (2014) Some studies on tribological properties of lubricating oil with nanoparticles as an additive. *Int J Adv Eng Tech* V(I):01–04
2. Noorawzi N, Samion S (2016) Tribological effects of vegetable oil as alternative lubricant: a pin-on-disk tribometer and wear study. *Tribol Trans* 59:831–837
3. Mohan N, Sharma M, Singh R et al (2014) Tribological properties of automotive lubricant SAE 20W-40 containing nano- $Al_2O_3$  particles. Epub ahead of print 13 October 2014. <https://doi.org/10.4271/2014-01-2781>
4. Fu X, Li J, Sun L et al (2017) Synergistic effect between organic borate esters and phosphorus-based additives on tribological performances as lubricant additives in mineral oil. *Proc Inst Mech Eng, Part J: J Eng Tribol* 231:1030–1040
5. Maurya JL, Jaiswal V, Rastogi RB (2016) Highly efficient sulfur and phosphorous-free antiwear additives for paraffin oil. *Proc Inst Mech Eng, Part J: J Eng Tribol* 230:222–237
6. Jatti VS, Singh TP (2015) Copper oxide nano-particles as friction-reduction and anti-wear additives in lubricating oil. *J Mech Sci Technol* 29:793–798
7. Wang X, Wu J, Wei X et al (2017) The effect of serpentine additive on energy-saving and auto-reconditioning surface layer formation. *Ind Lubric Tribol* 69:158–165
8. Wu YY, Tsui WC, Liu TC (2007) Experimental analysis of tribological properties of lubricating oils with nanoparticle additives. *Wear* 262:819–825
9. Le VNA, Lin JW (2017) Influence of aluminum nanoparticles additives on tribological properties of base oil. *Key Eng Mater* 737:184–191
10. Singh H, Bhowmick H (2018) Tribological behaviour of hybrid AMMC sliding against steel and cast iron under MWCNT-oil lubrication. *Tribol Int* 127:509–519
11. Singh H, Singh P, Bhowmick H (2018) Influence of MoS<sub>2</sub>, H<sub>3</sub>BO<sub>3</sub>, and MWCNT additives on the dry and lubricated sliding tribology of ammc–steel contacts. *J Tribol* 140:041801
12. Specific Wear Rate, Taguchi Method, ANOVA, Steady State. *Int J Comp M ater* 7
13. <https://www.chemistry.msu.edu/faculty/reusch/virtxtjml/alhalrx1.htm>—Google Search, [https://www.google.com/search?q=12.www2.chemistry.msu.edu/faculty/reusch/virtxtjml/alhalrx1.htm&rlz=1C1NDCM\\_enIN741IN741&gbv=1&sei=WT0sXlZ5Ho69rQGam4-4Aw](https://www.google.com/search?q=12.www2.chemistry.msu.edu/faculty/reusch/virtxtjml/alhalrx1.htm&rlz=1C1NDCM_enIN741IN741&gbv=1&sei=WT0sXlZ5Ho69rQGam4-4Aw). Accessed 2 Jan 2019

# Performance Evaluation on the Smartness of Malaysian Timber



Amirah Abdull Razak, Nasrul Izan Shahrin, Jaronie Mohd Jani,  
and Norul Hisham Hamid

**Abstract** Smart wood materials have been widely developed as green alternatives to the current infrastructures. The main property of wood that contributes to its smartness is hygroscopic, the ability of exchanging water with its environment. The objective of this work is to review and evaluate some of Malaysia's tropical woods in terms of the effects of their hygroscopic capability. Several well-known species in industries are chosen as the samples: Kembang Semangkok, Meranti, Merpauh, Nyatoh, and Rubberwood. The samples were observed to change in their shape as a response to water's diffusion. The factors that affect the rate and magnitude of shape change in the woods are their fibered structure composition and their grain orientation. Wood structure composition has an influence on the rate of water diffusion, thus affects the rate of responsiveness of the woods. The responsiveness of the investigated woods in this work is ranked from low to high as follows: Rubberwood, Merpauh, Nyatoh, Meranti, and Kembang Semangkok. While woods' grain orientation gives an impact on the deflection of the woods, a tangential cut orientation gives a higher magnitude on the shape change. These two factors can be utilized in designing new facilities by using Malaysia's smart woods in the future.

**Keywords** Smart Wood · Hygroscopic · Malaysian Timber · Water Diffusion · Shape Memory Effect

---

The original version of this chapter was revised: An acknowledgement has been included. The correction to this chapter is available at [https://doi.org/10.1007/978-981-15-5753-8\\_71](https://doi.org/10.1007/978-981-15-5753-8_71)

---

A. Abdull Razak (✉) · N. I. Shahrin · J. Mohd Jani  
Malaysia Italy Design Institute (MIDI), Universiti Kuala Lumpur, Kuala Lumpur, Malaysia  
e-mail: [amirahar@unikl.edu.my](mailto:amirahar@unikl.edu.my)

N. I. Shahrin  
e-mail: [nasrul.shahrin@s.unikl.edu.my](mailto:nasrul.shahrin@s.unikl.edu.my)

J. Mohd Jani  
e-mail: [jaronie.mohdjani@unikl.edu.my](mailto:jaronie.mohdjani@unikl.edu.my)

N. H. Hamid  
Department of Forest Production, Universiti Putra Malaysia (UPM), Seri Kembangan, Malaysia  
e-mail: [h\\_noroul@upm.edu.my](mailto:h_noroul@upm.edu.my)

## 1 Introduction

Wood is the main renewable resource that is available widely in Malaysia. Its usage is widely known in furniture industry. With 59.5% of the region covered by the wood, this resource should be studied and commercialized further on other industries, such as in construction and public infrastructures. A lot of researches around the world have been covered on the wood's unique behavior which is its smartness. Wood features as a smart material are due to its capability to react, remember, and return to its original shape [known as shape memory effect (SME)] as a response to external stimuli. Wood materials such as oak, pine, spruce, and birch were found to exhibit smart behavior, where these smart woods were responsive to electricity and humidity changes [1]. Other smart materials such as metal alloys, ceramics, and polymers also possess this behavior [2, 3] as a response to various stimuli.

The design of the smart materials with equipped stimuli responsiveness and shape memory effect (SME) is one of the most rapidly growing fields in material science [4]. Smart materials have been used widely in various domains, specifically to enhance the products' functionality, for instance for safety, comfort, and fuel economy in automotive engineering, as passive and active controls for vibrations and earthquakes in civil engineering, as responsive biocompatible implants in biomedical engineering, and as aerodynamic performance controllers with morphing technology in aerospace engineering [3]. Numerous smart wood developments based on cellulose modification also have been introduced, which will potentially change the design and concepts of existing wood-based applications, such as the electro-active paper (EAPap) [5, 6], drug delivery systems, sensors [7], self-healing concrete using natural wood fibers [8], and torsional actuators [9].

The main property of wood that contributes to its smartness is hygroscopy. This property is related to moisture content of the wood that maintains its shape in nature [10]. Changes in humidity will cause swelling and shrinking of the wood, which has become one of the major drawbacks in construction due to its instability. However, this material can as well be considered as a valuable smart material for its competency to generate reversible and complex visible movements [4]. The opening of pine cones and the movement of wheat awns are examples of the unidirectional moisture-activated actuations in nature [11].

Due to this hygroscopic property of wood, researchers are inspired to develop more responsive designs that give a response toward range of humidity changes, such as a tracker for solar modules [4], humidity-driven shading system [12], and a hygroscopic building façade panel [10]. This green sustainable development is required for new and rehabilitate deteriorated infrastructures. The main objective of this work is to review and evaluate some of Malaysia's tropical woods in terms of their hygroscopic capability, an evaluation on the effect of diffusion of water on the wood fibered structure to their shape-changing capability.

## 2 Materials and Methods

Five species were chosen for this study as shown in Table 1.

The species were divided into two groups as shown in Table 2; the species for Group 1 were prepared in crown cut cross section (tangential board) where the grain direction is  $0^{\circ}$ – $35^{\circ}$  relative to the face of the board. For Group 2, the species were prepared in quarter cut cross section (radial board) where the grain direction is  $65^{\circ}$ – $90^{\circ}$  relative to the face of the board. The species for both groups were taken from air-dried stock.

For each species of the groups, two different samples of a tangential and a longitudinal cut were prepared, with approximately the same dimensional ratio of 2:3 (width to length). The samples were used to study the effect of diffusion of water on the species' fibered structure in terms of their mechanical response. Both ends of each sample were attached to microscope slide with a masking tape. The samples were conditioned under room temperature of 50–70% relative humidity (RH). Three holes were punched, in a L shape, on the samples with approximately 1 mm distance from each other by using a pin as shown in Fig. 1a.

Before starting the test, each sample was put under  $5\times$  objective lens of OLYMPUS BX53M microscope and the initial dimension of the holes was measured by using OLYMPUS Stream image analysis software. The initial height of the samples' contour was taken as well by using a surf-test machine. A droplet of water was then dripped onto the sample. By using Mitutoyo SurfTest SV-3100, the contour of the sample was taken for every 5 min up to 40 min, for a fixed 5 mm in length as shown in Fig. 1b. The changes in the displacement of the sample for every 5 min were calculated by finding the differences in the height of the contour for every 5 min to the initial height before the experiment. The dimension of the holes of wet fibered structure was taken after the water droplet was fully diffused into the sample

**Table 1** List of species used in this study

Native name	Botanical name
Kembang Semangkok	<i>S. macropodum</i>
Meranti Bakau	<i>Shorea uliginosa</i>
Merpauh	<i>S. schwenkii</i>
Nyatoh	<i>Palaquium gutta</i>
Rubberwood	<i>Hevea brasiliensis</i>

**Table 2** Species were divided and tested under two types of cross sections

Group 1	Group 2
Crown cut	Quarter cut
Kembang Semangkok	Kembang Semangkok
Merpauh	Meranti
Rubberwood	Nyatoh



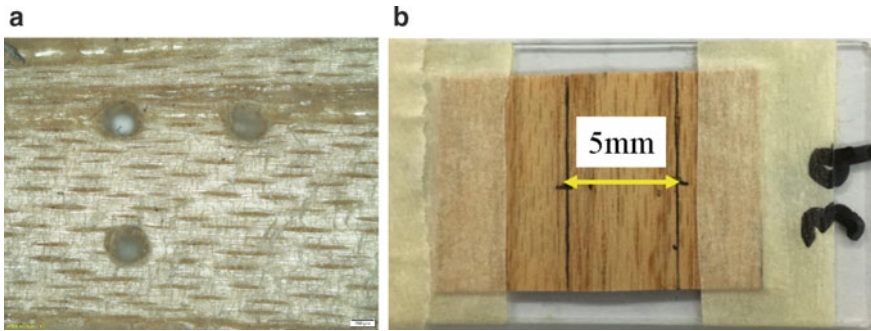


**Fig. 1** **a** Left: the sample with three punched holes before starting of experiment. **b** Right: the height of the contour of the sample was taken, for a fixed 5 mm in length, in every 5 min

approximately after 10–40 min. Graphs of the rate of shape change in the samples (displacement versus time) were plotted, and the expansions of the samples were tabulated.

### 3 Results and Discussion

#### 3.1 Rate of Shape Change

The rate of shape change data was plotted for each species. The graphs in Figs. 2 and 3 illustrate the displacement of samples versus time in tangential and longitudinal cut conditions for both groups. Based on the observation, all species expanded and bulged as a response toward the water's diffusion in their fibered structure. The samples' fibered structure continued to expand as the water droplet diffused until they reached an equilibrium state where no further expansion could occur. This expansion is controlled by swelling and de-swelling of the hemicelluloses and lignin constrained by the helically wound cellulose microfibrils [9].

However, the rate of water's diffusion is different for each species due to the differences in their structures' composition, which affects the rate of shape change [12]. Certain species such as Kembang Semangkok have higher diffusion rates, which took less than 5 min to fully change in shape. While other species, such as Merpauh, require more time for water to be fully diffused and change the shape. These phenomena may be resulted from the presence of hydroxyl group in the hydrophilic polymers of the cell wall, celluloses, and hemicelluloses to fix the water molecules through hydrogen bonds; however, hydroxyl groups of the adjacent molecules which are in parallel arrangement cannot be reached by the water molecules due to the forming of crystalline regions in the cellulose molecules [13].

Furthermore, the differences in grain orientation also give implication on the rate and magnitude of shape change in the samples. Wood, generally, is an anisotropic



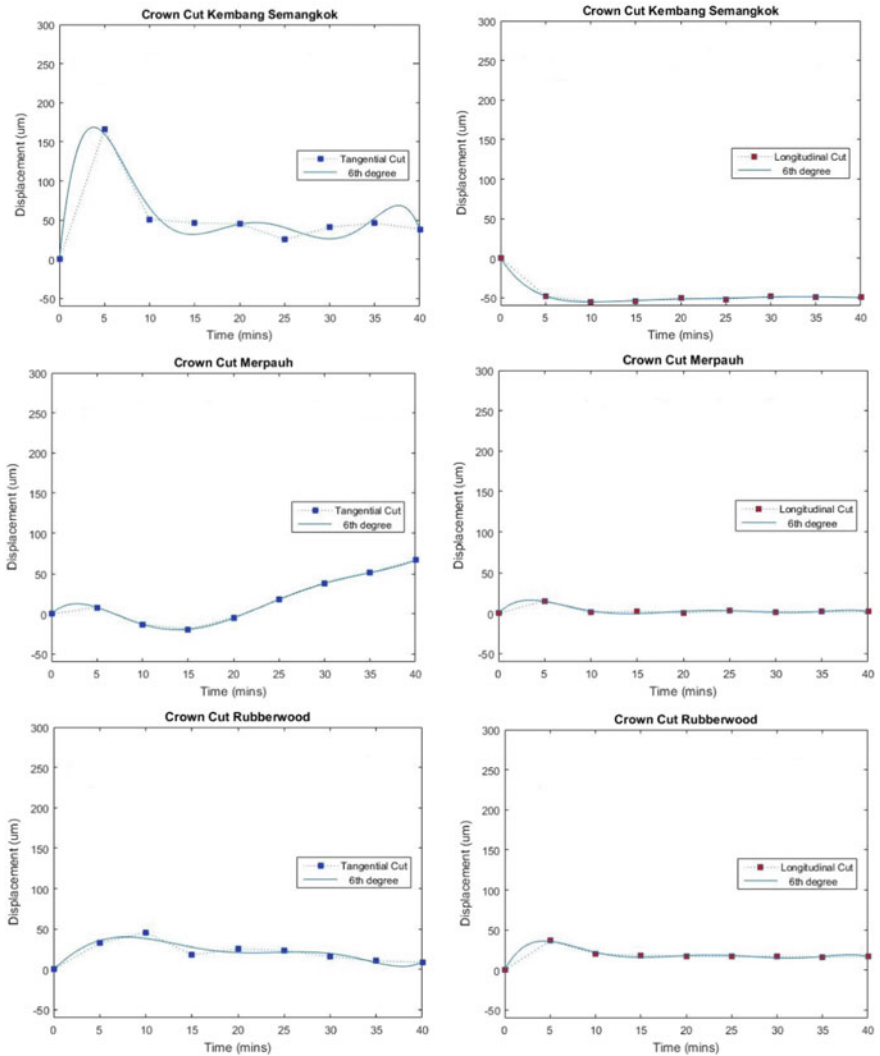


**Fig. 2** The rate of shape change in Group 1 when react to a water droplet in tangential and longitudinal cut conditions

material which its mechanical properties significantly differ when evaluated along the three directions (LRT directions) of the woodcut. This property is accountable for the mechanical properties' variations along the three perpendicular axes [10]. Based on the graph, the tangential cut orientation shows a better deflection of the fibered structure, which remarks this cut orientation has a better mechanical response compared with longitudinal orientation, which is much stiffer, and swells less in the L direction. The values of displacements for all the samples are within 50 μm or

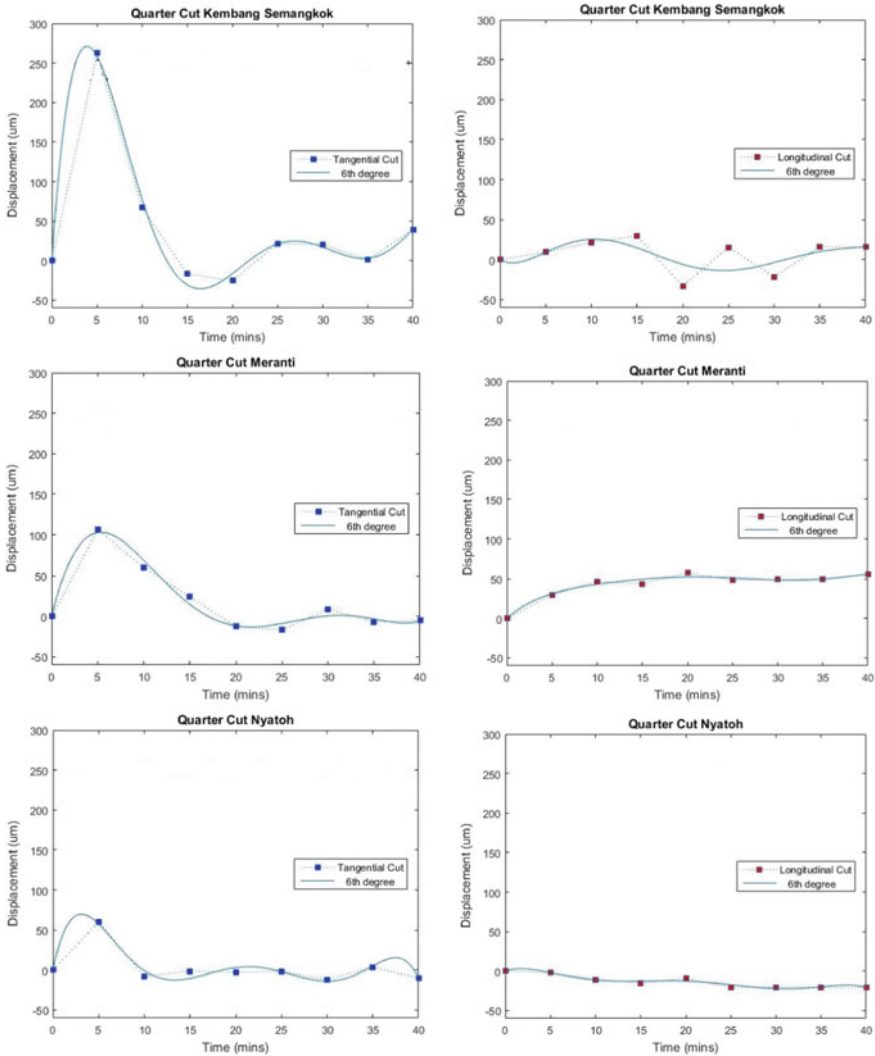


**Fig. 3** The rate of shape change in Group 2 when react to a water droplet in tangential and longitudinal cut conditions

less in longitudinal cut orientation, while the displacements for tangential cut can achieve up to 250 μm (for Kembang Semangkok quarter cut).

Comparing the deflection between Group 1 and Group 2 conditions for Kembang Semangkok in Fig. 4, crown cut cross section (tangential board) from the log shows a stable rate of shape change compared with quarter cut cross section (radial board). This shows that the deformation of the material is dependent on its grain orientation.

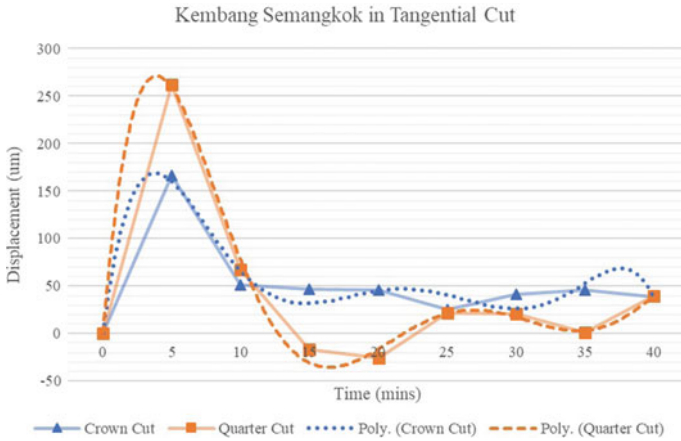


**Fig. 4** The comparison of rate of shape change in Kembang Semangkok (in tangential cut) for Group 1 (crown cut cross section) and Group 2 (quarter cut cross section)

According to Abdelmohsen et al. [10], the anisotropic property has an important implication on the response of wood toward humidity.

### 3.2 Expansion of the Fibered Structure

Based on the observation, the holes on the samples became smaller after water was fully diffused into their fibered structure, which shows that the structure can substantially swell as shown in Fig. 5.

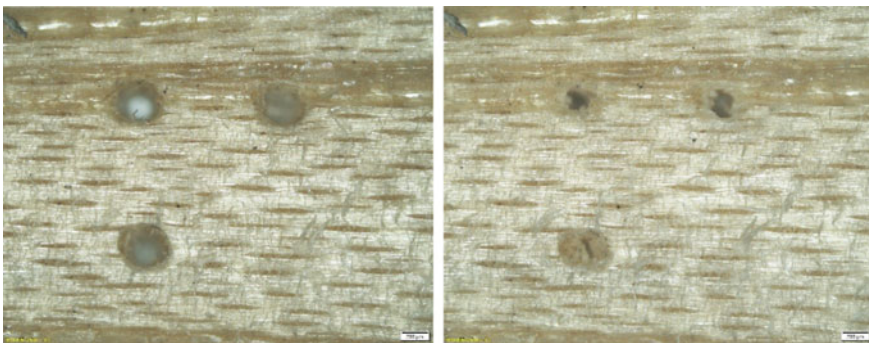


**Fig. 5** The fibered structure of the sample swells thus closes the holes. On the left is the picture of the holes before the experiment, while on the right is the picture of the holes after water fully diffused into the sample

**Table 3** The percentage of the samples' expansion for Group 1 and Group 2

	Samples	Tangential cut			Longitudinal cut		
		Initial dimension of holes ( $\mu\text{m}$ )	Final dimension of holes ( $\mu\text{m}$ )	Expansion (%)	Initial dimension of holes ( $\mu\text{m}$ )	Final dimension of holes ( $\mu\text{m}$ )	Expansion (%)
Group 1: crown cut	Kembang Semangkok	309.67	203.74	34	279.24	191.30	31
	Merpauh	289.65	207.42	28	338.38	217.00	36
	Rubberwood	390.54	307.97	21	300.04	152.77	49
Group 2: quarter cut	Kembang Semangkok	287.36	225.39	22	342.09	277.61	19
	Meranti	294.22	174.71	41	425.02	258.74	39
	Nyatoh	298.35	149.41	50	295.02	221.57	25

The average values of the initial and final dimensions of the holes were calculated in order to find the percentage of the expansion

Table 3 shows the percentage of the fibered structures' expansion of the samples for both groups.

The data show that the percentages of the expansion vary for both groups, in both tangential and longitudinal cut conditions. This proves that the expansion effects of the fibered structure (swelling and de-swelling of hemicellulose and lignin) associated with the diffusion of water are also anisotropic [10] in nature.

## 4 Conclusion

Malaysia's tropical woods exhibit shape-changing capability as a response toward different moisture contents. Based on the experiment, different species have different rates of responsiveness based on their structures' composition. Kembang Semangkok is the most responsive species (active sample) which absorbs water and changes shape faster than the others, followed by Meranti, Nyatoh, Merpauh, and Rubberwood (the least responsive). The shape changing of the species is also affected by their grain orientation. For a maximum deflection, the active sample shall be in a tangential cut orientation. The anisotropic property of wood does not only affect the macroscopic movement of the sample (change in shape), but also affects the microscopic expansion of its fibered structure.

**Acknowledgements** The authors would like to express their profound gratitude and deepest appreciation to the Ministry of Higher Education (MOHE), Malaysia, for funding this project through the Fundamental Research Grant Scheme (FRGS) under the grant reference code FRGS/1/2017/TK05/UNIKL/02/4. The authors would also like to express their special thanks to Enviri Industries Sdn. Bhd. for their specimen samples.

## References

1. Kim J, Yun S (2006) Discovery of cellulose as a smart material. *Macromolecules* 39:4202–4206
2. Gorbacheva G, Ugolev B, Sanaev V et al (2015) Methods of characterization of memory effect of wood. *Pro Ligno* 11:65–72
3. Jaronie MJ, Martin L, Aleksandar S et al (2013) A review of shape memory alloy research, applications and opportunities. *Mater Des* 56:1078–1113
4. Rüggeberg M, Burgert I (2015) Bio-inspired wooden actuators for large scale applications. *PLoS ONE* 10:1–16
5. Kim J, Yun S, Lee SK (2008) Cellulose smart material: possibility and challenges. *J Intell Mater Syst Struct* 19:417–422
6. Kim J, Yun S, Mahadeva SK et al (2010) Paper actuators made with cellulose and hybrid materials. *Sensors* 10:1473–1485
7. Qiu X, Hu S (2013) Smart materials based on cellulose: a review of the preparations, properties, and application. *Mater (Basel)* 6:738–781
8. Gard W, De Rooij M, Qian S et al (2010) Using natural wood fibers to self-heal concrete. In: *Concrete repair, rehabilitation and retrofitting II*
9. Plaza N, Zelinka SL, Stone DS et al (2013) Plant-based torsional actuator with memory. *Smart Mater Struct* 22:7
10. Abdelmohsen S, Adriaenssens S, El-Dabaa R et al (2019) A multi-physics approach for modeling hygroscopic behavior in wood low-tech architectural adaptive systems. *CAD Comput Aided Des* 106:43–53
11. Jakes JE, Plaza N, Zelinka SL et al (2014) Wood as inspiration for new stimuli responsive structures and materials
12. Vailati C, Bachtar E, Hass P et al (2018) An autonomous shading system based on coupled wood bilayer elements. *Energy Build* 158:1013–1022
13. Simpson W (1980) Sorption theories applied to wood. *Wood Fiber* 12:183–195

# A Brief Overview of Bending Operation in Sheet Metal Forming



**Omolayo M. Ikumapayi, Esther T. Akinlabi, Nkosinathi Madushele, and Samuel O. Fatoba**

**Abstract** Bending operation in sheet metal forming has been extensively used in manufacturing technology for mass production especially in automotive industry as one of the tools for shaping into a desired shape and geometry, therefore to keep abreast some of the trends in bending operation. In this short overview paper, different types of bending techniques were exploited and presented varying from old age to modern age of bending operation. Theory of bending was also discussed extensively in this paper.

**Keywords** Bending operation · Manufacturing technology · Shape · Sheet metal forming

## 1 Introduction

Researchers have shown that sheet metal forming has made major and crucial contributions in many industries especially automotive and transportation companies in terms of development [1, 2]. The most common metal sheet forming process being the bending process, also known as metalworking, produces a V shaped (channel or U shape) shape along the axis of a material by applying a force to a metal sheet causing it to bend into the desired shape. This is done in ductile materials. Such materials are used in brake presses, pan brakes and specialized machine processes [3]. Wipe bending needs the sheet to be held against the die by using a pressure pad, causing the sheet to bend against the radius of the edge. There are two main quality considerations when doing the sheet metal bending process which include but are not limited to formability and dimension. Consistency is also mandatory which is minimizing the variations in dimensions which is a key requirement within mass production [4]. In this paper, the recent developments within the manufacturing space particularly with the focus on bending operations are analysed.

---

O. M. Ikumapayi (✉) · E. T. Akinlabi · N. Madushele · S. O. Fatoba  
Department of Mechanical Engineering Science, University of Johannesburg, Johannesburg,  
South Africa  
e-mail: [oikumapayi@uj.ac.za](mailto:oikumapayi@uj.ac.za)

It is a known fact that advancement of the fourth industrial revolution will bring about changes in all industries and technological processes. Metal forming, as a technological process, will also be impacted by this rapid change. These changes include but are not limited to the improvement of production productivity, increased production rate of completed products, reducing technological difficulties between the adjusting equipment and the die and also a reduction in the time it takes to set up the die. These improvements will be brought about by an intelligent press system mainly consisting of four basic elements: control, identification, prediction and monitoring [2]. Bending along a straight line or path is one of the most common types of processes in sheet metal forming. Bending of metal sheets can be done in a variety of processes such as wiping, flanging or folding using specialist machinery, bending the metal in a die or bending the sheet in a die that has a radius.

### 1.1 Bending and Forming Operations

Bending operation is a technique that involves plastic deformation of materials especially metals around a linear axis, known as the bending axis with little or no change in the surface area [5]. This results in the uniform straining of the sheet metal. Simply put, bending occurs when a portion of the part is deformed along the linear axis until such a desired or undesired bending occurs. This bending process does not only occur in a straight line or a linear axis but along curved lines and paths as well. An important observation needs to be noted about the characteristics of the metal that occurs during bending operations. It was established that tensile strength becomes lower towards the middle of the sheet metal thickness and zero at the neutral axis, but there was increase in compressive stress from the neutral axis towards the middle of the bend. It is cogent to establish that in bending operation, there is no cutting of metal sheet but there is a change in the contour of the workpiece to get the desired product. Bending operation can be categorized into various types as depicted in Fig. 1a, which are (a)

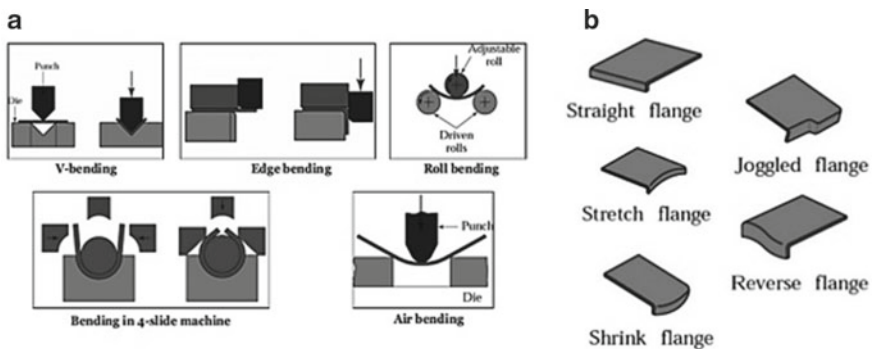


**Fig. 1** a Types of bending and b types of flange

V bending, (b) stretch forming, (c) edge bending, (c) beading, (d) roll bending, (e) flanging, (f) press break forming, (g) dimpling, (h) roll forming, (i) bulging, (j) air Bending and (k) tube forming [6]. When bending occurs in a curved path, flanging or stretching occurs in the metal sheet. Some of the flanges that occurred are illustrated in Fig. 1b. When flanging occurs in a bending operation it is classified into two forms namely shrinkage flanges and stretching flanges. Shrinkage flanges imply that the sheet metal is compressed or squeezed during the metal forming process and stretched flanges imply that the metal is stretched and subsequently thinned during its forming process. In order for a metal sheet to be considered as undergone a bending process, the cross-sectional area of the bent or flanged metal sheet must have the same thickness as the rest of the sheet in which it was made [6].

## 1.2 Bend Radius

Two important factors considerably affect bending of sheet metals. They are the bend radius and the size of the bend angle. At large bend angle, many materials can be bent to this degree without a great degree of difficulty since a little difference exists in the flat material and the one that has been formed. The bending radius greatly affects the desired bending results. The bending size depends on the thickness of the material and the hardness of the material. The smallest radius attained by bending can be expressed in Eq. 1 [7].

$$BR_{\min} = kt \quad (1)$$

where  $BR_{\min}$  is the minimum bending radius,  $t$  is the thickness of the material and  $k$  is the coefficient of the minimum radius for a given material.

## 1.3 Types of Bending Operations

Different types of manufacturing processes can accomplish different bending operations. There are supported as shown in Fig. 2a and unsupported bending operations as shown in Fig. 2b.

Unsupported bending can be described as the process in which stretching a sheet metal stretches in a retained die. V-die and U-die can be regarded as unsupported bending at their initial stages. As shown in Fig. 2b, as the bending process continues, and the material is pulled down into the recess, all the way down, the bending becomes supported, as shown in Fig. 2c [7].

Complex geometric shapes have helped humanity save space and be able to design structures that can be observed in cars, ships, airplanes and many other applications



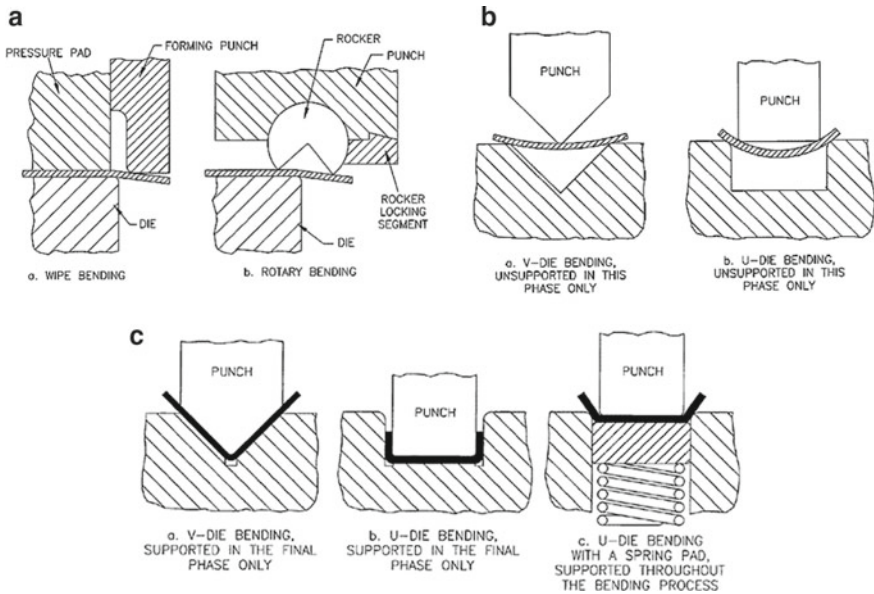


**Fig. 2** a Supported and partially supported bending [7]. b Unsupported bending [7]. c Supported bending [7]

[8]. One of these shapes is bending, and many structures have bending geometries in their designs and this structural shape can save space and give beautiful designs but also can render the structures of the material weaker than their initial structure [9]. The material may crack, tire or buckle depending on the nature of the material used. Bending of materials can increase its economic value and save space for specific applications which require it. The process is used to manufacture structures such as flanges, clutches and brake pressure levers, and I-beams for building towers, and the applications are limitless but they increase the economic value of the starting workpiece since its being appropriately shaped for the required application [8].

### 1.4 Theory of Bending

The workpiece is plastically deformed within the plastics deformation region of the stress–strain graph of the material it is made from. The reduction in the radius of the workpiece is limited by the ductility of the material, usually materials that are categorized as having a high ductility usually possess high radius of curvature and vice versa. One of the most important bending parameters in design is the bending allowance, which models the failure point in the radius where the workpiece may start to crack under bending, and to help prevent it [10, 11], the principle of bending allowance,  $L_b$  as shown in Eq. 2, is adopted.

$$L_b = \alpha (R + kt) \tag{2}$$

where  $\alpha$  is the bend angle,  $R$  is the radius, and  $t$  is the thickness.

$k$  is a constant which is obtained from the following details:

K—Constant		
Radius	$R < 2t$	$R > 2t$
$K$ value	0.3333	0.5

The material particles in a bent workpiece experience tensile forces of the out surface and compressive forces in the inner surface. This forces the particles on the outer surface to stretch retaining a lot of elastic energy in that region [1]. This results in an overload of energy beyond the materials capacity and then cracks begin to form on the outer surface, in order to find the strain ( $e$ ) on the outer surface the following Eq. 3 is used, where  $R$  is the radius of curvature, and  $t$  is the thickness [1].

$$e = \frac{1}{\frac{2R}{t} + 1} \tag{3}$$

An expression for the minimum radius as presented in Eq. 4 can be achieved during bending and specific materials allow for a radius of zero, which indicates that the material can be folded on itself [1].

The minimum radius that can be achieved is expressed in the ratio of radius over thickness ( $R/t$ ):

$$\frac{R_{min}}{t} = \frac{1}{2r} - 1 \tag{4}$$

This expression is used to find the minimum radius allowable where  $r$  is the reduction area of the bended sheet. A 50% reduction in the bending area results in the minimum radius being zero; hence, the radius is equal to zero [1]. From the graphical expression in Fig. 3, we could see that the reduction area at the bent sight is inversely proportional to the minimum radius.

### 1.5 The Modern Method for Bending Workpieces in Manufacturing.

The bending process has expanded into many sectors in the engineering industries, and it continues to grow with new techniques and methods being developed for better economic growth in value due to quality but also not sacrificing the engineering integrity of the workpieces being bent. Many bending processes exist in industry but only a few will be addressed in this paper. The bending processes can be classified

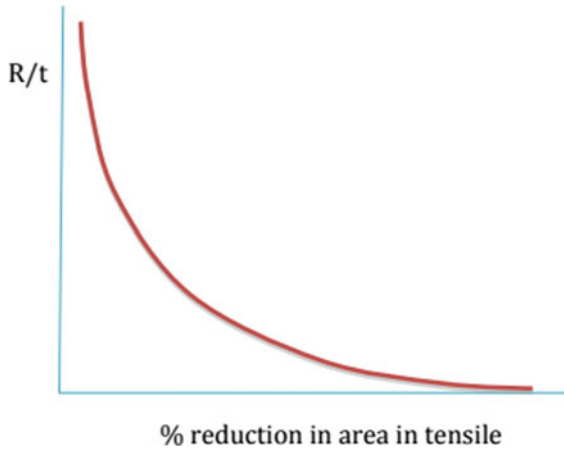


**Fig. 3**  $R/t$  versus percentage reduction in area

into two categories, linear die bending and rotatory die bending. Linear die bending is conventional and simple, a gradual force is exerted on the punch and the punch gradually bends the workpiece at a constant velocity to form a desired product based on the applications [12]. Rotatory die bending involves a rotatory motion, a die specifically constructed for the bending process. The workpiece is placed in lower die, and the upper dies contain the rocker which makes contact with the workpiece and bends it in desired manner to obtain the desired shapes. Modern bending operation has been developed from ancient art practised by the armour makers and the immortalized village blacksmith. Nowadays, sophisticated equipment has been deployed into bending operation industries to replace punch and die techniques which are updated versions of the ancient methods of bending. Some of the new technologies used in bending operations are presented in Fig. 4 [2].

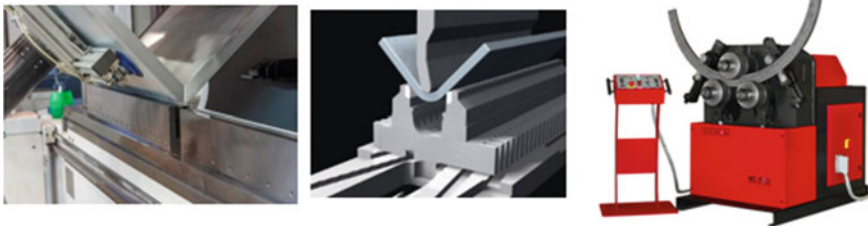


**Fig. 4** Today's bending Industry

## 2 Illustrative Case Study

The most common material that usually undergoes bending operation is metal. Different types of bend formation use different apparatus in the process of bending the specimen. The basic apparatus that is used in bend operations include the following: (a) punch, (b) die (c) pressure pad, (d) forming roll and (d) downholder.

### 2.1 Procedures

As these processes differ, so does the procedures that follow. The basic procedures to achieve sheet metal bending operations are itemized below. According to [5], these go through process analysis, simulative procedure, measurement, control and testing.

**Process analysis:** This is the first step into the process of bending. In order to understand extensively continuous bending as well as punch bending techniques, it is important to make an analysis of the tool design, the behaviour of the machines and the process design. In the process of punch bending, the first thing to be investigated is the behaviour of the cam disc machine that is used in the production series. To enable the use of the required measurement devices, the use of multi-body simulation models makes a possibility to obtain velocity and force general information.

The aim of the analysis is to get unambiguous machine behaviour, which includes the speed, the forces and the travel of an axis in the machine. The analysis also looks into the dimensional correctness of the parts produced by bending. It then goes into analysing the heating of the machine in the operation process, the specific machine characteristics and the effect of punch motion change.

**Simulative Technique:** The information acquired from the process analysis is utilized for demonstrating and simulating the bending process. A number of modelling strategies for metal bending process are developed [13]. For this situation, the simulation will serve to recognize both the important procedure parameters and the suitable commitment positions for correction activity. At that point, in view of these simulation models, the fundamental correction procedures are structured and investigated. This makes it conceivable to essentially decrease costly and tedious tests on the test facilities.

**Measurement:** Subsequent to process analysis, the following stage in the V-model is used to build up the measurement devices. To catch ordinary attributes of the part created, for example, a geometrical reference measurement, it is important to choose fitting sensors. To actualize the corrective action for changing a geometrical reference measurement, extraordinary actuators should be created. Sensors will quantify the current condition of the process and give the data to the control unit. The control unit gives the actuators the data required to change the ideal procedure variable. For this situation, the information of different parameters like elasticity or extension is not

significant to enlighten, the fact that it is wanted to address the deviation from the set point freely from these parameters.

The estimation technology in the punch bending process is utilized both for checking the bending process and for online procedure control. It is separated into two gatherings: one is for securing of procedure factors, for instance, the punch position and the bending force, while the other is for gathering of the significant parameters of semi-finished items. The difficulties for the estimation are exactness, elements and combination into the existing instrument. Laser sensors are hence chosen for position estimation, and piezo sensors for force measurement. For recognizing geometric dimensions, optical measuring devices can be utilized. A check should, be that as it may, be led to see whether the current market items are reasonable for gathering the prerequisites.

**Control strategy:** Self-correcting strategies are designed and used when using V-models. In the punch bending process, the test for the revision system lies in characterizing the factors from the shaping procedure which are of importance for online procedure control. The punch movements are utilized as impelling factors. The control system itself comprises of a feedback controller and disturbance compensator. The plan of the controller parameters is performed based on models utilizing streamlining algorithms. The controlled variable is an important geometrical normal for the work-piece for the opening measurement. On account of deviations of the real geometry from the wanted geometry, the corresponding axes will be modified.

In the event that the actual geometry of the genuine part is bigger than the ideal size, one probability is adjusting the punch movement to change the opening dimension of the following part. Various input variables must be handled, and numerous output variables must be discharged then record profile attributes of the opening measurement at various positions in the assembling procedure should be recorded to be utilized. A proper choice is the model-based plan of a multivariable control. Therefore, the control technique is first planned and tried on the model and after that executed on the genuine model plant.

**Testing:** The developments are analysed on test facilities as shown in Fig. 5a before being executed in the prototype system. Test facilities have been structured and built for the two processes. This makes it conceivable to investigate the conduct of the forming process under sensible conditions, while profiting by a laboratory circumstance. Therefore, as to re-enact the process forces, a hydraulic force-controlled cylinder is balanced in connection to the bearing block [14]. The object of the investigation included accomplishing right measurements on the mechanical and electrical segments. Further examination factors were the effect of backlash in the segments on the situating precision of the bearing block and its position retention exactness. The test facilities for the two procedures make it feasible to work independently of the machines utilized for arrangement generation which have high use rates. Along these lines, the estimation devices can be tried and enhanced, while having the control technique that has been created and executed in a modern control system. Figure 5b shows the details of bending [15].

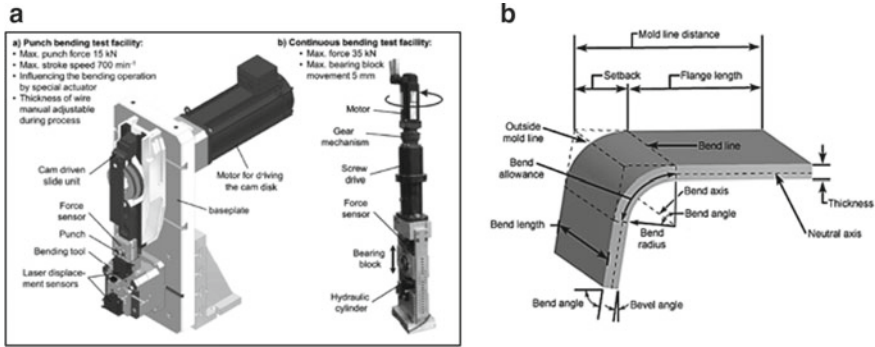


**Fig. 5** a Test facilities [5], b nomenclatures in bending

Some of the products produced from bending types such as v punch and edge bending have been explored with the specific interest on L-shaped products. The product of each process is illustrated with the use of images and given a description based on the resulted image.

**V Punch Bending Operation Products**

Figure 6a represents the illustration of V bending process of an aluminium metal sheet that is subjected to a plastic deformation punch to form a 90° L-shaped product in Fig. 6b. The line of action or contact with the specimen is illustrated in Fig. 6a, and in Fig. 6b the punch has applied a punching force all the way in the specimen and stopped before it alters the thickness of the aluminium specimen.

**Edge Bending Operation Products**

Figure 4 shows how the press has deformed the shape of the aluminium specimen to produce the desired shaped product. From the V punch, it can be deduced that the angle between the planes after unloading the punch is on the specimen which is smaller than the bending die angle by a tolerance of around  $-1^\circ$ . This difference represents the spring-back phenomenon [16]. It can also be noted that the thickness of the material does not influence the spring-back value significantly. Observing the

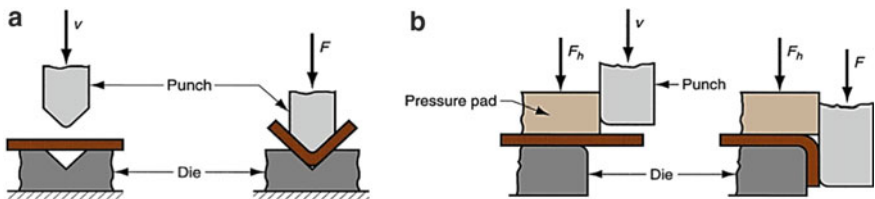


**Fig. 6** a V bending, b edge bending

L-shaped specimen from edge bending Fig. 6b, the specimen forms the perfect shape as desired from the bending process. The differences learnt between the two, aside their nature of operations, have been that V bending is relatively easy to set up and the possibility for error is relatively smaller than edge bending.

### 3 Conclusion

Metal bending is a huge industry, especially for mass productions such as in automotive engineering where the body panels are punched out of sheet metal [17]. From the research and the discussions, it can be concluded that the basic types of bending include V bending as well as edge bending. It was established that when punch and die with the included angle are employed in the bending operation, it is called V bending whereas when the punch forces a cantilevered sheet metal section over a die in order to achieve desired and optimum bend angle, it is called edge bending. Other processes to be acknowledged for bending operations include air bending, beading, seaming, flanging and tube bending [18, 19]. From the bending operation explored on this assignment, it can be concluded that V bending can be used for larger sophisticated projects and edge bending can be used for relatively small projects. Irrespective of which method used, there is always a spring-back force on the material.

### References

1. Tisza M (2013) Recent development trends in sheet metal forming. *Int J Microstruct Mater Propert* 8(1/2):125–500
2. Groover MP (2013) *Principles of modern manufacturing*, 5th edn. Wiley publisher
3. Wanisevic A, Milutinovi M, Strbac B, Skakum P (2013) Stress state and spring back in V-bending operations. *J Technol Plast* 39(2):157–168
4. Lim Y, Venugopal R, Galip AU (2008) Advances in controls of sheet metal forming. In: *Proceedings of the 17th world congress, the international federation of automatic control Seoul, Korea, July 6–11*, pp 1875–1883. <https://doi.org/10.3182/20080706-5-KR-1001.1201>
5. Damerowa U, Tabakajew D, Borzykh M, Schaermann W, Homberg W, Trächtler A (2014) Concept for a self-correcting sheet metal bending operation. *Procedia Technol* 15:439–446
6. Hosford WF, Duncan JL (1999) Sheet metal forming: a review. *JOM* 39–44
7. Groche PD, Fitteshe D (2007) Incremental bulk forming. *Ann CIRP*
8. Suchy I (2006) *Handbook of die design*, 2nd edn. McGraw-Hill, New York
9. Bressan JD (2008) Influence of thickness size in sheet metal forming. *Int J Mater Form suppl* 1:117–119
10. Cai S (2019) Investigations of sheet metal forming by vaporizing metal foils. *Int J Adv Manuf Technol* 102:3265–3270
11. Alexandrov S, Hwang YM (2009) The bending moment and spring-back in pure bending of anisotropic sheets. *Int J Solids Struct* 46:4361–4368
12. Tisza M, Lukacs Z, Gal G (2008) Integrated process simulation and die-design in sheet metal forming. *Int J Mater Form suppl* 1:185–188
13. Oyibo ST, Ikumapayi OM, Jen TC, Ismail SO (2020) Experimental and numerical prediction of extrusion load at different lubricating conditions of aluminium 6063 alloy in backward cup extrusion. *Eng Solid Mech* 8:119–130

14. Atzema E, Abspoel M, Kömmelt P, Lambriks M (2009) Towards robust simulations in sheet metal forming. *Int J Mater Form* 2(Suppl 1):351–354
15. Kirkhorn L, Frogner K, Andersson M, Ståhl JE (2012) Improved tribotesting for sheet metal forming. *Procedia CIRP* 3:507–512
16. Duflou JR, Vancza J, Aerens R (2005) Computer aided process planning for sheet metal bending: a state of the art. *Comput Ind* 56:747–771
17. Adeoti OM, Dahunsi OA, Awopetu OO, Oladosu KO, Ikumapayi OM (2019) Optimization of clay-bonded graphite crucible using D-optimal design under mixture methodology. *Int J Sci Technol* 8(7):455–461
18. Ikumapayi OM, Oyinbo ST, Bodunde OP, Afolalu SA, Okokpujie IP, Akinlabi ET (2019) The effects of lubricants on temperature distribution of 6063 aluminium alloy during backward cup extrusion process. *J Mater Res Technol* 8(1):1175–1187. <https://doi.org/10.1016/j.jmrt.2018.08.006>
19. Azeez TM, Ikumapayi OM, Bodunde OP, Babalola SA, Ogundayomi MO (2019) Measurement of surface roughness on a transmission shaft using CNC and conventional lathes machining. *Int J Sci Technol* 8(10):1626–1633



# Emerging Trend in Forging Operation



Omolayo M. Ikumapayi, Esther T. Akinlabi, and Peter Onu

**Abstract** Forging is one of the most popularly known metal-forming techniques in manufacturing process globally. Materials (metal) are transformed through a plastic deformation stage, which is a fast, energy-efficient, and low waste generation process. The operation may be considered to be economically attractive because of the initial cost of the forge. However, the benefit of an improved forging process far outweighs the loss. The present study aims to review forging operation by investigating techniques and developmental trends over the years, while proffering pathways based on technology and knowledge transfer. An experimental case was accessed on the use of Thyrotherm 2999 EFS SUPRA to exemplify recent development in drop forging technique. Advance computer models will improve product and process efficiency to satisfy the time, cost, and quality demands of customers, and promote competition in the market mix. The forging plant of the future will leave an environment that is safe, clean, and eco-friendly. Operations will be highly automated, and high-level excellence due to nascent technological solution will result in manufactured products having superior consistency and dimensional control.

**Keywords** Forging · Manufacturing process · Metal forming

## 1 Introduction

Forging is a process in manufacturing that presses a metal under great pressure into strong parts called forgings [1]. Different techniques of forging have been applied in different areas, and for manufacturing of diverse, both simple and complex industrial or machine parts. Forging is achieved through diverse approaches and methods and

---

O. M. Ikumapayi (✉) · E. T. Akinlabi  
Department of Mechanical Engineering Science, University of Johannesburg, Auckland Park  
Kingsway Campus, Johannesburg 2006, South Africa  
e-mail: [oikumapayi@uj.ac.za](mailto:oikumapayi@uj.ac.za)

P. Onu  
Department of Quality and Operation Management, Doornfontein Campus, University of  
Johannesburg, Johannesburg, South Africa

may be categorized based on working temperatures and techniques applied [2]. The forging techniques, however, are dependent on the temperature condition at which the operation is conducted (warm or cold forging). Conventional forging in manufacturing includes open and impression-die, and flashless forging. The expectation is to ensure sustainable, energy-efficient, and optimal operational performance in industrial manufacturing processes [3–6].

## 1.1 Literature Review

**The History of Forging.** The earliest signs of metalworking can be traced back to 4500 B.C. The ‘Sumerians’, which was a mixture of many ethnic backgrounds, had inhabited in the then, Mesopotamia region where the true founders of metallurgy, as we know it today were resident. The art of forging, shaping metal using heat pressure, progressed throughout the ‘Dark Ages’. Before this time, the possession of metals was highly regarded as wealth in their time, such that, the Romans committed greatly towards its exploits and had gods dedicated to the forge practice, the most notable being Vulcan [7] (Fig. 1).

Historically, forging depended greatly on the skill of the operator. The manufacture of forgings still depends on people, but developments in equipment and process control technology are increasingly changing the nature of jobs and skills needed in the forge shop [8]. Advancements in technology involved in the forging process gave more advantages over the old manufacturing processes. These advantages include higher strength, superior internal quality, tight dimensional tolerances, and more consistent and higher metallurgical properties [9]. Forging as an art form started with the desire to produce decorative objects from precious metals [10]. Today, forging is a major worldwide industry that has greatly contributed to the development of man. Modern forging is a sector that has developed from ancient art practised by the armour makers and the immortalized village blacksmith. Nowadays, powerful

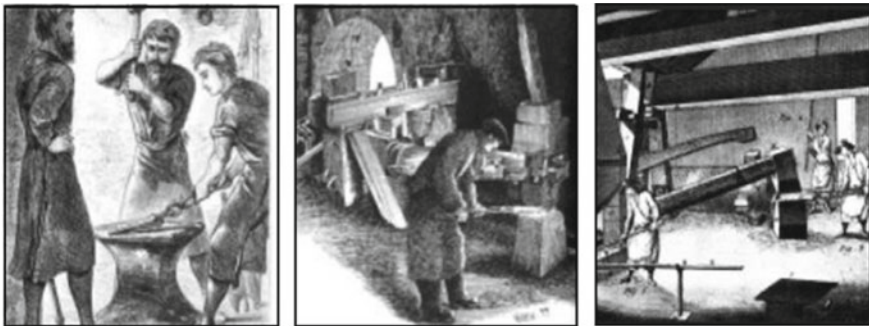


**Fig. 1** The art of forging in the dark ages



**Fig. 2** Today's forging industry

hammers and mechanical presses replace the strong arm, the hammer, and the anvil, and modern metallurgical knowledge helps the art and the skill of the craftsman in controlling the heating and handling of the metal (Fig. 2).

## ***1.2 The Importance of Forging***

Forging has a unique value among other manufacturing processes. It is the basic metal-forming operation which allows critical manufacturing segments and metal suppliers as well as end-user industrial manufacturers to join and exchange ideas. Forgings find application in a wide variety of areas: vehicles and heavy equipment, which have the potential to transform a country's economy [11]. Forgings are versatile as they can be manufactured easily from available bar stock, and almost all metals and alloys can be forged with few limitations in part size and yet accommodate high tolerance features. The products made from forging are fully recyclable, and they have relatively low life cycle costs [12]. Ultimately, forgings impart high strength and reliability in metal components, which is essential for industrial development.

## ***1.3 The Forging Industry***

Forgings are commonly used to make parts that are stronger than those manufactured by any other metal processes. For this reason, forgings are used where there is a need for high reliability and human safety. However, forgings are rarely in our sights as they are usually used for the production of sophisticated component parts as part of an assembled item, such as in airplanes, automobiles, tractors, ships, and engines. This is with regard to parts, ranging from the common hammer and wrench in small toolboxes to highly tolerant precise components in today's aircrafts, like the Boeing 747 and NASA space shuttles. Although forged parts may differ in shape, size, and structure for application consideration, there exist more than 18 000 forgings contained in a Boeing 747. It therefore draws inference to the level of importance and the customer base (forging in aerospace). Other areas include defence, automotive, agriculture, construction, mining, and general industrial equipment [13]. Different categories of forging techniques applied in the manufacturing operations include,

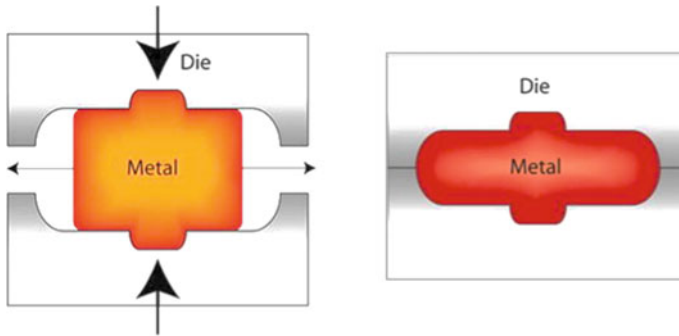


**Fig. 3** Impression-die forging

but not limited to, custom forgings—produce parts to meet customers’ requirement; captive forgings—create parts to meet own company’s internal use; and catalogue forgings produce standardized parts for resale. Although metal forging is a widely accepted technique, however, the most forged metals are carbon, alloy, and stainless steels, hard tool steels, aluminium, titanium, brass, and copper and high-temperature alloys, which contain cobalt, nickel, or molybdenum.

## 2 New Techniques and Forging Operation

### 2.1 *Impression-Die Forging*

Impression-die forging applies two dies, an upper die and a lower die. The latter is stationary, while the upper die transfers the pressure that is used to forge the workpiece into the desired geometry [14]. The illustration shown in Fig. 3 depicts the impression-die forging set-ups, having different forged geometries.

### 2.2 *Open-Die Forging*

The open-die forging process like many other forging techniques utilizes high enough pressure (blow) to alter the physical shape and size of a metal/work component. As such, during open-die forging, the material is impacted upon by hammers or stamps, while resting on an anvil. Also, while the material is being hammered, the dies allow the metal to expand in lateral direction [15]. The illustration in Fig. 4 depicts open-die forging.

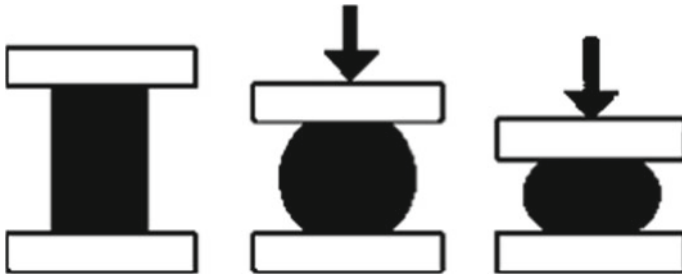


**Fig. 4** Simple illustration of open-die forging principles

This process is similar to the processes which have been used for years by blacksmiths to fabricate metals. Therefore, it is more often called smith forging. In manufacturing, open-die forging is very important and useful because of the numerous advantages. The use of super and/or robust forging machine can greatly impart the physical appearance and the characteristics of the finally finished material. For these processes, specialized open anvils are a must, and consequently, the workpiece to manoeuvre, and gyrate the produce in all directions. The accuracy due to degree of measure, in size and tolerance, is judiciously met by this process, regardless of the concept or the idea that it may be a simple design or very complex, both ways. More so, forging is a metal-forming process which is a cost-effective lean process that also increases material strength and leads to grain refinement. Unfortunately, open-die forging operation pays little attention/control to accuracy and precision, and may require addition final finishing operation to meet dimensionality.

### ***2.3 Drop Forging***

Drop forging is a metal-forming process where hot pieces of metal are forged between a stationary and dropping/hammer part of a 2-piece hollow metal die, also known as a forging die, in one/several operation(s) (Fig. 5). The upper die is the hammer of which when dropped deform the workpiece. The billet is inserted into a die and then hammered to the point where it has taken the shape of the used die. Drop forging can be operated at high or room temperature. Similar to other forging methods, drop forging improves the material properties and products' performance. This is an effective technique and process for the manufacturing of axles, crankshafts, gears, lathe tool, etc. [8, 9, 16].

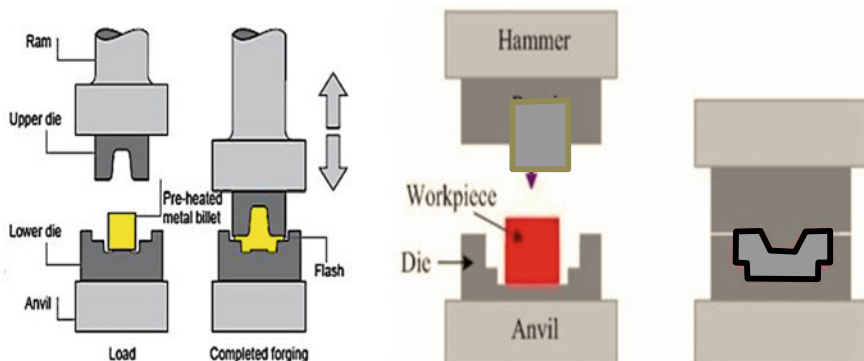


Fig. 5 Drop forging hot metal shaping hammer

### 2.4 Developments in Impression-Die Forging

Recent developments in impression-die forging include the utilization of computer-controlled preform (CCP) forging method. As such, with the third and fourth industrial revolution on the rise, the industry produces high volumes and it is a known fact that traditional impression forging produces small volume [17]. The recent development of CCP is made possible through the advancement of recent software and servocontrols that enable manipulators to function autonomously. The programming is done by the forge operator in dialogue with the machine. After each part is manufactured, the programme is later stored and can be used at a later stage. Any of the selected programmes could be changed or altered at any stage if improvements were needed on any specific parts.

### 2.5 Developments in Open-Die Forging

#### Open Die with No Friction

This is an open-die forging operation conducted under ideal conditions, thereby implying that there is no friction between the surfaces of the dies, material, and anvils [18]. For these particular conditions, strain is defined and calculated as shown in Eq. 1 (Fig. 6).

$$\epsilon = \ln \frac{h_o}{h} \tag{1}$$

The force applied on the die is a function of stress flow, represented in Eq. 2

$$F = Y_f A \tag{2}$$

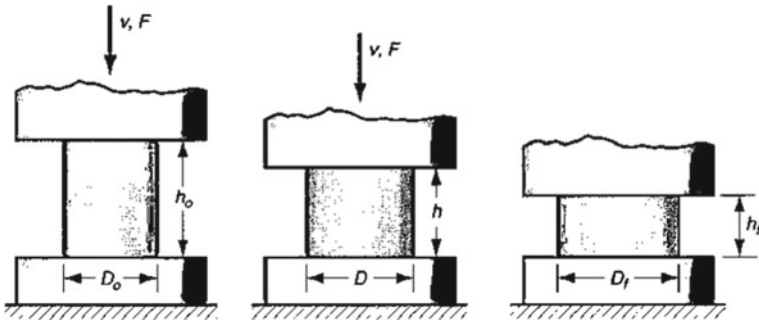


Fig. 6 Open-die forging with no friction

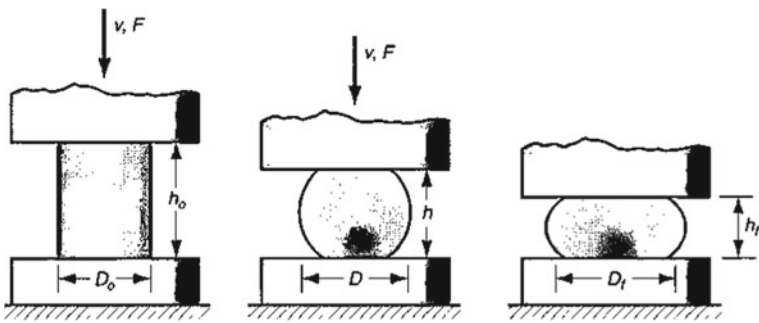


Fig. 7 Open-die forging with friction

**Open die with friction.** In open-die forging, the membranes and surfaces of the dies might experience friction between them, and the friction usually affects the shape of the workpiece, typically how it expands in the lateral direction, and results in barrelling effect (Fig. 7).

Since open-die forging is typically used for mass production, it is imperative to examine and optimize the forging operation to determine increased influence of production quality and quantities. Open-die forging has been developed to become cost-effective [19]. The forging instruments for this type of process are designed such that they are easy to use with little or no waste material disposal [5, 20]. Moreover, open-die forging permits the production of almost any type or shape of metals to be forged.

### 2.6 Developments in Drop Forging (Case)

Experimental determination on the advancement of hot-tool drop forging operation has been determined and proved with excellent wear resistance of the stimulus

for different industrial applications and has been tested [21] and compared to the most recently available processes. A forging die was used on a first case study on a Maxi press. A Thyrotherm 2999 EFS SUPRA was used in the tempering and hardening condition (46-47HRC) without any other further surface treatments. The Thyrotherm produced more than 10,000 forgings with tool productivity improved by more than 60%. In a second case study, the components of a drive shaft were produced by a customer. Carbon steel, C-35, was forged at a temperature of 1250 °C on a 10M-N eccentric press. The Thyrotherm was used in hardening and tempering conditions (48-52 HRC), which had resulted in the production of 3500 parts per die. The Thyrotherm tools improved productivity by 50%. In the third case study, a customer produced parts from carbon steel C-45. The production of Thyrotherm tools led to the production of about 17,000 parts per tool due to the high Thyrotherm wear resistance without any further surface treatment. Thyrotherm tools increased productivity by 50%.

### 3 Forging Industry Vision of the Future

The advent of the industrial revolution and the Internet way of doing things presses for the new intervention and includes forging operations. In order to keep up with technology, the forging industry needs to address specific areas such as materials, modelling, and design of the die, while applying different dedicated tools for modelling and optimization, sensors, process controls, real-time preventative maintenance, to mention a few among the primary and secondary processing equipment available for use. In particular, tooling, materials' selections, and technology advancements must concentrate on developing more reliable, longer-lasting, and high-performance die. Die design and modelling software help metallurgical improvements by giving a greater magnitude to the life of tooling. Advanced fast prototyping will be implemented into forged product design and engineering processes. These actions will facilitate operations and speed up completion of projects. Advanced computer models will improve product and process efficiency to satisfy the time, cost, and quality demands of customers in the future. Powerful computer codes and software that are available to every forging company are required to quickly and accurately model material flow during forging process and predict forged product microstructure and mechanical properties [22, 23]. New advanced technological processes, procedures, and devices will allow single-minute changeover, making one-piece workflow economically feasible for families of parts. Lastly, it is important to note that advanced lubricants will yield greater progress towards the environment and this increases the die life and process efficiency, and improves product quality, reliability, and predictability [24, 25].



## 4 Conclusion

The nature of types of technological entry in the global industry and the manufacturing sector is leading new possibilities for increased performance and imparts on forging operations as well. Future operations will become cost-effective, with preferred processes which produce metal components of superior quality, integrity, and performance for critical and demanding applications. The forge plant of the future will leave an environment that is safe, clean, and eco-friendly. Operations will be highly automated, and high-level excellence will result in manufactured products having superior consistency and dimensional control. Emerging forge companies will be more of a virtual enterprise, with cloud communication possibilities and able to successfully communicate designs and specifications to customers, and vice versa, thus exchanging information about a forged product. Computer-controlled preform, CCP, forging technique will become associative in all regards, and the current improvements in the open die—with, or without friction or drop forge techniques—will continue to evolve to lead development in metal forming.

## References

1. Bhaduri A (2018) Forging. In: Springer series in materials science
2. Floersheim LB (2009) Forging the future of American security with a total force strategy. *Orbis*
3. Onu P, Mbohwa C (2019) Industrial energy conservation initiative and prospect for sustainable manufacturing. *Procedia Manuf*
4. Siemens (2011) Energy management and energy optimization in the process industry
5. Onu P, Mbohwa C (2018) The interlink between sustainable supply chain management and technology development in industry. In: Proceedings of the international conference on industrial engineering and operations management, pp 425–430
6. Abdu YA, Onu P, Gupta UK (2016) Lean concepts and methods: 3P. *Int J Sci Res Comput Sci Eng Inf Technol* 1(2):20–24
7. Product design for manufacture and assembly, 3rd edn
8. El Wakil SD (2019) Metal forming. In: Processes and design for manufacturing
9. Juneja BL (2010) Fundamentals of metal forming processes. New Age International Pvt Ltd.
10. Reardon AC (2011) Discovering metals: a historical overview. In: Metall. non-metallurgist
11. Behrens BA, Doege E, Reinsch S, Telkamp K, Daehndel H, Specker A (2007) Precision forging processes for high-duty automotive components. *J Mater Process Technol*
12. Kim DH, Kim BM, Kang CG (2005) Estimation of die service life for a die cooling method in a hot forging process. *Int J Adv Manuf Technol*
13. Onodera S, Awai SN (1994) Modern cold forging applications for the manufacture of complex automotive parts. *J Mater Process Tech*
14. Altan T, Ngaile G (2005) Cold and hot forging
15. Debin S, Lin Y (2014) Hot forging. In *Comprehensive materials processing*
16. Bhaduri A (2018) Rolling. In: Springer series in materials science
17. Fuchs KD (2009) Hot-work steels with improved properties for die casting applications. *Foundry Trade J*
18. Rathi MG, Jakhade NA (2014) An overview of forging processes with their defects. *Int J Sci Res Publ*
19. Bayramoglu M, Polat H, Geren N (2008) Cost and performance evaluation of different surface treated dies for hot forging process. *J Mater Process Technol*

20. Onu P, Mbohwa C (2018) Future energy systems and sustainable emission control: Africa in perspective. In: Proceedings of the international conference on industrial engineering and operations management, pp 793–800
21. Berns H, Wendl F (1989) Influence of bainite on properties of hot work tool steel X40CrMoV5 1 (Thyrotherm 2344). Thyssen Edelstahl Tech. Ber. Int J Fatigue 13(912):122–129
22. Ikumapayi OM, Oyinbo ST, Bodunde OP, Afolalu SA, Okokpujie IP, Akinlabi ET (2019) The effects of lubricants on temperature distribution of 6063 aluminium alloy during backward cup extrusion process. J Mater Res Technol 8(1):1175–1187. <https://doi.org/10.1016/j.jmrt.2018.08.006>
23. Oyinbo ST, Ikumapayi OM, Jen TC, Ismail SO (2020) Experimental and numerical prediction of extrusion load at different lubricating conditions of aluminium 6063 alloy in backward cup extrusion. Eng Solid Mech 8:119–130
24. Adeoti OM, Dahunsi OA, Awopetu OO, Oladosu KO, Ikumapayi OM (2019) Optimization of clay-bonded graphite crucible using D-optimal design under mixture methodology. Int J Sci Technol 8(7):455–461
25. Azeez TM, Ikumapayi OM, Bodunde OP, Babalola SA, Ogundayomi MO (2019) Measurement of surface roughness on a transmission shaft using CNC and conventional lathes machining. Int J Sci Technol 8(10):1626–1633

# Effect of AFM Scan Size on the Scaling Law of Sputtered Aluminium Thin Films



F. M. Mwema, Esther T. Akinlabi, O. P. Oladijo, Stephen A. Akinlabi, and S. Hassan

**Abstract** The effect of scan size of the atomic force microscopy (AFM) imaging on the fractal characteristics of aluminium thin films deposited on stainless steel substrates by radiofrequency magnetron sputtering is presented. Three scan sizes of  $3 \times 3 \mu\text{m}$ ,  $5 \times 5 \mu\text{m}$  and  $10 \times 10 \mu\text{m}$  were used to obtain the images on the AFM facility. Visual examination revealed that using very high scan size ( $10 \times 10 \mu\text{m}$ ) captured poorer images, although with more features. One-dimensional fractal dimensions were obtained as  $1.610 \pm 0.012$ ,  $1.606 \pm 0.011$  and  $1.563 \pm 0.014$  for scan sizes of  $3 \times 3 \mu\text{m}$ ,  $5 \times 5 \mu\text{m}$  and  $10 \times 10 \mu\text{m}$ , respectively. Multifractal analyses revealed that images obtained at lower scan sizes ( $3 \times 3 \mu\text{m}$  and  $5 \times 5 \mu\text{m}$ ) were mono-fractal, whereas those obtained at scan size of  $10 \times 10 \mu\text{m}$  were multifractal. The results suggest that the scan size can significantly influence the scaling results of the AFM measurements and therefore should be carefully chosen.

**Keywords** Aluminium · Atomic force microscopy (AFM) · Scan size · Sputtering · Thin films

---

F. M. Mwema (✉) · E. T. Akinlabi · O. P. Oladijo  
Department of Mechanical Engineering Science, University of Johannesburg, Auckland Park  
Campus, Johannesburg 2006, South Africa  
e-mail: [fredrick.mwema@dkut.ac.ke](mailto:fredrick.mwema@dkut.ac.ke)

F. M. Mwema  
Department of Mechanical Engineering, Dedan Kimathi University of Technology, Private Bag,  
Nyeri 10143, Kenya

O. P. Oladijo  
Department of Chemical, Materials and Metallurgical Engineering, Botswana International of  
Science and Technology, Private Bag, 16, Palapye, Botswana

S. A. Akinlabi · S. Hassan  
Department of Mechanical Engineering, Walter Sisulu University, Butterworth Campus, Mthatha,  
South Africa

## 1 Introduction

Utilization of atomic force microscopy (AFM) surface topography is a common practice in most thin film industries for quality control and characterization of the surface roughness [1, 2]. In AFM facilities, there are various parameters involved in accurate determination of the surface topography, some of which include scan rate (speed), integral gain, proportional gain, scan size and amplitude setpoint [3]. In most cases, the choice of combination of the parameters is based on the experience of the operator and therefore, it means different results can be reported for the same surface by different parameter choices. It has been claimed that fractal results on AFM images are not dependent on the facility settings [4, 5]. This is because fractal theory uses scaling characteristics of the surfaces. The claim is viable for mono-fractal dimensions and not clear for multifractal cases. In this case, the variation of multifractal characteristics with scan size is illustrated for sputtered aluminium thin films on stainless steel surfaces.

## 2 Methods

The samples were prepared by radiofrequency magnetron sputtering at a power of 150 W as reported in our previous methodology [6]. Atomic force microscopy (AFM) was used to measure the topography of the sample at different scan sizes of  $3 \times 3 \mu\text{m}$ ,  $5 \times 5 \mu\text{m}$  and  $10 \times 10 \mu\text{m}$ . Further details on the AFM facility and other parameters are available in our publications [7, 8]. The obtained images were evaluated for fractal characteristics based on the image analysis procedure described in references [9, 10]. The complex fractal and multifractal equations described in literature were implemented in the freely available plugin *FracLac* tool in *Fiji* software [11–13]. The fractal results were discussed in relation to the AFM scan size.

## 3 Results and Discussion

Figure 1 shows the representative AFM images of Al thin films obtained at the three scan sizes. In addition, a scale bar representing the contour colouring of the images is shown below the images. As the scan size increases, the more surface features are captured; however at  $10 \times 10 \mu\text{m}$ , the quality of the image is very poor. These observations are further illustrated by the 2D-fast Fourier transformation (2D-FFT) spectra of the three images as shown in Fig. 2. As the scan size increases, the region of low frequency (white central patch) increases, which indicates changes in topography features [14].

The one-dimensional fractal dimensions were computed using the box counting method at 1000 grids and the following values obtained were  $1.610 \pm 0.012$ ,  $1.606$

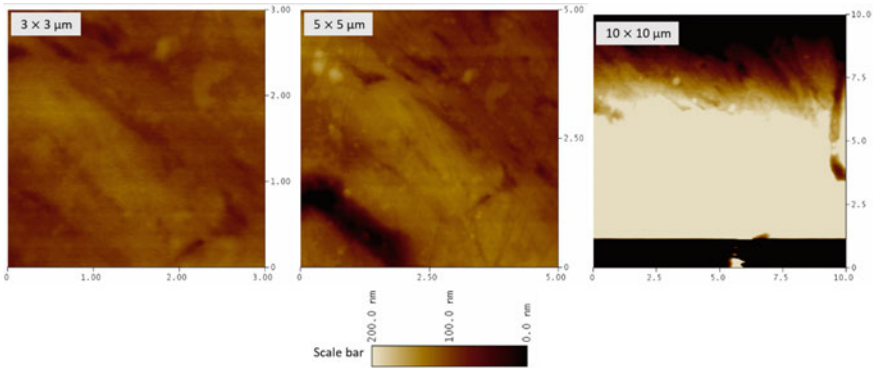


**Fig. 1** Representative atomic force microscope (AFM) images of sputtered aluminium thin films at different scan sizes

$\pm 0.011$  and  $1.563 \pm 0.014$  for scan sizes of  $3 \times 3 \mu\text{m}$ ,  $5 \times 5 \mu\text{m}$  and  $10 \times 10 \mu\text{m}$ , respectively. The change in fractal dimensions at small scan sizes ( $3 \times 3 \mu\text{m}$ ,  $5 \times 5 \mu\text{m}$ ) is insignificant, whereas at considerably large scan size, there is significant variation in the fractal dimensions. These results mean that when undertaking AFM measurements, closer scan sizes should be chosen to maintain the fractality of the thin films measurements.

The multifractal spectra ( $f(\alpha)$ ) plotted against the singularity index are shown in Fig. 3. The shapes of the spectra are clearly dependent on the scan size. At small scan sizes ( $3 \times 3 \mu\text{m}$ ,  $5 \times 5 \mu\text{m}$ ), the spectrums are skewed to the right with a left hook, whereas at large scan size, the spectrum is nearly a balanced semi-oval shape. These imply that images at scan size of  $10 \times 10 \mu\text{m}$  show multifractal behaviour, whereas those obtained at smaller scan sizes are mono-fractal. The widths and peaks of the spectra are also affected by the scan size, with wider spectrums observed at the smallest scan size in this report (Fig. 3).

The results on generalized fractal dimensions of the AFM images at different scan sizes are shown in Figs. 4 and 5. Similarly, the plots reveal that the generalized fractal

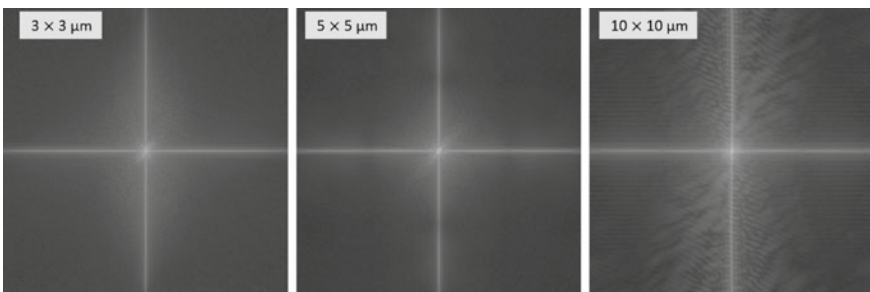


**Fig. 2** 2D-fast Fourier transform spectra of AFM images of aluminium thin films obtained at different scan sizes

**Fig. 3** Multifractal spectra ( $f(\alpha)$ ) versus singularity index ( $\alpha$ ) AFM images of aluminium thin films obtained at different scan sizes

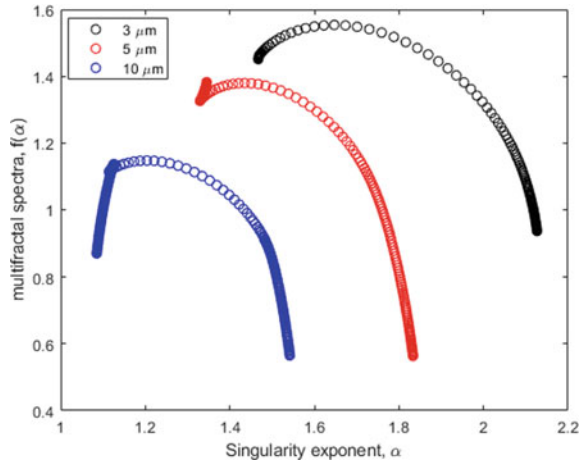
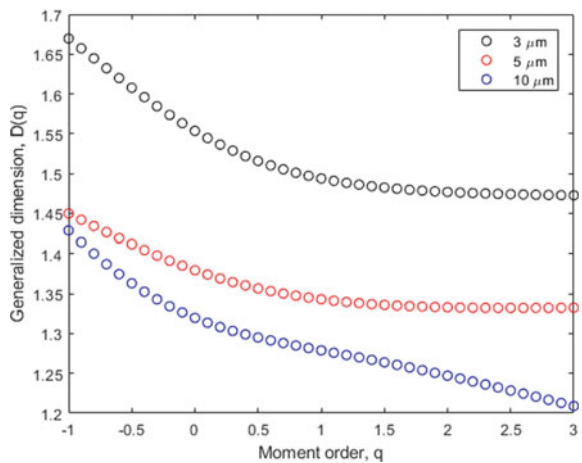


**Fig. 4** Plot of ordering for the  $D(q)$  versus  $q$  at the different AFM scan sizes



dimension against the moment order depends on the scan size of the AFM image. At  $3 \times 3 \mu\text{m}$ , the plot consists of well-defined three regions (namely gradual decrease of  $D(q)$  with  $q$ , transition at  $q = 0$  and constant variation of  $D(q)$  with  $q$ ) as shown in Fig. 4. These regions are not clear on the other two scan sizes. The plot of  $10 \times 10 \mu\text{m}$  is a characteristic of multifractal feature. The ordering of the generalized fractal dimension reveals nearly constant values at scan size of  $5 \times 5 \mu\text{m}$ , indicating that the fractality of the films at this scan size is reserved and may be the ideal scan size for the present measurement.

The plots of mass exponent  $\tau(q)$  as function of moment order ( $q$ ) are shown in Fig. 6. Like the other results, there is variation of the shape of the profiles with AFM scan size. The plots at small scan sizes are nearly linear, with the inflection point

**Fig. 5** Mass exponent  $\tau(q)$  as function of moment order,  $q$  for AFM images taken at different scan size

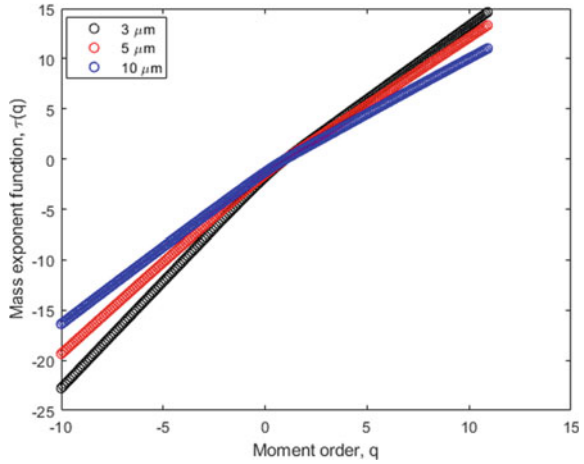
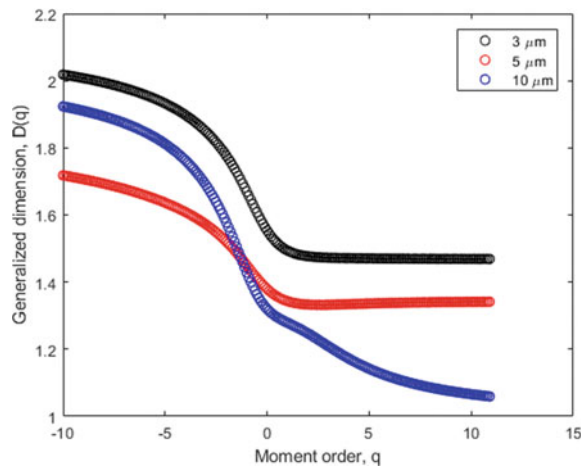


**Fig. 6** Generalized fractal dimension versus moment order for AFM images taken at different scan sizes



unclear, whereas the plot at  $10 \times 10 \mu\text{m}$  has a clear point of inflection, indicating multifractal nature of the images.

### 4 Conclusions

The relationship between the scan size of AFM images and the fractal characteristics of sputtered aluminium thin films was presented. It was seen that at a very high scan size, the quality of the images reduces and hence compromises the information of topography. However, at high scan sizes, more information can be captured but with difficulties. It was demonstrated that the influence of the scan size on the fractal

dimension is minimal between  $3 \times 3 \mu\text{m}$  and  $5 \times 5 \mu\text{m}$  but significant at  $10 \times 10 \mu\text{m}$ . The multifractal analyses are also influenced by the choice of the scan size. In this study, it was shown that the aluminium films exhibit fractal characteristics at lower scan sizes but become multifractal at higher scan sizes. These results imply that proper choice of the scan size during AFM imaging is very important.

**Acknowledgements** The Global Excellence and Stature (GES) 4.0 funding for Postdoctoral Research Fellowship by the University of Johannesburg is acknowledged.

## References

1. Amirzada MR, Tatzel A, Viereck V, Hillmer H (2016) Surface roughness analysis of SiO<sub>2</sub> for PECVD, PVD and IBD on different substrates. *Appl Nanosci* 6(2):215–222
2. Grayeli K et al (2019) Minkowski functional characterization and fractal analysis of surfaces of titanium nitride films. *Mater Res Exp* 6(8):086463
3. Sulchek T, Yaralioglu GG, Quate CF, Minne SC (2002) Characterization and optimization of scan speed for tapping-mode atomic force microscopy. *Rev Sci Instrum* 73(8):2928
4. Gong Y, Misture ST, Gao P, Mellott NP (2016) Surface roughness measurements using power spectrum density analysis with enhanced spatial correlation length. *J Phys Chem C* 120(39):22358–22364
5. Senthilkumar M, Sahoo NK, Thakur S, Tokas RB (2005) Characterization of microroughness parameters in gadolinium oxide thin films: a study based on extended power spectral density analyses. *Appl Surf Sci* 252(5):1608–1619
6. Mwema FM, Akinlabi ET, Oladijo OP, Krishna S, Majumdar JD (2019) Microstructure and mechanical properties of sputtered Aluminum thin films. *Procedia Manuf* 35:929–934
7. Mwema FM, Oladijo OP, Sathiaraj TS, Akinlabi ET (2018) Atomic force microscopy analysis of surface topography of pure thin aluminium films. *Mater Res Exp* 5(4):1–15
8. Mwema FM, Oladijo OP, Akinlabi ET (2018) Effect of substrate temperature on aluminium thin films prepared by RF-magnetron sputtering. *Mater Today Proc* 5(9):20464–20473
9. Mwema FM, Oladijo OP, Akinlabi ET (2019) The use of power spectrum density for surface characterization of thin films. In: Yang X-Y (ed) *Photoenergy and thin film materials*. Wiley Inc., Hoboken, NJ, USA, pp 379–411
10. Mwema FM, Akinlabi ET, Oladijo OP (2019) Correction of artifacts and optimization of atomic force microscopy imaging. In: Kumar K, Paulo Davim J (eds) *Design, development, and optimization of bio-mechatronic engineering products*. IGI Global, pp 158–179.
11. T̄əlu S, Stach S, Alb SSF (2015) Multifractal characterization of a dental restorative composite after air-polishing. *Chaos, Solitons Fractals* 71:7–13
12. Ghosh K, Pandey RK (2019) Fractal and multifractal analysis of In-doped ZnO thin films deposited on glass, ITO, and silicon substrates. *Appl Phys A* 125(2):98
13. Mwema FM, Akinlabi ET, Oladijo OP (2019) Fractal analysis of hillocks: a case of RF sputtered aluminum thin films. *Appl Surf Sci* 489:614–623
14. Mwema FM, Akinlabi ET, Oladijo OP (2019) Complementary investigation of SEM and AFM on the morphology of sputtered aluminum thin films. In: *Proceedings of the eighth international conference on advances in civil, structural and mechanical engineering—CSM*, pp 10–14



# Energy Content Modelling for Municipal Solid Waste Using Adaptive Neuro-Fuzzy Inference System (ANFIS)



Oluwatobi Adeleke, Stephen A. Akinlabi, Paul A. Adedeji,  
and Tien-Chien Jen

**Abstract** Recovery of energy from municipal solid waste (MSW) will not only add to the national electrical energy generation capacity, but it will also minimize the quantity of waste that ends up in landfill, consequently mitigating its environmental impact. This study has developed ANFIS model to forecast the energy content of waste generated in Johannesburg, South Africa, based on the physical component of the waste: plastic, paper, organics, metals, and textile as input against the energy content. The fuzzy c-means (FCM) clustering technique was explored for data clustering in the ANFIS model. The model was trained with 70% of the data and 30% for validation. The performance of the network was evaluated using root mean square error (RMSE), mean absolute deviation (MAD), and mean absolute percentage error (MAPE). The RMSE, MAD, and MAPE of the model were 0.3418, 0.2692, and 7.7991, respectively. The forecast accuracy of ANFIS was compared with ANN, giving a MAPE of 7.7991 and 13.7870, respectively. ANFIS gave a better forecast accuracy and recommended for energy content prediction of municipal solid waste.

**Keywords** Adaptive neuro-fuzzy inference system · Season · Municipal solid waste

## 1 Introduction

Waste management in South Africa is greatly contingent on landfilling till present time. About 108 million tons of waste was generated in South Africa in 2011, out of which 90.1% of the waste generated was disposed of to landfill and only 10% was recycled [1]. Landfill is an immense anthropogenic source of atmospheric methane emission globally. There is an estimation of about 531735tCH<sub>4</sub>/annum and

---

O. Adeleke (✉) · P. A. Adedeji · T.-C. Jen  
Department of Mechanical Engineering Science, University of Johannesburg, Johannesburg,  
South Africa  
e-mail: [thobyadeleke@gmail.com](mailto:thobyadeleke@gmail.com)

S. A. Akinlabi  
Department of Mechanical Engineering, Walter Sisulu University, Mthatha, South Africa

635207tCH<sub>4</sub>/annum emission for landfill in South Africa for 2015 and 2020, respectively [2]. The contribution of renewable source to electrical power generation is quite low in South Africa; however, recovery of energy from waste generated in South Africa could oil the wheel of environmental sustainability and play a major role in curtailing the footprint of municipal solid waste on the environment and add to the national grid electricity production.

Depletion of these fossil fuels, e.g. coal, oil, and natural gas, has been predicted to be in the next 40–50 years [3]. For this reason coupled with the environmental impact of these fossil fuels, the rapid increase in global energy demand has posed a threat to humans. This quest has led to search for alternative renewable and sustainable energy resources which are easily accessible and have close to zero impact on the environment [4]. This motivated this study to evaluate and predict the energy content of municipal solid waste.

Data of waste characteristics such as the physical composition, proximate analysis, elemental composition, ash, and moisture content and the heating value are important parameters to be considered in the design implementation of a fitting conversion technology for municipal waste [5]. The use of MSW as fuel for power plant in Indonesia can abridge the use of coal by 19.5%, and 1 ton of MSW can generate 0.5 MWh electricity and power of 21 kW [6]. Energy potential, steam generation potential, and net electrical energy potential per day on the average for the ten cities in Indonesia were also presented as 41.836 MWhr/day, 40,971 ton/day, and 3212 MWh/day, respectively.

The literature is proliferated with a number of data-mining techniques and regression analysis methods to forecast the heating value of waste, which can be recovered through thermochemical and biological processing for heat and electricity. Ample number of such researches made use of the elemental, physical, and proximate analysis of the MSW as input to forecast its heating value and energy content. Some researchers developed artificial neural network (ANN) model with different architectures using the elemental compositions [7, 8] or proximate analysis [9, 10] to forecast heating value of the waste. Hybrid models, such as Genetic Algorithm (GA)-ANFIS [11] and Particle Swarm Optimization (PSO)-ANFIS [12], were created for energy prediction of waste and other biomass. The performances of these models were laudable.

Linear equations were fitted by multiple regression analysis to predict energy content of waste, notable among them were found in [13–18]. However, energy content prediction of waste generated particularly in South Africa based on physical composition has not been widely researched; therefore, this study is aimed at developing an adaptive neuro-fuzzy inference system model to predict the potential of energy content using the physical composition generated waste.

Subsequent sections of this paper are organized as follows: Sect. 2 presents the methodology used, while Sect. 3 discusses the result of the technique, and the conclusion and recommendation are made in Sect. 4.

## 2 Methodology

### 2.1 Data Description and Analysis

Several samples of waste characterization data collected in two different seasons in 2015 and 2016 at some landfills Johannesburg, South Africa, were used in this paper. The percentage composition of each fraction of physical content in the total waste was used as independent variables, and the output variable is the energy content of the waste in (Giga Watt-Hour). Table 1 is the statistics of the input variables: the percentage composition of organics, plastics, paper, metal, glass, textile and other waste fractions, and the output variable, which is the energy content. Waste collected and dumped at the landfills in Johannesburg, South Africa, was of two sources. The daily non-compacted (DNC) waste is collected daily from hotels, stores, restaurants, and fast food shops, while the round collected refuse (RCR) is collected once a week from households. The maximum organic waste fraction is collected at the RCR, while the maximum plastic waste fraction is collected at the DNC waste. However, significant variation occurs in the percentage composition of each fraction of the waste at different seasons. Normalization of the data was done using the ‘mapminmax’ function inside MATLAB m-file script using Eq. (1)

$$y = \frac{x - x_{\min}}{x_{\max} - x_{\min}} \tag{1}$$

### 2.2 Adaptive Neuro-Fuzzy Inference System Approach

ANFIS is a technique which fuses both artificial neural network (ANN) and fuzzy logic reasoning for mapping a set of inputs to an output. The uncertainty and unreliability of model with the neural network are taken care of by the fuzzy logic [19]. Adaptive neuro-fuzzy inference system (ANFIS) is employed for prediction and training in this paper. Figure 1 shows an ANFIS structure.

**Table 1** Statistics of input and output data

Statistics	Organic (%)	Plastic (%)	Paper (%)	Metal (%)	Glass (%)	Textile (%)	Others (%)	Energy content (GWh)
Maximum	50.30	36.5	46.70	18.90	31.90	34.20	33.70	7.861
Minimum	3.10	5.00	1.90	0.00	0.00	0.00	4.50	1.233
Average	25.11	20.73	15.02	5.94	6.73	7.47	18.16	4.658

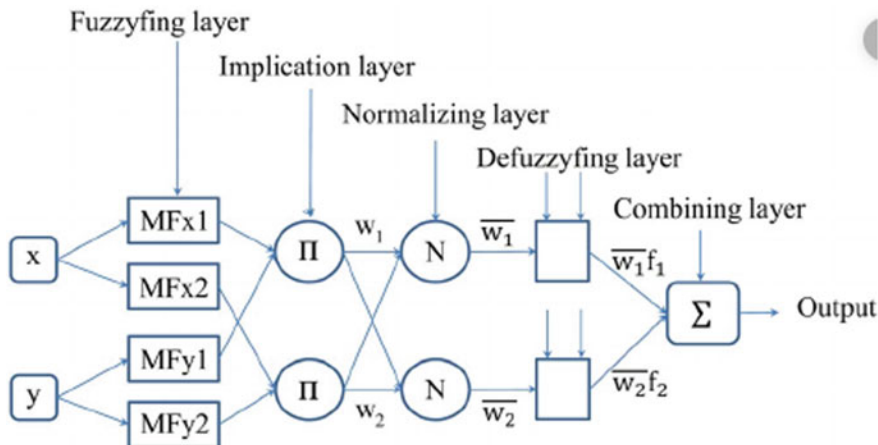


Fig. 1 ANFIS structure with two inputs and two rules [20]

A total of 8 epochs use a fuzzy c-means (FCM) clustering technique and a Sugeno-type fuzzy inference system. The purpose of clustering is to identify natural groupings of data from a large data set to produce a concise representation of a system’s behaviour.

A FCM data clustering technique allows a piece of data to belong to 2 or more clusters by minimizing objective function in Eq. 2:

$$J_m = \sum_{i=1}^N \sum_{j=1}^C U_{ij}^m \|x_i - c_j\|^2 \quad 1 \leq m \leq \infty \tag{2}$$

where

- $U_{ij}$  degree of membership  $x_i$  of in cluster  $j$
- $x_i$   $i$ th of measured data
- $c_j$  centre of cluster
- $\|*\|$   $n$ -dimensionless Euclidean spaces for sample data.

### 2.3 Artificial Neural Network Approach

ANN learns from a set of input data by identifying the hidden pattern in the data without being programmed with task-specific rules. The nodes transmit information through the interconnected neurons organized into layers. Attributed to each layer is the weight and bias, and the adjustment of the weight and bias is called training the network. Summation of weighed input signals from each output neurons gives the output according to Eq. 3:

$$y_j = F \left( \sum_{i=1} W_{ij} X_i + b_j \right) \tag{3}$$

where

- $y_j$  output signal
- $F$  activation function
- $W_{ij}$  weight connection of  $i$ th neuron in the input layer and  $j$ th neuron in the hidden layer
- $X_j$  input signal
- $b_j$  bias weight of  $j$  unit.

In this paper, a Levenberg–Marquardt training algorithm was used with a softmax transfer function. The architecture consists of 7 neurons in the input layer, 20 neurons in the hidden layers, and 1 neuron in the output layer.

### 3 Results

An M-file script was written in MATLAB 2015a for the ANFIS model, and 70% and 30% of the total sample data were used for training and validation, respectively, using the fuzzy c-means clustering method with a total of 8 epochs with a Sugeno-type fuzzy inference system. The model was run on a workstation with the following configurations: 64 bits, 4 GB ram Intel(R) core(TM) i3 for a computational time of 3.66 s. The performance of the model was evaluated using root mean square error (RMSE), mean absolute deviation (MAD), mean percentage error (MAPE), and the standard deviation (SD). Table 2 presents RMSE, MAD, MAPE, and SD for both training and testing in the ANFIS model.

ANN model was developed, and its forecast accuracy was compared to what is obtained using ANFIS, as presented in Table 3. Energy content of waste was forecasted using ANFIS, and a prediction accuracy of 92.2% (MAPE = 7.7991) was obtained, while the neural network predicted the energy content with an accuracy of 86.2 (MAPE = 86.2%).

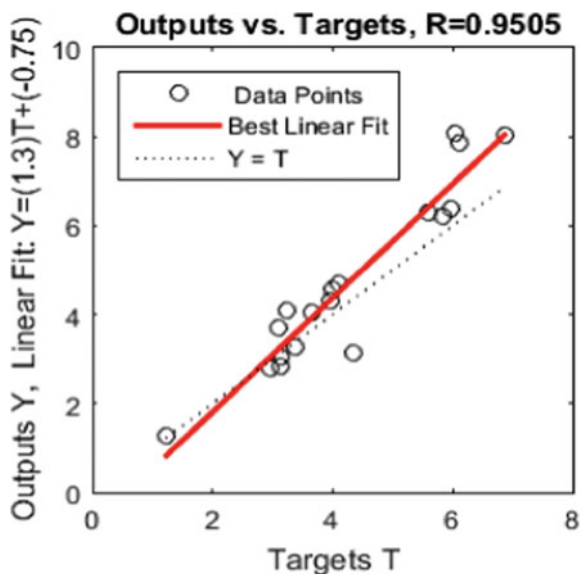
The best neural network was obtained using an architecture of 3 neurons at the input layer, 20 neurons in the hidden layer, and 1 neuron in the output layer. Figure 2 is a regression plot of the prediction test using ANN giving test error value of 0.9505.

**Table 2** ANFIS model performance for testing and training

Error	Training	Testing
RMSE	$1.4449 \times 10^{-8}$	0.3418
MAD	$8.8419 \times 10^{-8}$	0.2692
MAPE	$2.069 \times 10^{-6}$	7.7991
Error SD	$1.336 \times 10^{-7}$	0.3506

**Table 3** ANFIS and ANN performance

Error	ANFIS	ANN
RMSE	0.3418	0.8529
MAD	0.2692	0.5267
MAPE	7.7991	13.7870
Error SD	0.3506	0.7493

**Fig. 2** ANN prediction test plot

Energy content plot of the predicted and observed value for the ANFIS model is shown in Fig. 3. There is no variation in the trend of the observed and predicted energy content values. The predicted energy content of waste is very close to the observed values. A closer look at Figs. 3 and 4 with Table 3 revealed that ANFIS model predicts the energy content of waste from its physical component better than the ANN model.

There is significant variation in the observed and predicted energy content values of ANN model plot represented in Fig. 4, especially at test sample indexes of 10, 13, and 17. Theoretically, these points are identified as waste samples from the DNC source with high plastic content and consequently high energy potential. This is because of the high heating value of plastics. Highest fraction of waste from the RCR source is the organics yielding a lower potential for energy.

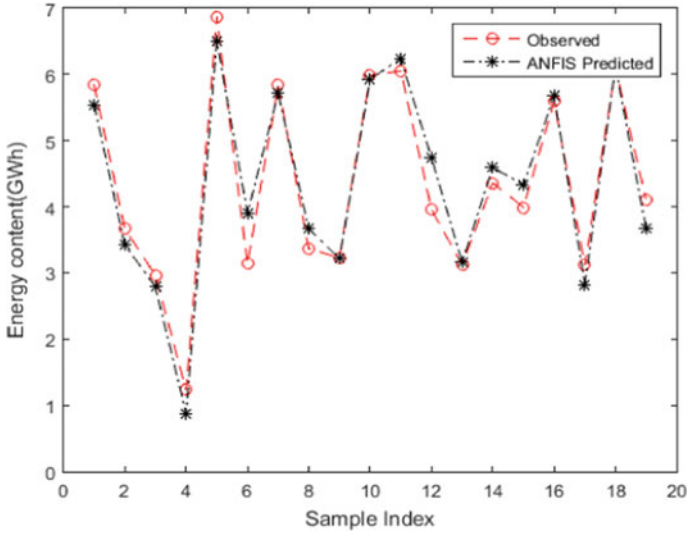


Fig. 3 ANFIS model prediction versus observed plot

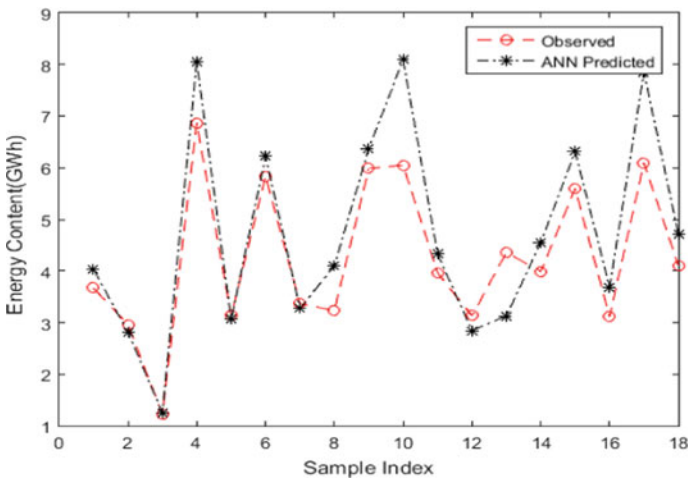


Fig. 4 ANN plot of predicted versus observed

## 4 Conclusions

This study has revealed the capacity of the ANFIS model to accurately predict the energy content of municipal solid waste generated in South Africa. The physical content of municipal waste is highly correlated with its energy content. Advancement in waste management and environmental sustainability in South Africa can be

achieved through recovery of energy from waste. The result of the prediction gives a MAPE value of 7.7991, which implies 92.2% accuracy with ANFIS model against 86.2% using ANN. In this study, ANFIS model for energy content prediction using the physical content performed better than ANN model. For future forecast, this study recommends the use of hybrid model of ANFIS with evolutionary algorithm, and test of other clustering data clustering techniques is also recommended.

## References

1. Department of Environmental Affairs (DEA) (2012) National Waste Information Baseline Report
2. Bhailall S (2015) Landfills gas emissions and the associated air quality, energy and climate change implications in South Africa. PhD Dissertation, University of the Witwatersrand.
3. Estiati I, Freire FB, Freire JT, Aguado R, Olazar M (2016) Fitting performance of artificial neural networks and empirical correlations to estimate higher heating values of biomass. *Fuel* 180:377–383
4. ÖzyüğÜran A, Yaman S (2017) Prediction of calorific value of biomass from proximate analysis. *Energy Procedia* 107:130–136
5. Sheng C and Azevedo JLTÄ (2005) Estimating the higher heating value of biomass fuels from basic analysis data. *Biomass Bioenergy* 28:499–507
6. Anshar M, Negeri P, Pandang U, Nasir F, Universiti A, Anshar M (2015) The energy potential of municipal solid waste for power generation in Indonesia. *Jurnal Mekanikal* 37:42–54
7. Gong S, Sasanipour J, Shayesteh MR, Eslami M, Baghban A (2017) Radial basis function artificial neural network model to estimate higher heating value of solid wastes. *Energy Source Part A Recover Util Environ Eff* 39(16):1778–1784
8. Akkaya E, Demir A (2010) Predicting the heating value of municipal solid waste-based materials: an artificial neural network model. *Energy Source Part A Recover Util Environ Eff* 32(19):1777–1783
9. Shu HY, Lu HC, Fan HJ, Chang MC, Chen JC (2006) Prediction for energy content of taiwan municipal solid waste using multilayer perceptron neural networks. *J Air Waste Manag Assoc* 56(6):852–858
10. Ch Ogwueleka T, Ogwueleka FN (2010) Modelling Energy content of municipal solid waste using artificial neural network. *J Environ Heal Sci Eng* 7(3):259–266
11. Baghban A, Ebadi T (2019) GA-ANFIS modeling of higher heating value of wastes: application to fuel upgrading. *Energy Source Part A Recover Util Environ Eff* 41(1):7–13
12. Suleymani M, Bemani A (2018) Application of ANFIS-PSO algorithm as a novel method for estimation of higher heating value of biomass. *Energy Source Part A Recover Util Environ Eff* 40(3):288–293
13. Drudi KCR, Drudi R, Martins G, Antonio GC, Leite JTC (2019) Statistical model for heating value of municipal solid waste in Brazil based on gravimetric composition. *Waste Manag* 87:782–790
14. Eboh FC, Ahlström P, Richards T (2016) Estimating the specific chemical exergy of municipal solid waste. *Energy Sci Eng* 4(3):217–231
15. Akkaya E and Ahmet D (2009). Energy Content of Municipal Solid Waste by Multiple regression Analysis. In: 5th International Advanced Technology Symposium. Karabuk, Turkey, May, pp 13–15
16. Shi H, Mahinpey N, Aqsha A, Silbermann R (2016) Characterization, thermochemical conversion studies, and heating value modeling of municipal solid waste. *Waste Manag* 48:34–47



17. Chang YF, Lin CJ, Chyan JM, Chen IM, Chang JE (2007) Multiple regression models for the lower heating value of municipal solid waste in Taiwan. *J Environ Manage* 85(4):891–899
18. Lin X, Wang F, Chi Y, Huang Q, Yan J (2015) A simple method for predicting the lower heating value of municipal solid waste in China based on wet physical composition. *Waste Manag* 36:24–32
19. Karaboga D & Kaya E (2018) Adaptive network based fuzzy inference system (ANFIS) training approaches: a comprehensive survey. In: *Artificial Intelligence Review*. pp 1–31
20. Akbarzadeh S, Arof AK, Ramesh S, Khanmirzaei MH, Nor RM (2014) Prediction of conductivity by adaptive neuro-fuzzy model. *PLoS ONE* 9(3):e92241

# Predicting the Effect of Seasonal Variation on the Physical Composition of Municipal Solid Waste: A Case Study of the City of Johannesburg



Oluwatobi Adeleke, Stephen A. Akinlabi, S. Hassan, and Tien-Chien Jen

**Abstract** Several factors influence the physical, chemical, and thermal properties of waste at different sources. One of the major indexes to variation in the morphological composition of municipal solid waste is the season. A significant discrepancy in the composition of municipal solid waste at different seasons has been reported in the literature. However, this study explores the adaptive neuro-fuzzy inference system (ANFIS) with a fuzzy c-means (FCM) clustering technique to predict the physical content of waste in South Africa based on the varying weather parameters at different seasons. Four different models (I–IV) were developed to forecast the percentage fraction of organics, plastics, paper, and textile, respectively. The choice of these streams was because a closer look at the historical data reveals a significant variation in the percentage of these waste fractions at different seasons with little or no difference in other waste streams. The percentage composition of samples of waste collected and characterized at Marie Louise Landfill, Johannesburg, in summer 2015 and winter 2016 was used as the output variable. Weather parameters for the same period were extracted from South Africa Weather Service data and used as the input variables. M-file script was written and computed on a workstation with configurations of 64 bits, 4 GB ram Intel(R) core(TM) i3. The performance of the ANFIS models I–IV was evaluated using mean absolute deviation (MAD), root mean square error (RMSE), and mean absolute percentage error (MAPE).

**Keywords** Adaptive neuro-fuzzy inference system · Clustering technique · Seasonal variation · Municipal solid waste

---

O. Adeleke (✉) · T.-C. Jen  
Department of Mechanical Engineering Science, University of Johannesburg, Johannesburg,  
South Africa  
e-mail: [thobyadeleke@gmail.com](mailto:thobyadeleke@gmail.com)

S. A. Akinlabi · S. Hassan  
Department of Mechanical Engineering, Butterworth Campus, Walter Sisulu University,  
Butterworth, Eastern Cape, South Africa

## 1 Introduction

Sustainable waste management is contingent on reliable data of waste characterization, generation, composition, and properties. The priority of sustainable waste management in South Africa is to ensure that all generated waste does not necessarily end up in landfills, especially when most landfills are reported to be running out of space for waste disposal. Several factors influence the physical, chemical, and thermal properties of waste at different sources. One of the major indexes of variation in the morphological composition of municipal solid waste is the season. A significant discrepancy in the composition of municipal solid waste at different seasons has been reported in the literature. For instance, the organic content of the waste tends to be higher in winter than in summer, likewise the percentage of leather and textile waste increased during winter. The disparity in the content of the waste can be attributed to the difference in the consumption pattern at different times of the year. Decision-makers obligated for waste management operations must possess appropriate information of waste generation, sources, and composition to design appropriate strategy of waste collection techniques and disposal plans [1].

Waste fractions such as organic materials, paper, metal, and plastic differ significantly at different seasons [2]. The seasonal variation in the physical composition of the municipal solid waste in the city of Lahore, Pakistan, has been investigated by Kamran et al. [1]. In the same socio-economic category, the highest fraction of food and yard waste is generated in spring. Plastic and textile waste also follows same pattern in all socio-economic categories; however, their highest fraction is in winter. The result of his research is presented in Fig. 1. A similar study analysed the composition and generation rate of municipal solid waste in four different seasons in Gulberg town of Lahore, Pakistan, by Jadoon et al. [3]. The result of their study on waste composition in different seasons is similar to [1]. His study further revealed that the

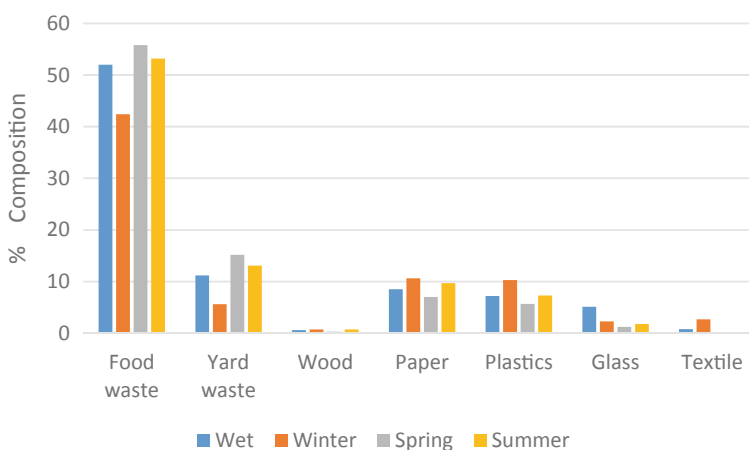


**Fig. 1** Waste composition in different seasons in the city of Lahore, Pakistan

total waste generation rate per day was 0.79 kg/capita, 0.77 kg/capita, 0.86 kg/capita, and 0.76 kg/capita in spring, summer, monsoon, and winter, respectively.

Aslani et al. [4] also studied seasonal variation of solid waste generation rate and composition in three northwest cities of Iran. His study reveals that waste composition follows a different pattern in different seasons. The highest organic and paper waste fraction in all the three cities was generated in winter and summer, respectively. The content of each waste stream in each season differs significantly across all the four seasons in Iran [4] went further to reveal that the elemental composition of waste generated in these three cities of Iran does not follow the same pattern. Obviously, the waste fraction varies independently in its physical and elemental compositions.

Effect of seasonal variation in composition of MSW in four European cities was investigated by Denafas et al. [2]. A report of increase in packaging waste in summer seasons on the island of Crete was given by Gidarakos et al. [5]. Waste generation rate in a low-temperature season in January is 28% lower than the rate in April in Chihuahua, Mexico [6]. Several factors such as vacation activities, summer events, and change in student population account for the seasonal variation in the generation rate and composition of MSW [7]. The literature is replete with studies which have majorly focused on experimental evaluation and determination of the quantitative extent of seasonal variation on waste composition. However, only few researches aimed at predicting the fraction of waste in different seasons [2] applied time series analysis to MSW fraction generation data to predict the monthly fraction of MSW. He tested several non-parametric methods such as simple exponential smoothing (SimpleES), double exponential smoothing (DES), seasonal exponential smoothing (SES), and linear exponential smoothing (LES). Using the SES, he established an expression for monthly MSW fraction ( $y_t$ ) given in Eq. 1:

$$Y_t = L_t + S_{t-p} + \varepsilon_t \quad (1)$$

where  $Y_t$  = monthly MSW fraction,  $S_{t-p}$  = fraction associated with time  $t$  with one of  $p$  season factors, and  $\varepsilon_t$  = error terms.

The use of data-mining techniques such as ANFIS, and artificial neural network (ANN) for forecasting seasonal disparity in waste composition, especially in South Africa, has not been widely researched. In this paper, the influence of changes in seasonal parameters on composition of municipal solid waste has been predicted using ANFIS model.

### 1.1 Description of Case Study Area

The city of Johannesburg is the capital of Gauteng Province of South Africa. It is the largest city in South Africa with latitude of 26° 12' 08" S and longitude of 28° 02' 37" E [8]. It has an area of about 1645 km<sup>2</sup> and an elevation of 1767 m. It is the constitutional headquarters of South Africa. In 2016, the population of the city was

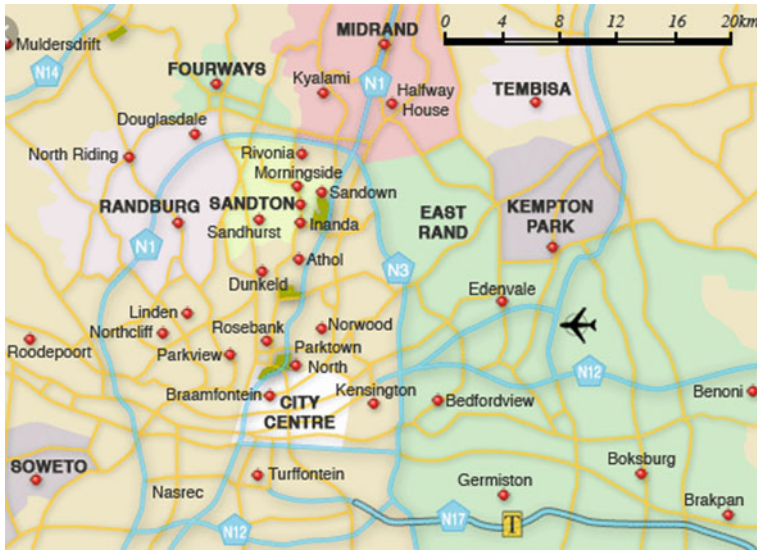


**Fig. 2** Map of City of Johannesburg

estimated at about 4.86 million. Johannesburg has a subtropical highland climate with mild sunny winter and moderately warm at summer. Figure 2 represents the map of Johannesburg, South Africa.

There are majorly four seasons in South Africa: summer (December–February), winter (June–August), spring (September–November), and autumn (March–May). On the average, the maximum temperature in summer and winter is 25 and 16 °C, respectively. The sunniest time of the year is observed at winter with temperature dropping as low as 4.1 °C. The maximum annual rainfall about 713 mm occurs during summer. The lowest temperature in Johannesburg from record is  $-8.2$  °C in 1979. Moreover, January is the warmest and wettest month, while July is the driest and coolest month. About 1.4 million tonnes of waste is generated per annum in the city of Johannesburg which are collected from two different sources, the round collected refuse (RCR) and the daily non-compacted waste (DNW), and dumped at different landfills [8].

## 2 Methodology

### 2.1 Data Description

Weather parameters for summer and winter were extracted from South Africa Weather Service data collected for two years of 2015 and 2016. However, due to unavailability of waste characterization in springs and autumn, the effect of seasonal

variation in both seasons was not considered. Waste at the landfill is a collection of waste at different parts of the city; therefore, average daily weather data for the city of Johannesburg was used. The waste characterization data consists of physical composition of different fractions of waste sampled between December–January 2015 and June–July 2016 representing summer and winter periods, respectively. Waste collection is basically from two different sources in the city of Johannesburg, the daily non-compacted (DNC) and the round collected refuse (RCR). However, there are significant variations in the percentage compositions of each of the waste streams from the two sources with slight impact of seasonal changes on the composition in winter and summer.

### 2.2 ANFIS Approach

The ANFIS model is a kind of artificial neural network (ANN) based on Takagi–Sugeno fuzzy inference system which integrates both neural network and fuzzy logic reasoning in a single network. It is a universal approximator using a set of fuzzy if–then rules for input–output mapping to obtain the distribution of the objective function [9]. ANFIS has five layers: the fuzzification layer, which takes input and determines the membership function, is the first layer. The second layer is called the rule layer since it generates the firing of the rule. The third layer computes the firing strength, while the normalized values and parameter sets from the third layer are taken as outputs in the fourth layer. Defuzzificated output from the fourth layer is received at the fifth layer as the final output. The structure of a typical ANFIS model architecture is shown in Fig. 3.

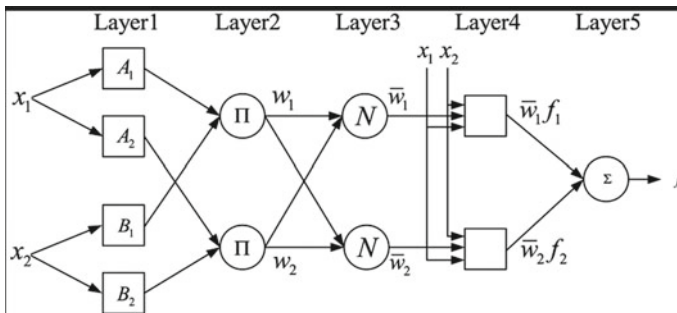


Fig. 3 ANFIS model architecture with two inputs and two rules

### 2.2.1 Fuzzy C-Means (FCM) Clustering Technique

The FCM is a type of fuzzy clustering technique which allows a set of data to be assigned to two or more clusters. The membership function bounds data to each other representing the fuzzy behaviour of the algorithm. The FCM aims at minimizing the objective function using the error function Eq. 2.

$$E = \sum_{i=1}^N \sum_{j=1}^C U_{ij}^m x_i - c_j^2 \quad (2)$$

where

$m$  Fuzzier, i.e. any real number greater than one ( $1 \leq m \leq \infty$ ).

$U_{ij}$  Degree of membership,  $U_{ij} \in (0, 1)$ .

$x_i$  Data points.

$c_j$  Centroid of clusters.

$C$  Number of clusters.

The degree of membership of the data point  $x_i$  in  $j$  cluster at any iteration is given by Eq. 3:

$$U_{ij} = \left( \sum_{k=1}^C \left( \frac{x_i - c_j}{x_i - c_k} \right)^{\frac{2}{m-1}} \right)^{-1} \quad (3)$$

## 3 Results

### 3.1 Data Analysis

Table 1 illustrates the statistics of waste composition from different sources. It presents the maximum and minimum values of each of the physical waste streams and the sources of the maximum and minimum values.

**Table 1** Statistics of the waste physical streams and sources

Waste stream	Organics (%)	Paper (%)	Plastics (%)	Textile (%)
Maximum	40.09	28.50	38.90	15.46
Source of maximum waste fraction	RCR	DNC	DNC	RCR
Minimum	11.20	11.21	15.40	0.00
Source of minimum waste fraction	DNC	RCR	RCR	DNC
Average	25.65	19.85	27.15	7.73

**Table 2** Weather parameter statistics

Weather parameter (WP)	Minimum temperature (°C)	Maximum temperature (°C)	Humidity (%)	Wind speed (m/s)
Highest WP	20.3	38.3	83.0	7.50
Season of highest WP	Summer	Summer	Winter	Summer
Lowest WP	-2.9	10.1	56.0	0.00
Season of lowest WP	Winter	Winter	Summer	Winter and Summer
Average WP	8.7	24.2	69.5	3.75

The highest fraction of organic and textile waste fraction were collected at the RCR and the lowest at the DNC; however, its composition varies slightly during winter and summer. RCR has the highest composition of paper and plastic waste streams, also with a little variation in winter and summer. Table 2 presents the statistics of the input of weather parameters (WP). Weather parameters used as input variables are minimum temperature, maximum temperature, humidity, and wind speed in winter and summer.

### 3.2 ANFISN Model Result

Four different models (I–IV) were developed to forecast the percentage composition of organics, paper, plastics and textile, respectively, using four inputs of weather parameters: minimum temperature, maximum temperature, humidity, and wind speed. M-file script was written in MATLAB 2015a, and the algorithm was computed on a system with configuration of 64 bits, 4 GB ram Intel(R) core(TM) i3. Root mean square error (RMSE), mean absolute deviation (MAD), and mean absolute percentage error (MAPE) were computed using Eqs. 3–5, respectively, to evaluate the accuracy of the four models. Prediction accuracy for models I–IV was 83.2%, 86.6%, 85.5%, and 79.5%, respectively.

$$RMSE = \left( \sum_{i=1}^N \frac{(P_i - O_i)^2}{N} \right)^{1/2} \tag{4}$$

$$MAD = \sum_{i=1}^N \left( \frac{O_i - P_i}{N} \right) \tag{5}$$



**Table 3** Model I performance parameters for training and testing

	RMSE	MAD	MAPE
Training	2.9484	2.1315	9.9462
Testing	4.6189	3.3270	16.80

**Table 4** Model II performance parameters for training and testing

	RMSE	MAD	MAPE
Training	2.2990	1.7257	11.0307
Testing	3.6727	2.5691	13.34

**Table 5** Model III performance parameters for training and testing

	RMSE	MAD	MAPE
Training	2.0388	1.4634	6.9996
Testing	5.2878	3.2928	13.52

**Table 6** Model IV performance parameters for training and testing

	RMSE	MAD	MAPE
Training	1.7997	1.3287	3.2388
Testing	5.4630	3.7691	20.56

$$MAPE = \frac{1}{N} \sum_{i=1}^N \left| \frac{O_i - P_i}{O_i} \right| \times 100\% \tag{6}$$

where  $N$  = numbers of samples,  $P_i$  = predicted values,  $O_i$  = observed values.

Each of the models was trained with 70% of the data, and 30% was used for validation. The FCM clustering technique was employed with a Sugeno-type fuzzy inference system in a total of 8 epochs. Tables 3, 4, 5 and 6 present the performance parameters of the training and testing for models I–IV, respectively.

The ANFIS models I–IV were predicted with different degrees of accuracy using the same input variable. Table 7 compares the prediction performance parameters and computational times for the four models.

The content of the organic waste stream in the waste mixture varies significantly in the DNC and RCR sources with the highest predicted and observed value of 43.2%

**Table 7** Prediction performance and computational time for models I–IV

Models	RMSE	MAD	MAPE	Computational time
Organics (Model I)	4.6189	3.3270	16.80	4.05
Paper (Model II)	3.6727	2.5691	13.34	3.80
Plastics (Model III)	5.2878	3.2928	13.52	3.66
Textile (Model IV)	5.4630	3.7691	20.56	3.67

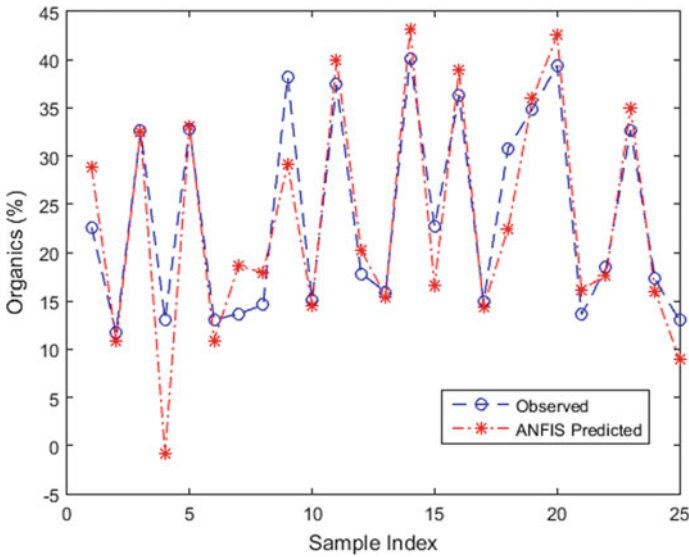


Fig. 4 Predicted and observed test plots of model I (organic waste fraction)

and 40.1, respectively, from the RCR, and the lowest predicted and observed value of  $-0.8\%$  and  $11.7\%$ , respectively, from the DNC. This explains the rise and fall in Fig. 4.

There is a similar pattern of organic fraction at the highest points (RCR) and at the lowest points (DNC). There is no significant variation in the observed and predicted values of organic waste. The prediction of ANFIS model in forecasting the composition of organic waste stream in winter and summer was  $83.2\%$  (MAPE =  $16.8\%$ ).

However, a deviation from the trend is observed at test sample 4, which could be due to the usual climatic minimum and maximum temperatures recorded for the day. The sample index represents different days in summer and winter.

From Fig. 5, the rising and falling trend in the paper waste stream for both observed and predicted values is due to the slight differences in the percentage composition of paper in the DNC and RCR sources. These values are relatively in closer range than what was obtained for organics in Fig. 3 with the highest values ( $28.5\%$ ) at DNC source and lowest at RCR ( $11.21\%$ ).

Despite this rise and fall, a similar trend is observed between the predicted and the observed values except for samples 1, 2, 4, and 20. The reason, as earlier identified, was because of the usual climatic conditions experienced at these days. ANFIS predicted paper waste composition better than organic with accuracy of  $86.66\%$  and lower computational time.

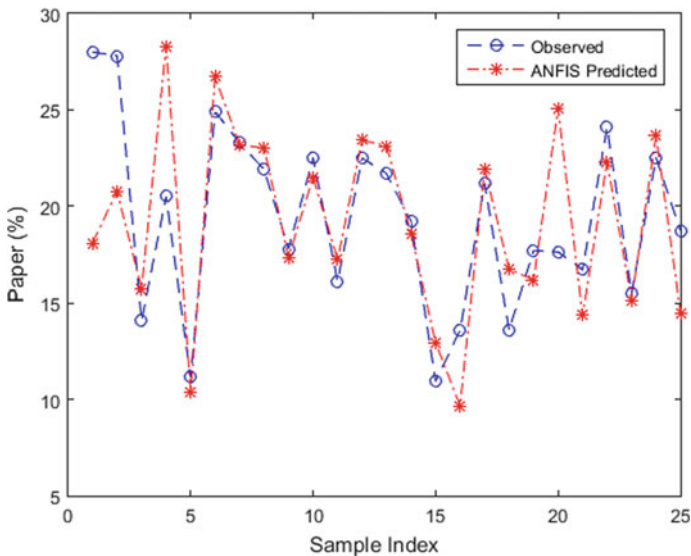


Fig. 5 Predicted and observed test plots of model II (paper waste fraction)

Generally, the rare and far-out climatic conditions recorded at test samples 1, 2, 4, 19, and 20 have notable effect on the predicted values of all waste categories at these points. The outliers of weather data on these days are reflected on the predicted waste fraction. This same trend is observed for plastics in Fig. 6. The content of plastic waste is not the same at different sources. The DNC has the highest plastic content, while the RCR has the lowest, justifying the rise and fall in Fig. 5. ANFIS prediction for plastic waste was off by 13.52% and has the least computational time.

The values of textile waste are in a closer range than the other waste fractions as seen in Fig. 7. The weather parameter has more influence on textile waste. A higher percentage prediction of textile was observed at sample 20. This occurs in winter season and the lowest in summer. The model was off by 20.56%, and the forecast has the highest root mean square error (5.4630) and mean absolute deviation (3.7691). Prediction accuracy of model IV is the least, which is due to irregular and unstable generation pattern of textile waste.

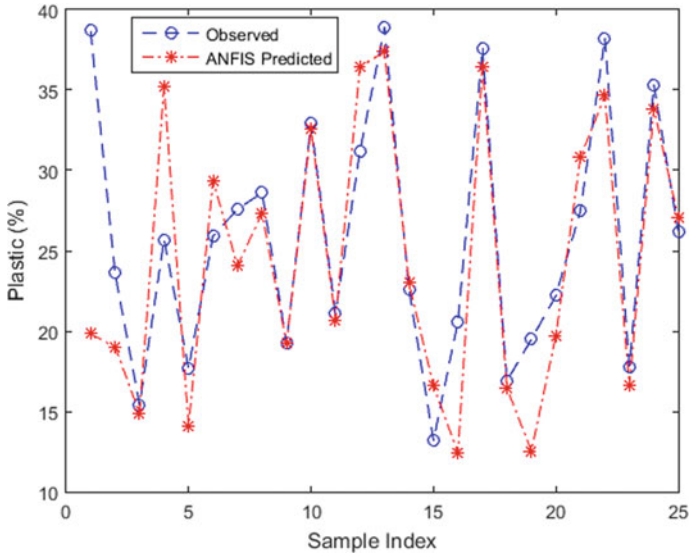


Fig. 6 Predicted and observed test plots of model III (plastic waste fraction)

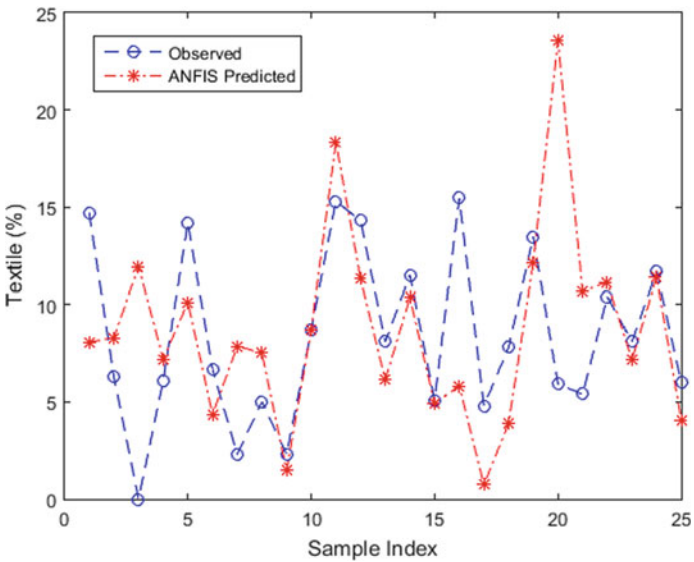


Fig. 7 Predicted and observed tests plot of model IV (textile waste fraction)

## 4 Conclusions

Slight differences are observed by comparing the waste physical compositions and seasonal variations. The same trend goes on in the case study used in this paper. The effect of the varying weather parameters during summer and winter on physical waste stream content has been predicted by ANFIS model I–IV representing organics, paper, plastics, and textile wastes, respectively. The prediction accuracy of the models I–IV was 83.2%, 86.7%, 86.5%, and 79.4%, respectively. ANFIS model forecasted paper waste with the highest prediction accuracy, and textile was predicted with the least accuracy. The result showed that ANFIS was capable of predicting effect of varying weather and climatic conditions in different seasons on the physical composition of municipal solid waste. However, due to unavailability of waste characterization data in other seasons, only winter and summer weather parameters were used; therefore, a consideration of the effect of other seasons such as spring and autumn is hereby recommended for further researches. To better compare the prediction performance, the use of hybrid clustering technique for the ANFIS model is recommended for further researches.

## References

1. Kamran A, Chaudhry MN, Batool SA (2015) Effects of socio-economic status and seasonal variation on municipal solid waste composition: a baseline study for future planning and development. *Environ Sci Eur*
2. Denafas G, Tomas R, Dainius M et al (2014) Seasonal variation of municipal solid waste generation and composition in four East European cities. *Resour Conserv Recycl* 89:22–30
3. Jadoon A, Batool SA, Chaudhry MN (2014) Assessment of factors affecting household solid waste generation and its composition in Gulberg Town, Lahore Pakistan. *J Mater Cycles Waste Manag* 16(1):73–81
4. Aslani H, Taghipour H (2018) Seasonal characterization and quantification of municipal solid waste: energy content and statistical analysis. *J Adv Env Heal Res* 6:34–43
5. Gidaracos E, Havas G, Ntzamilis P (2006) Municipal solid waste composition determination supporting the integrated solid waste management system in the Island of Crete. *Waste Manag* 26(3):668–679
6. Gómez G, Meneses M, Ballinas L et al (2009) Seasonal characterization of Municipal Solid Waste (MSW) in the city of Chihuahua, Mexico. *Waste Manag* 29(7):2018–2024
7. Zeng Y, Trauth KM, Peyton RL et al (2005) Characterization of solid waste disposed at Columbia sanitary landfill in Missouri. *Waste Manag Res* 23(1):62–71
8. Masebinu SO, Akinlabi ET, Muzenda E et al (2017) Assessing the morphological composition and energy potential of MSW, the case of the city of Johannesburg. In: *Proceedings of international conference on industrial engineering and operation management (Morocco)*. IEOM Society International, USA, pp 5696–5702
9. Roger J, Jyh S (1993) ANFIS: adaptive-network-based fuzzy inference system. *IEEE Trans Syst Man Cybern* 23(3)

# Optimization of Process Parameters Using Taguchi for Friction Stir Welding of Dissimilar Aluminum Alloys



Olatunji P. Abolusoro and Esther T. Akinlabi

**Abstract** Friction stir welding (FSW) is a major welding system employed to join aluminum alloys. This welding method is governed by so many variable parameters. These parameters control the quality and reliability of the welds. This paper gives attention to the optimization of two most prominent of these variable parameters which are the rotational speed and the travel speed of the tool through Taguchi technique of design of experiments. The friction stir welding was done on the 7075-T651 and 6101-T6 aluminum alloys with  $L_{16}$  orthogonal array of Taguchi method for the welding trials. 1550 rpm and 20 mm/min rotational speed and travel speed, respectively, were established to produce the maximum hardness at the nugget zone, while 950 rpm and 50 mm/min gave the optimum conditions for the ultimate tensile strength. The analysis of variance (ANOVA) gave rotational speed as the parameter with highest influence for achieving optimum tensile strength but gave tool travel speed in the case of hardness optimization.

**Keywords** Friction stir welding · Hardness · Taguchi technique · Ultimate tensile strength

## 1 Introduction

Introduction FSW is a system of welding that utilized a tool with shoulder and a probe which produce heat due to its frictional rotation on the workpiece. The heat plasticized the material at the interface of the joint thus enabling the tool pin to penetrate and stir the materials together and form bonding [1, 2]. This technology was invented in 1991 and has been successfully used to weld aluminum alloys in aerospace, marine, automobile, and spacecrafts applications. The use of FSW has now been extended to other alloys such as magnesium, copper, steel, and composites [2–4]. There are factors that influence the integrity of the welds produced in FSW. These factors include among others, tool rotational speed, tool geometry, travel speed, the spindle tilt angle, axial

---

O. P. Abolusoro (✉) · E. T. Akinlabi  
Department of Mechanical Engineering Science, University of Johannesburg, Johannesburg,  
South Africa  
e-mail: [abolusoroolatunji@yahoo.com](mailto:abolusoroolatunji@yahoo.com)

© Springer Nature Singapore Pte Ltd. 2020  
S. S. Emamian et al. (eds.), *Advances in Manufacturing Engineering*, Lecture Notes  
in Mechanical Engineering, [https://doi.org/10.1007/978-981-15-5753-8\\_19](https://doi.org/10.1007/978-981-15-5753-8_19)

force, and plunge depth [5]. Many researchers have reported the impact of these factors on mechanical properties and microstructures of welds [6–9]. Optimizations of these parameters, therefore, become important to save time and cost of experiments and to obtain high quality of welds. Researchers have employed various methods of optimizing these parameters [10, 11]. Prominent among them is the Taguchi technique which has found tremendous usage for optimizations. Taguchi is an experimental design method for systematic design and analysis of experimental output for quality characteristics. Many research works on Taguchi optimization technique in FSW have been reported. For instance, Elanchezhian et al. [12] used a mathematical model to optimize the parameters of the FSW of AA8081 and 6062 considering the impact and tensile strength performance. Taguchi  $L_9$  orthogonal array and ANOVA were used to arrive at the optimum conditions. Similarly, Prasad and Namola [13] used ANOVA optimization technique to optimize the processing parameters of FSW of AA5083 and 6061 with experimental design of Taguchi  $L_9$  orthogonal array. Hardness and ultimate tensile strength (UTS) were used as the outputs to determine the optimum parameter. Ugrasan et al. [14] also optimized the parameters using  $L_9$  orthogonal array Taguchi method for FSW of 6061 and 7075 aluminum alloys. The UTS and Vickers hardness were utilized to evaluate the optimized and significant parameters. Panda et al. [15] employed Taguchi method to optimize welding speed, tool pin geometry, and tool rotational speed using the tensile strength of the welds. Their result indicates that welding speed is a significant factor influencing the tensile strength. Jayaraman et al. [16] employ ANOVA and signal-to-noise ratio to obtain the optimum welding conditions for FSW of cast aluminum alloys. The tensile strength was correlated with non-linear regression model created which was discovered to be helpful in the prediction of the tensile strength. Gomathisankar et al. [17] used a complex proportional assessment (COPRAS) model to optimize tool rotational and travel speeds, tilt angle, and dwell time.  $L_9$  Taguchi orthogonal array was designed for the experiment. Confirmation test was later carried out for the outcome verification. Some researchers have established that the tool rotational and travel speed are the most important factors that influence the quality of welds obtained in FSW [18–21]. These two factors are therefore considered for optimization in this work. Generally, selection of optimum conditions where a parameter is varied and others held constant is difficult. It involves large number of experiments which is time- and money-consuming. Taguchi experimental design method has been developed to address this challenge. This work, therefore, employ the Taguchi design of experiment with  $L_{16}$  orthogonal array to optimize tool rotational and travel speed in the friction welding of 7075-T651 and 6101-T6 aluminum alloys.

Multiple performance characteristics optimization requires an overall evaluation of the signal-to-noise ratio. This is necessary as a result of differences in  $S/N$  which may be higher for a performance characteristic and correspondingly lower in another.

## 2 Experimental Procedures

The elemental components of the parent alloys (6101-T6 and 7075-T651) and their mechanical properties are illustrated in Tables 1 and 2, respectively.

The two aluminum alloys (7075-T651 and 6101-T6) were cut into 130 mm × 60 mm each and arranged in butt configuration for the welding. The 6101-T6 was kept on the advancing side, while the 7075-T651 was on the retreating side. Threaded pin welding tool used was fabricated with H13 mild steel made up of shoulder diameter of 22 mm, pin length of 5.6 mm, root pin diameter of 7.5 mm, and pin mouth diameter of 5.5 mm. Tool rotational speed and travel speed were selected as welding variables to be optimized. Other parameters for instance plunge depth and tilt angle were held constant at 2° and 0.2 mm, respectively. The experiment was designed using Taguchi technique at four levels for each of the two parameters under considerations. This gave an L<sub>16</sub> orthogonal array as shown in Table 3. The welding was carried out based on this experimental design, and the mean including the signal-to-noise ratio were evaluated. Three tensile samples were cut according to ASTM E8 standard from the center of each weld for testing. The average ultimate tensile strength for each parameter was evaluated and shown in Table 3. The Vickers hardness test was carried out perpendicular to the welding directions. A 300 kgf was applied for 15 s during the test, and about 27 indentations were taken on each sample. The average hardness values in the nugget zone of the weld were also evaluated and shown in Table 7.

**Table 1** Elemental components

Alloy	Si	Cu	Fe	Mn	Mg	Ti	Cr	Zn	Al
6101-T6	0.53	0.01	0.14	0.002	0.600	0.008	0.001	0.003	Others
7075-T651	0.40	1.70	0.50	0.300	2.40	0.20	0.22	5.50	Others

**Table 2** Mechanical properties

Alloy	Tensile strength (MPa)	Ultimate tensile strength (MPa)	Elongation (%)
6101-T6	172	180	21
7075-T651	462	575	18



**Table 3** Tensile test results

S. No.	Rotational speed (rpm)	Traverse speed (mm/min)	Ultimate tensile strength (MPa)
1	950	20	138.41
2	950	50	143.39
3	950	80	142.97
4	950	110	154.00
5	1250	20	141.85
6	1250	50	143.79
7	1250	80	66.98
8	1250	110	147.57
9	1550	20	141.31
10	1550	50	145.41
11	1550	80	144.73
12	1550	110	146.80
13	1850	20	137.14
14	1850	50	135.46
15	1850	80	141.88
16	1850	110	118.21

### 3 Results and Discussion

#### 3.1 Ultimate Tensile Strength

The results obtained for the ultimate tensile strength (UTS) for each parameter are given in Table 3. The results show that highest UTS was obtained at 950 rpm tool rotational speed and 110 mm/min tool traverse speed, while the lowest UTS occurred at 1850 rpm and 110 mm/min.

##### 3.1.1 Analysis of Variance (ANOVA)

In this work, larger is better approach was employed for the signal-to-noise ratio since maximum UTS is desired in any welding joint. Values of  $F$  in the ANOVA table shown in Table 4 show the impact of the variable process parameters to achieve the peak UTS, while values of  $P$  show uncontrollable factors probability known as noise. Maximum  $F$  and minimum  $P$  is the optimization target. Any variable parameter below 5% is taken as a significant parameter. The  $F$  values in Table 4 indicate that the rotational speed of the tool has a greater influence on tensile strength. It contributes about 63%, while the travel speed contributes 37%. The response to mean and signal-to-noise ratio ( $S/N$ ) evaluated using the larger is better approach are presented in Tables 5 and 6, respectively. The main effects for mean and  $S/N$  are illustrated in

**Table 4** Analysis of variance (ANOVA)

Source	DF	Adj SS	Adj MS	F-Value	P-Value
Rotational speed	1	45.31	45.31	0.10	0.759
Traverse speed	1	28.67	28.67	0.06	0.807
Error	13	6001.84	461.68		
Total	15	6075.82			

**Table 5** Response for means

Level	Rotational speed	Traverse speed
1	144.7	139.7
2	125.0	142.0
3	144.6	124.1
4	133.2	141.6
Delta	19.6	17.9
Rank	1	2

**Table 6** Response for signal-to-noise ratios

Level	Rotational speed	Traverse speed
1	43.20	42.90
2	41.52	43.04
3	43.20	41.47
4	42.47	42.98
Delta	1.68	1.58
Rank	1	2

Figs. 1 and 2, respectively. The interactions between the means and *S/N* for the two processing parameters accessed for optimizations, i.e., the welding tool rotational and travel speed are demonstrated in Figs. 3 and 4 for the means and signal-to-noise ratios, respectively.

### 3.1.2 Response Optimization for the UTS.

The response optimization for the rotational and travel speed for the UTS can be deduced from Tables 5 and 6 for mean and signal-to-noise ratio, respectively, and also from main effects plot for mean in Fig. 1 and *S/N* ratio effects plot in Fig. 2. The analysis gave 950 rpm rotational speed and 50 mm/min traverse speed as the optimized parameters. The mean and signal-to-noise ratio interactions with the two factors and four levels were illustrated in Figs. 3 and 4, respectively.

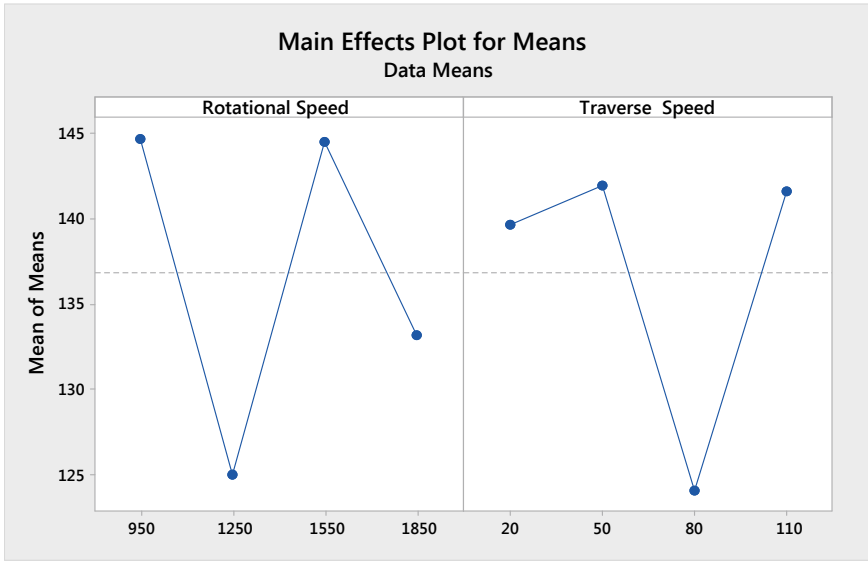


Fig. 1 Main effects plot for means

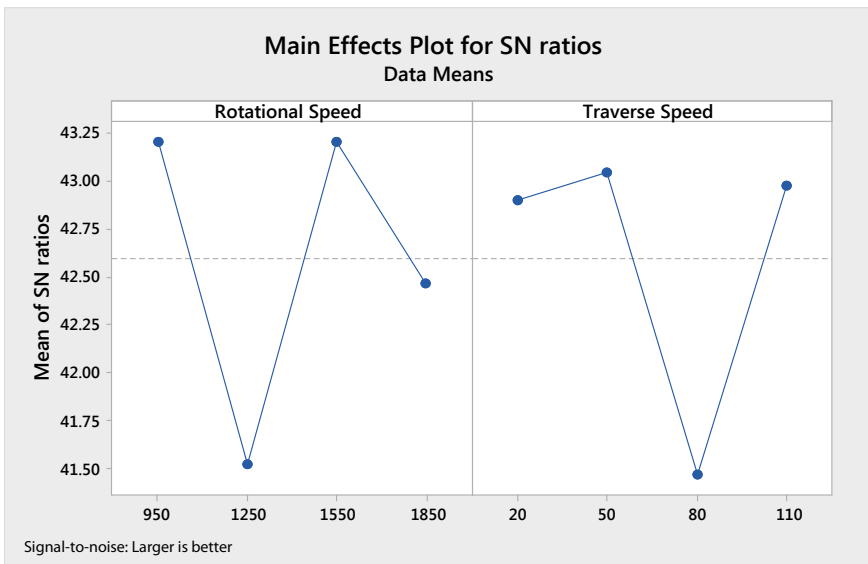


Fig. 2 Main effects plot for S/N ratios

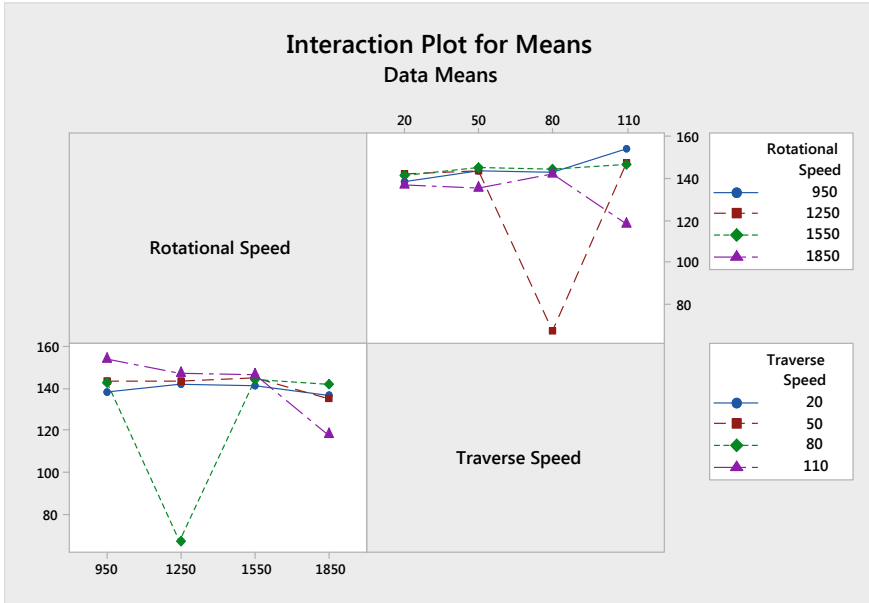


Fig. 3 Interaction plot for means

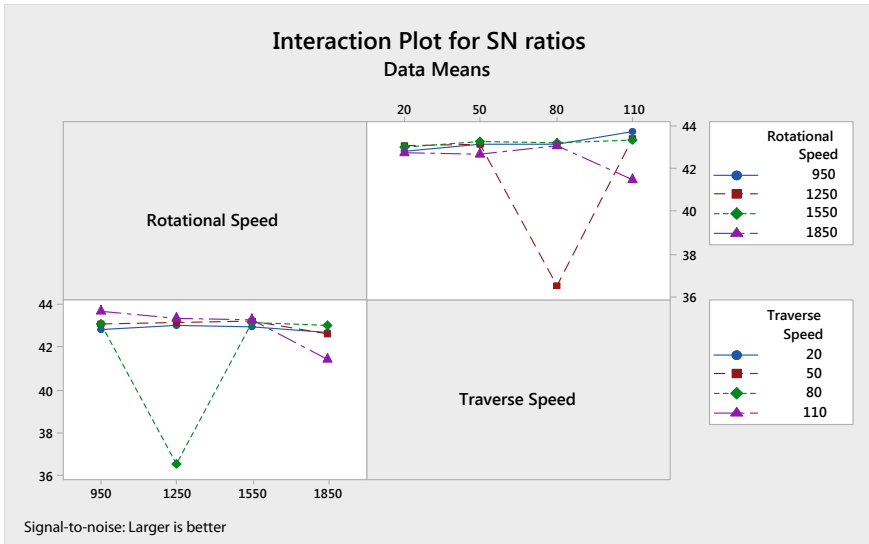


Fig. 4 Interaction plot for SN ratios

**Table 7** Hardness test results

S. No.	Rotational speed (rpm)	Traverse speed (mm/min)	Hardness (HV)
1	950	20	120.31
2	950	50	81.48
3	950	80	111.71
4	950	110	118.44
5	1250	20	98.51
6	1250	50	104.41
7	1250	80	74.56
8	1250	110	105.44
9	1550	20	121.08
10	1550	50	124.36
11	1550	80	126.64
12	1550	110	107.71
13	1850	20	100.43
14	1850	50	99.85
15	1850	80	133.26
16	1850	110	65.18

### 3.2 Hardness

Hardness The average hardness values taken at the weld nugget zone for each parameter are presented in Table 7. 1550 rpm and 80 mm/min rotational and traverse speed, respectively, gave the highest Vickers hardness at the nugget zone.

#### 3.2.1 Analysis of Variance (ANOVA)

The ANOVA analysis outcome is shown in Table 8. Since hardness is ability of material to resist plastic deformation, the larger the better approach is used to evaluate the *S/N* which is presented in Table 8. The contribution of the rotational speed to the hardness at the nugget zone is insignificant, while the travel speed contributes

**Table 8** Analysis of variance (ANOVA)

Source	DF	Adj SS	Adj MS	F-Value	P-Value
Rotational speed	1	0.10	0.097	0.00	0.988
Traverse speed	1	111.89	111.888	0.27	0.612
Error	13	5400.02	415.386		
Total	15	5512.00			

**Table 9** Response table for means

Level	Rotational speed	Traverse speed
1	107.99	110.08
2	95.73	102.53
3	119.95	111.54
4	99.68	99.19
Delta	24.22	12.35
Rank	1	2

**Table 10** Response table for signal-to-noise ratio (*S/N*)

Level	Rotational speed	Traverse speed
1	40.56	40.79
2	39.54	40.12
3	41.56	40.74
4	39.7	39.71
Delta	2.02	1.08
Rank	1	2

majorly to the hardness results. The response to mean and *S/N* taking the larger is better approach are given in Tables 9 and 10, respectively. The main effects for mean and *S/N* are illustrated in Figs. 5 and 6, respectively. The interactions between the

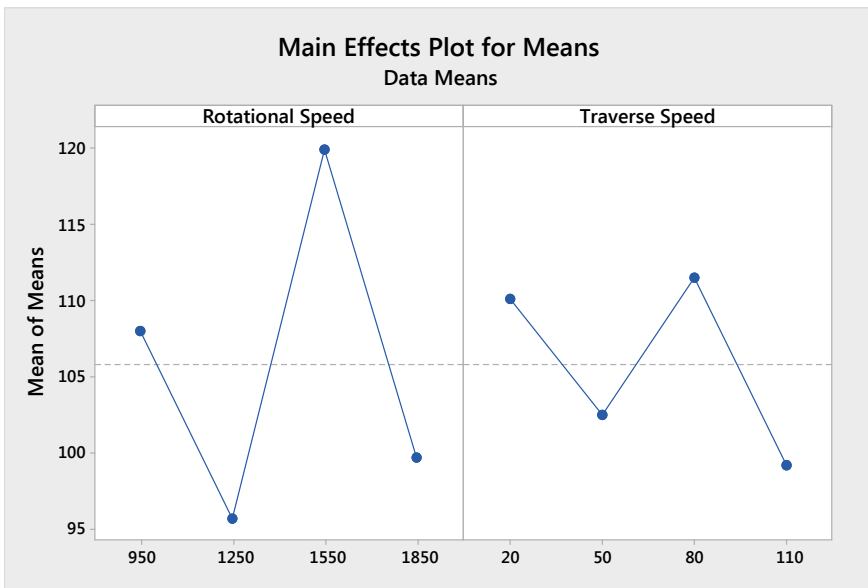


**Fig. 5** Main effects plots for means

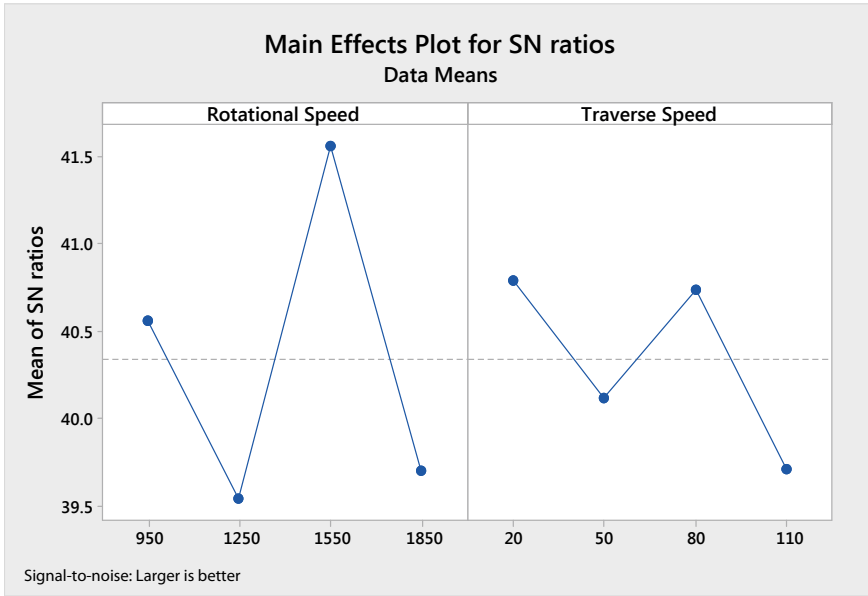


Fig. 6 Main effects plot for *S/N ratios*

two processing parameters considered for the optimizations are illustrated in Fig. 7 for the means while that of the *S/N* is shown in Fig. 8.

### 3.2.2 Response Optimization for Hardness

The response optimization for the rotational and travel speed for the hardness as analyzed from the *S/N* response and main effect plots in Fig. 6 gave the optimized parameters as 1550 rpm rotational speed and 20 mm/min traverse speed.

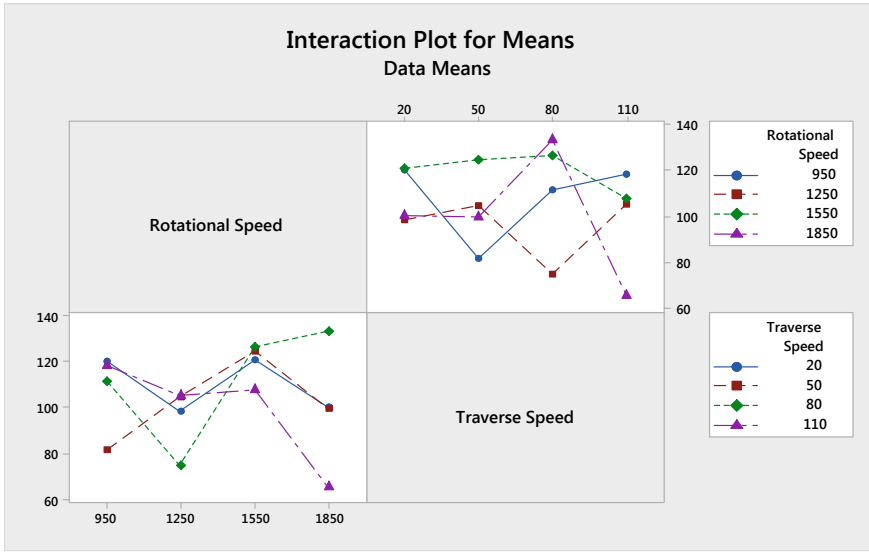


Fig. 7 Interaction plot for means

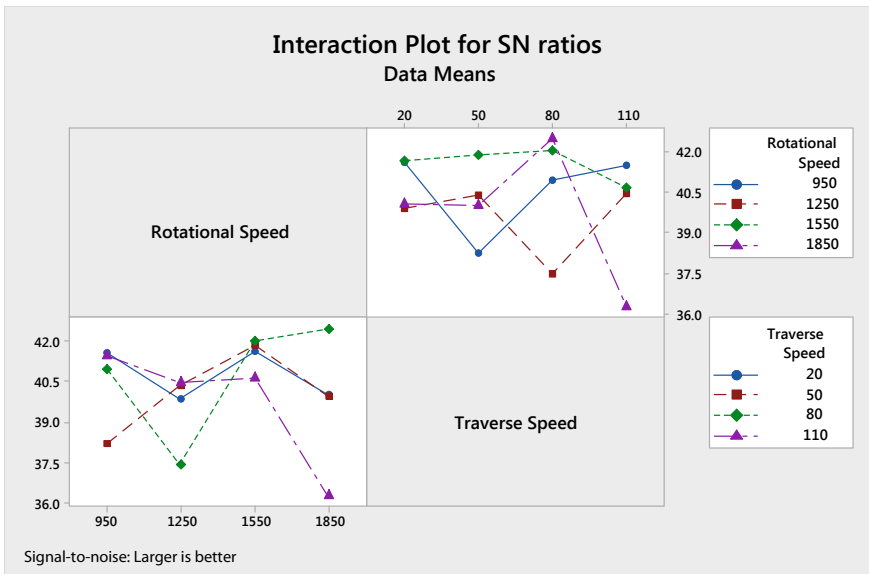


Fig. 8 Interaction plot for the *S/N* ratios



## 4 Conclusions

- The optimum rotational speed and travel speed for achieving maximum UTS are 950 rpm and 50 mm/min, respectively.
- The percentage contributions of the rotational speed toward attaining optimum UTS is 63% while that of transverse speed is 37%.
- Maximum hardness was obtained at an optimum rotational speed of 1550 rpm and 20 mm travel.
- The travel speed is the predominant factor toward attaining optimum hardness. The rotational speed contribution is very insignificant.

## References

1. Nandan R, DebRoy T, Bhadeshia HKDH (2008) Recent advances in friction-stir welding—process, weldment structure and properties. *Prog Mater Sci* <https://doi.org/10.1016/j.pmatsci.2008.05.001>
2. Kumar K, Kailas SV (2008) The role of friction stir welding tool on material flow and weld formation. *Mater Sci Eng, A*. <https://doi.org/10.1016/j.msea.2007.08.013>
3. Mishra A (2018) Friction stir welding of dissimilar metal: a review. *Int J Res Appl Sci Eng Technol*. <https://doi.org/10.22214/ijraset.2018.1237>
4. Abolusoro OP, Akinlabi ET (2019) Wear and corrosion behaviour of friction stir welded aluminium alloys—an overview. *Int J Mech Prod Eng Res Dev (IJMPERD)* 9:967–982
5. Shah PH, Badheka VJ (2017) Friction stir welding of aluminium alloys: an overview of experimental findings—process, variables, development and applications. *Proc Inst Mech Eng Part L J Mater Des Appl*. <https://doi.org/10.1177/1464420716689588>
6. RajKumar V, VenkateshKannan M, Sadeesh P, Arivazhagan N, Devendranath Ramkumar K (2014) Studies on effect of tool design and welding parameters on the friction stir welding of dissimilar aluminium alloys AA 5052–AA 6061. *Procedia Eng*. <https://doi.org/10.1016/j.proeng.2013.11.019>
7. Abnar B, Kazeminezhad M, Kokabi AH (2015) Effects of heat input in friction stir welding on microstructure and mechanical properties of AA3003-H18 plates. *Trans Nonferrous Met Soc China (English Edition)*. [https://doi.org/10.1016/S1003-6326\(15\)63826-2](https://doi.org/10.1016/S1003-6326(15)63826-2)
8. Palanivel R, Koshy Mathews P, Dinaharan I, Murugan N (2014) Mechanical and metallurgical properties of dissimilar friction stir welded AA5083-H111 and AA6351-T6 aluminum alloys. *Trans Nonferrous Met Soc China (English Edition)*. [https://doi.org/10.1016/S1003-6326\(14\)63028-4](https://doi.org/10.1016/S1003-6326(14)63028-4)
9. Rao RV, Senthil Kumar M (2018) Experimental investigation on effect of welding parameters on the friction stir welding of AA 6061. *Mater Today: Proc* 5:12265–12272. <https://doi.org/10.1016/j.matpr.2018.02.205>
10. Farzadi A, Bahmani M, Haghshenas DF (2017) Optimization of operational parameters in friction stir welding of AA7075-T6 aluminum alloy using response surface method. *Arab J Sci Eng* 42:4905–4916. <https://doi.org/10.1007/s13369-017-2741-6>
11. Prasad MVRD, Kumar Namala K (2018) Process parameters optimization in friction stir welding by ANOVA. *Mater Today: Proc* 5:4824–4831. <https://doi.org/10.1016/j.matpr.2017.12.057>
12. Elanchezian C, Vijaya Ramnath B, Venkatesan P, Sathish S, Vignesh T, Siddharth RV et al (2014) Parameter optimization of friction stir welding of AA8011-6062 using mathematical method. *Procedia Eng*. <https://doi.org/10.1016/j.proeng.2014.12.308>

13. Nourani M (2011) Taguchi optimization of process parameters in friction stir welding of 6061 aluminum alloy: a review and case study. *Engineering* 03:144–155. <https://doi.org/10.4236/eng.2011.32017>
14. Ugrasen G, Bharath G, Sagar R, Shivu PR, Keshavamurthy R (2018) Science direct optimization of process parameters for Al6061-Al7075 alloys in friction stir welding using Taguchi's technique. *Mater Today Proc* 5, 3027–3035. <https://doi.org/10.1016/j.matpr.2018.01.103>
15. Panda MR, Mahapatraand SS, Mohanty CP (2015) Parametric investigation of friction stir welding on AA6061 using taguchi technique. *Mater Today Proc*. <https://doi.org/10.1016/j.matpr.2015.07.177>
16. Jayaraman M, Sivasubramanian R, Balasubramanian V, Lakshminarayanan AK (2009) Optimization of process parameters for friction stir welding of cast aluminium alloy A319 by Taguchi method. *J Sci Ind Res*
17. Gomathisankar M, Gangatharan M, Pitchipoo P (2018) A novel optimization of friction stir welding process parameters on aluminum alloy 6061–T6. *Mater Today Proc* 5:14397–14404. <https://doi.org/10.1016/j.matpr.2018.03.025>
18. Saravanan V, Rajakumar S, Muruganandam A (2016) Effect of friction stir welding process parameters on microstructure and mechanical properties of dissimilar AA6061-T6 and AA7075-T6 aluminum alloy joints. *Metallogr Microstruct Anal* 5:476–485. <https://doi.org/10.1007/s13632-016-0315-8>
19. Kalembe-Rec I, Kopyściański M, Miara D, Krasnowski K (2018) Effect of process parameters on mechanical properties of friction stir welded dissimilar 7075–T651 and 5083–H111 aluminum alloys. *Int J Adv Manuf Technol*. <https://doi.org/10.1007/s00170-018-2147-y>
20. Pattanaik AK, Pradhan S, Panda SN, Bagal DK, Pal K, Patnaik D (2018) Effect of process parameters on friction stir spot welding using grey based taguchi methodology. *Mater Today Proc* 5:12098–12102. <https://doi.org/10.1016/j.matpr.2018.02.186>
21. Abolusoro OP, Akinlabi ET (2019) Experimental investigation of tool pin geometry and process parameter influence on the mechanical property of friction stir welded 6101-T6 and 7075-T651 Aluminium alloys, IOP conference series. *J Phys* 1378:032077. <https://doi.org/10.1088/1742-6596/1378/3/032077>

# Effect of Equal Channel Angular Pressing Die Angle on Corrosion Behavior of Bulk Nanostructured Metal



N. A. N. Mokhtar, D. N. Awang Shri, and M. M. Mahat

**Abstract** Equal channel angular pressing technique was used to process bulk nanostructured commercial pure titanium Cp2(Ti Cp2) and aluminium alloy 6061 (Al6061). The samples were processed at two different die channel angles of 120° and 126°. Hardness test shows that the hardness for Al6061, using channel angle 120° ECAP-ed, has increase 15.55% while using channel angle 126° the increase was 14.89% compared to non-ECAP-ed sample. Hardness test for Ti Cp2, using channel angle 120° ECAP-ed has increase 32.89% while using channel angle 126° the increase was 27.05%. The hardness for these both materials has shown that Ti Cp2 has higher hardness compared to Al6061 since the highest increment is 5.84% for 120° ECAP-ed than 126° ECAP-ed for Ti Cp2 samples. The corrosion behavior of the ECAP-ed Al6061 was investigated in 3.5% sodium chloride (NaCl) solution relative to seawater concentration while Ti Cp2 was investigated in phosphate-buffered saline (PBS) solution. Corrosion resistance on 120° ECAP-ed for both Al6061 and Ti Cp2 has shown improved corrosion behavior indicated by the least value of corrosion current density when compared to non-ECAP. By using channel angle 120°, Al6061 have shown the lowest corrosion current density ( $I_{\text{corr}}$ ) value of  $1.61\text{E}-7$  while Ti Cp2 has also shown lowest  $I_{\text{corr}}$  value of  $1.19\text{E}-08$ . This indicates ECAP-ed Al6061 using 120° is the most noble sample with lowest corrosion value, when applied with current, among all samples.

**Keywords** Equal channel angular pressing · Bulk nanostructured materials · Severe plastic deformation · Corrosion resistance

---

N. A. N. Mokhtar · D. N. Awang Shri (✉)  
Department of Mechanical Engineering, College of Engineering, University Malaysia Pahang,  
Lebuhraya Tun Razak, 26300 Gambang, Kuantan, Pahang, Malaysia  
e-mail: [noorfazidah@ump.edu.my](mailto:noorfazidah@ump.edu.my)

N. A. N. Mokhtar  
Institute of Postgraduate Studies, University Malaysia Pahang, Lebuhraya Tun Razak, 26300  
Gambang, Kuantan, Pahang, Malaysia

M. M. Mahat  
School of Physics and Material Studies, Faculty of Applied Sciences, Universiti Teknologi  
MARA, 40450 Shah Alam, Selangor, Malaysia

## 1 Introduction

The well-established Ti Cp2 in the biomedical application has an open interest among the scientists worldwide. It is currently developed with the enhancement of the severe plastic deformation through the process of ECAP. Besides, the lightweight and high material corrosion resistance significantly were demanded throughout the years. These lightweight materials are titanium [1] and aluminum alloys [2]. The SPD techniques help in grain refinement from micrometer in size until nanometer size. This smaller size of grain has developed the high strength, high ductility and advanced physical and mechanical properties [3, 4]. ECAP is one of the outstanding techniques between SPD techniques including high pressure torsion (HPT), friction stir processing (FSP), accumulative roll bonding (ARB), multi-directional forging, and equal channel forward extrusion (ECFE). Among these, ECAP is the best method which its grain refinement significantly has a high impact on the mechanical properties [5]. This ECAP exploit shear strain leads to deformation without no shape changes in its cross-sectional area [6]. The techniques involve specimen being pressed within inner arc of die through channels of die. This ECAP comprised of inner and outer arc of die angle [4]. The ECAP processing is influenced by the internal heating during ECAP, back pressure, pressing temperature, pressing speed, channel angle, and angle of curvature [7]. Ti Cp2 has been investigated since it is the most utilized among the series of titanium which has shown superior biocompatibility, low density, high strength to weight ratio, improved corrosion resistance and its osseo-integration properties [3, 8]. The advantages of mechanical properties in this metal in terms of low density and definite elastic modulus have encouraged the application of titanium and its alloys in wide industries such as sports appliances, aviation, automotive, ship-building, architecture and power and biomedical equipment [9]. Titanium is usually protected by the formation of spontaneous passive oxide layer. However, corrosion resistance of nanocrystalline titanium in human physiological fluid has shown to improve [8]. On the other hand, AA6061 is investigated due to its good mechanical and metallurgical properties among other AAs, such as good weldability, high corrosion resistance, heat treatable, workability, and proper affinity to various coatings. Corrosion behavior of metals and alloys is mainly caused by the effect of environment due to its high acidity and alkaline concentration [10]. The corrosion rate using the 3.5% NaCl has shown a higher value when the amount of  $Al_2O_3$  percentage used is higher [11]. Corrosion rate involves the anodic and cathodic processes in the solution. The anodic process for aluminium in seawater is the dissolution of aluminium ions with electrons. The cathodic process, which is involved in corrosion of aluminium in seawater is the reduction of dissolved oxygen and production of hydroxide ions. Some amount of aluminium ions will react with the hydroxide ions and form aluminium hydroxide on the aluminium surface. The aluminium hydroxide will precipitate on the surface because of its low solubility. The aluminium will gradually change to aluminium oxide resulting the formation of passive oxide film on the surface [12]. Even though changes in grain size have shown to improve the corrosion behavior of Ti Cp2 and AA6061; however, the analysis on the effect of

nanostructuring due to ECAP process at different angles is rarely discussed. Thus, the present work addresses the influence of ECAP die angle on the hardness and corrosion behavior of AA6061 and Ti Cp2.

## 2 Methodology

### 2.1 Sample Preparation

Commercial AA6061 and Ti Cp2 rods with 10 mm diameter and 150 mm length were used for ECAP. For Al6061, the furnace was heated until 526 °C then the samples were put inside for 3 h. This Al6061 was quenching in water for 15 s at room temperature which are followed by repeated heating at 204 °C for 1 h. For Ti Cp2, the furnace was heated in the range of 538–704 °C, then the samples were put inside for 2 h and then they were slow cooled at room temperature.

ECAP dies with two conditions internal die angles ( $\Phi$ ),  $\Phi$  of 120° channel angle and 126° channel angle which made of tool steel as shown in Fig. 1. The ECAP die was built in-house with interchangeable die slot with two channels, equal in cross-section, intersecting at an angle near the center of the die. Two different dies with channel angles of 120° and 126°, respectively, were used in this work. To reduce the friction between the rod and the die walls, a lubricant with molybdenum disulfide ( $\text{MoS}_2$ ) was used. A hydraulic press machine was used to carry out the ECAP process at room temperature.

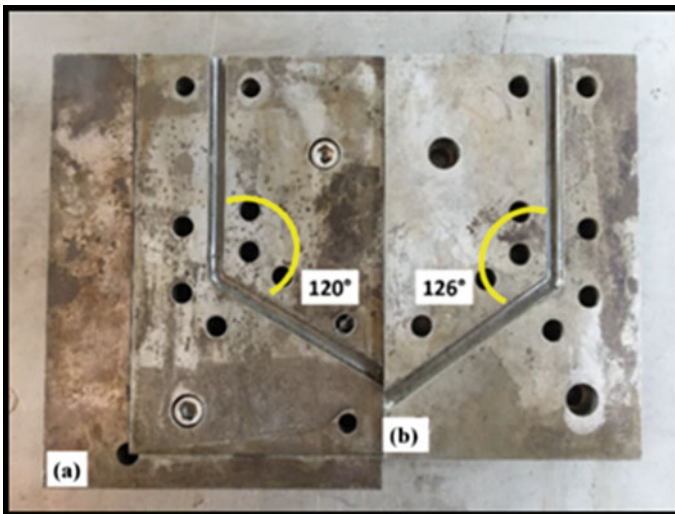


**Fig. 1** ECAP dies **a**  $\Phi = 120^\circ$  and **b**  $\Phi = 126^\circ$

### 2.2 Vickers Hardness Test

The evaluation of the hardness test is to identify the mechanical properties of the material. The test was taken from about 10 points horizontally and 3 points vertically to obtain the average of the hardness values and avoid the parallax error.

### 2.3 Corrosion Test

For the both samples of Al6061 and Ti Cp2, a potentiostat (Gamry Instruments Interface 1000 E Potentiostat) was used. For this study, using Al6061 samples, the corrosion test was done on 3.5% NaCl to stimulate seawater condition. The corrosion behavior of Al6061 was investigated in 3.5% NaCl solution at the same concentration with seawater. Meanwhile, the corrosion behavior of pure Ti Cp2 was investigated in PBS solution. The mechanically polished samples were left in the test electrolyte until a steady state was reached (~30 min from electrode immersion), then Tafel polarization was performed. The corrosion current density,  $I_{corr}$ , and corrosion potential,  $E_{corr}$ , were calculated from both the OCP and Tafel polarizations from electrode immersion in the test solution.

## 3 Result and Discussion

**Hardness Test.** A graph has been drawn after the hardness test was run on the 4 samples of Ti Cp2. It is obvious from the obtained results that ECAP-ed 120° has shown an increment in hardness by 32.89% and for ECAP-ed 126°, the increment hardness is 27.05% when compared to non-ECAP (see Fig. 2a).The closest values

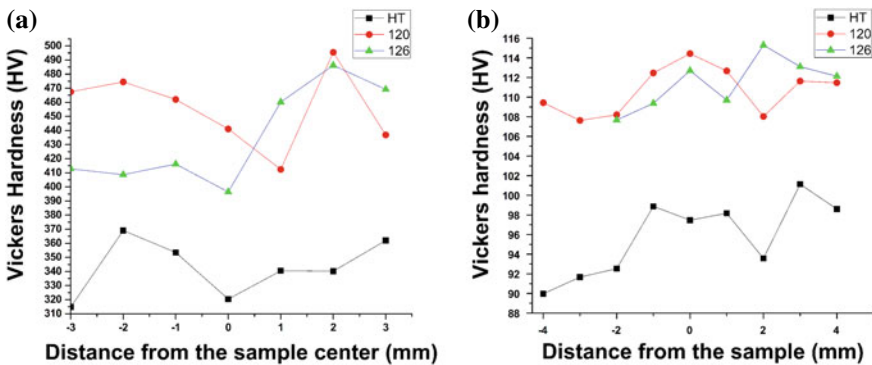


Fig. 2 Vickers hardness profile for a Ti Cp2 and b AA6061

of 120° ECAP-ed condition and 126° ECAP-ed condition are 495.5 HV and 486.27 HV, respectively, at point 2 mm from the center which is also the hardest point of all series. Meanwhile, the farthest values of 120° ECAP-ed condition and 126° ECAP-ed condition are at point -2 mm which are 474.6 HV and 408.7 HV, respectively. The percentage of the 120° ECAP-ed condition is higher than the 126° ECAP-ed condition. The influence of ECAP-ed Ti Cp2 can be associated with the development of hardness properties [4]. Standard deviation for 120° ECAP-ed is 27.56, for 126° ECAP-ed is 35.25, and for non-ECAP is 20.3.

A graph has been drawn after the hardness test was run on 4 samples of AA6061 (see Fig. 2b). ECAP process reduces the grain size of AA6061 according to the Hall-Petch relationship which states that the hardness of material will increase with decreasing of particle size. It was proved by the ECAP-ed samples hardness results which showed improvements in the mean hardness, which for the ECAP-ed 120° sample it is 110.66 HV (increment of 15.55% from non-ECAP-ed for heat treat sample). And for the ECAP-ed 126° sample, it is 110.03 HV (increment of 14.89% from non-ECAP-ed of heat-treated sample), respectively. There is a slightly higher increment for hardness when the channel angle is reduced from 126° to 120° because when the channel angle is reduced, the induced plastic strain in cross-section of sample is increased; therefore, the grain size for ECAP-ed 120° sample is a bit smaller than the ECAP-ed 126° sample. These results are in agreement with high stress distribution that was identified using die angle 120° compare to the 126°. Thus, there is a slight increase in hardness for the ECAP-ed 120° sample. Standard deviation for 120° ECAP-ed is 2.42, for 126° ECAP-ed is 4.31 and for non-ECAP is 3.89.

**Corrosion Behavior.** The results of the OCP measurements for all samples after reaching the steady state are presented in Figs. 3a and 4a, respectively. These results were confirmed by Tafel polarization. An increase in the corrosion resistance of Al6061 and Ti Cp2 with longer immersion time in test solution was recorded.

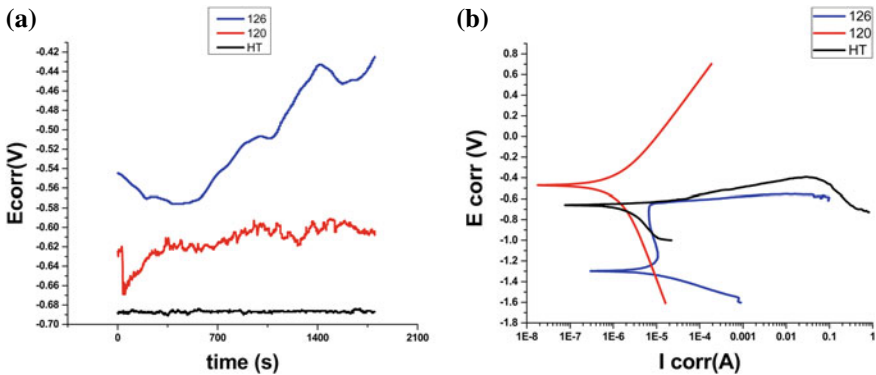


Fig. 3 Comparison of a OCP curves and b Tafel curves for AA6061

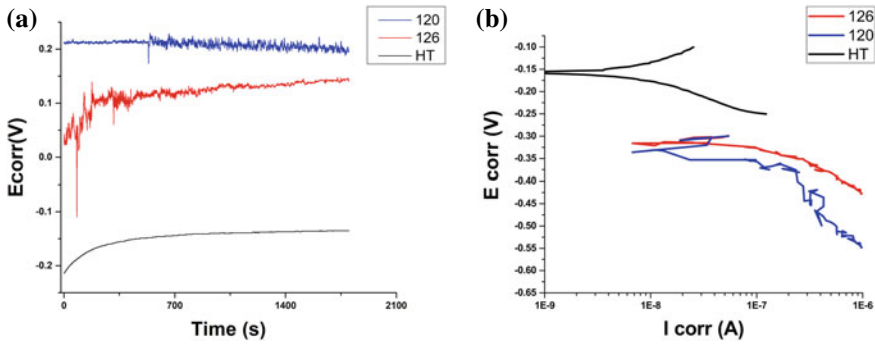


Fig. 4 Comparison of **a** OCP curves **b** Tafel curves for Ti Cp2

**Open Circuit Potential Measurements.** The characteristic of the passive film on the surface of Al6061 and Ti Cp2 was studied using the OCP with time in 3.5% NaCl solution for Al6061 and PBS solution for Ti Cp2. The OCP with the time variation of the 120° ECAP-ed, 126° ECAP-ed, and as-received are shown in Figs. 3a and 4a. The OCP curves have shown the corrosion potential,  $E_{corr}$ , fluctuation behavior through low OCP value. It can be due to the repassivation and dissolution occurred within electrolyte due to different proportions of impurities activity and different bulk orientations in area fractions [13]. However, a constant OCP value has showed that a stable surface and absolutely nobler passive film will be produced [14]. It can be observed that all the Al6061 ECAP-ed and Ti Cp2 ECAP-ed samples had imposed the free corrosion potential. These results are in agreement with the previous studies [13] reported that the ECAP samples have free corrosion potential compared to the non-ECAP samples. This may be attributed to the lower electrochemical reaction and the oxide film upgrading on the surface.

**Corrosion Behavior.** The results of the OCP measurements for all samples after reaching the steady state are presented in Figs. 3a and 4a, respectively. These results were confirmed by Tafel polarization. An increase in the corrosion resistance of Al6061 and Ti Cp2 with longer immersion time in test solution was recorded.

**Open Circuit Potential Measurements.** The characteristic of the passive film on the surface of Al6061 and Ti Cp2 was studied using the OCP with time in 3.5% NaCl solution for Al6061 and PBS solution for Ti Cp2. The OCP with the time variation of the 120° ECAP-ed, 126° ECAP-ed, and as-received are shown in Figs. 3a and 4a. The OCP curves have shown the corrosion potential,  $E_{corr}$ , fluctuation behavior through low OCP value. It can be due to the repassivation and dissolution occurred within electrolyte due to different proportions of impurities activity and different bulk orientations in area fractions [13]. However, a constant OCP value has showed that a stable surface and absolutely nobler passive film will be produced [14]. It can be observed that all the Al6061 ECAP-ed and Ti Cp2 ECAP-ed samples had imposed the free corrosion potential. These results are in agreement with the previous studies [13] reported that the ECAP samples have free corrosion potential compared to the



non-ECAP samples. This may be attributed to the lower electrochemical reaction and the oxide film upgrading on the surface.

The corrosion potential is directly proportional to corrosion resistance in which the corrosion resistance of 120° ECAP-ed and 126° ECAP-ed samples have shown higher corrosion resistance compared to heat-treated samples of titanium (see Figs. 3a and 4a). It can be noted that to the influence of the formation of biofilm on the surface of titanium due to the culture medium produced which blocked the corrode process occurred on it [15]. This may be reflected from the simulated biological reaction in the electrolyte comprised of PBS solution. This PBS solution contains 137 mM NaCl, 2.7 mM KCl, 8 mM Na<sub>2</sub>HPO<sub>4</sub>, and 2 mM KH<sub>2</sub>PO<sub>4</sub> (pH = 7.4) [8].

**Tafel Polarization.** The Tafel polarization characteristics in a wide range of anodic and cathodic polarization were performed with the scan rate of 1 mV s<sup>-1</sup> from the starting current density  $I_{\text{corr}}$  value of 1.650  $\mu\text{A}$  to the final current density achieved value of 1.0 A. All samples of Al6061 were immersed in 3.5% NaCl solution for about 30 min before polarization tests to achieve their stable OCP values. It can be observed from both polarization curves that the cathodic polarization curves showed a regular pattern.

Potentiodynamic data of AA6061 in 3.5% NaCl for ECAP-ed 120°, ECAP-ed 126°, and heat-treated AA6061 are shown in Table 1. The resulting Tafel polarization curves are shown. The potentiodynamic study revealed that the anodic and cathodic reactions minimize the corrosion potential ( $E_{\text{corr}}$ ). The cathodic ECAP-ed samples influenced the shift in the values of corrosion potential  $E_{\text{corr}}$  to more negative side relative to heat-treated sample. This was more noticeable for the sample ECAP-ed Al6061 (see Fig. 3b and Ti Cp2 Fig. 4b). Obviously, it has shown the cathodic performance which is more corrosion resistant. Other studies also found that reduced grain sizes through ECAP will improve corrosion resistant [16]. **Table 1** Polarization data for ECAP-ed 120°, ECAP-ed 126°, and heat-treated AA6061 in PBS solution

Potentiodynamic data of Titanium Cp2 in PBS solution for ECAP-ed 120°, ECAP-ed 126°, and heat treated are shown in Table 2. Larger cathodic reaction was observed

**Table 1** Polarization data for ECAP-ed 120°, ECAP-ed 126°, and heat-treated AA6061 in PBS solution

Conditions	$E_{\text{corr}}$ (V)	$I_{\text{corr}}$ (A)	Corrosion rate (mils per year)
HT	-0.659	1.65E-7	0.212
120°	-0.472	1.61E-7	0.207
126°	-0.130	8.44E-6	1.087

**Table 2** Polarization data for ECAP-ed 120°, ECAP-ed 126°, and heat-treated Ti Cp2 in PBS solution

Conditions	$E_{\text{corr}}$ (V)	$I_{\text{corr}}$ (A)	Corrosion rate (mils per year)
HT	- 0.157	2.06E-09	3.74E-03
120°	- 0.346	1.19E-08	4.27E-10
126°	- 0.325	2.19E-08	3.97E-10

on 120° ECAP-ed and 126° ECAP-ed Ti Cp2 when corrosion potential,  $E_{corr}$ , was reduced. It can contribute to improved corrosion resistance by time. This may be attributed to the less electrolyte ions diffusion and predominant oxide film formation [17].

## 4 Conclusion

The corrosion behavior of bulk nanostructured AA6061 and Ti CP2 processed by ECAP in two different die angles was investigated. From the studies, the following conclusions were drawn:

- (i) Hardness test reveals that ECAP introduces grain refinement that causes the hardness for both AA6061 and Ti Cp2 to increase. It was found that the samples that have ECAP at 120° have higher hardness compared to samples processed at 126°.
- (ii) Grain refinement, due to ECAP process, significantly affects the corrosion behavior for Ti Cp2 in PBS solution and Al6061 in 3.5% NaCl. Both samples were showing active dissolution based on OCP curves. This may be attributed to the formation of passive layer as ECAP causes grain refinements that help accelerate repassivation.

**Acknowledgement** This paper was fully supported by facilities and resources from University Malaysia Pahang. The authors would like to acknowledge the support of grants from University Malaysia Pahang No. RDU180318 and Fundamental Research Grant Scheme, Ministry of Higher Education, Malaysia No. RDU190110.

## References

1. Marin E, Pressacco M, Fusi S, Lanzutti A, Turchet S, Fedrizzi L (2013) Characterization of grade 2 commercially pure Trabecular Titanium structures. *Mater Sci Eng, C* 33(5):2648–2656
2. Santiago JA et al (2018) Adhesion enhancement of DLC hard coatings by HiPIMS metal ion etching pretreatment. *Surf Coat Technol* 349
3. Saleema N, Sarkar DK, Paynter RW, Gallant D, Eskandarian M (2012) A simple surface treatment and characterization of AA 6061 aluminum alloy surface for adhesive bonding applications. *Appl Surf Sci* 261:742–748
4. Zahari ZS, Awang Sh'ri DN, Abu Hassan MAH, Wan Harun WS (2019) Effect of ECAP die angle to the microstructure and mechanical properties of bulk nanostructured Al-6061. *IOP Conf Ser Mater Sci Eng* 469:012054
5. Sureshkumar P, Uvaraja VC, Rajakarunakaran S (2019) Addition of metallic reinforcement enhanced deformation and properties of ceramic reinforced composite by adapting ECAP with increment number of passes. *Mater Res Exp* 6(8):086502
6. Ansarian I, Shaeri MH, Ebrahimi M, Minárik P, Bartha K (2019) Microstructure evolution and mechanical behaviour of severely deformed pure titanium through multi directional forging. *J Alloys Comp* 776:83–95

7. Valiev RZ, Langdon TG (2006) Principles of equal-channel angular pressing as a processing tool for grain refinement. *Prog Mater Sci* 51(7):881–981
8. Sotniczuk A, Kuczyńska-Zemła D, Kwaśniak P, Thomas M, Garbacz H (2019) Corrosion behavior of Ti-29Nb-13Ta-4.6Zr and commercially pure Ti under simulated inflammatory conditions—comparative effect of grain refinement and non-toxic  $\beta$  phase stabilizers. *Electrochimica Acta* 312:369–379
9. de Viteri VS, Fuentes E (2013) Titanium and titanium alloys as biomaterials. In: *Tribology—fundamentals and advancements*. InTech, pp 155–181
10. Abbass MK, Hassan KS, Alwan AS (2015) Study of corrosion resistance of aluminum alloy 6061/SiC composites in 3.5% NaCl solution. *Int J Mater Mech Manuf* 3(1):31–35
11. Natesan M, Selvaraj S, Manickam T, Venkatachari G (2008) Corrosion behavior of metals and alloys in marine-industrial environment. *Sci Technol Adv Mater* 9(4):045002
12. Gao B, Zhang X, Sheng Y (2008) Studies on preparing and corrosion inhibition behaviour of quaternized polyethyleneimine for low carbon steel in sulfuric acid. *Mater Chem Phys* 108(2–3):375–381
13. El Aal MIA, Sadawy M (2015) Influence of ECAP as grain refinement technique on microstructure evolution, mechanical properties and corrosion behavior of pure aluminum. *Trans Nonferrous Met Soc China* 25(12):3865–3876
14. Porcayo-Palafox E, Carrera-Chavez S, Casolco S, Porcayo-Calderon J, Salinas-Bravo V (2019) Electrochemical performance of Ti-based commercial biomaterials. *Adv Mater Sci Eng*
15. Burnat B, Walkowiak-Przybyło M, Błaszczak T, Klimek L (2013) Corrosion behaviour of polished and sandblasted titanium alloys in PBS solution. *Acta Bioeng Biomech* 15(1)
16. Balyanov A et al (2004) Corrosion resistance of ultra fine-grained Ti. *Scripta Mater* 51(3):225–229
17. Bahraminasab M, Bozorg M, Ghaffari S, Kavakebian F (2019) Corrosion of  $\text{Al}_2\text{O}_3$ -Ti composites under inflammatory condition in simulated physiological solution. *Mater Sci Eng C* 102:200–211

# Investigation of Maximum Erosion Zone in the Horizontal 90° Elbow



Rehan Khan, H. H. Ya, William Pao, T. V. V. L. N. Rao, Azad Alam, and M. Azeem

**Abstract** Sand transportation within flow devices causes major problems for the hydrocarbon production industry and entails crucial material removal from pipelines and leads to failure and malfunction of the piping system. The 90° elbow configuration is an indispensable flow changing device used to redirect the flow direction in hydrocarbon and mineral processing industries. This paper highlights a comprehensive approach to quantify erosion in 90° elbow configuration ensues from fine particle transportation with the carrier fluid. A multilayer paint modeling (MPM) technique and computational fluid dynamics (CFD) are adopted to map the erosion distribution inside the elbow under liquid–solid flow in a flow loop setup. The experiments for horizontal-to-horizontal (H–H) orientation elbow with 50.8 mm inner diameter are performed with fine sand of 50 μm size entertains in a carrier fluid at 3 m/s. The high erosion zones have been located near the outlet of the 90° elbow under fine particle impact with a maximum erosion rate of 1.82 mm/year in horizontal–horizontal (H–H) oriented elbow.

**Keywords** Erosion · Multilayer paint modeling · Elbow · CFD

## 1 Introduction

Erosion of flow changing devices is an important concern of hydrocarbon production, chemical, and mineral processing industries. Erosion induces severe detriment to flow devices and abridges their lifetime and affects the operating safety of the whole production processes [1, 2]. Practical wall interaction within the pipelines is the ultimate cause of the disintegration of the pipe wall [2–4]. A prime concern in the hydrocarbon extraction and mineral processing industry is the inhabitation of the sand

---

R. Khan (✉) · H. H. Ya · W. Pao · A. Alam · M. Azeem  
Mechanical Engineering Department, Universiti Teknologi PETRONAS, Bandar Seri Iskandar,  
Tronoh, Perak, Malaysia  
e-mail: [Muhammad\\_15001294@utp.edu.my](mailto:Muhammad_15001294@utp.edu.my)

T. V. V. L. N. Rao  
Department of Mechanical Engineering, SRM Institute of Science and Technology,  
Kattankulathur 603203, India

© Springer Nature Singapore Pte Ltd. 2020  
S. S. Emamian et al. (eds.), *Advances in Manufacturing Engineering*, Lecture Notes  
in Mechanical Engineering, [https://doi.org/10.1007/978-981-15-5753-8\\_21](https://doi.org/10.1007/978-981-15-5753-8_21)

particles called fine. Fine is mainly sand particles with sizes less than  $62\ \mu\text{m}$ , which can generate erosive effects on pipelines. These particles affect operational safety and reduce the flow efficiency of production processes. To understand the erosion-induced damage due to sand particles and [5] factors influencing erosion in terms of the target wall properties, carrier fluid characteristics, and erodent properties, various investigations were directed in previous studies.

In order to change the flow direction, an inertia force toward downstream results in particle impact on the inner surface of the flow devices [6]. As a result, energy is transferred from particles to the inner wall of the flow devices and induces wear on the wall surface [7]. It is, therefore, essential to prolong the lifetime of these components by better understanding the physics of erosive wear mechanisms.

Vieira et al. [8] employed an experimental loop with the ultrasonic technique to capture the wall thickness loss of the  $90^\circ$  elbow with 300 and  $150\ \mu\text{m}$  grains of sand. They concluded that  $300\ \mu\text{m}$  sand particles generate 3.1 times more metal removal in comparison with  $150\ \mu\text{m}$  sand particles. Bourgoyne et al. [9] quantified the erosion rate bend configuration under multiphase flow to find the influence of elbow ratio on erosion intensity. Liu et al. [10] assessed two methods (CFD and flow loop test) to describe the relation of carrier phase velocity on the erosion of  $90^\circ$  elbow and found that erosion intensity changes significantly with altering flow velocity.

Peng and Cao [11] measured erosion-induced damage for  $90^\circ$  bend configuration using CFD and concluded the erosion significantly occurs at the boundary walls of the flow pipeline, near to the elbow exit and the outer side of the elbow. Chen et al. [12] adopted CFD-DEM techniques to quantify the erosion rate of different elbow configurations with  $150\ \mu\text{m}$  sand particles and found the location maximum erosion-induced damage closest to exit for all elbows configurations.

Published literature in this domain of erosive wear has focused on the sand diameter of greater size, and none has investigated erosion with fine particles. Additionally, the relevant literature survey yielded a limited study to identify the zone of maximum erosion for  $90^\circ$  elbows under fine particles impact of liquid dominant flow. Therefore, the present investigation in this paper contributes to mapping the zone of the erosion in long radius carbon steel  $90^\circ$  elbow configuration with a particle size of  $50\ \mu\text{m}$ . The present work pertains both numerical and simultaneous multilayer paint modeling (MPM) experiment to map erosion distribution which showed identical results compared with the available literature data. The maximum locations of erosion-induced damage are closest to exit in  $90^\circ$  elbow under fine particles impact.

## 2 Erosion Test

A multiphase close flow loop was developed and configured using a transparent acrylic tube to visualize flow pattern within 50.8 mm diameter pipe for erosion tests. The flow loop consisted of a water tank with sand stirring unit, a Warner abrasive pump, a Yokogawa gas flow meter, a magnetic flowmeter with ceramic lining, and flow-controlled valve. Typical silica sand of  $50\ \mu\text{m}$  average size was used as erodent

medium in the carrier fluid. For the present study, the carrier liquid phase is water and the solid phase is fine particles with a 2.5% (w/w) concentration. The slurry was re-circulated at 3 m/s velocities in a closed flow loop for the present study. Before the test, the internal surface of the 90° elbow was painted using enamel paint of red and silver colors with uniform thickness. The zone of high erosion was visualized by a paint removal map of the first layer (silver) on the internal surface of the elbow specimen. The detail of the experimental setup used for the present study was presented in previous research [13, 14].

### 3 Computational Fluid Dynamics (CFD) Simulations

The ANSYS FLUENT code was employed for current research of erosive wear quantification. CFD tools offer the advancement of computational capabilities in providing better accuracy of solving flow physics in complex geometries. The geometrical configuration of the CFD model consists of the long radius elbow with an inner radius of 0.0254 m. For CFD simulation, the computational mesh and refinement techniques were adopted based on mesh independence study performed by Khan et al. [15]. To extract erosion rate and particle trajectories (discrete phase modeling), DPM approach was introduced in simulation stages with discrete random walk model. The simulation parameters used to extract the erosion profile of the elbow configurations are set identical with experimental operating conditions.

## 4 Results and Discussion

The results and discussion are outlined with discrete phase modeling, the Multilayer paint modeling, to visualize erosion pattern under liquid-sand flow in the first section. Thereafter the particle trajectories under liquid dominant flow along the 90° elbow under the impact of fine particles are discussed.

### 4.1 Discrete Phase Modeling

The zone of erosion distribution along an axial angle from the inlet of the elbow starts with angle 0°, and the outlet angle is 90° with maximum erosion zone as illustrated in Fig. 1. A CFD-DPM contour of the erosion zones with 3 m/s liquid velocity and 50 μm particle size transported in long radius 90° elbows is outlined in Fig. 2a, b. As presented in Fig. 2, the elbow was defined as the bottom half and the upper half to map the erosion pattern inside elbow similar to the experimental condition. Erosion was observed in bottom half-section with larger erosion zone distribution as compared to the upper half-section of the elbow as shown in Fig. 2a, b. Furthermore,

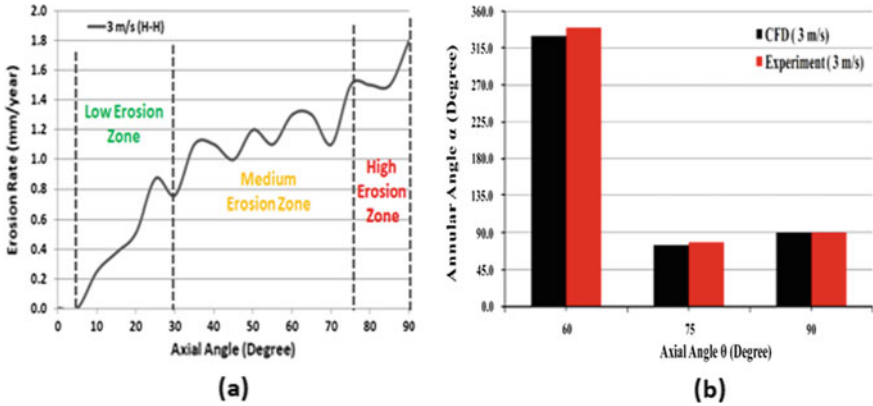


Fig. 1 a Erosion rate versus axial angle and b comparison of DPM Erosion location with MPM

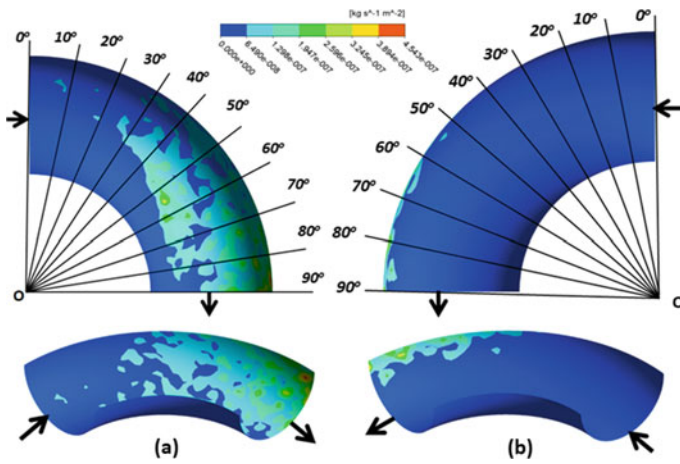
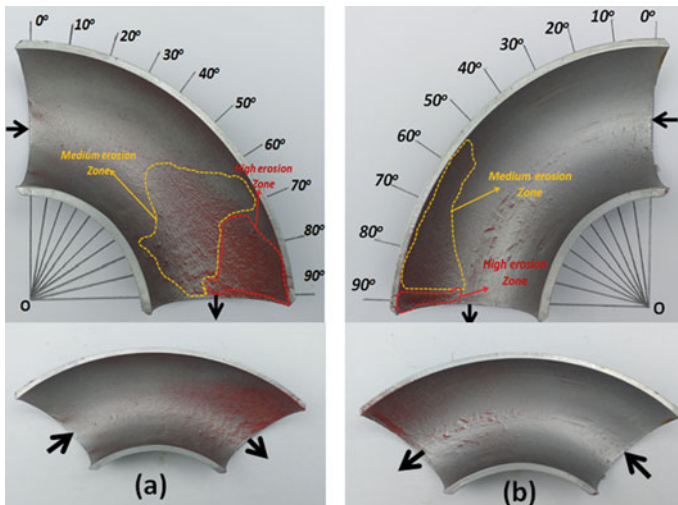


Fig. 2 DPM erosion contour 90° horizontal–horizontal elbow section for liquid–solid simulation with  $V_L = 3$  m/s, for a bottom half and b upper half

high erosion was observed at the outlet of elbow configuration between axial angles of 75° and 90° in the bottom half and between 88° and 90° in the upper half-section. The location of the medium erosion zone under the same operating condition yielded within 30° and 74° axially in the bottom half-section and between 65° and 88° in upper half-section. Comparison of experiment and CFD data presented in Fig. 1b shows a similar trend of erosion distribution along the elbow annular and axial angles with maximum erosion at the outlet.

### 4.2 Multilayer Paint Modeling

The multilayer paint modeling (MPM) is an inexpensive qualitative visual tool to accurately map the erosion in significantly less time using the flow loop at high transportation velocities [16]. The (MPM) test was repeated several times to ensure the measurement uncertainties and accuracy of the erosion map. After each test, the 90° elbow sample was unmounted from the test section for visualization of the paint removal location on the inner elbow wall. Figure 3a, b shows the qualitative paint erosion pattern with the location of maximum erosion inside elbow configuration and the liquid–solid flow with an impact of 50 μm fine particles. Figure 3a shows the zone of high erosion at the outlet in the bottom half-section with a carrier fluid velocity of 3 m/s. The high erosion zone was observed between axial angles of 72° and 90° in the bottom half-section and between 86° and 90° in the upper half-section. The location of the medium erosion zone was between 50° and 70° in the bottom half bend and between 65° and 85° in the upper half elbow section under similar flow conditions. The CFD-DPM simulation and qualitative experimental results from the present study were compared with previously published research of Peng et al. [11] and found the maximum erosion zone within 70° and 90° (downstream) for 50 μm particle sizes. The results extracted from the present study revealed the zone of maximum erosion distribution between 72° and 90° (Downstream) in 90° elbow configuration at the outlet for horizontal orientation. The results extracted from the simulation study match closely with the MPM test. Thus, the adopted methodology for the present study can be used to extract accurate erosion patterns with the identification of erosion zones.



**Fig. 3** Removed paint locations 90° horizontal–horizontal elbow section for liquid–solid flow with  $V_L = 3$  m/s, for **a** bottom half and **b** upper half-section



### 4.3 Erosion Pattern and Particle Trajectories

Figure 4 presents the extracted particle's path followed under carrier fluid flowing at 3 m/s with fine particles. In liquid–sand flow, the erosion distribution relies on the path of the sand under flow conditions towards the wall surface. Figure 4 reflects that fine particle impacts multiple times on the inner wall of the bottom half-section which generates an erosion map with the larger erosion rate at the bottom half-section of the elbow. In addition, the largest erosion zone was generated due to the particle–wall interaction at high impact angle at the bottom half-section of the elbow under horizontal–horizontal conditions. Figure 4 displays that fine particles impact the wall with larger angles at locations  $x$ ,  $y$ , and  $z$  at downstream which significantly contribute to escalating the erosion region. Thus, the smaller particle in the carrier fluid leads to a catastrophic impact to the wall surface and disintegrates significant walls mass at the bottom half-section. The selected particle trajectories and trajectory of fine particles inside a standard  $90^\circ$  elbow are shown in Fig. 4. For liquid–solid flow, the particles follow the independent path and impact the bottom half elbow wall section as outlined in Fig. 4. Both the simulated and MPM results showed the maximum erosion-induced damage found at the annular angles ( $75^\circ$ ,  $90^\circ$ ,  $135^\circ$ , and  $345^\circ$ ) inside elbow and reflect the reasonably good agreement with observations from flow loop experiments.

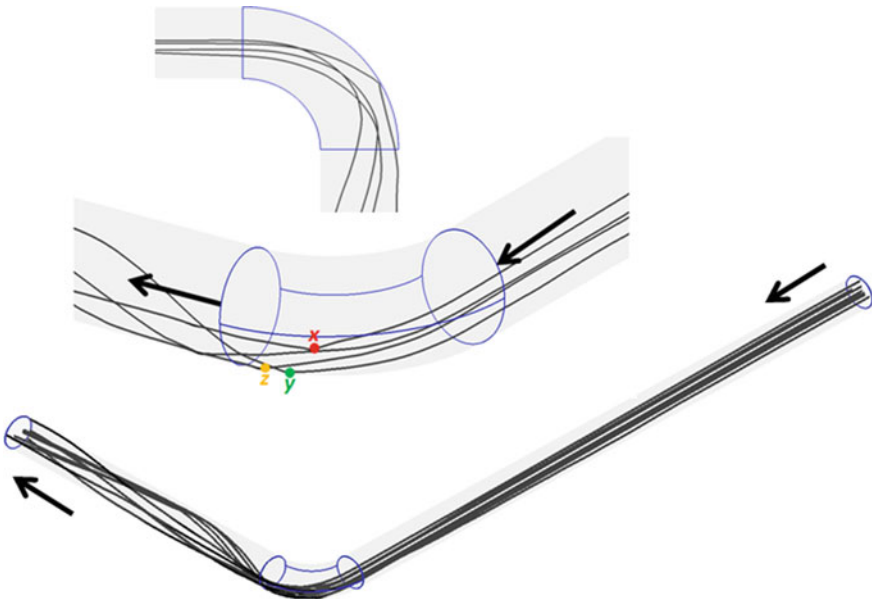


**Fig. 4** Fine trajectories for chosen particles and standard case

## 5 Conclusions

In this research, an experimental and numerical investigation was performed to identify the zone of peak erosion in horizontal 90° elbow. CFD-DPM technique was employed for the numerical study of fine particle erosion in long radius carbon steel 90° elbow. The investigations were conducted at 3 m/s water velocity with 50 μm sand particles. The following conclusions can be summarized from the current research:

1. The numerical simulation of erosion in the elbow's geometrical configuration shows that fine particles significantly contribute to the escalating erosion-induced damage on the outer wall of the outlet. Additionally, the high erosion zones have been located near the outlet of the 90° elbow under fine particle impact with a maximum erosion rate of 1.82 mm/year.
2. The experimental technique adopted in this study is suitable for the design and development of flow devices by identifying the location of the peak erosion region, without altering the material properties. The comparison of CFD erosion with the experimental results yields good recognition with the available literature.

**Acknowledgments** The authors acknowledge the financial support given by the Universiti Teknologi PETRONAS under grant YUTP-FRG 0153AA-H19 for this research.

## References

1. Tan Y, Zhang H, Yang D, Jiang S, Song J, Sheng Y (2012) Numerical simulation of concrete pumping process and investigation of wear mechanism of the piping wall. *Tribol Int* 46:137–144
2. Zhang H, Tan Y, Yang D, Trias FX, Jiang S, Sheng Y, Oliva A (2012) Numerical investigation of the location of maximum erosive wear damage in elbow: effect of slurry velocity, bend orientation and angle of elbow. *Powder Technol* 217:467–476
3. Khan MR, Ya HH, Pao W, Majid MAA (2020) Numerical investigation of sand particle erosion in long radius elbow for multiphase flow. Springer, Singapore, pp 41–49
4. Khan R (2019) Numerical investigation of the influence of sand particle concentration on long radius elbow erosion for liquid-solid flow. *Int J Eng* 32:1485–1490
5. Mazumder QH (2006) Prediction of erosion due to solid particle impact in single-phase and multiphase flows. *J Pressure Vessel Technol* 129:576–582
6. Chen X, McLaury BS, Shirazi SA (2004) Application and experimental validation of a computational fluid dynamics (CFD)-based erosion prediction model in elbows and plugged tees. *Comput Fluids* 33:1251–1272
7. Najmi K, McLaury BS, Shirazi SA, Cremaschi S (2015) Experimental study of low concentration sand transport in wet gas flow regime in horizontal pipes. *J Nat Gas Sci Eng* 24:80–88
8. Vieira RE, Mansouri A, McLaury BS, Shirazi SA (2016) Experimental and computational study of erosion in elbows due to sand particles in air flow. *Powder Technol* 288:339–353
9. Bourgoyne AT Jr (1989) Experimental study of erosion in diverter systems due to sand production. In: SPE/IADC drilling conference. Society of Petroleum Engineers, New Orleans, Louisiana, pp 10
10. Liu J, BaKeDaShi W, Li Z, Xu Y, Ji W, Zhang C, Cui G, Zhang R (2017) Effect of flow velocity on erosion–corrosion of 90-degree horizontal elbow. *Wear* 376–377:516–525

11. Peng W, Cao X (2016) Numerical simulation of solid particle erosion in pipe bends for liquid–solid flow. *Powder Technol* 294:266–279
12. Chen J, Wang Y, Li X, He R, Han S, Chen Y (2015) Erosion prediction of liquid-particle two-phase flow in pipeline elbows via CFD–DEM coupling method. *Powder Technol* 275:182–187
13. Khan R, Ya HH, Pao W, Khan A (2019) Erosion-corrosion of 30°, 60°, and 90° carbon steel elbows in a multiphase flow containing sand particles. *Materials* 12:3898
14. Khan R, Ya HH, Pao W (2019a) An experimental study on the erosion-corrosion performance of AISI 1018 carbon steel and AISI 304L stainless steel 90-degree elbow pipe. *Metals* 9:1260
15. Khan R, Ya HH, Pao W (2019b) Numerical investigation of the elbow angle effect on solid particle erosion for liquid-solid. *Int J Mech Mech Eng* 19:1–13
16. Wu J, Graham LJW, Lester D, Wong CY, Kilpatrick T, Smith S, Nguyen B (2011) An effective modeling tool for studying erosion. *Wear* 270:598–605

# An Overview: Mechanical and Wear Properties of HDPE Polymer Nanocomposites Reinforced with Treated/Non-treated Inorganic Nanofillers



Tauseef Ahmed, H. H. Ya, Shuhaimi Mahadzir, Rehan Khan, and Muhammad Azad Alam

**Abstract** Recently, several review papers on the topic of polymer nanocomposites have been written. Specifically, the scope of this article is aimed to include mechanical and tribological properties of reinforced high-density polyethylene owing to correlation of such properties in engineering and science applications. This paper provides reconsideration of mechanical and tribological properties of HDPE polymer nanocomposites reinforced with treated and non-treated inorganic nanofillers focusing on  $\text{CaCO}_3$ ,  $\text{SiO}_2$ , and nano clay. Some fundamental concepts and certain contradictions to the established facts are narrated. Moreover, classifications, comparisons, and the factors necessary for consideration of properties of HDPE are included as well.

## 1 Introduction

Polymer nanocomposite is a class of composite, in which the size of reinforcement must be in the range of 1–100 nm as by the definition of nanocomposites. Polymer nanocomposites, as indicated by the name, are composed of a polymeric material as a primary phase and nano-scaled reinforcements as a secondary phase [1]. Thermoplastics such as polypropylene (PP), high-density polyethylene (HDPE), PVC, polyamide, and thermosets such as epoxy, polyesters, and bakelite show remarkable performance while used as a primary phase for PNCs. While fillers such as calcium carbonate ( $\text{CaCO}_3$ ), mica, wollastonite, glass fiber, glass bead, jute, curaua fiber, silica ( $\text{SiO}_2$ ), nano clay, and CNT are the examples of reinforcements used as a reinforcing phase in nanometer range [2].

---

T. Ahmed (✉) · H. H. Ya · S. Mahadzir · R. Khan · M. A. Alam  
Mechanical Engineering Department, Universiti Teknologi PETRONAS, Bandar Seri Iskandar,  
Tronoh, Perak, Malaysia  
e-mail: [tauseef.17007229@gmail.com](mailto:tauseef.17007229@gmail.com)

H. H. Ya  
e-mail: [hamdan.ya@utp.edu.my](mailto:hamdan.ya@utp.edu.my)

Moreover, polymer nanocomposite is highly in demand in both industry and academia for research because of its remarkable mechanical properties such as high elastic strength, and hardness and because of ability to be improved in properties with very low concentration of fillers. The choice of particular nanofillers for a polymer matrix depends upon the intended application of polymer nanocomposite. As generally, polymer/filler is bonded by weak intermolecular forces, as a result such polymer composites can be used for mild applications. While in other cases, if the polymer is reinforced with nano-sized fillers having dispersion at molecular level, there is a strong polymer/filler chemical bond created, which can be employed for robust applications [3]. Polymeric phase used as a matrix can be categorized as follows:

1. Thermoplastics,
2. Thermosets,
3. Elastomers,
4. Natural and Biodegradable polymers.

The aforementioned types of the polymer have been used as a primary phase for fabricating PNCs; nevertheless, the choice of a polymer matrix over one another depends upon the required mechanical, electrical, magnetic, optical, biocompatibility, chemical stability, and the ability of functionalization of a polymer. However, the ability to recycle and retain the properties, even after heating, determines the superiority of thermoplasts over other polymeric matrices [4, 5].

On the other hand, application of polymer nanocomposites (PNCs) is limited by some factors as compared to metals and ceramics. Polymers are less dense than metals and ceramics. They have low coordination of number and lighter carbon and hydrogen as their main foundation chain; therefore, pure polymers have low performance in mechanical, thermal, and electrical properties [6]. Nonetheless, reinforced polymers are currently in high demand because of high surface area of nanometer-sized fillers. High surface energy of nanofillers if on one place increases stress transfer potential between matrix and reinforcements by increasing polymer/filler interaction; on the other hand, it decreases the distance between the fillers resting in a polymeric matrix mitigating the required outcome of selecting nano-sized fillers over macro- or micro-sized filler [7]. Additionally, it is a mainstream concept adopted in investigation of wear such that layered structure of fillers, such as layered silicates and graphene can enhance wear of a polymer when used as reinforcement yet, infrequently investigated in literature [8].

Clay polymer nanocomposites are the distinct class of PNCs reinforced with layered silicates, for enhanced wear properties which are also identified by their high stiffness and added into a polymer matrix particularly to improve tensile properties. The aforementioned property of clay PNCs is based on the fundamental concept of chain entanglement of a soft polymer matrix with the clay particles if the clay/matrix adhesion has an adequate chemical interaction. However, the case of a non-polar polymer, such as most of the polyolefins, exhibits the matter of very less or no compatibility with the inorganic clay particles. The matter arises owing to the microstructural property of clays having water molecules trapped between the layers of clay giving rise to a hydrophilic nature.

Additionally, tribological/wear properties are equally important because of friction and wear account for a substantial amount of resource loss in terms of energy and power in the commercial sector. Addition of nano-sized SiO<sub>2</sub> and layered silicates such as nano clays improves wear performance of HDPE polymer nanocomposites apart from rendering strength to HDPE polymers because of layered microstructural characteristics.

## 2 Factors Affecting Mechanical Properties

The final properties of PNCs cannot be estimated by considering only bulk mechanical properties of the reinforcement but also certain external factors such as size of nanofillers [9], morphology of the system, wt% of fillers in matrix, polymer/filler interfacial interaction [10–12], fabrication technique, and degree of distribution and dispersion [9, 13–15] which also contributes to manipulating the final properties of the PNCs as indicated in Fig. 1. It is an established fact that all mentioned factors essentially are interrelated which contribute to or alter bulk mechanical properties of fillers in a polymer matrix to decide the final properties of PNCs [16, 17].

For instance, a particular state of distribution and dispersion is the foremost requirement of PNCs which means that the nano-sized reinforcement must be properly distributed i.e., every site of the matrix should be reinforced having no empty site and the nanofillers need to be dispersed properly such that there are no agglomerated nanofillers. The corresponding relationship between dispersion and distribution can be well understood by looking at Fig. 2a in which a virtual polymer matrix is shown with the black dots representing nanofillers. In Fig. 2a, subdivision (a), the fillers are distributed at minimal state. Most of the sites, not all in the matrix have the reinforcement but there are still agglomerated fillers. Subdivision (b) of Fig. 2a is

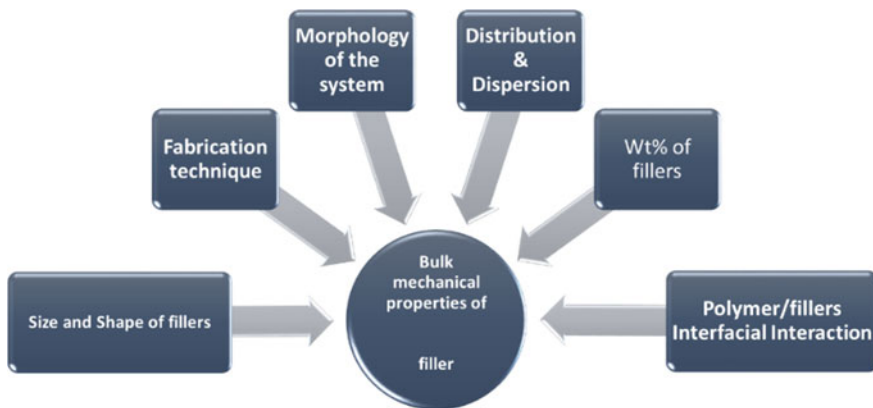


**Fig. 1** External factors contributing or effecting bulk properties of nanofillers to determine final properties of a polymer matrix

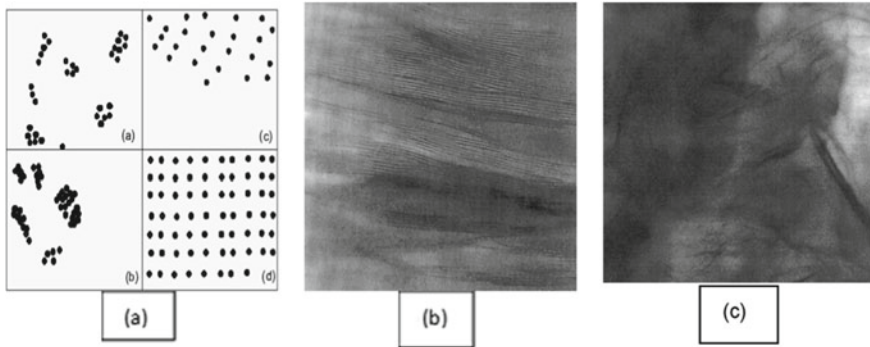


**Fig. 2** **a** Demonstration of different states of dispersion and distribution. **b** Horizontally resting alternate polymer/fill layers in intercalated PNCs. **c** Evenly distributed fillers in exfoliated PNCs. Represented with the permission from [18, 19]

the worst case of dispersion and distribution, while subdivision (c) has the excellent dispersion but there are empty sites in the matrix which is not reinforced. Eventually, subdivision (d) is the best demonstration having proper dispersion and distribution and ideally a polymer matrix with such degree of dispersion and distribution attains the maximum values of mechanical properties [18].

### 3 Reinforced High-Density Polyethylene (HDPE)

Polyethylenes are commodity polymers with the  $-\text{CH}_2-$  as their repeating unit (monomer). They are organic compounds having thermoplastic nature. Polyethylenes can be classified into six different classes based on their molecular weight, density, and degree of branching. Some of the well-known polymers among polyethylenes and corresponding properties are reported in Table 1.

**Table 1** Comparison among different types of polyethylene

Thermoplasts	Density ( $\text{gm}/\text{cm}^3$ )	MFI ( $\text{gm}/10 \text{ min}$ )	Molecular weight ( $\text{g}/\text{mol}$ )	No of monomers
UHMWPE	0.97–0.99	0.06	3.1 million	100,000–250,000
HDPE	0.941–0.965	0.2–3.0	30,000–200,000	700–1800
MDPE	0.926–0.940	1–2.0	–	–
LDPE	0.926–0.940	0.3–2.6	–	100
LLDPE	0.926–0.940	0.3–2.6	–	–
VLDPE	0.926–0.940	0.3–2.6	–	–

*Note* All data are presented based on information included in [20–23]

Furthermore, high-density polyethylene (HDPE) is a thermoplastic polymer that has substantial importance when used as primary phase to develop a polymer nanocomposite (PNC). It is one of the most searched polymeric phases for development of novel PNCs because of its outstanding performances in mechanical [6], thermal [7], and chemical [8] applications. Additionally, low cost, less energy demand, ease of processing [9, 10], recyclability [11], resistance to corrosion, and abrasion make it ideal for diverse applications [10]. However, HDPE is susceptible to fail in mechanical properties and wear resistance because of low tensile strength [12] and low wear resistance [7, 13].

For this purpose, HDPE is reinforced with different treated or not treated inorganic nanofillers for improvement in mechanical properties. Moreover, layered silicates or nano clays are excellent choices to improve not only mechanical properties but also wear properties. Liu et al. enhanced wear resistance of HDPE and reported the ability of layered nanofillers to improve wear performance owing to the stacked layers of layered silicates. As in illustration, wear behavior is improved if force is applied and the layers start sliding over one another [8].

As an important multipurpose nanofiller, nano clay is used for improvement in properties like mechanical properties [16], barrier properties [17], and chemical separation of contents from one another [18]. Such attractive uses of nano clay are attributed to its nanometric sized structural and functional characteristics of layer-by-layer stacking of sheets over one another. On the other hand, for practical applications of load-bearing joints replacement mechanical properties coexists with wear properties [12]. Therefore,  $\text{CaCO}_3$  as a nanofiller is considered a suitable candidate as a reinforcement for PNCs for mechanical properties [20] at low cost. Addition of nano-sized  $\text{CaCO}_3$  to HDPE polymeric phase has been reported to improve stiffness, resistance to environmental stress cracking, and high impact resistance [21].

A polymer/filler system, having no adequate chemical interactions, performs identically as conventional macro- or micro-composites. It is important to realize that just a mere physical mixture between a polymer matrix and nanofillers does not form a nanocomposite. Hence, it is pivotal to obtain an adequate polymer/filler chemical interaction to obtain an enhanced polymer composite [24]. Based on matrix/filler bonding, majorly two classes of PNCs are thermodynamically distinguished as presented in Table 2. They are as follows:

1. Intercalated PNCs
2. Exfoliated PNCs.

## 4 Mechanical Properties

Young's modulus of HDPE is improved virtually in all occurrences for a particular weight percentage of fillers which also improves the stiffness. Alexandre and Dubois [19], reviewing mechanical properties of clay PNCs, reflected that Young's modulus of a polymer matrix completely depends upon the weight percentage or the clay content, no matter what technique is employed for fabrication [19]. This comment is



**Table 2** Comparison between properties of intercalated and exfoliated polymer nanocomposites

Properties	Types of polymer nanocomposites	
	Intercalated PNCs	Exfoliated PNCs
Order of fillers	They are identified by having alternate polymer chain entangled between the layered silicate structures	Virtually no ordered polymer or fillers phases. Nanofillers are randomly distributed
Polymeric chain	The number of polymer chains residing between the two layers of silicate ranges from a single chain or more	Number of polymeric chains cannot be identified as there is random and even distribution of polymers/fillers
Polymer/fillers interaction	Polymer/fillers interact via low wander walls forces	This particular case occurs when there is a superior chemical polymer/fillers interaction
Characterization	XRD results clearly show the interlayer distances between the layers of silicates, owing to swollen layers as a result of penetration of polymer chains	TEM images are used for interlayer characterization owing to the large interlayer spacing and no alternate polymer chains
Morphology	Morphological analysis or dispersion and other properties are performed via TEM or FESEM	XRD is principally used to perform morphological analysis such as crystallinity

Note All information is based on data included in [19]

manifested when Young's modulus (tensile modulus) was examined at 120 °C [25]. It is reported that for a particular type of clay MMT as the clay content increases the value of young's modulus increases and may reach as high as 0.7 GPa [26]. This behavior is attributed to the aspect ratio of the dispersed clay, which plays an influential role in improving the performance [19]. However, the increase of Young's modulus with corresponding increase of weight percentage of nanofillers is nullified when the concentration of fillers is increased to a certain limit. This fact is explained by the process of agglomeration of nanofillers. Additionally, surface chemistry of inorganic fillers controls Young's modulus significantly. For instance, nano clays such as montmorillonite modified with octadecyl ammonium, magadiite modified with octadecyl ammonium, and magadiite modified with methyl octadecyl ammonium showed a variable behavior to improve Young's modulus.

In the result obtained by Alexandre and Dubois [19], it is visible that for epoxy composites with filler more than 4 weight percentage C18A-montmorillonite upgraded the modulus of elasticity superiorly, which is attributed to the difference in charge density of layers in nano clays. Likewise, the effect of surface modification cannot be ignored because if HDPE is reinforced with surface modified nanofillers, it alters Young's modulus of pure HDPE substantially. Zhang et al. displayed in their experimental investigation that grafted nano-silica (SiO<sub>2</sub>) particles increased the tensile modulus of elasticity of pure HDPE to approximately 1070 MPa, which

was 900 MPa when the nano-silica ( $\text{SiO}_2$ ) particles were not treated. Moreover, the variation of tensile modulus depends upon the nature and type of surface treatment performed as in case of  $\text{SiO}_2$ -g-PS-HDPE the value of tensile modulus was comparable to neat HDPE resin. HDPE composite was upgraded only in the case of  $\text{SiO}_2$ -g-PBA-HDPE which indicated the dependence of tensile modulus upon a specific surfactant compatible with both the polymer and the fillers [27].

#### ***4.1 Tensile Strength***

It is a well-established fact that not all, yet for most of the cases, inorganic nanofillers such as nano clay and nano-sized  $\text{CaCO}_3$ , not only increase the Young modulus but also the tensile strength as well [28, 29]. The undesirable results of very low strength in other situations are affected by the surface chemistry of polymer/filler interface which is manipulated by surfactants used to alter the surface chemistry [29]. Furthermore, experimental investigation of Zhang et al. indicates that tensile strength of a composite is contingent to the polymer/filler interfacial interaction [27]. Min et al. compared tensile strength of HDPE as a function of different MMT clay contents and asserted that compatibilizer assists to increase stress transfer capability. The increase in tensile strength was reported to be up to 70% with increasing clay content owing to the application of maleic anhydride acting as a compatibilizer [15].

#### ***4.2 Elongation at Break***

Addition of fillers generally decreases the ductility of polymers or elongation at break [29]. For inorganic nanofillers, such as nano clay, the reduction in the value of elongation at break is more as compared to increase in the value of tensile strength as shown in some experimental work [30], but generally speaking elongation of the PNCs is connected to the ductility which is controlled by the glass transition temperature. However, above the glass transition temperature, there is no such a meaningful change in elongation at break if a polymer matrix is reinforced with nano clay [29].

### **5 Tribological Properties**

Tribology is the study of friction (the resistance of lateral motion of two bodies in contact) and wears (the loss of material) because of materials sliding against one another [31]. In some studies, tribology is the name of a combination of friction, wear, and lubrication [32]. Particularly whenever two bodies come in contact and slide over one another, there is a material loss from the surfaces of both materials, which is called

**Table 3** Factor influencing wear behavior of PNCs

Factors	Examples
Bulk mechanical properties	Strength, toughness, fatigue, hardness
Surface properties	Surface energy, surface roughness, coefficient of friction
Experimental setup	Applied load, testing time, sliding distance, sliding speed

*Note* All information produced based on data included in [22]

as wear phenomenon, while the wear rate of a material is conventionally defined as the volume or mass lost from the material per unit of sliding distance [33]. Even so, the wear behavior of polymers is not well understood because it is dependent upon a combination of factors.

Literature in summing all the reviews shows that wear properties mainly depend upon bulk mechanical properties, surface properties, and experimental setup as shown in Table 3. Specifically, the effect of the applied load and testing time on friction and wear performance were considered [34]. In any case, the results of these parameters present a few inconsistencies during variation for the purpose of experiments. Furthermore, it was found in certain investigations that the friction coefficient of certain materials is significantly influenced by the sliding speed, particularly by the normal load.

Moreover, Clerico [35] investigated that the friction coefficient of polymers rubbing against metals diminishes with increasing the connected load. Unal et al. discovered dissimilarity and stated that friction coefficient decreases straightly with the increase of the contact pressure while the wear rate has demonstrated almost no affectability to the contact pressure. In reality, numerous different examinations demonstrated the contrary performance, that is reduction of friction coefficient with increasing the applied load [36, 37].

Da Silva et al. [1] have investigated the influence of applied load on rubbing coefficient of HDPE tests with galvanized steel plate [36]. Principally, there are three main types of wear mechanisms namely abrasive, adhesive, and fatigue wear which can be identified in polymers. The following Table 4 shows a brief comparison between wear mechanisms.

Moreover, the mechanisms of wear, which are reported in the sliding of polymers against metal counter faces, are mainly adhesion and abrasion [22]. Adhesive wear of polymers can be decreased by the formation of transfer film [37], while abrasive wear of polymers can be decreased by manipulating experimental parameters such as sliding distance, applied load, and material counter face [38].

**Table 4** Wear mechanisms in polymer nanocomposite

Types of wear mechanism	Explanation	
	Properties	Figures
Abrasive wear	<p>When a hard rough surface happens to grind against a soft surface</p> <p>Two subtypes such as (a) two-body wear and (b) three-body wear as shown in the image</p> <p>It is identified by its characteristics of plowing, cutting, and cracking</p>	
Adhesive wear	<p>It occurs as a result of material transfer from one sliding body to others</p> <p>It can be witnessed following the process of welding, and physical or chemical interaction if the bond between the two surfaces exceeds the strength of materials</p>	
Fatigue wear	<p>It occurs as a result of the weakness of material during cyclic loading</p> <p>Cracks start at the surface and spread to the subsurface region which may possibly cause delamination</p>	

Note All information is based on data included in [22, 39, 40]

## References

1. Usuki A et al (1993) Synthesis of nylon 6-clay hybrid. *J Mater Res* 8(5):1179–1184
2. Ray SS, Masami O (2003) Polymer/layered silicate nanocomposites: are view from preparation to processing. *Prog Polym Sci* 28(11):1539–1641
3. Mai Y-W, Yu Z-Z (2006) *Polymer nanocomposites*. Woodhead Publishing, Cambridge
4. Koo JH (2006) *Polymer nanocomposites*. McGraw-Hill Professional Pub., New York
5. Lampman S (2003) *Characterization and failure analysis of plastics*. Asm International, Ohio
6. Thostenson ET, Li C, Chou T-W (2005) Nanocomposites in context. *Compos Sci Technol* 65(3–4):491–516
7. Winey KI, Vaia RA (2007) *Polymer nanocomposites*. *MRS Bull* 32(4):314–322
8. Liu T, Wang Y, Eyler A, Zhong W-H (2014) Synergistic effects of hybrid graphitic nanofillers on simultaneously enhanced wear and mechanical properties of polymer nanocomposites. *Eur Polym J* 55:210–221
9. Liu H, Brinson LC (2008) Reinforcing efficiency of nanoparticles: a simple comparison for polymer nanocomposites. *Compos Sci Technol* 68(6):1502–1512

10. Lee SH, Cho E, Jeon SH, Youn JR (2007) Rheological and electrical properties of polypropylene composites containing functionalized multi-walled carbon nanotubes and compatibilizers. *Carbon* 45(14):2810–2822
11. Shang S, Williams J, Söderholm K-J (1994) How the work of adhesion affects the mechanical properties of silica-filled polymer composites. *J Mater Sci* 29(9):2406–2416
12. Gopakumar T, Lee J, Kontopoulou M, Parent J (2002) Influence of clay exfoliation on the physical properties of montmorillonite/polyethylene composites. *Polymer* 43(20):5483–5491
13. Inan T (2017) Thermoplastic-based nanoblends: preparation and characterizations. In: Recent developments in polymer macro, micro and nano blends. Elsevier, Amsterdam, pp 17–56
14. Manas-Zloczower I (1997) Analysis of mixing in polymer processing equipment. *Rheol Bull* 66(1):5–8
15. Min KD, Kim MY, Choi K-Y, Lee JH, Lee S-G (2006) Effect of layered silicates on the crystallinity and mechanical properties of HDPE/MMT nanocomposite blown films. *Polym Bull* 57(1):101–108
16. Jordan J, Jacob KI, Tannenbaum R, Sharaf MA, Jasiuk I (2005) Experimental trends in polymer nanocomposites—a review. *Mater Sci Eng A* 393(1–2):1–11
17. Jeon I-Y, Baek J-B (2010) Nanocomposites derived from polymers and inorganic nanoparticles. *Materials* 3(6):3654–3674
18. Ajayan PM, Schadler LS, Braun PV (2006) Nanocomposite science and technology. Wiley, Hoboken
19. Alexandre M, Dubois P (2000) Polymer-layered silicate nanocomposites: preparation, properties and uses of a new class of materials. *Mater Sci Eng R Rep* 28(1–2):1–63
20. Khanam PN, AlMaadeed MAA (2015) Processing and characterization of polyethylene-based composites. *Adv Manuf Polym Compos Sci* 1(2):63–79
21. Panin S, Kornienko L, Alexenko V, Buslovich D, Dontsov YV (2017) Extrudable polymer-polymer composites based on ultra-high molecular weight polyethylene. In: AIP conference proceedings, vol 1915, no 1. AIP Publishing, Melville, p 020005
22. Xu S (2014) Mechanical and tribological properties of carbon nanofiber reinforced high density polyethylene. North Dakota State University, North Dakota
23. Ramakrishna S, Huang ZM (2016) Biocomposites.
24. Biswas M, Ray SS (2001) Recent progress in synthesis and evaluation of polymer-montmorillonite nanocomposites. In: New polymerization techniques and synthetic methodologies. Springer, Berlin, pp 167–221
25. Ruiz-Hitzky E, Aranda P, Casal B, Galvan JC (1995) Nanocomposite materials with controlled ion mobility. *Adv Mater* 7(2):180–184
26. Kojima Y et al (1993) Mechanical properties of nylon 6-clay hybrid. *J Mater Res* 8(5):1185–1189
27. Zhang MQ, Rong MZ, Zhang HB, Friedrich K (2003) Mechanical properties of low nano-silica filled high density polyethylene composites. *Polym Eng Sci* 43(2):490–500
28. Stretz H, Paul D, Cassidy P (2005) Poly (styrene-co-acrylonitrile)/montmorillonite organoclay mixtures: a model system for ABS nanocomposites. *Polymer* 46(11):3818–3830
29. Fornes T, Yoon PJ, Keskkula H, Paul DR (2002) *Polymer* 43:2121
30. Nam BU, Son Y (2010) Evaluations of PP-g-GMA and PP-g-HEMA as a compatibilizer for polypropylene/clay nanocomposites. *Polym Bull* 65(8):837–847
31. Bobzin K, Bartels T (2011) Industrial tribology: tribosystems, friction, wear and surface engineering, lubrication. Wiley, Hoboken
32. Asgari M, Abouelmagd A, Sundararaj U (2017) Silane functionalization of sodium montmorillonite nanoclay and its effect on rheological and mechanical properties of HDPE/clay nanocomposites. *Appl Clay Sci* 146:439–448
33. Rodkiewicz C, Wang Y (1994) A dry wear model based on energy considerations. *Tribol Int* 27(3):145–151
34. Watanabe M, Yamaguchi H (1986) The friction and wear properties of nylon. *Wear* 110(3–4):379–388
35. Clerico M (1969) A study of the friction and wear of nylon against metal. *Wear* 13(3):183–197

36. Da Silva CH, Tanaka DK, Sinatora A (1999) The effect of load and relative humidity on friction coefficient between high density polyethylene on galvanized steel—preliminary results. *Wear* 225:339–342
37. Palabiyik M, Bahadur S (2000) Mechanical and tribological properties of polyamide 6 and high density polyethylene polyblends with and without compatibilizer. *Wear* 246(1–2):149–158
38. Unal H, Sen U, Mimaroglu A (2004) Dry sliding wear characteristics of some industrial polymers against steel counterface. *Tribol Int* 37(9):727–732
39. Chairman CA, Babu SK, DuraiSelvam M, Balasubramanian K (2011) Investigation on two-body abrasive wear behavior of titanium carbide filled glass fabric-epoxy composites-a Box-Behnken approach. *Int J Eng Sci Technol* 3(4)
40. Xue Y, Wu W, Jacobs O, Schädel B (2006) Tribological behaviour of UHMWPE/HDPE blends reinforced with multi-wall carbon nanotubes. *Polym Testing* 25(2):221–229

# Liquid Desiccant Membrane Regeneration of DES for Air Conditioning Systems Using Electrodialysis Technique



Temidayo Lekan Oladosu, Aklilu Tesfamichael Baheta, and P. B. Hussain

**Abstract** The quest for energy-saving dehumidification approach paved the way to liquid desiccant air conditioning system (LDAC). Non-corrosive and hygroscopic ionic liquids are compelling as potential liquid desiccants. However, toxicity, biocompatibility, biodegradability, and viscosity of ionic liquids still pose concerns. Binary deep eutectic solvent (DES) of choline chloride and ethylene glycol is proposed as potential greener liquid desiccant in air conditioning systems, by considering desiccant regeneration performance via electrodialysis technique. A parametric study of the liquid desiccant regeneration was investigated numerically using COMSOL Multiphysics commercial software. The results showed the influence of the operational parameters on the overall performance prediction. Electrodialytic regenerated desiccant in a single-cell analysis optimally yielded about  $74 \text{ mol/m}^3$  of aliphatic choline species at 313.15 K working temperature and 1.25 V DC power input.  $3.59\text{E}-02 \text{ g/m}^2\text{s}$  DES flux was obtained in the regenerated channel at 2 V power input. The results aid in predicting DES desiccant regeneration capacity, understanding electrodialysis phenomenon, and performance influential parameter interactions.

**Keywords** DESs · Desiccant regeneration · Electrodialysis · Ion flux · Dehumidification · Membrane

## 1 Introduction

Having established energy-saving potential of liquid desiccant air conditioning system (LDAC) over vapor compression technique, attention has been given to overcome limitations associated with liquid desiccant moisture handling mechanism. At

---

T. L. Oladosu (✉) · A. T. Baheta · P. B. Hussain  
Department of Mechanical Engineering, Universiti Teknologi PETRONAS, Bandar Seri Iskandar,  
32610 Seri Iskandar, Perak, Malaysia  
e-mail: [temidayooladosu@gmail.com](mailto:temidayooladosu@gmail.com); [temidayo\\_18000263@utp.edu.my](mailto:temidayo_18000263@utp.edu.my)

A. T. Baheta  
e-mail: [aklilu.baheta@utp.edu.my](mailto:aklilu.baheta@utp.edu.my)

the early stage of LDAC system development, desiccant carry-over due to direct contact between the liquid desiccant solution and the air stream instigates desiccant loss. This, in turn, increases operating costs and reduces air quality. Desiccant entrant into the conditioned air can be hazardous to human health depending on the chemical composition of the solution in question. The introduction of membrane into liquid desiccant configurations provided an acute remedy to carryover limitation.

Dehumidification and regeneration capability of few chemical compounds have been investigated for liquid desiccant suitability, and the most widely used are lithium chloride (LiCl), magnesium chloride ( $\text{MgCl}_2$ ), lithium bromide (LiBr), calcium chloride ( $\text{CaCl}_2$ ), and triethylene glycol (TEG) [1]. The halide salt solutions are corrosive to metallic equipment despite favorable thermodynamics and physiochemical properties. Potassium formate (HCOOK) is found to be less corrosive and quite cheap, and possesses a negative crystallization temperature as compared with aqueous salts solution. However, it is only suitable for high humidity [2, 3]. Qiu et al. [4] in the study of a novel air dehumidifier desiccant tested HCOOK solution experimentally and claimed over 25% decrease of relative humidity for highly humid air (>75% RH). However, it does not dehumidify efficiently if the air relative humidity is lower than 43% even if strong HCOOK desiccant solution is used.

The advent of ionic liquids and applicability to air conditioning system was a remarkable leap in the liquid desiccant air conditioning systems. Ionic liquids are non-corrosive, highly hygroscopic, non-volatility, and thermally stable [5]. Despite attractive thermodynamics and thermos-physical properties of ionic liquids, the high viscosity, biocompatibility, biodegradability, and toxicity are concerns to the research community [6]. The ongoing advancement in ionic liquids is deep eutectic solvent (DES) formulation. DES was first reported by Singh et al. [6] as greener solvent in lieu of ionic liquids. It is a compound of hydrogen bond donor and hydrogen bond acceptor with improved properties. DES has been applied in many applications such as biomedical, chemical separations, pharmaceutical,  $\text{CO}_2$  capturing and sequestration, and bio-fuel synthesis [7]. Investigating DES as potential liquid desiccants in air condition moisture handling applications would foster energy optimization in HVAC industries. Synthesizing novel DES and stringent investigation of available DES are crucial to their adaptability in liquid desiccant dehumidification systems.

Electrodialysis (ED) liquid desiccant regeneration has found to be more stable, energy-efficient, and cost-effective compared to the conventional solar thermal regeneration technique through a few theoretical and laboratory experimentation as reported in the literature [8–11]. The low-temperature regeneration capability of this method makes it favorably applicable in desiccant regeneration capable of working at ambient temperature which prevents re-cooling occurrence as it is in thermal desiccant regeneration. Therefore, in this study, we proposed binary DES as desiccant for LDAC systems. The investigation of DESs as desiccants in air conditioning system can overcome the limitation of the conventional liquid desiccant. Organic compounds of choline chloride and ethylene glycol in a molar ratio of 1:2 with melting temperature of 207.15 K [7], high hygroscopic, and reasonable viscosity were numerically investigated using electro-dialytic regeneration technique. The working fluid temperature, flow rate, and input voltage as performance influential factors were examined



relatively to the ion flux and concentration gradient across ion exchange membrane in an electro-dialytic cell. Finally, the parametric analysis was carried out to determine effective performance input parameters.

## 2 Materials and Methods

Binary DES of choline chloride and ethylene glycol solution with 17.5% weight of water was considered for this analysis. The self-diffusion coefficient of its ions was characterized by Pulsed Field Gradient, Nuclear Magnetic Resonance (PFG-NMR) [12, 13] was used as input parameters for the numerical computation in this work. The details of the other important parameters are tabulated in the input parameters section of Table 1.

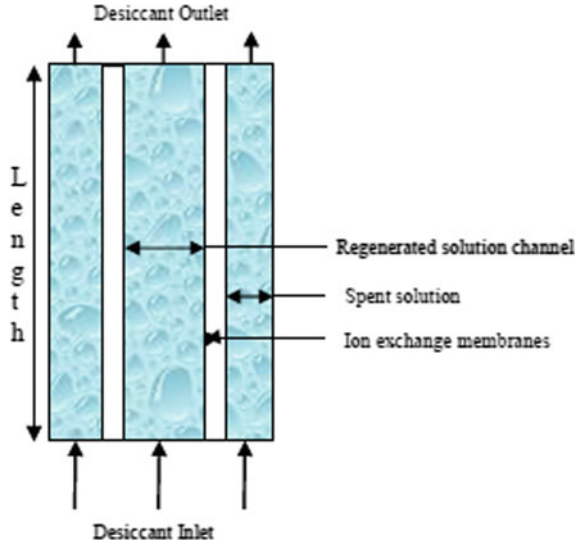
COMSOL Multiphysics commercial software was used to numerically solve a 2-D electro-dialytic separation problem. A steady-state, adaptive mesh refinement (AMR) analysis was executed on core i-7, hyperthreading processor computer resources. Figure 1 pictorially described the model used for this analysis while input parameters are illustrated in Table 1. The design of experiment synopsis derived from design expert tool was used in determining parametric couplings. Response surface method (Box–Behnken design) suggested seventeen different scenarios or parameter combination runs for this analysis. Each set of parametric combination was set as a study on

**Table 1** Input parameters and dialytic cell dimensions

Parameter	Value/Value range	Unit	Description
$V_{\text{tot}}^a$	0.5–2	V	Total potential drop over unit cell
DCH-A	6e–11	m <sup>2</sup> /s	Diffusion coefficient of aliphatic choline
DCH-OH	18e–11	m <sup>2</sup> /s	Diffusion coefficient of hydroxyl choline
DEG-OH	17.8e–11	m <sup>2</sup> /s	Diffusion coefficient of hydroxyl ethylene glycol
DEG-A	9e–11	m <sup>2</sup> /s	Diffusion coefficient of aliphatic ethylene glycol
$T^a$	293.15–333.15	K	Temperature
cMem	1000	mol/m <sup>3</sup>	Membrane charge concentration
$v_{\text{avg}}^a$	0.005–0.01	m/s	Channel average flow velocity
$L$	0.01	m	Channel length
$W_{\text{ch}}$	0.001	m	Channel width
$W_{\text{m}}$	1.3E–4	m	Membrane width
cEG_0	190	mol/m <sup>3</sup>	Inlet concentration of ethylene glycol
cEGOH_0	190	mol/m <sup>3</sup>	Inlet concentration of hydroxyl ethylene glycol
cCHOH_0	318	mol/m <sup>3</sup>	Inlet concentration of hydroxyl choline

<sup>a</sup>Varying parameters

Fig. 1 Electrolytic cell



COMSOL Multiphysics. Thereafter, the performance indices from numerical analysis were updated back as responses in the design expert to run statistical analysis of how overall performance is influenced by temperature, flow rate, and input power supply.

### 2.1 Governing Equations and Boundary Conditions

Fundamental physics of electrohydrodynamics and electrokinetics was solved for solution approximation based on finite element method (FEM). A multiphysics coupling of electrochemistry, tertiary current distribution, and Nernst–Planck tertiary electroneutrality enables diffusion mechanism analysis and mass conservation of the desiccant flowing through electrolysytic cells [14] were used in this analysis. Electrolysis (ED) analysis is governed by the following equations:

Nernst–Planck equation	$Ni = -Di \left[ \frac{dc_i}{dx} + z_i c_i \cdot \frac{F}{R.T} \cdot \frac{d\phi}{dx} \right] + c_i v$	(1)
Nernst–Planck equation with magnetic vector potential and electric field	$\frac{\partial c}{\partial t} = \nabla \left[ D \nabla c - uc + \frac{Dze}{K_B T} c (\nabla \phi + \frac{\partial A}{\partial t}) \right]$	(2)
Butler–Volmer equation	$i_{b-v} = i_o \cdot \left( \exp \left[ \frac{\alpha \cdot n \cdot F \cdot \mu}{R.T} \right] - \exp \left[ \frac{-\beta \cdot n \cdot F \cdot \mu}{R.T} \right] \right)$	(3)
Electrode kinetic equation	$i_m = \frac{i_{lim} \cdot i_{b-v}}{i_{lim} + i_{b-v}}$	(4)
Bruggeman coefficient equation for porous electrode	$i_i = -\sigma_{l,eff} \cdot \nabla \phi_l \cdot \sigma_{l,eff} = \epsilon_l^{1.5} \cdot \sigma_l$ $i_i = -\sigma_{l,eff} \cdot \nabla \phi_l \cdot \sigma_{l,eff} = \epsilon_l^{1.5} \cdot \sigma_l$	(5)

(continued)

(continued)

Continuity equation	$\frac{\partial p}{\partial t} + \nabla \cdot (\rho \bar{v}) = 0$	(6)
Naiver–Stokes conservation of momentum equation	$\frac{\partial \bar{v}}{\partial t} + (\bar{v} \cdot \nabla) \bar{v} = -\nabla p + \mu \nabla^2 \bar{v}$	(7)
Energy equation	$\rho C_p \frac{\partial T}{\partial t} + \rho C_p u \cdot \nabla T = \nabla \cdot (k \nabla T) + Q$	(8)

### 3 Results and Discussion

#### 3.1 Model Validation

Model validation was achieved through a comparative analysis between results obtained from our numerical model and reported results from models in the literature. In Zourmand et al. [15], analysis of brackish water desalination using NaCl solution, ion flux, and ion concentration outcome across membrane is found to comply with the trend of our result. However, little difference in total flux is a result of regenerated region interchange. Zourmand model described desalination while our model is for desiccant regeneration; therefore, the variation is justifiable. Further validation was done with Al-Jubainawi et al. [16] published outcome of both experimental and numerical analysis of desiccant regeneration using LiCl. The comparative plot of total salt flux of the simulated and experimental analysis was compared with DES total flux from our analysis which is shown in Fig. 2, and the DES flux at 0.005 m/s and 2 V is  $9.30E-03$  and  $3.59E-02$   $g\ m^{-2}\ s^{-1}$ , respectively. Ion flux trend plots are quite in agreement.

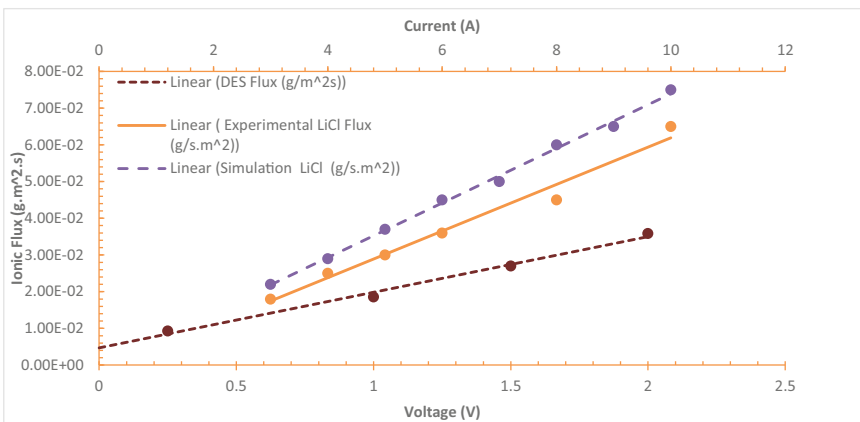
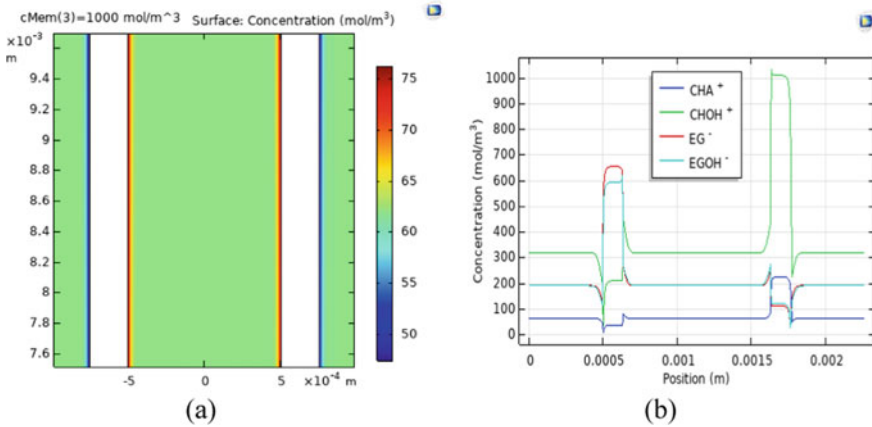


Fig. 2 Ionic flux trend of LiCl and DES desiccants



**Fig. 3** Concentration gradient representation of DES solution, **a** concentration gradient analyses and **b** species concentration profile ( $\text{mol/m}^3$ )

### 3.2 Concentration Profile and Species Flux Analysis

The regions near membrane show noticeable gradient in the ion concentration according to Fig. 3a which is the evidence of near boundary charge effect. The concentration at the diluate reduces while the regenerated solution at the middle channel gains ions concentration. Figure 3b represents average concentration of the ions that are involved in this analysis while the estimate of aliphatic and hydroxyl associated ions of choline illustrated moisture affinity of choline as a hygroscopic material. OH-CH has high mobility rate, and this is a clear indication of adverse effect of electroosmosis which is prevalent to electrodialysis separations method. EG- and OH-EG plots almost superimpose with a little lower value in OH-EG as shown in Fig. 3b. From this fact, one can predict how little EG ions can contribute to electroosmosis occurrence.

The concentration modulation at the membrane interface shows performance modification possibility as a result of contact area increment. The cell conductivity can be improved through spacers, turbulent raiser, and nano-particles embedded in the ion exchange membrane matrix. The effect of input voltage is also illustrated in Fig. 4, using  $\text{CHA}^+$  ion mobility to analyse the relationship between ions concentration at the outlet and energy input.

### 3.3 Performance Influential Factors Interaction

The parameters' interaction and the corresponding response revealed the optimum performance which can be used to configure electrodialyzer for DES regeneration towards energy saving design specification. The input power supply to the system

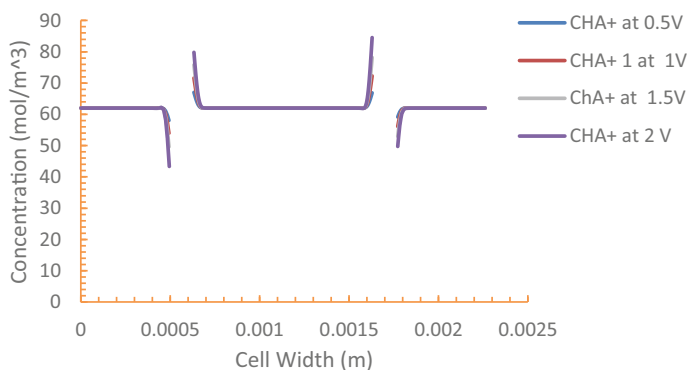


**Fig. 4** Concentration of  $\text{CHA}^+$  distribution of the solution through the ED cell at different applied voltages

above optimum voltage will lead to effect of over limiting current which is a major concern in electro dialysis systems. In Fig. 5a, the temperature increased from 293.15 to 333.15 K and  $\text{CHA}^+$  optimum ion concentration is found to be about  $74 \text{ mol/m}^3$  at about 1.25 V and 313.15 K. The increase in voltage has a very clear contribution to the DES regeneration. Figure 5b illustrates how resident time is crucial to electro dialysis operation. From the color legend of interaction contour plot, low entry velocity and low temperature are more favorable to the yield of ions concentration. Figure 5c compares input power and inlet velocity contributions to ion regeneration. The high yield of ions migration is obtainable at low inlet velocity and high input power. However, high input power beyond optimum threshold would lead to electroosmosis effect and as well as increasing solution dissociation.

### 3.4 3D Surface Analysis Plots

3D surface analysis, as shown in Fig. 6, illustrates three-dimensional parameters interaction view to corroborate established facts about parameters performance influence on the overall performance. Temperature has little effect on the performance compared with the contributing effect of velocity and input voltage, yet about 313.15 K is found to be the optimum temperature. The performance trend of voltage–temperature interaction predicts the regeneration technique to the best performance at low temperature.

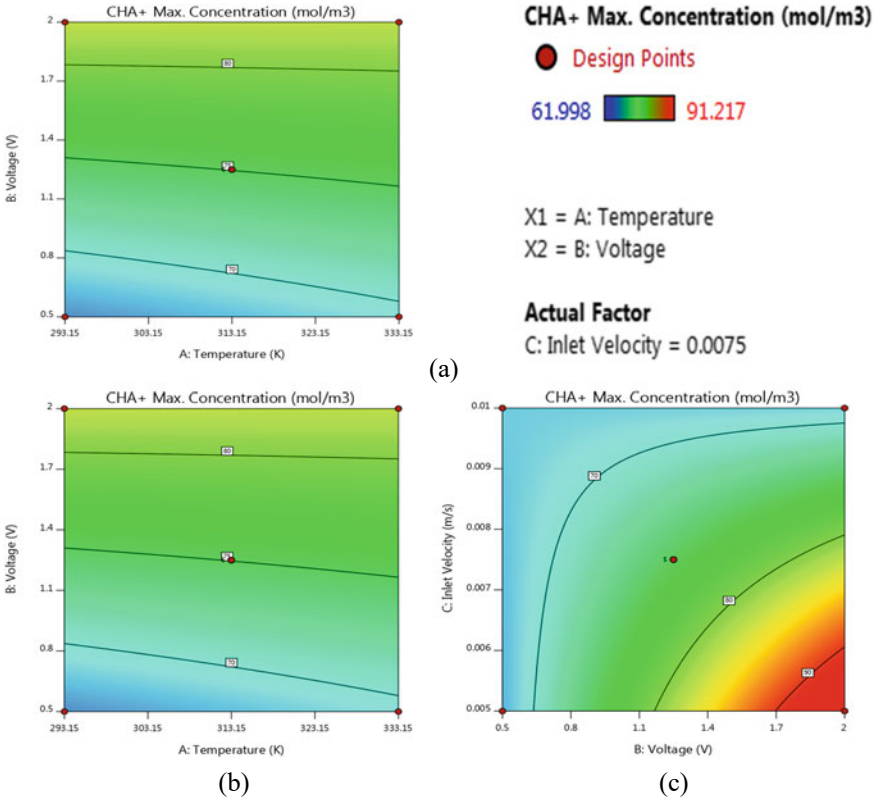


**Fig. 5** Parameter interaction and contour plots, **a** voltage–temperature interaction, **b** inlet velocity–temperature interaction, and **c** voltage–inlet velocity interaction

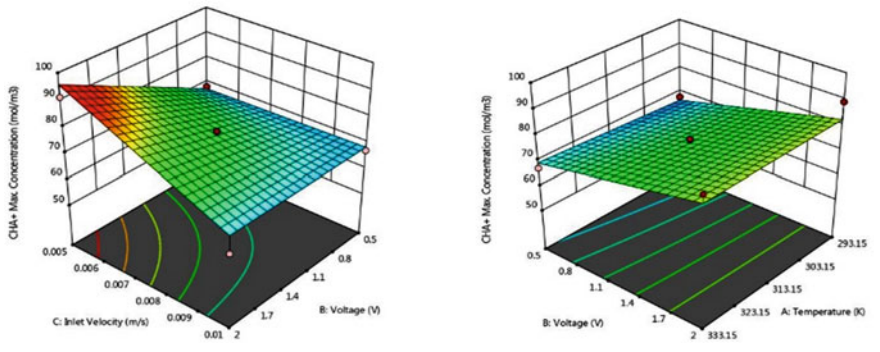


**Fig. 6** 3D Surface response analysis of parameters interaction, **a** voltage and inlet velocity and **b** temperature and voltage

## 4 Conclusions

Binary DES of choline chloride and ethylene glycol was numerically regenerated in electro-dialytic single cell. The parametric analysis of the performance influential factors was carried out for predicting energy-saving threshold for electro-dialysis regeneration of DES as a green solvent in liquid desiccant air conditioning system. The ion concentration of aliphatic choline species at 293.15 K and 0.0075 m/s desiccant velocity yielded about  $74 \text{ mol/m}^3$ . The response of the parametric interaction revealed high temperature insignificant to electro-dialytic cell performance. Therefore, electro-dialysis will perform optimally at low temperature. At 298.15 K, 0.005 m/s DES ion flux of  $3.59\text{E}-02 \text{ gm}^2/\text{s}$  is obtainable in the regeneration channel. The effect of joule heating, Debye ionic interaction, Lorentz force, turbulent raiser phenomenon, nonlinear electrokinetic phenomenon, double layer dipole effect, and membrane fouling in electro-dialytic regeneration still need more investigations. Finally, synthesizing novel DESs that can compete with conventional liquid desiccants in terms of thermo-physical properties and environmentally hazard-free capability will enhance air quality control device configurations.

**Acknowledgements** The authors gratefully acknowledge the support received from Universiti of Teknologi PETRONAS and financial assistance from grant (YUTP-FRG, 015LC0-082).

## References

1. Bubalo MC, Radošević K, Redovniković IR, Halambek J, Srček VG (2014) A brief overview of the potential environmental hazards of ionic liquids. *Ecotoxicol and Environ Saf* 99:1–12
2. Chen Z, Zhu J, Bai H, Yan Y, and , Zhang LJATE (2017) Experimental study of a membrane-based dehumidification cooling system. *Appl Therm Eng* 115:1315–1321
3. Chen S-Y, Soriano AN, Leron RB, Li M-H (2014) Density and vapour pressure of mixed-solvent desiccant systems (propylene glycol or dipropylene glycol or tripropylene glycol+ magnesium chloride+ water). *J Chem Thermodyn* 79:235–241
4. Sahlot M, Riffat SB (2016) Desiccant cooling systems: a review. *International J Low-Carbon Technol* 11:489–505
5. Qiu G, Riffat S, Zhu J (2008) Novel liquid regeneration system with solar evacuated tubes and evaporative bed. *J Energy Ins* 81:92–96
6. Singh BS, Lobo HR, Shankarling GS (2012) Choline chloride based eutectic solvents: Magical catalytic system for carbon–carbon bond formation in the rapid synthesis of  $\beta$ -hydroxy functionalized derivatives. *Catal Commun* 24:70–74
7. García G, Aparicio S, Ullah R, Atilhan M (2015) Deep eutectic solvents: physicochemical properties and gas separation applications. *Energy Fuels* 29:2616–2644
8. Chehayeb KM, Farhat DM, Nayar KG (2017) Optimal design and operation of electro-dialysis for brackish-water desalination and for high-salinity brine concentration. *Desalination* 420:167–182
9. Davidson SM, Andersen MB, Mani A (2014) Chaotic induced-charge electro-osmosis. *Phys Rev Lett* 112(12):128302
10. Nandigana VV, Aluru NR (2016) Avalanche effects near nanojunctions. *Phys Rev E*. 94(1):012402

11. Tufa RA, Rugiero E, Chanda D, Hnàt J, van Baak W, Veerman J, et al. (2014) Experimental and computational studies of choline chloride-based deep eutectic solvents. *J Membr Sci* 59(11):3652–3662
12. Perkins SL, Painter P, Colina CM (2019) Experimental and computational studies of choline chloride-based deep eutectic solvents. *J Chem Eng Data* 59:3652–3662
13. D'Agostino C, Gladden LF, Mantle MD, Abbott AP, Ahmed EI, Al-Murshedi AY, et al (2017) Correction: molecular and ionic diffusion in aqueous–deep eutectic solvent mixtures: probing inter-molecular interactions using PFG NMR. *Phys Chem Chem Phys* 19(2):1686–1686
14. Alizadeh H-R, Mortezaipoor H, Akhavan H-R, Balvardi M (2019) Performance of a liquid desiccant-assisted solar juice concentration system for barberry juice. *Solar Energy* 184:1–10
15. Zourmand Z, Faridirad F, Kasiri N, Mohammadi T (2015) Mass transfer modeling of desalination through an electrodialysis cell. *Desalination* 359:41–51
16. Al-Jubainawi A, Ma Z, Guo Y, Nghiem LD, Cooper P, Li W (2017) Factors governing mass transfer during membrane electrodialysis regeneration of LiCl solution for liquid desiccant dehumidification systems. *Sustain Cities Soc* 28:30–41



# Effects of Process Conditions on Calorific Value and Yield of Charcoal Produced from Pyrolysis of Coconut Shells



Rabi K. Ahmad, S. A. Sulaiman, M. Inayat, and Hadiza A. Umar

**Abstract** Charcoal, a black carbon residue, is mostly produced from the major conventional method where the biomass is allowed to be heated for several days in a kiln without studying the process condition. Most of the studies on the pyrolysis process focus on the liquid and gaseous by-products neglecting the solid to be used as a combustion fuel. For this study, charcoal was produced from coconut shells by the thermochemical conversion method of pyrolysis in a controlled nitrogen environment at temperatures of 300 °C, 400 °C, and 500 °C, and residence times of 15 min, 30 min, and 60 min. This was conducted to evaluate the process conditions' effects concerning the charcoal calorific value and yield. From the results obtained, a high process condition increases the calorific value, which results in a decrease in the charcoal yield. The lowest temperature gives a yield of 70.18 wt% and calorific value of 25.30 MJ/kg while the highest temperature produces a yield for as low as 26.57 wt% and a high calorific value of 30.15 MJ/kg. Furthermore, the charcoal yield tends to decrease from 51.99 to 33.10 wt% and the calorific value increases as the residence time increases from 15 to 45 min. Consequently, the thermal conversion undergone by the biomass may cause the changes of the quality parameters. Thus, charcoal can replace the use of fossil fuels because it presents energy content higher than that of lignite and similar to that of coal.

---

R. K. Ahmad (✉) · S. A. Sulaiman · M. Inayat · H. A. Umar  
Department of Mechanical Engineering, Universiti Teknologi PETRONAS, Bandar Seri Iskandar,  
32610 Seri Iskandar, Perak, Malaysia  
e-mail: [rabi\\_17000319@utp.edu.my](mailto:rabi_17000319@utp.edu.my)

R. K. Ahmad  
Department of Agricultural and Environmental Engineering, Bayero University Kano, Gwarzo  
Road, Kano 3011, Nigeria

## 1 Introduction

Wood, coal, charcoal, and many other plant-based materials (biomass) have been in use for decades as a primary source of fuel worldwide [1]. Fossil fuels are known to be the conventional sources of energy, and energy demand is increasing due to ever-increasing population all over the world [2], hence, the need for renewable energy. Almost up to 80% of all household energy requirements of developing countries are being fulfilled by the burning of these fuel sources. This burning of unprocessed biomass has well-characterized impacts on health and environmental issues [1].

The known and current practice of charcoal production is the traditional method of charcoal. It is the major method practiced all over, mostly in the growing countries. The biomass is allowed to be heated for several days. The charcoal piles, earth kilns, or pit kilns and pit methods are examples of the most widely used production methods of a charcoal [3, 4]. The downside of these processes includes, but not limited to, inefficiency caused by long processing time, poor processing control, low yield, high energy loss, and adverse change in the atmosphere [3, 5]. In combustion process, some portion of the feedstock is also used internally for the heat needed to start and drive the reaction [6]. The commercial charcoal usually contains 75% carbon, 20% volatile, and 5% ash in line with the production conditions and the type of raw material used for the process [3].

The emerging technology of thermochemical conversion method of pyrolysis is one of the relatively simple and inexpensive thermochemical technologies that transform biomass into a useful by-product (solid, liquid, or gas) in the absence or little oxygen [7–9]. In a laboratory-scale experiment, the processing variables are controlled, unlike the traditional method, and the controlled burning of the biomass is CO<sub>2</sub> neutral. Different studies have been conducted on charcoal produced from wood, bamboo, and agricultural wastes [3, 10–12].

Traditionally for thousands of years, the prime and common way for charcoal production is known to be the slow pyrolysis [13–15]. It favors the production of the solid. The process involves heating the biomass in an airtight reactor with a moderate temperature and a slow rate of heating with longer residence time [14–16]. The aim of the process results in a high-carbon solid product, liquid products, and combustible gases [6, 17]. Slow pyrolysis usually occurs at a low process time ranging between 5 and 30 min up to some hours and a temperature (200–500 °C) [8, 18] which gives a more solid product with about 35%, less liquid of 30%, and 35% combustible gases [15].

Pyrolysis process conditions greatly alter the structure and proportion of the slow pyrolysis by-products. The temperature has been identified as the main factor which influences the solid product [19]. The breakdown of heavy hydrocarbons, as a result of the high temperature, decreases the solid by-product, which increases liquid and gaseous products [6, 17, 20]. Therefore, a low temperature is suitable for the production of solid products. In the case of the residence time, a clear impression of its role with regard to solid by-product production is very challenging [20, 21] as other pyrolysis processing factors also hinder it. The available energy present in a material

is predicted by the energy density; as such it is an important factor for solid fuels. The energy present in parent biomass is less than the energy of the produced charcoal, because of the thermochemical conversion process undergone by the biomass [22]. The heating value of a product is affected by the operating temperature [15].

Despite the potential application of the pyrolysis solid products, the studies on the pyrolysis process mostly focus on the liquid and gaseous by-products. The solid product is mostly neglected and is used as a combustion fuel for other processes. Charcoal, which is the product of pyrolysis solid product, is used for several applications ranging from metallurgical and industrial fuel, in purification, cooking, medicine, and as a carbon source and so on. It is a cleaner, easier, and less smoky and smelly fuel than other biomass fuels made from any organic material, like the woods, straws, coconut shells, rice husks, and bones [23]. Charcoal is also obtained as a by-product from other thermochemical conversion methods, for the basis of other products production.

Coconut shells are used at a substantial scale for the production of charcoal [23] as it has certain advantages of adsorbing certain molecular species. This makes it a good feedstock for activated carbon that serves as a raw material in many industrial applications such as chemical mixing and preparation of pharmaceutical products, in preserving fruits and vegetables and many other applications. It also has a high amount of lignin which supports high solid by-products [20].

The objective of this work is to investigate the pyrolysis process conditions effect on the calorific value and yield of charcoal produced from coconut shells from thermochemical conversion methods of pyrolysis, and to compare the results with that of coal. This will highlight an appropriate selection of pyrolysis process parameters that will ascertain the quality of the charcoal in terms of its applications.

## 2 Methods

The coconut shell was used as a feedstock and the tools include machete, oven, hammer, granulator, digital scale, bomb calorimeter, and pyrolysis reactor. The process was carried out under different pyrolysis process conditions. The temperature was between 300 and 500 °C and residence time was between 15 and 45 min. These values were chosen as they were within the range of pyrolysis process condition as suggested by Basu [15].

### 2.1 *Sample Preparation and Experimental Procedure*

The coconut shells were chosen as the feedstock for the study, mainly because of their abundance and suitability for the pyrolysis process, ease of operation, low initial moisture content, less feedstock preparation time, density, and its energy capacity. The experiment was conducted at a biomass research laboratory, at Universiti Teknologi PETRONAS. Coconut outer fibrous portion was removed with a

machete, and the shells were crushed using a hammer and a granulator into the required size. ASTM E871-82 standard procedure [24] was used to dry the feedstock's sample to obtain its initial moisture content. The initial and final mass of the coconut shell was measured using a digital scale before and after drying. The dried and desired particle sizes of samples were used for the experiments. The amount of moisture content was calculated by:

$$MC\% = \frac{\text{Initial Weight} - \text{Final Weight}}{\text{Initial Weight}} \times 100 \quad (1)$$

The feedstock was weighed to 100 g for each experiment and was fed to an electric-powered reactor. It was heated gradually at different specific pyrolysis conditions according to experimental design. 20 mL/min of inert gas (nitrogen) was connected and purged to the pyrolysis process reactor for 10 min. The condensable and combustible gases pass through a cooling system before being channeled to a collection pipe. The pyrolysis reactor was switched off to collect the produced charcoal for further analysis. The ASTM standard procedure was used for the ash [25] and the calorific value [26] content determination. The yield of the charcoa ( $y$ ) was calculated by:

$$y = \frac{M_c - M_{\text{ash.c}}}{M_{\text{dry.b}} - M_{\text{ash.b}}} \times 100\% \quad (2)$$

where  $M_c$  represents the charcoal (kg),  $M_{\text{dry.b}}$  represents the oven-dry weight of biomass, and  $M_{\text{ash.c}}$  and  $M_{\text{ash.b}}$  are the ash content of the charcoal and biomass.

### 3 Results and Discussion

The moisture content and the ash content of the biomass were found to be 6.18% and 4.27%, respectively. The reaction conditions in a pyrolysis process are important factors. The operating process conditions greatly affect the production of the solid by-product and its quality [20]. Analysis with a kiln reactor shows that the moisture content of the biomass affects the yield of the charcoal and the residence time [3]. The calorific value for the entire charcoal sample is higher in comparison with its parent biomass as shown in Table 1. It was also higher with increasing the process conditions.

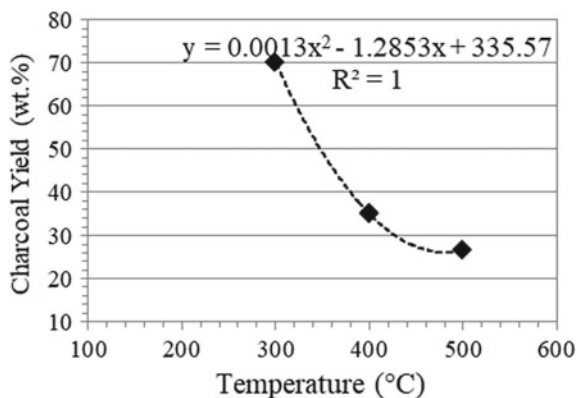
**Table 1** Yield and calorific value of the coconut shell biomass and the produced charcoal

Parameter		Calorific value (MJ/kg)	Yield (%)
Temperature (°C)	300	25.30	70.1
	400	27.83	34.99
	500	30.15	26.57
Residence time (min)	15	24.93	51.99
	30	26.36	33.57
	45	26.70	33.40

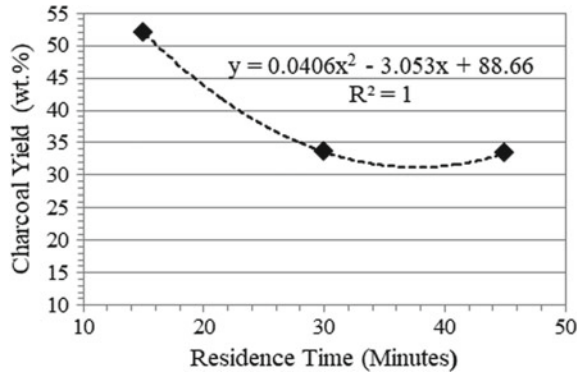
### 3.1 The Interrelation of the Operating Temperature and the Charcoal Yield

The lowest temperature (300 °C) achieved the highest yield of 70.18 wt% charcoal, while the yield was as low as 26.57 wt% at the highest temperature of 500 °C (Fig. 1). A polynomial relation between the temperature and the charcoal yield was observed which shows a significant difference. The volatiles present in the charcoal escapes as the process temperature is increased, which results in the yield decrease. This could be because at higher temperatures, the percent weight loss is high, thus, produces a lower yield. The thermal breakdown of hemicellulose and other extractives present within the feedstock occurs in a range of 190 and 270 °C, which may lead to the high yield at low temperatures [27, 28]. This trend agrees with those reported in other literature [29–32]. The interrelation between the yield and the temperature was established using Microsoft excel tool pack for regression. It was observed that when the operating temperature increases, the yield decreases as shown by the polynomial regression equation.

The biomass type and process conditions affect the solid by-product production [33]. Solid yield of 75 and 95 wt% were obtained from different biomasses after

**Fig. 1** Interrelation between the pyrolysis temperature and charcoal yield

**Fig. 2** The interrelation of charcoal yield and residence time



pyrolysis process at temperatures of 350 and 750 °C [29]. This result agrees with those of Khanna et al. [30].

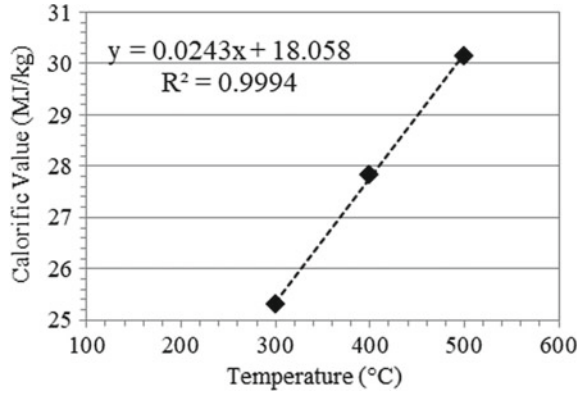
### 3.2 *The Interrelation of the Residence Time and the Charcoal Yield*

A negative correlation was shown by the two variables. The yield tends to decrease from 51.99 to 33.10 wt% at increasing time of 15 to 45 min (Fig. 2). It shows a polynomial relation among the observed variables. The characteristics and quality of the solid product are also affected by the residence time [20]. The relationship between the charcoal yield and residence time was established using Microsoft Excel tool pack for regression. The polynomial regression equation shows a decreasing charcoal yield pattern as the residence time increases. This was also observed in the results of different solid yields [29].

### 3.3 *The Relation Between Temperature and Calorific Value*

It was noted that the product's calorific value is affected by the operating temperature [15]. It was found that the calorific value tends to increase from 25.30 to 30.15 MJ/kg with increasing temperature. This could be as a result of the carbon enrichment in the charcoal as a result of the thermal conversion process. It was known that the charcoal chemical composition is strongly affected by the pyrolysis temperature [34]. The relationship between the temperature and calorific value was established using Microsoft Excel tool pack for regression. The linear regression equation shows that the calorific value tends to increase with increasing the temperature (Fig. 3).

**Fig. 3** The relation between the temperature and the charcoals calorific value



### 3.4 The Relation Between Residence Time and Calorific Value

The charcoal’s calorific value tends to increase from 24.93 to 26.70 MJ/kg with increasing residence time (Fig. 4). A slight difference in the calorific value was noted from residence time of 30 to 45 min. This could be as a result of the carbonization process being nearly completed. This peculiar observation was explained with the certainty that the energy compaction takes place in the organic proportion of the biomass only [29]. The relationship between the residence time and the charcoal calorific value was established using Microsoft Excel tool pack for regression. The polynomial regression equation shows that the calorific value tends to increase with increasing residence time, even though the difference in calorific value of 35 and 45 min residence time was slight (difference of 0.34 MJ/kg).

**Fig. 4** The relation between residence time and calorific value of the charcoal

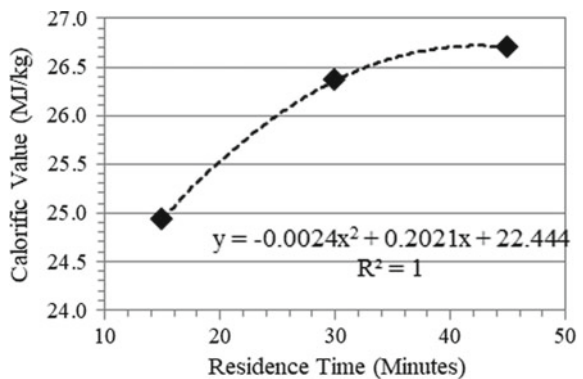


**Table 2** Calorific value of different biomass and the carbonaceous product

Fuel	Calorific value (MJ/kg)		References
	Feedstock	Carbonaceous product	
Coconut shell	19.40	30.15	Current study
Chestnut shell	15.49	25.86	[35]
Apricot stone	19.28	30.76	[35]
Hazelnut shell	18.33	29.08	[35]
Grapeseed	20.51	26.73	[35]
Rapeseed cake	8.34	28.4	[38]
Coal	24	31.7	[39, 40]
Lignite	14.6–19.3	22.4–29.5	[39, 41]

### 3.5 Comparison of the Calorific Value and Yield of the Charcoal with Other Studies

The result of the calorific value of different solid pyrolysis product samples is higher in comparison with its parent biomass as shown in Table 2. The present results are comparable with those on various carbonaceous materials such as apricot stone, hazelnut shell, grapeseed, and chestnut shell [35] that are used for various application. The calorific value of the biomass ranges from 15.49 MJ/kg to 20.51 MJ/kg, and the solid products are in the range of 25.86 MJ/kg and 30.76 MJ/kg, respectively. Apricot stone carbonized product shows the highest calorific value, whereas chestnut shell shows the lowest between the samples. In comparing the biomass fuel with the carbonaceous solid product, there is an increase in the calorific value. The produced charcoal can be characterized as a solid pyrolysis product with high calorific value. It can be utilized in various industrial applications as an alternative to solid non-renewable fuels [35]. This can be deduced from the calorific value of different types of coals from Table 2. A charcoal yield of 29.68% was obtained from wood waste [36], 36.9% blackbutt [37], and 38.40% from rapeseed [32] at a temperature of 400 °C. At 500 °C, the yield was 33.23% rapeseed [32] and blackbutt [37]. Similar results of 5.50% was found at 450 °C and residence time of 30 min [38] from rapeseed. The results are comparable with the current study at the same process condition.

## 4 Conclusion

The thermochemical conversion method of pyrolysis allows a clean production of charcoal with its simple, quick, and non-smoky technology. In the study, charcoal was produced from a coconut shell under different pyrolysis conditions. The relation between the pyrolysis conditions and the output variables was observed. The charcoal yield tends to decrease with increasing process conditions. On the contrary,



increasing the pyrolysis conditions increases the charcoal's calorific value. From this experimental study, it was observed that low pyrolysis conditions maximize the yield and minimize the calorific value and vice versa. This was also confirmed by some research on rapeseed, wood waste, and blackbutt. Therefore, the relatively high reported results show that coconut shells can be carbonized effectively at low pyrolysis conditions to obtain a high charcoal yield, and at high pyrolysis conditions to obtain a high energy value. The shells will serve as a promising source of energy using the pyrolysis method as it can replace the use of fossil fuels.

**Acknowledgements** The authors gratefully acknowledge the financial support of Universiti Teknologi PETRONAS for this research work.

## References

1. Action P (2009) Fuel from the fields: charcoal from agricultural waste 44(871954)
2. Sulaiman SA, Inayat M, Basri H, Guangul FM, At Naw SM (2016) Effect of blending ratio on temperature profile and syngas composition of woody biomass co-gasification. *J Mech Eng Sci (JMES)* 10(2):2177–2187
3. Tippayawong N, Saengow N, Chaiya E, Srisang N (2010) Production of charcoal from woods and bamboo in a small natural draft carbonizer. *Int J Energy Environ (IJEE)* 1(5):911–918
4. Clarke GC (2010) Analysis of charcoal production systems in Guyana. In: Clarke environmental consulting, pp 57–69
5. Patil KN, Ramana PV, Singh RN (2000) Performance evaluation of natural draft based agricultural residues charcoal system. *Biomass Bioenergy* 18(2):161–173
6. Williams PT, Besler S (1996) The influence of temperature and heating rate on the slow pyrolysis of biomass. *Renew Energy* 7(3):233–250
7. Mettler MS, Vlachos DG, Dauenhauer PJ (2012) Top ten fundamental challenges of biomass pyrolysis for biofuels. *Energy Environ Sci* 5(7):7797–7809
8. Mohan D, Pittman CU Jr, Steele PH (2006) Pyrolysis of wood/biomass for bio-oil: a critical review. *Energy Fuels* 20(3):848–889
9. Puig-Arnavat M, Bruno JC, Coronas A (2010) Review and analysis of biomass gasification models. *Renew Sustain Energy Rev* 14(9):2841–2851
10. Msuya N, Masanya E, Temu AK (2011) Environmental burden of charcoal production and use in Dar es Salaam, Tanzania. *J Environ Prot* 2:1364–1369
11. Nisgoski S, Magalhães WLE, Batista FRR, França RF, de Muñiz GIB (2014) Anatomical and energy characteristics of charcoal made from five species. *Acta Amazonica* 44(3):367–372
12. Sugumaran P, Seshadri S (2009) Evaluation of selected biomass for charcoal production. *J Sci Ind Res* 68:719–723
13. Jafri N, Wong WY, Doshi V, Yoon LW, Cheah KH (2018) A review on production and characterization of biochars for application in direct carbon fuel cells. *Process Saf Environ Prot* 118:152–166
14. Yaman S (2004) Pyrolysis of biomass to produce fuels and chemical feedstocks. *J Energy Convers Manage* 45(5):651–671
15. Basu P (2010) Biomass gasification and pyrolysis: practical design and theory. Elsevier, The Boulevard, Langford Lane Kidlington, Oxford, OX5 1GB, UK. All rights reserved
16. Qian K, Kumar A, Zhang H, Bellmer D, Huhnke R (2015) Recent advances in utilization of biochar. *Renew Sustain Energy Rev* 42:1055–1064
17. Bulushev DA, Ross JR (2011) Catalysis for conversion of biomass to fuels via pyrolysis and gasification: a review. *Catal Today* 171(1):1–13

18. Balat M, Balat M, Kırtay E, Balat H (2009) Main routes for the thermo-conversion of biomass into fuels and chemicals. Part 1: pyrolysis systems. *J Energy Convers Manage* 50(12):3147–3157
19. Budai A et al (2014) Surface properties and chemical composition of corncob and *Miscanthus* biochars: effects of production temperature and method. *J Agric Food Chem* 62(17):3791–3799
20. Tripathi M, Sahu JN, Ganesan P (2016) Effect of process parameters on production of biochar from biomass waste through pyrolysis: a review. *Renew Sustain Energy Rev* 55:467–481
21. Fassinou WF, Van de Steene L, Toure S, Volle G, Girard P (2009) Pyrolysis of *Pinus pinaster* in a two-stage gasifier: influence of processing parameters and thermal cracking of tar. *Fuel Process Technol* 90(1):75–90
22. da Silva MF, Fortes MM, Sette CR Jr (2018) Characteristics of wood and charcoal from eucalyptus clones. *Floresta e Ambiente* 25
23. Bhattarai T (1998) Charcoal and its socio-economic importance in Asia: prospects for promotion. In: Regional training on charcoal production, Pontianak, Indonesia
24. ASTM-E871-82 (2013) Standard test method for moisture analysis of particulate wood fuels. ASTM International, pp 1–2
25. A.-E. 01 (2015) Standard test method for ash in biomass. ASTM International, pp 1–3
26. ASTM-D4809-18 (2018) Standard test method for heat of combustion of liquid hydrocarbon fuels by bomb calorimeter. ASTM International, pp 1–10
27. White RH (1986) Effect of lignin content and extractives on the higher heating value of wood. *Wood Fiber Sci* 19(1):440–446
28. F. Forestry Department (1987) Simple technologies for charcoal making. Food and Agriculture Organization of the United Nations, Rome, Italy
29. Ronsse F, Van Hecke S, Dickinson D, Prins W (2013) Production and characterization of slow pyrolysis biochar: influence of feedstock type and pyrolysis conditions. *Bioenergy* 5(2):104–115
30. Khanna R et al (2017) Novel multidimensional carbons from structural transformations of waste lignin: a low temperature pyrolysis investigation. *Fuel Process Technol* 166:312–321
31. Demirbas A (2004) Effects of temperature and particle size on bio-char yield from pyrolysis of agricultural residues. *J Anal Appl Pyrol* 72(2):243–248
32. Ucar S, Ozkan AR (2008) Characterization of products from the pyrolysis of rapeseed oil cake. *Bioresour Technol* 99(18):8771–8776
33. Cao D, Sun Y, Wang G (2007) Direct carbon fuel cell: fundamentals and recent developments. *J Power Sources* 167(2):250–257
34. Guizani C, Jeguirim M, Valin S, Peyrot M, Salvador S (2019) The heat treatment severity index: a new metric correlated to the properties of biochars obtained from entrained flow pyrolysis of biomass. *Fuel* 244:61–68
35. Özçimen D, Ersoy-Meriçboyu A (2010) Characterization of biochar and bio-oil samples obtained from carbonization of various biomass materials. *Renew Energy* 35(6):1319–1324
36. Oyedun OA, Lam KL, Hui CW (2012) Charcoal production via multi stage pyrolysis. *Chin J Chem Eng* 20:455–460
37. Somerville M, Jahanshahi S (2015) The effect of temperature and compression during pyrolysis on the density of charcoal made from Australian eucalypt wood. *Renew Energy* 80:471–478
38. Karaosmanoglu ECF (2000) Rapeseed charcoal: production and characterization. *Energy Sour* 22(7):625–630
39. Cooper BR, Ellingson WA (1984) The science and technology of coal and coal utilization. Plenum Press, New York
40. Wu T, Gong M, Lester E, Hall P (2013) Characteristics and synergistic effects of co-firing of coal and carbonaceous wastes. *Fuel* 104:194–200
41. Demirbas A (2008) Relationships proximate analysis results and higher heating values of lignites. *Energy Sour Part A Recovery Utilization Environ Eff* 30(20):1876–1883

# Palm Kernel Shell as Potential Fuel for Syngas Production



Hadiza A. Umar, S. A. Sulaiman, Mior Azman B. Meor Said,  
and Rabi K. Ahmad

**Abstract** This study investigated the elemental content, proximate analysis, morphological nature, calorific value and ultimate analysis of the *Elaeis guineensis* palm kernel shell (PKS), to determine its suitability for use in syngas generation. The elemental content was studied using the X-ray fluorescence spectroscopy (XRF) analysis, and the presence of elements like Ca, Fe, Si, K and P with their oxides was detected. Field emission scanning electron microscopy (FESEM) with energy dispersive electron microscopy (EDX) was applied to detect the structural properties of PKS, with details of light surface elements. The PKS has a porous structure for a free flow of air and volatile matter, and carbon and oxygen were seen as the major surface elements, 64% and 29.4%, respectively. It had a high calorific value of 18.84 MJ/kg. The ultimate analysis revealed suitable contents of carbon 48.4%, oxygen 45% and hydrogen 5.85%. The proximate analysis showed the presence of high volatile matter of 73.4%, low moisture of 6.0% and ash content of 5.8%. Overall, PKS has a good prospect to be used as a fuel for syngas production via gasification.

## 1 Introduction

The global energy situation is facing a lot of challenges resulting from high population boom, increasing urbanisation, industrialisation and commercialisation which all translate into high energy demand. The effect of such increasing activities is the depletion of fossil fuel resources, increased environmental and air pollution, global warming, poor water quality and healthy lifestyle deterioration [1]. This has been the twenty-first-century global challenge and has forced both developed and developing countries to look for alternatives to cater for their energy demands sustainably [2, 3]. Biomass has been identified by several researchers as a source of green energy

---

H. A. Umar (✉) · S. A. Sulaiman · M. A. B. M. Said · R. K. Ahmad  
Department of Mechanical Engineering, Universiti Teknologi PETRONAS, Bandar Seri Iskandar,  
32610 Seri Iskandar, Perak, Malaysia  
e-mail: [ummihadiza@gmail.com](mailto:ummihadiza@gmail.com)

H. A. Umar · R. K. Ahmad  
Faculty of Engineering, Bayero University Kano, PMB 3011 Kano, Nigeria

© Springer Nature Singapore Pte Ltd. 2020  
S. S. Emamian et al. (eds.), *Advances in Manufacturing Engineering*, Lecture Notes  
in Mechanical Engineering, [https://doi.org/10.1007/978-981-15-5753-8\\_25](https://doi.org/10.1007/978-981-15-5753-8_25)

that is eco-friendly, renewable and sustainable. Thus, biomass conversion means such as gasification, pyrolysis and combustion have been embarked on as means of harnessing renewable energy.

Malaysia happens to be among the top palm oil producers globally, as such, 90% of its biomass comes from oil palm waste. The palm kernel shell (PKS) being among the principal biomass, obtained after oil extraction [4], occurs as an abundant secondary product of the oil palm processing factories in Malaysia. The annual expansion in the production yield of oil palm led to the ever increasing rate of palm kernel shell (PKS) biomass accumulation. This important biomass that is usually used as boiler fuel in oil palm industries for steam generation has the potential to be used for bioenergy generation by the production of syngas through the method of gasification. Therefore, there is a need to undertake a physicochemical analysis to prove the suitability of this fuel for use as a gasification feedstock. In 2018, about 5.4 million ha of oil plantation was cultivated, with about 97,803,919 million tonnes (Mt) of harvested fruits processed to remove oil. According to the established ratio of biomass to processed fruit rate [5–8], about 4.57 Mt of PKS was obtained while the other biomass was 22.82 Mt of oil palm frond (OPF), 7.53 Mt of empty fruit bunch (EFB), 7.92 Mt of mesocarp fibre (MF) and 65.5 Mt of palm oil mill effluent (POME). The PKS is predominantly utilised for combustion purposes, usually as boiler fuel for steam generation [9]. It has the potential of being used as a fuel for thermochemical conversion due to its lignocellulosic nature. The degradation pattern of PKS was investigated, and it was reported to have a slow decomposition trend as a result of its high lignin content [10–12]. In another research, PKS was characterised based on its physicochemical properties and was reported to have sufficient calorific value of 17 MJ/kg, possessed pores having a volume of 0.0473 cm<sup>3</sup>/g with a specific surface area of 239 m<sup>2</sup>/g, low moisture content and high volatile matter. Overall, it was also proven to be a suitable fuel for bioenergy generation.

This study intends to conduct a physicochemical study on PKS, which involves its chemical constituents, physical morphology, energy content and degradation characteristics to determine its potential for use as a fuel for syngas generation.

## 2 Methodology

### 2.1 Sample Preparation

The palm kernel shell (PKS) sample was collected from FELCRA Berhad Nasaruddin, an agricultural organisation that specialises on palm oil production situated in Bota, Lumut highway Perak, Malaysia. The PKS was washed and air-dried for 24 h, and later dried for a period of 12 h in an oven set at 105 °C ± 5. The sample was then crushed using a granulator to reduce its size; it was later ground to powder form and sieved to 250 µm size. The PKS powder was stored in an airtight container to avoid moisture absorption.



**Fig. 1** Images of raw PKS **a** original form, **b** granulated form and **c** ground powder 250  $\mu\text{m}$

## 2.2 Characterisation Methods

The methods that were employed for the characterisation of the PKS sample were ultimate analysis, field emission scanning electron microscope (FESEM) with energy dispersive X-ray spectroscopy XRD, proximate analysis, X-ray fluorescence (XRF) and calorific value. The ultimate analysis was used to find out the percentage composition of carbon (C), hydrogen (H), nitrogen (N) and sulphur (S) present in the sample. It was conducted according to ASTM D3176-15 standard by using the Leco CHNS-932 model analyser. The weight percentages of the elements were reported directly while oxygen was determined by difference [13]. The proximate analysis gives the amount of carbon content (FC), volatile matter (VM), moisture (M) and ash content. This was conducted according to the TGA analyser (Pyris-1 TGA) based on ASTM E1131-98 standard test method. The energy content, otherwise referred to as the calorific value, was determined using the Leco AC-350 bomb calorimeter based on ASTM D240-17. The FESEM-EDX and XRF analyses were used to get the elemental distribution and composition (elemental and oxide) of the PKS. The XRF analysis was conducted with SUPRA 55VP model field emission scanning

electron microscopes (FESEM) analyser to obtain the inorganic constituents of the biomass samples, in combination with energy dispersive X-ray spectroscopy (EDX) in non-conducting specimens mode.

### 3 Results and Discussions

The ultimate and proximate results of the PKS sample analysis along with the calorific value are shown in Table 1 based on weight percentages.

#### 3.1 *Ultimate and Proximate*

The ultimate analysis is very crucial in determining the suitability of biomass as fuel for gasification or thermal energy conversion [17]. It expresses the make-up of the hydrocarbon fuel with reference to its basic elements of C, H, N, S and O [18]. The level of carbon in a given sample determines the calorific value of the fuel; the more the carbon level, the more the calorific value. A high content of carbon in fuel makes it suitable for power generation. From Table 1, the carbon content of PKS was high (48.37%) when compared with other biomasses like RH and CS, of carbon, both having 40.87% and 46.93%, respectively. The carbon content of the wood was quite higher than that of PKS, 50.3%. The nitrogen and sulphur contents of the biomass are required at low levels; larger quantities of such compounds make the fuel unsuitable for power generation as it leads to the release of harmful gases  $\text{SO}_x$  and  $\text{NO}_x$  to the atmosphere. The levels of nitrogen and sulphur in the PKS are low, 0.6% and 0.1%, respectively, and comparing with other biomasses, PKS has less of these elements when compared to CS. However, wood biomass has less of the elements with nitrogen 0.07% and sulphur 0%. These exhibit the capabilities of these fuels including PKS as environmental-friendly fuels.

The rates of ash, moisture, FC and VM contents are given by the proximate analysis. The level of moisture in a biomass should be less than 30% as a requirement for good calorific value and satisfactory ignition capability [19]. More so, less ash content is also required as a prerequisite to slagging and agglomeration free gasification process. This ensures cutting down of expenses in terms of ash-handling system requirement. The moisture content of the PKS was 6% higher than that of CS 2.29% but lower than that of rice husk 9.12%. The ash content was also comparable; PKS has 5.80% ash higher than that of CS and wood which were 0.83% and 0.5%, respectively. However, rice husk has much ash content about 15% compared to the other biomasses. The volatile matter of PKS was high, 73.40%, and comparable to the other biomasses such as RH 61.9%, CS 81.67% and wood 84.3%. High volatile matter coupled with low ash content is required to achieve gasification at low temperature range of 600–750 °C low [20, 21]. The degradation trend of the PKS is shown in Fig. 2; it displays the weight loss of PKS with change in temperature. The initial

**Table 1** Ultimate, proximate and calorific values of PKS

Biomass sample	Ultimate				Proximate				Calorific value MJ/kg	References	
	Carbon	Hydrogen	Oxygen <sup>a</sup>	Nitrogen	Sulphur	MC	VM	Ash			FC
	PKS	48.37	5.86	45.07	0.60	0.10	6.00	73.40			5.8
PKS	46.05	5.14	45.40	0.62	0.14	7.52	69.35	2.67	20.46	18.96	[14]
Rice husk (RH)	40.87	5.59	53.09	0.45	0.0	9.12	61.90	15.0	17.89	15.3	[15]
Coconut shell (CS)	46.93	3.96	48.21	0.71	0.19	2.29	81.67	0.83	17.50	19.43	[3]
Wood	50.3	6.4	42.7	0.07	0.0	5.70	84.3	0.50	15.20	20.3	[16]

<sup>a</sup>By difference

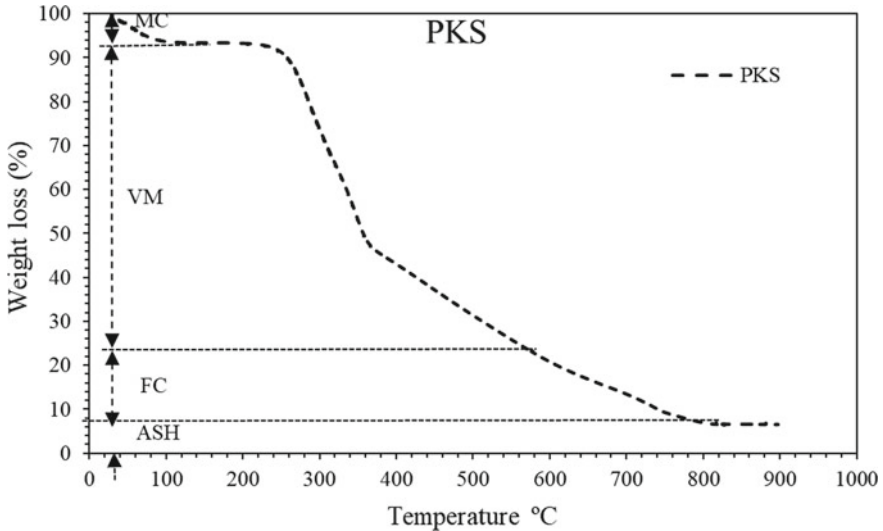


Fig. 2 Percentage weight loss of PKS with temperature

curve represents the removal of moisture content; the continuous curve that succeeds depicts the release of volatile matter. After that step comes a steady reducing slope indicating degradation of fixed carbon content. An almost straight line marks the end of the curve which indicates the ash content.

### 3.2 Calorific Value

The energy content, otherwise the calorific value, was obtained to be 18.84 MJ/kg using a bomb calorimeter as shown in Table 1. It was higher than that of RH 15.3 MJ/kg which may be due to the difference in moisture contents. The low moisture content in the PKS 6.00% led to higher calorific value obtained. In the case of high moisture content, extra energy is required to remove the excess moisture, thereby reducing the energy level of the biomass. Both CS and Wood had higher calorific value than the PKS, while RH had a lower value. However, all the biomasses were in the range that is suitable for use as fuel gas.

### 3.3 XRF and EDX Analyses

The chemistry of PKS is given by the XRF result as presented in Table 2. The PKS is composed of both elements and oxides of the elements. The main elements with the highest quantity are Ca with about 62% followed by Fe, Si, K, P, Cl, Cr, Mg and S



**Table 2** Metal and metal oxides present in PKS

Metal	Concentration (wt%)	Metal oxide	Concentration (wt%)
Ca	61.9	CaO	58.0
Fe	15.0	Fe <sub>2</sub> O <sub>3</sub>	12.9
Si	7.00	SiO <sub>2</sub>	11.6
K	5.99	K <sub>2</sub> O	5.33
P	1.94	P <sub>2</sub> O <sub>5</sub>	3.42
Cl	1.66	Cl <sub>2</sub> O	1.18
Cr	1.51	Cr <sub>2</sub> O <sub>3</sub>	1.23
Mg	1.35	MgO	1.76
S	1.25	SO <sub>3</sub>	2.35
Ni	0.827	NiO	0.572
Al	0.799	Al <sub>2</sub> O <sub>3</sub>	0.985
Mn	0.223	MnO	0.199
Cu	0.212	CuO	0.182
Zn	0.136	ZnO	0.113
Mo	0.112	MoO <sub>3</sub>	0.0862
Sr	0.0618	–	–
–	–	RuO <sub>3</sub>	0.0721
–	–	Rb <sub>2</sub> O	0.0641

with 15%, 7%, 5.99%, 1.94%, 1.66%, 1.51%, 1.35% and 1.25%, respectively. Other elements that were present in traces include Ni, Al, Mn, Cu, Zn, Mo and Sr which constituted 2.371% of the PKS biomass. In terms of metal oxides, the major one was CaO with 58.0%, Fe<sub>2</sub>O<sub>3</sub> with 12.9% and SiO<sub>2</sub> with 11.6% followed by K<sub>2</sub>O, P<sub>2</sub>O<sub>5</sub>, SO<sub>3</sub>, MgO, Cr<sub>2</sub>O<sub>3</sub> and Cl<sub>2</sub>O with 5.3%, 3.42%, 2.35%, 1.76%, 1.23% and 1.18%, respectively. The metal oxides present in trace constituted 2.2732%, and they include Al<sub>2</sub>O<sub>3</sub>, NiO, MnO, CuO, ZnO, MoO<sub>3</sub>, RuO<sub>3</sub> and Rb<sub>2</sub>O. The predominant metals in PKS are the Ca, Fe and their oxides, and high amount of such elements suppresses agglomeration, thereby making PKS a suitable fuel for gasification [22]. Usually presence of SiO<sub>2</sub> and K<sub>2</sub>O leads to formation of a compound K<sub>2</sub>O-SiO which may provoke agglomeration, although they are not in high quantity in PKS, but the presence of CaO, Fe<sub>2</sub>O<sub>3</sub>, MgO and Al<sub>2</sub>O<sub>3</sub> counterbalances their effects.

### **3.4 Field Emission Scanning Electron Microscopy (FESEM) with Energy Dispersive X-Ray (EDX) Spectroscopy**

It should be noted that XRF can only detect elements with atomic number 12 to 92 that is magnesium to uranium. Therefore it does not quantify light elements such as

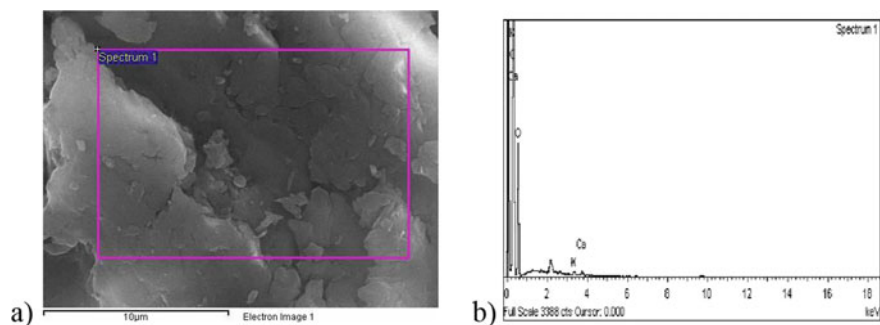


**Fig. 3** a FESEM image b EDX spectrum of raw PKS

**Table 3** Analysed elements on the EDX spectrum

Element	Weight %	Atomic %
C	64.01	70.46
O	35.57	29.40
K	0.17	0.06
Ca	0.24	0.08

nitrogen, oxygen, carbon, fluorine and sodium. Conversely EDX gives the predominant percentage elemental composition analysed on the surface of the spectrum. Thus such major elements like the carbon and oxygen are shown on the EDX spectrum. The image and spectrum is given by Fig 3, while Table 3 gives the EDX analysed surface elements.

The images obtained from the FESEM analysis show that PKS is composed of microstructure with adequately distributed micropores. This will allow for sufficient flow of air and liquids. The structural build-up of a biomass fuel is very crucial to the design of thermal reactors as it influences fluidisation behaviour and feeding system performance during the biomass gasification process [23]. More so, the presence of pores influences the release of volatile matter during thermal conversion processes. The presence of pores in PKS is shown in Fig. 4, which indicates the suitability of converting PKS to gaseous fuels via thermochemical conversion. Enlargement of the pore size and macropores takes place at pyrolysis temperature [24] which eases the release of volatiles.

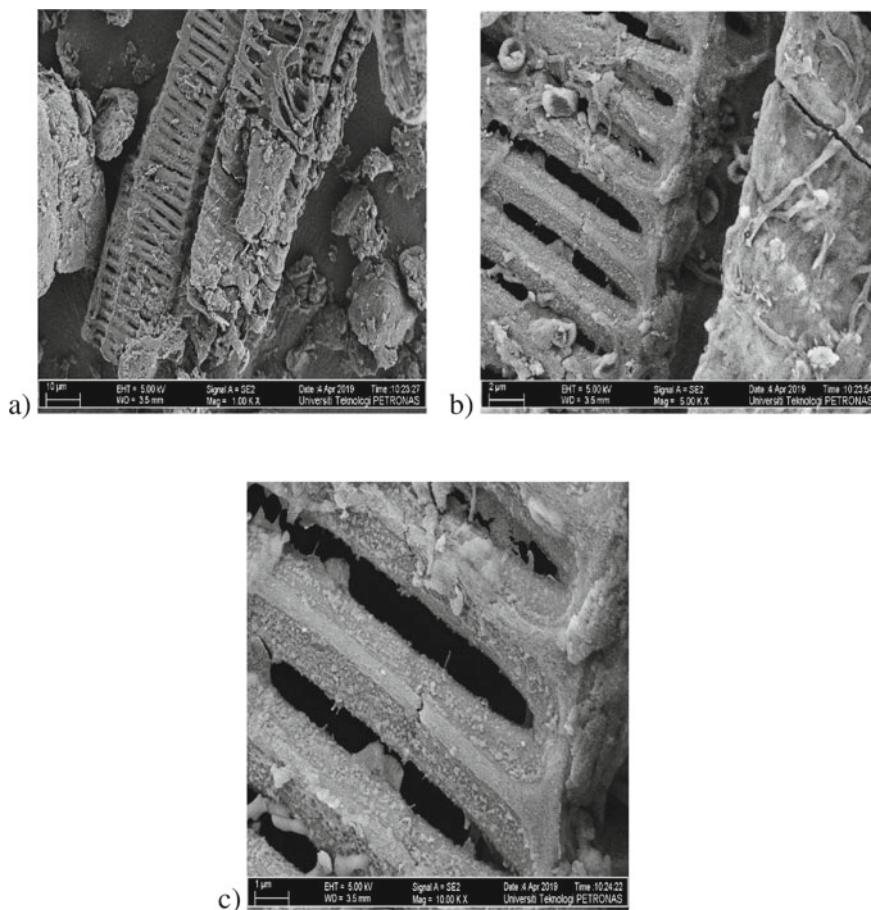


**Fig. 4** PKS FESEM images at different magnifications **a** at 1000 $\times$ , **b** at 5000 $\times$  and **c** at 10,000 $\times$

## 4 Conclusions

The characterisation of palm kernel shells has been conducted based on thermal, chemical and morphological properties in order to determine its feasibility for use as a gasification fuel. The PKS had a remarkable calorific value, 18.84 MJ/kg, its chemical constituents as given by the ultimate analysis suit a gasification fuel requirement having sufficient carbon 48.37%, hydrogen 5.86% and oxygen 45.07% with minute amounts of sulphur and nitrogen. The proximate analysis depicted the PKS to be having low moisture content, 6.0%, very high volatile matter, 73.40%, with less ash content, 5.8%. The XRF analysis showed that it also contained less amount of metals that make a fuel prone to causing sintering and agglomeration, thereby leading to a cost-effective gasification process free of ash-handling requirements. From the XRF analysis, CaO and FeO happen to be the major oxides with 58.0%

and 12.9%, respectively. The surface structure of the PKS is a porous one making it viable for adequate fluid passage and release of volatile matter. The EDX detected the major light elements, carbon and oxygen, as 64.01% and 35.57%, respectively. These properties make the PKS a suitable fuel for the generation of syngas via gasification and for use in other thermochemical processes.

**Acknowledgements** The authors wish to show their appreciation to Universiti Teknologi PETRONAS for the assistance rendered financially under the grant 0153AA-E06 (YUTP) and technically to conduct this study.

## References

1. Gollakota ARK, Kishore N, Gu S (2018) A review on hydrothermal liquefaction of biomass. *Renew Sustain Energy Rev* 81:1378–1392
2. Thiagarajan J, Srividhya PK, Balasubramanian P (2018) Thermal behavior and pyrolytic kinetics of palm kernel shells and Indian lignite coal at various blending ratios. *Bioresour Technol Rep* 4:88–95
3. Inayat M, Sulaiman SA, Naz MY (2018) Thermochemical characterization of oil palm fronds, coconut shells, and wood as a fuel for heat and power generation. In: MATEC web of conferences, vol 225. EDP Sciences, p 01008
4. Loh SK (2017) The potential of the Malaysian oil palm biomass as a renewable energy source. *Energy Convers Manage* 141:285–298
5. Basiron Y (2000) *Advances in oil palm research: Malaysian palm oil board*, v. 2
6. Basiron Y, Weng CK (2004) The oil palm and its sustainability 16(1)
7. Kong S-H, Loh S-K, Bachmann RT, Rahim SA, Salimon J (2014) Biochar from oil palm biomass: a review of its potential and challenges 39:729–739
8. Liew WL, Kassim MA, Muda K, Loh SK, Affam AC (2015) Conventional methods and emerging wastewater polishing technologies for palm oil mill effluent treatment: a review 149:222–235
9. Subramaniam V, Ma AN, Choo YM, Meriam NMN (2008) Life cycle inventory of the production of crude palm oil—a gate to gate case study of 12 palm oil mills 20(June):484–494
10. Ma Z, Chen D, Gu J, Bao B, Zhang Q (2015) Determination of pyrolysis characteristics and kinetics of palm kernel shell using TGA–FTIR and model-free integral methods 89:251–259
11. Luangkiattikhun P, Tangsathitkulchai C, Tangsathitkulchai M (2008) Non-isothermal thermogravimetric analysis of oil-palm solid wastes 99(5):986–997
12. McKendry P (2002) Energy production from biomass (part 2): conversion technologies. *Bioresour Technol* 83(1):47–54
13. Guangul FM (2013) Gasification of OPF with preheated inlet air. PhD, Mechanical Engineering, Universiti Teknologi Petronas
14. Acevedo J, Posso F, Durán J, Arenas E (2018) Simulation of the gasification process of palm kernel shell using Aspen PLUS. *J Phys Conf Ser* 1126(1):012010
15. Fauzan RFS et al (2018) Torrefaction and degradative solvent extraction as means of processing rice husk waste 32(3):3460–3468
16. Link S, Yrjas P, Hupa L (2018) Ash melting behaviour of wheat straw blends with wood and reed. *Renew Energy* 124:11–20
17. Sulaiman SA, Bamufleh HS, Tamili SNA, Inayat M (2016) Characterization of date palm fronds as a fuel for energy production 30(3):465–472
18. Basu P (2010) *Biomass gasification and pyrolysis: practical design and theory*. Academic Press

19. McKendry P(2002) Energy production from biomass (part 3): gasification technologies 83(1):55–63
20. Hussain M, Tufa LD, Yusup S, Zabiri H (2019) Thermochemical behavior and characterization of palm kernel shell via TGA/DTG technique 16:1901–1908
21. Khan Z, Yusup S, Ahmad MM, Rashidi NA (2014) Integrated catalytic adsorption (ICA) steam gasification system for enhanced hydrogen production using palm kernel shell 39(7):3286–3293
22. Guangul FM, Sulaiman SA, Raghavan VR (2012) Elemental and thermo-chemical analysis of oil palm fronds for biomass energy conversion. In: AIP conference proceedings, vol 1440, no 1. AIP, pp 1197–1205
23. Garcia-Perez M et al (2008) Fast pyrolysis of oil mallee woody biomass: effect of temperature on the yield and quality of pyrolysis products 47(6):1846–1854
24. Apaydin-Varol E, Pütün E, Pütün AE (2007) Slow pyrolysis of pistachio shell 86(12–13):1892–1899

# Potential Roles of Artificial Intelligence in the LCI of Renewable Energy Systems



Paul A. Adedeji, Stephen A. Akinlabi, Nkosinathi Madushele,  
and Obafemi O. Olatunji

**Abstract** Energy revolution from the conventional fossil fuels to clean energy is fast gaining traction with renewable and clean energy sources blazing the trail on the global scale. This has consequentially reduced electricity prices in certain countries and reduced carbon footprints in both manufacturing and service industries. Besides the advantages of these clean energy technologies, the assessment of their life cycle has recently gained more attention with life cycle inventory playing a major role. Life cycle inventory is a critical component in life cycle assessment. However, a life cycle inventory study is as accurate as the data used. This study presents a roadmap to the use of artificial intelligence (AI) techniques in life cycle inventory (LCI). The data chain for efficient local resident data availability for LCA studies was considered with a focus on AI integration. In addition, a framework for the use of AI in LCI was developed. The study concluded that it was possible to proffer solution to LCI data unavailability problem using AI with the joint support of public and private partners.

**Keywords** Artificial intelligence · Energy systems · Life cycle assessment · Life cycle inventory · Renewable energy sources

## 1 Introduction

The quest to mitigate climate change and ensure sustainable environment is a topmost concern among the nations. This mantra has necessitated a revolution towards clean energy for industrial (service and manufacturing systems), residential and non-residential systems. As part of this revolution, a paradigm shift has been experienced in the energy sector from the use of fossil fuels to the use of clean fuels. It is believed that the energy of the future will be a nexus of clean and renewable energy sources

---

P. A. Adedeji (✉) · N. Madushele · O. O. Olatunji  
Department of Mechanical Engineering Science, University of Johannesburg, Johannesburg,  
South Africa  
e-mail: [pauladedeji2k5@gmail.com](mailto:pauladedeji2k5@gmail.com)

S. A. Akinlabi  
Department of Mechanical Engineering, Walter Sisulu University, Mthatha, South Africa

if sustainability, efficiency and intermittency issues are resolved. Renewable energy source exploration has lately increased on the global scale with developing countries rising up to this global challenge [1, 2]. For example, Kenya, a developing country in Africa with one of the highest wind potentials [3], has the largest wind farm in Africa with 310 MW of capacity. Besides, the country added 11 MW of geothermal energy source to the national energy mix [ref]. As much as the electricity sector is gradually going green and clean, there is a need to evaluate the environmental impacts of these technologies to ensure their environmental sustainability. Life cycle assessment has been a potent tool in evaluating this, with life cycle inventory (LCI) being a crucial part of the process and data collection being the most difficult part of the LCI process. However, in the era of the fourth industrial revolution, the question of how artificial intelligence can help in real-time data collection to improve the LCI process is the focus of this discussion. The energy of the future is envisaged to be a nexus of clean energy from multiple sources. Harnessing the prowess of artificial intelligence in these energy sources predicates their effectiveness, cost and operational efficiency, and sustainability.

Life cycle assessment (LCA) has its origin from material flow accounting towards ensuring sustainability. This was further stepped to include emissions and their potential impacts, and other latent aspects of sustainability [4]. LCA is a methodology employed in quantifying the environmental impacts of products and processes from point of cradle to grave [5, 6]. The LCA tool is both a quantitative analysis technique built on factual information and an integrated model of natural and judgement process that evaluates the importance of different life cycle stages and emissions relative to environmental concerns [7]. This tool has been widely used in product and process development to minimize carbon footprints and associated environmental impacts. While many studies applied LCA on operational systems [8–10], some advocate performing the study at the product or process design stage [11]. All these approaches are aimed at ensuring a sustainable environment.

Life cycle inventory (LCI) is an integral part of the LCA process which is concerned with the data to be used for the LCA process. With growth of intelligence both in systems and in systems of systems, the integration of artificial intelligence in LCI studies will upscale the usefulness of real-time process data from real-time forecasting to real-time life cycle analysis. In this study, we examined the role of LCA in renewable energy (RE), the LCI and its associated processes. This study further develops a framework, which integrates artificial intelligence into life cycle assessment towards solving the problem of data unavailability.

## 2 LCA Studies in Renewable Energy System

Renewable energy is apparently globally preferred to the non-renewable energy due to associated demerits of the non-RE technologies for power generation in different spaces. Renewable energy technologies have, however, been viewed as not completely “green” in nature [12]. Many have argued that Anthropocene emerged

from industrial revolutions; however, industrial evolution is concomitant to energy revolution. Hence, a bottom-up process-oriented and impact-conscious mitigation strategy is considered the best for effective management of the environment and climate. The sustainability of the RE system has lately become a growing concern with more studies evolving at component, system and process levels. Common to harvesting many renewable energy sources is rather environmental impact assessment (EIA) as this is mandatory for the development of such projects with significant sizes.

According to Fava [13], rather than LCA being the only tool to address environmental performance, it should rather be seen as one of the tools to be used in acquiring a holistic understanding of a system, product or process. For example, in a wind farm or hydropower station, an LCA conducted on its sub-systems or the whole system itself reveals key areas for a more efficient use of resources. However, LCA will not be an appropriate method for a study whose goal is to address workers' concerns regarding health and toxic effects, but rather an ecological risk assessment would be more appropriate. A holistic perspective of a renewable energy system can rather be obtained by integrating LCA with several other relevant tools.

One of the main focuses of life cycle assessment (LCA) is to enable informed decision regarding operations, processes and products at strategic management level [14]. The question of the integration point between artificial intelligence and LCA in the next generation of clean energy has to be well established.

LCA in renewable energy sources has received less attention in the literature; however, recent concerns about how green the "green" energy is have instigated few studies in this area [15–17]. In addition, the quest for energy sustainability in the future has placed the renewable and clean energy sources at the frontline of the energy nexus of the future. Their increased use in electricity generation, transportation and other energy-intensive processes also contributes to the LCA paradigm shift towards them. For example, the importance of LCA of renewable energy sources was explained by Singh et al. [18]. The study emphasises the significance of environmental, social and economic sustainability of renewable energy resources, thus looking beyond their pros to their cons. Pehnt [15] also developed a dynamic approach to the LCA of renewable energy sources and compared the results with that of conventional fossil fuels. The study concluded that even though the emissions of greenhouse gases exist in the renewable energy resources investigated, this percentage is very low compared to the conventional sources. The relevant environmental impacts of renewable energy in the future of the German energy mix were projected to be 20% for electricity, 15% of reference mix for heat and 55% for future diesel cars. The findings in this study do not establish a clear verdict for or against renewable energy relative to other environmental impacts. Hence, regardless of the percentage of environmental impacts contributed by renewable energy resources, its effect requires critical investigation towards preventing an accumulated effect of these impacts on the biosphere.



### 2.1 Energy System Components

Harnessing renewable energy resources (Fig. 1) in their crude form requires the use of energy harvesting technologies. These technologies are made of components and sub-systems, which all constitute the functional system. For example, the wind turbine generator (WTG) is made of several components and sub-systems, which synergize together to convert the mechanical energy from the wind to active electrical energy. Similarly, the solar photovoltaic (PV), concentrated solar power (CSP) and geothermal energy sources are made up of the same. The effectiveness and efficiency of these systems during their useful life are hinged on their maintenance.

Many of these energy harvesting systems now come with real-time monitoring integrated systems for real-time condition monitoring. For example, the WTG used in large wind farms is a massive system of systems, which consists of hydraulic, gearbox, electrical wiring systems in the nacelle. These systems all have sensors which monitor their conditions, and data from these are logged within a defined resolution of time. Similarly, the solar, geothermal and biomass plants all have similar condition monitoring systems from which the data evolving can be further harvested towards use for LCI process.

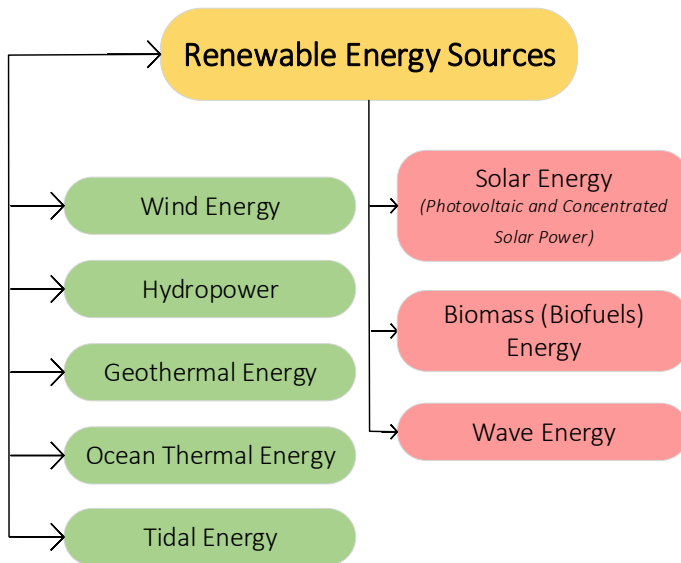


Fig. 1 Renewable energy sources

### 3 Life Cycle Inventory and Its Associated Stages

Extraction of inputs and outputs to the product or service system forms the crux of LCI process. Obtaining relevant data for the system process being examined is one of the major challenges of LCA studies. There exists paucity of data for inventory databases to draw from. Moreover, many of the available data do not capture dynamics of the system under study, which makes sensitivity analysis and process alternatives for environmental improvements technically impossible [19].

System modelling in LCA studies involves a trade-off between tractability and complexity. In ensuring tractability of every model, modellers often trade-off tractability for complexity, thereby making the system models simple. These simple models do not often represent the actual reality and often less describe the system being analysed. Many critical upstream and downstream processes are often relaxed due to unavailability of data [14]. The new generation of renewable energy systems generates real-time operational data intermittently, which can be harnessed using sensor technology.

#### 3.1 Life Cycle Inventory Stages

Primal to LCA studies is the life cycle inventory (LCI). The LCI process involves quantification of inputs and outputs into a system including the material and energy flow across the system. Basically, the LCI processes are divided into four stages as shown in Fig. 2.

The first stage involves identification of the whole products or processes involved in the LCA. The second stage focuses on the collection of data from various processes involved. The third stage defines the system boundaries, and the fourth stage adjusts the inputs and outputs to the system functional unit [20]. The data collection stage, however, has been identified as the most difficult and time-consuming step in the LCI process [20]. It often involves collection of a large data set from relevant companies, which includes activity data for assessing both background and foreground processes

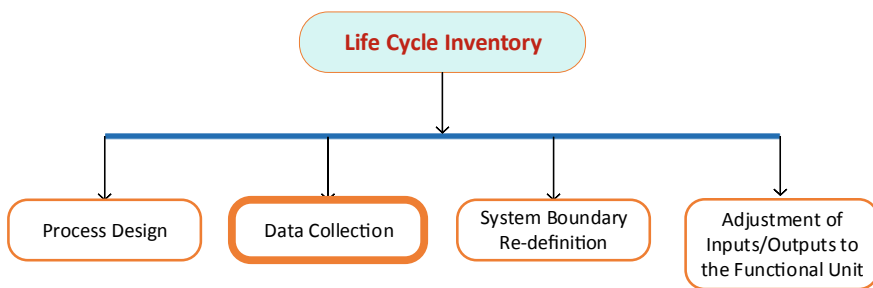


Fig. 2 The LCI processes with emphasis on the data collection process

[5]. These data are highly fundamental to an efficient LCA study and are mostly found in common LCA databases. Significant developments have evolved on databases for LCA studies over the years; however, these data are based on industry averages. Besides the effort required in the data collection process, the challenge of data quality and archiving has substantial impacts on the reliability of LCA results [5].

Over the years, the quest to replace classical decision-making technologies with intelligent ones in production systems has dominated the century. Artificial intelligence (AI) refers to computational techniques capable of demonstrating human cognition at the highest level and performing at such [21]. There are numerous agents associated with AI, some of which include machine learning, cognitive intelligence and deep learning [21]. These agents possess highly dynamic algorithms capable of imitating the human behaviour in terms of decision-making. They possess ability to study patterns in highly complex problems and make logical inference with a high level of precision. The use of AI has gained significant development in industrial systems for continuous production within the past few decades so much that its smartness is fast going out of control [22]. This is seen in the automated factories, intelligent robots for material handling and hazardous unit processes, and complex nexus of systems requiring precision in decision-making. In the last decade, the emergence of the Fourth Industrial Revolution (4IR) characterized by the evolution of cyber-physical systems has necessitated advanced manufacturing technologies across the globe [23]. This revolution has concomitantly translated into increased data complexity, velocity and size [24]. This is presently having significant influence on the energy sector as observed in the new generation of energy systems. A paradigm shift from the obsolete power generating plants to the smart power plants is observed not only in the renewable energy space but also in the non-renewable energy space.

## **4 Integrating Artificial Intelligence into Life Cycle Inventory—Proposed Roadmap**

Artificial intelligence techniques consist of integrated white and black box models, which study hidden patterns and features within data towards intelligent decision-making. Its integration into LCI offers high prospects in evaluating environmental impacts of global and local concerns in LCA studies of renewable energy systems. A roadmap towards integration of artificial intelligence in LCI of renewable energy systems is illustrated in Fig. 3. The critical points in the data flow are further explained briefly in this section.

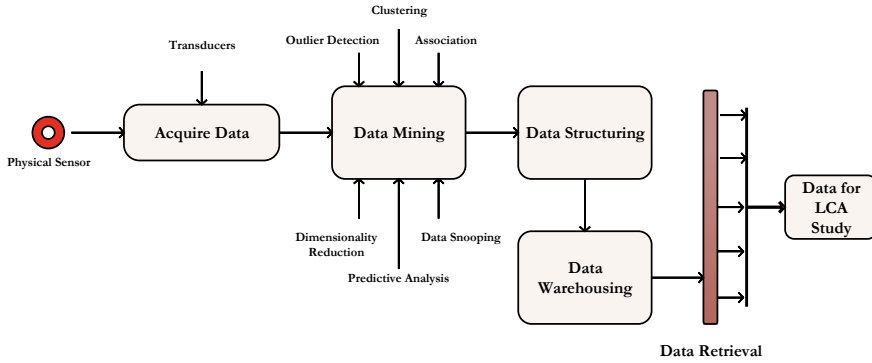


Fig. 3 Data flow from acquisition to retrieval with artificial intelligence integration

### 4.1 Data Acquisition

This forms a crucial step towards an effective LCI in LCA studies. Effective LCI in LCA is dependent on the availability, accuracy and recency of the data used. Data in this category can be obtained from primary and secondary sources. Primary source data can be obtained via the use of sensor technologies. One of the major contributors to the avalanche of data we have today and years to come is the sensor technologies. These technologies transmit data in real time according to a communication protocol from devices to which they are embedded.

In recent times, continuous production processes employ the supervisory control and data acquisition (SCADA) systems. Through the SCADA, data acquisition, monitoring, control and over-limit triggers are ensured in continuous production systems [25]. These systems, through sensor technology, generate an avalanche of data of process parameters and conditions in real time whose warehousing offers a high prospect for the future of LCA studies of such systems. The use of sensor technology with real-time data logging offers a great potential for future LCA studies enabling all processes to be incorporated in the product or process life cycle study. Many LCA studies are static studies. They define system processes as static processes without considering dynamics of the process. Assumptions are often made in life cycle software that every process works as expected. An example is seen in modelling the transportation of raw materials or end products to end-users. Breakdowns and corrective maintenance processes which might have occurred along the process, as well as materials used up in such processes, are often never accounted for. The dynamics of the process obtainable from real-time data of upstream and downstream processes enables a good sensitivity analysis to be performed at the interpretation phase in the course of the product or process LCA. Besides from the possibility of the system dynamics, the availability of region-specific data is ensured, when process machineries are manufactured with future LCA study in view.

However, a critical challenge in sensing continuous processes and real-time data logging is data storage and structuring. Humongous volume of data is bound to

be generated from these processes in real time leaving a critical challenge to data management. Management of this big data can be achieved using the proposed framework in Fig. 3. Notable in big data studies are their five Vs. These include the volume, velocity, variety, veracity and value. These five concepts therefore require an intelligent solution approach towards ensuring that they become advantages and not disadvantages in the LCI process.

The secondary data are process data archived in plant books. To increase the availability of these data, digital copies of these data are recommended to be structured under which product, process and plant-specific data can be stored for future retrieval.

### 4.2 Data Mining

Making deductive information from avalanche of data requires studying the patterns, trends, anomalies and correlations, from a large data set. Data mining forms the crux of knowledge discovery process (KDP). The process follows two techniques: the descriptive and the predictive approaches [26]. Shown in Fig. 4 are the examples of data mining techniques. In renewable energy systems, the predictive and descriptive techniques have significant applications towards acquiring useful information from the database of the acquired data for the LCA process. Predictive analysis from the data pool gives a projection of the equipment status at specific instance which will increase the novel field of “Predictive LCA” studies. Several intelligence algorithms in the literature have proved efficient in predictive analysis like artificial neural network (ANN), hybrid and standalone adaptive neuro-fuzzy inference system (H-ANFIS/S-ANFIS) and support vector machine (SVM), [27–30].

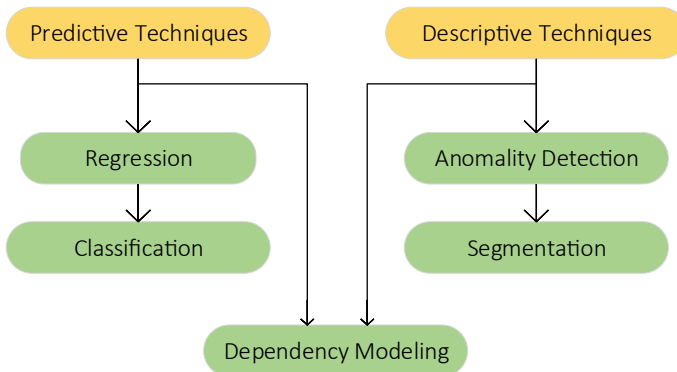


**Fig. 4** Some data mining techniques

### **4.3 Data Structuring**

Data structuring is highly essential for archiving and easy reference at the point of use. This technique involves the use of local and central servers to optimize data volume and variety. The data from renewable energy harvesting equipment are often resident on the SCADA system. The present SCADA system, however, presents real-time status of the equipment or farm for informed decision-making. The SCADA system requires a database management system (DBMS) of which the relational DBMS is often used. The relational database monitoring system (DBMS) stores data in the form of tables consisting of rows and columns for easy and rapid retrieval [31]. Integrating the structured query language (SQL) with the SCADA system enables data from the SCADA's DBMS to effectively communicate with other enterprise software. Prospect of communication between LCA software and the SCADA system will offer a high prospect in localized LCA studies, thus reducing the problem of LCI data unavailability.

The conventional means of data structuring has proved effective over the years; however, an integration of AI methodologies in this process offers a higher prospect in reducing throughput and increasing accuracy. Mined useful data can be intelligently clustered to associate related data with one another in the system. Product and process with high level of similarities can be structured together for easy drill down during the retrieval stage.

### **4.4 Data Warehousing and Retrieval for LCA Studies**

This is one of the crucial stages in data preparation for intended purpose. Data warehousing has been observed to be the centre for the architecture of the future information systems. A data warehouse is defined as an integrated decision support database whose content emanates from numerous operational databases [32]. The warehouse architecture is tripartite vis-à-vis the backend data extraction process, the warehouse and the front-end data access process. A data warehouse takes into consideration the subject-oriented, integrated, time-variant and non-volatile concepts of data. An LCI for renewable energy sources requires data from numerous databases. It is expected of a data warehouse to contain current detailed data, older detailed data, a lightly summarized data, a highly summarized data and a metadata [33]. Efficient data warehousing for easy accessibility is highly essential for real-time data availability for LCI in LCA studies.

An efficient front-end data retrieval process is highly essential for efficient and effective LCI for LCA studies where accuracy and speed of retrieval help to minimize the throughput of the process. At data retrieval process, it should be ensured that data quality is maintained such that specific data for intended purpose are made available without trade-off between dimensionality and quality.

## 5 Conclusion

Environmental sustainability of emerging renewable energy sources has become a global concern. LCA tool has proven to be highly efficient in quantifying these impacts. However, its procedure consists of several processes in which LCI forms a significant part. In this study, we identified the integration points between LCI process and artificial intelligence towards ensuring availability of quality and reliable data for the LCA process. The data value chain was studied from data acquisition to data retrieval. Real-time data collection and processing using artificial intelligence techniques was proposed in this study at specific echelons of the data chain. AI techniques can be used in data mining and structuring processes, which we believe will reduce throughput of the process, increase data quality, enhance data structuring and warehousing, and increase efficiency in data retrieval.

## References

- Olatunji OO, Akinlabi SA, Ayo OO, Madushele N, Adedeji PA, Fatoba SO (2019) Drivers and barriers to competitive carbon footprint reduction in manufacturing supply chain: a brief review. In: 2nd International conference on sustainable materials processing and manufacturing, vol 35. Elsevier B.V., Amsterdam, pp 992–1000. <https://doi.org/10.1016/j.promfg.2019.06.047>
- Olatunji OO, Ayo OO, Akinlabi S, Ishola F, Madushele N, Adedeji PA (2019) Competitive advantage of carbon efficient supply chain in manufacturing industry. *J Clean Prod* 238:1–9
- Kazimierczuk AH (2019) Wind energy in Kenya: a status and policy framework review. *Renew Sustain Energy Rev* 107:434–445. <https://doi.org/10.1016/j.rser.2018.12.061>
- Helling RK (2017) The role of LCA in sustainable development, vol 1. Elsevier, Amsterdam. <https://doi.org/10.1016/B978-0-12-409548-9.10063-6>
- Bicalho T, Sauer I, Rambaud A, Altukhova Y (2017) LCA data quality: a management science perspective. *J Clean Prod* 156:888–898. <https://doi.org/10.1016/j.jclepro.2017.03.229>
- Hanbury O, Vasquez VR (2018) Life cycle analysis of geothermal energy for power and transportation: a stochastic approach. *Renew Energy* 115:371–381. <https://doi.org/10.1016/j.renene.2017.08.053>
- Hertwich EG, Hammitt JK (2001) A decision-analytic framework for impact assessment part I: LCA and decision analysis. *Int J Life Cycle Assess* 6:5–12. <https://doi.org/10.1007/BF02977588>
- Dunmade I (2014) Lifecycle assessment of a stapling machine. *Int J Eng Technol* 4:12. <https://doi.org/10.14419/ijet.v4i1.3813>
- Tang L, Yokoyama T, Kubota H, Shimota A (2014) Life cycle assessment of a pulverized coal-fired power plant with CCS technology in japan. *Energy Procedia* 63:7437–7443. <https://doi.org/10.1016/j.egypro.2014.11.780>
- Mbohwa C (2013) Life cycle assessment of a coal-fired old thermal power plant. In: Proceedings of World congress on engineering 2013, I
- Madushele N, Adedeji PA (2019) Plausibility of assessing environmental impacts of a domestic biogas digester in the design stage. *Environ Prog Sustain Energy* 1–8. <https://doi.org/10.1002/ep.13228>
- Gibson L, Wilman EN, Laurance WF (2017) How green is ‘green’ energy? *Trends Ecol Evol* 32:922–935. <https://doi.org/10.1016/j.tree.2017.09.007>
- Fava JA (1997) LCA: concept, methodology, or strategy? *J Ind Ecol* 1:8–10. <https://doi.org/10.1162/jiec.1997.1.2.8>

14. Frankl P, Rubik F (2000) Life cycle assessment in industry and business. <https://doi.org/10.1007/978-3-662-04127-7>
15. Peht M (2006) Dynamic life cycle assessment (LCA) of renewable energy technologies. *Renew Energy* 31:55–71. <https://doi.org/10.1016/j.renene.2005.03.002>
16. Jensen JP (2019) Evaluating the environmental impacts of recycling wind turbines. *Wind Energy* 22:316–326. <https://doi.org/10.1002/we.2287>
17. Polit DJ, Maldonado D, Dávalos D (2016) Solar might not always be a green source of energy. *Procedia Eng* 145:611–621. <https://doi.org/10.1016/j.proeng.2016.04.051>
18. Singh A, Olsen SI, Pant D (2013) Importance of life cycle assessment of renewable energy sources. *Green Energy Technol* 1–11. [https://doi.org/10.1007/978-1-4471-5364-1\\_1](https://doi.org/10.1007/978-1-4471-5364-1_1)
19. Wallace RJ, Marvuglia A, Benetto E, Tiruta-Barna L (2014) A new approach to optimization with life cycle assessment: combining optimization with detailed process simulation. In: *Lecture notes in computer science (including subseries Lecture notes in artificial intelligence and Lecture notes in bioinformatics)*, 8581, LNCS, pp 707–720. [https://doi.org/10.1007/978-3-319-09150-1\\_52](https://doi.org/10.1007/978-3-319-09150-1_52)
20. Nabavi-Pelesaraei A, Rafiee S, Mohtasebi SS, Hosseinzadeh-Bandbafha H, Chau K (2018) Integration of artificial intelligence methods and life cycle assessment to predict energy output and environmental impacts of paddy production. *Sci Total Environ* 631–632:1279–1294. <https://doi.org/10.1016/j.scitotenv.2018.03.088>
21. Salehi H, Burgueño R (2018) Emerging artificial intelligence methods in structural engineering. *Eng Struct* 171:170–189. <https://doi.org/10.1016/j.engstruct.2018.05.084>
22. Hood D (2018) Is artificial intelligence a threat or a saviour? *Globe Mail Inc.*, pp 18–19. [https://doi.org/10.1016/S1353-4858\(18\)30046-1](https://doi.org/10.1016/S1353-4858(18)30046-1)
23. Integrated CY, Manufacturing I (2017) Perspectives and enablers. *Engineering* 3:588–595. <https://doi.org/10.1016/J.ENG.2017.04.009>
24. Torrecilla JL, Romo J (2018) Data learning from big data. *Stat Probab Lett* 136:15–19. <https://doi.org/10.1016/j.spl.2018.02.038>
25. Sanislav T, Căpătână D, Dancea O (2007) Application of data mining techniques to improve a Scada system's performance. *IFAC* 40. <https://doi.org/10.3182/20070709-3-RO-4910.00036>
26. Mohan S, Ramsundram N (2013) Data-mining models for water resource applications. *ISH J Hydraul Eng* 19:211–218. <https://doi.org/10.1080/09715010.2013.798905>
27. Olatunji O, Akinlabi S, Madushele N, Adedeji PA (2019) Estimation of municipal solid waste (MSW) combustion enthalpy for energy recovery. *EAI Endorsed Trans Energy Web* 6
28. Adedeji P, Madushele N, Akinlabi S (2018) Adaptive neuro-fuzzy inference system (ANFIS) for a multi-campus institution energy consumption forecast in South Africa. In: *Proceedings of the International conference on industrial engineering and operation management, Washington, DC, USA, 27–29 Sept 2018*, pp 950–958
29. Adedeji PA, Akinlabi S, Ajayi O, Madushele N (2019) Non-linear autoregressive neural network (NARNET) with SSA filtering for a university energy consumption forecast. In: *16th Global conference on sustainable manufacturing for global circular economy, 2019*, pp 176–183. <https://doi.org/1037//0033-2909.126.1.78>
30. Olatunji OO, Akinlabi S, Nkosinathi M, Adedeji PA (2019) Estimation of the elemental composition of biomass using hybrid adaptive neuro-fuzzy inference system. *Bioenergy Res*
31. Ignition. The next big thing in SCADA: how SQL is redefining SCADA. *Inductive Autom* 1–7. <https://doi.org/10.1109/MC.2007.148>
32. Merritt K (2008) Data warehousing and the internet: converging technologies. *J Internet Commer* 1:49–61. [https://doi.org/10.1300/J179v01n02\\_04](https://doi.org/10.1300/J179v01n02_04)
33. Gray P, Watson HJ (1998) Present and future directions in data warehousing. *Data Base Adv Inf Syst* 29:83–90. <https://doi.org/10.1145/313310.313345>



# Fault Detection System for Long-Distance Gas Mixture Pipelines Using Statistical Features



Syed Muhammad Mujtaba, Tamiru Alemu Lemma,  
and Mebrahitom Asmelash Gebremariam

**Abstract** Integrity management of gas pipelines can be enhanced by incorporating state-of-the-art failure detection, diagnostics and prediction tools. A plethora of methods are available for real-time monitoring and leak detection, the majority of which reported for liquid pipelines that can be quickly introduced for real-life applications. The present paper, however, proposes dynamic principal component analysis (DPCA) for it has not been tested for gas pipelines under transient conditions. Mass flow rate, temperature and pressure values are used separately and in combined form to establish the reference models. Measured data are projected into the new dimension based on selected principal components. For leak detection, Hotelling's  $T^2$ -statistics and  $Q$ -statistics are monitored in real time. The validation tests for simple as well as dynamic PCA show that both methods successfully detect a leakage that has an opening of 10% of pipeline diameter. DPCA significantly magnified the information on leak in terms of  $T^2$ -statistics, thus reducing the probability of missed faults.  $T^2$ -statistics is found to be more sensitive to small leaks than  $Q$ -statistics. Overall, it can be said that the proposed technique has the potential to accurately identify small leaks under transient conditions.

**Keywords** OLGA · Dynamic principal component analysis · Real-time leak detection · Hotelling's  $T^2$ -statistic ·  $Q$ -statistics · GERG-2008

---

S. M. Mujtaba · T. A. Lemma (✉)  
Department of Mechanical Engineering, Universiti Teknologi PETRONAS, Bandar Seri Iskandar,  
31750 Seri Iskandar, Perak, Malaysia  
e-mail: [tamiru.lemma@utp.edu.my](mailto:tamiru.lemma@utp.edu.my)

S. M. Mujtaba  
e-mail: [akbarmujtaba1994@gmail.com](mailto:akbarmujtaba1994@gmail.com)

M. A. Gebremariam  
College of Engineering, Industrial Engineering Department, University Malaysia Pahang,  
Gambang, Malaysia

# 1 Introduction

Pipelines are the preferred and economical means for the transportation of natural gas around the globe. However, pipelines may be exposed to several environmental conditions based on location and demand. Pipelines may be offshore, onshore or buried. Pipelines became extremely dangerous because of the faults like leakage and blockage. Old pipelines usually face material degradation due to corrosion which may lead to leakage and pipeline explosion resulting in several losses [1]. Various studies have been conducted in the past for fault detection in pipelines, but still there is a room to improve these techniques to meet industry expectation [2–4].

Fault detection techniques can be classified into model-based and data-driven methods (Fig. 1). Model-based techniques require mathematical modelling of the process to interpret abnormal events, while data-driven techniques extract features of the system using process data with minimal process knowledge [2]. Statistical process control (SPC) is one of the data-driven fault detection techniques. It monitors and controls a process or a system using statistical measures (control charts)-originated from manufacturing processes [5]. Statistical measures do not require mathematical model of the complex process, like other data-based techniques; it only relies on the process historical data [6]. These techniques can further be divided into univariate and multivariate statistical techniques. Typical control charts such as Shewhart chart, cumulative sum (CUSUM) chart and exponentially weighted moving average (EWMA) chart consider monitoring of single variable having independent samples [5]. However, there could be a correlation between system variables which is beyond the capabilities of univariate statistics [7], thus, for real systems, correlation between variables must be incorporated. Multivariate statistics maintains the

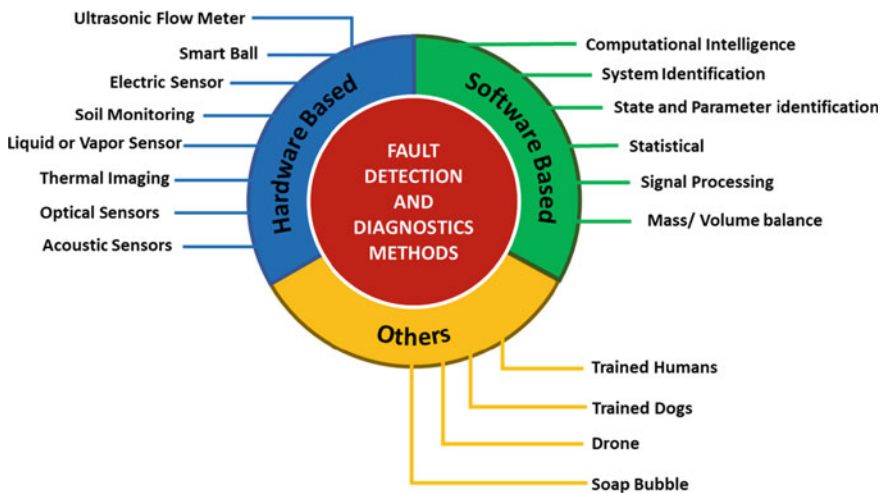


**Fig. 1** Classification of fault detection and diagnostic techniques

correlation among several variables and makes calculation of new features from the data. The most common multivariate statistics used for fault detection and diagnostics is principal component analysis (PCA) combined with Hotelling's  $T^2$ -statistics and  $Q$ -statistics. Detection of leak using multivariate approach is similar to other FDD techniques, i.e. by setting control limits (CL) [5, 7].

Increase in number of variables causes curse of dimensionality which can be partially resolved by dimensionality reduction techniques [2, 8]. Principal component analysis (PCA), partial least squares (PLS), Fisher's discriminant analysis (FDA) and independent component analysis (ICA) are some of the techniques that are being used for dimension reduction of data [2, 8]. Lower dimensions of data are calculated in such a way that the remaining variance retains maximum information of the original data [6]. In PCA, data with a high number of variables are projected into low number of principal components (new variables) using linear transformations [9].

From previous studies, for leak detection in water pipelines, Gertler et al. [10] used PCA to monitor the changes in flow residuals in case of small leaks. Hu et al. [11] used PCA in oil pipelines to identify negative pressure waves which lead towards leak detection. Torres et al. [12] used PCA coupled with  $T^2$ -statistics and  $Q$ -statistics to monitor natural gas pipelines; once there is a leak in a pipeline, these statistics violate the control limits.

The challenge in time-dependent systems like gas pipelines is to consider correlation between variables and the system dynamics at the same time. Simple PCA only handles the correlation between static variables. As such it is unable to handle temporal correlations [13]. This issue can be resolved by using dynamic PCA (DPCA) proposed by Jackson [14]. In DPCA, a sample of a variable is augmented with its previous samples [7]. Usage of DPCA for fault detection and diagnostics (FDD) is found in applications like chemical plants [5] and industrial boilers [15, 16]. Furthermore, Rato et al. [17] compares the performance of several modified forms of PCA. Santos-Ruiz et al. [18] proposed the use of DPCA to detect and quantify leak of various sizes in liquid pipelines by monitoring  $T^2$ - and  $Q$ -statistics as residuals. One study found that Hotelling's  $T^2$ -statistics is good for small as well as large leakages, whereas  $Q$ -statistics is good for large leaks only. To our knowledge, none of the past study applied DPCA for the purpose of FDD in case of natural gas long-distance pipelines. In this study, OLGA simulation is performed to generate data for a long distance natural gas pipeline under transient conditions. Mass flow rate, pressure and temperature will be used to find the principal components using simple and dynamic PCA. Then,  $T^2$ -statistics and  $Q$ -statistics will be calculated and monitored through control limits for the detection of leaks. Detection results using simple and dynamic PCA for both statistics will be studied. This paper is arranged in the following sections. Section 2 is describing mathematical details of the simple PCA and DPCA models. Section 3 is on the calculations of  $T^2$ -statistics and  $Q$ -statistics with their control limits. Section 4 is defining the methodology of the proposed technique. Section 5 covers the results and discussion of our findings. Finally, Sect. 6 concludes the findings followed by future recommendations.

## 2 PCA Mathematics

### 2.1 Simple PCA

PCA is a multivariate statistical approach that transforms matrix of measured data into orthogonal and linearly integrated variables called principal components. Typical advantage of PCA is dimensionally reduced model. According to [7, 19], if  $\mathbf{X} \in \mathbb{R}^{n \times m}$  implies the matrix formed by measured data (scaled and normalized to standard deviation of unity), then the corresponding covariance matrix  $\mathbf{S}$  can be written as

$$\mathbf{S} = \frac{1}{n-1} \mathbf{X}^T \mathbf{X} \quad (1)$$

Alternatively, by using singular value decomposition,  $\mathbf{S}$  can be written as

$$\mathbf{S} = \overline{\mathbf{P}} \mathbf{\Lambda} \overline{\mathbf{P}}^T \quad (2)$$

where  $\mathbf{\Lambda}$  is a diagonal matrix consisting of eigenvalues in decreasing order and columns in  $\overline{\mathbf{P}}$  are representing loading or eigenvectors.  $n$  is the total number of samples and is the number of observed variables, and if  $n > m$ , resulting eigenvalues and eigenvectors will give  $m \times m$  matrix [19].

$$\mathbf{\Lambda} = \begin{bmatrix} \lambda_1 & 0 & 0 & 0 \\ 0 & \lambda_2 & \dots & 0 \\ \vdots & \vdots & \ddots & 0 \\ 0 & 0 & \dots & \lambda_m \end{bmatrix} \quad (3)$$

Eigenvalues basically signify the variance corresponding to the eigenvectors. Resulting variables in the diagonal of matrix  $\mathbf{\Lambda}$  are arranged in order of decreasing order so that the variable with the highest magnitude will be  $\lambda_1$ .

The matrix  $\overline{\mathbf{P}}$  can be split into two matrices,

$$\overline{\mathbf{P}} = [\mathbf{P} \ \tilde{\mathbf{P}}] \quad (4)$$

$\mathbf{P}$  consists of vectors (vectors with maximum variance of the data) called principal components, while  $\tilde{\mathbf{P}}$  contains remaining or complementary vectors [18]. The transformation of old matrix into new space (Score matrix)  $\mathbf{Y}$  can be written as

$$\mathbf{Y} = \mathbf{X} \mathbf{P} \quad (5)$$

Now, the predicted data into original dimensions can be written as

$$\hat{\mathbf{Y}} = \mathbf{Y} \mathbf{P}^T + \text{error} \quad (6)$$

Here, error is due to the complementary vectors which can be explained as

$$\text{error} = X\tilde{P}\tilde{P}^T \tag{7}$$

## 2.2 Dynamic PCA

Simple PCA resolves the issue of correlation between variables but assumes that each sample is independent from the next sample, in temporal sense. So, PCA is suitable in steady-state conditions and cannot incorporate the dynamics of the system. PCA can be extended to dynamic PCA by adding previous samples of a variable in a new column of data matrix  $X_1$  (Eq. 8) [7, 18]. For a variable  $x_1$ , dynamic matrix can be written as

$$X_1 = \begin{bmatrix} x_1(1) & x_1(1-1) & \dots & x_1(1-r) \\ x_1(2) & x_1(2-1) & \dots & x_1(2-r) \\ \vdots & \vdots & \ddots & \vdots \\ x_1(n) & x_1(n-1) & \dots & x_1(n-r) \end{bmatrix} \tag{8}$$

Here,  $x_1(1)$  is representing the first sample of a variable  $x_1$ ,  $x_1(2)$  is representing the value of a second sample, and so on. The second column of the matrix contains the same variable  $x_1$ , but shifted one sample backward, i.e. each sample of a variable in the first column is followed by their preceding sample in the second. Third and above columns of the matrix are arranged with the similar approach, where  $r$  decides the number of previous samples to be included. For more than one variable, the same matrix can be generated for each variable and finally combined to get final matrix (Eq. 9) [7].

$$X = [X_1 \ X_1 \ \dots \ X_m] \tag{9}$$

The rest of the procedure to calculate principal components is the same as that of simple PCA.

## 3 Fault Detection Formulation

### 3.1 Hotelling's $T^2$ -Statistics

The basic concept of  $T^2$ -statistics was developed in 1947 by Hotelling [20]. Since then, it has been used to measure the variance in the principal components [19] that

can be used to monitor a process. Using covariance matrix  $S$ , calculated from the training data and new data matrix  $X_{New}$ ,  $T^2$ -statistics can be calculated as [18]

$$T^2 = X_{New} S^{-1} X_{New}^T \tag{10}$$

Thresholds  $T_\alpha^2$  for  $T^2$ -statistics can be calculated by [21]

$$T_\alpha^2 = \frac{m(n^2 - 1)}{n(n - m)} F_{\alpha(m, n-m)} \tag{11}$$

where  $F_{\alpha(m, n-m)}$  is the  $F$ -distribution with  $m$  and  $n - m$  degrees of freedom.

If  $p$  represents the number of considered principal components, then Eq. 11 becomes [18, 19]

$$T_\alpha^2 = \frac{p(n^2 - 1)}{n(n - p)} F_{\alpha(p, n-m)} \tag{12}$$

### 3.2 *Q-Statistics*

The squared prediction error (SPE) or  $Q$ -statistics is responsible for measuring the variability in the residuals. If  $Rs$  is representing the residuals between actual and predicted variables, then  $Q$ -statistics can be written as [19]

$$Q = Rs Rs^T \tag{13}$$

$$Rs = X_{New} - \hat{Y} \tag{14}$$

$$\hat{Y} = Y_{New} P^T \tag{15}$$

$$Y_{New} = X_{New} P \tag{16}$$

Threshold  $Q_\alpha$  for  $Q$ -statistics can be calculated by the following formula [21]

$$Q_\alpha = \theta_1 \left[ \frac{h_0 c_\alpha \sqrt{2\theta_2}}{\theta_1} + 1 + \frac{\theta_2 h_0 (h_0 - 1)}{\theta_1^2} \right]^{\frac{1}{h_0}} \tag{17}$$

$$\theta_i = \sum_{j=a+1}^n \sigma_j^{2i} \tag{18}$$

$$h_0 = 1 - \frac{2\theta_1\theta_3}{3\theta_2^2} \tag{19}$$

Here,  $c_\alpha$  is representing Student's  $t$ -distribution with  $m$  degrees of freedom and  $1 - \alpha$  confidence interval.

## 4 Methodology

Figure 2 is representing the steps involved in defining the control limits and how these limits can be used to detect the faults like leakage.

### 4.1 Benchmarking and Validation

Due to unavailability of field data, OLGA simulator is used to model a long natural gas pipeline and generate data enough to train and test PCA and DPCA models. A recent study by Uilhoorn [22] is considered as a benchmark to validate OLGA model. For the validation, mass flow rate values of OLGA model and benchmark study are compared at the same boundary conditions.

### 4.2 Case Study

A case is developed to generate natural gas pipeline data under normal and leakage conditions. Mass flow rate is excited at the inlet to design the system for training [23]. Mass flow rate, temperature and pressure readings are measured at six different

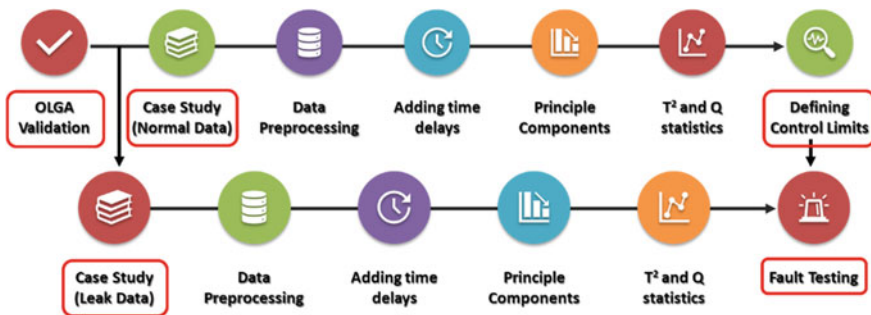


Fig. 2 Methodology of leak detection by monitoring  $T^2$ -statistics and  $Q$ -statistics with control limits

locations in the pipeline. Simulations are performed to generate data for normal, validation and testing conditions.

### ***4.3 Determination of Principal Components***

For the training, mass flow rate, pressure and temperature measurements are used independently and in a combined form to calculate principal components. To find the principal components, data are normalized to convert all data to zero mean and standard deviation of one, then, normalized data matrix is extended to obtain dynamic matrix using Eqs. 8 and 9. After that, covariance matrix is calculated using Eq. 2. This covariance matrix is then used to solve eigenvalues (variance) and eigenvectors (principal components) using SVD function in MATLAB.

### ***4.4 Fault Detection***

A new data set under pipeline normal operating conditions is generated using the same model to calculate the residuals between actual and predicted values. These data are then used to calculate  $T^2$ -statistics and  $Q$ -statistics using Eqs. 10 and 13, respectively. For normal conditions, control limits (CL) are also defined for these statistics using Eqs. 12 and 17, where the confidence intervals for  $F$ -distribution and Student's  $t$ -distribution are tuned for each variable. Data with a leakage of 10% are generated, and residual statistics are calculated again for faulty data. It is observed that after 10 min (time of leak), the defined limits are violated indicating the existence of fault (leak) in a pipeline. PCA and DPCA using different variables and several shifted samples are calculated to study their effect in detection of 10% leakage in a pipeline. Outcomes of the study are presented in the following section.

## **5 Results and Discussion**

### ***5.1 Simulation Setup***

A 150-km horizontal pipeline transporting natural gas is modelled using OLGA simulator. Mass flow rate and pressure sources are modelled at the boundaries of the pipeline. Inlet boundary condition is excited with random signals based on design of experiment (DOE), and outlet boundary condition is fixed to 7.2 MPa. Composition of the natural gas (methane, 84.385%; nitrogen, 0.416%; carbon dioxide, 1.919%; ethane, 8.871%; propane, 3.179%; n-butane, 0.658%; i-butane, 0.346%; n-pentane, 0.091%; i-pentane, 0.0897%; hexane, 0.0317%; heptane, 0.0073%; octane, 0.0016%;



**Table 1** OLGA simulation parameters

Parameters	Values
Length, diameter	150 km, 1.4 m
Pipeline Thickness	0.101 m (4 in.)
Pipe material	Carbon steel
Flowing fluid	Natural gas
Surface roughness	0.016 mm
Ambient temperature	278.15 K
Heat transfer coefficient	$2.84 \frac{W}{m^2 K}$
Inlet mass flow	Refer to Figure 3
Outlet pressure	7.2 MPa
Friction factor	Colebrook equation
Equation of state	GERG-2008
Leakage (testing)	Maximum 0.14 m (10% opening)

hydrogen, 0.0020%; and oxygen, 0.0010%) and the required pipeline details are adopted from [22]. Table 1 provides the further details needed for the simulation.

Figure 3 is representing the amplitude-modulated pseudo-random binary signals (APRBS) of mass flow rate at the inlet of the pipeline for the simulations of training, testing and validation case. Mass flow rate, pressure and temperature measurements are captured at six different locations in a pipeline. 1200 samples are captured in a

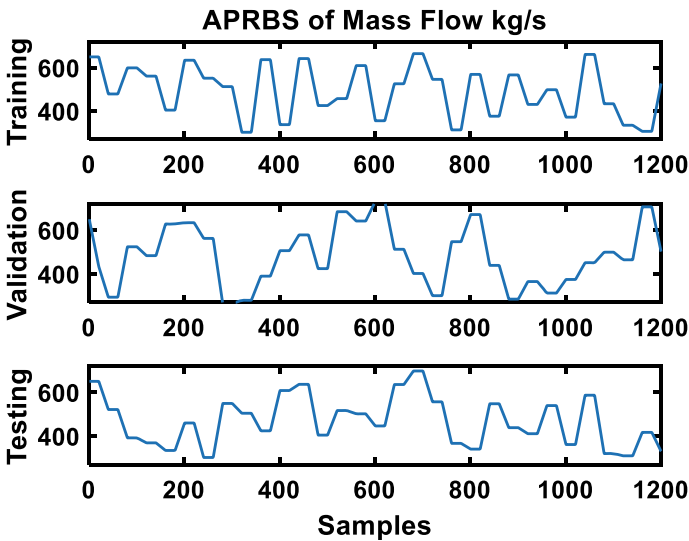


**Fig. 3** Amplitude-modulated pseudo-random binary signals (APRBS) at the inlet of the pipeline for training, validation and testing phase

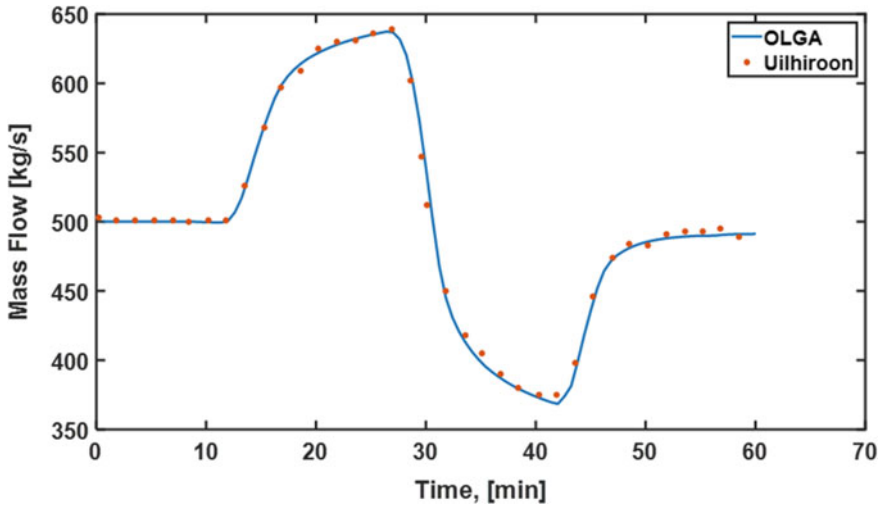


Fig. 4 Comparison between the mass flow rate of OLGA model and the benchmarked study [22]

period of 60 min. Simulations are performed to get the data for normal and leakage conditions. For testing condition, 10% leakage is introduced after 10 min.

## 5.2 Benchmarking and Validation

Validation of OLGA model from the literature is presented in Fig. 4. Mass flow rate values at 120 km from the inlet are compared. It can be observed that the results of OLGA model are very close to the benchmarked study with root mean square error (RMSE) of 5.42 kg/s. This small difference is due to usage of different solvers and discretization schemes used by OLGA and the benchmarked study [22].

## 5.3 Data Normalization

Mass flow rate, pressure and temperature measurements are normalized to zero mean and standard deviation of one; this is to give equal weightage to all variables. For instance, normalized variables of training data are shown in Fig. 5. S1 to S6 are representing the readings of sensors at 0, 30, 60, 90, 120 and 150 km, respectively. It can be seen that all variables are scaled to similar numbers having exactly similar trends as indicated in the training boundary condition (Fig. 5).

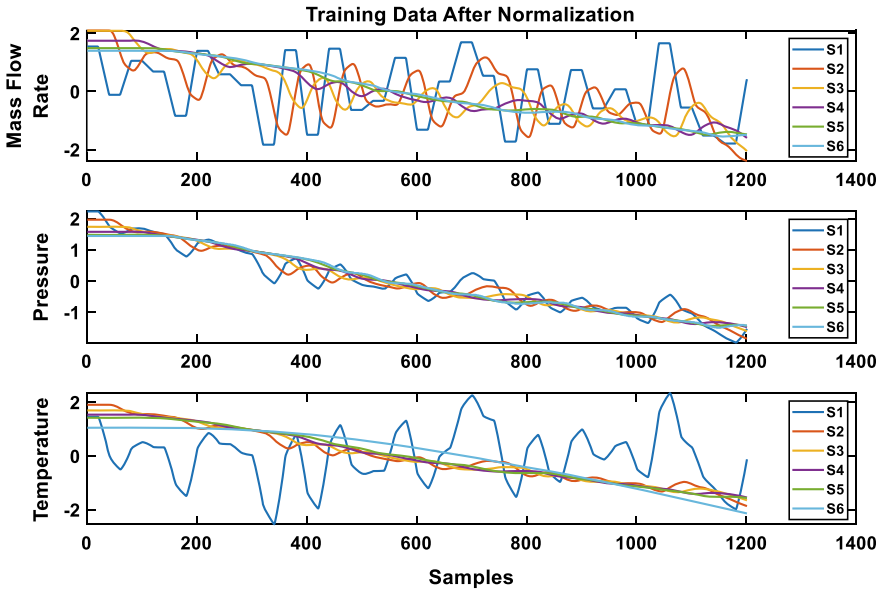


Fig. 5 Normalized data for mass flow rate, pressure and temperature used for the calculations of principal components

### 5.4 Fault Detection

Figures 6, 7, 8, 9, 10, 11, 12 and 13 are representing the results of leak detection by monitoring  $T^2$ -statistics and  $Q$ -statistics, respectively, under 0.01% white noise. Simple PCA (zero delays) results are mentioned in the left side of figures, and DPCA results are mentioned in the right. For DPCA, several  $r$  values are studied, and the one with the best results is presented.

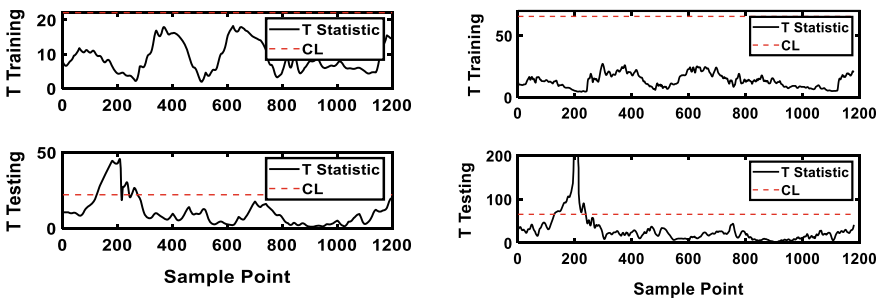


Fig. 6 Results of  $T^2$ -statistics obtained from mass flow rate measurements. The left figure is using zero delays (normal PCA), and the right figure is using twenty delays (DPCA)

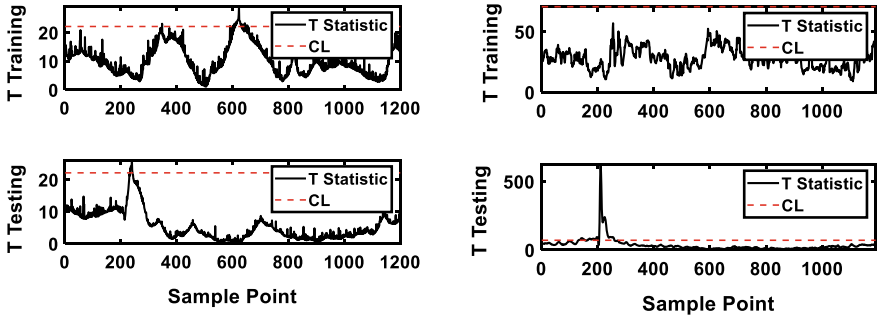


Fig. 7 Results of  $T^2$ -statistics obtained from pressure measurements. The left figure is using zero delays (normal PCA), and the right figure is using twenty delays (DPCA)

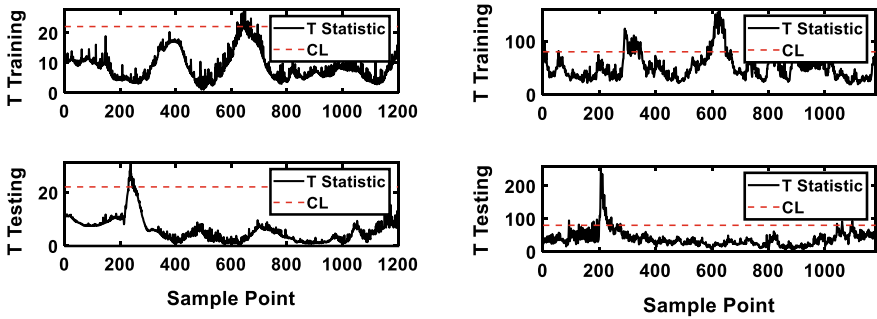


Fig. 8 Results of  $T^2$ -statistics obtained from temperature measurements. The left figure is using zero delays (normal PCA), and right figure is using twenty delays (DPCA)

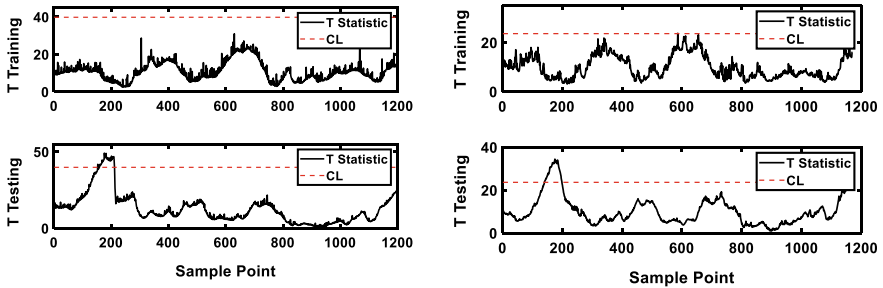


Fig. 9 Results of  $T^2$ -statistics obtained from mass flow rate, pressure and temperature measurements. The left figure is using zero delays (normal PCA), and the right figure is using thirty delays (DPCA)

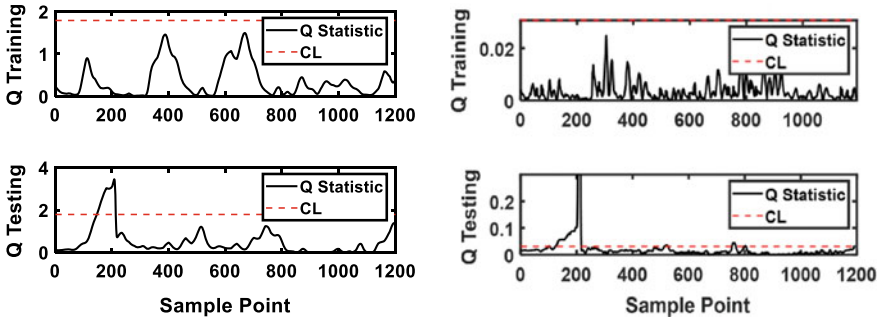


Fig. 10 Results of  $Q$ -statistic obtained from mass flow rate measurements. The left figure is using zero delays (normal PCA), and the right figure is using eight delays (DPCA)

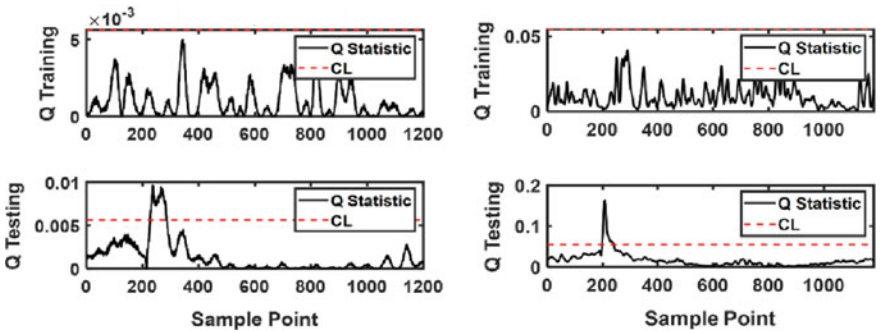


Fig. 11 Results of  $Q$ -statistic obtained from pressure measurements. The left figure is using zero delays (normal PCA), and the right figure is using twenty delays (DPCA)

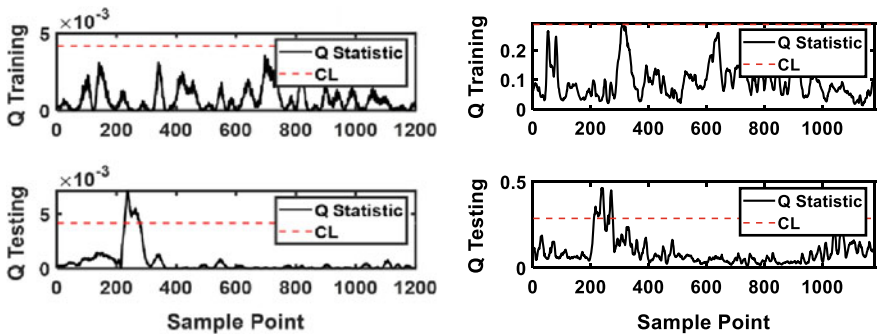
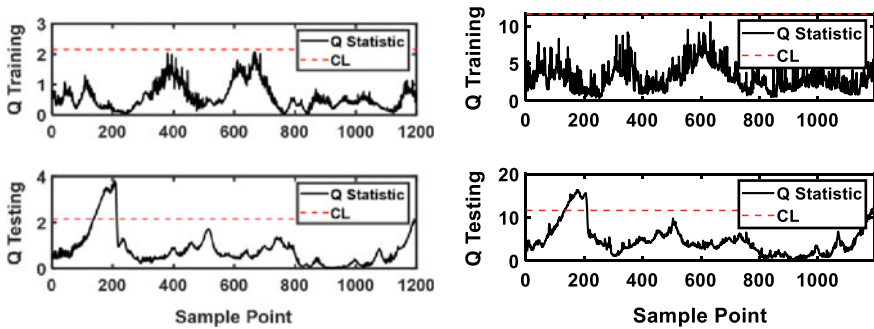


Fig. 12 Results of  $Q$ -statistics obtained from temperature measurements. The left figure is using zero delays (normal PCA), and the right figure is using twenty delays (DPCA)



**Fig. 13** Results of  $Q$ -statistics obtained from mass flow rate, pressure and temperature measurements. The left figure is using zero delays (normal PCA), and the right figure is using five delays (DPCA)

### 5.4.1 Hotelling's $T^2$ -Statistics

Leak detection results, by monitoring of  $T^2$ -statistics for mass flow rate, pressure, temperature and all three variables, are shown in Figs. 6, 7, 8 and 9, respectively. Dynamic PCA (right side) successfully detects leakage for almost all cases with big significant margin except for temperature (Fig. 8). But, simple PCA in cases of pressure and temperature fails to detect leakage (Figs. 7 and 8).

### 5.4.2 $Q$ -Statistics

Leak detection results by monitoring of  $Q$ -statistics residuals of mass flow rate, pressure, temperature and all three variables are shown in Figs. 10, 11, 12 and 13, respectively. It can be observed that using  $Q$ -statistics, both PCA (zero delays) and DPCA are able to detect the leak by selecting the appropriate principal components (PCs) and delays for all variables. For example, DPCA, using pressure measurements (Fig. 11), requires 27 PCs and 20 delayed terms to detect leakage, while only 3 PCs are required in case of mass flow rate with zero delays (Fig. 10). Summary of results obtained by monitoring  $Q$ -statistics for several variables is presented under discussion section.

## 5.5 Discussion

Tables 2 and 3 are representing the summary of detection results obtained through  $T^2$ -statistics and  $Q$ -statistics, respectively. As simple PCA is not able to capture the changes with time,  $T^2$ -statistics, which is the measure of variations in the data, suffers to detect leak using simple PCA. By incorporating dynamic PCA, detection results due to  $T^2$ -statistics improved notably. It can be seen in Figs. 6, 7 and 8 that the use

**Table 2** Summary of  $T^2$ -statistics results, SWLM: successful with low margin; SWHM: successful with high margin

Variable	$T^2$ -Statistics				
	PCA		DPCA		
	Components	Testing	Components	$r$ Value	Testing
Mass (Fig. 9)	6	SWLM	12	20	SWHM
Pressure (Fig. 10)	6	Not successful	22	20	SWHM
Temperature (Fig. 11)	6	Not successful	35	20	Not successful
Mass, pressure and temperature (Fig. 12)	7	SWLM	8	30	SWLM

**Table 3** Summary of  $Q$ -statistics results, SWLM: successful with low margin

Variable	$Q$ -Statistics				
	PCA		DPCA		
	Components	Testing	Components	$r$ Value	Testing
Mass (Fig. 5)	3	SWLM	9	8	SWLM
Pressure (Fig. 6)	5	SWLM	27	20	SWLM
Temperature (Fig. 7)	5	SWLM	26	20	SWLM
Mass, pressure and temperature (Fig. 8)	4	SWLM	8	5	SWLM

of DPCA allows  $T^2$ -statistics to successfully detect leak by significantly violating the control limits. Thus, it can be said that  $T^2$ -statistics is a good measure to detect small leaks; similar conclusion is made by [18].

It can be noted that results of  $Q$ -statistics due to 10% leak violate the limits but with low margin. Even the incorporation of dynamic PCA does not make any significant improvements in  $Q$ -statistics results. This might be due to the reason that  $Q$ -statistics calculates prediction errors but not the variations in the data [21]. Thus, it can be said that although in our case (10% leak)  $Q$ -statistics successfully detected the leak, it is not suitable for smaller leaks.

To monitor changes in time due to small leakage, one must switch to DPCA coupled with  $T^2$ -statistics. From the study, it is observed that higher number of delays is required to detect leak with big margin, e.g. in Fig. 7. It requires twenty delayed terms to excite the leakage to a reasonable margin. Temperature measurements do not show any noticeable changes due to 10% leak, so it is not recommended to use temperature in case of small leaks. It can also be said from our findings that using all three variables for leak is not fruitful instead of using individual variables like mass flow rate and pressure which are highly recommended.

There are several aspects that need to be considered for application of proposed technique in actual pipelines, such as gas composition, pipeline boundary conditions, presence of system and sensor noise, length of pipeline and pipeline roughness. The

results obtained in this study are dependent on the parameters that are mentioned in Sect. 5.1. For instance, the pipeline that is considered in this study is working under a high pressure of around 8.0 MPa at inlet, having fluctuations in mass flow rate between 300 and 700 kg/s and with the specific natural gas compositions. Under these conditions,  $Q$ -statistics and  $T^2$ -statistics are both able to detect 10% leakage. If pipeline conditions and parameters are changed, there is a need to tune the proposed technique accordingly.

## 6 Conclusions

Real-time leak detection and diagnostics tools are essential parts of a pipeline integrity management system. In the present paper, a new leak detection system (with DPCA as the primary algorithm) is introduced and its performance is assessed by considering various delay models, controlled leaks and simulated measurement noise. As per the validation tests and analysis, the following conclusions are drawn:

- a. Both simple and dynamic PCA are able to detect 10% leak under transient conditions and 0.01% white noise.
- b.  $Q$ -statistic detects leak using all variables for simple as well as dynamic PCA, but with low margins; thus, it may not be able to detect smaller leaks.
- c.  $T^2$ -statistics almost failed to detect leak using simple PCA, but modification to DPCA allows  $T^2$ -statistics to successfully detect leak with significant margin.
- d. Increasing the number of delayed terms notably increased the violation of  $T^2$ -statistics due to leakage.
- e. Pressure or mass flow rate measurements are recommended to detect small leakage using DPCA coupled with  $T^2$ -statistics.

**Future Work** will be on the extension of the current method for leak diagnostics, which can be materialized by considering ANN, fuzzy systems or Bayesian network. Another potential aspect for further research is the application of DPCA for fault detection and diagnostics in multiphase flow pipelines.

**Acknowledgements** The authors are pleased to recognize the support of Universiti Teknologi PETRONAS in terms of financial assistance and providing the facilities sought for the research. The invaluable feedbacks from the reviewers are also much appreciated.

## References

1. Datta SS (2016) A review on different pipeline fault detection methods. *J Loss Prev Process Ind* 41:97–106
2. Alauddin M, Khan F, Imtiaz S et al (2018) A bibliometric review and analysis of data-driven fault detection and diagnosis methods for process systems. *Ind Eng Chem Res* 57:10719–10735



3. Adegboye MA, Fung W-K, Karnik A (2019) Recent advances in pipeline monitoring and oil leakage detection technologies: principles and approaches. *Sensors* 19:2548
4. Ayati AH, Haghighi A, Lee P (2019) Statistical review of major standpoints in hydraulic transient-based leak detection. *J Hydraul Struct* 5:1–26
5. Ku W, Storer RH, Georgakis C (1995) Disturbance detection and isolation by dynamic principal component analysis. *Chemomet Intell Lab Syst* 30:179–196
6. Venkatasubramanian V, Rengaswamy R, Kavuri SN et al (2003) A review of process fault detection and diagnosis. Part III: process history based methods. *Comput Chem Eng* 27:327–346
7. Chiang LH, Russell EL, Braatz RD (2000) *Fault detection and diagnosis in industrial systems*. Springer Science & Business Media, Berlin
8. Lemma TA (2018) A hybrid approach for power plant fault diagnostics
9. Verde C, Torres L (2017) *Modeling and monitoring of pipelines and networks: advanced tools for automatic monitoring and supervision of pipelines*. Springer International Publishing, Berlin
10. Gertler J, Romera J, Puig V et al (2010) Leak detection and isolation in water distribution networks using principal component analysis and structured residuals. In: 2010 Conference on control and fault-tolerant systems (SysTol). IEEE, pp 191–196
11. Hu R, Ye H, Wang G et al (2004) Leak detection in pipelines based on PCA. In: ICARCV 2004 8th control, automation, robotics and vision conference. IEEE, pp 1985–1989
12. Torres MJ, Posada JD, Garcia JR et al (2012) Real-time fault detection application for natural gas pipelines. In: ASME 2012 international mechanical engineering congress and exposition. American Society of Mechanical Engineers, pp 769–774
13. Dai X, Gao Z (2013) From model, signal to knowledge: a data-driven perspective of fault detection and diagnosis. *IEEE Trans Industr Inf* 9:2226–2238
14. Jackson JE (1959) Quality control methods for several related variables. *Technometrics* 1:359–377
15. Dong Y, Qin SJ (2018) A novel dynamic PCA algorithm for dynamic data modeling and process monitoring. *J Process Control* 67:1–11
16. Sun X, Marquez HJ, Chen T et al (2005) An improved PCA method with application to boiler leak detection. *ISA Trans* 44:379–397
17. Rato T, Reis M, Schmitt E et al (2016) A systematic comparison of PCA-based statistical process monitoring methods for high-dimensional, time-dependent processes. *AIChE J* 62:1478–1493
18. Santos-Ruiz I, López-Estrada F, Puig V et al (2018) Diagnosis of fluid leaks in pipelines using dynamic PCA. *IFAC-PapersOnLine* 51:373–380
19. Joe Qin S (2003) Statistical process monitoring: basics and beyond. *J Chemometr J Chemometr Soc* 17:480–502
20. Hotelling H (1947) *Multivariate quality control. Techniques of statistical analysis*. McGraw-Hill, New York
21. Jackson JE, Mudholkar GS (1979) Control procedures for residuals associated with principal component analysis. *Technometrics* 21:341–349
22. Uilhoorn F (2017) Comparison of Bayesian estimation methods for modeling flow transients in gas pipelines. *J Nat Gas Sci Eng* 38:159–170
23. Mikleš J, Fikar M (2007) Process modelling, identification, and control

# Feasibility Study on Metal Inert Gas (MIG) Welding on Zincalume G550 Steel



WaliSiJiang Tayier, Shamini Janasekaran, and Arvinth Rajandran

**Abstract** The Metal Inert Gas (MIG) welding is commonly used to weld similar and dissimilar metals in many metal processing sectors because it welds efficiently and it is low cost, as well as it produces low fume that is one of the environmentally friendly aspects. In the present study, the Zincalume G550 steel was welded at a lap joint technique using MIG welding machine. The effect of welding parameters on Zincalume G550 steel was investigated using Digital Microscope (DM). The welded specimens were cold-mounted and cut with cutting machine, and the cross-section of the joints ground with three different abrasive papers (220, 1000, 2000) and etched with ferric chloride ( $\text{FeCl}_3$ ) for observing welded bead geometry. The results showed the wire speed was the most significant parameter in the experimental testing, in which direct variation was found in size of penetration, bead width, and wire speed mean, and when wire speed was increasing, the size of penetration and bead width also increased. In addition, the result showed the experimental testing for penetration reached to predicted values for penetration in fuzzy logic technique. In the meantime, the experimental testing for the bead width was much higher than predicted values for the bead width.

**Keywords** MIG welding · Zincalume G550 steel · Lap joint

## 1 Introduction

Nowadays, similar metal joining of light metal steel is performed in the manufacturing fields in order to reduce weight and cost in any requirements for construction and industry [1]. Metal joining in conventional method is an inconsistent process due to its low welding quality and inaccuracy of measurement such as welding speed [2]. Some highly advanced welding techniques are used by researchers such as laser-beam welding, friction-stir welding, and brazing welding. However, these highly advanced methods not only need more expensive equipment, but also energy spent is

---

W. Tayier · S. Janasekaran (✉) · A. Rajandran  
Centre for Advanced Materials and Intelligent Manufacturing, Faculty of Engineering and the Built Environment, SEGi University, 47810 Petaling Jaya, Malaysia  
e-mail: [shaminijanasekaran@segi.edu.my](mailto:shaminijanasekaran@segi.edu.my)

© Springer Nature Singapore Pte Ltd. 2020  
S. S. Emamian et al. (eds.), *Advances in Manufacturing Engineering*, Lecture Notes in Mechanical Engineering, [https://doi.org/10.1007/978-981-15-5753-8\\_28](https://doi.org/10.1007/978-981-15-5753-8_28)

costly [3]. Zinc-alloyed metal and zinc-coated steel have been expanded to be used in construction and building industries for their high corrosion resistance in different climate conditions, as well as humid tropical areas [4].

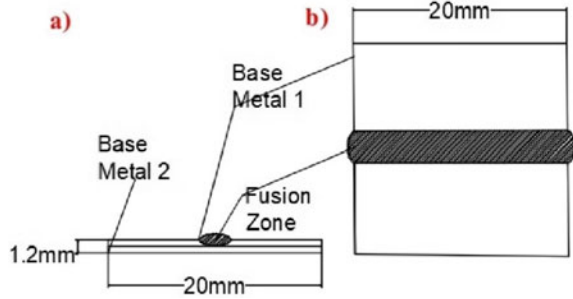
Zhang et al. [5] have investigated the microstructure and properties of copper joint in Metal Inert Gas (MIG) welding. Different parameters were set for experimental testing that it included wire feed rate (10.5 mm/min) and arc voltage (31 V). As a result, the copper plate has not fully penetrated of 3.5 mm depth with V-grooving [5]. Some researchers studied on aluminum and stainless steel in MIG welding that the welding voltage (13–15 V), welding current (20–40 A), wire feed (5.8–6.8 mm/min) are set into parameters for testing. The results showed that dissimilar metal plate has a lower melting point compared to stainless steels. However, the aluminum joined with low melting point in Stainless-aluminum plate [6]. Meanwhile, Nguyen and Huang [7] studied on Aluminum alloys with SS400 steel joint in MIG, that study set to three different parameters for influences on welding appearance and microstructure. The results showed they obtained results reached to Yufeng Zhang testing results [6] that the aluminum alloys is easy to melt with wire by low melting point. In contrast, the SS400 steel was melted with wire in high melting point; for the combination, the SS400 steel is less than Aluminum alloy sheet [7]. However, the similar novel metal joining process also has been investigated until the present, in which the issues of low welding quality, energy, and materials cost still exist in metal joining processing fields. Hence, this study conducts an experiment on Zinalume G550 metal joining which aims to solve some issues related to Zinc/Aluminum coated steel (Al–Zn alloy coated steel) joint with lower cost welding equipment (such as MIG). The aim of this study is investigating on the effects of different welding parameters on welded pool geometry of Zinalume metal welded joint using MIG through Design of Experiment (DOE) that contribute to sustainable environment in metal joining process, besides, it helps to solve some problems of metal joining in construction areas.

## 2 Experimental Procedure

### 2.1 Material and Sample Preparation

Figure 1 shows the sheets of Zinalume G550 steel (20 mm \* 20 mm \* 1.2 mm) were welded successfully by Metal Inert Gas (MIG) on lap joint configuration. The chemical deposit of metal wire is given in Table 1. The metal wire (ER70S-6, wire diameter is 1 mm) used on the Zinalume steel for welding and the chemical compositions of base metal are given in Table 2. The samples are ground through three different types of silicon carbide (SiC) abrasive papers, namely 220 grit, 1000 grit, and 2000 grit. It removes burrs on the joining interface.

**Fig. 1** Configuration joint (closed square in lap jointing). **a** Front view, **b** top view



## 2.2 Metal Inert Gas (MIG) Machine

The Hero Tech IM1680 160A inverter MIG welding was used to weld the joints. The IM1680 MIG welding machine range of output current is from 40 to 160 A with output voltage of 16–22 VDC. The specimens were clamped with G-clamp on the welding table for stability of samples in lap joint configuration.

The effect of wire speed (3, 3.75, and 4.5 m/min) was studied at a constant welding current of 70 A. In addition, the welding voltage (16.5, 17, and 17.5 V) was investigated at a constant gas flow rate of 15 L/min in this article.

## 2.3 Metallographic Characterizations

In this paper, the weld appearance of lap joint is evaluated via the visual inspection. In the analysis of metallographic characteristics, the welded specimens were cold-mounted (15 mL resin and 2 mL hardener/per sample) and cut perpendicular to the welding direction. The specimens were grounded with three types of abrasive papers (SiC) which consist of 220 grit, 1000 grit, and 2000 grit. Finally, these specimens were etched for 10 s and brushed to surface for two times. The welded samples were etched using ferric chloride ( $\text{FeCl}_3$ ) (25 mL of distilled water and 8 mL hydrochloric acid mixed with 4 g iron metal). The cross-sectioned surface (penetration and bead width) was detected using Digital Microscope (DM) from Celestron Micro Direct 1080 HDMI, and the configuration of penetration and bead width were given in Fig. 2.

## 2.4 Taguchi Method and Fuzzy Logic

The orthogonal arrays (OAs) in Taguchi method are an optimal design which helps finding the best values for experimental processes. The signal to noise (S/N) ratio is an analysis tool in Taguchi method that analyses each factor in the experimental result.

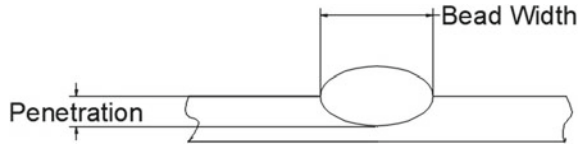
**Table 1** Chemical compositions for ER70S-6 wire (Iron: 96.11%)

Element of metal	C	Mn	Si	P	S	Cr	Ni	Mo	Ti	Cu
Percentage of value (%)	0.06–0.14	1.4–1.6	0.8–1	≤0.025	≤0.025	≤0.15	≤0.15	≤0.15	≤0.15	≤0.5

**Table 2** Chemical compositions of base metal (Zincalume G550 steel, (99.59%))

Element of metal	C	Mn	S	P	Si	Al
Percentage of value (%)	0.02–0.07	0.14–0.22	0.01–0.02	0.01–0.02	0–0.02	0.03–0.06

**Fig. 2** Configuration of penetration and bead width



The S/N ratio is divided to three main categories that included Smaller is Better, Normal is Better, and Larger is Better [8]. In this paper, the L9 (3<sup>3</sup>) orthogonal arrays are employed to optimize the parameters. The fuzzy logic is one of the analysis methods that can predict the output values from the input values with creating roles between the input values and the output values [9].

### 3 Results and Discussion

#### 3.1 Results of Testing for Penetration and Bead Width in Welded Metal

The parameters of wire speed and welding voltage were set via orthogonal arrays (OAs) of Taguchi method in design of experiment (DOE) and the testing results from parameter setting are given in Table 3.

**Table 3** Parameters testing results for penetration and bead width

Trial number	Welding voltage (V)	Wire speed (m/min)	Penetration (mm)	Bead width (mm)
1	16.5	3	0.66	3.256
2	16.5	3.75	0.67	3.119
3	16.5	4.5	0.692	3.825
4	17	3	0.651	2.645
5	17	3.75	0.636	3.589
6	17	4.5	0.807	3.288
7	17.5	3	0.699	3.051
8	17.5	3.75	0.551	4.07
9	17.5	4.5	0.813	4.699

The setting rules' relationship in between input variables (welding voltage and wire speed) and output variables (penetration and bead width) were set via fuzzy logic in Matlab software. The rules are shown in Table 4. The errors in between predicted values and measured values for parameters are given in Table 5.

The graphic of membership for input variables (welding voltage and wire speed) and output variables (penetration and bead width) was set via fuzzy logic in Matlab software. The graphic for membership is shown in Fig. 3.

**Table 4** The rules for input and output variables (L—low, M—medium, H—high)

Parameters	Input (welding voltage)	Input (wire speed)	Output (penetration)	Output (bead width)
1	L	L	M	M
2	L	M	M	L
3	M	L	M	H
4	M	M	L	L
5	L	H	L	L
6	H	L	H	H
7	H	M	M	H
8	H	H	L	H
9	M	H	L	M

**Table 5** The errors in between predicted values and measured values

Trial number	Penetration (mm)			Bead width (mm)		
	Measured	Predicted	Error (%)	Measured	Predicted	Error (%)
1	0.66	0.7	0.6	3.256	3	0.9
2	0.67	0.629	0.7	3.119	3	0.5
3	0.692	0.597	1.6	3.825	2.98	2.8
4	0.651	0.65	0.02	2.645	3.01	1.2
5	0.636	0.597	0.7	3.589	3.33	0.8
6	0.807	0.654	2.3	3.288	3.01	0.9
7	0.699	0.793	1.5	3.051	3.42	1.1
8	0.551	0.639	1.4	4.07	4.2	0.3
9	0.813	0.76	0.7	4.699	4.5	0.4

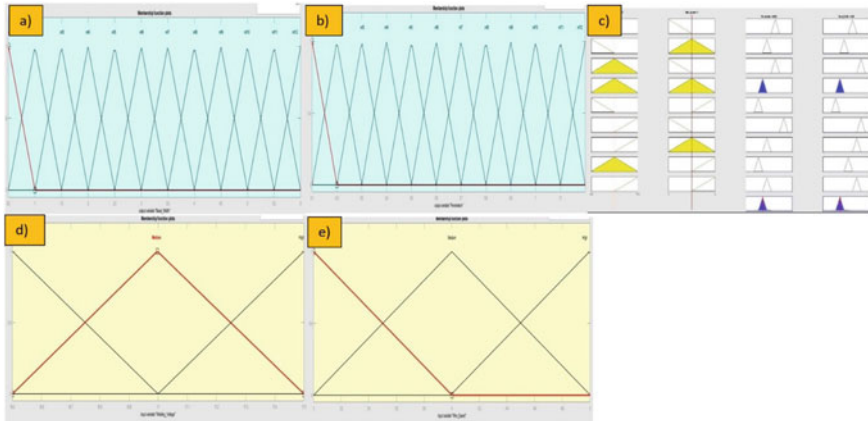


**Fig. 3** The fuzzy logic system for **a** output (penetration), **b** output (bead width), **c** rules set, **d** input (welding voltage), **e** input (wire speed)

### 3.2 Discussion on Testing Result of Penetration and Bead Width

In the geometry shape for bead width and penetration, the welding wire speed and welding voltage are the most significant parameters in many of the previous articles. In the MIG welding process, the size of bead width and penetration are decided by the welding voltage. The welding voltage increases; then, dimension of bead width increases and becomes wider. Meanwhile, an optimum value of welding voltage decides to the penetration increasing [10]. In this paper, the testing results of penetration and bead width are parallel with the Sakhivel et al. [10] results that when the welding voltage increases, the size of bead width increases from 2.645 to 4.699 mm. In the meantime, the penetration increases when the welding voltage reaches an optimum value at 17 V, which is given in the Fig. 4. In Fig. 5, the wire speed is a significant parameter in the experimental testing when the wire speed increases; then, the bead width and penetration increase. This result is consistent with the Yang et al. [11] result that when the wire speed and welding voltage increase, then heat input increases, and the bead width and penetration also increase. In addition, Fauzi et al. [12] reported that the lower welding voltage can decrease the penetration of weld pool [11, 12]. In Fig. 6, the real experimental testing for penetration and bead width approximately reached to prediction of penetration and bead width in fuzzy logic. It was found that the percentages of errors were less than 3% for all the tested data, and this percentage of errors is better than the results of prediction of error from the Shamini Janasekaran research [13, 14]. Thus, the predicted values for penetration and bead width are accepted by experimental testing. For the optimum value of penetration and bead width, this paper recommended the 17.5 V of welding voltage and 4.5 m/min of wire speed according to the S/N ratio in Fig. 4.



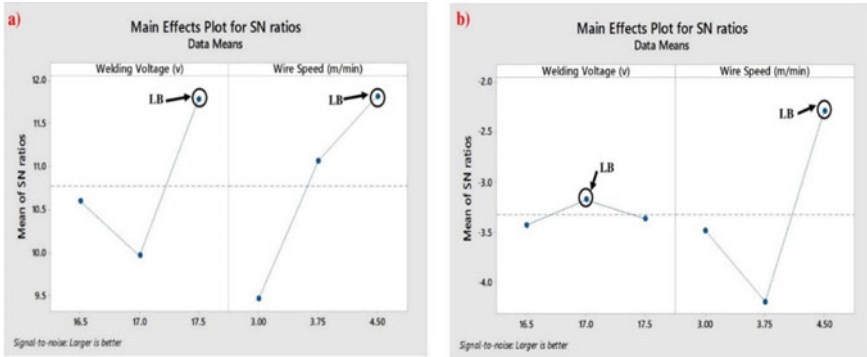


Fig. 4 S/N ratio for a bead width and b penetration (LB—Larger is Better)

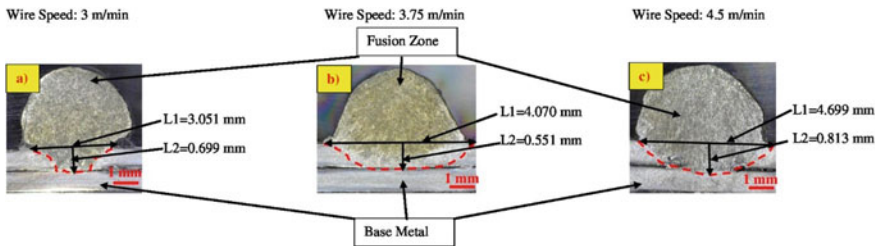


Fig. 5 Penetration and bead width value and structure in Digital Microscope at constant welding current 70 A. a Trial 7, b Trial 8, c Trial 9

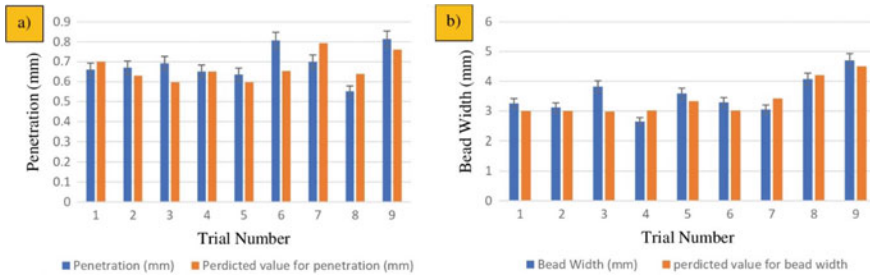


Fig. 6 The errors graphic for a penetration and b bead width

### 4 Conclusion

The following conclusions can be drawn from the results of this study:

1. The sheets of Zinalume G550 steel (20 mm \* 20 mm \* 1.2 mm) are successfully jointed by MIG welding using the suitable parameters.

2. The experimental testing values for penetration reached the predicted values of penetration, and experimental testing values for bead width are much higher than predicted values of bead width.
3. When the welding voltage and wire speed increase, then the penetration and bead width increase.

**Acknowledgements** This research was funded by SEGi University Sdn Bhd. The authors would like to thank Mr. Low Ping Hing and Mr. Vijaya Prakash Vijayasree from Swissma Building Technology Sdn Bhd for their kind contribution.

## References

1. Li J, Li H, Wei H, Gao Y (2015) Effect of torch position and angle on welding quality and welding process stability in pulse on pulse MIG welding–brazing of aluminum alloy to stainless steel. *Int J Adv Manuf Technol* 23:1–12
2. Tan CW, Li LQ, Chen YB, Mei CX, Guo W (2014) Interfacial microstructure and fracture behavior of laser welded-brazed Mg alloys to Zn-coated steel. *Int J Adv Manuf Technol* 1179–1188
3. Moinuddin SQ, Sharma A (2015) Arc stability and its impact on weld properties and microstructure in anti-phase synchronised synergic-pulsed twin-wire gas metal arc welding. *Mater Des* 293–302
4. Tru NN, Quang VA, Tam LH (2017) Understanding corrosion behavior of Zn and Zn alloy galvanized steels in humid tropical climate. *Vietnam J Sci Technol* 55:140–152
5. Zhang L-J, Bai Q-L, Ning J, Wang A, Yang J-N, Yin X-Q, Zhang J-X (2016) A comparative study on the microstructure and properties of copper joint between MIG welding and laser-MIG hybrid welding. *Mater Des* 110:35–50
6. Zhang Y, Huang J, Cheng Z, Ye Z, Chi H, Peng L, Chen S (2016) Study on MIG-TIG double-sided arc welding-brazing of aluminum and stainless steel. *Mater Lett* 172:146–148
7. Nguyen QM, Huang S-C (2015) An investigation of the microstructure of an intermetallic layer in welding aluminum alloys to steel by MIG process. *Materials* 12(8):8246–8254
8. Otto KN, Antonsson EK (1991) Extensions to the Taguchi method of product design. *Engineering and Applied Science in Caltech*, pp 1–26
9. Hynes NRJ, Kumar R, Angela J, Jesudoss AJS (2016) Modeling of process parameters of friction stud welding using fuzzy logic system. *Int J Adv Eng Technol* 7(1):413–417
10. Sakthivel R, Venkadeshwaran P, Sridevi R, Meeran RA, Chandrasekaran K (2015) Effect of welding current, arc voltage and gas flow rate on depth of penetration during MIG welding of AA2014 plate. *Int J Adv Res Technol Eng Sci* 2(2):1–7
11. Yang J-N, Zhang L-J, Ning J, Bai Q-L, Yin X-Q (2017) Single-pass hybrid laser-MIG welding of 8-mm-thick pure copper (T2) without preheating: weld geometry and integrity. *Int J Adv Manuf Technol* 91:1–7
12. Fauzi ERI, Samad Z, Jamil MSC, Nor NM, Boon GP (2017) Parametric modeling of metal inert gas (MIG) welding process using second-order regression model analysis. *J Adv Manuf Technol* 367–381
13. Janasekaran S, Yusof F, Zin HM, Jamaludin MF, Shukor MHA (2017) A fuzzy logic-based prediction model for fracture force using low-power fiber laser beam welding. *Int J Adv Manuf Technol* 91:1–8
14. Janasekaran S, Jamaludi MF, Yusof F, Shukor MHA, Ariga T (2017) Influence of BA4047 filler addition through Mamdani fuzzy logic optimization for double-sided T-joint welding of aluminum alloys using low-power fiber laser. *Int J Adv Manuf Technol* 93:1–11

# The Influence of Welding Parameters on the Microhardness of Zincalume Steel Welded Joint Using Taguchi Technique in Metal Inert Gas (MIG)



Walisijiang Tayier, Shamini Janasekaran,  
and Abdullah Hussein Ali Alzubydi

**Abstract** Nowadays, the Metal Inert Gas (MIG) welding is widely used to join similar and dissimilar metals in many industrial and manufacturing sectors because it welds efficiently, and it is low cost. In the present study, the Zincalume G550 steel was joined with a lap joint technique using MIG welding machine. The effect of welding parameters on microhardness of Zincalume G550 steel was investigated using Vickers hardness machine and digital microscope (DM) for the weld appearance. The welded specimens were cold mounted and cut with cutting machine, and the cross section of the joints was grounded at three different abrasive papers (220, 1000, 2000 grit). The results showed the wire speed is the most significant parameter in the experimental testing in which the direct variation was found in microhardness value, wire speed, and welding voltage mean when wire speeds, and when the welding voltage increase, the microhardness also increases.

**Keywords** MIG welding · Zincalume G550 steel · Lap joint · Microhardness

## 1 Introduction

In recent years, the Metal Inert Gas (MIG) welding technique is widely used in the metal processing fields in order to improve the welding quality and the welding accuracy [1]. A variety of materials, for instance, aluminum, copper, and plastic, are widely used in many industrial and manufacturing areas. However, these lightweight materials not only do not have high strength and toughness, but also do not have anti-resistance capability and easy of corrosion in the humid area [2]. In this study, the Zincalume G550 steel is used for metal joint in MIG welding, which is lightweight, highly resistant, and has a high strength. Many studies have been reported on alloyed metal welded joint using the fusion welding processes such as MIG [3–5]. Li et al. investigated the microhardness of commercial pure titanium using MIG welding with different parameters (20 mm/s of welding speed, 50L/min of gas flow rate, and

---

W. Tayier · S. Janasekaran (✉) · A. H. A. Alzubydi  
Centre for Advanced Materials Research and Manufacturing Processes, Faculty of Engineering  
and the Built Environment, SEGI University, 47810 Petaling Jaya, Malaysia  
e-mail: [shaminijanasekaran@segi.edu.my](mailto:shaminijanasekaran@segi.edu.my)

18.8 V of welding voltage). The results showed the microhardness of the welded zone is higher than the heat affected zone (HAZ) and the base metal [6]. In contrast, Li et al. studied the mechanical properties of aluminum alloy with various parameters (290 A of welding current, 27 V and 28 A of welding voltage and 8.5, 7.5 and 6.5 mm/s of welding speed). In the results, the hardness value in the welded zone was much lower than HAZ and base metal [7]. In addition, some researchers reported on mechanical properties of 7005 aluminum alloy using different parameters. From the results, the microhardness in base metal is much higher than HAZ and welded zone that it is parallel with Li results [8]. However, the joining of coated steels (such as Zinalume steel) has not been fully studied by researchers yet. Thus, the aim of this paper is investigating the effect of welding parameters on microhardness of Zinalume G550 steel welded joint in MIG welding that conduct on full factorial design of experiment (DOE) and analyzing data frame with Taguchi approach.

## 2 Experimental Procedure

### 2.1 Material and Sample Preparation

The sheets of Zinalume G550 steel (20 mm \* 20 mm \* 1.2 mm) were jointed via Metal Inert Gas (MIG) on lap joint configuration that is given in Fig. 1. The chemical compositions of metal wire are given in Table 1. The metal wire (ER70S-6, wire diameter is 1 mm) used on the Zinalume steel for welding and chemical compositions of the base metal is given in Table 2. The samples are ground through three different types of silicon carbide (SiC) abrasive paper, namely 220 grit, 1000 grit, and 2000 grit. It removes burrs on the joining interface.

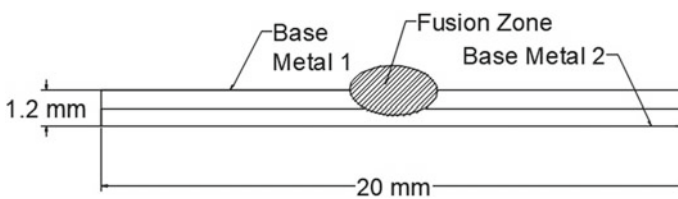


**Fig. 1** Configuration joint (closed square in lap jointing at the front view)

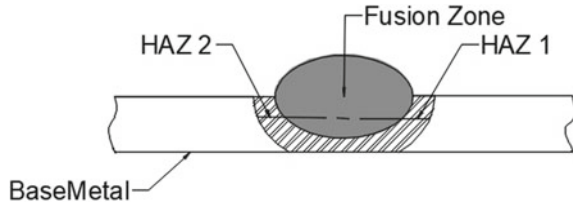
**Table 1** Chemical compositions for ER70S-6 wire (Iron: 96.11%)

Element of metal	C	Mn	Si	P	S	Cr	Ni	Mo	Ti	Cu
Percentage of value (%)	0.06–0.14	1.4–1.6	0.8–1	≤0.025	≤0.025	≤0.15	≤0.15	≤0.15	≤0.15	≤0.5

**Table 2** Chemical compositions of base metal [Zincalume G550 steel, (99.59%)]

Element of metal	C	Mn	S	P	Si	Al
Percentage of value (%)	0.02–0.07	0.14–0.22	0.01–0.02	0.01–0.02	0–0.02	0.03–0.06

**Fig. 2** Configuration of hardness distribution



### 2.2 Metal Inert Gas (MIG) Machine

This study used Hero Tech IM1680 160 A inverter MIG welding machine for joining the metals. The IM1680 MIG welding machine range of output current is from 40 to 160 A with output voltage of 16–22 VDC. The workpieces were clamped with G-clamp on the welding table for stability of samples in lap joint configuration.

The effect of welding voltage (16.5, 17, and 17.5 V) was investigated at a constant gas flow rate of 15 L/min. In addition, the wire speed (3, 3.75, and 4.5 m/min) was studied at a constant welding current of 70 A in this article.

### 2.3 Metallographic Characterizations

In this study, the weld appearance of lap joint is evaluated by the visual inspection for the hardness testing. In the hardness value testing, the welded specimens were cold mounted (15 mL resin and 2 mL hardener/per sample) and cut perpendicular to the welding direction. The specimens were ground with three types of abrasive papers (SiC) consisting of 220 grit, 1000 grit, and 2000 grit. The microhardness is tested via Vickers microhardness testing machine (401MVD, WOLPERT) with the load of 25 gf [2]. The hardness distribution crossed the cross section of welded pool on which the microhardness values were measured for the base metal (BM), fusion zone (FZ), and head affected zone (HAZ) [9], and the configuration of the microhardness distribution is given in Fig. 2.

### 2.4 Taguchi Method

The Taguchi orthogonal arrays (OAs) are a robust experimental design for optimizing process of parameters in which each factor is evaluated randomly by OAs. Normally,

**Table 3** Parameters of testing results for microhardness

Trial number	Microhardness values			
	HAZ1 (HV)	Welded pool (HV)	HAZ2 (HV)	Average (HV)
1	346.9	293.4	186.2	275.5
2	564.8	449.1	410.3	474.7
3	362.4	420.5	341.6	374.8
4	352.4	272.2	271.4	298.7
5	407.2	374.9	346.9	376.3
6	405.7	392.6	317.2	350.8
7	295.3	222	430.3	315.9
8	447.4	317.7	248.5	337.9
9	450	524.7	595.9	523.5
Average of each factor	403.6	356	349.8	
	Base metal		43.3	

there are three different categories for the analysis of signal–noise ratio (S/N) which are Small is Better, Normal is Better, and Larger is Better. In this study, the L9 ( $3^3$ ) orthogonal arrays are used to set the parameters in the Taguchi method in which the total number of trial is nine times [10].

### 3 Results and Discussion

#### 3.1 Results of Testing for Microhardness in Welded Metal

The parameters of wire speed and welding voltage were set via orthogonal arrays (OAs) of Taguchi method in design of experiment (DOE), and the testing results from parameter setting are given in Table 3.

#### 3.2 Discussion on Testing Result of Microhardness

From the previous studies about microhardness, the welding parameters greatly affect the hardness and toughness of the weldment. The size of grain structure of welded metal (WM) and the size of grain structure of heat affected zone (HAZ) are much smaller than the base metal (BM), and an increase in size of grain structure leads to a decrease in hardness [11]. In Fig. 3, the wire speed is a significant factor in this experiment which leads to an increase in hardness in the weldment. As a result, when the wire speed welding voltage increases, then the microhardness increases from 275.5 to 523.5 HV. The result is consistent with Li et al. [12] testing result and

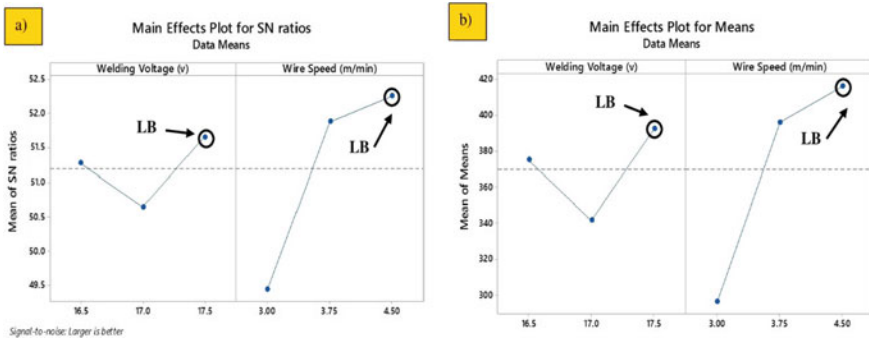


Fig. 3 a S/N ratio and b means for microhardness (LB-larger is better)

Sundararaj [13] in which the microhardness increases significantly when the wire speed and welding current increase. In Fig. 4, the hardness value in HAZ is higher than WM and BM (HAZ > WM > BM) at 403.6 HV results better than the results in a study by Hao et al. with 155 HV [14]. In the meantime, Berczeli found that the hardness value is the highest in HAZ at 190 HV [15]. According to the Taguchi results, this paper recommended the optimum value of results which included 4.5 m/min of wire speed and 17.5 V of welding voltage. The latest result is given in Table 4.

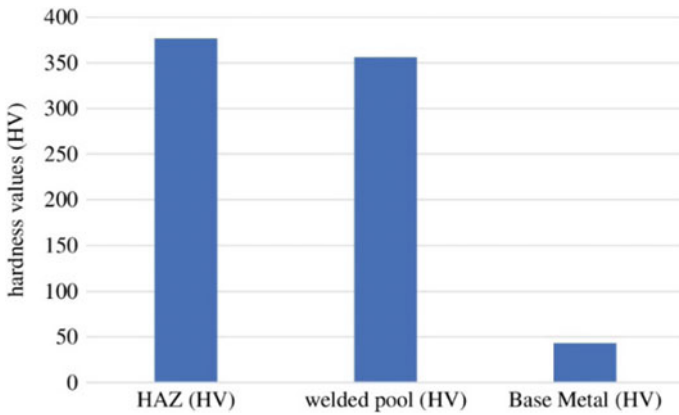


Fig. 4 Comparison of microhardness among the three positions in the welded metal

Table 4 Optimum values of results

Parameters	Wire speed (m/min)	Welding voltage (V)
Value	4.5	17.5

## 4 Conclusion

The following conclusions can be drawn from the results of this study:

1. The sheets of Zinalume G550 steel (20 mm \* 20 mm \* 1.2 mm) are successfully jointed by MIG welding using suitable parameters.
2. In the experimental results, when the wire speed and welding voltage increase, then the microhardness also increases.
3. The hardness value in HAZ is higher than BM and WM at 403.6 HV.

**Acknowledgements** This research was funded by SEGi University Sdn Bhd. The authors would like to thank Mr. Low Ping Hing and Mr. Vijaya Prakash Vijayasree from Swissma Building Technology Sdn Bhd for their kind contribution.

## References

1. Zhao J, Hua X, Huang L, Wu D, Li F, Zhang Y (2018) Double-sided hybrid laser-MIG welding plus MIG welding of 30-mm-thick aluminium alloy. *Int J Adv Manuf Technol* 97:1–9
2. Basak S, Das H, Pal TK, Shome M (2016) Characterization of intermetallics in aluminum to zinc coated interstitial free steel joining by pulsed MIG brazing for automotive application. *Mater Charact* 112:229–237
3. Das H, Basak S, Das G, Pal TK (2013) Influence of energy induced from processing parameters on the mechanical properties of friction stir welded lap joint of aluminium to coated steel sheet. *Int J Adv Manuf Technol* 64:1653–1661
4. Yang S, Zhang J, Lian J, Lei Y (2013) Welding of aluminum alloy to zinc coated steel by cold metal transfer. *Mater Des* 49:602–612
5. Dong H, Hu W, Zhang X (2013) Detachment of interfacial layers during arc-brazing of aluminum alloy to carbon steel with filler wire. *Trans Nonferrous Metals Soc* 23:1583–1588
6. Li R, Zhang F, Sun T, Liu B, Chen S, Tian Y (2019) Investigation of strengthening mechanism of commercially pure titanium joints fabricated by autogenously laser beam welding and laser-MIG hybrid welding processes. *Int J Adv Manuf Technol* 101:377–389
7. Li S, Dong H, Shi L, Li P, Ye F (2017) Corrosion behavior and mechanical properties of Al-Zn-Mg aluminum alloy weld. *Corr Sci* 123:243–255
8. Li Y, Zhang X, Ma X-J (2016) Microstructures and mechanical properties of MIG welding joint of 7005 aluminum alloy. In: 2nd annual international conference on advanced material engineering (AME 2016)
9. Janasekaran S, Jamaludin MF, Yusof F, Shukor MHA, Ariga T (2017) Influence of BA4047 filler addition through Mamdani fuzzy logic optimization for double-sided T-joint welding of aluminum alloys using low-power fiber laser. *Int J Adv Manuf Technol* 93:2133–2143
10. Mohamed MA, Manurung YHP, Berhan MN (2015) Model development for mechanical properties and weld quality class of friction stir welding using multi-objective Taguchi method and response surface methodology. *J Mech Sci Technol* 29(6):2323–2331
11. Hahn EN, Meyers MA (2015) Grain-size dependent mechanical behavior of nanocrystalline metals. *Mater Sci Eng* 646:101–134
12. Li R, Zhang F, Sun T, Chen S, Tian Y (2019) Investigation of strengthening mechanism of commercially pure titanium joints fabricated by autogenously laser beam welding and laser-MIG hybrid welding processes. *Int J Adv Manuf Technol* 101:377–389



13. Sundararaj P, Muthukumar M (2018) Characterisation of microstructure, mechanical and corrosion properties of pulsed MIG welded modified P91 steel weld metal. *Int Conf Adv Metall Mater Manuf* 314:1–6
14. Huang H, Yang B, Mo J, Geng Y, Zhou H, Zhang F (2018) Study on microstructures and properties of 7a52 aluminum alloy joints in laser-MIG hybrid welding. *Mater Sci Eng* 392:1–7
15. Berczeli M, Weltsch Z (2018) Experimental studies of different strength steels MIG brazed joints. *Periodica Polytechnica Transp Eng* 46(2):63–68

# Construction of a Hybrid Geometric Model for an Injection Mould Using CAD/CAM System



Jian Xin Tan and Mohd Salman Abu Mansor

**Abstract** The design of a mould, which is manually performed, is time-consuming and quite complicated. This research presents a study on the procedures for automatic feature recognition to help in mould design. A hybrid representation approach is used in automatic feature recognition to extract geometric information from a feature to identify undercut features. Boundary representation is applied in the shape representation using topology and geometry. The proposed approach uses a face adjacency hypergraph to describe the shape of the undercut features by representing the relationships amongst the feature faces. Face-to-face composition is applied to represent the relationship between the main and the undercut features. Parts A, B, and C are created, and automatic feature recognition is used to classify the depression and protrusion features. Algorithms based on a heuristic rule are adopted to determine the optimal parting line and direction of the parts by comparing their feature's geometric information. The automatic feature recognition approach identifies the shape of concave and convex features in accordance with the depression or protrusion of faces and the face adjacency relationship. This approach can be helpful in automatically creating the core and cavity. The proposed approach will help simplify the process and reduce the time for mould design. Therefore, this approach will significantly affect the increase in productivity in the manufacturing industry.

**Keywords** Automatic Feature Recognition · Undercut Features · Hybrid Representation · Parting Direction · Parting Line

## 1 Introduction

An injection mould is widely used in the manufacturing industry. Mould design is manually carried out, which is time-consuming and quite complicated. The automatic feature recognition will help promote automatic mould construction for industrial

---

J. X. Tan · M. S. Abu Mansor (✉)

School of Mechanical Engineering, Engineering Campus, Universiti Sains Malaysia, Seri Ampangan, 14300 Nibong Tebal, Seberang Perai Selatan, Pulau Pinang, Malaysia  
e-mail: [mesalman@usm.my](mailto:mesalman@usm.my)

© Springer Nature Singapore Pte Ltd. 2020

S. S. Emamian et al. (eds.), *Advances in Manufacturing Engineering*, Lecture Notes in Mechanical Engineering, [https://doi.org/10.1007/978-981-15-5753-8\\_30](https://doi.org/10.1007/978-981-15-5753-8_30)

323

uses. Several feature recognition and representation methods have been implemented to represent the feature shape and determine the undercut feature. However, some of these methods have limitations for specific features, and they are complex and require considerable geometric data to support the scheme.

The hybrid representation method is the key to generating a feature recognition algorithm based on geometric data and entities. The hybrid representation in the present research consists of an extended attributed adjacency graph (EAAG), boundary representation (B-rep), face adjacency hypergraph (FAH), and face-to-face composition (FFC). The parts and features can be represented by faces and edge and adjacency information relationship through the use of these representations. The details can be extracted and transformed into useful data. The data can generate some rules to help in feature recognition. These rules include determining the protrusion and depression. In CAD and solid modelling, B-rep is a method for representing feature shapes using limits. B-rep will focus on 3D structures, such as cylinder, cube, cuboid, sphere, and pyramid, by analysing the different entities in the model. This representation can effectively recognise various isolated features.

This research aims to use the hybrid representation method for generating several algorithms. Such an undertaking is initiated to help the feature recognition in the 3D model. The undercut features, such as protrusion and depression, can be determined through these algorithms. These algorithms will be inserted in the ACIS program. Subsequently, the mould construction for injection moulding will be automatically carried out.

## 2 Literature Review

Injection moulding is a manufacturing process of injecting molten materials into a designed mould to produce parts. The mould design is directly related to the mould quality and the time required to generate a mould [16]. The mould design process can be automatically carried out using the advanced knowledge in CAD/CAM software; this task is conducted to replace the manual method which is time-consuming [7].

In designing a mould through injection moulding, the part feature must be carefully analysed to ensure good mould quality. Moreover, the mould must be unaffected by the presence of undercut features. The method for determining and classifying the undercut features is crucial. The undercut features can be classified into two types, namely concave (protrusion) and convex (depression). Concave regions, such as pockets, holes, and slots, can probably become undercut features. By contrast, convex regions, such as bosses, spheres, cylinders, and cones, have low potential as undercut features [7]. The identification of non-convex regions on the part determines the part obstruction, and the region probably contains undercut features. Chakraborty and Venkata Reddy [5] reported that the external and internal undercut features are the major concerns to be solved. The internal undercut features are moulded by form pins or split cores inside the cavity and core. However, the external undercut features are moulded in the side cavities or cores.

A candidate retraction space is used for retracting the corresponding undercut facet, firstly in the horizontal direction and secondly in the vertical one, without intersecting with the part. However, the solid body is huge with a finite dimension attached to every undercut facet during retraction. This solid body volume and size will be the same as the core or cavity. The retraction space of the undercut facet will be computed [1]. Md Yusof and Abu Mansor [13] proposed an algorithm to detect feasible undercut features and generate the cavity and core using edge convexity and face connectivity approaches.

The 3D part can only focus on the square, triangle, rectangle, and loop containing a circular or partially circular arc [11]. Recognition rules that focus on regular shape recognition are simpler than those of a free-form-shaped one. Recognition rules applicable to all free-form shapes are difficult to generate. The free-form surface recognition method is restricted because the free-form features have no common pattern similarity [2]. Such a method can be applied using principle curvatures [4]. Entities, such as vertices, edges, and faces, are clustered into a curvature region and then grouped into features if they have the same curvature type. This method can be applied to regular-shaped and free-form features. Langerak [10] proposed a free-form feature recognition method. The global match on a free form is determined between the feature and the target shapes through an evolutionary computation procedure. If some dissimilarities still exist, then the shape's similarity is further expanded in another evolutionary procedure.

In the graph-based representation, a class of features has been determined by the required topological and geometric constraints. Gao and Shah [8] proposed an EAAG for the feature recognition method by extending the AAG and adding several edge and face attributes. The EAAG consists of five attributes, namely convexity, loop, geometry, existence, and blend type. The node attributes were used to verify the coincidence between faces. The other node attributes were used to verify the number of loops in the faces and concave hull and whether the face is planar or non-planar.

Nasr et al. [15] presented an approach for an automatic feature recognition system. The part data were extracted from the STEP file. The geometric information was analysed, and then a simple algorithm was developed to extract the feature face dimension. The maximum and minimum  $X$ ,  $Y$ , and  $Z$  values of the part were determined to estimate its volume size [18]. The common edge between the faces and the face group was verified to extract the dimension from the edge loop of the grouped faces through dimensional algorithms. The algorithms and checking common edge method helped identify part holes and pockets [9]. Ye et al. [20] proposed an extended attributed face edge graph (EAFEG) which is also a B-rep that extends the AAG to represent a solid model by adding edges and face attributes. The EAFEG has two attributes, namely face property and geometric type. The unique faces and edges were combined to generate the geometric information. The analytical result of the arc attributes indicates that the edge convexity is important for undercut feature recognition.

Concave edge is defined as the angle that is less than  $180^\circ$  between the sharing faces. The sharing faces which are greater than  $180^\circ$  are considered a convex edge. Sakkalis et al. [17] claimed that a valid B-rep model must be represented by a model

node if only one external shell exists, and no shell intersection and independent shell are present. Wu and Liu [19] proposed that the rule-based representation scheme for generating a set of heuristic rules is used to describe the characteristics and definition of a feature class. The graph-based representation scheme can also be converted into a rule-based one. Falcidieno [6] mentioned that the FAH model is used for shape feature recognition. The representation described the object faces, whereas the hyperarcs and arcs represented the face relationships. Bruzzone and Floriani [3] proposed that the FFC model of a feature is based on the decomposition into face adjacent parts. The two kinds of the components in the FFC model are negative and positive components. The former consists of depression features, whereas the latter consists of protrusion features.

Md Yusof and Abu Mansor [12] presented an algorithm that can automatically generate cavity and core for regular and free-form faces of a 3D CAD model. The optimal parting direction was selected using a normal vector approach. By contrast, holes and undercuts were detected using a scanning ray approach. Md Yusof and Abu Mansor [14] introduced a new algorithm for another alternative to determine parting direction automatically using the B-rep of a visibility map for generating the cavity and core of a two-plate mould.

### **3 Methodology**

#### ***3.1 Construction Part of the Injection Moulding in ACIS***

Three parts were constructed using the ACIS system. Part A consisted of depression features, such as blind and through-hole. Part B was composed of an external cuboid and a cylindrical protrusion feature. Part C consisted of protrusion and depression features which were the combined concepts of Parts A and B.

#### ***3.2 Obtain the Feature Geometry and Topology***

The global topological traversal functions were applied to obtain geometric information lists of lumps, shells, wires, faces, edges, and vertices of the parts. The number for each list of the parts was calculated and recorded using the global topological traversal functions.

### ***3.3 Classification of Undercut Features***

Solid objects bounded by two manifold features were considered. The FAH model was used to analyse the face relationship of the undercut features by constructing the FAH representation which uses the nodes to describe the object faces. The FFC composition was used to identify the face adjacent information between the features based on the component decomposition in the feature. The face classification categorised the faces in accordance with the shape and interaction. The types of undercut features were classified in accordance with the number of undercut faces, the type of faces, and the composition of features.

### ***3.4 Generating the Rule-Based Representation to Determine the Undercut Feature***

The EAAG and rule-based representations (heuristic rule) generated the attributes and rules which were based on the hybrid representation of FAH and FFC. The AAG was extended to determine the depression and protrusion features. The face attributes were added to the EAAG. Such attributes included convexity, type of face, number of adjacency faces, number of faces in the undercut feature, and geometry.

The rule-based representation was generated by the previous representation in this research to describe the undercut feature. The new heuristic rules are presented as follows:

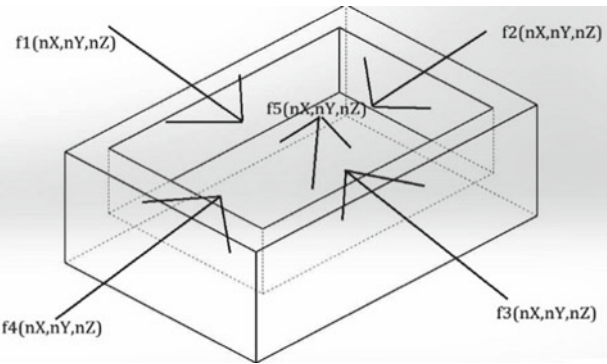
- Cuboid depression feature
  1. A concave feature is present.
  2. The feature consists of five depression faces.
  3. The feature only consists of cubic or rectangular planar faces.
  4. Only one interacting face is present on the depression feature.
- Cylindrical through a hole depression feature
  1. A concave feature is present.
  2. The feature only consists of one depression face.
  3. The circular edge is present on the feature.
  4. The feature only consists of one cylindrical face which is a non-planar one.
  5. Two interacting faces are present on the depression feature.
- Cylindrical blind hole depression feature
  1. A concave feature is present.
  2. The feature consists of two depression faces.
  3. The feature has one cylindrical face and one circular face.
  4. Only one interacting face is present on the depression feature.

- External cuboid protrusion feature
  1. A convex feature is present.
  2. The feature consists of five protrusion faces.
  3. The feature only consists of square and rectangular planar faces.
  4. Only one interacting face is present on the protrusion feature.
- External cylindrical protrusion feature
  1. A convex feature is present.
  2. The feature consists of two protrusion faces.
  3. The feature has one cylindrical face and one circular face.
  4. Only one interacting face is present on the protrusion feature.

### 3.5 Determination of the Parting Direction

The parting direction,  $d$ , should be identified to select the optimal direction to allow the core to move away from the cavity in the right direction. To identify the parting direction of the part, the normal direction,  $n$ , of the depression faces was identified and recorded to analyse their direction and find the parting direction of the depression feature. Table 1 displays the method for finding the parting direction of different features.

**Table 1** Determination of the parting direction of the cuboid depression feature

Normal direction of the faces in the depression feature	
Summation normal direction of each face in the depression feature	$X\text{-direction: } nX(f1) + nX(f2) + nX(f3) + nX(f4) + nX(f5) = dX$ $Y\text{-direction } nY(f1) + nY(f2) + nY(f3) + nY(f4) + nY(f5) = dY$ $Z\text{-direction } nZ(f1) + nZ(f2) + nZ(f3) + nZ(f4) + nZ(f5) = dZ$
Parting direction, $d$	$(dX, dY, dZ)$

### 3.6 Determination of the Parting Line

The parting line should be identified to separate the core and cavity. The parting line could be identified by gathering the mid-point information of the protrusion feature. If the mid-points of the protrusion features are sharing the same axis planar plane, then the parting line could be formed in the core and cavity generation.

### 3.7 Construction of the Core and Cavity

The structure and size of the core and cavity were constructed on the basis of the parting direction and line identified in the program.

## 4 Case Study

The automatic feature recognition programme is applied to Part C (Fig. 1). Such a programme consists of protrusion and depression features.

The undercut features of Part C were identified using the program. The topology information was known initially in this program. The programme showed that Part C consists of 1 lump, 1 shell, 29 faces, 60 edges, 44 vertices, and 48 loops. The maximum  $(x, y, z)$  coordinate was  $(9, 2, 4.5)$ , and the minimum was  $(-9, -2, -3)$ . The mould minimum should not be smaller than  $540 \text{ mm}^3$ . The programme extracted the protrusion and depression features information in accordance with the EAAG and

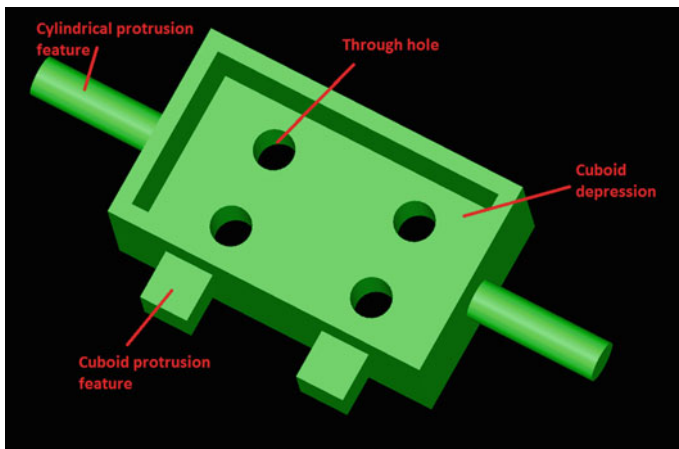


Fig. 1 Part C



heuristic hybrid representation. Such a programme showed that Faces 23–29 have no undercut feature.

*For depression feature*

The maximum ( $X_{\max}$ ,  $Y_{\max}$ ,  $Z_{\max}$ ) and minimum ( $X_{\min}$ ,  $Y_{\min}$ ,  $Z_{\min}$ ) values in this cuboid depression feature are (4.5, 2.0, 2.5) and (-4.5, -0.5, -2.5), respectively.

The volume of the cuboid depression feature is constructed as follows:

$$(X_{\max} - X_{\min}) \times (Y_{\max} - Y_{\min}) \times (Z_{\max} - Z_{\min}) = (4.5 - (-4.5)) \times (2.0 - (-0.5)) \\ \times (2.5 - (-2.50)) = 112.5\text{mm}^3.$$

To find the parting direction:

For the  $X$ -direction:

$$X(f4) + X(f5) + X(f6) + X(f7) + X(f8) = 0 + 1 + 0 + 0 + (-1) = 0$$

For the  $Y$ -direction:

$$Y(f4) + Y(f5) + Y(f6) + Y(f7) + Y(f8) = 0 + 0 + 0 + 1 + 0 = 1$$

For the  $Z$ -direction:

$$Z(f4) + Z(f5) + Z(f6) + Z(f7) + Z(f8) = (-1) + 0 + 1 + 0 + 0 = 0$$

The parting direction of Part C is (0, 1, 0) after comparing the parting directions of the depression features.

*For protrusion feature*

Find the normal direction of cuboid protrusions 1 and 2.

For the  $X$ -direction:

$$X(f9) + X(f10) + X(f11) + X(f12) + X(f13) = 0 + 0 + (-1) + 0 + 1 = 0$$

For the  $Y$ -direction:

$$Y(f9) + Y(f10) + Y(f11) + Y(f12) + Y(f13) = 0 + (-1) + 0 + 1 + 0 = 0$$

For the  $Z$ -direction:

$$Z(f9) + Z(f10) + Z(f11) + Z(f12) + Z(f13) = 1 + 0 + 0 + 0 + 0 = 1$$

This finding indicated that these features are sharing the same axis plane ( $Y = 0$ ). The results can be used to determine the parting line. The parting surface should be generated ( $134\text{ mm}^2$ ) to determine the parting line and should be located at ( $Y = 0$ ) as follows:

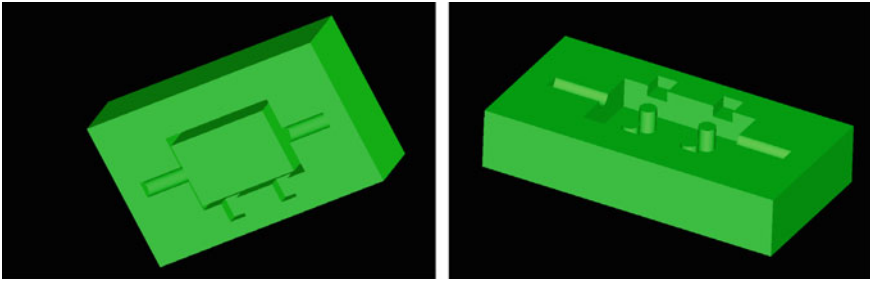


**Fig. 2** Core and cavity of Part C

$$\begin{aligned}
 \text{The parting surface} &= (X_{\max} - X_{\min}) \times (Z_{\max} - Z_{\min}) \\
 &= (9 - (-9)) \times (4.5 - (-3)) \\
 &= 134 \text{ mm}^2
 \end{aligned}$$

The programme combined the results by mixing the determination of depression and protrusion methods and created the ideal core and cavity for the mould (Fig. 2).

The result showed that the hybrid representation can combine the feature recognition and representation methods to produce another method that can ideally represent the part features, such as undercut features and feature shapes. The parting line and direction had also been identified and demonstrated by the algorithm.

## 5 Conclusions

The case study shows that different concave and convex features consist of various depression and protrusion faces, respectively. The parting direction is determined by the summation normal direction of the depression face algorithm in the depression feature, and the parting directions of the depression features are compared to find the optimal direction for ejecting the core away from the cavity. The parting line is determined by the algorithm wherein the mid-points of the protrusion features are compared to find the optimal parting surface for separating the core and cavity. In terms of contribution to knowledge, the determination of undercut features and the selection of the optimal parting direction and line can be automatically performed to help in the mould design. The mould design method can be simplified to save time.

**Acknowledgements** This research is supported by the Ministry of Higher Education Malaysia and Universiti Sains Malaysia under the Fundamental Research Grant Scheme (FRGS) (Reference No. 6071369).

## References

1. Banerjee AG, Gupta SK (2007) Geometrical algorithms for automated design of side actions in injection moulding of complex parts. *Comput Aided Des* 39(10):882–897. <https://doi.org/10.1016/j.cad.2007.05.014>
2. Bok AY, Abu Mansor MS (2013) Generative regular-freeform surface recognition for generating material removal volume from stock model. *Comput Ind Eng* 64(1):162–178. <https://doi.org/10.1016/J.CIE.2012.08.013>
3. Bruzzone E, Floriani L De (1991) Extracting adjacency relations IPS from a modular boundary model. *Comput Aided Des* 23(5):344–355. [https://doi.org/10.1016/0010-4485\(91\)90028-U](https://doi.org/10.1016/0010-4485(91)90028-U)
4. Cai N, Bendjebba S, Lavernhe S, Mehdi-Souzani C, Anwer N (2018) Freeform machining feature recognition with manufacturability analysis. *Procedia CIRP* 72:1475–1480. <https://doi.org/10.1016/J.PROCIR.2018.03.261>
5. Chakraborty P, Venkata Reddy N (2009) Automatic determination of parting directions, parting lines and surfaces for two-piece permanent molds. *J Mater Process Technol* 209(5):2464–2476. <https://doi.org/10.1016/j.jmatprotec.2008.05.051>
6. Falcidieno B (1989) Automatic recognition and representation of shape-based features in a geometric modeling system. *Comput Vis Graph Image Process* 48(1):93–123. [https://doi.org/10.1016/0734-189X\(89\)90106-0](https://doi.org/10.1016/0734-189X(89)90106-0)
7. Fu MW, Fuh JYH, Nee AYC (1999) Undercut feature recognition in an injection mould design system. *Comput Aided Des* 31(12):777–790. [https://doi.org/10.1016/S0010-4485\(99\)00070-6](https://doi.org/10.1016/S0010-4485(99)00070-6)
8. Gao S, Shah JJ (1998) Automatic recognition of interacting machining features based on minimal condition subgraph. *Comput Aided Des* 30(9):727–739. [https://doi.org/10.1016/S0010-4485\(98\)00033-5](https://doi.org/10.1016/S0010-4485(98)00033-5)
9. Han J, Kang M, Choi H (2001) STEP-based feature recognition for manufacturing cost optimization. *Comput Aided Des* 33(9):671–686. [https://doi.org/10.1016/S0010-4485\(01\)00071-9](https://doi.org/10.1016/S0010-4485(01)00071-9)
10. Langerak TR (2010) Local parameterization of freeform shapes using freeform feature recognition. *Comput Aided Des* 42(8):682–692. <https://doi.org/10.1016/j.cad.2010.02.004>
11. Liu C, Perng D, Chen Z (1994) Automatic form feature recognition and 3D part reconstruction from 2D CAD data. *Comput Ind Eng* 26(4):689–707. [https://doi.org/10.1016/0360-8352\(94\)90006-X](https://doi.org/10.1016/0360-8352(94)90006-X)
12. Md Yusof M, Abu Mansor MS (2017) Automatic core and cavity generation for 3D CAD model using normal vector and scanning ray approaches. *ARPN J Eng Appl Sci* 12(14):4250–4254
13. Md Yusof M, Abu Mansor MS (2018a) Undercut feature recognition for core and cavity generation. *IOP Conf Ser Mater Sci Eng* 290(1): 012070. <https://doi.org/10.1088/1757-899X/290/1/012070>
14. Md Yusof M, Abu Mansor MS (2018b) Alternative method to determine parting direction automatically for generating core and cavity of two-plate mold using B-rep of visibility map. *Int J Adv Manuf Technol* 96(9–12): 3109–3126. <https://doi.org/10.1007/s00170-018-1695-5>
15. Nasr ESA, Khan AA, Alahmari AM, Hussein HMA (2014) A feature recognition system using geometric reasoning. *Procedia CIRP* 18:238–243. <https://doi.org/10.1016/j.procir.2014.06.138>
16. Ratzlaff J, Giovannetti T (2016) Injection molding. In: *Handbook of industrial polyethylene technology*, vol 2. <https://doi.org/10.1002/9781119159797.ch15>
17. Sakkalis T, Shen G, Patrikalakis NM (2000) Representational validity of boundary representation models, *Comput Aided Design* 32(12):719–726. [https://doi.org/10.1016/S0010-4485\(00\)00047-6](https://doi.org/10.1016/S0010-4485(00)00047-6)
18. Sundararajan V, Wright PK (2004) Volumetric feature recognition for machining components with freeform surfaces. *Comput Aided Des* 36(1):11–25. [https://doi.org/10.1016/S0010-4485\(03\)00065-4](https://doi.org/10.1016/S0010-4485(03)00065-4)

19. Wu MC, Liu CR (1996) Analysis on machined feature recognition techniques based on B-rep. *Comput Aided Design* 28(8):603–616. [https://doi.org/10.1016/0010-4485\(95\)00075-5](https://doi.org/10.1016/0010-4485(95)00075-5)
20. Ye XG, Fuh JYH, Lee KS (2001) A hybrid method for recognition of undercut features from moulded parts. *Comput Aided Des* 33(14):1023–1034. [https://doi.org/10.1016/S0010-4485\(00\)00138-X](https://doi.org/10.1016/S0010-4485(00)00138-X)

# Development of a Face Sculpture Prototype Using a Reverse Engineering Technique



Mohd Zhafran Anwar Mohd Tahar and Mohd Salman Abu Mansor

**Abstract** This paper uses a reverse engineering technique to develop a face sculpture prototype from a real part without an original design documentation. Reproducing the model of a face sculpture becomes a considerable issue in the absence of such a documentation. Therefore, a data point was acquired for generating a 3D face sculpture in computer-aided design. The Delaunay triangulation and mesh of the point cloud were created using the computer-aided three-dimensional interactive application software. The surface of the mesh part was rebuilt, and the generated surface model of the face sculpture was analysed. To fabricate the face sculpture prototype via computer numerical control milling machine, machining simulation was performed using a computer-aided manufacturing software called Mastercam. The simulation showed different surface finishes for the face sculpture prototype when various parameters, such as cutting tool size, step over of the cutting tool and tool path style, were considered.

**Keywords** Reverse engineering · Computer-aided design · Prototype · Machining

## 1 Introduction

Reverse engineering (RE) allows a user to generate a computerised representation from an existing part surface based on the point data acquired [16]. RE consists of two processes, namely digitising a physical part and creating a 3D part modelling from digitised data. Different types of materials, such as stone, ceramic, bone, plastic, clay, metal, polyurethane or polystyrene, can be digitised [2, 4, 8]. An existing product or part of the geometrical shape is measured from the physical part, and then a complete computer-aided design (CAD) model is created [19]. Contact or non-contact method is used to collect 3D point data in creating a CAD model and in subsequent manufacturing processes [14]. RE input includes the focal physical object, and the CAD model is the output either as a volume representation or a surface reconstruction

---

M. Z. A. Mohd Tahar · M. S. Abu Mansor (✉)  
School of Mechanical Engineering, Engineering Campus, Universiti Sains Malaysia, Seri  
Ampangan, 14300 Nibong Tebal, Seberang Perai Selatan, Pulau Pinang, Malaysia  
e-mail: [mesalman@usm.my](mailto:mesalman@usm.my)

[18]. Existing RE software includes computer-aided three-dimensional interactive application (CATIA) [8, 16], SolidWorks, Pro-Engineer, CopyCAD, Rapidform and Geomagic Studio [3, 18]. RE is a versatile and highly popular technology in the currently advanced manufacturing world.

RE begins with data acquisition, wherein hardware is used to capture the data point cloud of the surface object. The physical object is scanned using different types of hardware which can be classified into the contact and non-contact methods. Contact methods involve the probe and mechanical contact between the physical object during the scanning process. For non-contact method, no probe and mechanical contact are found between the physical object during scanning [1]. An example of the contact method hardware is the coordinate measurement machine (CMM) with probe, and counterparts for the non-contact approach include computer tomography, magnetic resonance imaging, laser and ultrasonic scanners [18]. In contrast to their non-contact counterparts, contact-type devices are slow but can more accurately acquire data.

Varaday et al. [14], Lee and Woo [8] and Budaka et al. [3] discussed certain data acquisition issues, including data point accuracy, calibration, massive point data, measurement error, redundant data, the surface effect of the object (e.g. a shining object) and unfinished data that are associated with less accurate surface reconstruction. Budaka et al. [3] presented several solutions to these issues, such as the 3D digitisation preparation result via data filtering, data reduction and data smoothing. These steps usually imply a RE process at the pre-processing phase. Varaday et al. [14] also suggested calibrating the sensing device to identify accurate parameters or data points and utilising multiple scanning devices and views to resolve accessibility problems. Errors in acquired data are introduced by multiple views because of registration problems. Lee and Woo [8] proposed a procedure that overcomes certain resulting concerns and integrates RE and rapid prototyping.

Moreover, Son et al. [12] proposed an automated measuring system for partial inclusion of a free-form surface. To automate a measuring process, suitable hardware and software systems are needed. The software modules create optimal scan plans such that the scanning operation can be performed consequently. The hardware systems consist of setup fixtures and a laser scanning device that can give proper orientation and location for the part to be measured. Bernard and Véron [2] proposed a method that can scan a part automatically using a CMM with offline programming, and they employed a software module called Paint to locate the illuminated region using a laser beam, and thus, facilitate the data acquisition process. However, the system required enhancement in terms of its scanning effectiveness for a complex part. Vidvans and Basu [15] put forward a scalable open-source 3D reconstruction system for RE, which involves normalisation from a digital image correlation of surface speeds during a rotational motion of the focal part.

Pre-processing eliminates noisy points and obtains the required points. Despite technology utilised for scanning, a pre-processing phase is still needed to filter the point clouds from the deficiencies due to accuracy limitations and the noise introduced during the acquisition phase, thereby ultimately combining the point clouds that represent dissimilar views of the object and optimise the cloud's density

[6]. Budaka et al. [3] proposed a programmed system for the 3D digitisation pre-processing of data point. This commonly used system was derived from a cross-sectional approach. Data points acquired from a 3D digitisation system were rendered acceptable, sufficiently prepared and modified for the CAD model reconstruction. Carbone et al. [4] suggested combining a CMM and vision system for free-form surface RE by pre-processing point clouds through properly developed procedures for data reduction and ordering. Two algorithms were presented for reducing massive point data. Firstly, the random algorithm permitted the deletion of curves according to the probability specified by the consumer. This algorithm is very valuable when a large point number should be eliminated in the smooth shape areas. Secondly, a data reduction algorithm was developed on the basis of the change tolerance of the curvature or tangent [4].

According to Hsiao and Chuang [7], the data should be retrieved and reduced after reaching the acquisition data point. Scanned data will be overlooked at times for several reasons, including having a partition line or a concavity on the model. Moreover, the data point number can be reduced when the scanned data density is too high. A point cloud reduction method proposed by Lee and Woo [8] was employed to reduce the redundant point. The new point should be generated before creating the surface reconstruction. The first two steps in point cloud processing involve sampling and filtering [17]. Xu et al. [17] mentioned that these two steps directly influence the quality of model rebuilding and are the key stages in RE technology. This method may filter more noise on the high variability and low variability which could reflect the boundary and form points. Zhang [19] developed a programme for the format transformation of measurement data. Initially, the measurement data output format must be converted into a format that can be received by the Unigraphics software. Subsequently, the measurement data out of the tolerance range must be filtered out in a visualised way. The processed data can be employed directly for generating the die model.

Delaunay triangulation is defined as all the empty circumcircle of the triangle in the net. It is performed by creating a bounded circle from three random points and without any other points existing in the circle [9]. A triangle that is small and with a narrow angle must be avoided for stereolithography (STL) creation and actual fabrication using a rapid prototyping equipment. Hence, even the smallest among all triangle angles is sizeable. A vertex that makes an error that is smaller than the tolerance is selected and removed to reduce the point data. The Delaunay triangulation then retriangulates to the region around the vertex. A triangular mesh is one of the most popular shape representations in computer graphics and in the CAD and computer-aided manufacturing (CAM) domains. Such mesh comprises a set of triangles which is typically in 3D and is connected by common edges or corners. Sansoni and Docchio [11] used the Polyworks IMMerge module to generate or create a triangular mesh from the point cloud. The said module allows the operator or user to lightly adjust several parameter values that make this step flexible and feasible, and it also optimises the mesh both in terms of the number of the model triangles and in accuracy with respect to the original point cloud.

After creating and saving a solid model, it is transferred to a special file known as the STL. This file format was derived from the leading 3D systems in stereolithography. An STL file format stands for the virtual CAD model of the focal object to be modelled as a triangular facet. When taken together, this triangular facet describes a polyhedral estimation of the object's surface—such an estimation is a polyhedral approximation of the boundary involving the material and non-material. Using the scanned data to direct the STL file creation reduces the error and time in the modelling process. The number of point data reduction is important when producing STL file directly with retained precision from the measured point data. Lee et al. [9] demonstrated a novel approach for reducing the data size by segmentation and Delaunay triangulation. Chen et al. [5] focused on STL creation by specifying error bounds and percentages in data reduction. The region to be triangulated was chosen by the triangle deviation and its surrounding ones, and triangulation was executed according to the distance between the region points. Masood et al. [10] generated tool paths directly from point cloud data in the STL format based on direct machining. They proposed the machining of free-form surface geometries with complex machining areas and used three-axis milling with a ball end mill cutter and B-spline curves as the toolpaths [10].

RE is an important tool within the CAD modelling process, particularly in relation to complex surfaces which are often very complicated or almost impossible to model by using the tools offered in contemporary CAD systems. In the current study, a RE technique is used to develop a face sculpture prototype from its real part as the original design documentation of the face sculpture does not exist. Reproducing the model of the face sculpture becomes a great problem in the absence of the original design documentation.

## 2 Methodology

Figure 1 shows the flow chart of the overall RE process. In an early stage, CATIA is used to create the 3D part modelling from the digitised data. It is one of the most powerful and commonly used tools in many industries.

The first step in RE is accessing the workbench by using CATIA software for importing the point cloud from the scanned data file. To import the point cloud, the CATIA Digitised Shape Editor (DSE) workbench must be accessed. The DSE is used in the early stages of the RE cycle. In RE, the geometry of an existing physical object is captured by 3D scanning. The result is obtained in the form of digitised data. CATIA DSE allows for various operations on this digitised data. With DSE, many forms of digitised data can be imported, including meshes, grids, scans and point cloud to extract characteristic curves and create tessellated meshes. First, the CATIA DSE workbench must be accessed by selecting Start > Shape > Digitised Shape Editor. The point cloud is then imported using the 'cloud import tool'. This point cloud file can be in ASCII, Hyscan, Opton or stl file formats. The ASCII file format is selected to import the data by clicking 'Apply'.



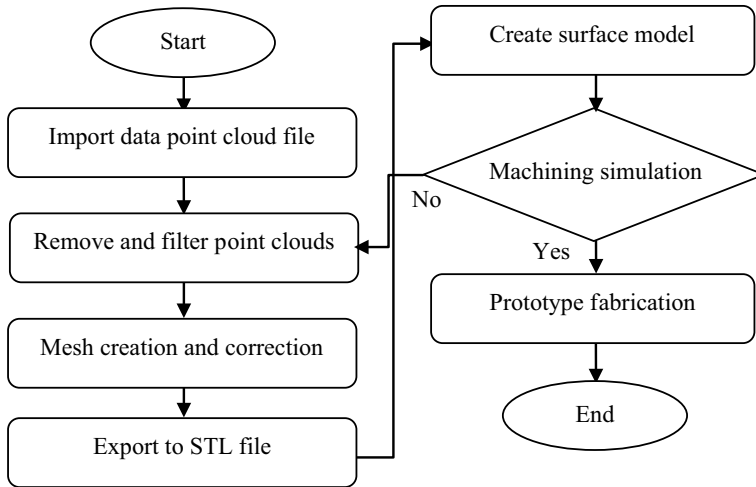


Fig. 1 Flow chart of the prototype development process

The number of points can be reduced to hasten further operation. The point to be removed can be selected either through using each of the points or the spline line to trap the certain region that must be removed. The ‘remove tool’ icon is clicked to remove the unnecessary points. Different modes (pick, trap or brush) can then be chosen to remove the point. This step filters the points and identifies the equilibrium gap between each of the points. When the scans or grids are filtered, the filtered points are hidden, and new scan or grids are created. The points can also be recalled using the ‘reset’ tab.

The next step is the mesh creation. In this step, facets can be created on the point cloud using the ‘mesh creation’ tool. The principle is that a mesh is created on all the active point clouds. The maximum facet edge is set via the neighbourhood parameter.

The mesh creation toolbox will appear after clicking on the ‘mesh creation’ tool. The standard or recommended neighbourhood value will be shown when the part or point cloud is clicked. The neighbourhood value is the maximum length of the facet edge. If one edge of the facet is greater than this maximum, then the facet will not be created. The neighbourhood value is increased to close unwanted holes in the mesh. In the display icon, the shading and triangles must be activated so that mesh with its triangles can be seen. In certain cases, identifying a neighbourhood value that can fill the holes without creating unwanted triangles may be difficult.

Figure 2 shows a complete mesh surface after hiding the point clouds. For the cloud export, an external format file can be created from the cloud, scans or meshes using the ‘Export’ tool.

The mesh elements that must be first exported are selected. The selected element is displayed in the ‘Element(s)’ field. The ‘Grouped’ feature selects all the elements for export into a single file. The ‘...’ button is then clicked to enter the name and the path of the file to be created. Subsequently, the ‘Save As’ dialogue box is displayed.

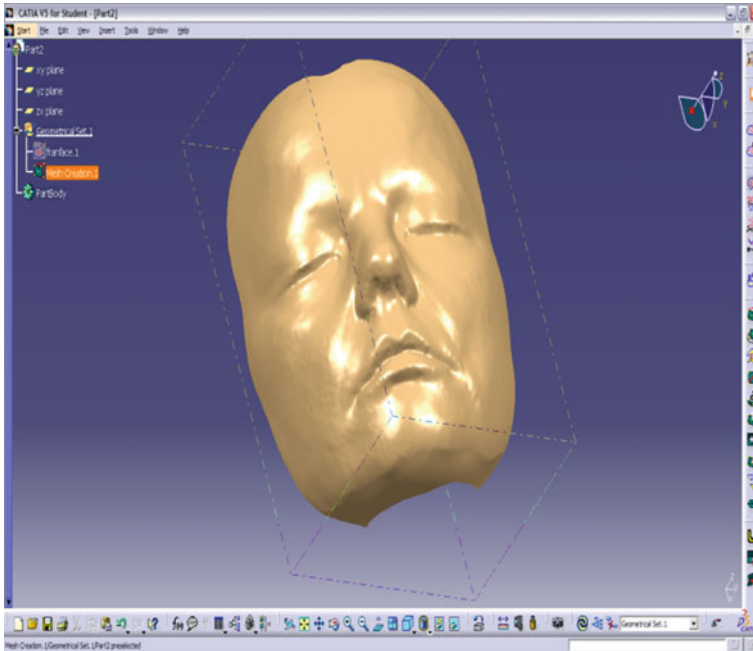


**Fig. 2** Complete mesh surface after hiding the point clouds

The file name is entered to create and select the needed file format, such as the STL file. Finally, the 'Save' button is pressed to revert to the main dialogue box.

A surface model is then generated for machining simulation. The tool and parameter selections are required for machining simulation using the CAM of the Mastercam software. Roughing is one of the processes for removing the bulk of the waste material during the machining process. This process is the first step of machining. The end mill tool is commonly used during roughing. This type of tool can be employed for removing the bulk of the material. In computer numerical control (CNC) milling, an end mill tool can perform many tasks, including cutting blind holes, flattening edges and making holes. However, such a tool cannot cut a square hole. Roughing is performed at high speed and depth. Conversely, finishing is the cutting process for completing the part and achieving the final dimension, tolerances and surface finish. Finishing is carried out at low speed and depth. In production machining tasks, one or more roughing cuts are usually performed on the work followed by one or two finishing cuts. Figure 3 shows the selected tool parameter. Finally, prototype fabrication is performed.

The face sculpture prototype was developed through RE. A CNC milling machine was used to fabricate the prototype. Perspex is the workpiece material utilised to fabricate this prototype. At the beginning of the process, the workpiece raw material was prepared into the required size, i.e. 200 mm × 150 mm × 50 mm (length × width × height). The thickness of the face sculpture to be fabricated is approximately 50 mm,

**Fig. 3** Final selection of the tool parameter

- Tool parameter:
- 1) Roughing
  - End mill D10
  - stepover 3mm
  - radius 0mm
- 2) Sweeping
  - Ball end mill D6
  - stepover 1mm
  - radius 3mm

but the available thickness of the workpiece raw material is only 25 mm. Hence, two blocks of Perspex material were employed and joined by using chloroform.

### 3 Result and Discussion

The surface of the face sculpture is almost similar to the actual one, and the apperancy is more clear (Fig. 4) because the data point cloud used in CATIA is larger. The larger the data point cloud used, the higher the probability that the shape of the face sculpture will be apparent. Each of the point clouds will connect to each other to create a triangle

**Fig. 4** Surface generation from CATIA



in a process known as Delaunay triangulation. This triangle will define the surface of the face sculpture. Therefore, the more the triangle is developed, the more apparent the shape of the face sculpture becomes.

Figure 5 shows that the smoothness of the surface model increased after the final selection of the tool parameter. The generated shapes obtained before this simulation are also rougher. The shape and contour of this machined surface model are also observed to be almost the same as those of the actual shape.

The set-up of the Perspex material was achieved with the CNC milling machine. After the complete set-up of the machine, the CNC code programme generated from the Mastercam software was transferred to the CNC milling machine to execute the machining operation. Machining started with the roughing process where the workpiece was roughly cut and was followed by the finishing process. Figure 6 shows the finished part of surface sculpture prototype.

**Fig. 5** After the machining simulation

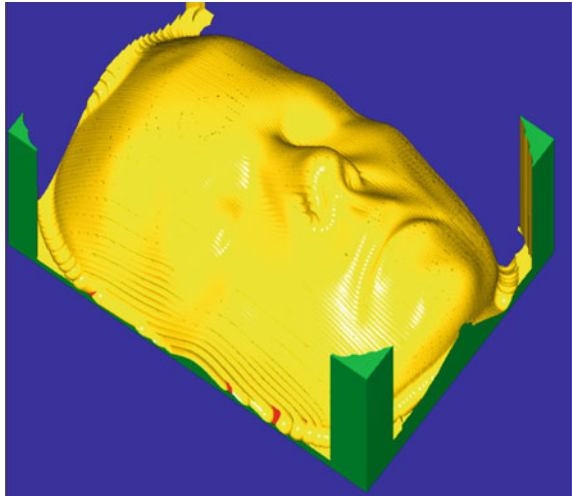


**Fig. 6** Finished face sculpture prototype



The simulation indicated that the size of tool used for each process (including roughing and finishing) influenced the surface quality of the final product. Tool size selection also depends on the size of the product that must be machined. This observation is because using a large tool for machining a small part will damage the part during machining. Furthermore, the step over of the cutting tool also plays an important role in producing a good surface finish. The larger the step over of the cutting tool used for the machining process, the lower is the surface quality produced.

A new paradigm for CNC carving of 3D surfaces on metallic or wooden plaques [13] can be related to this research as regards to the development of a face sculpture prototype. In contrast to the present work, prior research is focused on a 3D free-form surface representation in the form of a STL format and point cloud data from the conversion of a 2D digital image. However, their toolpath data for three-axis CNC finish machining was generated from the 3D surface data by using a ball end mill tool and validated by using a machining simulation, which is generally identical to the one in the current study. Therefore, the RE technique proposed for this work seems quite flexible, as indicated by the result for prototype development.

## 4 Conclusions

Several software applications can be used to develop a product design using the RE technique. However, software selection depends on the complexity of the part or the product that must be reverse engineered. In this study, CATIA software is used because it can import large file sizes given its lack of limitations regarding file sizes, and the quality of the final product also has its advantages. Surface analysis and comparison on the simulation can be performed for the CAD model of the face sculpture using CATIA. Furthermore, the Mastercam software was employed for machining simulation to fabricate the part prototype. This CAM software has its own benefits. Specifically, the quality of the part would be similar for the machining simulation and for the finished prototype of the face sculpture. Consequently, the step over of the tool is crucial in the finishing or sweeping process because it will influence the final surface quality of the product. In terms of contribution to knowledge, the RE technique presented in this paper can be employed flexibly, though no existing original design documentation is present.

**Acknowledgements** This research is supported by the Universiti Sains Malaysia and Ministry of Higher Education Malaysia under the Research University Grant (No: 811118) and Fundamental Research Grant Scheme (FRGS) (Reference No.: 6071369).

## References

1. Abu Mansor MS (2006) Free-form surface models generation using reverse engineering technique—an investigation. In: Proceedings of Malaysian Research Group International Conference 2006, United Kingdom, pp 379–385
2. Bernard A, Véron M (1999) Analysis and validation of 3D laser sensor scanning process. *Ann CIRP* 48(1):111–114
3. Budaka I, Hodolic J, Sokovic M (2005) Development of a programme system for data-point preprocessing in reverse engineering. *J Mater Process Technol* 162:730–735
4. Carbone V, Carocci M, Savio E, Sansoni G, De Chiffre L (2001) Combination of a vision system and a coordinate measuring machine for the reverse engineering of freeform surfaces. *Int J Adv Manuf Technol* 17:263–271
5. Chen YH, Ng CT, Wang YZ (1999) Generation of an STL file from 3D measurement data with user-controlled data reduction. *Int J Adv Manuf Technol* 152:127–131
6. Corbo P, Germani M, Mandorli F (2004) Aesthetic and functional analysis for product model validation in reverse engineering applications. *Comput Aided Des* 36:65–74
7. Hsiao SW, Chuang JC (2002) A reverse engineering based approach for product form design. *Des Stud* 24(2):155–171
8. Lee KH, Woo H (1998) Use of Reverse Engineering method for rapid product development. *Comput Ind Eng* 35(1):21–24
9. Lee SH, Kim HC, Hur SM, Yang DY (2002) STL file generation from measured point data by segmentation and delaunay triangulation. *Comput Aided Des* 34(10):691–704
10. Masood A, Siddiqui R, Pinto M, Rehman H, Khan MA (2015) Tool path generation, for complex surface machining. Using Point Cloud Data *Procedia CIRP* 26:397–402
11. Sansoni G, Docchio F (2004) Three-dimensional optical measurements and reverse engineering for automotive applications. *Robot Computer-Integr Manufact* 20:359–367
12. Son S, Park H, Lee KH (2002) Automated laser scanning system for reverse engineering and Inspection. *Int J Mach Tools Manuf* 42:889–897
13. Sood S, Duvedi RK, Bedi S, Mann S (2018) 3D representation and CNC machining of 2D digital images. *Procedia Manuf* 26:10–20
14. Varaday T, Martin RR, Cox J (1997) Reverse engineering of geometric model—an introduction. *Comput Aided Des* 29(4):255–268
15. Vidvans A, Basu S (2018) Smartphone based scalable reverse engineering by digital image correlation. *Opt Lasers Eng* 102:126–135
16. Woo H, Kang E, Wang S, Lee KH (2002) A new segmentation method for point cloud data. *Int J Mach Tools Manuf* 42(2):167–178
17. Xu L, Lin M, Li J, Wang Z, Chirende B (2008) Three-dimensional geometrical modelling of wild boar head by reverse engineering technology. *J Bionic Eng* 5:85–90
18. Yang Z, Chen Y (2005) A reverse engineering method based on haptic volume removing”. *Comput Aided Des* 37(1):45–54
19. Zhang Y (2003) Research into the engineering application of reverse engineering technology. *J Mater Process Technol* 139:472–475

# Experimental Investigations on the Surface Hardness of Synthesized Polystyrene/ZnO Nanocomposites



Mohammad Azad Alam, H. H. Ya, P. B. Hussain, M. Azeem, S. M. Sapuan,  
Rehan khan, and Tauseef Ahamad

**Abstract** The addition of inorganic spherical nanoparticles fillers to polymers matrix enables in the enhancement in the polymer's mechanical properties as well as the addition of new features in the polymer matrix. In the present study, ZnO/polystyrene composite was synthesized by bulk polymerization route and the hardness of composites was studied. The prepared nanocomposites were injected into a compression mold in a compression-molding machine. The prepared test specimen was subjected to Rockwell hardness tests. Further, to ensure proper morphology of nanocomposites, scanning electron microscopy (SEM) and X-ray diffraction (XRD) were carried out. Results revealed that by increasing nano-ZnO up to 0.3%, there is a remarkable increment approximately 47% in the hardness. Also, an analysis of variance (ANOVA) has been applied to find the optimal input parameter levels and to analyze the effect of these parameters on hardness. The composite produced is envisioned to have applications as the building blocks for the manufacturing of various automotive parts, sensors, transducers, actuators, UV detectors, and optoelectronic devices.

**Keywords** Polystyrene · Rockwell hardness · ZnO · Bulk polymerization

## 1 Introduction

In today's industrialization world, polymer-based composites are gaining their popularity as structural materials owing to their versatile properties. In order to enhance various properties like mechanical properties, tribological properties, and thermal stability, polymers are used to filled with nano-sized fibers, metals, and minerals;

---

M. A. Alam · H. H. Ya (✉) · P. B. Hussain · M. Azeem · R. khan · T. Ahamad  
Department of Mechanical Engineering, Universiti Teknologi PETRONAS, 32610 Seri Iskandar,  
Perak, Malaysia  
e-mail: [hamdan.ya@utp.edu.my](mailto:hamdan.ya@utp.edu.my)

S. M. Sapuan  
Department of Mechanical and Manufacturing Engineering, Universiti Putra Malaysia, 43400  
UPM Serdang, Selangor, Malaysia

however, in some previous studies ZnO nanoparticles have been studied as reinforcements for a number of polymers such as polyacrylonitrile [1, 2], polystyrene [3, 4], polystyrene butyl acrylate [5], and polyurethane [6]. However, the degree of property enhancement relies on the polymer matrix and on the particle size, distribution, and dispersion of the nanoparticles and on the adhesion at the interface of the filler matrix. Polystyrene is a widely used polymer, and its main features include low cost, transparency, and ease of processing. Due to its unique characteristics, polystyrene is to be used in a broad spectrum of applications area [7]. Polystyrene finds its applications in various industrial sectors that include electronics appliances, insulation of building and constructions, food utensils, and packaging [8]. The nano-sized zinc oxide (ZnO) has offered great attention as one of the multitask inorganic nanofillers due to its highly significant suitability like infrared adsorption, increased chemical stability, and low dielectric constant [9].

The main issue faced during processing or fabrication of polymer nanocomposites is to disperse the nano-sized fillers in a polymer matrix homogeneously [10]. The nano-sized fillers dispersion originates a greater interface area, and hence, nanocomposites got differentiated from traditional composites and filled plastics. Traditionally, there are usually three methods to fabricate polymer nanocomposites. They are melt intercalation, solution methods, and in situ polymerization. Hardness is purely a relative term, and hence, hardness of materials is impressed in number scale; so, it has no unit. Various evaluation approaches are developed to determine the hardness. Various types of hardness tests are the Rockwell hardness test, Durometer (shore) hardness test, Brinell hardness test, Knoop hardness scale, and Vickers scale.

The objectives of the present work are to synthesize new PS/ZnO nanocomposites using in situ polymerization methods and to analyze the influence of ZnO nanoparticles on the mechanical behavior, i.e., hardness of prepared composites and to characterize the prepared composites using SEM and XRD. The enhanced hardness nanocomposites are expected to be used in various fields such as field emission display, UV shielding, photocatalysis, and gas sensing.

## 2 Experimental Procedure

Prior to the fabrication of the nanocomposites, neat polystyrene samples were synthesized at 85 °C with the addition of initiator, namely benzoyl peroxide. The processing time for the polymerization is approximately 120 min, and the level of initiator was taken as 0.40% by weight. The experimental environment was chosen in order to get polystyrene with a melt flow index (MFI) value that is similar to commercially available polystyrene. The synthesis was done using polymerization (in situ) methods which include dispersing the nano-ZnO in monomer styrene and followed up by polymerization (free radical) process initialized by the addition of benzoyl peroxide (BPO). The monomer (styrene) with a suitable amount of ZnO was mixed (mechanically) with stirrer for half an hour. The mixture obtained is further gone in an ultrasonic bath for half an hour in order to obtain better dispersion. The benzoyl



peroxide was added to the prepared mixture to initiate the process (polymerization) at 95 °C for 180 min. The composites finally obtained were molded into the molds made up of aluminum and were kept in an oven at 110 °C to accomplish the process.

## ***2.1 Sample Preparation and Testing***

In order to prepare the specimens for hardness testing of the synthesized nanocomposite, synthesized composites are compression-molded between two compression-molding plates at a temperature of 160 °C. Before starting compression mold, the PS composite chunks and gauge are heated up to 160 °C. After this, pressure was applied manually in steps by a hand lever projected in the hydraulic press. The full pressure was applied for a minimum of 2 min. When the last step has taken place, the plates were cooled down to room temperature by giving the water bath. Then the compressed sheet of PS composite was taken out from the gauge. Ten sheets were prepared in a similar fashion. The capacity of this hydraulic press was 20 Ton.

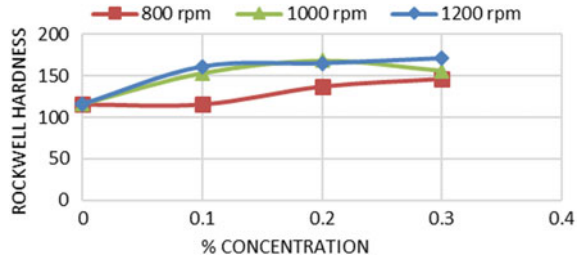
### **2.1.1 Hardness Test Procedure**

In Rockwell hardness test for all samples, M scale indenter is used and 100 kgf load is applied. Rockwell hardness test is most commonly used for relatively hard plastics. ASTM D785, standard test method for Rockwell hardness of plastics and electrical insulating materials was adopted for the Rockwell hardness test. ASTM D785 was adopted, and the test was carried out at a controlled atmosphere of  $23 \pm 2$  °C and  $50 \pm 5\%$  RH. A test scale preselected from the table was taken for measurement. This test was based on ASTM D785 according to the material. Accordingly, the major load was selected and was set, and the indenter was fitted. The test sample was placed on the anvil and minor load was applied by lowering the steel ball indenter onto the surface of the specimen. Minor load ensures good contact of indenter and test specimen. The dial of equipment was set to zero position, and major load is applied within 10 s by releasing the trip lever. After 15 s, major load is removed and the specimen is allowed to recover for another 15 s. During this period, the needle of the scale passing from zero position is counted. Rockwell hardness was calculated from the dial scale based on the difference in the number of times the needle of dial passes from zero. The Rockwell hardness was reported in number.

## **3 Results and Discussion**

The hardness of the nanocomposites synthesized at a different speed and concentration shows a notable increment as depicted in Fig. 1. This improvement can be attributed to the uniform dispersion of nano-filler in the polymer matrix. The uniform

**Fig. 1** Rockwell hardness variation with the concentration of ZnO at three different stirrer speeds



dispersion of nano-PS is also revealed that as the speed increases, the dispersion improves. In the present work, the maximum increment in Rockwell hardness is 47.41% at 1200 rpm with only a 0.3% level of concentration which is comparable with the previous works [11].

### 3.1 Characterization

The XRD pattern of the ZnO nanoparticles sample is shown in Fig. 2. It can be observed from Fig. 2 that the significant reflections are between  $30^\circ$  and  $40^\circ$  ( $2\theta$  values), which reveals a more crystalline regime in the zinc oxide sample. Figure 3 shows the XRD pattern of neat polystyrene. Figure 4 shows the XRD pattern of prepared composites at 1200 rpm and its comparison with base and filler materials.

The nano-ZnO peaks in the composite pattern confirm the formation of zinc oxide dispersed PS composite and development of crystallinity in the polystyrene matrix.

**Fig. 2** XRD pattern of nano-ZnO

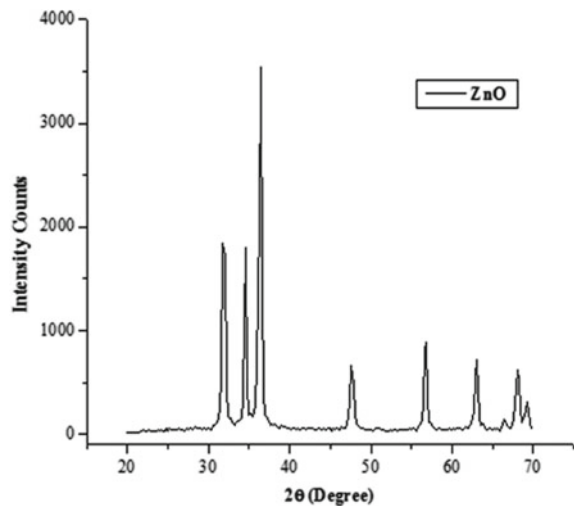


**Fig. 3** XRD pattern of polystyrene

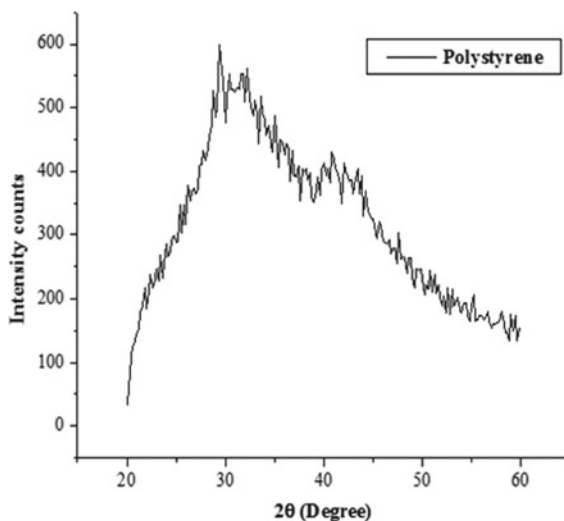
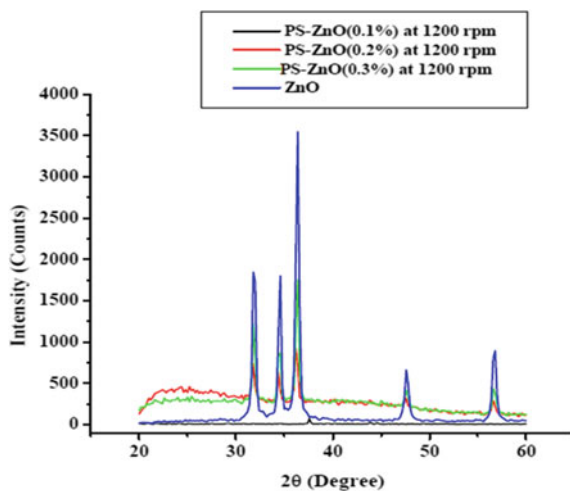


**Fig. 4** Comparison of XRD of ZnO with nanocomposites at different concentrations at 1200 rpm

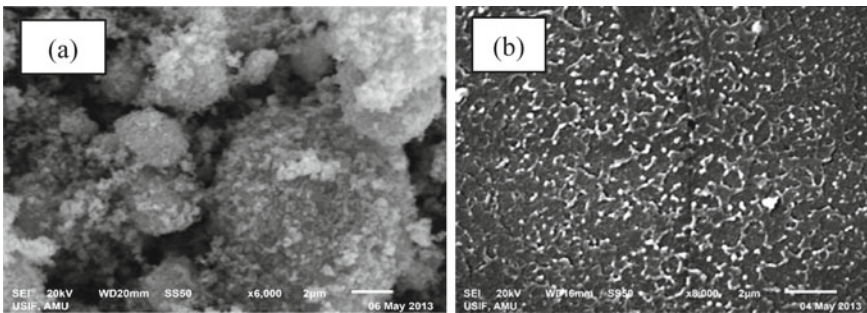


In this case, all the three composites peaks match with peaks of nano-ZnO, indicating the good dispersion of ZnO in the matrix.

Peak details of ZnO nanopowder obtained by powderx software are summarized in Table 1.

**Table 1** Peak details obtained by powderx

Sample	ZnO and nanocomposites
Crystal system	Hexagonal
Lattice type	<i>P</i>
Lattice parameter	$a = 4.9168, b = 4.9168, c = 5.4089$
Lattice parameter	Alpha = 90, Beta = 90, Gamma = 120
Radiation	Cu
Wavelength:	1.540598
2 $\theta$ start	20
2 $\theta$ end	70

**Fig. 5** SEM micrographs of **a** nano-ZnO and **b** PS/ZnO nanocomposites

### 3.1.1 Scanning Electron Microscopy

The scanning electron microscope (SEM) is one of the most flexible instruments for the assessment and investigation of the structural qualities of materials. The crack system of a polymer is a significant subject of intrigue identified with the structure of the material. The initiation of cracks and voids occurs in the weak region when a point load is applied on the surface of the polymer or composites. These voids can be detected by small angle X-ray scattering when they reach a size of about 20 to several hundred Angstrom units, and the structure can be observed directly by SEM. SEM micrographs for nano-ZnO and nanocomposites are shown in Fig. 5a, b, respectively.

## 3.2 ANOVA Analysis

The two-way ANOVA table for hardness against speed and concentration generated by MINITAB 15 is summarized in Table 2. From the table, it can be inferred that contribution of concentration is 19.93%, and while the contribution of speed

**Table 2** ANOVA table general linear model for hardness

Source	DF	SS	MS	F	P	Contribution%
Speed of stirrer (r.p.m)	2	1597.56	798.778	40.05	0.002	76.25
Conc. of ZnO	2	417.56	208.778	10.47	0.026	19.93
Error	4	79.78	19.944			3.82
Total	8	2094.89				100.00

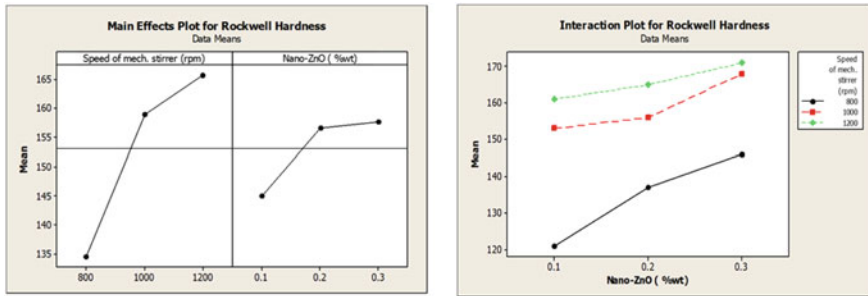


**Fig. 6** Main effects and interaction plot for rockwell hardness

is 76.25%, it means that the effect of concentration is more on tensile strength as compared to speed. Their contribution to error is 3.82%. The more the error, lesser will be the simultaneous effect of input parameter on the output parameter. The main effects plot and interaction effects plot are shown in Fig. 6. The concentration and stirring speed have an effect of 19.93% and 76.25%, respectively, as analyzed by ANOVA.

### 4 Conclusions

This research is focused on an experimental investigation of the effect of nano-ZnO and stirrer speed on the Rockwell hardness of prepared polymer nanocomposites. Polystyrene (PS)–zinc oxide (ZnO) nanocomposites were synthesized at three different concentrations and different stirrer speeds by in situ polymerization. Concentration and speed of stirring during polymerization are important parameters for the enhancement of mechanical properties. Nano-ZnO gives crystalline nature to nanocomposites. The optimum ZnO content to improve Rockwell hardness is 0.3%. At this ZnO content, the increment in Rockwell hardness is 47.41%. The dispersion of nanopowder enhances the crystallinity of PS. ANOVA results exhibit that in the case of Rockwell hardness, the concentration and stirring speed have an effect of 19.93% and 76.25%, respectively.

## References

1. Tang J, Wang Y, Liu H, Xia Y, Schneider B (2003) Effect of processing on morphological structure of polyacrylonitrile matrix nano-ZnO composites. *J Appl Polym Sci* 90(4):1053–1057
2. Chae DW, Kim BC (2006) Effects of zinc oxide nanoparticles on the physical properties of polyacrylonitrile. *J Appl Polym Sci* 99(4):1854–1858
3. Ma CCM, Chen YJ, Kuan HC (2006) Polystyrene nanocomposite materials—preparation, mechanical, electrical and thermal properties, and morphology. *J Appl Polym Sci* 100(1):508–515
4. Hooda A, Goyat M, Gupta R, Prateek M, Agrawal M, Biswas A (2017) Synthesis of nano-textured polystyrene/ZnO coatings with excellent transparency and superhydrophobicity. *Mater Chem Phys* 193:447–452
5. Xiong M, Gu G, You B, Wu L (2003) Preparation and characterization of poly (styrene butylacrylate) latex/nano-ZnO nanocomposites. *J Appl Polym Sci* 90(7):1923–1931
6. Song H-J, Zhang Z-Z, Men X-H, Luo Z-Z (2010) A study of the tribological behavior of nano-ZnO-filled polyurethane composite coatings. *Wear* 269(1–2):79–85
7. Tu Y et al (2010) Transparent and flexible thin films of ZnO-polystyrene nanocomposite for UV-shielding applications. *J Mater Chem* 20(8):1594–1599
8. Cao JP, Zhao J, Zhao X, Hu GH, Dang ZM (2013) Preparation and characterization of surface modified silicon carbide/polystyrene nanocomposites. *J Appl Polym Sci* 130(1):638–644
9. Ong CB, Ng LY, Mohammad AW (2018) A review of ZnO nanoparticles as solar photocatalysts: synthesis, mechanisms and applications. *Renew Sustain Energy Rev* 81:536–551
10. Alam MdA, Arif S, Ansari AH (2017) Mechanical and morphological study of synthesized PMMA/CaCO<sub>3</sub> nanocomposites. In: IOP conference series: materials science and engineering, vol 225 no 1. IOP Publishing
11. Xu J, Pan Q, Tian Z (2000) Grain size control and gas sensing properties of ZnO gas sensor. *Sens Actuators B Chem* 66(1–3):277–279

# A Review: Hybrid Welding of High Strength Materials



Okwudili S. Ogbonna, Stephen A. Akinlabi, Nkosinathi Madushele, Abiodun A. Abioye, and S. Hassan

**Abstract** Hybrid welding of high-strength materials such as stainless steel, aluminum alloy, and titanium alloy has become more important due to an ever-increasing demand for structural parts with combined properties of lightweight, low cost, enough strength, and energy saving and high performance in adverse environments for automobile, aerospace, petrochemical, and marine applications. Welding of such materials with conventional fusion processes has not always been possible due to wide disparity between their physical and thermal properties, residual stress, as well as the precipitation of thick and brittle intermetallic compounds, IMCs. Mechanical and corrosion properties depend so much on the thickness of IMCs, which conventionally must be less than 10  $\mu\text{m}$ . Although friction stir welding, laser welding, electron beam welding, and ultrasonic welding can give quality hybrid weld with reduced thickness of IMCs as low as 4  $\mu\text{m}$ , their application is limited by size and shape of base metals, need for vacuum environment in the case of electron beam welding, high cost, and special tool requirements. As a result of this, modified fusion arc welding processes remain the most widely applied welding processes in the industries. The improvement in the microstructural properties of hybrid arc fusion welding processes has been observed to achieve quality weld joint with enhanced performance. Comprehensive details of MIG–TIG hybrid welding of some high-strength materials have been developed in the subsequent sections of this review.

**Keywords** Hybrid welding · Intermetallic compound · Brazing · Microstructure · Mechanical

---

O. S. Ogbonna (✉) · N. Madushele  
Department of Mechanical Engineering Science, University of Johannesburg, Johannesburg,  
South Africa  
e-mail: [okwudilisimeon@gmail.com](mailto:okwudilisimeon@gmail.com)

S. A. Akinlabi · S. Hassan  
Department of Mechanical Engineering, Walter Sisulu University, East London, South Africa  
e-mail: [stephenakinlabi@gmail.com](mailto:stephenakinlabi@gmail.com)

A. A. Abioye  
Department of Mechanical Engineering, Covenant University, Ota, Nigeria

## 1 Introduction

Manufacturing processes are broadly classified into forming, casting, material removal, and joining processes [1]. Conventionally, welding is a manufacturing process in which similar or dissimilar metals are joined together by heat to form a formidable bond upon solidification different from brazing, riveting, and use of bolts and nuts [2]. Over the years, various welding processes have been developed such as friction stir welding (FSW), metal inert gas (MIG) welding, electron beam welding (EBW), ultrasonic welding (USW), tungsten inert gas (TIG) welding, submerged arc welding (SAW), laser beam welding (LBW), resistance spot welding (RSW), and plasma arc welding (PAW) [3] due to their superior strength over other metal joining processes. Hybrid welding entails a combination of two welding processes to form a joint [1]. There are about five types of welding joints based on applicability. They include lap joint, corner joint, butt joint, tee joint, and edge joint [2].

Properties of welded materials such as the fatigue, strength creep resistance, impact toughness and yield strength, and corrosion properties are affected by the chemical composition, residual welding stresses, and microstructural evolutions such as the formation of intermetallic compounds which arise from phase transformation during the heating process [4, 5]. The need for structural components with a combination of high specific strength, lightweight, and excellent corrosion properties in aerospace, automobile, railway, petrochemical, and marine industries increases. This increase is aimed to reduce cost, environmental pollution, weight, and energy consumption. Thus, welding of high-strength materials (most metal alloys) that meet these requirements or obtain high-performance workpiece becomes more important [6, 7]. However, welding of these materials demands adequate care to ensure that their excellent properties are not compromised during the welding process.

Most of the time, considering the disparities in chemical composition, and thermal and physical properties of high-strength materials, their weld joints often have properties different from their parent materials due to the introduction of residual stresses and formation of thick and brittle intermetallic compounds (IMCs) [7]. Several studies have examined arc fusion welding of similar and dissimilar high-strength materials [2, 8–27].

Tungsten inert gas welding (GTAW or TIG), a type of fusion welding, that utilizes arc between a non-consumable tungsten electrode and the workpiece [28], has also been widely investigated in joining of high-strength materials [29–38].

Although conventional MIG or TIG has been used to achieve a quality weld joint of high-strength materials with good performance through various strategies such as optimization of welding parameters, use of improved filler wire, use of adhesive bond, post-weld heat treatment, peening of surface to be welded, and numerical modeling [2, 8–27, 29–38], they are not without their shortcomings. Some of these shortcomings include low productivity due to low heat input and deposition rate of TIG welding process [39] and especially the formation of massive thick IMCs which has been seen to possess a great effect on the integrity, properties, and performance of welded joints [40].



Friction stir welding, laser beam welding, ultrasonic welding, and electron beam welding have been observed to achieve high-performance weld joints with very thin IMCs due to low heat input [41–44]. However, their application is limited by the size and shape of the workpiece, need for vacuum environment in the case of electron beam welding, and high cost of equipment. Arc welding, therefore, remains the most widely applied welding process in the construction and automobile industries. It is then obvious that there is need for MIG–TIG hybrid welding to be adopted instead of utilizing either MIG or TIG alone in welding of high-strength materials. This paper, therefore, has focused on the hybrid arc welding (MIG–TIG) of high-strength materials.

## 2 Methodology

Some scholars have investigated the microstructure of MIG–TIG hybrid welding. Zhang et al. [45] examined the microstructure of MIG welded joint of 7005 aluminum alloy to 321 stainless steel with auxiliary TIG arc. A welding–brazing joint mode with enhanced back and front appearance was observed due to the incorporation of the TIG arc, which was used to heat up the steel part with lower heat conductivity. The microstructure of IMCs of the weld bead was homogenous without abnormal lath-shaped intermetallic compound and less than 10  $\mu\text{m}$ . The IMCs of the joint obtained with conventional MIG process alone were not uniformed with serrated and some abnormal lath-shaped IMCs, which grew into the weld metal, thereby reducing the quality of the weld. The energy dispersive electroscopic study (EDS) conducted showed that the IMCs on the steel side possessed more dissolved nickel and chromium atoms than there were in the case of conventional MIG welding.

Still in an attempt to reduce the thickness of IMCs in order to enhance the quality of fusion welded joint, Ye et al. [46] also studied the synergistic effect of TIG and MIG double-sided arc welding on the microstructural and aesthetic properties of aluminum alloy and steel butt weld. The poor weld appearance often experienced in single-sided arc welding due to oxidation would be mitigated with the TIG torch at the reserve side of the weld if its current did not exceed 70 A. The Al–Fe IMC in the welding–brazing joint mode also was optimal at this TIG current value with thickness of 2.07  $\mu\text{m}$  on the steel brazing interface, which is lower than 2.23  $\mu\text{m}$  obtained at higher TIG current. It is also observed that the thickness of the IMCs became massive when the MIG voltage exceeded 13 V. The thickness of the IMCs at this voltage value decreased from 3.8 to 2.43  $\mu\text{m}$  also on the steel brazing interface.

Cheng et al. [6] observed the microstructural evolution of butt welded titanium alloy (Ti–6Al–4 V also known as TC4) and 304 stainless steel using MIG–TIG double-sided arc welding (DSAW). In the study, four different joint modes were used in the study by regulating the amount of heat input. It was observed that the stainless steel welding–TC4 brazing joint mode showed the best joint integrity. The welding–brazing mode achieved was different from the conventional welding–brazing joint mode, which involves the fusion of the two base metals with the base metal with

a lower melting point to braze the one with a higher melting point. Here, copper interlayer used formed brazing on the titanium alloy side and welding on the stainless steel side which suppressed the precipitation of brittle Ti–Fe IMCs. The stainless steel side interface of the joint contained two phases of copper and iron melted zones with curved morphology, which improved the quality of the joint.

Cheng et al. [7] also examined the microstructure of MIG–TIG double-sided arc welding of 304 stainless steel to pure copper without preheating and grooving. The heat input was regulated to examine its effect on the microstructure of the joint. It was found that at low heat input, a brazing mode was observed on the stainless steel side without pores and cracks. At intermediate heat input, dual welding and brazing were seen at the stainless steel side.

However, there was the presence of cracks and pores. At higher heat input, fusion on the stainless steel side was observed with pores and cracks. In all the three cases, there was fusion on the copper side of the joint. Therefore, copper welding–stainless steel brazing mode gave the best weld quality with good front and back appearances due to low heat. The positioning of the TIG arc at the reverse side of the joint during welding also protected the weld zone from oxidization.

The welding–brazing interface on the stainless steel side showed that the flat morphology and the weld zone consisted of single copper phase. At higher heat input, the fusion joint mode showed a scraggy morphology and the weld zone consisted of double phase of iron and copper due to the diffusion of iron atom at higher heat input. The microstructural evolution of MIG–TIG hybrid welded joints that has been discussed is given in Table 1.

**Table 1** Microstructural observations

Authors	Workpiece	Microstructure
Zhang et al. [45]	3.5-mm plates of 7005 aluminum alloy and 321 stainless steel	Homogenous lath-shaped Fe–Al IMCs with a thickness of less than 10 $\mu\text{m}$ Increased diffusion of nickel and chromium atoms in the $\alpha$ (Al) matrix
Ye et al. [46]	Q235 low-carbon steel and AA5052 aluminum alloy (3 mm $\times$ 60 mm $\times$ 200 mm)	Good front and back appearances obtained. With a proper combination of welding parameters, the Al–Fe IMC layer was less than 3 $\mu\text{m}$
Cheng et al. [6]	TC4 and 304 stainless steel plates (2 mm $\times$ 60 mm $\times$ 200 mm)	Thin IMCs with curved morphology and suppressed brittle Ti–Fe IMCs
Cheng et al. [7]	Pure copper and 304 stainless steel plates (3 mm $\times$ 60 mm $\times$ 200 mm)	At low heat input, stainless steel/weld interface showed a flat morphology Scraggy morphology was noticed at higher heat input due to the coarsening of grains

### 3 Study of Mechanical Properties

The mechanical properties of MIG–TIG hybrid welded joint have been investigated. Zhang et al. [45] observed the effect of auxiliary TIG arc on the mechanical behavior of MIG welded joint of 7005 aluminum alloy to 321 stainless steel. The hardness of the joint was lower than that of the aluminum base metal due to the replacement of iron atoms in the IMCs by nickel and chromium atoms. The reverse was observed without auxiliary TIG arc. The average tensile strength of the joint with auxiliary TIG arc increased from 96.7 to 146.7 MPa, and the fracture surface showed that the crack had penetrated through the weld metal, unlike in the case of conventional MIG where the crack initiated and ran through the IMCs alone.

Among four different joint modes observed between titanium alloy (TC4) and 304 stainless steel [6], stainless steel welding–titanium alloy brazing joint mode indicated the maximum tensile strength of 319 MPa which is higher than 63 MPa, 227 MPa, and 273 MPa obtained in TC4 welding–stainless steel brazing, TC4–stainless steel fusion, and TC4–stainless steel brazing joint modes, respectively. In MIG–TIG double-sided arc welding of pure copper to 304 stainless steel [7], as the heat input was increased, there was a reduction in the hardness of the heat-affected zone (HAZ) on the copper side of the joint. Their weld zone also changed from single phase of copper at low heat input to double phase of copper and iron. This increased the hardness of the weld zone to 139.1 and 136.1 HV at intermediate and higher heat inputs, respectively, which are significantly higher than 98.6 HV observed at lower heat input.

The tensile strength of all the joints obtained was lower than that of the base copper, the best tensile strength was 229 MPa, and fracture occurred on the HAZ of the copper base metal in all the cases due to increased softening. However, elongation observed was higher than that of the base copper. Table 2 gives the summary of the

**Table 2** Mechanical property observations

Authors	Workpiece	Response in mechanical property
Zhang et al. [45]	321 stainless steel plates and 3.5-mm 7005 aluminum alloy	Microhardness of welded bead was less than the aluminum base metal. Tensile strength increased from 96.7 to 146.7 MPa
Cheng et al. [6]	2 × 60 × 200 mm TC4 and 304 stainless steel plates	The joint with TC4 brazing–stainless steel welding mode showed a maximum tensile strength of 319 MPa
Cheng et al. [7]	3 × 60 × 200 mm plates of 304 stainless steel and pure copper	The hardness of the weld zone increased at higher heat input. Tensile strength decreased, but the elongation increased. The fracture occurred at the HAZ on the copper side in all the joint modes

mechanical properties of MIG–TIG hybrid welding of some high-strength materials that have been discussed.

#### 4 Study of the Effect of Welding Input Parameters

The weld pool behavior, arc shape, and manner of molten metal transfer in welding are determined by the choice of welding input parameters. These parameters, as well, have a great effect on the mechanical behavior and microstructure of the weld joint. Chen et al. [39] investigated the influence of auxiliary TIG arc on high-speed TIG–MIG hybrid welding. A bead on plate was used in the study. It was observed that when the auxiliary TIG arc was leading, the MIG arc was stable, the welding speed rose to 1.5 m/min, and undercut defect and spatters were not observed. In addition, even when the heat input was increased significantly, the microstructure of the weld did not deteriorate by the additional heat generated by the auxiliary TIG arc.

In MIG–TIG double-sided arc butt welding of aluminum alloy to low-carbon steel, Ye et al. [46] obtained optimal welding parameters. It was observed that TIG current, MIG voltage, and welding speed of 70 A, 13 V, and 2 cm/s gave the best IMC layers with best mechanical properties. Cracks were formed when the heat input was too high that was by increasing MIG voltage beyond 13 V or TIG current above 70 A. It was then observed that for optimal weld performance, MIG/TIG voltage ratio must be within 1.35–1.64. Beyond this ratio, the IMC layers were massive, which comprised the integrity of the weld joint.

In a MIG–TIG double-sided arc welding–brazing, Zhang et al. [47] studied the influence of welding parameters on the intermetallic compounds and mechanical properties of titanium alloy (Ti–6Al–4 V)/aluminum alloy (5A06) butt joints. The phase composition, thickness, and morphology of the Ti–Al IMCs were determined by the magnitude and concentration of the heat input. When the heat input was increased by increasing the TIG current from 70 to 100 A or by reducing the welding speed from 17 mm/s to 13 mm/s, the thickness of the Ti–Al IMCs increased. As a result, the morphology was transformed into serrated shape from the lamellar shape and the phase changed from  $\text{TiAl}_3$  to  $\text{TiAl}$  at the titanium alloy side of the joint. The maximum tensile strength of 240.3 MPa and IMCs of thickness from 2 to 6  $\mu\text{m}$  were obtained when the TIG current, welding speed, and TIG position were 80–90 A, 15 mm/s, and 0 mm, respectively.

Zhang et al. [40] also studied the effect of welding parameters on the microstructure of MIG–TIG double-sided arc welding–brazing of 1060 pure aluminum and 304L austenitic stainless steel. The argon flow rate of 15 L/min and welding rate were maintained at 200–400 mm/min at the two welding torches, while the MIG voltage was varied from 13 to 15 V and the wire-feeding rate from 5.8 to 6.8 m/min.

The TIG current was varied from 20 to 40 A. With the double-sided arc welding, due to its low heat input, a good weld was obtained with good front and back appearances and the thickness of IMCs was less than 5  $\mu\text{m}$  compared to 15  $\mu\text{m}$  observed in conventional MIG welding. The average tensile strength reached 80 MPa at fracture occurred at the HAZ of aluminum. However, this was reduced to 30 MPa with fracture at IMC layer when the TIG current, MIG voltage, and wire feed were raised to 40 A, 15 V, and 6.8 m/min, respectively, and welding speed reduced to 200 mm/min. This was due to increase in heat input, which increased the thickness of brittle IMC layers.

A challenge that is often encountered in the MIG–TIG double-sided arc welding (DSAW) is the welding depression defect. As a result, with the advantages of DSAW retained, Miao et al. [48] examined the effect of bypass current on the arc behavior and mode of molten metal transfer in high-speed butt welding of 304 stainless steel in order to eliminate welding depression. Due to the bypass current, a good weld seam appearance with significantly reduced depression was obtained at 0.87 m/min welding speed. The HAZ also became narrower, average tensile strength reached 618 MPa, the manner of metal transfer changed to globular transfer from short-circuiting transfer, and its rate of transfer was improved by 50%. These effects were attributed to the reduction of the base metal heat input and the increase in the filler wire melting heat by the bypass current.

From the foregoing, it is obvious that MIG–TIG double-sided arc welding has significantly improved the quality and performance of welded high-strength materials. However, in the welding of magnesium alloy to stainless for lightweight applications, the problems faced cannot sufficiently be solved by DSAW, since according to binary system, magnesium and iron do not interact with each other. Hence, Ding et al. [49] utilized copper as an interlayer between lap joints of AZ31B magnesium alloy and 430 ferritic stainless steel.

The joining was made possible because copper has great interaction with both. The TIG and MIG touches were arranged with an angle of  $75^\circ$  between them. In addition, two different copper foils of thicknesses 0.02 and 0.1 mm were chosen to study their effect on the properties of the weld joint. Optimal welding parameters were carefully chosen as follows: Welding current, voltage, shielding gas flow rate, and welding speed were 134A, 15.2 V, 15 L/min, and 30 mm/min, respectively.

With these values, when the thickness of the foil was lower than 0.01 mm, there was no proper spreading of the Mg on the Fe, while cracks began to occur when the thickness of the foil was above 0.15 mm. The lap joint with 0.1-mm copper foil gave the best quality joint. This was attributed to the higher conductivity and better heat distribution with the thicker foil, which promoted proper wetting, and hence better joint integrity with 47% improvement in tensile shear strength. The effects of welding parameters on the MIG–TIG hybrid welding have been summarized in Table 3.

**Table 3** Study of the effect of welding parameters

Authors	Workpiece	Processing parameter	Observation
Chen et al. [39]	Steel plate (5 mm × 70 mm × 250 mm)	Addition of auxiliary TIG arc current of 50 A, MIG current of 250 A, and argon shielding gas flowing at 20 L/min	The weld bead decreased by 48%, and no spatter and undercut defect detected. Stable current–voltage characteristics observed. There was no grain coarsening in the weld zone, and HAZ became narrower as welding speed increased
Ye et al. [46]	Q235 low-carbon steel and AA5052 aluminum alloy (3 mm × 60 mm × 200 mm)	MIG voltage was varied from 11 to 15 V, TIG current was varied from 50 to 90 A, and the welding speed was varied from 1.6 to 2.4 cm/s	Optimal welding parameters of MIG voltage 13 V, TIG current 70 A, and welding speed 2 cm/s gave the best weld quality with Al–Fe IMC layer less than 3 μm. The MIG/TIG voltage ratio must also be within 1.35–1.64 to avoid cracks
Zhang et al. [47]	Ti6Al4V and 5A06 Al (3 mm × 60 mm × 200 mm)	Welding speed: 13–19 mm/s, TIG current: 70–100 A	Maximum tensile strength obtained with TIG current, welding speed, and TIG position being 80–90 A, 15 mm/s, and 0 mm, respectively. The morphology of the Ti–Al IMCs changed from lamellar to serrated shape with a thickness of 2–6 μm, and their phase changed from TiAl <sub>3</sub> to TiAl on Ti6Al4V side of the joint

(continued)

**Table 3** (continued)

Authors	Workpiece	Processing parameter	Observation
Zhang et al. [40]	1060 pure aluminum and 304L austenitic stainless steel (2 mm 60 mm × 200 mm)	Welding rate: 200–400 mm/min, wire feed: 5.8–6.8 m/min, argon flow rate: 15 L/min, MIG voltage: 13–15 V, and TIG current: 20–40 A	A good weld appearance without defect was obtained with DSAW. In addition, the thickness of IMCs reduced at low heat input, the tensile strength reached 80 MPa with fracture at the HAZ of aluminum, and this was reduced to 30 MPa at higher heat input with fracture at the thick IMC layer
Miao et al. [48]	304 stainless steel (3 mm × 50 mm × 200 mm)	Bypass current of 50 A, filler melting current of 110 A, 32 V, 0.87 m/min welding speed, argon flow rate at 15 and 5 L/min for MIG and TIG, respectively, and wire feeding at 6.8 m/min	Depression reduced, metal transfer mode became globular instead of short-circuiting, fusion amount reduced, HAZ became narrower, average tensile strength reached 618 MPa, and the rate of metal transfer increased by 50%
Ding et al. [49]	AZ31B Mg alloy (3 mm × 60 mm × 150 mm) and 430 stainless steel (2 mm × 60 mm × 150 mm)	Welding current, voltage, shielding gas flow rate, and welding speed were 134 A, 15.2 V, 15 L/min, and 30 mm/min, respectively	Joint with 0.02-mm interlayer fractured at the Cu–Fe interface with brittle fracture mode, while the joint with 0.1-mm interlayer fractured at the intermetallic compound alloy which was not formed with 0.02-mm interlayer and propagated through the weld seam with quasi-cleavage fracture mode. The hardness of the Mg alloy was 55 HV. After welding, its HAZ rose to 83.2 HV with 0.02-mm foil and 64.4 HV with 0.1-mm foil. The tensile shear strength of 0.1-mm foil joint was 47% higher than the one with 0.02-mm foil

## 5 Conclusions

From the various studies examined, the following conclusions can be drawn:

- (1) High-strength materials such as titanium alloy, aluminum alloy, stainless steel, and magnesium alloy can successfully be welded with MIG–TIG hybrid welding.
- (2) The major challenges in welding of dissimilar materials are differences in their physical and thermal properties.
- (3) Welding of materials leads to the precipitation of intermetallic compounds at the weld and base metal interface. However, the properties of the welded joint are largely determined by the microstructure and thickness of intermetallic compound layer.
- (4) The thickness of intermetallic compounds is determined by the amount of heat input, which can be regulated by the welding parameters such as the welding current, voltage, speed, and shielding gas. Increasing the heat input increases the thickness of IMCs, which must be less than 10  $\mu\text{m}$  for optimal performance of the welded joint.
- (5) Although other welding processes, such as electron beam welding, ultrasonic welding, and friction stir welding, can be used to achieve a high-quality weld, their application is limited by the high cost of equipment, size and shape of base metal, special tooling, and their need for special preparation.
- (6) Hybrid MIG–TIG arc welding especially in DSAW has a great potential in the welding of high-strength materials without groove and preheating due to its low heat input, which reduces the thickness of IMCs formed during welding which improves the mechanical behavior of the welded joint. In addition, due to the positioning of the welding torches at both sides of the weld, a good spreadability of the molten metal is achieved, which yields a weld seam with excellent front and back appearances. The weld is also protected from oxidation at the backside of the weld.

## 6 Recommendations

From the literature reviewed, the following recommendations are made:

- Although from the reports given by the researchers on the MIG–TIG hybrid welding of high-strength materials, quality weld joint with excellent performance can be achieved, only a few studies in this regard have been reported and as such, more studies need to be done.
- The thickness of the workpiece that has been investigated is 3 mm and below without groove. Therefore, there is a need for more investigations to be made with workpieces with higher thicknesses. The result should then be compared with traditional MIG or TIG welding.



- Corrosion and thermal properties are crucial considerations for high-strength material structural components in an adverse and high-temperature environment. The studies that were reviewed in this paper have not considered the effect of MIG–TIG hybrid welding on these properties. Hence, more studies are required in this regard.

## References

1. Das S, Biswas A, Debbarma J, Deoghare AB (2018) Study of hardness of the weld bead formed by partial hybrid welding by metal inert gas welding and submerged arc welding at three different heat inputs. *Mat Today Proc* 5(5):13650–13657
2. Sen R, Choudhury SP, Kumar R, Panda A (2018) A comprehensive review on the feasibility study of metal inert gas welding. *Mat Today Proc* 5(9):17792–17801
3. Bu Y, Gardner L (2019) Finite element modelling and design of welded stainless steel I-section columns. *J Constr Steel Res* 152:57–67
4. Hu M, Li K, Cai Z, Pan J (2018) A new weld material model used in welding analysis of narrow gap thick-walled welded rotor. *J Manuf Process* 34:614–624
5. Kucharczyk P, Madia M, Zerbst U, Schork B, Gerwien P, Münstermann S (2018) Fracture-mechanics based prediction of the fatigue strength of weldments material aspects. *Eng Fract Mech* 198:79–102
6. Cheng Z, Huang J, Ye Z, Liu H, Yang J, Chen S, Zhao X (2018) Interfacial microstructure evolution and mechanical properties of TC4 alloy/304 stainless steel joints with different joining modes. *J Manuf Process* 36:115–125
7. Cheng Z, Huang J, Ye Z, Chen Y, Yang J, Chen S (2019) Microstructures and mechanical properties of copper-stainless steel butt-welded joints by MIG–TIG double-sided arc welding. *J Mat Process Technol* 265:87–98
8. Meena SL, Butola R, Murtaza Q, Jayantilal H, Niranjana MS (2017) Metallurgical investigations of microstructure and micro hardness across the various zones in synergic MIG welding of stainless steel. *Mat Today Proc* 4(8):8240–8249
9. Ghosh N, Pal PK, Nandi G (2017) GMAW dissimilar welding of AISI 409 ferritic stainless steel to AISI 316L austenitic stainless steel by using AISI 308 filler wire. *Eng Sci Technol Int J* 20(4):1334–1341
10. Khanna P, Maheshwari S (2018) Residual stress analysis in MIG welding of stainless steel 409 M. *5:4939–4947*
11. Li D, Uy B, Aslani F, Hou C (2019) Behaviour and design of spiral-welded stainless steel tubes subjected to axial compression. *J Construct Steel Res* 154:67–83
12. Vijaya SB, Daniel LI, Jayabal S (2018) Experimental study and analysis of weld parameters by GRA on MIG welding. *Mat Today Proc* 5(6):14309–14316
13. Dong H, Yang L, Dong C, Kou S (2012) Improving arc joining of Al to steel and Al to stainless steel. *Mat Sci Eng A* 534:424–435
14. Costanza G, Sili A, Tata ME (2016) Weldability of austenitic stainless steel by metal arc welding with different shielding gas. *Procedia Struct Integrity* 2:3508–3514
15. Rosado-Carrasco J, Krupp U, López-Morelos VH, Giertler A, García-rentería MA (2019) Effect of a magnetic field applied during fusion welding on the fatigue damage of 2205 duplex stainless steel joints. *Int J Fatigue* 121:243–251
16. Li D, Yang D, Luo X, Zhang G (2018) Effects of shielding gas on GMAW of 10Ni5CrMoV HSLA steel using high Cr-Ni austenitic wire. *J Mat Process Technol* 259(92):116–125
17. Ratan A, Chakraborty S, Sarathi P, Bose D (2018) Study of parametric effects on mechanical properties of stainless steel (AISI 304) and medium carbon steel (45C8) welded joint using GMAW. *Mat Today Proc* 5(5):12384–12393

18. Anant R, Ghosh PK (2017) Ultra-narrow gap welding of thick section of austenitic 19. stainless steel to HSLA steel. *J Mat Process Technol* 239:210–221
19. Májlinger K, Kalácska E, Russo P (2016) Gas metal arc welding of dissimilar AHSS sheets. *Mat Design* 109:615–621
20. Huang L, Hua X, Wu D, Jiang Z, Ye Y (2019) A study on the metallurgical and mechanical properties of A GMAW-Welded Al-Mg alloy with different plate thicknesses. *J Manuf Processes* 37:438–445
21. Yagati KP, Bathe RN, Rajulapati KV, Sankara KB, Padmanabham G (2014) Journal of materials processing technology fluxless arc weld-brazing of aluminium alloy to steel. *J Mat Process Technol* 214(12):2949–2959
22. Ru JI, Ram C (2007) Effect of preheating temperature and filler metal type on the microstructure, fracture toughness and fatigue crack growth of stainless steel welded joints. *Mat Sci Eng* 453:235–243
23. García AL, Salas R, Centeno L, Velásquez A (2011) Crack growth study of dissimilar steels (Stainless-Structural) butt-welded unions under cyclic loads. *Procedia Eng* 10:1917–1923
24. Tasalloti H, Kah P, Martikainen J (2017) Effect of heat input on dissimilar welds of ultra high strength steel and duplex stainless steel: microstructural and compositional analysis. *Mat Charact* 123:29–41
25. Shiri SG, Nazarzadeh M, Sharifitabar M, Afarani MS (2012) Gas tungsten arc welding of CP-Copper to 304 stainless steel using different filler materials. *Trans Nonferrous Met Soc China* 22(12):2937–2942
26. Anant R, Ghosh PK (2017) Advancement in narrow gap GMA weld joint of thick section of austenitic stainless steel to HSLA steel. *Mat Today Proc* 4(9):10169–10173
27. Ghosh N, Kumar P, Nandi G (2016) Parametric optimization of MIG welding on 316L austenitic stainless steel by grey-based taguchi method. *Procedia Technol* 25:1038–1048
28. Singh AK, Dey V, Rai RN (2017) Techniques to improve weld penetration in TIG welding (A review). *Mat Today Proc* 4(2):1252–1259
29. Wu B, Wang B, Zhao X, Peng H (2018) Effect of active fluxes on thermophysical properties of 309L stainless-steel welds. *255:212–218*
30. Kumar A, Sharma G, Dwivedi DK (2018) TIG spot weld bonding of 409 L ferritic stainless steel. *Int J Adhes Adhes* 84:350–359
31. Jegdić B, Bobić B, Radojković B, Alić B, Radovanović L (2019) Corrosion resistance of welded joints of X5CrNi18-10 stainless steel. *J Mat Process Technol* 266:579–587
32. Xin J, Song Y, Fang C, Wei J, Huang C, Wang S (2018) Evaluation of inter-granular corrosion susceptibility in 316LN austenitic stainless steel weldments. *Fusion Eng Des* 133:70–76
33. Kumar D, Sahoo G, Basu R, Sharma V, Mohtadi-bonab MA (2018) Investigation on the microstructure — mechanical property correlation in dissimilar steel welds of stainless steel SS 304 and medium carbon steel EN 8. *J Manuf Process* 36:281–292
34. Sadeghi B, Shari H, Ra M, Tayebi M (2018) effects of post weld heat treatment on residual stress and mechanical properties of GTAW : the case of joining A537CL1 pressure vessel steel and A321 austenitic stainless steel. *94:396–406*
35. Ghorbani S, Ghasemi R, Ebrahimi-kahrizsangi R, Hojjati-najafabadi A (2017) An effect of post weld heat treatment (PWHT) on the microstructure, mechanical properties, and corrosion resistance of dissimilar stainless steels. *Mat Sci Eng A* 688:470–479
36. Chuaiphan W, Srijaroenpramong L (2018) Optimization of gas tungsten arc welding parameters for the dissimilar welding between AISI 304 and AISI 201 stainless steels. *Diffr Technol* 1–9
37. Chandrasekar G, Kailasanathan C, Vasundara M (2018) Investigation on un-peened and laser shock peened dissimilar weldments of inconel 600 and AISI 316L fabricated using activated-TIG welding technique. *J Manuf Process* 35:466–478
38. Sayyar N, Shamanian M, Niroumand B (2018) Arc weldability of incoloy 825 to AISI 321 stainless steel welds. *J Mat Process Technol* 262:562–570
39. Chen J, Zong R, Wu C, Kumar G, Hu Q (2017) Influence of low current auxiliary TIG arc on high-speed TIG-MIG hybrid welding. *J Mat Process Technol* 243:131–142

40. Zhang Y, Huang J, Cheng Z, Ye Z, Chi H, Peng L, Chen S (2016) Study on MIG–TIG double-sided arc welding-brazing of aluminum and stainless steel. *Mat Lett* 172:146–148
41. Venkatesh KM, Arivarsu M, Manikandan M, Arivazhagan N (2018) Review on friction stir welding of steels. *Mat Today Proc* 5(5):13227–13235
42. Sun GF, Wang ZD, Lu Y, Zhou R, Ni ZH (2017) Investigation on microstructure and mechanical properties of NV E690 steel joint by laser-MIG hybrid welding. *Mat Des* 127:297–310
43. Hajitabar A, Naffakh-moosavy H (2017) Electron beam welding of difficult-to-weld austenitic stainless steel/Nb-based alloy dissimilar joints without interlayer. *Vacuum* 146:170–178
44. Ni ZL, Ye FX (2018) Ultrasonic spot welding of aluminum alloys: a review. *J Manuf Process* 35:580–594
45. Zhang H, Liu J, Feng J (2014) Effect of auxiliary tig arc on formation and microstructures of aluminum alloy/stainless steel joints made by mig welding-brazing process. *Trans Nonferrous Met Soc China* 24(9):2831–2838
46. Ye Z et al (2017) Combined effects of MIG and TIG arcs on weld appearance and interface properties in Al/ steel double-sided butt welding-brazing. *J Mat Process Technol* 250:25–34
47. Zhang Y, Huang J, Ye Z, Cheng Z, Yang J, Chen S (2018) Influence of welding parameters on the IMCs and the mechanical properties of Ti/Al butt joints welded by MIG/ TIG double-sided arc. *J Alloy Compd* 747:764–771
48. Miao Y, Xu X, Wu B, Han D, Zeng Y, Wang T (2015) Effects of bypass current on arc characteristics and metal transfer behaviour during MIG–TIG double sided arc welding. *J Mat Process Technol* 224:40–48
49. Ding M, Liu SS, Zheng Y, Wang YC, Li H, Xing WQ, Yu XY, Dong P (2015) TIG–MIG hybrid welding of ferritic stainless steels and magnesium alloys with Cu interlayer of different thickness. *Mat Des* 88:375–383

# Image Segmentation and Particle Size Analysis of Vibratory Disc Milled Titanium Alloy Powder



Okwudili S. Ogbonna, Stephen A. Akinlabi, Nkosnathi Madushele, Paul A. Adedeji, and Stephen Ekolu

**Abstract** Composite materials constitute two or more constituents with significant differences in their physical and chemical behaviours which combine to form a single material with superior properties than any of the individual constituents. Particle-reinforced composite is a class of composite materials in which particles (metallic, fibre, polymer, etc.) of various sizes are used to improve the property of the base material. The properties of particle-reinforced composite are greatly dependent on the particle size of the component used as reinforcement in the base or matrix material among other factors. This is due to a change in the interface bonding of the particles with the matrix component as the particle size changes. However, these reinforcing materials do not always come in the required particle size desired by the composite manufacturer. As a result of this, there is a need to reduce the particles to the required sizes. Vibratory disc milling is one of the techniques used in reducing the reinforcing material into the required size. In this study, the effect of milling duration on the particle size of titanium alloy powder has been analysed with MATLAB software. The result shows that when other milling parameters are held constant, the particle size reduces with increasing milling duration.

**Keywords** Titanium · Milling · Powder · Composite · Particle

---

O. S. Ogbonna (✉) · N. Madushele · P. A. Adedeji  
Department of Mechanical Engineering Science, University of Johannesburg, Johannesburg,  
South Africa  
e-mail: [okwudilisimeon@gmail.com](mailto:okwudilisimeon@gmail.com)

S. A. Akinlabi  
Department of Mechanical Engineering, Walter Sisulu University, East London, South Africa  
e-mail: [stephenakinlabi@gmail.com](mailto:stephenakinlabi@gmail.com)

S. Ekolu  
Department of Civil Engineering Science, University of Johannesburg, Johannesburg, South  
Africa

## 1 Introduction

Composite materials constitute two or more constituents with significant differences in their physical and chemical characteristics which combine together to form a single material with superior properties than any of the individual constituents [1]. Composite materials are conventionally made of two phases, namely: the matrix phase (the load distribution phase) and the reinforcement phase (the dispersed phase) [1]. The properties of composite material are a function of the relative quantity, quality, geometry, orientation and chemical composition of the constituent phases [2]. Composites are categorized based on the matrix phase as polymer matrix composites, ceramic matrix composites and metal matrix composites and also based on dispersed constituent as particulate-reinforced composites, structural composites and fibre-reinforced composites [3].

Particle-reinforced composites can be classified into two, namely: large-particle-reinforced and dispersion-strengthened composites. Concrete is an example of the large-particle-reinforced composite, while dispersion-strengthened composites include metals/metal alloys, polymer and ceramic matrices which contain finely dispersed inert material as reinforcement [4]. Particle-reinforced composites are widely utilized due to their excellent high specific strength, high strength, elastic stiffness, good dimensional stability, creep resistance, good fatigue property and enhanced tribological properties [5]. Titanium and its alloys display superior physical, mechanical and chemical behaviours which make them very useful for particle-reinforced composite fabrication for applications in industries such as aerospace, marine and automobile industries [6]. The titanium alloy used in this study is an  $\alpha + \beta$  type (Ti-6Al-2Sn-2Zr-2Mo-2Cr-0.25Si) with high ductility, high strength, high density, high corrosion resistance with reduced cold formability [7].

There are two major routes in the fabrication of particle-reinforced composite (ceramic matrix), namely: through liquid-state and solid-state processes. Liquid-state process of ceramic matrix composite fabrication includes various casting techniques, while the solid-state process involves powder metallurgy technique. Mechanical milling is often employed in the production of powder from the bulk material or in reduction of already obtained powder to the required size. Vibratory disc milling and ball milling have widely been utilized to this end [8]. In vibratory disc milling, the substance is milled by the pressure and frictional force generated between a gyrating disc and another fixed disc. The milling operation involves preliminary crushing by the grinding disc before the samples are transferred to the exterior regions of the grinding discs via centrifugal force where they are then finely ground to the required size depending on the set milling parameters [6].

Several studies have investigated the significance of milling operation on the microstructural transformation and properties of materials for various applications. Garroni et al. [9] stated that the reduction in grain size induced in metals during milling is determined by the processing technique, relative amount of metals present in the mixture and the differences between their respective hardness values. Dikici and Sutcu [6] reported a reduction in the average particle size of Ti-6Al-4 V flake powders without a change in the crystal structure.

Singh et al. [10] reported that the microhardness and compressive strength of Al-MWCNT nanocomposite reinforced by ball-milled aluminium were higher compared with nanocomposite without milled aluminium powders. Chen et al. [11] reported in cold pressing operation, milling operation increases the rate of microstructural evolution. Li et al. [12] also observed the consequences of milling on the particle size of tungsten–copper alloy below 48 h. Above this milling time, only the lattice parameters changed.

Madavali et al. [13] reported the growth of copper grains during the milling operation. The powder was milled under both air and argon atmospheres with varying milling time. After 80 h of milling, copper powder milled under air atmosphere due to contamination with oxygen showed higher particle size compared to the one milled under argon atmosphere. However, there was no observable change in their crystal structure as well as lattice parameters under both conditions of milling and at the end of many hours of milling. Ozkaya and Canakci [14] achieved a reduction in density and an increase in microhardness value of hot-pressed boron carbide-reinforced aluminium alloy matrix composite (AlCuMg–B<sub>4</sub>C) as the content of the boron carbide and milling duration progressed. The increased hardness of the reinforced composite was attributed to the even dispersion of the B<sub>4</sub>C particles in the aluminium alloy matrix.

Similarly, Yu et al. [15] also observed an increase in microhardness and refinement in the particle size of magnesium matrix-reinforced composite. Zhao et al. [16] utilized mechanical milling in spark plasma sintering of tungsten–yttrium (W<sub>3</sub>Y) composite. According to the study, as the milling time increased, there was corresponding increase in the crystallite size of the resultant composite. There was also slight increase in the microhardness of the composite as the milling duration was increased. In this study, the image segmentation and particle size analysis of vibratory disc-milled titanium alloy powder using MATLAB software were explored.

## 2 Experimental Procedure

An  $\alpha + \beta$  titanium alloy powder (Ti–6Al–2Sn–2Zr–2Mo–2Cr–0.25Si) produced and delivered by TLS Technik GmbH & Co company, South Africa, was used in this study. The mechanical milling process was carried out on vibratory disc milling machine model 2MZ-200 at 2 min intervals from 0 to 10 min. Prior to milling, the compartment was properly cleaned with water and detergent and then dried before finally cleaning with acetone to ensure that there is no contaminant left behind. The microscopic image of the powder obtained from the milling operation was analysed by scanning electron microscopy equipped with energy-dispersive spectrometer. The scanning electron images of the powder with their corresponding processed images are shown in Fig. 1a–f.

Vibratory disc milling machine specification has two chambers and can contain about 20 g weight of powder. Its feed size, motor capacity and speed are less than 15 mm, 380 V/50 Hz, 1.5 KW and 940 rpm, respectively.

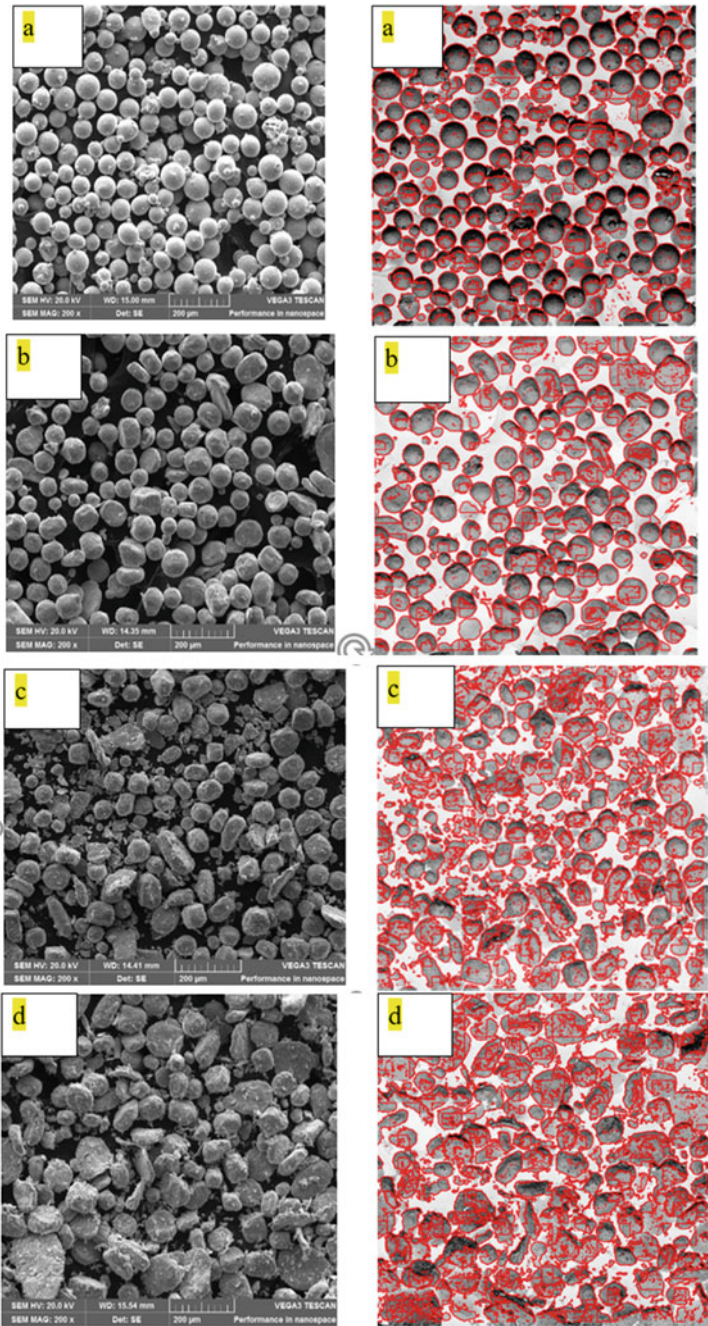


**Fig. 1** SEM of the **a** un-milled powder; **b** milled for 2 min; **c** milled for 4 min; **d** milled for 6 min; **e** milled for 8 min; and **f** milled for 10 min and their corresponding segmented images



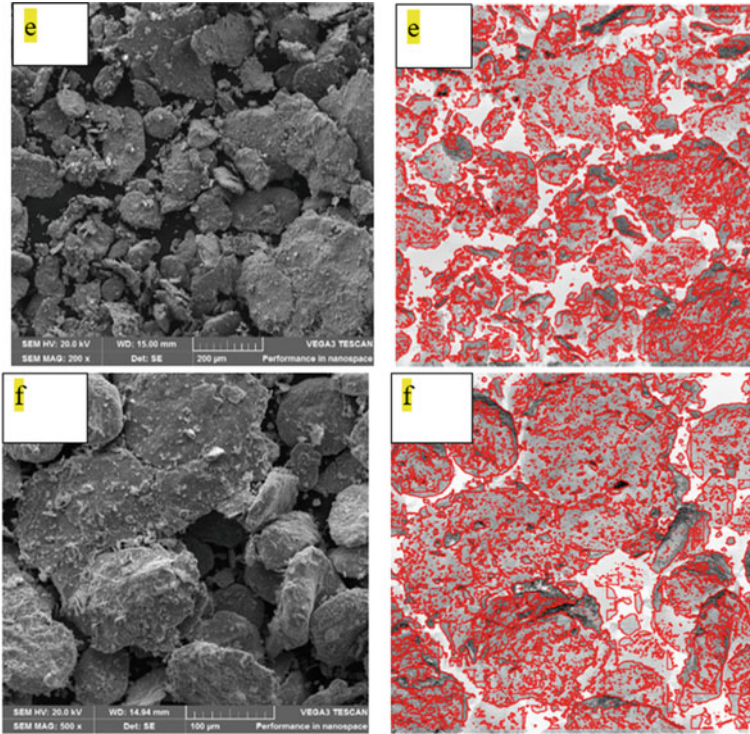


Fig. 1 (continued)

The image segmentation and particle size analysis of the scanning electron microscopic images of the powder were analysed by MATLAB software.

### 3 Image Segmentation

In image processing for morphological analysis, thresholding is a common segmentation technique as it separates the foreground pixel from background pixel, thereby improving the visual quality of the image [17]. To minimize data complexity during the thresholding, greyscale microscopic images are transformed into binary images. One of the advantages of threshold segmentation is that it simplifies calculation due to its fast operation and lack of complexity [18].



## 4 Methodology

### 4.1 Otsu Image Segmentation

In this study, the image thresholding was carried out via Otsu approach [19]. This approach is nonparametric and one-dimensional. It utilizes maximization of the intraclass variance of binary images. Bimodal class of the image is assumed which incorporates the foreground and background pixels which the microscopic images used in this study satisfy. After the global threshold value, the particle sizes of the images were obtained by using the different milling times after thresholding.

Given the local thresholds  $t_1, t_2, t_3, \dots, t_n$  to be selected from, the thresholds subdivide the images into  $n + 1$  classes of  $C_1, C_2, C_3, \dots, C_n$  by maximizing the objective function given by the sum of all threshold variances [20]. The flow chart is as follows:

$$J_1(t_1, t_2, t_3, \dots, t_n) = \sigma_0^2 + \sigma_1^2 + \sigma_2^2 + \sigma_3^2 + \dots + \sigma_n^2 \tag{1}$$

where

$$\begin{aligned} \sigma_0^2 &= \omega_0(\mu_0 - \mu_T)^2, & \omega_0 &= \sum_{i=0}^{t_1-1} p_i, & \mu_0 &= \sum_{i=0}^{t_1-1} \frac{ip_i}{\omega_0} \\ \sigma_1^2 &= \omega_1(\mu_1 - \mu_T)^2, & \omega_1 &= \sum_{i=t_1}^{t_2-1} p_i, & \mu_1 &= \sum_{i=t_1}^{t_2-1} \frac{ip_i}{\omega_1} \\ \sigma_2^2 &= \omega_2(\mu_2 - \mu_T)^2, & \omega_2 &= \sum_{i=t_2}^{t_3-1} p_i, & \mu_2 &= \sum_{i=t_2}^{t_3-1} \frac{ip_i}{\omega_2} \\ \sigma_3^2 &= \omega_3(\mu_3 - \mu_T)^2, & \omega_3 &= \sum_{i=t_3}^{t_4-1} p_i, & \mu_3 &= \sum_{i=t_3}^{t_4-1} \frac{ip_i}{\omega_3} \\ \sigma_n^2 &= \omega_n(\mu_n - \mu_T)^2, & \omega_n &= \sum_{i=t_n}^{t_{n+1}-1} p_i, & \mu_n &= \sum_{i=t_n}^{t_{n+1}-1} \frac{ip_i}{\omega_n} \end{aligned}$$

and  $\sigma_0^2, \sigma_1^2, \sigma_2^2, \sigma_3^2, \dots, \sigma_n^2$  are the class variances,  $\omega_0, \omega_1, \omega_2, \omega_3, \dots, \omega_n$  represent the class probabilities and  $\mu_0, \mu_1, \mu_2, \mu_3, \dots, \mu_n$  represent the mean values of the segmented classes. The intensity of the whole image is  $\mu_T \subseteq \mu_T = \omega_0\mu_0 + \omega_1\mu_1 + \omega_2\mu_2 + \omega_3\mu_3 + \dots + \omega_n\mu_n$  and  $\omega_0 + \omega_1 + \omega_2 + \omega_3 + \omega_n = 1$ .

Segmentation of the SEM images was performed at different milling times using a MATLAB script implemented in MATLAB R2015a installed on a laptop computer with configuration 64 bits, 6 GB RAM Intel (R) Core (TM) i7. The statistical analysis of the particles is displayed in Table 1.

**Table 1** ANOVA: two factors without replication

Summary	Count	Sum	Average	Variance
0.00	2.00	45,330.00	22,665.00	196,099,208.00
2.00	2.00	53,261.00	26,630.50	308,736,400.50
4.00	2.00	43,204.00	21,602.00	156,574,208.00
6.00	2.00	40,885.00	20,442.50	152,617,920.50
8.00	2.00	34,309.00	17,154.50	54,236,112.50
10.00	2.00	28,610.00	14,305.00	31,728,578.00
Particle size (micrometres)	6.00	73,699.00	12,283.17	1,688,072.57
StDev	6.00	171,900.00	28,650.00	54,807,137.20

## 5 Result and Discussion

As shown in Fig. 1a–f, the thresholding segmentation technique with MATLAB software was able to distinguish the foreground from the background pixels, thereby enabling the particle sizes to be calculated. It can be deduced from Table 1 that the average particle size of the un-milled powder is 22,665  $\mu\text{m}$ . After two minutes of milling operation, the average particle size increased to 26,630.50  $\mu\text{m}$ . However, after 4, 6, 8 and 10 min of milling, the average particle size decreased to 21,602  $\mu\text{m}$ , 20,442.50  $\mu\text{m}$ , 17,154.50  $\mu\text{m}$  and 14,305  $\mu\text{m}$ , respectively.

This shows that if other milling parameters are kept constant, increasing the milling time decreases the particle size of the powder. The increase in the particle size of the powder after 2 min milling suggests that the milling time is too low to cause complete fracturing of the particles; rather, they are experiencing some deformation from spherical to flake-like shape, which is most likely responsible for the increase in the average particle size. However, as the milling progressed, the particles began to fracture by plastic deformation indicated by the transformation of the spheroidal shape of the powder into flattened irregular morphology.

## 6 Conclusion

From the result obtained, the following conclusions were drawn:

1. Vibratory disc milling is an effective technique to obtain the desired particle size from the bulk material for application in powder metallurgy and composite fabrication.
2. Increasing the milling time while other milling parameters are kept constant leads to a significant reduction in the particles of the material being milled.
3. Threshold segmentation with MATLAB software can be used for image processing to determine the particle size of a sample.

## References

1. Shekar HSS, Ramachandra M (2018) Green composites: a review. *Mater Today Proc* 5(1):2518–2526
2. Henrique P, Camargo C, Satyanarayana KG, Wypych F (2009) Nanocomposites: synthesis, structure, properties and new application opportunities. *Mater Res* 12(1):1–39
3. Low LF, Bakar AA (2011) Advanced hollow epoxy particle-filled composites. *J Compos Mater* 45(22):2287–2299
4. Wang R-M, Zheng S-R, Zheng Y-P (2011) Introduction to polymer matrix composites. *Polym matrix Compos Technol*, 1–548
5. Cabeza M et al (2017) Effect of high energy ball milling on the morphology, microstructure and properties of nano-sized TiC particle-reinforced 6005A aluminium alloy matrix composite. *Powder Technol* 321:31–43
6. Dikici T, Sutcu M (2017) Effects of disc milling parameters on the physical properties and microstructural characteristics of Ti6Al4V powders. *J Alloys Compd* 723:395–400
7. Shah FA, Trobos M, Thomsen P, Palmquist A (2016) Commercially pure titanium (cp-Ti) versus titanium alloy (Ti6Al4V) materials as bone-anchored implants — is one truly better than the other? *Mater Sci Eng C* 62:960–966
8. Albaaji AJ, Castle EG, Reece MJ, Hall JP, Evans SL (2017) Effect of ball-milling time on mechanical and magnetic properties of carbon nanotube reinforced FeCo alloy composites. *Mater Des* 122:296–306
9. Garroni S, Soru S, Delogu F (2014) Sciencedirect reduction of grain size in metals and metal mixtures processed by ball milling. *Scr Mater* 88:9–12
10. Singh LK, Bhadauria A, Laha T (2018) Al-MWCNT nanocomposite synthesized via spark plasma sintering: effect of powder milling and reinforcement addition on sintering kinetics and mechanical properties. *Integr Med Res* xx:1–10
11. Chen Y, Chen T, Zhang S, Li P (2015) Effect of ball milling on microstructural evolution during partial remelting of 6061 aluminium alloy prepared by cold-pressing of alloy powders. *25:2113–2121*
12. Li C, Zhou Y, Xie Y, Zhou D, Zhang D (2018) Effects of milling time and sintering temperature on structural evolution, densification behaviour and properties of a W-20wt.% Cu alloy. *J Alloys Compd* 731:537–545
13. Madavali B, Lee J, Kyu J, Young K, Challapalli S, Hong S (2014) Effects of atmosphere and milling time on the coarsening of copper powders during mechanical milling. *Powder Technol* 256:251–256
14. Ozkaya S, Canakci A (2016) Effect of the B 4 C content and the milling time on the synthesis, consolidation and mechanical properties of AlCuMg-B 4 C nanocomposites synthesized by mechanical milling. *Powder Technol* 297:8–16
15. Yu H, Sun Y, Hu L, Zhou H, Wan Z (2016) Microstructural evolution of AZ61-10 at.% Ti composite powders during mechanical milling. *JMADE* 104:265–275
16. Zhao M, Zhou Z, Tan J, Ding Q, Zhong M (2015) Effects of ball milling parameters on microstructural evolution and mechanical properties of W-3% Y composites. *J Nucl Mater* 465:6–12
17. Lei B, Fan J (2019) Image thresholding segmentation method based on minimum square rough entropy. *Appl Soft Comput J* 84:105687
18. Zaitoun NM, Aqel MJ (2015) Survey on image segmentation techniques. *Procedia Procedia Comput Sci* 65(Iccmit):797–806
19. Smith P, Reid DB, Environment C, Palo L, Alto P, Smith PL (1979) A threshold selection method from gray-level histograms. *C(1):62–66*
20. Li L, Sun L, Kang WEI, Guo J, Han C, Li S (2016) Fuzzy multilevel image thresholding based on modified discrete grey wolf optimizer and local information aggregation. *IEEE Access* 4:6438–6450

# Hydrodynamic Analysis of Floating Offshore Solar Farms Subjected to Regular Waves



A. M. Al-Yacouby, Emiruddin Redza Bin Abdul Halim, and M. S. Liew

**Abstract** In the Malaysian water, most of offshore platforms rely on fossil fuels to produce electricity for their power generation. However, due to concerns related to depletion of fossil fuels and the greenhouse gas (GHG) emissions, the Malaysian government is moving towards the application of renewable energy resources. Floating solar farms are comparatively new in the Malaysian water, and in-depth investigation is needed to better understand the performance of these types of floaters when placed in the open sea. This paper is intended to conduct a parametric study on the dynamic responses of a floating solar farm for Malaysian offshore applications. In this study, the dynamic responses of the floating solar farm are determined using analytical methods, and then the results are validated using Computational Fluid Dynamics (CFD). The important parameters covered in this study are the wave heights, wave periods, water depths, and the diameter of pontoons. The results show that wave heights, wave periods, and pontoon diameters have major influence on the hydrodynamic forces, while the water depth has comparatively minor influence on the dynamic responses of the floating offshore solar farm.

**Keywords** Hydrodynamic analysis · Floating offshore solar farms · RAO · CFD · Dynamic responses

## 1 Introduction

Increasing awareness of climate change has increased the demand for renewable energy resources [1]. Offshore solar panels have already been pioneered across the globe where several such solar farms have been built on large lakes [2]. However, installing such floating solar farms in open sea is a challenging task as their responses to the environmental loads are not fully understood. Malaysian offshore platforms rely on non-renewable energy sources during the exploration and production of oil and gas. Solar energy is the most promising alternative energy for such a particular

---

A. M. Al-Yacouby (✉) · E. R. B. A. Halim · M. S. Liew  
Department of Civil and Environmental Engineering, Universiti Teknologi PETRONAS, Seri Iskandar, 32610 Perak Darul Ridzuan, Malaysia  
e-mail: [ahmad.aliyacouby@utp.edu.my](mailto:ahmad.aliyacouby@utp.edu.my); [aalyacouby@gmail.com](mailto:aalyacouby@gmail.com)

country that has strategic geographical location near the equator that gives abundance source of sunlight and high solar irradiance levels. Malaysia lies between  $1^\circ$  and  $7^\circ$  in north latitude and  $100^\circ$  and  $120^\circ$  in east longitude, which possesses high yearly average values of solar irradiance [3]. It can be observed that most regions in Malaysia are highly exposed to the radiant energy, thus making the solar energy a good alternative to generate electricity. Malaysia is currently on the path to become a major competitor in solar energy industry, particularly in the manufacturing of photovoltaic (PV) solar panels. Reason why solar power is foreseen to have high acceptance is because the generated power has contributed to zero greenhouse gas emission, resulting in a clean energy source that seems viable in Malaysia [4]. As such, implementing solar power to generate energy panel will help Malaysia reduce the emission of carbon dioxide by 35% by the year 2030 [5]. The review of the literature shows that many countries including Malaysia have started implementing large-scale solar projects [6]. For instance, Japan has occupied more solar energy capacity than any country in the world and their solar farms are installed on both land-based and lake-based units as presented in Fig. 1. However, installing floating offshore solar farms in open sea is a new concept and needs fundamental investigations to better understand the dynamic responses of these floating platforms when subjected to environmental loads. Thus, the objective of this paper is to conduct parametric study on the hydrodynamic responses of floating offshore solar farms when subjected to regular waves. For additional material on the topic, the reader can refer to [7–9]. In this paper, the remainder is organized as follows. Section 2 presents the theoretical background formulation of Linear Airy Wave Theory, and commonly used wave spectra in offshore engineering. In Sect. 3, the research methodology, Response Amplitude Operators (RAOs), and Computational Fluid Dynamics (CFD)

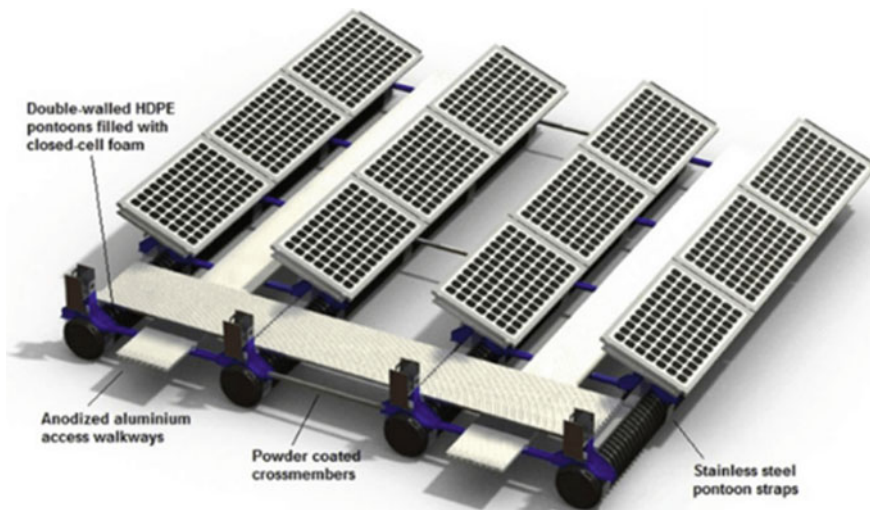


Fig. 1 Typical floating solar panel system [10]

adopted in this paper are briefly discussed. Results and discussion for the numerical analysis of hydrodynamic forces and the corresponding RAOs are presented in Sect. 4. Finally, investigated conclusions based on the observation are summarized in Sect. 5.

## 2 Theoretical Background

### 2.1 Linear Airy Wave Theory

Airy waves are defined as the first-order, small-amplitude gravity waves with a sinusoidal shape, which can be modelled in deep water using the equations of waves proposed by Airy [11]. It is essential for all offshore structural analysis to estimate the forces generated by fluid given the description of the wave and current environment [12]. This can be carried out by defining the coordinate system and the parameters that will be used in the development of the wave theories. Figure 2 shows the coordinate system with  $x$  measured in the direction of the wave propagation,  $y$  measured upwards from the ground surface, and  $z$  orthogonal to  $x$  and  $y$ . It is assumed that the waves are two-dimensional in the  $x$ - $y$  plane and that they propagate over a smooth horizontal bed in water of constant undisturbed path [13].

### 2.2 Formulation of Linear Airy Wave Theory

A Linear Airy wave theory and the associated assumptions are discussed in this section. Based on this theory, analytical expressions for the water particle's velocities,

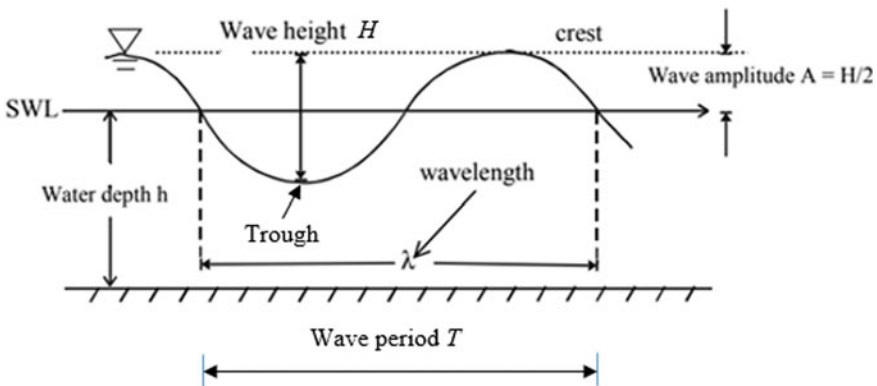


Fig. 2 Linear Airy wave theory characteristics

particle paths, particle accelerations, and pressure are established. Even though this theory is not strictly applicable to typical design waves in offshore engineering, it is a preliminary calculation to reveal the basic characteristics of wave-induced water motion. Airy's linear theory gives an expression for horizontal and vertical water particle velocities at  $(x, y)$  and time,  $t$ , as depicted in the following equations:

The horizontal water particle velocity,  $u$ ;

$$u = \frac{\pi H \cosh ks}{T \sinh kd} \cos(kx - \omega t) \quad (1)$$

The vertical water particle velocity,  $v$ ;

$$v = \frac{\pi H \sinh ks}{T \sinh kd} \sin(kx - \omega t) \quad (2)$$

The wave number,  $k$ , and wave angular frequency,  $\omega$ , are related in linear dispersion which are

$$\omega^2 = gk \tanh kd \quad (3)$$

By using the linear dispersion equation, the wave speed can be expressed as

$$c^2 = \left( \frac{g}{k} \tanh kd \right) \quad (4)$$

The water particle accelerations in  $x$  (horizontal) and  $y$  (vertical) directions can be calculated by applying the second derivative to Eqs. (1) and (2):

$$\text{horizontal : } \frac{\partial u}{\partial t} = \frac{2\pi^2 H \cosh ks}{T^2 \sinh kd} \sin(kx - \omega t) \quad (5)$$

$$\text{vertical : } \frac{\partial v}{\partial t} = -\frac{2\pi^2 H \sinh ks}{T^2 \sinh kd} \cos(kx - \omega t) \quad (6)$$

The inherent assumption in the derivation of linear airy wave theory has a limit of  $y = d$ , which does not allow computation above the SWL (i.e.  $y > d$ ). This predicament is resolved by the linear surface correction,  $\eta$  [14]:

$$\eta \text{ (wave surface elevation)} = \frac{H}{2} \cos(kx - \omega t) \quad (7)$$

Dynamic pressure,  $p$ , can be expressed as:

$$p = \rho g \frac{H \cosh ks}{2 \sinh kd} \cos \theta \quad (8)$$

### 2.3 Commonly Used Wave Spectra

Short-term stationary irregular sea waves can be described by its energy density spectrum formulated by several parameters such as the significant wave height and peak period [15]

- Pierson–Moskowitz (PM) spectrum

$$S(f) = \frac{ag^2}{(2\pi)^4 f^5} \exp\left[-1.25\left(\frac{f_0}{f}\right)^4\right] \tag{9}$$

where  $\alpha = 0.0081$  and  $f_0 = \frac{1}{T_p}$ .

- JONSWAP spectrum

$$S(f) = \frac{ag^2}{(2\pi)^4 f^5} \exp\left[-1.25\left(\frac{f_0}{f}\right)^4\right] \gamma^{\exp\left[-\frac{(f-f_0)^2}{2\pi^2 f_0^2}\right]} \tag{10}$$

where

$$\gamma = 3.30$$

$$\tau_a = 0.07 \text{ for } f \leq f_0$$

$$\tau_b = 0.09 \text{ for } f > f_0$$

$$\tau_a = 0.0081$$

## 3 Research Methodology

### 3.1 Response Amplitude Operators (RAOs)

In the design of floating structures, the extreme responses of the structure due to ocean waves must be determined. The amplitude of the response is normalized with respect to the amplitude of the wave. The RAO can be determined theoretically or using physical models [16, 17]. In the following sections, the equations used to determine RAOs in three degrees of freedom are discussed in the following sections.

#### 3.1.1 Surge RAO

Total mass of surge is calculated using the following formula:



$$\text{Added Mass} = \rho(C_m - 1) \left( \frac{\pi}{4} \times D^2 \right) \times d \quad (11)$$

- $\rho$  density of sea water (1025 kg/m<sup>3</sup>)  
 $C_m$  1.9  
 $D$  diameter of pipe  
 $d$  draft to baseline

$m_{surge}$ , total mass of surge = mass + added mass  
 Stiffness is calculated using the following formula:

$$k_{surge} = \left( \frac{2\pi}{T_n} \right)^2 \times m_{surge} \quad (12)$$

- $T_n$  natural period  
 $m_{surge}$  total mass of surge

The natural frequency can be calculated as follows:

$$\omega = \sqrt{\frac{k_{surge}}{m_{surge}}} \quad (13)$$

$$\text{Surge}_{RAO} = \frac{\left( \frac{F_{surge}}{H/2} \right)}{\left[ \left( K_{surge} - M_{surge}\omega^2 \right)^2 + (C\omega)^2 \right]^{\frac{1}{2}}} \quad (14)$$

### 3.1.2 Heave RAO

Total mass of heave is calculated using the following formula:

$$\text{Added Mass} = \rho(C_m - 1) \times A \times d$$

- $\rho$  Density of sea water (1025 kg/m<sup>3</sup>)  
 $C_m$  1.9  
 $A$  water plane area of floating platform  
 $d$  draft to baseline

$m_{heave}$ , total mass of heave = mass + added mass  
 Stiffness is calculated using the following formula:

$$k_{heave} = \rho \times g \times A$$

Natural Frequency

$$\omega = \sqrt{\frac{k_{\text{heave}}}{m_{\text{heave}}}}$$

$$\text{Heave}_{\text{RAO}} = \frac{\left(\frac{F_{\text{heave}}}{H/2}\right)}{\left[\left(K_{\text{heave}} - M_{\text{heave}}\omega^2\right)^2 + (C\omega)^2\right]^{\frac{1}{2}}} \tag{15}$$

### 3.1.3 Pitch RAO

The total mass of pitch is calculated using the following equations:

$$\text{Added Mass} = (\text{Actual Mass} \times r^2) \times \frac{m_{\text{heave}}}{\text{Actual Mass}}$$

$r$  radius of gyration

$$m_{\text{pitch}}, \text{ total mass of pitch} = \text{mass} + \text{added mass}$$

The stiffness is calculated as follows:

$$k_{\text{pitch}} = \left(\frac{2\pi}{T_n}\right)^2 \times m_{\text{pitch}}$$

$T_n$  natural period

$m_{\text{pitch}}$  total mass of pitch

From which the pitch RAO can be estimated using the following equation:

$$\text{Pitch}_{\text{RAO}} = \frac{\left(\frac{\text{Moment}_z}{H/2}\right)}{\left[\left(K_{\text{pitch}} - M_{\text{pitch}}\omega^2\right)^2 + (C\omega)^2\right]^{\frac{1}{2}}} \tag{16}$$

## 3.2 Computational Fluid Dynamics (CFD) Simulation

The hydrodynamic forces on the floating solar platform have been validated using CFD simulation. ANSYS Fluent was used for the validation purposes. Figure 3 shows the general overview of a typical floating solar farm used for CFD simulation. The mass of the platform is 10,000 kg, and the materials used for the pontoons are high-density polyethylene. Pipe diameters of 0.8 m, 1 m, and 2 m are used in this simulation, and the hydrodynamic forces are determined for water depths of 50 m, 62 m, and 100 m, respectively. The CFD simulation was conducted using Large Eddy Simulation (LES) method.

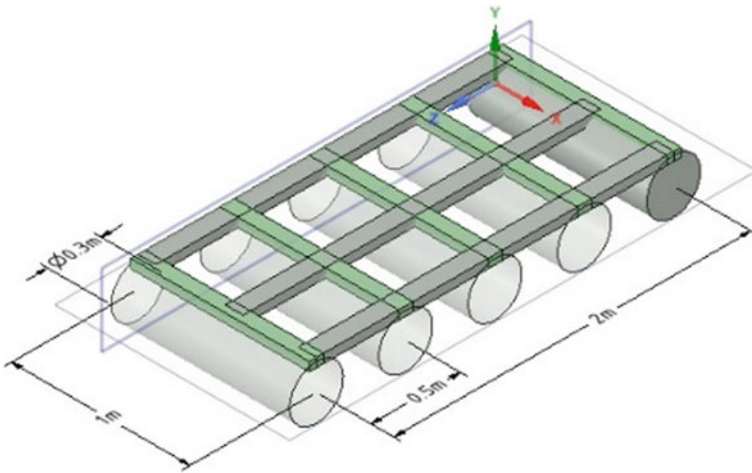


Fig. 3 Typical floating solar farm model for CFD simulation

## 4 Results and Discussion

### 4.1 Numerical Analysis of Hydrodynamic Forces

A MATLAB code was developed to determine the effect of input variables on the hydrodynamic forces acting on the four pontoons that form the floating offshore solar farm unit. The numerical calculations are done based on Morison's equation, in which the time interval varied from  $t = 0$  to  $t = 50$  s. Figure 4 shows the plan view of the proposed floating solar farm unit and the direction of wave propagation.

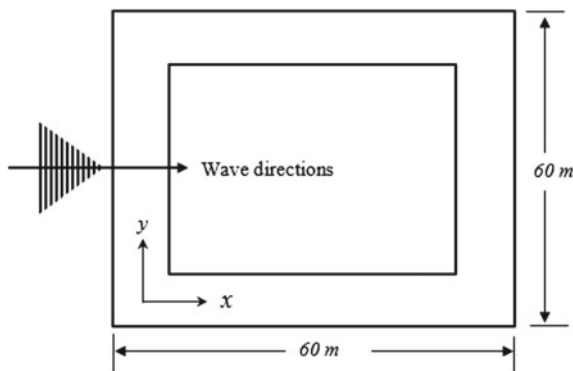


Fig. 4 Plan view of floating solar platform

### 4.2 Effect of Wave Periods on Hydrodynamic Forces

Figures 5, 6, 7 show the variation of the hydrodynamic forces on the floating solar farms as a function of wave period. The graphs show that increasing the wave height has increased the hydrodynamic forces. The graphs also show that as the wave frequencies decreased, the hydrodynamic force increased to 580 kN at  $T_{ass} = 9s$ . In addition, from the graphs one can conclude that increasing the outer diameter of the pipe by 50% has resulted in an increment of 60% on the hydrodynamic forces.

### 4.3 Effects of Water Depth on Hydrodynamic Forces

The variation of hydrodynamic forces with the water depth is presented in Figs. 8, 9, 10. The figures show that when the water depth is increased from 50 m to 100 m,

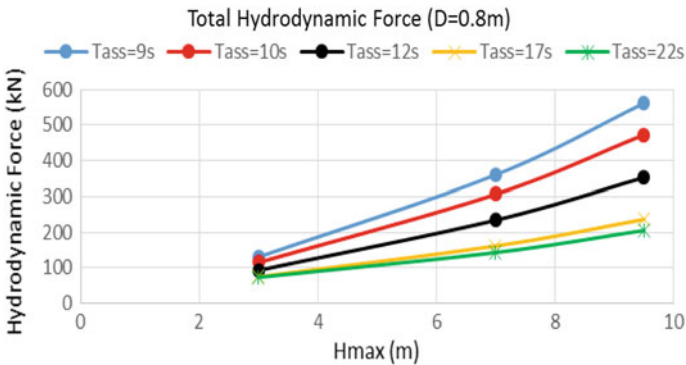


Fig. 5 Variation of hydrodynamic forces with wave periods,  $D = 0.8\text{ m}$ ,  $d = 50\text{ m}$

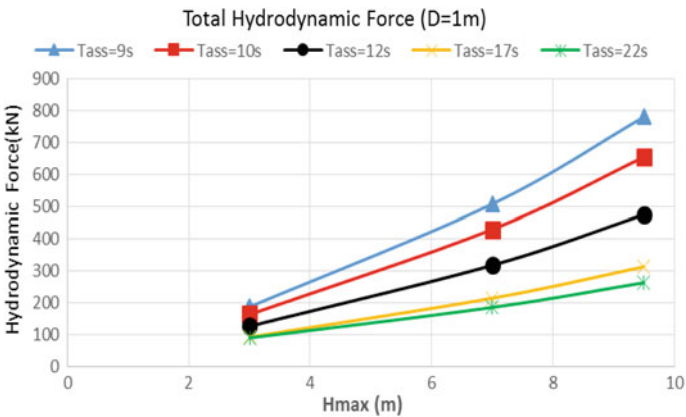


Fig. 6 Variation of hydrodynamic forces with wave periods,  $D = 1\text{ m}$ ,  $d = 50\text{ m}$

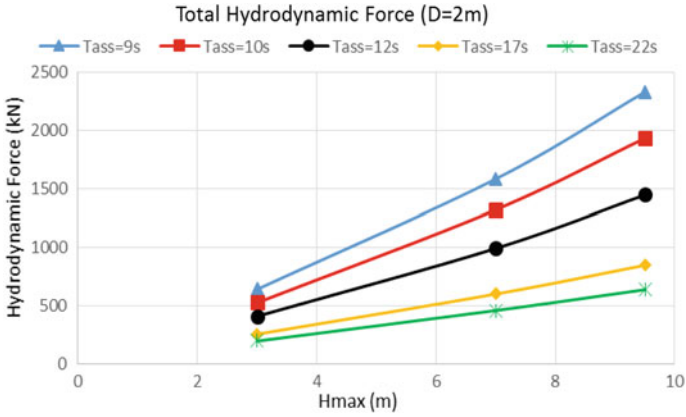


Fig. 7 Variation of hydrodynamic forces with wave periods,  $D = 2$  m,  $d = 50$  m

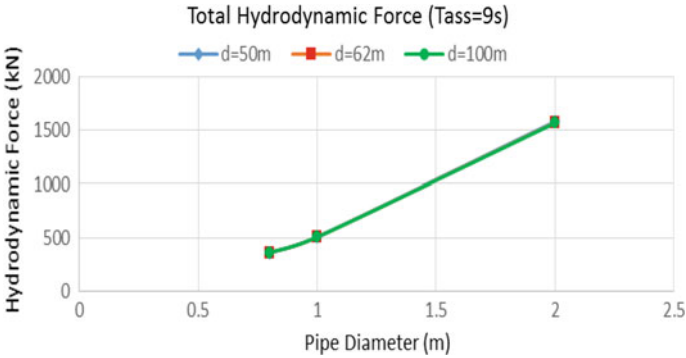


Fig. 8 Variation of total hydrodynamic forces with water depth,  $T_{ass} = 9$  s

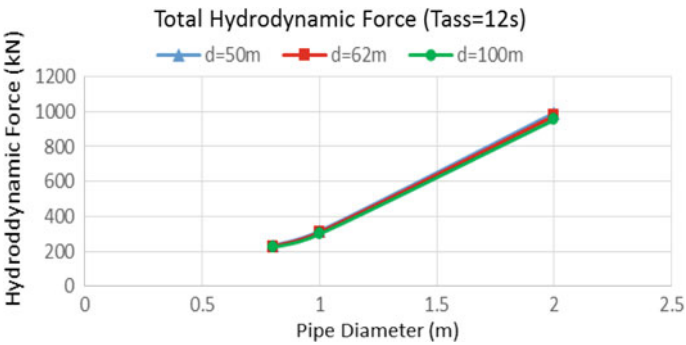
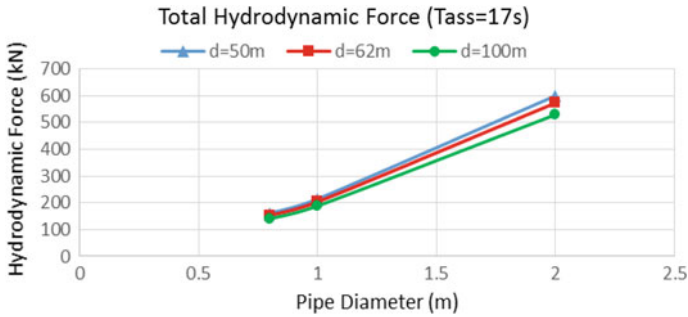


Fig. 9 Variation of total hydrodynamic forces with water depth,  $T_{ass} = 12$  s



**Fig. 10** Variation of total hydrodynamic forces with water depth,  $T_{ass} = 17$  s

the total hydrodynamic force was slightly increased by 1% only. The maximum total hydrodynamic force was observed on the pontoon with outer diameter,  $D = 2$  m. From the graphs, it can be observed that different water depths have comparatively minimal effects on the total hydrodynamic forces, with a maximum variation of less than 20%.

#### 4.4 Effects of Pipe Diameters on Total Hydrodynamic Forces

The variation of hydrodynamic forces as function of wave periods for various pipe diameters is presented in Figs. 11–13. The graphs show that increasing the pipe diameters has significantly increased the hydrodynamic forces. For instance, increasing the pipe diameters from 0.8 to 1 m has increased the total hydrodynamic forces by 28% as shown in Fig. 11. Similarly, when a 0.8 m pipe diameter was increased to 2 m, the total hydrodynamic force was increased by 76% as depicted in Fig. 12. Similarly, an increase of 67% on the total hydrodynamic force was observed when the pipe

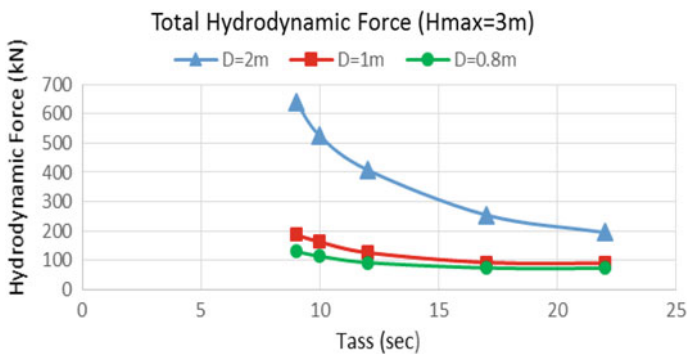


**Fig. 11** Variation of total hydrodynamic forces with pipe diameter,  $H_{max} = 3$  m

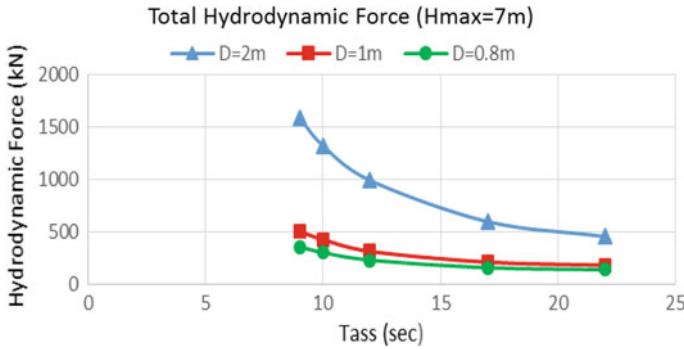


Fig. 12 Variation of total hydrodynamic forces with pipe diameter,  $H_{max} = 7$  m

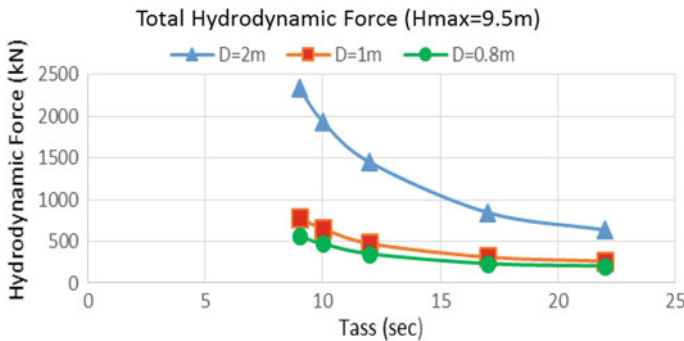


Fig. 13 Variation of total hydrodynamic forces with pipe diameter,  $H_{max} = 9.5$  m

diameter was increased from 1 to 2 m as shown in Fig. 12. It can also be observed from the graphs that the maximum total hydrodynamic force is recorded at  $T_{ass} = 9$  s. In addition, one can observe that as the wave frequency increased, the hydrodynamic forces on the pontoons decreased. However, the graphs indicate that increasing the wave height by 35.7% has resulted in an increase of 60% on the hydrodynamic forces as depicted in Figs. 12 and 13.

### 4.5 Response Amplitude Operators (RAOs)

#### 4.5.1 Surge RAO

The surge RAO for the floating unit is depicted in Fig. 14. The graph shows that surge RAO for the pontoon with outer diameter of 2 m is comparatively higher than the other pipe diameters. The maximum value of surge RAO occurred at  $T = 9$  s. Generally, RAO decreased with increasing wave periods, in the meantime, the graph

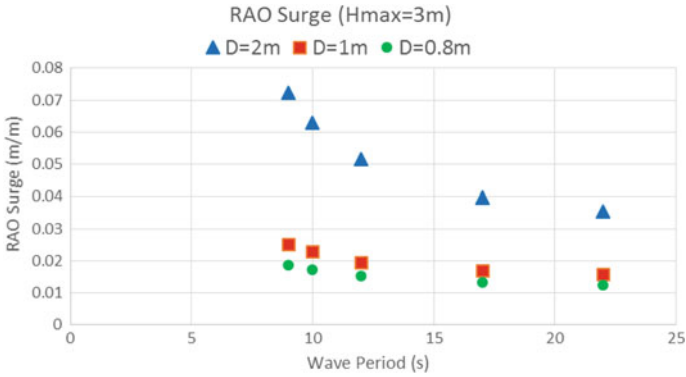


Fig. 14 Surge RAO,  $D = 0.8$  m,  $1.0$  m, and  $2.0$  m, at  $H_{max} = 3$  m

shows that increasing the wave heights has slightly increased the RAO from  $0.02$  m/m to  $0.075$  m/m.

### 4.5.2 Heave RAO

The variation of heave RAO with wave periods for different pipe diameters at  $H_{max} = 9.5$  m is presented in Fig. 15. The graph shows that pontoon with outer diameter of  $2$  m has experienced the highest RAO in heave as compared to other pipe diameters when subjected to different wave heights and wave periods. The graph also shows that the maximum heave RAO occurs at  $T_{ass} = 9$  s. Generally, the responses of the model decreased with increasing wave periods.

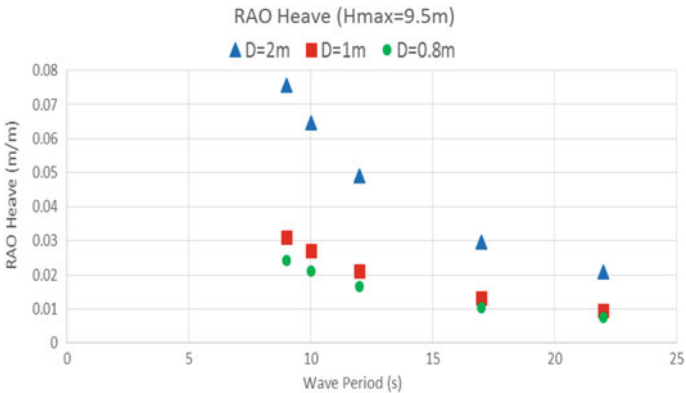


Fig. 15 Heave RAO,  $D = 0.8$  m,  $1.0$  m, and  $2.0$  m, at  $H_{max} = 9.5$  m



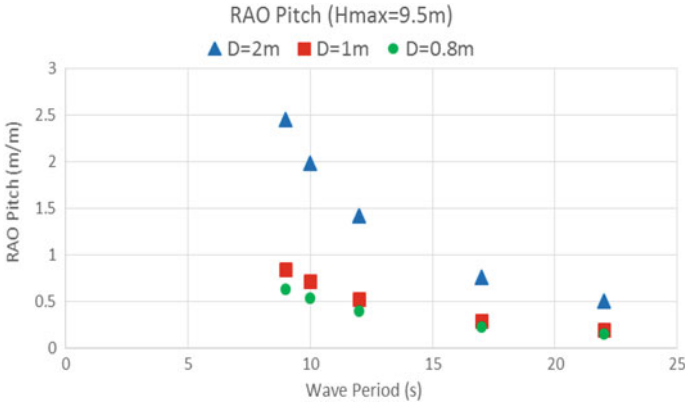


Fig. 16 Pitch RAO,  $D = 0.8$  m,  $1.0$  m, and  $2.0$  m, at  $H_{max} = 9.5$  m

### 4.5.3 Pitch RAO

Figure 16 shows the variation of heave RAO with the wave periods for different pipe diameters at  $H_{max} = 9.5$  m. The graph shows that the pipe diameter with  $D = 2$  m has comparatively experienced higher RAO as compared to other pipe diameters. Increasing the wave height has produced an increment in the pitch moment with a difference of 18%. It can be observed that maximum pitch RAO values occur at  $T_{ass} = 9$  s.

## 4.6 Validation of the CFD Results

CFD simulation was used in this study to determine the hydrodynamic forces on the floating solar farm model. The total forces determined from CFD simulations are then used to validate the hydrodynamic forces determined analytically using the Morison equation. Then, these forces were used to estimate the RAO for surge, heave, and pitch. Figure 17 shows the comparison of total hydrodynamics forces on a horizontal pipe with outer diameter of 2 m, subjected to various wave heights and wave periods. The comparison of the numerical methods with the CFD simulations shows a good agreement, with a total variation ranging from 3–4%.

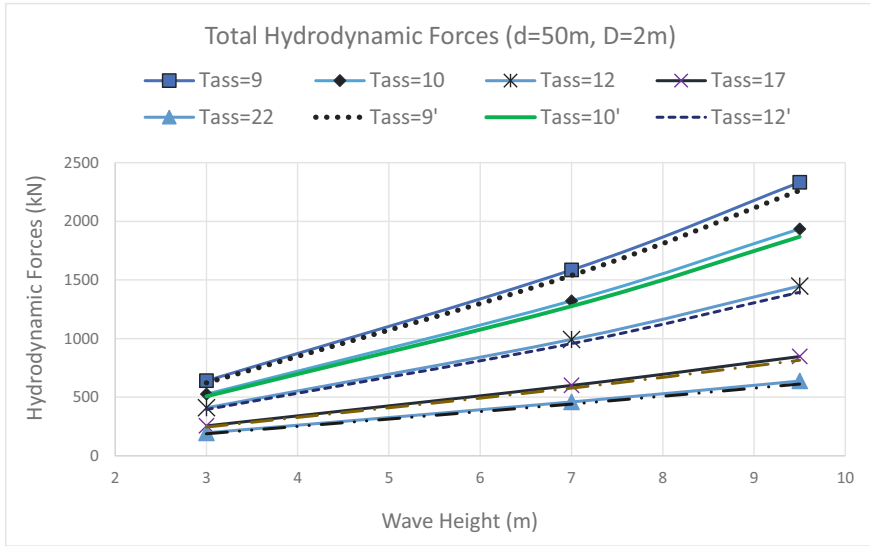


Fig. 17 Comparison of numerical analysis versus CFD simulation

## 5 Conclusions

This paper presented a fundamental research on the dynamic responses of a floating solar farm using analytical and CFD simulation techniques. The important parameters covered in this study are the wave heights,  $H$ , wave periods,  $T$ , water depths,  $d$ , and the diameters of pontoon,  $D$ . The results show that wave heights, wave periods, and pontoon diameters have major influences on the hydrodynamic forces, while the water depth has comparatively a minor influence on the dynamic responses of the floating offshore solar farm unit. Generally, the comparison of hydrodynamic forces between the numerical analysis and CFD simulation shows a fair agreement. The comparison of the results shows a version of 3–4% between the two methods, which is within the acceptable limits.

**Acknowledgements** This research is financially supported by Yayasan UTP Fundamental Research YUTP Cost Centre 015LC0-094 and 015LC0-095.

## References

1. Sims RE, Rogner H-H, Gregory K (2003) Carbon emission and mitigation cost comparisons between fossil fuel, nuclear and renewable energy resources for electricity generation. *Energy Policy* 31(13):1315–1326
2. Muscat M (2014) A study of floating PV module efficiency. University of Malta

3. Rafeq S, Zulfattah Z, Najib A, Rody M, Fadhli S, Abdollah MFB, Hafidzal M (2013) Preliminary study of CST in Malaysia based on optical efficiency. *Procedia Eng* 68:238–244
4. Samsudin A, Suhandi A, Rusdiana D, Kaniawati I (2016) Preliminary design of ICI-based multimedia for reconceptualizing electric conceptions at universitas pendidikan Indonesia. *J Phys: Conf Ser*, IOP Publishing
5. Commission E, Energy in Malaysia. vol 12, Energy Commission
6. Wasfi M (2011) Solar energy and photovoltaic systems
7. Sahu A, Yadav N, Sudhakar K (2016) Floating photovoltaic power plant: a review. *Renew Sustain Energy Rev* 66:815–824
8. Ranjbaran P, Yousefi H, Gharehpetian G, Astarai FR (2019) A review on floating photovoltaic (FPV) power generation units. *Renew Sustain Energy Rev* 110:332–347
9. Dai J, Zhang C, Lim HV, Ang KK, Qian X, Wong JLH, Tan ST, Wang CL (2019) Design and construction of floating modular photovoltaic system for water reservoirs. *Energy*, pp 116549
10. Trapani K, Redón Santafé M (2015) A review of floating photovoltaic installations: 2007–2013. *Prog Photovolt Res Appl* 23(4):524–532
11. Airy G (1845) Tides and waves, Art. 192 in *Encyc. Encyc Metrop*, pp 241–396
12. Borthwick A, Herbert D (1988) Loading and response of a small diameter flexibly mounted cylinder in waves. *J Fluids Struct* 2(5):479–501
13. Noorzaei J, Bahrom SI, Jaafar MS, Thanoon WAM, Mohammad S (2005) Simulation of wave and current forces on template offshore structures. *Suranaree J Sci Technol* 12(3):193–210
14. Chakrabarti SK (1987) Hydrodynamics of offshore structures. WIT press
15. Chen H, Uddin M (2013) Optimization of a floating platform design
16. Rodriguez Marijuan A (2017) Offshore floating platforms: analysis of a solution for motion mitigation
17. Kurian V, Baharuddin NH, Magee A, Hashim AM (2013) Model tests for dynamic responses of float-over barge in shallow wave basin. In: The twenty-third international offshore and polar engineering conference. International Society of Offshore and Polar Engineers

# Open-Hole and Filled-Hole Failure Envelopes of BFRP and GFRP: A Comparative Study



Z. Sajid, S. Karuppanan, and S. Z. H. Shah

**Abstract** Open- and filled-hole analysis is essential in the calculation of allowable stresses of composite structures as open- and filled-hole strengths of a structure can be limiting factors. Considering the end of product life management, most companies are starting to replace traditional composite materials with green materials. One of the best options is to substitute glass fibers with basalt fiber. Basalt fibers are less costly than glass fibers. Importantly, basalt is a green material along with excellent recyclability. Therefore, this research aims to compare the BFRP and GFRP with respect to the open- and filled-hole laminates. In this research work, strain-based failure envelopes of open- and filled-hole laminates made up of E-glass, S2-glass, and basalt were compared and discussed. Classical laminate theory and Lekhnitskii solution were used to develop the failure envelopes. In addition, the effect of first ply failure (FPF) and last ply failure (LPF) on failure envelopes was also discussed. In longitudinal and transverse tensions, basalt fiber has large failure strains as compared to E-glass and has a reasonably comparable failure strains with S2-glass. In compression, basalt is better than E-glass and S2-glass.

## 1 Introduction

Fiber-reinforced plastics (FRPs) are commonly used in aerospace, automotive, marine, and civil industries, because of their high specific stiffness, specific strength, and their elastic tailoring properties. However, composite structure performance is degraded in the presence of holes. This is because holes lead to stress concentration. Reduction in ultimate strain and ultimate strength occurs due to the introduction of the holes in composite laminates. Therefore, notched testing is used to determine the reductions in ultimate strain and strength. Composites present a much greater challenge, as compared to metals for which stress concentrations and strength reductions, due to the presence of holes, are relatively simple to calculate. The directionally

---

Z. Sajid (✉) · S. Karuppanan · S. Z. H. Shah  
Mechanical Engineering Department, Universiti Teknologi PETRONAS, Bandar Seri Iskandar,  
32610 Perak, Malaysia  
e-mail: [zubair\\_17005303@utp.edu.my](mailto:zubair_17005303@utp.edu.my)

influenced stiffness of composite laminates considerably increases the complexity of stress concentration calculations in composites. Moreover, the damage states in composite laminates around holes are considerably more complicated than the yielding around holes in metallic structures. These damages are influenced by the composite material, loading directions, and the ply-stacking sequence. Due to these complications, the strength reduction is very difficult to predict.

Another source of stress concentration is in the joining of composites. Composites can generally be joined through a variety of methods. Among many, bolts and rivets can be identified as the most used mechanical fastening methods. Stress concentration resulted by the interaction of bolt and the hole is called as bolt–hole damage. The damage to the bolt–hole is caused by the bearing stress on the contact surface. This could cause the hole to elongate resulting in laminate splitting or damage to the upper plies. The inappropriate design of any joint can cause structural problems or influence the integrity of the structure. Furthermore, any conservative design can indirectly add weight to the structure. The testing of the filled-hole laminates is used to determine the strength and strain reductions that occurred due to fastener filled holes.

After the introduction of the hole in a composite structure, the strength of the structure reduces. Open- and filled-hole strengths are therefore important for the estimation of the allowable stresses for the composite structures. Therefore, the first objective of the current study is to predict the failure envelope of open- and filled-hole laminates.

FRP is a material made of a polymer matrix, reinforced by high-strength fibers. The fibers may consist of carbon, glass, aramid, or basalt. The laminate properties are determined by fiber quality, shape, orientation, and the fiber volumetric ratio. The polymer matrix is made up of epoxy resin, vinyl ester, or polyester thermosetting plastic. The fibers added into a polymer matrix contribute to the strength and stiffness of the composite, while resin transfers the load into the reinforcement fibers and protects the fibers from the environment [1, 2]. Carbon fiber (CFRP), glass fiber (GFRP), aramid fiber (AFRP), and basalt fiber (BFRP) are mainly used in industry as common FRPs [1]. Basalt fiber is a type of molten rock produced at 1400°C, which is extruded by tiny nozzles to produce fine fiber without the addition of any material [3, 4]. Basalt FRP (BFRP) in comparison with carbon FRP (CFRP) and glass FRP (GFRP) is a newcomer to the FRP. Basalt fiber is an eco-friendly material. It is superior in terms of strength-to-weight ratio, ductility, and durability, and has high thermal resistance and excellent resistance to corrosion. It offers excellent properties at low cost as compared to the other FRP materials. BFRP has been used in many engineering sectors, including civil engineering, automotive, and marine. However, its failure envelopes have not been studied in detail. In order to reliably predict structural performance, understanding of the material properties of BFRP is crucial.

Many studies have been conducted on the mechanical and thermal properties of BFRP. Colombo et al. [5] studied BFRP composite's static material characteristics, produced by the vacuum infusion method instead of the hand layup method. Two types of polymer matrices have been tested, i.e., epoxy resin and vinyl ester resin. Epoxy resin composite has been found to have better mechanical properties than vinyl

ester composite. Failure behavior is totally different for both the matrix systems. The epoxy resin composite generally fails with the fiber still attached to the matrix, whereas the vinyl ester composite fails due to the separation between the fibers and the matrix. The mechanical properties of BFRP with two different fabric types (plain weave and twill weave) were investigated by Valentino et al. [6] under tensile load. It has been found that the type of fabric has no effect on the values of stiffness. However, the failure mode and location of the failure were found to be different for two types of fabric. High et al. [7] improved the flexural properties of concrete members by the addition of chopped basalt fibers.

In view of the good mechanical and thermal performance of basalt fibers, many authors compared BFRP with various FRPs. Lopresto et al. [8] compared the mechanical characteristics of BFRP and GFRP composites. Young's modulus, compressive strength, bending strength, and impact resistance were compared. The findings of the experiment indicated that BFRP has higher Young's modulus, compressive and bending strength, higher impact force resistance, and energy absorption capacity compared to GFRP. Wu et al. [9] investigated the behavior of basalt fibers under the influence of a corrosive environment. Wu et al. investigated the fatigue performance of several FRP composites made of carbon, glass, basalt fiber, and hybrid fibers. It was observed that the failure mode of the composite is highly dependent on the tensile modulus of fibers. The fatigue performance has been improved significantly in hybrid carbon/basalt composites.

Recently, most of the industries start implementing end-of-life management to their product. Two factors need to be satisfied to achieve the end-of-life management. These factors are recyclability and environmental friendliness of the product. Therefore, the material must have these two characteristics [10]. Considering the end-of-life management of the products, most of the industries start replacing conventional composite materials with green materials. One of the best options is to use basalt as the replacement of glass fibers. As discussed earlier, basalt fibers are cheaper than glass fibers. In addition, basalt fibers have better mechanical and thermal properties than glass fibers. Importantly, basalt is a green material along with excellent recyclability [11, 12].

Considering the excellent mechanical performance of BFRP, many authors proposed that BFRP would be a useful substitute for GFRP. This research work will, therefore, focus on the comparative study between BFRP and GFRP. Analytical methods consisting of classical laminate theory and Lekhnitskii solutions were used to generate open- and filled-hole laminate failure envelopes. In this research work, strain-based failure envelopes of open- and filled-hole laminates made up of E-glass, S2-glass, and basalt were compared and discussed.

## 2 Methodology

To compare the performance of open- and filled-hole laminates made up of different materials, three materials made of QI laminate,  $[0/\pm 45/90]_s$ , were considered. These three materials were E-glass, S2-glass, and basalt fibers. In order to study the effect of different materials, all the factors should remain the same, except the fiber material. Importantly, the fiber volume fraction greatly influences the stiffness and strength properties of the material. However, there is a limitation in obtaining the exact amount of fiber volume fractions in all laminates experimentally. It is plausible that a slight variation in fiber volume fraction could influence the results obtained. Therefore, the fiber volume fraction should be the same for all the materials. This problem could be avoided by using analytical relations. The micromechanical approach is a viable alternative in obtaining the same volume fraction. Therefore, a micromechanical approach was used to calculate stiffness and strength [13] of three different laminates. The properties of fiber and matrix are listed in Table 1.

Properties of laminates, which were calculated using a micromechanical approach, are shown in Table 2.

In the product design process, the first stage is to use some analytical techniques. These analytical techniques could save a lot of time and effort for detailed designing in the later stage. Therefore, an analytical approach was considered to study the response of open- and filled-hole laminates working under different scenarios. Classical laminate theory (CLT) [14] is considered as a fundamental analytical approach to study the response of laminates. However, it could only be used for un-notched laminates. This was considered to be the main limitation of using CLT alone for notched laminates. As discussed earlier, some researchers have shown the compatibility of CLT with Lekhnitskii [15] solutions. Therefore, the methodological approach taken in this study is a mixed methodology based on the combination of CLT and Lekhnitskii solutions. Combination of these approaches was particularly useful in studying the response of open- and filled-hole laminates. Hashin failure criteria [16] were opted for the prediction of failure index of the laminates. Equations (1)–(4) listed different failure modes, namely fiber failure in tension, fiber failure in compression,

**Table 1** Material properties of fiber and matrix

Properties	E-glass	S2-glass	Basalt	Matrix
$E_{11}$ (GPa)	74	87	90	3.20
$E_{22}$ (GPa)	74	87	90	3.20
$G_{12}$ (GPa)	30.8	36.3	35.7	1.18
$\nu_{12}$	0.2	0.2	0.26	0.35
$\nu_{23}$	0.2	0.2	0.26	–
$X_T$ (MPa)	2150	2850	2950	73
$X_C$ (MPa)	1450	2450	2950	120
$V_f$	0.6	0.6	0.6	0.4

**Table 2** Material properties of laminates

Properties	E-glass	S2-glass	Basalt
$E_{11}$ (GPa)	45.68	53.48	55.28
$E_{22}$ (GPa)	8.84	8.93	8.95
$G_{12}$ (GPa)	3.30	3.33	3.32
$G_{23}$ (GPa)	2.81	2.83	2.70
$\nu_{12}$	0.26	0.26	0.29
$\nu_{23}$	0.33	0.33	0.40
$X_T$ (MPa)	1327.18	1751.93	1811.95
$X_C$ (MPa)	895.08	1506.04	1811.95
$Y_T$ (MPa)	49.51	49.34	49.29
$Y_C$ (MPa)	127.82	127.92	127.97
$S$ (MPa)	87.00	87.47	87.42

matrix failure in tension, and matrix failure in compression, respectively.

$$FFT = \frac{\sigma_{11}^2}{X_t^2} + \frac{\sigma_{12}^2}{S^2} \tag{1}$$

$$FFC = \frac{-\sigma_{11}}{X_t} \tag{2}$$

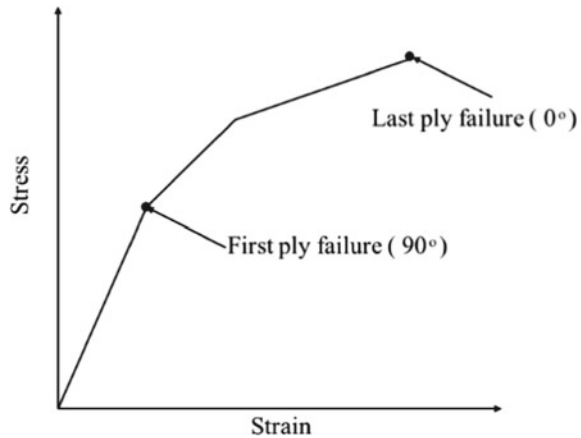
$$MFT = \frac{\sigma_{22}^2}{Y_t^2} + \frac{\sigma_{12}^2}{S^2} \tag{3}$$

$$MFC = \frac{\sigma_{22}^2}{4S^2} + \left[ \left( \frac{Y_C}{2S} \right)^2 - 1 \right] \frac{\sigma_{12}}{Y_C} + \frac{\sigma_{12}^2}{S^2} \tag{4}$$

Two definitions of failure are commonly used in the composite industry. These two failure definitions were considered in this study, namely first ply failure (FPF) and last ply failure (LPF). FPF is different from LPF in a number of aspects. Figure 1 highlights the change in slope for FPF. Even though the failure occurred according to the FPF, laminate still poses some load-bearing capacity. This is because the fiber can still continue to bear load as FPF indicates the transverse failure of the matrix. To sum up, FPF indicates the failure initiation of 900 plies, whereas LPF is the ultimate failure of laminate. Unlike the FPF, after LPF has occurred, laminate has no load-bearing capacity. Therefore, LPF indicates the failure of fiber [17]. For LPF analysis, stiffness and strengths were decreased by a degradation factor equal to 0.1.



**Fig. 1** LPF and FPF comparison



### 3 Results and Discussion

As indicated in Fig. 2a, there was a huge difference in the shape and size of FPF and LPF failure envelopes. Closer inspection of Fig. 2a revealed that failure envelopes of FPF are very small as compared to LPF. Interestingly, there was not much difference found in the failure envelope of E-glass, S2-glass, and basalt when FPF was considered. In addition, significant variations were found in the failure envelopes for all the three materials when LPF was considered. Therefore, only LPF-based failure envelopes have been discussed from now on.

Next, the failure envelopes of un-notched, open-hole, and filled-hole laminates are compared. Figure 2a–c compares the failure envelopes of un-notched, open-hole, and filled-hole laminates, respectively. By analyzing Fig. 2a–c, it was observed that the shapes of the failure envelopes are different for all the three cases (un-notched, open-hole, and filled-hole laminates). Also, the values of the failure strains differ for each case. The highest values of failure strains in all directions were shown by the un-notched laminates, as can be seen in Fig. 2a. Among these three cases (un-notched, open hole, and filled hole), open-hole laminates produced the smallest failure envelope.

Lastly, the effect of materials (E-glass, S2-glass, and basalt fibers) on the LPF failure envelope was considered. Points A and B in Fig. 2a, c illustrate that all the three materials of un-notched and filled-hole laminates exhibit the same values of failure strains when subjected to tension loadings (longitudinal and transverse). However, this behavior is not reflected for open-hole case, as shown in Fig. 2b. For open-hole laminates, E-glass shows lower strain values as compared to the other two materials. In all the three cases (un-notched, open hole, and filled hole), basalt produces higher failure strains when subjected to compression loadings, as highlighted by points C and D in Fig. 2a–c. This is due to the larger diameter of the basalt fiber compared to the glass fiber. Compressive performance of a laminate depends upon the diameter of the fiber. Larger diameter fibers exhibit more compressive strength than the smaller

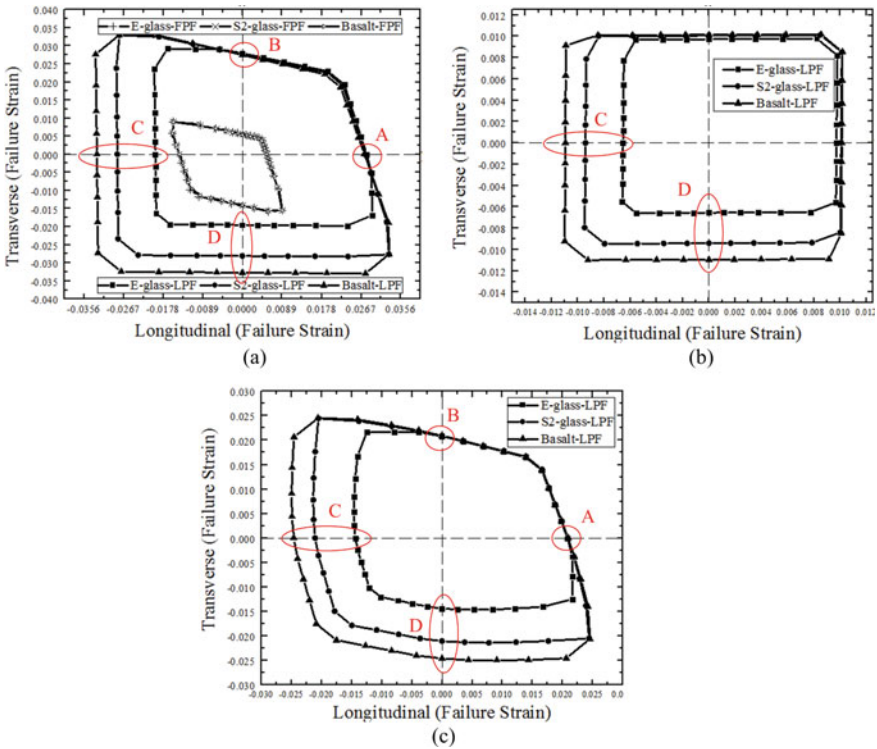


Fig. 2 Effect of material on failure envelop of a un-notched b open hole c Filled hole laminates

diameter fibers [18]. Overall, it could conceivably be hypothesized that basalt fibers offer larger failure strains than the other two materials, especially under compression loadings.

### 4 Conclusions

The aim of the current research work is to compare the failure strains of open and filled-hole laminates comprised of BFRP and GFRP. Following are the few observations from the current study:

- These findings suggest that basalt fibers have more capacity to bear load than E-glass and S2-glass fibers.
- In longitudinal and transverse tensions, basalt fiber has larger failure strains as compared to E-glass and has a reasonably comparable failure strains with S2-glass. In compression, basalt is better than E-glass and S2-glass.

- There is not much difference in the failure envelopes of all the three materials when generated using FPF theory. However, a considerable difference was found for all the three materials when considering LPF.

**Acknowledgements** The authors would like to acknowledge the support of the Mechanical Engineering Department of Universiti Teknologi PETRONAS.

## References

1. Chen J-F, Smith S, Lam L, Teng JG (2013) Behaviour and strength of FRP-strengthened RC structures: a state-of-the-art review. In: Proceedings of The Institution of Civil Engineers-structures and Buildings—PROC INST CIVIL ENG-STRUCT B, vol 156, pp 51–62, 01/02/2003
2. Skuturna T, Valivonis J (2016) Experimental study on the effect of anchorage systems on RC beams strengthened using FRP. *Compos Part B: Eng* 91:283–290, 2016/04/15
3. Dhand V, Mittal G, Rhee KY, Park S-J, Hui D (2015) A short review on basalt fiber reinforced polymer composites. *Compos Part B: Eng* 73:166–180, 2015/05/01
4. Fiore V, Scalici T, Di Bella G, Valenza A (2015) A review on basalt fibre and its composites. *Compos Part B: Eng* 74:74–94, 2015/06/01
5. Colombo C, Vergani L, Burman M (2012) Static and fatigue characterisation of new basalt fibre reinforced composites. *Compos Struct* 94:1165–1174, 2012/02/01
6. Valentino P, Furgiuele F, Romano M, Ehrlich I, Gebbeken N (2013) Mechanical characterization of basalt fibre reinforced plastic with different fabric reinforcements—tensile tests and FE-calculations with representative volume elements (RVEs), pp 231–237
7. High C, Seliem HM, El-Safty A, Rizkalla SH (2015) Use of basalt fibers for concrete structures. *Constr Build Mater* 96:37–46, 2015/10/15
8. Lopresto V, Leone C, De Iorio I (2011) Mechanical characterisation of basalt fibre reinforced plastic. *Compos Part B: Eng* 42:717–723, 2011/06/01
9. Wu G, Wang X, Wu Z, Dong Z, Zhang G (2014) Durability of basalt fibers and composites in corrosive environments. *J Compos Mater* 49:873–887, 2015/03/01
10. Sakai S, Noma Y, Kida A (2007) End-of-life vehicle recycling and automobile shredder residue management in Japan. *J Mater Cycles Waste Manag* 9:151–158, 2007/09/01
11. Jamshaid H, Mishra R (2016) A green material from rock: basalt fiber—a review. *J Text Inst* 107:923–937, 2016/07/02
12. Johnny HA, Randall TS, Robert AL, Daryl A (2014) Vehicle component including basalt and method for making same. United States Patent
13. Huang Z-M, Xin L-M (2017) In situ strengths of matrix in a composite. *Acta Mech Sinica* 33:120–131, 2017/02/01
14. Bert CW (1989) Classical lamination theory. In: Pendleton RL, Tuttle ME (eds) *Manual on experimental methods for mechanical testing of composites*. Springer Netherlands, Dordrecht, pp 11–16
15. Lekhnitskii SG (1968) Anisotropic plates
16. Hashin Z (1980) Failure criteria for unidirectional fiber composites. *J Appl Mech* 47:329–334
17. Muhamad Irwan MD, Zurri Adam MA, Mahmud J (2014) Failure analysis of composite laminates under biaxial tension: a review and framework. *Appl Mech Mater* 680:160–163
18. Yerramalli C, Waas A (2004) A nondimensional number to classify composite compressive failure. *J Appl Mech* 71, 05/01

# Investigation on Effect of Fly Ash Volume Percentage on Microstructure and Microhardness of AA7075—Fly Ash Surface Composites via FSP



Namdev Ashok Patil, Ng Zhongyan, Srinivasa Rao Pedapati,  
and Othman Bin Mamat

**Abstract** In this study, friction stir processing (FSP) technique is used to fabricate aluminium AA7075 alloy reinforced with fly ash (FA) metal matrix composites (MMCs). The cheap and abundantly available industrial-waste fly ash (FA) micropowder is used as a reinforcing medium. The main focus of this study is to find out the optimal volume percentage that will bring out good mechanical properties on the selected base metal AA7075. The surface blind holes method is used for depositing the FA particles, and inter-cavity spacing is utilized as a parameter to control the volume percentage. For inter-cavity spacing of 4 mm (S1), 6 mm (S2), 8 mm (S3), and 10 mm (S4), the volume percentages of FA particles to be inserted are 2%, 4%, 6%, and 8%, respectively. After producing the MMCs, the microhardness and tensile tests have been conducted to study the mechanical properties of the MMCs. The microstructural analysis of Al 7075-FA MMCs has been conducted using field emission scanning electron microscopy (FESEM). The highest average microhardness value 178 HV and the highest UTS 240 MPa are observed for the sample of S-2 combination. The microstructural observations confirm that breaking of FA microparticles and their more uniform distribution facilitates grain refinement which contributes to obtain enhanced microhardness and tensile strength. The FESEM-EDX and mapping confirm the presence of FA micropowder in the form of silicon oxide and other constituents.

**Keywords** Fly ash · Aluminium matrix composites · Friction stir processing · Mechanical properties · Microstructure

---

N. A. Patil (✉) · N. Zhongyan · S. R. Pedapati · O. B. Mamat  
Department of Mechanical Engineering, Universiti Teknologi PETRONAS, Seri Iskandar, 32610  
Perak, Malaysia  
e-mail: [namdev\\_17003401@utp.edu.my](mailto:namdev_17003401@utp.edu.my)

## 1 Introduction

In the material industry, the demand of high-strength and low-cost material is rising globally. Aluminium matrix composites (AMCs) are highly sought after in industries which produce automobiles, aircraft, rockets, military vehicles structural components, etc. The justification for the popularity of AMCs among these sectors is its good wear resistance, low cost, and high stiffness besides having a high strength-to-weight ratio [1]. However, the cost of aluminium matrix composite (AMC) production is high. Yet, the cost can be reduced by utilizing natural and industrial waste materials as reinforcement particles in its fabrication [2]. To promote sustainability and reduce pollution, it is crucial for engineers to look for suitable industrial waste and further utilize it. The usage of coal in thermal plants to produce energy worldwide has raised environmental issues as the process usually produces a waste known as fly ash (FA) which is being disposed into ponds or supporting landfill initiatives which causes soil and water pollution due to its high salinity [3]. It is reported by Prabhakar et al. [4] that the use of FA as a composite material in AMC by using friction stir processing (FSP) can enhance the mechanical properties, such as microhardness, of the base alloy. Hence, in order to utilize FA to produce AMCs, considering that FA contains constituents mainly silicon oxides ( $\text{SiO}_2$ ) and other oxides is getting more attention from researchers worldwide [3].

FSP is a thermomechanical processing method based on the friction stir welding (FSW) process principles. An FSP machine comprises a rotating tool with a pin and shoulder. Two of the most important variables in FSP are the tool rotational speed and tool traverse speed. Both of these factors will account most of the heat generation that is required to soften or plasticize the metal through friction [5]. Enhancement of the material properties after applying FSP is because there is a transition of the microstructure from heterogeneous to a refined homogenous microstructure [6]. The microstructural changes are mainly observed at the three crucial zones such as stir zone (SZ), thermomechanically affected zone (TAZ), and heat-affected zone (HAZ) [5]. Within these zones, the microstructure will develop as a consequence of plasticized material flow, plastic deformation, and elevated temperature. Sometimes, comparing to conventional strength improvement methods, such as heat treating, FSP has provided a better solution in providing the localized enhanced properties [6].

Various approaches have been implemented in producing a defect-free MMC with uniformly reinforced AMCs. In case of deposition by groove method, Rathee et al. [7] found out that defect-free surface composites can be fabricated when the ratio of groove width ( $w$ ) to tool pin diameter ( $d$ ) is not more than 0.5. They mentioned that the width must not be more than the ratio of 0.5 since it may lead to lack of proper plasticization in the base alloy with the reinforcement particles within the groove. The abundance of the reinforcement particle is believed to reduce the heat generated by the tool rotation as the particles tend to absorb more heat as the volume percentage of particle increased within the groove. Single FSP pass and multiple FSP passes are the other important parameters for MMC fabrications. Increasing number of passes

has resulted in reduction of cluster size along with homogeneous dispersion of the reinforcement particle, ultimately being able to reduce the grain size successively [5]. However, Weglowski et al. [5] stated that there will not be any significant reduction of grain size after more than six passes. Employing multiple-pass technique might be useful on certain types of metals, but it will not work as well on age-hardened alloys as it might lead to weakening which is associated with Ostwald ripening of the strengthening precipitate. Another alternative has been proposed by Gangil et al. [8] in which they used unit stirring parameter defining certain relationship between tool dimensions and machine parameters. It was inferred that when the unit stirring is high, it is likely that the reinforcement particles slip more and less likely to stick to the matrix material [8]. However, reports on how volume percentage affects the properties of AA7075-FA MMC are hardly submitted. Therefore, the objective of this study is to study the relationship between volume percentage of FA and resultant mechanical properties of Al alloy MMCs.

## 2 Materials and Methods

In aerospace grade, AA7075-T651 aluminium alloy samples with dimensions of (110 mm × 150 mm × 6.35 mm) were used as the base metals. The fly ash micropowder (99% pure) with average particle size of 40–50 μm was selected as the reinforcement particle. The H13 steel tool with straight cylindrical profile having 4.5-mm pin length, 6-mm pin diameter, and 20-mm shoulder diameter was selected for FSP. The chemical compositions of Al 7075-T651 base alloy and fly ash powder are presented in Tables 1 and 2, respectively.

**Table 1** Chemical composition of Al 7075-T651 alloy

Component	wt%	Component	wt%	Component	wt%
Al	87.1–91.4	Mg	2.1–2.9	Si	Max 0.4
Cr	0.18–0.28	Mn	Max 0.3	Ti	Max 0.2
Cu	1.2–2	Others, each	Max 0.05	Zn	5.1–6.1
Fe	Max 0.5	Others, total	Max 0.15		

**Table 2** Chemical composition of fly ash micropowder

Component	wt%	Component	wt%
SiO <sub>2</sub>	51.57	MgO	1.74
Al <sub>2</sub> O <sub>3</sub>	22.57	SO <sub>3</sub>	0.99
Fe <sub>2</sub> O <sub>3</sub>	14.91	Loss in ignition	3.56
CaO	4.82	Na <sub>2</sub> O + K <sub>2</sub> O	0.68

**Table 3** Fly ash volume percentages

No.	Inter-cavity spacing (mm)	Number of blind holes	FA volume percentage (%)
1	4	23	8
2	6	16	6
3	8	12	4
4	10	10	2

## 2.1 Surface Blind Holes Deposition Method

The types of deposition holes used in this study are blind holes of equal size of 2-mm diameter and 3-mm depth. The volume percentage of the fly ash is controlled by changing the number of blind holes on each band. The volume of the composite to be fabricated is calculated by using the formula

$$\text{Volume of FSP Region} = L \times \text{PD} \times \text{PL} \quad (1)$$

where  $L$  is the length of plate, PD is the pin diameter, and PL is the pin length.

$$\text{Volume of 1 Hole} = \pi \times R^2 \times D \text{ mm} \quad (2)$$

where  $R$  is the radius of hole and  $D$  is the depth of the hole.

The volume percentage of FA into AA 7075 is defined using the expression:

$$\text{Vol\%} = (\text{Total Volume occupied by Holes} / \text{Vol. of FSP Region}) \times 100 \quad (3)$$

By changing the inter-cavity spacing of the blind holes within the plates, different numbers of blind holes could be obtained, and thus, the FA volume percentages are given in Table 3. The blind holes were machined onto AA7075 using a vertical milling machine. The selection of the inter-cavity spacing was kept less than the radius of the shoulder diameter to ensure continuous dispersion of FA particles during the process. The variation in volume percentage of FA with inter-cavity spacing is represented in Table 3.

## 2.2 Capping and Friction Stir Processing

The capping process was done by using a 20-mm diameter pinless H13 steel tool. The capping parameters used are: tool rotational speed 1000 rpm and traversing speed 30 mm/min. The FSP parameters were selected by using unit stirring parameters and tool plunge depth relation. Gangil et al. [8] reported that the derivation of unit stirring parameter has been proved to provide a clearer picture on how the particle disperses within the aluminium matrix. It was reported that when the unit stirring parameter

$\omega = 0.00223$ , there will be good degree of mixing and dispersion with less defects on the aluminium.

The unit stirring parameters were given by:

$$\omega = T / (R \times SD) \quad (4)$$

where  $T$  is the traverse speed,  $R$  is the rotational speed, and  $SD$  is the shoulder diameter.

Plunge depth is also reported to affect the mechanical properties and microstructures in FSP. When the plunge depth is not carefully set, over-plunging of tool will cause undesirable flash formation. However, when the plunge depth is not sufficient, vertical motion of the matrix will not occur, hence preventing sufficient plasticization of material due to lack of forging action [9]. The tool plunge depth relation provides a better judgement on how to select the right plunge depth. The relation proposed by Khan et al. [9] is given as below:

$$PD = (R + r) \sin \alpha + l \cos \alpha \quad (5)$$

where  $R$  is the shoulder radius,  $r$  is the pin radius,  $l$  is the pin length, and  $\alpha$  is the tool tilt angle. The final FSP parameters were designed for this study by applying concepts of unit stirring parameters and tool depth–tilt angle relationships as discussed above. The parameters used in this study are  $R$  670 rpm,  $T$  30 mm/min,  $\alpha$  2DP,  $PD$  5.3 mm, and single-pass processing.

### 2.3 Microstructural Characterization

The square-shaped samples of 20 mm × 20 mm were cut using wire EDM machine. The specimens were mounted and polished with silicon carbide paper by increasing grit of 600, 800, 1200, and 2400. The sample was oriented 90° with each increment of silicon carbide paper. Further polishing of the sample was done by applying diamond slurry, 6-μm diamond paste, and 3-μm diamond paste. Keller's reagent was used for etching with immersion time of 30 s, immediately cleaned with running water, and dried. Optical microscopy (OM) of 5× and 50× magnification was used to observe the grain boundaries and validate the presence of the FA within the AA7075/FA-AMC along the SZ, TMAZ, and HAZ. FESEM analysis was used to capture microscopic images within the SZ. Energy-dispersive X-ray (EDX) and mapping using FESEM were used to further analyse the elements contained within the stir zone as well as the dispersion of each element.



## 2.4 Microhardness and Tensile Testing

The flash that has been formed during the FSP was removed by using diamond file to prevent misalignment of the specimen when the scope and indenter moved. The specimen was tested with 200 gf with 15 s dwell time. The indentation was measured on two diagonals (d1 and d2 in  $\mu\text{m}$ ). Ten readings were recorded on the advancing side (AS), stir zone (SZ), and retreating side (RS), and the average value is utilized for further analysis. The dog bone sample was prepared according to ASTM E8M subsize and tested with strain rate of 2 mm/mm until fracture occurs. The tensile specimens were cut such that the gauge length was incorporated within composite zones.

## 3 Results and Discussion

### 3.1 Vickers Microhardness Test

The microhardness values of three important zones were measured for each composite sample. The readings of four composite samples were recorded, and the average of the results is given in Table 4 and plotted in Fig. 1.

All the samples above received an increase in microhardness compared to the base alloy (140 HV). For this study, the highest average hardness value was recorded at S2. Gangil et al. [8] observed that with unit stirring of ratio  $\omega = 0.00223$ , rotational speed is sufficient such that the reinforcement particles slip easier in the aluminium matrix rather than attaching evenly throughout the surface of the aluminium matrix. As discussed before, FSP is a process whereby the material experiences plastic deformation and causes large strains in the material. Dinaharan et al. [10] tried to produce MMC from AZ231 aluminium alloy, Mg, and Cu alloy with FA through FSP and observed that most of the FA particles break during the FSP process as they were unable to sustain the large strain that was applied. Besides that, the broken-down fly ash became debris which was not seen to cluster together; instead, they blended well with the metal, forming the composite desired. They also mentioned that the debris was dispersed homogenously in the composites resulted in higher resistance for particle dislocation. The disintegrated FA also fills up the spaces between the

**Table 4** Microhardness results of Al 7075-T651-FA MMCs

Sample	Volume % of FA particles	AS	SZ	RS	Avg. HV
S1	2	161.53	170.06	184.19	171.7
S2	4	179.63	180.88	174.52	178.3
S3	6	174.23	163.43	150.13	162.6
S4	8	163.31	172.61	167.69	167.87

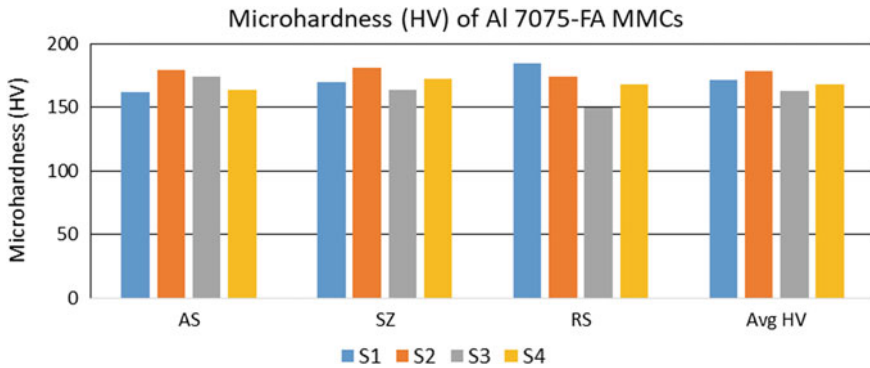


**Fig. 1** Microhardness of AA7075 FA-AMCs on AS, SZ, RS, and average microhardness values

magnesium alloy particles which produces higher microhardness with lower grain size.

Besides showing positive mechanical properties on magnesium alloy, various metals such as AA6061 and AA5083 that were reinforced with FA as reinforcement particles also produced desirable results as well. Through FSP, the final appearance of the composite is seen to be shiny and there is no defect on the surface of the MMCs [11, 12]. By looking the microstructure of the processed composite, the FA particles were observed to be mixed homogenously along the stir zone without reduction in the size of the FA particles [11, 12]. The microhardness of all the samples in their study also proved that the hardness value of the composite will be higher when compared to the original base metal. After FSP, smaller and finer grains are formed which contribute to the increase of microhardness.

### 3.2 Tensile Tests

The dog bone-shaped samples were cut and tested with a strain rate of 2 mm/min, and the results were observed. Both of the samples with least defect were compared. S2 exhibits a higher tensile strength when compared to S4. The result is in line with the findings in the microhardness test where S2 exhibited highest hardness. When a material has a higher hardness value, the material itself will be able to resist more localized deformation with less ductile properties. Therefore, the trend of increased hardness is close to the relationship of increased tensile strength. However, there is the presence of tunnels within the dog bone sample itself for both S2 and S4. The flaw within the specimen acts as a stress concentrator which inhibits the specimen to distribute the force evenly throughout the whole cross-sectional area. Therefore, when a force is applied, localized stress happens at the flaw, which propagates the crack throughout the specimen of the material. The FA-reinforced aluminium alloy

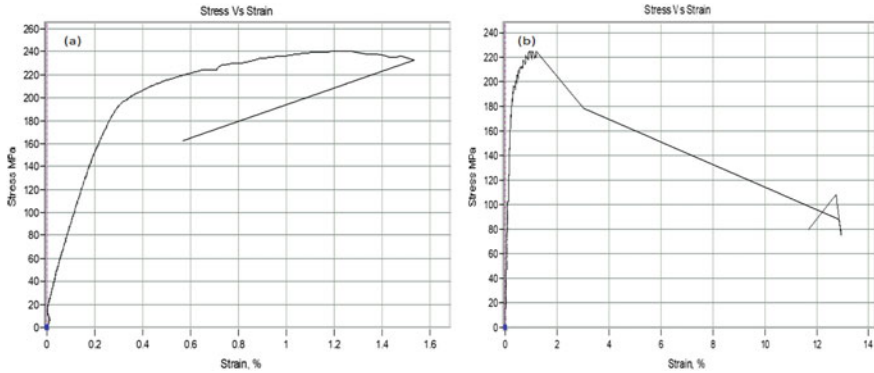


**Fig. 2** Stress–strain curve for **a** S2 and **b** S4

now exhibits the characteristics of a brittle fracture. There is no necking of the fractured samples, and the fracture of the specimen occurs without prior indications. The results obtained for S2 sample were: peak load = 9.15 kN and UTS = 240.24 MPa. For the S4 sample, the results obtained were: peak load = 8.55 kN and UTS = 224.49 MPa.

Figure 2a shows the stress–strain curve of S2 which shows a distinct elastic region below 180 MPa. S2 reaches the yield point at 200 MPa and starts to deform plastically. At the fracture point, the graph showed a sudden drop towards 0.6% strain rate due to specimen slippage from the extensometer. Figure 2b, stress–strain curve for S4, shows the stress–strain curve for S4 which shows a distinct elastic region below 180 MPa which reaches yield point at 220 MPa. As S4 enters the plastic region after yield point, the graph started to move towards lower stress with larger strain %. The phenomenon was caused by loose gripping of the extensometer which started to record lower stress as the elongation occurred. However, both of the specimens have a similar elongation length of  $1 \pm 0.5$  mm. However, in other studies, it was observed that the presence of FA hindered the movement between the FA particles as it increased the strength required to dislocate the particles [11]. It is also reported that the ultimate tensile strength (UTS) and yield strength (YS) influentially improved in the copper matrix composites with FA [3].

### 3.3 Microstructural Observations

The fly ash seemed to be dispersed homogeneously within the aluminium matrix as shown in Fig. 3. It is noticed that the size of the original fly ash powder (40–50  $\mu\text{m}$ ) was broken down into smaller sizes. Irregularities of the shape and sizes of the fly ash were due to the intense rotating motion of the tool which breaks the particles into finer particles to be deposited within the aluminium matrix [11]. As per Fig. 4 observations, it showed that there were cracks beneath the surface of the composite.

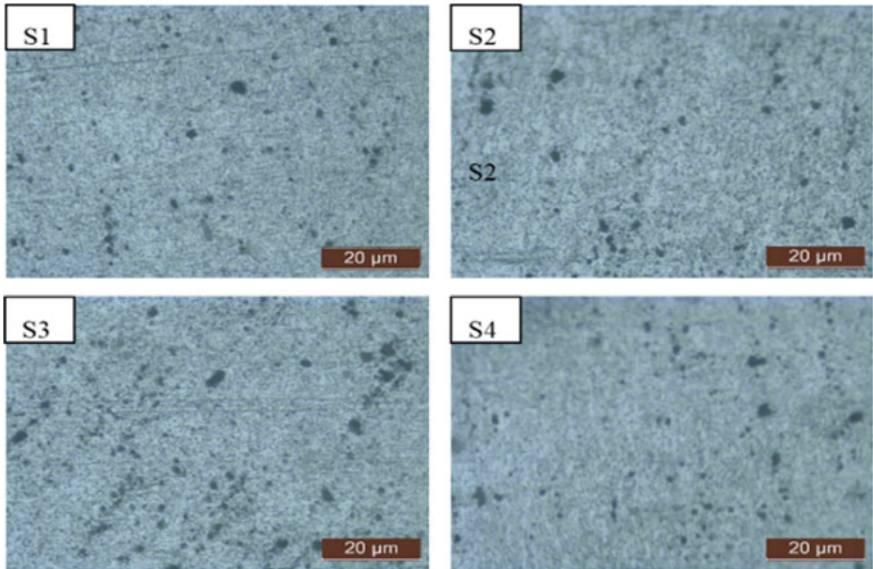


Fig. 3 Microscopic images of 50× magnification taken around the stir zone of S1–S4

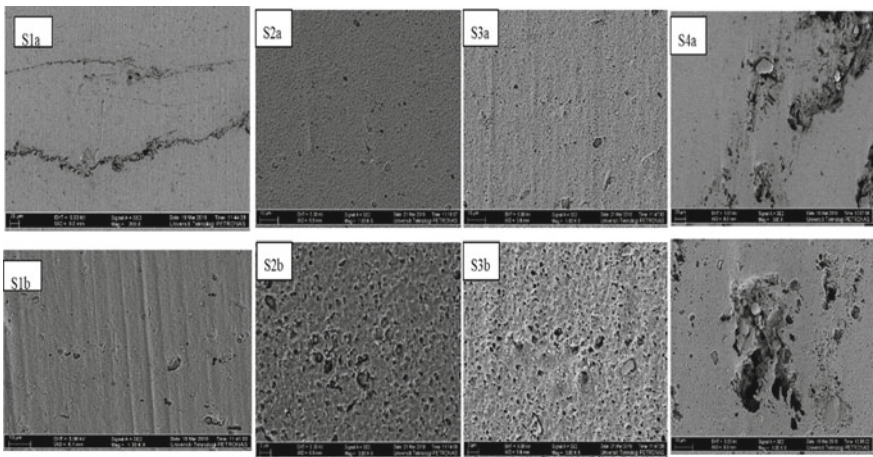
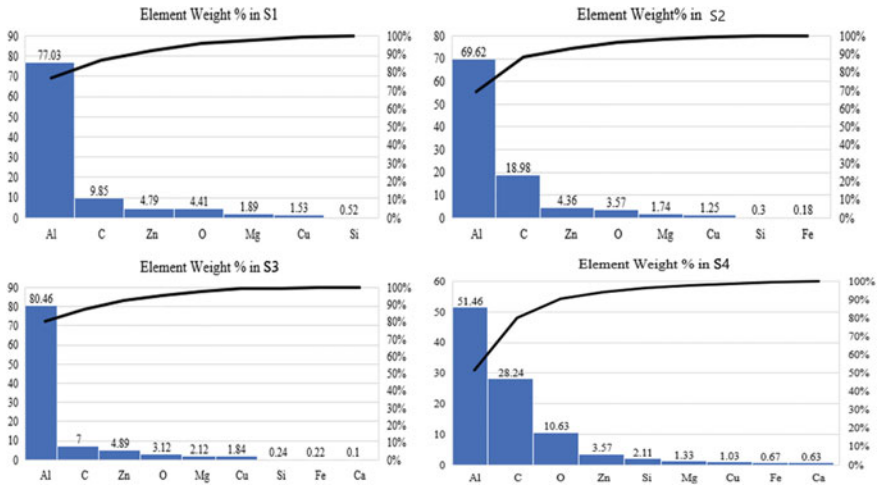


Fig. 4 FESEM images for samples S1–S4: a 200× magnification and b 1000× magnification

The plasticization of the base alloy, which moves the aluminium matrix layer by layer, did not occur intensively. When the tool traverses, frictional heat is provided to melt the aluminium, hence moving the material from AS to RS.

In imaging, it is confirmed that there are cracks beneath the surface of the composite due to poor interfacial bonding as shown in Fig. 4. The intense plasticization, which moves the aluminium matrix layer by layer, did not happen sufficiently,



**Fig. 5** FESEM-EDX elemental analysis results of Al 7075-FA composite samples S1–S4

and thus, agglomeration of particles and poor interfacial bonding took place. When the tool traverses, frictional heat is provided to melt the aluminium, hence moving the material from AS to RS. Figure 4 shows that homogeneous distribution of particles is achieved in sample S2 and sample S3. It is confirmed that by using unit stirring parameter, a better particle–matrix bonding is accomplished within 1 pass of FSP. The high volume of fly ash does not have a good particle–matrix bonding as before due to the high-volume percentage of fly ash. The axial force with suitable stirring parameters will help in plasticizing the matrix to provide a better condition for the fly ash to stick when the aluminium moves layer by layer.

The FESEM-EDX elemental analysis results of Al 7075-FA composite samples S1–S4 are shown in Fig. 5. The matrix of aluminium has some dark spots which contains the FA particles. On the same area, the intensity of the silicon and oxygen elements is higher compared to other regions. For other elements, such as carbon, calcium, and iron have been dispersed homogeneously within the aluminium matrix which enhances their hardness. However, oxides, silicon, iron, and carbon were present in the region as the fly ash particles were lodged into matrix site of the surface composite. EDX analysis confirmed the presence and distribution of fly ash through the mapping of carbon (9.85–28.24%), oxygen (3.12–18.98%), and calcium (0.1–0.63%) within the composite samples as shown in Fig. 6.

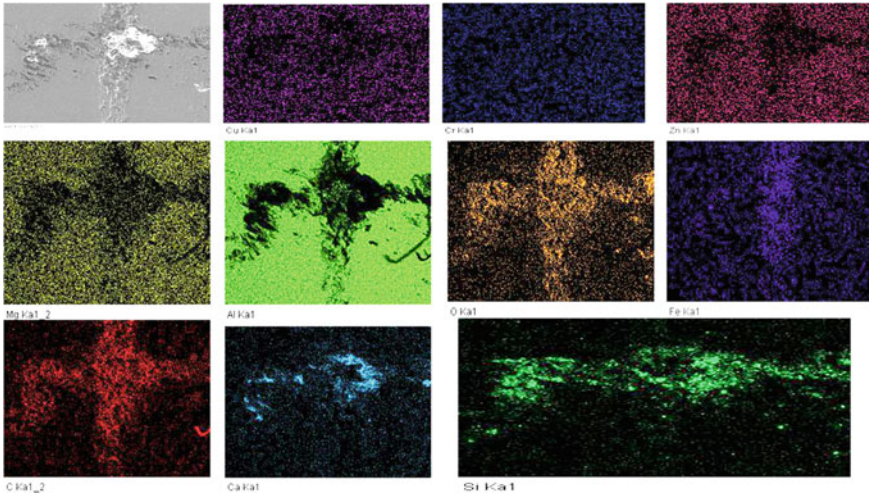


**Fig. 6** FESEM mapping results of Al 7075-FA composite sample S4

## 4 Conclusion

In this study, AA7075/FA-AMCs were successfully produced through FSP. The tests have been conducted to further analyse the mechanical properties and microstructure of the composites. AA7075/FA-AMC with 4% volume percentage (S2) exhibited the highest increase of microhardness value of 178.3 HV. The low 2% FA has not increased the hardness of the AA7075/FA-AMC due to lack of more strengthening particles. High-volume 6 and 8% FA insertions have not been as efficient in increasing hardness value due to agglomeration of micropowder and poor interfacial bonding. The OM and FESEM micrographs showed homogenous distribution of FA particles. The FA particles have been broken into finer particles embedded within the aluminium matrix due to sufficient stirring which breaks the particles and is spread across the AS to RS. Finally, the EDX analysis confirmed the presence and distribution of fly ash in the composites in terms of its constituent's elements such as carbon (9.85–28.24%), oxygen (3.12–18.98%), and calcium (0.1–0.63%).

**Acknowledgements** We are thankful to Centre of Graduate Studies, Universiti Teknologi PETRONAS, for providing financial support for this publication.



## References

1. Mishra P, Rana R (2018) Effect of rice husk ash reinforcements on mechanical properties of aluminium alloy (LM6) matrix composites. *Mater Today Proc* 5(2):6018–6022
2. Dinaharan I, Kalaiselvan K, Murugan N (2017) Influence of rice husk ash particles on microstructure and tensile behavior of AA6061 aluminium matrix composites produced using friction stir processing. *Compos Commun* 3:42–46
3. Kumar H, Prasad R, Srivastava A, Vashista M, Khan M (2018) Utilisation of industrial waste (Fly ash) in synthesis of copper based surface composite through friction stir processing route for wear applications. *J Cleaner Prod* 196:460–468
4. Prabhakar G, Ravi Kumar N, Ratna Sunil B (2018) Surface metal matrix composites of Al5083—fly ash produced by friction stir processing. *Mater Today Proc* 5(2):8391–8397
5. Węglowski M (2018) Friction stir processing—state of the art. *Arch Civil Mech Eng* 18(1):114–129
6. Smith C, Mishra R (2014) Concept of friction stir processing for enhanced formability. *Friction stir processing for enhanced low temperature formability*, pp 1–6
7. Rathee S, Maheshwari S, Siddiquee A, Srivastava M (2017) Investigating effects of groove dimensions on microstructure and mechanical properties of AA6063/SiC surface composites produced by friction stir processing. *Trans Indian Inst Metals* 70(3):809–816
8. Gangil N, Maheshwari S, Nasr E, El-Tamimi A, El-Meligy M, Siddiquee A (2018) Another approach to characterize particle distribution during surface composite fabrication using friction stir processing. *Metals* 8(8):568
9. Khan NZ, Siddiquee AN, Khan ZA (2018) Proposing a new relation for selecting tool pin length in friction stir welding process. *Measurement* 129:112–118
10. Dinaharan I, Akinlabi E (2018) Low cost metal matrix composites based on aluminium, magnesium and copper reinforced with fly ash prepared using friction stir processing. *Compos Commun* 9:22–26
11. Dinaharan I, Nelson R, Vijay S, Akinlabi E (2016) Microstructure and wear characterization of aluminium matrix composites reinforced with industrial waste fly ash particulates synthesized by friction stir processing. *Mater Charact* 118:149–150
12. Sharma V, Gupta Y, Manoj Kumar BV, Prakash U (2015) Friction stir processing strategies for uniform distribution of reinforcement in a surface composite. *Mater Manufact Process* 31(10):1384–1392

# Design-Point Performance Adaptation of Small Gas Turbine Using Particle Swarm Optimization



Affiani Machmudah and Tamiru Alemu Lemma

**Abstract** Modeling of design-point performances is an important step for designing the gas turbine engine. It is also a necessary step in an off-design performance analysis where during the modeling of design-point performance, some engine parameters are typically not known. These unknown parameters should be estimated and adapted to obtain design-point target performances. This paper employs meta-heuristic optimizations, namely genetic algorithm (GA), particle swarm optimization (PSO), gray wolf optimizer (GWO), and whale optimizer algorithm (WOA) to solve the design-point adaptation of a small gas turbine designed for marine applications. Target parameters are shaft power, fuel flow, turbine exit temperature, turbine exit pressure, and thermal efficiency with seven adapted parameters as the optimization parameters. Due to multiple solutions and constraints of the searching area, the meta-heuristic optimization can encounter the computational difficulty. The PSO shows an outstanding performance among other meta-heuristic optimizations where it has the smallest fitness value, i.e., 0.02233. The GWO has the minimum fitness value as compared with the GA and WOA, but the value of turbine inlet temperature (TIT) is approaching its upper bound, in which this condition is not expected. The GA has a problem of escaping from the initial value for the TIT parameter. The WOA has the largest fitness value, i.e., 0.0971, although it does not have a problem of escaping the initial value and approaching the upper/lower bound.

## 1 Introduction

Engine performance modeling is an important step during the gas turbine design. It should be started from the design-point modeling [1]. In most cases, values of engine parameters are not known and the user does not have access to the information, since they are manufacturer's properties. Thus, design-point parameter estimation should

---

A. Machmudah (✉) · T. A. Lemma  
Mechanical Engineering, Universiti Teknologi PETRONAS, Bandar Seri Iskandar, Perak,  
Malaysia  
e-mail: [de.affela@gmail.com](mailto:de.affela@gmail.com)



be conducted to predict their values in such a way that the engine target parameters are obtained. This process is also known as the design-point adaptation [2].

Performance adaptation is an inverse mathematical problem with the objective to adapt an engine model in such a way so that the real engine data as target parameters can be obtained [3]. Design-point adaptation can be modeled as the optimization problem. Stamatis et al. [4] presented a computational procedure for developing a performance model adaptation by employing optimization technique. Yi et al. [2] proposed the method for adapting the design-point performance of industrial gas turbine using pseudoinverse technique. Li and Pilidis [5] employ GA and influence coefficient matrix to solve the design-point adaptation of the industrial gas turbine. TURBOMATCH/PYTHIA software was employed to simulate the proposed method. Mohammed et al. [6] presented design-point performance simulation and adaptation of an industrial GE LM2500+ gas turbine engine. PYTHIA software was employed with target parameters of fuel flow rate, compressor exit pressure, turbine exit temperature, and compressor exit temperature. Kiaee et al. [7] presented a method to estimate the specification components for design-point and off-design performance analysis of a micro-gas turbine. Design-point and off-design-point adaptations of 30 MW gas turbine GE LM 2500+ were presented in [3]. Simulation was conducted in PYTHIA software employing the GA.

Using small gas turbines as propulsion system of marine vehicle has been of interest due to its lightweight and high power [8]. The small gas turbine has the range of power from 1 to 40 MW [9]. This paper addresses the design-point adaptation to design the small gas turbine engine with power of 3 MW. The meta-heuristic optimizations, namely GA, PSO, GWO, and WOA, are employed to solve the design-point adaptation. Their performance to estimate the value of adapted parameters to achieve the targeted parameters is investigated. To be adapted, parameters consist of inlet mass flow, compressor pressure ratio, compressor polytropic efficiency, turbine polytropic efficiency, power turbine polytropic efficiency, burner pressure loss, and TIT. Target performances involve design specification parameters of engines, which are the shaft power and the thermal efficiency, and gas generator turbine parameters, which are the exit turbine temperature and pressure. Gas turbine engine has performance limiters which include the surge, TIT, minimum spool speed, maximum spool speed, maximum spool speed, and flameout limits that construct fuel boundaries. The TIT limit presents because of material temperature properties, while the surge limit should be considered because of the compressor blade design property [10, 11]. Besides the performance of the meta-heuristic optimizations, the fuel flow boundary of the designed small gas turbine is further presented in discussions.

## 2 Thermodynamics Models of Gas Turbine Design-Point Performance

Figure 1 illustrates the two-shaft gas turbine engine used in this work. Design-point performance modeling is the first step of the design process where the results will be used for the next steps, which are the off-design performance modeling and the control system design. Its calculation aims to obtain the unknown design-point parameter at the expected design performance, i.e., targeted parameters. This work models the gas turbine components at the design-point level using standard thermodynamics model. It should be noted that the thermodynamics model of the design-point performance will be different from the off-design performance modeling. In the off-design performance analysis, designer should consider the detail of the gas turbine components, such as compressor, turbine, and power turbine.

### 2.1 Inlet

Total temperature and total pressure of ambient conditions can be expressed as follows:

$$T_{oa} = T_{amp} + \frac{v_{amp}^2}{2C_p}; P_{oa} = P_{amp} + \left( \frac{T_{oa}}{T_{amp}} \right)^{\frac{\gamma}{\gamma-1}} \tag{1}$$

where  $C_p$ ,  $\gamma$ ,  $T_{amp}$ , and  $P_{amp}$  are the specific heat at ambient condition, the specific heat ratio, the ambient temperature, and the ambient pressure, respectively.

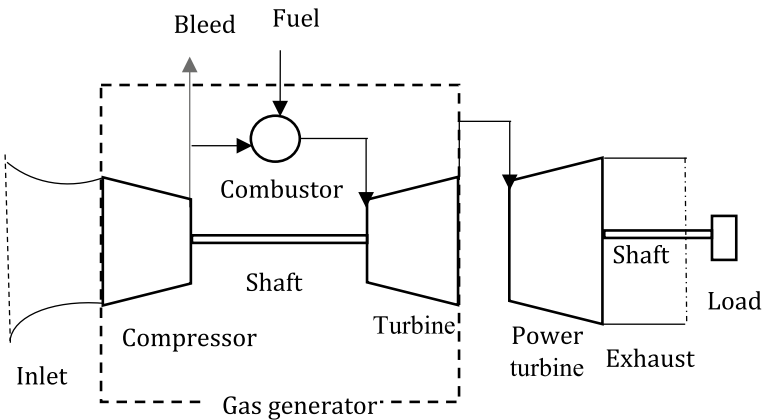


Fig. 1 Two-shaft engine layout

Assuming the  $v_{amp}$  is relatively low, Eq. (1) can be expressed as:

$$T_{oa} = T_{amp}; P_{oa} = P_{amp} \quad (2)$$

Pressure at inlet can be expressed as follows:

$$P_{o1} = P_{oa}(1 - \Delta PR_{inlet}); \Delta PR_{inlet} = 1 - \frac{P_{o1}}{P_{oa}} \quad (3)$$

where  $\Delta PR_{inlet}$  is the pressure loss at inlet.

Mass flow at inlet is expressed in the following equation:

$$m_1 = m_a \quad (4)$$

where  $m_l$  and  $m_a$  are the mass flow at compressor inlet and the air mass flow, respectively.

## 2.2 Compressor

Pressure and temperature at exit point of compressor can be obtained as follows:

$$P_{o2} = P_{o1} PR_c \quad (5)$$

$$T_{o2} = T_{o1} + \left( \frac{T_{o1}}{\eta_{pc}} \right) \left( \frac{T_{o2s}}{T_{o1}} - 1 \right); T_{o2s} = T_{o1} (PR_c)^{\frac{\gamma-1}{\gamma}} \quad (6)$$

where  $PR_c$  and  $\eta_{pc}$  are the compressor pressure ratio and the compressor polytropic efficiency, respectively.

Compressor power is obtained as follows:

$$C_{power} = m_1 (h(T_{o2}) - h(T_{o1})) \quad (7)$$

where  $C_{power}$  and  $h$  are the compressor pressure ratio and the specific enthalpy, respectively.

## 2.3 Combustor

Fuel flow and pressure at turbine can be expressed as follows:

$$\dot{m}_f = m_{21}(h_{\text{air}}(T_{o3}) - h_{\text{air}}(T_{o21})) / (\text{HV} \cdot \text{Bn} - h_{\text{air}}(T_{o3})) \quad (8)$$

$$P_{o3} = P_{o2}(1 - \Delta \text{PR}_b) \quad (9)$$

$$T_{o3} = \text{TIT}; m_{21} = m_2; m_3 = m_{21} + \dot{m}_f$$

where  $\dot{m}_f$ , HV, TIT, and  $\Delta P_b$  are fuel flow, heating value, turbine inlet temperature, and pressure loss at burner, respectively.

## 2.4 Gas Generator Turbine

Power by gas generator turbine is expressed as follows:

$$\text{HPT Power} = \left( \frac{C_{\text{power}}}{M_n} \right) + \text{Aux} \quad (10)$$

where HPT Power, Aux, and  $M_n$  are power of gas generator turbine, auxiliary power, and mechanical efficiency, respectively.

Exit temperature and pressure of the power turbine can be expressed as follows:

$$T_{o4} = T_{o31} - \left( \frac{\text{HPT power}}{\eta_{pc} \cdot m_{31}} \right) \quad (11)$$

$$P_{o4} = P_{o3} / \text{PR}_t; \text{PR}_t = \left( \frac{T_{o31} T_{o4}}{T_{o4}} \right)^{\frac{\gamma}{(\gamma-1)\eta_{pT}}} \quad (12)$$

where  $\eta_{pc}$  and  $\eta_{pT}$  are polytrophic efficiencies of compressor and turbine, respectively.

## 2.5 Power Turbine

Power of power turbine can be obtained as follows:

$$\text{LPT Power} = m_{41}(h_{\text{air}}(T_{o41}) - h_{\text{air}}(T_{o5})) \quad (13)$$

$$T_{o5} - T_{o41} + (T_{o5s} - T_{o41})\eta_{pPT}; T_{o41} = T_{041} \quad (14)$$

where LPT Power and  $\eta_{pPT}$  are power of power turbine and the power turbine polytropic efficiency, respectively.

## 2.6 Shaft Power

Shaft power and thermal efficiency of the gas turbine engine can be obtained as follows:

$$\text{Shaft Power} = \text{LTP power} \cdot M_n \cdot \text{GB}_n \quad (15)$$

$$\eta_{\text{thermal}} = \frac{\text{Shaft Power}}{\dot{m}_f \text{HV}} \quad (16)$$

where  $M_n$ ,  $\text{GB}_n$ , and  $\eta_{\text{thermal}}$  are mechanical efficiency, gearbox efficiency, and thermal efficiency, respectively.

## 3 Optimization

Using the optimization approach, the objective optimization is to minimize the error of targeted parameters with actual parameters. Using meta-heuristic optimization, adapted parameters become the searching agents or optimization parameters. The adapted parameters are the air mass flow, the compressor efficiency, the compressor polytropic efficiency, the turbine polytropic efficiency, the power turbine polytropic efficiency, burner pressure loss, and turbine inlet temperature. Searching area for air mass flow, compressor pressure ratio, burner pressure loss, and turbine inlet temperature are  $3 < \dot{m}_a < 22$ ,  $5 < \text{PR}_c < 15$ ,  $0.07 < \Delta P_b < 0.1$ , and  $1000 < \text{TIT} < 1220$ , respectively. Target parameters are the fuel flow, the efficiency thermal, the shaft power, power turbine inlet temperature, and power turbine inlet pressure.

### 3.1 Fitness Function

Since the number of adapted parameters is more than the number of targeted parameters, mathematically there are multiple solutions. It is necessary to ensure that the meta-heuristic optimization lays within the valid solution. For example, the negative value of polytropic efficiency should be avoided. Fitness function should accommodate these requirements. This work employs the death penalty in the fitness function as Eq. (17a) to avoid the unfeasible solution.

$$F = \begin{cases} \infty & (3 < \dot{m}_a < 22) \text{ or } (5 < PR_c < 15) \text{ or } (0 < \eta_{pc}, \eta_{pT}, \eta_{pPT} < 1) \text{ or} \\ & (0.07 < \Delta P_b < 0.1) \text{ or } (1000 < TIT < 1230) \\ F_{ob} & \text{else} \end{cases} \tag{17a}$$

$$F_{ob} = \sum a_i b_i |x_{\text{target}(i)} - x_{(i)}| \tag{17b}$$

### 3.2 Genetic Algorithm

There are three main operators in the GA: reproduction, crossover, and mutation. The optimization parameter is represented in the chromosomes to code it in the evolution process to find the best individual with the best performance. Using real code GA, the chromosome is a string of numbers, which represents the number in sequence. The selection is the process of choosing two individuals as parents from the population for mating to born the new offspring. A crossover is a process of randomly picking one or more individuals as parents and swapping segments of the parents. This paper uses random resetting mutation. In this scheme, randomly chosen gene is assigned to be changed with a random value. Detailed procedure of the GA can be referred to [12].

### 3.3 Particle Swarm Optimization

The optimization parameter is represented as particles that have positions and velocities. The particle will move with a certain velocity. Velocities and positions will be updated according to the local and global best solutions.

Eberhart and Shi [13] proposed the velocity by utilizing constriction factor,  $\chi$ , in the following equation:

$$v_{i+1} = \chi \{wv_i + \phi_1 \beta_1 (p_i - x_i) + \phi_2 \beta_2 (p_g - x_i)\};$$

$$\chi = \frac{2}{2 - \varphi - \sqrt{\varphi^2 - 4\varphi}}; \phi = \phi_1 + \phi_2, \phi > 4 \tag{18}$$

The velocity for each particle is needed to be updated and adds this velocity to the particle position. If the best local solution has a fitness less than the fitness of the current global solution, then the best local solution replaces the best global solution. Detailed procedure of the PSO can be referred to [13].

### 3.4 Gray Wolf Optimizer

Inspiring from the leadership hierarchy and hunting mechanism of gray wolves, there are four types of gray wolves which are alpha, beta, delta, and omega. The computation of GWO involves four steps, namely hunting, searching for prey, encircling prey, and attacking prey. The fittest solution is considered as the alpha ( $\alpha$ ). The beta ( $\beta$ ) and delta ( $\delta$ ) are the second and third best solutions, respectively. The remaining of the candidate solutions are omega ( $\omega$ ).  $\omega$  wolves follow the guidance from  $\alpha$ ,  $\beta$ , and  $\delta$  wolves in the hunting mechanism. Detailed procedure of the GWO can be referred to [14].

### 3.5 Whale Optimization Algorithm

The WOA is a meta-heuristic optimization technique inspired from the bubble-net hunting strategy of humpback whales proposed by Mirjalili et al. [15]. Humpback whales have an ability to recognize the location of prey and encircle them. Because the optimal solution in the search space is not known a priori, the current best candidate solution is assumed as the target prey or is close to the optimum solution. The search agents will update their positions approaching the best search agent. Humpback whales search for prey randomly according to the position of each other. In the exploitation phase, the position of the search agent is updated according to a randomly chosen search agent instead of the current best search agent. Detailed procedure of the WOA can be referred to [15].

## 4 Results and Discussion

This section presents the results of design-point adaptation of small gas turbine engine using the meta-heuristic optimizations. At design-point level, the value target parameters for shaft power,  $\eta_{thermal}$ ,  $\dot{m}_f$ ,  $T_{o4}$ , and  $P_{o4}$  are 3 MW, 0.27, 0.26, 970 K, and 260 kPa, respectively. The values of input parameter for design-point performance modeling are presented in Table 1.

The value of weighting factor and normalized factor in Eq. (17b) is, respectively, as follows

$$a_i = [0.1 \ 0.1 \ 0.3 \ 0.3 \ 0.2];$$

$$b_i = [100 \ 100 \ 0.005 \ 0.005 \ 0.005]$$

The computation of design-point adaptation using the meta-heuristic optimization is conducted by writing the computer program in MATLAB environment. For each

**Table 1** Parameter values of design-point input

Components	Symbol	Value	Parameter
Inlet	$\Delta PR_{\min}$	4 (in H <sub>2</sub> O)	Inlet total pressure loss
Compressor	$B_c$	0.015	Compressor bleed fraction
Combustor	$\eta_b$	99%	Combustion efficiency
	HV	43,100 kJ/kg	Fuel heating value
Exhaust	$\Delta PR_{\text{exhaust}}$	8 (in H <sub>2</sub> O)	Exhaust total pressure loss
Shaft	$\eta_{\text{mech}}$	99%	Mechanical efficiency
Load	$\eta_{\text{gear}}$	100%	Gearbox efficiency

meta-heuristic optimization, the computation uses 20 search agents in the population with 5000 number of iterations. For the GA, the selection rate and mutation rate are 0.5 and 0.008, respectively. For the PSO, the constriction parameter, the cognitive parameter, and the social parameter are 1, 1.5, and 1.5, respectively. To give the objective evaluation, this study considers to input the initial searching parameter  $[\dot{m}_a PR_c \eta_c \eta_T \eta_{PT} \Delta P_b TIT]_{\text{initial}} = [14.3 \ 7.75 \ 0.94 \ 0.8 \ 0.9 \ 0.009 \ 1216]$ . Figure 2 shows the fitness value evaluation of the meta-heuristic optimizations. It shows that the PSO has outperformed other methods.

Table 2 presents the detailed results of the adapted parameters from the GA, the PSO, the GWO, and the WOA. It can be observed that from the fitness value, the PSO and the GWO have almost the same value; however, they have different values of the compressor efficiency, turbine efficiency, power turbine polytrophic efficiency, and

**Fig. 2** Fitness value evolutions

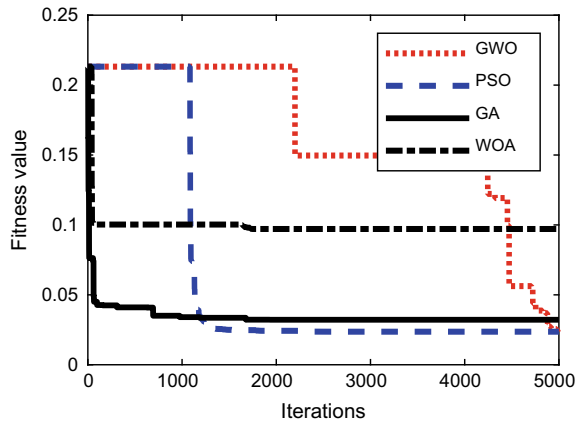




**Table 2** Optimization results of the adapted parameter

	Fitness	Best optimization parameter						
		$\dot{m}_a$	$PR_c$	$\eta_{pc}$	$\eta_{pT}$	$\eta_{pPT}$	$\Delta P_b$	TIT
GA	0.032182	14.400	7.8359	0.9378	0.7997	0.9068	0.0825	1216
PSO	0.02233	14.288	7.6141	0.941	0.7946	0.91777	0.08946	1213.1999
GWO	0.0226	14.2164	7.3012	0.8606	0.8618	0.9201	0.0741	1228.8084
WOA	0.0971	14.2439	6.3029	0.8881	0.9485	0.8975	0.0868	1210.3695

TIT. Especially for the TIT value, the TIT obtained from the GWO is approaching the upper bound, i.e., 1230 K. The WOA does not have a good performance where it has the largest fitness value, but different with the GWO, the WOA result of TIT is not approaching the upper bound value. In terms of the fitness value, the GA has a better performance than the WOA; however, the TIT value does not move from the initial value.

In the optimization point view, avoiding the value near to the upper bound and lower bound of the constraints is a positive value. Thus, in the case of multiple solutions, the PSO has a good performance in searching the optimization parameters where they are quite far from the upper bound and lower bound values. Table 3 presents the details of the target parameter obtained from the optimization results of each meta-heuristic optimization. Generally speaking, since this case has multiple solutions, the meta-heuristic optimization can encounter the computational problem of approaching the lower/upper bound and being trapped in the initial value for TIT parameter. Among the meta-heuristic optimizations that have been employed in this study, the PSO has an outstanding performance where it avoids such problems.

After the design-point modeling, the off-design performance should be conducted. The gas turbine also operates at off-design conditions where the variation of speed, power, or load is necessary. The results of the optimal adapted parameters are used in the off-design performance analysis. Computational procedures of the off-design analysis need a compressor map in the calculation. In the preliminary design, in which the compressor is still under development, the compressor map can be obtained through the scaling method. Employing the scaling method as in [16], Fig. 3a shows the compressor map of the designed gas turbine.

**Table 3** Value of the adapted parameter obtained from meta-heuristic optimization

	Target				
	Shaft power (kW)	$\eta_{thermal}$	$\dot{m}_f$	$To_4$	$Po_4$
GA	2999.991	0.26792	0.2598	967.3834	265.4347
PSO	3000	0.26782	0.25989	969.9991	260.8092
GWO	2999.8768	0.26962	0.25815	970.0611	259.9617
WOA	3000	0.26544	0.26223	983.5893	268.8245

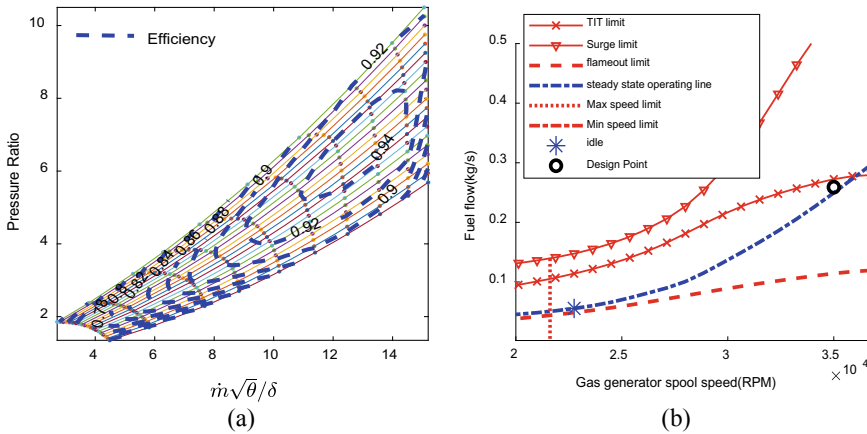


Fig. 3 a Compressor map and b fuel flow boundaries

Accurate prediction of engine performance is very important for the user to maintain the engine operating in the safe zone. Gas turbine has performance limitations that should be considered during its operation. According to Saravanamuttoo et al. [17], the fuel boundaries can be obtained through the compatibility of flow and compatibility of work during the steady-state off-design performance considering the limiters. Based on material properties of the gas turbine components, the maximum transient gas generator TIT and over-temperature of TIT are 1250 and 1300 K, respectively. Minimum fuel-to-air ratio is 0.0081 to avoid engine flameout [1]. These limit values are necessary in the computation of the fuel boundaries using the component-matching method. Employing the Newton–Raphson method to solve the compatibility requirements, the graph of fuel flow boundaries of the designed gas turbine is illustrated in Fig. 3b. The fuel boundaries represent the safe zone of the operational gas turbine. To protect the components of the engine from being damaged, control system needs to be designed in such a way so that the engine operates within the fuel flow boundaries. Acceleration and deceleration schedules should be designed inside these boundaries.

The design-point modeling to obtain 3 MW of the gas turbine power has been presented. This is the first step of the comprehensive design of the gas turbine engine. Applying the optimal design-point obtained from PSO, which has the best performance among other meta-heuristic optimizations, the fuel boundary graph has been obtained in this present study. Next steps that need to be conducted are transient off-design performance, acceleration/deceleration scheduling, and designing the control system of the small gas turbine, which are currently under development. The optimal control system considering performance limiter employing the meta-heuristic optimizations will be conducted for future research.

## 5 Conclusions

Modeling the design-point performance adaptation using the meta-heuristic optimization for design purpose of the small gas turbine has been studied. The PSO has the best performance among the other meta-heuristic optimizations, which are the GA, the GWO, and the WOA. For future research, employing other meta-heuristic optimizations that can give the best performance without involving the problem of trapping the initial condition and approaching the upper/lower bound values is encouraged. The next step of design process, which is designing optimal control system of the small gas turbine for marine application, is very essential to be conducted.

**Acknowledgements** The authors would like to acknowledge the funding received from YUTP (015LC0-028) grant for completing this work.

## References

1. Walsh PP, Fletcher P (1998) Gas turbine performance. Blackwell Science, Oxford, UK
2. Li Y-G, Pilidis P, Newby MA (2006) An adaptation approach for gas turbine design-point performance simulation. *J Eng Gas Turb Power* 128(4):789–795
3. Tsoutsanis E, Li Y-G, Pilidis P, Newby M (2017) Non-linear model calibration for off-design performance prediction of gas turbines with experimental data. *Aeronaut J* 121(1245):1758–1777
4. Stamatis A, Mathioudakis K, Papailiou KD (1990) Adaptive simulation of gas turbine performance. *J Eng Gas Turbines Power* 112(2):168–175
5. Li Y-G, Pilidis P (2010) GA-based design-point performance adaptation and its comparison with ICM-based approach. *Appl Energy* 87(1):340–348
6. Mohammed A, Adeniyi AA, Hassan AB et al (2012) Design-point performance simulation and adaptation of a gas turbine engine. *Int J Emerg Trends Eng Dev* 4(2):665–672
7. Kiaee M, Tousi AM, Toudefallah M (2015) Performance adaptation of a 100 kW microturbine. *Appl Therm Eng* 87:234–250
8. Goldstein L, Hedman B, Knowles D et al (2003) Gas-fired distributed energy resource technology characterizations. National Renewable Energy Laboratory (NREL), Golden, Colorado
9. Molland AF (2008) The maritime engineering reference book: a guide to ship design, construction and operation. Butterworth-Heinemann, Oxford
10. Gaudet SR (2007) Development of a dynamic modeling and control system design methodology for gas turbines. M.Sc. thesis, Carleton University, Ottawa, Ontario
11. Lember JA, Ritchie RO (2012) Mo-Si-B alloys for ultrahigh-temperature structural applications. *Adv Mater* 24(26):3445–3480
12. Goldberg D (1989) Genetic algorithms in search, optimization, and machine learning. Addison-Wesley Professional, Boston, MA
13. Eberhart RC, Shi Y (2000) Comparing inertia weights and constriction factors in particle swarm optimization. In: *Proceedings Congress Evolutionary Computation*, pp 84–88
14. Mirjalili S, Lewis A (2016) The whale optimization algorithm. *Adv Eng Softw* 95:51–67
15. Mirjalili S, Mirjalili SM, Lewis A (2014) Grey wolf optimizer. *Adv Eng Softw* 69:46–61

16. Saravanamuttoo HIH, Maclsaac BD (1983) Thermodynamic models for pipeline gas turbine diagnostics. *J Eng Power* 105(4):875–884
17. Saravanamuttoo HIH, Rogers GFC, Cohen H (2001) Gas turbine theory. Pearson Education Limited

# Finite Element Analysis of the Heat Generated During FSP of 1100 Al Alloy



Adedotun Adetunla and Esther Akinlabi

**Abstract** FSP is a solid-state technique for microstructural modification using the heat from friction and stirring; hence, the temperature during the experiment may alter the microstructural behaviour of the material if not properly controlled. In this study, the in situ temperature during the experiment was measured and compared with the simulation result. The finite element analysis was done using ABAQUS to study the heat generated due to friction during the process. The experimentally measured temperature results are in agreement with the generated heat energy of the developed model, which is less than 10 °C difference. Hence, this study shows that the peak temperature during the process from the experiment and simulation is well below the melting point of the material.

**Keywords** Aluminum alloy · Finite element simulation · Friction stir processing · heat generation

## 1 Introduction

Friction stir processing (FSP) is a technology that involves severe plastic deformation caused by the contact between the base material and the non-consumable workpiece [1]. The working principle of both friction stir welding (FSW) and FSP is one that has a tool with cylinder shoulder consisting of a smaller pin shaped with a specific design, and the tool rotates while the pin is plunged into the surface of the material. The material is softened due to a combined frictional and adiabatic heat caused by friction as a result of the contact between the surface of the material and the non-consumable tool, thereby leading to plastic deformation and consequently altering the microstructure of the material. In FSP, a volume of the workpiece is being processed which is determined by the design of the tool pin, the transverse pattern, and the tool parameters used. When FSP is applied to a material, the mechanical and the physical properties of the material may be improved while changing the macroscopic shape

---

A. Adetunla (✉) · E. Akinlabi

Department of Mechanical Engineering Science, University of Johannesburg, Johannesburg 2006, South Africa

e-mail: [dotunadetunla@yahoo.com](mailto:dotunadetunla@yahoo.com)

© Springer Nature Singapore Pte Ltd. 2020

S. S. Emamian et al. (eds.), *Advances in Manufacturing Engineering*, Lecture Notes in Mechanical Engineering, [https://doi.org/10.1007/978-981-15-5753-8\\_39](https://doi.org/10.1007/978-981-15-5753-8_39)

of the material [2, 3]. The tool rotational speed, tool traverse along the processed path, and plastic deformation of the tool result in rapid heat and steep gradients in the temperature and strain rate.

Ramadam et al. [4] developed a heat generation model of an FSP tool with cylindrical shape used to fabricate Al alloys, and the temperature field was measured with thermocouples during the experiment and compared with the central differential scheme used to calculate the heat transfer during the plunging stage, transverse stage, and the tool removal from the workpiece. Thermocouple measurements were done by Lebaal et al. [5] using the inverse problem approach. The effect of tool rotational speed on the temperature of the workpiece was predicted by Cartiguyen et al. [6] by using a numerical model which was subsequently validated with the results gotten from thermocouple measurements. The effect of tool rotational speed on the quality of the fabricated alloy has not been extensively studied. Also, as far as the authors know, the effect of heat generated due to friction on the mechanical properties of the alloys has been moderately studied; in particular, no published literature has predicted the peak temperature for different alloys and materials using ABAQUS to ensure a temperature as the melting point of the material. Therefore, this study aims to investigate the heat generated due to friction and studies the effect of rotational speed on the thermal history of the interface between the tool and the workpiece using finite element analysis software (i.e. Abaqus).

## 2 Methods

### 2.1 Experimental Procedure

Sequel to the work done by Adetunla et al. [7], in situ measurement of temperature during different stages of the fabrication of aluminium alloy by using different process parameters is carried out. In their work, the base material used was 1100 aluminium alloy sheet of 5 mm thickness. The sheets were subjected to three cumulative passes with 100% overlap using constant traverse speed of 30 mm/min and varying tool rotational speeds of 600 and 1200 rpm. Table 1 shows the mechanical properties and temperature at different process parameters. Workpiece material was cooled down to room temperature after each pass before subjecting it to another FSP pass; hence, the temperature measurements of the second and third passes are negligible [8].

**Table 1** Mechanical properties and temperature measurements of fabricated 1100 alloy [9]

Number of pass	Tool rotational speed (RPM)	Hardness (HV)	Tensile properties (UTS)	In situ temperature measurements at 20 s (°C)
1 pass	600	26.58	91.77	405
1 pass	1200	26.14	88.20	385

## 2.2 Simulation Procedure Using ABAQUS

A three-dimensional (3D), transient, nonlinear thermal model was developed by using ABAQUS 2019 edition to simulate the thermal history during FSP of 1100 aluminium. The modelling of the aluminium plate with a length of 150 mm, breadth of 50 mm, and base extrusion depth of 200 mm was performed in order to investigate the heat generated due to friction caused by the base material and the FSP tool during the process when subjected to two different tool rotational speeds (i.e. 600 and 1200 rpm), as shown in Fig. 1. A linear static and nonlinear transient modelling method for the nodal temperature at nodes was used to predict the heat generated during the process.

The assumptions made in developing the model are as follows:

- Material sheet is homogenous and isotropic.
- Workpiece material was cooled down to room temperature after each pass before subjecting it to another FSP pass.
- Uniform boundary conditions are along the processed part.
- The contact between the FSP tool and the base material has perfect contact with 100% sticking condition.
- The tool pin only generates 2% of the total heat, which is negligible [10].

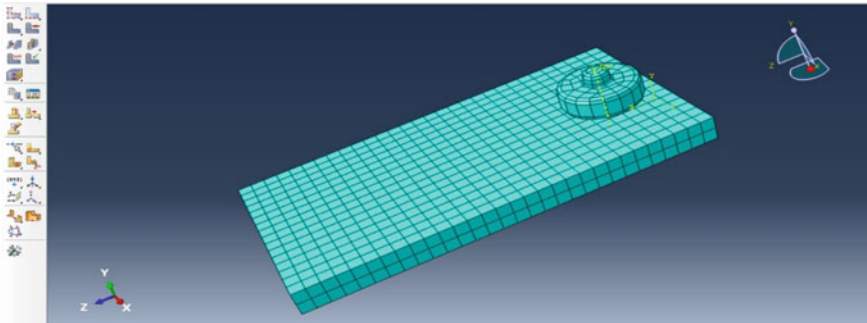


**Fig. 1** Surface contact of the FSP tool and aluminium plate

**Table 2** Simulation parameters

Parameters	Values
Young's modulus of elastic	70 GPa
Poisson's ratio	0.3
Thermal conductivity	0.15 (W/(m K))
Coefficient of friction	0.1
Density	27,000 kg/m <sup>3</sup>
Specific heat capacity	670,000 J/K

- Heat transferred to the clamp from the workpiece is negligible. Table 2 shows the properties of 1100 aluminium used in finite element modelling.

### 3 Finite Element Analysis of the Heat Generated Due to Friction During the Process

The temperature fields measured from the material during FSP can be used to determine the heat generated during the process. To analyse the heat generated due to friction, the transient temperature ( $T$ ) which is a function of time ( $t$ ) and the spatial coordinates ( $x, y, z$ ) can be calculated using Fourier's law of heat conduction in Eq. (1) [11].

$$K \left( \frac{\partial^2 T}{\partial x^2} + \frac{\partial^2 T}{\partial y^2} + \frac{\partial^2 T}{\partial z^2} \right) + Q_{\text{int}} = c\rho \frac{\partial T}{\partial t} \quad (1)$$

where  $K$  is the thermal conductivity,  $Q_{\text{int}}$  is the rate of internal heat,  $c$  the heat capacity, and  $\rho$  the density of the material.

The thermal history of a material can be determined by heat transfer coefficients on several surfaces. The loss of heat ( $qs$ ) is calculated using Eq. 2

$$qs = \beta(T - T_0) + \varepsilon\sigma(T^4 - T_0^4) \quad (2)$$

where  $\beta$  the convection coefficient ( $61 \text{ W/m}^2 \text{ K}$ ),  $T$  is in Kelvin, which is the absolute temperature of the workpiece materials,  $T_0$  is the ambient temperature ( $300 \text{ K}$ ),  $\varepsilon$  the emissivity of the plate surfaces ( $0.11$  for aluminium), and  $\sigma$  the Stefan–Boltzmann constant ( $5.67 \times 10^{-8} \text{ W/m}^2 \text{ K}^4$ ).

With the assumptions made in this study, the heat produced due to the friction between the material and the tool shoulder is the only source of heat generated. The heat generation rate ( $qr$ ) is obtained by using Johnson et al. [12] in Eq. 3 for this model.

$$qr = \frac{3Q_r}{2\pi(r)} \quad (3)$$

where the shoulder radius is  $r$ , the material's coefficient of friction is  $\mu$  which is  $0.3$  for aluminium, the heat input ( $Q_r$ ) is calculated by Eq. 4, while the downward force is denoted with  $F$  and the tool speed is  $\omega$  or this model, the heat flux ( $qr$ ) from Eq. 4 is applied as surface load by using the appropriate conditions at the boundary.

$$Q_r = \frac{\pi\omega\mu F(r^2 + r)}{45(r)} \quad (4)$$



Experimental data achieved from the tensile test carried out on the specimens were used to complete some simulation parameters needed. The finite element modelling utilizes parameters of aluminium alloy such as specific heat capacity (0.385 kJ/KgK), density (8930 kg/m<sup>3</sup>), and thermal conductivity (400 W/mK), while the boundary conditions were specified. The results from this model are compared with the experimental results for validation. Figures 2 and 3 show the finite element model results generated with ABAQUS software. The heat is generated due to friction during the experiment, and initially the temperature of the plate was 20 °C and it rose up to different peak temperatures when fabricated with different tool rotational speed.

The temperature–time curves for the contact point (in situ) are compared with the simulation results. The simulated temperature history of FSP and the experimental result of the 3-passes sample produced with tool rotational speed of 600 rpm are presented in Fig. 4.

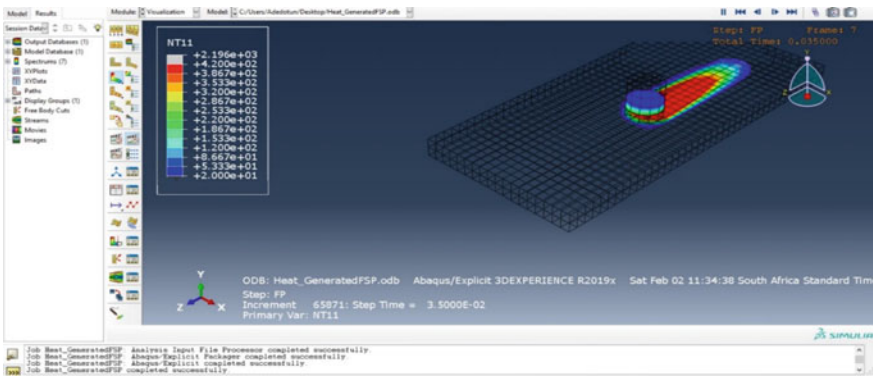


Fig. 2 Temperature distributions obtained by ABAQUS on the aluminium alloy on  $\omega = 600$  rev/min and  $v = 30$  mm/min

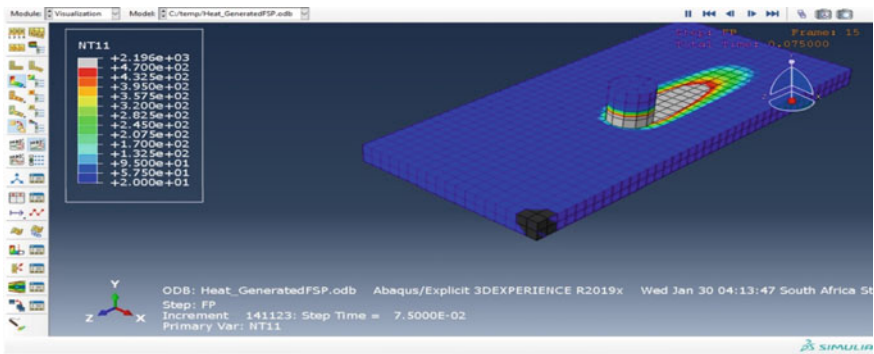
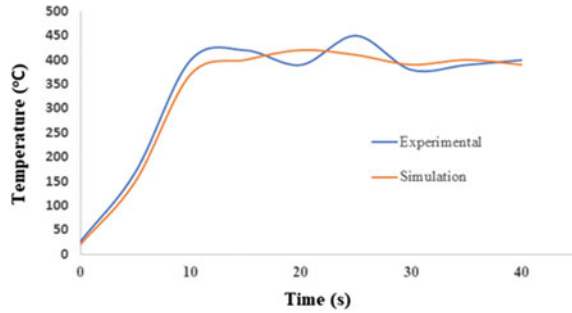
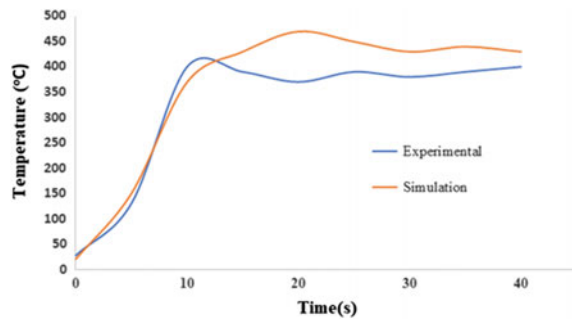


Fig. 3 Temperature distributions obtained by ABAQUS on the aluminium alloy on  $\omega = 1200$  rev/min and  $v = 30$  mm/min

**Fig. 4** Temperature profiles of simulated and experimented values at 600 rpm and 30 mm/min



**Fig. 5** Temperature profiles of simulated and experimented values at 1200 rpm and 30 mm/min



The 3-passes sample fabricated with 1200 rpm is shown in Fig. 5. Increasing speed from 600 to 1200 rpm causes significant changes in the thermal history where the maximum temperature of 423 °C is observed at 600 rpm. However, at 1200 rpm, a higher peak temperature of 475 °C is observed. The results observed in this study are in agreement with other studies [13]. It can be said that the generated heat energy and the maximum temperature by the model and experimentally measured results are in good agreement.

## 4 Conclusions

In this study, the heat generated due to friction during the process was investigated through three-dimensional transient heat transfer model developed by ABAQUS in a moving coordinate and compared with the experimental data. The following conclusions can be drawn:

- A good agreement of numerically and experimentally determined time dependence of the temperature has been obtained. Workpiece (plate) temperature suddenly increases when the tool shoulder establishes contact with it.
- The developed model described in this study can be used to predict the peak temperature for different alloys and materials. Thermal modelling is useful in

predicting the temperature of the material around the tool. The simulation and the experimental results are in agreement, with a temperature difference of less than 10 °C.

- The peak temperature during the process from the experiment and simulation is well below the melting point of the material. The findings of this study reveal that the peak temperature increases as the tool rotational speed increases.

## References

1. Mishra RS, Ma ZY, Charit I (2003) Friction stir processing: a novel technique for fabrication of surface composite. *Mater Sci Eng, A* 341(1–2):307–310
2. Dixit M, Newkirk JW, Mishra RS (2007) Properties of friction stir-processed Al 1100-NiTi composite. *Scr Mater* 56(6):541–544
3. Mishra RS, Ma ZY (2005) Friction stir welding and processing. *Mater Sci Eng R: Rep* 50:1–78
4. Ramadan A, Essa S, Mohamed M, Ahmed Z, Ahmed AY, El-nikhaily AE (2016) An analytical model of heat generation for eccentric cylindrical pin in friction stir welding. *Integr Med Res* 5(3):234–240
5. Lebaal N, Chamoret D, Schlegel D, Folea M (2017) Thermal modelling of friction stir process (Fsp) and identification parameters. *Mater Phys Mech* 32:14–20
6. Cartigueyen S, Suresh OP, Mahadevan K (2014) Numerical and experimental investigations of heat generation during friction stir processing of copper. *Procedia Eng* 97:1069–1078
7. Adetunla A, Akinlabi E (2018) Mechanical characterization of Al/Ti-6Al-4 V surface composite fabricated via FSP: a comparison of tool geometry and number of passes. *Mater Res Express* 5(11):115015
8. Rahsepar M, Jarahimoghadam H (2016) The influence of multipass friction stir processing on the corrosion behavior and mechanical properties of zircon-reinforced Al metal matrix composites. *Mater Sci Eng, A* 671:214–220
9. Adetunla A, Akinlabi ET (2019) Fabrication of aluminum matrix composites for automotive industry via multipass friction stir processing technique. *Int J Auto Tech* 20(6):12239
10. Mil DŠČIĆ, Stamenkovi DŠĆ (2009) Heat generation during friction stir welding process. *Tribol Ind* 31(1):8–14
11. Ikumapayi OM, Akinlabi ET, Majumdar JD (2018) Review on thermal, thermomechanical and thermal stress distribution during friction stir welding. *Int J Mech Eng Technol* 9(8):534–548
12. Johnson AR, Chen T (1985/2000) Coupled thermo-mechanical analyses of dynamically loaded rubber cylinders
13. Taysom BS, Sorensen CD, Hedengren JD (2016) Dynamic modeling of friction stir welding for model predictive control. *J Manuf Process* 23:165–174

# A Concise Review of the Effects of Hybrid Particulate Reinforced Aluminium Metal Matrix Composites on the Microstructure, Density and Mechanical Properties



**Ndudim Ononiwu, Esther T. Akinlabi, Chigbogu G. Ozoegwu, and Victor Aigbodion**

**Abstract** The area of aluminium metal matrix composites has seen considerable research done to further produce materials capable of meeting the current industrial needs of adequate material selection. This has led to improvements in both cost savings, mechanical properties and sustainability in production processes in AMMCs. This work attempts to highlight this point by adequately reviewing selected recent sources of literature which highlights the selection of reinforcements used in the production of AMMCs. The need highlighted earlier has been met through the production of MMCs reinforced using two or more particles defined as hybrid reinforced MMCs. Research to this end has reported the engineering of lightweight MMCs with improved tensile and compression strengths, hardness values, impact energy and corrosion resistance among others. Most of the research highlighted in this work has selected stir casting and powder metallurgy as their preferred route for the production of the MMCs. The works reviewed in this paper suggest the importance of materials regarded as ‘waste’ as investigations done in hybrid reinforced MMCs.

**Keywords** AMMCs · Hybrid reinforcements · Sustainability · Production

---

N. Ononiwu (✉) · E. T. Akinlabi  
Department of Mechanical Engineering Science, University of Johannesburg, Johannesburg,  
South Africa  
e-mail: [219122653@student.uj.ac.za](mailto:219122653@student.uj.ac.za); [ndudim.ononiwu@unn.edu.ng](mailto:ndudim.ononiwu@unn.edu.ng)

N. Ononiwu · C. G. Ozoegwu  
Department of Mechanical Engineering, University of Nigeria, Nsukka, Nigeria

V. Aigbodion  
Department of Materials and Metallurgical Engineering, University of Nigeria, Nsukka, Nigeria

## 1 Introduction

Metal matrix composites (MMC) have become a household choice during the material selection phase of most design and manufacturing endeavours. MMCs are produced to cater for the need of selecting lightweight materials in producing structural and mechanical members across several industrial sectors. This statement holds true due to the addition of reinforcements regarded as the dispersed phase to the MMC. These reinforcements are high strength, high modulus refractory particles [1] which act as the primary load-carrying components of the resulting composite [2]. The addition of these reinforcements into the continuous phase, known as the matrix, produces a composite material with improved properties such as density, tensile strength, toughness, hardness and compressive strength [3–5]. The properties of a composite material are highly dependent on the constituents of the dispersed phase, relative proportion, size, shape, orientation and distribution. Composites can be classified based on the reinforcement, and by this definition, composites can be reinforced with continuous fibres, short fibres/whiskers and particulates. Of these classifications, MMC R&Ds have leaned towards particulate composites owing to their isotropic properties, overall cost saving and reduced post-processing requirements [6] of the reinforcement particles. Another merit of particulate reinforcements in MMCs is the availability of production routes required to produce these MMCs.

Aluminium and its alloys are the most utilized continuous phase in the production of MMCs owing to properties such as corrosion resistance, lightweight, ductility and wear resistance. Other metals employed as base metals in MMC production include magnesium, copper, titanium and iron. Other than the properties highlighted earlier, aluminium is favoured in MMC production due to its availability. It is the most commonly used metal in engineering industrial applications [7]. Magnesium-based MMCs, although sought after because of their mechanical properties, have limitations due to their ductility, low fracture resistance and high reactivity at elevated service temperatures [8]. On the other hand, iron-based MMCs are brittle and have low impact strength. Copper-based MMCs have low strength, although they have found applications in areas where thermal and electrical conductivity are important factors for the MMCs' application [9].

Particulate reinforced composites, mostly hard enabled aluminium alloy matrix such as aluminium 2, 6 and 7 series are attractive due to their ductility, strength and toughness as well as their ability to be processed using conventional methods [10]. For particulate reinforced MMCs, the most utilized materials are SiC, Al<sub>2</sub>O<sub>3</sub>, TiC, B, BN and B<sub>4</sub>C [2]. Of these particles, the most utilized is SiC owing to its close density values to that of aluminium [11]. On the other hand, B<sub>4</sub>C powder has limited interest owing to its high cost and poor wettability [12]. The need for sustainability in the production of components and materials has generated high interest in the use of alternative materials for particulate reinforcements for MMCs. This identified need for sustainability commonly dubbed as 'waste-to-wealth' has promoted research into the use of waste materials as reinforcements. These waste materials are usually categorized into agricultural and industrial wastes as shown in Fig. 1.

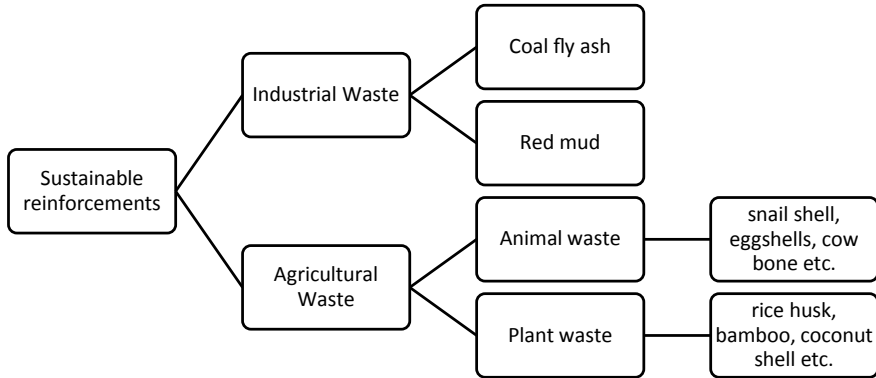


**Fig. 1** Classification of sustainable reinforcement materials

**Table 1** Properties of selected sustainable materials used as reinforcements in MMCs

Sustainable material	Chemical constituents	Density (g/cm <sup>3</sup> )	References
Fly ash	SiO <sub>2</sub> , Al <sub>2</sub> O <sub>3</sub> , Fe <sub>2</sub> O <sub>3</sub> , CaO, MgO, SO <sub>3</sub> , K <sub>2</sub> O, Na <sub>2</sub> O	2.17–2.47	[13–15]
Eggshells	CaCO <sub>3</sub>	1.98–2.22	[4, 16]
Coconut shell	SiO <sub>2</sub> , Al <sub>2</sub> O <sub>3</sub> , Fe <sub>2</sub> O <sub>3</sub> , CaO, MgO, SO <sub>3</sub> , K <sub>2</sub> O, Na <sub>2</sub> O, ZnO	1.16–2.2	[17]
Red mud	SiO <sub>2</sub> , Al <sub>2</sub> O <sub>3</sub> , Fe <sub>2</sub> O <sub>3</sub> , K <sub>2</sub> O, Na <sub>2</sub> O, TiO <sub>2</sub>	3.05	[18]

These materials, such as those highlighted in Fig. 1, have been researched, of which certain constituents are identified to fit the profile of the sought-after reinforcement particles. These constituents, often regarded as phases, include CaCO<sub>3</sub>, Fe<sub>2</sub>O<sub>3</sub>, Al<sub>2</sub>O<sub>3</sub>, SiO<sub>2</sub>, graphene, magnesium and carbon among others. Apart from these identified phases, these materials usually have low densities, making them ideal candidates for producing lightweight MMCs. Table 1 highlights selected sustainable materials used as reinforcements in MMC research, along with their chemical constituents and densities.

### 1.1 Production Routes

Over time, research into the production of MMCs has given birth to several methods which aims to effectively produce composites having uniform particle distribution and minimum production defects. The uniform particle distribution is a major factor that defines the isotropy of the resulting MMC produced. In the production of MMCs, two factors are considered to meet an applied need [19]. The first is to produce the composite, and the second is to shape the composite to its final application. Various

**Table 2** Advantages and limitations of stir casting and powder metallurgy

Stir casting	Powder metallurgy
Relatively cheaper production route	Expensive when compared to stir casting
Easier to perform	A more complex operation
Ability to produce a variety of simple and complex shapes	Produces composites in rolls only
Can produce net shape products	Requires further manufacturing operations to produce the required component
There could be losses particularly that of the reinforcements due to oxidation or reduction reactions during stirring	There is no loss of materials during production
Uniform distribution is highly dependent on a number of factors which could be difficult to control	There is always uniform distribution of reinforcement in the matrix pool

methods of producing composites are defined based on the working temperature and the phase of the metallic matrix during the production process [20]. Based on this definition, there are essentially five classifications of process used as production routes for MMCs [21]: liquid-phase processes, solid–liquid processes, deposition techniques, in situ processes and two-phase (solid–liquid) processes. Stir casting and powder metallurgy are the most used routes in MMC production. Stir casting has been identified as the most economical production route in production of MMCs [22–26]. Table 2 highlights the advantages and limitations of powder metallurgy and stir casting.

The reinforcement phases in particulate reinforcement can be single or hybrid. A hybrid particulate reinforcement composite is regarded as the use of two or more reinforcements for the production of an MMC. In this case, the use of a hybrid reinforcement could be as a result of factors such as cost savings, and in some cases improvements of certain properties such as mechanical properties, weight and corrosion resistance among others. In this regard, most researchers have attempted to produce MMCs reinforced with a synthetic material and a sustainable material. In most cases, citing cost is the identified need to be addressed. In some cases, these research attempts have tried to improve the machinability of the resulting MMC without compromising its strength and hardness. This article will attempt to review the current state of research of hybrid reinforcements and their effects on the MMCs.

## 2 Literature Review

The production of MMCs has sought to study the effects of the dispersed phase on the matrix material. These researches, in this regard, have produced ample evidence that the reinforcement particles/fibres/whiskers alter certain properties of the matrix, resulting in the production of entirely new material (composites). Most researches

have recorded improvements in properties such as hardness, density, tensile strength, temperature and corrosion resistance among others. Hybrid particulates as reinforcements are sought after for reasons such as improvements in a particular property or sets of properties and cost in some cases [27]. This has led to the production of MMCs with different reinforcements such as research carried out by Sharma et al. [28] which attempted to reinforce the selected matrix material with a mix of a sustainable material and a synthetic material for sustainability sake and research done by Ashok et al. [29] which was conducted to reinforce the matrix material with two synthetic materials mostly for the improvement of the mechanical properties and machinability of the resulting MMC. Sustainable materials are regarded as ‘waste materials’ obtained from industrial and agricultural processes. These materials, in some cases, are further processed through pyrolysis (carbonization) or other processes before they can be used as reinforcements for composite production. The succeeding sections of this work will highlight research done in the area of hybrid composites and their effects on microstructure, density and mechanical properties.

## 2.1 Microstructure

Using powder metallurgy route, Naim Shaikh [30] produced a hybrid aluminium MMC reinforced with fly ash and SiC whiskers attempting to study their effect on properties such as microstructure, density, hardness and wear. The analysis of the microstructure to study the grain structure, reinforced particles shape and the distribution of the dispersed phase in the matrix showed good interfacial bonding between the constituent phases of the MMC and adequate dispersion of the reinforcements in the matrix pool. It was also reported that with the increasing wt% of fly ash, the uniformity and homogeneity of the specimen began to decrease as a result of the formulation of agglomerate by the fly ash particles. Citing the issue of environmental degradation, Sharma and Dwivedi [31] studied the effects of waste eggshell and SiC on the thermal and specific strength of AA 2014 matrix. Results from the microstructure analysis, as shown in Fig. 1, show uniform distribution, proper wettability and good face bonding between the AA 2014/SiC/eggshell ash particles. The microstructural analysis was conducted on only the AA 2014/7.5% eggshell/2.5% SiC due to the maximum specific strength and minimum cross-sectional reduction after thermal expansion. It was also reported that beyond a certain wt%, it was observed that there was clustering of the reinforcements as shown in Fig. 2b. These clusterings also resulted in porosity in the interface of the MMC.

Ravi Kumar et al. [32] investigated the microstructure among other mechanical properties of Al 6082 reinforced with coconut shell ash and zirconium oxide ( $ZrO_2$ ). The composite having been produced using stir casting route was checked for the presence of pores which were not present, indicating proper casting. There was also uniform distribution of reinforcements in the continuous phase with clustering of coconut shell ash along some sections of the surface. This resulted in a non-uniform mixture in those areas. The SEM also showed a good intermolecular bonding between



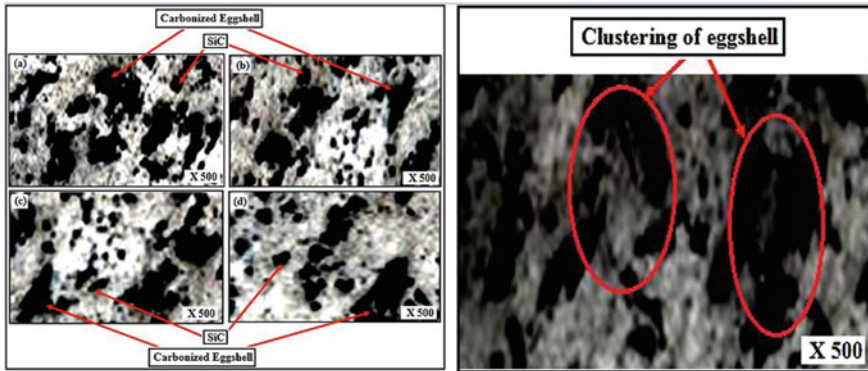


**Fig. 2** Microstructure of AA2014 reinforced with 2.5% SiC and 7.5% eggshell, microstructure of AA2014 reinforced with 2.5% SiC and 12.5% eggshell [31]

the MMC constituents. Quader et al. reported fairly uniform distribution of the SiC particles in the matrix pool [18]. The work was centred on the characterization of AA 6061 reinforced with  $\text{Al}_2\text{O}_3$  and red mud. It was concluded from the SEM analysis that the dispersion of the coarser sizes resulted in a more uniform distribution when compared to the finer particles. An investigation into the mechanical properties of Al 7015/boron carbide/coconut shell ash by [33] reported that the dispersed phases of the composite were uniformly distributed and randomly oriented. It was also reported that the as produced MMC had good interfacial bonding and minimum porosity. The results of these studies have shown that with good production processes, production of MMCs by using the stir casting and powder metallurgy will produce composites that possess minimal microstructural defects while promoting isotropic characteristics during the service life of the produced composite materials.

## 2.2 Density

With the introduction of low-density reinforcements into the matrix pool of an MMC, it is expected to produce lightweight composites with reduced density values compared to the matrix. Research is conducted in the area of hybrid. Aluminium MMCs, as summarized in Table 3, indicated reduced density values with increasing wt% of reinforcements.

## 2.3 Mechanical Properties

The main objectives of studies in AMMC are to produce components with improved mechanical properties among other properties. These mechanical properties are

**Table 3** Summary of density values of selected research in hybrid AMMCs

S. No.	Researchers	Aluminium metal matrix composite	wt% of reinforcements	Density values of matrix (g/cm <sup>3</sup> )	Density values of AMMC (g/cm <sup>3</sup> )
1	Prakash and Satpal [28]	A356/SiC/Fly ash	5, 10, 15, 20	2.70	2.65, 2.48, 2.35, 2.21
2	Kulkarni et al. [34]	A356/Al <sub>2</sub> O <sub>3</sub> /Fly ash	2, 4, 6	2.69	2.605, 2.549, 2.534
3	Chethan et al. [35]	AA 6061/bamboo char/B4C micro fillers	1, 2, 3	2.70	2.66, 2.59, 2.57
4	Sharma and Dwivedi [31]	AA 2014/SiC/Carbonated eggshell	25 variations SiC and Carbonated eggshell, (5 and 10) (5 and 12.5) (12.5 and 10) (12.5 and 12.5), respectively	2.8	2.68, 2.66, 2.68, 2.66
5	Hima Gireesh et al. [36]	Al 6061/SiC/Al <sub>2</sub> O <sub>3</sub> /Fly ash	SiC and Al <sub>2</sub> O <sub>3</sub> (5, 7.5, 10). Fly ash kept constant at 5%	2.67	2.48, 2.56, 2.44

poised to be replacements of materials selected for components already in service. Such applications include pipelines, aircraft body, automobiles, sporting equipment, structural applications and marine applications among others. Most research into all areas of MMC production, regardless of the reinforcement types, investigates properties such as specific strength, hardness, impact energy and toughness [37–40]. Saravanakuma et al. [41] produced a hybrid composite of AA 6063 reinforced with Al<sub>2</sub>O<sub>3</sub> and graphite. The mechanical properties, including compression strength, toughness and hardness, were investigated.

For the production of these composites, the wt% of Al<sub>2</sub>O<sub>3</sub> varied from 3 to 12% while graphite was kept constant at 1%. The investigation led to the conclusion that the hardness, compressive strength and impact strength were best at 6wt% Al<sub>2</sub>O<sub>3</sub> as evident in Fig. 3; [42] investigated the characteristics of Al2024/SiC/red mud produced using stir casting. It was observed that the tensile strength is influenced greatly by the increase in wt% of red mud. The resulting hybrid composite saw an increase in tensile strength by 34%. The tribological behaviour of Al 1100 reinforced with coconut shell ash and graphite was studied by Siva et al. [43]. The mechanical properties of the produced composite are summarized in Table 4.

Hima Gireesh et al. [36] conducted an experimental investigation into the mechanical properties of Al6061/SiC/Al<sub>2</sub>O<sub>3</sub>/fly ash. The wt% of the fly ash was kept constant at 5 wt% while that of the SiC and Al<sub>2</sub>O<sub>3</sub> were varied as shown in Table 5.

The tensile test, hardness and impact strength test were conducted on the specimens. Sample B had the best values for hardness and impact strengths, 63.66 BHN

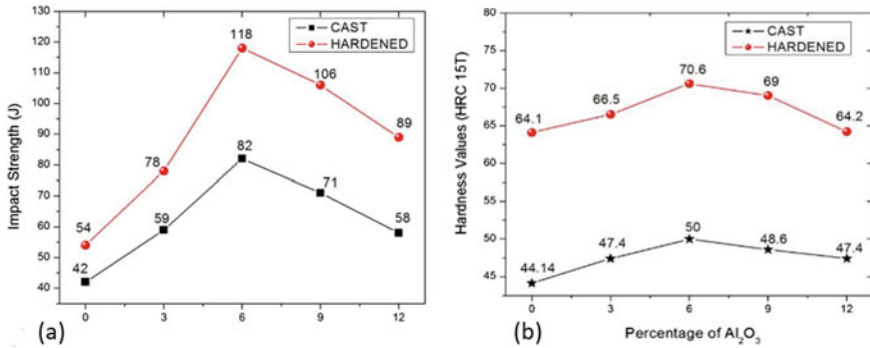


**Fig. 3** Impact strength and hardness values of AA 6063/Al<sub>2</sub>O<sub>3</sub>/graphite [41]

**Table 4** Mechanical properties obtained according to [43]

Composite	BHN	Elongation (mm)	T.S (N/mm <sup>2</sup> )	Specific strength (N-mm/kg)
Al 1100	28.30	21.91	104.3	43.40
Al + Al <sub>2</sub> O <sub>3</sub>	50.53	13.27	146.74	52.76
Al + Al <sub>2</sub> O <sub>3</sub> + Gr	49.97	17.11	126.91	51.30
Al + CSA	51.33	13.85	173.50	63.29
Al + CSA + Gr	50.42	18.23	154.48	60.40

**Table 5** Composition of Al6061/SiC/Al<sub>2</sub>O<sub>3</sub>/fly ash [36]

Specimen	Al 6061 (wt%)	SiC (wt%)	Al <sub>2</sub> O <sub>3</sub>
A	85	5	5
B	80	7.5	7.5
C	75	10	10

and 1.75 J/mm<sup>2</sup>, respectively. Specimen C had the best value for tensile strength (129 mPa) followed by sample B then A with values of 126 mPa and 117 mPa, respectively. It was concluded that the hybrid AMMC exhibited improved tensile strength, yield strength and hardness when compared to the base material but no significant change in impact strength. David et al. [44] conducted a study into the microstructure and mechanical characterization of AA 6061/TiB<sub>2</sub>/Al<sub>2</sub>O<sub>3</sub> hybrid MMC processes using an electric stir casting furnace. The tensile strength and microhardness values showed an increasing trend with higher wt% of the reinforcement. The values for these properties were highest at 15wt% with tensile strength and hardness values of 287 mPa and 122HV, respectively. [33] showed that the tensile strength and hardness values of Al 7075/B<sub>4</sub>C/coconut shell ash increased with increasing wt% of the reinforcement. The impact strength of the composite also increased from 3 to 12wt%. ‘Further addition of reinforcement reduced the impact energy of the MMC due to

the micropores in the composite and crack initiation in the reinforcement matrix interface, which resulted in the failure at the earlier stage’.

### 3 Conclusion

This work in detail summarizes using recent and relevant literature in the current state of events regarding the research in the area of hybrid reinforced AMMCs. The effects of these hybrid reinforcements on selected mechanical properties, microstructure and density were reviewed. Based on this study, the following conclusions and recommendations were drawn:

1. Results from the reviewed literature highlight cost savings and sustainability as the drive for this area of research.
2. With the positive results obtained from the relevant literature, more investigations can be carried out using new combinations of reinforcements to ascertain their effects on selected matrix materials.
3. Avenues for the production of hybrid materials using sustainable materials should be explored.

### References

1. Hashim J, Looney L, Hashmi MSJ (1999) Metal matrix composites: production by the stir casting method, vol. 93, pp 1–7
2. Haghshenas M (2015) Metal–matrix composites. In: Reference module in materials science and materials engineering, p 28, Jan 2015
3. Saenpong P, Talangkun S, Laonapakul T, Boonma A (2018) Microstructures and hardness of A356-SiC composites produced by the mechanical stir casting. *Mater Today Proc* 5(3):9489–9496
4. Hassan SB, Aigbodion VS (2015) Effects of eggshell on the microstructures and properties of Al–Cu–Mg/eggshell particulate composites. *J King Saud Univ Eng Sci* 27(1):49–56
5. Sharma VK, Singh RC, Chaudhary R (2017) Effect of flyash particles with aluminium melt on the wear of aluminium metal matrix composites. *Eng Sci Technol Int J* 20(4):1318–1323
6. Balasubramanian M (2014) Composite materials and processing, 1st edn. CRC Press, Boca Raton
7. David S (2017) Materials for the 21st century, 1st edn. Croydon
8. Arunachalam R, Kumar P, Muraliraja R (2019) A review on the production of metal matrix composites through stir casting. In: Furnace design, properties, challenges, and research opportunities, vol. 42, pp 213–245
9. Acker R, Martin S, Meltke K (2016) Casting of Fe–CrMnNi and ZrO<sub>2</sub>-based metal–matrix composites and their wear properties. *Steel Res Int* 87:1111–1117
10. Toptan F, Kilicarslan A, Karaaslan A, Cigdem M, Kerti I (2010) Processing and microstructural characterisation of AA 1070 and AA 6063 matrix B4Cp reinforced composites. *Mater Des* 31(SUPPL. 1):S87–S91
11. Bilal M, Shaikh N, Arif S (2018) Fabrication and characterization of aluminium hybrid composites reinforced with fly ash and silicon carbide through powder metallurgy fabrication and

- characterization of aluminium hybrid composites reinforced with fly ash and silicon carbide through powder metallurgy
12. Raj R, Thakur DG (2016) ScienceDirect Qualitative and quantitative assessment of microstructure in Al-B 4 C metal matrix composite processed by modified stir casting technique. *Arch Civil Mech Eng* 16(4):949–960
  13. Ikumapayi OM, Akinlabi ET (2019) Effects of vibratory disc milling time on the physiochemical and morphological properties of coal fly ash nanoparticles. *Key Eng Mater* 796(March):38–45
  14. Kumarasamy SP, Vijayananth K, Thankachan T, Pudhupalayam Muthukutti G (2017) Investigations on mechanical and machinability behavior of aluminum/flyash cenosphere/Gr hybrid composites processed through compocasting. *J Appl Res Technol* 15(5):430–441
  15. Rao CRP, Bhagyashekar MS, Viswanath N (2014) Machining behavior of Al6061-fly ash composites. *Procedia Mater Sci* 5:1593–1602
  16. Dwiwedi SK, Srivastava AK, Sugimoto K, Chopkar M (2018) Microstructural and mechanical characterization of chicken eggshell-reinforced Al6061 matrix composites. *Open J Metal* 08(01):1–13
  17. Apasi A, Madakson PB, Yawas DS, Aigbodion VS (2012) Wear behaviour of Al-Si-Fe alloy/coconut shell ash particulate composites. *Tribol Ind* 34(1):36–43
  18. Quader SM, Murthy BSN, Reddy PR (2017) Processing and characterization of particulate reinforced aluminum 6061 hybrid metal matrix composites. *Int J Eng Stud* 9(1):11–19
  19. Pawar PB, Wabale RM, Utpat AA (2018) A comprehensive study of aluminum based metal matrix composites: challenges and opportunities. *Mater Today Proc* 5(11):23937–23944
  20. Skibo MD, Schuster DM (1998) Process for preparation of composite materials containing non-metallic particles in a metallic matrix, and composite materials. Patent No. 4,786,467
  21. Kandpal BC, Kumar J, Singh H (2018) Manufacturing and technological challenges in Stir casting of metal matrix composites—a review. *Mater Today Proc* 5(1):5–10
  22. Baburaja K, Teja Sainadh S, Sri Karthik D, Kuldeep J, Gowtham V (2017) Manufacturing and machining challenges of hybrid aluminium metal matrix composites. *IOP Conf Ser Mater Sci Eng* 225(1)
  23. Alaneme KK, Bodunrin MO (2013) Mechanical behaviour of alumina reinforced AA (6063) metal matrix composites developed by two step—stir casting process, pp 105–110
  24. Annigeri UK, Veeresh GB (2017) Method of stir casting of aluminum metal matrix composites: a review. *Mater Today Proc* 4(2):1140–1146
  25. Sankara Raju RS, Panigrahi MK, Ganguly RI, Srinivasa Rao G (2019) Tribological behaviour of al-1100-coconut shell ash (CSA) composite at elevated temperature. *Tribol Int* 129:55–66
  26. Shamim S, Singh H, Sasikumar C, Yadav DK (2017) Microstructures and mechanical properties of Al-Si-Mg-Ti/egg shell particulate composites. *Mater Today Proc* 4(2):2887–2892
  27. Bodunrin MO, Alaneme KK, Chown LH (2015) Aluminium matrix hybrid composites: a review of reinforcement philosophies; Mechanical, corrosion and tribological characteristics. *J Mater Res Technol* 4(4):434–445
  28. Prakash S, Satpal D (2015) Microstructure and mechanical behavior of A356/SiC/fly-ash hybrid composites produced by electromagnetic stir casting, pp 57–67
  29. Kumar RA, Devaraju A, Arunkumar S (2018) Experimental investigation on mechanical behaviour and wear parameters of TiC and graphite reinforced aluminium hybrid composites. *Mater Today Proc* 5(6):14244–14251
  30. Naim Shaikh MB (2018) A statistical analysis of wear behaviour of fly ash reinforced Al-SiC hybrid composites. *J Powder Metall Mining* 7(1):1–5
  31. Sharma S, Dwivedi SP (2017) Effects of waste eggshells and SiC addition on specific strength and thermal expansion of hybrid green metal matrix composite. *J Hazard Mater* 333:1–9
  32. Ravi Kumar K, Pridhar T, Sree Balaji VS (2018) Mechanical properties and characterization of zirconium oxide (ZrO<sub>2</sub>) and coconut shell ash (CSA) reinforced aluminium (Al 6082) matrix hybrid composite. *J Alloys Compounds* 765:171–179
  33. Subramaniam B, Natarajan B, Kaliyaperumal B, Chelladurai SJS (2018) Investigation on mechanical properties of aluminium 7075—boron carbide—coconut shell fly ash reinforced hybrid metal matrix composites. *China Foundry* 15(6):449–456

34. Kulkarni SG, Meghnani JV, Lal A (2014) Effect of fly ash hybrid reinforcement on mechanical property and density of aluminium 356 alloy. *Procedia Mater Sci* 5:746–754
35. Chethan KN, Pai A, Keni LG, Singhal A, Sinha S (2018) Fabrication and tribological response of aluminium 6061 hybrid composite reinforced with bamboo char and boron carbide micro-fillers. *IOP Conf Ser Mater Sci Eng* 310(1)
36. Hima Gireesh C, Durga Prasad K, Ramji K (2018) Experimental investigation on mechanical properties of an Al6061 hybrid metal matrix composite. *J Compos Sci* 2(3):49
37. Lancaster L, Lung MH, Sujan D, Ash ACS (2013) Utilization of agro-industrial waste in metal matrix composites: towards sustainability. *Int J Environ Chem Ecol Geol Geophys Eng* 7(1):25–33
38. Agunsoye JO, Bello SA, Talabi IS, Yekinni AA, Raheem IA, Oderinde AD, Idegbekwu TE (2015) Recycled aluminium cans/eggshell composites: evaluation of mechanical and wear resistance properties. *Tribol Ind* 37(1):107–116
39. Thirumoorthy A, Arjunan TV, Senthil Kumar KL (2018) Latest research development in aluminum matrix with particulate reinforcement composites—a review. *Mater Today Proc* 5(1):1657–1665
40. Jims John Wessley G, Gaith Franklin A, Vijay SJ (2018) Fabrication and mechanical characterization of stir cast AA6063-borosilicate-fly ash hybrid metal matrix composites. *Int J Eng Technol* 7(3):101
41. Saravanakumar A, Sasikumar P, Sivasankaran S (2014) Synthesis and mechanical behavior of AA 6063-x wt%  $Al_2O_3$ -1% Gr (x = 3, 6, 9 and 12 wt%) hybrid composites. *Procedia Eng* 97:951–960
42. Singh J, Chauhan A (2017) Fabrication characteristics and tensile strength of novel Al2024/SiC/red mud composites processed via stir casting route. *Trans Nonferrous Metals Soc China (English Edition)* 27(12):2573–2586
43. Siva Sankara Raju R, Panigrahi MK, Ganguly RI, Srinivasa Rao G (2017) Investigation of tribological behavior of a novel hybrid composite prepared with Al-coconut shell ash mixed with graphite. *Metall Mater Trans A Phys Metall Mater Sci* 48(8):3892–3903
44. David Raja Selvam J, Dinaharan I, Vibin Philip S, Mashinini PM (2018) Microstructure and mechanical characterization of in situ synthesized AA6061/(TiB<sub>2</sub> + Al<sub>2</sub>O<sub>3</sub>) hybrid aluminum matrix composites. *J Alloys Compounds* 740:529–535

# Application of Molecular Dynamics Simulation: A Case Study to Estimate Wettability



Vahid Khosravi, Syed Mohammad Mahmood, and Davood Zivar

**Abstract** Enhanced oil recovery (EOR) has always been a significant pillar in the oil industry, and lots of laboratory studies have been conducted for this technology. However, experimental research in EOR encounters several problems such as expensive materials and equipment, and long-term duration of measurements that could take from weeks to years. In this backdrop, molecular dynamics simulation (MDS) appears to be an efficient complementary method that can be used for first-order approximation once it is validated. The objective of this work is to evaluate the efficacy of molecular dynamics (MD) for the understanding of wetting condition of a given rock/fluid system by calculating the free energy which could yield contact angles (a measure of wettability). The interaction between polyethylene surface and n-decane oil as the first system as well as polyethylene surface and cyclohexane oil as the second system was simulated by MDS, and the total free energies were calculated to be  $-7.515$  (kcal/mol) and  $-1.872$  (kcal/mol), respectively. Contact angles were calculated from MDS and computed 15.4 degrees for the first, and 28.6 degrees for the second system. The deviation for n-decane was 3.1-degree, and cyclohexane was 0.4-degree on the same surface compared to the published results. Data shows that the MDS is a reliable method for the first-order estimation of wettability determination for the purpose of initial screening and optimization of EOR processes relying upon wettability alteration.

**Keywords** Molecular dynamics simulation (MDS) · Solvation free energy (SFE) · Contact angle · Wettability

## 1 Introduction

Since primary and secondary oil recovery stages are able to recover only 20–40% of the original oil in place (OOIP), enhanced oil recovery (EOR) techniques are needed to increase oil recovery (up to 60% or higher) [1, 2]. However, field application of

---

V. Khosravi (✉) · S. M. Mahmood · D. Zivar  
Petroleum Engineering Department, Universiti Teknologi PETRONAS, Perak, Malaysia  
e-mail: [Vahid\\_17006746@utp.edu.my](mailto:Vahid_17006746@utp.edu.my); [vahid.khosravi87@gmail.com](mailto:vahid.khosravi87@gmail.com)

EOR is technically challenging, requiring extensive and time-consuming geological and laboratory studies. Research continues to find quick alternatives, albeit as a first approximation. In this regard, MDS is a tool that has shown promising results. In one MDS study for enhancing oil recovery, intermolecular dynamics calculations were utilized to explain and predict the interaction between different components (polar or non-polar) and organic/inorganic surfaces. It was found that increasing temperature leads to decreasing interfacial tension (IFT) in the case of CO<sub>2</sub>, N<sub>2</sub>, and CH<sub>4</sub> injection in the presence of alkanes [3]. This could be achieved by Large Atomistic/Molecular Massively Parallel Simulator (LAMMPS) [4] package. In another study, interaction energy was calculated for swelling of the CO<sub>2</sub>-alkane system at various temperatures and pressures using the molecular simulator [5, 6]. Wang and Wu [7] also showed that the wettability alteration of rock can be simulated by MDS. They investigated the effect of surfactant solution and hydrophobic nanoparticles on oil detachment from the solid surface [7].

Several theories exist for calculating surface free energy, including Zisman, OWRK, Fowkes, and van Oss acid–base for single or multicomponent interaction calculations. Among them, Zisman theory is one of the most reliable ones to calculate surface free energy for the non-polar surfaces. In this theory, liquid/solid contact angles are used to compute solid surface energy (SSE) [8].

This study was conducted in view of the importance of rapid wettability estimation for EOR method screening and optimization. The molecular free energies for a non-polar surface with two different oils were calculated by utilizing MDS, and their corresponding contact angles were determined to understand wetting characteristics. Results were validated by wettability determined by the Zisman plot.

## 2 Literature Review

Three different CO<sub>2</sub> flooding systems were studied [9]: (1) without sodium dodecyl sulfate (SDS) and nanoparticles, (2) with SDS but without nanoparticles, and (3) with SDS and nanoparticles. Thus, the system involved: (1) CO<sub>2</sub>-water–water/hexane system, (2) CO<sub>2</sub>-water/SDS-water/hexane system, and (3) CO<sub>2</sub>-water/SDS/silica nanoparticle (SiO<sub>2</sub>)-water/hexane system, respectively. MDS was used to calculate the diffusion coefficients and interfacial tensions of SDS, Hexane, CO<sub>2</sub>, and water on the SiO<sub>2</sub> surface at two different temperatures (298 K and 383 K). Material Studio (MS [10]) was used with Condensed-Phase Optimized Molecular Potential For Atomistic Simulation Studies (COMPASS) [11] forcefield and NPT ensemble (constant number of particles, pressure, and temperature) as a functional group. It is found that the temperature helps in the diffusion process. The diffusion coefficient increased with increasing temperature. Adding SDS reduced the interfacial tension of the system. Adding SiO<sub>2</sub> along with SDS further reduced IFT, thus resulted in better oil recovery. Although oil type and boundary conditions used in his study were slightly different than the other similar studies, simulation results were close to the published experimental results.



In another research [12], equilibrium molecular dynamics (EMD) simulation was used to investigate the effect of CO<sub>2</sub> injection into oil shales. In fact, physics behind the interaction between injected CO<sub>2</sub>, synthetic oil mixture, and nanopores of the organic material was investigated. The CO<sub>2</sub> was at supercritical condition (scCO<sub>2</sub>), i.e., miscible with the oil. The molecular simulator was LAMMPS along with the graphical processing unit (GPU [13–15]) and visual molecular dynamics (VMD) [16] packages for MD visualization. The Statistical Associating Fluid Theory (SAFT- $\gamma$  coarse-grained forcefield developed [17]) was employed for components and COMPASS forcefield to describe atoms, bonds, and angles interactions. NVT (constant number of particles, volume, and temperature) and NPT as functional groups were selected. Density profiles were plotted using MDS, and the recovery factor was calculated. The results showed good agreement with the laboratory data. They showed that the heavy oil components (C7<sup>+</sup>) had more absorbance on the kerogen surface than the lighter hydrocarbon components. In addition, increasing the injection pressure of scCO<sub>2</sub> increased the soaking time required to achieve maximum process performance (for gas which completely mixed with oil). The tendency of scCO<sub>2</sub> molecules for being absorbed onto the surface of the kerogen resulted in the separation of the synthetic oil molecules. Synthetic oil recovery factor was found to increase from 24.4 to 49%, which was in good agreement with laboratory data. Due to higher adsorption of heavy oil components on kerogen surfaces, recovery of heavy components was much less than light oil components.

Furthermore, the CO<sub>2</sub>/N<sub>2</sub> flooding at the molecular level was studied [18], and the interaction energy, diffusion coefficient, density profile, radial density function (RDF), and velocity profile were determined. LAMMPS and MS software were used with Chemistry at Harvard Macromolecular Mechanics (CHARMM [19, 20]) and CLAYFF [21] forcefields (for octane and silica, respectively) and NVT ensemble. Three different injection scenario studies were: (1) mixture gas flooding, (2) CO<sub>2</sub> slug + N<sub>2</sub> (pre-CO<sub>2</sub>) flooding, and (3) N<sub>2</sub> slug + CO<sub>2</sub> (pre-N<sub>2</sub>) flooding. The medium was hydroxylated silica nanoslit in the presence of octane. The results showed a weak movement of carbon dioxide and a weak reaction of nitrogen and crude oil which resulted in short residence time in the nanosilicate. However, CO<sub>2</sub>/N<sub>2</sub> slug flooding displacement efficiency was better than both CO<sub>2</sub> and N<sub>2</sub> or mixture gas flooding. The displacement efficiency was the best when the front slug was CO<sub>2</sub>.

Another study was performed for the alteration of calcite wetting characteristics by low salinity brine (CaCl<sub>2</sub>, MgSO<sub>4</sub>, NaCl, and KCl salts), TiO<sub>2</sub> nanoparticles, and dioctyl sulfosuccinate sodium (AOT) ionic surfactants in the presence of crude oil [22]. The LAMMPS simulator was used with the CHARMM forcefield and the NVT, NPT, and NVE (constant number of particles, volume, and energy) ensembles. Potential of mean force (PMF) calculations showed the adjustment of the nanoparticles near the surface of the brine–oil interface. The nanoparticles (NPs) interaction with the surfactant produced surface pressure, which in combination with multi-component ion exchange (MIE) and cation-bridge, resulted in the separation of the oil from the calcite surface. The results showed that the combination of NPs + surfactant + low salinity brine leads to the maximum synergy and minimum contact angle. This

combination resulted in the maximum separation of oil from the calcium carbonate surface. Results were validated by experimental data from the literature.

Furthermore, oil recovery improvement by the water-alternating-gas (WAG) using CO<sub>2</sub> as gas was studied [23]. The interactions between CO<sub>2</sub>-WAG, scCO<sub>2</sub>, and water in the presence of oil on the silica surface were investigated. MD simulations were conducted using the NVT ensemble at 330 K with the Nosé–Hoover thermostat. Molecular interaction energy and RDF were calculated by non-equilibrium molecular dynamics (NEMD) method and LAMMPS with CLAYFF forcefield (for silica) and CHARMM forcefield (for oil). It is understood that the apolar oil component dissolved by scCO<sub>2</sub> slug, and miscible decane/scCO<sub>2</sub> is taken out of the nanoslit by water slug. In this regard, four synergistic phenomena, namely high dissolution efficiency, easy discharging of residual water, broadening of the fluid channel, and desirable displacement consequence, were observed. The high oil recovery efficiency by CO<sub>2</sub>-WAG injection at low injection pressure due to the phenomena above happened.

Furthermore, the interaction among propylamine surfactant, dodecyl amine surfactant, functionalized (silica) nanoparticle, *n*-tridecane, and the water in the presence of bitumen on the surface of silica was studied [24]. EMD and NEMD methods were used to simulate nanoparticle surfactant behavior in static and dynamic conditions. It was done by LAMMPS software with CLAYFF forcefield and Nosé–Hoover thermostat. Molecular calculations of the interaction energy, interfacial tension, and density profile showed that the movement of the nanoparticles is effective in the displacement of the oil film from the rock surface. Increasing the temperature and adding surfactants also increased the ability of the oil to be swept from colloidal nanosuspensions. Changes in interfacial tension and density with functionalized silica NPs and surfactant-NP compositions were observed. The potential for change of wettability and surfactant transferability of nanoparticles was also observed. These observations were consistent with the study of Eskandar et al. [25]. It is concluded that they have the potential for EOR applications due to their surface-active properties observed on the oil–water interface (Table 1).

### 3 Materials and Method

#### 3.1 Surface and Fluids

Polyethylene (plastic) was considered as surface, and *n*-decane/cyclohexane was selected as fluids. This selection was made to be able to validate the results by Zisman theory which is for calculating SSE of one component on the non-polar surface through contact angle. The surface energy of a liquid is identical to its surface tension [8].

**Table 1** Details of literature review

Item No.	Authors & year	Solid surface	Fluid mixture	Simulation software	Force field	Ensemble	Calculation	Validation by
1	Salwani et al. (2019)	Silica nanoparticle (SiO <sub>2</sub> )	Sodium dodecyl sulfate (SDS), silica nanoparticle (SiO <sub>2</sub> ), hexane, CO <sub>2</sub> , water	MS	COMPASS	NPT	Diffusion coefficient, interfacial tensions (IFT)	Literature experimental results
2	Kazemi et al. (2019)	Shale oil (a 3D Kerogen nanochannel (type IIC))	Synthetic oil mixture, scCO <sub>2</sub>	LAMMPS, GPU, VMD	SAFT coarse-grained for components, COMPASS class2 for atoms, bonds, and angles	NVT (Nosé-Hoover thermostat) and NPT	Density profile, recovery factor	Laboratory measurements
3	Fang et al. (2019)	Hydroxylated silica nanoslit	Octane, CO <sub>2</sub> /N <sub>2</sub> slug, the gas mixture	LAMMPS, MS (library)	CHARMM (for octane) and CLAYFF (for silica)	NVT (Nosé-Hoover thermostat)	Interaction energy, diffusion coefficient, density profile, RDF, velocity profile	-
4	Aminian and ZareNezhad (2019)	Calcite	low salinity brine, TiO <sub>2</sub> NPs, and AOT ionic surfactant, crude oil	LAMMPS	CHARMM	NVT, NPT, and NVE	Surface free energy or PMF, density profile, RDF, contact angle	Experiment data

(continued)

Table 1 (continued)

Item No.	Authors & year	Solid surface	Fluid mixture	Simulation software	Force field	Ensemble	Calculation	Validation by
5	Yan et al. (2017)	Silica	CO <sub>2</sub> WAG, scCO <sub>2</sub> , water, oil	LAMMPS, VMD	CLAYFF (for silica) and CHARMM (for oil)	NVT (Nosé-Hoover thermostat)	Interaction Energy, RDF	-
6	Mazyar et al. (2017)	Silica	Propylamine surfactant, dodecylamine surfactant, bitumen, functionalized (silica) nanoparticle, <i>n</i> -tridecane, water	LAMMPS	CLAYFF	(Nosé-Hoover thermostat)	Interaction energy, interfacial tension, density profile	Literature [25]

### 3.2 *Molecular Dynamics Simulation (MDS)*

MS was used as Molecular Dynamics Simulator. Calculations were done by the Forcite module using a thermodynamic integration algorithm for electrostatic and van der Waals non-bond interactions. The energy of interaction between the solvent and the solute, called solvation free energy (SFE), as well as creating the cavity relating to the solvent entropy that disturbs the solvent mixture was considered in this study. Therefore, solvation free energy was calculated by simulating two components of the Zisman plot. Thereby, the interaction between non-polar surfaces, which are polyethylene and two different components (*n*-decane and cyclohexane), was simulated. Then, contact angles were obtained and compared with Zisman contact angles for the same components.

Simulation stages started by building the molecular structure. Polyethylene was built via homopolymer function from MS library, and components were made by the “Sketch Atom” tool. Also, the “Cleaning” tool was utilized for aligning correct molecular angles.

The molecules needed to be prepared for the following calculations. For the system relaxation, molecular dynamics energy was needed to be minimized. Hence, the geometrical optimization was done for all systems including surface and fluids, one by one. In this regard, the COMPASS forcefield was selected for group-based non-bond electrostatic and van der Waals interactions with cutoff distance 12.5 Å. COMPASS forcefield can predict the structure and property of a wide range of organic and inorganic substances.

Then, the amorphous cells were built for preparing a platform to initiate the dynamics of molecular calculations. For this, ten polyethylene molecules and one fluid for each component were loaded individually as the composition of the amorphous cell, which provided a trajectory document.

Before equilibrating the system for starting the calculation, it must be realized that there is a possibility of having stress points or density heterogeneity in different parts of the structure. The thermostat tool will remove the excess heat from the system. Nosé–Hoover thermostat is a good choice for simultaneous production and equilibration runs. Therefore, for attaining the equilibrium in the system, the NVT ensemble at 298 K with Nosé–Hoover thermostat was chosen with 10 ps total simulation time through the Forcite dynamics module.

For reducing calculation time, 1000 and 5000 runs with 1 fs time step were used for equilibration and production steps, respectively. For this purpose, polyethylene was defined as solvent, and *n*-decane and cyclohexane were defined as solute atoms for simulation runs. In the end, SFE was calculated for both systems which include ideal, van der Waals and electrostatic free energy contributions. The ideal contribution calculation was quick, but the other contributions took a longer time. After finishing the molecular dynamics simulation, contact angles were determined.

## 4 Results and Discussion

As it is shown in Figs. 1 and 2, two molecular lattice systems were simulated, polyethylene-*n*-decane as the first system and polyethylene-cyclohexane as the second system.

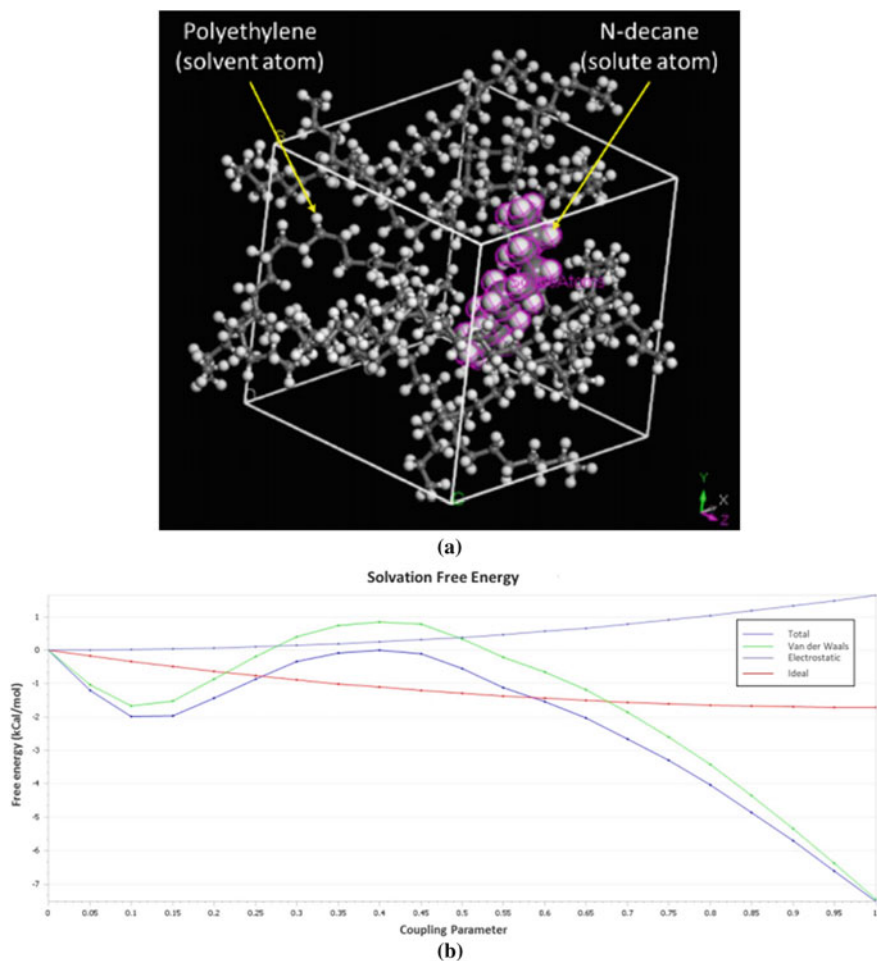


**Fig. 1** Molecular dynamics simulation: **a** amorphous cell: polyethylene as solvent and *n*-decane as solute and **b** total SFE calculation: ideal, van der Waals and electrostatic free energies

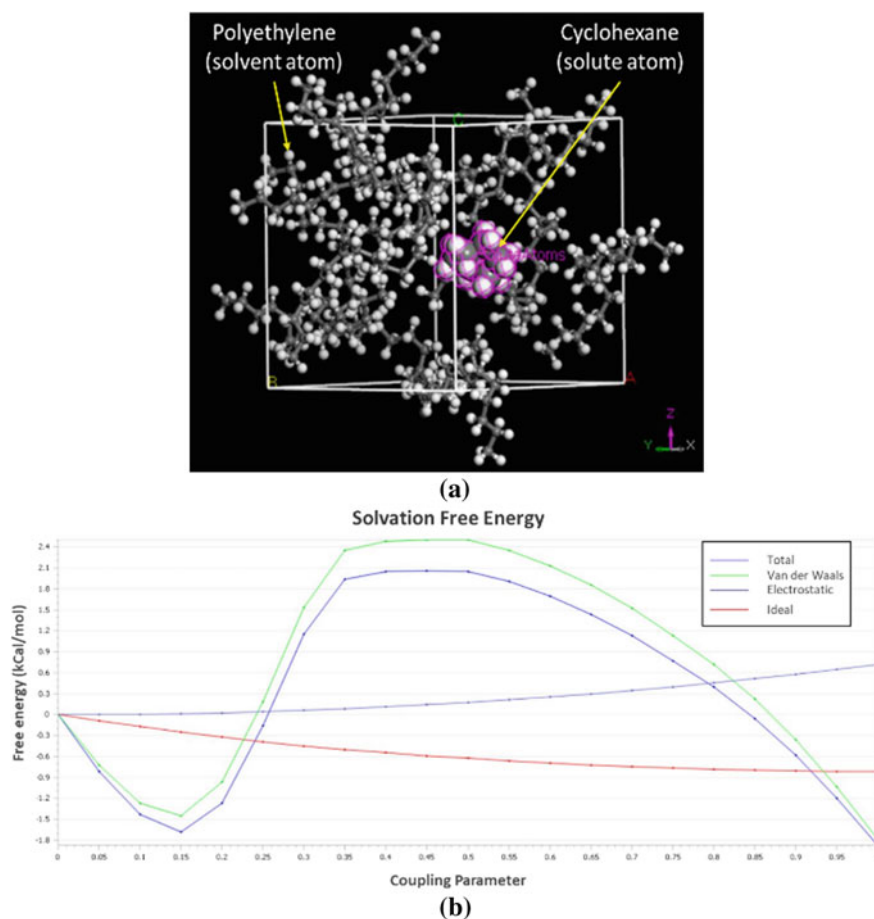


**Fig. 2** Molecular dynamics simulation: **a** amorphous cell: polyethylene as solvent and cyclohexane as solute, **b** total SFE calculation: Van der Waals and electrostatic free energies

#### 4.1 Polyethylene-*n*-Decane SFE Molecular Calculations

In Fig. 1, (a) is the MDS of the first system (polyethylene-*n*-decane). In (b), the vertical axis is free energy in kcal/mol, and the horizontal axis is the coupling parameter ( $\lambda$ ), which measures the degree of interaction between the solute molecule and the solvent. Usually,  $\lambda = 0$  corresponds to no coupling, and  $\lambda = 1$  corresponds to full interaction [9].

According to SFE molecular dynamics calculation, ideal, van der Waals and electrostatic free energies obtained were  $-1.715$  kcal/mol,  $-7.444$  kcal/mol, and  $1.645$  kcal/mol, respectively. The total free energy calculated was  $-7.515$  kcal/mol.

## 4.2 Polyethylene-Cyclohexane SFE Molecular Calculations

For the second system (Fig. 2), the results for the ideal, van der Waals and electrostatic free energies were  $-0.813$  kcal/mol,  $-1.776$  kcal/mol, and  $0.718$  kcal/mol, respectively. And the total free energy calculated was  $-1.872$  kcal/mol.

Based on calculated total free energies, contact angles obtained for System 1 and System 2 were  $15.4^\circ$  and  $28.6^\circ$ , respectively. According to the Zisman plot, contact angles for the untreated low-density polyethylene (LDPE) film were calculated to be  $18.5$  and  $28.2$  for the same fluids, respectively. It shows that the results were in good agreement with Zisman-computed contact angles. Thus, MDS can be a good means for estimating contact angles and wettability conditions of the non-polar surfaces. Furthermore, our simulation observations were in agreement with Zisman in which it was indicated that the increased surface tension resulted in increasing contact angle [8], i.e., decreasing surface and fluid contact area. Thus, a correlation was observed between free energies and contact angles/wettability.

## 5 Conclusions

Experimental determination of wettability is a complex, time-consuming, and costly process, and researchers continue to find an alternative for its quick first-order approximation for screening and optimization purposes.

This study shows the below results:

- Molecular dynamics simulation (MDS) is such a reliable alternative.
- Wettability obtained from MDS only had a maximum deviation of 3.1-degree from experimental data which is acceptable in many situations prior to a final laboratory determination.

## References

1. Tengku Mohd TA, Baco J, Noor Fitrah AB et al (2016) Effects of particle shape and size on nanofluid properties for potential enhanced oil recovery (EOR). MATEC Web Conf 69:03006
2. Rezk MG, Foroozesh J, Zivar D et al (2019) CO<sub>2</sub> storage potential during CO<sub>2</sub> enhanced oil recovery in sandstone reservoirs. J Nat Gas Sci Eng 66:233–243
3. de Lara LS, Michelon MF, Miranda CR (2012) Molecular dynamics studies of fluid/oil interfaces for improved oil recovery processes. J Phys Chem B 1(16):14667–14676
4. Plimpton S (1995) Fast parallel algorithms for short-range molecular dynamics. J Comput Phys 117:1–19
5. Liu B, Shi J, Sun B et al (2015) Molecular dynamics simulation on volume swelling of CO<sub>2</sub>-alkane system. Fuel 143:194–201
6. Zhang J, Pan Z, Liu K, Burke N (2013) Molecular simulation of CO<sub>2</sub> solubility and its effect on octane swelling. Energy Fuels 27–5:2741–2747



7. Wang F-C, Wu H-A (2013) Enhanced oil droplet detachment from solid surfaces in charged nanoparticle suspensions. *Soft Matter* 9:7974
8. Kruss C (1999) Models for surface free energy calculation. Technical note
9. Salwani M, Rosli NR, Tengku Mohd TA et al (2019) Diffusion coefficient and interfacial tension with addition of silica nanoparticles in CO<sub>2</sub>-surfactant-water-hexane for enhanced oil recovery (EOR) using molecular dynamic simulation. *Key Eng Mater* 797:375–384
10. A. S. I. S. D. Material Studio, CA
11. Sun H et al (2016) COMPASS II: extended coverage for polymer and drug-like molecule databases. *J Mol Model* 22:1–10
12. Kazemi M, Takbiri-Borujeni A, Hansel J et al (2019) Enhanced oil recovery of shale oil: a molecular simulation study. In: SPE/AAPG/SEG unconventional resources technology conference
13. Brown WM, Yamada M (2013) Implementing molecular dynamics on hybrid high performance computers—three-body potentials. *Comput Phys Commun* 184:2785–2793
14. Brown W, Kohlmeyer A, Plimpton S et al (2012) Implementing molecular dynamics on hybrid high performance computers—particle-particle particle-mesh. *Comput Phys Commun* 183:449–459
15. Brown W, Wang P, Plimpton S et al (2011) Implementing molecular dynamics on hybrid high performance computers—short range forces. *Comput Phys Commun* 182:898–911
16. Humphrey W, Dalke A, Schulten K (1996) VMD: visual molecular dynamics. *J Mol Graph* 14–1:33–38
17. Herdes C, Totton T, Müller E (2015) Coarse grained force field for the molecular simulation of natural gases and condensates. *Fluid Phase Equilib* 406:91–100
18. Fang T, Wang M, Gao Y et al (2019) Enhanced oil recovery with CO<sub>2</sub>/N<sub>2</sub> slug in low permeability reservoir: molecular dynamics simulation. *Chem Eng Sci* 197:204–211
19. Zoete V, Cuendet M, Grosdidier A et al (2011) SwissParam: a fast force field generation tool for small organic molecules. *J Comput Chem* 32–11:2359–2368
20. Vorobyov I, Anisimov VM, Greene S et al (2007) Additive and classical drude polarizable force fields for linear and cyclic ethers. *J Chem Theory Comput* 3–3:1120–1133
21. Cygan RT, Liang J-J, Kalinichev AG (2004) Molecular models of hydroxide, oxyhydroxide, and clay phases and the development of a general force field. *J Phys Chem B* 108–4:1255–1266
22. Aminian A, ZareNezhad B (2019) Oil-detachment from the calcium carbonate surfaces via the actions of surfactant, nanoparticle and low salinity brine: an insight from molecular dynamic simulation. *Chem Eng Sci* 202:373–382
23. Yan Y, Li C, Dong Z, Fang T et al (2017) Enhanced oil recovery mechanism of CO<sub>2</sub> water-alternating-gas injection in silica nanochannel. *Fuel* 190:253–259
24. Mazyar OA, Darugar QA, Khabashesku VN (2017) Functions of nanoparticles and surfactants in enhanced oil recovery: molecular dynamics studies. In: Abu Dhabi international petroleum exhibition & conference
25. Eskandar NG, Simovic S, Prestidge CA (2007) Synergistic effect of silica nanoparticles and charged surfactants in the formation and stability of submicron oil-in-water emulsions. *Phys Chem Chem Phys* 9–48:6426–6434

# A Comparison of Single-Vacuum-Bag and Double-Vacuum-Bag Methods for Manufacturing High-Quality Laminated Composites



Yasir Mujahid, Nabihah Sallih, and Mohamad Zaki Abdullah

**Abstract** Selection of an appropriate vacuum-bagging technique is critical for producing high-quality laminated composites. However, the comparative study among various choices of vacuum-bagging techniques is not readily available. This study investigates the contribution of various bagging techniques and laminate thicknesses in achieving lower void content. Six laminates were produced, and their contents of surface porosity and through-thickness void were evaluated. The lowest contents of surface porosity and through-thickness void are achieved using a double-vacuum-bagging technique, i.e., 0.04% and 0.5%, respectively. The reduced void content is a result of the ballooning effect due to a pressure difference between the inner and outer bags. The laminate void content increased with an increase in thickness. The highest content of void is reported in the laminate with 3.2 mm thickness, i.e., 0.79%. This comparative study conclusively elucidates the importance of selecting appropriate processing parameters in reducing the formation of voids in laminated composites.

**Keywords** Laminated composites · Single-vacuum-bag method · Double-vacuum-bag method · Image processing · Surface porosity · Through-thickness void content

## 1 Introduction

The demand for advanced composite materials is increasing enormously in recent years because they offer commendable advantages over metallic materials including a significant weight reduction without compromising mechanical strength [1], design

---

Y. Mujahid (✉) · N. Sallih · M. Z. Abdullah  
Mechanical Engineering Department, Universiti Teknologi PETRONAS, 32610 Perak, Malaysia  
e-mail: [yasir\\_mb93@yahoo.com](mailto:yasir_mb93@yahoo.com)

N. Sallih  
e-mail: [nabihah.sallih@utp.edu.my](mailto:nabihah.sallih@utp.edu.my)

N. Sallih  
Institute of Health and Analytics, Universiti Teknologi PETRONAS, 32610 Perak, Malaysia

flexibility [2], and fatigue resistance. They also offer outstanding specific strength and stiffness [3]. Advanced composites are being used in a wide range of applications including the aerospace industry, oil and gas industry, automobiles, and biomedical applications [1, 3]. Vacuum bagging (VB) is a promising technique to manufacture advanced laminated composites and sandwich structures. Traditionally, such composites were produced using vacuum bagging with an autoclave (VBA). The vacuum-bagging setup is placed inside an autoclave vessel, achieving partial or full vacuum in the bag, as shown in Fig. 1. The vessel temperature is raised following a specified curing profile, and the vessel is pressurized. The prepregs are compressed by the consolidation pressure differential to acquire the required shape [4]. VBA is commonly known to produce high-quality composites with very minimal void content. However, manufacturing process for composites using VBA process is extremely costly because of high procurement, operation, and maintenance costs involved in a specialized autoclave vessel [5, 6]. The vessel size also limits the sizes of parts to be produced. Their unavailability in required sizes certainly affects the production rate or required components in the industry. Furthermore, a longer cure cycle is required to heat up a large autoclave vessel which at the end of the operation also takes longer to cool down. Occasionally, a slower ramp rate is used to ensure an even distribution of temperature distribution on both the tool and the parts themselves [6].

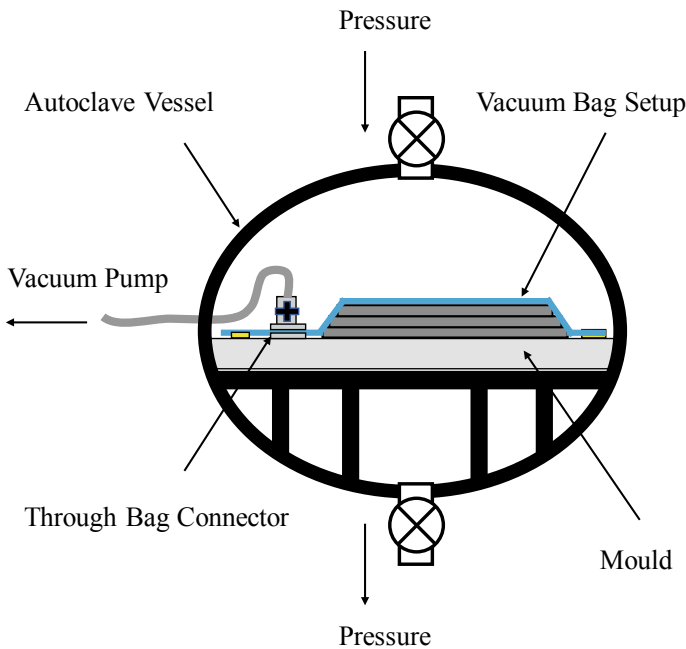


**Fig. 1** Vacuum bagging with the autoclave curing process

As the demands, desired sizes and complexity for these composite parts increase, the need for a faster and more economical manufacturing process increases [5, 2]. However, the challenges associated with a VBA process prohibit it from achieving all the advantages in a single manufacturing process. Vacuum-bagging-only (VBO) is another promising composite manufacturing process which has the potential to produce autoclave quality high-performance composite structures, mostly with the use of partially impregnated prepregs [7]. VBO is an economical and cost-effective manufacturing process. It solves major limitations associated with autoclave processes such as high operational and setup cost, longer curing cycles, and size dependency on autoclave chambers. It only uses atmospheric pressure differential to consolidate the prepregs to achieve the required shape of molds [8, 9]. VBO prepreg processing allows the composite parts to be cured in conventional ovens. A void is the most commonly known manufacturing-induced defect associated with VBO. The acceptable void content in polymer composites may vary depending on desired applications. However, many researchers often use aircraft standards for benchmarking purpose. The primary structures of the aircraft industry have less than 1% void content, while the secondary structures allow up to 5% void content [10]. Manufacturing of such quality composite parts is a challenging activity. It depends on several factors including consolidation pressure, curing cycle, raw material, prepregs, breather density, and release film perforation. Usually, a vacuum is pulled in VBO at room temperature prior to the curing of composites at elevated temperature [11]. This technique is efficient to prevent any leakages in the bag at an early stage of the process. Conventionally, a single bag is used to form a vacuum chamber in vacuum-bagging method, hereby known as single-vacuum-bagging (SVB). A typical SVB setup consists of composite plies stacked on a mold/tool of the desired shape, covered with a release fabric, perforated (or unperforated) film, and a breather cloth layer, and then sealed in a vacuum bag using sealant tape [12]. Vacuum pump with fittings (i.e., valve, pressure gauge, pressure regulator, hoses) is connected to the vacuum-bagging setup using a through-bag-connect, as shown in Fig. 2a.

Release fabric is a smooth woven fabric which is placed on top of the laminate plies to create a separation film between the breather cloth and the laminate. It allows the excess epoxy to penetrate through laminate and still can be peeled off, as it does not bond with resin. An example of a commonly used release fabric is a finely woven polyester fabric. A perforated plastic film is often placed on top of a release fabric which aims in holding the resin within laminate when a high consolidation pressure is applied. Clamping pressure, resin's viscosity, and its out-time define the selection of a suitable perforated film which varies in pore sizes and its patterns [13]. On top of a perforated film, a breather cloth is placed to allow air evacuation from the inner environment to through-bag-connector by providing a separation between the bag and the laminate [13, 1]. Edge breather or porous dams are also used on the edges of a composite; they prevent resin loss while allowing air evacuation [12]. Before applying sealant bag on top of the setup, the through-bag connector is placed inside which helps evacuating entrapped air to the atmosphere through a vacuum pump. The setup is then sealed with a plastic bag using sealant tape to provide an airtight environment. It is recommended to use a transparent bag for easy inspection.

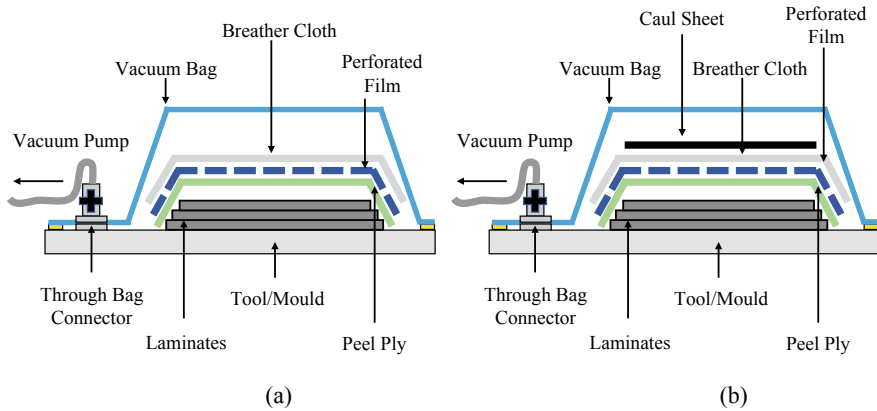


**Fig. 2** An example of **a** vacuum-bagging-only schematics and **b** laminates subjected to atmospheric pressure using a vacuum-bagging-only technique

After setting a vacuum bag on top of the setup and sealing to avoid any leakages, the vacuum port is then connected to the vacuum pump. Any leakages in the bag or near through-bag-connector can be sealed using sealant tape. Before starting the vacuum pump of a vacuum-bagging setup, the inside and outside pressures of the bag are the same, i.e., one atmospheric pressure. Once the air-evacuation process from inside of the bag starts, the inner pressure starts to drop, while the outer pressure of the bag remains at 1 atm [14]. This pressure difference forces the bag to tightly hold everything inside together, applying uniform pressure, as shown in Fig. 2b. For composites to be cured at a temperature higher than ambient conditions, the SVB setup is then placed inside an air-circulating oven. The required cure cycle is then followed to increase the temperature with an appropriate ramp rate and dwells [15, 16]. Modified SVB (MVSb) is similar to SVB, except that it incorporates caul sheets or pressure strips as pressure intensifiers to facilitate the intensification of pressure distribution on composites, especially for composites with complex shapes. MSVB is suitable for composites with convex, concave, or semi-spherical corners. The intensifiers, however, block the air passages for entrapped air to escape which causes porosity [1].

The concept of the double-vacuum-bagging technique was first introduced in 1990 by NASA Langley Research Centre. DVB technique is a superior alternative to an SVB and offers exceptional void management [17]. There are two types of DVB setups. For the first DVB type, vacuum-bagging setup (similar to SVB) is placed inside a rigid chamber, which acts as a second vacuum environment, as shown in Fig. 3 [18]. The rigid chamber is vacuumed during a low-temperature hold stage to create a second vacuum environment, as shown in Fig. 3a, and then purged to the atmosphere during a high-temperature hold, as shown in Fig. 3b. Initially, a partial vacuum is drawn in the vacuum bag during low temperature while the bag is fully vacuumed during the high-temperature hold. This technique is, however, not favorable because of its limitation on composite size flexibility. VBO process was

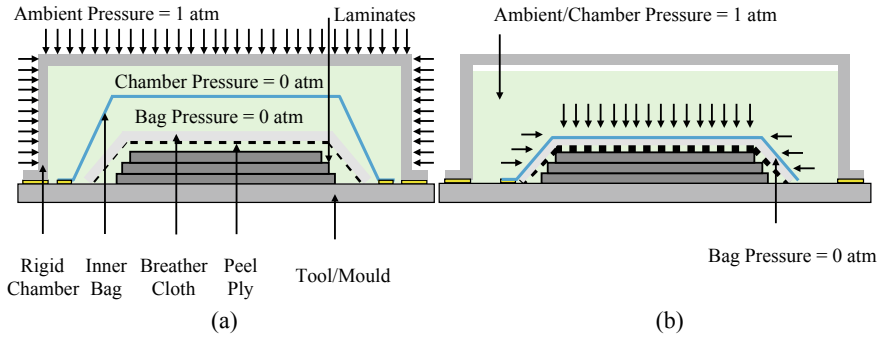


**Fig. 3** Schematics of a double-vacuum-bagging setup within a rigid chamber during **a** degassing phase and **b** compaction phase

introduced to eliminate the need for autoclave shells. Introducing rigid chambers would again limit the sizes of composites, which is not desirable. It also involves added costs for manufacturing and maintenance of the rigid chambers. The second type of DVB setup includes an SVB setup placed inside another plastic bag which is separated by a perforated steel tool, as shown in Fig. 4. This tool prevents outer bag from collapsing onto the inner bag while creating a second vacuum environment. A double-vacuum-bagging assembly creates two vacuum environments, one inside inner bag and one in between inner and outer bags, for fabricating composites using prepreps while eliminating the possibilities of void formation. This process is conducted in two phases, namely degassing and compaction. Degassing phase occurs at B-stage (low-temperature dwell) of the cure, while the compaction phase occurs at C-stage (high-temperature dwell) of the cure. A full vacuum in the outer bag is drawn by applying 1.01 bar pressure which tends to create a ballooning effect inside the inner bag, as shown in Fig. 4a. A partial vacuum of 0.95 bar is created in the inner bag, say 0.95 bar [19, 17]. During B-stage of a cure cycle, volatile by-products

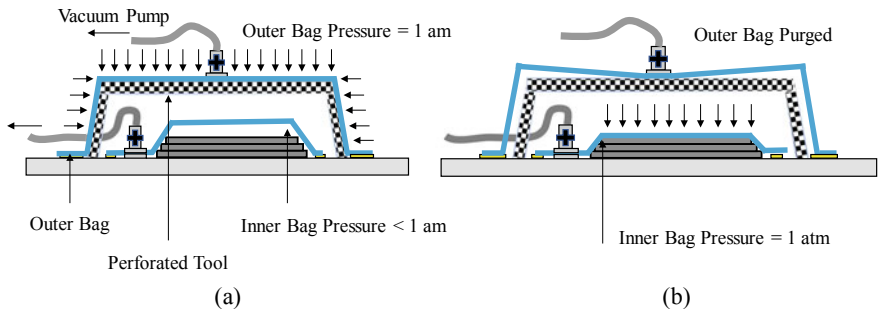


**Fig. 4** Schematics of a flexible double-vacuum-bagging setup with a perforated tool during **a** degassing phase and **b** compaction phase

are produced, which are free to evacuate easily due to the ballooning effect created inside the inner bag.

A suitable cure cycle with enough curing time is very essential to ensure volatiles and air evacuation from inner bag so as to manufacture void-free composites. In DVB arrangement, the composite lay-up assembly is not compacted by the atmospheric pressure because the Inner bag remains loose. The vacuum in the outer bag is discontinued by purging it to the atmosphere at the end of the B-stage, while the vacuum inside the inner bag is maximized to complete 1.01 bar pressure. This helps in the consolidation of composites during the high-temperature ramp-and-hold period of the cure cycle, as shown in Fig. 4b. Although the concept of DVB has been introduced for a while now, this setup is yet to be fully understood and applied in the laboratory/industry. The literature on the performance of the technique is not readily available. Therefore, this work compares the compatibility and performance of the double-vacuum-bagging with conventional single-vacuum-bagging techniques for manufacturing high-quality composites.

## 2 Materials

Out-of-autoclave carbon preregs XC110 3K, 210g, 2/2 Twill with 58% fiber content by weight were used to manufacture composite samples with both SVB and DVB techniques to investigate and compare their behaviors. All the laminate samples were stacked using an  $[0^\circ]_n$  orientation, where  $n$  is the number of the prepreg plies used. The consumables for VB assembly comprised of polyester-woven breather cloth, nylon bagging film, and polyolefins perforated release film.

## 3 Specimens Manufacturing Method

Carbon preregs XC110 3K were given an adequate four-day out-time at 20 °C before producing laminates. Total of six laminate samples were produced using two difference bagging techniques (SVB and DVB) and laminate thicknesses (1.6, 2.5 and 3.2 mm), as shown in Table 1.

For each sample, preregs of dimensions 220 mm × 220 mm were stacked on a flat aluminum mold. Laminates using SVB technique were covered with first release fabric, followed by a perforated film and on top, a breather fabric was placed. A plastic bag 20% larger than the laminate dimensions was cut to accommodate the stacking without disturbing its orientation. Composites were then sealed within the vacuum bag using sealant tape on the edges. A second bag was used in the DVB to create a second vacuum environment which was separated from the inner bag by a steel-perforated tool. A manufacturer's recommended cure cycle (MRCC) was used for SVB and DVB techniques, as shown in Fig. 5a, b. The MRCC for SVB technique consists of 4-h dwell at 70 °C (B-stage) and 1-h dwell at 120 °C (C-stage).

**Table 1** Manufacturing plan for laminate samples (for example, Sample 1 is produced using SVB technique which is 1.6 mm thick)

Samples	Bagging techniques	Laminate thickness (mm)
1	SVB	1.6
2	SVB	2.5
3	SVB	3.2
4	DVB	1.6
5	DVB	2.5
6	DVB	3.2

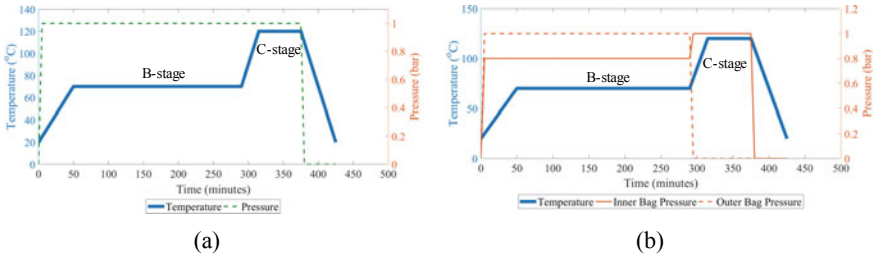


**Fig. 5** Manufacturer’s recommended cure cycle used in **a** SVB and **b** DVB techniques

Two ramp rates are used: 1 °C/min up to 70 °C and 2 °C/min from 70 to 120 °C. A full vacuum is pulled at room temperature by applying 1.01 bar pressure until the end of C-stage. The temperature profile in the MRCC for DVB is similar to SVB. However, it consists of two pressure profiles due to the two vacuum bags used. The pressure inside the inner bag is 0.95 bar (partial vacuum) during B-stage and 1.01 bar pressure (full vacuum) during C-stage. A full vacuum is drawn inside the outer bag during B-stage (to create a ballooning effect in the inner bag) while it is purged to the atmosphere during C-stage.

### 4 Quantification of Void Content

Content of surface porosity and through-thickness void is quantified using MATLAB code for image processing. First, high-resolution images of mold-laminate and laminate-bag sides were acquired for all samples produced, using a Nikon D7000 DSLR camera with an AF-S XD NIKKOR 18–105 mm VR lens. Specimens were then cut into 15 mm × 200 mm dimensions using a diamond blade cutter. Specimens’ cross-sectional areas were then polished using 1000-grit and 1500-grit sandpapers, respectively. High-resolution images were taken to quantify through-thickness void content. To avoid discrepancies and human error, twenty images on each side of the specimens were analyzed to evaluate void content.



### 5 Results and Discussion

Surface porosity or pitting effect is a frequent concern which often arises in VBO prepreg-processed laminates. This effect is the repercussion of air trapped between prepreg ply in contact with the tool surface. While the effect of surface porosity on mechanical performance is not significant, it is an aesthetic issue that may include costly methods for remedies such as paints, resin-rich surfacing films, and filling gel coats. However, the mechanical properties and overall life cycle of composite parts are deeply dependent on the through-thickness void content. An example of surface porosity and through-thickness void content using a MATLAB code for image processing is shown in Fig. 6.

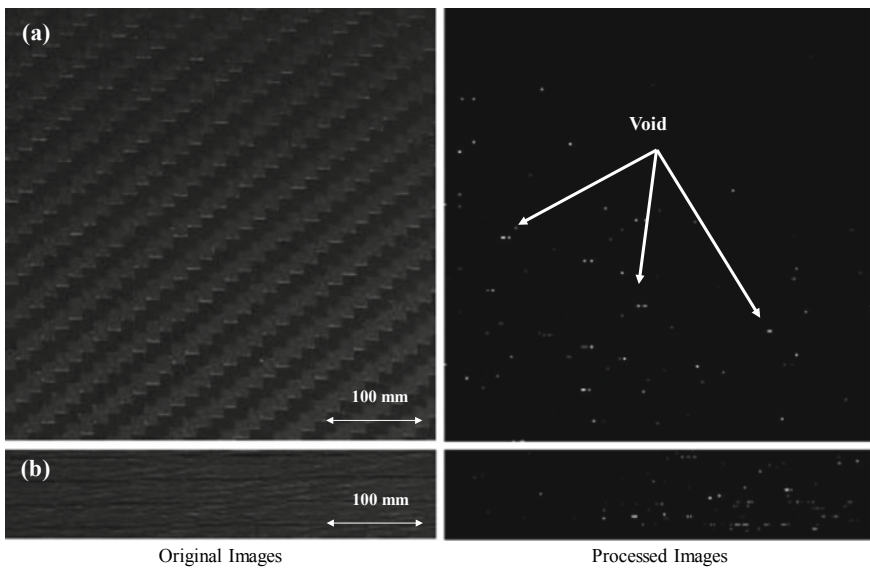


**Fig. 6** Original and processed images for **a** surface porosity and **b** through-thickness void

**Table 2** Surface porosity and through-thickness void content

Samples	Bagging techniques	Laminate thickness (mm)	Surface porosity (%)	Though-thickness void (%)
1	SVB	1.6	0.100	0.484
2	SVB	2.5	0.117	0.754
3	SVB	3.2	0.120	0.904
4	DVB	1.6	0.030	0.229
5	DVB	2.5	0.040	0.462
6	DVB	3.2	0.036	0.675

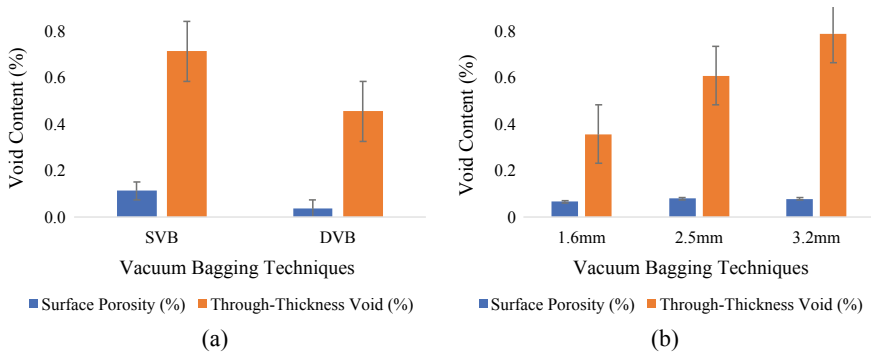


**Fig. 7** Surface porosity and through-thickness void in laminates produced using **a** various vacuum-bagging techniques and **b** various laminate thicknesses

The contents for surface porosity and through-thickness void are listed in Table 2. Laminates produced using DVB technique exhibited the lowest manufacturing-induced void content, as shown in Fig. 7a. The lowest content of surface porosity and through-thickness void is reported when using DVB, i.e., 0.04% and 0.5%, respectively. These results are superior when compared to laminates produced using SVB technique which demonstrated the content of surface porosity and through-thickness void of 0.1% and 0.7%, respectively. The SVB technique holds the laminate tightly during the entire curing process, leaving minimal space for entrapped air to be evacuated, which results in the worse pitting effect. On the contrary to the SVB technique, the ballooning effect in DVB allows entrapped volatiles to be evacuated, resulting in a reduction of 69% lower content of surface porosity and 36% through-thickness void. These observations conclusively elucidate that the DVB technique is better in vigorously removing the entrapped volatiles so as to achieve a lower content of voids. It is observed that the increment of thickness in laminates further hinders the air-evacuation process and worsens the void contents, as shown in Fig. 7b.

The content of surface porosity is almost similar in all laminates with an average of 0.07%. This similar pitting effect indicates that the evacuation process of entrapped (in between tool-part and bag-part sides) volatiles is not affected by the addition of prepreg layers after some threshold. However, an increasing trend in through-thickness void content is observed with the increase in laminate thickness. The through-thickness void content in laminates increased by 41% when thickness increased from 1.6 to 2.5 mm (an addition of four layers), and by 55% when double the laminate thickness from 1.6 to 3.2 mm thickness. This increase in the void content with the increase in laminate thickness demonstrates the complexity of the volatile-evacuation process. Although partially impregnated prepreps contain channels to facilitate the air-evacuation process, however, the further increase in the laminate thickness hinders the air-evacuation process and worsen the void content.

## 6 Conclusions

This study investigates the effects of vacuum-bagging techniques along with laminate thickness on the formation of surface porosity and through-thickness void content. Void contents in the laminated composites could be further reduced by considering the contribution of various bagging techniques and laminate thickness. Six laminates were produced using single-vacuum-bagging and double-vacuum-bagging techniques with laminate thicknesses of 1.6, 2.5, and 3.2 mm. High-resolution images of laminate surfaces and cross-section areas were analyzed to quantify the contents of surface porosity and through-thickness void using a MATLAB® code for image processing. Among bagging techniques, the double-vacuum-bagging technique was found to be better in achieving the lowest content of surface porosity and through-thickness void. This is achieved by the ballooning effect during the low-temperature hold stage which ensures an adequate time for the entrapped volatiles to be evacuated which is followed by the consolidation at the high-temperature hold stage which helps in achieving the shape conformation to the mold. The surface porosity trend in each bagging technique was almost similar in all samples of laminates with different thicknesses and indicates that the surface porosity is not affected after some threshold. However, the through-thickness void content got worse with the increase in the laminate thickness. An increment of 55% void content was observed when the laminate thickness was doubled. This present investigation of comparison of laminates produced using various bagging techniques and laminate thicknesses suggests that the formation of void due to the entrapped volatiles can be minimized by the introduction of second bagging technique to allow easy evacuation process during the low-temperature hold.

**Acknowledgements** The authors are thankful to Universiti Teknologi PETRONAS for providing financial assistantship and facilities to conduct this research. This work was partially funded by the Institute of Health and Analytics, Universiti Teknologi PETRONAS (Cost center: 015NC0-001).

## References

1. Hassan M, Othman A (2017) Contribution of processing parameters on void content in the vacuum bagging configurations of L-shaped composite laminates. *Int J Adv Manuf Technol* 93:1333–1345
2. Kourkoutsaki T, Comas-Cardona Sébastien, Binetruy C, Upadhyay R et al (2015) The impact of air evacuation on the impregnation time of out-of-autoclave prepregs. *Compos A Appl Sci Manuf* 79:30–42
3. Park SY, Choi CH, Choi WJ, Hwang SS (2018) A comparison of the properties of carbon fiber epoxy composites produced by non-autoclave with vacuum bag only prepreg and autoclave process. *Appl Compos Mater* 1–18
4. Ma Y, Centea T, Nutt SR (2017) Defect reduction strategies for the manufacture of contoured laminates using vacuum BAG-only prepregs. *Polym Compos* 38:2016–2025

5. Centea T, Grunenfelder LK, Nutt SR (2015) A review of out-of-autoclave prepregs—material properties, process phenomena, and manufacturing considerations. *Compos A Appl Sci Manuf* 70:132–154
6. Lee J, Ni X, Daso F, Xiao X, King D, Gómez JS, Varela TB, Kessler SS, Wardle BL (2018) Advanced carbon fiber composite out-of-autoclave laminate manufacture via nanostructured out-of-oven conductive curing. *Compos Sci Technol*
7. Helmus R, Centea T, Hubert P et al (2016) Out-of-autoclave prepreg consolidation: coupled air evacuation and prepreg impregnation modeling. *J Compos Mater* 50:1403–1413
8. Hu W, Nutt SR, Gill MC (2017) In-situ monitoring of air removal during vacuum bag-only (VBO) processing
9. Park SY, Choi CH, Choi WJ et al (2019) A comparison of the properties of carbon fiber epoxy composites produced by non-autoclave with vacuum bag only prepreg and autoclave process. *Appl Compos Mater* 26:187–204
10. Hassan M, Othman AR, Kamaruddin S (2017) A review on the manufacturing defects of complex-shaped laminate in aircraft composite structures. *Int J Adv Manuf Technol* 91:4081–4094
11. Kratz J, Hubert P (2013) Vacuum bag only manufacturing of honeycomb sandwich panels. In: *International conference of composite materials (ICCM)*
12. Centea T, Hubert P (2014) Out-of-autoclave prepreg consolidation under deficient pressure conditions. *J Compos Mater* 48:2033–2045
13. Epoxy WS (2010) Vacuum bagging techniques, p 56
14. Grunenfelder L, Dills A, Centea T et al (2017) Effect of prepreg format on defect control in out-of-autoclave processing. *Compos A Appl Sci Manuf* 93:88–99
15. Hou T-H (2014) Cure cycle design methodology for fabricating reactive resin matrix fiber reinforced composites: a protocol for producing void-free quality laminates
16. Dong A, Zhao Y, Zhao X et al (2018) Cure cycle optimization of rapidly cured out-of-autoclave composites. *Materials* 11:421
17. Khan LA, Mahmood AH, Ahmed S, Day RJ (2013) Effect of double vacuum bagging (DVB) in quickstep processing on the properties of 977-2A carbon/epoxy composites. *Polym Compos* 34:942–952
18. Sherwin GR (1999) Non-autoclave processing of advanced composite repairs. *Int J Adhes Adhes* 19:155–159
19. Hou T, Jensen B (2004) Evaluation of double-vacuum-bag process for composite fabrication

# Experimental Studies of FPSO Responses with Validation by Numerical and Artificial Neural Network Prediction



N. L. Azizan, Ruly Irawan, M. S. Liew, A. M. Al-Yacouby,  
and Kamaluddeen Usman Danyaro

**Abstract** There will be a force on the floating systems after applied environmental load which has an important effect on the performance and safety of the structure. Therefore, the research on orientation of the structure and wave impact has a practical significance. Experimental and numerical simulation becomes valuable in predicting the performance during the system operation. Hence, in this article, a study on the effect of FPSO response by changing the orientation of FPSO has been presented by conducting experiments in the UTP wave basin subjected to regular wave condition. The results are used to be validated with numerical models using a commercial software AQWA by the 3D frequency domain theory and presented in terms of Response Amplitude Operators (RAO) of six degrees of freedom. To accurately consider the effect of response, artificial neural network (ANN) is adopted to predict the FPSO behaviour under different orientations and validate the results. ANN can provide meaningful solutions and can process information in extremely rapid mode ensuring high accuracy of prediction, especially for long response in time histories. Results show that three methods were achieved to generalize the responses.

**Keywords** Floating · Production · Storage and Offloading (FPSO) · Experimental · Numerical Simulation · Response Amplitude Operators (RAO) · Artificial Neural Networks (ANN) · Universiti Teknologi Petronas (UTP)

## 1 Introduction

Recently, floating production platforms have been accepted by the offshore industry as reliable, efficient, and economic solutions for oil and gas production for large and marginal fields. To achieve the expected results, it is necessary to have a combination of both, the model basin results and the analysis, although there is a poor correlation between the model tests and simulations [1]. Many authors have mentioned the involvement of wind, waves, and current as external loads to the structure which

---

N. L. Azizan (✉) · R. Irawan · M. S. Liew · A. M. Al-Yacouby · K. U. Danyaro  
Department of Civil and Environmental Engineering, Universiti Teknologi PETRONAS, 32610  
Seri Iskandar, Perak, Malaysia  
e-mail: [nur\\_17005249@utp.edu.my](mailto:nur_17005249@utp.edu.my)

needs a dynamic study [2]. Wicher [3] had performed an experiment to investigate the response of the turret-moored FPSO for water depth of 6000-ft. A similar experiment has been done by Howell [4] to find the extreme response of a turret-moored FPSO in the Gulf of Mexico. The model tests have some limitations to calculate the interaction effects of rigid body and slender cables at deep-water condition due to depth restrictions of wave basins. Another major problem of physical model testing is differential Reynolds number between the cable lines and the prototype. Recently, researchers have changed their focus to develop the modelling and simulation tools for the analysis of an FPSO. Likewise, a second-order diffraction radiation theory has been incorporated into the hydrodynamic analysis on the turret-moored FPSO by Kim [5]. To estimate the response behaviour of FPSO under dynamic environment condition, the time domain analysis has been preferred more over the frequency domain analysis [6].

Neural network model can learn a complex and nonlinear relationship between the inputs and the outputs. Forecasting is required extensively in offshore engineering problems such as fatigues, maximum stress, and reliability of structures. ANN model has a robust alternative if it is applied in the right ways; therefore, the ability to understand the advantages and the limitations of ANNs is highly important [7, 8].

Neural network-based surrogate model is applied for the intensive computational simulation to design moorings and risers. Neural networks show a good accuracy as those calculated by finite element method (FEM) with a great reduction on calculation in time domain [7]. Hybrid integration of neural network model and FEM are also used to predict the responses and forces in time domain. The hybrid method shows that the approach has a better efficiency within 20 times faster compared to a complete simulation [8].

Wavelet neural network model is a hybrid of wavelet transform and feed-forward neural network. Wavelet neural network can give good accuracy and speed for the prediction of nonlinear dynamic finite element problems [9]. The use of ANN, surrogate, and other meta-model has been widely considered in structural mechanics. Practically, in offshore engineering, the prediction of sea-state characteristics, dynamic positioning systems, mooring forces, and recently, fatigue behaviour of risers is using neural network models. Kim used a meta-model based on quadratic Volterra kernels to predict the dynamic behaviour of catenary risers in the time domain, which also had been studied before [10, 11].

Mazaheri et al. started developing the design and analysis of mooring system using neural network model. ANN was used to predict the extreme values of the offsets of FPSO with a spread mooring system under specific metocean conditions. Using the specific mooring configuration, the use of models has been presented to obtain the tension forces, both moorings and risers, in full time domain [11].

Therefore, this paper investigated an approach for an experimental study conducted on FPSO to observe the effect of waves on the hydrodynamic responses in six degrees of freedom. The numerical analysis is then used to validate the experimental results. Finally, to achieve the expected results in both methods, artificial neural network is used for prediction of FPSO responses.

## 2 Methods

The general approach of predicting the FPSO responses can be categorized according to the model set-up and numerical analysis methods.

### 2.1 Modelling Law

In order to simulate the prototype responses, the important factor is to determine the modelling laws that were required for the system to be examined by the following parameters [12]:

- Geometric similitude,
- Hydrodynamic similitude.

The limitation of the experimental facilities affected the choice of scale for the tests. Normally, the choice of scale that provides the most economical and the most effective solution will be chosen. The common ranges of scaling factors for coastal studies are in the range of 1:150 to 1:20 in 2D tank, 1:150 to 1:80 for 3D wave tank, and 1:100 to 1:10 is the common range of scale for free and moored floating platforms. The most practical scaling law for the free and moored floating platform tests is the Froude’s law, where the Froude’s number,  $F_r$  is given as [12]:

$$F_r = \frac{u^2}{gD} \tag{1}$$

where  $u$  = fluid velocity,  $g$  = gravitational acceleration, and  $D$  = characteristic dimension platform.

The Froude model should satisfy the relationship, where a model scale of  $\lambda$  and geometric similarity are assumed [12]:

$$F_r = \frac{u_p^2}{gD_p} = \frac{u_m^2}{gD_m} \tag{2}$$

where  $p$  = prototype,  $m$  = model, and  $\lambda$  = scaling factor.

The model linear dimensions will be scaled linearly with the scale factor according to the geometric similarity [12]:

$$I_p = \lambda I_m \tag{3}$$

while

$$u_p = \sqrt{\lambda u_m} \tag{4}$$

## **2.2 Wave Kinematics**

The solution of the boundary value problem can be found in different ways using the existing wave theories. The simplest solution of the hydrodynamic equations involves further assumptions that the waves are of small amplitude compared to the water depth and the wave length. This solution was introduced by Airy (1845) and became known as the linear Airy wave theory or sinusoidal wave theory. This assumption allows the free surface boundary condition to be linearized dropping the wave height terms beyond the first order. It was used to provide a good solution in deep water when water-depth-to-wave-length ratio is greater than 0.5. For the range of water depths, wave periods and wave heights were used for the first-order analysis using regular waves, and the linear wave theory was used since it is simple and reliable over a large segment of whole wave regime and sufficient to obtain the kinematics of waves to be used in the analysis of FPSO [12, 13].

## **2.3 Case Study**

For the purpose of comparative evaluation, a generic FPSO has been selected as the study case. The results of the coupled versus non-coupled analyses of the case study are presented. The same study case is used for evaluating the model test techniques and sensitivity analyses of FPSO responses.

## **2.4 Model Description**

The FPSO model, as shown in Fig. 1, was used to perform experimental tests. The model was fabricated by adopting a scale ratio of 1:100 by using plywood and timber. The model test is based on full load condition with four numbers of mooring lines. The details of model are presented in Table 1.

## **2.5 Test Facilities and Instrumentations**

The experimental test was executed in the wave basin at Universiti Teknologi Petronas, Malaysia, with the dimensions of 22 m long, 5 m wide, and 1.2 m depth. It is equipped with eight wave paddles to generate regular and random waves. The wave absorber functioned to minimize the wave reflection and three skidded remotely controlled bridges were used to support personnel and equipment instruments. The wave basin also aided with the wave probes and inclinometer, load cells, data logger,



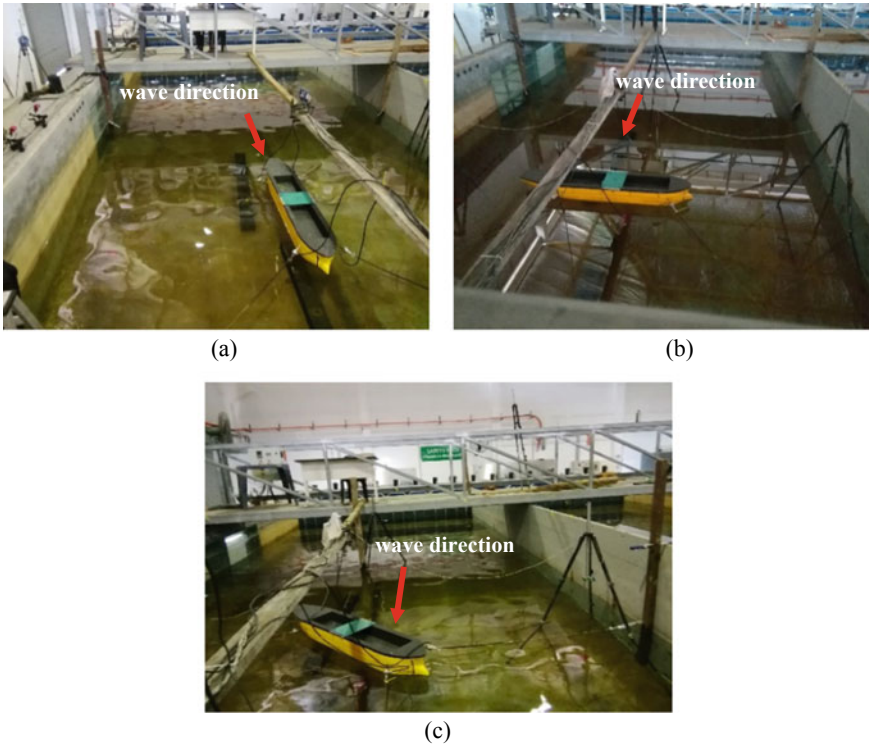


**Fig. 1** a FPSO in head sea, b FPSO in beam sea, and c FPSO in quarter sea direction

**Table 1** Hydrostatic particular FPSO

Measurement	Full scale	Model (1:100)	Unit
Overall length	177.3	1.7730	m
Beam of ship	32.2	0.3220	m
Draft to baseline	12.6	0.1260	m
Displacement	58,095	0.0581	tonne

slamming gauge, velocimeters, pressure transducers, accelerometers, Qualisys, and optical tracking system are also available in the laboratory.

### 2.6 Metocean Data

The experiment was conducted based on metocean conditions in Table 2 and Fig. 1 for the FPSO position and wave heading direction.

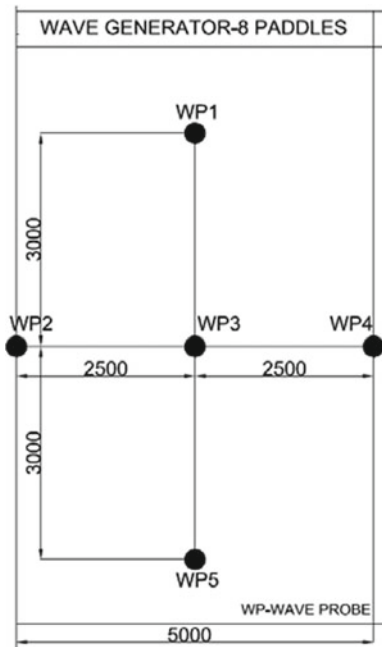
**Table 2** Metocean conditions (model scale)

Parameters	Notation	Value	Unit
Wave height	$H_s$	4	m
Time period	$T_p$	8–30	s
Water depth	$d$	70	m

### 2.7 Laboratory Tests

Before starting the model tests, wave height, as per Table 2, which are intended to be used in the tests, were calibrated at the model position. The instantaneous wave elevation was measured using the twin-wire wave probes for the set water depth. Wave probes were calibrated, and the required water depth was set with free surface set to zero position. During wave calibration, five wave probes were installed, with one wave probe being at the centre of the tank. Figure 2 shows the wave probe arrangement for wave calibration. To enable the generation of wave conditions, it is necessary to know the dimensionless paddle transfer function (PTF), which relates the desired wave height up on the model and the associated paddle movement. This relationship is dependent on both water depth and frequency. Hence, it is mandatory to calibrate the waves with the same wave height and period if they are used at different water depths. For regular waves, the theoretical wave height and wave period are similar with the measured wave height and wave period obtained from the

**Fig. 2** Wave probe position in wave basin



wave probe in the model position, by adjusting the gain factor in the HR WaveMaker software.

## 2.8 Seakeeping Tests

To investigate the dynamic motion responses of the model in the seakeeping condition, regular waves were generated. The six DOF motion responses were captured using the optical track system. To obtain the six DOF response amplitude operators for the model, the wave elevations were generated and measured prior to the installation of the models by the wave probe placed at the same location where the models were installed. Long-crested regular waves were recorded for the duration of 5 min [12].

Seakeeping tests were done for two purposes: for validating the numerical model and for conducting parametric studies. The frequency-dependent motion RAOs for the first-order systems (linear) are obtained as [12]:

$$\text{RAO}(\omega) = \sqrt{\frac{S_R(\omega)}{S(\omega)}} \quad (5)$$

The effect of wave heading direction was studied under the action of long-crested regular waves for 0.7 m water depth. The wave module defined the regular wave as the sine function. The motion RAOs, when subjected to regular waves, are obtained as [12]:

$$\text{RAO} = \frac{\text{Response}(\tau)}{\eta(\tau)} \quad (6)$$

## 2.9 Time Domain Analysis

Moored compliant offshore platforms could be analysed by either coupled or uncoupled analysis. In this study, uncoupled analysis was adopted. In uncoupled analysis, the platform and the mooring system are considered as two different components. The force vector, stiffness, mass, and damping matrices are formulated for each platform elements. Mooring lines are modelled as mass-less springs, and the contribution to the inertia, damping, and excitation force is ignored [12].

The governing equations for the rigid platform EOM with three degrees of freedom are derived by considering the conditions of equilibrium in the longitudinal direction, transverse direction, and the rotational direction around CG. In the case of both spars and semi-submersible platform prototypes, the general equation is given as [13, 14]:

$$[M]\{\ddot{X}\} + [C]\{\dot{X}\} + K\{X\} \tag{7}$$

### 2.10 Artificial Neural Networks (ANNs)

The ANN methodology was first started by McCulloch and Pitts (1943) which then artificial model of a neuron was known as McCulloch–Pitts neuron. Figure 3 shows the process of how neural network systems are working. The network is created as a group by combinations of neurons. The input signals that come to the network will be processed before being transmitted to the other neurons. This process of transmitting inputs to neurons has a performance on the network systems. Based on this assumption, artificial neural networks (ANN) models are developed [15].

## 3 Results and Discussions

The RAOs for each six DOFs were analysed for the FPSO model. The directions of the waves were corresponding to the FPSO in head sea (180°), beam sea (90°), and quartering sea (135°) conditions. The experiments were carried out under the action of regular waves. The wave height was 4 m, and time period range was between 8 and 30 s. The water depth was 70 m. In this paper, the comparison of model responses in surge, sway, heave, yaw, pitch, and roll for FPSO, in terms of response amplitude operator (RAO) are presented. As mentioned earlier, the result is verified with numerical methods and predicted by using artificial neural networks (ANNs). To study the effect of motions response of the model subjected to waves, the model was positioned in different angles, which are head sea, beam sea, and oblique sea.

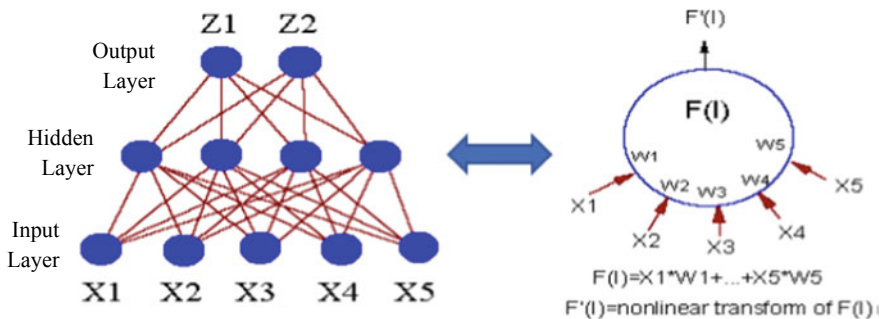


Fig. 3 Typical neural network architecture

### 3.1 Combine Model Testing and Analysis Approach

The overall FPSO responses can be well predicted by either the numerical tools or the model tests. Both have their advantages and limitations. Until now, the model test method is still perceived as a more reliable mean to correctly predict the deep-water floater responses [1]. A numerical simulation is conducted in order to verify the validity of the modelling process by comparing the results obtained from the experimental works. Artificial neural networks (ANNs) can give prediction based on input and output data because the system is encouraged by biological systems, such as human brain. Each processing element is fully interconnected to other processing elements called “connection inputs”. The selection of inputs is a key element for the analysis. Meaning, the data selection inputs, which can capture the main feature of prediction element, are very important. From that, it can generate a number of predictions. For this paper, the time series analysis of a result, which is based on the experimental and numerical simulations by AQWA, will be used for the prediction. The results obtained from the experiment, numerical works, and ANN are shown in Figs. 4, 5, 6, 7, 8 and 9, respectively. All the result is based on the model scale.

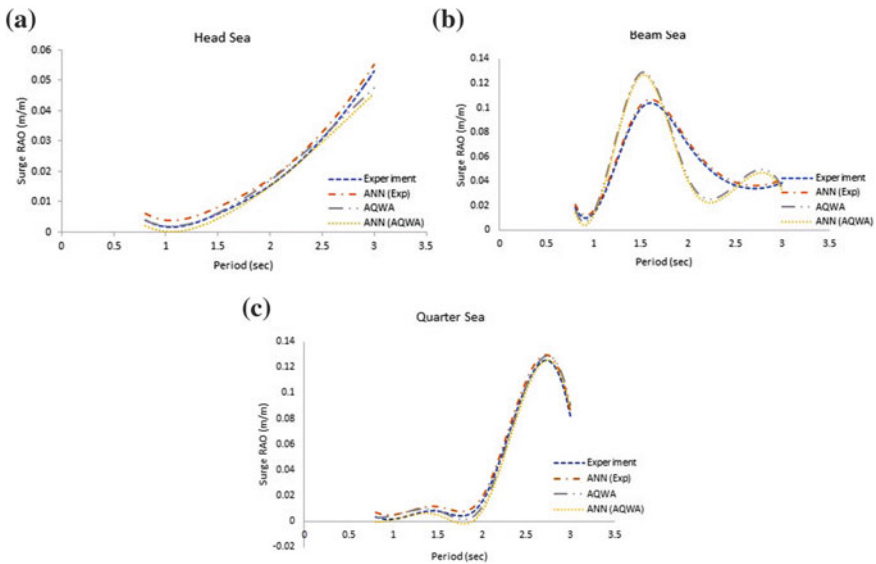


Fig. 4 Response in surge a head sea, b beam sea, and c quarter sea

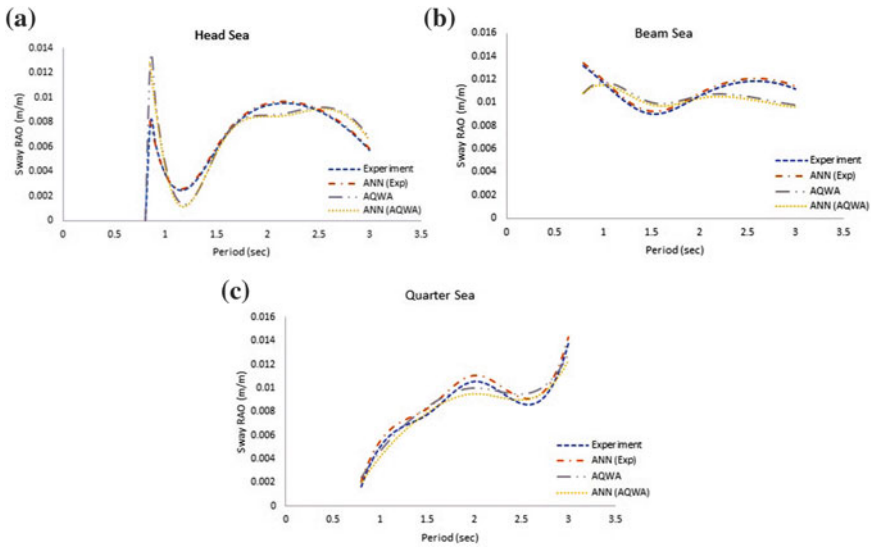


Fig. 5 Response in sway **a** head sea, **b** beam sea, and **c** quarter sea

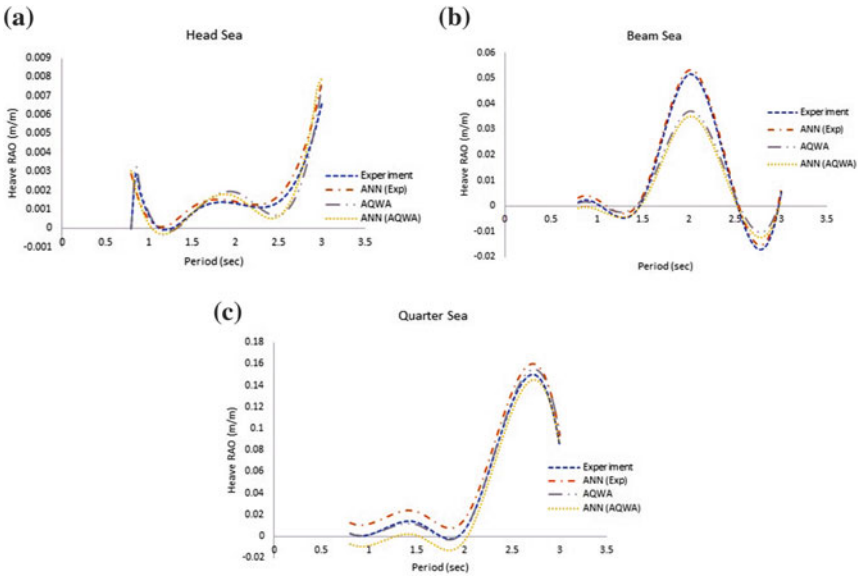


Fig. 6 Response in heave **a** head sea, **b** beam sea, and **c** quarter sea

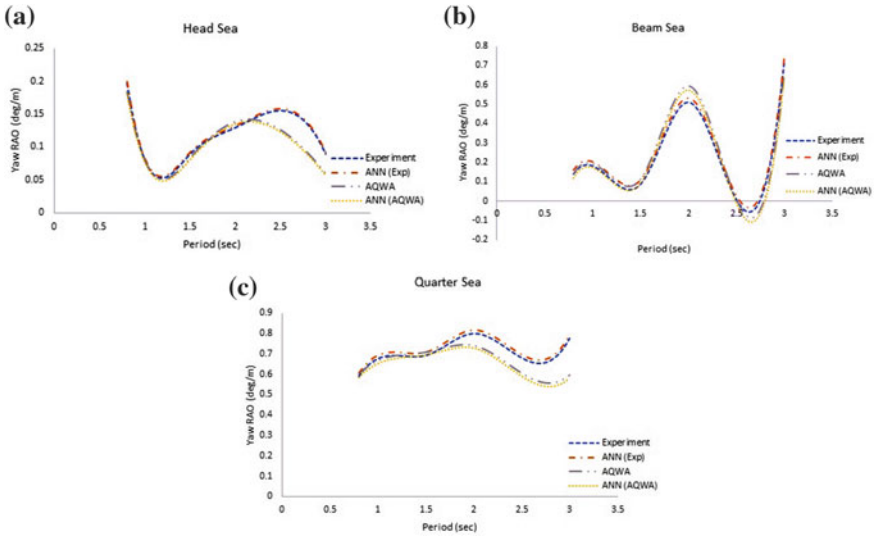


Fig. 7 Response in yaw a head sea, b beam sea, and c quarter sea

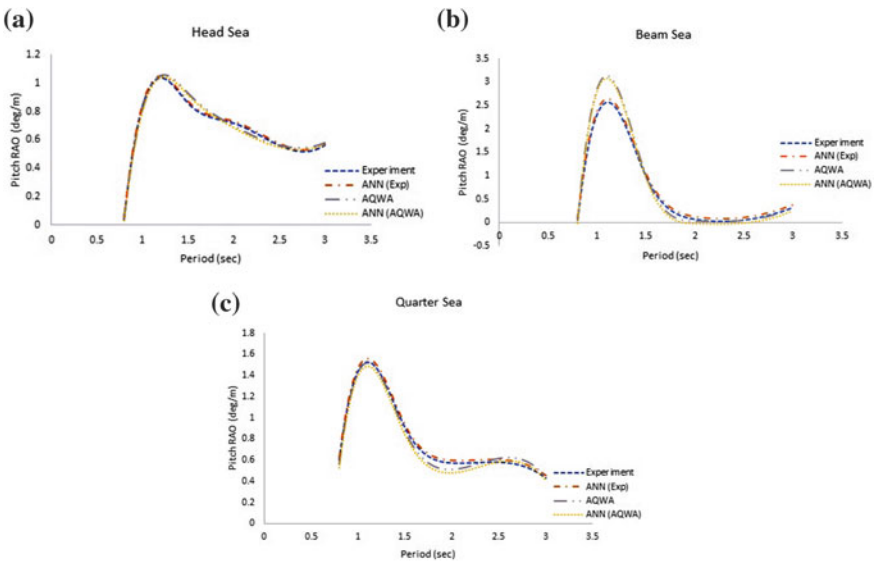


Fig. 8 Response in pitch a head sea, b beam sea, and c quarter sea

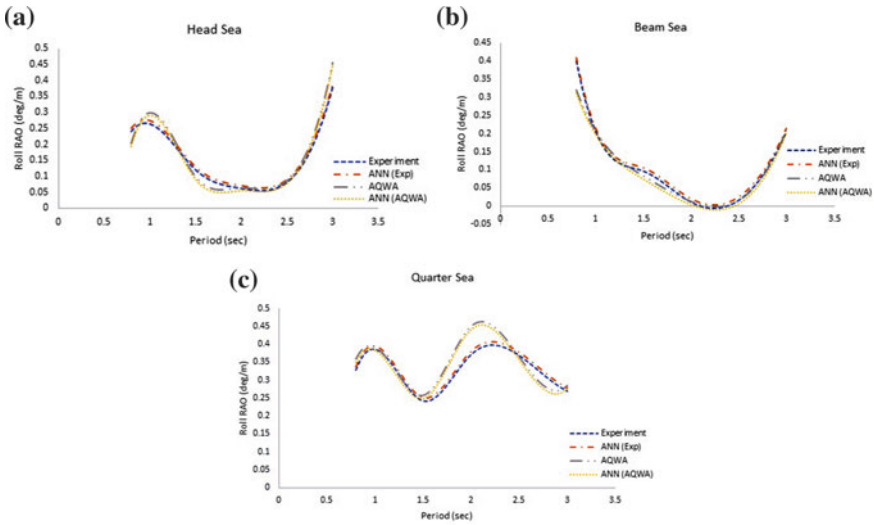


Fig. 9 Response in roll **a** head sea, **b** beam sea, and **c** quarter sea

### 3.2 FPSO Motion Responses

The surge, sway, heave, roll, pitch, and yaw motion RAOs are all important. All six DOF motions, shown in the result, provide a good agreement between experiment and numerical simulation. ANNs also predict accurate values for the responses on both analyses. Thus, the measured RAOs for the model FPSO are reliable to produce the prototype FPSO to calculate the other environmental condition vs numerical analysis or ANN model.

For the surge RAO (Figs. 4), beam sea (BS) and quarter sea (QS) give (0.12 m/m) which is slightly higher compared to head sea (HS) (0.05 m/m). It means surge motion is important to BS and QS conditions. For the sway RAO (Figs. 5), BS is smaller (0.008 m/m) compared to BS and QS (0.014 m/m). For the heave RAO (Figs. 6), BS possesses a higher motion (0.051 m/m) compared to QS (0.014 m/m) and HS (0.007 m/m). For the yaw RAO (Figs. 7), BS and QS were observed with the same motions (0.7 deg/m), while HS was smaller (0.2 deg/m) which the motion does not affect much. For the pitch RAO (Figs. 8), BS has a higher motion (2.1 deg/m) followed QS (1.48 deg/m) and HS (1.04 deg/m). For roll RAO (Fig. 9), no significant differences were found to the response which is 0.4 deg/m. Therefore, the characteristics of roll damping were identified to be important for RAO, while the others for surge, sway, yaw, pitch, and heave shown to be less impact. The feature for roll motion RAO is low because it is influence by the resonant response which excessive from the viscous effects due to the vortices that are generated by the bilge keels of the FPSO model. However, the model used for experiment does not have bilge keel, which is usually present in real scenario, while the other motion RAOs are largely governed by the inertia of the FPSO model [12].



## 4 Conclusions

There are several methods is adopted to be capable for generating motion responses of the model. Based on the present results, the motion responses of the RAOs are influence to the direction of waves heading. It is measured that the FPSO model was testing is more crucial on beam and quartering sea. The impact of FPSO RAOs by experimental analysis is more reliable compare to numerical simulations. In such case, a combined model testing and analysis approach is required to correctly predict the system responses. However, the difference affect is not much and still acceptable. Thus, further analysis for others metocean data condition can be done by using software analysis. The results also observed that the ANN approach is competence to provide a good accuracy and reduce times for predicting long response time histories. The responses obtained from the ANN approach are similar to the input from the experimental and numerical analysis and give a good prediction. Thus, ANN tool is one of the prediction methods to measure the responses by saving the time duration.

**Acknowledgements** This research was supported by Universiti Teknologi PETRONAS, Malaysia. The authors would like to appreciatively present their gratitude to the university for providing financial support and good facilities

## References

1. API RP-2SK (2005) Design and analysis of station keeping systems for floating structures, 3rd edn. American Petroleum Institute
2. Ma QW, Yan S, Greaves D, Mai T, Raby A (2015) Numerical and experimental studies of Interaction between FPSO and focusing waves. In: Proceedings of the 25th ISOPE, Hawaii, USA
3. Wicher JEW, Devlin PV (2001) Effect of coupling of mooring lines and risers on the design values for a Turret Moored FPSO in deep water of Gulf of Mexico. In: Proceedings of 11th international offshore & polar engineering, vol 3, pp 480–487
4. Howell G, Duggal A, Heyl C, Ihonde O (2006) Spread Moored or Turret Moored FPSO's for deepwater field developments. offshore West Africa
5. Kim Y (2003) Dynamic analysis of multiple-body floating platforms coupled with mooring lines and risers. Texas A&M University
6. Lopez JT, Tao L, Xiao L, Hu Z (2017) Experimental study on the hydrodynamic behaviour of an FPSO in a deepwater region of the Gulf of Mexico. *Ocean Eng* 129:549–566
7. de Pina AC, de Pina AA, Albrecht CH (2013) ANN-based surrogate models for the analysis of mooring lines and risers. *Appl Ocean Res* 41
8. Guarize R, Matos NAF, Sagrilo LVS (2007) Neural networks in the dynamic response analysis of slender marine structures. *Appl Ocean Res* 29:191–198
9. Jacob P, Bahiense RA, Correa FN, Jacovazzo BM (2012) Parallel implementations of coupled formulations for the analysis of floating production systems, part I: coupling formulations. *Ocean Eng* 55:206–218
10. Hong, SY, Kim JH, Kim HJ, Choi YR (2002) Experimental study on behavior of tandem and side-by-side moored vessels. In: Proceedings of 12th international offshore and polar engineering conference (ISOPE), Kita-Kyushu, Japan

11. Mazaheri S, Downie MJ (2005) Response-Based method for determining the extreme behaviour of floating offshore platforms. *Ocean Eng* 32:363–393
12. Chakrabarti SK (1998) Physical model testing of floating offshore structures. In: Proceedings of MTS dynamic positioning conference
13. Chakrabarti SK (2001) Hydrodynamic of offshore structures. WIT Press
14. DNV Offshore Standard DNV-OS-E301 (2013) Position mooring, Det Norske Veritas
15. Alhaz Uddin Md., Jameel M, Abdul Razak H, Saiful Islam ABM (2011) Response prediction of offshore floating structure using artificial neural network

# Surface Coating Processes: From Conventional to the Advanced Methods; a Short Review



A. D. Baruwa, Esther T. Akinlabi, and O. P. Oladijo

**Abstract** This study considers a short review of the coating methods from conventional methods to the recent methods. Surface coating is a surface engineering process by which the surface of a material is subjected to another overlay, such as powder, film or bulk for intended applications based on the coating material and the surface to be coated. Some view samples of convectional and advanced coating processes were considered including their evolving properties. Some of the disadvantages associated with each of the processes were also mentioned. Conclusions were drawn from the literature review, and future concerns were also enumerated.

**Keywords** Advanced Method · Convectional Method · Deposition · Surface Coating

## 1 Introduction

Surface coating is an engineering aspect that deals with surface layer deposition, process or modification in order to improve, protect or beautify the surface. Surface engineering is required in a state where the substrate could not perform its function as a result of the environment or stress in a particular application. Surface modification has found its application in the areas of food processing, aviation, medicine, defence, automobile, microelectronics and petrochemical machine tools, among others to serve the purpose of decoration, tribology resistance and surface-passivation applications [1]. Surface engineering can be achieved in three different ways; changing or altering surface chemistry, changing or altering the surface metallurgy, and addition of a top layer (surface coating). Altering of the surface chemistry occurs by changing the elementary composition of the material's surface such as

---

A. D. Baruwa (✉) · E. T. Akinlabi · O. P. Oladijo  
Department of Mechanical Engineering Science, University of Johannesburg, Johannesburg,  
South Africa  
e-mail: [darebaruwa@gmail.com](mailto:darebaruwa@gmail.com)

O. P. Oladijo  
Department of Chemical, Material and Metallurgical Engineering, Botswana International  
University of Science and Technology, Gaborone, Botswana

© Springer Nature Singapore Pte Ltd. 2020  
S. S. Emamian et al. (eds.), *Advances in Manufacturing Engineering*, Lecture Notes  
in Mechanical Engineering, [https://doi.org/10.1007/978-981-15-5753-8\\_44](https://doi.org/10.1007/978-981-15-5753-8_44)

carburization, vanadizing, boronizing, nitriding, laser alloying and ion implantation [2, 3]. In some processes, the engineered surfaces generate entirely new surfaces as a result of processing through lattice-structure formation, transformational behaviour or disruption. Changing of surface metallurgy happens by modifying the surface characteristics without altering the chemical matrix such as grain size-refinement, strain hardening, and transformation hardening. These characteristics are usually established by either thermal energy treatment (transformational hardening and grain refinement) and mechanical energy treatment (strain hardening) [4]. Surface coating, however, is a method by which another layer or multi-layer materials are deposited on the material's surface for the resistance or appearance improvement depending on the area of application which varies from soft to hard and metal to ceramic to organic materials [5].

Surface coating, therefore, could be classified into three categories based on the applications and functions. A coating can serve as a barrier coating by impeding the diffusion of oxygen through the film unto the underlying substrate and suppressing the ionic-solution transmission when densely prepared [6]. Some of these types of coatings often offer permeability to water without jeopardizing the resistance ability to the oxygen diffusivity and ionic-solution transmission [7]. Another category a coating can exhibit is an inhibitive nature. This is a method by which the substrate-primer interfacial environment is chemically modified for an associated application [8]. The pigment is usually added to the topcoat to release the passivating moieties and oxidizing ions into the matrix of the aqueous phase against the interface. This type of coatings is usually found in the aviation and automobile industries. Another category is the zinc-rich coating which is done by incorporating zinc dust into the pigment; this anodizes the coating and renders the substrate as a cathode [8]. The sacrificial nature of this type of coating poses it to be different from the barrier and inhibitive coatings because it undergoes corrosion to protect the substrate.

The coating methods vary from one another depending on the application, and the choice of a method is dependent on the type of materials to be deposited and the intended applications.

Both conventional coating and the advanced coating methods have been summarized in Table 1 by Sulzer [9].

This review focuses on conventional and advanced coating processes as well as the coating materials and their area of applications including their evolving properties.

## 2 Conventional Coating

The conventional coating is the type of coating that is very common and generally accepted and applied on the surface of a material. Few processes are mentioned below.

**Table 1** Lists of a few examples of types of coating and their associated features

Coating process	Typical coating thickness	Coating material	Characteristics	Examples
PVD	1–5 $\mu\text{m}$ (40–200 $\mu\text{in}$ )	Ti(C,N)	Wear resistance	Machine tools
CVD	1–50 $\mu\text{m}$ (40–2000 $\mu\text{in}$ )	SiC	Wear resistance	Fibre coating
Baked polymers	1–10 $\mu\text{m}$ (40–400 in)	Polymers	Corrosion resistance	Automobile
Thermal spray	0.04 – 3 mm (0.0015–0.12 in)	Ceramics and metallic alloys	Wear resistance, corrosion resistance	Bearing
Hard chromium plate	10–100 $\mu\text{m}$ (40–4000 $\mu\text{in}$ )	Chrome	Wear resistance	Rolls
Weld overlay	0.5–5 mm (0.02–0.2 in)	Steel, stellite	Wear resistance	Valves
Galvanize	1–5 $\mu\text{m}$ (40–200 $\mu\text{in}$ )	Zinc	Corrosion resistance	Steel sheet
Braze overlay	10–100 $\mu\text{m}$ (40–4000 $\mu\text{in}$ )	Ni–Cr–B–Si alloys	Very hard, dense surface	Shafts

## 2.1 Thermal Spray

It is often adopted where there is a requirement for hybrid improved properties such as wear/corrosion, corrosion/temperature, corrosion/oxidation or any combination. It can be easily defined as the coating process whereby functionalized molten or semi-molten particles are sprayed and deposited on the substrate [10]. FeCoCr and FeCoCrNi alloys were thermally sprayed on a steel structure by Bastos et al. [11] to improve the wear and corrosion resistance in an aggressive marine environment.

It was observed that porosity, usually associated with thermal spray coating process, was also evident.

## 2.2 Weld Overlay

This type of coating finds its application in the area of wear resistance by a simple process of overlaying high-strength steels. It is done by marrying the carbides abrasion resistance with the metal matrix toughness. Adopting tungsten inert gas (TIG) welding process, alloys of stellite 21, stellite 6 and Inconel 625 were overlaid on H11 steel substrate for the purpose of wear resistance applications by Kashani et al. [12], and improved wear resistance was observed more than the substrate material. Liyanage et al. [13] adopted plasma-transferred arc welding (PTAW) process to overlay different alloys of NiCrBSi varied by the concentration of chromium

constituent and made comparison with a typical NiCrBSi by understudying the influence of alloy chemistry on the microstructural and mechanical properties evolution, and it was observed that the permuted alloys of NiCrBSi showed an improved hardness. Materials such as Ultimet, Iron—Aluminide 316L SS, Inconel-625, Hastelloy-C22 and Stellite-6 were overlaid on ductile-wrought superalloy materials by Levin et al. [14] using plasma-transferred arc welding (PTAW) process, and it was clear after investigations that three overlays (Ultimet, Inconel-625, and 316L SS) were able to produce an improved high hardness and low wear rate which helped in defining a set of parameters for toughness determination.

This method of the coating process is very known to deposit a defect-free and efficient wear resistance structure [15], but it has been limited in application deployments as a result of its cost application [16].

### **2.3 Galvanize**

This process can be achieved in three ways; either by hot-dipping, zinc-enriched plating or by spraying. It is the type of coating process that is usually associated with corrosion resistance, and it has been widely deployed [17]. Anti-corrosion capability of galvanized steel treated by zinc was investigated by Pistofidis et al. [18], and it was observed that molecules of O<sub>2</sub>, H<sub>2</sub>O and CO<sub>2</sub> formed a denser and adherent film on the surface of the metal which caused a barrier to the propagation of aggressive ions and electrolyte because of their insolubility. Akamphon et al. [19] employed a process-based cost modelling (PBCM) to enhance corrosion resistance. This was achieved by reducing the zinc composition in the chemical matrix, and it was observed that corrosion resistance was still achievable at reduced zinc content and cost. The effect of continuous galvanizing and galvannealing by the hot-dip method on the morphology kinetics of interlayer formation was investigated by Chen et al. [20] that confirmed that the influence duration of the sample in the zinc bath, aluminium concentration and temperature defines the microstructural evolution of the sample and influences the diffusion path of the ions or electrolyte by defining the kinetic model for the inhibition layer growth. Also, in conclusion of Shibli et al. [21], the efficiency of a coating in a specific application is based on the process parameter factors which are determined by the in situ physicochemical control, characteristics of the structure and its applicability.

### **2.4 Hard Chromium Plate**

Corrosion and wear are the major characteristics of hard chromium coating or materials processing. Processes such as duplex chromium coating, crack-free coating and hard chromium coating were investigated for both corrosion and wear resistance reasons by Sohi et al. [22] and Dhondt et al. [23], and it was established

that hard chromium coating performed better in both wear and corrosion resistances than the other two processes investigated. Danilov et al. [24] investigated properties such as surface structure, wear behaviour, hardness and corrosion resistance of a nanocrystalline hard chromium deposited on stainless steel 403 from the trivalent chromium-rich in carbide and formic acid by adoption of electrodeposition process. It was discovered that trivalent chromium coating has improved wear resistance and corrosion resistance and has exhibited stable chemical structure but without significant hardness improvement in comparison with the hexavalent chromium process. The same results were reported by Liang et al. [25] using the aforementioned trivalent and hexavalent chromium coating processes.

Evidence of microcracks and porosity have limited the adoption of the process within the aviation and marine and other sectors [7, 8, 26, 27].

## **2.5 Braze Overlay**

The process works on the basis of overlaying a more cathodic material onto another substrate for corrosion or wear resistance. This is achieved by joining of dissimilar metals in order to function in a specific application. It involves heating the braze metal above the melting temperature and depositing it on the base material at a lower temperature. Improved corrosion resistance was achieved by brazing AISI 316 with the Cu-Ag-Ti and Cu-Ag-In-Ti in the investigation conducted by Kvrryan et al. [28]. Ban et al. [29] investigated the corrosion resistance of Inconel 625 brazing on ASTM A333 Gr6 material at different elevated temperatures and observed no iota of pitting corrosion on the surface of the base material.

Inconsistence in the bonding strength of this process has limited its application.

## **3 Advanced Coating Process**

This type of process usually involves a specialized machine(s) to carry out the target task. Most of the shortcomings usually exhibited by the conventional coating processes are near annihilation using advanced coating process.

### **3.1 Physical Vapour Deposition (PVD)**

It operates on the basis of ions bombardment to release atoms of depositing material from the target onto the substrate in a reaction chamber. The PVD is of four different processes which are dependent on the plasma make-up, the vaporized material's way of ion plating or plasma creation. The processes are: (a) low-voltage electron beam evaporation; (b) magnetron sputtering; (c) cathodic- arc deposition; and (d) triode

high-voltage electron beam evaporation [30]. It is an advanced coating method that is suitable for multiphase coating, multi-layer coating, multi-component coating and gradient coating [31]. This type of processes has a vast range of applications such as the deposition of piezoelectric films for dielectric materials, interconnection-wiring on semi-conductors, the deposition of wear and corrosion-resistant materials. In the investigation conducted by Lin et al. [32], titanium nitride/zirconium nitride (TiN/ZrN) was deposited on the AISI 304 via PVD in a simulated oxygen (O<sub>2</sub>)-rich environment of a regenerative fuel cell for improved corrosion and wear resistance. It was established that the process showed a nearly non-defective result, and it has been used to deposit metal unto the targets.

### 3.2 Chemical Vapour Deposition (CVD)

CVD process was developed to alleviate the least defects usually associated with PVD [33], although it is usually employed for thin film surface modification. It operates by pulsing the precursors into the reacting chamber accommodating preheated substrates, and the gaseous precursors react at near surface to form a film [34]. It has been very useful in diverse applications such as optics, microelectronics, synthesis, sensors, adhesion enhancements, nanoparticle water resistance with their applications, scalable resistant coatings and anti-corrosive coatings [35], and its applications range from scalable [36] to large-scale applications [37]. This process can be conducted in five ways which are detailed in Fig. 1

Benson et al. [38] performed an experiment to establish the five types of CVD process; pyrolysis or thermal decomposition ( $\text{CH}_3\text{SiCl}_3 \rightarrow \text{SiC} + 3\text{HCl}$ ), reduction ( $\text{WF}_6 + 3\text{H}_2 \rightarrow \text{W} + 6\text{HF}$ ), oxidation ( $\text{SiH}_4 + \text{O}_2 \rightarrow \text{SiO}_2 + 2\text{H}_2$ ), hydrolysis ( $2\text{AlCl}_3 + 3\text{H}_2\text{O} \rightarrow \text{Al}_2\text{O}_3 + 6\text{HCl}$ ) and coreduction ( $\text{TiCl}_4 + 2\text{BCl}_3 + 5\text{H}_2 \rightarrow \text{TiB}_2 + 10\text{HCl}$ ). CVD process shown to have improved seemingly impossible properties such as chemical and mechanical properties of asymmetrical structures, with any type of material that can exhibit gaseous state.

CVD coating process was adopted to deposit poly-para-xylylene organic compound on implantable medical devices. This was shown to have improved the mechanical stability and adhesion when compared with other known coating methods [39]. Ren et al. [40] deposited metamaterial niobium nitride (NbN) film doped with silver via CVD to achieve a hard hydrophobized surface, and a high level of hardness greater than 20 Gpa was found when investigated using Berkovich nanoindenter. The ability of the coating process to terminate hydrogen bond, oxidize or deoxidize made the process to be an advanced method as a result of inner chamber reaction or deposition process. It was used to achieve chemical and thermal stability and improve corrosion resistance when SiO<sub>x</sub> in combination with tetraethyl orthosilicate (TEOS) precursor in form of post-plasma coating was deposited as a thin film for enhanced photoactive receptions [41]. For nanoscale applications, Elias et al. [42] deposited a



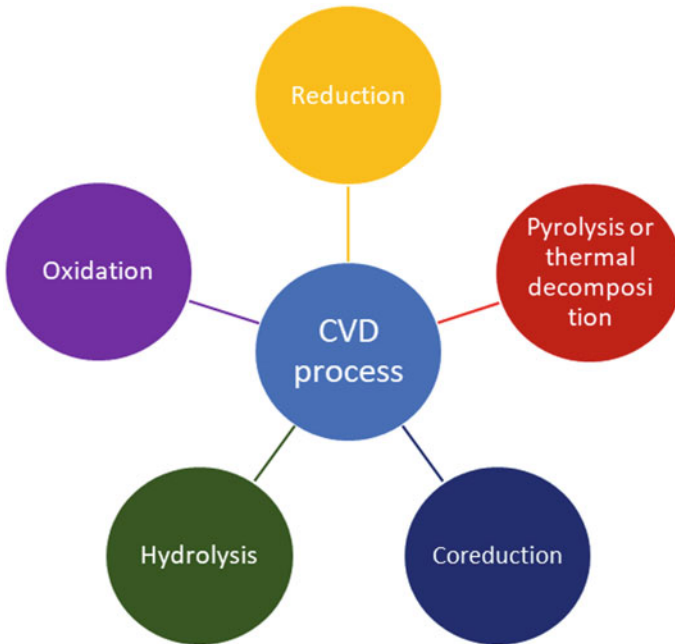


**Fig. 1** Outline of different types of the CVD process

thin carbon nanotube (CNT) material by thermal CVD method for improved mechanical properties; the material exhibited a stable microstructure, a high level of hardness and a superhydrophobic surface which could not be achieved via dipping process.

The high degree of roughness associated with this kind of process led to the development of another advanced coating process called atomic layer deposition.

### **3.3 Atomic Layer Deposition (ALD)**

ALD is an advanced and high-precision coating process of depositing or growing a film from precursors through a chemical reaction in sequential order in a self-limiting way [43]. It is an advanced state of CVD to eliminate the dichotomy limitations. The dichotomy is an issue related to the higher temperature of the precursors and the lower melting temperature of the substrate which frequently affects the integrity, stability and the quality of the coating or deposited film. The precursors of ALD are categorized according to the physical state into three: (1) gases; (2) high vapour pressure (from 5 to 40 Torr) at room temperature; and (3) low vapour pressure (less than 0.5 Torr) at room temperature.

Langereis et al. [44] developed tantalum nitride ( $\text{TaN}_x$ ) from the reaction of  $\text{Ta}[\text{N}(\text{CH}_3)_2]_5$  and  $\text{H}_2$ , as well as  $\text{H}_2\text{-N}_2$  and  $\text{NH}_3$  for conductivity and semi-conductivity resistance with adequate structural stability, deposited by the aid of ALD. An improved electrical resistance was registered, and a conductive  $\text{TaN}_x$  could be achieved when the film was deposited within temperature range of 150–250 °C. It is the most appropriate coating process for nanostructures, complex nanostructures and surface synthesis when it is used for diverse applications such as optics and photonic crystals, medicine, biomedical, nanopatterning, microelectronics and semiconductor conformal coating [45]. Hosseini et al. [46] used ALD to deposit  $\text{SiO}_2$  on a silicon wafer for microelectronic application and discovered that the film of 38 nm thickness behaved in an ohmic manner and caused a breakdown of approximately 10MV/cm.

In the same way, the CVD process has many types, and ALD process has different types which can be grouped into three: (1) batch (single wafer); (2) energy enhanced (thermal) and (3) spatial (temporal) [47]. The various types of ALD are presented in Table 2 and are based on their area of applications.

The ALD processes can also be classified according to chamber pressure starting from atmospheric to ultra-high vacuum [59], as well as the flow rate [60]. The process is classified in two ways: (a) pressures higher than or equal to 100 mTorr which operate under viscous/transition flow conditions; these types of reactors are similar to that of CVD reactor, and (b) pressures at high/ultra-high vacuum reactors which operate under molecular flow conditions; they are in resemblance with the molecular beam epitaxial reactors.

## 4 Conclusion

The conventional and advanced coating of the metal process has been considered in this short review. It has been established that in the conventional coating process, the type of process is dependent on the application, which also defines the kind of material to be deposited. The advanced coating process has shown to deposit wide varieties of material (both metals and non-metals) for different applications. Different improved properties associated with each process were highlighted. Shortcomings of each process are listed, and the reasons for seeking an alternative method were listed. However, some gaps are observed in the case of advanced coating process;

- (a) There are large-scale productions with advanced coating process, but there are no provisions for large structures to be processed like conventional coatings.
- (b) The functionally graded deposition has not been widely exploited using advanced coating process
- (c) Although the future of manufacturing is tending towards nanoprocessing, the advanced coating processes have not seen much attention for processes above 00  $\mu\text{m}$ .

**Table 2** Types of atomic layer deposition with associated processes and area of applications

Type	Process	Attribute
Thermal ALD process (TALD)	The substrate is stationary, and the precursor is pulsed into the chamber	This is the best-known ALD; it is based on a high-quality industrial deposition technique [48]
Plasma ALD	The energy is delivered by distributing power either directly to the base material (substrate) stage	This plasma is made of free, charged particles and many reactive atomic or molecular gas-phase species [44, 49, 50]
Spatial ALD process (SALD)	The reactor of the spatial ALD is separate; it moves underneath the substrate below the target precursor by depositing precursors at atmospheric pressure up to 70 nm/min deposition rate	This a good method to use for the deposition of industrial high-quality metal oxides on a substrate [48]
Particle ALD	It deposits a conformed nanothick coating on the particles of the substrate, with the aid of a fluidized bed reactor [56]	It is a self-limiting reaction technique that can meritoriously functionalize the nanoparticles' surface without showing a significant shift in particle size, loss or the surface area of the powder [57]
Polymer ALD	It is a self-limiting method has been described as an alternating vapour deposition polymerization (AVDP) [33]	It is very helpful in growing polymeric thin film. The chemistry of the polymer ALD usually comprises a two-step AB reaction cycle, using homo-bifunctional reactants [58]
Metal ALD	This type of reactor operates on the generation of hydrogen radicals that would reduce the precursors of either the metal or the semiconductor. This type of ALD is usually adopted whereby the thermal ALD could be difficult to employ, such as single-element ALD material (metal and semiconductors) [51, 52]. It is operated on a low-temperature growth that would accommodate “back end of the line” (BEOL) [43]	This type of deposition process is useful when there is a need for a process with an excellent conformability to the nanoscale base structure – lower than 100 nm [53–55]

## References

1. Chopra KL, Kaur I (1983) Surface engineering applications, In: Chopra KL, Kaur I (eds) *Thin film device applications*. Springer, Boston, pp 255–273
2. Hutchings I, Shipway P, Halada GP, Clayton CR (2017) *Surface engineering*. In: *Tribology*, 2nd edn. Elsevier, Amsterdam, pp 237–281
3. Dwivedi DK (2018) Surface engineering: enhancing life of tribological components
4. Dwivedi DK, Dwivedi DK (2018) Surface engineering by changing the surface metallurgy. In: *Surface engineering*, pp 73–90
5. Podgurski V et al (2012) Coatings and surface engineering. *Industry oriented research. Est J Eng* 18(3):176
6. Günthner M et al (2011) High performance environmental barrier coatings, part I: passive filler loaded SiCN system for steel. *J Eur Ceram Soc* 31:3003–3010
7. Kuzminova A, Shelemin A, Petr M, Kylian O, Biederman H (2013) Barrier coatings on polymeric foils for food packaging. In: *Wds*, pp 128–133
8. Van Droffelaar H, Atkinson JTN (1995) Corrosion and its control. *Corrosion* 332
9. Metco S (2013) An introduction to thermal spray
10. Fauchais P, Vardelle A (2012) Thermal sprayed coatings used against corrosion and corrosive wear. In: *Advanced plasma spray applications*, pp 3–39
11. Antunes FJ, dos de Sá Brito VRS, Bastos IN, Costa HRM (2013) Characterization of FeCr and FeCoCr alloy coatings of carbon steels for marine environment applications. *Appl Adhes Sci* 1(1):1–10
12. Kashani H, Amadeh A, Ghasemi HM (2007) Room and high temperature wear behaviors of nickel and cobalt base weld overlay coatings on hot forging dies. *Wear* 262(7–8):800–806
13. Liyanage T, Fisher G, Gerlich AP (2010) Influence of alloy chemistry on microstructure and properties in NiCrBSi overlay coatings deposited by plasma transferred arc welding (PTAW). *Surf Coatings Technol* 205(3):759–765
14. Levin BF, Dupont JN, Marder AR (1998) Solid particle erosion resistance of ductile wrought superalloys and their weld overlay coatings. *J Mater Sci* 33(8):2153–2163
15. Rozmus-Górnikowska M, Cieniek L, Blicharski M, Kusiński J (2014) Microstructure and microsegregation of an inconel 625 weld overlay produced on steel pipes by the cold metal transfer technique. *Arch Metall Mater* 59(3):1081–1084
16. Mendez PF et al (2014) Welding processes for wear resistant overlays. *J Manuf Process* 16(1):4–25
17. Mackowiak J, Short NR (1979) Metallurgy of galvanized coatings. *Int Met Rev* 24(1):1–19
18. Pistofidis N, Vourlias G, Konidaris S, Pavlidou E, Stergiou A, Stergioudis G (2006) Microstructure of zinc hot-dip galvanized coatings used for corrosion protection. *Mater Lett* 60(6):786–789
19. Akamphon S, Sukkasi S, Boonyongmaneerat Y (2012) Reduction of zinc consumption with enhanced corrosion protection in hot-dip galvanized coatings: a process-based cost analysis. *Resour Conserv Recycl* 58:1–7
20. Chen L, Fourmentin R, McDermid JR (2008) Morphology and kinetics of interfacial layer formation during continuous hot-dip galvanizing and galvannealing. *Metall Mater Trans A Phys Metall Mater Sci* 39(9):2128–2142
21. Shibli SMA, Meena BN, Remya R (2015) A review on recent approaches in the field of hot dip zinc galvanizing process. *Surf Coatings Technol* 262:210–215
22. Sohi MH, Kashi AA, Hadavi SMM (2003) Comparative tribological study of hard and crack-free electrodeposited chromium coatings. *J Mater Process Technol* 138(1–3):219–222
23. Dhondt M, Shubina V, Homette R, Chirani SA, Calloch S (2018) Effect of mechanical (monotonic and cyclic) stress on the corrosion resistance of chromium-plated steel rods. *Procedia Eng* 213:598–605
24. Danilov FI, Protsenko VS, Gordiienko VO, Kwon SC, Lee JY, Kim M (2011) Nanocrystalline hard chromium electrodeposition from trivalent chromium bath containing carbamide and formic acid: structure, composition, electrochemical corrosion behavior, hardness and wear characteristics of deposits. *Appl Surf Sci* 257(18):8048–8053

25. Liang A, Li Y, Liang H, Ni L, Zhang J (2017) A favorable chromium coating electrodeposited from Cr(III) electrolyte reveals anti-wear performance similar to conventional hard chromium. *Mater Lett* 189:221–224
26. Daure JL, Carrington MJ, Shipway PH, McCartney DG, Stewart DA (2018) A comparison of the galling wear behaviour of PVD Cr and electroplated hard Cr thin films. *Surf Coatings Technol* 350(March):40–47
27. Sarraf SH, Soltanieh M, Aghajani H (2016) Repairing the cracks network of hard chromium electroplated layers using plasma nitriding technique. *Vacuum* 127:1–9
28. Kvyran A et al (2016) Microgalvanic corrosion behavior of Cu-Ag active braze alloys investigated with SKPFM. *Metals (Basel)* 6(4):91
29. Ban S-D, Shin Y-T, Lee SR, Lee H-W (2016) Corrosion resistance of Inconel 625 overlay welded inside pipes as a function of heat treatment temperature. *Int J Electrochem Sci* 11:7764–7774
30. Sproul WD (2002) Multilayer, multicomponent, and multiphase physical vapor deposition coatings for enhanced performance. *J Vac Sci Technol Vac Surf Film* 12(4):1595–1601
31. Holleck H, Schier V (1995) Multilayer PVD coatings for wear protection. *Surf Coatings Technol* 76–77(1995):328–336
32. Lin MT, Wan CH, Wu W (2014) Enhanced corrosion resistance of SS304 stainless steel and titanium coated with alternate layers of TiN and ZrN in a simulated O<sub>2</sub>-rich environment of a unitized regenerative fuel cell. *Int J Electrochem Sci* 9(12):7832–7845
33. Pedersen H, Elliott SD (2014) Studying chemical vapor deposition processes with theoretical chemistry. *Theor Chem Acc* 133(5):1–10
34. ASM International (2010) Introduction to chemical vapour deposition
35. Dong J, Wang A, Ng KY S, Mao G (2006) Self-assembly of octadecyltrichlorosilane monolayers on silicon-based substrates by chemical vapor deposition. *Thin Solid Films* 515(4):2116–2122
36. Su M, Zheng B, Liu J (2000) A scalable CVD method for the synthesis of single-walled carbon nanotubes with high catalyst productivity
37. Yang P, Zheng B, Liu J (2010) Large scale Cvd synthesis of single-walled carbon nanotubes. *Chem Nanostructured Mater* 101–125
38. Benson J, Boukhalfa S, Magasinski A, Kvit A, Yushin G (2012) Chemical vapor deposition of aluminum nanowires on metal substrates for electrical energy storage applications. *ACS Nano* 6(1):118–125
39. Hogg A (2014) Development and characterisation of ultrathin layer packaging for implantable medical devices. University of Bern
40. Ren P et al (2017) Tailoring the surface chemical bond states of the NbN films by doping Ag: achieving hard hydrophobic surface. *Appl Surf Sci* 407:434–439
41. Post P, Jidenko N, Weber A, Borra J-P (2016) Post-plasma SiO<sub>x</sub> coatings of metal and metal oxide nanoparticles for enhanced thermal stability and tunable photoactivity applications. *Nanomaterials* 6(5):91
42. Koumoulos EP, Charitidis CA (2017) Surface analysis and mechanical behaviour mapping of vertically aligned CNT forest array through nanoindentation. *Appl Surf Sci* 396:681–687
43. Kim H (2003) Atomic layer deposition of metal and nitride thin films: current research efforts and applications for semiconductor device processing. *J Vac Sci Technol B Microelectron Nanom Struct* 21(6):2231
44. Langereis E, Knoops HCM, Mackus AJM, Roozeboom F, Van De Sanden MCM, Kessels WMM (2007) Synthesis and in situ characterization of low-resistivity films by remote plasma atomic layer deposition. *Cit J Appl Phys* 102:83517
45. Knez M, Nielsch K, Niimistö L (2007) Synthesis and surface engineering of complex nanostructures by atomic layer deposition. *Adv Mater* 19(21):3425–3438
46. Hosseini SF, Soleimani MR, Nikkhah M (2018) Chitosan/sodium tripolyphosphate nanoparticles as efficient vehicles for antioxidant peptidic fraction from common kilka. *Int J Biol Macromol* 111(8):730–737
47. Locquet J-P, Marchiori C, Sousa M, Fompeyrine J, Seo JW (2006) High-K dielectrics for the gate stack. *J Appl Phys* 100(5):051610

48. Werner F, Stals W, Görtzen R, Veith B, Brendel R, Schmidt J (2011) High-rate atomic layer deposition of  $\text{Al}_2\text{O}_3$  for the surface passivation of Si solar cells. *Energy Procedia* 8:301–306
49. Potts SE, Kessels WMM (2013) Energy-enhanced atomic layer deposition for more process and precursor versatility. *Coord Chem Rev* 257(23–24):3254–3270
50. Knoops HCM et al (2015) Atomic layer deposition of silicon nitride from Bis(*tert* - butylamino)silane and  $\text{N}_2$  plasma. *ACS Appl Mater Interfaces* 7(35):19857–19862
51. MacKus AJM, Garcia-Alonso D, Knoops HCM, Bol AA, Kessels WMM (2013) Room-temperature atomic layer deposition of platinum. *Chem Mater* 25(9):1769–1774
52. George SM (2010) Atomic layer deposition: an overview. *Chem Rev* 110(1):111–131
53. Aaltonen T, Ritala M, Sajavaara T, Keinonen J, Leskelä M (2003) Atomic layer deposition of platinum thin films. *Chem Mater* 15(9):1924–1928
54. Christensen ST et al (2010) Supported Ru-Pt bimetallic nanoparticle catalysts prepared by atomic layer deposition. *Nano Lett* 10(8):3047–3051
55. Hämäläinen J, Ritala M, Leskelä M (2014) Atomic layer deposition of noble metals and their oxides. *Chem Mater* 26(1):786–801
56. King DM, Liang X, Carney CS, Hakim LF, Li P, Weimer AW (2008) Atomic layer deposition of UV-absorbing ZnO films on  $\text{SiO}_2$  and  $\text{TiO}_2$  nanoparticles using a fluidized bed reactor. *Adv Funct Mater* 18(4):607–615
57. Didden AP, Middelkoop J, Besling WFA, Nanu DE, van de Krol R (2014) Fluidized-bed atomic layer deposition reactor for the synthesis of core-shell nanoparticles. *Cit Rev Sci Instrum* 85:13905
58. George SM, Yoon B, Dameron AA (2009) Surface chemistry for molecular layer deposition of organic and hybrid organic–inorganic polymers. *Acc Chem Res* 42(4):498–508
59. Sinha AK (2006) Design and characterization of materials and processes for area selective atomic layer deposition
60. Wang W, Xiong K, Wallace RM, Cho K (2012) High-k gate dielectrics for CMOS technology. *High-k Gate Dielectr C Technol* 407–431

# Surface Coating Processes: From Conventional to Silane Organic Compound Applications: Recent and Prospects



A. D. Baruwa, Esther T. Akinlabi, O. P. Oladijo, and F. M. Mwema

**Abstract** Silane is a chemical compound that has been widely deployed for both inorganic and organic applications. It has the capability to unilateral function or gets doped for optimal ability. This review enumerates where silane compounds have found its application in diverse engineering applications and stated the areas where the improvements are pronounced. It also states the potential application they can be employed. The future research and expected improved properties that can make the compound materials to potentially replace known carcinogenic coatings are mentioned.

## 1 Introduction

Silane can be described as a silicon compound that has a hydrolytic center that can react with an inorganic substrate such glass. Textile, metal, silicon, plastics, fabrics ceramics, silicon (to mention a few) chemically in order to form a stable covalent bond and also has the capacity to substitute organic branch which can be used to make alteration between the inorganic substrate and the physical interaction of the organic compound.

The silane film preparation, modification and abilities have been investigated in several ways; among them is the development of silicon nanocrystals from two silane precursors- pure silane ( $\text{SiH}_4$ ) and silicon tetrachloride ( $\text{SiCl}_4$ ) through non-thermal plasma synthesis for structural stability determination; a distortion in the Si–Si chain (silicon) and destabilized structural formation was observed as a result of bombardment of nanocrystal with chlorine atoms which terminated the particles generation from  $\text{SiCl}_4$  [1]. In another way, Arkhireeva et al. [2] experimented a versatile hybrid of

---

A. D. Baruwa (✉) · E. T. Akinlabi · O. P. Oladijo · F. M. Mwema  
Department of Mechanical Engineering Science, University of Johannesburg, Johannesburg,  
South Africa  
e-mail: [darebaruwa@gmail.com](mailto:darebaruwa@gmail.com)

O. P. Oladijo  
Department of Chemical, Material and Metallurgical Engineering, Botswana International  
University of Science and Technology, Palapye, Botswana

organic-silica nanoparticles of silsesquioxane prepared organically modified precursors, and it was observed that a higher concentration of emulsifier can be achieved by adopting a non-ionic surfactant and, also, a 3 nm spherical nanoparticle can be achieved. They discovered that hydrolytic and non-hydrolytic showed an effect on the surface chemistry of the particles which was established as a result of solvent polarity during the synthesis. Another method was developed by Brook et al. [3] by developing sugarsilane and alkoxysilane precursors from sugar and its alcohol; it was observed that the curing behaviour of sugarsilanes and other alkoxysilanes such as tetraethylorthosilicate (TEOS) and tetramethylorthosilicate (TMOS) is different by showing a distinction in pH and solubility in water solubility. Silane precursors have also been developed from dimethyldiethoxysilane and bis(trimethoxysilylpropyl) amine doped in silica aerogels and were used to examine the recovery effect by Randall et al. [4]. Soares et al. [5] use lipase activity prepared from tetraethoxysilane (TEOS), methyltrimethoxysilane (MTMS) and polydimethylsilane (PDMS) to produce an alkyl-substituted silane that was used to study the influence of the precursor in the substrate. It was registered that the performance of all the samples was improved as a result of encapsulated lipase, as well, the surface ability was enhanced [6].

In this study different silanes applications will be reviewed, and area of success will be highlighted.

## 2 Chemistry of Silane Deposition

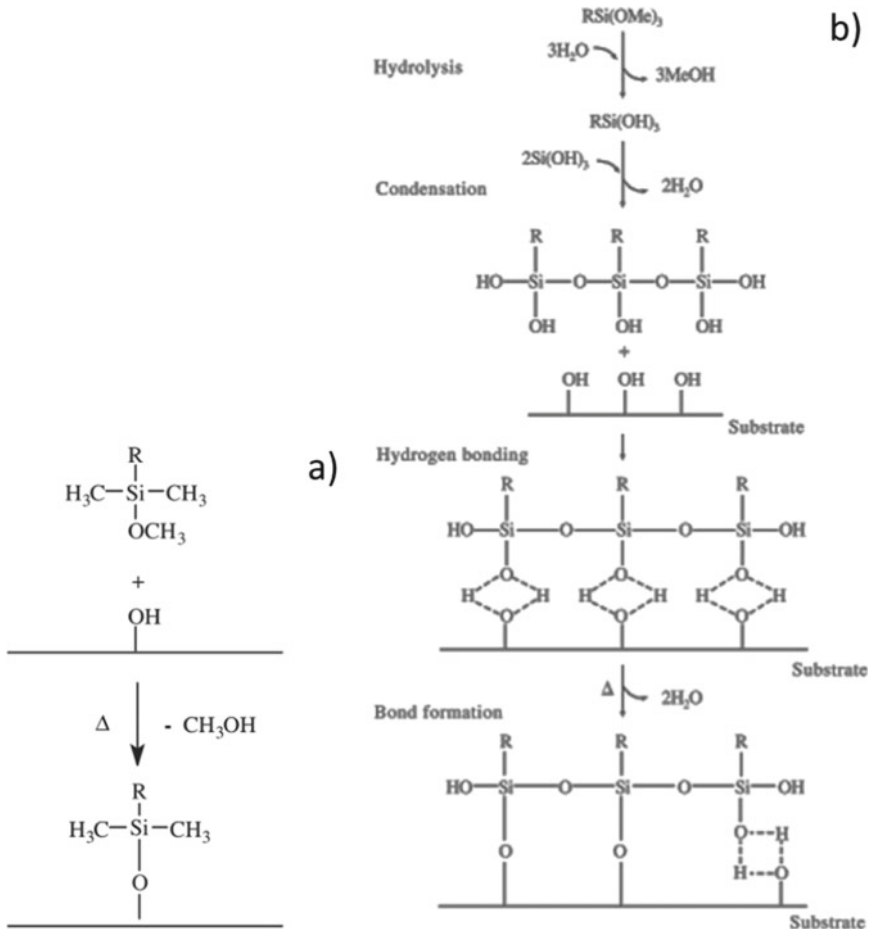
The chemistry behind deposition and its eventual application of silane compound are categorized into two; a hydrolytic deposition and an anhydrous deposition by Arles [7]. The chemistry is represented in Fig. 1.

Figure 1a described the chemistry of surface modification by adopting the anhydrous deposition condition, this is very effective in the absence of catalysis except for the methoxysilanes which are synonymous adequate and efficient vapour deposition and monolayer deposition.

Figure 1b, however, showed a detailed hydrolytic condition process stage. Hydrolysis served as the first stage with liable ( $\text{RSiOM}_e$ ),  $3\text{M}_e\text{OH}$  and  $\text{RSi}(\text{OH})_3$ , the second stage entailed the condensation of oligomer's reaction which formed a bond with the surface hydroxyl group of the substrate; this formation is lead to the third stage by producing a hydrogen bond, last stage involved the formation of a covalent bond with the substrate during the curing process.

This type of deposition in Fig. 1 led Senkevich et al. [8] to investigate short-chain chemistry of alkoxysilane molecular layer for structural growth; a good metallic diffusion barrier was discovered after it possessed a molecular silane layer dielectric control as a function of surface chemistry. Jonsson et al. [9] investigated the role of deposited silane-dextran chemistry the role of silane chemistry in the lateral flow of the polymer chip. In their conclusion, hydrophilization and immobilization extended the life span of the cycloolefin-copolymer test chips.





**Fig. 1** Reaction process of organosilane compounds with a substrate using **a** an anhydrous method and **b** the hydrolytic method [7]

The silane chemistry was also used to define the type of silane compound and this is based on the functionality of the silane compound itself; (a) non-functional silane compound and (b) functional silane compound. non-functional silane compound is known to have two hydrolyzable X group molecules at either end of the carbon chain [10]. This is termed as a crosslinking agent but lacked good properties such as strong adhesion. It only portrayed a non-reactive group, which interacted or reacted with the inorganic surfaces [11]. Functional silane compound, however, has general formula  $X_3\text{Si}(\text{CH}_2)_n\text{Y}$ , where X could be any of the groups of ethoxy ( $\text{OC}_2\text{H}_5$ ) or methoxy ( $\text{OCH}_3$ ) group which could readily hydrolyze while Y is the organofunctional group like epoxy or chlorine [12].

### 3 Recent Application of Silane Compounds

Application of organic silane is based on the intention on the surface behavior of a material which could be hydrophilic/oleophilic, hydrophobic/oleophobic, superhydrophobic/superoleophobic. Hydrophilic is a state of a solid's surface, which with water makes an angle less than  $90^\circ$  when deposited [13], while the hydrophobic surface has a water contact angle greater than  $90^\circ$  but less than  $150^\circ$  [14] and superhydrophobic is a solid state, where the surface of the material has a water contact angle above  $150^\circ$  [15]. These states of the surface behaviour inform the subjected applications.

**Biomedical:** A thin  $\text{TiO}_2$ -modified 3-glycidoxypopyl)-trimethoxysilane (GPTMS) coating was applied on the surface AZ31 and ZE41 Mg alloys for biodegradable implants by Córdoba et al. [16].  $\gamma$ -methacryloxypropyltrimethoxysilane, vinyltriisopropoxysilane, and Tris (3-trimethoxysilylpropyl)isocyanurate coatings on titanium implants were investigated by Matinlinna et al. [17] for medical dental application. Tan et al. [18] also deposited Octadecyltrichlorosilane (OTS), 3-aminopropyltriethoxysilane (APTES) and glycidoxypopyltrimethoxysilane (GPTMS) on the surface of titanium to improve the shear strength for the purpose dental implant.

**Anti-stiction:** for a surface to show anti-stiction properties, Van der Waals, electrostatic and capillary forces are to be overcome. Octadecyltrichlorosilane (OTS) self-assembled monolayer and dichlorodimethylsilane (DDMS) employed octadecyltrichlorosilane (OTS) self-assembled monolayer and dichlorodimethylsilane (DDMS) monolayer silanes were employed by Ashurst et al. [19] to improve the anti-stiction properties of glass substrate for micro-mechanical structural applications. The surface of a silicon wafer substrate was improved by the addition of 1H, 1H, 2H, 2H-perfluorodecyltrichlorosilane and octadecyltrichlorosilane by showing enabled anti-stiction, improved wear resistance, high-temperature tolerance, even in oxygen-rich environments [20].

**Energy:** Yan et al. [21] achieved a self-cleaning coating on a solar panel for power generation using 2-[acetoxo (polyethyleneoxy) propyl] triethoxysilane (SIA) while Matin et al. [22] used octadecyltrichlorosilane (ODTS) to achieve a self-cleaning solar panel. The efficiency of a solar cell from dye synthesis was improved using a dry solvent with alkyl(trialkoxo)silanes by Spivack et al. [23]; while octyl(trimethoxy)silane was used to increase the optimum performance of the solar cell. A hydrogenated amorphous silicon was used by Shin et al. [24] for a solar cell application, and by adopting the Urbach energy-silane depletion-fraction relationship, homogeneous film deposited from the optimization improved the photon capturing on the solar panel, as well as the photovoltaic conversion efficiency. Han et al. [25] showed an improved hydrogen generation fuel cell by deposition of silane such as 1,1,3,3,5,5-hexachloro-1,3,5-trisilacyclohexane, 1,1,4,4-tetrachloro-2,5-bis(trichlorosilyl)-1,4-disilacyclohexane, 1,1,1,3,3,5,5,5-octachloro-1,3,5-trisilapentane, 1,1,2-tris(trichlorosilyl) ethane, and 1,2,3-tris(trichlorosilyl)propane on the cell container. Kim et al. [26] used

carbonsilane-based hydrides to dope 1,3,5-trisilacyclohexane silanes to achieve a fast releasing hydrogen releasing fuel cell while Brunel [27] used polysilane to achieve the same result.

**Anti-icing:** This is a method by which a chemical or material is deposited on a surface of a material to prevent a bond between the ice and the surface. Matsumoto et al. [28] deposited  $\gamma$ -aminopropyltri-ethoxysilane and triethoxy- 1H,1H,2H,2H-tridecafluoro-n-octylsilane to suppress the force of adhesion that exist between the glass and copper surfaces and the ice. 1H,1H,2H,2H- perfluorodecyltriethoxysilane and methyltrimethoxy- silane were deposited on AISI 1045 steel surface nullify the adhesion force between the metal and icing in an extreme condensing environment [29].

**Anti-reflective:** This type of application is adopted to reduce the reflection of surface without loosing its functionality. Keun et al. [30] deposited tetraethoxysilane (TEOS) via spin-coating on a quartz substrate which showed more broadened band. Hydrolyzed-polymerized tetraethoxysilane (TEOS) was also employed for antireflective and electromagnetic-wave-shielding coating; it showed a better result by suppressing the absorption of the colloid growth on the deposited film; this film has been deployed on a large industrial scale coating on glass panel for CRTsKeu [31].

**Coupling agent:** Some silane compounds have also demonstrated to possess high Van der Waals forces by showing to be a good coupler. Zhu et al. [32] used Vinyltriethoxysilane (VTES) produced by a dry process to improve the coupling capability between magnesium hydroxide sulfate hydrate (MHSH) whiskers and with the polymer. Octadecyltrichlorosilane (OTS), 3-aminopropyltriethoxysilane (APTES) and glycidoxypropyltrimethoxysilane (GPTMS) were used as coupling agents to adhere titanium to biomimetic hydroxyapatite film strictly for biomedical implants [18]. 3-aminopropyltrimethoxysilane (APTMS) and trimethylchlorosilane (TMCS) were adopted as adhesion between polyethersulfone (PES) and MCM-41 mesoporous together; it showed an improved mechanical and thermal strength, as well as improved gas separation techniques [33].

## 4 Prospects in the Application of Silane Compounds

**Corrosion resistance:** Corrosion can be termed as the degradation or systemic breakdown of material properties as a result of chemical or electrochemical process or attack subject to the environment or conditions in which such material functions [34]. Most common materials are woods, concrete, plastic, polymer, ceramics and metals to mention a few. Metallic corrosion is governed by the breakdown of chemical composition to form oxides and it is a menace that needs to be militated against. Many achievements have been made with regards to limiting corrosion propagation; improving alloying compound and coating of the surface have been widely accepted. Most of the coating materials are chromium-based and eventual breakdown of the chromium compounds leads to carcinogens [168]. Green coatings have been sought as an alternative material to the carcinogenic chromium-based coating

[169]. Some silanes have found their applications in this regards, but none has been able to withstand the extreme conditions to which chromium based coatings have been subjected.

Geoger et al. [35] used perfluorooctyltriethoxy silane to coat a nuclear turbine blade made of 9Cr–1Mo ferritic steel for corrosion resistance; it was observed that the silane compound failed at extreme temperature. Chico et al. [36] used 3-aminopropyltriethoxysilane ( $\gamma$ -APS), 3-glycidoxypropyltrimethoxysilane ( $\gamma$ -GPS) and bis(3-triethoxysilylpropyl)amine to pretreat the surface of a steel panel, and bis-( $\gamma$ - trimethoxysilylpropyl)amine (BAS) and 1,2-bis(triethoxysilyl)ethane (BTSE) silane as a topcoat to prevent the steel from corrosion. Vaezis et al. [37] and Zhu et al. [38] deposited 3-Aminopropyl triethoxysilane(APTES), modified with graphene oxide on mild steel and aluminium in order to prevent corrosion propagation. 3-glycidoxy-propyl-trimethoxy-silane (3-GPTMS) and methyl-triethoxy-silane (MTES) modified with lanthanum triflate and silica nanoparticles were used to protect the surface of low carbon steel from corrosion when subjected to more than 168 h electrochemistry [39]. A Zr-doped Bis-[trimethoxysilylpropyl]amine (BAS) and vinyltriactoxysilane (VTAS) were used to coat the carbon steel, in order to improve the self-healing property of the steel [40]. In all these silane compounds, there was no major report on a silane compound that has combined chemical and mechanical viability in the literature making it the subject of future investigation.

## 5 Conclusion

Silane compound as a material has been described. The chemistry behind the silane deposition or coating were analyzed and the two types were logically presented. The recent achievements in the adoption of silanes compounds for diverse applications were mentioned including their improved properties. The prospect of the silane compound in serving as alternative material for the replacement of chromium-based coatings were shown while few of the successfully deposited silanes were mentioned.

However, from the literature survey, with regards to the prospect of silane, none of the developed and applied silane showed to have combined improved properties which the chromium-based coatings have demonstrated in the past. There are achievements made in the chemical, microstructural, and in some cases, electrochemical properties of silanes, but little or no achievement have been made in the area of mechanical stability. The future research should focus more on the mechanical and thermal stability of the silane compounds in applications.

## References

1. Yasar-Inceoglu O, Lopez T, Farshihagro E, Mangolini L (2012) Silicon nanocrystal production through non-thermal plasma synthesis: A comparative study between silicon tetrachloride and silane precursors. *Nanotechnology* 23(25):255604
2. Arkhireeva A, Hay JN, Oware W (2005) A versatile route to silsesquioxane nanoparticles from organically modified silane precursors. *J Non Cryst Solids* 351(19–20):1688–1695
3. Brook MA, Chen Y, Guo K, Zhang Z, Brennan JD (2004) Sugar-modified silanes: Precursors for silica monoliths. *J Mater Chem* 14(9):1469–1479
4. Randall JP, Meador MAB, Jana SC (2013) Polymer reinforced silica aerogels: effects of dimethyldiethoxysilane and bis(trimethoxysilylpropyl)amine as silane precursors. *J Mater Chem A* 1(22):6642–6652
5. Soares CMF, Dos Santos OA, Olivo JE, De Castro HF, De Moraes FF, Zanin GM (2004) Influence of the alkyl-substituted silane precursor on sol-gel encapsulated lipase activity. *J Mol Catal B Enzym* 29(1–6):69–79
6. Sanz-Moral LM, Rueda M, Nieto A, Novak Z, Knez Ž, Martín Á (2013) Gradual hydrophobic surface functionalization of dry silica aerogels by reaction with silane precursors dissolved in supercritical carbon dioxide. *J Supercrit Fluids* 84:74–79
7. B. Ardes, “Gelest - Hydrophobicity, hydrophilicity and silane surface modification,” 2011
8. Senkevich JJ, Mitchell CJ, Yang GR, Lu TM (2002) Surface chemistry of mercaptan and growth of pyridine short-chain alkoxy silane molecular layers. *Langmuir* 18(5):1587–1594
9. Jönsson C et al (2008) Silane-dextran chemistry on lateral flow polymer chips for immunoassays. *Lab Chip* 8(7):1191–1197
10. Franquet A, Le Pen C, Terry H, Vereecken J (2003) Effect of bath concentration and curing time on the structure of non-functional thin organosilane layers on aluminium. *SPEC, Electrochim Acta* 48(9):1245–1255
11. Qiao W et al (2016) The Role of Silane Coupling Agents and Universal Primers in Durable Adhesion to Dental Restorative Materials - a Review. *Curr Oral Heal Reports* 3(3):244–253
12. BinSabi MH, Galal A, Al Kharafi FM, Abditon M (2019) Improving corrosion protection of Al97Mg3alloy in neutral sodium chloride solution by 1,2-bis(trimethoxysilyl)ethane coating. *Appl Surf Sci* 465(8859):143–153
13. Ma Y, Cao X, Feng X, Ma Y, Zou H (2007) Fabrication of super-hydrophobic film from PMMA with intrinsic water contact angle below 90°. *Polymer (Guildf)* 48(26):7455–7460
14. Zhu M, Zuo W, Yu H, Yang W, Chen Y (2006) Superhydrophobic surface directly created by electrospinning based on hydrophilic material. *J Mater Sci* 41(12):3793–3797
15. Fridgen TD, McMahon TB, MacAleese L, Lemaire J, Maitre P (2004) Infrared spectrum of the protonated water dimer in the gas phase. *J Phys Chem A* 108(42):9008–9010
16. Córdoba LC, Montemor MF, Coradin T (2016) Silane/TiO<sub>2</sub>coating to control the corrosion rate of magnesium alloys in simulated body fluid. *Corros Sci* 104:152–161
17. Matinlinna JP, Lassila LV, Vallittu PK (2004) The effect of a 3-methacryloxypropyltrimethoxysilane and vinyltriisopropoxysilane blend and tris(3-trimethoxysilylpropyl)isocyanurate on the shear bond strength of composite resin to titanium metal. *Dent Mater* 20:804–813
18. Tan G et al (2016) Effect of amino-, methyl- and epoxy-silane coupling as a molecular bridge for formatting a biomimetic hydroxyapatite coating on titanium by electrochemical deposition. *J Mater Sci Technol* 32(9):956–965
19. Ashurst WR, Yau C, Carraro C, Maboudian R, Dugger MT (2001) Dichlorodimethylsilane as an anti-stiction monolayer for MEMS: A comparison to the octadecyltrichlorosilane self-assembled monolayer. *J Microelectromechanical Syst* 10(1):41–49
20. Maboudian R, Ashurst WR, Carraro C (2000) Self-assembled monolayers as anti-stiction coating for MEMS: characteristics and recent progress. *Sensors, Actuators A, Phys* 82:219–223
21. Yan H, Yuanhao W, Hongxing Y (2017) TEOS/silane coupling agent composed double layers structure: a novel super-hydrophilic coating with controllable water contact angle value. *Appl Energy* 185:2209–2216

22. Matin A, Merah N, Ibrahim A (2016) Superhydrophobic and self-cleaning surfaces prepared from a commercial silane using a single-step drop-coating method. *Prog Org Coatings* 99:322–329
23. Spivack J, Siclován O, Gasaway S, Williams E, Yakimov A, Gui J (2006) Improved efficiency of dye sensitized solar cells by treatment of the dyed titania electrode with alkyl(trialkoxo)silanes. *Sol Energy Mater Sol Cells* 90(9):1296–1307
24. Shin C et al (2013) Optimization of intrinsic hydrogenated amorphous silicon deposited by very high-frequency plasma-enhanced chemical vapor deposition using the relationship between Urbach energy and silane depletion fraction for solar cell application. *Thin Solid Films* 547:256–262
25. Han WS et al (2011) Silane-based hydrogen storage materials for fuel cell application: Hydrogen release via methanolysis and regeneration by hydride reduction from organosilanes. *Int J Hydrogen Energy* 36(19):12305–12312
26. Kim Y, Yoon CW, Han WS, Kang SO, Nam SW (2012) A portable power-pack fueled by carbonsilane-based chemical hydrides. *Int J Hydrogen Energy* 37(4):3319–3327
27. Brunel JM (2017) Polysilanes: the grail for a highly-neglected hydrogen storage source. *Int J Hydrogen Energy* 42(36):23004–23009
28. Matsumoto K, Sakaguchi T, Tsubaki D, Kubota H, Minamiya K, Sekine K (2015) Investigation on characteristics of thin films made from two kinds of silane-couplers to control adhesion force of ice to solid surfaces. *Int J Refrig* 53:177–183
29. Wang N, Xiong D, Li M, Deng Y, Shi Y, Wang K (2015) Superhydrophobic surface on steel substrate and its anti-icing property in condensing conditions. *Appl Surf Sci* 355(July):226–232
30. Keun H, Kyeong J, Joon H, Ki S, Hoon K (2003) Fabrication of CuIn<sub>(1-x)</sub>Ga<sub>x</sub>Se<sub>2</sub> thin film solar cells by sputtering and selenization process. *Thin Solid Films* 435:186–192
31. Abe K, Sanada Y, Morimoto T (2003) Anti-reflective coatings for CRTs by sol-gel process. *J Sol-Gel Sci Technol* 26(1–3):709–713
32. Zhu D, Nai X, Lan S, Bian S, Liu X, Li W (2016) Surface modification of magnesium hydroxide sulfate hydrate whiskers using a silane coupling agent by dry process. *Appl Surf Sci* 390:25–30
33. Laghaei M, Sadeghi M, Ghalei B, Shahrooz M (2016) The role of compatibility between polymeric matrix and silane coupling agents on the performance of mixed matrix membranes: Polyethersulfone/MCM-41. *J Memb Sci* 513:20–32
34. Roberge P (2008) corrosion engineering: principles and practice. 52
35. Vizhi ME, Vanithakumari SC, George RP, Vasantha S, Mudali UK (2016) Superhydrophobic coating on modified 9Cr—1Mo ferritic steel using perfluoro octyl triethoxy silane. *Surf Eng* 32(2):139–146
36. Chico BN, De La Fuente D, Pérez ML, Morcillo M, Pé Rez ML, Morcillo M (2012) Corrosion resistance of steel treated with different silane/paint systems. *J Coatings Technol Res* 9(1):3–13
37. Pourhashem S, Rashidi A, Vaezi MR, Bagherzadeh MR (2017) Excellent corrosion protection performance of epoxy composite coatings filled with amino-silane functionalized graphene oxide. *Surf Coatings Technol* 317:1–9
38. Zhu H et al (2016) Fabrication and characterization of self-assembled graphene oxide/silane coatings for corrosion resistance. *Surf. Coatings Technol.* 304:76–84
39. Balan P, Raman RKS, Chan ES, Harun MK, Swamy V (2016) Effectiveness of lanthanum triflate activated silica nanoparticles as fillers in silane films for corrosion protection of low carbon steel. *Prog Org Coatings* 90:222–234
40. Xian X, Nai C, Li L, Zhao S (2017) The formation process of Zr-doped silane film on carbon steel during immersing in Zr(NO<sub>3</sub>)<sub>4</sub>/silane mixed solutions. *Anti-Corrosion Methods Mater* 64(1):1–9

# Study of Additive Manufactured Ti–Al–Si–Cu/Ti–6Al–4V Composite Coating by Direct Laser Metal Deposition (DLMD) Technique



L. C. Naidoo, O. S. Fatoba, Stephen A. Akinlabi, R. M. Mahamood, M. Y. Shatalov, E. V. Murashkin, S. Hassan, and Esther T. Akinlabi

**Abstract** Direct laser metal deposition (DLMD) is an additive manufacturing technique that is favourable in industries such as aerospace, biomedical, sports and automotive. Its advanced three-dimensional printing via layer-by-layer additive of a material allows for high-dimensional accuracy of the manufacturing of a part, but the surface finishing is still a limitation for the technology. Complex geometrical parts can be manufactured or repaired by employing the technology. This study focuses on the DLMD of Ti–Al–Si–Cu-based composite coatings on Ti–6Al–4V substrate, with the processing parameters such as the laser power and scanning speed being varied, while the other parameters were invariant. The microstructural evolution was analysed, and its influence on the anisotropy of the mechanical properties, the hardness property, and the corrosion performance of the material was investigated. The results showed that at low laser power and scan speed of 900 W and 1.0 m/min of Ti–Al–13Si–6Cu, which had the highest addition of alloying content, the highest hardness

---

L. C. Naidoo · O. S. Fatoba (✉) · R. M. Mahamood  
Department of Mechanical Engineering Science, University of Johannesburg, Auckland Park  
Kingsway Campus, Johannesburg 2006, South Africa  
e-mail: [drfatobasameni@gmail.com](mailto:drfatobasameni@gmail.com)

S. A. Akinlabi · S. Hassan  
Department of Mechanical Engineering, Walter Sisulu University, Butterworth Campus, Mthatha,  
South Africa

R. M. Mahamood  
Department of Material and Metallurgical Engineering, University of Ilorin, Ilorin, Nigeria

M. Y. Shatalov  
Department of Mathematics and Statistics, Tshwane University of Technology, Pretoria, South  
Africa

E. V. Murashkin  
Ishlinsky Institute of Problems in Mechanics, Russian Academy of Science, Moscow, Russia

O. S. Fatoba  
Kent State University, College of Aeronautic and Engineering, Ohio 44240, USA

E. T. Akinlabi  
Covenant University, Department of Mechanical Engineering, Ota, Ogun State, Nigeria  
e-mail: [etakinlabi@gmail.com](mailto:etakinlabi@gmail.com)

and improvement on the substrate was achieved. Large intermetallics compounds were formed of which the grains varied between columnar and backbone-like structures. The composite coating with the best corrosion rate was Ti–Al–7Si–Cu at  $1.305 \times 10^{-3}$  mm/year.

## 1 Introduction

In many of the various sectors in the engineering industry, there has been great development and innovations by using titanium alloy grade-five (Ti–6Al–4V) material through the available additive manufacturing techniques. The solutions are proposed to the problems, and challenges are provided by the great properties the material possesses for applications. The societal standards and the production quality are improved by the ability to design and repair complex and customized parts prudently, timeously and efficiently [1]. The products manufactured are now more easily sustainable and have much less environmental consequences than conventionally manufactured products.

Additively manufactured products possess great value in attribution to the benefitting characteristics that the material possesses in its suitability to be employed in various application cases. They provide performance at high temperatures, a weight ratio which is low, great corrosion resistance and high strength [2]. Many industries that benefit are the sports, automotive, medical, aerospace, chemical and oil/gas industries [3]. Ti–6Al–4V is suitable and serves as a better material to be used than the conventionally used stainless steels and cobalt-chromium in biomedical applications such as the manufacturing of medical products of orthopaedic and oral implants because of its high biocompatibility, Young's modulus (110 GPa), weight which is 50% less and excellent corrosion resistance [4–6]. The application of the material in the aerospace industry provided volume reduction and weight benefits that conventional aluminium and steels do not match when it comes to the design of the flaps engine mountings and airframes [7]. Its resistance to fatigue is high and exhibits high-thermal structural properties [8].

Literature indicates that the mechanical properties and metallurgical morphology of a fabricated laser metal deposited Ti–6Al–4V component are affected by the manufacturing parameters which are introduced into the process. The most common properties in fatigue, hardness, corrosion, strength, ductility and wear are sensitive to the resulting microstructure [9]. Commonly, products fabricated with the Ti–6Al–4V alloy by DLMD technique result in the microstructure consisting of constituents such as prevailing Widmanstätten structures that comprise of alpha lath structures with a minimal amount of beta phase within, martensitic acicular alpha phase in a sequence and beta grains [9].

However, the original microstructural features of the material are seen to possess a composition of alpha and beta phases, which has a crystal structure that is hexagonal closed-packed and body-centred cubic in structure, respectively. The alpha phase appears in white and the beta phase in dark. Observations have showed that the beta



phase can take formation into a martensitic alpha phase and a crystal structure of HCP when the material is subjected to high temperatures and then follows rapid solidification process from high thermal energy [10]. The alpha and beta have the aluminium and vanadium as stabilizers, respectively [7]. It has been that the alpha phase crystal structure is stabilized in room temperature as well as when the material is subjected to approximately 995 °C (beta transus) and more in which the structure morphs into a body-centred cubic structure [11].

The two phases (alpha and beta) that are present standardly in additively manufactured Ti–6Al–4V can be altered by employing the various available processing procedures and prior heat conditioning, which influences the morphology and distribution of the grains. It is of importance to note the rate of cooling of the alloy once it has been heated to and above the beta transus temperature as the metallurgical modifications occurs during this process [12]. The microstructural evolution that is commonly evident is that of the formation of large lamellar beta grains [1].

The alpha Widmanstätten structures nucleate and grow inside the beta matrix attributed to a rate of solidification which is approximately less than 20 °C/s [12]. The traditional wrought and casts display the mentioned microstructural features. Literature showed that the tensile strength of the Ti–6Al–4V alloy material may be enhanced when the alpha lamellar structures have their length and thickness reduced, attributed to cooling the material in the range of 20–410 °C/s [13]. The martensitic alpha phase results from the beta phase when the applied cooling rate is higher than 410 °C/s [3, 12]. It is of importance to produce parts that are dense and possess the highest percentages of densities as possible, which is one of the challenges of using the additively manufacturing technologies. The cause of a relatively less dense part is the formation of processing defects during the fabrication process. The formation of defects is detrimental to the tensile properties of a material, and that defiled area initiates growth of cracks [14, 15].

The current state of literature has delved into the importance of processing parameters on the mechanical properties of additively manufactured Ti–6Al–4V parts, with consideration to the procedure of fabrication, thermal histories and post-processing heat treatments. This present study contributes to literature by surface engineering of Ti–6Al–4V with a hybrid composite reinforcement at varying laser power and scanning speeds, as the remaining processing parameters were invariant. The microstructural evolution and mechanical properties were studied consequential to the methodology of fabrication.

## 2 Methods

The direct laser metal deposition (DLMD) was conducted by employing the Ytterbium Laser System (YLS-2000-TR) which operates at 3 kW maximum power and incorporates a Kuka robot for the operation of controlling the process of deposition. The deposits were designed and manufactured at The Council for Scientific and Industrial Research, National Laser Centre (CSIR NLC), Pretoria, South Africa.

**Table 1** Experimental matrix

Sample	Laser intensity (W)	Scan speed (m/min)	Powder rate (g/min)	Gas rate (L/min)
Ti–Al–7Si–Cu	1000	1	2	2.5
		1.2	2	2.5
Ti–Al–12Si–2Cu	900	1	2	2.5
		1.2	2	2.5
Ti–Al–13Si–6Cu	900	1	2	2.5
		1.2	2	2.5

The laser head of the Kuka robot irradiated the laser through the centre nozzle which created a molten pool on the substrate, and the reinforcement powders were deposited into the melt through the concentric nozzle by using argon gas to accelerate the powders. The argon gas was also used to protect the deposition process from oxidation.

The substrate used in the deposition operation was a solid titanium grade 5 Ti–6Al–4V which had a volumetric dimension of  $72 \times 72 \times 5 \text{ mm}^3$ . A cleaning preparation was conducted on the substrates whereby they were sandblasted to remove the surface impurities and to roughen the surface layer of the material to aid the metallurgical bond of the clad to the surface of the substrate. All the residue after sandblasting was washed off with acetone and then dried in air. The powders used to create the hybrid composite coatings were Titanium, Aluminium, Silicon and Copper which had particle sizes that varied from 50 to 150  $\mu\text{m}$ . Table 1 provides the experimental matrix of processing parameters which were used for the operation. The argon gas served to prevent oxidation of the deposit and served as a carrier gas for the powders which moved from the hoppers to the nozzle through hoses. The laser intensity and the scanning speed were the parameters which were variants, and the other processing parameters were kept constant throughout the operation. A 4 mm beam diameter was used, and the length of the tracks was ceased at 65 mm. A 12 mm standoff distance from the nozzle was maintained for the operations.

Twelve deposits were manufactured and labelled as 1A to 6B. The deposits were cleaned with a brush post-deposition to eliminate the residue of powders which were un-melted on the surface. The deposits were subjected to metallurgical preparation, whereby they were cut transversely and prepared for material characterization process, according to the Struers standard guide (ASTM E3-11) of the metallographic preparation for specimens. The samples were etched for 15 s in Kroll's reagent, and then, the necessary material characterization tests were carried out that included observing the microstructural evolution using SEM and an optical microscope.

## 2.1 Microhardness

The Vickers Microhardness Tester was used to ascertain the hardness property of the samples by applying six indentations on the cross section from the top of the deposit towards the substrate. A test force of 100 gf was used.

## 2.2 Microscopy

The microstructural features were observed by using the optical microscope, BX51M Olympus. The deposited zone of the cross section was the area of focus.

## 2.3 Corrosion

The corrosion performance of the samples was tested using the DY2300 Series Potentiostat, of which the surface of the deposition of the samples was the area tested in 3.5% NaCl.

# 3 Results and Discussion

## 3.1 Microhardness

The microhardness for each sample was measured across the deposit, the heat-affected zone and the substrate. Table 2 summarizes the mean hardness values, and the subsequent Figs. 1 and 2 provide the hardness values at different zones of the samples.

**Table 2** Mean microhardness values

Sample	Laser intensity (W)	Scan speed (m/min)	Mean microhardness (HV <sub>0.1</sub> )
Ti–6Al–4V	–	–	428
Ti–Al–7Si–Cu	1000	1.0	409
		1.2	412
Ti–Al–12Si–2Cu	900	1.0	400
		1.2	434
Ti–Al–13Si–6Cu	900	1.0	591
		1.2	588

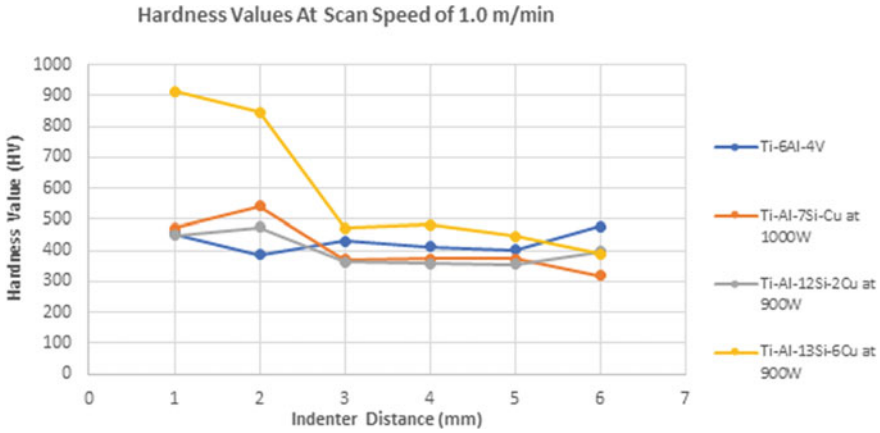


Fig. 1 Microhardness at 1.0 m/min scan speed and varied Laser Power

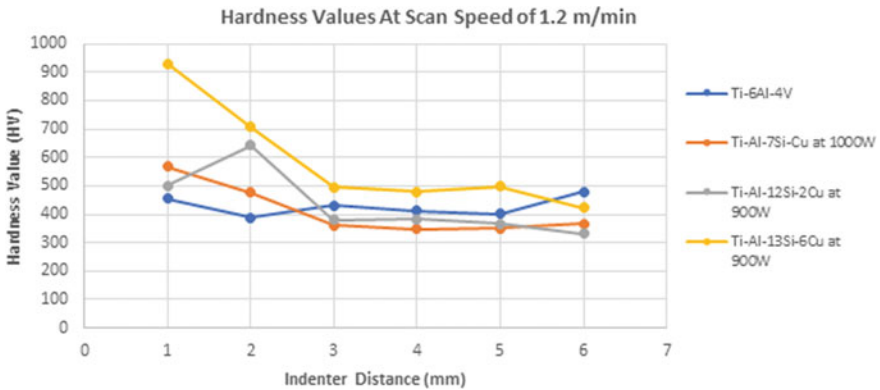


Fig. 2 Microhardness at 1.2 m/min scan speed and varied Laser Power

The mean hardness values provided in Table 2 show the correlation between maintaining a constant power and increasing the scanning speed, which improves the hardness of the material. This is observed with Ti–Al–7Si–Cu, where the scanning speed was increased from 1.0 to 1.2 m/min at a constant laser power of 1000 W, and the hardness increased slightly from 409 to 412HV<sub>0.1</sub>, respectively. The same is observed with Ti–Al–12Si–2Cu; at a constant power of 900 W and increased scanning speed from 1.0 m/min to 1.2 m/min, the hardness of the material was enhanced from 400 to 434HV<sub>0.1</sub>. However, Ti–Al–13Si–6Cu does not perform in accordance with the trend as it is seen to decrease in hardness when the scanning speed was increased from 1.0 m/min to 1.2 m/min at a constant laser power of 900 W [16]. Despite this, Ti–Al–13Si–6Cu had the highest mean hardness value at the given processing parameters and showed an improvement on the Ti–6Al–4V alloy (substrate).

Figures 1 and 2 show that the hardness is highest at the centre of the sample and decreases towards the HAZ and substrate. Moreover, it is observed that Ti–Al–13Si–6Cu has the highest hardness across its zones compared to the other samples and the addition of Cu allows the mechanical properties to be altered through age hardening [17].

### 3.2 Microstructural Evaluation

Optical observation of the deposit for all the samples showed that the grains became more prominent with increasing scanning speed. Ti–Al–7Si–Cu (Fig. 3) appears to have a martensitic microstructure with small alpha and beta grains at a scanning speed of 1.0 m/min and 1000 W of laser power. The microstructure developed acicular alpha grains and darker beta grains when the scan speed was increased to 1.2 m/min. Ti–Al–12Si–2Cu resulted in a martensitic microstructure, as can be seen in Fig. 4, with more acicular alpha grains appearing when the scanning speed was increased but a

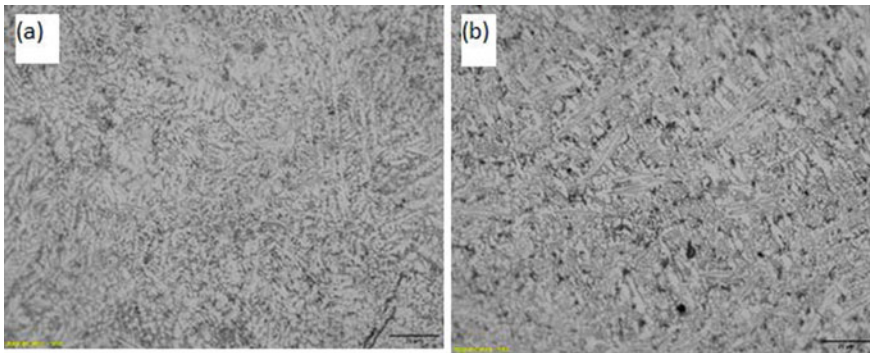


Fig. 3 Optical Micrograph of Ti–Al–7Si–Cu at (a) 1.0 m/min, 1000 W and (b) 1.2 m/min, 1000 W

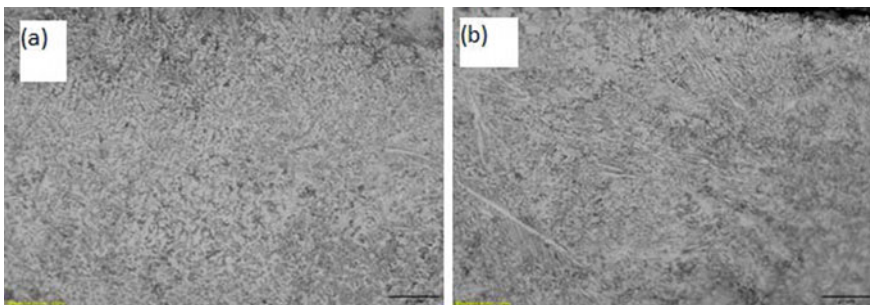


Fig. 4 Optical Micrograph of Ti–Al–12Si–2Cu at (a) 1.0 m/min, 900 W and (b) 1.2 m/min, 900 W

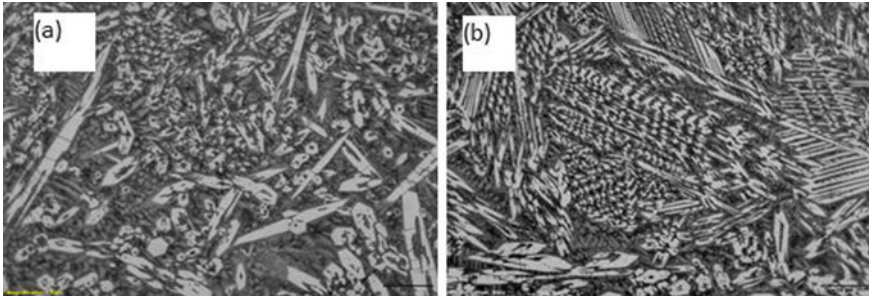


Fig. 5 SEM image of Ti–Al–13Si–6Cu at (a) 1.0 m/min, 900 W and (b) 1.2 m/min, 900 W

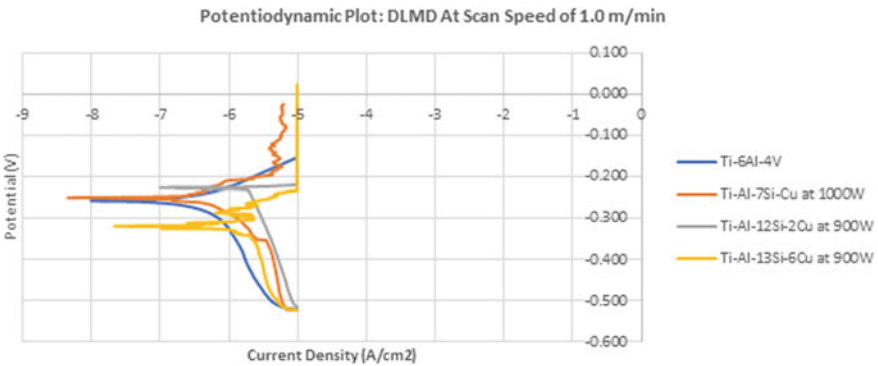
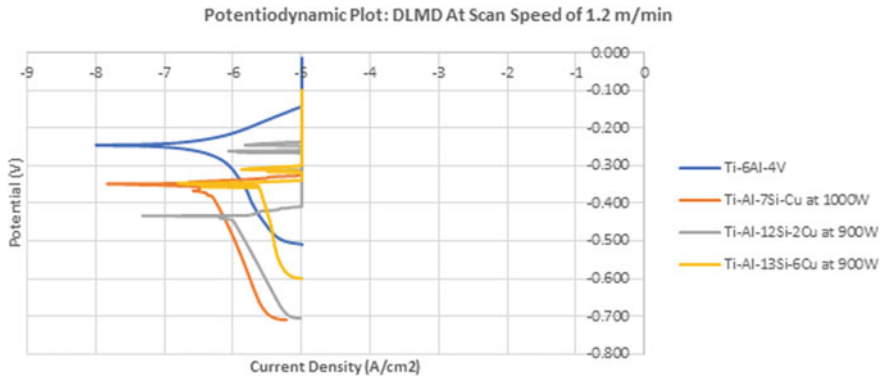


Fig. 6 Potentiodynamic curves of Ti–Al–Si–Cu/Ti–Al–4V composite coatings at 1.0 m/min and varied laser power

few beta grains at the top of the deposit. Acicular alpha martensite is also referred to as alpha-prime microstructure [18–27]. Figure 5 shows a unique development of the microstructure, compared to the other samples. The intermetallic compounds formed appear to be more prominent in Ti–Al–13Si–6Cu, which was inevitable since the powder had the most addition of alloying elements to the titanium substrate—the highest content of silicon and copper in the reinforcement powder [17]. The intermetallic compounds that were formed at a scan speed of 1.0 m/min had a mixture of small grains and columnar grains. When the scanning speed was increased to 1.2 m/min, backbone-like structures formed. This appears to be in attribution to the sample having the highest hardness.

### 3.3 Corrosion

Table 3 shows the correlation between Ti–Al–7Si–Cu and Ti–Al–12Si–2Cu. As the scanning speed was increased from 1.0 to 1.2 m/min, the corrosion potential had



**Fig. 7** Potentiodynamic curves of Ti–Al–Si–Cu/Ti–6Al–4V composite coatings at 1.2 m/min and varied laser power

**Table 3** Potentiodynamic data of Ti–Al–Si–Cu/Ti–6Al–4V composite coatings

Powder composition	Process parameters	E <sub>corr</sub> (V)	I <sub>corr</sub> (A/cm <sup>2</sup> )	Polarization resistance (Ω.cm <sup>2</sup> )	Corrosion rate (mm/yr)
Ti–6Al–4V alloy	–	–0.245	5.578 × 10 <sup>–7</sup>	46070	8.961 × 10 <sup>–4</sup>
Ti–Al–7Si–Cu	1.0 m/min, 1000 W	–0.372	8.123 × 10 <sup>–7</sup>	31630	1.305 × 10 <sup>–3</sup>
	1.2 m/min, 1000 W	–0.347	1.398 × 10 <sup>–6</sup>	18380	2.246 × 10 <sup>–3</sup>
Ti–Al–12Si–2Cu	1.0 m/min, 900 W	–0.465	1.957 × 10 <sup>–5</sup>	1313	3.144 × 10 <sup>–2</sup>
	1.2 m/min, 900 W	–0.432	5.622 × 10 <sup>–6</sup>	4571	9.032 × 10 <sup>–3</sup>
Ti–Al–13Si–6Cu	1.0 m/min, 900 W	–0.319	1.645 × 10 <sup>–6</sup>	15620	2.643 × 10 <sup>–3</sup>
	1.2 m/min, 900 W	–0.344	1.876 × 10 <sup>–5</sup>	1369	3.014 × 10 <sup>–2</sup>

improved from –0.372 to –0.347 V and –0.465 to –0.432 V, respectively. However, Ti–Al–7Si–Cu is more corrosion resistant at 1000 W of laser power and 1.0 m/min of scanning speed. Ti–Al–13Si–6Cu seems not to improve its corrosion performance when the scanning speed is increased. The corrosion potential shows –0.319 V at 1.0 m/min. Whereas, the other two samples show improvement in corrosion potential at 1.2 m/min. Ti–6Al–4V alloy (substrate) displays corrosion potential of –0.245 V and corrosion rate of 9.961 × 10<sup>–4</sup> mm/year (Figs. 6 and 7).

## 4 Conclusions

The hardness of the material was enhanced compared to the Ti–6Al–4V substrate when the contents of silicon and copper were at highest and 1.0 m/min scan speed. This is in regard to the reinforcement powder of Ti–Al–13Si–6Cu. The Optical micrographs and SEM Image showed that the intermetallic compounds which had formed in the microstructure may have been in attribution for the high hardness produced. Ti–Al–13Si–6Cu showed the best corrosion potential of  $-0.319$  V amongst the other composites AT 900 W and 1.0 m/min. However, Ti–Al–7Si–Cu corrodes the least amongst the samples at  $1.305 \times 10^{-3}$  mm/year at 1000 W and scan speed of 1.0 m/min.

**Acknowledgements** This project was supported by NRF-IRG SA/Russia Bilateral and technical research collaboration grant No.: NRF/UID No. 118905 and NRF/RFBR No. 19-51-60001.

## References

1. Azarniya A, Colera X, Mirzaali M, Sovizi S, Bartolomeu F, St Weglowski M, Wits W, Yap C, Ahn J, Miranda G, Silva F, Madaah Hosseini H, Ramakrishna S, Zadpoor A (2019) Additive manufacturing of Ti–6Al–4V parts through laser metal deposition (LMD): Process, microstructure, and mechanical properties. *J Alloys Compd*
2. Vaithilingam J, Hague R, Edmondson S (2016) The effect of laser remelting on the surface chemistry of Ti6Al4V components fabricated by selective laser melting. *Mater Process Technol* 232:1–8
3. Raju R, Petle V, Rajendran R (2015) Microstructural and mechanical characterization of Ti6Al4 V refurbished parts obtained by laser metal deposition. *Mater Sci Eng, A*(643):64–71
4. Bartolomeu F, Carvalho O, Alves N, Alves N, Silva F, Miranda G (2017) Tribological behavior of Ti6Al4V cellular structures produced by Selective Laser Melting. *Mechanical Behav Biomed Mater* 69:128–134
5. Miranda G, Bartolomeu F, Carvalho O, Silva F (2019) Design of Ti–6Al–4V–HA composites produced by hot pressing for biomedical applications. *Mater Des* 108:488–493
6. Wolff S, Faierson E, Cao J (2016) Anisotropic properties of directed energy deposition (DED)-processed Ti–6Al–4V. *J Manuf Process* 24:397–405
7. Liu Q, Zheng H, Ding L, Gong S (2016) Microstructure and mechanical properties of LMD–SLM hybrid forming Ti6Al4V alloy. *Mater Sci Eng* 660:24–33
8. Sterling A, Shamsaei N, Seely D (2016) Fatigue behavior and failure mechanisms of direct laser deposited Ti–6Al–4V. *Mater Sci Eng A*(655):100–112
9. Li P, Huang W, Lin X (2015) Thermomechanical response of 3D laser-deposited Ti–6Al–4V alloy over a wide range of strain rates and temperatures. *Mater Sci Eng A*(647):34–42
10. Mei W, Wen Y, Sun J (2017) Martensitic transformation from  $\beta$  to  $\alpha$  and  $\alpha$  phases in Ti–V alloys: A first-principles study. *J Mater Res* 32:3183–3190
11. Bartolomeu F, Pinto E, Silva F, Miranda G (2017) Wear behavior of Ti6Al4V biomedical alloys processed by selective laser melting, hot pressing and conventional casting. *Trans Nonferrous Met Soc* 27:829–838
12. Shunmugavel M, Polishetty A, Littlefair G (2015) Microstructure and Mechanical Properties of Wrought and Additive Manufactured Ti–6Al–4V Cylindrical Bars. *Procedia Technology* 20:231–236



13. Murr L, Gaytan S, Rodela A, Hernandez D, Medina F (2009) Microstructure and mechanical behavior of Ti–6Al–4 V produced by rapid layer manufacturing, for biomedical applications. *Mechanical Behav Biomed Mater* 2:20–32
14. Clark D, Whittaker M, Bache M (2012) Microstructural characterization of a prototype titanium alloy structure processed via direct laser deposition (DLD). *Metall Mater Trans B*(43):388–396
15. Vilaro T, Colin C, Bartout J (2011) As-fabricated and heat-treated microstructures of the Ti–6Al–4V alloy processed by selective laser melting. *Metall Mater Trans A*(42):3190–3199
16. Erinoshio MF, Akinlabi ET, Johnson O, Owolabi G Effect of scanning speed on the material characterisations of laser deposited titanium alloy and copper. University of Johannesburg, Johannesburg
17. Erinoshio MF, Akinlabi ET, Pityana S Laser metal deposition of Ti6Al4 V/Cu composite: A study of the effect of laser power on the evolving properties. University of Johannesburg, Johannesburg
18. Akinlabi ET, Tayob MA, Pietra F (2016) Experimental and Numerical Analysis of Geometrical Properties of Laser Metal Deposited Titanium. University of Johannesburg, Johannesburg
19. Makhatha ME, Fatoba OS, Akinlabi ET (2017) Effects of rapid solidification on the microstructure and surface analyses of laser-deposited Al-Sn coatings on AISI 1015 steel. *Int J Adv Manuf Technol* 1–15. <https://doi.org/10.1007/s00170-017-0876-y>
20. Fatoba OS, Popoola API, Aigbodion VS (2018) Laser alloying of Al-Sn binary alloy onto mild steel: insitu formation. hardness and anti-corrosion properties. *Lasers Eng* 39(3–6):292–312
21. Fatoba OS, Akinlabi ET, Akinlabi SA (2018) Numerical investigation of laser deposited al-based coatings on Ti–6Al–4V alloy. In: Proceedings at the 2018 IEEE 9th international conference on mechanical and intelligent manufacturing technologies (ICMIMT 2018), Cape town, South Africa, pp 85–90. <https://doi.org/10.1109/icmimt.2018.8340426>
22. Gharehbaghi R, Fatoba OS, Akinlabi ET (2018) Influence of scanning speed on the microstructure of deposited Al-Cu-Fe coatings on a titanium alloy substrate by laser metal deposition process. In: Proceedings at the 2018 IEEE 9th international conference on mechanical and intelligent manufacturing technologies (ICMIMT 2018), Cape town, South Africa, pp 44–49. <https://doi.org/10.1109/icmimt.2018.8340418>
23. Gharehbaghi R, Akinlabi ET, Fatoba OS (2018) Experimental investigation of laser metal deposited icosahedral Al-Cu-Fe coatings on grade five titanium alloy. Proceedings at the 2018 IEEE 9th international conference on mechanical and intelligent manufacturing technologies (ICMIMT 2018), Cape town, South Africa, pp 31–36. <https://doi.org/10.1109/icmimt.2018.8340416>
24. Fatoba OS, Akinlabi ET, Akinlabi SA (2018) Effects of Fe addition and process parameters on the wear and corrosion properties of laser deposited Al-Cu-Fe coatings Ti–6Al–4V Alloy. In: Proceedings at the 2018 IEEE 9th international conference on mechanical and intelligent manufacturing technologies (ICMIMT 2018), Cape town, South Africa, pp 74–79. <https://doi.org/10.1109/icmimt.2018.8340424>
25. Fatoba OS, Adesina OS, Popoola API (2018) Evaluation of microstructure, microhardness, and electrochemical properties of laser-deposited Ti-Co coatings on Ti–6Al–4V Alloy. *Int J Adv Manuf Technol*. <https://doi.org/10.1007/s00170-018-2106-7>
26. Fatoba OS, Akinlabi SA, Gharehbaghi R, Akinlabi ET (2018) Microstructural Analysis, Microhardness and Wear Resistance Properties of Quasicrystalline Al-Cu-Fe Coatings on Ti-6Al-4V Alloy. *Mater Express Res* 5(6):1–14. <https://doi.org/10.1088/2053-1591/aaca70>
27. Fatoba OS, Akinlabi SA, Akinlabi ET (2018) Numerical modelling and performance effects of laser deposited Ti-Al-Sn coating on ASTM A29 steel. In: Presented at the international conference on mechanical stress evaluation by neutron and synchrotron (MECASSENS 2017, 19th–22nd September 2017, Kruger Park, South Africa. *Materials Research Proceedings*. 4, pp 135–140. <http://dx.doi.org/10.21741/9781945291678-21>

# Experimental Investigation of Laser Metal Deposited Al–Cu–Ti Coatings on Ti–6Al–4V Alloy



A. M. Lasisi, O. S. Fatoba, Stephen A. Akinlabi, R. M. Mahamood, M. Y. Shatalov, E. V. Murashkin, S. Hassan, and Esther T. Akinlabi

**Abstract** The aim of this research is to study the effect of aluminum-based coatings on the new emerging surface properties, producing improved thermal, mechanical, tribological and metallurgical properties, which can withstand adverse environmental conditions using laser metal deposition technique. In this study, laser metal deposition was used to produce a hybrid coating on Ti–6Al–4V at a scanning speed of 0.8 m/min. The laser power of the process was also varied between 900 and 1000 W. The microstructure was characterized by using the scanning electron microscope (SEM) and an optical microscope (OPM). The mechanical properties of the samples were characterized using microhardness test. From the results, the higher the scanning speed, the more the microhardness of the samples.

**Keywords** Additive manufacturing · SEM · Microstructure · Microhardness · Titanium-alloy composite · Laser metal deposition (LMD)

---

A. M. Lasisi · O. S. Fatoba (✉) · R. M. Mahamood · E. T. Akinlabi  
Department of Mechanical Engineering Science, University of Johannesburg, Auckland Park  
Kingsway Campus, Johannesburg 2006, South Africa  
e-mail: [drfatobasameni@gmail.com](mailto:drfatobasameni@gmail.com)

E. T. Akinlabi  
e-mail: [etakinlabi@uj.ac.za](mailto:etakinlabi@uj.ac.za)

S. A. Akinlabi · S. Hassan  
Department of Mechanical Engineering, Butterworth Campus, Walter Sisulu University,  
Butterworth, South Africa

R. M. Mahamood  
Department of Material and Metallurgical Engineering, University of Ilorin, Ilorin, Nigeria

M. Y. Shatalov  
Department of Mathematics and Statistics, Tshwane University of Technology, Pretoria, South  
Africa

E. V. Murashkin  
Ishlinsky Institute of Problems in Mechanic, Russian Academy of Science, Moscow, Russia

## 1 Introduction

Titanium and titanium alloys have been used widely in numerous applications due to the various attractive properties they possess. These properties are namely high temperature performance, high modulus of elasticity, high strength-to-weight ratio, and biocompatibility [1]. Titanium and its alloys find their applications in numerous industries such as energy, chemical, electronics, aerospace, and biomedical due to their exceptional properties [1]. Ti-6Al-4V is the most frequently used titanium alloy in the aerospace industry for aeronautical applications; all the applications are possible due to properties such as low weight, high mechanical strength, and super plasticity [6]. It is a very versatile material; hence, it finds its place in the work environment of almost every industry. In some applications, where specific service requirements need to be met, such as a work environment in which it is necessary for it to come in contact with other materials, the wear resistance property of Ti-6Al-4V is found to be very poor, as well as the corrosion resistance, hence, resulting in the loss of strength of the products and finally failure [6]. It is therefore necessary to perform surface modifications aimed at improving the corrosion and wear resistance properties of titanium.

Laser metal deposition (LMD) is one of the most effective additive manufacturing techniques in the expanding field of additive manufacturing. It is a versatile manufacturing technique that can be used for numerous applications such as directly creating hybrid surface coating on parts, production of fully dense solid objects from porous powders, and manufacturing of freeform shapes. It is also extremely effective because it produces minimal waste after the manufacturing process is completed. These are the qualities that make it a valuable manufacturing technique in the biomedical, aerospace, energy, electronics, and chemical industries [6]. Based on researched material, the use of hybrid coatings (Al-Cu-Fe) on titanium alloy (Ti-6Al-4V) is limited in the aerospace industry. Other titanium alloys also play a crucial role in the aerospace industry, which are used for the manufacturing of engine parts, landing gears, and anti-crash frames. They are used in Boeing B787 and Airbus A350XWB [6].

## 2 Methods

A particle with size (50-105  $\mu\text{m}$ ) aluminum-based powder was used as reinforcement while Ti-6Al-4V alloy was used as the substrate. Before the laser metal deposition process was initiated, a chemical balance was done on the titanium substrate. After the deposition was completed, the aluminum powder particles which were not fully melted and were clinging to the substrate and the deposit were removed. To obtain a homogeneous mixture of the powdery substances which possessed varying particle sizes and specific weights, a tubular shaker-mixer was used. The mixture of the powders occurred in a closed clean container.

## ***2.1 Parent Material***

Ti–6Al–4 V alloy was used as the substrate. Before deposition took place, the substrate was sand blasted and cleaned with acetone to remove any impurities, to aid the laser absorption before the deposition process.

## ***2.2 Experimental Setup***

The laser deposition operation was conducted at the National Laser Center, Council of scientific Research (NLC-CSIR). The laser created a melted pool on the surface of the titanium substrate, while a nozzle was used to deposit the aluminum-based reinforcement powders onto the surface of the substrate.

## ***2.3 Material Characterization***

The following materials characterizations were conducted on the samples produced to ascertain the integrity of the deposit. These include.

## ***2.4 Microstructure***

The titanium substrate is not only affected by varying the laser power but also by the addition of the deposited powder on the surface of the substrate. Hence, the emerging microstructure of the product will be different from that of the substrate. The optical microscope image is used to discuss the general microstructure, while the images from scanning electron microscope were used to explain the composition of the microstructure, and how the molecules were arranged in the product.

## ***2.5 Hardness***

Hardness is the measure of a materials ability to resist localized plastic deformations. Hardness testing involves a technique of forcing an indenter into a material to be tested under a controlled load. The size and depth of the measured dent is then compared to a hardness value. The Vickers hardness test is the chosen method of determining the hardness of the composite.

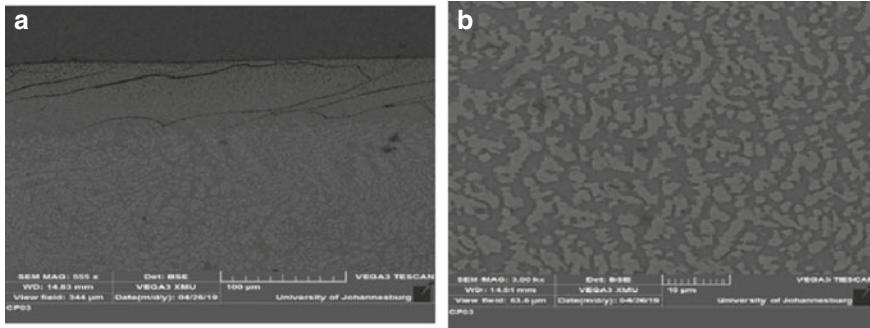


**Fig. 1** Microstructure of Ti-6Al-4V/Al-4Cu-7Ti at **a** 900 W and **b** 1000 W

### 3 Results and Discussion

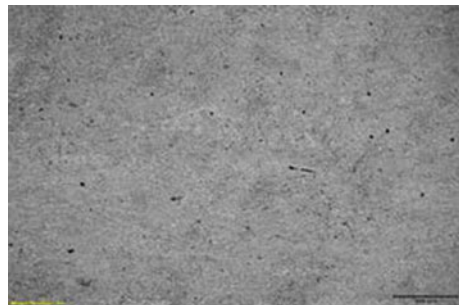
#### 3.1 Microstructure (Optical Microscope)

The laser metal deposition process of nickel-based powder on the titanium substrate shows the beta phase grains exist at a high scanning speed and the alpha phase grains exist at a lower scanning speed [7]. There is a reduction in the geometrical properties of the samples such as width, height, and heat-affected zone, with increasing scanning speed due to the laser metal interaction. The corrosion and microhardness of each sample tend to increase with increasing the scanning speed (Fig. 1).

#### 3.2 Substrate Microstructure

Figure 2 illustrates the grain structure of the titanium substrate used for the investigation. The average grain size is approximately 78  $\mu\text{m}$ . The microstructure of the titanium substrate is visibly characterized by the formation of light and dark regions which represent two phases, namely alpha ( $\alpha$ ) and beta ( $\beta$ ) phases. They

**Fig. 2** Microstructure of Ti-6Al-4V substrate



are distributed through the area of the substrate as shown in Fig. 2. This is the basic microstructure of the titanium substrate that was used for the investigation.

### 3.3 Scanning Electron Microscope (SEM)

The high-resolution images, which show the microstructures of the samples, are achieved using SEM. Figure 1 shows the structure of the grains. The solidification mechanism is due to laser beam interaction. The coating powder particles melt and create a liquid pool on the titanium (substrate) surface that undergoes a limited melting. Therefore, only small dilution of addition elements is obtained. The very small amount of nickel in various zones of the coating supports this theory. Solidification begins with formation of some large particles such as Al and Cu. Since Cu is well known as a strong  $\beta$ -stabilizing element, it can be observed that atomic migration of Cu into Ti lattice results in the  $\beta$ -Ti phase formation during cooling and travels a longer distance in the Ti lattice than other elements which opens more crystallographic structure of the  $\beta$  matrix. Thus, aluminum and copper powders recoated with titanium for better photon absorption, resulting in better deposit quality [7].

### 3.4 Microhardness

The hardness values were recorded at different points on the intermetallic section where formation of the composite takes place. Then the average of these values for each sample was recorded as shown in Tables 1 and 2.

The mean hardness value increases with increasing laser power. In this case, at the start of material deposition, the heat rapidly dissipated by the substrate heat conduction. At the beginning stage of the LMD process, the initial thermal transience produced a rapid quenching rate effect, which resulted in increase of the hardness. It can be observed that the mean hardness value increases with increasing laser power which is due to the limited interaction within the powder and the laser. Only a small amount of energy was supplied during the melting process. This energy limited the amount of time available for growth, thus, increasing the hardness. It is evident

**Table 1** Microhardness results (surface)

Samples	Laser power (W)	Scanning speed (m/min)	Mean surface hardness (HV)
Ti–6Al–4V	1000	0.8	417.54
Ti–6Al–4V/Al–4Cu–7Ti	900	0.8	423.54
Ti–6Al–4V/Al–4Cu–7Ti	1000	0.8	346.10
Ti–6Al–4V/Al–7Cu–5Ti	900	0.8	338.30

**Table 2** Microhardness results (cross-section)

Samples	Laser power (W)	Scanning speed (m/min)	Mean cross-section hardness (HV)
Ti-6Al-4V	1000	0.8	418.00
Ti-6Al-4V/Al-4Cu-7Ti	900	0.8	318.20
Ti-6Al-4V/Al-4Cu-7Ti	1000	0.8	375.92
Ti-6Al-4V/Al-7Cu-5Ti	900	0.8	355.62

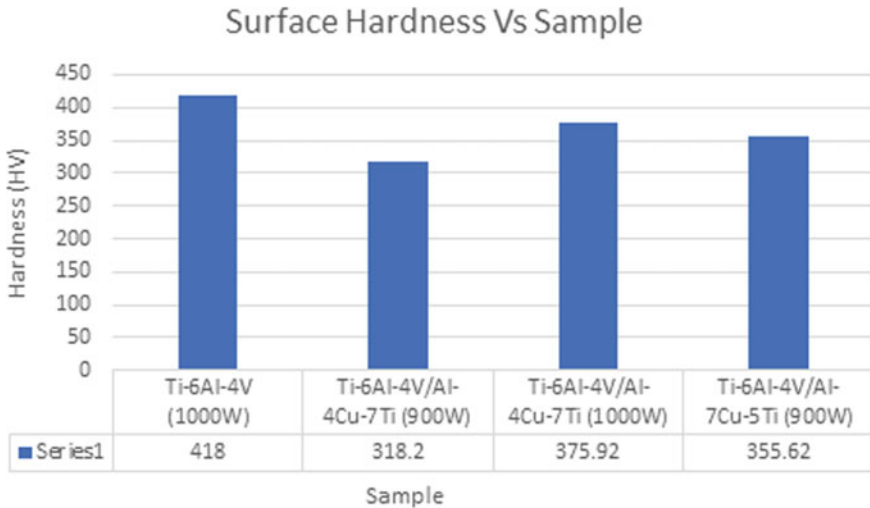


**Fig. 3** Hardness graph of titanium substrate and samples (surface)

that the composites have the highest mean hardness values at higher laser powers (1000 W) (Figs. 3 and 4).

### 4 Conclusions

The aim of the research project was to analyze the effect of hybrid coating (Al-Cu-Ti) powder on Ti-6Al-4V. The experiments were conducted at different laser powers and scanning speeds in order to improve material properties as well as to find the best combination of process parameters for the composite to form. The optimization of process parameters for the LMD process was accomplished by quantifying and characterizing the formed composite through metallurgical evaluation and geometrical measurements. Based on the obtained results, the laser power of 1000 W and laser scanning speed of 0.8 are the optimum process parameters. The significant effect of hybrid coating powder on a grade five titanium alloy is an increase in the hardness.

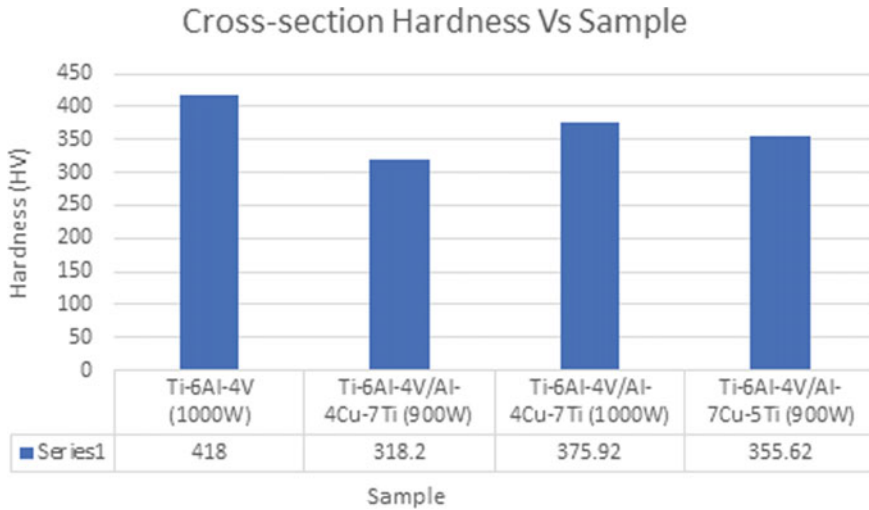


Fig. 4 Hardness graph of titanium substrate and samples (cross-section)

**Acknowledgements** This project was supported by NRF-IRG SA/Russia Bilateral and technical research collaboration grant No.: NRF/UID No. 118905 and NRF/RFBR No. 19-51-60001.

## References

- Banerjee D, Williams JC (2013) Perspectives on titanium science and technology. *Acta Mater* 61:844–879
- Attar H, Prashanth KG, Chaubey AK, Calin M, Zhang LC, Scudino S, Eckert J (2015) Comparison of wear properties of commercially pure titanium prepared by selective laser melting and casting processes. *Mater Lett* 142:38–41
- Weng F, Chen C, Yu H (2014) Research status of laser cladding on titanium and its alloys: A review. *Material Design* 58:412–425
- Mao YS, Wang L, Chen KM, Wang SQ, Cui XH (2013) Tribo-layer and its role in dry sliding wear of Ti–6Al–4 V Alloy, *Wear*, 297 (1–2), 1032–1039. Org/, Doi. <https://doi.org/10.1016/J.Wear.2012.11.063>
- Attar H, Calin M, Zhang LC, Eckert Scudino SJ (2014) Manufacture by selective laser melting and mechanical behaviour of commercially pure titanium. *Mater Sci Eng, A* 593:170–177
- Baumer M, Dickens P, Tuck C, Hague R (2016) The cost of additive manufacturing: Machine productivity, economies of scales and technology-push. *Technol Forecast Soc Chang* 102:193–201
- Vrancken B, Thijs L, Kruth JP, Van Humbeeck J (2014) Microstructure and mechanical properties of a novel beta titanium metallic composite by selective laser melting. *Acta Mater* 68:150–158
- Makhatha ME, Fatoba OS, Akinlabi ET (2018) Effects of rapid solidification on the microstructure and surface analyses of laser-deposited Al-Ni coatings on AISI 1015 steel. *Int J Adv Manuf Technol* 94(1–4):773–787
- Salonitis K, Zeng B, Mehrabi HA, Jolly M (2016) The challenges for energy efficient casting processes, *Procedia Cirp*, 24–29



10. Fatoba OS, Akinlabi ET, Akinlabi SA (2018) Numerical investigation of laser deposited Al-Based coatings on Ti-6Al-4 V Alloy. In: Proceedings at the 2018 IEEE 9th international conference on mechanical and intelligent manufacturing technologies (ICMIMT 2018), Cape town, South Africa, pp 85–90. <https://doi.org/10.1109/icmimt.2018.8340426>
11. Fatoba OS, Popoola API, Aigbodion VS (2018) Laser alloying of Al-Sn binary alloy onto mild steel: In situ formation. Hardness and anti-corrosion properties. *Lasers in Eng* 39(3–6):292–312
12. Gharehbaghi R, Fatoba OS, Akinlabi ET (2018) Influence of scanning speed on the microstructure of deposited Al-Cu-Fe coatings on a titanium alloy substrate by laser metal deposition process. In: Proceedings at the 2018 IEEE 9th international conference on mechanical and intelligent manufacturing technologies (ICMIMT 2018), Cape town, South Africa, pp 44–49. <https://doi.org/10.1109/icmimt.2018.8340418>
13. Gharehbaghi R, Akinlabi ET, Fatoba OS (2018) Experimental investigation of laser metal deposited icosahedral Al-Cu-Fe coatings on grade five titanium alloy. In: Proceedings at the 2018 IEEE 9th international conference on mechanical and intelligent manufacturing technologies (ICMIMT 2018), Cape town, South Africa, pp 31–36. <https://doi.org/10.1109/icmimt.2018.8340416>
14. Fatoba OS, Akinlabi ET, Akinlabi SA (2018) Effects of Fe addition and process parameters on the wear and corrosion properties of laser deposited Al-Cu-Fe coatings Ti-6Al-4 V Alloy. In: Proceedings at the 2018 IEEE 9th international conference on mechanical and intelligent manufacturing technologies (ICMIMT 2018), Cape town, South Africa, pp 74–79. <https://doi.org/10.1109/icmimt.2018.8340424>
15. Fatoba OS, Adesina OS, Popoola API (2018) Evaluation of microstructure, microhardness, and electrochemical properties of laser-deposited Ti-Co coatings on Ti-6Al-4 V Alloy. *Int J Adv Manuf Technol*. <https://doi.org/10.1007/s00170-018-2106-7>
16. Fatoba OS, Akinlabi SA, Gharehbaghi R, Akinlabi ET (2018) Microstructural Analysis, Microhardness and Wear Resistance Properties of Quasicrystalline Al-Cu-Fe Coatings on Ti-6Al-4 V Alloy. *Mater Express Res* 5(6):1–14. <https://doi.org/10.1088/2053-1591/aaca70>
17. Fatoba OS, Akinlabi SA, Akinlabi ET (2018) Numerical modelling and performance effects of laser deposited Ti-Al-Sn coating on ASTM A29 Steel. In: Presented at the international conference on mechanical stress evaluation by neutron and synchrotron (MECASSENS 2017, 19th–22nd September 2017, Kruger Park, South Africa. *Materials Research Proceedings*. 4, pp 135–140. <http://dx.doi.org/10.21741/9781945291678-21>

# Effect of Process Parameters on the Hardness Property of Laser Metal Deposited Al–Cu–Ti Coatings on Ti–6Al–4V Alloy



A. M. Lasisi, O. S. Fatoba, Stephen A. Akinlabi, R. M. Mahamood, M. Y. Shatalov, E. V. Murashkin, S. Hassan, and Esther T. Akinlabi

**Abstract** The aim of this investigation is to characterize the effect of process parameters applied to the laser metal deposition of Al–Cu–Ti coatings on titanium substrate (Ti–6Al–4V). After the deposition process was completed, a new hybrid coated surface emerged with improvements in the following areas: improved thermal, mechanical, and metallurgical properties. During the laser metal deposition procedure to obtain a hybrid coating on Ti–6Al–4V, certain process parameters were employed to achieve the optimum results which are the scanning speed (1.0 m/min) and the laser power of the procedure, which was varied between 900 and 1000 W. The microstructural analysis was carried out using the scanning electron microscope (SEM) and an optical microscope (OPM). The mechanical properties of the samples were characterized using microhardness test.

**Keywords** Additive manufacturing · SEM · Microstructure · Microhardness · Titanium-alloy composite · Laser metal deposition (LMD)

---

A. M. Lasisi · O. S. Fatoba (✉) · R. M. Mahamood · E. T. Akinlabi  
Department of Mechanical Engineering Science, University of Johannesburg, Auckland Park  
Kingsway Campus, Johannesburg 2006, South Africa  
e-mail: [drfatobasameni@gmail.com](mailto:drfatobasameni@gmail.com)

E. T. Akinlabi  
e-mail: [etakinlabi@uj.ac.za](mailto:etakinlabi@uj.ac.za)

S. A. Akinlabi · S. Hassan  
Department of Mechanical Engineering, Walter Sisulu University, Butterworth Campus,  
Butterworth, South Africa

R. M. Mahamood  
Department of Material and Metallurgical Engineering, University of Ilorin, Ilorin, Nigeria

M. Y. Shatalov  
Department of Mathematics and Statistics, Tshwane University of Technology, Pretoria, South  
Africa

E. V. Murashkin  
Ishlinsky Institute of Problems in Mechanics, Russian Academy of Science, Moscow, Russia

## 1 Introduction

The titanium alloy is a very versatile material which has numerous industrial applications. The most applicable alloy of the titanium alloys is the Ti-6Al-4V alloy. Titanium and its alloys are materials of choice in a wide range of industrial applications owing to their high strength-to-weight ratio, exceptional biocompatibility, and corrosion resistance. These properties are obtained as a result of allotropic property possessed by these materials which is dependent on temperature and the effect of alloying on phase stability [1–5]. The alloy itself is limited in application due to its poor hardness, low wear resistance, and its ability to oxidize readily when exposed to extreme temperatures. It is therefore important for the alloy to be re-enforced regularly to avoid failure in the working environment. Various conditions affect the behavior of titanium alloys; hence, surface modification is a very important technique that should be employed for the improvement of the material properties of the titanium alloys [6–8], therefore, increasing the production cost of parts. Thus to reduce such cost of replacements, research into solutions that will solve this problem is important and by researching the relationship between the alloys and mechanical properties of their finished products, material failure will be eliminated.

The microstructures of titanium alloys are primarily described by the amount and arrangement of  $\alpha$  and  $\beta$  phases. The microstructures and mechanical properties of titanium alloys depend upon the processing history and heat treatment that the material had gone through [9–13]. To obtain fine microstructure, high cooling rate is however advised; the use of lasers as a modification tool for materials, however, makes this possible.

## 2 Methods

The investigation was performed with Al-Cu-Ti, which possessed particle size of 50–105  $\mu\text{m}$ . Ti-6Al-4V titanium alloy was used as the substrate while the Al-Cu-Ti powder was used to reinforce the titanium alloy. After the deposition was completed, the Al-Cu-Ti powder particles which were not fully melted and were clinging to the substrate and the deposit were removed. To obtain a homogeneous mixture of the powdery substances which possessed varying particle sizes and specific weights, a tubular shaker-mixer was used.

### 2.1 Parent Material

Ti-6Al-4V alloy was used as the substrate. Before the laser metal deposition took place, the substrate was sand blasted and sterilized with acetone to remove any unwanted impurities, which was one to aid the laser absorption before the deposition process.

## **2.2 *Experimental Set-Up***

The laser deposition operation was conducted at the National Laser Center, Council of scientific Research (NLC - CSIR). The laser created a melted pool on the surface of the titanium substrate, while a nozzle was used to deposit the Al–Cu–Ti reinforcement powders onto the surface of the substrate.

## **2.3 *Material Characterization***

The following material characterizations were conducted on the produced samples to ascertain the integrity of the deposit. These include.

### **2.3.1 *Hardness***

The hardness of a material is the measure of a material's ability to resist localized plastic deformations. Hardness testing involves a technique of forcing an indenter into a material to be tested under a controlled load. The size and depth of the measured dent is then compared to a hardness value. The Vickers hardness test is the chosen method of determining the hardness of the composite.

### **2.3.2 *Microstructure***

The optical microscope image is used to discuss the general microstructure, while the images from scanning electron microscope were used to explain the composition of the microstructures and how the molecules were arranged in the product. The titanium substrate is not only affected by varying the laser power but also by the addition of the deposited powder on the surface of the substrate. Hence, the emerging microstructure of the product will be different from that of the substrate.

## **3 *Results and Discussion***

### **3.1 *Microstructure (Optical Microscope)***

Using Al–Cu–Ti-based powders as re-enforcement by laser metal deposition enables the microstructure of the samples to be more observable, which further helps to illustrate the grain boundaries and formation. It shows the beta phase grains exist at a high scanning speed and the alpha phase grains exist at a lower scanning speed [14–16]. There is a reduction in the geometrical properties of the samples, such as

width, height, and heat-affected zone, with increasing the scanning speed due to the laser metal interaction.

### 3.1.1 Substrate Microstructure

Figure 1 illustrates the grain structure of the titanium substrate used for the investigation. The microstructure of the substrate is characterized by the formation of dark and light regions which represent two phases, namely beta ( $\beta$ ) phase and alpha ( $\alpha$ ) phase. The average grain size is approximately  $77\ \mu\text{m}$ . They are distributed through the area of the substrate as shown in Fig. 1. This is the basic microstructure of the substrate that was used for the investigation.

## 3.2 Scanning Electron Microscope (SEM)

The high-resolution images, which depict the microstructures of the samples, are taken using SEM. Figure 2 shows the structure of the grains. The solidification mechanism is due to laser beam interaction. The coating powder particles melt and create a liquid pool on the titanium (substrate) surface that undergoes a limited melting. Therefore, only small dilution of added elements is obtained. The amount of Al–Cu–Ti found in various zones of the coating supports this theory. Solidification begins with formation of some large particles such as Al and Cu [17, 18].

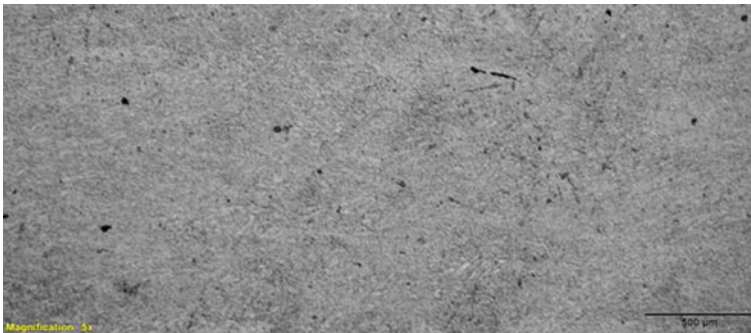


**Fig. 1** Microstructure of Ti–6Al–4V substrate

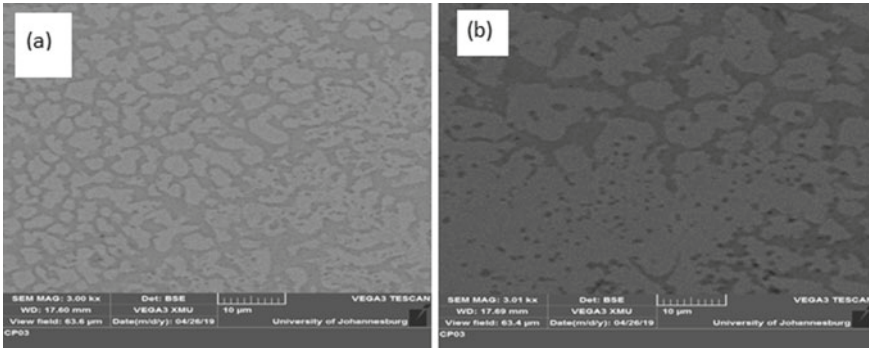


**Fig. 2** Microstructure of Ti-6Al-4V/Al-7Cu-5Ti at **a** 900 W and **b** 1000 W

### 3.3 Microhardness

The hardness values were recorded at different points on the intermetallic section where formation of the composite takes place. Then the average of these values for each sample was recorded as shown in Tables 1 and 2 (Fig. 3).

The mean hardness value increases with increasing the laser power. In this case, at the start of material deposition, the heat rapidly dissipated by the substrate heat conduction. It can be observed that the mean hardness value increases with increasing the laser power and this is due to the limited interaction within the powder and the laser. It is evident that in the composites, the highest mean hardness values are obtained at higher laser power of 1000 W for surface and 900 W for cross-section.

**Table 1** Microhardness test results (surface)

Samples	Laser power (W)	Scanning speed (m/min)	Mean surface hardness (HV)
Ti-6Al-4V	1000	1.0	417.54
Ti-6Al-4V/Al-4Cu-7Ti	900	1.0	619.86
Ti-6Al-4V/Al-7Cu-5Ti	900	1.0	652.66
Ti-6Al-4V/Al-7Cu-5Ti	1000	1.0	718.06

**Table 2** Microhardness test results (cross-section)

Samples	Laser power (W)	Scanning speed (m/min)	Mean cross-section hardness (HV)
Ti-6Al-4V	1000	1.0	418.00
Ti-6Al-4V/Al-4Cu-7Ti	900	1.0	476.18
Ti-6Al-4V/Al-7Cu-5Ti	900	1.0	335.74
Ti-6Al-4V/Al-7Cu-5Ti	1000	1.0	354.04

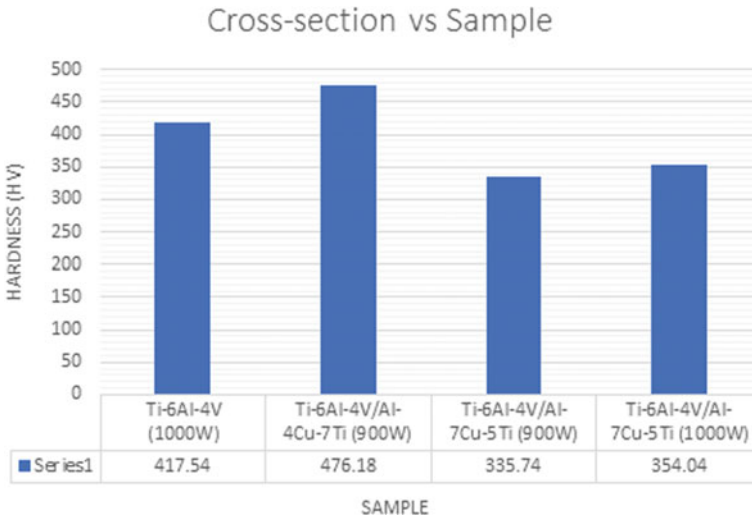


**Fig. 3** Hardness graph of titanium substrate and samples (surface)

## 4 Conclusions

The aim of the research project was to analyze the effect that hybrid coating (Al–Cu–Ti) powder has on Ti–6Al–4V. The experiments were conducted at different laser powers and scanning speeds. The optimization of process parameters for the LMD process was accomplished by quantifying and characterizing the composite formed. Based on the obtained results, the laser power of 1000 W and laser scanning speed of 1.0 are the optimum process parameters. The significant effect of the hybrid coating powder on a grade five titanium alloy is an increase in the hardness.

**Acknowledgements** This project was supported by NRF-IRG SA/Russia Bilateral and technical research collaboration grant No. NRF/UID, No. 118905 and NRF/RFBR No. 19-51-60001.

## References

1. Bansala D, Eryilmazb O, Blau P (2011) Surface engineering to improve the durability and lubricity of Ti–6Al–4 V alloy. *Wear* 271(9–10):2006–2015
2. Viswanathan V, Laha T, Balani K, Agarwal A, Seal S (2006) Challenges and advances in nanocomposite processing techniques. *Mater Sci Eng* 54:121–285
3. Dutta B, Froes FS (2017) The additive manufacturing (AM) of titanium alloys. In: *Metal powder report*, Volume 00
4. Hagedorn Y (2017) Laser additive manufacturing of ceramic components: materials, processes, and mechanisms. In: Brandt M (ed) *Laser additive manufacturing*. Woodhead Publishing Series, North Rhine-Westphalia, Germany, pp 163–180

5. Konečná R, Kunz L, Baca A, Nicoletto G (2017) Resistance of direct metal laser sintered Ti6Al4V alloy against growth of fatigue cracks. *Eng Fract Mech*
6. Raju R, Duraiselvama M, Petley V, Verma S, Rajendran R (2015) Microstructural and mechanical characterization of Ti6Al4 V refurbished parts obtained by laser metal deposition. *Mater Sci Eng A* 643:64–71
7. Liu ZC, Ning FD, Cong WL, Zhang HC (2016) Laser engineered net shaping of metal powders: a study on energy consumption. In: *Solid freeform fabrication 2016: Proceedings of the 26th annual international solid freeform fabrication symposium—An additive manufacturing conference reviewed paper*
8. Wang ZM, Ezugwu EO (1997) Titanium alloys and their machinability a review. *J Mater Process Technol* 68:262–270
9. Zhu YY, Liu D, Tian XJ, Li J, Wang HM (2014) Microstructure evolution and layer bands of laser melting deposition Ti–6.5 Al–3.5 Mo–1.5 Zr–0.3 Si titanium alloy. *J Alloys Compd* 616:468–474
10. Fatoba OS, Popoola API, Aigbodion VS (2016) Experimental study of hardness values and corrosion behaviour of laser alloyed Zn–Sn–Ti coatings of UNS G10150 mild steel. *J Alloy Compd* 658:248–254
11. Gong X, Lydon J, Cooper K, Chou K (2014) Beam speed effects on Ti–6Al–4 V microstructures in electron beam additive manufacturing. *J Mater Res* 29:1951–1959
12. Makhatha ME, Fatoba OS, Akinlabi ET (2017) Effects of rapid solidification on the microstructure and surface analyses of laser-deposited Al–Sn coatings on AISI 1015 steel. *Int J Adv Manuf Technol* 1–15. <https://doi.org/10.1007/s00170-017-0876-y>
13. Fatoba OS, Akinlabi ET, Akinlabi SA (2018) Numerical investigation of laser deposited Al-based coatings on Ti–6Al–4 V alloy. In: *Proceedings at the 2018 IEEE 9th international conference on mechanical and intelligent manufacturing technologies (ICMIMT 2018)*, Cape town, South Africa, pp 85–90. <https://doi.org/10.1109/icmimt.2018.8340426>
14. Fatoba OS, Popoola API, Aigbodion VS (2018) Laser alloying of Al–Sn binary alloy onto mild steel: inSitu formation. Hardness and anti-corrosion properties. *Lasers Eng* 39(3–6):292–312
15. Gharehbaghi R, Akinlabi ET, Fatoba OS (2018) Experimental investigation of laser metal deposited icosahedral Al–Cu–Fe coatings on grade five titanium alloy. In: *Proceedings at the 2018 IEEE 9th international conference on mechanical and intelligent manufacturing technologies (ICMIMT 2018)*, Cape town, South Africa, pp 31–36. <https://doi.org/10.1109/icmimt.2018.8340416>
16. Fatoba OS, Akinlabi ET, Akinlabi SA (2018) Effects of Fe addition and process parameters on the wear and corrosion properties of laser deposited Al–Cu–Fe coatings Ti–6Al–4 V alloy. In: *Proceedings at the 2018 IEEE 9th international conference on mechanical and intelligent manufacturing technologies (ICMIMT 2018)*, Cape town, South Africa, pp 74–79. <https://doi.org/10.1109/icmimt.2018.8340424>
17. Fatoba OS, Adesina OS, Popoola API (2018) Evaluation of microstructure, microhardness, and electrochemical properties of laser-deposited Ti–Co coatings on Ti–6Al–4 V Alloy. *Int J Adv Manuf Technol*. <https://doi.org/10.1007/s00170-018-2106-7>
18. Fatoba OS, Akinlabi SA, Gharehbaghi R, Akinlabi ET (2018) Microstructural analysis, microhardness and wear resistance properties of quasicrystalline Al–Cu–Fe coatings on Ti–6Al–4V alloy. *Mater Express Res* 5(6):1–14. <https://doi.org/10.1088/2053-1591/aaca70>



# Feasibility Study of Through Hole Fabrication on Aluminium Nitride Ceramic Using Die-Sinking Electro-Discharge Machining



Asif Rashid, M. P. Jahan, D. Talamona, and A. Perveen

**Abstract** A series of experiments were carried out to machine aluminium nitride (AlN) ceramic by die-sinking electro-discharge machining (EDM) process. EDM is a non-conventional machining process that requires the workpiece to be electrically conductive. An assisted-electrode method is used to make the surface of the workpiece conductive enough to machine. A combination of graphene paste, carbon nanotube, and copper tape has been used to make the coating surface. Tungsten carbide tool has been used. The findings indicate that, for low pulse energy, it is possible to generate through holes in this process. A combination of low peak current and high gap voltage proved to be successful in this method. The surface of the machined hole reveals that thermal spalling is present as material removal mechanism, which results in a rough surface. The energy dispersive spectroscopy (EDS) analysis proves that carbon deposition occurs in the wall of the holes to promote successful machining. Copper is also present in the machined surface. A feasible process has been developed to machine AlN ceramics using EDM process.

**Keywords** Coating · Carbon nanotube · Ceramics · Through hole · Pulse energy · Die-Sinking EDM

## 1 Introduction

Electrical discharge machining (EDM) has established itself as a viable non-conventional machining process for difficult-to-cut materials. Complex shapes to materials with high wear resistance can be achieved through EDM process [1–3]. Creating structures like bores, grooves, and undercuts in miniaturized hard components is also possible through EDM [4, 5]. Although EDM requires the workpiece

---

A. Rashid · M. P. Jahan

Department of Mechanical and Manufacturing Engineering, Miami University, Oxford, OH 45056, USA

D. Talamona · A. Perveen (✉)

Department of Mechanical & Aerospace Engineering, Nazarbayev University, Nur-Sultan 010000, Kazakhstan

e-mail: [perveen.asma@gmail.com](mailto:perveen.asma@gmail.com)

© Springer Nature Singapore Pte Ltd. 2020

S. S. Emamian et al. (eds.), *Advances in Manufacturing Engineering*, Lecture Notes in Mechanical Engineering, [https://doi.org/10.1007/978-981-15-5753-8\\_49](https://doi.org/10.1007/978-981-15-5753-8_49)

to be electrically conductive in order for it to be machined, recent experiments with modifications have been carried out where insulators, like ceramic materials, were machined using this process [5, 6].

In EDM process, removal of materials occurs by means of precisely controlled electrical sparks. Voltage difference applied between electrode and workpiece causes generation of sparks. Material removal occurs in the form of micro-size craters. Dielectric medium is needed between the electrode and workpiece. High voltage difference forces the dielectric to break down and creates a channel for electric pulses to reach the workpiece [7]. Ceramic materials are generally electrically non-conductive by nature and offer high hardness, great resistance to wear and chemical changes. Three basic mechanisms such as natural electrical conduction by free lattice electrons, doping with conductive materials, and adding impurity atoms can be used to generate electrical conductivity to insulating ceramic materials [8]. Assistive electrode method was the first successful attempt at machining non-conductive ceramics by EDM process. For assisting electrode methodology, EDM process is initiated by a conductive layer on the surface of insulating ceramics, where a carbonaceous oil is used as dielectric. Molecules of the hydrocarbon dielectric oil as well as the workpiece are cracked because of the high temperature generated by the electric discharges. This process assists carbon molecules to bind itself with ceramic materials. Since these carbon molecules are conductive in nature, discharge may continue to occur even though the conductive layer is removed. As a result, both the conductive layer and ceramic materials beneath that layer will be removed. A star-shaped through hole of 3.5 mm diameter was constructed in sialon ceramic. A copper conductive layer was used along with a copper electrode. Material removal rate was improved by adding tool rotation and flushing to the system, this setup also allowed better surface finish to the drilled hole [9]. It was later concluded that both the conductive layer and dielectric have an effect on machining ceramics by EDM [10]. Incorporating advanced carbon compounds during ceramic machining by EDM process is one of the newest approaches in this field. Carbon nanotubes (CNT) have excellent conductive properties and can improve the overall electrical conductivity of a system [11–13]. Adding carbon nanotubes with ceramic composites in a modified assisted-electrode method greatly affects its material and machining properties [14]. Material removal rate is greatly affected by combining carbon nanostructure with assisted-electrode method while machining Si<sub>3</sub>N<sub>4</sub>. Surface roughness also is improved by adding carbon nanotubes in assisted-electrode process [15]. In the previous work, blind hole was fabricated using die-sinking EDM on AlN ceramics [16]. In this study, new conductive coating, consisting of graphene paste as well as four layers of copper tape, where carbon nanotubes were sandwiched between two layers of copper, is proposed which acts as an assisting electrode. It was demonstrated that this method was applied successfully to fabricate through hole on AlN ceramics by die-sinking EDM.

## 2 Experimental Setup, Parameters and Materials

### 2.1 Experimental Setup

The experiments were carried out on EXCETEK ED 400 die-sinker EDM machine. For our experiments, only z-direction movement was utilised as the goal of the study was to machine through holes. In the experiments, a tungsten carbide electrode with 1.98 mm diameter was used. A vice is used to hold the workpiece tightly. Coatings had to be applied in a manner that it could form a conductive circuit with the vice of the machine. The machining is only carried out in z-direction to generate holes. The flushing is turned on while machining. The tool rotation is turned off during the machining process. Aluminium nitride (AlN) ceramic material is used as the workpiece. The thickness of the workpiece is 1.4 mm. Graphene paste, carbon nanotube (CNT), and copper tape have been used as coating materials. The peak current was kept at 1 Amp for all sets of experiments. The pulse-on time was fixed at 100 microseconds ( $\mu\text{s}$ ). The pulse-off time was varied between 200 and 300 microseconds ( $\mu\text{s}$ ). High voltage discharge of 235 V DC was selected, and the low voltage current was kept at 1.2 Amp for all experiments. The gap voltage was kept at 80 Volts. The servo speed was kept at a relatively lower setting. Flushing was always present during machining. The tool rotation was turned off to initiate better condition for carbon deposition.

### 2.2 Applying the Coating

In the experiments, a simple and easy to remove coating setup has been used. Such a setup made sure that the coating can be removed simply after machining. So, the sample can be analysed effectively. The step-by-step coating process is mentioned below: 1. A thin layer of graphene paste is added to the top of the ceramic surface. A ceramic is then kept in the oven for an hour with temperature reaching 300 °C. This makes sure that the graphene paste is placed uniformly over the surface. 2. The workpiece is taken out of the oven and cooled down. Then a layer of carbon nanotube powder is added on the top. The powder is then covered by a layer of copper tape that makes sure that the powder stays in place. This process with CNT and copper tape is then repeated for two more times. Finally, a layer of copper tape is added to make the overall outside structure of the workpiece conductive. Therefore, there are three layers of CNT, three layers of copper tape around CNT plus one layer at the top, and an initial thin layer of graphene paste. This coating makes the surface of the ceramic material electrically conductive. Copper tape is added not only to hold the CNT powder in place, but also to create a conductive channel as copper tape is conductive.

### 3 Results and Discussions

The two cases for successful machining have been found with the same coating setup (Table 1). Figure 1 shows the top surface of the fabricated through holes. The coating is a thin layer of graphene paste baked at 300 °C for 1 h and four layers of copper tape on top. Beneath each layer of copper tape, there is a low amount of carbon nanotube. As can be seen in Fig. 2a, b, CNT powders are stuck to the tape adhesive on the side wall of through hole and the layer is very thin. The surface of the machined hole reveals a relatively rough surface and degree of hole roundness is not very clear due to the presence of deformed copper layer. For the case 2, the hole seems to have quite high degree of out of roundness issue. Thermal spalling is present on the surface. Thermal cracks and porosity are also present on the surface.

EDS analysis (Fig. 3) for the machined surface reveals the reason behind the achievement of through holes generation. There is a very high amount of carbon deposition around the wall of the machined surface. Copper is also present in these regions. These conductive materials can make the wall of the workpiece conductive, and EDM can be used to machine these conductive regions. Therefore, presence

**Table 1** Machining conditions for two different successful through hole machining

Parameters	Case 1	Case 2
Coating	Thin layer of graphene paste baked at 300 °C for 1 h, four layers of copper tape on top. Beneath each layer of copper tape, there is a low amount of carbon nanotube. CNT powders are stuck to the tape adhesive and the layer is very thin	Thin layer of graphene paste baked at 300 °C for 1 h, four layers of copper tape on top. Beneath each layer of copper tape, there is a low amount of carbon nanotube. CNT powders are stuck to the tape adhesive and the layer is very thin
Tool	Tungsten carbide	Tungsten carbide
Tool diameter	1.98 mm	1.98 mm
Tool rotation	No	No
Dielectric	Hydrocarbon oil	Hydrocarbon oil
Flushing	Yes	Yes
Depth reached	Through hole (1.4 mm)	Through hole (1.4 mm)
Peak current	1 Amp	1 Amp
Pulse-on time	100 $\mu$ s	100 $\mu$ s
Pulse-off time	200 $\mu$ s	300 $\mu$ s
High voltage discharge	235 V	235 V
Low voltage current	1.2 Amp	1.2 Amp
Servo speed	10 steps	10 steps
Gap voltage	80 V	80 V
Machining time	80 min	80 min

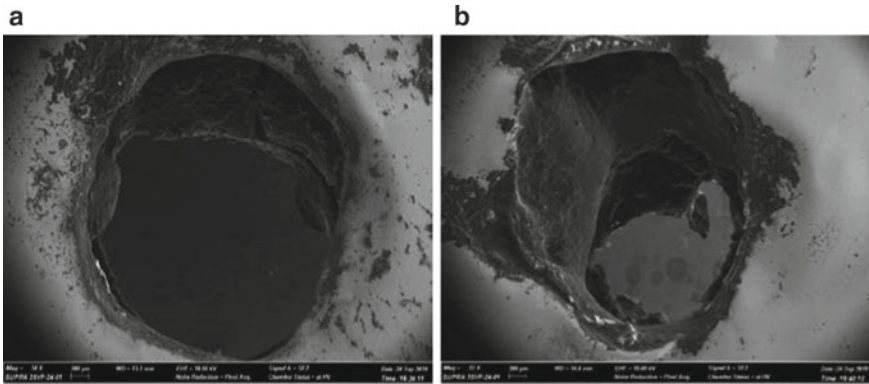


**Fig. 1** a Top surface of the machined through hole for case 1, b Top surface of the machined through hole for case 2

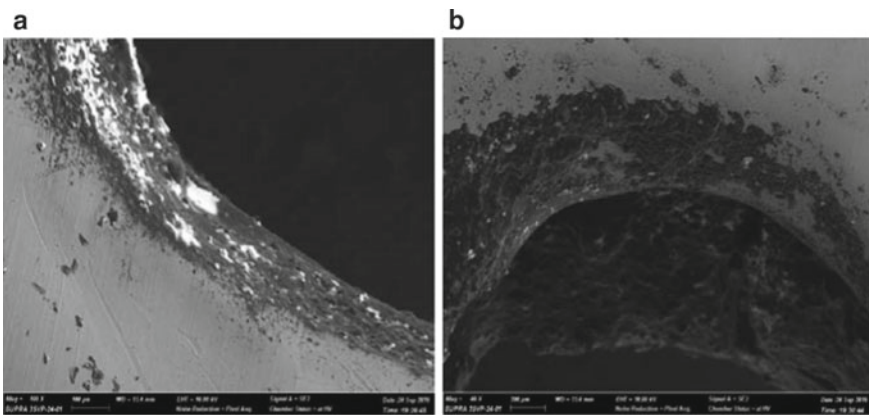


**Fig. 2** a Edge of the machined through hole viewed from top (case 1), b Edge and machined surface viewed from the top

and deposition of these conductive materials allow EDM to work on non-conductive aluminium nitride material.

## 4 Conclusions

This study investigates the feasibility of machining through hole on aluminium nitride (AlN) ceramic using assisted-electrode method. Three layers of CNT, three layers of copper tape around CNT plus one layer at the top, and an initial thin layer of graphene paste act as assistive electrodes in this study. The following conclusions can be made from the experiments:

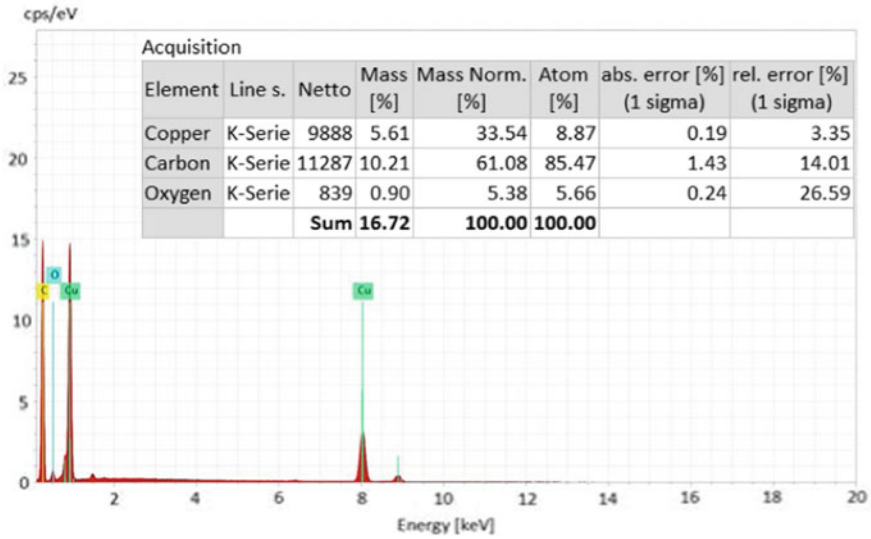


Fig. 3 Spectral analysis of the interest region around machined surface

- Through holes can be machined successfully in AlN ceramics using EDM process. Proper machining setup and right machining parameters are prerequisite for successful machining. The combination of carbon nanotube and copper tape as coating materials is very effective.
- Low energy sparks are effective for machining ceramic by EDM. Very low peak current and pulse-on time is necessary for obtaining successful through hole.
- There is very high amount of carbon deposition around the machined surface. Copper is also present near the walls of the holes. This carbon deposition is the key to achieve successful through holes in ceramic materials by EDM process.

**Acknowledgements** This research study is funded by Nazarbayev University under the project “Multi-scale Investigation of the Machining Behaviour of Non-conductive Ceramics Using Electro-Discharge Machining” (Grant No: 090118FD5324).

**References**

1. Uhlmann E, Domingos DC (2013) Investigations on vibration-assisted EDM-machining of seal slots in high-temperature resistant materials for turbine components. Proc CIRP 6:71–76
2. Sabyrov N, Jahan MP et al (2019) Ultrasonic vibration assisted electro-discharge machining (edm)—an overview. Materials 12(3):522
3. Kumar S, Kumar A, Kumar V, Singh NK (2018) Study of machining of Inconel 825 super alloy using powder mixed EDM process. Mater Today Proc 5(9):18129–18134

4. Chen X, Wang Z, Xu J et al (2018) Sustainable production of micro gears combining micro reciprocated wire electrical discharge machining and precision forging. *J Clean Prod* 188:1–11
5. Bilal A, Jahan MP et al (2019) Electro-discharge machining of ceramics: a review. *Micromachines* 10(1):10
6. Yongfeng G, Yerui F et al (2018) Experimental investigation of EDM parameters for ZrB<sub>2</sub>-SiC ceramics machining. *Proc CIRP* 68:46–51
7. Schumacher BM (2004) After 60 years of EDM the discharge process remains still disputed. *J Mater Process Technol* 149(1):376–381
8. König W, Dauw DF et al (1988) EDM-future steps towards the machining of ceramics. *CIRP Ann* 37(2):623–631
9. Mohri N, Fukuzawa Y, Tani T, Saito N, Furutani K (1996) Assisting electrode method for machining insulating ceramics. *CIRP Ann* 45(1):201–204
10. Hösel T, Müller C et al (2011) Spark erosive structuring of electrically nonconductive zirconia with an assisting electrode. *CIRP J of Manuf Sci Tech* 4(4):357–361
11. Dalkılıç AS et al (2018) Experimental study on the thermal conductivity of water-based CNT-SiO<sub>2</sub> hybrid nanofluids. *Int Commun Heat Mass Transf* 99:18–25
12. Van Trinh P, Anh NN et al (2018) Experimental study on the thermal conductivity of ethylene glycol-based nanofluid containing Gr-CNT hybrid material. *J Mol Liq* 269:344–353
13. Hassanzadeh-Aghdam MK, Mahmoodi MJ et al (2018) Effect of CNT coating on the overall thermal conductivity of unidirectional polymer hybrid nanocomposites. *Int J Heat Mass Transf* 124:190–200
14. Chaudhury P, Samantaray S (2017) Role of carbon nano tubes in surface modification on electrical discharge machining a review. *Mater Today Proc* 4(2):4079–4088
15. Hanaoka D, Fukuzawa Y, Ramirez C et al (2013) Electrical discharge machining of ceramic/carbon nanostructure composites. *Proc CIRP* 6:95–100
16. Sarsen A, Bilal A et al (2019) Assistive electro discharge machining of AlN ceramics. *Mater Sci Forum* 947:109–113

# CFD Study on the Thermal Performance of n-Octadecane (PCM) Doped with Graphene Nanoparticles as a Potential Thermal Energy Storage Medium for Trombe Walls



Chukwumaobi K. Oluah, Esther T. Akinlabi, and Howard O. Njoku

**Abstract** Thermal energy storage is one of the methods used in reducing energy consumption and heat recovery from thermal systems. Some of the major applications of heat storage systems are in buildings, solar energy technologies, and waste heat recovery from high-temperature applications. Thermal energy storage could be in the form of sensible heat, latent heat, or chemical heat arising from bond breaking and formation in chemical reactions. Among all these forms of solar energy storage aforementioned, latent heat thermal energy storage is greatly explored because it is generally safe to use and its ability to store a large quantity of heat in a relatively small volume. Phase change materials (PCMs) are widely used in latent heat thermal energy storage systems. Some of the setbacks encountered with the use of PCMs are its low-thermal conductivity and subcooling characteristics. Nanoparticles have been found very useful in improving the thermal conductivity of PCMs, thereby improving its general performance. The nano-PCM considered in this work is (graphene + octadecanol). The top surface of the nano-PCM enclosure was exposed to ambient solar radiation. The solar radiation data for Johannesburg (26.2041° S, 28.0473° E) was used for the simulation. A two-dimensional heat transfer equation was solved numerically using initial, boundary, and phase transition conditions. The effect of volume fractions of nanoparticles on the melt fractions was investigated. From the result obtained, the PCM with 4% loading of nanoparticles yielded the best result.

**Keywords** CFD · Phase change materials (PCMs) · Graphene nanoparticles  
Trombe walls

---

C. K. Oluah (✉) · E. T. Akinlabi · H. O. Njoku  
Department of Mechanical Engineering Sciences, University of Johannesburg, Johannesburg  
2006, South Africa  
e-mail: [218107364@student.uj.ac.za](mailto:218107364@student.uj.ac.za)

Department of Mechanical Engineering, University of Nigeria, Nsukka 410001, Enugu State,  
Nigeria



## 1 Introduction

Space conditioning in buildings has been identified as one of the major consumers of the final global energy production. This figure was reported to be about 40% of annual global energy production by the international energy agency [1]. A greater majority of the global energy resource is fossil-based and comes with increased CO<sub>2</sub> production. The rapidly growing population of the world and the effect of climate change accounts for the rise in energy demand. Some of the adverse effects of global warming as listed by the IPCC include but not restricted to the following; a continuous rise in temperature, increased hurricane, more drought, heatwaves, etc. [2]. It is due to this cause that scientists have sought to reduce global CO<sub>2</sub> emission while maintaining reasonable thermal comfort. Over the past decades, researches have studied various novel renewable approaches to meet the energy requirements of residential or commercial buildings while keeping the environment safe. Thermal energy storage (TES) is one way that many researchers have proposed, that can sufficiently reduce a building's energy demand. It finds a useful application in solar thermal systems as well as heat recovery systems [3]. Thermal energy storage (TES) mediums are green systems that result in zero-emission of carbon into the atmosphere. Thermal energy storage (TES) systems absorb heat, store it, and release it when required for use; this helps in load shedding in buildings. TES is further classified based on their mode of operation as; chemical heat storage (CHTES), sensible heat storage (SHTES), or latent heat storage (LHTES) [4]. Trombe walls are passive solar structures used for thermal energy storage and delivery [5]. It consists of a massive wall installed a few distances from glazing. The Trombe wall absorbs solar radiation through the glazing and the heat is transferred by conduction into the room. The massive wall serves as a thermal battery used for either heating or cooling application. Scientists have made various modifications to the conventional Trombe wall in order to improve its performance, most of which are documented in literature. Researchers have identified the massive wall as the most germane component of the Trombe wall system. Some researchers have tried to improve the thermal mass of the wall by using bricks, aerated concrete, and PCMs. Krishna et al. [6] induced aluminum oxide nanoparticles in tricosane for electronic cooling application; a 25% in evaporation temperature was recorded; Das et al. [7], introduced carbon-based nanocomposites to n-eicosane; a melting rate of 27% and 40% was recorded SWCNT and graphene respectively. Mahdi and Nsofor [8] doped aluminum oxide nanoparticles with rubitherm 82 (RT82), an improvement in the melting process was reported by the authors. Sciacovelli et al. studied the enhancement of the thermal properties of n-octadecane using copper nanoparticles; the experimental findings showed that when 4% volume fraction of the nanoparticle was inoculated in the base PCM, a 16% improvement in heat flux and consequently a 15% reduction in the melting rate were recorded [9]. Wu et al. studied the improvement in thermal properties of paraffin wax using copper nanoparticles. The nanoparaffin wax was contained in a vertical cylindrical tube and heat source was introduced at the bottom of the enclosure. A 13% improvement in thermal properties was achieved with the introduction of 1 wt%

of nanoparticle [10]. Putra et al. experimentally studied the effect of graphene on rubitherm-22. They obtained graphene platelets of particle size range of 21.5–65.5. They reported a thermal conductivity enhancement of 306% upon inoculation of 0.05 wt% of graphene nanoparticle [11]. Babaei et al. experimentally investigated the thermal conductivity enhancement of bio-based PCM using carbon nanotubes of particle size 100 nm; the thermal conductivity of the nano-PCM increased from 0.15 to 0.41 W/mK for a 1 wt% concentration of the CNT.

The foregoing discussions have revealed that the introduction of nanoparticles in phase change materials generally improves their thermal conductivity. PCMs are materials of interest in thermal energy storage in engineering applications due to the advantage of storing large quantities of heat in a relatively small volume and lightweight. Research findings have shown that the limitations of PCMs in thermal conductivity can be overcome by doping with nanoparticles. The essence of this work is to simulate the performance of PCM doped with graphene nanoparticles, as a potential thermal energy storage medium in Trombe walls. Some researchers have used PCM in Trombe walls but there is no literature on the application of nanoenhanced phase change materials as massive wall materials in Trombe walls, hence the need for this study. The environmental condition of Johannesburg where the project is being executed was used in the simulation. Furthermore, we seek to find the optimum nanoparticle loading which will yield best performance when installed in a Trombe wall system.

## 2 Problem Formulation

A cylindrical storage enclosure is considered, with physical dimensions of length ( $L = 150$  mm) and diameter of 150 mm as shown below (Fig. 1).

The walls are adiabatic but the top surface is exposed to receive solar radiation. The cylinder is filled with the nano-PCM. For simplicity of analysis, it is assumed that the nanoparticles are evenly dispersed in the PCM and are in thermal equilibrium. The

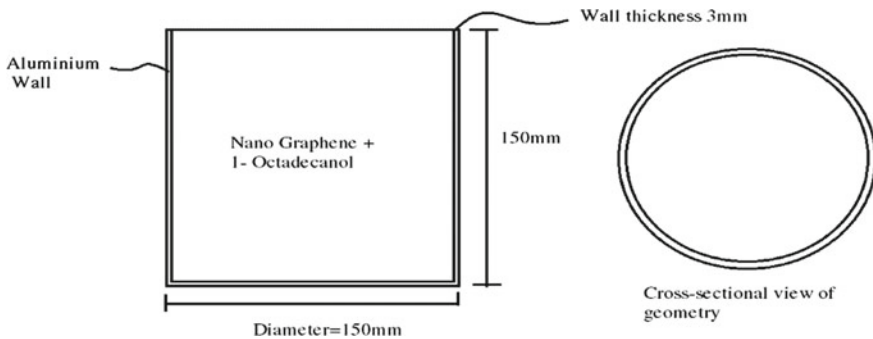


**Fig. 1** Geometry description of the PCM storage wall

walls of the container are adiabatic except the top which is exposed to solar insolation. Thermal energy from the sun ( $T_{\text{sun}}$ ) penetrates through the top to the bottom. The melting process starts when the energy from the sun exceeds the fusion temperature of the PCM denoted as  $T_m$ . The initial temperature of the nano-PCM is denoted as  $T_o$ , which is less than  $T_m$ . When the melting proceeds, there will exist liquid–solid interphase; this liquid phase is assumed to be Newtonian and incompressible.

## 2.1 Governing Equations

From the problem formulation, the governing equations are the conservation of mass equation, momentum, and energy equation in cylindrical coordinates. Presented below are these equations.

Conservation of mass:

$$\frac{\partial u}{\partial r} + \frac{u}{r} + \frac{\partial w}{\partial z} = 0 \quad (1)$$

r-momentum equation:

$$\frac{\partial u}{\partial t} + u \frac{\partial u}{\partial r} + w \frac{\partial u}{\partial z} = -\frac{1}{\rho} \frac{\partial P}{\partial r} + \mu \left( \frac{\partial^2 u}{\partial r^2} + \frac{1}{r} \frac{\partial u}{\partial r} - \frac{u}{r^2} + \frac{\partial^2 u}{\partial z^2} \right) \quad (2)$$

z-momentum equation:

$$\frac{\partial w}{\partial t} + u \frac{\partial w}{\partial r} + w \frac{\partial w}{\partial z} = -\frac{1}{\rho} \frac{\partial P}{\partial z} + \mu \left( \frac{\partial^2 w}{\partial r^2} + \frac{1}{r} \frac{\partial w}{\partial r} - \frac{u}{r^2} + \frac{\partial^2 w}{\partial z^2} \right) \quad (3)$$

Energy equation:

$$\rho c_p \frac{\partial T}{\partial t} + \rho c_p \left[ u \frac{\partial T}{\partial r} + w \frac{\partial T}{\partial z} \right] = k \left[ \frac{1}{r} \frac{\partial}{\partial r} \left( r \frac{\partial T}{\partial r} \right) + \frac{\partial^2 T}{\partial z^2} \right] \quad (4)$$

## 2.2 Thermophysical Properties

The thermophysical properties of the graphene and 1-octadecanol are summarized in the table below.

Material	$T_m$	$K$ (W/m °C)		$C$ (J/mol °C)		$P$ (Kg/m <sup>3</sup> )		$\Delta H$ (KJ/Kg)
		Solid	Liquid	Solid	Liquid	Solid	Liquid	
1-octadecanol	28.8	0.358	0.148	485	564	814	778	245
Graphene	3652	119		15		2267		–

### 2.3 Phase Transition Relations

There is no sharp transition between the solid and the liquid phases, rather it occurs over a small temperature interval  $\Delta T_m$ . Approximations can be made for the thermo-physical properties of the nano-PCM at the onset of phase transition. The following mathematical expressions are approximations of the thermophysical properties of the nano-PCM at phase transition.

Density:

$$\rho = \begin{cases} \rho_{ns} & T < T_m \\ \frac{\rho_{ns} + \rho_{nl}}{2} & T_m \leq T \leq T_m + \Delta T_m \\ \rho_{nl} & T \geq T_m + \Delta T_m \end{cases} \quad (5)$$

Thermal conductivity:

$$k = \begin{cases} k_{ns} & T < T_m \\ \frac{k_{ns} + k_{nl}}{2} & T_m \leq T \leq T_m + \Delta T_m \\ k_{nl} & T \geq T_m + \Delta T_m \end{cases} \quad (6)$$

Heat capacity:

$$\rho C_p = \begin{cases} (\rho C_p)_{ns} & T < T_m \\ \frac{(\rho C_p)_{ns} + (\rho C_p)_{nl}}{2} + \frac{\rho_{ns} + \rho_{nl}}{2} \left( \frac{L_{hf,n}}{\Delta T_m} \right) & T_m \leq T \leq T_m + \Delta T_m \\ (\rho C_p)_{nf} & T \geq T_m + \Delta T_m \end{cases} \quad (7)$$

where  $L_{hf,n}$  is the latent heat of fusion of the nano-PCM and can be evaluated as;

$$L_{hf,n} = (1 - \varphi)L_{sf}. \quad (8)$$

Dynamic viscosity:

The dynamic viscosity for the solid nano-PCM is assumed too large while that of the liquid nano-PCM can be approximated using Eq. (9).

$$\mu = \begin{cases} \frac{\mu_f}{(1-\varphi)^{2.5}}, & T \geq T_m + \Delta T_m \\ 10^6 & T < T_m \end{cases} \tag{9}$$

The thermophysical relations for the nano-PCM is summarized in the table below

Properties	Liquid nano-PCM	Solid nano-PCM
Density	$\rho_{nl} = (1 - \varphi)\rho_f + \varphi\rho_n$	$\rho_{ns} = (1 - \varphi)\rho_s + \varphi\rho_n$
Heat capacity	$(\rho C_p)_{nl} = (1 - \varphi)(\rho C_p)_l + \varphi(\rho C_p)_n$	$(\rho C_p)_{ns} = (1 - \varphi)(\rho C_p)_s + \varphi(\rho C_p)_n$
Expansion coefficient	$(\rho\beta)_{nl} = (1 - \varphi)(\rho\beta)_l + \varphi(\rho\beta)_n$	$(\rho\beta)_{nl} = (1 - \varphi)(\rho\beta)_l + \varphi(\rho\beta)_n$
Thermal conductivity	$k_{nl} = \frac{k_n + 2k_l - 2\varphi(k_l - k_n)}{k_n + 2k_l + \varphi(k_l - k_n)} k_l$	$k_{ns} = \frac{k_n + 2k_s - 2\varphi(k_s - k_n)}{k_n + 2k_s + \varphi(k_s - k_n)} k_s$
Dynamic viscosity	$\mu_{nl} = \frac{\mu_l}{(1-\varphi)^{2.5}}$	

### 2.4 Initial and Boundary Conditions

Before the initialization of the melting process, time,  $t = 0$ . The temperature of the Nano-PCM is  $T = T_0$ . Mathematically, initial condition:  $u = w = 0, T = T_0$

All the surfaces are assumed to be insulated except the surface ( $z = H$ ) which is open to receiving solar radiation. Therefore, we have the following set of boundary conditions

$$u = w = 0, \frac{\partial T}{\partial r} = 0 \quad u = w = 0, \frac{\partial T}{\partial z}(\text{at } z = 0) = 0$$

$$u = w = 0, T(\text{at } z = H) = T_{\text{sol}}, \quad u = w = 0, \frac{\partial T}{\partial z} = -\frac{h}{k}(T_{\text{sol}} - T_a)$$

### 3 Results and Discussion

The following results were obtained for various loadings of nanoparticles in the PCM. The melt fraction, which determines the degree of heat absorption or release and a critical factor for the performance of a PCM, was considered at various times of the day. The melt fraction is evaluated thus.

$$M_f = \frac{\text{mass of liquid NPCM}}{\text{mass of liquid NPCM} + \text{mass of solid NPCM}}$$

The results of the melt fractions of volume concentrations of 0%, 4%, and 10%, respectively were presented. Also presented were graphs showing the combined performance of the various concentrations of nanoparticles at different times of the day.

### 3.1 Result of Pure PCM with 0% Graphene Content

The results presented below are melt fractions of the phase change material at various times of the day. A greater fraction of the PCM melted between the hours of 2 p.m.–3 p.m. Also presented alongside is the CFD image showing the mass fractions of the melted PCM (Figs. 2, 3, 4, and 5).

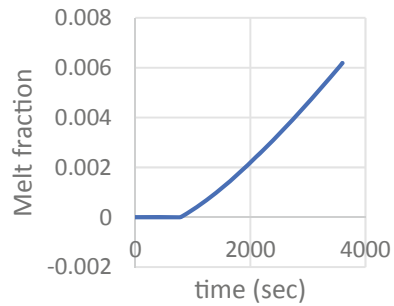
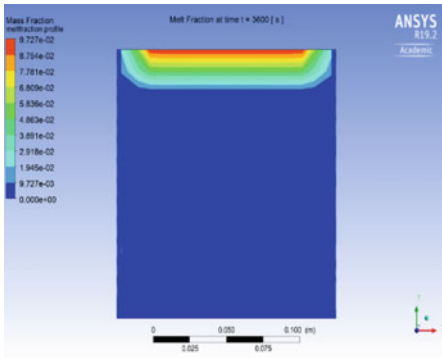


Fig. 2 Melt fraction profile of PCM with 0% graphene between 8 a.m. and 9 a.m.

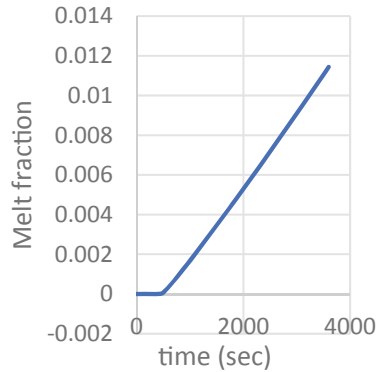
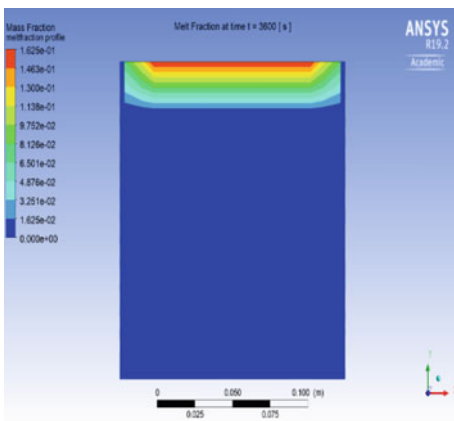


Fig. 3 Meltfraction profile of PCM with 0% graphene between 12 a.m. and 1 p.m.



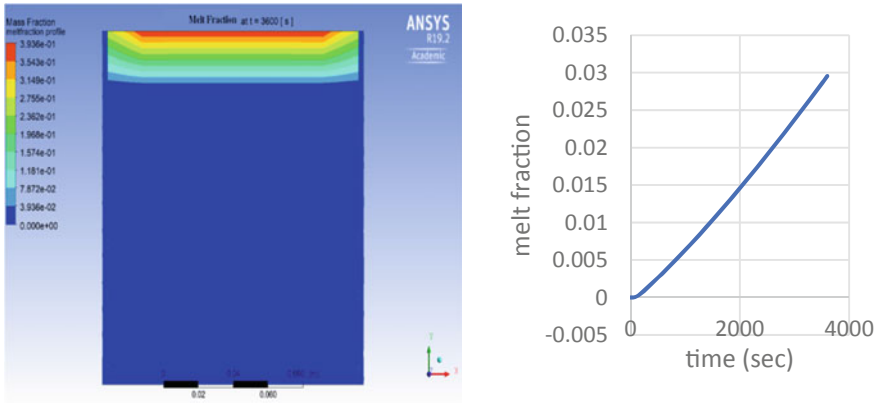


Fig. 6 Meltfraction profile of PCM with 4% graphene between 8 a.m. and 9 a.m.

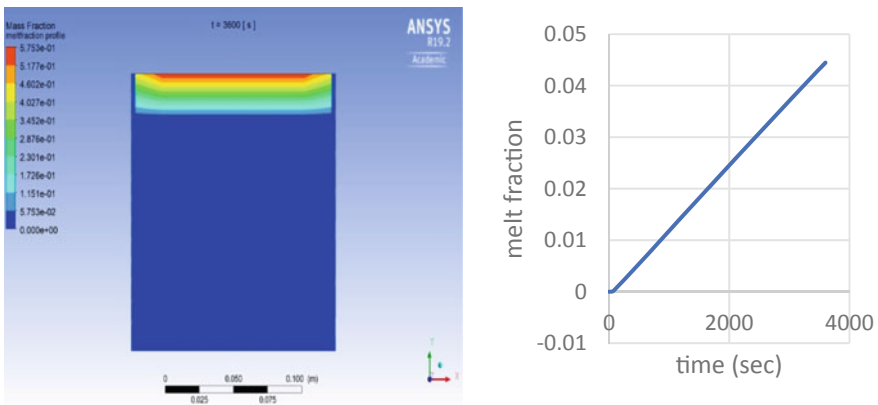


Fig. 7 Meltfraction profile of PCM with 4% graphene between 12 p.m. and 1 p.m.

### 3.3 Result of Pure PCM with 10% Graphene Content

A similar trend in result was obtained for the nano-PCM with 10% graphene content the (Figs. 10, 11, 12, 13, and 14).

From the results presented, a comparative performance graph was plotted as shown in Figs. 15, 16, 17, and 18, respectively. In the early hours of the morning, the PCM containing 4% graphene had a greater quantity melted followed by 10% loaded nanoparticle and 0%. At late hours of the morning and the mid-day, the PCM with 10% loading of nanoparticles showed a higher percentage of melted PCM, while at



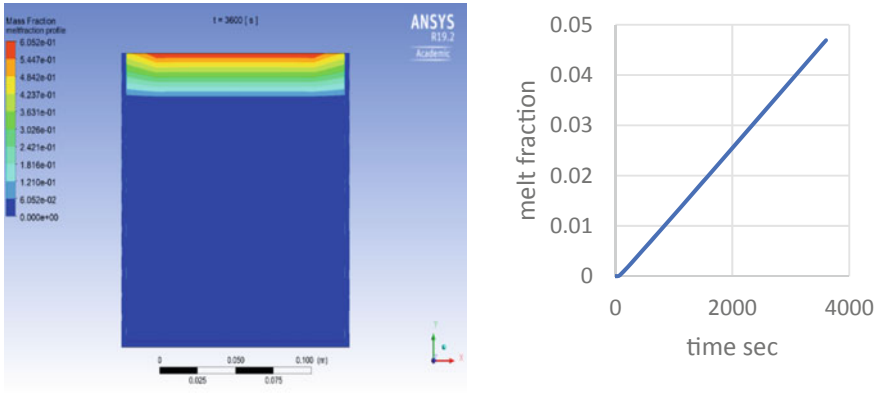


Fig. 8 Meltfraction profile of PCM with 4% graphene between 2 p.m. and 3 p.m.

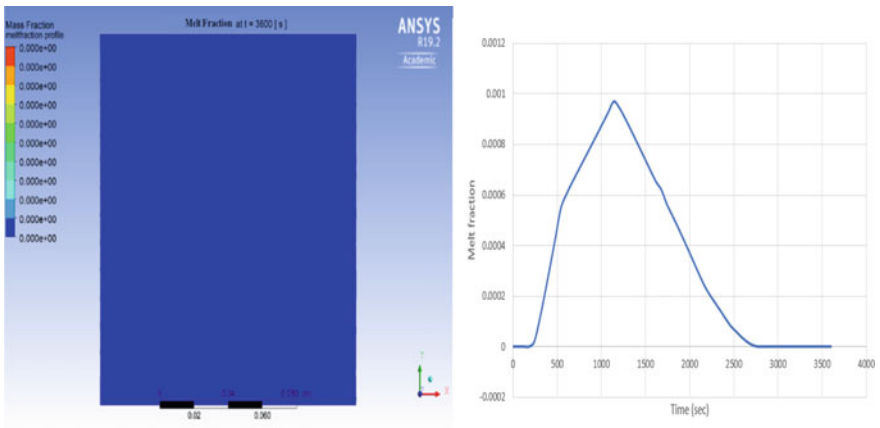


Fig. 9 Meltfraction of PCM with 4% graphene between 6 p.m. and 7 p.m.

night time, when the sunlight is gone, the PCM with 4% loading was seen to have retained more heat with higher melt fraction than both the pure PCM and the PCM with 10% graphene loading. The increased concentration of nanoparticles in the 10% nano-PCM led to faster charging and discharging of the nano-PCM. Whereas the ability of the PCM with 4% loading to retain heat at non-sunshine hours makes it the most suitable for use in real-life applications.

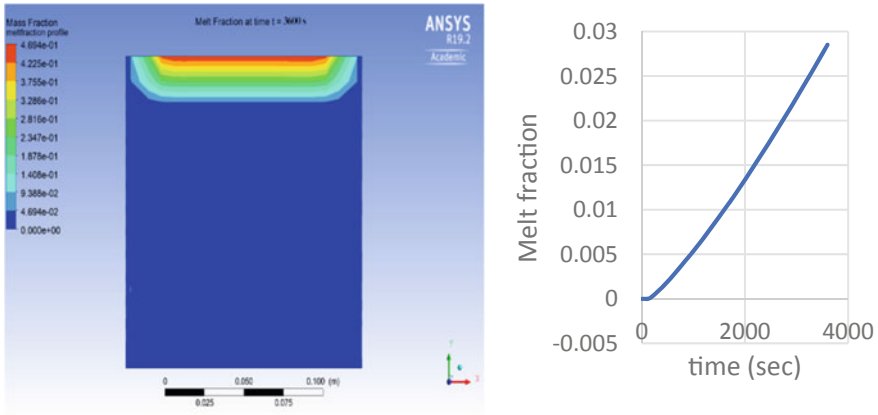


Fig. 10 Meltfraction profile of PCM with 10% graphene between 8 a.m. and 9 a.m.

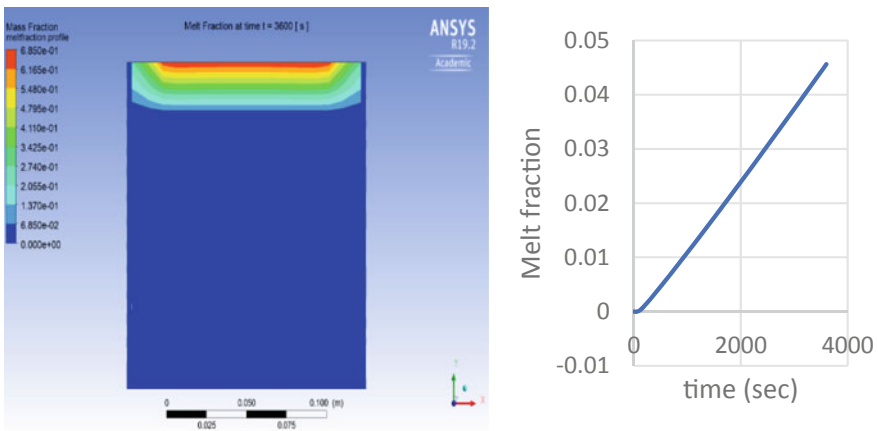


Fig. 11 Meltfraction profile of PCM with 10% graphene between 10 a.m. and 11 a.m.

### 4 Conclusion

The CFD studies on the melting performance of n-octadecane doped with various concentrations of graphene nanoparticle were studied in this work. The result presented has shown an hourly performance of the normal PCM and the PCM doped with nanoparticles. The results established that melt fraction increased as nanoparticles were introduced into the base PCM. One of the objectives of this study was to find the optimum concentration of nanoparticles that will yield the best result, and

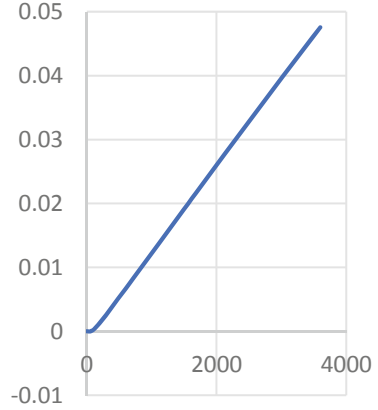
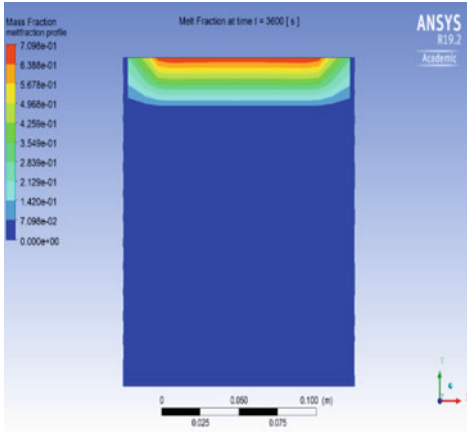


Fig. 12 Meltfraction profile of PCM with 10% graphene between 12 p.m. and 1 p.m.

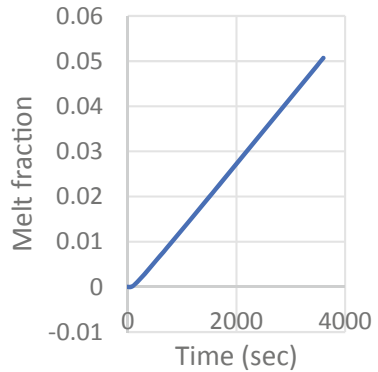
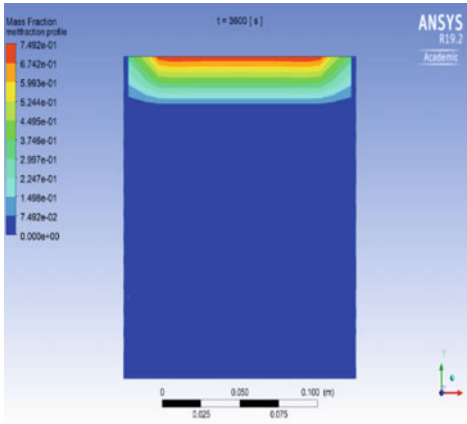


Fig. 13 Meltfraction of PCM with 10% graphene between 2 p.m. and 3 p.m.

as seen from the results presented, at 4% volume concentration, the nano-PCM gave an overall better performance than the rest. In the morning hours, the 4% volume concentration showed better heat conduction, while during the mid-day, the 10% volume concentration showed better heat conduction with a small margin; during the evening hours, the 4% volume concentration retained heat more than both the

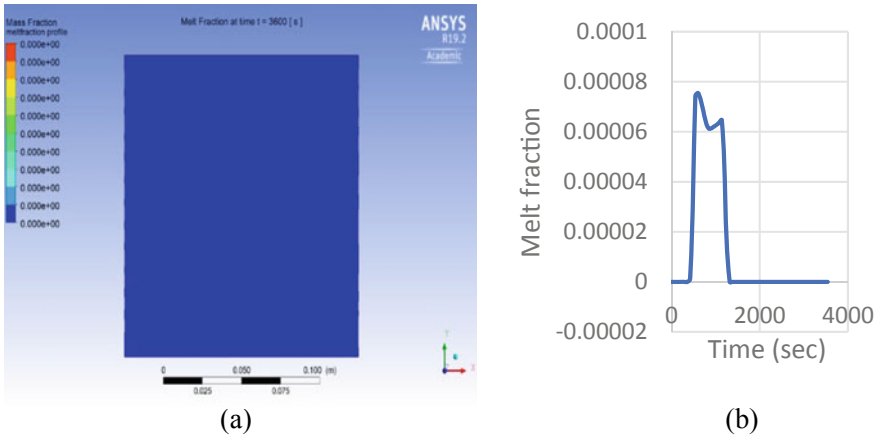


Fig. 14 a and b Meltfraction of PCM with 10% graphene between 6 p.m. and 7 p.m.

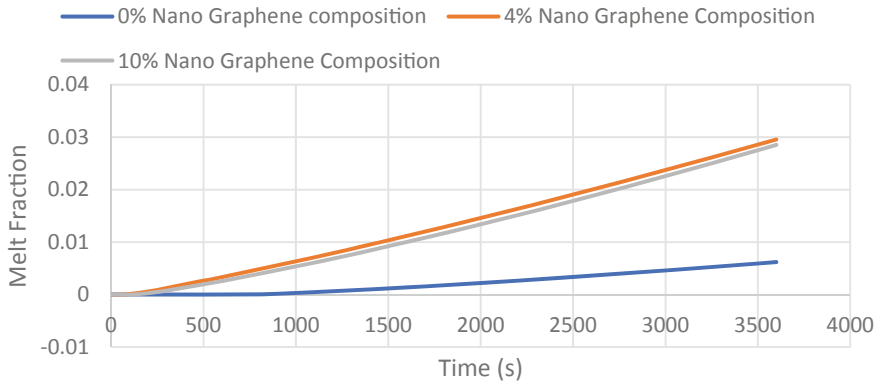


Fig. 15 Melt fraction of PCM with 0, 4, and 10% graphene between 8 a.m. and 9 a.m.

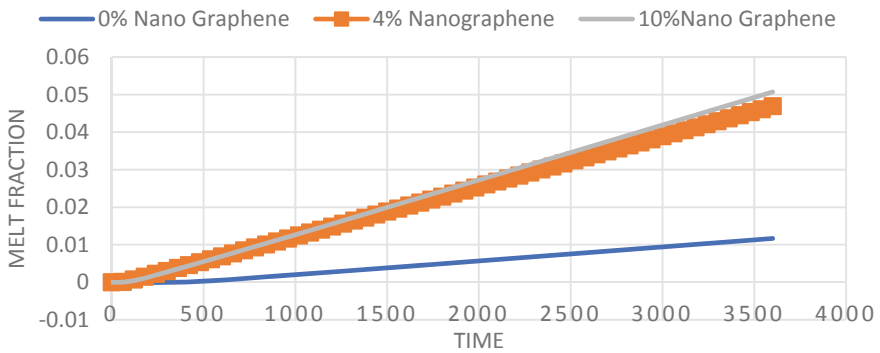


Fig. 16 Melt fraction of PCM with 0, 4, and 10% graphene between 12 p.m. and 1 p.m.

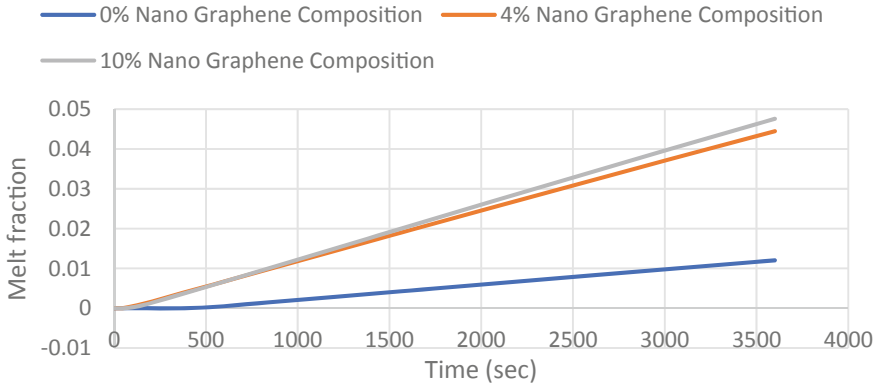


Fig. 17 Melt fraction of PCM with 0, 4, and 10% graphene between 2 p.m. and 3 p.m.

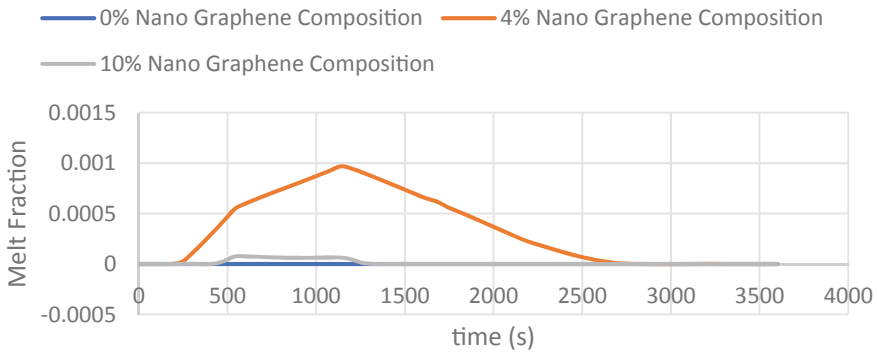


Fig. 18 Melt fraction of PCM with 0, 4, and 10% graphene between 6 p.m. and 7 p.m.

10 and 0%, which is important in keeping the room warm. Hence, the 4% volume concentration yielded the optimal result relevant to heat storage properties in Trombe wall applications. In furtherance to this work, an experimental investigation is being carried out to validate the simulation studies done.

## References

1. IEA roadmap targets <https://www.iea.org/publications/freepublications/publication/IEASolar>
2. IPCC 2007, Summary for policymakers. In: Climate change 2007: impacts, adaptation and vulnerability. Contribution of working group II to the fourth assessment report of the inter-governmental panel on climate change. Cambridge University Press, Cambridge, UK, p 17
3. Oysterman E et al (2012) Review of PCM based cooling technologies for buildings energy and buildings

4. Hassan N, Mariah B, Bolivar Osorio FJ, Marllory I, Xinhai Y, Vignarooban K, Patrick P, Inamuddin, Kannan AM (2019) Recent developments in phase change materials for energy storage applications: a review. *Int J Heat Mass Transf* 129:491–523
5. Bellos E, Tzivanidis C, Zisopoulou E, Mitsopoulos G, Antonopoulos KA (2016) An innovative Trombe wall as a passive heating system for a building in Athens-a comparison with the conventional Trombe wall and the insulated wall. *Energy Build* 133:754–769
6. Krishna J, Kishore PS, Solomon AB (2017) Heat pipe with nano enhanced-PCM for electronic cooling application. *Exp Thermal Fluid Sci* 81:84–92
7. Das N, Takata Y, Kohno M, Harish S (2017) Effect of carbon nano inclusion dimensionality on the melting of phase change nanocomposites in vertical shell-tube thermal energy storage unit. *Int J Heat Mass Transf* 113:423–432
8. Mahdi JM, Nsofor EC (2017) Melting enhancement in triplex-tube latent thermal energy storage system using nanoparticles-fins combination. *Int J Heat Mass Transf* 109:417–427
9. Sciacovelli A, Colella F, Verda V (2013) Melting of PCM in a thermal energy storage unit: numerical investigation and effect of nanoparticle enhancement. *Int J Energy Res* 37:1610–1623
10. Wu S, Wang H, Xia S, Zhu D (2012) Numerical simulation on thermal energy storage behavior of cu/paraffin nanofluids PCMs. *Procedia Eng* 31:240–244
11. Putra N, Amin M, Kosasih EA, Luanto RA, Abdullah NA (2017) Characterization of the thermal stability of RT 22 HC/graphene using a thermal cycle method based on thermoelectric methods. *Appl Therm Eng* 12:62–70. <https://doi.org/10.1016/j.applthermaleng.2017.06.009>

# Laser Metal Deposition of Titanium Composites: A Review



Esther T. Akinlabi, Ganiyat A. Soliu, R. M. Mahamood,  
Stephen A. Akinlabi, S. Hassan, M. Y. Shatalov, Evgenii Murashkin,  
and O. S. Fatoba

**Abstract** Composite materials are used for the manufacturing of light weight components and structures in many industries. Composite materials are obtained by combining materials with preferred properties and by synthesizing a new material using two or more materials having the desired properties. The composite material obtained has an enhanced proportion of the desired property of each of the constituent materials. Titanium alloy has been modified by adding another material to it to form titanium composites. Its properties make it suitable for most applications where low density and good corrosion resistance is necessary such as in turbine engine components, high-performance automotive parts, aircraft structural components, marine applications, aerospace fasteners, medical devices, biomedical applications (implant and prostheses) and sport equipment. Titanium composites are often used for surface modification to improve certain mechanical properties. The efficient fabrication of these composite materials is a significant challenge faced by manufacturers. The advent of additive manufacturing technology made it easier to fabricate composite materials like titanium. Laser metal deposition, an additive manufacturing process, is a process that offers excellent opportunities in fabrication of titanium and its composites. This process also helps to fabricate complex and innovative parts which

---

E. T. Akinlabi · R. M. Mahamood · O. S. Fatoba  
Department of Mechanical Engineering Science, University of Johannesburg, Auckland Park  
Kingsway Campus, 2006 Johannesburg, South Africa

G. A. Soliu  
Department of Mechanical Engineering, Federal Polytechnic Offa, Offa, Nigeria

R. M. Mahamood (✉)  
Department of Materials and Metallurgical Engineering, University of Ilorin, Ilorin, Nigeria  
e-mail: [mahamoodmr2009@gmail.com](mailto:mahamoodmr2009@gmail.com)

S. A. Akinlabi · S. Hassan  
Department of Mechanical Engineering, Walter Sisulu University, Butterworth Campus, East  
London, South Africa

M. Y. Shatalov  
Thwane University of Technology, Pretoria, South Africa

E. Murashkin  
Ishlinskiy Institute of Problems in Mechanic, Russian Academy of Science, Moscow, Russia

cannot be effectively manufactured using substantial manufacturing process. This paper provides an overview of laser metal deposition processes used for fabricating titanium composites.

**Keywords** Additive manufacturing · Aerospace · Corrosion · Titanium composite · Wear

## 1 Introduction

The unique properties presented among composite materials allow them to offer a lot of advantages over other engineering materials. These advantages make them suitable to be used for lightweight components and structures in various industries [1]. Currently, approximately 50% of the airframe of aircrafts is fabricated from composite materials [2]. In addition, composite materials have an increased usage in automotive industry. Research showed an increase of 5% in its annual growth in the automotive industry since 2015.

The worldwide demand for composite materials increases on a daily basis [3]. Titanium composites exhibit a wider range of application compared to conventional Titanium alloys because of their higher stiffness and strength [4, 5]. Another feature of titanium composites is the high wear resistance and resistance to corrosion [6]. This is because of the particles like TiC or TiB that have been added which exhibit some self-lubricating behaviors. Titanium composites show a much lower wear of the counterpart because the particles like TiC or TiB show some self-lubricating behavior [7]. Titanium composites are also very attractive which also makes them suitable for a broad range of automotive and aerospace applications [8, 9]. The better mechanical strength, excellent biocompatibility, low density, corrosion resistance and high temperature performance make titanium composites to be applicable in a majority of industries where lightweight material is required such as in turbine engine components, food processing plants, high-performance automotive parts, aerospace, nuclear power plants, chemical industries, oil refinery heat exchanger, marine applications, medical devices, electronics, biomedical applications (implant and prostheses), energy and defense areas [8–10].

Titanium requires surface modification to impact certain properties in it, which will make it more suitable in some areas where it is applicable. Additive manufacturing technology (AMT) is the recommended manufacturing technology that can be used to process several types of composites because it addresses most of the problems of the traditional manufacturing of composites [8]. Composite materials typically consist of a defined matrix as a continuous phase, a reinforcement as a discontinuous or dispersed phase, and an interface or binder which joins the materials together [11, 12]. The mechanical properties and microstructure of composite materials can be controlled through the proper selection of the constituent materials which form the fabrication method for various composites [13]. Additive manufacturing (AM) is the best technology for multi-directional fabrication [14]. Due to the



important advantages offered by AM, this makes it suitable to produce geometric and material complexities which cannot be created using subtractive manufacturing processes [15]. However, several researches have been done to improve the physical and mechanical properties of titanium by introducing other materials to make up composites which are suitable materials for many industrial applications.

This paper reviews the application of different AM technologies for the fabrication of lightweight composites, in particular titanium alloy composites.

## 2 Laser Metal Deposition of Titanium Composites

Laser metal deposition (LMD) process is an additive manufacturing technology in the direct energy deposition (DED) group. LMD is capable of producing complex parts directly from the three-dimensional model (3D) of CAD models [16]. In this process, nozzles can move in multiple directions, which allow materials to be deposited from any angle. The deposited materials are then melted using a laser which fuses the material together. LMD has an advantage over all other additive manufacturing processes as it can be used in repairing high valued components which could not be done by other processes [17]. It performs repairs without causing damages to parts as compared with traditional manufacturing methods. This technology is also capable of repairing and reducing part weight in one single step.

Ti-6Al-4V is the most widely produced and most widely used titanium alloy in aerospace industry because of its unique property which is the lightness in weight with high strength and its structural efficiency which also makes it suitable in critical and high-performance applications such as jet engine parts and frame components [18]. The addition of other materials to titanium forms composite materials. This helps to impart certain properties into the material to improve its usefulness. Materials such as TiB and TiC are normally added to titanium alloys to improve hardness and wear resistance of the material.

## 3 Microstructure and Mechanical Properties of Titanium Composites

Jingwei et al. [19] carried out a research on a microstructure and hardness study of functionally graded materials (Ti-6Al-4V/TiC) that were produced using laser metal deposition process. Their study focused on the influence of laser processing parameters and TiC compositional distribution on microstructure. The TiC and gas-atomized Ti6Al4V powders were premixed at different ratios, using a laser power ranged from 400 to 700 W, and scanning speed between 200 and 400 mm/min, and parts of crack free functionally graded material (FGM) Ti-6Al-4V/TiC were successfully fabricated. The presence of primary carbide, eutectic carbide and unmelted carbide was

observed on the deposits. At an increased laser power, the primary and secondary dendrite arm spacing were observed to have increased. The values of scanning speed and laser power used did not influence the hardness distribution on the samples. It was concluded that the addition of TiC powder to the material plays an important role in improving hardness value of fabricated parts from 300 to 600 HVI. Also, Popoola et al. [20] examined the corrosion and hardness characteristics of laser surface modified Ti-6Al-4V/Zr + TiC and Ti-6Al-4V/Ti + TiC composites obtained through LMD process. Commercial titanium alloy of Ti-6Al-4V was laser clad with the combination of Zr and TiC ceramic powders. The research revealed that a moderate amount of ceramic coatings helps to increase the surface properties of Ti-6Al-4V alloy. From the electrochemical and hardness study, the combination of ceramic and metallic powder has significant influence on the property enhancement of surface modified Ti6Al4V alloy. With 70% Ti + 30% TiC and 70% Zr + 30% TiC, using a laser power of 1.4 kW, the hardness of the composites was greatly improved. Laser surface modified composites result in better corrosion resistance composites and also increased hardness of the composites. TiC powder is therefore a suitable ceramic powder when hardness is required to be impacted on surface modified samples. Subsequently, Sampedro et al. [21] researched on how to improve the mechanical properties of Ti Grade 2 and Ti6Al4V surfaces. This was achieved by depositing Ti6Al4V powder and the mixture of Ti6Al4V and TiC, respectively, using laser metal deposition process. Using a weight ratio of 30% of Ti6Al4V and 60% of TiC, a defect-free coating of Ti6Al4V and TiC on metal matrix composites of free pores and cracks was obtained. An increase in laser power to 800 W allows the TiC particles to be completely dissolved resulting in the formation of improved surface, free of defects. Also, the hardness of the base material was improved from the initial value of 120–300 HV. In addition, there was an improved wear resistance and coefficient of friction observed on the samples. This result obtains help to affirm the fact that laser metal deposition is a suitable technology for enhancing the properties of manufactured titanium components. Further studies were conducted by Mahamood et al. [22] to characterize laser deposited Ti6Al4V/TiC composite. The composites were achieved by varying the laser power between 0.4 and 3.2 kW and keeping the scanning speed constant at 0.005 m/s. To avoid oxidation from taking place, the process was shielded with argon gas. The microhardness and the wear resistance are significantly dependent on laser power. In these studies, the optimal laser power required for better wear resistance performance of the composite is 2 kW. Further increase in laser power beyond 2.0 kW, resulted in the decrease in microhardness of the composites. This is because if more power is introduced, more TiC will be melted which results into low unmelted carbide in the composites and thus provides less reinforcement for the composites. Therefore, there is a limit to which the laser power should be increased in order to retain the required unmelted carbide and to improve the microhardness of the composites. It was also observed that the wear resistance was not improved at lower laser power but with a laser power of 2.0 kW, the unmelted carbide was well bonded in the matrix of the Ti-6Al-4V grains which serves as powder lubricant during the sliding wear process. The TiC powder particle shows irregular shape morphology, while the morphology of Ti-6Al-4V powder particle is

spherical in shape. The microstructure of the surface of the Ti-6Al-4V substrate is characterized by a finely dispersion of alpha grains in the matrix of beta grain structure. The microstructure of Ti-6Al-4V + TiC MMCs ceramic and Zr + TiC MMCs TiC using laser metal deposition process was studied by Ochonogor et al. [23]. Ti-6Al-4V/TiC and Zr/TiC composites were obtained with varying compositions of gas-atomized Ti-6Al-4V powder. The microstructure of the TiC-based composites revealed the presence of partially melted TiC particles embedded in the metal matrix, and Ti in solid solution was observed on the microstructure of Zr-based composite. There was an improvement in the microhardness of the composites which was due to the addition of TiC ceramic powder. This correlates with previous studies which reveal that when increase in strength is required in component part, TiC ceramic powder is suitable to be added to the material to achieve the desired microhardness and good corrosion resistance. This can be effectively achieved through LMD process. Functionally graded materials of commercially pure titanium (CPTi) and titanium carbide (TiC) powders were fabricated using laser metal deposition (LMD) technique [17]. During the deposition process, 50 wt% TiC and 50 wt% CPTi powder were used. Investigations on the structural integrity of the composites were carried out. During the fabrication process, all the processing parameters used for the process were varied. Processing parameters such as the laser power and the scanning speed played a very crucial role on the evolving properties of the deposits as the hardness of the material was observed to have increased. It was deduced from the obtained microstructures that the laser power had much influence on the grain growth of the material as the hardness was highly influenced by the laser power. In addition, varying the percentages of the titanium and titanium carbide during the deposition process causes the sharp boundaries of the titanium carbide to reduce greatly and resulted into customized tailored microstructure. This is one of the best characteristic of functionally graded materials [17].

Pouzet et al. [24], manufactured titanium matrix composite walls, using a premixed powder containing Ti-6Al-4V + B<sub>4</sub>C with the B<sub>4</sub>C contents ranging from 0.5, 1.5 and 3.0 wt%. The research aimed to study the surface finish, microstructures, hardness, and mechanical resistance of the composites produced at ambient temperatures using various process parameters. Ti-6Al-4V and B<sub>4</sub>C particles that were homogeneously mixed were successfully used for the deposition process. A sound and homogeneously refined grain of Ti-6Al-4V/TiB microstructures was obtained. High cooling rate during the deposition process results into boron segregation during  $\beta$ -Ti solidification. 1.5% B<sub>4</sub>C and 3% B<sub>4</sub>C mixture show nearly the same microstructural and mechanical properties. The ductility of the samples was seen to be reduced at high and ambient temperatures. Also, there was an increase in the modulus of elasticity and ultimate tensile strength at temperature of 500 °C which resulted from the B<sub>4</sub>C used as the reinforcement material. They suggested that further studies should be carried out on how to precisely measure the carbon content present in a composite after fabrication. Similarly, in the work of Ogunlana et al. [25], the surface effect of laser power during laser metal deposition on microstructural evolution and hardness behavior of titanium matrix composite was investigated. Boron carbide (B<sub>4</sub>C) and Ti6Al4V powder were used for the experiment. These were deposited in the ratio

of 1:4 in weight percent. The laser power used was varied between 800 and 2400 W with 200 W intervals.  $B_4C$  powder was dissolved into the melt pool to alloy the surface of the sample. This produces microstructure of the composites with a defect free intermetallic phase. The laser power plays an important role on the evolving properties of the deposits. It was revealed that with the set of processing parameters used for the study, the sample produced at a laser power of 2200 W was observed to have good intermetallic bonding and free of porosity. Also, the laser power has great influence on the hardness of the composites in the sense that an increase in the laser power leads to an improved microhardness of the composites.

Erinosho et al. [26] conducted an experiment on how to use laser metal deposition process to improve the microstructure and wear behavior of fabricated samples of Ti-6Al-4V/Cu composites. Ti-6Al-4V and Cu powders were deposited on Grade 5 titanium alloy substrate. Processing parameters selected for the experiment included a scanning speed between 0.30 and 0.72 m/min and laser powers between 1300 and 1600 W. The system operates at a maximum power of 2 kW with a wavelength of 1.047  $\mu\text{m}$ . The micrograph reveals that all Ti-6Al-4V/Cu samples obtained have sound integral properties which are free of voids. Widmatt structure was observed which was attributed to the cooling rate and the deviation in the heat input which has strong effect on the grain boundaries around the heat-affected zone and the fusion zone. A lesser coefficient of friction and a lower rate of wear were observed when a laser power of 1397 W and a scanning speed of 0.30 m/min were used. This was as a result of the martensitic structure which was seen to be formed during cooling and solidification. The experiments were conducted that successfully improve the poor abrasive wear of Ti-6Al-4V by adding Cu powder through laser metal deposition. Therefore, the addition of Cu into Ti-6Al-4V has greatly enhanced the mechanical properties of the deposited composite. Erinosho et al. [27], further estimated the surface topography and wear loss of laser metal deposited samples of Ti-6Al-4V and Cu. The effects of processing parameters on the evolving properties of the deposited composite were studied. Ti-6Al-4V alloy and Cu powders were premixed in two different ratios. The first ratio was achieved by mixing 3 wt% of Cu with Ti-6Al-4V alloyed powder while the second mixture contained 5 wt% of Cu mixed with Ti-6Al-4V alloyed powder. With scanning speed values varied between 0.5 and 2 m/min, beam diameter of 4 mm, and keeping all other parameters constant, Ti-6Al-4V/Cu composites were successfully deposited. A spherical-shaped morphology was observed in the two powders and the particle sizes were seen to be equiaxed in nature. Ti-6Al-4V was observed to have smooth surfaces with the presence of dust particles on it while Cu particle sizes revealed denser faces. XRD analyses identify that the two powder mixtures exhibit similar trend having sharp and narrow edges with Ti observed at the highest peak, while Al was observed at the lowest peak. The Cu powder is added to Ti which played an important role as it helped in the formation of additional oxides of Ti which resulted in the formation of protective films over the surfaces of the deposited Ti-6Al-4V/Cu. From the roughness values obtained, it was deduced that the roughness values fall within the roughness number required for the intended application. Also, it was discovered that when a laser power of 1200 W was used, samples obtained were seen to present a minimum wear loss. The addition of

Cu powder to fabricate Ti-6Al-4V/Cu helps to improve and enhance the properties of the titanium alloy to be suitable in areas like marine application.

Moreover, Lakshimi et al. [28] studied the microstructural and texture development in laser fabricated In718 using commercially available gas-atomized In718 powder. During the deposition, the laser beam was focused on the substrate at a spot size of 0.7 mm, keeping the spacing between built layers at 0.3 mm, and argon gas was used as a carrier gas with a flow rate of 5.5 l/min. Oxidation was prevented by keeping the oxygen level below 50 ppm. Laser power of 390 W and laser scan speed of 200 mm/min were used and all other processing parameters were kept constant. In this study, three layers were deposited. During the first deposition, laser system was switched off between the layers for a time equal to deposit a layer. The laser head was moved back to the initial position ensuring stable powder flow and cooled by flowing cool gas through the carrier gas along the deposited samples. The second layer was deposited by moving laser beam backward and forward without any cooling medium between the layers. A third layer was also deposited by using two directional deposition paths with a laser power of 910 W. Also, the powder feed rate was reduced during the third build layer to 7 g/min to prevent the built layer from getting in contact with the nozzle due to the enhanced powder catchment efficiency caused by the increase laser power which led to increased melt pool. When a lesser laser power was used, a mixture of fine and coarse grains with a weak texture was observed on the microstructure. But when the laser power was increased, the particle phase became larger with the presence of carbide with fine dendritic network which was formed as a result of the cooling effect. The porosity test revealed a lower porosity level when a reduced laser power was used and it was seen to increase with an increase in laser power. Laser power has a significant effect as it showed a significant variation in grain structure and grain size of direct laser fabricated samples.

In the research carried out by Tlotleng et al. [29], effect of laser power on microstructure, hardness and composition of the produced TiAl coatings was studied. Commercially available pure aluminide and pure titanium powder were used for the experiment with Ti-6Al-4V sheet as the substrate. The fabrication of TiAl coatings was successfully achieved through direct laser metal deposition process by setting the powder carrier gas to deposit 80% Ti and 20% Al. Keeping the beam spot size at 4 mm, and laser scanning speed at 2.5 m/min, gas flow rate at 10 l/min, powder flow rate at 2 l/min, while varying the laser power, Ti and Al powders were injected simultaneously from different hoppers. At laser powers of 1.0, 1.3 and 1.5 kW, Ti and Al powders showed a lamellar structure, but when the laser power was increased to 2.0 kW, a refined dendritic structure was observed. The result obtained also showed that the coatings contained  $TiAl_3$  and  $TiAl_5$  at stable and uniform phases at high temperature processes. Finally, hardness evaluation confirmed that the produced coatings had their microhardness value within the expected range of that of TiAl/TiAl<sub>3</sub> based.

Zhang et al. [30] use laser metal deposition process to fabricate Ti-6Al-4V/TiB composites by keeping beam size at 3 mm away from the substrate with gas flow rate of 20 l/min. Composites of Ti-6Al-4V/TiB were manufactured from gas-atomized

prealloyed Ti-6Al-4V/TiB powder. The influence of processing parameters on properties and microstructure of the samples was examined. Scanning speed and laser power were varied. After the deposition process, specimens were heat treated by annealing at 1100 °C for 1 h and allowed to cool inside furnace. It was observed that the Ti-6Al-4V  $\beta$ -grains structure changes from fine equiaxial grains in the heat-affected zone and the melt pool into large columnar grains in the deposited samples. These changes resulted into an increase in the fatigue resistance, ductility and strength of the composites. TiB was seen to add to the hardness value of the samples containing boron when compared to Ti-6Al-4V deposits. TiB is a reinforcement material that increases the hardness of composites. It was also observed that the hardness value dropped after the  $\beta$ -annealing process, which is attributed to the formation of near equiaxed  $\alpha$  grains. The importance of laser metal deposition in making complex-shaped component made with composite material at a single manufacturing run cannot be over emphasized [31]. It reduces the product lead time and the overall cost of manufacturing or remanufacturing of customized part with metals, alloys as well as composite materials [32–34].

#### **4 Conclusion and Future Research Direction for Laser Metal Deposition of Titanium Composites**

Complex components produced by additive manufacturing technology are lighter when compared with those produced using conventional manufacturing methods. Laser metal deposition process is capable of producing composite materials when desired property is required on a component part and in one manufacturing run. LMD has been used to fabricate various composite materials by adding other metallic materials to improve its mechanical properties. Materials such as TiC, TiB, B<sub>4</sub>C and Cu are added to improve the wear resistance and microhardness of titanium and its alloys.

In this research article, a review of the mechanical properties and microstructure of titanium composites produced by laser metal deposition is presented by studying their relationship with the process parameters used during the deposition process. It was confirmed that the processing parameters have significant effect on the microstructure and properties of components produced through LMD. In general, the proper combination of processing parameters to fabricate composite materials is a great challenge faced by manufacturers. Inadequate process parameters may cause changes to the mechanical properties and material microstructure and results into formation of low-quality composites. LMD process involves complex physical phenomena. These physical phenomena interact with each other and require proper understanding of processing parameters required for obtaining the desired mechanical properties and microstructure.

To maintain proper process control, further research in the area of LMD of titanium composite is required. Hence, these challenges need to be studied for the long-term growth of the additive manufacturing of titanium and its composite materials.

## References

1. Hegab HA (2016) Design for additive manufacturing of composite materials and potential: a review. *Manuf Rev* 3. <https://doi.org/10.1051/mfreview/2016010>
2. Mostafa Y, Elbestawi MA (2017) Additive manufacturing of composite materials: an overview. In: 6th international conference on virtual machining process technology (VMPT), Montréal, Canada, 29 May–2 June 2017
3. Quan Z, Wu A, Keefe M et al (2015) Additive manufacturing of multi-directional preforms for composites: opportunities and challenges. *Mater Today* 18:503–512
4. Lu Y, Tang HB, Fang YL et al (2012) Microstructure evolution of sub-critical annealed laser deposited Ti–6Al–4V alloy. *Mater Des* 37:56–63
5. Graf B, Gumenyuk A, Rethmeier M (2011) Laser metal deposition as repair technology for stainless steel and titanium alloys. *Phys Procedia* 39:376–381
6. Rastegari HA, Asgari S, Abassi SM (2011) Producing Ti-6Al-4V/TiC composite with good ductility by vacuum induction melting furnace and hot rolling process. *Mater Des* 32(10):5010–5014
7. Peters M, Kumpfert J, Ward CH, Leyens C (2003) Titanium alloys for aerospace applications, titanium and titanium alloys. *Adv Eng Mater* 5:419–427
8. Boyer R, Welsch G, Colling EW (1994) *Materials properties handbook: titanium alloys*. ASM International, Materials Park, OH
9. Moiseyev VN (2006) *Titanium alloys: Russian aircraft and aerospace applications*. CRC Press Taylor & Francis Group, pp 169–180
10. Mahamood RM, Akinlabi ET (2015) Effect of processing parameters on wear resistance property of laser material deposited titanium-alloy composite. *J Optoelectron Adv Mater* 17(9–10):1348–1360
11. Baufeld B, Biest OV, Gault R (2010) Additive manufacturing of Ti-6Al-4V components by shaped metal deposition: microstructure and mechanical properties. *Mater Des* 31:S106–S111
12. Ding D, Pan Z, Cuiuri D et al (2015) Wire-feed additive manufacturing of metal components: technologies, developments and future interests. *Int J Adv Manuf Technol* 8:465–481
13. Tekinalp HL, Kunc V, Velez-Garcia GM et al (2014) Highly oriented carbon fiber-polymer composites via additive manufacturing. *Compos Sci Technol* 105:144–150
14. Balla VK, Das M, Mohammad A et al (2016) Additive manufacturing of g-TiAl: processing, microstructure, and properties. *Adv Eng Mater* 18:1208–1215
15. Chastanda V, Tezenas A, Cadoret Y et al (2016) Fatigue characterization of titanium Ti-6Al-4V samples produced by additive manufacturing. *Procedia Struct Integr* 2:3168–3176
16. Löber L, Schimansky FP, Kühn U et al (2014) Selective laser melting of a beta-solidifying TiAl–Ni–Ti–Zr–Al–Cu–Nb–Zr titanium aluminide alloy. *J Mater Process Technol* 214:1852–1860
17. Akinlabi ET, Akinlabi SA (2015) Characterization of functionally graded commercially pure titanium (CPTI) and titanium carbide (TiC) powders. *Proc World Congr Eng* 2:978–988
18. Shin K-H, Natu H, Dutta D et al (2003) A method for the design and fabrication of heterogeneous objects. *Mater Des* 24:339–353
19. Zhang J, Zhang Y, Liou F et al (2015) A microstructure and hardness study of functionally graded materials Ti-6Al-4V/TiC by laser metal deposition. In: *Proceedings of the 26th solid freeform fabrication symposium*, Austin, TX, pp 664–673
20. Popoola API, Ochonogor OF, Abdulwahab M (2013) Corrosion and hardness characteristics of laser surface-modified Ti-6Al-4V/Zr + TiC and Ti-6Al-4V/Ti + TiC composites. *Int J Electrochem Sci* 8:2449–2458

21. Sampedro J, Petrez I, Carcel B et al (2011) Laser cladding of TiC for better titanium components. *Phys Procedia* 12:313–322
22. Mahamood RM, Akinlabi ET, Shukla M et al (2014) Characterization of laser deposited Ti6Al4V/TiC composite powders on a Ti6Al4V substrate. *Lasers Eng* 29:197–213
23. Ochonogor OF, Meacock C, Pityana SL (2012) Microstructure characterization of laser deposited titanium carbide and zirconium based titanium metal matrix composites. *J South Afr Inst Mining Metall* 112:105–110
24. Pouzet S, Peyre P, Gorny C et al (2006) Additive layer manufacturing of titanium matrix composites using the direct metal deposition laser process. *Mater Sci Eng* 677:171–181
25. Ogunlana OM, Akinlabi ET, Musbau O (2016) Surface effect of laser power on microstructural evolution and hardness behaviour of titanium matrix composites. *IAENG Proc World Congr Eng* 2:978–988
26. Erinosh FM, Akinlabi ET et al (2014) Laser metal deposition of Ti-6Al-4V/Cu composite: a study of the effect of laser power on the evolving properties. *Proc World Congr Eng* 2:978–988
27. Erinosh FM, Akinlabi ET et al (2016) Estimation of surface topography and wear loss of laser metal deposited Ti-6Al-4V and Cu. *Adv Eng Mater* 18(8):1396–1405
28. Lakshmi LP, Ravi GA, Daniel CM et al (2014) Microstructural and texture development in direct laser fabricated In718. *Mater Charact* 89:102–111
29. Tlotleng M, Masina B, Pityana S (2016) Characteristics of laser in-situ alloyed titanium aluminides coatings. *Procedia Manuf* 7:39–45
30. Zhang Y, Zhang J, Liou F et al (2011) Microstructure and property of TiB-reinforced Ti alloy composites by laser metal deposition. *Rare Met Mater Eng* 40:27
31. Mahamood MR (2018) Laser metal deposition process of metals, alloys, and composite materials. Springer, Switzerland
32. Mahamood RM, Akinlabi ET, Owolabi MG (2017) Laser metal deposition process for product remanufacturing. In: Gupta K (ed) *Advanced manufacturing technologies*. Springer, Switzerland, pp 267–291
33. Akinlabi ET, Mahamood RM, Akinlabi SA (2016) *Advanced Manufacturing Techniques Using Laser Material Processing*. IGI Global USA
34. Pityana S, Mahamood RM, Akinlabi ET, Shukla M (2013) Gas flow rate and powder flow rate effect on properties of laser metal deposited Ti6Al4V. *Proceedings of the International MultiConference of Engineers and Computer Scientists 2013 Vol II, IMECS 2013, March 13 - 15, 2013, Hong Kong*



# Efficacy of Quasi Agro Binding Fibre on the Hybrid Composite Used in Advance Application



J. O. Dirisu, O. S. I. Fayomi, and S. O. Oyedepo

**Abstract** The choice for natural fibre obtained from agricultural products is on the rise due to its solution to eco-friendly, environmental and improved mechanical properties concerns. Its abundant availability, low cost, emission reduction and adaptability to base material for composite make it a prime material for selection. This review explores diverse perspectives to the future trend of agro fibre in terms of the thermo-mechanical properties as it applies to advanced application in building structures. It is important to investigate the ecofriendliness of the products of composites from fibres in agricultural wastes so as to achieve a green and sustainable environment. This will come to fore by the combined efforts of both researchers and feedback from building stakeholders.

## 1 Introduction

The abundance of natural resources, fertile land mass, waste plant produce and free renewable energy in developing country such as Nigeria calls for deep attention to invest in developing composite products that will be applicable to diverse sectors in the globe [1, 2]. Natural composites which stem from agricultural waste are focal studies in the research community [3, 4]. There is now diversification from polymer reinforced composites to natural composites. Polymers reinforced composites are trailed with associated health risk, non-biodegradable and environmental concerns [5–13]. The polymer production process involved the synthesis of different chemicals which unfortunately has oestrogenic activities that can cause detrimental effect to

---

J. O. Dirisu (✉) · O. S. I. Fayomi · S. O. Oyedepo  
Department of Mechanical Engineering, Covenant University, Ota P.M.B 1023, Ogun State,  
Nigeria  
e-mail: [joseph.dirisu@covenantuniversity.edu.ng](mailto:joseph.dirisu@covenantuniversity.edu.ng)

O. S. I. Fayomi  
Department of Chemical Metallurgical and Materials Engineering, Tshwane University of  
Technology, Pretoria P.M.B. X680, South Africa

human even with minor ingestion [6]. The aim of this study is to explore the potentials of agricultural waste in their application as fibre and binding agents to composite matrix for building structure.

## 2 Agricultural Waste

“Waste is abstract, it doesn’t exist. No material is a waste to a scientist, even our human waste is an energy source. A waste becomes a mine of wealth to a wealth creator and a visionary. The waste in our environment is a potential product to solve human challenge” quote by Adeniran Olukokun. Agricultural waste is a waste produced due to agricultural processes such as plant, animal and chemical wastes [14]. The plant wastes are not limited to shell, husk, bagasse, straw, cob, stalk which can be utilized to create wealth [15]. Agricultural wastes or agro wastes are also residue from agricultural products such as fruit and manure waste. Manure is a natural fertilizer and biodegradable which is a benefit to the soil unlike the chemically produced fertilizers. Chemical waste is a function of presence of heavy metals such as lead and mercury in fertilizers that pose a threat to the environment and ecosystem. It can degrade or mutate the soil structure which when crop product from this is consumed can stress the human body system.

### 2.1 Agro Waste Conversion and Application

Agricultural waste was preferred in removing heavy metals suspended in the atmosphere to other methods due to its low cost and high efficiency [16]. It was applied in removing heavy metal from wastewater [17]; production of hydrogen which is an acclaimed replacement for fossil fuel [18]; garlic peel was applied as a stain remover in aqueous solution as it becomes a ready replacement to costlier absorbent employed for dye [19–21]; treatment of wastewater [22, 23], supplies energy through biofuels [24–28]; inexpensive nitrogen and low-cost carbon were used in minimizing polyhydroxyalkanoate (PHA) production cost [29]; and refining of gold was achieved using shell of apricot stone from agricultural waste [30]; textile application [31], aeronautic application; production of activated charcoal [32]. Agricultural waste has high biomass content when pulverized and pyrolyzed that can be applied to electricity generation [33–36].

## 3 Different Types of Binding Agents

Epoxy resin is appreciated as a binder as it is suitable to various industrial applications such as surface coating, laminated circuit, fibre filler and adhesive. Its limitation

of brittleness, low impact strength and fracture toughness can be overcome when the chemical characteristics are modified [37–39]. Organic binding agents are of the following examples: bentonite, bitumen, clay, corn starch, aluminium silicate, water, waste paper amongst others. Binding agents in pharmaceutical industry that exist are starch, microcrystalline cellulose, polyvinyl pyrrolidone, liquid glucose amongst others. Binding agents employed in the building and ceramic industries are not limited to bentonite, sodium silicate, clay, magnesium aluminium silicate, polyvinyl alcohol, starches amongst others.

### **3.1 Agro Binding Agents**

A binder holds material together by cohesion to give it a structural stability. It gives a frame structure to powdered materials that can crumble easily. It imparts cohesiveness to the particulates [40]. It binds flour or crumb together giving it structural stability. Binder can be liquid, semi-solid or powder in substance that hardens when materials like fibre or other particles mix with it. Examples are adhesives such as glue, cement, wheat flour, starch, tapioca flour, lactose powder and thickener. Binders can be organic in nature, e.g. asphalt, polymers and plant or animal glues. Inorganic binders are cement, liquid glass and gypsum. Cement as a binder is low in tensile strength but high in compressive strength, as such will need a reinforcement from a fibrous material. Resin is elastic, however will require the support of reinforcement to improve the tensile strength in composite materials with resin as the matrix. Eggs and eggshell act as binding agent, due to the presence of calcium in it.

Concrete uses cement as binder in building construction. High amount of natural resources is needed for concrete production. To reduce this consumption, agricultural waste is introduced to achieve similar mechanical strength feat and to minimize negative environmental effect due to raw material consumption [41]. Sand is included to increase compressive strength, hardness and reduce shrinkage. Traditionally straw and natural fibres are used to strengthen clay in wattle-and-daub construction and in the building material cob which would otherwise become brittle after drying. Bitumen is used as a binder for asphalt in road construction.

#### **3.1.1 Binding Fibres**

Fibre is the indigestible part of plant or animal. It helps in food flow through the body. It is thin or threadlike in shape which is longer in dimension than its breadth. Fibres are eco-friendly and as well environmentally friendly which account for it being a focal study for reinforcement [4]. Engineering composites usually rely on fibre as a reinforcement to improve its desired mechanical properties. Fibre can be natural or man-made in type. Natural fibres are seen in plant, animal and minerals. Plant types are not limited to examples such as bamboo, coconut, oil palm, cotton, hemp, jute, bagasse, sisal, kenaf and coir. Animal fibres are horse hair, wool, silk, spider silk,

**Table 1** Binding agent types and application

Product	Type	Example of use
Accroides	Resin	Binder in fireworks and flares
Candelilla	Wax	Binder in chewing gum
Gum Arabic	Gums	Binder in baking, ceramic glazes and paints
Guar	Gums	Binder in baking and tablets
Karaya	Gums	Binder in baking and paper manufacturing
Shellac	Shellac	Binder in mascara, eyeliners and pyrotechnics
Tragacanth	Gums	Binder in icing, tablets and paints

**Table 2** Extract of natural fibres [75]

Fibre type	Fibre diameter (mm)	Specific gravity	Tensile strength (Ksi)	Elastic modulus (Ksi)	Elongation at break (%)	Water absorption (%)
Wood fibre	0.025–0.075	1.5	51–290	1500–5800	–	50–75
Coconut	0.1–0.4	1.12–1.15	17–29	2750–3770	10–25	130–180
Sisal	0.2–0.4	1.45	40–82	1880–3770	3–5	60–70
Cane sugar	0.2–0.4	1.2–1.3	27–42	2175–2750	1.1	70–75
Bamboo		1.5	51–73	4780–5800	–	40–45
Jute		1.02–1.04	36–51	3770–4640	1.5–1.9	28.64
Elephant grass		0.818	26	710	3.6	–

camel hair amongst others. Asbestos is a notable example of mineral fibre which is a hybrid of six naturally occurring silicate minerals each having their fibrous nature. Man-made fibres are synthetic in composition such as polymers, rayon, glass amongst others. Properties of natural and man-made fibres are shown in Tables 1 and 2. The properties of synthetic fibres are shown in Table 3.

In all, plant fibres are abundantly available and can be harvested within short period making it the most reliable of all types of fibres for reinforcement of base material [74].

## 4 Agro Waste and Composites Efficacy Synergy

Varied properties in engineering are used to explore the nature of agro fibres in the overall composite [42]. Dynamic mechanical analysis was adopted to provide additional information to thermal analytical techniques such as storage modulus, loss modulus and damping factor which are all temperature dependent [43]. Pineapple

**Table 3** Properties of extracted synthetic fibres [72, 73]

Fibre type	Fibre diameter (mm)	Specific gravity	Tensile strength (Ksi)	Elasticity modulus (Ksi)	Elongation at break (%)	Water absorption (%)	Melting point (°C)	Maximum working temperature (°C)
Steel	0.1-1	7.8	70-380	30,000	0.5-3.5	-	1370	760
Glass	0.0075-0.02	2.5	220-580	10,400-11,600	2.4	-	1300	1000
Carbon	0.0075-0.00875	0.90	260-380	33,400-55,100	0.5-1.5	-	3652-3697	-
Nylon	0.00225	1.14	140	750	20-30	2.8-5.0	220-265	199

and sisal leaves fibres were explored as bio-fillers on polymer matrix [44]. Their low-cost, non-abrasiveness and lightweight edge make them promising for base materials. However, these fibres need to be modified to improve the engineering properties and to overcome the shortcoming of poor wettability, poor adhesion to the parent substance and water absorption [45]. Chemical treatment of fibre helps in improving the flexural strength [46]. The tensile strength of natural fibre reinforced polymer increment is dependent on the bond between the matrix and the filler. It also increases with increase in percentage content of reinforcement [47]. Comparison was made between reinforced jute epoxy composite and jute polyester composite. The latter exhibited some better mechanical properties than jute–polymer combination due to the differences in reinforcement [48]. Wall nut and coconut shell with rice husk that served as fillers to bio epoxy resin proved better properties under mechanical loading compared to glass reinforced composite [49]. The correlation between the morphology and the tensile strength of some natural fibres was investigated which revealed that there is a direct relationship between the cell wall thickness to fibre strength and Young's modulus [50]. The disparity in fibre types influences the mechanical properties of natural composites [51]. Long natural fibre and carbon fibre had some similar laminate properties while short natural fibre had a higher scatter profile unlike the long fibre [52]. Different binding agents subsist and are utilized based on application of end products and desired properties. Examples are epoxy resin, cement, bentonite, bitumen. Epoxy resin is adjudged to have an excellent chemical, thermal and mechanical properties and can be used to bind composite thereby yielding different products [37].

#### ***4.1 Agricultural Waste for Ceiling Tile Production***

Agricultural waste is utilized in producing ceiling panel by combining it with other materials such as wood dust or industrial waste that are eco-friendly in composition [53–58]. Water melon peel finds its usefulness as a probable alternative to particle board. Recycled low density polyethylene was appropriated as a binder. The internal bonding strength, modulus of rupture and modulus of elasticity were investigated and compared with particle board. All results met with European standard requirements for panelling, partitioning and ceiling. Banana peel was explored by Babatunde [59] which was bonded with sawdust and cement. This is another exploit of agricultural waste in ceiling production. Bamboo waste combined with polystyrene to produce particleboard [60]. Particleboard was further produced by bonding cement with combination of flakes, flake-sawdust and sawdust [61–64]. Rice husk particleboard was produced as a ceiling composite; urea formaldehyde was used as the binder [65]. Zea mays was introduced to develop cement-particleboard hybrid composite [66–68]. Different agricultural wastes had been proven to form particleboard that is used for ceiling construction [69–71].

## 5 Conclusion

Agricultural wastes can be utilized to form novel viable product currently applied in building construction. These wastes used as fibres are abundantly available in Nigeria. Viable products from these fibres and selected matrix to produce composite material has been investigated by researchers. The impact of fibre particle size, their orientation in the matrix and percentage admixture should be critically studied. The morphology of the interaction between fibre and the base material will reveal clearly their bond nature, strength and combustion properties. More focus should be made on the appraisal of the combustion and emission nature of these products from agricultural waste so as to establish its suitability for use in building construction especially in ceiling tiles. It is important to investigate the ecofriendliness of the products of composites from fibres in agricultural wastes so as to achieve a green and sustainable environment.

**Acknowledgements** The authors wish to appreciate the management of Covenant University for her unflinching publication support.

## References

1. Anyanwu CN, Ibeto CN, Eze IS et al (2013) Present and prospective energy use potentials of selected agricultural wastes in Nigeria. *J Renew Sustain Energy* 5(3):032703
2. Satyanarayana KG, Arizaga GG, Wypych F (2009) Biodegradable composites based on lignocellulosic fibers—an overview. *Prog Polym Sci* 34(9):982–1021
3. Milanese AC, Cioffi MOH, Voorwald HJC (2011) Mechanical behavior of natural fiber composites. *Procedia Eng* 10:2022–2027
4. Lau KT, Hung PY, Zhu MH et al (2018) Properties of natural fibre composites for structural engineering applications. *Compos B Eng* 136:222–233
5. Teow Y, Asharani PV, Hande MP et al (2011) Health impact and safety of engineered nanomaterials. *Chem Commun* 47(25):7025–7038
6. Yang CZ, Yaniger SI, Jordan VC et al (2011) Most plastic products release estrogenic chemicals: a potential health problem that can be solved. *Environ Health Perspect* 119(7):989–996
7. Schlagenhauf L, Nüesch F, Wang J (2014) Release of carbon nanotubes from polymer nanocomposites. *Fibers* 2(2):108–127
8. VomSaal FS, Akingbemi BT, Belcher SM et al (2007) Chapel Hill bisphenol A expert panel consensus statement: integration of mechanisms, effects in animals and potential to impact human health at current levels of exposure. *Reprod Toxicol* (Elmsford, NY) 24(2):131
9. Thakur VK, Thakur MK, Raghavan P et al (2014) Progress in green polymer composites from lignin for multifunctional applications: a review. *ACS Sustain Chem Eng* 2(5):1072–1092
10. Gurunathan T, Mohanty S, Nayak SK (2015) A review of the recent developments in biocomposites based on natural fibres and their application perspectives. *Compos A Appl Sci Manuf* 77:1–25
11. Bambach MR (2017) Compression strength of natural fibre composite plates and sections of flax, jute and hemp. *Thin-Walled Struct* 119:103–113
12. Sanjay MR, Madhu P, Jawaid M et al (2018) Characterization and properties of natural fiber polymer composites: a comprehensive review. *J Clean Prod* 172:566–581

13. Shekar HS, Ramachandra M (2018) Green composites: a review. *Mater Today Proc* 5(1):2518–2526
14. Obi FO, Ugwuishiwu BO, Nwakaire JN (2016) Agricultural waste concept, generation, utilization and management. *Niger J Technol* 35(4):957–964
15. Owanaba DB (2015) Conversion of agricultural wastes into poultry feed for sustainable environment. Doctoral dissertation, Federal University of Technology, Owerri
16. Sud D, Mahajan G, Kaur MP (2008) Agricultural waste material as potential adsorbent for sequestering heavy metal ions from aqueous solutions—a review. *Bioresourcetechnology* 99(14):6017–6027
17. Mohan D, Singh KP (2002) Single- and multi-component adsorption of cadmium and zinc using activated carbon derived from bagasse—an agricultural waste. *Water Res* 36(9):2304–2318
18. Guo XM, Trably E, Latrille E et al (2010) Hydrogen production from agricultural waste by dark fermentation: a review. *Int J Hydrogen Energy* 35(19):10660–10673
19. Hameed BH, Ahmad AA (2009) Batch adsorption of methylene blue from aqueous solution by garlic peel, an agricultural waste biomass. *J Hazard Mater* 164(2–3):870–875
20. Namasivayam C, Radhika R, Suba S (2001) Uptake of dyes by a promising locally available agricultural solid waste: coir pith. *Waste Manag* 21(4):381–387
21. Tsai WT, Chang CY, Lin MC et al (2001) Adsorption of acid dye onto activated carbons prepared from agricultural waste bagasse by  $ZnCl_2$  activation. *Chemosphere* 45(1):51–58
22. Garg UK, Kaur MP, Garg VK et al (2007) Removal of hexavalent chromium from aqueous solution by agricultural waste biomass. *J Hazard Mater* 140(1–2):60–68
23. Garg U, Kaur MP, Jawa GK et al (2008) Removal of cadmium (II) from aqueous solutions by adsorption on agricultural waste biomass. *J Hazard Mater* 154(1–3):1149–1157
24. Yevich R, Logan JA (2003) An assessment of biofuel use and burning of agricultural waste in the developing world. *Glob Biogeochem Cycles* 17(4)
25. Macias-Corral M, Samani Z, Hanson A et al (2008) Anaerobic digestion of municipal solid waste and agricultural waste and the effect of co-digestion with dairy cow manure. *Biores Technol* 99(17):8288–8293
26. Aina OM (2006) Wood waste utilization for energy generation. In: *Proceedings of the international conference on renewable energy for developing countries*, p 2
27. Olorunnisola A (2007). Production of fuel briquettes from waste paper and coconut husk admixtures
28. Oluoti K, Megwai G, Pettersson A et al (2014) Nigerian wood waste: a dependable and renewable fuel option for power production. *World J Eng Technol* 2:234–248
29. Soleimani M, Kaghazchi T (2008) Adsorption of gold ions from industrial wastewater using activated carbon derived from hard shell of apricot stones—an agricultural waste. *Biores Technol* 99(13):5374–5383
30. Summerscales J, Dissanayake N, Virk A et al (2010) A review of bast fibres and their composites. Part 2—composites. *Compos A Appl Sci Manuf* 41(10):1336–1344
31. Hong CK, Wool RP (2005) Development of a bio-based composite material from soybean oil and keratin fibers. *J Appl Polym Sci* 95(6):1524–1538
32. Yahya MA, Al-Qodah Z, Ngah CZ (2015) Agricultural bio-waste materials as potential sustainable precursors used for activated carbon production: a review. *Renew Sustain Energy Rev* 46:218–235
33. Saeed MA, Medina CH, Andrews GE et al (2015) Agricultural waste pulverised biomass: MEC and flame speeds. *J Loss Prev Process Ind* 36:308–317
34. Neugebauer M, Sołowiej P, Piechocki J (2014) Fuzzy control for the process of heat removal during the composting of agricultural waste. *J Mater Cycles Waste Manage* 16(2):291–297
35. Simonyan KJ, Fasina O (2013) Biomass resources and bioenergy potentials in Nigeria. *Afr J Agric Res* 8(40):4975–4989
36. Oladeji JT (2010) Fuel characterization of briquettes produced from corncob and rice husk residues. *Pac J Sci Technol* 11(1):101–106
37. Saba N, Jawaid M, Alothman OY et al (2016) A review on dynamic mechanical properties of natural fibre reinforced polymer composites. *Constr Build Mater* 106:149–159



38. Cruz J, Figueiro R (2016) Surface modification of natural fibers: a review. *Procedia Eng* 155:285–288
39. Badrinath R, Senthilvelan T (2014) Comparative investigation on mechanical properties of banana and sisal reinforced polymer based composites. *Procedia Mater Sci* 5:2263–2272
40. Shailendra P, Shikha A, Singh LB (2012) Natural binding agents in tablet formulation. *Int J Pharm Biol Arch* 3(3):466–473
41. Shafiqh P, Mahmud HB, Jumaat MZ et al (2014) Agricultural wastes as aggregate in concrete mixtures—a review. *Constr Build Mater* 53:110–117
42. Rajesh M, Pitchaimani J (2017) Mechanical properties of natural fiber braided yarn woven composite: comparison with conventional yarn woven composite. *J Bionic Eng* 14(1):141–150
43. Saba N, Jawaid M, Alothman OY et al (2016) Recent advances in epoxy resin, natural fiber-reinforced epoxy composites and their applications. *J Reinf Plast Compos* 35(6):447–470
44. Faruk O, Bledzki AK, Fink HP et al (2012) Biocomposites reinforced with natural fibers: 2000–2010. *Prog Polym Sci* 37(11):1552–1596
45. Mishra S, Mohanty AK, Drzal LT et al (2004) A review on pineapple leaf fibers, sisal fibers and their biocomposites. *Macromol Mater Eng* 289(11):955–974
46. Sood M, Dwivedi G (2017) Effect of fiber treatment on flexural properties of natural fiber reinforced composites: a review. *Egypt J Pet*
47. Ku H, Wang H, Pattarachaiyakoo N (2011) A review on the tensile properties of natural fiber reinforced polymer composites. *Compos B Eng* 42(4):856–873
48. Gopinath A, Kumar MS, Elayaperumal A (2014) Experimental investigations on mechanical properties of jute fiber reinforced composites with polyester and epoxy resin matrices. *Procedia Eng* 97:2052–2063
49. Chandramohan D, Kumar AJP (2017) Experimental data on the properties of natural fiber particle reinforced polymer composite material. *Data in Brief* 13:460–468
50. Fidelis MEA, Pereira TVC, Gomes OD (2013) The effect of fiber morphology on the tensile strength of natural fibers. *J Mater Res Technol* 2(2):149–157
51. Elanchezian C, Ramnath BV, Ramakrishnan G et al (2018) Review on mechanical properties of natural fibercomposites. *Mater Today Proc* 5(1):1785–1790
52. Torres JP, Vandi LJ, Veidt M et al (2017) The mechanical properties of natural fibre composite laminates: a statistical study. *Compos A Appl Sci Manuf* 98:99–104
53. Dirisu J, Oyedepo S, Fayomi O et al (2019) Ignition time of selected ceiling materials and escape temperature time prediction of fire fighter rescue mission. *J Chem Technol Metall* 54(1)
54. Dirisu JO, Asere AA, Oyekunle JA et al (2017) Comparison of the elemental structure and emission characteristics of selected PVC and non PVC ceiling materials available in Nigerian markets. *Int J Appl Eng Res* 12(23):14755–14758
55. Dirisu JO, Oyedepo SO, Fayomi OSI et al (2018) Effects of emission characteristics on elemental composition of selected PVC ceiling materials. *Mater Focus* 7(4):566–572
56. Youngquist JA, English BE, Spelter H et al (1993) Agricultural fibers in composition panels. In: *Proceedings of the 27th international particleboard/composite materials symposium*. Washington State University, Pullman, WA, pp 30–31
57. Youngquist JA, Krzysik AM, English BW et al (1996) Agricultural fibers for use in building components. In: *Proceedings of the conference on the use of recycled wood and paper in building applications*, pp 123–134
58. Osarenmwinda JO, Nwachukwu JC (2010) Development of composite material from agricultural wastes. *Int J Eng Res Afr* 3:42–48 (Trans Tech Publications)
59. Babatunde A (2003) Assessment of the dimensional stability of cement-bonded particleboard from post-harvest banana stem residues and sawdust. *ASSESSMENT* 488:A2
60. Abdulkareem SA, Adeniyi AG (2017) Production of particle boards using polystyrene and bamboo wastes. *Niger J Technol* 36(3):788–793
61. Sotannde OA, Oluwadare AO, Ogedoh O et al (2012) Evaluation of cement-bonded particle board produced from Afzelia African a wood residues. *J Eng Sci Technol* 7(6):732–743
62. Badejo SO (1988) Effect of flake geometry on properties of cement-bonded particleboard from mixed tropical hardwoods. *Wood Sci Technol* 22(4):357–369

63. Okuneye PA, Akande SO, Banwo PA (1986) Forestry residues, wood wastes and fibreboard production and possible uses in Nigeria. *Agric Wastes* 18(3):215–223
64. Erakhrumen AA, Areghan SE, Ogunleye MB et al (2008) Selected physico-mechanical properties of cement-bonded particleboard made from pine (*Pinus caribaea* M.) sawdust-coir (*Cocos nucifera* L.) mixture. *Sci Res Essay* 3(5):197–203
65. Osarenmwinda JO, Nwachukwu JC (2007) Effect of particle size on some properties of rice husk particleboard. *Adv Mater Res* 18:43–48 (Trans Tech Publications)
66. Babatunde A (2011) Durability characteristics of cement-bonded particleboards manufactured from maize stalk residue. *J For Res* 22(1):111–115
67. Pinto J, Paiva A, Varum H et al (2011) Corn's cob as a potential ecological thermal insulation material. *Energy Build* 43(8):1985–1990
68. Akinyemi AB, Afolayan JO, Oluwatobi EO (2016) Some properties of composite corn cob and sawdust particle boards. *Constr Build Mater* 127:436–441
69. Khazaeian A, Ashori A, Dizaj MY (2015) Suitability of sorghum stalk fibers for production of particleboard. *Carbohydr Polym* 120:15–21
70. Olorunnisola AO, Adefisan OO (2002) Trial production and testing of cement-bonded particles board from rattan furniture waste
71. Ndububa EE, Nwobodo DC, Okeh IM (2015) Mechanical strength of particleboard produced from Fonio Husk with gum Arabic resin adhesive as binder. *Int J Eng Res Appl* 5(4):29–33
72. Kosmatka SH, Kerkhoff B, Panarese WC (2002) Design and control of concrete mixtures, Portland cement association. Skokie, Illinois, USA
73. Wang X, Taylor P, Yurdakul E et al (2018) An innovative approach to concrete mixture proportioning. *ACI Mater J* 115(5)
74. Pickering KL, Efendy MA, Le TM (2016) A review of recent developments in natural fibre composites and their mechanical performance. *Compos A Appl Sci Manuf* 83:98–112
75. <https://www.afsuter.com/application/binding-agents/Binding>. Agents—Shellac, Waxes, Natural Gums, Resins, Menthol Crystals & Zein 2/5/2019

# Review on Ergonomics Application on Car Modification for Limbs Disabled Drivers



**Salami Bahariah Suliano, Siti Azfanizam Ahmad, Azizan As'arry, and Faieza Abdul Aziz**

**Abstract** Individuals with disabilities in Malaysia can be considered as a standout among the most vulnerable of the minority bunch in the Malaysian population. World Health Organization (WHO) estimated that 15% of the world populations have some forms of disabilities. According to *Jabatan Kebajikan Masyarakat Malaysia* (JKM), there is an expanding trend in the number of registered disabled as per recorded in their annual statistic. With a projected rise in the number, the quantity of referred group that use the road also continuously increases over time. In addition, they are the majority of those who are likewise, depended on the private cars for their versatility. It is likely that future adjustments in vehicle configuration will be connected in some parts to the physical ailments frequently confronted by them. With incongruous design today in the market, the disabled facing poor driving experience that contributed to the diminishing of physical and emotional impact on them. Thus, this research discusses available interior designs and redesigns for lower limb or upper limb or combined limb disabled in market together with recommendation for future works with intense highlight of most sought after needs for satisfactory requirements of their ergonomics.

**Keywords** Limbs disabled · Redesign · Interior car · Ergonomics · Inclusive design

## 1 Introduction

There are growing numbers of the population of the disabled (DOSW, 2016), and as a result, the population of the disabled drivers show a parallel increase. Driving is an important activity for the disabled to maintain their activities and keep their independence optimized in the tasks such as shopping, attending doctor's as well as maintaining social reintegration [1]. Therefore, having independency in driving is very much important for the disabled peoples' daily life.

---

S. B. Suliano (✉) · S. A. Ahmad · A. As'arry · F. A. Aziz  
Department of Mechanical and Manufacturing, Universiti Putra Malaysia, Selangor, Malaysia  
e-mail: [salami.suliano@gmail.com](mailto:salami.suliano@gmail.com)

The automotive industry is a symbol of technical marvel by humankind, being one of the fastest-growing sectors in the world in which its dynamic growth phases are explained by few criteria such as nature of competition, product lifecycle, and consumer demand. Though Nag et al. (2007) believe that today's global automotive industry is more concerned about consumer demands for styling, safety, and comfort, and few other elements to achieve an effective outcome [2]. Additionally, there are numbers of studies such as by Mutoh, (1988) and Sadler, (2016) on a continuous fascination with the automotive industry and its significant impact on socio-economic life of mankind and its impact continuing to the present [3, 4].

Automotive requires long lead times for design, development, and production planning. Hence, a redesigned product is a derivative work, with changes made to make it more suitable and to improve production besides having a new design or a factory-customized vehicle [5]. However, product optimization and efficiency are the other's another areas that should be analyzed during the redesign process [6].

Presently, the quality of human life is constantly improving and market demands are much more different than in the past. An everyday product that helps one to maintain independence at home, in public, in traveling, and in leisure activities plays a crucial role in one's life [7]. In line with the growing of demands is a constant development of vehicles' design and their performance. With aid of technologies, the vehicles are now equipped with many features such as reverse camera, navigators, and intelligent parking assistance that assist and simplify the users while driving. Therefore, to be competitive in the modern industry, companies need to quickly release vehicles to meet rapidly changing market demands. Products often need to be equipped with more functions to satisfy customers' needs.

Presently, an automotive industry faces new challenges and economic limitations, and one such challenge is determining the needs of the inclusive group to produce an inclusive design [8]. Therefore, with aid of inclusive design, identifying needs or requirements for the group of people with functional limitations will improve their driving quality, also, for those with no limitations [9]. Moreover, inclusive design is an important approach to ensure needs of users with various physical, cognitive, and sensory ability limitation are included and meet [10].

Erroneous choice over product in a way there are mismatch over user demands and user [7]. In specific, as stated by Persad et al. (2007), the combination of attributes in everyday products highlights capability versus demand relation [11]. Therefore, in order for a product to be accessible, individual capabilities have to be greater than product demand unless the product is understood to be inaccessible. Accessibility refers to the user's ability to observe, understand, and interact physically with the product [12].

## 2 Discussion

### 2.1 *Problem Faced by Disabled Drivers (Door to Door)*

Living as a disabled reflects to live in different ways of lifestyle as compared to normal people. The ability of person with disabilities toward using a vehicle was found to be very important as one of survival factors in community integration [10] and employment opportunities. Therefore, it is an important measure for the disabled to have access to every single equipment or facilities from door to door in order to move. The term door to door, illustrating the independent moves of the disabled, starts from exiting the house door to closing the car door. Then after, they can start to move, and this sequence is repeated again along the way throughout their daily journeys. In process, multiple problems might be faced by the disabled such as complexity of transferring wheelchairs into cars (arm and reach) and accessibility to car interior [13]. Besides, there are numbers of barriers to move for the disabled [14] as follows:

#### **Social Problems**

- Different and awkward treatment.
- Less opportunity in societies, work, etc.
- Poverty, discrimination, and inequality in society as a whole.
- Lack of respect toward their daily activities.

#### **Commercial Problems**

- The cost of driving (Including petrol, maintenance, insurance, tax, high adaptive equipment for person with disabilities such as wheelchair and other modifications for assistive driving).
- Lack of job vacancies.
- Heavy traffic.
- High-speed traffic.
- Weather.
- Insufficient parking [15].
- Licensing.

### 2.2 *Disabled Car*

Being disabled makes that particular person has an inner strength to “stand with their own two feet,” and achieving mobility is an important step in doing this [16]. Either disabled with a wheelchair or without a wheelchair both need to drive their own vehicle to attain greater autonomy in their daily life [17]. Likewise, driving is considered a complex task for the disabled as it requires physical attentions, ability to make decisions, quick response, and accurate perception [18]. This is the reason behind steps taken by Ministry of Health of Malaysia in introducing occupational

therapist role as a Pre-Driving Screening as discussed in previous section. Assessments toward the car for the disabled are very much needed. It includes a full check of both off- and on-road of functional ability and cognitive awareness [19]. Table 1 shows the suggested modifications for cars in Malaysia with respect to individual disabilities in which the modifications can be done at any registered vehicle workshop registered with Road Transport Department (RTD).

Ordinary controls such as steering, accelerator, and pedal in a standard production are design to help and provide feedback to drivers [20]. For example, steering wheel and pedals are designed for a rotational distribution of control toward drivers' hands and feet. However, there are certain points or types of disabilities that limit the driver from driving conventionally controlled cars [20]. Having modifications of adaptive equipment is said to be a proven process for maintaining freedom on the road for the disabled [21]. With adaptation, it meets the user needs in different ways as well as allowing the disabled who could not drive before, to drive more easily and more independently [22]. In general, the usefulness of an adaptation or modification depends on several factors [23–25]. These factors include:

- Characteristics of individual users  
(Example: person's particular impairment)
- Characteristics of technology itself  
(Example: ease of use, ease of maintaining, reliability, durability, etc.)
- Environmental circumstances  
(Example: social attitudes, health care professional).

### ***2.3 Ergonomic Car for Disabled***

Ergonomics has been considered since the culture of Ancient Greece [26]. The ergonomics term is derived from the word *ergon* (work) and *nomos* (natural laws) as the scientific discipline is concerned with designing according to the human needs, and the profession that applies theory, principles, data, and methods [27] to design in order to optimize human well-being and overall performance which is also called human engineering and human factor [28]. Within this view, the ergonomics problems contain all elements of the mankind, and environmental systems, comprising people's interactions with hardware, software, and other people both individually and as social groups [29]. In considering the design of an ergonomic car, there are five aspects of ergonomics as listed below [30]:

- Safety [31]
- Comfort [32, 33]
- Ease of use [22, 34]
- Productivity and performance [31]
- Aesthetics [35].

**Table 1** Driving aids guidelines with respect to disabilities

Disability	Effects on driving	Suggested driving aids
Left leg missing or non-functional	<ul style="list-style-type: none"> <li>● Possible inability to maintain body balance</li> <li>● Inability to use clutch</li> <li>● Possible interference of leg or foot with driving mechanisms</li> </ul>	<ul style="list-style-type: none"> <li>● Automatic transmission</li> <li>● A restrain</li> </ul>
Right leg Missing or non-functional	<ul style="list-style-type: none"> <li>● Inability to use standard accelerator</li> <li>● Possible inability to maintain body balance</li> <li>● Inability to use clutch</li> </ul>	<ul style="list-style-type: none"> <li>● Accelerator adapted to the left side</li> <li>● Automatic transmission</li> <li>● A restrain</li> </ul>
Both legs missing or non-functional	<ul style="list-style-type: none"> <li>● Inability to use brake and accelerator</li> <li>● Possible difficulty entering car</li> </ul>	<ul style="list-style-type: none"> <li>● Hand-operated brake and accelerator</li> <li>● Automatic transmission</li> <li>● Transfer board/swivel seat</li> </ul>
Left arm below elbow missing or non-functional	<ul style="list-style-type: none"> <li>● Difficulty performing hand-over-hand steering maneuvers</li> <li>● Inability to shift gears while steering</li> </ul>	<ul style="list-style-type: none"> <li>● Power steering and spinner knob attached to steering wheel mounted at 3 or 4 o'clock positions for the sound hand</li> <li>● Automatic transmission</li> </ul>
Right arm below elbow missing or non-functional	<ul style="list-style-type: none"> <li>● Difficulty performing hand-over-hand steering maneuvers</li> <li>● Inability to shift gears while steering</li> </ul>	<ul style="list-style-type: none"> <li>● Power steering and spinner knob attached to steering wheel, mounted at 8 or 9 o'clock positions for the sound hand</li> <li>● Automatic transmission is easier</li> </ul>
Both arms below the elbow level are missing or not working	<ul style="list-style-type: none"> <li>● Cannot hold and rotate the standard steering wheel</li> <li>● Difficult to handle components in the dashboard</li> <li>● Difficult to hold, pull or twist small controllers such as locking car doors, radio knobs, and window cranks</li> </ul>	<ul style="list-style-type: none"> <li>● Use prosthesis</li> <li>● Driving ring or steering knob is placed in the steering wheel with the dominant hand</li> <li>● Place the ring on the control dashboard</li> <li>● Ring is placed in a small controlled device for easy operation</li> <li>● Without using prosthesis:                             <ul style="list-style-type: none"> <li>● Can rotate steering using both arms, if not using extended telescopic steering is recommended</li> </ul> </li> <li>● Dashboard extension</li> <li>● Power door locks and power windows</li> </ul>

(continued)

**Table 1** (continued)

Disability	Effects on driving	Suggested driving aids
Left arm above elbow missing or non-functional	<ul style="list-style-type: none"> <li>• Inability to perform hand-over-hand steering maneuvers</li> <li>• Disability reaching left-hand dashboard controls</li> <li>• Difficulty to reach left-hand dashboard controls</li> <li>• Difficulty activating horn while right hand is occupied</li> </ul>	<ul style="list-style-type: none"> <li>• Steering knob or other steering aid mounted on the right</li> <li>• Right-hand extension on left-hand dashboard controls</li> <li>• Parking brake release adapted for use by the left foot</li> <li>• Automatic transmission</li> <li>• Horn ring that can be reached without letting go of the steering knob</li> </ul>
Right arm above elbow missing or non-functional	<ul style="list-style-type: none"> <li>• Inability to perform hand-over-hand steering maneuvers</li> <li>• Difficulty reaching right-hand dashboard controls</li> <li>• Possible difficulty turning the ignition key</li> <li>• Inability to shift gears on standard transmission</li> </ul>	<ul style="list-style-type: none"> <li>• Steering knob or another device mounted on the left</li> <li>• Left-hand extensions for right-hand dashboard controls/signals</li> <li>• Ignition key reachable with the left hand while parked or adapted for the left hand</li> <li>• Automatic transmission</li> </ul>
Both arms above the elbow level are missing or do not work	<ul style="list-style-type: none"> <li>• Cannot use standard steering</li> <li>• Cannot handle standard gear</li> <li>• Cannot handle signal, ignition key, handling dashboard components, horn, parking brake release, and gear conversion</li> </ul>	<ul style="list-style-type: none"> <li>• Steering control using the legs</li> <li>• Automatic transmission</li> <li>• Handling gear using right foot</li> <li>• Remote control using knee to control the ignition key, light</li> </ul>

## 2.4 Objective

The main aim of this paper is to solve the difficulties in the automotive of the disabled people by performing some researches and literary survey on various journal articles mainly about disabled drivers and ergonomics. This will be helpful for knowledge added to discover a best desired technology in the pre-existing modified parts to be implemented in the interior design of the cars for the disabled according to their ergonomics and to achieve their desired goals.

### 2.4.1 Literature Survey

**Goswami et al. (1987)** “Anthropometric characteristics of disabled and normal Indian men.” This research paper describes a preliminary study of anthropometric characteristics of disabled Indian men, undertaken in order to facilitate the design of



mobility aid which compares growth and affected parts of limbs between these two groups [36].

**Benktzon (1993)** “Designing for our future selves: the Swedish experience.” This is a study of the ergonomics of handicapped people driving any type of adapted vehicle due to the absence of guidelines for both adapted control design and installation that analyze the reach zones for each type of handicapped and the normal position of vehicle controls to establish criteria for the correct ergonomic adaptation of vehicle controls [37].

**Dols et al. (1997)** “Procedure for improving the ergonomic design of driving positions adapted for handicapped people.” This research addresses particular aspects of design for people with specific difficulties, and problems associated with the use of everyday items, which has led to designs which are acceptable to a broader range of users [38].

**Nicolle and Peters (1999)** “Elderly and Disabled Travelers: Intelligent Transport Systems (ITS) Designed for the 3rd Millennium.” This article describes the methods of the handbooks development, including an overview of the methodology for capturing the requirements of elderly and disabled travelers, a survey of existing guidelines, and empirical results and lessons learned from simulator testing. The authors conclude that although general guidelines are necessary, the most specific and useful guidelines emerge only when carefully chosen research questions can be investigated. The development of such guidelines should help us come closer to achieve usability of ITS not only for elderly and disabled people but for everybody as we enter the third millennium [39].

**Newell and Gregor (2002)** “Long papers Design for older and disabled people—where do we go from here?” This paper brings together a number of proposals to improve both specialists and mainstream design methods in the field as a contribution to the debate about design for older and disabled people and the concept of universal usability [40].

**Kaklanis et al. (2013)** “Virtual user models for the elderly and disabled for automatic simulated accessibility and ergonomic evaluation of designs.” This paper presents a framework for automatic simulated accessibility and ergonomic testing of virtual prototypes of products using virtual user models. The proposed virtual user modeling framework describes virtual humans focusing on the elderly and people with disabilities. Geometric, kinematic, physical, behavioral, and cognitive aspects of the users affected by possible disabilities are examined, in order to create virtual user models able to represent people with various functional limitations [41].

**Wu et al. (2015)** “A Concept Compact City Vehicle Design for the Disabled Aging People.” The paper focused on observation of six disabled aged users of light to moderate physical disabilities in moving inside and getting in and out of a car. From the video and interviews, problems the disabled aged people encountered in using compact cars were addressed. To solve the inconvenience and the difficulties that the elderly disabled passengers have in a compact car, a concept design of a welfare vehicle was developed. In the concept welfare vehicle, a big hand bar on the side of the car door that could be controlled with the operation of car door was proposed to help the aging people support their body [42].

**Suliano et al. (2019)** “Limbs disabled needs for an ergonomics assistive technologies and car modification.” This paper dealt with the survey outcome from 30 independent limbs disabled drivers in Selangor, Malaysia. The main objective of this survey is to find the real need of limbs disabled in respect to any activities related to car driving as a driver enters, drives, and exits the car. At the present time, the car’s interior is equipped with few assistive technologies and modifications available to be installed ranging from hand to foot, and also, to those with or without wheelchair users according to the type of limbs disabilities. From the survey, it was found that interior parts such as handling, upholstery, and steering are in high need to be ergonomically redesigned [43].

#### **2.4.2 Assistive Driving Comparison**

Medical conditions which are accompanied by physical impairments and relative individual functional performance (varies depending on personal characteristics) are often reasons that cause challenges in assessing driving abilities of the disabled [44]. However, independent driving is an important aspects particularly for people with disabilities as significant activities of daily life [45]. For improvement of quality of life, a majority of the disabled are driving an adapted or modified car as a most important means of independency [20] on access to personal vehicular transportation [46]. Modification or assistive driving has led to improvements for limbs disabled drivers [45]. Here, some of the literature on available assistive driving parts together with review on each one are presented as in Table 2.

### **3 Future Recommendation**

It is very important to ensure disabled drivers experience the most ergonomic driving experience as their physical limitation can be caused the worst impact toward them physically and psychologically. Therefore, five main aspects of ergonomics such as safety, comfort, ease of use, productivity and performance, and esthetic were implied in this inclusive design to support disabled drivers as well as normal drivers. Therefore, when we design for the disabled, we provide benefits for all.

**Table 2** Comparison on literature survey

No.	Authors (years)	Parts of car	Remarks		Ergonomics (Yes/No)
			Type	Strength (S)/recommendation (R)/gaps (G)	
[47]	Boyce et al. (2013)	Hand control	PHC-3 and TNT	<p><b>S:</b> Highlight the usability of portable assistive driving devices as it relates to driver performance and safety</p> <p><b>R:</b> To increase the sample population and improves quantitative measuring tools to assess functional capacity</p> <p><b>G:</b> Only consider two ergonomic aspect which is safety and performance</p>	Yes. Partially
[48]	Yamashita (2014)		Omni Haptic hand control	<p><b>S:</b> Designed model predictive controller, combined with the admittance controller, achieves excellent tracking performance in both an autonomous mode and assistive mode</p> <p><b>R:</b> Wider age area. Only consider older driver aged 65 above. Malaysian with age 65 above rarely drive</p> <p><b>G:</b> Only consider one ergonomic aspect which is safety</p>	Yes. Partially
[20]	Peters et al. (2005)		Joystick control	<p><b>S:</b> Joystick was designed for severe locomotor disabled drivers</p>	Yes. Partially

(continued)

**Table 2** (continued)

No.	Authors (years)	Parts of car	Remarks	Ergonomics (Yes/No)	
				Strength (S)/recommendation (R)/gaps (G)	
			Type		
[16]	Murata and Yoshida (2013)	Driving interface	Gesture driving	<p><b>G:</b> only consider one ergonomic aspect which is ease of use</p> <p><b>S:</b> Steering operation interface designed for disabled people that uses right and left gesture operations</p> <p><b>R:</b> Main device is sensor. Having sensor in driving environment to replace real body parts cooperated with safety issues. Safety issues highlight</p> <p><b>G:</b> No ergonomics elements</p>	No
[49]	Morton and Yousuf (2011)	Driving interface	Electronics	<p><b>S:</b> Specifically for pedestrians and travelers with visual impairment or other disabilities</p> <p><b>G:</b> No ergonomics elements</p>	No
[50]	Jones et al. (2010)	Pedal	Flip accelerator pedal	<p><b>G:</b> No ergonomics elements</p> <p><b>S:</b> Restore independence to people with left limbs disabled</p> <p><b>R:</b> Dual advantage consideration. Those with right-sided pathology are disadvantaged in this respect</p> <p><b>G:</b> No ergonomics elements</p>	No
[51]	Nilsson (1989)	Pedal	Combined accelerator-brake	<p><b>S:</b> Eliminate the operator's risk of pressing the wrong pedal as well as to reduce his or her reaction time in braking</p>	Yes, Partially

(continued)

**Table 2** (continued)

No.	Authors (years)	Parts of car	Remarks Type	Strength (S)/recommendation (R)/gaps (G)	Ergonomics (Yes/No)
				<p><b>R:</b> Safety feature installation. Might cause unintended or mixed function of brake or accelerator</p> <p><b>G:</b> Only consider ease of use and safety</p>	
[52]	Nilsson (2002)		Brake–accelerator pedal (Improved)	<p><b>S:</b> Eliminate the operator’s risk of pressing the wrong pedal as well as to reduce his or her reaction time in braking</p> <p><b>R:</b> Safety feature installation. Might cause unintended or mixed function of brake or accelerator</p> <p><b>G:</b> Only consider ease of use and comfort</p>	Yes. Partially
[53]	Arora (2016)		Combined accelerator–brake	<p><b>S:</b> Eliminate the operator’s risk of pressing the wrong pedal as well as to reduce his or her reaction time in braking, develop in a way the brake and accelerator work in instant and reduce delay in action and design to improve confusion issues</p> <p><b>G:</b> Only consider ease of use, safety and comfort</p>	Yes. Partially

(continued)

**Table 2** (continued)

No.	Authors (years)	Parts of car	Remarks	Ergonomics (Yes/No)	
				Strength (S)/recommendation (R)/gaps (G)	
[54]	Lawton et al. (2008)	Seat	Postural support	<p><b>S:</b> Postural stability of disabled drivers, Improved driving performance, reduced physical exertion, maintain an upright driving position</p> <p><b>R:</b> Not based on real-world driving environment</p> <p><b>G:</b> Not ease to use</p>	Yes, Partially
[55]	Said et al. (2015)		Postural support	<p><b>S:</b> Focus on compact car</p> <p><b>G:</b> Only consider is safety and comfort</p>	Yes, Partially
[56]	Neville (2005)		Postural support	<p><b>Strength:</b> Study on impact of seating and positioning</p> <p><b>Gaps:</b> Not considering ease to use and esthetic factor</p>	Yes, Partially
[57]	Klarborg et al. (2012)	Speed	Intelligent speed	<p><b>S:</b> cognitive workload of driving by demanding less attention for monitoring speedometer and speed limit signs, decision-making processes associated with choosing an appropriate speed and using GPS located at dashboard to do monitoring</p> <p><b>Gaps:</b> Only for acquired brain injury driver and not ergonomic</p>	No

**Acknowledgements** This research has been supported by Grant Putra (GP-IPS) from Universiti Putra Malaysia. The authors would like to acknowledge Road Transport Department Malaysia and Social Welfare Department who provided insight, expertise, and documentation that greatly guided the research.

## References

1. Patrick EJ, Mohd EF, Yang CT (2012) Ability to return to driving after major lowerlimb amputation. *J Rehabil Med* 44:19–23
2. Nag B, Benerjee S, Chatterjee R (2007) Changing features of the automobile industry in Asia : comparison of production, trade and market structure in selected countries
3. Mutoh H (1988) *The automotive industry*. Academic Press, San Diego
4. Sadler D (2016) The geographies of just-in-time: Japanese investment and the automotive components industry in Western Europe. *J Econ Geogr* 70:41–59
5. Shen YT, Smith S (2009) Product redesign using TRIZ and contradictory information from the Taguchi method. In: Chou SY, Trappey A, Pokojski J et al (eds) *Global perspective for competitive enterprise, economy and ecology*. In: *Proceedings of the 16th ISPE international conference on concurrent engineering*. Springer, London, pp 487–497
6. Hill K, Edwards M, Szakaly S (2007) How automakers plan their products
7. Bieber M (2003) The struggle for independence. In: Clarkson J, Keates S, Coleman R et al (eds) *Inclusive design: design for the whole population*. Springer, London, pp 50–57
8. Bhise VD (2012) *Ergonomics in automotive design process*. CRC Press, Florida
9. Karali S (2015) *Vehicle ergonomics and older drivers*
10. Persad U, Langdon P, Clarkson J (2006) Exploring user capabilities and health: a population perspective. *Contemp Ergon*
11. Persad U, Langdon P, Clarkson J (2007) Characterising user capabilities to support inclusive design evaluation. *Univ Access Inf Soc* 6:119–135
12. Keates S, Clarkson J (2003) Countering design exclusion: bridging the gap between usability and accessibility. *Univ Access Inf Soc* 2:215–225
13. Branowski B, Pohl P, Rychlik M et al (2011) Integral model of the area of reaches and forces of a disabled person with dysfunction of lower limbs as a tool in virtual assessment of manipulation possibilities in selected work environments. In: *Universal access in human-computer interaction*, vol 6766, pp 12–21
14. SACOG (2006) *Senior and disabled mobility study*. Sacramento
15. Sanmargaraja S, Wee ST (2011) *Kajian Penyediaan Fasiliti Orang Kurang Upaya (OKU) di Institusi Kerajaan di Nusajaya Johor Bahru*, pp 1–11
16. Murata Y, Yoshida K (2013) Automobile driving interface using gesture operations for disabled people. *Int J Adv Intell Syst* 6:329–341
17. Monacelli E, Dupin F, Dumas C et al (2009) A review of the current situation and some future developments to aid disabled and senior drivers in France. *IRBM* 30:234–239
18. MyHealth (2019) Pre-driving assessment for people with disabilities. <http://www.myhealth.gov.my/en/pre-driving-assessment-people-disabilities/>. Last accessed 19 Dec 2017
19. Frye A (2013) *Disabled and older persons and sustainable urban mobility*. London
20. Peters B, Ostlund J (2005) *Joystick controlled driving for drivers with disabilities*
21. NHTSA (2015) *Adapting motor vehicles for people with disabilities*
22. Field M, Jette A (2007) *The future of disability in America*. The National Academies Press, Washington
23. Batavia AI, Hammer GS (1990) Toward the development of consumer-based criteria for the evaluation of assistive devices. *J Rehabil Res Dev* 27:425–436

24. Scherer MJ (2005) *Living in the state of stuck: how assistive technology impacts the lives of people with disabilities*. Brookline Books, Cambridge MA
25. Thorkildsen R (1994) *Research synthesis on quality and availability of assistive technology devices*. Washington, DC
26. Marmaras N, Poulakakis G, Papakostopoulos V (1999) Ergonomic design in ancient Greece. *Appl Ergon* 30:361–368
27. Samuji MSBM (2009) Development of ergonomics passenger car driver seat concept design
28. Wickens CD, Lee JD, Liu Y et al (2004) *An introduction of human factors engineering*. Pearson Prentice Hall, New Jersey
29. Wilson JR (2000) Fundamentals of ergonomics in theory and practice. *Appl Ergon* 31:557–567
30. Vinay S (2013) *Automotive design with respect to ergonomics*. Virginia Area
31. Woodcock A (2012) New insights, new challenges; Person centred transport design. *Work* 41:4879–4886
32. Giacomini J, Quattrocchio S (1997) An analysis of human comfort when entering and exiting the rear seat of an automobile. *Appl Ergon* 28:397–406
33. Haug E, Trameeon A, Allain JC et al (2001) Modelling of ergonomics and muscular comfort. *KSME Int J* 15:982–988
34. Waller S, Cardoso C, Clarke S et al (2007) *Inclusive design toolkit*. Engineering Design Centre, University of Cambridge, Cambridge
35. Liu Y (2000) Engineering aesthetics and ergo-aesthetics : theoretical and methodological foundations. In: *Industrial engineering-theory and practice*, pp 1–12
36. Goswami A, Ganguli S, Chatterjee BB (1987) Anthropometric characteristics of disabled and normal Indian men. *Ergonomics* 30:817–823
37. Benktzon M (1993) Designing for our future selves: the Swedish experience. *Appl Ergon* 24:19–27
38. Dols JF, Garcia M, Sotos JJ (1997) Procedure for improving the ergonomic design of driving positions adapted for handicapped people
39. Nicolle C, Peters B (1999) Elderly and disabled travelers: intelligent transport systems designed for the 3rd Millenium. *J Transp Hum Factors* 1:121–134
40. Newell AF, Gregor P (2002) Long papers design for older and disabled people—where do we go from here? *Univiers Access Inf Soc* 2:3–7
41. Kaklanis N, Moschonas P, Moustakas K et al (2013) Virtual user models for the elderly and disabled for automatic simulated accessibility and ergonomoy evaluation of designs. *Univiers Access Inf Soc* 12:403–425
42. Wu JC, Lee TL, Chang CC (2015) A concept compact city vehicle design for the disabled aging people. *J Heal Sci* 3:62–70
43. Suliano SB, Ahmad SA, Assary A et al (2019) Limbs disabled needs for an ergonomics assistive technologies and car modification. In: *4th international conference on mechanical manufacturing and plant engineering*
44. Greve JMDA, Santos L, Alonso AC et al (2015) Driving evaluation methods for able-bodied persons and individuals with lower extremity disabilities: a review of assessment modalities. *Clinics* 70:638–647
45. Dahuri MKAM, Hussain MN, Yusof NFM et al (2017) Factors, effects, and preferences on vehicle driving modification for the Malaysia independent disabled. *J Soc Automot Eng Malays* 1:103–110
46. Roosmalen VL, Paquin GJ, Steinfeld AM (2017) Quality of life technology: the state of personal transportation. *Phys Med Rehabil Clin* 21:111–125
47. Boyce MW, Fekety DK, Smither JA (2013) Resource consumption and simulator driving performance using adaptive controls. *Assist Technol* 25:158–165
48. Yamashita M (2014) Assistive driving simulator with haptic manipulator using model predictive control and admittance control. *Procedia Comput Sci* 39:107–114
49. Morton T, Yousuf M (2011) *Technological innovations in transportation for people with disabilities*. Washington, DC



50. Jones C, Abbassian A, Trompeter A et al (2010) Driving a modified car: a simple but unexploited adjunct in the management of patients with chronic right sided foot and ankle pain. *Foot Ankle Surg* 16:170–173
51. Nilsson R (1989) 10 Evaluation of a combined accelerator-brake pedal, pp 99–100
52. Nilsson R (2002) Evaluation of a combined brake-accelerator pedal. *Accid Anal Prev* 3:175–183
53. Arora S (2016) A combined pedal for brake and accelerator. *Int J Res Aeronaut Mech Eng* 4:131–138
54. Lawton C, Cook S, May A et al (2008) Postural support strategies of disabled drivers and the effectiveness of postural support aids. *Appl Ergon* 39:47–55
55. Mohd Said MA, Ahmad MK, Wennedy BH et al (2015) Modeling compact driver car seat and analysis of its ergonomic for driver postural using Catia software. *J Sci Res Dev* 2:125–131
56. Neville L (2015) The fundamental principles of seating and positioning in children and young people with physical disabilities
57. Klarborg B, Lahrman H, Nielsagerholm, Tradisauskas N, Harms L (2012) Intelligent speed adaptation as an assistive device for drivers with acquired brain injury: a single-case field experiment. *Accid Anal Prev* 48:57–62

# Hybrid Microgrid Systems: Operational Schedule Optimization Considering Time of Use Demand Response and Battery Wear Cost



Topé Roseline Olorunfemi and Nnamdi Nwulu

**Abstract** This study develops a multi-objective optimization model, for the optimal operational schedule for a grid-connected microgrid. A combination of renewable and non-renewable energy sources were considered in the microgrid. This consists of photovoltaic (PV) solar energy, battery, and diesel generator. The optimization model has an objective function which seeks to simultaneously minimize diesel generator fuel cost, grid electricity, and battery wear cost. Two microgrid configurations were developed and compared to obtain the configuration with the minimal operational cost. The Advanced Interactive Multidimensional Modeling System (AIMMS) software was used to solve the model. Obtained results show the practicality of the developed model.

## 1 Introduction

Electricity is a vital element that forms a part of human social economic development which influences all spheres of human social lifecycle. Therefore, there is a need for a balance in the demand and supply for electricity. The conventional sources for electricity generation include, but not limited to: coal and oil which pollute the environment and cause bad effects on human health [1]. Consequently, the integration of renewable energy sources has a great role to play in the electricity generation to overcome the previously mentioned problems. Furthermore, advantages of deploying renewable energy resources in a microgrid include reduction of power loss during transmission, reserve generation capacity, and grid security [2]. According to Twaha and Ramli [2] by 2040, there is going to be a rise in the global energy demand by 30% which will aggravate the need for renewable sources to emerge as the prime solution in the electricity industry, as the conventional method of generation is no longer sustainable to meet the demand [3, 4]. Additionally, the electricity industry contributes to the largest amount of greenhouse gas emissions, specifically 25% of the total global

---

T. R. Olorunfemi (✉) · N. Nwulu  
Department of Electrical and Electronic Engineering Science, University of Johannesburg,  
Johannesburg, South Africa  
e-mail: [topyrose6@gmail.com](mailto:topyrose6@gmail.com)

greenhouse gas emissions. However, most countries such as South Africa, Estonia, Poland, and Australia are still heavily dependent on electricity generation from the burning of coal, while other developed countries Brazil, Germany, Denmark, India, USA, China, and Russian are doing their best to integrate renewable energy sources [5]. Consequently, those of the leading countries in renewable energy sources are utilizing the technology and the countries that are yet to utilize the technology who have to learn some lessons from the leading countries in renewables. Findings show that in recent years, the price of renewable energy sources has dropped considerably, especially photovoltaic (PV) cells which make their integration more viable [6]. However, as good as the integration of renewable energy resources could be, it is essential to optimize the sizing of the systems and other objective parameters (such as cost reduction and maximize profit and the like) to get the technical, environmental, and economic advantages, so that their potential can be fully utilized. This study investigates the use of renewables in a grid-connected microgrid and a diesel generator (DG) at the supply side to minimize the grid cost and battery wear cost.

### ***1.1 Microgrid System***

The currently available microgrid system consists of one or more distributed energy resources (DER) located close to the end users over a small area of land. There are many benefits with the deployment of DER. These range from low energy tariffs compared to tariff from the grid, reduction of CO<sub>2</sub> emissions, and long-lasting DER systems [7]. The distributed energy resources can either be the conventional methods of power generation, storage systems, or renewable energy sources. Furthermore, examples of the conventional methods of electricity generating are diesel generator units and gas generator units. Also, examples of renewable energy resources include solar energy and wind energy while that of storage systems include pump storage, batteries, and flywheels. Microgrids can either be in a connected mode or an islanded mode. The connected mode means it has a connection with the main grid while the islanded mode means that there is no connection whatsoever with the main grid [8]. Microgrids that consist of solar energy, wind energy, batteries, and gas generator unit are economically viable in supplying electricity at present and in future following the high demand in electricity and the depletion in the fossil fuels. Therefore, optimization of the system is essential to determine the system cost and its reliability [8]. Due to the wide spread deployment of the microgrids into power systems, there have been many researches to optimally size or operate already sized microgrids. This work falls under the operational optimization of microgrid. Many researchers have investigated the operational aspect of the microgrids. Reference [9] proposed the minimization of operating cost in a neighborhood made up of a microgrid system for their source of energy supply. While in [10], their work was based on an optimization model which optimally reduced the life cycle cost of the various microgrid components which were comprised of PV, wind, diesel generators, and battery energy system. Also, authors in [11] determined the optimal power in

the microgrid in order to reduce the total cost at the demand side with the system connected to the main grid. Reference [12] presented a conditional value at risk (CVaR) formulation to optimally manage the battery energy system to enhance the microgrid while still keeping the operational cost to the lowest level. Also [13], puts forward the minimization of the battery degradation cost of the microgrid since the battery life time depends on the rate of charging and discharging of the battery. Also [14], integrates a battery energy storage system into a microgrid which was formulated as a day-ahead forecast of the battery. Their aim was to minimize the degradation cost and the operational cost of the entire system using rainbow algorithm of particle swarm optimization for the system simulations. The contributions of this paper include:

1. Investigating two different microgrid operational strategies and their impact on battery wear cost.
2. Evaluate the impact of a TOU-DR tariff on the operational schedule of the microgrid by extension on the cost metrics.
3. Sensitivity analysis of various parameters.

The rest of the paper is organized as follows: Sect. 2 presents the system configurations and formulations, showing the proposed model objective and constraints. Section 3 detailed the numerical analysis of the simulation results Sect. 4 gives the conclusion, and future works.

## 2 System Configurations and Formulations

### 2.1 Modeling of the Photovoltaic (PV) System

The active energy output of a PV generator depends solely on the ambient temperature and the density of solar irradiation [15]. Also, the aim of utilizing a PV generator is to achieve its maximum energy output. Therefore, each component and modules in the system including how the output power is generated must be investigated. However, the mathematical model used to calculate the hourly energy generated from a photovoltaic generator of specified area can be stated as follows [16]:

$$Y_{pv} = E_{pv} N A_m G_t \quad (1)$$

where  $Y_{pv}$  is the hourly output of the PV generator,  $E_{pv}$  means instant PV generator efficiency,  $N$  is the number of modules used in the system,  $A_m$  represents the area of the PV array ( $m^2$ ), and lastly  $G_t$  stands for the global irradiation incident on the titled plane in ( $w/m^2$ ). The energy losses in the system are all assumed to be zero. While the instant PV generator efficiency is represented as follows [15]:

$$E_{pv} = \text{Ref}_{pv} f_{pv} E_{pt} [1 - \beta_t (T_c - T_r)] \quad (2)$$

where  $\text{Ref}_{\text{pv}}$  is the reference efficiency of the PV generator,  $E_{\text{pt}}$  is the power tracking equipment efficiency which is normally equal to 1 if the perfect tracker is used.  $T_c$  stands for the PV array temperature ( $^{\circ}\text{C}$ ) while  $T_r$  is also the PV array reference temperature, and lastly  $\beta_t$  is the temperature coefficient of efficiency usually ranging from 0.004 to 0.006 ( $^{\circ}\text{C}$ ) for each cell.

## 2.2 Modeling of Battery System

The battery lifetime modeling is a crucial part of the hybrid energy systems. Therefore, the approach for managing the energy storage systems will significantly influence the performance of the overall system [17]. There are several types of lifetime models for battery systems, but the two commonly used are: Post-processing and performance degradation.

1. Post-processing models: These real-life models can be used to evaluate and measure data from real systems. Unlike the performance model, which combines lifetime model with performance model, which is being updated during the simulation efficiency of the battery as it gets older.
2. Performance degradation models: The usage of the battery from charge and discharge is referred to as battery “degradation.” For a battery to attain its full utilization, the percentage of its nominal capacity must be 80%. If then a battery, that has been operating for some years, is only able to give an output of 75% of its total nominal capacity, then the battery is considered dead [18].

Also, there are several approaches in calculating the life time consumption of a battery: These include the Ah-throughput and the cycle counting approach.

The Ah-throughput approach counts the quantity of charge that has passed through the battery. In this model, it is assumed that certain quantities of power must have passed through a battery before it is due for replacement. In order to calculate the total throughput over a battery lifetime, the following would be involved in the depth of discharge (DoD) and cycles to failure (CTF) datasheets which are usually provided by the manufacturer. It is represented mathematically as follows [19]:

$$\lambda_L = \text{DoD} * \text{BC} * \text{CTF} \quad (3)$$

where DoD is the depth of discharge considered, and in this work, the DoD used is 50%, BC is the battery capacity, and CTF stands for cycles to failure. The constant charge and discharge of the battery especially when having prolonged periods of low discharge, this account for the battery wear. This leads us to one of our objective functions, which is the battery wear cost. The battery wear cost (BWC) gotten from the literature and can be modeled as follows [20]:

$$\text{BWC} = cb/\lambda_l \quad (4)$$

where  $cb$  is the cost of battery and  $\lambda_l$  is the estimated throughput of the battery lifetime. The output of the battery's hourly state of charge (SOC) is determined by the previous hour's SOC charge and discharge of the battery. State of charge at a time ( $t$ ) can be modelled mathematically as [21]:

$$B_{\text{soc}} = B_{\text{soc}-1} + \eta_c \text{pfib} - \eta_d \text{pfob} \quad (5)$$

where  $\eta_c$  is the battery charging efficiency,  $\eta_d$  is the discharging efficiency, pfib represents the power flow in the battery at time ( $t$ ), and pfob stands for power flow out of the battery at time ( $t$ ).

### 2.3 Modeling the Diesel Generator

The diesel generator serves as a good source of energy dispatch whenever the RES is not able to meet the energy demand at a particular period of time ( $t$ ). Therefore, it is normally used as a backup for dispatching energy when the demand is more than what the RES can supply or when they cannot supply at all, due to their stochastic nature. The cost function of the diesel generator is simplified and presumed to be a quadratic function in nature given as follow:

$$C_{\text{gen},t} = ay_t + b^2y_t \quad (6)$$

where  $a$  and  $b$  are the fuel cost coefficients of the diesel generator, respectively.

## 3 System Configurations

The parameters employed for the model are presented in Table 1 while the parameters for the time of use energy tariff are presented in Table 2.

Two system configurations were employed in this work and the outputs were compared. For the first model, the excess power from the DG and the PV was used to charge the battery while in the second model, the DG did not charge the battery but only the PV does. The first model contains the PV generator, diesel generator, a battery energy storage system, the energy from the grid, and the load demand to be met.

Figure 1 depicts the hybrid PV-DG battery grid-connected model (Case study 1) of the system configuration. The load demand is supplied by the PV generator and the DG while the excess energy from both is used to charge the battery system. The battery discharges whenever the PV and DG are not able to meet the load. Also, the system is designed in such a way that the load can also be met by the energy from the grid and vice versa. Therefore, the objective function was formulated to accommodate this, which was the reason why we gave a *weighting factor* to the variables in order to determine the best solution by varying the weighting factors.

**Table 1** Model parameters

S. no.	Types	Capacity
1	PV array	47 m <sup>2</sup>
2	Battery size	40 kWh
3	Allowable depth of discharge (DoD)	50%
4	Cost of battery	\$65 kWh
5	Discharge and charge efficiency	75 and 100%
6	Initial state of charge	0.6
7	Minimum and maximum state of charge	0.5 and 1
8	<i>a</i> and <i>b</i>	0.877 and 12
9	DG min (kW)	0
10	DG max (kW)	5 kW

**Table 2** The time of use energy tariff parameters

Hour (h)	0–5	5–8	8–11	11–17	17–22	22–24
Unit price (\$/kWh)	0.426	0.852	1.278	0.852	1.278	0.426

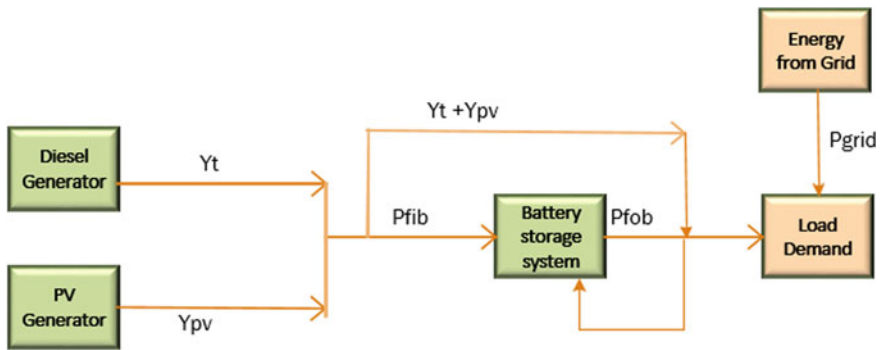


**Fig. 1** Hybrid PV-DG battery grid-connected model (Case study 1)

The second model as presented in Fig. 2 also comprises of the PV generator, DG, the battery storage, load from the grid, and lastly the demand. In this model, the strategy employed is based on the PV solely charging the battery system, while the DG and PV also supply the demand. The battery system can either charge (*p<sub>fib</sub>*) or discharge (*p<sub>fob</sub>*) to also meet the demand at the time when the demand is greater than the supply from the two generators. It can also buy from the grid with the utilization of time of use (TOU) tariff. The TOU tariffs is a prominent demand side management tools for curtailing customer demand [22–24]. Our main goal is to determine which of the models gives the minimum grid power cost and the battery wear cost. The objective function is represented mathematically as follows:

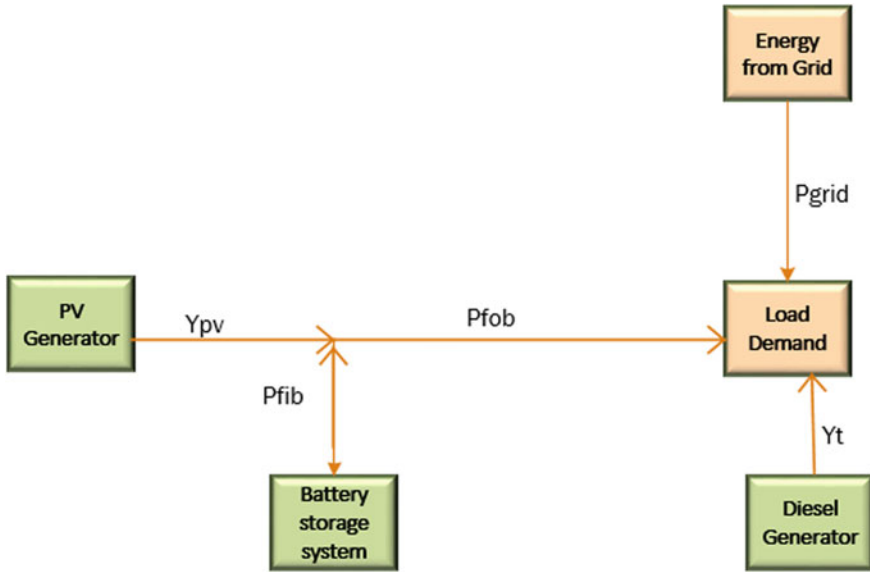


Fig. 2 Hybrid PV-DG battery grid-connected model (Case study 2)

$$\min \sum_{t=1}^N w1 a(y^2(t)) + b(y(t)) + w2 BWC(pfib(t)) + BWC pfob(t) + w3 pgrid(t) tou(t) \tag{7}$$

Weighting factor ( $w$ ) was used to combine the three objective functions into one since there were three of them namely: the fuel cost, battery wear cost, and the grid electricity cost. As such,  $w1$ ,  $w2$  and  $w3$  are the weighting factors which add up to 1,  $a$  and  $b$  are the fuel cost coefficients,  $y_t$  is the hourly power output at time ( $t$ ) from the generator, BWC is the battery wear cost,  $pfob_t$  is the power flow out of the battery at time ( $t$ ),  $pfib_t$  means the power flow into the battery at time ( $t$ ),  $pgrid_t$  is the power bought from the grid at time ( $t$ ), and lastly  $tou(t)$  is the time of use for the energy tariff, which is subjected to some load and generation constraints. The constraints of the case study 1 are given as follows:

$$y_t + Ypv_t + pfob_t + pgrid_t = load_t + pfib_t \tag{8}$$

$$pfib_t + pfob_t \leq y_t Ypv_t \tag{9}$$

$$Ypv_t \leq sr_t \tag{10}$$



$$\text{gen}_{\min} \leq \text{gencap} \leq_t \text{gen}_{\max} \quad (11)$$

$$\text{soc}_t \leq \text{bacap}_{\max} \quad (12)$$

The brief descriptions of the constraints are stated as follows:

Constraint (8) is the power balance constraint which satisfies the condition that at any given time ( $t$ ) the output from the generator, output from the battery, and finally output from the grid should be equal to the load and the power flow into the battery.

Constraint (9) is a constraint that balances both power charging and discharging powers from the battery which should be less or equal to the output from the DG generator and the PV generator.

Constraint (10) is the PV generator output refraining the output to be less or equal to the solar irradiation.

Constraint (11) shows that the generator's minimum and maximum capacities must not be exceeded.

Constraint (12) implies that the state of charge at any given time ( $t$ ) should be less or equal to the maximum battery capacity.

Case study 2 also satisfies the following constraints:

$$y_t + \text{pfob}_t + \text{pgrid}_t = \text{load}_t \quad (13)$$

$$\text{pfob}_t + \text{pfb}_t \leq Y_{pv}_t \quad (14)$$

$$\text{gen}_{\min} \leq \text{gencap} \leq_t \text{gen}_{\max} \quad (15)$$

$$\text{soc}_t \leq \text{bacap}_{\max} \quad (16)$$

$$Y_{pv}_t \leq sr_t \quad (17)$$

Constraint (13) is the power balance constraint which satisfies the condition that at any given time ( $t$ ), the output from the PV, output from the generator, output from the battery, and finally output from the grid should be equal to the load.

Constraint (14) constraint that balances both power charging and discharging power from the battery which should be less or equal to the output from the PV generator.

Constraint (15) shows that the generator's minimum and maximum capacities must not be exceeded.

Constraint (16) implies that the state of charge at any given time ( $t$ ) should be less or equal to the maximum battery capacity.

Constraint (17) implies that the PV generator output must be less or equal to the solar irradiation.

### 3.1 Solution Methodology/Results

The Advanced Interactive Multidimensional Modeling System (AIMMS) software was used to model and solve the obtained multi-objective mathematical model. CONOPT Solver and Outer Approximation Algorithm (OAA) were used. The solving time was 0.05 s on an Intel Pentium computer, windows 10 edition with central processing unit of 2.2 GHZ, RAM of 8 GB and 64-bit operating system.

The variables determined are as follows.

State of charge of the battery ( $soc_t$ ), power flow in of battery ( $p_{fib}_t$ ), power flow out of battery ( $p_{fob}_t$ ), The hourly output of PV generator ( $Y_{pv}_t$ ), the energy from the PV generator only starts to produce at time (8 a.m.–18 p.m.) because of the nature of the weather condition. The hourly output of the diesel generator ( $y_t$ ) and lastly the energy purchased from the grid ( $p_{grid}_t$ ).

#### 3.1.1 Case Study 1

The configuration in Fig. 1 is set up in such a way that both the DG and PV generators, respectively, supply the load demand. Then the excess power is used to charge the battery and discharged to the load when needed (for backup purposes, in the case where the DG and PV cannot supply the load at any given period of time) ( $t$ ). The time of use (TOU) type of tariff for unit prices of electricity was used to model the energy from the grid.

#### 3.1.2 Case Study 2

The configuration in this case study, as depicted in Fig. 2, shows that the load was supplied by the PV generator, DG, and also from the grid. The battery system gets charged from the PV generator and can also discharged by meeting the required load whenever the other systems cannot meet the load requirement.

#### 3.1.3 Discussions

In case study 1, it was observed that buying from the grid was cheaper than any other sources. The system picked from the grid and left the DG, as compared to the case study 2 where the system picked from both the DG and PV generators. In case study 2, the battery only gets charged from the PV, because the PV only works within the hour ranges from 8 a.m.–6 p.m. due to weather conditions. The PV gets charged from the solar irradiation from the sun. Also, worthy of note is the power flow out of the battery ( $p_{fob}$ ); the battery only discharges on the hours when the PV is not discharging, which means that it was only kept on reserve to only dispatch power when the other sources could not meet up with the demand. The time of power

generated from the PV is within the range of 8 a.m.–6 p.m. because of the weather conditions, so the PV generator was only able to dispatch power within those ranges. The power generated from the grid ( $P_{grid}$ ) was only generated at the time when the PV generator was not able to meet the demand. Figures 3 and 4 show the hourly output power from  $p_{grid}_t$ ,  $p_{fib}_t$ ,  $p_{fob}_t$ , and  $y_{pv}_t$  for case 1 and case 2, respectively.

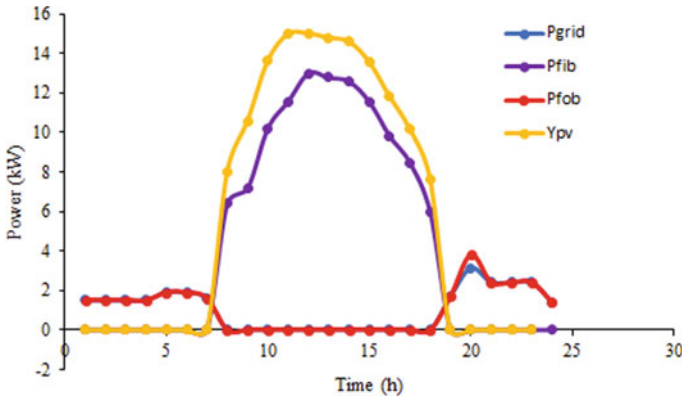


Fig. 3 Output power from  $P_{grid}$ ,  $P_{fib}$ ,  $P_{fob}$ , and  $Y_{pv}$

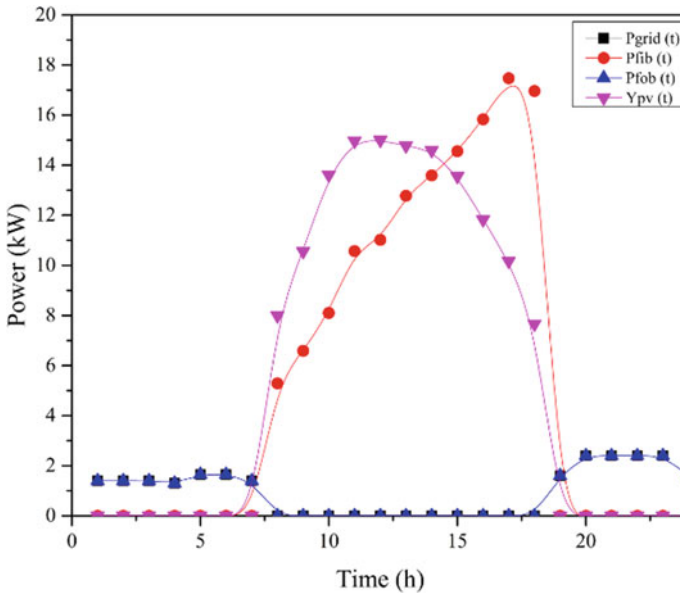


Fig. 4 Output power from  $P_{grid}$ ,  $P_{fib}$ ,  $P_{fob}$ , and  $Y_{pv}$

Figure 3 shows that the battery only gets to discharge when the PV is not able to meet the demand and also gets charged only when PV is able to supply the demand (between 8 a.m. and 6 p.m.).

## 4 Conclusions

A hybrid PV-battery grid-connected model was explored and investigated in this study to minimize the grid cost and the battery wear cost. Two cases were considered using the same data with different configuration settings. At the end of the analysis, it was observed that case study 2 gave the best solution of 5.40 as seen in Table 4 as compared to case study 1 with best solution of 6.40 shown in Table 3.

**Acknowledgements** The first author will like to thank the University Research Committee (URC) at the University of Johannesburg for the study scholarship award.

## References

1. Energy Overview. [Online]. Available: <http://www.worldbank.org/en/topic/energy/overview>. Accessed 09 May 2019
2. Twaha S, Ramli MAM (2018) A review of optimization approaches for hybrid distributed energy generation systems: off-grid and grid-connected systems. *Sustain Cities Soc* 41((May)):320–331
3. Hamed TA, Bressler L (2019) Energy security in Israel and Jordan: the role of renewable energy sources. *Renew Energy* 135:378–389
4. Gbadamosi SL, Nwulu NI, Sun Y (2018) Multi-objective optimisation for composite generation and transmission expansion planning considering offshore wind power and feed-in tariffs. *IET Renew Power Gener* 12(14):1687–1697
5. Nwulu NI, Agboola OP (2012) Modelling and predicting electricity consumption using artificial neural networks. In: 2012 11th international conference on environment and electrical engineering EEEIC 2012—conference proceedings, pp 1059–1063
6. Diesendorf M, Elliston B (2018) The feasibility of 100% renewable electricity systems: a response to critics. *Renew Sustain Energy Rev* 93(May):318–330
7. Jiang P, Yang H, Heng J (2019) A hybrid forecasting system based on fuzzy time series and multi-objective optimization for wind speed forecasting. *Appl Energy* 235(May 2018):786–801
8. Olorunfemi TR, Nwulu N (2018) Optimization applications in distributed energy resources : review and limitations. In: 2018 international conference on computational techniques, electronics and mechanical systems, pp 446–450
9. Ramli MAM, Bouchehara HREH, Alghamdi AS (2018) Optimal sizing of PV/wind/diesel hybrid microgrid system using multi-objective self-adaptive differential evolution algorithm. *Renew Energy* 121:400–411
10. Meena NK et al (2019) Optimal planning and operational management of open-market community microgrids. *Energy Procedia* 159:533–538
11. Jing Z, Luo Z (2018) An IGD-T model for capacity configuration optimization of island microgrid. *Energy Procedia* 158:2774–2779
12. Dulău LI, Bică D (2019) Optimization of generation cost in a microgrid considering load demand costing models capacity optimization in industry. *Procedia Manuf* 32:390–396

13. Tavakoli M, Shokridehaki F, Funsho M, Marzband M (2018) Electrical power and energy systems CVaR-based energy management scheme for optimal resilience and operational cost in commercial building microgrids. *Electr Power Energy Syst* 100(February):1–9
14. Hossain A, Roy H, Squartini S, Zaman F, Muttaqi KM (2019) Energy management of community microgrids considering degradation cost of battery. *J Energy Storage* 22(February):257–269
15. Hossain A, Roy H, Squartini S, Zaman F (2019) Energy scheduling of community microgrid with battery cost using particle swarm optimisation. *Appl. Energy* 254(August):113723
16. Nemati M, Braun M, Tenbohlen S (2018) Optimization of unit commitment and economic dispatch in microgrids based on genetic algorithm and mixed integer linear programming. *Appl Energy* 210:944–963
17. Kajela D, Manshahia MS (2017) Optimization of renewable energy systems : a review. *Int J Sci Res Sci Technol* 3(8):769–795
18. Zhao B, Guo L (2013) Operation optimization of standalone microgrids considering lifetime characteristics of battery energy storage system
19. Bindner H et al (2005) Lifetime modelling of lead acid batteries, vol 1515
20. Zhu B, Tazvinga H, Zhu B, Xia X (2015) Optimal power-ow management for distributed energy resources with batteries Optimal power flow management for distributed energy resources with batteries q. *Energy Convers Manag* 102(January):104–110
21. Sadati SMB, Moshtagh J, Shafie-khah M, Catalão JPS (2018) Smart distribution system operational scheduling considering electric vehicle parking lot and demand response programs. *Electr Power Syst Res* 160:404–418
22. Nwulu N (2017) Multi-objective optimization of a CHP-PV-battery islanded microgrid. In: 2017 international conference on energy, communication, data analytics and soft computing (ICECDS), pp 98–102
23. Nwulu NI, Fahrioglu M (2011) A neural network model for optimal demand management contract design. In: 2011 10th International conference on environment and electrical engineering. *EEEIC. EU 2011—Conference Proceedings*, pp 1–4
24. Fahrioglu M, Nwulu NI (2012) Investigating a ranking of loads in avoiding potential power system outages. *Electr Rev* (11):239–242

# A Review of Mathematical Optimization Applications in Renewable Energy-Powered Microgrids



Tope Roseline Olorunfemi and Nnamdi Nwulu

**Abstract** Renewable energy sources are being increasingly adopted because there is a need for alternative sources of power generation which are emission-free and environmentally friendly. These sources include solar energy, wind energy, marine energy, geothermal energy and battery storage systems. Mathematical optimization techniques have increasingly been deployed in sizing and scheduling renewable energy sources in microgrids. In this study, a systematic review of various energy sources, mathematical optimization techniques and applications of mathematical optimization techniques in renewable energy-powered microgrid is presented. It is observed from the review that mathematical optimization techniques have been used with great success in this domain. The review concludes with research gaps for future exploration.

## 1 Introduction

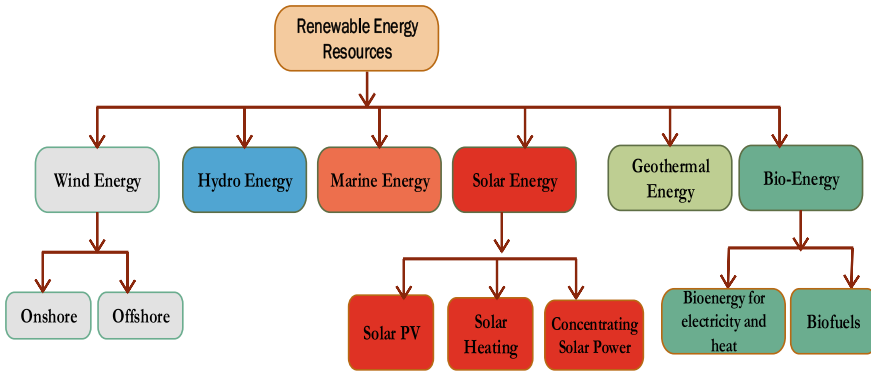
Renewable energy sources are abundant in nature and are not depletable which means they are continually available in abundance from nature. Renewable energy sources include wind energy, solar voltaic energy, hydro and geothermal energy and so on. Some of the resources are generated directly (photoelectric and photochemical) or indirectly (hydropower, tidal and wind) from the sun, water and other natural sources from the environment (geothermal and tidal) [1].

Figure 1 illustrates the summary of renewable energy resources.

The global outlook for renewable energy sources is at its peak, with many developed countries adopting and adjusting their energy policies to fit into renewable sources of energy generation. In 2017, a quarter of all the electricity generation globally was supplied from renewable resources. Also, findings reveal that renewable sources can deliver two-thirds of the world's energy demand, which is part of the progress to the greenhouse gas emission reduction that is needed between now and

---

T. R. Olorunfemi (✉) · N. Nwulu  
Department of Electrical and Electronic Engineering Science, University of Johannesburg,  
Johannesburg, South Africa  
e-mail: [topyrose6@gmail.com](mailto:topyrose6@gmail.com)



**Fig. 1** Renewable energy sources

2050, to reduce the average global warming temperature below 2 °C [2]. Aside from the wind, which is the most prominent and fast-growing renewable energy source, is the solar energy, which is environmentally friendly with no pollution, has low maintenance and running fee, unlimited in nature and has long-life time expectancy. In addition to these, countries are also increasingly deploying demand-side management tools all in a bid to control and manage electricity consumption [3–5].

The next section gives a brief description of some of the renewable energy sources.

### **1.1 Wind Energy**

Wind energy is generated by converting the flow of wind across the earth’s surface into electrical energy. It is one type of promising sources of renewable energy, because it is vast, clean, readily available and economically viable. The global outlook for a cumulative capacity of wind installed is approximately 486,749 MW as of 2017 [6]. Most of the developed countries are embracing the use of wind energy at its optimum level. An example of such is India’s high integration in renewable sources, especially to their rural area. According to statistics, more than two-thirds of their electricity generation comes from renewables and over 50% has been projected to come from renewables in 10 years to come [7].

### **1.2 Battery Energy System**

Battery energy systems have been widely deployed as a complement to other renewable energy resources. This is one of the major advantages of battery energy systems. The stochastic nature of PV and wind is the major drawback in their integration. Therefore, the hybridization of battery with other renewable energy sources (RES)

will be able to overcome the above problem in such a way that whenever the wind and PV are operating on a full-time basis, after meeting the required load, the excess energy is stored in the battery, and when they are affected by the atmospheric conditions, the stored energy is dispatched to meet the required demand. Considering the rate, at which wind and solar energy are accelerating in Africa, battery storage systems will be the solution to help accomplish the full potential in achieving the sustainable energy resources. Because of the intermittent nature of the wind and solar energies, battery storage systems can help overcome this problem of their nature by storing energy when the system is up and releasing it for use when the system is not capable of generating electricity. But the technology is still expensive, which brought together almost 200 participants from over the globe including private and public sectors at the World Bank Group Event “Batteries, Energy Storage & the Renewable Future” held at Cape Town, South Africa, in February this year to find a way out to the high cost. The total energy demand worldwide for battery storage systems is projected to reach 2300 GWh by 2030 [8]. Additionally, the grid system globally will need almost ten times more than the present projected energy storage system and 22,000 GWh will be needed by 2050 to deploy more solar and wind energy in the power system grid. To this end, the World Bank Group has taken the initiative to invest \$1 billion into battery storage systems also, raising \$4 billion extra from both private and public institutions with the aim of attaining 17.5 GWh of battery storage systems by 2050, which will triple the present capacity installed in developed countries (4.5 GWh). However, the World Bank Group is in partnership with the African Development Bank (ADB) and Clean Technology Fund (CTF) to support a significant battery storage system deployment in South Africa [8].

### ***1.3 Solar Photovoltaic (PV) System***

The technology of PV systems is seriously gaining grounds and is highly desired. More research is beginning to emerge in the area of the technology for its improvement and advancement. Photovoltaic technology converts sunlight directly into electrical energy with the use of semiconductors. Many countries have taken part in the deployment of PV, and it keeps growing and working for them. Such countries are China, USA and Indian who are currently the top three leading countries in the deployment of RES technologies [9]. “In 2017, cumulative solar PV capacity reached almost 398 GW and generated over 460 (TWh), representing around 2% of global power output. Utility-scale projects account for just over 60% of total PV installed capacity, with the rest in distributed applications (residential, commercial and off-grid). Over the next five years, solar PV is expected to lead renewable electricity capacity growth, expanding by almost 580 GW under the Renewables 2018 main case” [10].

Figure 2 shows the real and forecast PV generation capacity for the year 2017–2023.



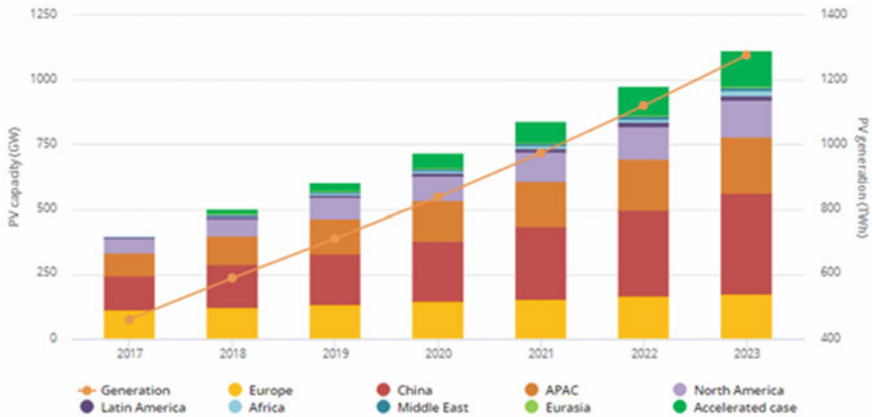


Fig. 2 Chart of solar PV generation and collective capacity, 2017–2023 [36]

## 2 Overview of Optimization Techniques in the Microgrid Integrating Renewables

Resources are always limited even in the real world that is why optimization of the available resource is very important. Therefore, optimization is a significant scientific and engineering research area that can be applied to every facet of life to give better results [11].

Optimization can be defined as finding the best way to perform an operation to give an optimal result or near-optimum result, whereas an optimization technique is finding a way to give the best solution from all feasible solutions to the optimization problem [12]. It can be either to minimize or to maximize a certain function depending on the objective or the number of the assessment criteria. Also, it could either be one objective function formulation termed as a single-objective function which gives the optimal solution for such objective, or be more than one objective function termed as multi-objective function problem formulation [13–15]. Single-objective type of optimization formulation has clear definitions of the objectives and straightforward result tactics, and gives a clear, single best optimum result. But this could weaken the model when other parameters tend to be neglected. Therefore, to overcome this problem, a multi-objective formulation type of optimization is encouraged, which takes into account several objectives to attain values for a set of solutions that represent the best trade-offs between the objectives, although it will be more challenging as there will be conflict among several objective functions [16].

However, several optimization techniques are presently being used, but generally there are two broad classifications of optimization techniques: meta-heuristics optimization techniques and mathematical programming optimization techniques. Figure 3 shows the classifications of optimization techniques.

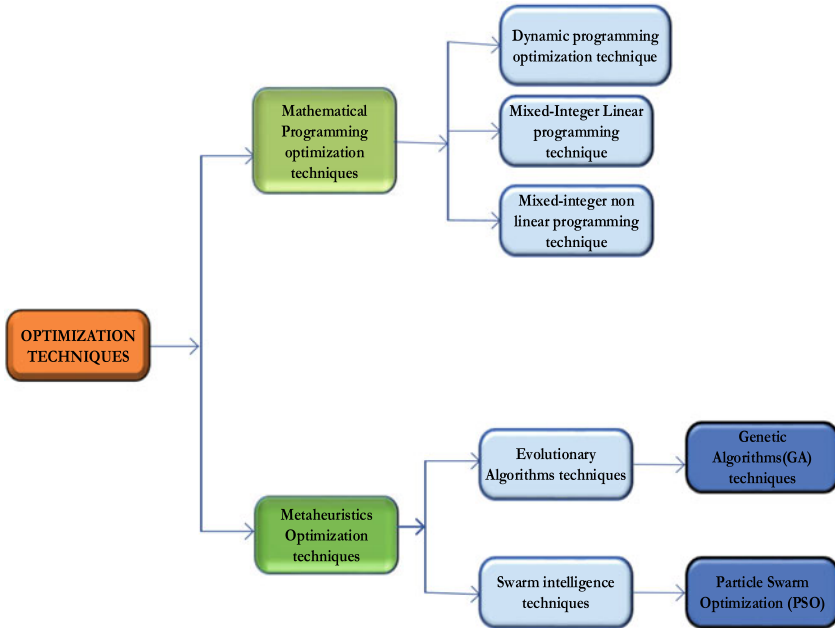


Fig. 3 Classification of optimization techniques

### 2.1 Mathematical Programming Optimization Technique

The mathematical programming optimization technique, otherwise known as deterministic technique, makes use of some particular types of mathematical approaches just as the name implies, such as simplex method, steepest decent, quasi-Newton and Newton. This has the capability of getting the accurate optimum solution when applied to simple problem types such as convex and linear [17], whereas the reverse is the case for meta-heuristics techniques, which gives approximate solutions and is not always accurate; therefore, users should take note of the accuracy of their result when using the technique. Notwithstanding, meta-heuristics still have their own advantages, and solutions can be easily achieved with the low computational load when compared with mathematical programming. Meta-heuristic means “high level to find optimal solution iteratively by trial and error method” [18]. Examples of meta-heuristics include, but not limited to, genetic algorithm optimization and particle swarm optimization.

Figure 3 gives the classification of optimization techniques.

### 2.1.1 Dynamic Programming Optimization Technique

Dynamic programming is one of the optimization methods which is classified under mathematical programming optimization methods. Examples of such include: mixed-integer linear programming (MILP) and mixed-integer nonlinear programming (MINLP). Bellman was the first man to develop dynamic programming in the 1950s with the aim of solving complicated problems by dividing the problems into subproblems which pacts with a fewer number of variables. It is computationally fast and efficient when considering large variables compared to smaller variable problems [19]. Dynamic programming has recently gained grounds from scholars, especially in the area of energy management systems. It is an optimization method that is capable of solving both linear and nonlinear problems with some objectives and constraints to attain the global optimum result, and it is mostly deployed to solve optimal control problems [20].

### 2.1.2 Mixed-Integer Linear Programming

Generally, a mixed-integer linear program can be defined as:

$$\begin{aligned} \text{Min } Z &= C^T X \\ \text{Subject to: } Ax &\geq b \quad j \in C \end{aligned}$$

$$X_j \in \{0, 1\} \quad j \in B$$

$$X_j \in Z \geq 0 \quad j \in 1 \text{ where}$$

$X$  is a vector of decision variables,  $C$  is a vector of objective constants,  $A$  is an  $m \times n$  matrix and  $b$  is a vector of right-hand constant. The set of binary variables is divided into two stages, i.e., set of general integer variables and set of continuous variables. Therefore, when the set of integer variables is empty, it is generally referred to as a 0-1 mixed-integer program [21]. Mixed-integer linear programming problems are stochastic in nature, which have a decomposable structure that can be deployed to design an effective optimization method [22].

### 2.1.3 Mixed-Integer Nonlinear Programming

Mixed-integer nonlinear programming belongs to a class of mathematical programming techniques in which problems are difficult to solve because of their nonlinear nature. They are comprised of nonlinear constraints, nonlinear objective functions and binary decision variables. Though they still cover a wide range of problems in which they can provide solutions, they are intricately difficult in nature, which has put a limitation on their use but they are still capable of efficiently tackling problems to give optimum results [23]. Resulting from the stated issues associated with

the MINLP, there are two major categories that have explored in the literature to tackle the nonlinear nature: (i) the model that solves the exact nonlinear continuous relaxation and (ii) the polyhedral approximations that are used to find approximate solutions to the continuous relaxations. Few solvers used in these approaches include the AIMMS outer approximation (AOA) algorithms in AIMMS and Bonmin [24].

## 2.2 *Meta-Heuristic Optimization Techniques*

By definition, “meta” means “high level” and “heuristics” means to “find by trial and error” to iteratively find an optimal solution. Meta-heuristic optimization techniques are fast developing algorithms which are heuristics in nature. They use heuristics for solving a whole range of optimization problems without having prior knowledge about the basis of the problem [25]. One of the advantages of them is that some solutions can be easily achieved with low computational time when compared with mathematical programming. Nevertheless, meta-heuristics get approximate solutions and not exactly like mathematical programming. Generally, meta-heuristic optimization techniques comprise two algorithms, which are evolutionary algorithm (EA) and swarm intelligence algorithm (SIA). A lot of hybrid algorithms are formed under the umbrella of these two, which combine the major features of the optimization algorithms such as evolutionary operators, methods for representing individual, methods for choosing population size and so on. Examples of meta-heuristic algorithms include genetic algorithm (GA), particle swarm optimization (PSO), Simulated Annealing (SA) [26] and so on.

### 2.2.1 **Evolutionary Algorithm (EA)**

Evolutionary algorithms are enlisted among the well-known and effective techniques to solve complex and non-convex optimization problems applied to various research areas. EAs imitate evolutionary perception. Evolutionary grounded approaches start with a random population and then assess the original population-based one or more features such as selection, crossover and mutation during the optimization procedure. It is worth knowing that these techniques do not take into account previous information about the population before executing and finding the best out of the search space. The general framework assumed by EA is (1) evaluating solutions, (2) selecting solutions and (3) creating new solutions [27].

Genetic algorithms can be categorized under the evolutionary algorithms. They are also renowned algorithms deployed by various optimization problems in the literature [28]. GA is based on the theory of Darwin for evolution, which uses some features of evolution to evaluate the initial population generated randomly, such as selection, crossover and mutation. It quests the solution space of the problem by performing searches stochastically. The composition comprises the population (set) and genes (structures); individual genes represent a solution to the problem. The

fitness function is used to verify the suitability of the set of the genes suitable for the problem. According to the fitness of individual genes, a new set (population) that inherits the best characteristics of their ancestors is obtained. Therefore, the new obtained population set is the outcome of several changes guided by the genetic operators such as the selection, crossover and mutation. Several iterative procedures will be repeated with a predefined number of iterations until a stop criterion is reached [29]. Other types of popular algorithms in this category include differential evolution (DE) and evolutionary programming (EP) [30].

### **2.2.2 Swarm Intelligence Algorithm (SIA)**

Swarm intelligence algorithms are derived from concepts based on the behavior of animals. There are many new and interesting algorithms now in the literature that have been developed based on the behaviors of animals. These have been used and deployed appropriately to solve complex optimization problems. Example of such algorithms includes particle swarm optimization (PSO), artificial bee colony, which is derived from fish conduct, ant colony optimization (ACO) which is also based on ant behaviors from finding the shortest route from the nest to the food and so on [31].

### **2.2.3 Particle Swarm Optimization (PSO)**

Kennedy and Eberhart proposed PSO algorithm in 1995 [32], based on the behavior, understanding and simulation of both the movement of individual bird herds or fish schools and their mutual behavior as a swarm. PSO has a general characteristic which is its simplicity; this is based on the fact that it takes just a few lines of computer codes coupled with simple mathematical operations to deploy the basis of PSO. As the name implies particle swarm optimizations, they exploit the swarm intelligence by simulating the communal interaction of the particles to find the optimum place in the search space [33]. It has demonstrated an effective performance on many optimization problems. It is easy to implement and gives good results. In each iteration, the particles travel round in a multidimensional design space conferring to its prior best location and best location of all other members; each particle varies its searching path toward attaining or approaching the optimum result [34].

## **3 Hybrid Renewable Energy System (HRES)**

Hybrid renewable energy systems can be defined as the combination of two or more forms of renewable energy sources (wind, solar PV, batteries and hydro) for energy generation. HRES can deliver host of benefits compared with single-source systems. These energy systems are perfect solutions since they can offer significant improvements in performance and cost saving which can be tailored to various end-user

requirements. There are several types of hybrid renewable energy systems. These include wind–solar hybrid system, solar–diesel hybrid system, wind–hydro hybrid system and wind–diesel hybrid system. HRES supports a substantial amount of reduction of CO<sub>2</sub> emissions, and it is used for a greater penetration of renewable energy sources, whose performance and reliability depend heavily on the interaction between demand, generation, storage and the energy management strategy as a whole [35]. The choice of sources for the hybrid systems depends on several considerations, but basically it depends on the availability of natural resources and the cost involved, and the types of end-users.

## 4 Conclusions

This study has undergone a comprehensive literature survey of renewable energies and how they can be deployed in the modern-day power system (microgrid) using mathematical optimization techniques. From the findings, it can be said that the evolutionary algorithms still give the best result to optimization, i.e., give near optimum as compared to other optimization methods. This suggests that researchers should concentrate their efforts in developing novel evolutionary optimization methods for sizing and scheduling practical renewable energy-powered microgrids.

**Acknowledgements** The first author would like to thank the University Research Committee (URC) at the University of Johannesburg for the Study Scholarship Award.

## References

1. Ellabban O, Abu-Rub H, Blaabjerg F (2014) Renewable energy resources: current status, future prospects and their enabling technology. *Renew Sustain Energy Rev* 39:748–764
2. Gielen D, Boshell F, Saygin D, Bazilian MD, Wagner N, Gorini R (2019) The role of renewable energy in the global energy transformation. *Energy Strateg Rev* 24((January)):38–50
3. Nwulu NI, Agboola PO (2012) Modelling & predicting electricity consumption using artificial neural networks. In: Proceedings of the 11th international conference on environmental & electrical engineering (EEEIC2012), Venice, Italy, 18–25 May 2012
4. Nwulu NI, Fahrioglu M (2011) A neural network model for optimal demand management contract design. In: Proceedings of the 10th international conference on environmental & electrical engineering (EEEIC2011), Rome, Italy, 8–11 May 2011
5. Fahrioglu M, Nwulu NI (2012) Investigating a ranking of loads in avoiding potential power system outages. *J Electr Rev (Przegląd Elektrotechniczny)* Warsaw, Poland 88(11a):239–242
6. Wang J, Du P, Niu T, Yang W (2017) A novel hybrid system based on a new proposed algorithm—Multi-Objective Whale Optimization Algorithm for wind speed forecasting. *Appl Energy* 208((September)):344–360
7. Gärtner J, Flath CM, Weinhardt C (2018) Portfolio and contract design for demand response resources. *Eur J Oper Res* 266:340–353

8. Batteries Can Help Renewables Reach Full Potential in Africa. [Online]. Available: <https://www.worldbank.org/en/news/feature/2019/02/28/batteries-can-help-renewables-reach-full-potential-in-africa>. Accessed: 09 May 2019
9. Jani V, Abdi H (2018) Optimal allocation of energy storage systems considering wind power uncertainty. *J. Energy Storage* 20((September)):244–253
10. Hales D (2018) Renewables 2018 global status report
11. Shadravan S, Naji HR, Bardsiri VK (2019) Engineering applications of artificial intelligence the sailfish optimizer : a novel nature-inspired metaheuristic algorithm for solving constrained engineering optimization problems. *Engineering Applications of Artificial Intelligence*, vol 80, July 2018, pp 20–34
12. Schmidt M, Schöbel A, Thom L (2019) Min-ordering and max-ordering scalarization methods for multi-objective robust optimization. *Eur J Oper Res* 275(2):446–459
13. Zapotecas-martínez S, García-nájera A, López-jaimés A (2019) Multi-objective grey wolf optimizer based on decomposition. *Expert Syst Appl* 120:357–371
14. Gbadamosi S, Nwulu NI, Sun Y (2018) Multi-objective optimization for composite generation and transmission expansion planning considering offshore wind power and feed in tariffs. *IET Renew Power Gener* 12(14):1687–1697
15. Damisa U, Nwulu NI, Sun Y (2018) Microgrid energy and reserve management incorporating prosumer behind-the-meter resources. *IET Renew Power Gener* 12(8):910–919
16. Pintari ZN, Kravanja Z (2015) The importance of proper economic criteria and process modeling for single- and multi-objective optimizations. *Comput Chem Eng* 83:35–47
17. Twaha S, Ramli MAM (2018) A review of optimization approaches for hybrid distributed energy generation systems: off-grid and grid-connected systems. *Sustain Cities Soc* 41(May):320–331
18. Ooka R, Ikeda S (2015) A review on optimization techniques for active thermal energy storage control. *Energy Build* 106:225–233
19. Kheiri F (2018) A review on optimization methods applied in energy-efficient building geometry and envelope design. *Renew Sustain Energy Rev* 92(May 2017):897–920
20. Bahlwan H, Morini M, Pinelli M, Ruggero P (2019) Dynamic programming based methodology for the optimization of the sizing and operation of hybrid energy plants. *Appl Therm Eng* 160(December 2018):113967
21. Guastaroba G, Savelsbergh M, Speranza MG (2017) Adaptive kernel search: a heuristic for solving mixed integer linear programs. *Eur J Oper Res* 263(3):789–804
22. Ogbe E, Li X (2018) Extended cross decomposition for mixed-integer linear programs with strong and weak linking constraints. *Comput Chem Eng* 119:237–257
23. Arcuri P, Beraldi P, Florio G, Fragiaco P (2015) Optimal design of a small size trigeneration plant in civil users: a MINLP (Mixed Integer Non Linear Programming Model). *Energy* 80:628–641
24. Vinel A, Krokhmal PA (2017) Discrete optimization mixed integer programming with a class of nonlinear convex constraints. *Discret Optim* 24:66–86
25. Seliverstov EY, Karpenko AP (2019) ScienceDirect hierarchical model of parallel metaheuristic optimization hierarchical model of parallel metaheuristic optimization algorithms. *Procedia Comput Sci* 150:441–449
26. Han F, Jiang J, Ling Q, Su B (2019) Neurocomputing a survey on metaheuristic optimization for random single-hidden layer feedforward neural network. *Neurocomputing* 335:261–273
27. Du W, Zhang M, Ying W, Perc M, Tang K (2018) The networked evolutionary algorithm: a network science perspective. *Appl Math Comput* 338:33–43
28. Salza P, Ferrucci F (2019) Speed up genetic algorithms in the cloud using software containers. *Futur Gener Comput Syst* 92:276–289
29. Diego-mas JA, Garzon-leal D, Poveda-bautista R, Alcaide-marzal J (2019) User-interfaces layout optimization using eye-tracking, mouse movements and genetic algorithms. *Appl Ergon* 78(March):197–209
30. Zhi H, Liu S (2019) Face recognition based on genetic algorithm. *J Vis Commun Image Represent* 58:495–502

31. Yapici H, Cetinkaya N (2019) A new meta-heuristic optimizer: Pathfinder algorithm. *Appl Soft Comput J* 78:545–568
32. Abadlia H, Abadlia H, Smairi N, Ghedira K (2018) ScienceDirect a hybrid Immigrants schema for particle swarm optimization algorithm a hybrid immigrants schema for particle swarm optimization. *Procedia Comput Sci* 126:105–115
33. Sedlaczek K, Eberhard P (2006) Using augmented Lagrangian particle swarm optimization for constrained problems in engineering. *Struct Multidisc Optim* 277–286
34. Li X, Wang H, Li G (2018) Reanalysis assisted metaheuristic optimization for free vibration problems of composite laminates. *Compos Struct* 206(July):380–391
35. Bartolucci L, Cordiner S, Mulone V, Rossi JL (2019) Electrical power and energy systems hybrid renewable energy systems for household ancillary services. *Electr Power Energy Syst* 107(August 2018):282–297
36. Olorunfemi TR, Nwulu N (2018) Optimization applications in distributed energy resources : review and limitations. In: 2018 international conference on computational techniques, electronics and mechanical systems, pp 446–450



# Optimal Grid-Connected Microgrid Scheduling Incorporating an Incentive-Based Demand Response Program



Tope Roseline Olorunfemi and Nnamdi Nwulu

**Abstract** This study investigates the optimal scheduling of a grid-connected microgrid incorporating an incentive-based demand response program (IBDRP) at the customer side to reduce electricity consumption. A mixture of renewable and non-renewable energy sources was deployed in the microgrid. This comprises wind energy, solar energy and power generating units (PGUs). A multi-objective model was formulated which seeks to simultaneously minimize the annual cost of electricity production, minimize the carbon dioxide emission and maximize the customers' participation in the IBDRP, to increase the customer benefit that comes with the program. The Advanced Interactive Multidimensional Modeling System (AIMMS) software was used to solve the formulated multi-objective optimization model. The simulation results obtained show the applicability of the model.

## 1 Introduction

Over the time electricity has become one of the greatest vital forms of amenities to man. However, modeling and planning of quantity of electricity consumed have been a major concern to both researchers and industry [1]. The balancing between the power generation and consumption is crucial for the smooth running of the power grids. Any disparity between power supply and demand would increase costs to both the load serving entity and consumers which may damage the entire grid. Thus, the electricity industry is undergoing a time of speedy and unprecedented transformation in the deployment of renewable energy generation technologies. Since 2012, renewable sources have generated more than half of the new energy generation capacity worldwide. In 2016, total renewable energy generation that was accounted for exceeded 2000 GW, doubling the quantity in the space of nine years [2].

---

T. R. Olorunfemi (✉) · N. Nwulu  
Department of Electrical and Electronic Engineering Science, University of Johannesburg,  
Johannesburg, South Africa  
e-mail: [toppyrose6@gmail.com](mailto:toppyrose6@gmail.com)

Today's microgrids consist of a combination of renewable and non-renewable sources of power generation to meet the ever-growing electricity demand. To this end, microgrids comprise small distributed energy resources (DER) located close to the consumers. This comes with advantages such as the ability to operate in either the grid-connected or island mode of operation to enhance the supply reliability. Additionally, it also improves the network performance resulting in loss reduction, voltage control and reduced congestion. Demand response (DR) is a useful tool in the electricity market. They are activities on the consumers' side, which helps to reduce the customer's electricity usage while maintaining the efficiency and reliability of the grid. They are usually divided into two broad groups: incentive-based demand response program (IBDRP) and price-based demand response program (PBDRP). The first type is typically formulated as a contractual agreement with consumers, where they get incentives in monetary value when they cut down their electricity usage, while the latter depends solely on the dynamic electricity price, which can be either peak or off-peak. Prices tend to be higher at peak periods to encourage energy curtailing and low at off-peak hours [3]. Over the years, there have been many researches in the area of dispatching and deployment of DER in the microgrids incorporating DR to curtail electricity at the customer's side [4]. Reference [5] worked on day-ahead scheduling for commercial buildings combining time of use (ToU) and demand pricing (DP) to plan the demand response program (DRP) with the goal of minimizing monthly electricity charge, while Asadinejad and Tomsovic [6] proposed a model deploying both ToU and IBDRP plans based on the demand price elasticity to design an optimal structure for achieving cost reduction and maximizing customer acceptance level of the DRP. Also, the work done in [7] modeled the responsive load behavioral model with linear and nonlinear modeling for the IBDR and PBDR programs. In [8], optimization of a home-based energy management controller integrating various categories of loads which could be curtailable, deferrable and non-deferrable appliances and sought to simultaneously minimize customer's electricity bill and the day-to-day capacity of energy curtailed. The contributions of this paper include:

1. Investigate an incentive demand response program with renewables to minimize annual cost and maximize the profit of customer participation.
2. Evaluate the impact of an IBDRP on the operational schedule of the microgrid and by extension on the cost metrics.

The rest of the paper is organized as follows: Sect. 2 presents the system modeling and formulations, Sect. 3 details the verified results, and Sect. 4 gives the conclusion and future works.

## 2 Methods

### 2.1 Microgrid Model

The sources of power deployed in a microgrid consist of both renewable and non-renewable sources, which comprises: 1 PV, 1 wind, 3 PGUs, a grid connection and 10 willing customers. The objective function is to minimize the annual cost of electricity production and carbon dioxide emission. The mathematical formulation is presented as follows:

$$\sum_{t=1}^N (c_{\text{fuel}} + c_{\text{grid}} - c_{\text{sub}}) \quad (1)$$

Subject to the following constraints:

$$yp_{it} \leq yp_{\text{max}_i} \quad (2)$$

$$yp_{i,t} + E_{\text{grid}t} + yw_t + ypv_t = \text{load}_t \quad (3)$$

$$ypv_t \leq sr_t \quad (4)$$

$$yw_t \leq w_t \quad (5)$$

where

$$c_{\text{fuel}} = \sum_{t=1}^T \sum_{i=1}^I ccng \times fng_{i,t} \times P \quad (6)$$

$$c_{\text{grid}} = \sum_{t=1}^T cc_{\text{grid}t} \times E_{\text{grid}t} \times P \quad (7)$$

$$c_{\text{sub}} = \sum_{t=1}^T cc_{\text{sub}} \times ypv_t \times P \quad (8)$$

The following is a brief description of the constraints:

Equation (2): The PGU's output ( $i$ ) at time ( $t$ ) must be less or equal to the maximum capacity of the PGU.

Equation (3): This constraint is referred to as the energy balance constraint, which means the output from the PGUs ( $yp_{i,t}$ ), the energy from the grid ( $E_{grid,t}$ ), output from the wind ( $yw_t$ ) and output from PV ( $ypv_t$ ) must be equal to the total load.

Equation (4): The PV output at time ( $t$ ) must be less or equal to the forecast solar power at time ( $t$ ).

Equation (5): The wind output at time ( $t$ ) must be less or equal to the forecast wind power at time ( $t$ ).

## 2.2 The Incentive-Based Demand Response Model

The aim of demand-side management program, which demand response falls under, is to regulate the demand for electricity amongst consumers by reducing load and improving system reliability. Clearly, demand response contract formulations give incentives to customers who were willing to engage in the load disruption with payments [9]. The demand response model in the study involved ten customers who are ready to participate in the contract and willing to declare the amount of load they want to reduce in return for incentive.

The mathematical formulation seeks to maximize the total customer benefit and is presented below:

$$\sum_{t \in T} EP_t (LRQ_{jt} \times CPART_{jt}) - (LRIC_{jt} + PLR_{jt} \times LQR_{jt} \times CPART_{jt}) \quad (9)$$

Subject to the following constraint:

$$LQR_{j,t} \times CPART_{j,t} \geq CCL \quad (10)$$

where

$$LRQ_{j,t} = \text{quantity of load reduction at each customer } (j) \text{ at time } (t). \quad (11)$$

$$LRIC_{j,t} = \text{load reduction initialization cost for each customer } (j) \text{ at time } (t). \quad (12)$$

$$CPART_{j,t} = \text{a binary variable indicator maybe customer participates or not.} \quad (13)$$

$$PLR_{j,t} = \text{a variable that determines the price of the load reduction by customers.} \quad (14)$$

$$EP_t = \text{energy price at time } (t). \quad (15)$$

The following is a brief description of the constraint:

Equation (10): The quantity of load reduction of a customer ( $j$ ) in time ( $t$ ) multiplied by the customer participation ( $j$ ) at time ( $t$ ) must be greater or equal to critical load.

### 2.3 Combined Mathematical Model

The combined mathematical model consists of mathematical models representing both the microgrid and the incentive-based demand response program. The multi-objective function and its constraints are given below:

$$w1 \sum_{t=1}^N (c_{\text{fuel}} + c_{\text{grid}} - c_{\text{sub}}) - w2 \sum_{t \in T} EP_t (\text{LRQ}_{jt} \times \text{CPART}_{jt}) - (\text{LRIC}_{jt} + \text{PLR}_{jt} \times \text{LQR}_{jt} \times \text{CPART}_{jt}) \quad (16)$$

Subject to the following constraints:

$$yp_{it} \leq yp_{\max_i} \quad (17)$$

$$yp_{i,t} + E_{\text{grid}_t} + yw_t + ypv_t = \text{load}_t \quad (18)$$

$$ypv_t \leq sr_t \quad (19)$$

$$yw_t \leq w_t \quad (20)$$

$$\text{LQR}_{j,t} \times \text{CPART}_{j,t} \geq \text{CCL} \quad (21)$$

$$w1 + w2 = 1 \quad (22)$$

## 3 Numerical Simulations, Results and Discussion

To verify the developed model in Eqs. (16)–(22), we use a case study of 1 PV, 1 wind, 3 PGUs and 10 willing customers. The Advanced Interactive Multidimensional Modeling System (AIMMS) software [10, 11] was used to build and solve the multi-objective mathematical model using outer approximation algorithm (OAA) [12]. The data used in this work is gotten from a site from Harare in Zimbabwe [13]. The variables to be determined are as follows.

**Table 1** Load curtailed and incentives

Customer number and hour of curtailment	Amount of load curtailed (kW)	Incentive (\$)
1 at hour 12	10	5
3 at hour 9	30	15
5 at hour 20	15	7.5
8 at hour 4	32	16
10 at hour 8	40	20
Total	127	63.5

$ypv_t$ —the hourly output of PV generator at time  $t$ ,  $yp_{i,t}$ —hourly output of the power generating units ( $i$ ) in time ( $t$ ),  $E_{grid,t}$ —energy bought from the grid at time  $t$ ,  $yw_t$ —hourly output of wind generator at time  $t$ ,  $CPART_{j,t}$ —the variable indicator that shows the customer participation in the demand and response contract and  $PLR_{j,t}$ —the determined price of the quantity of energy reduced by the customers.

Table 1 shows the customer load curtailed and corresponding incentive, while Table 2 presents the hourly output from the various microgrid sources.

From Table 1, it is clear that the higher the quantity of load reduced the higher the customer incentive. For example, customer 1 was willing to reduce 10 kW at hour 12, which gives payment of \$5, as against customer 10 who was willing to reduce 40 kW at hour 8 whose payment will be \$20, thus higher than the payment of customer 1.

From Table 2, it can be observed that the output from the PV only starts generating from 8 a.m. to 6 p.m. due to the weather conditions. The output from wind dispatches as appropriate without any form of hindrances, while the three PGUs also dispatch effectively.

## 4 Conclusions

This work investigates the energy management of a microgrid incorporating the incentive-based demand response program. A multi-objective optimization model is proposed to determine the annual cost of electricity production, which minimizes the carbon dioxide emission and maximizes the customers’ participation in the program. The Advanced Interactive Multidimensional Modeling System (AIMMS) software was used to solve the proposed model. Furthermore, obtained results show that incorporating demand response program could be helpful at both the supply and demand sides of the microgrid. Also, it was observed that the customers’ participation in the program was maximized which is one of the objective functions of the model.

**Table 2** Hourly output of the generating units

Time ( <i>t</i> )	PV	Wind	Grid	PGU		
				Diesel generator	Gas engine	Gas turbine
1		7.56	10	0.11	14.15	
2		7.5	10	4.68	9.21	
3		8.25	10	9.45	3.46	
4		8.48	11.17	11.52		
5		8.48	12.1	11.52		
6		9.42	12.97	10.58		
7		9.82	10	10.18		
8	7.99	10.35	10		5.76	
9	10.56	10.88	10		6.09	
10	13.61	11.01	10		3.71	
11	14.78	10.98	10		4.27	
12	14.59	10.68	10		5.9	
13	13.56	10.42	10		5.69	
14	14.59	10.15	14.1		6.96	
15	13.56	9.67	10		4.74	
16	11.83	8.98	10	10.86		
17	10.17	8.33	10	10.53		1.66
18	7.66	7.61	10	11.99		2.80
19		6.7	10	6.910		1.50
20		5.72	10	4.680		1.59
21		7.25	10	2.380		1.40
22		7.75	10	11.08		3.96
23		7.88	12.5	12.21		
24		7.69	24.31	12.31		

**Acknowledgements** The first author would like to thank the University Research Committee (URC) at the University of Johannesburg for the Study Scholarship Award.

**References**

1. Nwulu NI, Agboola OP (2012) Modelling and predicting electricity consumption using artificial neural networks. In: 2012 11th International conference on environment and electrical engineering EEEIC—conference proceedings 2012, pp 1059–1063
2. IRENA (2018) Renewable power generation costs in 2017
3. Sadati SMB, Moshtagh J, Shafie-khah M, Catalão JPS (2018) Smart distribution system operational scheduling considering electric vehicle parking lot and demand response programs. Electr Power Syst Res 160:404–418

4. Fahrioglu M, Nwulu NI (2012) Investigating a ranking of loads in avoiding potential power system outages. *J Electr Rev (Przegląd Elektrotechniczny)*, Warsaw, Poland 88(11a):239–242
5. Zhu K, Lu N, Zheng J, Sun G, Mei F (2019) Optimal day-ahead scheduling for commercial building-level consumers under TOU and demand pricing plan. *Electr Power Syst Res* 173(August 2018):240–250
6. Asadinejad A, Tomsovic K (2017) Optimal use of incentive and price based demand response to reduce costs and price volatility. *Electr Power Syst Res* 144:215–223
7. Rahmani-Andebili M (2016) Modeling nonlinear incentive-based and price-based demand response programs and implementing on real power markets. *Electr Power Syst Res* 132:115–124
8. Soares A, Gomes Á, Antunes CH (2014) Categorization of residential electricity consumption as a basis for the assessment of the impacts of demand response actions. *Renew Sustain Energy Rev* 30
9. Nwulu NI, Fahrioglu M (2011) A neural network model for optimal demand management contract design. In: 2011 10th International conference on environment and electrical engineering IEEEIC.EU 2011—conference proceedings, pp 1–4
10. Gbadamosi S, Nwulu NI, Sun Y (2018) Multi-objective optimization for composite generation and transmission expansion planning considering offshore wind power and feed in tariffs. *IET Renew Power Gener* 12(14):1687–1697
11. Damisa U, Nwulu NI, Sun Y (2018) Microgrid energy and reserve management incorporating prosumer behind-the-meter resources. *IET Renew Power Gener* 12(8):910–919
12. Kronqvist J, Bernal DE, Lundell A, Grossmann IE (2018) A review and comparison of solvers for convex MINLP, no. 0123456789. Springer, US
13. Nwulu NI, Xia X (2017) Optimal dispatch for a microgrid incorporating renewables and demand response. *Renew Energy* 101:16–28



# Free-End Damage Detection in Cantilever Steel Plate Using Wavelet Transform Method



Muyideen Abdulkareem and Norhisham Bakhary

**Abstract** Cantilever plates are widely applied in engineering structures. Monitoring these structures is extensive due to the uniqueness of the support system. However, identification of damage at the free-end has not been given adequate attention. In this study, a continuous wavelet transform (CWT) damage identification method is presented for cantilever plate. The WT method involves analysing mode shape difference of the plate with WT. This method analyses the difference between the intact and damaged mode shapes of the cantilever plate, and the damage is localized in the decomposed signal. Through this method, the problem of free-end damage detection is resolved. A numerical model of a cantilever plate with different levels of damage severity at different locations is applied to validate this method. The results indicate the proposed method is capable of detecting damage at the free-end as well as damage at other parts of the cantilever plate. In addition, a sensitivity study on noise effect is provided.

**Keywords** Cantilever plate · Damage detection · Free-end damage · Mode shape difference · Wavelet transform

## 1 Introduction

Cantilever plates are structures commonly used in engineering applications. They are typically used in mechanical and aerospace engineering to model helicopter rotor blades and aircraft wings, and in micro-electromechanical systems. The civil engineering application of these structures can be seen in bridges, building balconies, and gas stations. The rise in ageing, loading, and extreme environmental conditions has promoted the need to maintain the operational and non-operational safety of

---

M. Abdulkareem (✉) · N. Bakhary  
Institute of Noise & Vibration, Universiti Teknologi Malaysia, Kuala Lumpur, Malaysia  
e-mail: [moabdulkareem2@live.utm.my](mailto:moabdulkareem2@live.utm.my)

M. Abdulkareem  
Department of Civil Engineering, Faculty of Engineering, Technology and Built Environment,  
UCSI University, Kuala Lumpur, Malaysia

these structures. Hence, early identification of damage is needed to provide reliable safety and performance during the life service of these structures.

A relatively new area of research in damage detection through vibration response is the application of wavelet transform (WT) [1]. Being a mathematical tool, WT decomposes signals into time and frequency domains. Since the pioneering work of Wang and Deng [2] by applying WT to detect damage in beams, WT has been efficiently demonstrated in detecting damage in plate structures. Rucka and Wilde [3] showed a 2-D continuous wavelet transform (CWT) technique by applying reverse biorthogonal wavelet to obtain damage information. Damage was identified by the spikes in the transformed responses. Bombale et al. [4] showed WT efficiency in identifying defaults in a plate. Discrete wavelet transform (DWT) and CWT analysed the mode shapes to identify delamination. Bagheri et al. [5] proposed a 2-D DWT to detect linear damage in plate. Lam and Yin [6] applied a 2-D spatial WT to identify plate cracks. Nikravesh and Chegini [7] analysed a plate with two cracks using DWT.

Most damage cases have limited damage to the locations that are away from boundaries [8]. The “spike” indicating damage can reach high/low near the boundaries. In such case, where it is high, no damage may actually exist in this region, and when the value is low, damage might actually exist at such locations [3, 9]. These values can bury the singularity caused by the presence of damage and render small damage undetectable. According to Vafaei et al. [9], the spike at the support is caused by increase in stiffness at the supports. The same phenomenon can be adopted for the free-end which experiences a sudden reduction of stiffness as the structure terminates. Previous methods have smoothed the coefficient near the boundaries to solve border distortion; however, they were not efficient to detect damage around the boundaries.

This study proposes a technique of WT analysis of the mode shapes to identify damage at boundary regions. A 2-D CWT is utilized to analyse the difference between the plate’s undamaged and damaged mode shapes. With the application of the mode shape difference, this eliminates the effect of the sudden stiffness reduction at the plate’s free-end. Numerical model of a cantilever steel plate structure is used as an example. Several damage cases are considered by thickness reduction of elements. Various degrees of damage severities are induced at different locations in the plate. The results show that this technique addresses the problem of damage detection at boundary locations. Moreover, the technique is fast, simple, and accurate. A sensitivity study evaluating damage under different levels of noise is provided.

## 2 Wavelet Basis Function

In 2-D CWT, the function  $f(x, y)$  is [3]:

$$W^i f(u, v, s) = \frac{1}{s} \int_{-\infty}^{\infty} \int_{-\infty}^{\infty} f(x) \psi^i \left( \frac{x-u}{s}, \frac{y-v}{s} \right) dx dy$$

$$= \frac{1}{s} f * \psi^i \left( \frac{-u}{s}, \frac{-v}{s} \right) = f * \bar{\psi}_s(u, v), i = 1, 2$$

where  $s, u, v, Wf(u, v, s)$ , and  $f * \bar{\psi}_s$  are the scale, position, and wavelet coefficient of  $\psi_{u,s}(x)$  and the convolution of function.

### 3 Numerical Example

#### 3.1 Cantilever Plate Modelling

The plate dimensions are 560 mm × 560 mm × 2 mm. The properties of material are:  $E = 200$ ;  $\rho = 7850 \text{ kg/m}^3$ ; and  $Gpa, \nu = 0.3$ . For boundary conditions, the left side of the plate is fixed, while others are unsupported to resemble a cantilever condition. The plate has 3136 square shell elements that are 10 mm by 10 mm. Though higher modes are better to identify damage, they contain more dead areas where the quality of damage detection is poor when applying CWT [3, 10]. Thus, only the first mode shape is applied in the analysis. The damaged area is 80 mm × 80 mm. The percentage of the reduced thickness (severity) is 25% of the plate's thickness. The corresponding value of the plate's thickness as a result of damage is now 1.50 mm. Three damage locations were considered which are middle, top, and free-end of the plate and are shown in Fig. 1a–c, respectively. The mode shape difference is derived by deducting the damaged from undamaged mode shape.

#### 3.2 Frequency Evaluation

To evaluate the consequence of damage on natural frequencies of the cantilever plate, the trend of frequency change is examined as several types of damages involving different damage severities and locations are imposed on the plate. The damage severity ranges from 5 to 87.5%. The damage positions are at the top, middle, and free-end of the plate. The changes of the first frequencies for the damages are shown

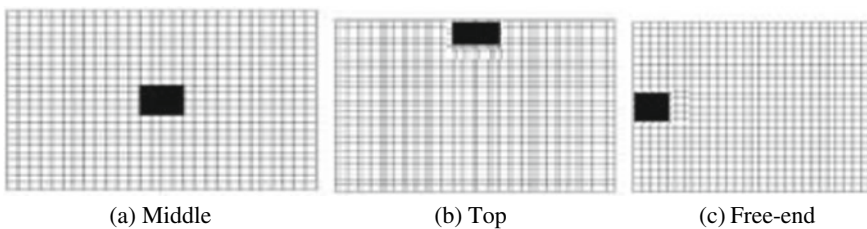
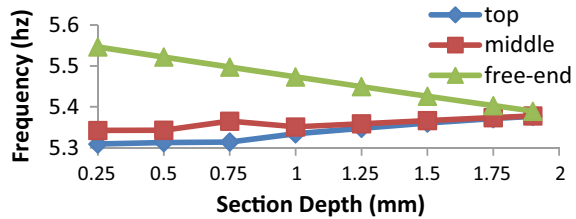


Fig. 1 Damage locations

**Fig. 2** Change in frequency of damaged plate



in Fig. 2. It is observed that this frequency decreases as the middle and top damages increase. This is unarguably as a result of stiffness reduction due to damage in the plate: the existence of damage at these locations serves as “weak points” in the plate structure. Contrary to this, the frequency increases as the free-end damage increases. This increase in frequency shows that the mass decrease (at the free-end) from damage simulation overrides stiffness loss due to damage, thus increasing the frequency as mass is inversely proportional to frequency. This can be explained as the closer a damage is to the support, the more the effect (decrease) on the stiffness is and vice versa. The damage leads to small change in frequency, and this change in frequency is contradictory (increasing frequency) confirming the limitation of change in frequency for damage identification. The result in this section confirms that the changes in frequency can be applied to detect damage on a plate structure, but this comes with several drawbacks. For example, different damage locations may have the same frequency change. Secondly, the free-end damage increases the frequency due to the mass effect overshadowing the stiffness loss. And lastly, there is inability of change in frequencies to differentiate damage positions in symmetrical structures. Therefore, the application of frequency change as a parameter for damage detection should be accompanied by another method to avoid inaccurate results.

### 3.3 Wavelet Analysis

Wavelets are family of basic functions capable of analysing signals in a localized time and frequency (or scale) domain. MATLAB wavelet toolbox is applied to analyse the mode shape difference. The mode shape difference is estimated by subtracting the displacement value at each node of the damaged mode shape from the undamaged mode shape of the plate, and it is decomposed using 2-D CWT.

The most appropriate mother wavelet is selected after several trials for damage identification. For damage identification at middle and top of the plate, the derivative of Gaussian (DOG) mother wavelet is chosen with scale 3 and angle 1. The detection of the free-end damage is done by first transposing the mode shape difference matrix signal, followed by the wavelet decomposition. Paul mother wavelet having scale and angle of 3 and 1, respectively, is applied to detect the free-end damage. The 2-D CWT is thereafter utilized to decompose the mode shape difference signal. The mode shape difference signal applied here contains no noise. Wavelet transform modulus

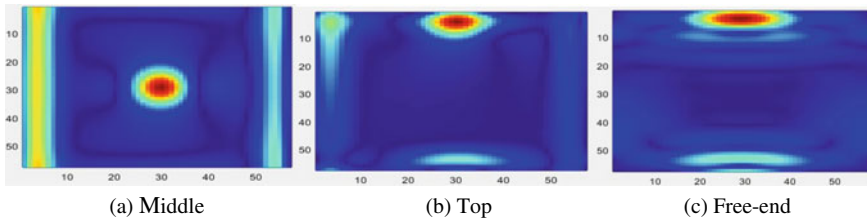


**Fig. 3** Wavelet transform moduli

of the decomposed signal identifies damage by image presentation. This is due to WT sensitivity to sudden change in the analysed signal. Figure 3 shows the WT modulus of the mode shape difference of each damage location. The damage positions are easily spotted as the red area in the decomposed images. Based on the results, it is observed that the proposed technique proves to provide solution to damage detection in plate structure, especially at the free-end without being confronted with the problem of border distortion.

### 4 Parametric Study

Since the effects of noise are certainly unavoidable in practice, more detailed studies are carried out in this section to evaluate the technique’s sensitivity to levels of noise. For this purpose, several degrees of damage severity and damaged areas are imposed by changing the thickness of the plate at the specified damage location. The maximum damaged area is 2.041% of plate’s area. Damage severity ranged from 5 to 87.5% of thickness of the plate (2 mm). Table 1 shows damage severities.

Figure 4 summarizes the results of this sensitivity study. The *y*- and *x*-axes represent the noise levels and damaged area, respectively. The damaged area is indicated as a percentage of the plate’s area, while the noise level represents the maximum noise level in a signal for damage to be detectable. The curves represent the noise-level limits for damage detectability for damage at different locations. The areas below and above each curve represent the allowable and unallowable noise levels for damage identification and the corresponding damage sizes. From Fig. 4, the smallest detectable damaged area at the top and middle is 0.51% of the plate area, while it is 0.76% of the plate for free-end damage. This implies that the minimum damage that can be detected at the top or middle of the plate is 0.51% of the plate’s area

**Table 1** Plate’s thickness reduction (damage)

Cases	1	2	3	4	5
Thickness reduction percentage (%)	5	25	50	75	87.5
Thickness of plate d (mm)	1.9	1.5	1.0	0.5	0.25

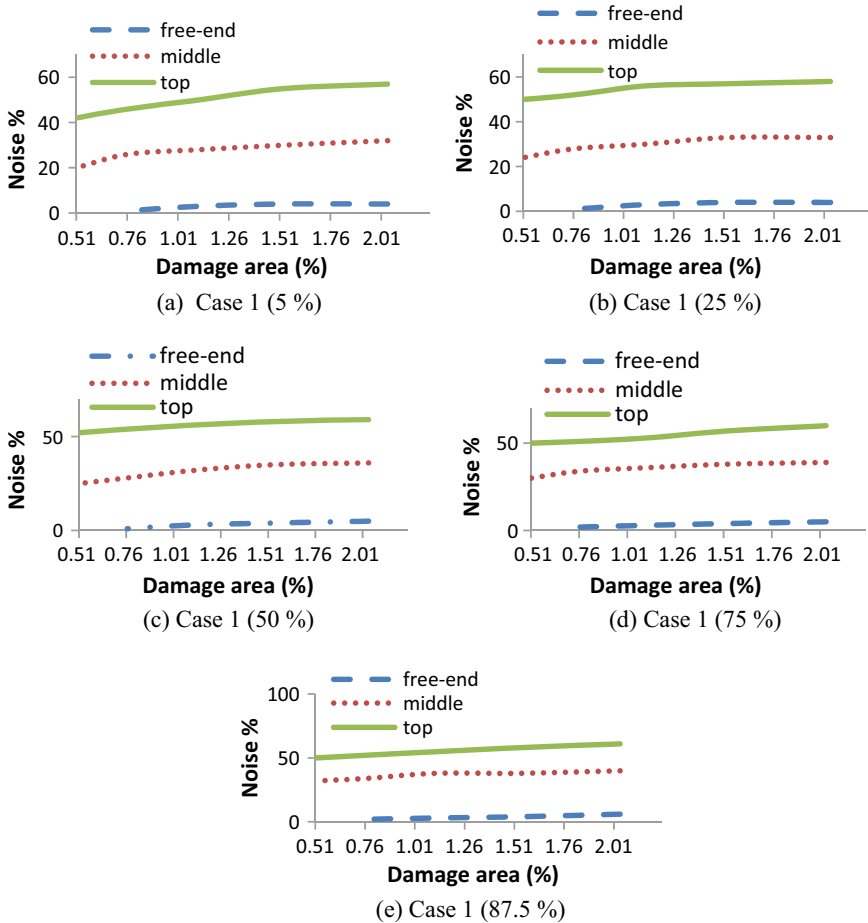


**Fig. 4** Damage detectable level with respect to noise for different damage severities

and 0.76% at the free-end. The damage fingerprint of the free-end damage in the mode shape difference is very small compared to the other locations in the plate. Figure 4a shows the sensitivity result of case 1 (damage severity is 5%). In Fig. 4a, when considering the middle damage, the maximum noise level for detecting 1.1% plate area damage is 28%. This indicates that this damage is not detectable at a noise level higher than 28%. Similar values for top and free-end damages are 50 and 3%, respectively. In addition, for the same severity (case 1) and damage of 1.53% of plate area, noise should not be above 55, 30, and 4% for top, middle, and free-end damages, respectively. Figure 4 shows the results of cases 2–5. The trend in Fig. 4 shows that the detectability of damage level increases with damaged area increment. It is also seen that as noise level increases, larger damage size is needed to detect damage confidently. This phenomenon is seen in all the damage locations. This is

because high noise level submerges damage information in the signal, leading to less accurate detection.

From the results, it is also noticed that the most sensitive damage location to noise is the free-end section of the plate, followed by middle and the top section being the least sensitive to noise. This is due to the effect each damage location has on the change of the plate's stiffness. The free-end damage, which has the highest sensitivity to noise, is accounted for due to its least damage information. The information includes the small changes in natural frequencies and mode shapes. Since changes in the modal parameters are small, the information is easily submerged in noise as mentioned earlier. This is shown in 3.2 which show that the top damage has the largest frequency change.

## 5 Conclusions

This paper investigated a WT damage identification method on a cantilever plate with damage (thickness reduction) at different locations. The locations of the damage are at the middle, top, and free-end of the plate. The wavelet decomposition is performed on the difference of the first mode shape. Two-dimensional CWT is employed for signal decomposition to provide damage detection information. This technique addresses the problem of border distortion that is associated with mode shape decomposition which may result in inaccurate damage detection at the boundaries. This study has demonstrated the effective performance of WT to detect damage when applying noisy signals. The frequency analysis shows that the position and size of damage in a plate have influence on the frequency. In this case, the influence causes an increase or a decrease in the frequency. The increase in frequency experienced is due to the effect of mass loss as a result of the free-end damage which exceeds the effect of stiffness.

**Acknowledgements** Financial support provided through Fundamental Research Grant Scheme (4F800) and HiCOE Grant (4J224) by Malaysia Ministry of Education and Universiti Teknologi Malaysia is appreciated.

## References

1. Abdulkareem M, Bakhary N, Vafaei M et al (2018) Non-probabilistic wavelet method to consider uncertainties in structural damage detection. *J Sound Vib* 433:77–98
2. Wang Q, Deng X (1999) Damage detection with spatial wavelets. *Intl J Sol Struct* 36:2332–2357
3. Rucka M, Wilde K (2006) Application of continuous wavelet transform in vibration based damage detection method for beams and plates. *J Sound Vib* 297(3–5):536–550
4. Bombale BS, Singha MK, Kapuria S (2008) Detection of delamination damage in composite beams and plates using wavelet analysis. *Struc Eng Mech* 30(6):699–712

5. Bagheri A, Ghodrati Amiri G, Khorasani M (2011) Structural damage identification of plates based on modal data using 2D discrete wavelet transform. *Struc Eng Mech* 40(1):13–28
6. Lam HF, Yin T (2012) Application of two-dimensional spatial wavelet transform in the detection of an obstructed crack on a thin plate. *Struct Con Health Mon* 19:260–277
7. Nikravesht MY, Chegini SN (2013) Crack identification in double-cracked plates using wavelet analysis. *Meccanica* 48:2075–2098
8. Abdulkareem M, Bakhary N, Vafaei M et al (2019) Experimental damage assessment of support condition for plate structures using wavelet transform. *Theor Appl Mech* 57(2):501–518
9. Vafaei M, Alih SC, Rahman ABA et al (2014) A wavelet-based technique for damage quantification via mode shape decomposition. *Struct Infra Eng* 11(7):869–883
10. Abdulkareem M, Bakhary N, Vafaei M et al (2019) Application of two-dimensional wavelet transform to detect damage in plate structures. *Measurement* 146:912–923



# Determining the Potentials of Renewable Energy Sources for Distributed Generation in Ghana



Ernestina Amewornu and Nnamdi Nwulu

**Abstract** Electricity is essential for the economic and social development of a country. However, most developing countries are yet to meet the full electrical load demand of their citizens. The generation of electricity in most of these countries is dependent on coal, although there are substantial amounts of renewable resources ranging from biomass, geothermal, solar, wind, hydro, etc. These renewable sources when fully exploited have the potential of significantly improving the level of available and quality electricity at the consumer ends. Significant quantity of electricity can be generated from solar and wind for the purpose of distributed generation (DG). This is based on analysis with the help of RETScreen clean energy project software and HOMER simulation software. In Ghana, the introduction of DG based on available renewable energy is more economical compared with generation from diesel generators, hence the need to pay attention to the development of renewable energy for electricity generation.

**Keywords** Renewable energy · Electricity · Distributed generation · Gas emission · Cost

## 1 Introduction

Ghana is a West African country located in the Gulf of Guinea Coast. The country lies about 4° north of the equator and extends in land to about 670 km to 12° south. The width is from about 1° east to a distance of about 560 km to 4° west. The northern border of Ghana is shared with Burkina Faso, the western border is shared with Ivory Coast, and the eastern boarder is shared with Togo. The Gulf of Guinea and the Atlantic Oceans are located to the south. This forms a coastline of about 550 km for Ghana. The coastal area is mainly used for the fishing activities. The Greenwich meridian passes through Tema located in the eastern part of Ghana. The

---

E. Amewornu · N. Nwulu (✉)

Department of Electrical and Electronic Engineering Science, University of Johannesburg,  
Johannesburg, South Africa

e-mail: [nnwulu@uj.ac.za](mailto:nnwulu@uj.ac.za)

© Springer Nature Singapore Pte Ltd. 2020

S. S. Emamian et al. (eds.), *Advances in Manufacturing Engineering*, Lecture Notes in Mechanical Engineering, [https://doi.org/10.1007/978-981-15-5753-8\\_58](https://doi.org/10.1007/978-981-15-5753-8_58)

631

total cross-sectional area is 238,533 km<sup>2</sup>, out of which about 8520 km<sup>2</sup>, representing 3.5%, is covered by water bodies.

Over 96% of Ghana is covered with various landscapes categorised as forest plains, low bush, park-like savannah and grassy plains. The characteristics of the various landscapes coupled with tropical climatic condition support the cultivation of various crops for domestic and export purposes.

The country's economic development is driven by activities such as exportation of various agricultural and non-agricultural products and other forms of business activities. The effectiveness of these economic development activities is dependent on the availability of energy.

The primary sources of energy exploited in Ghana [1] are crude oil, natural gas, hydro, solar and biomass. The consumed energies [1] are in the forms of petroleum products, electricity and biomass in various quantities. The high consumption of wood fuel is a potential cause of deforestation, hence the need to switch to more efficient energy consumption.

The available electricity in the country is sometimes lower than expected for predicted economic growth rate. The available electrical power in 2016 was far lower than the expected electricity range of 16,798 to 16,900 GWh required for a minimum economic growth range of 4–4.5%. The relative low electricity available for domestic use can be said to be one of the causes of the low economic growth of 3.7% [2] in the year 2016. This indicates the need to increase power generation for fostering economic development [3, 4]. This challenge prompts the idea of introducing distributed generation (DG) into the country's distribution network. The sources to be considered are non-renewable sources often accompanied by high-gas-emissions [5, 6] and renewable sources often accompanied by high initial cost.

## ***1.1 Renewable Energy Development in Developing Countries***

Renewable source of energy refers to the use of naturally occurring energy flux. The energy fluxes are sustainable and environmentally friendly. Hence, the energy produced from these sources is referred to as clean energy. The exploitation of renewable energy [7, 8] contributes to reduction in greenhouse gas emission and air pollution level. The use of renewable energy potentially prevents environmental effects and diseases associated with the use of non-renewable sources of energy. The development of renewable energies has the potentials of strengthening the security of electricity availability, thereby enhancing economic and social development of a country.

Despite the benefits of renewable energy, most developing countries are yet to take full advantage of it. Cameroon [8] has significant solar energy, wind energy, biomass energy and hydropower potentials. However, only 6.1% of the economical feasible hydropower is being developed. Mali depends on hydropower plant [7] in addition to electricity generated from imported crude oil. The provision in the country's

renewable energy policy aimed at improving the exploration of renewable energy is yet to yield results. Mali depends heavily on traditional methods of consuming biomass to compliment the low access to electricity. Nigeria is also yet to take advantage of the substantial renewable sources such as hydro, solar, wind and biomass energy [9] for electricity generation.

Hydro and geothermal energy sources form about 80% of the sources of energy for electricity generation in Kenya [10]. This renewable electricity generation is exploited from only 30% of potential hydropower resources, 4% of the potential geothermal resources and lower percentages of available wind and solar resources. The electricity supply from Kenya's national grid meets only about 18% of the national electricity demand. The country has also a heavy reliance on biomass which is responsible for deforestation of the land.

Most developing countries in Africa are endowed with various renewable energy sources. However, these countries are yet to fully develop the available renewable sources. The development of the renewable sources can contribute to improving the security of electricity with drastic reduction in harmful environmental effects. Developing countries need to take proactive steps towards the exploitation and production of efficient energy from renewable sources. This will contribute to the reduction in the release of environmental harmful gases. The renewable sources can also be considered for distribution generation (DG) since the resources are available at various parts of the country [11]. This can also be deployed in addition to demand-side management tools and techniques [12–15]

## ***1.2 Renewable Energy Resources in Ghana***

Ghana is identified with various renewable energy sources. Electricity from these renewable sources can be connected to the national grid at various points within the distribution network. This step has the potentials of improving the power stability of the country. The power losses associated with the introduction of DG can comparatively be low. Renewable sources of energy are environmentally friendly. Hence, it is worth considering the potentials of renewable energy sources within the country for distributed generation (DG).

### **1.2.1 Bio-Energy Potentials in Ghana**

One of the main occupations in Ghana is agriculture. About 15,900,000 hectares of land is marked suitable for the cultivation of various crops such as cereals (maize, millet, rice, wheat and sorghum) and other crops, which include sugarcane, cocoa, oil palm, coconut, among others. The preparation of these crops creates by products which are treated as waste. The farm wastes in addition to forest residues which are sources of biofuel [16] are often burnt in open air. Also, the average waste generated in Ghana [17] is about 0.47 kg/person/day, out of which 0.314 kg/person/day is organic.

About 0.376 kg/person/day organic waste generated in metropolitan cities, while about 0.249 kg/person/day is generated in municipals and about 0.172 kg/person/day is generated in districts. Improper disposal of these wastes pose health hazards that need to be avoided. A diversion of the Country's waste into energy will contribute to improving the nation's power quality as well as reducing health challenges in society.

### **1.2.2 Wind Energy Potentials in Ghana**

The generation of electricity from wind energy is dependent on the speed of wind which is believed to be proportional to the distance of a location from the equator. The speed of wind along the coast of Ghana according to Energy Commission of Ghana ranges from 3.4 to 7.37 m/s at a height of 50 m. Analysis based on the extrapolation of wind speed data which is available on RETScreen Plus also indicates wind speed [18] ranging from 3.77 to 8.24 m/s at 60 m height. Estimated capacity [19] indicates that wind energy in Ghana can potentially influence electricity generation. The potential of electricity generation from wind energy is enough to significantly influence electricity distribution in Ghana.

### **1.2.3 Solar Energy Potentials in Ghana**

Solar energy generation is highly dependent on the efficiency of the solar system as well as the sun radiation level at a location. The efficiency of solar system is also derived from the orientation of components used for intercepting sun rays. Based on the orientation of components, solar systems are broadly categorized as photovoltaic (PV) technology or the solar thermal system (concentrated solar power, CSP). The PV technology converts sun radiations directly into electrical energy. On the other hand, CSP uses the diffusion of solar energy to heat liquid which can be used for domestic or industrial purposes. The steam from the heated liquid can also be used to turn a thermal turbine for electricity generation. The average monthly solar radiation, according to energy commission of Ghana, is as shown in Fig. 1.

The solar energy that can be harnessed within a year varies with significant reduction within the months of April to September. A storage device may be considered to be included in a non-concentrated solar system, while backups are considered for concentrated solar systems. The solar PV systems, as stated earlier, depend on the radiation of the sun. Hence, there is the possibility of generating electricity throughout the year at various levels from solar PV systems. Solar photovoltaic systems can be relied on for the purpose of distribution generation in Ghana. Despite the high potential of solar energy in Ghana, enough electricity is yet to be generated from solar energy in the country.

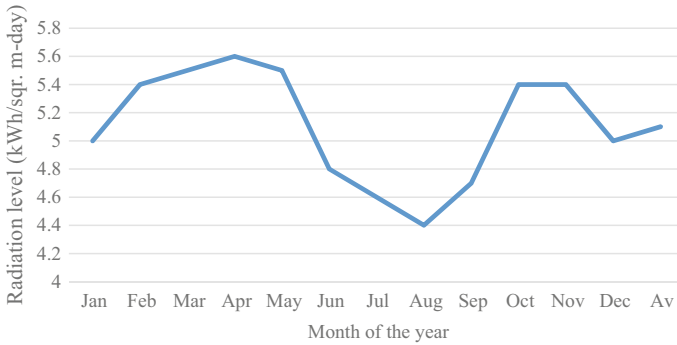


**Fig. 1** Monthly average solar radiation in Ghana

### 1.2.4 Hydropower Potentials in Ghana

Electricity generation from hydro involves the fall of water from a height to turn a turbine. Ghana has various sources [20] of water that can be considered for the generation of electricity [21]. The generation of hydropower in Ghana [17] is mainly dependent on rainfall pattern, evaporation and inflow from outside the country. Hydropower contributes about 47% of the total electricity generated in Ghana as of December 31, 2016. There are other various potential sites [22] on the major rivers in Ghana.

In addition, potential hydropower generation sites are the waterfalls which are located at various parts of Ghana. A total of about 2400 GWh electricity [23, 24] can potentially be generated from available medium-scale hydropower generation sites per year. Hydropower generation in Ghana can therefore be considered for introduction of distributed generation. The use of hydropower will also depend on the location of the DG.

### 1.3 Renewable Energy Policy Framework in Ghana

The current renewable policy structured towards taking measures to ensure sustainable provision of energy was passed into law in 2010. This policy is to help the country attain micro-economic stability and growth status by 2020. The policy among other things acknowledges the need to improve the level of exploitation of renewable sources such as solar, wind, hydro and biomass in Ghana. The use of biomass (wood fuel) accounts for about 60% of total energy used in the country as at the time of drafting the policy. The policy seeks to encourage the use of modern efficient technology for sustainable energy production.

There has been improvements with respect to the percentage of wood fuel use since the percentage has been reduced to about 39% as of December 2016. This

reduction may be associated with an increase in the use of improved stoves that uses less quantity of wood fuel for cooking and heating.

The level of wood fuel consumption needs to be reduced further to save the country from deforestation. The country is yet to see significant extraction and/or refinery of bio-oil as stated in the policy. This may be attributed to low cultivation of energy crop since the proposed energy crop recommended for Ghana (jatropha plant) is unable to withstand draught as expected. Alternative energy crops suitable for Ghanaian tropical climate need to be identified through the conduct of more research.

The policy prohibits the burning of waste, but this seems not to be enforced to latter. This may be attributed to the health repercussions of keeping waste within communities for a long period. There is the need for more motivation for the building of waste to energy plants to convert the wastes into useful energy.

There has been improvements in the solar energy generation capacity from 0 in 2010 to 22 MW in 2016. However, the target of energy commission of Ghana to have solar generation capacity of about 150 MW grid connection in 2020 is far from being achieved. There is the need for more motivation to encourage the generation of electricity from solar energy for grid connection. The energy policy of Ghana like that of Nigeria [9] encourages individuals and organizations to generate electricity from renewable sources in off-grid mode. Energy Commission of Ghana in an attempt to encourage boosting the level of solar electricity generation launched in 2016 a rooftop solar installation program aimed at installing about 200,000 solar systems within a year for commercial, industrial and residential purposes. The programme has enabled the installation of about 89 fully installed solar systems as at the end of 2016. There is low implementation of solar photovoltaic systems [25] in Ghana because individuals in the program are challenged by the inability to pay [26] for the cost of other associated items like installation, other than the solar panels (which is free for those sign up to the program).

It is the aim of the policy to encourage investors to generate electricity from renewable sources for grid connection purposes. However more needs to be done to attract investors into renewable electricity generation sector since government cannot do it alone.

## 2 Methodology

This study seeks to assess the quantity of electricity that can be generated from renewable source for distribution generation purpose in Ghana. Ten locations, randomly selected from the regions in Ghana, were considered for the assessment of solar power generation. The selected locations are Wa, Bawku, Tamale, Kintampo, Ejura, Axim, Cape Coast, Koforidua, Tema and Kete-Krachie.

The optimal position of the solar panel in terms of slope was determined by varying the slope angle while observing the expected average annual radiation. The positioning of the panels was considered in terms of the azimuth and slope angles respectively. The azimuth angles considered are  $0^\circ$ ,  $180^\circ$ ,  $90^\circ$ ,  $-90^\circ$ ,  $45^\circ$  and  $-45^\circ$ .

The azimuth angle was set to zero degree ( $0^\circ$ ) since the varied angles yielded the same average radiation level. The slope angles considered for the installation of PV panels are  $5^\circ$ ,  $10^\circ$ ,  $15^\circ$  and  $20^\circ$ .

The selected panel for the assessment is mono-Si-CSUN320-72 M model based on its relatively high efficiency (16.6%) of converting solar radiation of electrical power. Each of these panels has a cross-sectional area of  $1.936 \text{ m}^2$ . 80,000 units of the PV panels will be capable of generating up to about 25.6 MW on a minimum of  $153.9 \text{ m}^2$  area. RETScreen clean energy project software was used to estimate the quantity of electricity that can be generated from solar at each of the selected locations. Miscellaneous losses due to manufacturing deficiencies were considered [14] for the photovoltaic panel as 10%, while that for the inverter was set as 5%. In addition, an inverter capacity of 30 MW with 80% efficiency was considered.

An existing electrical load profile on Juansa network, a Ghanaian distribution network, was used as a case study to determine the economic feasibility of distributed generation based on power from solar and wind energy as well as a diesel generator. The assessment considered factors such as capital cost, replacement cost, maintenance and operation costs as well as gas emission cost [27] with the help of HOMER simulation software.

### 3 Results and Discussion

The slope angle for the installation of PV panel at Wa and Bawku for maximum interception of sun radiation ranges from  $10^\circ$  to  $15^\circ$ . The highest average sun radiation can be intercepted at Tamale, Kintampo and Kete-Krachie at a slope angle of  $10^\circ$ . The installation of solar panels at slope angle between  $5^\circ$  and  $15^\circ$  is expected to intercept the highest radiation at Ejura and Koforidua. The highest solar power is expected to be generated at Axim and Tema when solar panels are installed at slope angle between  $5^\circ$  and  $10^\circ$ . The quantity of power that can be generated from solar at the selected locations is as shown in Table 1.

The estimated electricity that can be generated from solar PV installed on about 0.67% of Ghana's land is 310 GWh a year. This is equivalent to increasing the 2016 solar grid-connected solar power by more than 1000 times. The generation of this electricity can contribute to serving the local electricity needs of the country as well as saving the country from carbon dioxide emission of 76,798 per year.

**Case study:** The average annual system cost is as shown in Fig. 2, and the annual cost in terms of gas emission is also shown for the various energy sources in Fig. 3.

The system annual cost for integrating diesel generator into the grid is GH¢ 26,974,240.13, out of which GH¢ 24,778,375.86 is for the system and GH¢ 2,195,864 is due to gas emission. Integrating wind generator into the grid costs a total of GH¢ 2,276,077.43 per year, out of which GH¢ 440,057.23 is for the system and GH¢ 1,836,020 for gas emission. The yearly cost on PV configuration is GH¢ 5,709,772.36 comprising of GH¢ 3,970,335.63 for the system and GH¢ 1,739,437 for gas emission.

**Table 1** Potentials of solar PV electricity generation in Ghana

Location	Potential generation [GWh/yr]	Emission reduction [tCO <sub>2</sub> /yr]	Savings due emission reduction [GH¢]
Wa	32.8	10,286	946,003.42
Bawku	33	10,356	952,441.32
Tamale	30.4	9537	877,117.89
Kintampo	31.1	9759	897,535.23
Ejura	29.5	9262	851,826.14
Axim	32.2	10,091	928,069.27
Cape coast	28	8774	806,944.78
Koforidua	29.7	9315	856,700.55
Tema	32.4	10,165	934,875.05
Kete-Krachie	30.9	9694	891,557.18
Total	310	76,798	706,3112.1

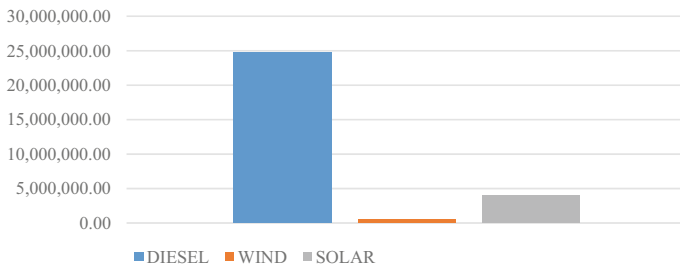


**Fig. 2** Annual system cost per generation source connected to grid

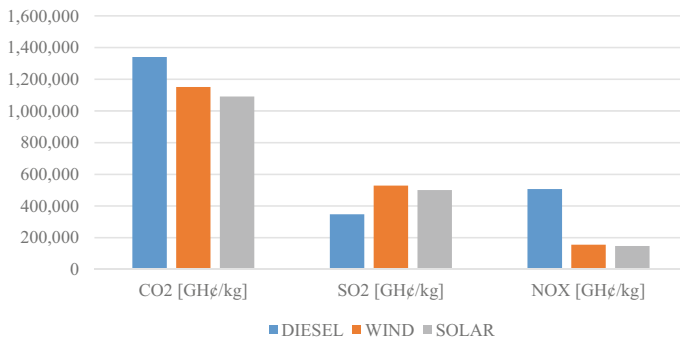


**Fig. 3** Gas emission cost



## 4 Conclusion

The study has shown that there is the possibility of generating enough electricity from renewable sources in Ghana. The generated electricity can be incorporated into the country's power network. The renewable plants can be sited at various parts of the country. Hence, renewable energy can be considered for the introduction of distributed generation into the Ghanaian power network. The DGs have the potentials of contributing to a reduction in power losses in the power network.

Increase in the level of generated power from renewable sources will promote a reduction in the level of harmful gas introduced into the atmosphere. The move also has the potential of creating jobs. In addition, there is the potential of improving economic and social development of individuals and the country at large. Ghana, therefore, needs to create enabling environment through the implementation of flexible renewable energy policy to promote investments into the development of the various renewable sources in the country.

## References

1. Energy Commission (2017) National energy statistics (2007–2016)
2. Ghana Statistical Service (GSS) (2018) Provisional 2017 annual gross domestic product. Accra: Ghana statistical service
3. Gbadamosi S, Nwulu NI, Sun Y (2018) Multi-objective optimization for composite generation and transmission expansion planning considering offshore wind power and feed in tariffs 12:1687–1697
4. Nwulu NI, Agboola PO (2012) Modelling & predicting electricity consumption using artificial neural networks. In: 11th international conference on environmental & electrical engineering (EEEIC2012)
5. Elbisy MS, Mlybari EA (2017) Environmental risk management and mitigation strategies for offshore gas well drilling projects (Case Study: Abu Qir Bay, Egypt). *J Civ Construct Environ Eng* 2:66–77
6. Ejiba IV, Onya SC, Adams OK (2016) Impact of oil pollution on livelihood: evidence from the Niger delta region of Nigeria. *J Sci Res Rep* 12:1–12
7. Maiga AS, Chen GM, Wang Q et al (2008) Renewable energy options for a Sahel country: Mali. *Renew Sustain Energy Rev* 12:564–574
8. Abanda FH (2012) Renewable energy sources in Cameroon: potentials, benefits and enabling environment. *Renew Sustain Energy Rev*
9. Mohammed YS, Mustafa MW, Bashir N et al (2013) Renewable energy resources for distributed power generation in Nigeria: a review of the potential. *Renew Sustain Energy Rev* 22:257–268
10. Kiplagat JK, Wang R, Li TX (2011) Renewable energy in Kenya: resource potentials and status of exploitation. *Renew Sustain Energy Rev* 15:2960–2973
11. Musasa K, Nwulu NI, Gitau MN, Bansal RC (2017) Review on DC collection grids for offshore wind farms with HVDC transmission system. *IET Power Electron* 10:2104–2115
12. Fahrioglu M, Nwulu NI (2012) Investigating a ranking of loads in avoiding potential power system outages. *J Electr Rev (Przegląd Elektrotechniczny)* 88(11a):39–242
13. Nwulu NI, Fahrioglu M (2011) A neural network model for optimal demand management contract design. In: 10th international conference on environmental & electrical engineering (EEEIC2011)

14. Maltitz G, Haywood L, Mapako M et al (2009) Analysis of opportunities for biofuel production in sub-Saharan Africa
15. Damisa U, Nwulu NI, Sun Y (2018) Microgrid energy and reserve management incorporating prosumer behind-the-meter resources. *IET Renew Power Gener* 12(8):910–919
16. Miezah K, Obiri-Danso K, Kada Z et al (2015) Municipal solid waste characterization and quantification as a measure towards effective waste management in Ghana. *Waste Manag* 15–27
17. Acakpovi A, Majeed IB, Fifatin FX et al (2017) Wind velocity extrapolation in Ghana by Weibull probability density function. *Wind Eng* 42:1–13
18. Angelin-Chaab M, Adaramola MS, Paul SS (2014) Assessment of wind power generation along the coast of Ghana. *Energy Convers Manag* 77:61–69
19. Yeleliere E, Cobbina SJ, Duwiejuah AB (2018) Review of Ghana's water resources: the quality and management with particular focus on freshwater resources. *Appl Water Sci*
20. Owusu PA, Asumadu-Sakodie S, Ameyo P (2016) A review of Ghana's water resource management and the future prospect
21. Ministry of Power of Ghana (2016) Renewable energy resources and potentials in Ghana
22. Zhang J, Adu D, Fang Y (2017) The potential for small hydropower plants in Ghana. *Innov Energy Res* 6:1–6
23. Dervedde S, Ofosu-Ahenkorah AK (2012) Mini hydro power in Ghana. Energy Found, Accra
24. Bawakyillenuo S (2012) Deconstructing the dichotomies of solar photovoltaic (PV) dissemination trajectories in Ghana, Kenya and Zimbabwe from the 1960s to 2007. *Energy Policy* 49:410–421
25. Awiah DM, Hackman I (2018) Rooftop Solar program faces financial crisis. Graphic Online, Accra
26. Emission factor (gasoline and diesel industrial engines)
27. Asumadu-Sarkodie S, Owusu PA (2016) A review of Ghana's solar energy potential

# Optimal Location of Distributed Generators in a Radial Distribution Network



Ernestina Amewornu and Nnamdi Nwulu

**Abstract** Electrical power loss and low-voltage profile represent loss of revenue to power utility providers as well as electricity end users. Utility providers therefore need to take steps towards minimizing power losses and ensure appreciable bus voltage at the load ends. There are various methods for improving the performance of a power network. However, the objective of this work is to determine optimal location of Distributed Generators (DGs) based on power loss index and voltage stability index, and this was accomplished using the Power System Analysis Tool (PSAT). The optimal location of DG in a radial distribution network based on a combination of voltage stability and power loss index produces significantly reduced power loss and improved voltage profile. It is therefore a suitable method for improving the performance of radial distribution networks.

**Keywords** Distributed generation · Radial distribution network · Optimal location · Power loss · Voltage profile

## 1 Introduction

Quality electricity provision is essential for effective operation at the consumer end towards a country's development. Quality electricity here refers to providing electrical energy to consumers within defined standards. Power loss and voltage profile are among other factors that affect the performance of a power network. Power losses incurred in transmission lines represent loss of revenue since the losses are paid for by the utility providers. Voltage level at the receiving end influences the operation of electrical load. Voltage levels outside standard range can cause malfunction of electrical and electronic gadgets. The malfunction of end loads contributes to loss of revenue. It is therefore important to minimize line losses and compensate for bus voltage within standard values.

---

E. Amewornu · N. Nwulu (✉)

Department of Electrical and Electronic Engineering Science, University of Johannesburg,  
Johannesburg, South Africa

e-mail: [nnwulu@uj.ac.za](mailto:nnwulu@uj.ac.za)

© Springer Nature Singapore Pte Ltd. 2020

S. S. Emamian et al. (eds.), *Advances in Manufacturing Engineering*, Lecture Notes in Mechanical Engineering, [https://doi.org/10.1007/978-981-15-5753-8\\_59](https://doi.org/10.1007/978-981-15-5753-8_59)

641

There are various methods of compensating for voltage and minimizing power losses in an electrical network. Among the compensation techniques is the use of Distributed Generation (DG), which involves the generation of power close to load centres. Various researches such as [1–5] have confirmed the ability of DGs to manipulate the power load flow of a network towards reducing power loss as well as maintaining bus voltage within acceptable levels in a distribution network. The level of influence of DG on the performance of a distribution network depends on the position of DG in the network [2, 6–14].

Researchers have identified different methods to determine the optimal location of DG in a power network. The principal method embraced by researchers utilizes mathematical optimization techniques (either classical or nature inspired approaches) which includes genetic algorithm (GA), which is a stimulation [9] process to determine the optimal location of DG. This method [12, 14, 15] helps improve the performance of a power network. The human opinion dynamics algorithm, based on the factors that influence human decision, is used to determine the optimal location of DG in a network. The solution provided by this method is more reliable [7] when compared with that from GA.

The particle swarm optimization (PSO) algorithm is based on the principles of birds or fishes moving in search for food. In this method, the position and velocity of a particle are based on information about that particle as well as that of the entire group. The PSO algorithm is recommended to be used to determine the optimal position of DG [16] to minimize power loss. The bacteria foraging optimization (BFO) algorithm is another method based on bacteria foraging for food in an environment. The BFO algorithm provides good solution [17] for the optimal placement of DG and DSTATECOM in a radial distribution network.

The competitive swarm optimizer (CSO) algorithm [18] is another recommended method for determining the optimal position of multiple DGs in a distribution network for low power loss and voltage drop. Another procedure for determining the position of DG(s) is the cuckoo search (CS) algorithm. This algorithm is based on the breeding behaviour of some cuckoo species. This algorithm also helps [10] to determine the position(s) of single and multiple DG units in radial distribution network. The solutions of this algorithm are of high quality with respect to PSO and GA.

Research [6] has shown that a combination of GA with Power Loss Index (PLI) gives better result than with GA only. A combination of PSO algorithm and Chu–Beasley genetic algorithm (CBGA) [3] can be used for locating the suitable site for DG. This approach can result in reducing the power loss of a network by about 50% of the base value. PSOGSA, which is a combination of PSO and GSA, on MATLAB platform [19] is also recommended for the siting of DG in a power network. Hybrid particle swarm (HPSO) algorithm [19] is also capable of assisting in the determination of DG position in a power network. The above researchers did not consider combination of voltage stability index and power loss reduction index when determining the optimal DG site in a power network. This work considers both and utilizes the PSAT simulation software. The main focus of this work is to identify optimal

location of DG in a Ghanaian radial distribution network for reduced power loss and improved bus voltage. This optimal DG site is determined based on combination of voltage stability index and power loss reduction index with the help of PSAT stimulation software.

## 2 Methodology

The voltage at a receiving bus in a power network without load ( $P_L + j Q_L$ ) is almost the same as that of the sending end bus since the drop across the line is ideally zero. This is because no current, apart from leakage current, flows through the line. The connection of load ( $P_L + j Q_L$ ) to the receiving bus causes current to flow through the line, depending on the magnitude of the connected load. The current flow through the line with impedance,  $Z$ , results in voltage drop across the line. The voltage at the receiving end bus, ‘ $V_r$ ’, as indicated in the modelled network as Fig. 1, is less than the voltage at the sending end ‘ $V_s$ ’ by the voltage drop across the impedance ‘ $Z$ ’.

The receiving end voltage at no-load ‘ $V_o$ ’ and that after connection of load ‘ $V_L$ ’ were used to determine the voltage stability of each bus within considered radial network with the help of Eq. (1) [20].

$$VSI = \frac{4(V_o V_L - V_L^2)}{V_o^2} \tag{1}$$

The IEEE standard voltage variation is  $\pm 5\%$ . Hence, the goal is to ensure a minimum bus voltage deviation as close as possible to 5%. Buses with VSI greater than 0.19 (equivalent to voltage deviation more than 5%) where therefore identified as the potential buses for DG installation.

20, 40, 60, 80 and 100% of the total load on the network were assumed to be DG capacities to be introduced into the network. DG of various capacities was connected to the buses with VSI greater than 0.19 one after the other. The power loss reduction indices of the entire network were determined according to Eqs. (2) and (3) after each DG connection.

$$\text{Active Power Loss Reduction Index, (APLRI)} = \frac{P_{\text{loss}} - P_{\text{loss, DG}}}{P_{\text{loss}}} \times 100\%$$

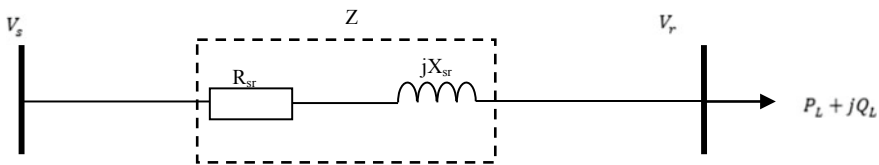


Fig. 1 Modelled electrical power network

$$APLRI = \left( 1 - \frac{P_{loss, DG}}{P_{loss}} \right) \times 100\% \tag{2}$$

$$\text{Reactive Power Loss Reduction Index, (QPLRI)} = \frac{Q_{loss} - Q_{loss, DG}}{Q_{loss}} \times 100\%$$

$$QPLRI = 1 - \frac{Q_{loss, DG}}{Q_{loss}} \times 100\% \tag{3}$$

The bus with DG connection that resulted in the maximum total power loss reduction index for the network is identified as the optimal location for DG installation. The IEEE 33 bus distribution network, IEEE 69 distribution network and an existing 167 bus distribution network in Ghana were used as case studies. PSAT simulation software was used to obtain the power flow for the various networks considered.

### 3 Results and Discussion

**Case 1:** This case considers the IEEE 33-bus radial distribution network. The voltage deviation at the network buses, from bus 6 to bus 18, is above the 5% of margin set. The bus 18 is with the lowest voltage of 0.90707 p.u. Introduction of 2.678214MVA represented 60% of the total load on the network, as DG capacity connected to bus 6 resulted in improved voltage profile as shown in Fig. 2. The effects of connecting DG to bus 6 on active and reactive power losses are as indicated in Figs. 3 and 4. The bus voltage improved up to about 5.98% when DG was connected to bus 6. The individual line active power loss reduced up to about 95%, while the individual line reactive power loss experienced up to 100% reduction. However, the total active loss of the entire 33-bus network reduced by 69.3%, while the reactive power reduced by 63.89%.

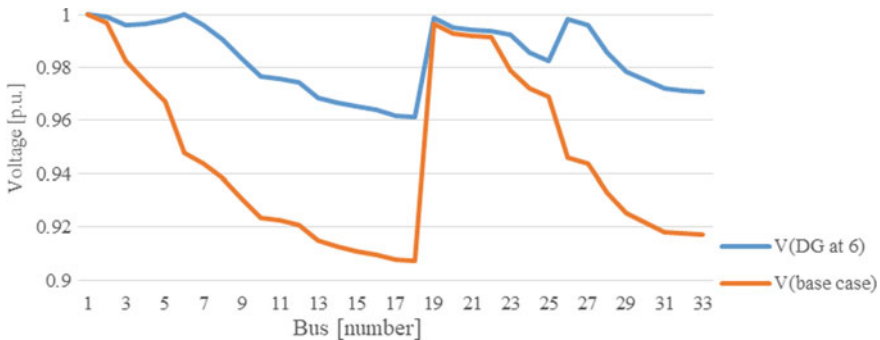


Fig. 2 33-bus network voltage profile before and after DG connected to bus 6

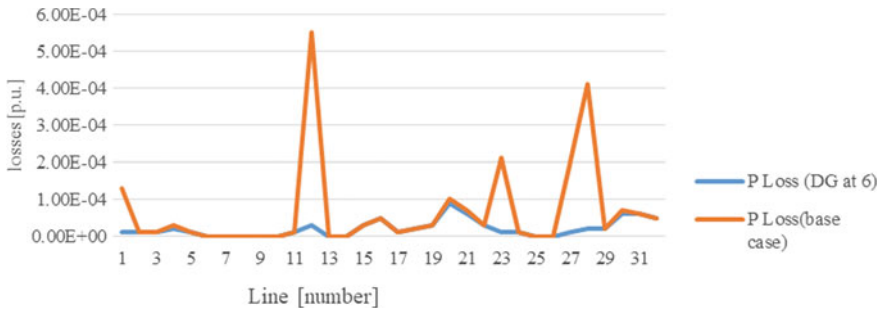


Fig. 3 33-bus network active power ( $P$ ) loss before and after DG connected to bus 6

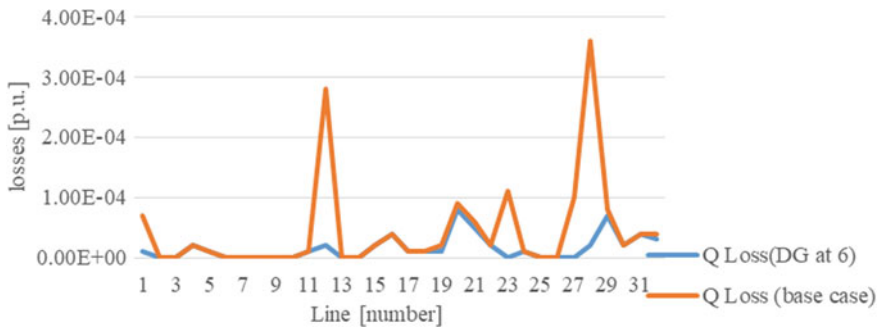


Fig. 4 33-bus network reactive power loss before and after DG connected to bus 6

**Case 2:** This case involves the determination of the optimal location of DG in IEEE 69-bus distribution network. Buses from 57 to 65 of this network have voltages below the 5% tolerance range with the lowest voltage of 0.90919 at bus 65. The connection of DG to bus 61, as the optimal location, resulted in bus voltage improving to about 9.67% with the minimum voltage of 0.97254 as indicated in Fig. 5. The individual active and reactive power line losses reduced up to 100% of the base line losses shown by Fig. 6. However, the total active and reactive power losses reduced by 89.78% and 86.27%, respectively (Fig. 7).

**Case 3:** This case is based on an existing Ghanaian distribution network. The network is made up of 167 buses and referred to as the Konongo-Juansa distribution network. The minimum bus voltage of this network is about 0.79 p.u.

The total active and reactive power losses are about 13.11% and 27.09% of the total active and reactive loads, respectively. The voltage deviation at bus 14 through to bus 167 is higher than 5%. The voltage profile of the 167-bus network with DG connected to bus 112 compared with the base case voltage profile is shown in Fig. 8. The minimum bus voltage after the connection of DG to bus 112 is about 0.94 pu representing about 18% voltage improvement. The individual line power losses are

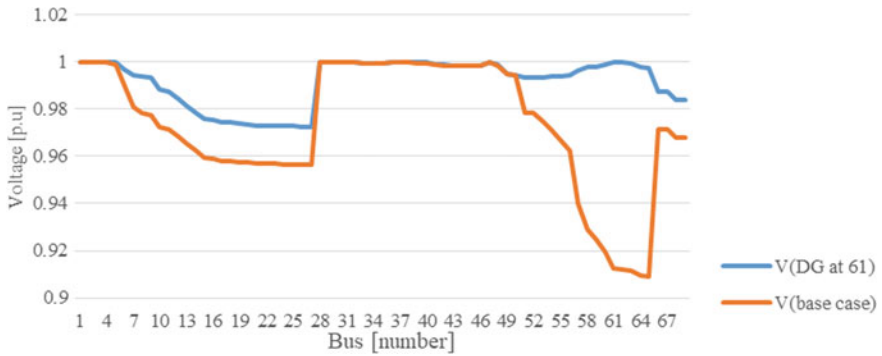


Fig. 5 IEEE 69-bus network voltage profile of with and without DG connected to bus 61

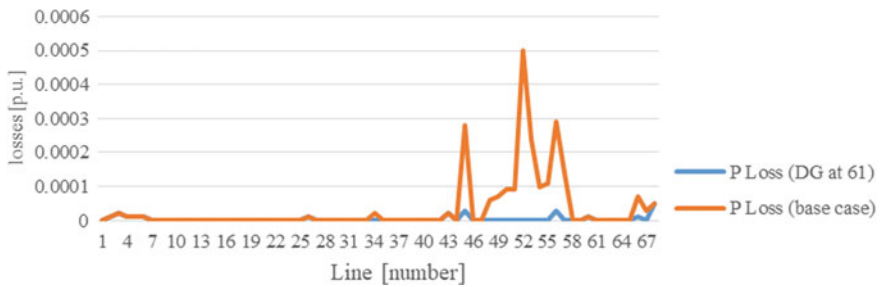


Fig. 6 IEEE 69 bus network active power loss with and without DG at bus 61

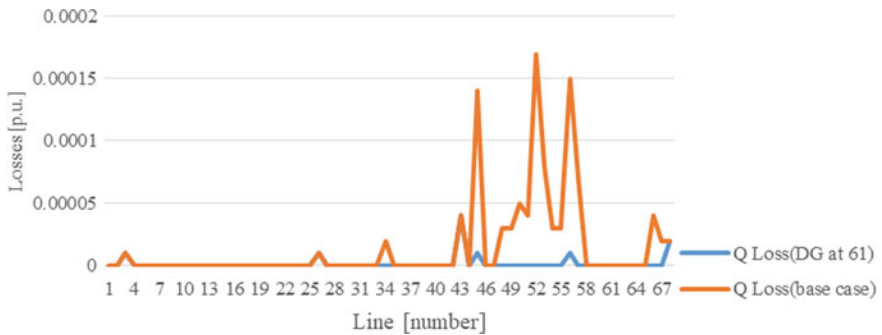
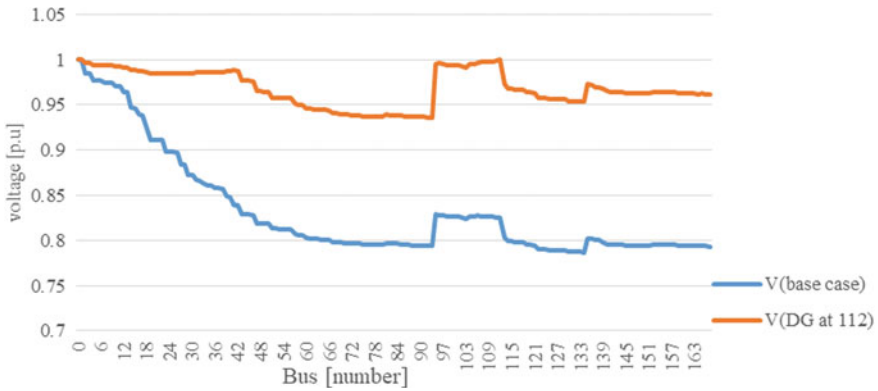


Fig. 7 IEEE 69 bus network reactive power loss with and without DG at bus 61

as indicated in Figs. 9 and 10. The total active and reactive power loss of the entire 167-bus networks are 0.00087 pu and 0.00068 pu, respectively. These represent total power loss reductions of about 79.77% in active power and 87.96% in reactive power, respectively.





**Fig. 8** Konongo-Juansah distribution network voltage profile with and without DG at bus 112

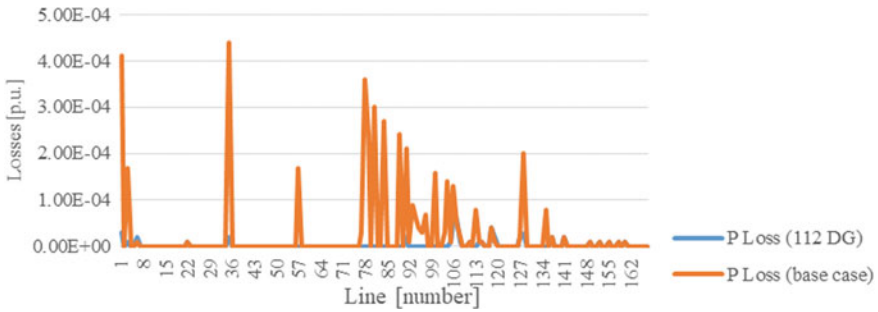


**Fig. 9** Konongo-Juansa distribution network active power loss with and without DG at bus 112

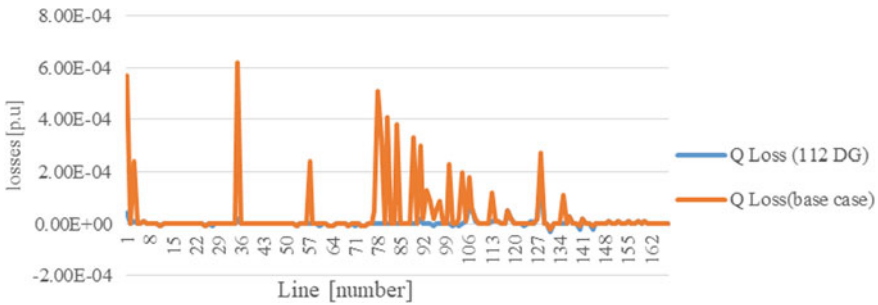


**Fig. 10** Konongo-Juansah distribution network reactive power loss with and without DG at optimal location

## 4 Conclusion

This study has shown that combination of voltage stability index and power loss reduction index helps to effectively determine the optimal location for DG connection in a radial distribution network. The optimal location of DG enables significant reduction in the power loss to be incurred in a power distribution network. The introduction of DG into radial distribution network at optimal location results in power loss reduction above 65%. The bus voltage profile of a radial distribution network is also significantly improved with the introduction of DG at the optimal location. Combination of power loss reduction indices and voltage stability index is therefore recommended for determining the optimal location of DG in radial distribution network.

Electrical distribution companies are encouraged to consider the use of DG for voltage compensation and reduction in line power losses. This step will contribute to the companies' increasing revenue as well as meeting the power demand voltage quality. Also, the move will contribute to support the extension of electricity to areas without electricity.

## References

1. Ahmad S, Asar AU, Sardar S, Noor B (2017) Impact of distributed generation on the reliability of local distribution system. *Int J Adv Comput Sci Appl (IJACSA)* 8:375–382
2. Elsherif A, Shaaban H (2015) Location and sizing of distributed generation units in primary networks for loss reduction and voltage enhancement. *MEPCON*
3. Grisales LF, Grajales A, Montoya OD, et al (2015) Optimal location and sizing of distributed generators using a hybrid methodology and considering different technologies. *Latin American Symposium on Circuits & Systems (LASCAS)*
4. Mahari A (2014) Optimal DG and capacitor allocation in distribution systems using DCIA. *J Eng Sci Technol*, 641–656
5. Pazouki S, Kerendian RF (2012) Effect of distribution generation on distribution network and compare with shunt capacitor. *Int Journal Adv Eng Technol (IJAET)* 4:298–303
6. Rakesh R, VenkataPanana P, Keerthi S (2017) A hybrid algorithm for optimal allocation of DG in radial distribution system. In: *Region 10 synposium (TENSYP)*
7. Kaur M, Mehta S (2016) Optimal placement and sizing of distributed generation unit using human opinion dynamics algorithm. In: *India international conference on power electronics (IICPE)*
8. Ogunjuyigbe AS, Ayodele TR, Alinala OO (2016) Impact of distributed generators on the power loss and voltage profile of sub-transmission network. *Electri Syst Inf Technol* 94–107
9. Shivarudraswamy R, Gaondar DN, Jayalakshmi SN (2016) GA based optimal location and size of the distributed generators in distribution system for different load condition. In: *1st International conference on power electronics, intelligent control and energy systems (ICPEICES)*
10. Tan WS, Hassan MY, Majid MS et al (2013) Allocation and sizing of DG using cuckoo search algorithm. In: *IEEE international conference on power and energy (PECon)*, pp 133–138
11. Sulaiman MH, Mustafa MW, Azmi A et al (2012) Optimal allocation and sizing of distributed generation in distribution system via firefly algorithm. In: *IEEE international power engineering and optimization conference*, pp 84–89

12. Talaat HE, Al-Ammar E (2011) Optimal allocation and sizing of distributed generation in distribution networks using genetic algorithms. In: International conference on electrical power quality and utilisation
13. Liu L, Bao H, Liu H (2011) Siting and sizing of distributed generation based on the minimum transmission losses cost. In: Power engineering and automation conference, pp 22–25
14. Pisica I, Bulac C, Eremia M (2009) Optimal distributed generation location and sizing using genetic algorithms. In: International conference on intelligent system applications to power systems
15. Priya R, Prakash S (2014) Optimal location and sizing of generator in distributed generation system. *Innovative Res Electr Electron Instrum Control Eng* 2:1272
16. Rajalakshmi J, Durairaj S (2016) Review on optimal distributed generation placement using particle swarm optimization algorithms. In: International conference on emerging trends in engineering, technology and science (ICETETS)
17. Devabalaji KR, Ravi K (2016) Optimal size and siting of multiple DG and DSTATCOM in radial distribution system using bacterial foraging optimization algorithm. *Ain Shams Eng J*, pp 959–971
18. Kumarappan N, Arulraj R (2016) Optimal installation of multiple DG units using competitive Swarm optimizer (CSO) algorithm. In: Congress on evolutionary computation (CEC), pp 3955–3960
19. Tolba MA, Tulskey VN, Diab AA (2017) Optimal siting and sizing of renewable distributed generations in distribution networks using a hybrid PSO-GSA optimization algorithm. In: IEEE International conference on environment and electrical engineering and IEEE industrial and commercial power systems europe (EEEIC/ I&CPS Europe), pp 1–7
20. Rahi OP, Yadav AK, Malik H et al (2011) Power system voltage stability assessment through artificial neural network. In: International conference on communication technology and system design, pp 53–60

# Integrated Appliance Scheduling and Optimal Sizing of an Autonomous Hybrid Renewable Energy System for Agricultural Food Production



Omolola A. Ogbolumani and Nnamdi Nwulu

**Abstract** This paper presents the optimal sizing of a solar photovoltaic (SPV), a wind turbine generator (WTG) and a battery-based autonomous hybrid renewable energy system (HRES) for a dairy farm. The multi-objective design and operational (sizing) optimisation problem integrate an appliance-scheduling strategy under the time of use demand response (TOU-DR) program to optimally schedule the load at the demand side. The objective function is to minimise the cost of energy (COE) of the system while satisfying all load demand constraints. The critical indicators of the technical and economic performance of the system are loss of power supply probability (LPSP) and the net present cost (NPC), respectively. The Advanced Interactive Multidimensional Modelling System (AIMMs) outer approximation (AOA) solver in AIMMS was used to formulate and solve the optimisation problem. A cost savings of R45,938.96 for the annualised cost was achieved due to appliance scheduling which indicates the benefit of integrating appliance-scheduling strategy using the TOU-DR program.

**Keywords** Battery energy storage · Dairy farm · Optimisation models · Solar PV · Wind turbine generator

## 1 Introduction

Due to the increase in population and changes in the pattern of food consumption, the demand for food has increased in tandem with constrained energy and water resources. There is an estimated increase in food demand by 60% to satisfy 9.7 billion people by 2050 [1]. There is more demand of 50% food, 40% additional energy and 30% extra water by 2030 [2].

For several decades, the world agricultural food production system has been dependent on fossil fuel. The burning of fossil fuels generates greenhouse gases (GHG), majorly CO<sub>2</sub>, in the atmosphere, which leads to serious health risks and

---

O. A. Ogbolumani · N. Nwulu (✉)  
Department of Electrical and Electronic Engineering Science, University of Johannesburg,  
Auckland Park, 2006, South Africa  
e-mail: [nnwulu@uj.ac.za](mailto:nnwulu@uj.ac.za)

many premature deaths every year [3]. CO<sub>2</sub> emission has given rise to an increase in global mean temperature, and future impact on climate is uncertain. Furthermore, the dependency on fossil fuels for power generation also has a negative impact in terms of exhaustion and rise in the price of fossil fuels [4]. Opportunely, renewable energy resources render an alternative for the issues arising from the vast use of fossil fuels for power generation [5, 6]. The duos, solar photovoltaic (PV) and wind turbine (WT) energy systems are well tested and their energies are abundant in nature. They are usually the preferred alternative energies amongst renewable energy technologies [7]. However, stand-alone solar-or wind-only renewable energy systems cannot generate a large amount of energy continuously nor satisfy high load demands without extensive battery energy storage system (BESS) installation. A solution is the autonomous HRES [8]. Issues such as nonlinear characteristics of system components, diversity between the output from renewable generators and load demand confront HRES at the design stage [7]. Overcoming these problems also requires large-capacity BESSs, increasing the capital cost and cost of energy (COE). Optimal sizing is required to overcome reliability issues that are present in the design and operation of such systems. Optimisation approaches have been used extensively in the literature to solve design and sizing issues in HRES [9–11] with economic and reliability objectives based on COE, NPC and LPSP.

Some works have been conducted on the use of fossil fuel to generate electricity in an agricultural production system [12, 13]. In [14], an energy audit process was used to investigate the level at which renewable energy and energy efficiency can aid in lowering energy intensity and operating costs for a small-scale dairy farm. Reference [15] developed a multi-objective model to satisfy energy requirements of a dairy farm located in South Africa by a micro hydro-wind-grid system while minimising the energy imported from the grid under the time of use tariff. Later on, [16] in their work identified the significant electricity and water components of a pasture-based automatic milking system on a dairy farm. They also established daily and seasonal consumption trends within the system.

There are limited studies on autonomous HRES comprising solar photovoltaic panels, wind turbines and battery for energy storage in the agricultural sector. From works in literature, we can conclude that apart from the challenges posed by the deployment of other sources of energy such as fossil fuel, a more significant challenge persists due to soaring energy cost which has contributed to low-profit margins for farmers in South Africa [17]. Therefore, it is necessary at this point to investigate what combination of WTG, SPV and BESS is needed to satisfy the load demand of a dairy farm.

Appliance-scheduling strategy of the TOU DR program sets out to reduce electricity cost, abate CO<sub>2</sub> emission and lower the total peak demand within the power system. It is a useful tool to attain optimised performance in a power system [18] and it is one of the demand side management tools and techniques used to curtail customer load/demand [19, 20]. In this work, we investigate if the integration of the appliance-scheduling strategy of the TOU DR program would reduce the cost of energy while providing a reliable autonomous HRES. A framework is designed to optimise the preference of renewable energy sources at the supply end of an autonomous HRES

while concurrently having optimality at the demand side by integrating appliance-scheduling strategy of the TOU-DR program. This strategy should be able to achieve a cost-effective and reliable system.

## 2 System Modelling

### 2.1 Solar PV (SPV)

In this work, a polycrystalline SPV module with a power rating of 200 W is used. SPV’s operation and maintenance (O&M) assumes zero value since its significantly small [7]. The hourly output power of the SPV, which is dependent on solar radiation and hybrid renewable microgrid configuration, is represented in Eq. (1) as in [21].

$$P_{spv} = A_{spv} \mu_{spv} I_{spv} \tag{1}$$

where  $A_{spv}$ ,  $\mu_{spv}$ ,  $I_{spv}$  depicts area, efficiency and solar irradiation of the SPV module.

### 2.2 Wind Turbine Generator (WTG)

According to the power law, the wind speed changes at different hub heights. The power law in Eq. (2) is a tool used in determining the wind speed with the reference height [22].

$$V_{wtg-t} = V_{wr-t} \times \left( \frac{h_{wtg-t}}{h_{ref}} \right)^\varphi \tag{2}$$

where  $V_{wtg-t}$  is the hourly wind speed at rotor height  $h_{wtg-t}$ ;  $V_{wr-t}$  is the wind speed at the measured height  $h_{ref}$ , while  $\varphi$  is the power-law exponent with the value taken as  $\frac{1}{7}$  [23].

Equation (3) computes WT generator power output [25]:

$$P_{wtg} = \frac{1}{2} \rho_{air} A \mu_{wtg} C_{wtg} V^3 \tag{3}$$

where  $P_{wtg}$ ,  $\mu_{wtg}$ ,  $C_{wtg}$  are WTG’s hourly power output, efficiency and power coefficient;  $\rho_{air}$ ,  $A$ ,  $V^3$  are the air density, swept area of wind turbine’s rotor and the hourly wind speed to reference height.

### 2.3 Battery Energy Storage System (BESS)

BESS is used to strike a balance between the energies from the renewable generators (SPV and WTG) and the supply. In this study, we utilised lead–acid batteries for their low cost and effectiveness even at very high temperatures [7]; the performance of the battery is described using the energy balance Eqs. (4)– (6) and state of charge (SOC) assessment based on charging and discharging, Eqs. (7) and (8).

$$P_{\text{spv}-t} + P_{\text{wtg}-t} = P_{l-t} \quad (4)$$

$$P_{\text{spv}-t} + P_{\text{wtg}-t} > P_{l-t} \quad (5)$$

$$P_{\text{spv}-t} + P_{\text{wtg}-t} < P_{l-t} \quad (6)$$

where  $P_{\text{spv}-t}$ ,  $P_{\text{wtg}-t}$ ,  $P_{l-t}$  are the energies generated by SPV and WTG hourly and load demand for each hour. Eq. (4) represents a context where there is no change in the BESS energy level. In Eq. (5), the BESS is in charging mode, while Eq. (6) shows the discharging mode where the BESS acts to satisfy the unmet energy demand by the renewable generators.

$$E_{\text{batt}-t} = E_{\text{batt}-(t-1)} \cdot (1 - \sigma) + \left[ (E_{\text{gen}-t}) - \frac{E_{l-t}}{\mu_{\text{inv}}} \right] \mu_{\text{batt}} \quad (7)$$

$$E_{\text{batt}-t} = E_{\text{batt}-(t-1)} \cdot (1 - \sigma) - \left[ \frac{E_{l-t}}{\mu_{\text{inv}}} - E_{\text{gen}-t} \right] \quad (8)$$

where  $E_{\text{batt}-t}$ ,  $E_{\text{batt}-(t-1)}$  are energies stored in BESS within the hour and a previous hour, respectively;  $\sigma$  is the BESS losses rate;  $E_{\text{gen}-t}$ ,  $E_{l-t}$  are the energies generated by the renewable resources and energy required by the load within an hour;  $\mu_{\text{batt}}$ ,  $\mu_{\text{inv}}$  are the BESS and inverter efficiencies.

### 2.4 Objective Functions with Constraints

#### 2.4.1 Supply-Side Objective Function with Constraints

The optimisation problem is conceptualised using annualised cost ( $C_{\text{annual}}$ ) Eq. (9). Capital cost ( $C_{\text{cap}}$ ), maintenance cost ( $C_{\text{con}}$ ) and replacement cost ( $C_{\text{sub}}$ ) constitute annual cost. The decision variables are  $N_{\text{spv}}$ ,  $N_{\text{wtg}}$ , and  $N_{\text{batt}}$  representing the number of SPV, number of WTG and number of BESS. Equation (10) defines  $C_{\text{total}}$  total cost of a single component. Equation (11) interprets the NPC, a key indicator of the systems economic performance.  $\text{salvage}$  represents the salvage value at

the end of the project life time. Equation (12) computes COE with the unit in R/kWh. LPSP represented in Eq. (13) was incorporated to alleviate the diversity between renewable energy resources and demand, resulting in a more reliable HRES. Equation (14) constraints LPSP to assume a value between 0 and 0.01. Equations (15)–(17) limits the  $N_{spv}$ ,  $N_{wtg}$ , and  $N_{batt}$  to assume only non-negative integer values.

$$\text{Min } C_{\text{annual}} = (N_{spv} * C_{\text{total}} + N_{wtg} * C_{\text{total}} + N_{batt} * C_{\text{total}} + C_{\text{inv}}) \quad (9)$$

$$C_{\text{total}} = C_{\text{cap}} + C_{\text{con}} + C_{\text{sub}} \quad (10)$$

$$NPC = (N_{spv} * C_{\text{total}} + N_{wtg} * C_{\text{total}} + N_{batt} * C_{\text{total}} + C_{\text{inv}} + C_{\text{salvage}}) \quad (11)$$

$$COE = \frac{C_{\text{annual}}}{\text{load served}} \quad (12)$$

$$LPSP = \sum_0^T \frac{(P_l - P_{spv} - P_{wtg} + P_{soc-m})}{\sum_0^T P_l} \quad (13)$$

$$LPSP \leq 0.01 \quad (14)$$

$$N_{spv} \geq 0 \quad (15)$$

$$N_{wtg} \geq 0 \quad (16)$$

$$N_{batt} \geq 0 \quad (17)$$

#### 2.4.2 Demand-Side Objective Function and Constraints

$$\text{Min } C_{\text{electric}} = \sum_{m=1}^{24} \sum_{l=1}^L B_l V_{ml} P_m \quad (18)$$

$$\sum_{S_l}^{E_l} V_{ml} = Z_l \quad (19)$$

$$\sum_{l=1}^l B_l V_{ml} \leq PE_l \quad (20)$$



Equation (18) defines the demand-side objective function, which minimises electricity cost of all loads ( $C_{\text{electric}}$ ). Binary  $V_{ml}$  is the decision variable that can assume 0 or 1 indicating the on/off status of the load in the hour  $l$ . 24 hrs. are available.  $B_l, P_m$ , are the energy utilised by the load in each hr. (Wh) and cost of electricity for every hour in South African Rands (R/kWh) [24]. Equation (19) defines the constraints in charge of load flexibility, ensuring ample hours for the load, while  $S_l, E_l, Z_l$  are the start hour, end hour and a total number of hours required by a load to complete its task. The second constraint in Eq. (20) limits the stress on the power system where  $PE_l$  is the previous energy level of the system.

### 2.4.3 Integrated Multi-objective Function and Constraint

$$\text{Min } C_{\text{optimum}} = \omega * (C_{\text{annual}}) + \omega * (C_{\text{electric}}) \quad (21)$$

$$\omega + (1 - \omega) = 1 \quad (22)$$

The integrated multi-objective function of the nonlinear optimisation problem is to minimise the COE ( $C_{\text{optimum}}$ ) while satisfying all the demand and reliability constraints with optimality at the demand side aided by an appliance-scheduling strategy of the TOU-DR program (Eq. 21). A weighting factor  $\omega = 0.5$  is employed, having the limits represented by Eq. (22). This factor gives equal preference to both objective functions avoiding minimising/maximising an objective function at the detriment of the other [6, 7, 9].

## 3 Case Study

A 200W SPV, WTG rated 2000W with 12V 200Ah lead–acid BESS form the energy sources of the proposed HRES. We used hourly average temperature, wind speed and solar radiation obtained from Solar Radiation Data (SoDa) website for the dairy farm located in Roodepoort, near Johannesburg, South Africa (26.096°S and 27.911°E). The optimisation models were solved using AOA solver in Advanced Interactive Multidimensional Modelling System (AIMMS) software. The model was modified using data adapted from [14]. LPSP and NPC are the performance metrics for reliability and economics, respectively. Based on the degree of flexibility, demand-side loads were classified into three classes: flexible, night time and inflexible (Table 1) for the optimisation process, and the TOU data was adapted from [24].

**Table 1** Classification of demand-side load with data for the dairy farm case study

	$S_l$ (h)	$E_l$ (h)	$Z_l$ (h)	$B_l$ (Wh)
<i>Flexible</i>				
Load 1	1	24	18	5680
Load 2	12	16	3	5200
Load 5	1 and 13	12 and 24	6	5595
Load 6	1, 9 and 17	8, 16 and 24	3	746
Load 7	1	24	18	10
<i>Night-time</i>				
Load 8	21	24	2	746
Load 10	1	4	1	746
Load 11	1 and 17	6 and 24	10	746
<i>Inflexible</i>				
Load 3	8	16	8	260
Load 4	6	18	12	100
Load 9	1	24	24	1.5

### 4 Results and Discussions

Figure 1 illustrates the hourly load profile for the case study of dairy farm. Figures 2 and 3 depict the optimal power output profiles for renewable sources within the HRES. From Fig. 2, we can see that the SPV generated significant power for 10 hrs concurrently (6 am—4 pm). While in Fig. 3, the hourly output power of the WTG shows a considerable amount of power output from 9 am to 4 pm (7 hrs).

Table 2 summarises the optimisation results and then goes further to compare the two approaches considered in this study. Appliance-scheduling optimisation gives a better mix of resources, as far as cost and reliability are concerned, over the one without it. Cost savings of 63.61 and 63.62% were realised in the annualised cost and cost of energy, respectively. The economic value of the proposed HRES system

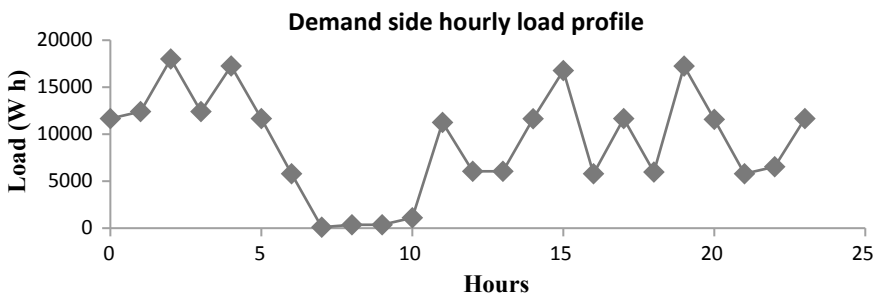


**Fig. 1** Demand-side hourly load profile

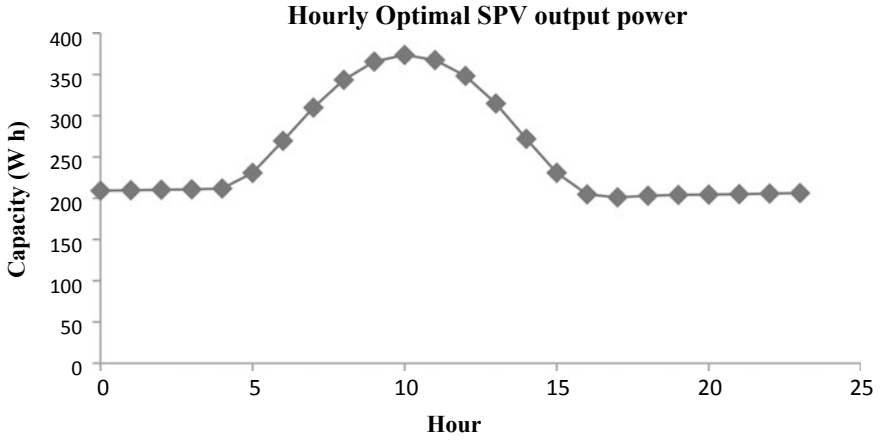


Fig. 2 Hourly optimal solar PV output power profile

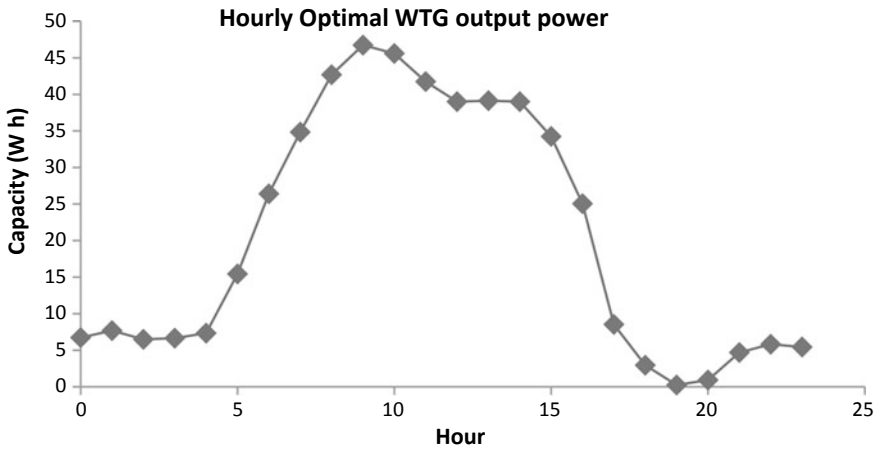


Fig. 3 Hourly optimal wind turbine generator output power profile

Table 2 Optimisation results

WTG capacity (W)	SPV capacity (W)	Strategy	$N_{wtg}$	$N_{spv}$	$N_{batt}$	$C_{annual}$ (R)	COE (R/kWh)
2000	200	Appliance scheduling exclusive	2	59	71	72,215.40	0.9029
2000	200	Appliance scheduling inclusive	0	43	45	26,276.44	0.3285

is further realised by computing simple payback time (SPB) [7] giving 9 years, 9 months and 25 days for the investors to realise their investment back.

## 5 Conclusion

This work presents an optimisation approach for sizing of solar PV, WTG and BESS based HRES for a dairy farm in South Africa. We integrated appliance-scheduling strategy TOU-DR program at the design stage of the autonomous HRES. The integrated model was set out to minimise the cost of energy (COE) of the system while satisfying the demand constraints. The formulated mixed-integer, nonlinear programming optimisation problem was solved using AIMMS outer approximation (AOA) module. Results obtained showed that optimal scheduling of the load demands using TOU-DR program has a positive effect on the design and operational cost of the entire autonomous HRES. A cost saving of R45,938.96 was achieved due to appliance scheduling.

## References

1. FAO (2011) The state of the world's land and water resources for food and agriculture (SOLAW)—Managing systems at risk. Food and Agriculture Organization of the United Nations, Rome and Earthscan, London.
2. White DJ, Hubacek K, Feng K, Sun L, Meng B (2018) The water-energy-food nexus in east Asia: a tele-connected value chain analysis using inter-regional input-output analysis. *Appl Energy* 210:550–567
3. Lehmann S (2018) Conceptualizing the urban nexus framework for a circular economy: linking energy, water, food, and waste (EWWF) in southeast-Asian cities. In: *Urban energy transition*, Elsevier, pp 371–398
4. Nwulu NI, Agboola OP (2012) Modelling and predicting electricity consumption using artificial neural networks. In: *2012 11th International Conference Environment Electrical Engineering EEEIC 2012-Conference Proceedings*, pp 1059–1063
5. Dincer I, Acar C (2014) Review and evaluation of hydrogen production methods for better sustainability. *Int J Hydrogen Energy* 40(34):11094–11111
6. Damisa U, Nwulu NI, Sun Y (2018) Microgrid energy and reserve management incorporating prosumer behind-the-meter resources. *IET Renew Power Gener* 12(8):910–919
7. Ma T, Javed MS (2019) Integrated sizing of hybrid PV-wind-battery system for remote island considering the saturation of each renewable energy resource. *Energy Convers Manag* 182:178–190 2018
8. Guangqian D, Bekhrad K, Azarikhah P, Maleki A (2018) A hybrid algorithm based optimization on modeling of grid independent biodiesel-based hybrid solar/wind systems. *Renew Energy* 122:551–560
9. Gbadamosi SL, Nwulu NI, Sun Y (2018) Multi-objective optimisation for composite generation and transmission expansion planning considering offshore wind power and feed-in tariffs. *IET Renew Power Gener* 12(14):1687–1697. <https://doi.org/10.1049/iet-rpg.2018.5531>

10. Belouda M, Hajjaji M, Sliti H, Mami A (2018) Bi-objective optimization of a standalone hybrid PV–Wind–battery system generation in a remote area in Tunisia. *Sustain Energy Grids Networks* 16:315–326
11. Hatata AY, Osman G, Aladl MM (2018) An optimization method for sizing a solar/wind/battery hybrid power system based on the artificial immune system. *Sustain Energy Technol Assessments* 27:83–93
12. Li M et al (2019) An optimal modelling approach for managing agricultural water-tenergy-food nexus under uncertainty. *Sci Total Environ* 651:1416–1434
13. Namany S, Al-Ansari T, Govindan R (2018) Integrated techno-economic optimization design and operations of energy, water and food nexus systems constrained as non-cooperative games. In: *Computer aided chemical engineering*, vol 44, Elsevier BV, pp 1003–1008
14. Houston C, Gyamfi S, Whale J (2014) Evaluation of energy efficiency and renewable energy generation opportunities for small scale dairy farms: a case study in Prince Edward Island, Canada. *Renew Energy* 67:20–29
15. Wamalwa F, Sichilalu SM, Xia X (2017) Optimal energy mix of a microhydro-wind-grid system powering a dairy farm in Western cape, South Africa. *Energy Procedia* 142:708–715
16. Shortall J, O'Brien B, Sleator RD, Upton J (2018) Daily and seasonal trends of electricity and water use on pasture-based automatic milking dairy farms. *J Dairy Sci* 101(2):1565–1578
17. Kuschke I, Geyer J (2016) Agriculture: market intelligence report, greencape, pp 1–60
18. Azar AG, Jacobsen RH (2016) Appliance scheduling optimization for demand response. 9(1): 50–64
19. Fahrioglu M, Nwulu NI (2012) Investigating a ranking of loads in avoiding potential power system outages. *Prz Elektrotechniczny* 88(11A):239–242
20. Nwulu NI, Fahrioglu M (2011) A neural network model for optimal demand management contract design. In: 2011 10th international conference environment electrical engineering EEEIC.EU 2011-conference proceedings, pp 1–4
21. Singh S, Singh M, Kaushik SC (2016) Feasibility study of an islanded microgrid in rural area consisting of PV, wind, biomass and battery energy storage system. *Energy Convers Manag* 128:178–190
22. Radhakrishnan BM, Srinivasan D (2016) A multi-agent based distributed energy management scheme for smart grid applications. *Energy* 103:192–204
23. Sawle Y, Gupta SC, Bohre AK (2018) Socio-techno-economic design of hybrid renewable energy system using optimization techniques. *Renew. Energy* 119:459–472
24. Eskom (2013) Schedule of standard prices for Eskom tariffs 1 April 2013 to 31 March 2014 for non-local authority supplies and 1 July 2013 to 30 June 2014 for local authority supplies. vol 0207, March, pp 1–48
25. Musasa K, Nwulu NI, Gitau MN, Bansal RC (2017) Review on DC collection grids for offshore wind farms with HVDC transmission system. *IET Power Electron* 10:2104–2115

# Cost Analysis of Hybrid Energy Storage System Benefits to Distribution Network Operators



Azizat Olusola Gbadegesin, Yanxia Sun, and Nnamdi Nwulu

**Abstract** Storage systems can be deployed on varying scales by different stakeholders. The stakeholders in grid-tied scenarios include residential, industrial or commercial consumers, distribution network operators, or transmission system network operators. For the purposes of this study, the distribution network operator has been selected as the primary beneficiary of the storage system. This study examines the economic benefits of investing in storage systems for distribution network operators. The consideration for time-of-use (ToU) rates, as they influence the operation of the storage system and in turn, the profit obtainable from a storage-in-distribution-network system, is considered. The economic analysis of the payback period for the investment in storage systems when the storage system provides energy arbitrage services only has been analysed under the ToU tariff schemes. For the distribution network operator owning a storage system, the payback period, when storage systems are incorporated into the network, ranges from 83 to 5 years when there is an increase in variation of consumer tariffs from 1 to 10% of the present electricity costs. Sensitivity analysis for other storage technology options is also considered and presented.

**Keywords** Distribution networks · Hybrid energy storage systems · Storage degradation cost · Payback period

---

A. O. Gbadegesin (✉) · Y. Sun · N. Nwulu  
University of Johannesburg, Johannesburg, South Africa  
e-mail: [azizatosg@gmail.com](mailto:azizatosg@gmail.com)

Y. Sun  
e-mail: [ysun@uj.ac.za](mailto:ysun@uj.ac.za)

N. Nwulu  
e-mail: [nnwulu@uj.ac.za](mailto:nnwulu@uj.ac.za)

# 1 Introduction

Recent upgrades to national grids and environmental concerns in many countries have seen an inclusion of renewable energy sources in national energy mixes. This inclusion has further led to the deployment of energy storage systems to handle intermittency of renewable energy sources, especially solar and wind sources. Other than intermittency, storage has also played a huge role in providing black-start services during grid outages [1], providing additional reliability and flexibility [2] and maintaining grid voltage by supplying reactive power to the system [3]. There is also a growing potential for energy storage systems in modern grid networks due to evolving energy demands in transportation and heating [1].

Storage systems have varying characteristics and constraints which make some more suitable than others in providing a particular service to a network. These may include the ability to charge and discharge rapidly to handle spikes and surges in demand and supply, or a high energy density to provide power during blackouts. The differing constraints which affect their suitability for a particular location also include requiring large volumes of water, the need for a large space for storage tanks or high capital costs. In this regard, a hybrid of two or more types of energy storage systems can be used to deliver a wider range of services required by the consumer [4]. In addition, having more than one type of storage in the network also helps to improve reliability, as the failure of one storage system would be handled by the second system, without interrupting normal system operation [1].

As the storage system owner (SSO), the distribution network operator (DNO), as shown in Fig. 1, invests resources into the design, building, operation and maintenance of a storage system. Apart from providing technical services to the consumers, the distribution network storage system owner's (DN-SSO) aim is to make maximum profit via energy trading and other services. The choice to act as a power supplier to the consumer to augment grid supply must also be balanced with acting as a consumer to the central grid operator while ensuring that customers' demands are met at all times [20]. While in operation, the degradation of the storage system must also be factored into the objective function to account for reduced efficiency after going through a number of charge–discharge cycles.

The practical problem that motivates this paper stems from: How can a DNO obtain maximum value from the inclusion of energy storage systems as part of its network infrastructure? In addition, a range of energy storage technologies abounds; which one is the most promising for the DNO to operate?

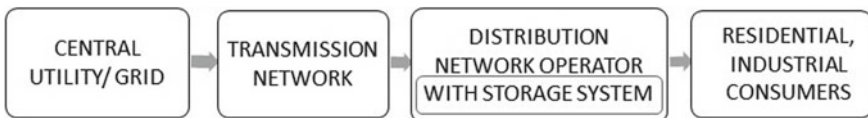


**Fig. 1** Storage incorporated within a grid-tied distribution network

The rest of the paper is organised as follows: a detailed literature review of energy storage systems and related literature is presented in Sect. 2. This is followed by the formulation of the mathematical model describing the system in Sect. 3. Section 4 presents the results and some cost analysis of variations in the network operating conditions. The study is concluded in Sect. 5.

## 2 Literature Review

Storage systems may be deployed within a network by a range of stakeholders, each having their own interests and expected benefits. These stakeholders include these three categories:

1. The consumer—residential, commercial and industrial consumers
2. The distribution network operator (DNO) as the storage system owner (DN-SSO)
  - The storage system owner (depending on grid supply only)
  - The storage system owner (depending on grid and owned-PV/wind power)
3. The transmission network operator [21]

The residential, commercial or industrial consumer seeks to make use of storage systems to provide power when there is a grid outage or when grid prices are high. An intelligent grid management system would take advantage of low grid prices to charge the storage system and run dispatchable electrical loads within the network. With these consumers, the ESS can provide reliable power during outages and replace back-up generators [3]. The DN-SSO invests in storage systems for technical, economical and environmental reasons—handling voltage fluctuations, energy arbitrage, peak shaving or reducing GHG emissions [5, 6]. The DNO can go further to include solar or wind power supply within the network to optimise the services offered by the installed storage system in their network. The transmission network invests in storage for network upgrade deferral, voltage regulation and improvements in transient stability [2].

A distribution network's operation was optimised to maximise profit when energy storage systems and distributed generation were incorporated in it [7]. The results of the study revealed that coordinated planning of the storage and distributed generation yielded increases in profits of 42, 37 and 59%, when distributed generation only, energy storage only and distributed generation-energy storage, respectively, were considered.

Based on the possible benefits of the storage system to different stakeholders [2], who sometimes have opposing interests, the optimisation of storage system operation must be done with consideration of its effect on the remunerability, which may vary for each stakeholder [8] and also depends on the incentive scheme being used [9]. For instance, under a ToU tariff scheme, a residential consumer seeks to minimise buying from the distribution network operator at peak periods and obtain maximum remuneration to make his storage investments profitable. A distribution



network operator on the other hand seeks to buy from the utility so that even when the customer demands reach peak periods, the high customer demands can be met while seeking to maximise remuneration [22–24].

Similarly, it is important to consider who the primary beneficiaries of the storage system's required function would be [8] in considering storage type, site and size to be deployed, as this affects the return on investment. In sizing a storage system performing energy arbitrage services in a distribution network, there needs to be a compromise between the invested capital and incomes realised from energy arbitrage [10]. When providing peak shaving services, high power and high energy capabilities of the storage system are required.

In an ideal situation when the beneficiaries do not have conflicting interests, one storage can serve multiple functions within the network and gain revenue for multiple services provided. However, this may not be a common case as the storage's performance in carrying out one function might be limited by other functions. One way to overcome this challenge is the inclusion of multiple storage systems within a network to obtain maximal functionality of the particular storage systems in the network [4]. Summarily, the objective of optimising storage system allocation involves a trade-off among the capital invested in the storage system, the services that the storage system can provide and the choice of storage technologies that can be considered [2].

Reviewed literature has considered the profitability of energy storage systems providing different services for a distribution network. As storage systems require consideration of both power and energy constraints unlike other conventional assets in a network [11], our work seeks to consider in detail the influence of the preceding time interval on profitability of the system. Therefore, while other works are limited to power demand constraints, which do not consider power demand or supply in the preceding time interval within the horizon, we have included time-dependent energy-related constraints in this study to give a more realistic approach to the operation of storage systems within a distribution network.

### 3 Methodology

A modified form of the IEEE 5-bus network [12] is used in this study. Buses 1–4 are selected as buses with residential consumers, while Bus 5 is selected as the bus for industrial consumers. The storage service considered in this study is the provision of energy arbitrage services.

Due to the huge variety of demand profiles available, peak demand, which is generally assumed for the demand profile, is not sufficient for proving the contribution of energy storage systems within a network [11]. Thus, in this study, the load profile is based on the IEEE 5-bus system peak demands (see Table 1), but modified to suit residential consumers at some buses and industrial consumers at one bus. The residential load profile framework from Eskom [13] is scaled to match the peak demand of the IEEE 5-bus data at each bus for every hour within a day. Similarly, the industrial load profile of [14] is used at Bus 5 and is scaled to match the IEEE 5-bus

**Table 1** IEEE 5-bus data: active loads at buses and lines

Bus	Peak power demand (MW)	Lines
1	0	1–2, 1–3
2	20	2–3, 2–4, 2–5
3	45	3–4
4	40	4–5
5	60	–

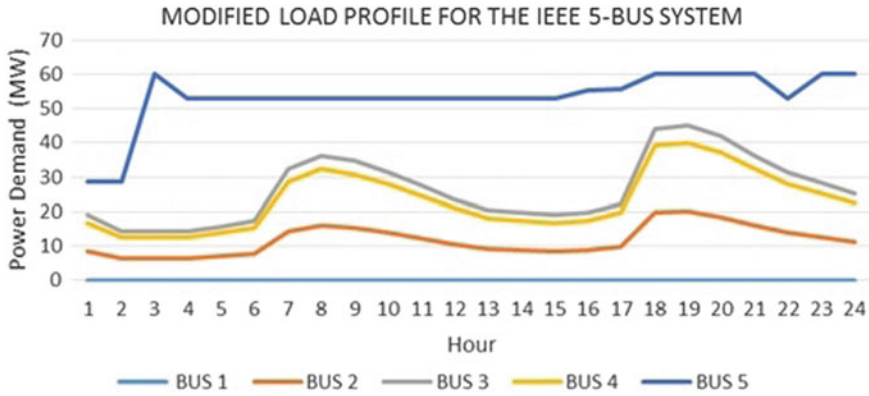


**Fig. 2** Hourly load profile

data. Thus, the demand at every hour comprises residential loads on Buses 2–4 and industrial loads on Bus 5. The resulting hourly load profile at all buses is presented in Fig. 2 below:

The objective of the model is to maximise profits from the sale of electricity to residential and industrial consumers, while considering degradation of the energy storage systems as shown in Eq. 1:

Maximise

$$\left( \sum_i^5 \sum_t^{24} P_{\text{dem}}(i, t) * \text{ToU}(i, t) - \sum_i^5 \sum_t^{24} P_{\text{grid}}(i, t) * C_{\text{munic}} \right) - (\mu_{s1} * P_{s1D}(i, t) + \mu_{s2} * P_{s2D}(i, t)) \tag{1}$$

The profit due from the storage system under the ToU is defined in Eq. 2.  $P_{\text{dem}}(i, t)$  and  $P_{\text{grid}}(i, t)$  represent the power demand from the consumer and power supplied by the grid respectively,  $\text{ToU}(i, t)$  are the electricity prices under time of use rates and  $C_{\text{munic}}$  is the cost of purchasing electricity from the central grid.  $\mu_{s1}$  and  $\mu_{s2}$  are the storage degradation costs for storage systems 1 and 2. The power discharged from storage systems 1 and 2 are represented by  $P_{s1D}(i, t)$  and  $P_{s2D}(i, t)$  respectively. Equations 3 and 4 define the sales of electricity to consumers,  $\text{ConSP}(i, t)$

which is a product of the power demanded by the consumers,  $P_{dem}(i, t)$ , and the time of use tariffs,  $ToU(i, t)$ . The cost of grid electricity ( $GridCP(i, t)$ ) purchased is shown in Eq. 4.

$$Act.Profit(i, t) = ConSP(i, t) - GridCP(i, t) \tag{2}$$

$$ConSP(i, t) = P_{dem}(i, t) * ToU(i, t) \tag{3}$$

$$GridCP(i, t) = P_{grid}(i, t) * CMunic \tag{4}$$

The constraints guiding the operations of system components in the distribution network are as shown in Eqs. 5– 9b below. Equation 5 depicts the power balance at buses within the day, where the balance of power within the network involves power generation and supply balancing out. The limits of the grid power supply are presented in Eq. 6, and the state of charge of the storage systems is presented in 7a and 7b.

$$\begin{aligned} &\sum_i^5 P_{grid}(i, t) + \sum_i^5 P_{S1D}(i, t) + \sum_i^5 P_{S2D}(i, t) \\ &= \sum_i^5 P_{dem}(i, t) + \sum_i^5 P_{S1C}(i, t) + \sum_i^5 P_{S2C}(i, t) \end{aligned} \tag{5}$$

$$P_{grid\ min}(i) \leq P_{grid}(i) \leq P_{grid\ max}(i) \tag{6}$$

$$ESOC_{s1}(i, t) = ESOC_{s1}(i, t - 1) + Ef_{s1} * P_{S1C}(i, t) - \left( \frac{P_{S1D}(i,t)}{Ef_{s1}} \right) \tag{7a}$$

$$ESOC_{s2}(i, t) = ESOC_{s2}(i, t - 1) + Ef_{s2} * P_{S2C}(i, t) - \left( \frac{P_{S2D}(i,t)}{Ef_{s2}} \right) \tag{7b}$$

These states of charge (SOC) of the energy storage systems are maintained between the highest and lowest SOC, to avoid possible overcharging or over discharging, as defined in 8a and 8b.

$$ESOC_{s1\ MIN} \leq ESOC_{s1}(i, t) \leq ESOC_{s1\ MAX} \tag{8a}$$

$$ESOC_{s2\ MIN} \leq ESOC_{s2}(i, t) \leq ESOC_{s2\ MAX} \tag{8b}$$

Simultaneous charging and discharging of the storage systems are prevented as shown in Eqs. 9a and 9b:

$$P_{c_{s1}}(i, t) * P_{d_{s1}}(i, t) = 0 \tag{9a}$$

**Table 2** Time-of-use tariffs for residential and industrial consumers in summer

		Residential	Industrial
	Hours	Summer charges (c/kWh)	Summer charges (c/kWh)
Peak	07–10, 18–20	162.57	155.99
Standard	06–07, 10–18, 20–22	128.60	117.44
Off-peak	00–06, 22–00	101.17	90.28

$$Pc_{s2}(i, t) * Pd_{s2}(i, t) = 0 \tag{9b}$$

Other data used in the model include the electricity tariffs of CityPower consumers as shown in Table 2 [15].

## 4 Results

The model is run with the data presented in the tables above using the CPLEX solver of the Advanced Interactive Multidimensional Modeling Software (AIMMS). The system daily profit with and without storage systems installed in the network is obtained from the simulation results. These results show the profit from buying electricity from the central utility at Municflex rates (CMunic (\$/MWh) of R583, (equivalent to \$38.33/MWh) was compared with when storage was included in the system. The HESS storage configuration considered in this analysis is a lithium-ion and lead–acid battery hybrid.

Without storage systems, a daily profit from sales of electricity under the ToU tariff system was realised as \$267,265. In this case, as there is no storage, all power obtained from the grid is immediately sold to the consumer at the ToU rates. It should be noted that this is not the actual profit generated by the distribution network, as other expenses such as network demand charges, transmission network charges, environmental levies and administrative charges are also borne by the distribution network operator daily and would reduce this value. However, for the purposes of this study, it is assumed that this is the profit received daily.

In comparison, when storage systems are included in the network, it was observed that:

$$\beta_A = \text{Total daily revenue without storage} = \$267,265$$

$$\beta_B = \text{Total daily revenue with storage} = \$265,672$$

$$\text{Savings made from system, } \beta_{AB} = \beta_B - \beta_A = -\$1593$$

On a superficial level, this simply implies that the inclusion of a storage system is not profitable to the distribution network operator under the existing conditions. However, a detailed analysis of some influencing factors presented below will give another perspective.

#### **4.1 Sensitivity Analysis I—Increasing ToU Tariffs**

As current electricity ToU tariffs (shown in Table 2) were used in the first cost analysis, a consideration for a 1–10% increase in tariff paid by the consumer shows the daily savings due to the inclusion of storage systems (Table 3):

##### **Payback Period**

The payback period is an economic analysis tool used to assess the time it would take to recover the capital costs invested in an energy storage system [16]. A simple payback period is used in this study and is described in Eq. 10 as [17]:

$$\text{Payback period} = \frac{\text{Cost of the storage system}}{\text{Annual cost savings}} \quad (10)$$

For a storage system to be deemed as profitable, the best scenario would be to have a payback period less than its lifetime [16]. Thus, from preceding results, the annual savings and payback periods at slightly increased consumer tariffs from 1 to 10% of the current consumer ToU tariff are presented in Table 4:

From the results presented in Table 4, the most beneficial tariff for the customer is the one in which there is at least 10% increment in the current time-of-use tariff rates, due to the lifetime of the storage used (lithium-ion and lead–acid HESS).

#### **4.2 Sensitivity Analysis II—Comparison of Different Storage Technologies**

Each storage type has particular characteristics associated with it. These include the roundtrip efficiency, power density, energy density, lifetime, response time, technology maturity, storage duration, etc. [18]. The technically viable energy storage system options for distribution networks include batteries, hydrogen fuel cell (HFC) systems, flywheel energy storage systems, supercapacitors and superconducting magnetic energy storage systems [18]. The charging and discharging efficiencies of the energy storage systems are assumed to have the same value [19].

A compromise between the cost and performance using the data provided in Table 5 is used to compare some of these technologies.

**Table 3** Daily revenue from the distribution network with increase in consumer tariffs

\$	1%	2%	3%	4%	5%	6%	7%	8%	9%	10%
\$β <sub>A</sub>	267,265.11	267,265.11	267,265.11	267,265.11	267,265.11	267,265.11	267,265.11	267,265.11	267,265.11	267,265.11
\$β <sub>B</sub>	269,413.37	273,154.36	276,895.34	280,636.33	284,337.32	288,118.31	291,859.30	295,600.28	299,341.27	303,082.26
\$β <sub>AB</sub>	2,148.26	5,889.25	9,630.24	13,371.22	17,112.21	20,853.20	24,594.19	28,335.18	32,076.16	35,817.15

**Table 4** Annual savings and payback period

	Annual savings ('000 \$)	Payback period (years)
1%	784.11	83.33
2%	2149.58	30.4
3%	3515.04	18.59
4%	4880.5	13.39
5%	6245.96	10.46
6%	7611.42	8.59
7%	8976.88	7.28
8%	10342.33	6.32
9%	11707.8	5.58
10%	13073.26	5

**Table 5** Data of costs and efficiency ranges of different storage systems [3, 17]

Storage technology	Cost ('000 \$/MW)	Cost ('000 \$/MWh)	Efficiency
Battery—lead–acid	300–600	200–400	0.63–0.90
Battery—lithium-ion type	1200–4000	600–2500	0.75–0.97
Battery—sodium sulphur	1000–3000	300–500	0.75–0.90
Hydrogen fuel cell	10,000	1,650	0.20–0.66

**Table 6** Annual savings and payback period for the lithium-ion battery-hydrogen fuel cell HESS

	0%	1%	5%	10%
Annual savings ('000 \$)	–1,672.24	2,068.75	17,032.70	35,737.64
Payback period (years)	–144.40	116.73	14.18	6.76

For this study, another HESS considered is the lithium-ion battery-hydrogen fuel cell hybrid. The payback period with this HESS is presented in Table 6.

The results from Table 6 show that under the existing ToU tariffs scheme, the lithium-ion battery hydrogen fuel cell HESS only becomes profitable when there is at least a 1% increase in the current tariff regime. In addition, it can be seen that the payback period, when there is a 10% increase in the current tariff, is 6.76 years.

## 5 Conclusion

The profitability of inclusion of energy storage systems when providing energy arbitrage services within a distribution network is influenced by a number of factors—the technology type, the capacity, existing tariff rates, lifetime of the storage technology,

etc. A few of these factors have been analysed in this study to highlight the influence they have on the payback period of storage systems within a network under the time-of-use tariff. This analysis would assist distribution network operators in choice of storage technologies that can be deployed to ensure that the investment on storage systems is profitable. Further work on this study will include the profit analysis when the storage system is providing other services such as peak shaving, voltage regulation, etc., concurrent with energy arbitraging.

## References

1. Brandon NP, Edge JS, Aunedi M, Barbour ER, Bruce PG, Chakrabarti BK, Esterle T et al (n.d.) UK research needs in grid scale energy storage technologies. [http://energysuperstore.org/wp-content/uploads/2016/04/IMPJ4129\\_White\\_Paper\\_UK-Research-Needs-in-Grid-Scale-Energy-Storage-Technologies\\_WEB.pdf](http://energysuperstore.org/wp-content/uploads/2016/04/IMPJ4129_White_Paper_UK-Research-Needs-in-Grid-Scale-Energy-Storage-Technologies_WEB.pdf)
2. Lorente JL, Liu XA Best R, Morrow DJ (2018) Energy storage allocation in power networks—a state-of-the-art review. In: Proceedings of 2018 53rd International University Power Engineering Conference UPEC 2018, pp 1–6
3. Wong LA, Ramachandaramurthy VK, Taylor P, Ekanayake JB, Walker SL, Padmanaban S (2019) Review on the optimal placement, sizing and control of an energy storage system in the distribution network. *J Energy Stor* 21:489–504
4. Gbadegesin AO, Sun Y, Nwulu NI (2019) Techno-economic analysis of storage degradation effect on levelised cost of hybrid energy storage systems. *Sustain Energy Technol Assess* 36:100
5. Das CK, Bass O, Kothapalli G et al (2018) Overview of energy storage systems in distribution networks: placement, sizing, operation, and power quality. *Renew Sustain Energy Rev* 91:1205–1230
6. Bozchalui MC, Sharma R (2014) Operation strategies for energy storage systems in distribution networks. In: IEEE Power and Energy Society General Meeting, vol 2014
7. Saboori H, Hemmati R (2017) Maximizing DISCO profit in active distribution networks by optimal planning of energy storage systems and distributed generators. *Renew Sustain Energy Rev* 71:365–372
8. Hartmann B, Vokony I, Sorés P, Táci I (2019) Service aspect assessment of energy storage under the ownership of distribution system operators. *J Energy Storage* (25)
9. Gbadamosi SL, Nwulu NI, Sun Y (2018) Multi-objective optimization for composite generation and transmission expansion planning considering offshore wind power and feed in tariffs. *IET Renew Power Gen* 12(14):1687–1697
10. Chen C, Que B, Zhou Z et al (2018) Cost-benefit analysis of distributed energy storage in distribution grids with renewables. In: 2018 international conference on power system technology: powercon 2018
11. Konstantelos IG, Strbac G (2018) Capacity value of energy storage in distribution networks. *J. Energy Storage* 18:389–401
12. 'APPENDIX 1 IEEE 5-BUS SYSTEM DATA'. [Online]. Available [https://shodhganga.inflibnet.ac.in/bitstream/10603/26549/14/14\\_appendix.pdf](https://shodhganga.inflibnet.ac.in/bitstream/10603/26549/14/14_appendix.pdf)
13. Eskom, 'Eskom Homeflex'. Available at [http://www.eskom.co.za/ Customer-Care/TariffsAndCharges/Documents/Eskom%20Booklet.pdf](http://www.eskom.co.za/Customer-Care/TariffsAndCharges/Documents/Eskom%20Booklet.pdf)
14. Paudyal S, Cañizares CA, Bhattacharya K (2015) Optimal operation of industrial energy hubs in smart grids. *IEEE Trans Smart Grid* 6(2):684–694
15. CityPower, 'Schedule of Approved Electricity Tariffs for FY2019/20'. [Online]. Available: <https://www.citypower.co.za/ReportsandDocuments/ScheduleofApprovedTariffs.1920.pdf>
16. Fong G, Moreira R, Strbac G (2017) Economic analysis of energy storage business models. *IEEE Manchester Power Tech*



17. Grantham A, Pudney P, Ward LA et al (2017) The viability of electrical energy storage for low-energy households. *Sol Energy* 155:1216–1224
18. Alhamali A, Farrag ME, Bevan G, Hepburn DM (2017) Review of Energy Storage Systems in electric grid and their potential in distribution networks. In: 2016 18th international middle-east power systems conference, MEPCON 2016—proceedings, pp 546–551
19. Fedjaev J, Amamra SA, Francois B (2016) Linear programming based optimization tool for day ahead energy management of a lithium-ion battery for an industrial microgrid. In: Proceedings IEEE international power electronics and motion control conference PEM, pp 406–411
20. Nwulu NI, Agboola PO (2012) Modelling and predicting electricity consumption using artificial neural networks. In: Proceedings of the 11th international conference on environmental and electrical engineering (EEEIC2012), Venice, Italy, 18–25 May 2012
21. Musasa K, Nwulu NI, Gitau MN, Bansal RC (2017) Review on DC collection grids for offshore wind farms with HVDC transmission system. *IET Power Electr* 10:2104–2115
22. Damisa U, Nwulu NI, Sun Y (2018) Microgrid energy and reserve management incorporating prosumer behind-the-meter resources. *IET Renew Power Gener* 12(8):910–919
23. Fahrioglu M, Nwulu NI (2012) Investigating a ranking of loads in avoiding potential power system outages. *J Electr Rev (Przegląd Elektrotechniczny)* Warsaw, Poland 88(11a):239–242
24. Nwulu NI, Fahrioglu M (2011) A neural network model for optimal demand management contract design. In: Proceedings of the 10th international conference on environmental and electrical engineering (EEEIC2011), Rome, Italy, 8–11 May 2011

# The Awareness and Obstacle Factor of Machine Maintenance Toward Total Productive Maintenance in Manufacturing Company



**Yunos Ngadiman, Md Fauzi Ahmad, Nor Aziati Abd Hamid, Raja Zuraidah Raja Mohd Rasi, Kamilah Ahmad, and Nor Hadilah Abdul Hamid**

**Abstract** Total productive maintenance (TPM) is intended to enhance equipment effectiveness and overall efficiency by introducing a comprehensive product management system to maintain equipment life, including equipment related to planning, applications, maintenance, and related matters. The participation of all employees from top management to floor worker level is fundamental in the implementation of TPM. It starts with management motivation or voluntarily to be developed by starting with small group activities. The objective of this research is to prepare an awareness procedure and explore the obstacle factors in machine maintenance toward TPM. Besides, this study intends to suggest the highest obstacle factors that appear in machine maintenances. In this study, 60 machine technicians randomly from manufacturing companies in Malaysia. The data collection instrument is to apply quantitative methods by distributing questions to respondents. In this study, awareness of machine maintenance and barrier factors in the maintenance of the machine is discussed.

## 1 Introduction

The sense of overall maintenance of technical skills is to maintain or control all parts to fulfill the functions required in the life expectancy [1]. The maintenance process is essential to keep up with all the work carried out to ensure that all equipment in the manufacturing system or service will work with the planned productivity targets [2]. Maintenance is one of the key roles in determining the strategic goals of a challenging organization today [3]. The maintenance process by the correct procedure

---

Y. Ngadiman (✉) · M. F. Ahmad · N. A. A. Hamid · R. Z. R. M. Rasi · K. Ahmad · N. H. A. Hamid

Department of Production and Operation Management, Faculty of Technology and Business, Faculty of Technology Management and Business, Universiti Tun Hussein Onn Malaysia Raja, Batu Pahat, Johor, Malaysia  
e-mail: [yunos@uthm.edu.my](mailto:yunos@uthm.edu.my)

is the easiest way toward production performance with a high productivity guarantee [4]. This process includes planned and unplanned goals to keep physical assets in a normal operating environment. This process aims to stabilize the reliability, safety, availability, and quality of manufacturing, equipment or building production at a minimal cost [5]. In the past, maintenance functions have been considered a stressful process and are not taken care of by organizational management. Only maintenance operations are limited when needed to repair and maintain during emergency hours. Obstacle factor means something that impedes the movement of the process or an obstacle or intentionally to make things worse [6]. In this research, the factors affecting machine maintenance processes will affect the performance of TPM in the manufacturing industry [7].

## **2 Research Background**

In the context of the business environment in the early 2000s, issues that arose were concerned with the reduction of the workforce or the reduction of labor. These efforts will impact the direct involvement of employees in implementing the TPM program [7]. The activity of TPM is derived from support by middle management [8]. Meanwhile, line workers began to contribute ideas to increase productivity because they knew their machines were in perfect condition [8]. Although most senior managers are not raised in machine operations, they are focusing on productivity and reduce production costs while focusing on increasing profits. Thus, the employee's involvement in implementing the TPM becomes less attention and thus, it affected the success of the TPM program [4].

### ***2.1 Research Problems***

Nowadays, most manufacturing companies suffered from significant losses/wastes from the manufacturing division. The level of quality management in manufacturing is particularly important in terms of raw material management, operation times, and the reputation of the company which is difficult to disclose [5]. Besides, other residues that not visible due to the speed of operation of the machine, loss of starting residue, engine breakdown, and bottleneck control [9]. Zero-oriented target concepts such as zero-tolerance for breakdown, spacing and zero accidents have become a prerequisite in the manufacturing and installation industry. In this regard, in addressing these issues, the concept of TPM has been adopted in many industries around the world [4]. The main objectives of the TPM program are to increase productivity and quality in line with increasing employee motivation and job satisfaction [5]. Maintenance before breakdown is the best step as a process of adding value in improving organizational performance [6]. It is also an important condition for the prolonged

lifespan of machining [7]. TPM is an innovative approach to maintenance to maximize equipment efficiency, prevent engine malfunctions, and introduce maintenance concepts through daily work activities that involve a large workforce [3].

In the difficulty of implementing TPM, it requires multiple procedures and takes a long time [9]. The smooth implementation of the TPM depends on the investment of the organization. Among the obvious side effects is the lack of support from management as they do not understand the final goals of the TPM program [8]. Management considers only production management and maintenance of employees. However, the results were not stimulating but rather a negative impact [4]. The success of TPM implementation will require the full support and commitment of top management, a greater sense of ownership and responsibility, cooperation and engagement of both operators and maintenance employees and disciplinary attitudes [8].

## **2.2 Research Objectives**

- (1) Identify the awareness and obstacle factor in machine maintenance toward TPM in a manufacturing company.
- (2) Prepare the awareness procedure in machine maintenance toward TPM in a manufacturing company.

## **3 Literature Review**

This section covered the concept and definition of awareness and obstacle factors in machine maintenance.

### **3.1 Awareness**

The meaning of consciousness is the knowledge that something exists or understands the current state of information or experience [3]. The goal of this course is to ensure that each participant will:

- determine the strategies required by performing machine maintenance
- identify the importance of data structure before work strategy begins
- identify to categorize assets
- understand different types of maintenance
- assessing the total likelihood of being involved in performing proper maintenance analysis
- identify similarities and differences in strategies

- spearhead the implementation of the Maintenance Strategy Study on the impact of replacement parts
- learn the classification of specific equipment that requires the right strategy.

### **3.2 *Obstacle Factors in Machine Maintenance***

#### **3.2.1 Definition**

- (1) The purpose of the obstacle is that it impedes forward movement or impedes action or makes it more difficult. This study was to study the factors of inhibition in machine maintenance against TPM in manufacturing companies [8]. The following are some of the difficulties faced by companies when starting the TPM program [4]:
- (2) The main difficulty is changing the attitude of the workers.
- (3) Most consider it a monthly activity and doubt its effectiveness.
- (4) It does not provide people who can train and does not provide sufficient funds and time.
- (5) Workers consider it extra work or burden.
- (6) The middle and upper managements do not clearly understand TPM.
- (7) Most consider the TPM to be owned by the maintenance division only.
- (8) Workers think that TPM does not carry out activities on the shop floor but workers are burdened with production targets only.
- (9) Lack of education and training in TPM.
- (10) Support to weak TPM team members in carrying out their activities.

## **4 Total Productive Maintenance (TPM)**

### **4.1 *Definition***

TPM is a productivity improvement practice that is considered to be equivalent to total quality management (TQM) [7]. It demonstrates the concept of Japanese equipment management to significantly improve equipment performance in a manufacturing company with the support and involvement of all employees [8]. The objective of the TPM is to continuously increase availability and prevent before the breakdown to equipment for maximum effectiveness. This objective requires strong management support as well as continuous teamwork and small group activities [8]. TPM starts with 5S activity [10]. The success of 5S is a decisive step in continuing the TPM. The 5S is considered the basis of TPM implementation and 5S activity emphasizes more on hygiene and layout. Unsuccessful workplaces are a major cause of problems [9]. Problems can be detected and seen if they are not properly organized. If the 5S

is not taken seriously, then it will lead to 5Ds being delayed, defective, dissatisfied customers lowered profits and disliked employees.

## **5 Preventive Maintenance**

Preventive maintenance (PM) is the basis of maintenance practiced in manufacturing to facilitate the production process and to improve the efficiency of equipment [11]. PM activities are organized according to work priorities and arrangements, preparation of labor resources, timeframes for performing tasks and planning of raw materials and parts [8]. Preventive maintenance (PM) programs have proven their effectiveness by effectively reducing machine failure rates [11].

## **6 Methodology**

### ***6.1 Introduction***

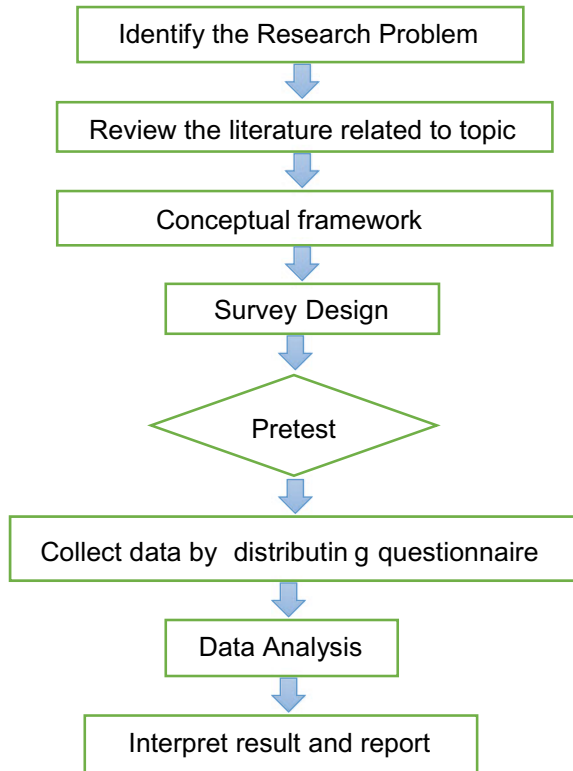
The methodology in this study is the method used in analyzing the systematic theory. Discussions on problem-solving, design, methods, research frameworks, and hypotheses [12], population studies, sampling techniques, and sampling frameworks, sample size, data measurement, and statistical analysis [13].

### ***6.2 Research Design***

Quantitative methods are the one way of providing the phenomenon with the collection of numerical data that are mathematically analyzed [14]. This method is particularly useful as it can identify the relationship between production machine maintenance, and maintenance consumption in the manufacturing industry [15]. All data were analyzed using SPSS software [16].

### ***6.3 Research Process***

See Fig. 1.

**Fig. 1** Research flow-chart

#### **6.4 Respondents**

Quantitative study method where random sampling is used to determine sample size [17]. The random samples selected to represent each unit in the population have similar opportunities. This study aims to population is the production machine operators of the manufacturing companies in Klang Valley. The respondents were chosen randomly from different manufacturing companies.

#### **6.5 Data Collection Instrument**

This study is made up of questions that are divided into three parts. The first part contains the questionnaire on respondents' demographic information [18], the second section covers the maintenance factor of machine maintenance with five items per dimension, while the third part is maintenance usage [19]. Measure each item in the second and third sections using a Likert scale with five points ranging from value 1 strongly disagree until value 5 strongly agree [18].

### 6.6 Pre-test of the Questionnaire

A pre-test is a very important step to reduce the errors associated with a survey [20]. The pre-test in the present study is conducted with ten production machine workers in different manufacturing companies from the sample to test the reliability of the questionnaire [18]. After pre-testing, the questionnaire was distributed to machine maintenance technicians in the manufacturing company [7].

### 6.7 Data Analysis

The data obtained were analyzed using the Statistical Package for Social Science (SPSS) version 22.0 [13]. SPSS is a software that is capable of managing and analyzing large-capacity data by producing fast and accurate results in the form of tables and graphs [21], whereas descriptive analysis works to identify data and characteristics related to the population or phenomenon under study [13]. Correlation relationships were used to measure inference statistics to identify factors of awareness and barriers to TPM [19] at manufacturing companies in the Klang Valley.

## 7 Data Analysis and Findings

Company profile distribution, reliability values, descriptive statistics, and normality test were presented in this chapter. Finally, the correlation test of the hypotheses was conducted to determine its significant level and interpret the final result [21] (Table 1).

### 7.1 Company Profile Analysis

The result shows that most of the respondents are male; there are four of the respondents with 80% of them while 16 of the respondents with 20% are female.

**Table 1** Frequency of gender

	Frequency	Percent
Male	64	80
Female	16	20
Total	100	100



**Table 2** Frequency of industry

	Frequency	Percent
Textile and clothing	15	18.75
Furniture	27	33.75
Paper and printing	8	10.0
Rubber or plastic	4	5.0
Non-metallic minerals	16	20.0
Machinery fabrication	10	10.0
Total	80	100.0

**Table 3** Frequency of job position

	Frequency	Percent
Production technician	12	15.0
Machine technician	45	56.25
Maintenance technician	23	28.75
Total	80	100.0

**Table 4** Frequency of technical working experience

	Frequency	Percent
Less than 1 years	4	5.0
1–5 years	20	25.0
5–10 years	40	50.0
More than 10 years	16	20.0
Total	80	100.0

Table 2 shows that most of the respondents are from furniture industries which 27 of the total respondents or 33.75%, while the least was from rubber or plastic industries which 4 of the respondents or 5%.

Table 3 shows that most of the respondents are machine technicians with the number 45 or 56.25%, followed by maintenance technicians which are 23 or 28.75% of the respondents and the least are production technicians which are 12 or 15.0% of the respondents.

Table 4 shows that most of the respondents had 5–10 years of technical working experience which was 40 (50%) of the respondents. Only 4 technicians have the technical working experience fewer than 1 year or 5%.

## 7.2 Reliability Analysis

Reliability analysis can be defined as the testing of consistency. In this research, Cronbach's alpha was used to determine the internal reliability [21]. For Cronbach's

**Table 5** Reliability statistics

Section	Variable	Cronbach alpha ( $\alpha$ )	Result
B	Obstacle factor in maintenance	0.712	Good
C	Awareness of maintenance	0.725	Good

alpha with a value below 0.7, improvements need to be made by discarding the problematic items from the group of questions to increase the alpha value [18].

Table 5 shows the value of Cronbach alpha ( $\alpha$ ) for the pilot test done in terms of obstacle factors in the maintenance and awareness of maintenance. The Cronbach alpha value for the pilot test of obstacle factor in maintenance is 0.712, and for awareness of maintenance is 0.725, it is an agreeable and valid questionnaire.

### 7.3 Descriptive Analysis

Descriptive analysis is a method of describing the study sample. Its function is to obtain the mean value and standard deviation [21]. If results are obtained with lower standard deviation values, then they are closer to the average value of the data. Table 5.10 illustrates the level of mean measurement at the level of central tendency [13].

### 7.4 Data Analysis and Results

#### 7.4.1 Summary of Analysis on Obstacle Factor

Table 6 shows the average mean score of the ten obstacle factors of machine maintenance toward TPM in the manufacturing companies and its ranking. The highest point to point out here is that technicians do not know what the appropriate problem is causing the machine to breakdown with the highest score of 3.8750, followed by the organizational feel that the organization does not have enough workers to perform maintenance [7], so the maintenance takes longer to work with the value of 3.5000.

Third place is that the engineer does not know how to make the inspection base for the machine before it breaks down to 3.35. Technicians feel that the organization does not provide machine maintenance training and it makes them not careful to do well maintenance once again with the value of 3.3000 and the technician does not know when the machine needs maintenance before it stops working with the value of 3.1000 in fifth place. Sixth and seventh places are too old technical think engineers, making the arrangement more difficult and technicians feel that the organization does not update maintenance knowledge, which makes them unable to perform well

**Table 6** Obstacle factor in maintenance

Obstacle factor	Average mean score	Ranking
Technicians do not know when a machine needs for maintaining before it stops function	3.1000	5
Technicians do not know what the appropriate problems due to breakdown	3.8750	1
Technicians do not know how to perform the basic inspection for the machine	3.3500	3
Technicians think that the maintenance step harder due to the machine is too old	3.0000	6
Technicians do not have the freedom and right to do the maintenance procedure	2.8500	8
Technicians feel the organizations do not provide machine maintenance training, lacked understanding in maintenance very well	3.3000	4
Technicians feel the organizations do not update the maintenance knowledge and influenced the maintenance performance	2.9000	7
Technicians feel the organization does not prepare enough budget to do the maintenance, affected by unable on-time maintenance	2.4000	10
Technicians feel the organizations do not have enough employees to do the maintenance	3.5000	2
Technicians feel the organization do not have proper personal protective equipment (PPE) to do the maintenance	2.7000	9

with values of 3.0000 and 2.9000. Technicians have no freedom and the right to perform their maintenance steps at eighth place with a value of 2.8500 and followed by technicians feel that the organization has no proper personal protective equipment (PPE) to perform maintenance [7], it makes maintenance run slowly and becomes more difficult and For technicians to feel that the organization does not provide enough budget for maintenance, it creates a damaged component that cannot replace the time and suspend maintenance with values of 2.7000 and 2.400. So, from this analysis, the technicians do not know the causes of the machine breaking down with the highest value 3.8750. It is the main obstacle factor in the machine maintenance toward TPM in the manufacturing companies in Klang Valley.

#### 7.4.2 Summary of Analysis on Awareness in Maintenance

Table 7 shows the average mean score of awareness in maintenance and its ranking. The highest analysis shows that technicians have maintenance planning and machine maintenance schedules to reduce unnecessary breakdowns and barriers with a mean

**Table 7** Summary of analysis on awareness in machine maintenance

Awareness in machine maintenance	Average mean score	Ranking
The technician should have maintenance planning and schedule on machine maintenance to prevent unnecessary breakdown and obstacle	4.8000	1
The technician should have their freedom and right to do every single step in machine maintenance	3.2000	3
The organizations should increase more technicians to reduce the obstacle factors of machine maintenance	2.9000	4
The organizations should increase the budget on machine maintenance	3.4000	2
The organizations should prepare maintenance courses for the technicians to increase their awareness and knowledge about machine maintenance	2.7000	5

score of 4.8000. Likewise, organizations should increase their budget in the maintenance of machines with a value of 3.4000. Third place onward is a technician must have his freedom and the right to do every step in the maintenance of the machine and the organization should increase more technicians to help reduce the factors that prevent the maintenance of the machine to increase total productivity with values of 3.2000 and 2.9000. Organizations should provide maintenance courses for technicians to increase their awareness in fifth place with the lowest average score of 2.7000. So, we knew the majority of the technicians think they should have maintenance planning and schedule on machine maintenance to reduce unnecessary breakdown [11] and obstacle factor of machine maintenance toward TPM in a manufacturing company in Klang Valley.

## 8 Discussion and Conclusion

In the following subchapters, the discussion was done to answer the study questions stated in this study. This study was conducted to identify the awareness and obstacle factor in the machine maintenance toward TPM in the manufacturing companies [9]. Additionally, it aimed to suggest an awareness procedure in machine maintenance toward TPM in the manufacturing companies.

### 8.1 Awareness Procedure

According to the results shown in Chap. 4, the main obstacle for technicians in machine maintenance is that they do not know the cause of the engine failure. The

next step for a technician is to provide a plan and a maintenance schedule for the machine to prevent damage [22].

Maintenance work is an important issue in manufacturing companies [5]. The maintenance process is not only focused on repair and replacement parts but also planning maintenance work.

Corrective maintenance (CM) and preventive maintenance (PM) operations must be planned [17]. Implementing a CM does not require a large amount of labor and less labor cost. This will have minimal impact on maintenance costs, whereas, PM is a basic maintenance technique applied in the manufacturing environment to facilitate production flow and improve equipment efficiency. PMs are usually scheduled on a daily, weekly, monthly, or appointed time basis [5].

The role of PM is important in designing maintenance schedules that are effectively coordinated with production scheduling, affecting efficiency and effectiveness in the manufacturing system [10]. Therefore, production planning and PM activities can be carried out to avoid re-planning [10].

So, a good preventive maintenance schedule can effectively reduce the breakdown [20] and the six maintenance planning principles are very important in the schedule [22]. When all six of these principles are used and combined correctly, maintenance planning can reach new levels.

- (1) Separate department
- (2) Focus on future work
- (3) Component-level files
- (4) Estimate job based on planner expertise
- (5) Recognize the skills of the craft
- (6) Measure performance with work sampling

The management should manage the schedule to avoid wasting work. The implementation of PM has proven that the rate of machine breakdown has been reduced and the production performance has improved [8].

## **8.2 Conclusion**

Finally, various knowledge and learning related to awareness and factors in machine maintenance against TPM at a manufacturing company in Klang Valley [9]. The majority of technicians face obstacles in their work, and they do not take it as a serious issue that causes productivity performance to decline. After the completion of this project, the implementation of TPM has an impact on productivity [9]. All the obstacle factors in machine maintenance need to be taken seriously and to increase the awareness of technicians to improve their productivity performance. The implementation of PM has proven that the rate of machine damage can be significantly reduced [20]. PMs are also not routinely implemented as they require precise planning on the maintenance dates of each machine [22]. However, the situation in the busy manufacturing industry has proven that PM operations are not effective [6]. The

lack of skilled manpower and the maintenance of a tight schedule are the factors that prevent the impact of achieving research objectives.

### 8.3 Future Study

This study is more of an exploratory study and is limited to case studies at a Malaysian-based company. It will benefit future researchers to research in case study mode where generalization ability can be identified. This case study can be done at manufacturing companies across Malaysia. The suggestion for future study is they can set up with additional procedures except this and planning maintenance procedure not only on manufacturing company, and other fields [22]. The analysis done due to machine downtime factors has created a technical problem which is usually caused by improper maintenance work to prove the importance of implementing PM.

**Acknowledgements** We thank the sponsorship of this research to the Center for Research and Commercialization, Universiti Tun Hussein Onn Universiti Malaysia (UTHM), for providing this research opportunity. The results of this research will benefit to all researchers who intend to enhance their knowledge in the similar field.

## References

1. Blanchard BS, Verm D, Peterson EL (1995) Maintainability: a key to effective and maintenance management. Wiley, New York, NY
2. Pintelon LM, Parodi-Herz A (2006) Maintenance: an evolutionary perspective. Complex System Maintenance Handbook, Springer Series in Reliability Engineering
3. Van Horenbeek A, Pintelon L, Muchiri P (2010) Maintenance optimization models and criteria. *Int J Syst Assur Eng Manag* 1(3):189–200
4. Kocher G, Kumar R, Singh A, Dhillon SS (2012) An approach for total productive maintenance and factors affecting its implementation in manufacturing environment. *Int J Emerg Technol* 3(1):41–47
5. Parida A, Kumar UU (2006) Maintenance performance measurement (MPM): issues and challenges. *J Qual Mainten Eng* 12(3):239–251
6. Swanson L (2001) Linking maintenance strategies to performance. *Int J Prod Econ* 70:237–244
7. Mwanzaa BG, Mbohwa C (2015) Design of a total productive maintenance model for effective implementation: a case study of a chemical manufacturing company. *Ind Eng Serv Sci IESS* 2015, p 462
8. Heizer J, ve Render B (2012) Operations management (11 edn). USA, Pearson Education Inc., ISBN-10: 0132921146. ISBN-13: 978-0132921145 Prentice Hall
9. Smith R, Hawkins B (2004) Lean maintenance: reduce costs; improve quality and increase market share. Butterworth-Heinemann Publication, Massachusetts
10. Singh R, Gohil AM, Shah DB, Desai S (2012) Total productive maintenance (TPM) implementation in a machine shop: a case study. Chemical, Civil and Mechanical Engineering Tracks of 3rd Nirma University International Conference on Engineering
11. Murray M, Fletcher K, Kennedy J, Kohler P, Chambers J, Ledwidge T (1996) Capability assurance: a generic model of maintenance. Maintenance Engineering Society of Australia

12. Midasm (2015) Best practise of maintenance planning and scheduling, genesis solutions, an ABS Group Company
13. Marquez AC (2007) The maintenance management framework, Springer, 2007 edition, ISBN-10: 1846288207. ISBN-13: 978-184628820
14. Hair JF, Black WC, Babin BJ, Anderson RE (2011) Multivariate data analysis, 7th edn. China Machine Press, Beijing
15. Aliaga M, Gunderson B (2005) Interactive statistics, 3rd edn. Pearson Education Inc, Upper Saddle River, NJ
16. Bryman A, Cramer D (2005) Quantitative data analysis with SPSS 14. Psychology Press, New York
17. Krathwohl DR (1998) Methods of educational and social science research: an integrated approach, reading. Longman, Massachusettes
18. Cavana RY, Delahaye BL, Sekaran U (2001) Applied business research: qualitative and quantitative methods. Wiley, Milton, Queensland
19. Krejcie RV, Morgan DW (1970) Determining sample size for research activities. *Educ Psychol Measur* 30:607–610
20. Dhillon BS (2006) Maintainability, maintenance, and reliability engineering. CRC Press Taylor & Francis Group, Florida
21. Sortrakul N, Nachtmann HL, Cassady CR (2005) Genetic algorithm for integrated preventive maintenance planning and production scheduling for a single machine. *Comput Ind* 56:161–168
22. Jonsson P (1997) The status of maintenance management in Swedish manufacturing firms. *J Qual Mainten Eng* 3(4):233–258
23. Neuman WL (2012) Basics of social research: qualitative and quantitative approaches. Pearson, Boston. Norman WT (2012) Toward an adequate taxonomy of personality attributes: Replicated factor structure in peer nomination personality ratings. *J Abnorm Soc Psychol* 66:574–583 (1963)
24. Ab-Samat H, Jeikumar LN, Basri EI, Harun NA, Kamaruddin S (2012) Effective preventive maintenance scheduling. School of Mechanical Engineering Universiti Sains Malaysia

# A Multifractal Study of Al Thin Films Prepared by RF Magnetron Sputtering



F. M. Mwema, Esther T. Akinlabi, O. P. Oladijo, Stephen A. Akinlabi, and S. Hassan

**Abstract** In this article, a multi-fractal approach has been employed to study the micromorphology of sputtered aluminium films by radio frequency magnetron sputtering method. The films were prepared at 150 and 200 W on stainless and mild steel substrates of 50 mm by 50 mm by 3 mm dimensions. The substrates and targets were maintained at room temperature. The surface microstructures of the films were imaged using atomic force microscopy (AFM). The images were then subjected to the cube counting method to calculate the fractal dimension ( $D$ ) and multifractal analysis to comprehend the complex nature of the sputtered Al films. The results show that the fractal dimension increases with power for mild steel substrates and decreases with RF power for stainless steel substrates. The multifractal behaviour determined through mass exponent as a function of moment order, singularity strength as a function of singularity exponent, and generalized fractal dimension as a function of moment order reveals that all the films are multifractal in nature.

**Keywords** Aluminium · Atomic force microscopy (AFM) · Microstructure · Multifractal theory · Substrates · Radio-frequency sputtering · Sputtering power · Thin films

---

F. M. Mwema (✉) · E. T. Akinlabi · O. P. Oladijo  
Department of Mechanical Engineering Science, University of Johannesburg,  
Auckland Park Campus, Johannesburg 2006, South Africa  
e-mail: [fredrick.mwema@dkut.ac.ke](mailto:fredrick.mwema@dkut.ac.ke)

F. M. Mwema  
Department of Mechanical Engineering, Dedan Kimathi University of Technology,  
Private Bag, 10143 Nyeri, Kenya

O. P. Oladijo  
Department of Chemical, Materials and Metallurgical Engineering,  
International of Science and Technology, Private Bag, 16, Palapye, Botswana

S. A. Akinlabi · S. Hassan  
Department of Mechanical Engineering, Walter Sisulu University,  
Butterworth Campus, South Africa



## 1 Introduction

The quantitative analysis of structure/topography of films is significant since most of their properties (such as optical, electrical, and tribology) and performance depend on surface morphology [1]. Atomic force microscopy (AFM) is used in acquiring morphological data of thin films due to its versatility and high resolution. As such, AFM has been extensively used to obtain morphological information of various thin films [2–5]. Various information on the properties of thin films can be obtained from AFM micrographs including surface roughness, grain sizes, growth mechanism, defects/porosity, lateral behaviour, distribution of structures, and so forth [6, 7]. In analysing AFM data, both statistical and fractal methods have been used in published works [8, 9]. Fractal geometry has been shown to provide detailed descriptions of complex surfaces and thereby enhancing understanding of morphology–property relationship of thin films. Through fractal theory, self-affinity, scaling laws, and lateral roughness of thin films have been described [2].

Aluminium thin films are widely used in optical, microelectronics, and solar devices due to the low resistivity, high reflectance, and availability of bulk aluminium [10]. Various methods of depositing Al thin films have been described [11–13], and sputtering has emerged as one of the most attractive methods since it deposits films at low temperatures [10]. Al thin films deposited by magnetron sputtering exhibit fractal behaviour as earlier reported [5, 9, 14, 15]. Notably lacking in the literature is the multifractal behaviour/studies of Al thin films deposited on metal substrates. In this study, therefore, multifractal characterization of Al thin films grown by RF magnetron sputtering is presented.

## 2 Methods

The experimental procedure used in this research was detailed in our earlier articles [14, 15]. In summary, the thin aluminium films were sputtered on steel substrates using the HHV TF500 deposition system (manufactured by HHV Limited, UK). The deposition was undertaken at 28 °C and at 150 and 200 W. The microstructure properties of these samples were determined using scanning electron microscopy and X-ray diffraction measurements and reported earlier [14].

The atomic force microscope (AFM) measurements used in this paper were described in detail in reference [14] in which statistical and mono-fractal (power spectral density function) analyses of the AFM micrographs were explained. The AFM images were obtained using Nanoscope 3100 Dimension AFM equipment in non-contact mode at ambient conditions in air.

### 3 Results and Discussion

Figure 1 shows 3D representative AFM micrographs for all the samples used in this study. The films deposited at 150 W for both films which consist of small and closely packed surface structures, whereas those deposited at 200 W have large and interconnected structures, indicating structural evolution with RF power. The AFM micrographs were binarized into 8-bit and then the threshold was applied to identify the surface features (Fig. 2). The values of  $D$  were computed by the box counting method, which uses the log–log plots of the number  $N(\epsilon)$  and size  $\epsilon$  of grids enough to cover the pixels of the image. A convergence study was used to determine the minimum number of grids to compute the accurate fractal dimensions in all the surfaces. The graph of the fractal dimension against the number of boxes is shown in Fig. 3, and as observed, 500 boxes were enough to accurately determine the fractal dimensions for all the samples.

The computed fractal dimensions ( $D$ ) for all the samples are summarized in Table 1. It is observed that samples on stainless steel surfaces prepared at both powers have very close values of  $D$  ( $\approx 1.6$ ), indicating similar fractal (lateral) surfaces are obtained at these powers. However, films deposited on mild steel substrates have very different fractal dimension values ( $\approx 1.5$  at 150 W and  $\approx 1.6$  at 200 W) indicating that increasing power from 150 to 200 W results in lateral growth during sputtering of Al

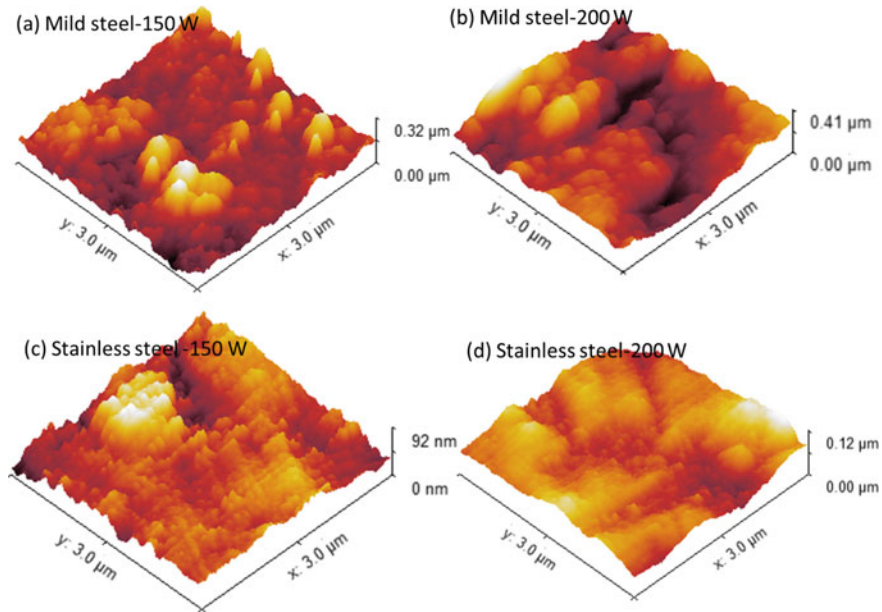


**Fig. 1** Representative 3D AFM images taken at scan area of  $3 \times 3 \mu\text{m}^2$  on the top surfaces of the aluminium thin films

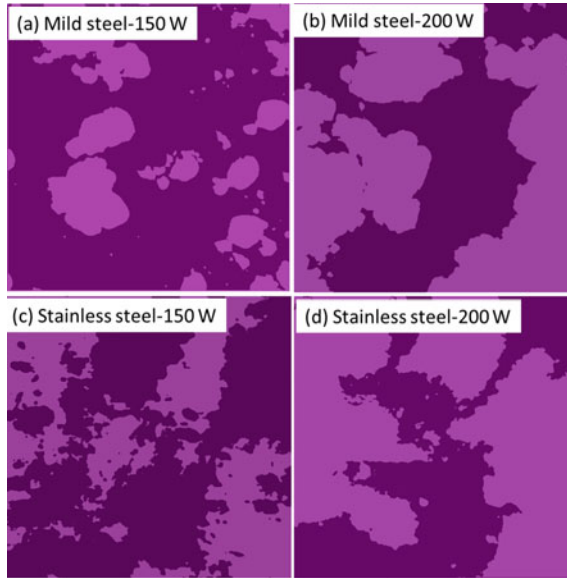


Fig. 2 Image processing for multifractal analysis of AFM micrographs shown in Fig. 1

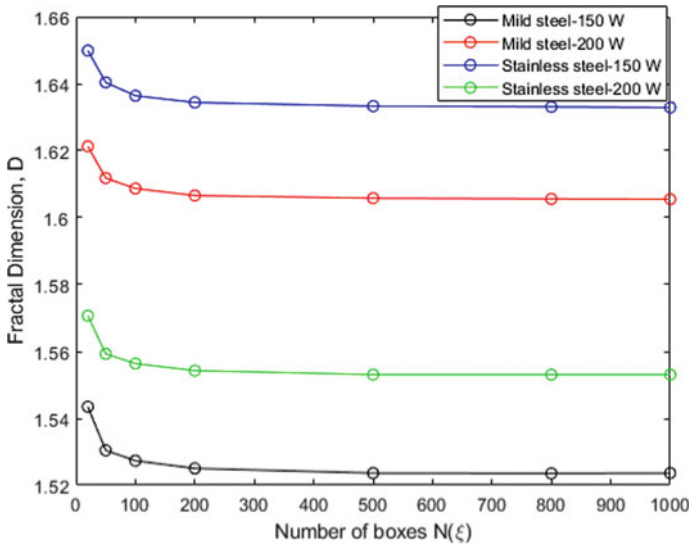


Fig. 3 Fractal dimension ( $D$ ) versus number of boxes ( $N(\epsilon)$ ). The values of  $D$  converged between 400 and 500 boxes. These results indicate that  $N = 500$  is enough for computation of fractal dimensions for all the surfaces in Fig. 1

**Table 1** Fractal and multifractal parameters of Al thin films grown on different substrates and powers

Samples	$\alpha_{min}$	$\alpha_{max}$	$\Delta\alpha$	$f(\alpha_{min})$	$f(\alpha_{max})$	$\Delta f(\alpha)$	$D$
MS 150 W	1.3560	2.1290	0.7730	1.3047	0.9278	0.3769	1.5230
MS 200 W	1.3000	1.9817	0.6817	1.2849	0.3741	0.9108	1.6060
SS 150 W	1.4952	2.0920	0.5968	1.4932	0.8333	0.6599	1.6330
SS 200 W	1.3642	2.100	0.7358	1.3642	0.5377	0.8265	1.5530

thin films. For all the surfaces, the values of fractal dimensions ( $D$ ) are observed to vary from one point to another indicating existence of multifractality of these films.

A multifractal analysis was then undertaken following the algorithms described in references [9, 16]. In these analyses, plots of mass exponent function ( $\tau(q)$ ) against moment order ( $q$ ) multifractal spectrum or singularity strength ( $f(\alpha)$ ) against singularity index ( $\alpha$ ) and generalized fractal dimension ( $D(q)$ ) versus  $q$  are used to characterize the multifractal behaviour of the Al films [17]. The graphs of these results are represented in Figs. 4, 5, and 6, respectively.

The mass exponent function,  $\tau(q)$ , is computed in the range of  $-10 < q < 10$  with steps of 0.2, and the results are presented in Fig. 4. As seen, the  $\tau(q)$  exhibits a nonlinear relationship with  $q$  for all the surfaces indicating that these films are multifractal. It has been reported that in computation of  $\tau(q)$ , larger values of  $q$  are not statistically significant due to small data sizes and therefore small range of  $q$  should be used [18]. The nonlinearity for all the surfaces is nearly equal, and all the curves exhibit an ‘inflection’ region about  $q = 0$ .

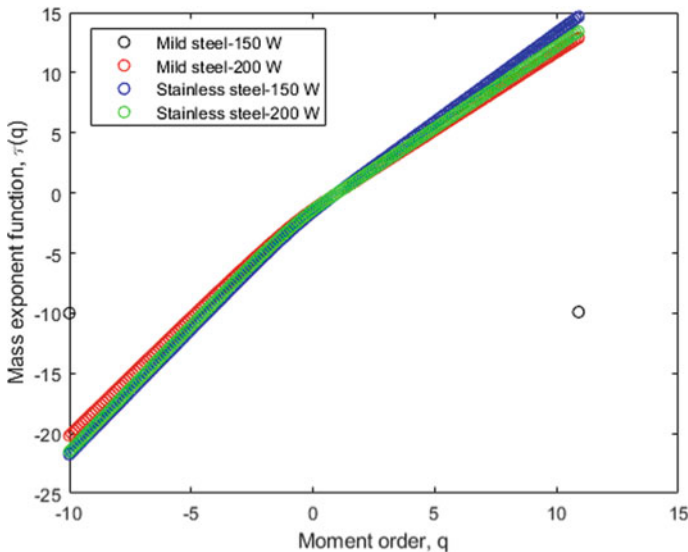


**Fig. 4** Mass exponent function ( $\tau(q)$ ) profiles for the sputtered Al thin films

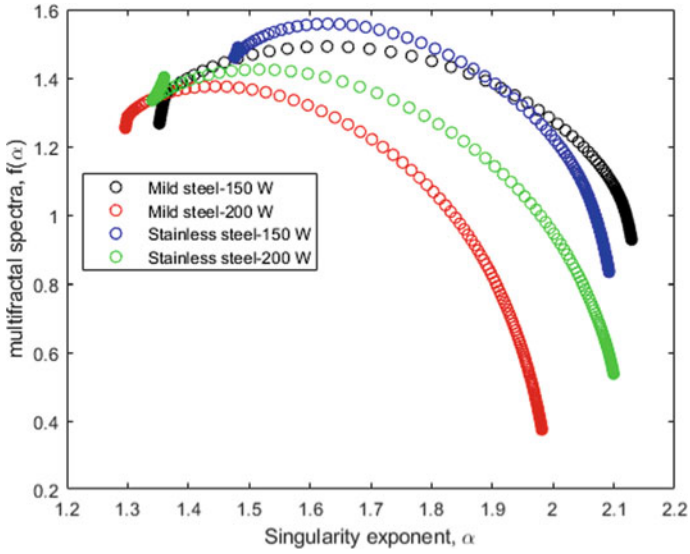


Fig. 5 Plots of singularity strength,  $f(\alpha)$ , versus singularity index,  $\alpha$  for the sputtered Al film samples

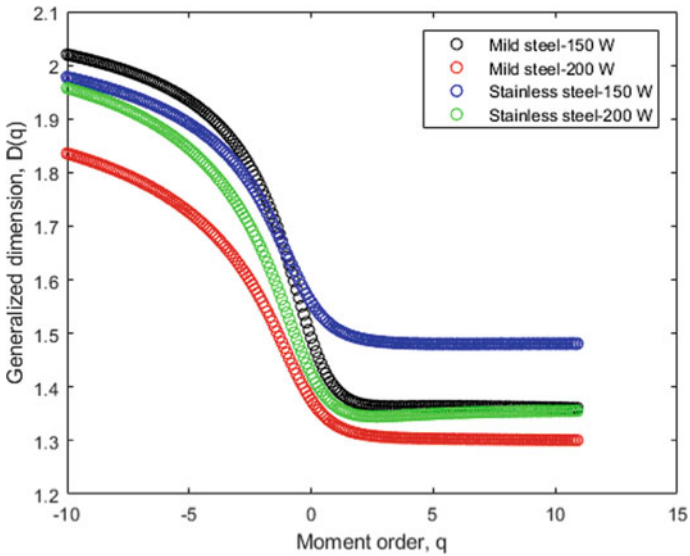


Fig. 6 Generalized dimension,  $D$ , as a function moment order,  $q$  of aluminium thin films at different powers

In Fig. 5, the singularity strength ( $f(\alpha)$ ) is expressed as a function of singularity index,  $\alpha$ . It is observed that  $f(\alpha)$  is a continuous function of  $\alpha$  and that width ( $\Delta\alpha$ ) and profile of each spectrum are different for all samples (Table 1). Additionally, all the spectra exhibited hook-like shapes skewed to the right with tips to the left. The highest value of  $\Delta\alpha$  can be observed on mild steel films at 150 W, whereas the lowest value is obtained on stainless steel substrates deposited at 150 W. It therefore means that the films sputtered on mild steel at 150 W have the highest average height surface features, whereas the stainless steel samples prepared at 150 W have the lowest height features as it was reported in our earlier results [14]. The samples with small values of  $\Delta\alpha$  are said to be less multifractal [1, 18]. The differences in fractal dimensions,  $\Delta f(\alpha) = f(\alpha_{\min}) - f(\alpha_{\max})$ , for all the samples are also shown in Table 1, and all the values are positive, which is consistent with the left hook-like profiles.

Figure 6 shows the generalized fractal dimension  $D$  plotted against  $q$ . As can be seen, the  $D(q)$  decreases with  $q$  confirming the multifractal behaviour of the films. There is a slower decrease in  $D(q)$  with  $q$  for samples on stainless steel surfaces at 150 W, which indicates that the films have less multifractality. All the plots show a point of inflection at  $q = 0$ , which are indicative of multifractal surfaces [9].

## 4 Conclusions

A multifractal analysis on the atomic force microscope (AFM) micrographs of Al thin films sputtered on mild and stainless steel samples at 150 and 200 W is presented in this article. There is no significant difference between the fractal dimensions ( $D$ ) for stainless steel samples prepared at both powers. For mild steel substrates, fractal dimension  $D = 1.5230$  is obtained at 150 W, which is considerably lower than that obtained at 200 W ( $D = 1.6060$ ). Mass exponent function ( $\tau$ ) exhibits a nonlinear relationship with moment order ( $q$ ) for all the samples indicating that all the surfaces are multifractal. The singularity strength parameters and generalized fractal dimensions confirmed the existence of multifractal behaviour of the films. It is also observed that the stainless steel samples at 150 W exhibit the lowest multifractal characteristics.

**Acknowledgements** The Global Excellence and Stature (GES) 4.0 funding for Postdoctoral Research Fellowship by the University of Johannesburg is acknowledged.

## References

1. Yadav RP, Dwivedi S, Mittal AK, Kumar M, Pandey AC (2012) Fractal and multifractal analysis of LiF thin film surface. *Appl Surf Sci* 261:547–553
2. Yadav RP, Kumar M, Mittal AK, Dwivedi S, Pandey AC (2014) On the scaling law analysis of nanodimensional LiF thin film surfaces. *Mater Lett* 126:123–125
3. Mwema FM, Akinlabi ET, Oladijo OP, Majumdar JD (2019) Effect of varying low substrate temperature on sputtered aluminium films. *Mater Res Expr* 6(5):056404
4. Dallaeva D, Talu S, Stach S, Skarvada P, Tomanek P, Grmela L (2014) AFM imaging and fractal analysis of surface roughness of AlN epilayers on sapphire substrates. *Appl Surf Sci* 312:81–86
5. Mwema FM, Oladijo OP, Akinlabi ET (2018) Effect of substrate temperature on aluminium thin films prepared by RF-magnetron sputtering. *Mater Today Proc* 5(9):20464–20473
6. Aqil M, Azam M, Aziz M, Latif R (2017) Deposition and characterization of molybdenum thin film using direct current magnetron and atomic force microscopy. *J Nanotechnol* 2017:1–10
7. Mwema FM, Akinlabi ET, Oladijo OP (2019) Complementary investigation of SEM and AFM on the morphology of sputtered aluminum thin films. In: Proceedings of the eighth international conference on advances in civil, structural and mechanical engineering—CSM, pp 10–14
8. Hosseinpanahi F, Raoufi D, Ranjbarghanei K, Karimi B, Babaei R, Hasani E (2015) Fractal features of CdTe thin films grown by RF magnetron sputtering. *Appl Surf Sci* 357:1843–1848
9. Mwema FM, Akinlabi ET, Oladijo OP (2019) Fractal analysis of hillocks: a case of RF sputtered aluminum thin films. *Appl Surf Sci* 489:614–623
10. Mwema FM, Oladijo OP, Akinlabi SA, Akinlabi ET (2018) Properties of physically deposited thin aluminium film coatings: a review. *J Alloy Compd* 747:306–323
11. Avinun M, Barel N, Kaplan WD, Eizenberg W, Naik M, Guo T, Chen LY, Mosely R, Littau Y, Zhou S, Chen L (1998) Nucleation and growth of CVD Al on different types of TiN. *Thin Solid Films* 320(1):67–72
12. Elajel MA, Sbeta SM (2008) Deposition of thin aluminum film on acrylic substrate using physical vapor deposition technique (PVD). *Metal*, pp 2–6
13. Khachatryan H, Lee S, Kim KB, Kim HK, Kim M (2018) Al thin film: the effect of substrate type on Al film formation and morphology. *J Phys Chem Solids* 122:109–117
14. Mwema FM, Oladijo OP, Sathiaraj TS, Akinlabi ET (2018) Atomic force microscopy analysis of surface topography of pure thin aluminium films. *Mater Res Expr* 5(8):1–15
15. Mwema FM, Oladijo OP, Akinlabi ET (2019) The use of power spectrum density for surface characterization of thin films. In: Yang X-Y (ed) *Photoenergy and thin film materials*. Wiley, Hoboken, NJ, USA, pp 379–411
16. Xu Y, Qian C, Pan L, Wang B, Lou C (2012) Comparing monofractal and multifractal analysis of corrosion damage evolution in reinforcing bars. *PLoS ONE* 7(1):1–8
17. Țălu S, Morozov IA, Yadav RP (2019) Multifractal analysis of sputtered indium tin oxide thin film surfaces. *Appl Surf Sci* 65(3):294–300
18. Nasehnejad M, Gholipour SM, Nabiyouni G (2016) Atomic force microscopy study, kinetic roughening and multifractal analysis of electrodeposited silver films. *Appl Surf Sci* 389:735–741

# Influence of Elbow Orientation on Solid Particle Erosion for Multiphase Flow



Rehan Khan, H. H. Ya, William Pao, Armaghan Khan, R. Zahoor, and Tauseef Ahmed

**Abstract** Erosive wear of equipment in hydrocarbon and mineral processing pipelines can occur under multiphase flow. The 90° elbow configuration is a common flow changing device in the pipeline network used to redirect the flow direction. This paper highlights a CFD approach to study erosion-induced damage in 90° elbows due to the transportation of sand particles in the carrier phase. A discrete phase modeling (DPM) technique is employed to decouple the relationship of elbow orientation and erosion-induced damage in 90° elbows. The computational geometry and simulation parameters consist of horizontal to horizontal (H–H), horizontal to vertical (H–V), and vertical to horizontal (V–H) orientated 90° elbows with 50.8 mm inner diameter and fine sand of 50  $\mu\text{m}$  size entrained in a liquid phase at 5 m/s flow velocity. The high erosion zones have been located near the outlet of the 90° elbow under fine particle impact with a maximum erosion rate of 5.5 mm/year in horizontal–vertical (H–V) oriented elbow.

**Keywords** Erosion · Multiphase flow · 90° elbow · CFD

## 1 Introduction

Hydrocarbon production process involving the sand particles transpiration entrained in a carrier phase induces erosion damage. Erosion may cause severe detriment to production equipment and devices and affect the operating safety and life of production equipment. [1–3]. Practical wall interaction within the flow changing devices

---

R. Khan (✉) · H. H. Ya · W. Pao · T. Ahmed  
Mechanical Engineering Department, Universiti Teknologi PETRONAS, Bandar Seri Iskandar,  
Tronoh Perak, Malaysia  
e-mail: [Muhammad\\_15001294@utp.edu.my](mailto:Muhammad_15001294@utp.edu.my)

A. Khan  
Department of Mechanical Engineering, McGill University, Macdonald Engineering Building,  
817 Sherbrooke Street, West Montreal, Canada

R. Zahoor  
Laboratory for Fluid Dynamics and Thermodynamics, Faculty of Mechanical Engineering,  
University of Ljubljana, Aškerčeva 6, 1000 Ljubljana, Slovenia



(i.e., elbows, tee, and valves) is the ultimate cause of erosion which induces damage [2]. Although sand collectors and separators are widely installed in pipelines to avoid the progression of solid particles, the transit of fine particles in pipes is unavoidable. Fine particles are mainly sand particles with sizes less than  $62\ \mu\text{m}$ , which can generate erosive effects on pipelines. These particles affect operational safety and reduce the flow efficiency of production processes. To understand the erosion-induced damage due to sand particles [4] and factors influencing erosion in terms of the target wall properties, carrier fluid characteristics, and erodent properties, various investigations were directed in previous studies [5–7]. To quantify the erosion intensity and damage in the wide range of geometries under different flow conditions, erosion equations should be implemented into CFD codes. Because of the significance of computational techniques in erosion quantification, a range of studies has been done by scholars for complex geometries [8–13].

Duarte et al. [14] identified that the adoption of coupling techniques may essentially alter the erosion pattern of the elbows. Zhang et al. [2] described a probability-based technique to predict sand erosion of pipes under multiphase flow. Jafari et al. [15] developed an equation to measure erosion by considering the effect of fluctuating velocity of the liquid phase in a horizontal pipe using the discrete random walk model with a turbulence model. For the present study to quantify erosion rate and particle trajectories, DPM approach was introduced in simulation stages with discrete random walk model in simulation parameters which was used to extract the erosion profile for different elbow configurations.

Many numerical and experimental efforts have been directed to investigate the wear of flow changing devices in the liquid–solid flow. Unfortunately, these studies were initiated to find the maximum erosion rate of the complete elbow configuration. Only a few studies were found that attempted to decouple the relationship of elbow orientation and erosion zone distribution for the  $90^\circ$  elbow. The study of the elbow in erosion research is significant since it is the common configuration that has the most influence on erosion failure under industrial operating conditions [16]. In the current work, the influential effect of elbow orientation on sand erosion was studied using computational fluid dynamics simulation. Furthermore, the relationship between elbow orientation and turbulence intensity in the elbow pipe has been discussed.

## 2 Computational Fluid Dynamics (CFD) Simulations

The ANSYS FLUENT code was employed for current research of erosive wear quantification. CFD tools offer the advancement of computational capabilities in providing better accuracy of solving flow physics in complex geometries. The geometrical configuration of the CFD model consists of the carbon steel elbow with an inner radius of 0.0254 m and radius of curvature  $1.5D$  as shown in Fig. 1a. For computational study, hexahedral mesh (Fig. 1b) with 0.003 m elements size was used for all the simulations and mesh independence study with model validation is presented in

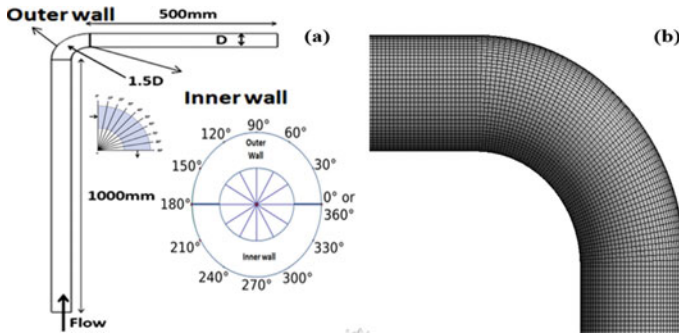


Fig. 1 90° Elbow a computational geometry, b computational mesh

the previous research [17]. For the present study to extract erosion rate and particle trajectories (discrete phase modeling), DPM approach was introduced in simulation stages with discrete random walk model. Typical silica sand of 50 μm was used as erodent medium in the carrier fluid. For the current work, the carrier liquid phase is water with a flow velocity of 5 m/s, and the solid phase is fine particles with a 2.5% (w/w) concentration.

### 3 Results and Discussion

#### 3.1 Relation of Elbow Orientation with Erosion Zone and Particle Trajectories

The relationship of elbow orientation on the high erosion zone for liquid–solid flow is studied using the CFD modeling technique details outlined in Sect. 2. To analyze the elbow orientation and the erosion zone relationship in more details, Figs. 2, 3, and 4 show the erosion contour of horizontal–horizontal (H–H), horizontal–vertical (H–V), and vertical–horizontal (V–H) elbow orientation under the same flow velocity. Figures 2, 3, and 4 show that with changing elbow orientation, the position of erosion gradually changes from the bottom half to upper half section of the elbow. As shown in particle track in Fig. 5a–c, multiple particles will impact downstream with larger kinetic energy which travel from the inlet to elbow outlet and then cause severe erosion between axial location 75° and 90° for all orientations. Additionally, the area of low erosion zone changes with the change of elbow orientation as outlined in Fig. 5a–c. The results in Fig. 6a reflect that for the 90° elbow with identical geometric configuration, the orientation of the elbow significantly contributes to escalating the high erosion zone. Furthermore, the erosion rate significantly changes with the change of elbow orientation as shown by distribution in Fig. 6b. However, the maximum erosion location will not significantly change with a change in elbow

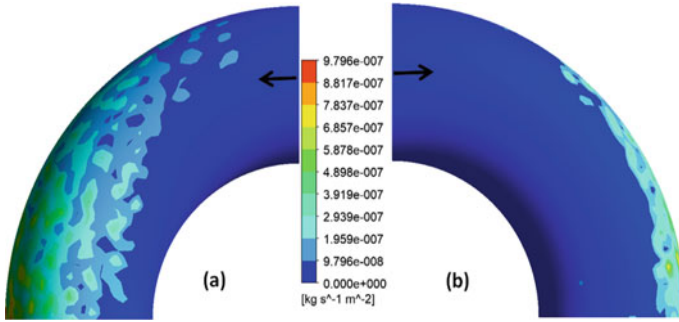


**Fig. 2** Erosion rate contour for H–H 90° elbow outer wall at transportation velocity 5.0 m/s **a** bottom view, **b** upper view

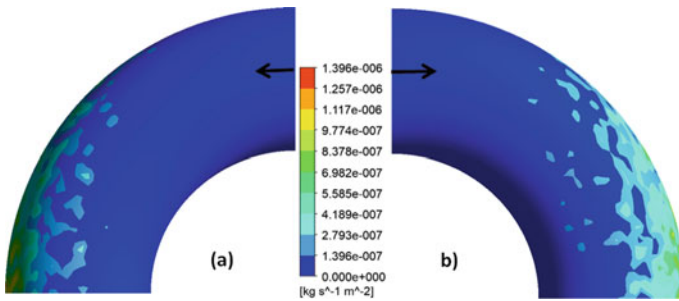


**Fig. 3** Erosion rate contour for H–V 90° elbow outer wall at transportation velocity 5.0 m/s **a** bottom view, **b** upper view

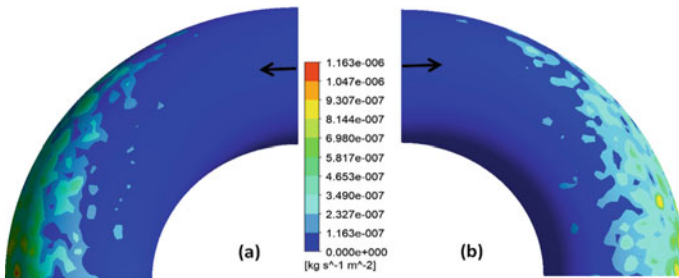


**Fig. 4** Erosion rate contour for V–H 90° elbow outer wall at transportation velocity 5.0 m/s **a** bottom view, **b** upper view

orientation as presented in Fig. 6b. Particles impact the outlet at 90° axial angle on the outer wall of elbow configuration for all orientations. The high erosion rate was found for H–V followed by V–H, and the minimum erosion rate was found for H–H orientation as presented in Fig. 6a. The erosion rates differed and varied for a flow

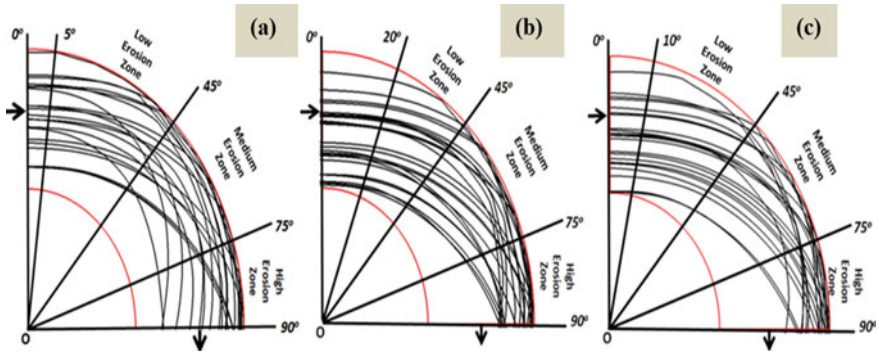


**Fig. 5** Fine particle trajectory for 5 m/s flow velocity **a** H–H 90° elbow, **b** H–V 90° elbow, **c** V–H 90° elbow

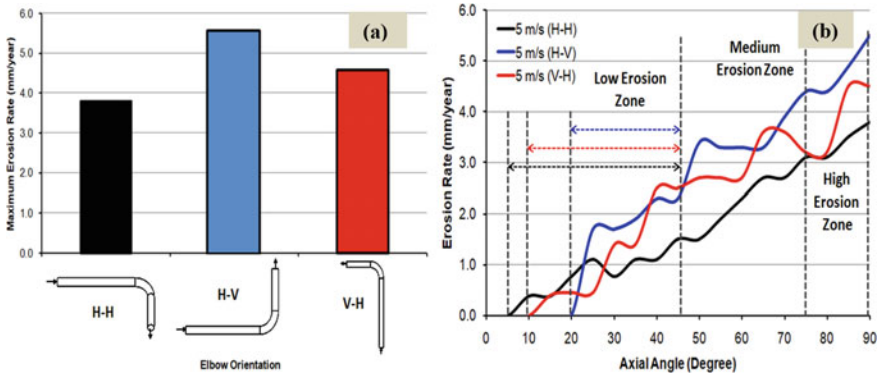


**Fig. 6** Erosion rate (CFD) for three elbows with different orientations **a** maximum erosion rate, **b** erosion rate distribution

velocity of 5 m/s from 1.5 to 4.3 mm/year between axial angles 47° and 76°, between 76° and 90° axial angles 3.1–5.5 mm/year. By comparing elbow erosion rate results for different orientations, the maximum erosion rate in H–H is 1.4 times less than H–V and 1.18 times less compared to V–H elbow.

### 3.2 Relationship of the Elbow Orientation and Turbulence Intensity

Figure 7a–c illustrates that turbulent intensity significantly contributes to enhancement of particle–wall interaction and erosion-induced damage at the elbow exit toward the outer wall. The peak turbulence zone near the outlet of 90° elbow outer wall boundary escalates particles and results in more particles impact of the outer

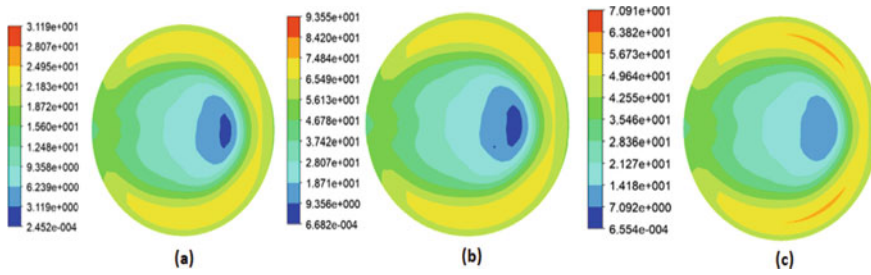


**Fig. 7** Turbulent intensity contours in the outlet for 90° elbows orientation **a** H–H, **b** H–V, **c** V–H

wall which causes more erosion in that region. For H–V oriented 90° elbow, the turbulence zone was found to be stronger at the outlet as compared to H–H and V–H oriented 90° elbows. Fine sand starts moving from the inner wall and impacts the outer wall due to centrifugal force, causing erosion of the wall. The centrifugal force enhances particle–wall interaction of the 90° elbow. Based on the simulation results, turbulence weighs more in the horizontal–vertical elbow orientation of the outlet which significantly contributes to enhancing the erosion region and erosion rate. The turbulent intensity contours imply that the contraction in the blue zone and the enlargement in the yellow zone signify the high turbulence in the region.

## 4 Conclusion

In this study, CFD-DPM simulations were carried out on carbon steel long radius 90° elbow to decouple the influence of the elbow orientation on erosion rate and particle trajectories. The following conclusions can be drawn from the CFD-DPM simulation results:

- The erosion rate shows a significant increase in the change of orientation from H–H to H–V and V–H. In addition, elbow orientation does not significantly affect the maximum erosion location and cause a more destructive impact to the outer surface at the outlet for all orientations with a maximum erosion rate of 5.5 mm/year for H–V elbow.
- The high turbulence toward the downstream region induces more catastrophic particle–wall interaction at the outlet side and affects the erosion pattern. However, high turbulence intensity is observed in H–V oriented 90° elbow as compared to H–H and V–H oriented configurations. Thus, the replacement of H–V with H–H and V–H oriented elbow is recommended for suitable cases.

**Acknowledgements** The authors acknowledge the financial support given by the Universiti Teknologi PETRONAS under grant YUTP-FRG 0153AA-H19 for this research.

## References

1. Tan Y, Zhang H, Yang D, Jiang S, Song J, Sheng Y (2012) Numerical simulation of concrete pumping process and investigation of wear mechanism of the piping wall. *Tribol Int* 46:137–144
2. Zhang H, Tan Y, Yang D, Trias FX, Jiang S, Sheng Y, Oliva A (2012) Numerical investigation of the location of maximum erosive wear damage in elbow: effect of slurry velocity, bend orientation and angle of elbow. *Powder Technol* 217:467–476
3. Khan R, Ya HH, Pao W (2019) An experimental study on the erosion-corrosion performance of AISI 1018 carbon steel and AISI 304L stainless steel 90° elbow pipe. *Metals* 9:1260
4. Mazumder QH (2006) Prediction of erosion due to solid particle impact in single-phase and multiphase flows. *J Pressure Vessel Technol* 129:576–582
5. Banakermanni MR, Naderan H, Saffar-Avval M (2018) An investigation of erosion prediction for 15°–90° elbows by numerical simulation of gas-solid flow. *Powder Technol* 334:9–26
6. Xu L, Zhang Q, Zheng JY, Zhao YZ (2016) Numerical prediction of erosion in elbow based on CFD-DEM simulation. *Powder Technol* 302:236–246
7. Khan R, Ya HH, Pao W, Khan A (2019) Erosion-corrosion of 30°, 60°, and 90° carbon steel elbows in a multiphase flow containing sand particles. *Materials* 12:3898
8. Chen J, Wang Y, Li X, He R, Han S, Chen Y (2015) Erosion prediction of liquid-particle two-phase flow in pipeline elbows via CFD-DEM coupling method. *Powder Technol* 275:182–187
9. Wee SK, Yap YJ (2019) CFD study of sand erosion in pipeline. *J Petrol Sci Eng* 176:269–278
10. Vieira RE, Mansouri A, McLaury BS, Shirazi SA (2016) Experimental and computational study of erosion in elbows due to sand particles in air flow. *Powder Technol* 288:339–353
11. Zhang Y (2006) Application and improvement of computational fluid dynamics (CFD) in solid particle erosion modeling; ProQuest. UMI Dissertations Publishing: Ann Arbor, MI, USA
12. Khan R (2019) Numerical investigation of the influence of sand particle concentration on long radius elbow erosion for liquid-solid flow. *Int J Eng* 32:1485–1490
13. Khan MR, Ya HH, Pao W, Majid MAA (Year) Numerical investigation of sand particle erosion in long radius elbow for multiphase flow. Springer Singapore, pp 41–49
14. Duarte CAR, de Souza FJ, dos Santos VF (2015) Numerical investigation of mass loading effects on elbow erosion. *Powder Technol* 283:593–606
15. Jafari M, Mansoori Z, Saffar Avval M, Ahmadi G, Ebadi A (2014) Modeling and numerical investigation of erosion rate for turbulent two-phase gas–solid flow in horizontal pipes. *Powder Technol* 267:362–370
16. Pereira GC, de Souza FJ, de Moro Martins DA (2014) Numerical prediction of the erosion due to particles in elbows. *Powder Technol* 261:105–117
17. Khan R, Ya HH, Pao W (2019) Numerical investigation of the elbow angle effect on solid particle erosion for liquid-solid. *Int J Mech Mechatr Eng* 19:1–13

# High-Speed Machining for CNC Milling Simulation Using CAM Software



Kwok Cheat Gan and Mohd Salman Abu Mansor

**Abstract** The two types of computer numerical control (CNC) machining are conventional and high-speed machining. In this work, the high-speed machining is investigated. The term ‘high-speed machining’ typically refers to milling machining at high levels of rotational speed, feed rate, and/or material removal rate. High-speed machining technology sometimes uses high revolutions per minute (rpm) rate and has a small step-over with significantly increased feed rate. Thus, the high-speed machining is suitable for replacing an existing machining process with increased flexibility and efficiency. Therefore, a gap of knowledge for high-speed machining information exists and must be explored on the basis of in-house resource availability. This work presents an investigation of high-speed machining for CNC milling simulation using Mastercam software. This work aims to study the difference between CNC machining strategies for high speed and conventional machining on a 3D part model containing a pocket with a protrusion island. The high-speed machining is compared with conventional machining using the same software to ensure the reliability of the former. Furthermore, the toolpath strategies for cutting methods are compared.

**Keywords** High-speed machining · CNC milling · Cutting methods · Toolpath strategies

## 1 Introduction

Salomon [1] proposed the definition of high-speed machining. He assumed that the temperature will start to reduce to a certain cutting speed which is five to ten times higher in a chip tool interface than in conventional machining. High-speed machining is frequently applied to all operations, particularly in small-sized tools [2]. High-speed machining can be defined in many different ways [3], such as high-feed machining ( $V_f$ ), high rotational speed machining ( $n$ ), high cutting speed machining

---

K. C. Gan · M. S. Abu Mansor (✉)  
School of Mechanical Engineering, Engineering Campus, Universiti Sains Malaysia, Seri Ampangan, 14300 Nibong Tebal, Seberang Perai Selatan, Pulau Pinang, Malaysia  
e-mail: [mesalman@usm.my](mailto:mesalman@usm.my)

© Springer Nature Singapore Pte Ltd. 2020  
S. S. Emamian et al. (eds.), *Advances in Manufacturing Engineering*, Lecture Notes in Mechanical Engineering, [https://doi.org/10.1007/978-981-15-5753-8\\_65](https://doi.org/10.1007/978-981-15-5753-8_65)

703

(Vc), high productive machining, or high-speed and feed machining. The suitable manufacturing conditions must be carefully selected for each operation to obtain dimensional accuracy and minimise cutting time in manufacturing in accordance with product specifications [4].

Generally, cutting conditions, such as cutting speed, depth of cut, and feed rate, are considered. The final result is affected by each component involved in machining. The machining centre is the basic element of the process; various characteristics, such as workspace dimensions, power, number of axes, travel speed on axes, spindle speed, and tool magazine capacity, available in the machining centre will affect the final product [5]. The cutting tool is another key to the machining element. The term high-speed milling is typically used to express end milling with a small diameter tool that is equal to or less than 10 mm and with high rotational speed up to 10,000 rpm [6]. Under these conditions, the high tendency of vibration and tool rigidity becomes a critical issue. However, this problem can be minimised or solved using a suitable tool holder.

Numerous commercial computer-aided manufacturing (CAM) systems currently have high-speed machining selections to provide proper machining strategies. Nevertheless, some researchers have allowed the cutting parameters to be calculated. The common features of CAM systems are based on geometric programming and not on selecting the cutting parameters requiring considerable information on tools and materials [7]. All the factors for machining are difficult to analyse.

Dagiloke et al.'s [8] research is limited to factors with a significant effect on dimensional accuracy and cycle time. In the analysis, the factors considered are provided as follows: (i) the type of tool holder to avoid tool failure and obtain a favourable surface finish because a good tool balance is critical; (ii) the cutting conditions, such as the programmed feed rate, to ensure high-speed milling in the process; and (iii) the interpolation type used to create the programme using distinctive circular and linear interpolation. Few researchers [9–11] have proposed methods for constructing spiral toolpaths for high-speed machining. The toolpaths for high-speed machining significantly affect the surface quality and the efficiency of the machining process [12, 13].

Several critical parameters are present for high-speed machining. One parameter is the depth of cut. Recommendations are provided by cutting tool manufacturers in terms of machining parameters that should be used. These parameters are generally a machining datum applicable for the parameter sets [14]. High-speed machining technology offers more advantages than conventional machining [15]. Many advantages of high-speed machining have been cited. The common claims are presented as follows: (i) high metal removal rates, (ii) low cutting forces and minimal workpiece distortion, (iii) an ability to machine thin-walled sections, and (iv) the use of simple fixturing.

High-speed milling is efficient in reducing machining time [16]. Machining is rapidly performed using high-feed rates, thereby resulting in enhanced surface quality when declining the distance between successive cutter paths. Consequently, this technology can abolish the manual polishing process and reduce costs and lead time. Minimal amounts of material per step can be subtracted given fast feed rates, thus



resulting in small forces on the geometry to be machined. Thus, thin walls can be machined through high-speed machining.

The number of literature in high-speed machining has drastically increased for the past few years. This finding demonstrates the growing success of evolutionary approaches in the machining production area. However, a gap of knowledge for high-speed machining information exists and must be explored on the basis of existing in-house resources. Thus, an extensive study on the investigation and application on high-speed machining with respect to various performance measures and approaches is necessary.

Therefore, the high-speed machining must be studied given its benefits, as previously mentioned, to fulfil the gap of knowledge and machining information that must certainly be explored on the basis of the availability of in-house resources. High-speed machining for CNC milling simulation will be investigated using Mastercam.

## 2 Methodology

A 3D part model with a pocket and protrusion island is prepared using a CAD system. The model is then exported to Mastercam to generate toolpath and G-code for the machining. Few toolpaths, such as contour, drill, pocket, and facing toolpaths, can be created using Mastercam. In this work, contour (Fig. 1) and pocket (Fig. 2) toolpaths are used. Contour toolpaths are used to remove materials along a path defined by a chain of curves. By contrast, pocket toolpaths are used to remove materials contained in a closed profile. The contour and pocket toolpaths are selected from the Operations Manager menu for creating contour and pocket toolpaths, respectively. This process is initiated to create a toolpath for the part. The Roughing or Finishing parameter menu is configured (Fig. 3).

For toolpath verification, the stock shape is updated whilst the tool moves along the toolpath and produces the final path. This step allows the resulting model to be inspected, thus ensuring that the programming errors are eliminated before they are transferred to the CNC machine. Similar to creating a part, the Operations Manager menu must be firstly opened to run toolpath verification. Secondly, the Verify button must be chosen, and the verification process is run by clicking the play button from the Verify menu (Fig. 4). After verifying all the toolpaths, the G-code can be created by selecting Post from the Operations Manager menu. Finally, the NC file and Edit are saved in the post-processing menu (Fig. 5).

The procedures for high-speed and conventional machining are the same from exporting a 3D part model to Mastercam until the G-code is created. In high-speed machining, the normally used method includes high speed, parallel spiral, and parallel spiral with clean corners. Thus, the only difference between the two machining methods is the different cutting methods chosen in the Roughing/Finishing parameter menu (Fig. 3).

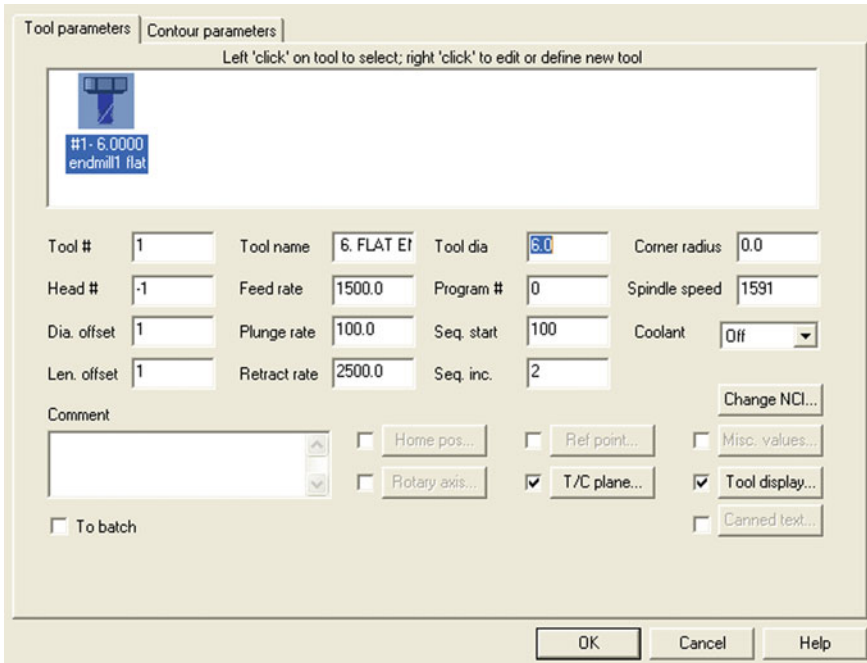


Fig. 1 Contour (2D) menu

### 3 Result and Discussion

Figure 6 illustrates the machining part used for this work. The machining part is divided into the following sections:

- (a) First section: Rectangular part,
- (b) Second section: Circular part, and
- (c) Third section: Pocket part.

Figure 7 demonstrates the toolpart strategy for the rectangular part that must be machined. The cutter begins its machining at Point 1. Then, the cutter moves to Point 2, 3, and 4 (refer to the yellow arrow).

Figure 8 exhibits the toolpart strategy for the circular part that must be machined. The cutter begins its machining at Point 1. Afterwards, the cutter moves in the clockwise direction (refer to the yellow arrow). The machining process is divided into the following four sections: the first quadrant at Point 2, the second quadrant at Point 3, the third quadrant at Point 4, and the last quadrant at Point 1.

Figure 9 presents the toolpart strategy for the pocket part that must be machined. The cutter begins its machining from 'Start'. The first layer of pocket is machined through the 'zigzag method' (refer to the yellow arrow). The machining process is

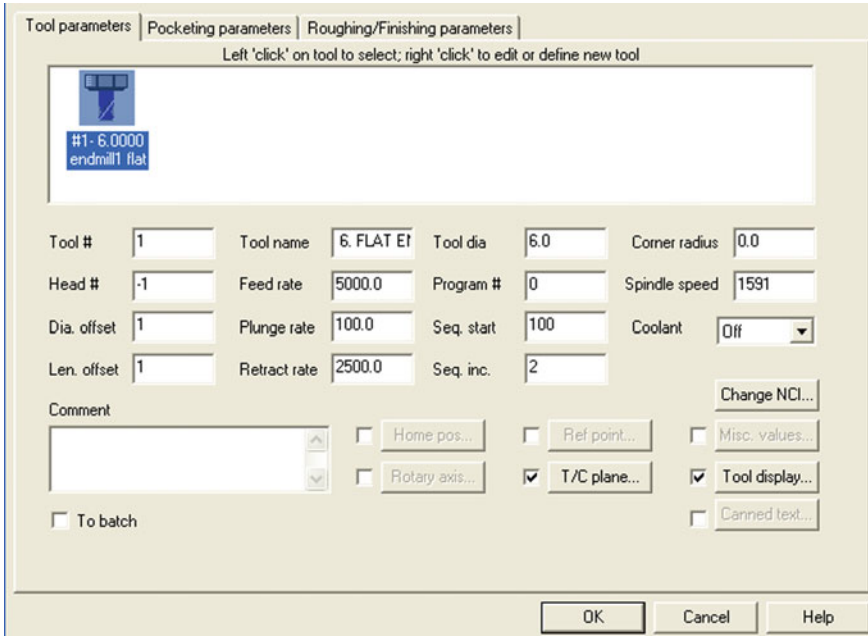


Fig. 2 Pocket (standard) menu

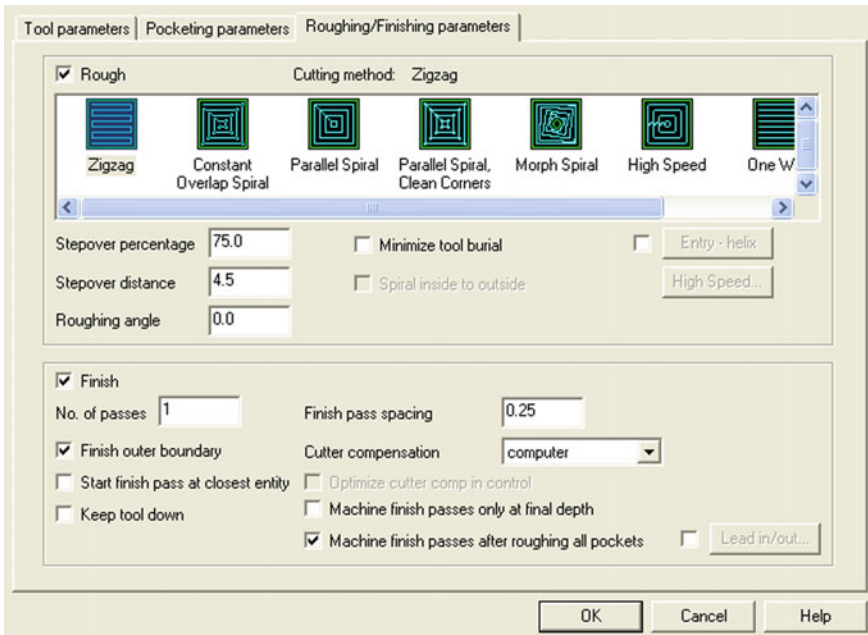


Fig. 3 Roughing/finishing parameter menu

Fig. 4 Verify menu



Fig. 5 Post-processing menu

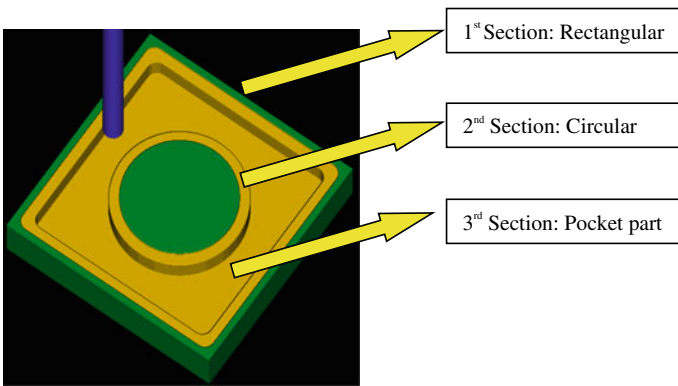
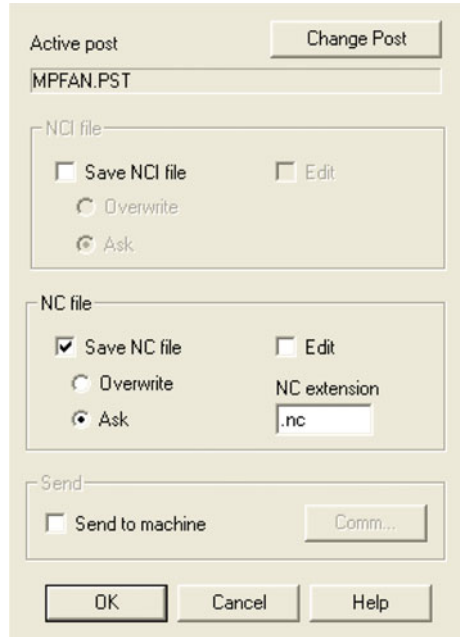


Fig. 6 Machining part

continued through the same method until a tenth layer of the pocket part is produced. Figure 10 depicts a completely machined product with a pocket.

The same 3D part model is used to investigate high-speed machining (Fig. 6). The only difference between conventional and high-speed machining is the utilised

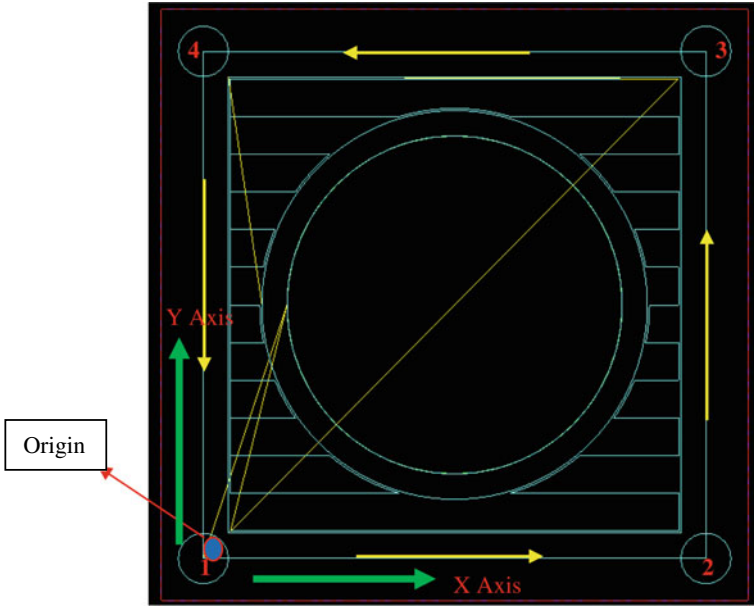


Fig. 7 Toolpart strategy for the zigzag cutting method—rectangular part

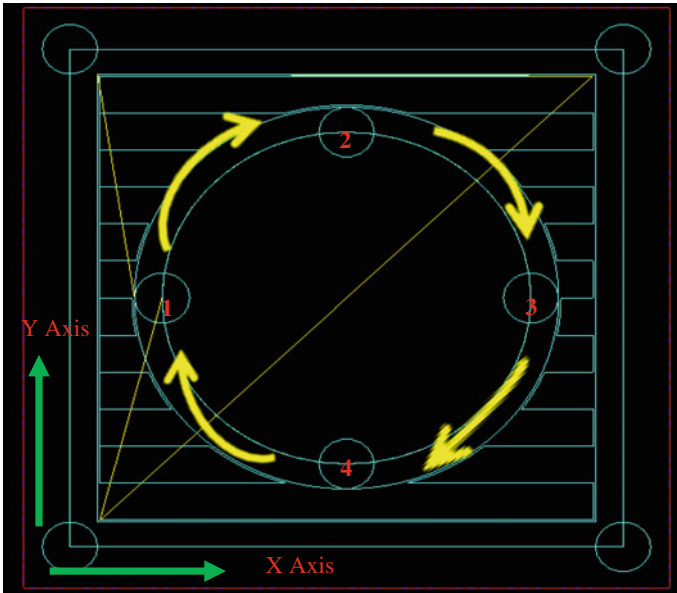


Fig. 8 Toolpart strategy for the zigzag cutting method—circular part

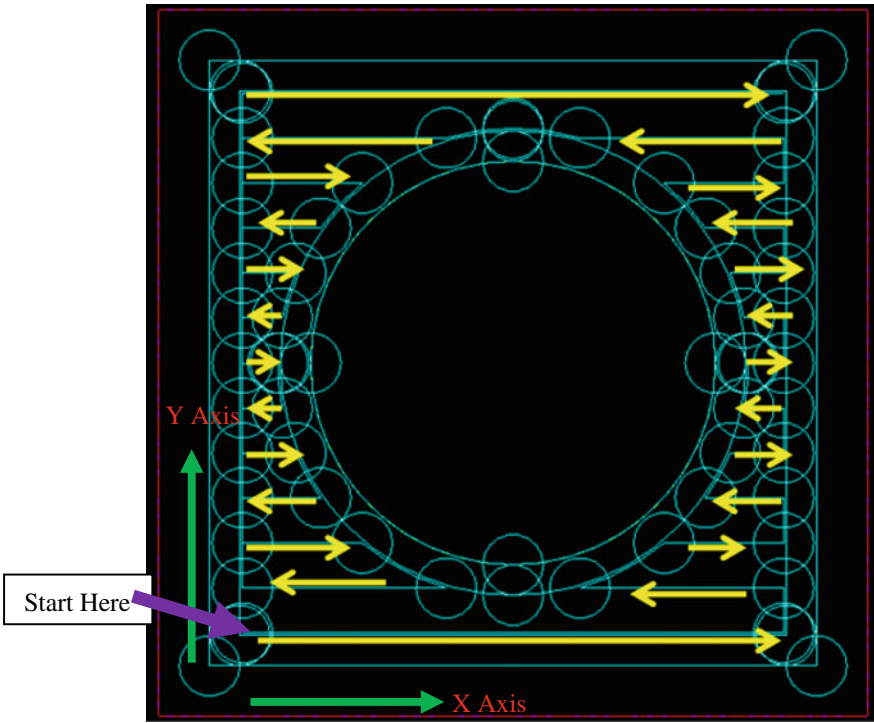
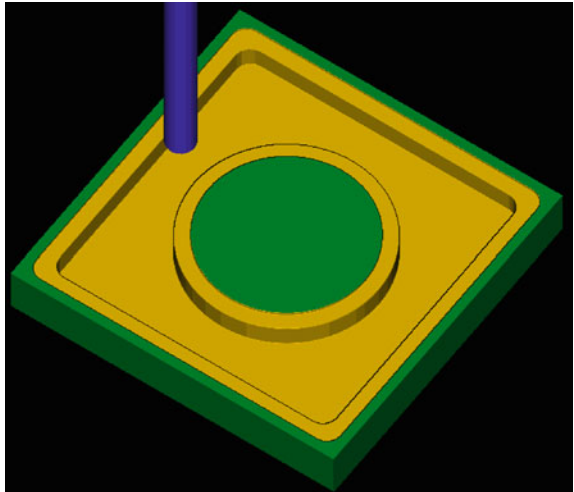


Fig. 9 Toolpart strategy for the zigzag cutting method—pocket part

Fig. 10 Completely machined product with a pocket



cutting method. As mentioned previously, the machining part can be divided into three sections, namely rectangular, circular, and pocket parts. In the rectangular and circular parts, the same machining method is used for high-speed machining. The NC code generated for high-speed machining is the same as that in conventional machining considering the same cutter orientation. In the pocket part, a different machining method is used between conventional and high-speed machining. High-speed machining uses a high-speed cutter orientation. By contrast, conventional machining uses a zigzag cutter orientation. The NC code generated for high-speed machining is different, given the cutter orientation difference.

Figure 11 illustrates a toolpath strategy for the high-speed cutting method. The tool is moved in small circles rather than in a straight line whilst cutting. The cutter begins its machining at Area 1 by moving the tool in small circles whilst cutting. The cutter maintains the same high-speed method until ten product layers are completely machined. Then, the cutter moves to Areas 2, 3, and 4 (refer to the yellow arrow) by performing the same machining steps. The surface finish process in the rectangular and circular parts will begin after cutting completely at Areas 1–4.

Table 1 displays a comparison of the zigzag and high-speed cutting methods. The tools in a zigzag cutting method are cutting in a straight line and low spindle speed.

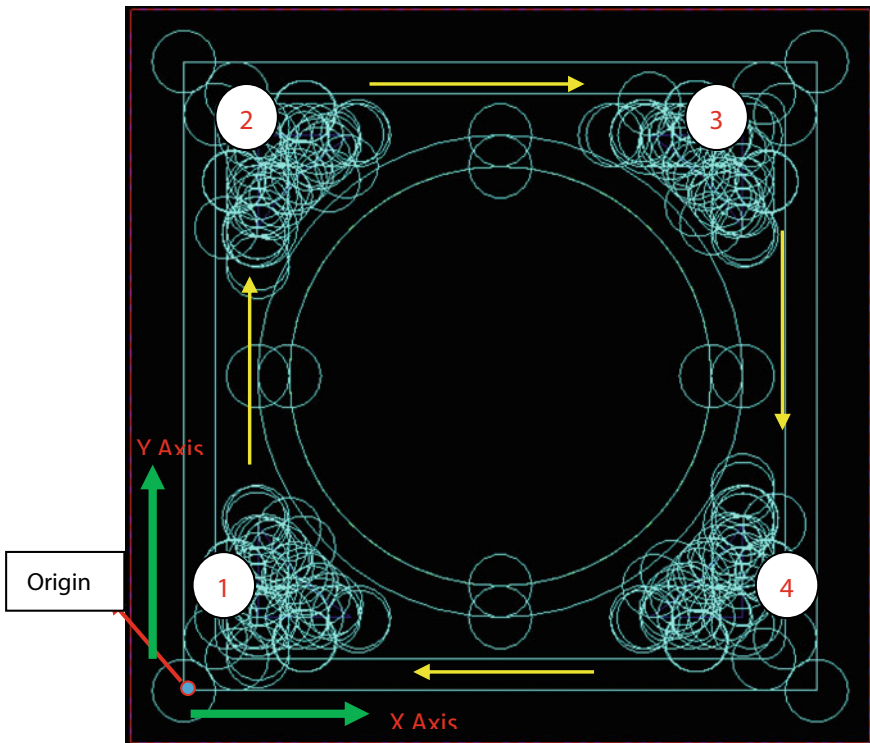


Fig. 11 Toolpath strategy for the high-speed cutting method

**Table 1** Comparison of the zigzag and high-speed cutting methods

No	Zigzag cutting method	High-speed cutting method
1	Cut in a straight line	Moves the tools in small circles whilst cutting
2	Unsuitable for high-speed machining	Suitable for high-speed machining
3	Inconsistent feed rate	Consistent feed rate
4	Cut in low speed	Cut in high speed

By contrast, the high-speed cutting method moves the tools in small circles whilst cutting, and the tools are cutting in high spindle speed.

A significant impact on the efficiency of the machining process and surface quality can be obtained from the toolpaths for high-speed machining [12, 13]. Tool wear is an important aspect in high-speed machining, which influences part quality and machining precision and requires a suitable method to predict and monitor tool conditions [17]. The investigation result shows that the toolpart generated for the high-speed machining for CNC milling simulation is found in different cutting methods in terms of tool movement and cutting parameters which can influence the process efficiency and surface quality.

## 4 Conclusions

In this work, the CNC milling simulation for high-speed machining is investigated. A significant finding in terms of the high-speed cutting method and its benefits is obtained. The cutting method for high-speed machining has generated numerous small circle toolpaths for the pocket part. The high-speed cutting method is suitable for high-speed machining because the cutting tool constantly moves along a curve with a constant radius. This condition also allows a consistent feed rate throughout the machining process. Therefore, enhanced surface quality can be produced and can eliminate the manual polishing process. Small cutting forces on the geometry can be created and can remove the small amounts of material per step. In terms of contribution to knowledge, high-speed machining can be considered to replace the existing machining processes with increased flexibility and efficiency.

**Acknowledgements** This research is supported by Universiti Sains Malaysia and Ministry of Higher Education Malaysia under the Incentive Grant (Reference No.: 2007/493) and Fundamental Research Grant Scheme (FRGS) (Reference No.: 6071369).



## References

1. Salomon CJ (1931) Process for machining metals of similar acting materials when being worked by cutting tools. German patent: 523594
2. Schulz H, Moriwaki T (1992) High—speed machining. *Ann CIRP* 41(2):637–642
3. Coromant S (1999) Die and mould making application guide
4. de Lacalle LN, Lamikiz A, Sánchez JA, Arana JL (2002) Improving the surface finish in high-speed milling of stamping dies. *J Mater Process Technol* 123:292–302
5. Alberti M, Ciurana J, Rodríguez CA (2007) Experimental analysis of dimensional error versus cycle time in high-speed milling of aluminium alloy. *Int J Mach Tools Manuf* 47:236–246
6. Toh CK (2005) Design, evaluation and optimization of cutter path strategies when high speed machining hardened mould and die materials. *Mater Des* 26(6):517–533
7. Alberti M, Ciurana J, Casadesús M (2005) A system for optimizing cutting parameters when planning milling operations in high speed machining. *J Mater Process Technol* 168(1):25–35
8. Dagiloke IF, Kaldos A, Douglas S, Mills B (1995) High-speed machining: an approach to process analysis. *J Mater Process Technol* 54:82–87
9. Abrahamsen M (2019) Spiral tool paths for high-speed machining of 2D pockets with or without islands. *J Comput Des Eng* 6(1):105–117
10. Held M, Spielberger C (2014) Improved spiral high-speed machining of multiply-connected pockets. *Comput Aided Des Appl* 11(3):346–357
11. Held M, Spielberger C (2009) A smooth spiral tool path for high speed machining of 2D pockets. *Comput Aided Des* 41(7):539–550
12. Lee E (2003) Contour offset approach to spiral toolpath generation with constant scallop height. *Comput Aided Des* 35(6):511–518
13. Zhou B, Zhao J, Li L (2015) CNC double spiral tool-path generation based on parametric surface mapping. *Comput Aided Des* 67:87–106
14. Plaza, M (1995) The prons and cons of high-speed machining. *Canadian Machinery and Metalworking*, pp 8–10
15. Juan H, Yu SF, Lee BY (2003) The optimal cutting-parameter selection of production cost in HSM for SKD61 tool steels. *Int J Mach Tools Manuf* 43:679–686
16. Knoppers R, Gunnink JW, Zwaags J, Whittington C (2003) No high speed milling without high speed programming. In: *Proceedings of the 1st international conference on advanced research in virtual and rapid prototyping*, p 485
17. Zhu K, Zhang Y (2019) A generic tool wear model and its application to force modeling and wear monitoring in high speed milling. *Mech Syst Signal Process* 115:147–161

# Structural Fabrication and Dynamic Simulation of Stress of a Vibrosieve for Efficient Industrial Applications



Enesi Y. Salawu, O. O. Ajayi, Fajobi Muyiwa, Felix Ishola, and Azeta Joseph

**Abstract** A reliable and accurate size determination of powder particles or solid particles, in general, depends on the vibrating efficiency of a vibrosieve. Thus, the study employed the inexpensive design concept of vibration mechanics and mass balance to improve the quality production of powder. Stress simulation of a vibrosieve was proposed. The result of the stress simulation using carbon steel materials showed that there is variation in both yield stress and shear stress. For a 7 N load, a yield stress of 2.817–2.835 N/m<sup>2</sup> and a corresponding shear stress of 2.817–2.821 N/m<sup>2</sup> were observed. Subsequently, simulation result using alloy steel revealed a yield stress ranging from 6.204 to 6.212 and a corresponding shear stress of 4.549–4.555 N/m<sup>2</sup>. The variation in the stress depicts the fatigue life of the machine overtime. Thus, the result of increased yield stress showed that the material might likely fail overtime. This will enable designers to carefully select their material and operating stress which will be safe for the machine, thereby increasing machine, reliability and efficiency.

**Keywords** Stress · Vibration · Powder · Production · Vibrosieve

## 1 Introduction

Sieving or screening is referred to as the separation of solids into two or more parts based on their size differences. This process has become a very important operation in the food processing industry as well as in the industrial separation of other solid particle sizes [1]. For instance, the separation of some particle-based systems has been found to be contaminated by some reagents during the process, especially in the pharmaceutical industries due to improper sieving during the process [2]. Consequently, Chen et al. [3] reported that the use of molecular sieves in the separation of hydrogen isotopes is highly significant but the mole fraction determination is still a challenge. Thus, previous studies on the domestic application of sieves in threshing of rice mixture showed that the process is laborious, and the rate of loss

---

E. Y. Salawu (✉) · O. O. Ajayi · F. Muyiwa · F. Ishola · A. Joseph  
Department of Mechanical Engineering, Covenant University, Ota, Nigeria  
e-mail: [enesi.salawu@covenantuniversity.edu.ng](mailto:enesi.salawu@covenantuniversity.edu.ng)

and quality of the product is highly dependent on the sieving machine [4]. However, the development of a highly efficient device that can be used for the separation of some processed agricultural produce remains a challenge due to mass transfer [5]. More so, the determination of the particle size is the key to quality production as well as having efficient and accurate powder production technique [6–9]. Further to this, the geometric factor in the design of sieves is still a problem as this relates to the dynamic and kinematic properties of the particles to be separated [10–12]. These factors can be simulated in the design process of the sieve in order to get the desired efficiency during the sieving operation. According to Carpin et al. [13], the surface area and the length of the particle size distribution limit the compressibility and the flowability of the powder. This is due to the fact that the size distribution is a function of the length of a single particle and gives more uncertainties when the morphology is complex [14–16]. To obtain accuracy and stability in powder production, various sieve designs must be of a reasonable peak height to reduce the sieving time [17–19]. Consequently, the drop size and mass transfer coefficient of the particle size distribution must be taken into consideration at the design stage to achieve a reliable product [20–24]. In the present study, the focus is on the development of an automated sieving machine based on the knowledge of vibration that can efficiently salvage the time wasted in processing and packaging of agricultural and industrial products which include wheat flour, yam flour, maize flour and industrial chemicals, etc., thus making it possible to separate or sieve the powder from impurities and also making the end product safe for consumption even in the local communities. More so, the study further investigated the strength of the assembled sieve via finite element approach to determine the effect of vibration on the yield strength of the material, hence improving machine reliability.

## 2 Problem Definition

Vibrosieves have been found to have major factors which pose problems during the design. These factors or problems include accumulation of materials at the centre of the sieve due to reduced vibration and the vibrator motor vibrating in the direction opposite to the expected and inadequate operating efficiency. These problems or factors contribute to the overall performance, wastage of time and poor quality of powder production [25, 26]. This research, therefore, focused on the fabrication, assembly and stress simulation of the vibrosieve to improve the smooth running and efficient operation of a vibrosieve.

### 3 Materials and Methods

#### 3.1 Materials Selection

The machine components include the frame which is cylindrical in shape and made of carbon steel due to its high strength and corrosion resistance. The frame is coupled with the wire mesh of which the sieve is attached as well as the electric motor. The sieve was made from stainless steel due to its corrosion resistance and its ability to resist failure under repeated loading. The base was made from mild steel because of its excellent strength and durability, while the springs were used to dampen the vibration produced by the motor. Cast alloy springs were selected based on compressive strength and resistant to failure due to repeated vibrations.

#### 3.2 Methods

##### 3.2.1 Design Concept and Calculations

The methods involved the design equations of component parts based on vibration requirement.

For a mass of 1 kg, speed of motor required for the sieve  $N = 950$  rpm [27]

$$\omega = \frac{2\pi N}{60} = 950 \times \frac{2\pi}{60} = 99.5 \text{ rad/s} \quad (1)$$

Unbalanced mass eccentricity is given by  $r = 50 \text{ mm} = 0.05 \text{ m}$ .

Force exerted by the electric motor to cause vibration is given by [26].

$$F = m\omega^2 r \quad (2)$$

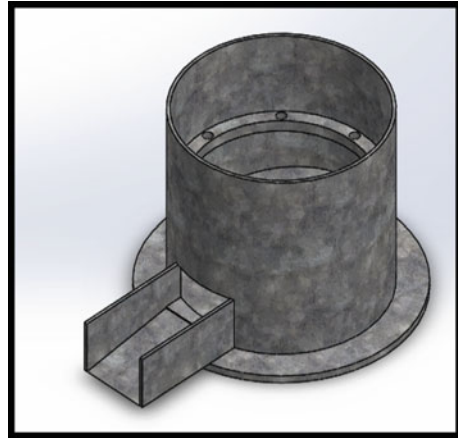
$$F = 1 \times 99.5^2 \times 0.05 = 495N$$

The force produces an amplitude on the powder given by

Mass of frame + sieve = 20.5 kg (as simulated in Solidwork)

$$F = ma$$

To find the vibration amplitude  $a = \frac{F}{m} = \frac{495}{20500} = 0.0241G$ .

**Fig. 1** Frame design

### 3.2.2 Solidworks Models of Components and Assembled Parts of the Sieve

The vibrosieve operates with a powerful single-phase electric motor which was designed and integrated to the body of the machine for mass balance. When the motor vibrates, the trough attached to the frame shakes making the sieve attached to the frame shake also and then, eventually, discharges a fine smooth and medium size product according to the design of the aperture. The vibration per minute is 1450, and an amplitude of 2–4 mm was selected for the design according to [28]. The component design and complete assembly of the vibrosieve are shown.

## 4 Figures

See Figs. 1, 2, 3, 4, 5 and 6.

## 5 Results and Discussion

Figures 1, 2, 3, 4 and 5 present the individual components of the vibrosieve, which include the frame design with an integrated trough, through which the sieved or screened particles flow. In addition, the design of the sieve is shown in Fig. 2. A size of about 75  $\mu\text{m}$  was selected for the aperture for smooth and quality production. More so, Figs. 3 and 4 represent the base support for the entire design, which is the sensitive part which supports the vibration and the movement of the springs, while Fig. 5 represents the springs which serve as vibration dampers and Fig. 5 is the complete assembly of the vibrosieve.

**Fig. 2** Sieve design

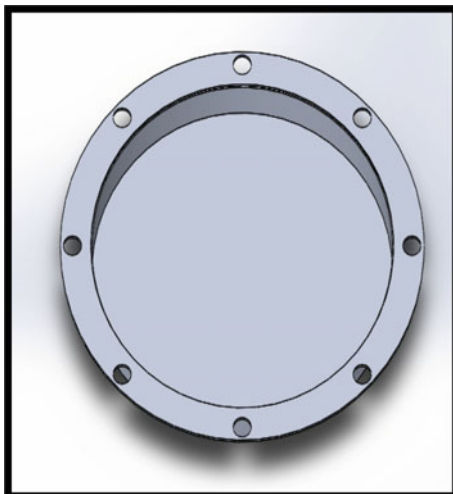


**Fig. 3** Base support of the machine

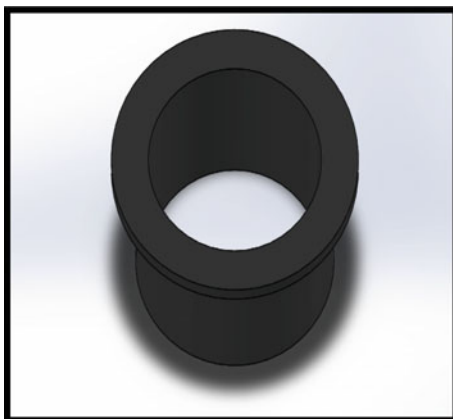


**Fig. 4** Single-phase electric motor

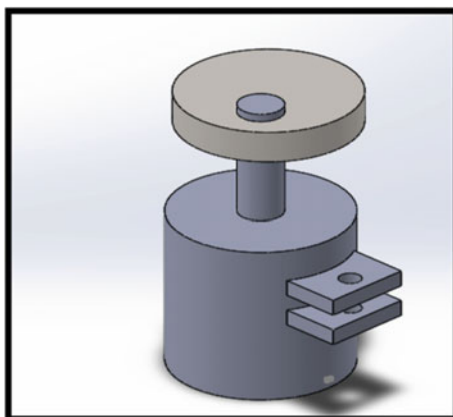


**Fig. 5** Spring for vibration damping

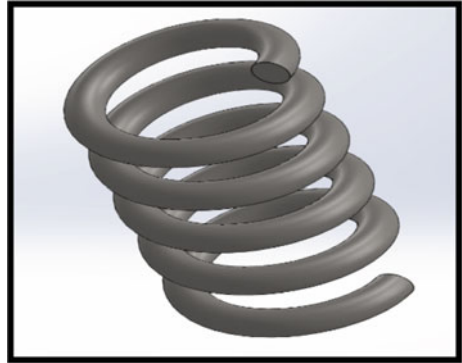
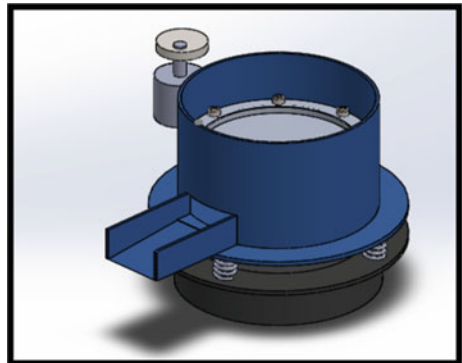


**Fig. 6** Complete assembly of vibrosieve



Further to this, the finite element approach was employed to study the variation in stresses between carbon steel and alloy steel for the fabrication materials. The yield stress and the shear stress observed were demonstrated on the simulation result.

Figure 7 displays variation in the yield stress as the material vibrates with an assumed force of 7 N causing vibration. A yield stress of 2.827–2.835 N/m<sup>2</sup> was observed. However, the equivalent shear stress was noted to be between 2.817 and 2.821 N/m<sup>2</sup> as seen on Fig. 8. Thus, fatigue might set in after a long operation.

Applying the same analysis using alloy steel for simulation of yield stress and shear stress, it was noted that the vibration effect was evenly distributed with a yield stress ranging from 6.204 to 6.212 N/m<sup>2</sup> and shear stress of about 4.54–4.555 N/m<sup>2</sup> (Figs. 9 and 10).

## 6 Conclusion

A vibrosieve was designed, fabricated and assembled by carefully selecting materials for the individual component. The entire assembly was subjected to stress simulation using different materials under a specified load of 7 N to determine the yield stress

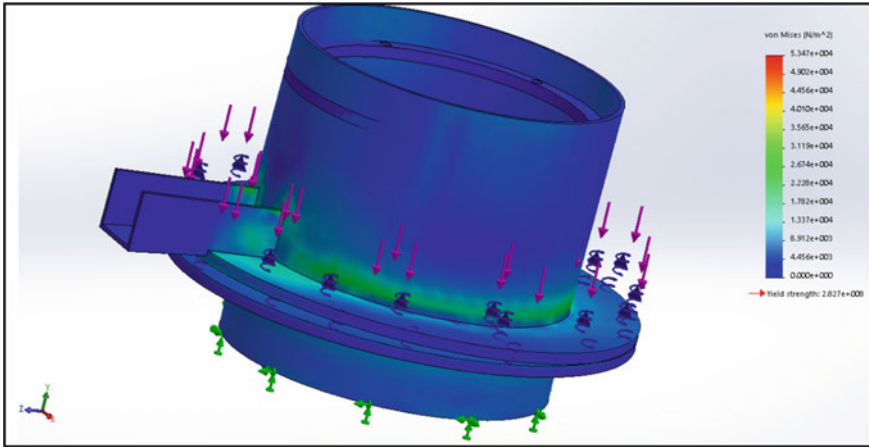


Fig. 7 Finite element model of yield stress (carbon steel)

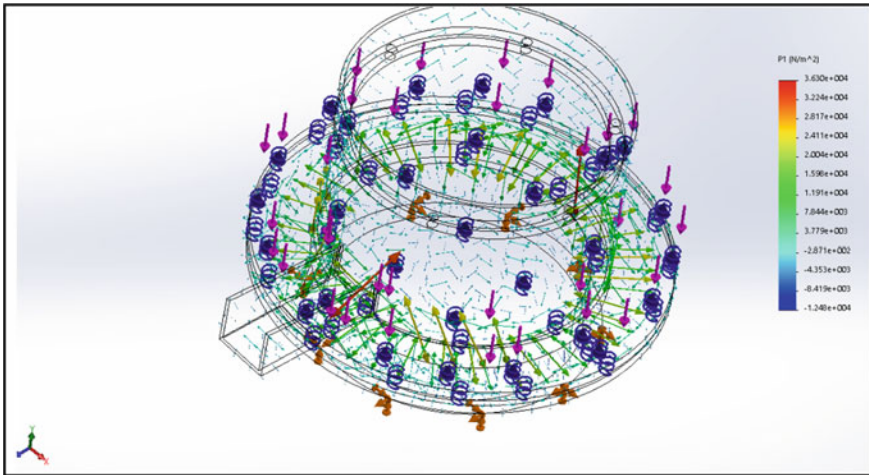


Fig. 8 Finite element model of shear stress (carbon steel)

and shear stress. The result of the simulation showed that carbon steel gave less yield stress and shear stress of 2.827–2.835  $\text{N/m}^2$  and 2.817–2.821  $\text{N/m}^2$  compared to the alloy steel having 6.204–6.212 and 4.549–4.555  $\text{N/m}^2$ . This implies that the former will perform better in service compared to the latter due to increased fatigue life overtime. The design and proposed simulation of the vibration process will help in improving machine design and reliability.



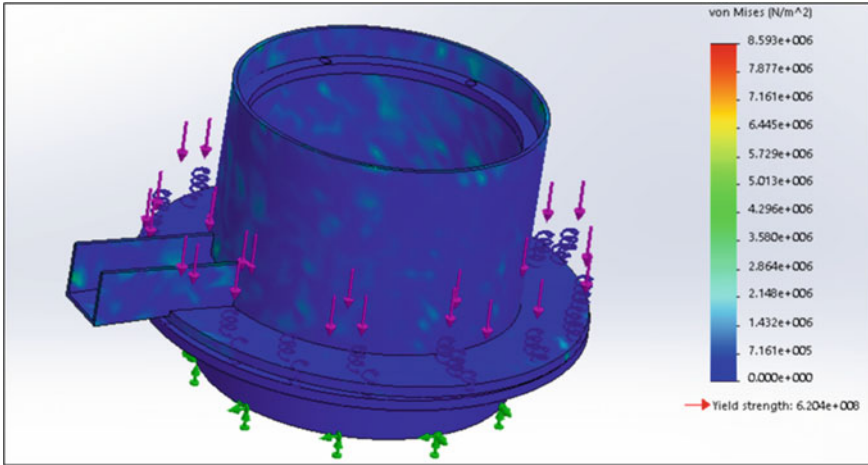


Fig. 9 Finite element model of yield stress (alloy steel)

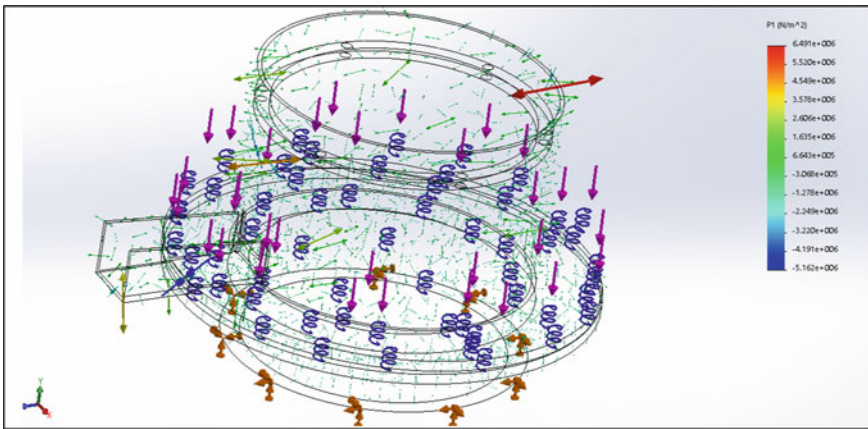


Fig. 10 Finite element model of yield stress (alloy steel)

**Acknowledgements** The authors would like to thank the management of Covenant University for the partial sponsorship of this research.

## References

1. Liu H, Jia J, Liu N, Hu X, Zhou X (2018) Effect of material feed rate on sieving performance of vibrating screen for batch mixing equipment. *Powder Technol* 338:898–904
2. Zhang Y, San Lee DY, Farwin A, Ying JY (2018) Sieve-through vertical flow platform for efficient liquid exchange in particle-based assays. *Analytica Chimica Acta*

3. Chen M, Song J, Li P, Yu B, Wang J, Yao Y, An Y (2019) A dynamic simulation of cryogenic hydrogen isotope adsorption in molecular sieve beds. *Fusion Eng Des* 138:159–163
4. Yuan J, Wu C, Li H, Qi X, Xiao X, Shi X (2018) Movement rules and screening characteristics of rice-threshed mixture separation through a cylinder sieve. *Comput Electron Agric* 154:320–329
5. Dijkshoorn JP, Wagterveld RM, Boom RM, Schutyser MAI (2017) Sieve-based lateral displacement technology for suspension separation. *Sep Purif Technol* 175:384–390
6. Kontopoulos I, Presslee S, Penkman K, Collins MJ (2018) Preparation of bone powder for FTIR-ATR analysis: the particle size effect. *Vib Spectrosc* 99:167–177
7. Asachi M, Hassanpour A, Ghadiri M, Bayly A (2018) Experimental evaluation of the effect of particle properties on the segregation of ternary powder mixtures. *Powder Technol* 336:240–254
8. Yohannes B, Liu X, Yacobian G, Cuitiño AM (2018) Particle size induced heterogeneity in compacted powders: effect of large particles. *Adv Powder Technol* 29(12):2978–2986
9. Becker L, Zaiter A, Petit J, Karam MC, Sudol M, Baudelaire E, Dicko A (2017) How do grinding and sieving impact on physicochemical properties, polyphenol content, and antioxidant activity of *Hieracium pilosella* L. powders. *J Funct Foods* 35:666–672
10. Cao B, Jia F, Zeng Y, Han Y, Meng X, Xiao Y (2018) Effects of rotation speed and rice sieve geometry on turbulent motion of particles in a vertical rice mill. *Powder Technol* 325:429–440
11. Zhao H, Li L, Jin J, Li Q (2018) CFD simulation of sieve-fixed valve tray hydrodynamics. *Chem Eng Res Des* 129:55–63
12. Ighathinathane C, Ulusoy U, Pordesimo LO (2012) Comparison of particle size distribution of celestite mineral by machine vision  $\Sigma$  volume approach and mechanical sieving. *Powder Technol* 215:137–146
13. Carpin M, Bertelsen H, Dalberg A, Bech JK, Risbo J, Schuck P, Jeantet R (2017) How does particle size influence caking in lactose powder? *J Food Eng* 209:61–67
14. Gil M, Teruel E, Arauzo I (2014) Analysis of standard sieving method for milled biomass through image processing. Effects of particle shape and size for poplar and corn stover. *Fuel* 116:328–340
15. Raclavská H, Corsaro A, Hartmann-Koval S, Juchelková D (2017) Enrichment and distribution of 24 elements within the sub-sieve particle size distribution ranges of fly ash from wastes incinerator plants. *J Environ Manage* 203:1169–1177
16. Azevedo JM, Serrenho AC, Allwood JM (2017) The deformation of metal powder particles: hardness and microstructure. *Procedia Engineering* 207:1200–1205
17. De Scheerder L, Sparén A, Nilsson GA, Norrby PO, Örnskov E (2018) Designing flexible low-viscous sieving media for capillary electrophoresis analysis of ribonucleic acids. *J Chromatogr A*
18. Sabzian M, Nasrabadi MN, Haji-Hosseini M (2018) Design and development of radioactive xenon gas purification and analysis system based on molecular sieves. *J Environ Radioact* 190:66–72
19. Jiang W, Hu S, Zhao L, Yan W, Yang Y (2010) Design and application of phase photon sieve. *Optik-Int J Light Electr Opt* 121(7):637–640
20. Li S, Yang K, Liu L, Zhao B, Chen Y, Li X, Zhang Y (2018) Surface sieving coordinated IMAC material for purification of His-tagged proteins. *Analytica Chimica Acta* 997:9–15
21. Yadav RL, Patwardhan AW (2008) Design aspects of pulsed sieve plate columns. *Chem Eng J* 138(1–3):389–415
22. Sun C, Bai B (2017) Molecular sieving through a graphene nanopore: non-equilibrium molecular dynamics simulation. *Science bulletin* 62(8):554–562
23. Lavasani MS, Rahimi R, Zivdar M (2018) Hydrodynamic study of different configurations of sieve trays for a dividing wall column by using experimental and CFD methods. *Chem Eng Process-Process Intens* 129:162–170
24. Park S, Yeon KM, Moon S, Kim JO (2018) Enhancement of operating flux in a membrane bio-reactor coupled with a mechanical sieve unit. *Chemosphere* 191:573–579
25. Yekini SE, Okokpujie IP, Afolalu SA, Ajayi OO, Azeta J (2018) Investigation of production output for improvement. *Int J Mech Prod Eng Res Dev* 8(1):915–922

26. Okokpujie IP, Okokpujie KO, Salawu EY, Ismail AO (2017) Design, production and testing of a single stage centrifugal pump. *Int J Appl Eng Res* 12(18):7426–7434
27. precisionmicrodrives.com <https://www.precisionmicrodrives.com/>
28. Precision microdrives <https://www.precisionmicrodrives.com/vibration-motors>

# Recycling of Polylactic Acid (PLA) Wastes from 3D Printing Laboratory



Thai Kiat Ong, Hui Leng Choo, Wei Jean Choo, Seong Chun Koay,  
and Ming Meng Pang

**Abstract** Material extrusion process, or commonly known as fused deposition modelling (FDM), is the most popular additive manufacturing process to date. Most universities use this technique along with PLA and ABS as the main materials for prototyping. A lot of wastes are generated in this process from support structures and scrapped parts, but they are not usually recycled indoor. Most commonly, these materials are thrown away as landfill. Therefore, the aim of this research was to investigate in-house recycling of PLA wastes using a standard desktop filament extruder. A total of two cycles were carried out (Cycle 0 being the new filament, Cycle 1 and Cycle 2). Mechanical properties, thermal properties and melt flow rate (MFR) were tested on the obtained samples at each cycle. After one recycling (Cycle 1), mechanical properties reduced drastically. This was attributed to hydrolytic degradation which is shown through an increase in MFR and percentage crystallinity. Increasing MFR can be attributed to the reduction in PLA molecular weight. Besides degradation, there were some extrusion and printing issues, which were magnified during Cycle 2. The clogging of extrusion nozzle was due to impurities as no filtering was used during extrusion. Overall, it can be concluded that in-house recycling is feasible, but it should be done with care as the resulting material has reduced mechanical properties.

**Keywords** Additive manufacturing · Polylactic acid · Recycling · Mechanical properties · Thermal properties · Fused deposition modelling

---

T. K. Ong

Tunku Abdul Rahman University College, Jalan Genting Kelang, Kampus Utama, Jalan Genting Kelang, 53300 Kuala Lumpur, Wilayah Persekutuan Kuala Lumpur, Malaysia

H. L. Choo (✉) · W. J. Choo · S. C. Koay · M. M. Pang

School of Computer Science and Engineering, Taylor's University, No. 1 Jalan Taylor's, 47500, Subang Jaya Selangor, Malaysia

e-mail: [HuiLeng.Choo@taylors.edu.my](mailto:HuiLeng.Choo@taylors.edu.my)

© Springer Nature Singapore Pte Ltd. 2020

S. S. Emamian et al. (eds.), *Advances in Manufacturing Engineering*, Lecture Notes in Mechanical Engineering, [https://doi.org/10.1007/978-981-15-5753-8\\_67](https://doi.org/10.1007/978-981-15-5753-8_67)

725

## 1 Introduction

Additive manufacturing (AM), colloquially known as 3D printing, has gained a lot of attention in the past decades. It is a layered manufacturing process whereby materials are deposited layer by layer according to the CAD design to create a 3D product. One of the most popular AM methods is based on material extrusion process, which is commonly known as fused deposition modelling (FDM). In this process, thermoplastic filament is heated to its melting temperature and then extruded via a nozzle to form the required shape. The most common materials used for FDM process are polylactic acid (PLA) and acrylonitrile butadiene Styrene (ABS). PLA has lower melting temperature and is easier to print than ABS. Research has also shown that PLA requires 25–55% less fossil energy than petroleum-based polymers for manufacturing [1]. In addition, PLA is also compostable. These have made PLA the most common material to be used in FDM.

In the FDM process, wastes are generated from the support structures, rafts and skirts that are removed after printing and from scrapped parts due to printing error. Wastes are also produced when prototypes are discarded after serving their purpose. These wastes are generally thrown away for landfill and are rarely recycled in-house for reuse.

Recycling of PLA using extrusion and injection moulding was investigated. Żenkiewicz et al. [2] studied the mechanical and thermal properties of PLA extruded up to ten cycles. The authors found a decrease of 5.2% in tensile strength and a decrease of 20% in impact strength. Melt flow rate (MFR) was found to increase by 236% at the end of the tenth extrusion. In terms of thermal properties, glass transition temperature ( $T_g$ ) and melting temperature ( $T_m$ ) were found to be relatively stable, whereas crystallinity of the samples increased from 18% to 34%. They attributed this to the formation of a higher number of crystallisation centres due to degradation and/or impurities found in the samples with subsequent extrusion. Scaffaro et al. [3] recycled PLA with plasticiser by extrusion and injection moulding up to three times and found that the material became stiffer and more brittle. The impact strength experienced a drop of around 50% upon first recycling and further recycling did not have as much influence.

To date, there is limited research in recycling of 3D printing wastes with a focus on the mechanical and thermal properties. Anderson [4] investigated the mechanical properties of recycled PLA from 3D printing wastes. The collected wastes were recycled using a desktop filament extruder. The mechanical properties of recycled PLA were found to decrease by 11% for tensile yield strength and 5% for tensile modulus. In addition, the variability of the data was found to increase. The author faced some difficulties in printing recycled PLA which could be due to impurities since filtering was not used during extrusion. Sanchez et al. [5] investigated the mechanical properties after five cycles and found that tensile modulus increased slightly after each cycle, whereas there was a large decrease in tensile modulus. Zhao et al. [6] studied the closed-loop recycling of PLA used in FDM. The authors extruded their own filament from virgin PLA pellets using a twin-screw extruder. It was found

that the material can only be used for two cycles in 3D printing due to significant deterioration in the viscosity brought about by thermomechanical degradation. They also blended recycled PLA with virgin material, which was able to improve the viscosity and thus facilitates the closed-loop recycling process.

The aim of this research was to investigate the feasibility of recycling PLA wastes from Taylor's University 3D printing laboratory for reuse in FDM process. A desktop filament single-screw extruder was used as this is a low-cost option that could be a more viable option. Mechanical and thermal properties were investigated to determine the quality of the recycled PLA filament and parts printed using the recycled filament.

## 2 Methods

### 2.1 Preparation of Wastes and Filament Extrusion

Printing wastes were collected from the 3D printing laboratory at Taylor's University. The laboratory uses PolyLite™ PLA filament from polymaker. Around 2.3 kg of wastes were collected in a month, which mostly consisted of failed parts and support structures. This is equivalent to more than two rolls of new filaments. The wastes collected were separated based on colours as mixing of colours may influence the properties of the recycled filaments. In this project, only white-coloured PLA wastes were used as it formed majority of the wastes collected. The wastes collected were shredded into pieces of around 3–5 mm, which is similar in size to most of the virgin PLA pellets. In this study, test specimens were also printed using new PLA filaments for results comparison. After testing, these samples were also recycled along with collected wastes.

The shredded PLA wastes were dried in an oven at a temperature of 80 °C for 12 h prior to extrusion to remove moisture. A Wellzoom Desktop Extruder Line II with a maximum extrusion speed of 4400 mm/min was used to produce the filaments. The filaments were extruded using a 1.75 mm die and a temperature profile of 210–205 °C. The extrusion speed and filament winding speed were adjusted manually using two independent controllers until filament of around  $1.75 \pm 0.10$  mm was obtained. The actual speed was unknown and not measured in this study.

### 2.2 3D Printing

Manufacturing was carried out using a material extrusion-type printer, Raise3D N2 Dual with a 0.4 mm nozzle. The main process parameters used are shown in Table 1. These parameters are the standard parameters used to print PLA parts in the laboratory. Tensile, flexural and impact tests specimens were printed according to ASTM

**Table 1** Process parameters for 3D printing

Process parameters	Values
Printing temperature (°C)	215
Bed temperature (°C)	60
Printing speed (mm/s)	60
Layer height (mm)	0.15
Fill density (%)	100

D638 Type I, ASTM D790 and ASTM D256 notched, respectively. At least five specimens were printed for each test. Test specimens printed using new PLA filaments are designated as Cycle 0, whereas PLA wastes that were recycled once and twice are designated as Cycle 1 and Cycle 2, respectively.

### 2.3 Mechanical and Thermal Properties Testing

Tensile and flexural tests were performed using a GT-TCS-2000 Universal Testing Machine according to ASTM D638 and D790, respectively. Tensile tests were carried out using a 20 kN load cell at a speed of 5 mm/min, and strain was measured using a 50 mm extensometer. For flexural tests, the support span was set at 53 mm with a crosshead speed of 1.4 mm/min. Impact tests were carried out according to ASTM D256 using an Izod Impact Tester GT-7045-HMH. The initial angle of the pendulum was set to 150.13°, and the weight of the pendulum used was 635.1 g.

Differential scanning calorimetry (DSC) was performed using a Perkin Elmer DSC 8000 to determine the thermal properties of the new and recycled filaments. Samples of around 10 mg were measured into an aluminium pan. Samples were heated from 30 to 200 °C at a heating rate of 10 °C/min and then cooled from 200 to 30 °C at a cooling rate of 10 °C/min. Finally, a second heating was done from 30 to 200°C at a heating rate of 10 °C/min. All heating and cooling were carried out in a nitrogen atmosphere at a rate of 20 ml/min. Crystallinity,  $\chi$ , is calculated using Eq. 1 [7]

$$\chi(\%) = \frac{\Delta H_m - \Delta H_{cc}}{\Delta H_m^{\circ}} \times 100 \quad (1)$$

where  $\Delta H_m$  (J/g) and  $\Delta H_{cc}$  (J/g) are the melting enthalpy and cold crystallisation enthalpy, respectively, and  $\Delta H_m^{\circ}$  (J/g) is the melting enthalpy for a 100% crystalline PLA which is 93.1 J/g [8].

### 2.4 Melt Flow Rate (MFR)

MFR was conducted using a TWELVindex to investigate the ease of flow of the PLA; the higher the MFR, the easier the flow is. Temperature, plunger weight and cut time were set as 190°C, 2.16 kg and 15 s, respectively, according to ASTM D1238. Around 10 g of new and recycled filaments were cut to pellet size and placed inside the barrel from the top of the machine and a plunger weighing 2.16 kg was used to extrude the specimen out through a die. Samples were cut automatically at 15 s interval. At least four samples were obtained for each cycle and weighed. MFR, in g/10 min, was calculated using Eq. 2

$$\text{MFR (g/10 min)} = w_{15} \times 40 \tag{2}$$

where  $w_{15}$  (g) is the average weight of material extruded in 15 s.

## 3 Results and Discussion

### 3.1 Mechanical Properties

Mechanical properties of PLA samples at Cycle 0, 1 and 2 are shown in Table 2. Due to extrusion and printing difficulties, only flexural tests were carried out after second recycling. No results were obtained for impact strength and tensile tests. All properties were observed to have deteriorated after one cycle. Tensile modulus and tensile strength decreased by around 48% and 50%, respectively. The samples were also observed to be more brittle with a reduction of 64% in elongation at

**Table 2** Mechanical properties of new PLA (Cycle 0), PLA after one recycling (Cycle 1) and after two recycling (Cycle 2)

	Cycle 0	Cycle 1	Cycle 2
Tensile modulus (GPa)	3.13 ± 0.08	1.64 ± 0.23	1.46*
Tensile strength (MPa)	25.50 ± 0.80	12.64 ± 1.66	11.00*
Elongation at break (%)	2.24 ± 0.52	0.81 ± 0.08	0.78*
Flexural modulus (GPa)	1.72 ± 0.09	1.33 ± 0.20	0.66 ± 0.26
Flexural Strength (MPa)	46.44 ± 0.75	34.92 ± 4.51	21.37 ± 10.00
Impact strength (kJ/m <sup>2</sup> )	3.96 ± 0.19	1.91 ± 0.11	No Result

*Note* \*Indicates that the sample size is one, hence results are not conclusive and are used as an indication only



break. Flexural properties also decreased but not as much when compared to tensile properties. Flexural modulus and flexural strength both decreased by about 23% and 25%, respectively. After second recycling, properties dropped drastically by 50% and 39%, respectively. Impact strength was also observed to decrease by 52%. The variation in the properties also increased in general after one cycle. Similar to the results obtained by previous researchers [2–6], the mechanical properties of the PLA were found to decrease with increasing number of cycles. However, the decrease in properties was found to be more drastic in this study.

As mentioned earlier, there were some difficulties during filament extrusion and printing. In the first cycle, the filaments can be extruded but it was observed that the output from the die was occasionally inconsistent. This resulted in filaments with varying diameter. During printing, the nozzle was sometimes clogged. The same was experienced by Anderson [4], who suggested that this could be because filtering was not used during extrusion causing impurities to enter the filament. The short screw length could also lead to inhomogeneous melting of PLA resulting in unmelted microparticles clogging the nozzle head. It is interesting to note that this research also used a desktop filament extruder and faced the same problem, whereas other literature using a twin-screw extruder did not mention similar observation. In the second cycle, the problem during extrusion was more pronounced. The diameter of the extruded filaments became more inconsistent and printing problem worsened. As shown in Fig. 1, the distance between each extrusion during printing increases from Cycle 0 to Cycle 2. The filaments with inconsistent diameter could have affected the amount of PLA melt pool in the nozzle, hence causing this problem. The drastic reduction in mechanical properties could be a direct result of the difficulties experienced during extrusion and printing.

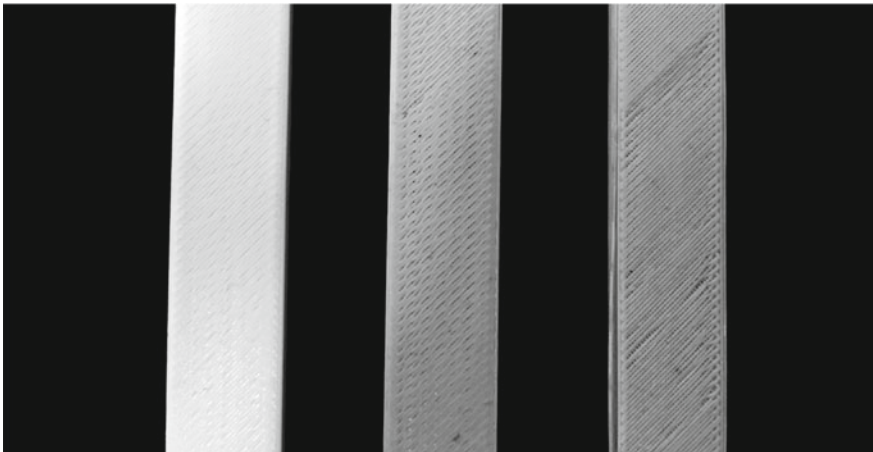


**Fig. 1** (L-R) specimens printed using new PLA filament (Cycle 0), after one recycling (Cycle 1) and after two recycling (Cycle 2). Each extrusion can be seen to be further apart from Cycles 0 to 2. This is notable for Cycle 2 as parts of the outer shells were loose

**Table 3** DSC results for new PLA (Cycle 0) and PLA after one recycling (Cycle 1)

Properties	Cycle 0	Cycle 1
$T_g$ (°C)	62.45	60.75
$T_m$ (°C)	152.15	152.65
$\Delta H_m$ (J/g)	24.4	32.2
$\chi$ (%)	26.2	34.6

**Table 4** MFR values of new PLA (Cycle 0), PLA after one recycling (Cycle 1) and after two recycling (Cycle 2)

	Cycle 0	Cycle 1	Cycle 2
MFR (g/10 min)	6.73 ± 0.58	15.04 ± 1.17	26.28 ± 1.43

### 3.2 Thermal Properties

Glass transition temperature ( $T_g$ ), melting temperature ( $T_m$ ), melting enthalpy ( $\Delta H_m$ ) and per cent crystallinity ( $\chi$ ) are shown in Table 3 for Cycle 0 and Cycle 1 PLA.  $T_g$  was found to decrease, whereas  $T_m$  was found to increase slightly. Percent crystallinity was found to increase from 26.2 to 34.6%, confirming that degradation had occurred. Zhao et al. [6] explained that 3D printing resulted in shorter polymer chains which are able to crystallise more easily, increasing the crystallinity. The impurities that were present in Cycle 1 could also act as nucleating site, thus increasing its crystallinity.

### 3.3 Melt Flow Rate

MFR values are shown in Table 4 for Cycle 0 to Cycle 2. MFR measures the flowability of the polymer and can indicate the molecular weight of the polymer. An increase in MFR could mean degradation as polymer chain scission has taken place, allowing the polymer to flow more easily. After one recycling, the MFR value increased by 123% and further recycling increased the MFR by a further 75%. According to Wang et al. [9], an MFR above 10 g/10 min shows good printability without blockage. This is true for Cycle 0, where it printed smoothly at 215 °C, above the 190 °C used for MFR test. However, for Cycles 1 and 2, when printing was done at 215 °C, blockage still occurred. The increasing MFR value could be correlated with the decrease in molecular weight due to degradation of the polymer by chain scission, which explains the lower mechanical properties. Even though the PLA was dried prior to extrusion, some moisture could still be present or absorbed during handling, resulting in hydrolytic degradation. In addition, the change in colour of the filament from white to dull white (Fig. 1) supports this theory.

## 4 Conclusions

This research looked into the recycling of PLA wastes collected from university 3D printing laboratory. A total of two cycles were carried out. In Cycle 1, the mechanical properties reduced drastically, which could be attributed to degradation. In Cycle 2, a lot of extrusion and printing problems were encountered, therefore limited samples were produced. The mechanical properties showed further degradation. Overall, this research has shown that it is viable to recycle PLA wastes in the university laboratory. However, a reduction in mechanical properties should be expected due to degradation. The printing quality was also affected as evident in the increase in distance between each extrusion. It should be noted that a single-screw desktop filament extruder may not be efficient for recycling as it may cause clogging during printing. Further investigation will be required to verify this. From the results of this research, it is suggested that PLA wastes are to be recycled only once, as further recycling was shown to create a lot of issues in extrusion and printing.

## References

1. Vink ETH, Rábago KR, Glassner DA et al (2003) Applications of life cycle assessment to NatureWorks<sup>TM</sup> polylactide (PLA) production. *Polym Degrad Stab* 80(3):403–419
2. Żenkiewicz M, Richert J, Rytlewski P et al (2009) Characterisation of multi-extruded poly(lactic acid). *Polym Test* 28(4):412–418
3. Scaffaro R, Morreale M, Mirabella F et al (2011) Preparation and recycling of plasticized PLA. *Macromol Mater Eng* 296(2):141–150
4. Anderson I (2017) Mechanical properties of specimens 3D printed with virgin and recycled polylactic acid 3D print. *Addit Manuf* 4(2):110–115
5. Cruz Sanchez FA, Boudaoud H, Hoppe S et al (2017) Polymer recycling in an open-source additive manufacturing context: mechanical issues. *Addit Manuf* 17:87–105
6. Zhao P, Rao C, Gu F et al (2018) Close-looped recycling of polylactic acid used in 3D printing: An experimental investigation and life cycle assessment. *J Clean Prod* 197:1046–1055
7. Kong Y, HayJN (2002) The measurement of the crystallinity of polymers by DSC. *Polymer (Guildf)*
8. Deroiné M, Le Duigou A, Corre Y-M et al (2014) Accelerated ageing of polylactide in aqueous environments: comparative study between distilled water and seawater. *Polym Degrad Stab* 108:319–329
9. Wang S, Capoen L, D'hooge DR et al (2018) Can the melt flow index be used to predict the success of fused deposition modelling of commercial poly(lactic acid) filaments into 3D printed materials? *Plast Rubber Compos* 47(1):9–16

# A Framework for the Optimal Sizing of Hybrid Solar PV-Battery-Hydro System for a Rural House in Malaysia



Bilawal A. Bhayo, Hussain H. Al-Kayiem, and Syed I. U. Gilani

**Abstract** This paper presents a framework for the optimal sizing of hybrid system utilizing the solar energy and direct rainfall for power generation to meet the load demand of rural house in Malaysia. The rainfall through catchment area is utilized to generate power when the power from PV is not enough to meet the load demand. The loss of power supply probability (LPSP) is considered as constant value for four different case studies. Case 1 and Case 2 are the PV-Battery system and PV-Battery-Hydro system, respectively, with LPSP of 0.0. Case 3 and Case 4 are the PV-Battery system and PV-Battery-Hydro system, respectively, with LPSP of 0.02. Using particle swarm optimization (PSO), the optimal sizing is determined based on the minimization of levelized cost of energy (LCE). For LPSP of 0.0, the integration of only 0.05 kWh rainfall-based hydropower systems with PV-Battery system resulted in reduction in the battery capacity of about 2.66%. Compared to other cases, the lowest LCE of about 0.3613 \$/kWh is found for Case 3. For the LPSP of 0.0, the power systems are oversized, which resulted in high LCE. The integration of rainfall-based hydropower system with PV-Battery system for LPSP of 0.0 and 0.02 has increased and decreased the surplus power by 0.8% and 2.5%, respectively, than the conventional PV-Battery system. It is intimated that with robust power management and water storage, the integrated solar/rainfall-based hydro system can be of more advantageous.

**Keywords** Hybrid renewable energy system, photovoltaic system · Levelized cost of energy · Loss of power supply probability

---

B. A. Bhayo (✉) · H. H. Al-Kayiem · S. I. U. Gilani  
Mechanical Engineering Department, Universiti Teknologi PETRONAS, 32610, Bandar Seri  
Iskandar Perak, Malaysia  
e-mail: [bilawal.bhayo@yahoo.com](mailto:bilawal.bhayo@yahoo.com)

B. A. Bhayo  
Department of Mechanical Engineering, Mehran University of Engineering & Technology  
Shaheed Zulifqar Ali Bhutto Campus, 66020 Khairpur Mirs, Sindh, Pakistan

## 1 Introduction

Integrated solar PV and rainfall-based hydropower system in Malaysia is motivating due to tropical weather. Average annual rainfall in Malaysia is more than three times the world average annual rainfall of 750 mm. In Peninsula, Sabah, and Sarawak, the average annual rainfall is 2540 mm, 2630 mm, and 3850 mm, respectively [1]. Whereas, the average solar radiation in Malaysia is also considerably high and about 4500 W/m<sup>2</sup>/day [2, 3]. Due to high potential of solar radiation and rainfall in Malaysia, the solar PV-hydro system can be installed to produce electricity at lower cost with high system reliability. The integration of rainfall based hydropower system with solar photovoltaic is very interesting. When, the PV system fails to produce power due to heavy rain, the hydro system will still be producing power by utilizing the rain water. Thus, the proposed hybrid solar PV-Battery-Hydro design can ensure the high reliability of power supply with less numbers of expensive batteries. Furthermore, if PV-Battery-Hydro system is optimized, it can lead to more economical and reliable power generation.

The optimization studies are being carried out from the previous two and half decades. The trend has exhibited that artificial intelligent algorithms are mostly used in the last decade due to reduced computation time, high accuracy, and good conversions [4]. The meta-heuristic approaches copied from natural processes (likewise, exchange of information between swarm of fish, flocks of birds) are being used to solve the complex optimization where the other optimization approaches are not able to acquire good results [5]. It is complex to determine the optimal sizing of HRES due to nonlinear behavior of the system components and stochastic nature of the renewable resources [6–8].

The meta-heuristic approaches, such as particle swarm optimization (PSO) and genetic algorithm (GA), have the tendency to optimize the hybrid renewable energy system (HRES) [9]. PSO is simple, easy to implement, and requires information of only few parameters. In contrast to GA, PSO has proved to be robust and efficient optimization approach [10–13].

The aim of this research is to develop a framework for the integration of solar PV-Battery system and rainfall-based hydropower system to meet the load demand of a rural house in Malaysia. PSO was applied for the optimal sizing of PV-Battery and PV-Battery-Hydro system by considering the LPSP of 0 and 0.02. The sizing of components involved in the power system was determined by minimizing the LCE. The comparative analysis of all four case studies was also attempted to determine effect of LPSP on the optimal sizing of PV-Battery system with hydropower system in tropical weather of Malaysia.

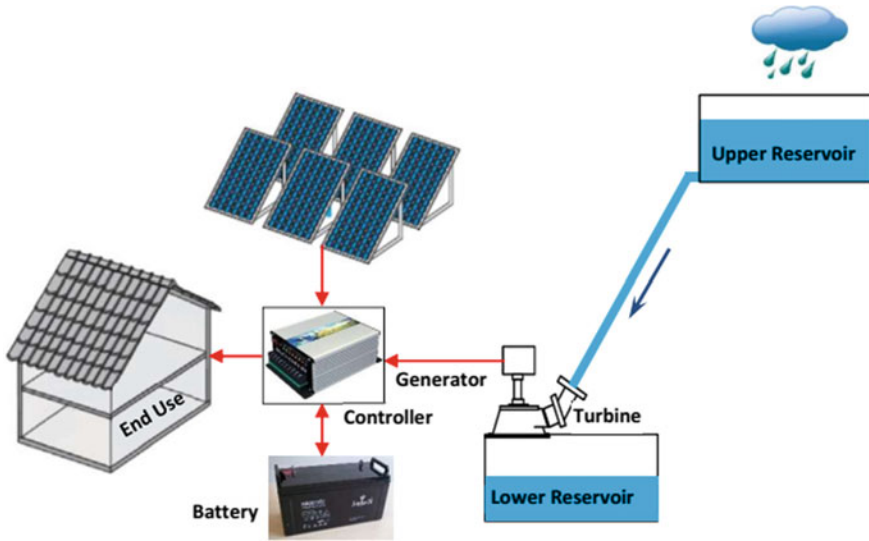


Fig. 1 Interconnection of the hybrid solar PV-battery-hydro components

## 2 Design, Materials and Methods

### 2.1 Design of PV-Hydro System

The integrated PV-hydropower is shown in Fig. 1. In the designed PV-hydro system, PV is the main source to meet the load demand and charge the batteries. When the solar radiations are absent or not enough to produce the needed power, i.e., in evening or during cloudy weather, the batteries will be used to supply the deficit power. However, in the rainy weather, rain water will be harvested through gutters to produce hydropower and minimize the power discharge from the batteries. The proposed strategy of utilizing the rainwater for power generation is expected to reduce the over sizing of standalone PV system in tropical weather.

### 2.2 Case Studies for Optimal Sizing in PSO

Sizing of PV-hydro system is determined in PSO using the framework presented in this paper. Four different case studies, as exhibited in Table 1, are considered for the optimal sizing. The weather data and specification inputs are identical for all four cases to provide a decisive comparison.

**Table 1** Categorization of cases for the optimal sizing

Case #	Power system	LPSP
Case 1	PV-battery	0.0
Case 2	PV-battery-hydro	0.0
Case 3	PV-battery	0.02
Case 4	PV-battery-hydro	0.02

### 2.3 Data Inputs for Sizing the Power System

The data inputs for sizing of power system are critical. Power system sizing is complex and site dependent. The objective function, LCE, for optimal system configuration is based on the input parameters [14]. Whereas, LPSP values are considered fixed as 0.0 and 0.02. The data inputs required for the execution of algorithm are weather data, house load profile, technical parameters, and cost of components. Therefore, the records of weather data used for the present analysis are from Jabatan Meteorologi Malaysia (Department of Metrology Malaysia). The daily house load demand for a rural remote house in Malaysia is taken as 3.1 kWh/day and the peak load demand is 0.274 kWh. In technical parameters, commercial photovoltaic module of 100 W<sub>p</sub> is considered. The inverter sizing is fixed to 0.350 kW for meeting the peak load demand. Whereas, the charge controller is 1.2 times the installed PV. Furthermore, the catchment area for rainfall-based hydropower system is 100 m<sup>2</sup> and the overall efficiency of hydropower system is taken as 80%.

The investment cost and life time in \$/W and in years of components in case studies are considered as 0.9 and 30, 0.4 and 5.0, 2.0 and 30, 0.2 and 10, and 0.2 and 10 for photovoltaic, battery, hydropower, inverter, and charge controller, respectively. However, the operation and maintenance (O&M) involved are only for photovoltaic and hydropower system in \$/W/Year as 0.018 and 0.04, respectively. The total cost was determined for LCE by considered the project lifetime as 30 years [14].

### 2.4 Constraint Values in the Optimization

In the optimal sizing, constrains define the boundaries for the search region. Each constrain considered in the problem specifies a parameter and number of constrains used in this study. For deciding number of PV panels, lower bound and upper bound as 0.0 and 10 are considered, respectively. For the battery, the minimum state of charge (SOC<sub>min</sub>) is 20% of maximum state of charge (SOC<sub>max</sub>), and SOC<sub>max</sub> is 90%. For determining the installed battery capacity, the SOC<sub>max</sub> lower bound and upper bound are taken as 0.0 and 5000, respectively. Also, there are several constrains associated with the rainfall-based hydropower system such as, catchment area, water storage capacity, water head, and minimum discharge for hydro turbine. However,

in the present study, the total rain falls on catchment areas of 100 m<sup>2</sup> at head of 6 m is utilized through gutters to generate power when the power generated by PV is not enough to meet the load demand.

### 3 Results and Discussion

Optimal sizing and cost analysis are carried out for four different case studies. Case 1 and Case 2 are with LPSP of 0.0, and Case 3 and Case 4 are with LPSP of 0.02, i.e., system power reliability of 100% and 98%, respectively. Using PSO, the LCE is obtained following to the optimal sizing. In the optimal sizing, the installation capacity of PV, battery, inverter, and charge controller are determined.

Table 2 shows the optimal sizing of all analyzed cases. It can be observed that in PV-Battery system with LPSP of 0.0, the battery installed capacity has decreased by 2.66% with the integration of rainfall-based hydropower system of only 0.05 kW. However, for LPSP of 0.0, the integration of hydropower system has led to a meager increase of installed PV of 0.64%. For LPSP 0.02, the battery installed capacity has increased by only 0.85% and installed PV capacity has decreased by 4.2%. A meager increase of battery capacity and considerable high decrease of PV capacity for LPSP of 0.02 is due to the trade off to achieve minimum LCE.

Analysis results presented in Table 3 show the LCE, house load, power generation, and total cost in lifetime for Case 1 to Case 4. The increase of power reliability has caused to increase the LCE due to oversizing of the components. The integration of hydropower system depending on rainfall has led to increase in the LCE due to dependency on the rainfall and applied condition that when PV system fails to meet the load demand.

**Table 2** Optimal sizing of components

Case#	PV (kWp)	Battery (kWh)	Inverter (kWh)	Charge controller (kW)	LPSP
Case 1	1.721	3.044	0.35	2.1	0
Case 2	1.732	2.963	0.35	2.1	0
Case 3	1.152	2.954	0.35	1.4	0.02
Case 4	1.104	2.979	0.35	1.4	0.02

**Table 3** LCE, total cost, power generation, and house load in lifetime

Case#	LPSP	Total cost (\$/lifetime)	Power generation (kWh/lifetime)	House load kWh/lifetime	LCE (\$/kWh)
Case 1	0	14947.9	75972.9	33397.5	0.425
Case 2	0	15101.6	76736.5	33397.5	0.4293
Case 3	0.02	12711.6	50847.2	33397.5	0.3613
Case 4	0.02	12961.7	49046.1	33397.5	0.3685



**Table 4** Surplus and deficient power in lifetime

Case#	Case#	Power generation kWh/lifetime	Loss of power supply kWh/lifetime	Surplus power %age/lifetime
Case 1	Case 1	75972.9	0	53.40%
Case 2	Case 2	76736.5	0	54.20%
Case 3	Case 3	50847.2	703.1	30.80%
Case 4	Case 4	49046.1	702.7	28.30%

The increase of LCE in Case 2 and Case 4 compared to Case 1 and Case 3 is 1.01% and 2.0%, respectively. Whereas, in Case 2 about 764 kWh/lifetime of power generated is higher due integration of rainfall-based hydro system. In Case 4, the increase of power generated due to integration of rainfall-based hydro system is higher of about 136.0% than the Case 2. Therefore, the hydropower system harvesting direct rainfall has high utility when the LPSP is 0.02. Furthermore, if all the generated power is utilized, then the Case 2 and Case 4 can lead to decreased LCE.

Table 4 exhibits the predicted surplus power and deficit power for all four investigated cases. The PV-Battery-Hydro system with LPSP of 0.0 has higher surplus power of about 0.8% than the PV-Battery system. However, it can be due to the decrease in the battery capacity of about 2.66%. In PV-Battery-Hydro system with LPSP of 0.02, the surplus power is about 2.5% lower than the system without hydropower. It can also be observed that when LPSP is high the surplus power is also high. The high surplus power can be due to the oversizing of the system components. In addition, the hydropower system has high utility when LPSP is low. In Case 3 and Case 4, the total loss of power supply is only around 1.4%/lifetime than the available surplus power. Therefore, robust power management is further needed for managing the surplus power to useful power and reduce unit cost of electricity.

Figure 2 exhibits the optimal sizing of PV in kW<sub>p</sub>, battery in kWh, and LCE in \$/kWh for four case studies. An appropriate system to meet the load demand of a rural remote house in Malaysia is PV-Battery system. However, integration of rainfall-based hydropower system can reduce the dependency on the battery bank and generate power in rainy events. If the hydropower system as proposed in this study is scaled up, it can lead to decrease the LCE.

## 4 Conclusions

In this paper a framework to integrate rainfall-based hydropower system with solar PV-Battery system is presented. With PSO and the developed framework, an optimal sizing has been determined to meet the load demand of a rural house in Malaysia. The objective function in this study is LCE. Whereas, the LPSP values are kept fixed at 0.0 and 0.02. At each value of LPSP, the PV-Battery system with and without

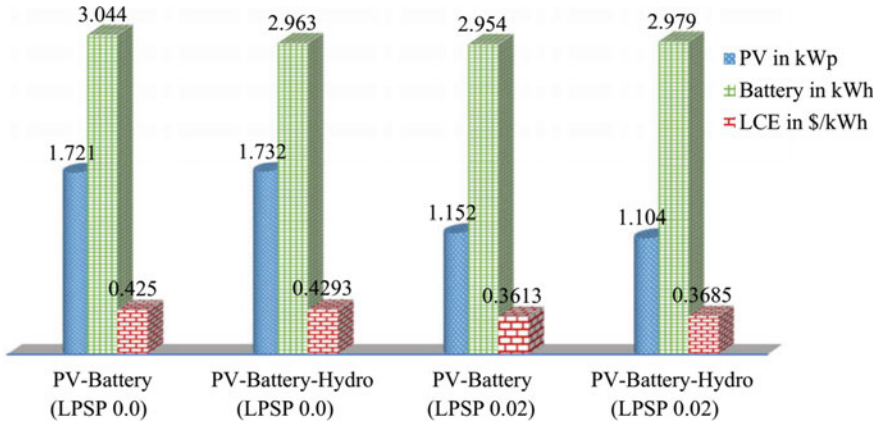


Fig. 2 Optimal sizing of PV in kW<sub>p</sub>, battery in kWh and LCE in \$/kWh for four case studies

integration of rainfall-based hydropower system is optimized for LCE. The integration of hydropower system of only 50 watts (net maximum power) has exhibited an average decrease in battery capacity of about 2.66% for LPSP of 0.0. For LPSP of 0.02, the PV installed capacity is reduced by 4.2% and battery installed capacity is increased by only 0.6%. In contrast to conventional PV-Battery system, the integrated PV-Battery system with rainfall-based hydropower system has increased the surplus power by 0.8% at LPSP of 0.0 and decreased the surplus power by 2.5% at LPSP of 0.02. The integration of rainfall-based power system can be more advantageous in standalone applications when all the generated power is utilized. It is suggested that instead of power generation from direct rainfall, the collected rainfall should be utilized with effective water storage system comprises ground storage tank and elevated storage tank of more than 6 m<sup>3</sup>.

**Acknowledgements** The authors acknowledge Universiti Teknologi PETRONAS (UTP) for providing the technical and logistic support to carry out the research and funding the publication cost under YAYASAN UTP (YUTP FRG; CS: 015LC0-206) and partially from RIPHEN joint research grant. In particular, the first author expresses his thankful remarks to UTP for supporting his PhD under the Graduate Assistance (GA) scheme.

## References

1. Kadier A, Kalil MS, Pudukudy M, Hasan HA, Mohamed A, Hamid AA (2018) Pico hydropower (PHP) development in Malaysia: potential, present status, barriers and future perspectives. *Renew Sustain Energy Rev* 81:2796–2805. <https://doi.org/10.1016/j.rser.2017.06.084>
2. Md Tasbirul Islam NH, Saidur R (2019) Current energy mix and techno-economic analysis of concentrating solar power (CSP) technologies in Malaysia. *Renew Energy* 140:789–806. <https://doi.org/10.1016/j.renene.2019.03.107>

3. Borhanazad H, Mekhilef S, Saidur R, Boroumandjazi G (2013) Potential application of renewable energy for rural electrification in Malaysia. *Renew Energy* 59:210–219. <https://doi.org/10.1016/j.renene.2013.03.039>
4. Sinha S, Chandel S (2015) Review of recent trends in optimization techniques for solar photovoltaic–wind based hybrid energy systems. *Renew Sustain Energy Rev* 50:755–769. <https://doi.org/10.1016/j.rser.2015.05.040>
5. Fodhil F, Hamidat A, Nadjemi O (2019) Potential, optimization and sensitivity analysis of photovoltaic-diesel-battery hybrid energy system for rural electrification in Algeria. *Energy* 169:613–624. <https://doi.org/10.1016/j.energy.2018.12.049>
6. Monotosh Das MAKS, Biswas Agnimitra (2019) Techno-economic optimization of an off-grid hybrid renewable energy system using metaheuristic optimization approaches—case of a radio transmitter station in India. *Energy Convers Manag* 185:339–352. <https://doi.org/10.1016/j.enconman.2019.01.107>
7. Dufo-Lopez R, Bernal-Agustín JL, Contreras J (2007) Optimization of control strategies for stand-alone renewable energy systems with hydrogen storage. *Renew Energy* 32(7):1102–1126. <https://doi.org/10.1016/j.renene.2006.04.013>
8. Luna-Rubio R, Trejo-Perea M, Vargas-Vázquez D, Ríos-Moreno G (2012) Optimal sizing of renewable hybrids energy systems: a review of methodologies. *Sol Energy* 86(4):1077–1088. <https://doi.org/10.1016/j.solener.2011.10.016>
9. Sharafi M, ELMekawy TY (2014) Multi-objective optimal design of hybrid renewable energy systems using PSO-simulation based approach. *Renew Energy* 68:67–79. <https://doi.org/10.1016/j.renene.2014.01.011>
10. Fadaee M, Radzi M (2012) Multi-objective optimization of a stand-alone hybrid renewable energy system by using evolutionary algorithms: a review. *Renew Sustain Energy Rev* 16(5):3364–3369. <https://doi.org/10.1016/j.rser.2012.02.071>
11. Askarzadeh A, dos Santos Coelho L (2015) A novel framework for optimization of a grid independent hybrid renewable energy system: a case study of Iran. *Sol Energy* 112:383–396. <https://doi.org/10.1016/j.solener.2014.12.013>
12. Zahraee S, Assadi MK, Saidur R (2016) Application of artificial intelligence methods for hybrid energy system optimization. *Renew Sustain Energy Rev* 66:617–630. <https://doi.org/10.1016/j.rser.2016.08.028>
13. Erdinc O, Uzunoglu M (2012) Optimum design of hybrid renewable energy systems: Overview of different approaches. *Renew Sustain Energy Rev* 16(3):1412–1425. <https://doi.org/10.1016/j.rser.2011.11.011>
14. Bhayo BA, Al-Kayiem HH, Gilani SI (2019) Assessment of standalone solar PV-Battery system for electricity generation and utilization of excess power for water pumping. *Sol Energy* 194:766–776. <https://doi.org/10.1016/j.solener.2019.11.026>

# Anaerobic Treatment of Chicken Manure Co-digested with Sawdust



H. Y. Kok, M. R. Shamsuddin, and A. Aqsha

**Abstract** The high total nitrogen content of chicken manure (CM) makes it suitable to undergo anaerobic digestion (AD) for the production of biogas. In this study, AD of CM was done using sawdust (SD) as co-substrate to investigate the quality of biogas produced. CM and SD were mixed to reach different carbon-to-nitrogen (C/N) ratios of 20, 25, 30, and 35. By using laboratory scale of 10L digesters, biogas production was investigated in anaerobic fermentation. Cow manure, as inoculum, was added in each digester to facilitate the anaerobic fermentation process. The process was performed in batch reactors at temperature of 35 °C, and a retention time of 60 days. Under mesophilic conditions, all co-digestions of CM and SD improved biogas and methane (CH<sub>4</sub>) yields significantly compared to control. Percentage of methane had increased up to 65.9% for CM and SD at C/N ratio of 30. The highest methane yields (percentages of methane) obtained from different C/N ratios were as follows: C/N 30 (65.9%), C/N 35 (47.0%), C/N 20 (46.5%) and C/N 25 (44.2%). Mono-digestion of CM generated only 20.5% methane on day 60, possibly due to the high amount of nitrogen that caused ammonia inhibition.

**Keywords** Anaerobic digestion · Chicken manure · Carbon-to-nitrogen ratio (C/N) · Sawdust · Co-digestion

## 1 Introduction

The poultry demand of Malaysia increases as the population increases. In 2015, the number of chicken farms was estimated around 662 establishments [1]. Adult chicken can produce up to 59 kg of manure a year [2]. With a large volume of manure generation, the waste has to be discarded safely without harming the environment. Manure is traditionally used as fertilizer by applying directly to croplands as chicken manure contains high nutrient value of nitrogen and phosphorus. However, abundant

---

H. Y. Kok · M. R. Shamsuddin (✉) · A. Aqsha  
HICoE, Centre for Biofuel and Biochemical Research, Institute of Self-Sustainable Building,  
Department of Chemical Engineering, Universiti Teknologi PETRONAS, 32610, Seri Iskandar  
Perak, Malaysia  
e-mail: [mrashids@utp.edu.my](mailto:mrashids@utp.edu.my)

manure may release nitrate that can enter ground water through runoff during raining season. This can lead to water pollution. Manure waste also contains growth hormone, antibiotics, microorganisms, and heavy metals which will cause pollution to the environment [3]. Moreover, untreated raw manure can also cause flies problem as flies are attracted to manure as a food source. Flies presence can lead to hygienic issue to nearby residents, affecting their health and living environment [4].

There is an alternative measure to treat chicken manure which is to use them as raw material for AD. Organic matters such as animal or food waste are decomposed to produce biogas and biofertilizer through the biological process of AD. This process happens in the absence of oxygen. CM has a higher energy content compared to other animal wastes such as cow and pig, thus, making it potential for biogas production [5]. The major components of biogas are methane gas (45–70%) and carbon dioxide (25–40%), as well as trace amounts of hydrogen, nitrogen, and hydrogen sulphide. Biogas produced can be converted into electricity and heat [6]. The organic material decomposed through four stages which are hydrolysis, acidogenesis, acetogenesis, and methanogenesis where each stage utilizes different types of anaerobic bacteria to digest the biomass.

In the process of AD, production of ammonia from organic nitrogen of raw material can cause inhibition, thus, resulting in reduced biogas production [7]. In order to reduce or prevent ammonia inhibition, CM can be co-digested with a low nitrogen content feedstock in order to achieve C/N ratio of 15–30, which is the optimum condition for AD process [8]. Various research have shown that the usage of agricultural waste as co-substrate in AD with CM can increase specific methane yield due to better nutrient mixtures [9]. Ideally, co-digestion materials should come from local organic waste in order to lower the overall cost, ensure sustainability and as a mean to value-add or treat the waste. Locally abundant natural sawdust from a local sawmill was selected as the additive material.

## **2 Materials and Methods**

### ***2.1 Raw Materials Collection***

Raw chicken manure was collected from a poultry farm located at Seri Manjung, Perak. Sawdust was collected from Wan Sang Sawmill Enterprise, located in Ayer Tawar, Perak. Moisture content, pH, elemental analysis of C and N, and concentration of P and K were determined for fresh CM and SD. Fresh cow manure was used as inoculum, which was collected from a cow farm in Tanjung Tualang, Perak.

**Table 1** Experimental design

C/N ratio	CM (kg)	SD (kg)	Water (kg)	Inoculum (kg)
8.10 (control)	2.0	0.0	6.0	0.60
20	1.388	0.612	6.0	0.60
25	1.209	0.791	6.0	0.60
30	1.059	0.941	6.0	0.60
35	0.933	1.067	6.0	0.60

## 2.2 Experimental Digester and Setup

A total of five laboratory anaerobic digesters, each with a total volume of 10L, were operated for 60 days. The operating temperature was kept at 35 °C by conducting the process in an oven. Feedstock (CM) and co-substrate (SD) are mixed to form substrate. The ratio of inoculums to substrates was controlled at 30:70 [10]. Water was added to the mixture at a ratio of 1:3 of substrate to water.

Four different mixing ratios of CM and SD were prepared in order to adjust the C/N ratios to 20, 25, 30, and 35. Mono-digestion of CM was also conducted as control. All treatments had the same total weight of substrates of 2 kg. The required mass of CM and SD to achieve specific C/N ratios was calculated using formula below. The substrate formulations are listed Table 1.

$$R = \frac{Q1[C1 \times (100 - M1)] + Q2[C2 \times (100 - M2)]}{Q1[N1 \times (100 - M1)] + Q2[N2 \times (100 - M2)]}$$

where

- $R$  C/N ratio of compost mixture
- $Q_n$  mass (kg) of material  $n$  (wet weight)
- $C_n$  carbon (%) of material  $n$
- $N_n$  nitrogen (%) of material  $n$
- $M_n$  moisture content (%) of material  $n$

## 2.3 Sampling Procedures

Biogas was collected into a gas bag at every 5 days for the first 30 days and every 10 days subsequently until retention time of 60 days. The gas collected was sent for gas composition analysis using GC-NGA (Perkin Elmer, 580 Clarus).

**Table 2** Characteristics of chicken manure and sawdust

Parameter	Concentration	
	Manure	Sawdust
Total C (%)	36.457	45.161
Total N (%)	4.502	0.331
C/N ratio	8.10	136.64
Total K (ppm)	2228.80	26.84
Total P (ppm)	560	nd
pH	5.55	7.14
Moisture Content (%)	39.73	15.33

nd = not detected; ppm = parts per million

### 3 Results and Discussions

#### 3.1 Physicochemical Properties of Substrates

The characterization parameters of CM and SD are shown in Table 2. The concentration of phosphorus (P) of the sawdust was not detected. It had been reported by various researchers that SD only contains a trace amount of P, which can be assumed negligible [12, 13].

The C/N ratios of CM and SD are 8.10 and 136.64, respectively, whereby on its own, they are not ideal for anaerobic bacteria to live in. It has been shown by various research that the optimum range of C/N ratio for microbial activity of methanogens is approximately 20–30 [14]. Raw materials with different C/N ratios can be used together in AD process to improve biogas production [2]. The results indicate that SD is high C content which can be used as an additive material for feedstock preparation at C/N ratios of 20–35.

#### 3.2 Methane Generation of Feedstock at Different C/N Ratio

Figure 1 illustrates the percentage of methane obtained from the mono-digestion and co-digestion setups under mesophilic state. In this experiment, all digesters, in which the C/N ratios were adjusted with SD, had higher methane production compared to the mono-substrate digester throughout all 60 days of retention period.

As shown in Fig. 1, mono-digestion of CM (Control) had the lowest methane percentage throughout the AD process. Methane started to increase after the digestion process took place for 30 days. The highest percentage of methane achieved by the control was 20.5% on day 60. Digesters with adjusted C/N ratio displayed similar trends at the beginning of AD. The production of methane started to increase steadily on day 10. However, methane percentages of C/N 20 digester decreased on day 20,

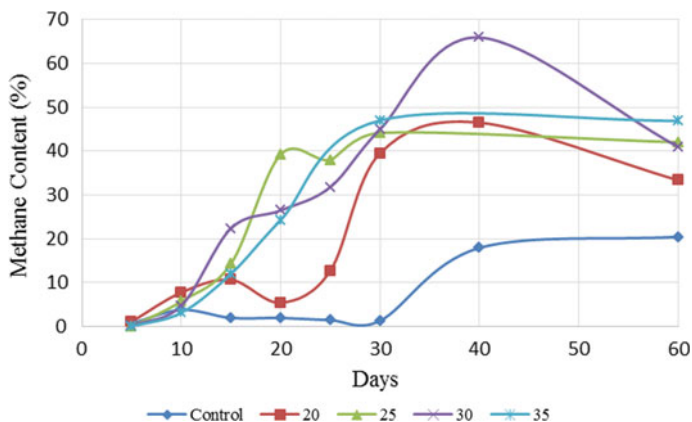


**Fig. 1** Percentage of methane from biogas

with low  $\text{CH}_4$  concentration of 5.4% and high  $\text{CO}_2$  concentration of 41.7%. This indicates that the digester was undergoing acidogenesis during this period [15].

Digesters with C/N ratio adjusted to 20 and 30 had a sharp increase of methane production started on day 25 and they reached the peak of methane percentages of 46.5% and 65.9%, respectively, on day 40. After day 40, methane percentage of digesters C/N 20 and 30 decreased drastically. On the other hand, content of methane produced from digesters C/N 25 and 35 increased steadily and remained constant with peak on day 30. Co-digestion at C/N ratio 30 produced the highest methane percentage (65.9%), followed by C/N 35 (47.0%), C/N 20 (46.5%), and C/N 25 (44.2%). These results have shown similar trends with former findings indicating that the C/N ratio of 25–30:1 is optimum to improve biogas production [16].

Figure 2 illustrates the methane and nitrogen contents of biogas from the digesters. The relationship between methane and nitrogen contents is similar in all the digesters. Methane percentage increased when nitrogen gas decreased. The low methane yield of CM is due to ammonia inhibition caused by the high concentration of nitrogen. Mono-digestion of CM generated more than 50% of nitrogen gas throughout the fermentation period, with average of 68.30%. Ammonia ( $\text{NH}_3$ ) and ammonium ( $\text{NH}_4^+$ ) are the main causes of inhibition during AD that were generated from degradation of proteins [17]. Nitrates can be reduced to nitrogen gas through denitrification, whereas nitrites and ammonia can transform directly into  $\text{N}_2$  gas through anaerobic ammonia oxidation [18], thus, causing the high percentage of  $\text{N}_2$ . The methane yield of CM only started to increase after retention time of 30 days because components that were unable to dissolve, such as proteins or fats, can only be broken down slowly into monomers after several days, hence, prolonging the digestion of CM [19].



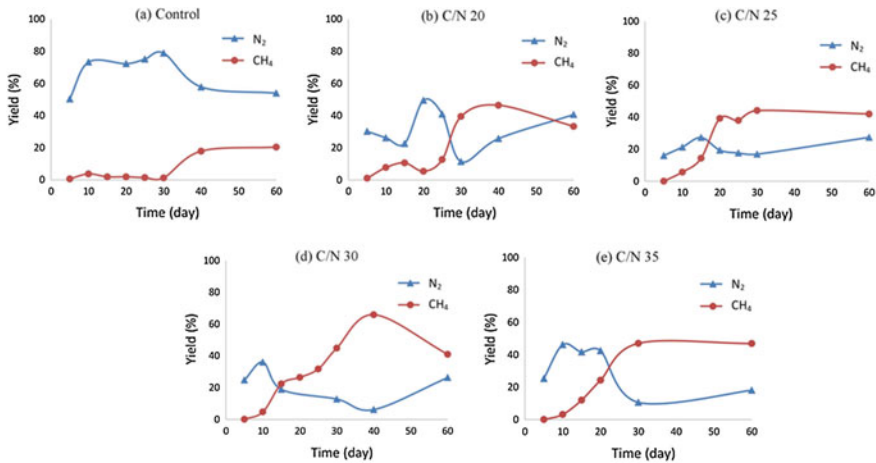


Fig. 2 Methane and nitrogen contents from digesters, **a** control, **b**, C/N 20, **c** 25, **d** 30 and **e** 35

### 3.3 Effect of Sawdust as Co-substrate on Biogas Composition

Anaerobic process of CM co-digested with SD in this experiment is relatively slow when compared to other co-substrates as carbon source. Methane production of CM co-digested with corn stover in biochemical methane potential (BMP) tests reached the peak (54.2–63.5%) around day 5–10 [20]. In AD of pig manure mixed with agricultural waste (rice straw) and kitchen waste, the methane content started to reach the highest percentage (50–60%) and subsequently remained stable on day 14 [21]. However, in this experiment, all C/N adjusted digesters reached the peak of methane production after retention time of 30 days. For digester C/N 20 and 30, methane reached the highest yield on day 40, whereas digester C/N 25 and 35 reached the peak earlier, on day 30. This can be due to the high lignin content in SD. Table 3 shows the lignocellulosic content of different co-substrates.

Dry wood mainly consists of cellulose, lignin, hemicelluloses, and with insignificant amounts (5–10%) of extraneous materials [22]. Hemicellulose can also cross-link with lignin to form complex bonds that provide structural strength to plant, hence further increasing the difficulty to undergo microbial degradation [23, 24]. Lignin's characteristic of resistant to degradation, either biologically, enzymatically or chemically [25, 26] resulted in low bioavailability of substrates [27].

**Table 3** Lignocellulosic content of various co-substrates

Parameter	Corn stover [20]	Rice straw [21]	SD [28]
Cellulose (%)	42.3 ± 1.3	34.96	55.30
Hemicelluloses (%)	29.8 ± 1.2	16.70	8.60
Lignin (%)	9.4 ± 1.1	23.34	27.88

## 4 Conclusions

AD is an alternative treatment process for animal manure with organic waste such as CM and SD are potential co-digestion materials to enhance biogas generation while also producing useful fertilizer. Mesophilic AD of CM with SD had improved methane content to 44.2–65.9% as compared to 20.5% for CM alone. Low methane yield of CM was due to ammonia inhibition on complete digestion of protein-based material in the feedstock. Co-digestion of CM and SD at C/N ratio 30 produced the highest methane percentage at 65.9% on day 40.

**Acknowledgements** The author would like to acknowledge the in-kind contribution from Dindings Poultry Sdn. Bhd. and Wan Sang Sawmill Enterprise as well as Universiti Teknologi PETRONAS for the research grant (YUTP 015LC0-198).

## References

1. D. o. S. Malaysia (2017) Economic Census 2016—Livestock. Available [https://www.dosm.gov.my/v1/index.php?r=column/cthemByCat&cat=405&bul\\_id=bEkvWDRrSWw4OGtVTduamVmWVN5UT09&menu\\_id=Z0VTZGU1UHBT1VJMF1paXRRR0xpdz09](https://www.dosm.gov.my/v1/index.php?r=column/cthemByCat&cat=405&bul_id=bEkvWDRrSWw4OGtVTduamVmWVN5UT09&menu_id=Z0VTZGU1UHBT1VJMF1paXRRR0xpdz09)
2. Wang X, Yang G, Feng Y, Ren G, Han X (2012) Optimizing feeding composition and carbon–nitrogen ratios for improved methane yield during anaerobic co-digestion of dairy, chicken manure and wheat straw. *Biores Tech* 120:78–83
3. Thu CTT, Cuong PH, Hang LT, Chao NV, Anh LX, Trach NX et al (2012) Manure management practices on biogas and non-biogas pig farms in developing countries—using livestock farms in Vietnam as an example. *J Cleaner Prod* 27:64–71
4. Singh G, Shamsuddin M, Aqsha R, Lim SW (2018) Characterization of chicken manure from Manjung Region. *IOP conference series: materials science and engineering*, vol 458, p 012084, 2018/12/24 2018
5. Bujoczek G, Oleszkiewicz J, Sparling R, Cenkowski S (2000) High solid anaerobic digestion of chicken manure. *J Agric Eng Res* 76:51–60
6. Sreekrishnan TR, Kohli S, Rana V (2004) Enhancement of biogas production from solid substrates using different techniques—a review. *Biores Tech* 95(1):1–10
7. Bolan NS, Szogi A, Chuasavathi T, Seshadri B, Rothrock M, Panneerselvam P (2010) Uses and management of poultry litter. *World's Poultry Sci J* 66:673–698
8. Wang X, Lu X, Li F, Yang G (2014) Effects of temperature and carbon–nitrogen (C/N) ratio on the performance of anaerobic co-digestion of dairy manure, chicken manure and rice straw: focusing on ammonia inhibition. *PLoS ONE* 9:e97265
9. Abouelenien F, Namba Y, Kosseva MR, Nishio N, Nakashimada Y (2014) Enhancement of methane production from co-digestion of chicken manure with agricultural wastes. *Biores Technol* 159:80–87
10. Weerayuttil P, Khoyun U, Khuanmar K (2016) Optimum ratio of chicken manure and napier grass in single stage anaerobic co-digestion. *Energy Proc* 100:22–25
11. Román P, Martínez M, Pantoja A (2015) Farmer's compost handbook, experiences in Latin America. FAO, Santiago
12. Eghball B (1997) Composting manure and other organic residues. Available <http://ianrwww.unl.edu/pubs/wastemgt/g1315.htm>
13. Galler WS, Davey CB (1971) High rate poultry manure composting with sawdust. *Livestock Waste Manag Pollut Abatement Proc*

14. Briefs E (2002) Methane (Biogas) from anaerobic digesters. office of energy efficiency and renewable energy. US Department of Energy
15. Kleyböcker A, Liebrich M, Kasina M, Kraume M, Wittmaier M, Würdemann H (2012) Comparison of different procedures to stabilize biogas formation after process failure in a thermophilic waste digestion system: influence of aggregate formation on process stability. *Waste Manag* 32:1122–1130
16. Danlami Yavini T (2014) comparative study of mesophilic biogas production potentials of selected agro-wastes. In: Yavini TD, Taura UH, Mohammed N, Namo JM 3
17. Yenigün O, Demirel B (2013) Ammonia inhibition in anaerobic digestion: a review. *Process Biochem* 48:901–911
18. Ghyselbrecht K, Monballiu A, Somers M, Sigurnjak I, Meers E, Appels L et al (2017) The fate of nitrite and nitrate during anaerobic digestion. *Environ Tech* 40:1–38
19. Weiland P (2010) Biogas production: current state and perspectives. *Appl Microbiol Biotechnol* 85:849–860
20. Li Y, Zhang R, Chen C, Liu G, He Y, Liu X (2013) Biogas production from co-digestion of corn stover and chicken manure under anaerobic wet, hemi-solid, and solid state conditions. *Bioresour Tech* 149:406–412
21. Ye J, Li D, Sun Y, Wang G, Yuan Z, Zhen F et al (2013) Improved biogas production from rice straw by co-digestion with kitchen waste and pig manure. *Waste Manag* 33:2653–2658
22. Horisawa S, Sunagawa M, Tamai Y, Matsuoka Y, Miura T, Terazawa M (1999) Biodegradation of nonlignocellulosic substances II: physical and chemical properties of sawdust before and after use as artificial soil. *J Wood Sci* 45:492–497
23. Lynch J (1993) Substrate availability in the production of composts. In *Science and engineering of composting: design, environmental, microbiological and utilization aspects*, ed: Renaissance Publications Ohio, pp 24–35
24. Ladisch M, Lin K, Voloch M, Tsao GT (1983) Process considerations in the enzymatic hydrolysis of biomass. *Enzyme Microbial Tech* 5:82–102
25. Zheng Y, Zhao J, Xu F, Li Y (2014) Pretreatment of lignocellulosic biomass for enhanced biogas production. *Prog Energy Combust Sci* 42:35–53
26. Yang L, Xu F, Ge X, Li Y (2015) Challenges and strategies for solid-state anaerobic digestion of lignocellulosic biomass. *Renew Sustain Energy Rev* 44:824–834
27. Richard T The effect of lignin on biodegradability. Cornell composting, Cornell Waste Management Institute, In <http://www.cfe.cornell.edu/compost/calc/lignin.html>, 996
28. Zumalla A, Sumardiono S (2018) Utilization of delignified sawdust as raw material of biogas production. in *MATEC Web of Conferences*, p 03054

# Temperature Distribution Investigation During Friction Stir Welding (FSW) Using Smoothed-Particle Hydrodynamics (SPH)



Bahman Meyghani, Mokhtar Awang, Chuan Song Wu, and S. Emamian

**Abstract** Fundamentally, heat is needed during friction stir welding (FSW) for joining materials together. This heat is mainly produced by the friction force which is a part of the force that is applied to the tool. Many researchers have tried to use finite element modelling for investigating the thermal and the material flow behaviour; however, the process large plastic deformation causes mesh distortion. To illustrate, the excessive mesh distortion should be considered as one of the key problems happening during the modelling of the process. In this paper, the thermo-mechanical behaviour of FSW is investigated using finite element modelling. The smoothed-particle hydrodynamics (SPH) method is used to solve the mesh distortion problem. The outcomes indicated that the temperature of the welding is around 524 °C that is less than the welding material melting point. Finally, the outcomes are matched with some scientific papers which this issue confirms the accuracy of the simulated model.

**Keywords** Friction stir welding (FSW) · Friction force · Finite element modelling · Large plastic deformation · Mesh distortion · Thermomechanical behaviour · Smoothed-particle hydrodynamics (SPH) · Material melting point

---

B. Meyghani · C. S. Wu

Institute of Materials Joining, Shandong University, 17923, Jingshi Road, Jinan 250061, China

M. Awang (✉)

Department of Mechanical Engineering, Faculty of Engineering, Universiti Teknologi PETRONAS (UTP), Bandar Seri Iskandar, 32610 Perak Darul Ridzuan, Malaysia  
e-mail: [mokhtar\\_awang@utp.edu.my](mailto:mokhtar_awang@utp.edu.my)

S. Emamian

Center of Advance Manufacturing and Material Processing (AMMP), Department of Mechanical Engineering, Faculty of Engineering, University of Malaya, Kuala Lumpur, Malaysia

## 1 Introduction

There is a growing necessity to reduce construction weight, especially for the aircraft panels and aerospace industries. Advanced welding techniques have a significant role in manufacturing of these lightweight structures. Friction stir welding (FSW) is a unique and relatively new solid-state welding method which was invented and patented in the last decades [1]. FSW was developed in the automotive industry as an alternative method for the welding of aluminium sheets in 2001 [2]. Nowadays, FSW can be used to join a variety of materials without the use of filler materials and the process currently is using in a lot of manufacturing applications, like railway, marine, land transportation, and aerospace [3–6]. As can be seen in Fig. 1, through this welding method, a rotational cylindrical tool (consists of a shoulder and a pin) plunges into the workpiece and then moves along the welding seam [7–9]. Some of key benefits of FSW are the removal of the solidification cracking, liquation cracking, and porosity, which results in better mechanical properties of the join [10–12]. Thus, FSW and similar processes like friction stir spot welding (FSSW) and friction drilling have been studied by a considerable amount of studies [13–16]. On the other hand, FSW is a complicated procedure, because the process involves highly nonlinear (coupled) physical phenomenon, such as severe plastic deformation, the complex flow of the material, the complicated interactions behaviour between the tool and the workpiece, and the complex thermomechanical behaviour [17–19]. These multiple parameters highly affect the joint quality and efficiency.

In the meantime, without finite element modelling, FSW can only be studied in experiments which is time consuming and expensive [13]. To illustrate, the application of finite element modelling is increasing in academic and industrial applications.

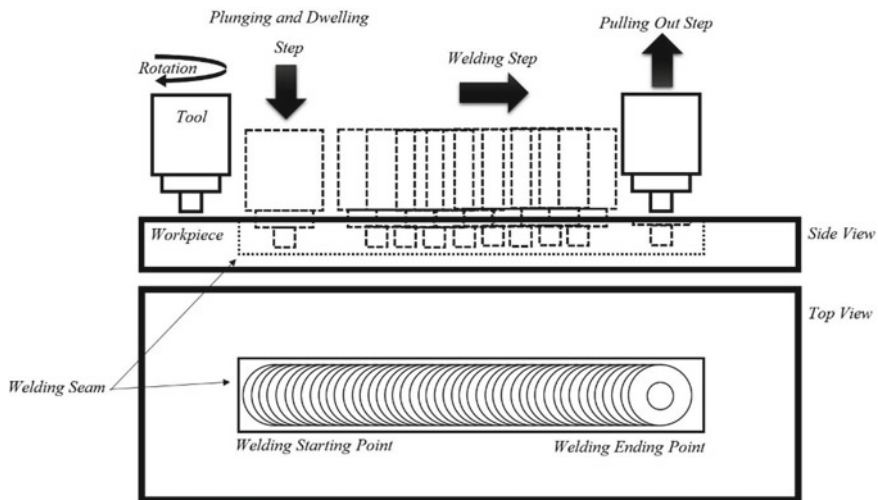


**Fig. 1** The stages of the friction stir welding (FSW)

Thus, many researchers studied the FSW process by using finite element methods (FEMs) [20–24]. However, the welding process has a very complicated deformation behaviour; therefore, the investigation of the FSW process such as predicting the temperature and the evaluation of the material behaviour during the weld is still challenging [25]. It should be mentioned that, by providing an effective way for analysing the joints formation and the behaviour of the weld in an appropriate finite element method, large plastic deformations and complicated governing equations can be solved [26, 27].

Basically, FEM is a technique in which approximate solutions of complex equations can be solved by using boundary conditions, because the calculation of variations in the FEM minimises the error and produces a stable condition [28, 29]. To illustrate, in the FEM, many tiny straight lines will produce a larger circle, because the method uses various simple elements for connecting all of the small subdomains (named finite elements) in order to find estimated shape over a larger domain [30]. In the meantime, modelling of the FSW is a very complicated process that involves complex thermomechanical behaviour and a highly nonlinear plastic deformation [31]. As an illustration, some nonlinear behaviours are extremely severe plastic deformations near the pin (in the stirring zone) and the heat transfer mechanics during the welding. Consequently, by using FEMs, the material behaviour and the thermal history during different process parameters and different tool geometries can be investigated. Some numerical models are claimed that FEMs are able to investigate significant features of the process [32, 33].

One of the most significant facts in modelling of the FSW process is the choice of the computational method (mesh technique). Many researchers have chosen different methods like the Lagrangian, the Eulerian, the Arbitrary Lagrangian–Eulerian (ALE), etc. [34–36]. Two contact conditions were used to investigate the heat generation which compared the classical and the modified Coulomb law [37]. The results showed that the temperature and the friction force are controlled by the contact pressure. Lagrangian and Eulerian methods have been used to investigate the FSW thermal properties using two important parameters in the contact condition including the friction coefficient and the slip rate. Several studies [38–40] have reported to estimate the temperature and the material flow during the process by measuring the tool torque and the axial pressure [41, 42]. It should be noted in some of the abovementioned literature, ALE technique in full sticking, full sliding or partial sliding/sticking conditions have been used. Lagrangian formulation in a full sliding condition was employed in some studies, but the pin depth was neglected [29, 43] and the contact geometry was not realistic. Moreover, by using a machine power input, different mesh techniques have been used in a study [44] in which a uniform shear stress in the tool work-piece surface was assumed. Meanwhile, in order to discover the mechanical and the thermal behaviours of FSW, a thermal model was proposed in a full sliding contact condition [45]. In addition, some past researchers [46, 47] were measured the plastic deformation in order to investigate the contact behaviour using computational fluid dynamics (CFD) method. Lagrangian method in full sliding and full sticking was

considered in a study [48], but unfortunately, both models were uncoupled due to the complexity of the process, while Gerlish et al. [49] and Schmidt et al. [50] showed that the contact condition has a partial sliding/sticking condition.

Although, the abovementioned papers used different mesh methods; however, in the Lagrangian technique, the material cannot flow between the elements. Additionally, the Eulerian method requires a very refine mesh and this issue increases the computational costs. ALE method also has some problems like the path-dependent behaviour plasticity modelling. To illustrate, for solving the treatment of the constitutive equation, the relationship between the mesh and the material should be calculated at each step.

Unlike other methods that are based on the mesh (connectivity between the simulation domain nodes), smoothed-particle hydrodynamics (SPH) is another technique in the numerical analysis that is based on the intermodal interaction. This issue makes this method as a mesh-free method. It should be mentioned that, in this method, the assignment of mass, kinetic energy, and other standard extensive properties is done to individual nodes and not to the elements of the mesh. Therefore, this method can be used to solve simulated models with more time that need to be computed resulting in more effort for the simulation. Consequently, SPH is a mesh-free method for simulating the large plastic deformation processes like the solid mechanics and the fluid flow problems. It should be noted that, compared to other mentioned methods, the resolution and the accuracy of SPH method are higher.

Based on the discussion above, in this paper, in order to increase the accuracy and the development of the modelling of the FSW process, SPH method is proposed to resolve the governing equations and investigate the thermomechanical behaviour.

## 2 Material and Methodology

Aluminium 6061-T6 was selected to be the workpiece material. During FSW, the interface temperature reaches up to 60–80% of the base material melting point [51, 52]. The simulation results are done in ABAQUS<sup>®</sup> software and SPH method is used for the mesh modelling technique. In this technique, three parts need to be defined including the die (rigid body with an almost thin thickness), the workpiece, and the tool. One among the earliest mesh-free techniques is smoothed-particle hydrodynamics (SPH) which considers the data points as a physical particle including mass and density, moving with time and possessing worth. It is a method that can be used to compute and simulate solid mechanics, fluid flows, and other continuum media mechanics. In 1977, Gingold, Monaghan, and Lucy built this technique to initially solve issues in astrophysics and now have been employed in research of ballistics, volcanoes, oceans, and astrophysics. SPH is a mesh-free Lagrangian technique, and in this method, the adjustment of the resolution can be done accurately with some variables like the density. Due to its advantages over the conventional mesh-based techniques, the use of SPH for modelling fluid motions is increasing. First of all, in SPH method, the particles are a self-representation of mass, and this issue guarantees



the conservation of the mass without additional computing. Moreover, computations in SPH are not based on resolving equations of linear systems, and they are based on the determination of the pressure from weighted contributions of the neighbouring particles. Furthermore, as the particles and the space are represented as the dense (water) and light (air) fluid, respectively, a free surface for the interaction of two-phase fluids is created by SPH, whereas the mesh-based techniques are in need to track the boundaries of the fluid. These reasons enable SPH to do a real-time simulation for fluid motions. However, in both mesh-based and non-mesh-based methods, a free surface geometry which can be rendered by making the use of polygonization technique like metal balls and marching cubes, point splatting or “carpet” visualisation needs to be generated. It should be noted that, to render a gas column density for gas dynamics, the kernel function can be considered as an appropriate method. The disadvantage of the mesh-based techniques is the need for a huge quantity of particles for simulating a similar resolution that can be done by using other methods. Basically, in this method, the water volumes will be filled with many particles that will never be rendered during the implementation of other methods. Nonetheless, the mesh-free technique can provide higher accuracy, in specific to the ones that are coupled with particle methods (such as particle level sets), as enforcing the incompressibility condition is easier in this systems. Thus, in this paper, SPH is selected as the mesh modelling technique. As can be seen in Fig. 2, 28,357 nodes and 23,832 elements have been created and C3D8R-type element is used for the element type in the workpiece. Dynamic explicit step type including the adiabatic definition is employed to extract the temperature results.

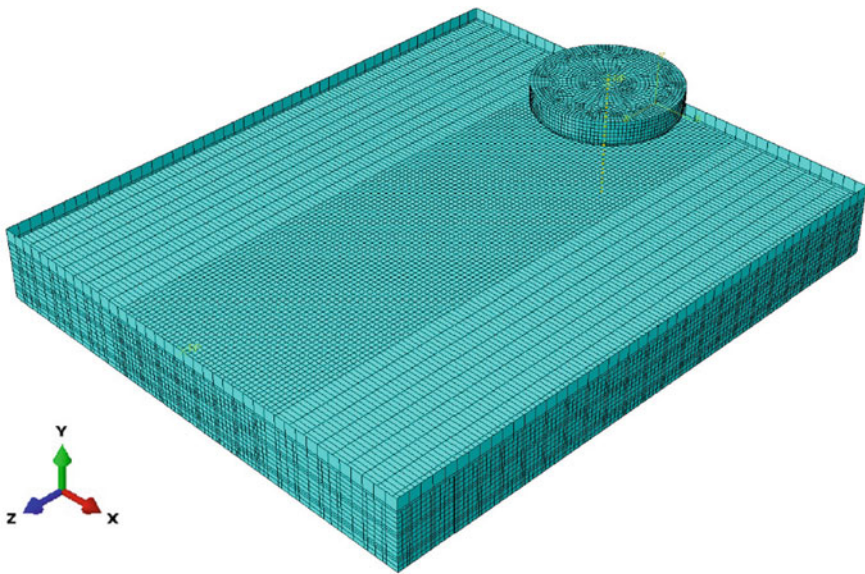


**Fig. 2** The considerations of the mesh for the tool and the plate



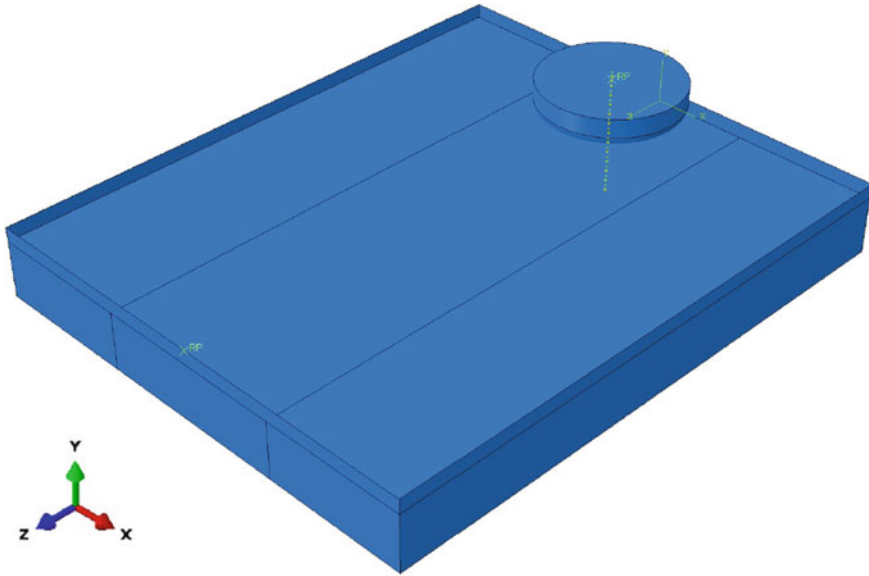


**Fig. 3** The parts for the tool and the workpiece

Shoulder diameter is set to be 30 mm and the pin diameter of 4 mm is considered. The workpiece has dimensions of  $120 \times 100 \times 12$  mm. It should be mentioned that the plate and the tool are also shown in Fig. 3. Moreover, temperature-dependent friction coefficient and material properties have been employed in the model [7]. The rotational velocity is 900 RPM and the transverse velocity is 100 mm/min and the room temperature of 25 °C is defined for the initial temperature.

The contact interfaces contain a pair of interactions is defined for the interactions between the workpiece and the frame. It should be noted that there are two different surfaces in the interaction part including the master and the slave surfaces. In this regard, this “balanced master–slave” arrangement is significant for getting more uniform pressure of the contact in the welding surfaces and also avoiding the hourglass effects [53]. The abovementioned complicated contact behaviour causes the large plastic deformation during the process which this issue results in the mesh distortion problem. In this research, in order to avoid mesh distortion problem, the frame is defined as the master surface, because its material is harder in comparison with the workpiece and the nodes of the workpiece are defined as the slave surface [54].

### 3 Results and Discussion

Figure 4 demonstrates the isometric view of the welding temperature of the process with the tool and Fig. 5 shows the isometric view of the welding temperature of the process without the tool. As can be seen, Fig. 4 illustrates that the welding peak temperature (524 °C) is between 60 and 80% of the melting point of the base material

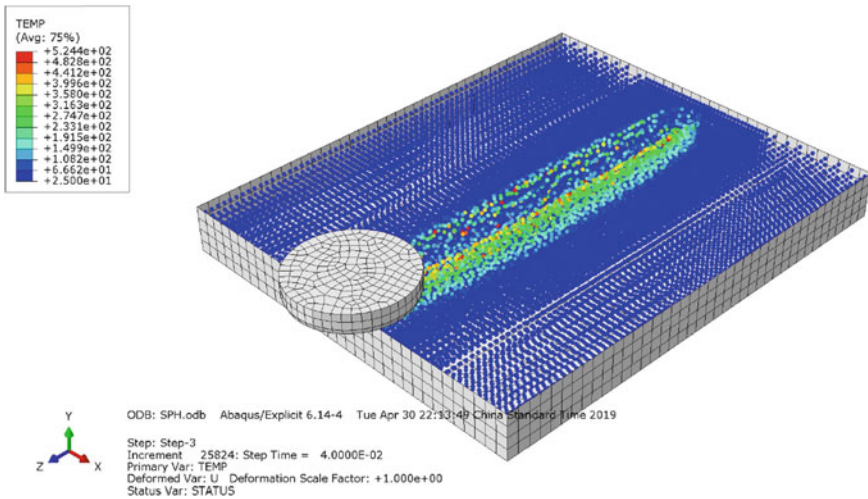


Fig. 4 The temperature distribution at the welding with tool

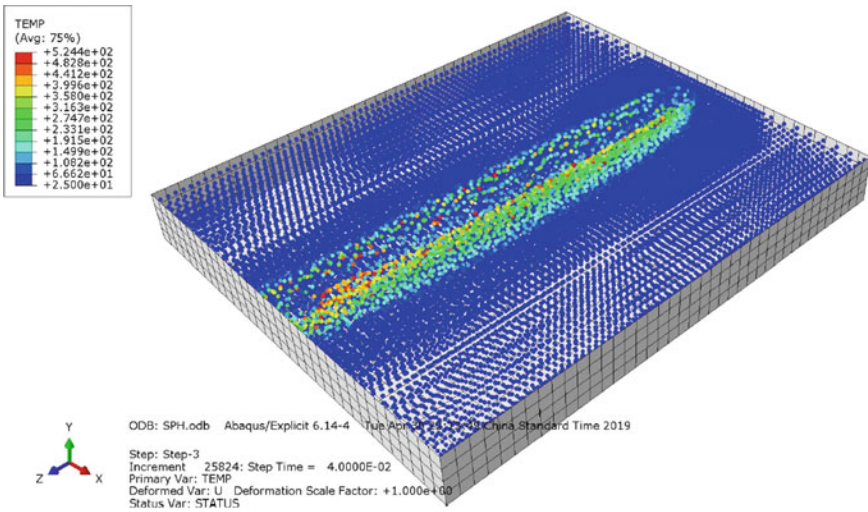
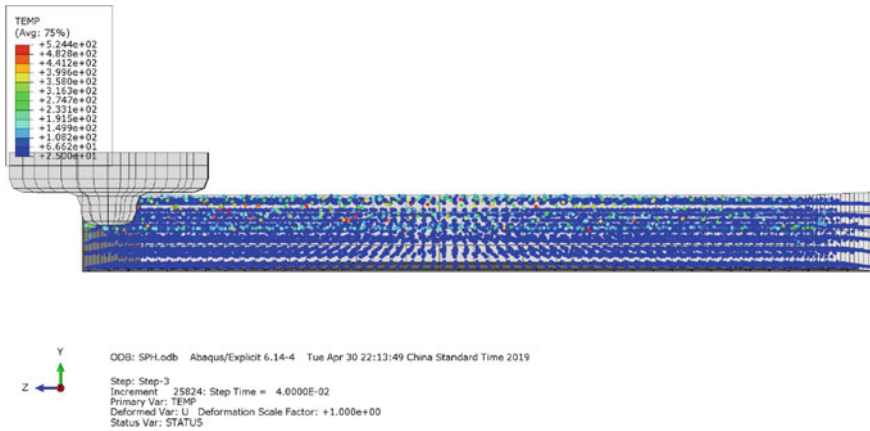


Fig. 5 The distribution of the temperature at the workpiece when the tool is removed



**Fig. 6** The temperature distribution at the horizontal viewpoint of the welding

[51]. From Fig. 5, it is observed that the maximum temperature is around 358 °C (2 mm far from the welding centre line). Furthermore, it can be seen that the welding temperature is higher below the shoulder compared to other parts. This is because more friction force is produced in the welding shoulder as the larger geometry will produce higher levels of friction. It should be noted that these findings are in line with what has reported in previous studies [7, 29].

Figure 6 shows the longitudinal view of the field distribution of the temperature along the joint line after the welding step. It could be seen that for generating the heat, the workpiece was penetrated by the rotating tool pin and then the tool shoulder touches the workpiece. As can be seen in Fig. 7, after moving the tool, the heat source started to move across the welding seam. Figure 7 also shows that the heat source and the material deformation at the upper surface of the workpiece are larger due to the higher friction force, higher deformation, and higher welding temperature produced by shoulder at this surface. This issue shows that the effect of the shoulder in generating of the heat is more than the pin, because the geometry of the contact area plays a significant role in producing the friction force which is one of the key sources of the heat generation during the process.

The cross-sectional view of the workpiece is shown in Fig. 8 that illustrates the workpiece temperature distribution, the material deformation, and the penetration of the tool at the end of the plunging step. It needs to be mentioned that some other advantages of the SPH method are its capability to make prediction about the stresses and strains during the simulation. Consequently, this has garnered the interest of scholars to investigate the stresses and strains to predict the plasticization of the workpiece and the tolerance of the failure during the FSW process. Scholars also advocated that examining the aforementioned parameters can help forecast any surface defects during the process including the formation of the flash. It is observed that the temperature and the material deformation at the welding advancing side are higher compared to the retreating side.

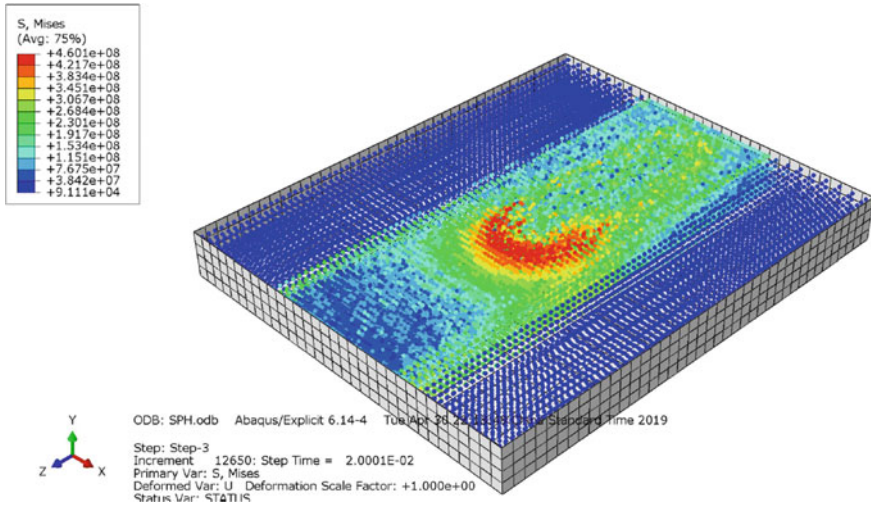


Fig. 7 The distribution of the temperature below the shoulder at the middle of the welding step

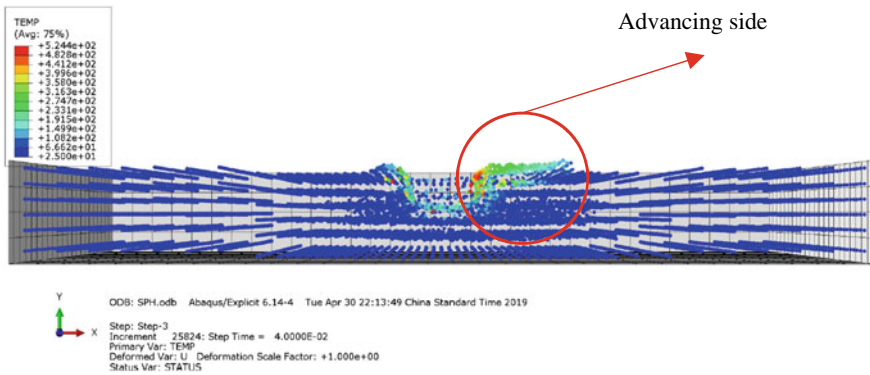
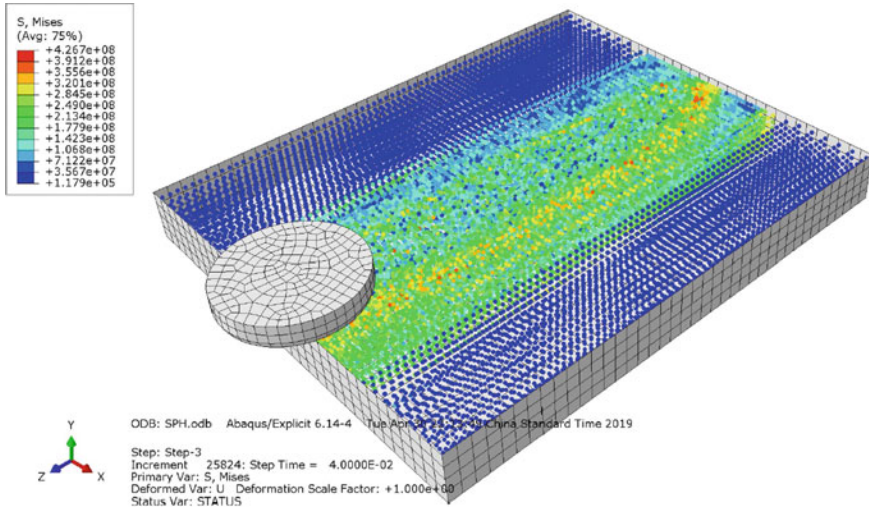


Fig. 8 The temperature distribution at the cross section of the welding (without tool)

Basically, thermal and mechanical loading which is produced by translating the rotating tool generates the structural stress in the interface of the tool and the work-piece. Moreover, the rigid element is in contact with the SPH workpiece particles maintains the continuity of the stress transfer between the workpiece and the FSW tool. Figure 9 illustrates the three-dimensional results of the effective stress at the end of the welding step which can be used to examine the effect of the plunge depth on the stress that is recorded during FSW. As expected, the stress field distribution smoothly decreased when the distance from the weld line becomes larger. This finding is in line with other studies and observations that focused on the welding joint line [24, 55–57]. It can be observed that the tool shoulder and the pin shoulder interface areas show the maximum equivalent plastic damages. Because of this issue, the maximum



**Fig. 9** The stress distribution at the welding workpiece during the process

stress is found inside the welding zone. In this light, for further investigations of the process in the future, observing the variations of the temperature distribution, the stresses, and the equivalent plastic strain with the changes in the process parameters will be recommended.

## 4 Conclusions

The results of the model indicate that compared to the welding retreating side, the temperature profile below the shoulder is asymmetrical and the welding advancing side shows a higher temperature. The study also found a gap for the values of the temperature in the stirring zone between the upper and the lower welding workpiece surfaces. Subsequently, the gap is reduced as it moves further from the weld centre. The peak temperature of the stirring zone was observed to be like a quasi-steady phenomenon, while the quasi-steady phenomenon gradually disappears as the heat source moves further across the welding seam. Like the temperature values, the welding stress is observed to be higher in the welding advancing side. Finally, the results showed a good agreement with the published papers.

**Acknowledgements** The authors would like to acknowledge the fellowship of the government of China, Shandong University from the International Postdoctoral Exchange Programme and the Universiti Teknologi PETRONAS (UTP), Malaysia, for the financial support from YUTP-FRG grant cost centre 0153AA-H18. Moreover, the authors would like to thank Professor Wallace Kaufman for his endless support.

## References

1. Wu C, Su H, Shi L (2017) Numerical simulation of heat generation, heat transfer and material flow in friction stir welding. *Acta Metall Sin* 54(2):265–277
2. Hancock R (2004) Friction welding of aluminum cuts energy costs by 99%. *WELDING JOURNAL-NEW YORK*- 83:40–43
3. Zhang H-W, Zhang Z, Jun B, Lei Z, Chen J-T (2006) Effect of viscosity on material behavior in friction stir welding process. *Trans Nonferrous Metals Soc China* 16:1045–1052
4. Meyghani B, Awang M (2019) A novel tool path strategy for modelling complicated perpendicular curved movements. *Key Eng Mater* 796:164–174
5. Meyghani B, Awang M, Emamian S, Akinlabi E (2018) A comparison between temperature dependent and constant Young's modulus values in investigating the effect of the process parameters on thermal behaviour during friction stir welding: Vergleich zwischen den temperaturabhängigen und konstanten Elastizitätsmodulwerten in der Untersuchung der Prozessparameter auf die Wärmewirkung beim Rührreibschweißen. *Materialwiss Werkstofftech* 49:427–434
6. Meyghani B, Wu C (2020) Progress in thermomechanical analysis of friction stir welding. *Chin J Mech Engi* 33:12
7. Meyghani B, Awang M, Emamian S, Khalid NM (2017) Developing a finite element model for thermal analysis of friction stir welding by calculating temperature dependent friction coefficient. In: 2nd international conference on mechanical, manufacturing and process plant engineering, pp 107–126
8. Meyghani B, Awang MB (2018) Prediction of the temperature distribution during friction stir welding (FSW) with a complex curved welding seam: application in the automotive industry. *MATEC Web Conf* 225:01001
9. Padhy G, Wu C, Gao S (2015) Auxiliary energy assisted friction stir welding—status review. *Sci Technol Weld Joining* 20:631–649
10. Kumar S, Wu C (2017) Review: Mg and its alloy—scope, future perspectives and recent advancements in welding and processing. *J Harbin Inst Technol (New Ed)* 24:1–37
11. Fu B, Qin G, Li F, Meng X, Zhang J, Wu C (2015) Friction stir welding process of dissimilar metals of 6061-T6 aluminum alloy to AZ31B magnesium alloy. *J Mater Process Technol* 218:38–47
12. Dialami N, Chiumenti M, Cervera M, de Saracibar CA (2017) Challenges in thermo-mechanical analysis of friction stir welding processes. *Arch Comput Methods Eng* 24:189–225
13. He X, Gu F, Ball A (2014) A review of numerical analysis of friction stir welding. *Prog Mater Sci* 65:1–66
14. Meyghani B, Awang MB, Emamian SS, Mohd Nor MKB, Pedapati SR (2017) A comparison of different finite element methods in the thermal analysis of friction stir welding (FSW). *Metals* 7:450
15. Wu C, Ma N, Guo Y, Hu W, Takada K, Okada H et al (2018) A dynamic ductile failure analysis of shell structures using a nonlocal XFEM method with experimental validation. *Adv Eng Softw* 123:1–12
16. Pan X, Wu C, Hu W, Wu Y (2019) A momentum-consistent stabilization algorithm for Lagrangian particle methods in the thermo-mechanical friction drilling analysis. *Comput Mech* 64:1–20
17. Emamian S, Awang M, Hussai P, Meyghani B, Zafar A (2016) Influences of tool pin profile on the friction stir welding of AA6061. *ARNP J Eng Appl Sci* 11:12258–12261
18. Sun Z, Wu C, Kumar S (2018) Determination of heat generation by correlating the interfacial friction stress with temperature in friction stir welding. *J Manuf Process* 31:801–811
19. Wu C, Zhang W, Lei S, Chen M (2012) Visualization and simulation of plastic material flow in friction stir welding of 2024 aluminium alloy plates. *Trans Nonfer Metals Soc China* 22:1445–1451
20. Su H, Wu CS, Bachmann M, Rethmeier M (2015) Numerical modeling for the effect of pin profiles on thermal and material flow characteristics in friction stir welding. *Mater Des* 77:114–125

21. Zhao Y-H, Lin S-B, Qu F-X, Wu L (2006) Influence of pin geometry on material flow in friction stir welding process. *Mater Sci Technol* 22:45–50
22. Dialami N, Chiumenti M, Cervera M, de Saracibar CA, Ponthot JP, Bussetta P (2014) Numerical simulation and visualization of material flow in friction stir welding via particle tracing. In: *Numerical simulations of coupled problems in engineering*, Springer, pp 157–169
23. Dialami N, Chiumenti M, Cervera M, Segatori A, Osikowicz W (2017) Enhanced friction model for friction stir welding (FSW) analysis: simulation and experimental validation. *Int J Mech Sci* 133:555–567
24. Dialami N, Cervera M, Chiumenti M, de Saracibar CA (2017) Local–global strategy for the prediction of residual stresses in FSW processes. *Int J Adv Manuf Technol* 88:3099–3111
25. Meyghani B, Awang M, Emamian S (2017) A mathematical formulation for calculating temperature dependent friction coefficient values: application in friction stir welding (FSW). *Defect Diff Forum* 379:73–82
26. He XC (2013) Numerical studies on friction stir welding of lightweight materials. *Adv Mater Res* 743:118–122
27. Meyghani B, Awang M, Emamian S (2016) A comparative study of finite element analysis for friction stir welding application. *ARPN J Eng Appl Sci* 11:12984–12989
28. Meyghani B, Awang M, Emamian S, Plank B, Heinzl C, Siow K (2019) Stress analysis of nano porous material using computed tomography images. *Materialwiss Werkstofftech* 50:234–239
29. Meyghani B, Awang M (2019) A comparison between the flat and the curved friction stir welding (FSW) thermomechanical behaviour. *Arch Comput Methods Eng* 27:1–14
30. Dialami N, Cervera M, Chiumenti M (2019) Effect of the tool tilt angle on the heat generation and the material flow in friction stir welding. *Metals* 9:28
31. Yang CL, Wu CS, Lv XQ (2018) Numerical analysis of mass transfer and material mixing in friction stir welding of aluminum/magnesium alloys. *J Manuf Process* 32:380–394
32. Neto DM, Neto P (2013) Numerical modeling of friction stir welding process: a literature review. *Int J Adv Manuf Technol* 65:115–126
33. Tutum CC, Hattel JH (2011) Numerical optimisation of friction stir welding: review of future challenges. *Sci Technol Weld Joining* 16:318–324
34. Schmidt H, Hattel J (2004) A local model for the thermomechanical conditions in friction stir welding. *Modell Simul Mater Sci Eng* 13:77
35. Zhang Z, Zhang H (2008) A fully coupled thermo-mechanical model of friction stir welding. *Int J Adv Manuf Technol* 37:279–293
36. Zhang Z, Liu Y, Chen J (2009) Effect of shoulder size on the temperature rise and the material deformation in friction stir welding. *Int J Adv Manuf Technol* 45:889–895
37. Zhang Z (2008) Comparison of two contact models in the simulation of friction stir welding process. *J Mater Sci* 43:5867–5877
38. Chao YJ, Qi X, Tang W (2003) Heat transfer in friction stir welding—experimental and numerical studies. *J Manuf Sci Eng* 125:138–145
39. Chen C, Kovacevic R (2003) Finite element modeling of friction stir welding—thermal and thermomechanical analysis. *Int J Mach Tools Manuf* 43:1319–1326
40. Song M, Kovacevic R (2003) Thermal modeling of friction stir welding in a moving coordinate system and its validation. *Int J Mach Tools Manuf* 43:605–615
41. Colligan KJ, Mishra RS (2008) A conceptual model for the process variables related to heat generation in friction stir welding of aluminum. *Scripta Mater* 58:327–331
42. Kumar K, Kalyan C, Kailas SV, Srivatsan TS (2009) An investigation of friction during friction stir welding of metallic materials. *Mater Manuf Processes* 24:438–445
43. Song M, Kovacevic R (2003) Numerical and experimental study of the heat transfer process in friction stir welding. *Proc Instit Mech Eng Part B: J Eng Manuf* 217:73–85
44. Khandkar M, Khan JA, Reynolds AP (2003) Prediction of temperature distribution and thermal history during friction stir welding: input torque based model. *Sci Technol Weld Joining* 8:165–174
45. Hamilton C, Sommers A, Dymek S (2009) A thermal model of friction stir welding applied to Sc-modified Al–Zn–Mg–Cu alloy extrusions. *Int J Mach Tools Manuf* 49:230–238



46. Ulysse P (2002) Three-dimensional modeling of the friction stir-welding process. *Int J Mach Tools Manuf* 42:1549–1557
47. Colegrove P, Shercliff H (2006) CFD modelling of friction stir welding of thick plate 7449 aluminium alloy. *Sci Technol Weld Joining* 11:429–441
48. Heurtier P, Jones M, Desrayaud C, Driver JH, Montheillet F, Allehaux D (2006) Mechanical and thermal modelling of friction stir welding. *J Mater Process Technol* 171:348–357
49. Gerlich A, Yamamoto M, North T (2007) Strain rates and grain growth in Al 5754 and Al 6061 friction stir spot welds. *Metall Mater Trans A* 38:1291–1302
50. Schmidt HNB, Dickerson T, Hattel JH (2006) Material flow in butt friction stir welds in AA2024-T3. *Acta Mater* 54:1199–1209
51. Tang W, Guo X, McClure J, Murr L, Nunes A (1998) Heat input and temperature distribution in friction stir welding. *J Mater Process Manuf Sci* 7:163–172
52. B. Meyghani (2018) Thermomechanical analysis of friction stir welding (FSW) on curved plates by adapting calculated temperature dependent properties. *Universiti Teknologi PETRONAS*
53. Emamian S, Awang M, Yusof F, Hussain P, Meyghani B, Zafar A (2018) The effect of pin profiles and process parameters on temperature and tensile strength in friction stir welding of AL6061 alloy. In: *The advances in joining technology*, Springer, pp 15–37
54. Meyghani B, Awang M, Emamian S, Nor MKBM (2019) Thermal modelling of friction stir welding (FSW) using calculated Young's Modulus values. In: *The advances in joining technology*, Springer, pp 1–13
55. Meyghani B, Awang M, Emamian S, Nor MKBM (2018) Thermal modelling of friction stir welding (FSW) using calculated Young's Modulus values.: *The advances in joining technology*, Springer, pp 1–13
56. Meyghani B, Awang MB, Poshteh RGM, Momeni M, Kakooei S, Hamdi Z (2019) The effect of friction coefficient in thermal analysis of friction stir welding (FSW). In: *IOP conference series: materials science and engineering*, p 012102
57. Meyghani B, Awang MB, Momeni M, Rynkovskaya M (2019) Development of a finite element model for thermal analysis of friction stir welding (FSW). In: *IOP conference series: materials science and engineering*, p 012101



# Correction to: *Advances in Manufacturing Engineering*



Seyed Sattar Emamian, Mokhtar Awang, and Farazila Yusof

## Correction to:

S. S. Emamian et al. (eds.), *Advances in Manufacturing Engineering*, Lecture Notes in Mechanical Engineering, <https://doi.org/10.1007/978-981-15-5753-8>

The original version of the chapter “Performance Evaluation on the Smartness of Malaysian Timber” has been revised. “Acknowledgement” section included.

And

The original version of the chapter “A Review of Recent Developments in Mechanical Properties of Polymer–Clay Nanocomposites” has been revised. In the Introduction section last two paras has been removed.

The correction chapters and the book have been updated with changes.

---

The updated version of these chapters can be found at  
[https://doi.org/10.1007/978-981-15-5753-8\\_11](https://doi.org/10.1007/978-981-15-5753-8_11)  
[https://doi.org/10.1007/978-981-15-5753-8\\_13](https://doi.org/10.1007/978-981-15-5753-8_13)

© Springer Nature Singapore Pte Ltd. 2021  
S. S. Emamian et al. (eds.), *Advances in Manufacturing Engineering*, Lecture Notes in Mechanical Engineering, [https://doi.org/10.1007/978-981-15-5753-8\\_71](https://doi.org/10.1007/978-981-15-5753-8_71)

C1